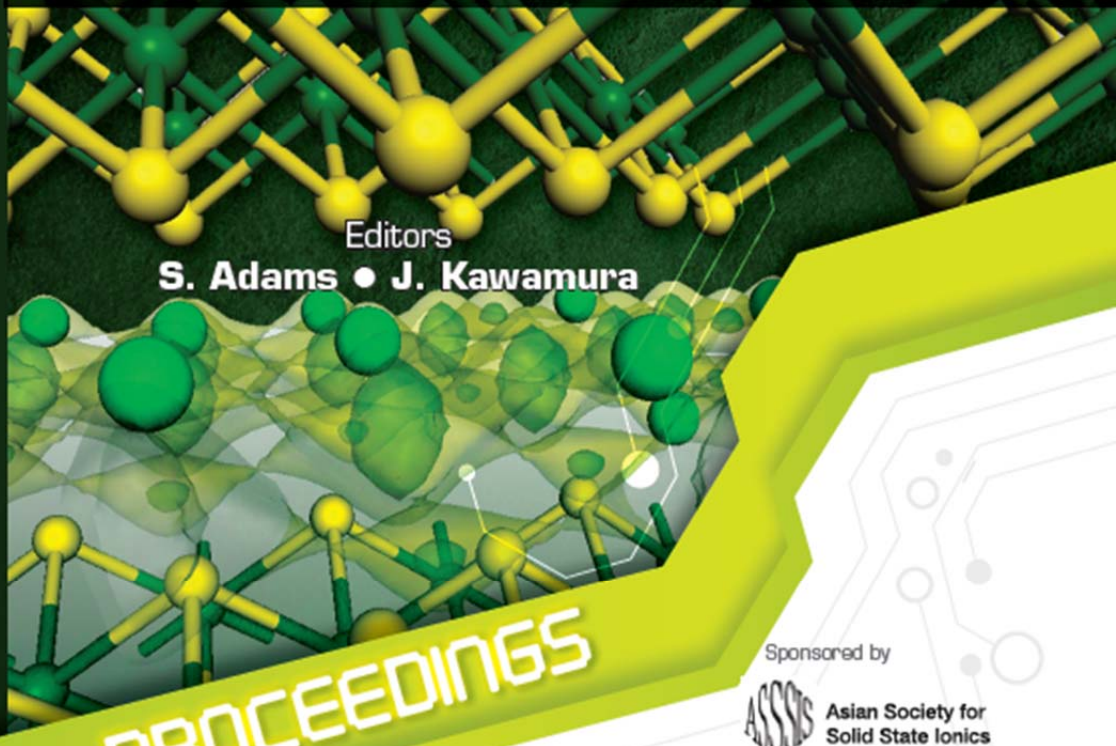
14th Asian Conference on

SOLID STATE IONICS

Solid State Ionics from Lab to Fab

24th to 27th, June 2014 | UTown, NUS, Singapore



Editors

S. Adams • J. Kawamura

PROCEEDINGS

Sponsored by

Asian Society for Solid State Ionics

National Research Foundation
Prime Minister's Office
Singapore
Research . Innovation . Enterprise

Organised by

NUS National University of Singapore

ITS SCIENCE & MEDICAL

RESEARCH PUBLISHING

14th Asian Conference on Solid State Ionics

Editors: S. Adams • J. Kawamura

Proceedings of the
14th Asian Conference on Solid State Ionics (ACSSI 2014)

Proceedings of the 14th Asian Conference on Solid State Ionics (ACSSI 2014)

Editors

S. Adams
J. Kawamura

RESEARCH PUBLISHING

Published by

Research Publishing
Blk 12 Lorong Bakar Batu, #02-11 Singapore.

India Office: New No: 61/1 First Cross Street, CIT Nagar, Chennai 600035.
e-mail: editorial@rpsonline.com.sg

Proceedings of the 14th Asian Conference on Solid State Ionics (ACSSI 2014)

Editors: S. Adams and J. Kawamura

Copyright © 2014 ACSSI 2014 Organisers. All rights reserved.

This book, or parts thereof, may not be reproduced in any form or by any means, electronic or mechanical, including photocopying, recording or any information storage and retrieval system now known or to be invented, without written permission from the Publisher.

All the papers in this volume have been peer-reviewed. However, the editors assume no responsibility for the accuracy, completeness or usefulness of the information provided in this proceedings. No responsibility is assumed by the publisher or editors for any use or operation of any methods, products, instructions or ideas contained in the materials presented.

ISBN-13: 978-981-09-1137-9
ISBN-10: 981-09-1137-8

Design, Typeset & Printed by iTEK CMS Web Solutions. e-mail:enquiries@itekcms.com

Printed in Singapore.

Contents

Welcome Message xviii

Committee xix

Abstracts for Plenary Sessions

Application of NMR and MRI for Lithium Ion Battery xx
Junichi Kawamura, Yoshiki Iwai, Reiji Takekawa, Nithya Hellar and Naoaki Kuwata

Lithium Superionic Conductor and its Application to all Solid-State Battery xxi
Ryoji Kanno

What is Special About Solid Ionic Conductors? xxii
Werner Weppner

Reversible Solid Oxide Fuel Cells Based on Chemically Stable Proton Conductorss xxiii
Enrico Traversa

Electrode Materials I

Enabling Lithium Metal Borate Cathodes: Synthetic and Electrochemical Insights 3
Prabeer Barpanda, Yasunobu Yamashita and Atsuo Yamada

Transport Properties of Layered Lithium Nickel Manganese Oxide ($LiNi_{0.5}Mn_{0.5}O_2$) Cathode Material for Lithium Ion Batteries 13
P. Senthil Kumar, A. Sakunthala, M. Prabu and M. V. Reddy

Batteries I

Solid Ceramic Electrolytes for Lithium Sulphur Rechargeable Batteries 25
R. Prasada Rao, D. Safanama, M. H. Chen, M. V. Reddy and S. Adams

Perfomances of TiO_2 as Cathode Material in Rechargeble Mg Batteries with Polyethylene Oxide Based Gel Electrolyte 32
H. N. M. Sarangika, W. A. R. B. Weerasekera, G. K. R. Senadeera, M. A. K. L. Dissanayake, K. V. L. Amarasinghe, H. K. D. W. M. N. R. Divaratne and V. A. Seneviratne

The Effect of Annealing Temperature on Morphology, Structure and Electrochemical Performance of Spinel - $LiMn_2O_4$ 41
Teguh Yulius Surya Panca Putra, Evvy Kartini, Deswita, Masao Yonemura, Shuki Torii, Toru Ishigaki and Takashi Kamiyama

Proceedings of the 14th Asian Conferenceon Solid State Ionics (ACSSI2014)
Copyright © 2014 Research Publishing.
ISBN: 978-981-09-1137-9

Polymer Electrolytes I

Optimization of Iodide Ion Conductivity in Electrolytes for Dye Sensitized Solar Cells 53
M. A. K. Lakshman Dissanayake

Fabrication of Lithium Polymer Battery Based on PVA: PVP: Li X ($X=ClO_4^-$, NO_3^-) Polymer lend Electrolyte 63
N. Rajeswari, S. Selvasekarapandian, S. Asath Bahadur, J. Kawamura and S. R. S. Prabaharan

Experimental Studies on Blend Based Polymer Gel Electrolyte Containing Nanofiller (PVA: PVK): $CHCOO_3NH_4$:EC:SiO_2 System 72
R. P. Kumhar, Neelesh Rai and S. L. Agrawal

Fundamentals I

Comparative AB Initio Study of Lithium Storage in Amorphous and Crystalline TiO_2 85
Fleur Legrain, Oleksandr Malyi and Sergei Manzhos

Elastic Constants of Ionic Conductors: A Theoretical Study 93
Haruhitosadakuni and Masaru Aniya

Electrode Materials II

Synthesis and Electrochemical Properties of Molybdenum Dioxide/Graphene Nanomaterial 103
Xue Yang, Yang Li, Yueli Liu, Wen Chen and Yanyuan Qi

VC-$LiNO_3$: A Hybrid Additive in Carbonic Ester Electrolytes for SEI Formation on Lithium Metal Electrode 111
Jing Guo, Zhaoyin Wen, Meifen Wu and Yu Liu

Electrochemical Impedance Spectroscopy Analysis of V_2O_5 Nanowires Electrode as Lithium-Ion Batteries 118
Zhaolong Li, Shanshan Jiang, Quanyao Zhu, Shengnan Huang, Chunxia Zhao, Wen Chen and Galina S. Zakharova

Solid Electrolytes II

All-Solid-State Lithium Batteries Using Li_6PS_5Br Solid Electrolyte 127
Chen Maohua, Rayavarapu Prasada Rao and Stefan Adams

Temperature — Dependent Dielectric and Electrical Characteristics of Undoped and Samarium Doped $SrBi_2Ta_2O_9$ Ferroelectric Ceramics 135
B. Rajesh Kannan and B. Harihara Venkataraman

A Model for the Non-Arrhenius Ionic Conductivity of Solid Electrolytes 142
Yohei Okada, Sahara, Masahiro Ikeda and Masaru Aniya

Diffusion Coefficient Measurement of Lithium Ion in β-Alumina Single Crystal by Pulsed Field Gradient NMR Spectroscopy 150
Mohammed Tareque Chowdhury, Reiji Takekawa, Yoshiki Iwai, Naoaki Kuwata and Junichi Kawamura

Solid Electrolytes III

Synthesis and Characterization of New Solid Electrolyte Layer $(Li_2O)_2(P_2O_5)_Y$ 163
Evvy Kartini, Wagiyo Honggowiranto, Supardi, Heri Jodi, Azis K. Jahya and Wahyudianingsih

Polymer Electrolytes II

Polyvinyl Alcohol Gel Polymer Electolyte Based Dye Sensitized Solar Cells 177
M. A. Careem, M. H. Buraidah, M. F. Aziz, H. C. Hassan and A. K. Arof

Electrical Characterization of Tetrabutylammonium Iodide Based Polymer Free Gel Electrolyte 187
E. M. T. K. Ekanayaka, V. A. Senavirathne, L. R. A. K. Bandara, K. V. L. Amarasinghe, C. A. Thotawaththage, J. M. K. W. Kumari and M. A. K. L. Dissanayake

Electrical, Structural, Optical and Thermal Properties of (1-X)Blend:XLi[$(CF_3SO_2)_2$N] Solid Polymer Electrolyte System 197
Ravindra Kumar Gupta and Hee-Woo Rhee

Poster Session

Enhancement of Dielectric Constant in $LaFeO_3NiFe_2O_4$ Composites 205
V. M. Gaikwad and S. A. Acharya

Influence of Aliovalent Dopants on the Structure and Defects of Ceria Under Fuel Cell Operating Temperature 215
S. A. Acharya and V. M. Gaikwad

Ionization Condition Scaled with Molecular Cooperativity in Ionic Liquids – Lithium Salt Mixtures 225
Masahiro Ikeda and Masaru Aniya

PGSE NMR Studies on Room Temperature Ionic Liquids C_N MIM TFSI 235
Arunkumar Dorai, Reiji Takekawa, Nithya Hellar, Naoaki Kuwata and Junichi Kawamura

Polyvinylidene Fluoride and Cobalt Based Nanocomposites Exhibiting High Dielectric Constant 244
K. Vasundhara, B. P. Mandal and A. K. Tyagi

A New Style Field Effect Transistor Based on Ionic-Electronic Conductor Composite Nanostructures 253
Guowei Zhang, Zhanmin Dong, Jinquan Wei, Jia-Lin Sun and Jia-Lin Zhu

Electrochemical Studies of 'Exfoliated Graphene Oxide-MoO_2' Composite Synthesized by Novel Graphenothermal Reduction 259
Shaikshavali Petnikota, Keefe Wayne Teo, Luo Chen, M. V. Reddy, Sandeep Kumar Marka, Vadali V. S. S. Srikanth, B. V. R. Chowdari

Development of Sri Lankan Natural Vein Graphite as Anode Material for Lithium-Ion Rechargeable Batteries 270
T. H. N. G. Amaraweera, N. W. B. Balasooriya, H. W. M. A. C. Wijayasinghe, A. N. B. Attanayaka, M. A. K. L. Dissanayake and B. -E. Mellander

Hierarchical Mesoporous Nanostructured $NiCo_2O_4$ Spinel: Facile Preparation and Application as Anodes for Rechargeable Sodium Batteries 278
Kun Rui, Yan Lu, Chen Shen and Zhaoyin Wen

Synthesis and Electrochemical Properties of Mesoporous Carbon Supported Well-Dispersed Cobalt Oxides Nanoparticles 288
Chunxia Zhao, Junshen Li, Wen Chen, Yunxia Yang, Ken Chiang and Nick Burke

Synthesis of EG-Ge Composite by Novel Graphenothermal Reduction and its Anodic Studies for Lithium Ion Batteries 297
Shaikshavali Petnikota, Sandeep Kumar Marka, M. V. Reddy, Vadali. V. S. S. Srikanth and B. V. R. Chowdari

Synthesis of Carbon-Encapsulated SnO_2 Nanoparticles as Anode Material with Superior Cyclability for Lithium Ion Batteries 307
Peng Peng, Zhaoyin Wen and Yu Liu

Li-Cycling Studies of MFe_2O_4(M=Ni,$Ni_{0.5}$&$Zn_{0.5}$) 316
M. V. Reddy, Chu Yao Quan, Keefe Wayne Teo, Lim Ji Ho, S. Adams and B. V. R. Chowdari

Li-Air Batteries with LAGP-Polymer Composite Membranes 327
Dorsasadat Safanama, Rayavarapu Prasada Rao and Stefan Adams

Synthesis and Characterization of $LiMnO_2$ Nanostructure at Various Temperatures 335
Wagiyo Honggowiranto, Evvy Kartini, Aziz Khan Jahja and Mardiyanto

Facile Synthesis of Electrospun Hierarchical $\alpha-Fe_2$-O_3-SiO_2 Binary Nanotubes for Libs 343
Y. Z. Wu, R. Murugan, M. V. Reddy, B. V. R. Chowdari and S. Ramakrishna

Methods of Preparation-Molten Salt and Mixed Hydroxides and Cathodic Studies on Layered-Structure Materials $Li(Ni_{13}Co_{13}Mn_{13})O_2$ for Li-Ion Batteries 355
M. V. Reddy, Nguyen Ngoc Minh Uyen, Toh Wei Qi, Wu Xiao Yue, S Adams and B. V.R. Chowdari

Improvement of Electrochemical Performance of Li_2MnO_3 Cathode Material by Bismuth Substitution 365
Wu Sha, Yu Zhiyong and Liu Hanxing

Li and Na Storage on TCNE: A Computational Study 374
Chen Ying Qian and Sergei Manzhos

Effects of Mesoporous Co_3O_4 on Electrochemical Properties of Lithium/Sulfur Battery 381
Guoqiang Ma, Zhaoyin Wen, Jun Jin, Peng Peng and Qingsong Wang

Preparation and Electrochemical studies of MnO_2 for Li-ion and Li-air batteries 391
Yun Hong Lee, M. V. Reddy and Stefan Adams

Development and Characterization of PVA: Cellobiose-NH_4NO_3 Polymer Membrane 401
Vinithra Gurunarayanan, S. Selvasekarapandian, Sindhuja Manoharan, D. Vinoth Pandi, C. Veeramanikandan and Arun Araichimani

Characetrization of PVA:Cellobiose – NH_4SCN Polymer Electrolyte 408
Sindhuja Manoharan, S. Selvasekarapandian, Vinithra Gurunarayanan, D. Vinoth Pandi, C. Veeramanikandan and Arun Araichimani

AC Conductivity Studies of PAN- NH_4Cl Polymer Electrolyte System 417
S. Sikkanthar, S. Karthikeyan, S. Selvasekarapandian, D. Vinoth Pandi, S. Nithya, C. Sanjeeviraja and G. Mani

Study of Bio-Degradable Polymer PCL with NH_4SCN 425
D. Vinoth Pandi, S. Selvasekarapandian, N. Vijaya and C. Sanjeeviraja

Bio-Polymer Pectin Based Proton Conducting Polymer Electrolyte 436
N. Vijaya, S. Selvasekarapandian, D. Vinoth Pandi, S. Sindhuja, A. Arun and S. Karthikeyan

Study of Natural Polymer Cellulose Acetatae with NH_4BF_4 446
S. Karthikeyan, S. Selvasekarapandian, D. Vinoth Pandi, N. Vijaya, Sindhuja Manoharan and Arun Araichimani

AC Conductivity, Vibrational and Structural Behaviour of Proton Conducting Gel Polymer Electrolyte based on Poly(Vinyl Alcohol) 456
K. P. Radha, S. Selvasekarapandian, D. Vinoth Pandi, S. Karthikeyan, M. Hema and C. Sanjeeviraja

Cellulose Acetatae Based Proton Conducting Polymer Electrolyte 467
S. Selvasekarapandian, N. Rubiya Evangelin, D. Vinoth Pandi, Arun Araichimani, N. Vijaya, Sindhuja Manoharan, S. Karthikeyan and T. Mathavan

Preparation and Characterization of PVA Complexed with Amino Acid, Arginine 477
R. Bhuvaneswari, S. Karthikeyan, S. Selvasekarapandian, D. Vinoth Pandi, N. Vijaya, Arun Araichimani and C. Sanjeeviraja

The Effect of Dopant Concentration on the Ionic Conductivity of Liquid PMMA Oligomer 488
Norashima Kamaluddin, Famiza Abdul Latif, Chan Chin Han, Ruhani Ibrahim, Sharil Fadli Mohamad Zamri and Fitrah Hadip

Electrical Properties of Rare Earth Salt Doped Irradiated MH-PPV 495
Famiza Abd Latif, Fitrah Bt Hadip and Kamariah Bt Muda

Electrical Properties of PPV Derivatives Synthesized via Microwave Irradiation Technique 503
Fitrah Bt Hadip, Famiza Bt Abd Latif and Kamariah Bt Muda

Structural, Impedance and Moisture Absorption Studies on Polymer Electrolytic Films Based on PVA and PAN 512
S. Siva Devi, S. Selvasekarapandian, C. Karthikeyan, F. Kingslin Mary Genova and N. Vijaya

Electrical Properties Investigation of Newly Synthesized Pema Ionogels Composite 522
Famiza Abd. Latif, Ruhani Ibrahim, Yusairie Mohd, Mohd Azri Ab Rani, Norashima Kamaluddin and Sharil Fadli Mohamad Zamri

Electrical and FT-IR Study of Fumed Silica Based Gel Electrolytes; $(Tetraglyme)_n KI$ and $(Ethylene\ Glycol)_n$ KI 528
K. V. L. Amarasinghe, V. A. Senaviratne, L. R. A. K. Bandara and M. A. K. L. Dissanayake

Investigations on Influence of Titania Content on the Properties of (PVdF-co-HFP) Based Polymer Electrolytes 538
P. Issac Nelson, P. Senthil Kumar, A. Sakunthala, M. Prabu, M. V. Reddy and K. Govindan

Investigations on Pure and Cu Doped Nanocrystalline LLTO for Lithium Ion Batteries 548
P. Christopher Selvin, K. P. Abhilash, B. Nalini and K. Somasundaram

Permeability Studies of Cellulose Acetate Doped with NH_4NO_3 and NH_4PF_6 560
T. Chidambaram, S. Selvasekarapandian, K. Govindan and Arun Araichimani

Studies on Blend Based Nanocomposite Polymer Gel Electrolyte: {(PVA:PEG):NH_4SCN:Al_2O_3} System 569
S. L. Agrawal and Neelesh Rai

Thin Film Solid Electrolyte of Garnet-Related $Li_7La_3Zr_2O_{12}$ by Tape Casting 578
Zhen Feng Yow, Wenyi Gu and Stefan Adams

Characterization of Lithium Borate and Lithium Silicate Thin-Films as a Solid Electrolyte for Thin-Film Battery 587
Haruka Itabashi, Naoaki Kuwata, Daichi Fujimoto, Yasutaka Matsuda and Junichi Kawamura

Towards Hydrolysis-Stable Thiophosphate Solid Electrolytes 595
Chen Haomin, Rayavarapu Prasada Rao and Stefan Adams

The Effect of Plasticizer Addition to Solid Polymer Electrolyte Based on Chitosan Monmorillonite Nanocomposite 606
Evi Yulianti and Sudaryanto

Fuel Cell Materials I

Designing Mixed Conducting Anodes for Solid Oxide Fuel Cells (SOFCs) 619
Wang Hay Kan, Behzad Mirfakhraei, Kalpana Singh, Hala T. Handal and Venkataraman Thangadurai

Fuel Cell Materials II

Performance of IT-SOFC Using Novel Nanostructured: $DY_{1-X}BA_XSR_{0.5}CO_{0.8}FE_{0.2}O_{3-\delta}$(DBSCF) and DBSCF-Doped Ceria Composite as Cathode 631
S. A. Acharya

Process for Mass Production and Characterization of Zirconates by an Optimized Solid-State Reaction Method 642
Jinduo Han, Zhaoyin Wen, Jingchao Zhang, Xiaowei Chi, Heng Liu and Guoqiang Ma

Synthesis and Characterization of $La_{0.6}Sr_{0.4}Co_{0.2}Fe_{0.8}O_{3-\alpha}$ Compound Prepared by an Activated Carbon-Assisted SOL Gel Method 651
Ismariza Ismail, Nafisah Osman and Abdul Mutalib Md Jani

Batteries II

Novel Li-Ion Capacitor Having an Ultrahigh Specific Capacity Comparable to that of Li-Ion Battery 661
Tsutomu Takamura, Kyouichi Sekine and Fuminori Mouri

Fundamentals II

Non-Debye Electrical Relaxation Processes and Understanding of Dynamical Conductivity in Ion Conducting Solids 667
G. Govindaraj

Study of Structural Phase Transition and Dielectric Behavior of $BiNaTiO_3$-$SrTiO_3$ (BNT-ST) Solid Solution 677
S. K. Sayyed and S. A. Acharya

Study of Morphology, Dielectric and Magnetic Behaviour of Lead Iron Niobate (PFN) With Sintering AIDSPbO-B_2O_3 Glass 685
T. Quazi and Kamal Singh

Abstracts

Cathode Materials for High Energy and Power LiIon Batteries 695
Jaephil Cho

Solid State Thin Film Batteries with 5V Class Cathode Materials 696
Naoaki Kuwata, Shota Kudo, Daichi Fujimoto Yasutaka Matsuda and Junichi Kawamura

Synthesis of Nonstoichiometric $LixCoO_2$(X>1) for All SolidState Lithium Ion Batteries using Li_2S-P_2S_5 Glass Ceramics 697
Sungwoo Noh, Junghoon Kim, Minjeong Kim and Dongwook Shin

Electrochemical Kinetics of $Li_3V_2(PO_4)_3$ Cathode by Parametric Impedance Spectroscopy Combined with GITT 698
Eui-Chol Shin, Jing Su, Yu- Guo Guo, Jaekook Kim and Jong Sook Lee

Key Points and Materials Design for Rechargeable Lithium Sulfur Battery 699
Zhaoyin Wen, Jun Jin, Guoqiang Ma and Xiangwei Wu

Cathode Interface Structures in Solid-State Lithium Batteries with Sulfide Solid Electrolytes 700
Kazunori Takada

Preparation and Cathodic Studies on α1-$LiVOPO_4$ and $LiVO(HPO_4)(C_2O_4)_{0.5}$ 701
M. V. Reddy, A. Shahul Hameed, J. J. Vittal and B. V. R. Chowdari

NCL behaviour and Ion Transport Property in Ion Conducting Polymers 702
Awalendra K. Thakur

Dynamic Heterogeneity in Organic Ionic Plastic Crystals 703
Fangfang Chen and Maria Forsyth

Relaxation Behavior in Clay Reinforced Polymer Nanocomposites 704
A. L. Sharma and Awalendra K. Thakur

Probing Interfaces in Lithium Ion Conductors at the Atomic Level 705
Craig Fisher Akihide Kuwabara, Hiroki Moriwake Xiang Gao, Shijian Zheng, Saiful Islam, Hideki Oki, Keiichi Kohama and Yuichi Ikuhara

In Situ Diffraction: Simultaneously Characterising Crystal Structure and Electrochemistry in Fully Functioning Batteries 706
Neeraj Sharma

New Insights Into Novel Solid Electrolyte Materials from Magnetic Resonance Experiments 707
Luke O'Dell, Daniel Gunzelmann, Yogita Oza, Cameron Pope, Haijin Zhu, Konstantin Romanenko and Maria Forsyth

Ionic and Electronic Transport in Composite Electrodes for Lithium Batteries: In-Situ Dielectric Spectroscopy Study from Low Frequencies to Microwaves 708
Jean Claude Badot, Kalid Ahmed, Seid Olivier Dubrunfaut, Patrick Soudan and Bernard Lestriez

Electrode Materials for Li/Na Ion Batteries 709
Boddu Venkata Rami Reddy, Raman Ravikumar, Chandrashekaran Nithya and Sukumaran Gopukumar

Development of $Li_2FeP_2O_7$ Cathode Glass GlassCeramic and Polycrystalline Systems for Lithium Ion Batteries 710
Hariharan K

Systematic Binder Design in High Capacity Silicon Anodes of Lithium Ion Batteries 711
Jang Wook Choi, You Kyeong Jeong, Tae-Woo Kwon and Ali Coskun

Development of Long Length MWCNTS/ SnO_2Nanocomposites with Increasing Capacity as Free Standing Anode for Li Ion Batteries 712
Indu Elizabetha, Bhanu. P. Singh, S. Gopakumar and R B Mathur

Low Cost Synthesis Method and Characterization of $Li_2FeP_2O_7$/C as Cathode Material for Lithium Ion Battery 713
Zheng Zhenning, Liu Hanxing, Li Wenji and Yu Zhiyong

Motion of Host Atoms in Some Cathodes in Li-Ion Batteries during Lithium Extraction and Insertion 714
Yinchun Lyu, Xiqian Yu, Rui Wang Kyung Wan Nam, Ruijuan Xiao, Lin Gu, Hong Li, Xiao- Qing Yang and Liquan Chen

Developing Solid Electrolytes for All-Solid-State Battery 715
Byoungwoo Kang

14 Years of Development in Garnet-Type Solid-State Li Ion Electrolytes and Future Trends 716
Venkataraman Thangadurai

Effect of Li^{+}Content on Lithium Ion Conductivity of Lithium Garnets 717
S Ramakumar and Ramaswamy Murugan

Metastable Lithium Iron Phosphate Under Two Phase Electrochemical Reaction Between $LiFePO_4$ and $FePO_4$ 718
Yuki Orikasa, Yukinori Koyama, Takashi Uyama, Katsutoshi Fukuda, Hajime Arai, Yoshiharu Uchimoto and Zempachi Ogumi

Impedance Spectroscopy for Beta-Alumina: Revisted and Settled 719
Jee Hoon Kim, Eui- Chol Shin, Dong Chun Cho, Sooseok Kim, Youngkoo Yoon, Keedeok Yang, Jinhyung Beom, Shu Yamaguchi, Jaekook Kim and Jong Sook Lee

Mixed Glass Former Effect in Mol% $50Li_2O50[xNb_2O_5\text{-}(1\text{-}x)P_2O_5]$ Glasses 720
Prashant Dabas and K Hariharan

Fast Proton Transport Mechanisms in the Triflic Acid Containing Guanidinium Triflate 721
Haijin Zhu, Usman Rana and Maria Forsyth

Preparation and Characterization of Novel Sulfobetaine based Polymer Electrolyte doped with NH_4PF_6 722
Manindra Kumar, Jagdish Kumar Chauhan, Madhavi Yadav and Neelam Srivastava

The Fabrication and Evaluation of Solid Oxide Fuel Cells Prepared by Spray Pyrolysis 723
Peter Hing, Montri Suklueng, Nyuk Yoong Voo and Lim Chee Ming

Enhancement of Ionic Conductivity of Dy-Doped Ceria: Role of Vacancy and Oxidation State 724
Smita Acharya and Shradha Joshi

Mixed Inorganic Salts Modified $CaZrO_3$ Based Proton Conductor with Improved Sinterability and Electrical Conductivity 725
Xiaowei Chi, Jingchao Zhang, Peng Peng, Zhaoyin Wen, Yu Liu and Jinduo Han

A New Approach to AC Analysis of Solid Electrolytes 726
Dong-Chun Cho, Jee-Hoon Kim, Young-Hun Kim, Gye-Rok Kim, Eui-Chol Shin and Jong-Sook Lee

Ion Dynamics in $Na_2NbXP_3O_{12}$ (X=Cu, Cd, Pb Zn) Glass with Unusual Complex Non-Debye Relaxation Function 727
N S. Krishna Kumar and G. Govindaraj

Hydration/Dehydration Kinetics in Protonic Ceramic Conductors: Moving Boundary Diffusion Problems 728
Gye-Rok Kim, Hyun-Ho Seo, Jung-Mo Jo, Eui-Chol Shin, Ji Haeng Yu and Jong Sook Lee

Three-Dimensionally Ordered Macroporous Cu_2O/Ni Inverse Opal Electrodes for Electrochemical Supercapacitors 729
Chien-Chia Wang

$Li(Ni_{1/3}Mn_{1/3}Co_{1/3-x}M_x)O_2$ M = Na, Mg, Ba and x = 0 - 0.33 as Potential Cathode Materials for Rechargeable Li-Ion Batteries 730
Gayani Amaraweera, Athula Wijayasinghe, Bengt-Erik Millander and M A. K. Lakshman Dissanayake

Kinetic Study of Reactions between $LiFePO_4/FePO_4$ and Redox Species 731
Qizhao Huang, James Jennings and Qing Wang

Al Doping Improves Si storage Energetics for Li, Na and Mg 732
Fleur Legrain, Oleksandr Malyi and Sergei Manzhos

DFT Study on Feasibility of Two Step Redox Process in Li Battery Electrodes 733
Shamik Chakrabarti, Awalendra K Thakur and Koushik Biswas

Nickel Substituted $LiCoO_2$ as Cathode Materials for All-Solid-State Lithium Secondary Batteries Using Li_2S- P_2S_5 Solid Electrolytes 734
Minjeong Kim, Junghoon Kim, Sungbo Hong and Dongwook Shin

High Performance Dye-Sensitized Solar Cells with PEO Based Gel Polymer Electrolyte Using TiO_2 Nano Fibers Developed by Electrospinning 735
H. N. M. Sarangika, G. K. R. Senadeera, H. K. D. W. M. N. R. Divaratne, P. M. P. C. Ekanayake, C. A. Thotawatthage and M. A. K. L. Dissanayake

Ion Dynamics in Nanocrystalline Graphene Wrapped $LiNiPO_4$ Composite 736
Rajesh Cheruku and G. Govindaraj

Synthesis and Electrochemical Characterization of Tin-Hollandites, $K_2(M_2Sn_6)O_{16}$ (M = In, Co) 737
M. V. Reddy, Tran Thuy Linh, Dang Thu Hien, Stefan Adams and B. V. R. Chowdari

Influence of Liquid Phase Sintering by ZnO-B_2O_3Glass on Sinterability of $Pb(Zr_{0.52}Ti_{0.48})O_3$ 738
Shradha Joshi and Smita Acharya

Studies on Nano-Gel Polymer Electrolyte Based EDLCs 739
Amrita Jain and S. K. Tripathi

Experimental Studies on Ionic Liquid Based Polymer Gel Electrolytes 740
S. K. Tripathi, Amrita Jain and Ashish Gupta

Synthesis and Impedance Analysis of Proton – Conducting Polymer Electrolyte Based on PAN: NH_4SCN 741
K Selvakumar, M Karthikeyan and Ramesh Prabhu

Structural and Electrical Characterisation of PVA:NH_4 SCN Nanocomposite Polymer Electrolyte Films 742
Niharika Kulshrestha and Prem Gupta

Cooling Rate Effects on Structure and Mobility of Garnetrelated Fast-ion Conductor $Li_7La_3Zr_2O_{12}$ 743
Wenyi Gu, Prasada Rao Rayavarapu and Stefan Adams

Electrical Evaluation of Chemical Gas Sensors Based on CuO Nanoflowers 744
Dang-Thanh Nguyen, Eui- Chol Shin, Duc Vuong Dang and Jong Sook Lee

Electrical Properties of Nanocrystalline Oxygen Deficient Barium Manganite 745
Namita Pandey and Awalendra Kumar Thakur

AC Conductivity Analysis and Dielectric Relaxation Behaviour of a Conducting Polymeric System Based on PMMA-$LiClO_4$ 746
Namrata Shukla, Awalendra K Thakur, Archana Shukla and Ratnamala Chatterjee

Oxygen Mobility and Lattice Dynamics in $Sr_2Fe_2O_5$and $Ca_2Fe_2O_5$ Brownmillerites 747
Sergey Danilkin, Chris Ling Josie Auckett and Gordon J Kearley

Novel Bi-functional Perovskite Catalyst for Oxygen Reduction and Evolution 748
Jae Il Jung and Jaephil Cho

Novel Cathodes for Solid Oxide Fuel Cells 749
Peter Hing, Montri Suklueng, Nyuk Yoong Voo and Lim Chee Ming

Novel Anode Catalytic Materials with Lithium-Ion Conducting Ability for Solid Oxide Fuel Cells with Improved Coking Resistance and Sulfur Tolerance 750
Wei Wang and Zongping Shao

The Effect of NiO and MgO on the Sinterability of Yttria Stabilized Zirconia and Gadolinium Doped Ceria 751
Peter Hing, Andrew Jung, Daniel Dodzi Setssoafia and Lim Chee Ming

Aqueous Lithium/Air Rechargeable Batteries with Protected Lithium Electrode 752
Nobuyuki Imanishi

Phase Diagram and Sodium Ordering in Sodium Layered Oxides 753
Marie Guignard, Christophe Didier, Benoit Mortemard de Boisse, Dany Carlier, Jacques Darriet and Claude Delmas

High-Voltage Sulphate Framework Cathode Materials for NaIon Batteries 754
Prabeer Barpanda, Gosuke Oyama, Shin-Ichi Nishimura, Sai-Cheong Chung, Chris D. Ling and Atsuo Yamada

Reversible Chemical Lithiation/Delithiation of Anatase TiO_2 for Redox Flow Lithiumion Batteries 755
Feng Pan, Qizhao Huang and Qing Wang

Application of Carbon Nanotube (CNT) Sheets as Current Collector of All-Solid-State Lithium Ion Batteries 756
Sunho Choi, Junghoon Kim, Chanhwi Park and Dongwook Shin

The 4^{th} Missing Passive Circuit Element - A Memristor 757
S R S Prabaharan

The Transformation of Conformers: A New Type of SolidSolid Phase Transition 758
Liyu Jin, Haijin Zhu, Kate Nairn, Jiaye Li, Jenny Pringle, Patrick Howlett and Maria Forsyth

Author Index 759

Welcome Message

The Asian Conference on Solid State Ionics provides a stage for the presentation and discussion of the latest advances in the Asia-Pacific region on solid state ionic materials, devices and related topics. It is the 14th meeting in this series and the first time that the conference returns home to Singapore, the place where it was founded in 1988.

Solid State Ionics is a growing inter-disciplinary branch of science and technology. Scientifically, it explores ionic motion and reactivity in a wide spectrum of functional materials covering inorganic ceramics, glasses, polymers, composites and nanoscale materials. At this conference we will particularly focus on the key role of ionic and mixed conductors in the design and optimisation of high performance devices.

In response to the urgent global need for intelligent solutions in energy conversion and storage ACSSI 2014 will highlight advances in high energy density batteries and fuel cells with high energy and power density as well as improved safety for key applications ranging from integrated solid state thin film devices via storage solutions for electric vehicles to the grid integration of renewable energy sources.

At the same time ACSSI 2014 will showcase progress of Solid State Ionics fruitful in a wider range of devices that rely ionic mobility in the solid state such as electrochromic displays, sensors and photoelectrochemical solar cells

Stefan ADAMS
Chairman
ACSSI 2014 Organization Committee

Proceedings of the 14th Asian Conferenceon Solid State Ionics (ACSSI2014)
Copyright © 2014 Research Publishing.
ISBN: 978-981-09-1137-9

International Advisory Committee

Stefan Adams, *National University of Singapore, Singapore*
B.V.R. Chowdari, *National University of Singapore, Singapore*
M.A.K.L. Dissanayake, *Institute of Fundamental Studies, Kandy, Sri Lanka*
Liu Hanxing, *Wuhan University & Technology, China*
Xuejie Huang, *Centre for Clean Energy, Institute of Physics, CAS, China*
Ryoji Kanno, *Tokyo Institute of Technology, Japan*
Evvy Kartini, *National Nuclear Energy Agency, Indonesia*
Junichi Kawamura, *Tohoku University, Japan*
Ajit Kulkarni, *Indian Institute of Technology Bombay, India*
Jong-Sook Lee, *Chonnam National University, Korea*
Junichiro Mizusaki, *Tohoku University, Japan*
S.R.S. Prabaharan, *VIT University, India*
S. Selvasekarapandian, *Karunya University, India*
V.A. Seneviratne, *University of Peradeniya, Sri Lanka*
A. K. Thakur, *IIT Patna, India*
Zhaoyin Wen, *Shanghai Institute of Ceramics, CAS, China*
Werner Weppner, *Kiel University, Germany*
Shu Yamaguchi, *The University of Tokyo, Japan*
Han-Ill Yoo, *Seoul National University, Korea*

Local Organizing Committee

Stefan ADAMS, *NUS Materials Science & Engineering (Chair)*
Daniel J. BLACKWOOD, *NUS Materials Science & Engineering (Treasurer)*
Palani BALAYA, *NUS Mechanical Engineering*
B.V.R. CHOWDARI, *NUS Physics*
Harry HOSTER, *TUM Create*
Jim-Yang LEE, *NUS Chemical and Biomolecular Engineering*
Poi See LEE, *NTU Materials Science*
Li LU, *NUS Mechanical Engineering*
Seeram RAMAKRISHNA, *NUS Mechanical Engineering*
Prasada Rao RAYAVARAPU, *NUS Materials Science & Engineering*
M.V. REDDY, *NUS Materials Science & Engineering*
Madhavi SRINIVASAN, *NTU Materials Science & Engineering*
Qing WANG, *NUS Materials Science & Engineering*

Conference Secretariat
Office of Professional Engineering
Executive Education, (OPE^3)
Faculty of Engineering
National University of Singapore,
Singapore 117578.
Tel : (65) 6516 5113; Fax : (65) 6874 5097
Email: acssi2014@nus.edu.sg
http://www.eng.nus.edu.sg/OPE3/

On-Line Web & Conference Management System
Ra. Sankaran
iTEK CMS Web Solutions
Blk 12 Lorong Bakar Batu, #02-11
Singapore 348745.
Tel: (65) 6492 1137, Fax: (65) 6748 2556
Email: sankaran@itekcms.com
www.itekcms.com

Abstracts for Plenary Sessions

Application of NMR and MRI for Lithium Ion Battery

Junichi Kawamura[a], Yoshiki Iwai, Reiji Takekawa, Nithya Hellar and Naoaki Kuwata
Tohoku University, Japan.
[a]kawajun@tagen.tohoku.ac.jp

ABSTRACT

Nuclear Magnetic Resonance (NMR) has been used as a powerful technique in Solid State Ionics field, which gives information of the local structure and the dynamics of ionic conductors [1]. In particular, recent advancement of pulse field gradient (pfg) technique enables us to obtain reliable diffusion coefficient values in liquids and solids [2]. Moreover, the pfg technique has opened the door of NMR micro-Imaging in the field of solid state ionics [3], which is the same technology as MRI (magnetic resonance imaging) used in medical diagnosis, although the space resolution is much higher. In this presentation, a tutorial lecture of these modern NMR/MRI techniques and its application to lithium ion battery is given[4]. Main topics are,

1. Principle of pfg-NMR
2. Diffusion data in electrolytes of LIB
3. Electrophoretic NMR
3. Principle of MRI
4. Example of MRI of LIB

Keywords: Nuclear Magnetic Resonance (NMR), Pulse Field Gradient (PFG), MRI (Magnetic Resonance Imaging).

References:
[1] "New aspects of NMR studies in solid electrolytes", D. Brinkmann, Solid State Ionics: *Science & Technology*, (ed. B.V.R. Chowdari *et al*., World Scientific Publ.Co., Singapore 1998) 93-102.
[2] Aihara, Yuichi, Kyoko Sugimoto, William S. Price, and Kikuko Hayamizu,J. Chem. Phys.,113,(2000)1981.
[3] Iwai, Yoshiki and Junichi Kawamura, *J. Physical Soci.Japan, Suppl.A*, 79,(2010)160-162.
[4] Miwa Murakami, Yoshiki Iwai, and Junichi Kawamura, "Nuclear Magnetic Resonance Study of Lithium-Ion Batteries.", (T.Osaka and Z.Ogumi Ed., Nanoscale Technology for Advanced Lithium Batteries, Springer, 2013, p. 143-166.

Lithium Superionic Conductor and its Application to all Solid-State Battery

Ryoji Kanno
Tokyo Institute of Technology, Japan.
kanno@echem.titech.ac.jp

ABSTRACT

All solid-state batteries are promising candidate for the future energy storage systems with high energy and power densities. To realize the all solid-state batteries, the most important issue to be solved is the materials for the solid electrolyte. Lithium superionic conductors promise the potential to replace organic liquid electrolytes and thereby improve safety of the next-generation high-energy batteries. The present paper reviews the materials of lithium superionic conductors and discuss the structure-property relationship, for example, in the Li10GeP2S12 (LGPS), which has high ionic conductivity of over 10^{-2} S cm^{-1} at room temperature and its value is comparable to that of liquid systems. The application of these materials to solid electrolyte of all-solid-state batteries is reviewed and the future issues to be solved the practical applications will be discussed.

Keywords: Lithium, Superionic conductor, All solid-state battery.

What is Special About Solid Ionic Conductors?

Werner Weppner
Institute of Materials Science, Christian-Albrechts University, Germany.
ww@tf.uni-kiel.de

ABSTRACT

Solids are considered to overcome potentially the presently existing limitations of lithium (ion) batteries. It is believed that simply the liquid electrolyte has to be replaced by a solid electrolyte. However, solids behave quite different in many regards from common liquid electrolytes and new approaches are necessary and extaordinarily challenging. The ionic conductivities of practically suitable solid electrolytes are commonly much lower than those of liquids and are inversely related to the electrochemical/thermodynamic stability. Further, crystalline solids show commonly large intergranular and contact resistances. But major progress has been achieved in recent years and new compounds have been identified with structural disorder in the lithium partial lattice, providing Li+ ion conductivities in the range of 10^{-3} S/cm at ambient temperature. Prominent representatives are oxides with garnet-type structures of the compositions $Li_5La_3M_2O_{12}$ (M=Nb, Ta) and $Li_7La_3Zr_2O_{12}$. While free electrons are commonly neglected in the case of liquid electrolytes, these play a major role in solid electrolytes. They have to equilibrate together with the ions across the interfaces between the electrolyte and electrodes. In the case of a 5 V battery, the electrons have to differ in concentration by 87 orders of magnitude. Nevertheless, electrons have to be minority charge carriers and equilibria have to be achieved even in the case of very low concentration. Furthermore, solid electrolytes have much shorter space charge regions in view of the much larger concentration of charge carriers compared to liquid electrolytes. These are in the range of atomic radii and may be strongly influenced by chemical reactions and segregation. While ionic conductors should have small ranges of stoichiometry in accordance with low electronic conductivities, electronically conducting electrodes should have wide ranges of non-stoichiometry. It is not expected that materials with such different properties exist in thermodynamic equilibrium. Furthermore, in order to provide both high energy and power densities, the requirements of fast diffusion and non-stoichiometry of electrodes are also contradictory. Materials development is accordingly the key issue in developing solid state ionic devices. With regard to the many conflicting requirements, there is one major advantage of solid materials. That is the tremendous versatility of the kinetic and thermodynamic properties of solids. Solids may behave kinetically similar to liquids and even gases and may have the highest chemical stability. Many features reported in this presentation are applicable to other solid state ionic devices, such as supercaps, fuel cells, thermoelectric converters, electrochromic devices and chemical sensors.

Keywords: Solid electrolyte, Electrochemical/thermodynamic stability, Liquid electrolytes.

Reversible Solid Oxide Fuel Cells Based on Chemically Stable Proton Conductors

Enrico Traversa

King Abdullah University of Science and Technology (KAUST), Thuwal, Saudi Arabia.

Enrico.Traversa@kaust.edu.sa

ABSTRACT

The development of alternative and renewable solar and photovoltaic power supply devices is attracting increasing attention for a sustainable future. However, solar power is intermittent and site-specific. Leverage of continuous energy supply needs to be achieved with the integration of energy storage systems in the grid. One possibility is the use of solid oxide electrolysis cells (SOECs), solid oxide fuel cells (SOFCs) operating in reverse, which are high temperature energy storage devices that convert heat and electrical power into chemical energy by producing hydrogen from steam. Hydrogen is attractive as energy carrier and as a clean fuel for a number of applications. Conventional SOECs use oxygen-ion conducting electrolytes, which possess several problems for practical applications, including the need of separating produced H_2 from unreacted H_2O, cell performance degradation due to the oxidation of hydrogen electrode, low current efficiency during the electrolysis process, etc. This talk will discuss the use of proton-conducting oxide electrolytes as an alternative that may solve some of the current issues; since water is formed at the air electrode, proton-conducting SOECs can produce dry H_2 and oxidation of Ni, commonly used for the hydrogen electrode, is prevented. Furthermore, the current efficiency of the cell is kept high by the water-rich environment, which facilitates proton formation depressing the formation of other charge carriers. The main problem of conventional proton-conducting electrolytes is their chemical stability in the presence of steam. The new and necessary direction for the research on proton-conducting SOECs will be discussed, which is the development of film electrolytes made of chemically stable proton-conducting oxides.

Electrode Materials I

ENABLING LITHIUM METAL BORATE CATHODES: SYNTHETIC AND ELECTROCHEMICAL INSIGHTS*

PRABEER BARPANDA

Faraday Materials Laboratory, Materials Research Centre, Indian Institute of Science, C.V. Raman Avenue, Bangalore, Karnataka 560012, India

YASUNOBU YAMASHITA

Department of Chemical System Engineering, The University of Tokyo, 7-3-1 Hongo, Bunkyo-ku, Tokyo, 113-8656, Japan

ATSUO YAMADA

Department of Chemical System Engineering, The University of Tokyo, 7-3-1 Hongo, Bunkyo-ku, Tokyo, 113-8656, Japan & Unit of Elements Strategy Initiative for Catalysts and Batteries, ESICB, Kyoto University, Kyoto 615-8510, Japan

Borate class of polyanionic insertion compounds ($LiMBO_3$) offers an alternative to design high capacity cathode materials with theoretical capacity exceeding 200 mAh/g. Though known for over a decade, it is difficult to extract Li^+ from borate compounds reversibly owing to their poor conductivity, material degradation and difficulty in synthesis. Here, with careful synthesis, materials handling and proper cathode optimization, we have enabled $LiFeBO_3$ cathode delivering a reversible capacity approaching 200 mAh/g with an Fe^{3+}/Fe^{2+} redox potential centered at 2.85 V (vs. Li/Li^+). This electrochemical activity in $LiFeBO_3$ can be realized by classical solid-state synthesis as well as solution combustion route. Moving on, we have enabled the electrochemical activity of $LiCoBO_3$ showing partial Li^+ extraction with a Co^{3+}/Co^{2+} redox potential located at 4 V (vs. Li/Li^+). The synthetic and electrochemical insights on these $LiMBO_3$ (M = Fe, Co) high-capacity cathodes are explained in this proceeding.

1. Introduction

Li-ion batteries have become ubiquitous in portable electronics segment and are fast becoming *numero uno* energy storage device for propelling the imminent (hybrid) electric vehicles revolution [1-3]. With its light weight and high-energy density, it offers commercially viable option for ever-growing electronics and automobiles markets of the 21st century. In addition to their electrochemical

* This work is supported by the Ministry of Education, Culture, Sports, Science and Technology, Japan (MEXT) under the 'Element Strategy Initiative for Catalysts & Batteries' (ESICB) and Japan Society for the Promotion of Sciences under the JSPS Postdoctoral Fellowship program.

Proceedings of the 14th Asian Conference on Solid State Ionics (ACSSI 2014)
Copyright © 2014 ACSSI 2014 Organizers. All rights reserved.
ISBN: 978-981-09-1137-9
doi:10.3850/978-981-09-1137-9_006

performance, the cost, safety and sustainability plays key role in real-life usages of Li-ion batteries. It has led to growing importance on Fe-based cathode materials owing to the abundance and economy associated with Fe precursors. In this pursuit, triphylite $LiFePO_4$ is the front-runner candidate that has already been commercialized [4]. Numerous other Fe-based polyanionic materials have been reported e.g. silicates (Li_2FeSiO_4), sulphate ($LiFe_{0.5}SO_4$), fluorophosphates (Li_2FePO_4F), pyrophosphates ($Li_2FeP_2O_7$) and fluorosulphates ($LiFeSO_4F$) etc [5-7]. These polyanionic compounds, owing to their weight penalty, invariably suffers from relatively lower capacity vis-à-vis the oxide cathodes. One way to maximize the net capacity is to utilize the lowest weight polyanion component (i.e. BO_3^{3-}) that can offer theoretical capacity exceeding 200 mAh/g.

Following the success story of $LiFePO_4$, the lithium metal borate ($LiMBO_3$; M = Fe, Mn, Co) family was first proposed by Legagneur *et al.* [8] in 2001. But, in the first article as well as all following reports for over a decade showed very poor electrochemical activity due to material instability and kinetic limitation of deintercalation process. Over the last few years, our groups effort has led to the success in realizing near theoretical electrochemical capacity in $LiFeBO_3$ [9-12], as a result of careful materials handling and proper cathode optimization. Also, we have demonstrated the first (de)insertion reaction in $LiCoBO_3$ at high voltage of 4 V [13]. The current proceedings briefly highlights some nuances of material synthesis and electrochemical characterization of borate family of cathodes.

2. Experimental Details

2.1. *Borate Materials Synthesis*

$LiFeBO_3$ was prepared by conventional solid-state reaction using Li_2CO_3, $FeC_2O_4.2H_2O$ and B_2O_3 precursors. An intimate precursor mixture was prepared by ball-milling with optional addition of carbon and was annealed at 600 °C for 12 h in a tubular furnace maintained in an Ar atmosphere. Alternately, $LiFeBO_3$ was synthesized by a two-step solution combustion method [14,15]: (i) low temperature heating (110-130 °C) of solution containing constituent precursors gradually forming an intermediate amorphous complex followed by (ii) high temperature (400-600 °C) annealing of intermediate complex to obtain the final $LiFeBO_3$ product. Using a stoichiometric amounts of various precursors (acting as oxidants) and citric acid (acting as fuel), gradual heating onsets an exothermic reaction leading to the formation of amorphous metal-nitrogen complex. The citric acid fuel plays multiple roles: (a) reducing Fe^{3+} to Fe^{2+} species, (b) acting as source of carbon to form carbon coating and (c) reacting with metal nitrates to

trigger exothermic combustion reaction. Various mixture of metal precursors and fuels can be used to form the final product. In some cases, the annealing at high-temperature can be limited to as short as 1 minute. As $LiFeBO_3$ is highly sensitive to moisture degradation (as discussed later), the as-synthesized $LiFeBO_3$ was immediately transferred inside an Ar-filled glove box.

$LiCoBO_3$ was prepared by a two-step solid-state process: (i) annealing a stoichiometric mixture of CoC_2O_4 and B_2O_3 at 800 °C for 6 h (in air) to obtain intermediate $Co_2B_2O_5$ pyroborate compound and (ii) annealing a mixture of Li_2CO_3 and $Co_2B_2O_5$ at 300-600 °C for 6 h (in Ar).

2.2. *Borate Materials Characterization*

X-ray diffraction of polycrystalline $LiMBO_3$ (M = Fe, Co) powder was acquired by a Bruker AXS D8 ADVANCE powder diffractometer operating at 35 mA/ 40 kV, equipped with a Co source (λ_1= 1.78897 Å) and a linear Vantec-1 position sensitive detector. Typical scan were collected in the 2θ range of 10-80° with a step size of 0.028°/sec. Full pattern matching and Rietveld refinement were conducted with TOPAS-Academic software. ^{57}Fe Mössbauer spectra were acquired on powder sample by a Topologic spectrometer equipped with a ^{57}Co(Rh) source. The Mossbauer spectra were analyzed with MossWinn 3.0 software to determine the isomer shift (δ) and quadrupole splitting (ΔE_q) values. Scanning electron microscopy on powder sample was conducted with a Hitachi S-4800 SEM unit operating at 5 kV under low vacuum. Transmission electron microscopy was performed using a JEOL JEM-2100 unit operating at 200 kV.

2.3. *Electrochemical Characterization*

For galvanostatic study, a slurry of active material ($LiMBO_3$), Ketjen carbon black and polyvinylidene fluoride (PVdF) (in 80:20:10 weight ratio) was prepared in minimal amount of N-methylpyrrolidone (NMP) medium. The slurry was cast on Al-current collector film. Post drying at 120 °C under vacuum to remove NMP, circular disks were punched out to be used as cathode in test cells. Typical cathode loading in these disks were ~5 mg/cm^2.

Standard 2023 type coin cells were prepared inside an Ar-filled glove box. The cathode disk was used as working electrode along with Li-metal foil as counter/ reference electrode separated by two sheets of polypropylene film separator. The separator was soaked with 1M $LiPF_6$ dissolved in 3/7 v/v mixture of ethylene carbonate- diethyl carbonate (EC-DEC) acting as electrolyte. These cells were tested at C/20 rate (1 Li in 20 h) (at 25 °C) with a TOSCAT-3100 battery tester (Toyo system) using the CC-CV mode.

3. Results and Discussion

Among all known polyanionic insertion compounds [XO_n; X =B, C, P, Si, S, V], the $LiMBO_3$ family offers pragmatic avenue for developing high-capacity cathodes with the capacity exceeding 200 mAh/g. It is possible owing to the lightest oxyanion (BO_3^{3-}) and the least weight penalty. In 2001, Li*M*BO_3 group was reported to have suitable tunnels for ion-migration along with mixed (electron-ion) conduction. $LiMBO_3$ assumes a monoclinic crystal structure (*C*2/*c* symmetry) with an open framework, suitable for easy Li^+-ion migration. The $LiMBO_3$ structure is illustrated in Figure 1 and the lattice parameters are listed in Table 1. It is built from edge-sharing FeO_5 trigonal bipyramids, edge-sharing chains of LiO_4 tetrahedra and BO_3 triangular planar units. The BO_3 planar units act as links between adjacent parallel FeO_5-chains forming a three-dimensional $[FeBO_3]_n^{n-}$ framework. The Li species are statistically (50:50) distributed among two face-sharing LiO_4 tetrahedral sites. Recently, the existence of commensurate modulation in $LiFeBO_3$ has been reported [16].

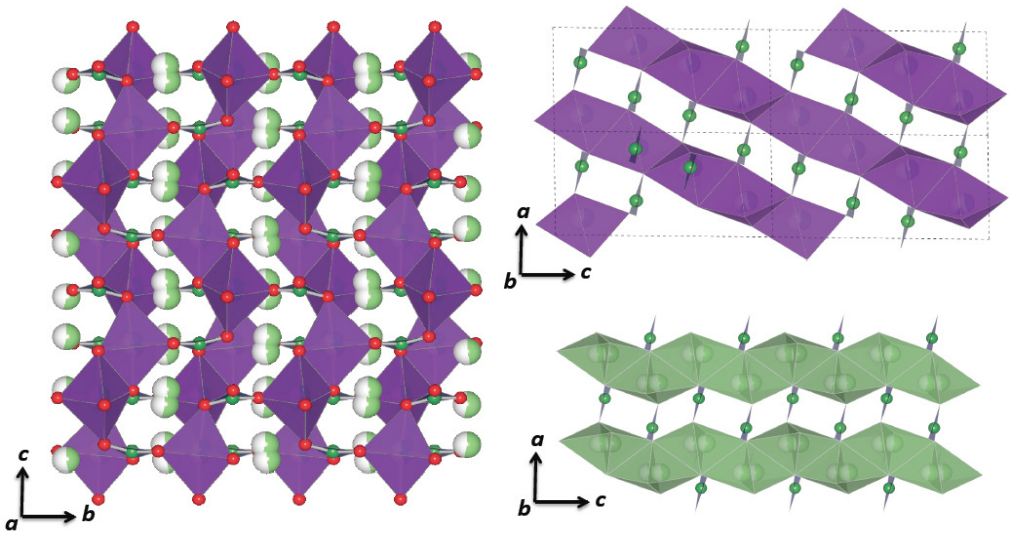


Figure 1. Structural illustration of $LiMBO_3$ borate insertion materials showing the FeO_5 trigonal bipyramids (velvet), BO_3 triangles (green), face-sharing LiO_4 tetrahedra (light green) and Li atoms (green/ white).

Table 1. Lattice parameters of $LiMBO_3$ insertion compounds in *C*2/*c* symmetry.

Material	a (Å)	b (Å)	c (Å)	β (°)	Volume (Å^3)
$LiMnBO_3$	5.1928(3)	8.9641(2)	10.3741(5)	91.36(3)	482.679(2)
$LiFeBO_3$	5.1597(2)	8.9127(5)	10.1559(4)	91.34(3)	466.922(5)
$LiCoBO_3$	5.1322(2)	8.8562(5)	10.1313(4)	91.31(3)	460.374(4)

3.1. *Study of $LiFeBO_3$*

Solid-state synthesis of $LiFeBO_3$ has been well-documented. Nevertheless, it was in 2010, our group produced electrochemically enabled $LiFeBO_3$ by optimized solid-state synthesis. Pursuing alternative energy-savvy synthesis, we have implemented solution combustion synthesis to get one-step carbon-coated nanostructured $LiFeBO_3$ cathode. Starting with aqueous precursors solution, it uses low-cost Fe^{3+}-based precursors [e.g. $Fe^{3+}(NO_3)_3.9H_2O$], which makes the processing very economic. Combustion synthesis involves a low temperature step facilitating mixing and partial reaction between individual precursors to form an amorphous intermediate complex showing broad XRD peak. It consists Fe^{3+}-metal-nitrate complex embedded in carbonaceous matrix. High temperature annealing undergo (i) rapid formation of $LiFeBO_3$ from the amorphous complex as evident from the XRD and (ii) *in-situ* Fe^{3+} to Fe^{2+} reduction owing to the presence of carbon as depicted by Mössbauer data (Figure 2). It is similar to carbothermal reduction (CTR [17]) process, with one-step formation of carbon coating on $LiFeBO_3$ particles. It is impressive to notice that within a minute of high-temperature exposure, it rapidly forms the $LiFeBO_3$ product, with complete synthesis accomplished in an hour vis-à-vis solid-state synthesis demanding at least 6-12 h annealing. The use of low cost Fe^{3+} precursors and short annealing duration make solution combustion synthesis economic and energy-savvy.

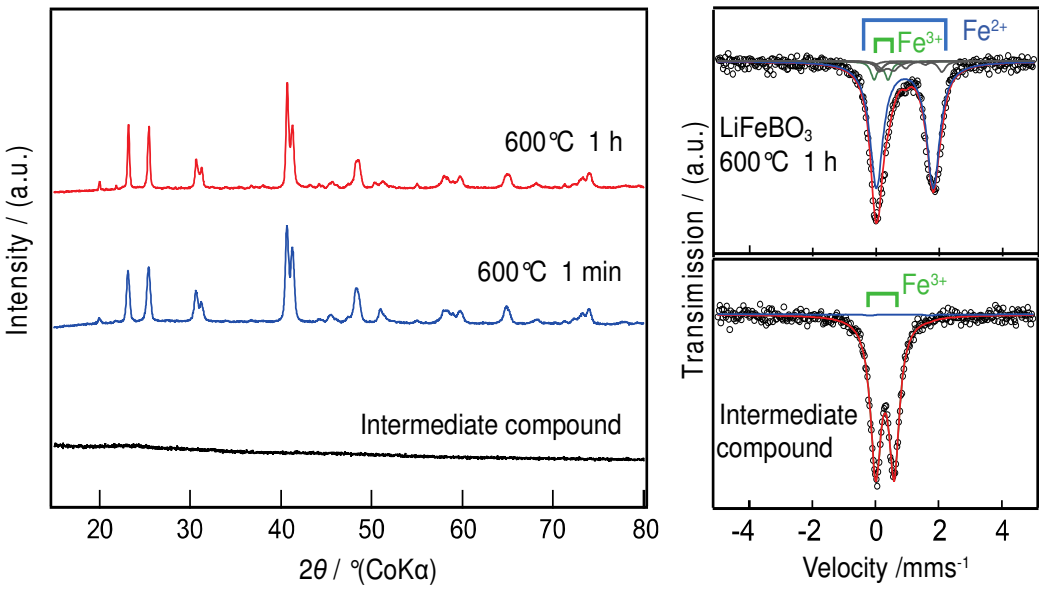


Figure 2. (Left) Structural evolution of $LiFeBO_3$ during annealing of amorphous intermediate complex. The amorphous Fe^{3+}-complex rapidly transform to Fe^{2+}-product within a minute as evident from the corresponding Mössbauer spectra (Right).

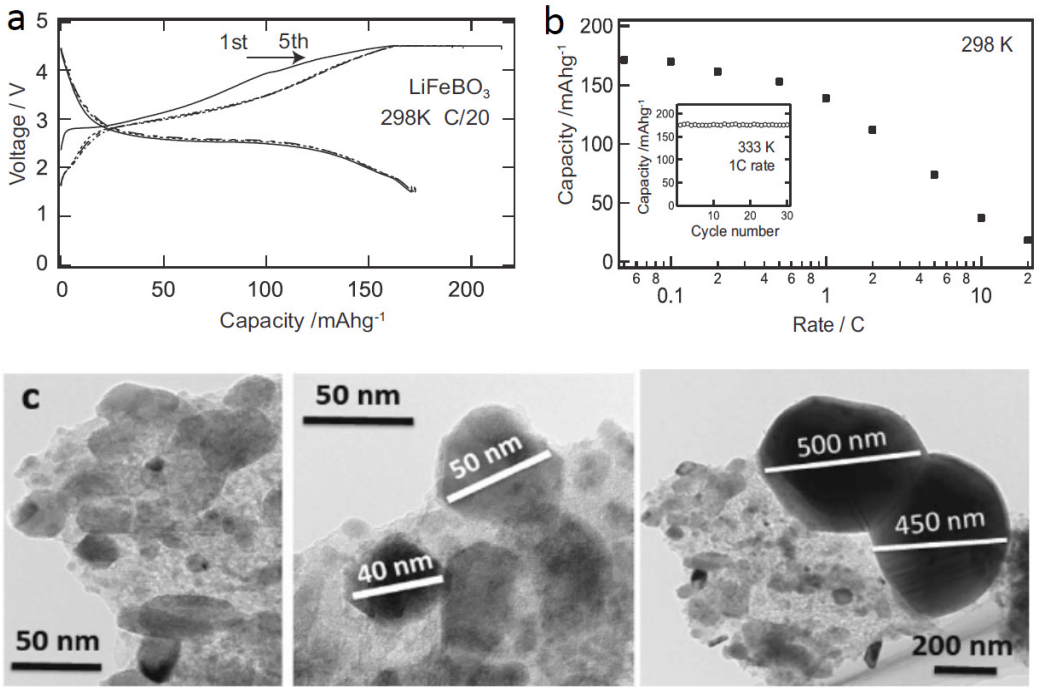


Figure 3. (a) Galvanostatic charge-discharge profile of solution combustion synthesized $LiFeBO_3$, cycled between 1.5-4.5 V at a rate of C/20 (1 Li in 20 h) at room temperature. (b) The rate kinetics of $LiFeBO_3$ at 25 ºC. (Inset) Cycling stability at 1C rate (1 Li in 1 h) conducted at 60 ºC. (c) Some representative TEM images of $LiFeBO_3$ nanoparticles in the size range of 40-500 nm.

The feasibility to prepare the target $LiFeBO_3$ with short exposure to high temperature and the presence of carbon coating inhibited excess grain growth, thus leading to homogeneous nanostructured particles in the range of 40-500 nm (Figure 3c). This formation of nanoparticle is beneficial to shorten the diffusion distance, enhance the Li-ion diffusivity and electrochemical activity in $LiMBO_3$. Since its discovery, numerous trysts on $LiMBO_3$ cathodes have been thwarted by poor Li-diffusivity, anti-site defects blocking Li-ion diffusion and insulating behavior [18]. The combustion synthesized $LiFeBO_3$, when tested at room temperature in half-cell architecture, delivered a reversible capacity approaching 180 mAh/g with steady reversibility (Figure 3a). We observed well-defined plateaus involving Fe^{3+}/Fe^{2+} redox reaction with an average potential of 2.85 V (vs. Li/Li^+). The sloppy voltage-capacity profile and minimal volume strain (2 %) during battery operation is a signature of solid-solution redox mechanism in $LiFeBO_3$ cathode. Following the solid-state synthesis by Yamada *et al* [9], this is only the second example of efficient and reversible Li^+ (de)intercalation from $LiFeBO_3$ cathode.

Following the successful demonstration of Li (de)insertion, the rate kinetics of $LiFeBO_3$ was tested at room temperature. As shown in Figure 3b, it retains the capacity fairly well even at faster rate: having 80% capacity at 1C and 40% capacity at 5C. Further, the high-temperature battery testing was conducted to test its operational safety. It offers excellent cycling stability at 60 °C delivering 175 mAh/g even at 1C rate (Figure 3b, inset). Overall, the solution combustion synthesized $LiFeBO_3$ offers excellent electrochemical activity and properties.

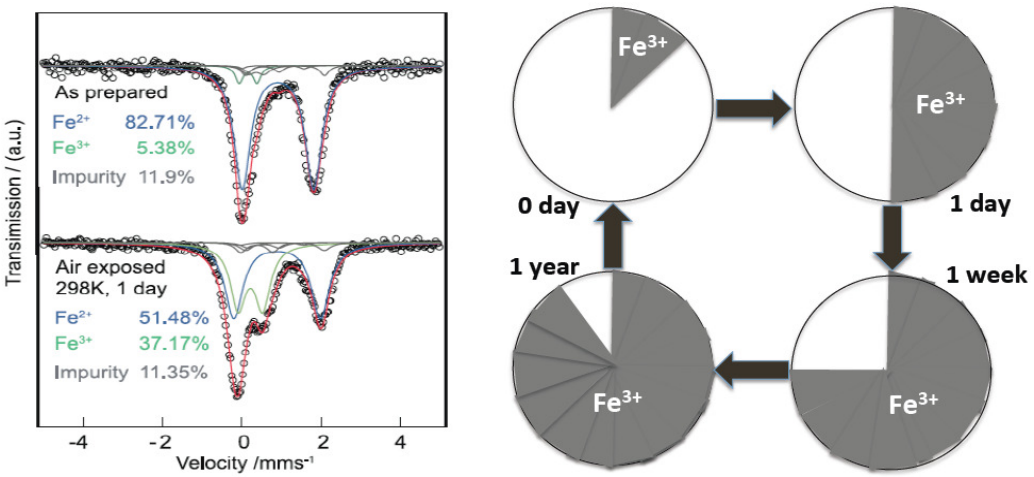


Figure 4. (Left) Mossbauer spectra of pristine and air-exposed $LiFeBO_3$ revealing the extreme Fe^{2+} to Fe^{3+} transition. (Right) This atmospheric poisoning and steady growth of Fe^{3+} species in $LiFeBO_3$ is shown as a function of time.

As originally pointed out by Yamada [9], the principal problem with $LiFeBO_3$ cathode is its quick atmospheric poisoning (i.e. Fe^{2+} to Fe^{3+} conversion) upon exposure to air. The solution combustion synthesis forms a protective carbon layer on each particles that may avoid the material degradation. The as-prepared materials' stability was tested with diligent Mössbauer study for over a year. As shown in Figure 4, $LiFeBO_3$ product is prone to degradation upon air exposure, where Fe^{3+} species grows from mere 5.4 % to 37 % in just a day. The exposure to air forms a core-shell structure with Fe^{3+}-rich shell, which grows thicker over longer duration. Progressive degradation was noticed as depicted in Figure 4 (right), where the Fe^{2+} content decreases to 50 % in just a day, 25 % in a week and <3% after a year. This aggressive materials degradation is certainly a great challenge to realize commercialization of high-capacity borate cathodes, similar to the case of Li_2FeSiO_4. One possible way to circumvent this problem is to coat the borate particles with a thin hydrophobic layer such as ionic liquid [19].

3.2. *Study of $LiCoBO_3$*

With the success in enabling $LiFeBO_3$ cathode, we next focused on isostructural $LiCoBO_3$ as a potential high voltage insertion compound, which has so far been electrochemically inactive. $LiCoBO_3$ offers an excellent combination of a theoretical capacity of 220 mAh/g and operational voltage ~4 V. If realized, it can deliver very high energy-density far exceeding that of all existing cathodes.

As Co-species can easily form metallic Co^0, we adopted a two-step route to form $Co_2B_2O_5$ pyroborate intermediate compound followed by reaction with Li_2CO_3 to obtain $LiCoBO_3$. Phase-pure $LiCoBO_3$ was successfully prepared by annealing the reaction mixture at 450 °C for 6 h (Figure 5a). While lower temperature (x< 400 °C) led to incomplete reaction, higher temperature (x> 500 °C) led to the decomposition and formation of CoO. Pure $LiCoBO_3$ thus has a narrow temperature window (400~500 °C) for formation. This use of moderate temperature makes the synthesis energy-miser as well as capable of forming homogeneous nanoscale (50-100 nm) product (Figure 5a, inset).

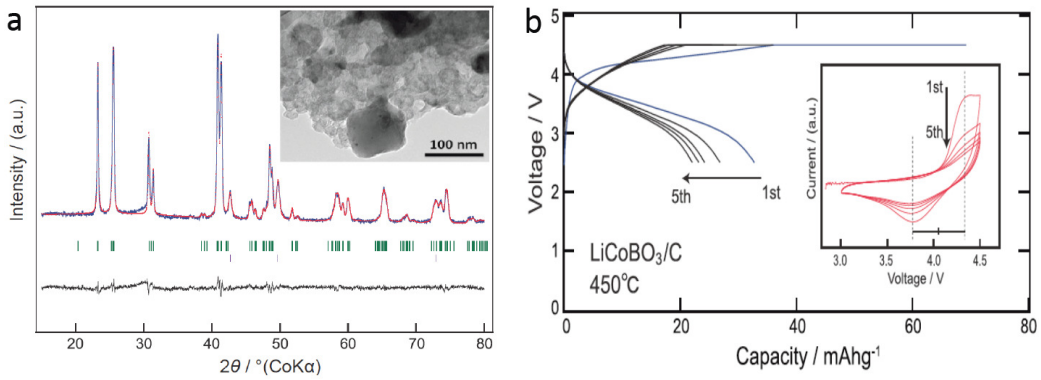


Figure 5. (a) X-ray diffraction pattern with Rietveld refinement of solid-state prepared $LiCoBO_3$. The blue line (experimental points), red dots (simulated pattern), their difference (black line) and Bragg positions (green ticks) are shown. (inset) Representative TEM image showing nanostructured morphology. (b) Charge-discharge curves of $LiCoBO_3$/C revealing a Co^{3+}/Co^{2+} plateau centered at 4 V (vs. Li). (inset) Respective cyclic voltammogram with reversible oxidation and reduction peaks.

Similar to other $LiMBO_3$, the $LiCoBO_3$ suffers from both electronic and ionic conductivity with very high energy barrier [18]. It can be avoided by using carbon coating and nano-sizing of cathode material. Our nanoscale $LiCoBO_3$, when tested vs Li, delivered a meager capacity of 20 mAh/g, with a Co^{3+}/Co^{2+} redox potential centered exactly at 4 V (Figure 5b). Cyclic voltammogram shows reversible cathodic/ anodic peaks located around 4 V. Although the capacity is limited, it is the first example of enabling Co^{3+}/Co^{2+} redox activity in $LiCoBO_3$.

Further optimization is needed to solve issues like poor conductivity, Co dissolution and amorphization at the electrode-electrolyte interface.

4. Conclusions

Lithium metal borate ($LiMBO_3$) offers a pedestal for realizing high-capacity insertion materials. However, it has been limited by difficulty in synthesis and poor electronic/ ionic conductivity. Here, we have shown the use of solution combustion synthesis with quick annealing and two-step solid-state route with low temperature treatment as effective ways to prepare $LiFeBO_3$ and $LiCoBO_3$ respectively. With these synthetic routes, careful materials handling and cathode optimization, near complete activity in $LiFeBO_3$ and partial activity in $LiCoBO_3$ has been demonstrated for the first time to present transition metal borates as a promising class of insertion materials for Li-ion batteries.

Acknowledgments

The authors would like to acknowledge T. Ye, Y. Yamada, S. Nishimura and S.C. Chung for scientific discussions and technical assistance. The financial help from the Ministry of Education, Culture, Sports, Science & Technology- MEXT under the 'Element Strategy Initiative for Catalysts and Batteries (ESICB)' program is gratefully acknowledged. PB sincerely thanks the Japan Society for the Promotion of Science for a JSPS Fellowship at the University of Tokyo.

References

1. J. M. Tarascon, *Phil. Trans. R. Soc. A.* **368**, 3227 (2010).
2. M. Armand and J. M. Tarascon, *Nature (London)* **451**, 652 (2008).
3. R. Marom, S. Francis Amalraj, N. Leifer, D. Jacob and D. Aurbach, *J. Mater. Chem.* **21**, 9938 (2011).
4. A. K. Padhi, K. S. Nanjundaswamy and J. B. Goodenough, *J. Electrochem. Soc.* **144**, 1188 (1997).
5. G. Rousse and J. M. Tarascon, *Chem. Mater.* **26**, 394 (2014).
6. C. Masquelier and L. Croguennec, *Chem. Rev.* **113**, 6552 (2013).
7. P. Barpanda, S. Nishimura and A. Yamada, *Adv. Energy Mater.* **2**, 841 (2012).
8. V. Legagneur, Y. An, A. Mosbah, R. Portal, A. Le Gal la Salle, A. Verbaere, D. Guyomard and Y. Piffard, *Solid State Ionics.* **139**, 37 (2001).
9. A. Yamada, N. Iwane, Y. Harada, S. Nishimura, Y. Koyama and I. Tanaka, *Adv. Mater.* **22**, 3584 (2010).

10. A. Yamada, N. Iwane, S. Nishimura, Y. Koyama and I. Tanaka, *J. Mater. Chem.* **21**, 10690 (2011).
11. P. Barpanda, Y. Yamashita, S. C. Chung, Y. Yamada, S. Nishimura and A. Yamada, *ECS. Trans.* **50**, 21 (2013).
12. P. Barpanda, Y. Yamashita, Y. Yamada and A. Yamada, *J. Electrochem. Soc.* **160**, A3095 (2013).
13. Y. Yamashita, P. Barpanda, Y. Yamada and A. Yamada, *ECS Electrochemistry Lett.* **2**, A75 (2013).
14. K. C. Patil, S. T. Aruna and T. Mimani, *Curr. Opin. Solid St. Mater. Sci.* **6**, 507 (2002).
15. P. Barpanda, S. K. Behera, P. K. Gupta, S. K. Pratihar and S. Bhattacharya, *J. Eur. Ceram. Soc.* **26**, 2603 (2006).
16. Y. Janssen, D. S. Middlemiss, S. H. Bo, C. P. grey and P. G. Khalifah, *J. Am. Chem. Soc.* **134**, 12516 (2012).
17. B. V. L'vov, *Thermochim. Acta.* **360**, 109 (2000).
18. D. H. Seo, Y. U. Park, S. W. Kim, I. Park, R. A. Shakoor and K. Kang, *Phys. Rev. B.* **83**, 205127 (2011).
19. P. Barpanda, R. Dedryvere, M. Deschamps, C. Delacourt, M. Reynaud, A. Yamada and J. M. Tarascon, *J. Solid State Electrochem.* **16**, 1743 (2012).

TRANSPORT PROPERTIES OF LAYERED LITHIUM NICKEL MANGANESE OXIDE ($LiNi_{0.5}Mn_{0.5}O_2$) CATHODE MATERIAL FOR LITHIUM ION BATTERIES*

P.SENTHIL KUMAR

Department of Physics, Karunya University
Coimbatore 641114, Tamilnadu, India

A.SAKUNTHALA#

Department of Physics, Karunya University
Coimbatore 641114, Tamilnadu, India

M.PRABU

Department of Energy Systems Engineering, Daegu Gyeongbuk Institute of Science & Technology
South Korea

M.V.REDDY

Department of Physics, National University of Singapore
Singapore 117542

The present study concentrates on the development of easy and inexpensive sol-gel method to prepare phase pure Lithium nickel manganese oxide using PVP as a chelating agent. The crystallinity and the purity of the prepared compound were confirmed by Rietveld XRD refinement. Vibrational studies like FTIR and Raman analysis show the formation of layered hexagonal structure. A SEM micrograph and particle size analyser study confirms the presence of sub-micron sized particle in the prepared compound. An EDX spectrum reveals the presence of the transition metal (Ni and Mn) in the compound LNMO. AC impedance analysis shows the electrical conductivity of the prepared compound as 2.57×10^{-7} S/cm.

1. Introduction

* This work is supported by Department of Atomic Energy - Board of Research in Nuclear Sciences (DAE-BRNS), India (Project No.2012/34/32/1221). The first author thanks the DAE-BRNS for Junior Research Fellowship.
# Corresponding author: meetsaku@gmail.com

Proceedings of the 14th Asian Conference on Solid State Ionics (ACSSI 2014)
Copyright © 2014 ACSSI 2014 Organizers. All rights reserved.
ISBN: 978-981-09-1137-9
doi:10.3850/978-981-09-1137-9_083

Recently, lithium ion batteries were considered as a promising rechargeable power sources for consumer electronics. Performance and safety of lithium ion batteries were determined by active materials such as cathode, anode and electrolyte. Basically lithium ion batteries use lithiated transition metal oxides as cathode materials. The commercially used $LiCoO_2$ has received considerable amount of attention as a cathode material for rechargeable Li-ion batteries due to its ease of synthesis, stable electrochemical cycling, high reversibility and long cycle life [1-2]. But cobalt is very expensive and toxic. Many researchers attempted to replace this commercial cathode with another suitable cathode material without compromising power, safety, and economical view. Mixed transition metal oxide cathode materials like $LiNi_{0.5}Mn_{0.5}O_2$ and $LiNi_{1/3}Co_{1/3}Mn_{1/3}O_2$ have been widely investigated for the past few years by various research groups [3-5]. Among the above two mixed transition metal cathode materials, $LiNi_{0.5}Mn_{0.5}O_2$ was considered as a next generation cathode material because of its low cost, higher specific capacity and excellent thermal stability [3,6-7]. The electrochemical performance of this electrode material was strongly affected by the synthesis conditions. Various methods have been used to synthesize $LiNi_{0.5}Mn_{0.5}O_2$ including solid state reaction, ion exchange, hydroxide co-precipitation, ball milling etc [5, 8-10]. Among these various methods, sol–gel method can provide homogeneous distribution of cations trapped in chelating agent, such as Li, Ni, and Mn in atomic scale, consequently leading to homogeneous and fine oxide products. So far, many literatures have been reported on the preparation of $LiNi_{0.5}Mn_{0.5}O_2$ by sol-gel method [11-14]. Particles prepared using the sol-gel method generally aggregate one another during calcination process. Polymers were considered as useful components in the formation of confined nano particles and they act as stabilizers for metal colloids and prevent from particle agglomeration [15-16]. Combustion nature of the polymer helps to particle growth and also reduces the calcination temperature for the preparation of cathode materials. The present work focus on the easy and inexpensive sol-gel method of preparing $LiNi_{0.5}Mn_{0.5}O_2$ cathode material using PVP (Polyvinylpyrrolidone) as a gelating agent.

2. Experimental

$LiNi_{0.5}Mn_{0.5}O_2$ was prepared using acetate and nitrate precursors in the presence of the polymer PVP (Polyvinylpyrrolidone) as a capping agent. All the chemicals used were received from Sigma-Aldrich. The preparation methodology of the **Sample PN950** was as follows: Required amount of PVP (M_W=40,000) was added to 100 ml of distilled water and stirred well. The stoichiometric ratio of high purity lithium nitrate (0.1M), nickel nitrate (0.05 M) and manganese nitrate (0.05 M) were

mixed with the above homogeneous polymer solution and stirred well. The PVP to metal ratio was fixed to 1:1.5. The pH of the solution was found to be neutral. The viscous solution was heated to 150°C on hot plate to get a dry powder. The obtained green colour powder was grinded well using mortar and pestle and calcined at different temperatures 850° and 950°C for 10 hrs in air. The heating rate was kept at 3°C/min. The sample code was fixed as PN950. The black powder obtained after calcination was ground and taken for further studies. **Sample PA950**: The above procedure was repeated using the acetate precursor instead of nitrate precursor was calcinated at 950 °C for 10 hr at a heating rate of 3°C / min. The sample code was given as PA950.

X-ray diffraction patterns (XRD) of the samples were obtained using SHIMADZU-XRD-6000 diffractometer with Cu-Kα radiation (λ = 0.1541 nm) as the source at 40 kV. Morphology and EDX analysis were made using JEOL-JSM 6000 scanning electron microscope. Particle size measurement was carried out using a MALVERN Zetasizer ZS-90. FTIR studies were carried out using a BRUKER-FTIR spectrometer in the range 400 to 4000 cm^{-1}. Raman spectra were recorded using 514.5 nm line of an Argon laser at the power level of 16 mW. The AC impedance studies were made using computer-controlled CH-Instrument (CHI-600E) in the frequency range of 40 Hz - 1MHz at room temperature. The amplitude was fixed as 50 mV during the measurement.

3. Results and discussion

3.1. XRD analysis

The Rietveld refined XRD pattern of the $LiNi_{0.5}Mn_{0.5}O_2$ compound prepared using nitrate precursor at a calcination temperature of 950°C for 10 hrs in air by sol gel method based on PVP (PN950) is shown in Fig. 1a. The obtained Bragg diffraction peaks could be indexed on the basis of α-$NaFeO_2$ structure with space group R3m. Generally α-$NaFeO_2$ hexagonal structure forms a close packed face centred (fcc) lattice with a distortion in the c-direction due to the oxygen sub-lattice [17], which is otherwise considered as a cubic structure. The presence of the distortion along c-direction can be confirmed by the splitting of the peaks at $2\theta \sim 37$ and 64° ((006/012) and (018/110) doublets) in the XRD pattern of the hexagonal structured compound $LiNi_{0.5}Mn_{0.5}O_2$. From our XRD patterns, the well clear doublets of (006/012) and (018/110) was observed for the sample PN950 (inset of fig.2a). This indicates that the synthesized $LiNi_{0.5}Mn_{0.5}O_2$ compound (PN950) has high degree of crystallinity, good hexagonal ordering and better layered characteristics [18]. The intensity ratio of 003/004 planes (I_{003}/I_{004}) depends on the degree of displacement of ions between lithium layers (at 3a site) and transition metal layers (at 3b site). Ohzuku and Makimura [6] et al reported

reactivity due to high concentration of inactive rock-salt domains in a layered solid matrix. When the intensity ratio of 003/104 peak is more than unity it indicates the compound to have no cation mixing [6, 8]. The intensity ratio (I_{003}/I_{004}) of the above compound was found to be 1.04. From Rietveld refinement the cation disorder was found to be 9 % and the lattice parameter values were found to be a = 2.89 Å and c = 14.30 Å. The cell volume and the ratio of lattice parameter (c/a) were found to be 103.62 Å and 4.95 respectively. A negligible amount of Li_2MnO_3 was observed in the XRD pattern. The Rietveld refinement results are well agreed with the experimental results.

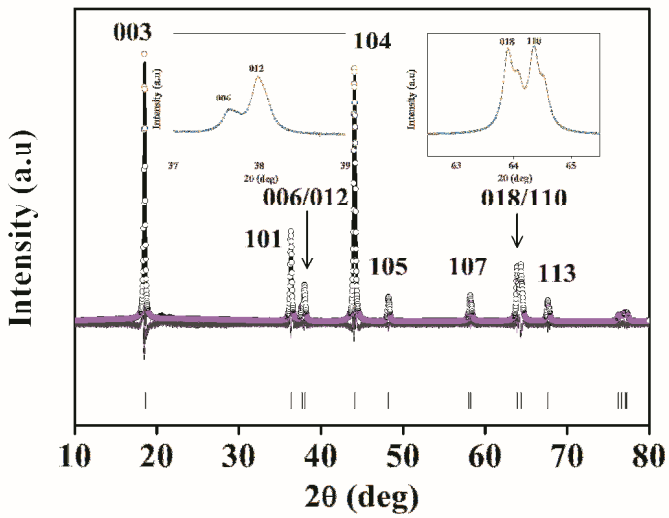


Figure 1(a). Rietveld refined XRD pattern of $LiNi_{0.5}Mn_{0.5}O_2$ (PN950)

The XRD pattern of the sample PA950 shows the formation of cubic phase (Fig. 1b) and no peak splitting at 2θ ~ 37 and 64^o (inset of Fig. 1b) were observed in the XRD pattern irrespective of the precursor taken. Also from Fig. 1b, it can be clearly seen that, a notable amount of Li_2MnO_3 impurity with high cation disorder was obtained in acetate precursor samples. This suggests the importance of the raw material choosing to synthesize phase pure hexagonal phase. Generally nitrate and acetate based chemicals are the products of strong HNO_3 and weak CH_3COOH respectively. So the reaction rate of the nitrate based precursor was always very fast comparing to acetate precursor and also nitrate acts as a mild oxidizer. This may enhance the homogeneity and sinterability of final product of the nitrate precursor based samples (PN950). Based on the XRD results further discussions of morphological, vibrational and electrical studies were made for the sample PN950.

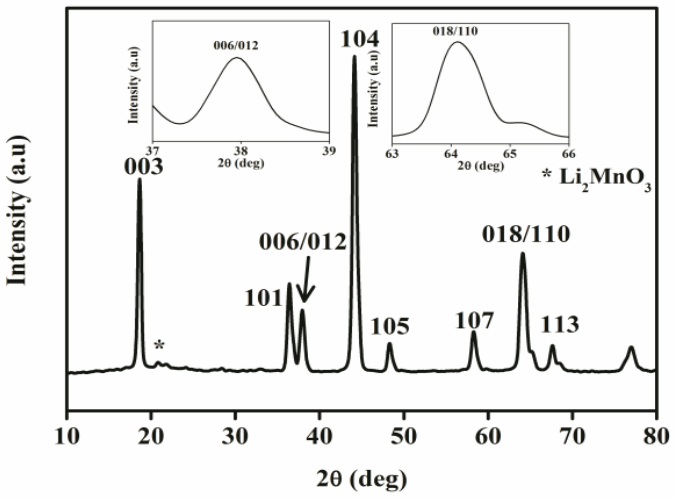


Figure 1(b) XRD pattern of $LiNi_{0.5}Mn_{0.5}O_2$ (PA950)

3.2. Surface and Elemental analysis

The SEM micrograph of $LiNi_{0.5}Mn_{0.5}O_2$ compound (Fig. 2a) shows agglomerated morphology with spherical and uniform distribution. The size of the particle was in sub-micron range. Energy dispersive spectra (Fig. 2b) confirm the presence of transition metal ions (Ni and Mn). The atomic percentage of Ni, Mn was found to be 14.41 and 15.40 respectively. Particle size distribution spectra of $LiNi_{0.5}Mn_{0.5}O_2$ sample is shown in fig 2 (c). This spectrum reveals the average size of the particle to be in sub-micron range.

3.3. Vibrational analysis

In addition to the X-Ray diffraction results, further evidence for the formation layered hexagonal structure of the compound $LiNi_{0.5}Mn_{0.5}O_2$ (PN950) was confirmed by the Fourier Transform Infrared spectroscopy and Raman studies. The IR spectra of layered structure compounds with space group R3m have four infrared active modes, namely $2A_{2u}$ and $2E_u$ by factor group analysis. The Figure. 3 shows deconvoluted IR spectrum for $LiNi_{0.5}Mn_{0.5}O_2$ in the 400 cm^{-1} to 700 cm^{-1} region. These recorded regions were associated with the vibrations of LiO_6 and MO_6 octahedral units. The peaks at 529 and 600 cm^{-1} are the bending modes of MO_6 (O-Mn-O (or) O-Ni-O), and the band at around 466 can be assigned to the asymmetric stretching Li-O in LiO_6 octahedral environments [19]. Figure. 4 shows the deconvoluted RS spectra of $LiNi_{0.5}Mn_{0.5}O_2$ compound (PN950). $LiNi_{0.5}Mn_{0.5}O_2$ has two Raman active modes, namely A_{1g} and E_g. A_{1g} vibrational active mode has greater oscillator strength and the intensity of the A_{1g} was twicer than E_g mode

[20]. Two Raman active modes A_{1g} and E_g were found to be at 583 and 469 cm^{-1} respectively in fig. 5. The appearance of these two vibrational bands confirms the formation of layered hexagonal structure. Carbon dominated D band at ~ 1300 cm^{-1} and G band at ~ 1500 cm^{-1} were not influenced in the recorded Raman spectra of the sample PN950.

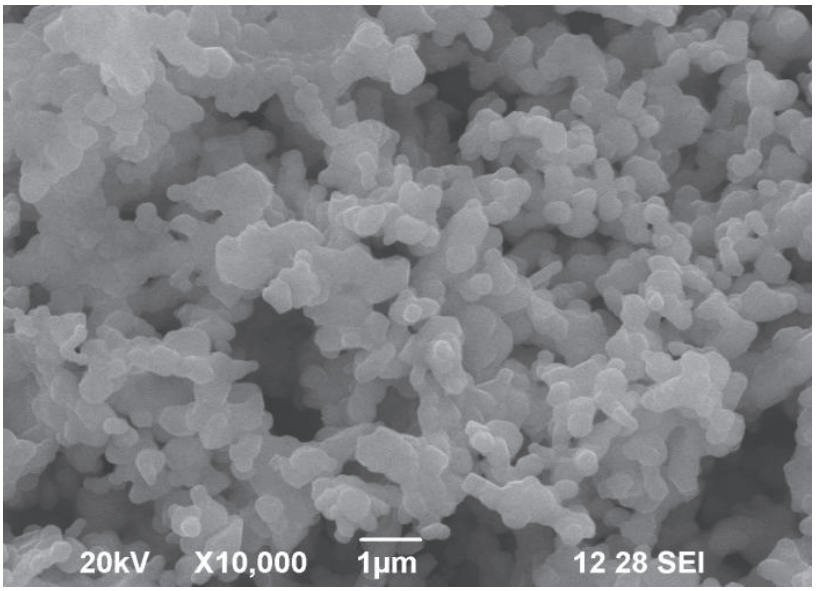


Figure. 2a SEM image

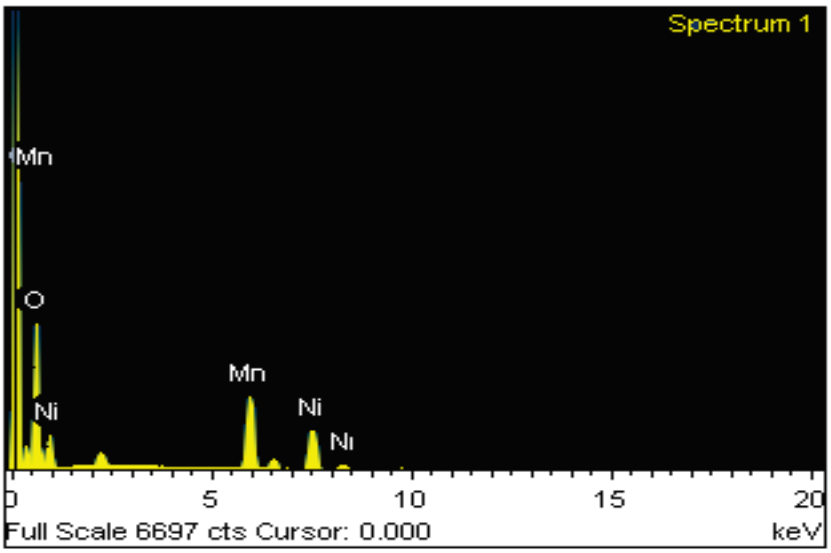


Figure. 2b EDX spectrum

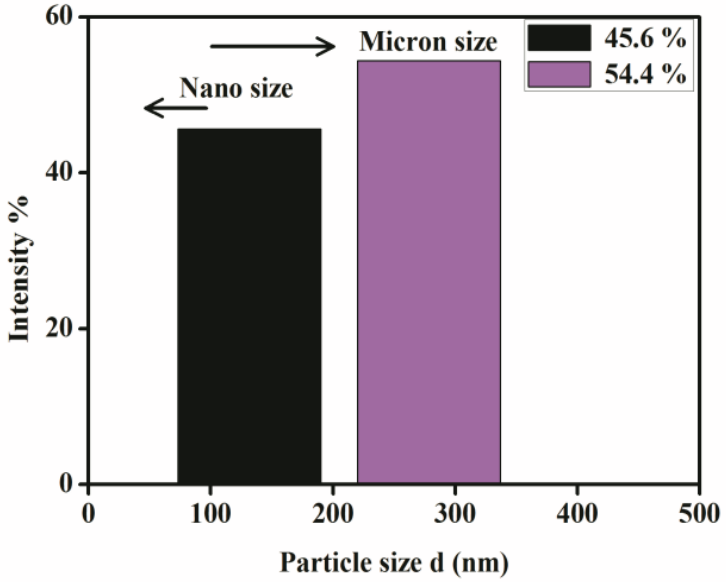


Figure. 2c Particle size distribution spectra

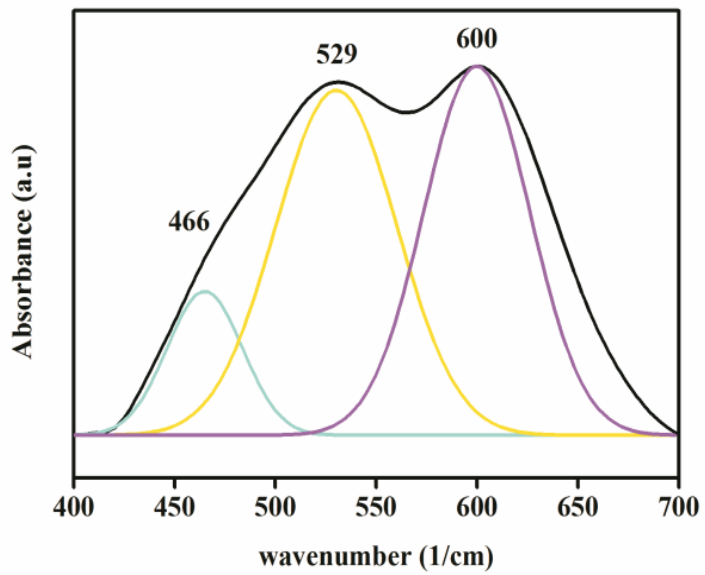


Figure.3 Deconvoluted FTIR spectra (PN950)

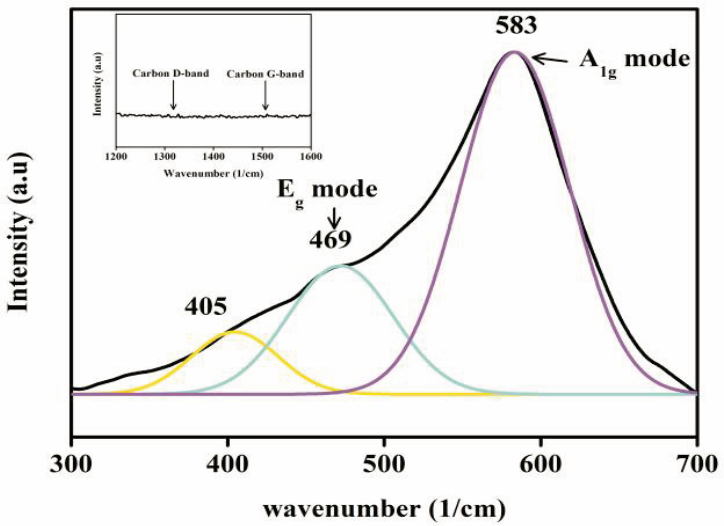


Figure.4 Deconvoluted Raman spectra (PN950)

3.4. AC impedance analysis

3.4.1. Cole-Cole plot analysis

Electrical behaviour of the $LiNi_{0.5}Mn_{0.5}O_2$ compound was studied by AC impedance technique. Figure. 5a represents the complex impedance plots of the $LiNi_{0.5}Mn_{0.5}O_2$ compound taken at room temperature (303 K) for the frequency range 42 Hz to1 MHz. The plot shows the overlapping of two semicircles related to the parallel combination of the resistor and a capacitor. High frequency semicircle is attributed to grain and mid frequency semi circle is related to grain boundary effect. The bulk resistance (R_b) of the sample was calculated by intercept of the low frequency spike on x-axis. The electrical conductivity of the $LiNi_{0.5}Mn_{0.5}O_2$ sample can be calculated using the conductivity formula given in Eq. (1).

$$\sigma = l / R_b A \qquad (1)$$

where l and A are the thickness and area of specimen, respectively. The calculated electrical conductivity at ambient temperature was found to be 2.57×10^{-7} S/cm.

3.4.2. Conductance spectra analysis

The frequency dependence of the conductivity for $LiNi_{0.5}Mn_{0.5}O_2$ compound at room temperature for the frequency range 42 Hz to1 MHz is shown in the fig. 5b. Within the measured frequency range the observed spectra has two distinct

regions. The frequency independent plateau region or the mid frequency (1 KHz to 10 KHz) region representing the dc conductivity (σ_{dc}) of the sample. The higher frequency (>10 KHz) dispersion region was attributed to the bulk relaxation phenomena. The conductivity value obtained from the conductance spectra (2.15×10^{-7} S/cm) was almost coincided with the value obtained from cole-cole plot.

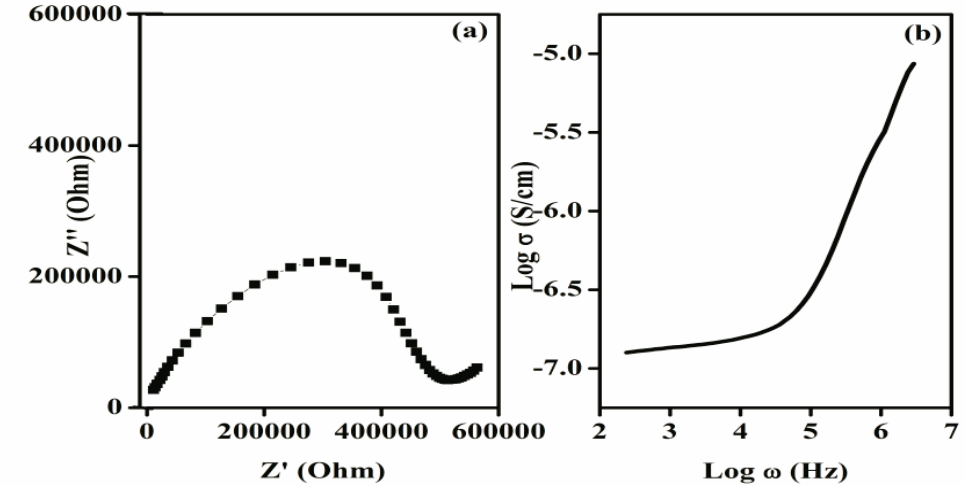


Figure. 5 a) cole-cole plot, b) conductance spectra (PN950)

4. Conclusion

The hexagonal layered lithium nickel manganese oxide cathode material, $LiNi_{0.5}Mn_{0.5}O_2$ has been successfully prepared by sol-gel method based on PVP as a chelating agent. XRD analysis shows the importance of raw materials in order to obtain phase pure hexagonal structure with good crystallinity and less cation disorder. FTIR and Raman analysis confirms the formation of layered structure. SEM image of the prepared compound have uniform spherical morphology with sub-micron sized particle. The electrical conductivity value obtained from cole-cole plot was well matched with the conductivity calculated from conductance spectra. The synthesized compound has low electrical conductivity value which must improved by alien metal ion doping or coating.

Acknowledgements

The authors would like to thank Karunya University, Coimbatore- 641114 for the Central research facilities. The authors are grateful to the Board of Research in Nuclear Sciences, Bombay (DAE-BRNS Project. No: 34/32/1221/2012) for providing funding for this research work and Junior Research Fellowship.

References

1. K.H.Jeong, H.W.Ha, N.J.Yun, M.Z.Hong and K.Kim, *Electrochimica Acta,* **50**, 5349, (2005).
2. S.H.Na, H.S.Kim and S.I.Moon, *Electrochimica Acta,* **50**, 449, (2004).
3. Z. Lu, D. D. MacNeil and J. R. Dahn, *Electrochem. Solid State Lett*. **4**, A191, (2001).
4. B. J. Hwang, Y. W. Tsai, D. Carlier and G. Ceder, *Chem. Mater*. **15**, 3676, (2003).
5. Y. Hinuma, Y. S. Meng, K. Kang and G. Ceder, *Chem. Mater*. **19**, 1790, (2007).
6. T. Ohzuku and Y. Makimura, *Chem. Lett*. **744**, (2001).
7. K. Kang, Y.S. Meng, J. Bréger, C.P. Grey and G. Ceder, *Science* **311**, 977, (2006).
8. Z. Lu, L.Y. Beaulieu, R.A. Donaberger, C.L. Thomas and J.R. Dahn, *J. Electrochem. Soc.* **149**, A778, (2002).
9. H. Xia, S.B. Tang and L. Lu, *J. Alloys Compd*. **449**, 296, (2008).
10. Y. Makimura and T. Ohzuku, *J. Power Sources* **119–121**, 156, (2003).
11. H. Li, Q. Xu, X.X. Shi, D.W. Song and L. Qi Zhang, *Rare metals,* (2013).
12. D. Bhuvaneswari, Gangulibabu and N. Kalaiselvi, *J Solid State Electrochem.* **16**, 3667*,* (2012).
13. B.J. Hwang, C.J. Wang, C.H. Chen, Y.W. Tsai and M. Venkateswarlu, *J. Power Sources* .**146**, 658, (2005).
14. X. Wanga, F. Zhoua, X. Zhaoa, Z. Zhanga, M. Jia, C. Tangb, T. Shenb and H. Zhenga, *J. Crystal Growth.* **267**, 184, (2004).
15. G. Xiong, X. Wang, L. Lu, X. Yang and Y.F. Xu, *J. Solid State Chem*. **141**, 70, (1998).
16. D.H. Chen and Y.W. Huang, *J. Colloid Interface Sci*. **255**, 299, (2002).
17. Y. Gao, M.V. Yakovleva and W.B. Ebner, *Electrochem. Solid-State Lett*. **1**, 117, (1998).
18. G.T.K. Fey, Z.F. Wang and T.P. Kumar, *Ionics*. 8, 351, (2002).
19. S.R.S. Prabakaran, M.S. Michael, S. Radhakrishnan and C. Julien, *J Mater Chem*. **7**, 1791, (1997).
20. C. Julien, *Solid State Ionics*, **136-137**, 887, (2000).

Batteries I

SOLID CERAMIC ELECTROLYTES FOR LITHIUM SULPHUR RECHARGEABLE BATTERIES

R. PRASADA RAO, D. SAFANAMA, M.H. CHEN, M.V. REDDY, S. ADAMS

Department of Materials Science and Engineering, National University of Singapore, Singapore, Singapore 117576

Lithium–sulphur (Li–S) and lithium–oxygen (Li–O_2) technologies have been identified as highly efficient technologies for energy storage devices for various electric vehicles and smart grid storage systems by large scientific community. However the formation of lithium dendrites and use of liquid electrolytes turned to be the major impediment in realising the potential of these batteries. Halide doped lithium Argyrodite-type thiophosphates Li_6PS_5X (where X = Cl, Br), $Li_{10}GeP_2S_{12}$ as solid electrolytes have been studied by our group and all these solid electrolytes exhibited ionic conductivity of the order of 10^{-4} S/cm at room temperature. Here we are presenting preliminary data using these electrolytes in all-solid-state battery. The first discharge capacity observed for all-solid-state battery with $Li_{10}GeP_2S_{12}$ electrolyte was 538 mAh/g at 20 mA/g current density.

1. Introduction

Lithium-based batteries as highly efficient energy storage devices have long been considered as promising power supply for various electric vehicles and smart grid storage systems [1,2]. However, presently available lithium-ion technology cannot satisfy the increasing demand for energy density. Among the conceivable high energy systems based on lithium metal anodes, lithium–sulphur (Li–S) and lithium–oxygen (Li–O_2) batteries appear to be particularly attractive candidates for next-generation high-energy density batteries [3]. In case of Li–S battery, the graphite as used in commercial batteries is replaced by a pure lithium metal that has both electronic and ionic conductivity and work as sink and source. And the metal oxide is replaced by low weight and low cost sulphur that can bond to two lithium atoms. All of that led to a high energy density and low cost advantages for Li–S technology. But the reaction between lithium and sulphur is the major impediment for this technology in realizing potential. As the battery is charged and discharged, soluble lithium polysulphides can seep into the liquid organic electrolyte, degrading the electrodes so that the battery loses charge and the cell gums up [4,5]. To answer these problems here we demonstrated the use of solid electrolytes in Li-S battery.

Proceedings of the 14th Asian Conference on Solid State Ionics (ACSSI 2014)
Copyright © 2014 ACSSI 2014 Organizers. All rights reserved.
ISBN: 978-981-09-1137-9
doi:10.3850/978-981-09-1137-9_141

In case of all-solid-state lithium batteries, the biggest challenge in the realization of such batteries is the need for a stable fast Li-ion conductor as the solid electrolyte, which significantly improves battery safety and widens electrochemical window relative to conventional liquid electrolyte containing batteries [3].

Halide doped lithium Argyrodite-type thiophosphates Li_6PS_5Br, $Li_{10}GeP_2S_{12}$ as solid electrolytes (SE) have been extensively studied by our group and all these solid electrolytes exhibited ionic conductivity exceeding 10^{-4} S/cm at room temperature [6-8]. Here, we investigated the performance of lithium batteries using these solid electrolytes.

2. Experimental

Li_6PS_5X (X=Cl,Br) and $Li_{10}GeP_2S_{12}$ were synthesized by reacting stoichiometric quantities of Li_2S (Alfa Aesar, 99.8%), P_2S_5 (Loba Chemie, 99%), GeS_2 (Sigma 99.8%), LiCl (Alfa Aesar, 99.8%) and LiBr (Alfa Aesar, 99.8%) The samples were prepared by high-energy mechanical milling using an zirconia bowl and balls (45 ml bowl and 15 balls of 10 mm diameter) for 20 h followed by heating at 550°C for 6h. All procedures were conducted under Ar atmosphere. The annealed samples were characterized by X-ray powder diffractometry using Cu K_α radiation (PANalytical X'Pert PRO) equipped with a fast linear detector. XRD data were collected in the 2θ° range 8-100° with a step size of 0.016° and a nominal scan rate of 120 s/step and at room temperature. Rietveld refinements of XRD powder patterns were performed with the Generalized Structure Analysis System (GSAS) by Larson and von Dreele [9], along with the graphical user interface EXGUI [10]. Initial structure models for the refinements are taken from published single crystal X-ray measurements by Deiseroth et al. [11] and our simulations [8]. Ionic conductivity measurements samples at different temperatures were carried out by impedance spectroscopy (Schlumberger Solartron SI1260) in the frequency range of 1 Hz to 10 MHz using stainless steel plates as electrodes. At each temperature the samples were kept for 20 min for thermal equilibration. The bulk resistance R_b was determined from fitting impedance data to Nyquist plots. The equivalent circuit consists of C_b, R_b and a Warburg element.

All solid state batteries were prepared using the configuration S:C:SE/SE/Li, where SE is the solid electrolyte Li_6PS_5Cl, Li_6PS_5Br and $Li_{10}GeP_2S_{12}$. For preparing the composite cathode 10 wt% of carbon black (AB) was added to sulphur and ball-milled for 30 hours. Then the SE was added yielding a SE : carbon black : S composite with the mass ratio 30:10:60 and ball milled for 30

min. The total mass of the composite cathode was kept at 7 mg, corresponding to 4.2 mg of active sulphur.
70 mg of the SE and 10 mg of cathode were cold-pressed (5 MPa) together forming a pellet of 12 mm diameter before being assembled into a coin cell using Li foil as the anode. Galvanostatic charge/discharge cycling studies of the cells were conducted using an Arbin BT2000 life cycle tester. The samples were cycled at room temperature in the range 1 - 3 V by applying a scan rate of 10 mA/g, using Li metal as the counter and reference electrode.

3. Results and discussion

The XRD patterns of ball-milled samples show partial crystallinity with peaks belonging to the Li_2S, P_2S_5, LiX (X=Cl, Br), GeS_2 phases. After annealing all samples yield the respective argyrodite phases with comparable crystallinity. Thus preparation time for argyrodites has been drastically reduced when compared to the original synthesis recipe. The final Li_6PS_5Cl and Li_6PS_5Br samples exhibit the high-symmetry aristotype argyrodite structure in space group *F-43m*. The lattice parameters of Li_6PS_5Cl and Li_6PS_5Br are 9.850(4) Å and 9.980(8) Å, respectively, in good agreement with reported values. Figure 1 shows the Rietveld refinement of the crystalline Li_6PS_5Br phase as an example. More details are reported in our previous manuscripts [6,7].

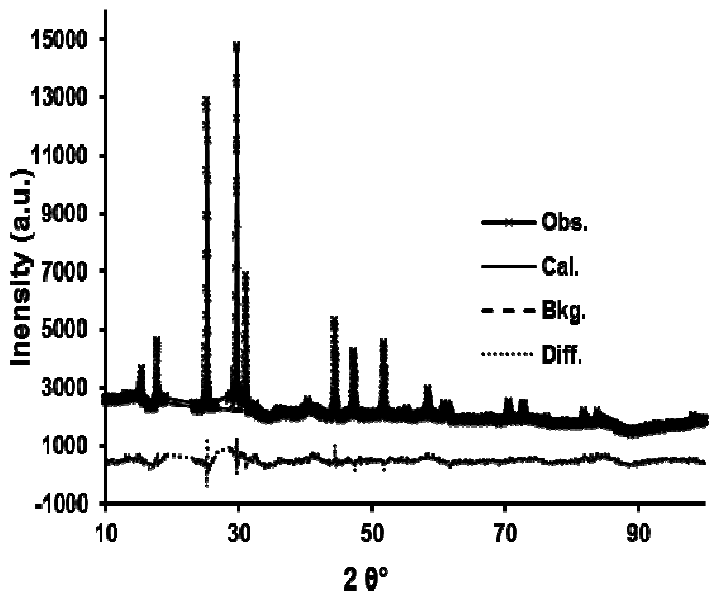


Figure 1. Rietveld refinement of Li_6PS_5Br prepared at 550°C with R_{wp}= 5%.

XRD patterns of $Li_{10}GeP_2S_{12}$ ball milled sample showed tetragonal structure with space group $P4_2/nmc$. The lattice parameters are a = 8.687(6) Å, c= 12.5816(10) Å, respectively, in good agreement with reported values. Figure 2 shows the Rietveld refinement of the crystalline $Li_{10}GeP_2S_{12}$ phase.

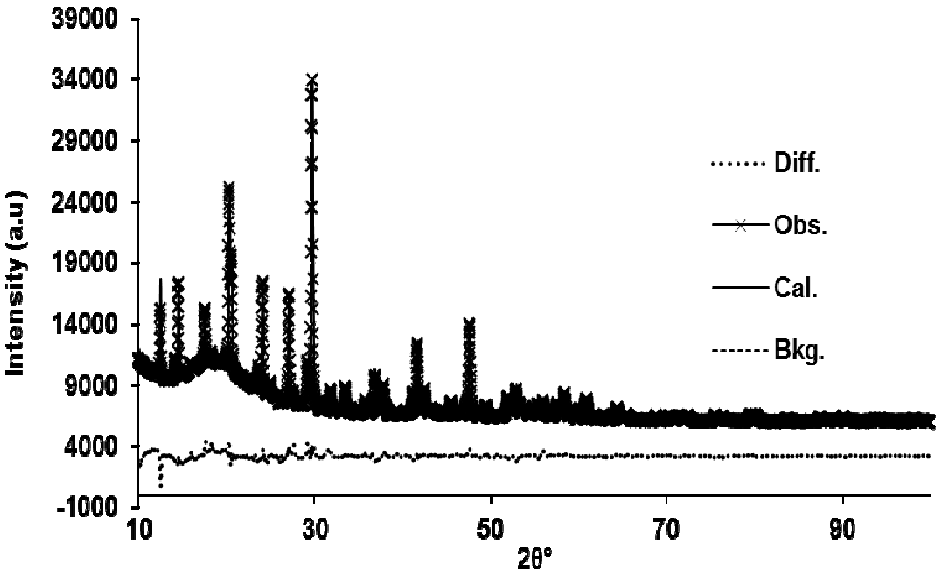


Figure 2. Rietveld refinement of $Li_{10}GeP_2S_{12}$ prepared at 550°C R_{wp}= 6%.

The bulk resistance R_b was determined from fitting impedance data to Nyquist plots. For the argyrodites the equivalent circuit consists of C_b, R_b and a Warburg element, yielding ionic conductivities of 7.4×10^{-4} S/cm for Li_6PS_5Cl and 7.2×10^{-4} S/cm for Li_6PS_5Br, both at 30°C with activation energies of E_a = 0.11 eV or 0.17 eV, respectively. In the case of $Li_{10}GeP_2S_{12}$ the conductivity was derived from the intercept of the Nyquist plot on x-axis (see figure 3), yielding 1.2×10^{-3} S/cm^{-1} at room temperature with an activation energy of 0.14 eV. This conductivity of $Li_{10}GeP_2S_{12}$ is substantially lower than the one previously reported by Kamaya et al.[12] but the same as observed by Hassoun et al. [13] .

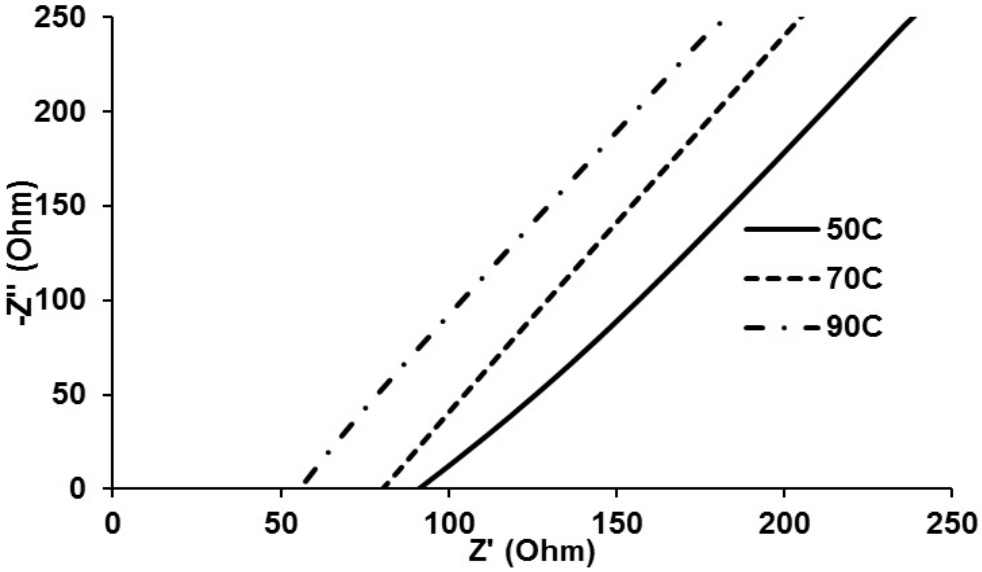


Figure 3. Nyquist plots of $Li_{10}GeP_2S_{12}$ at various temperatures.

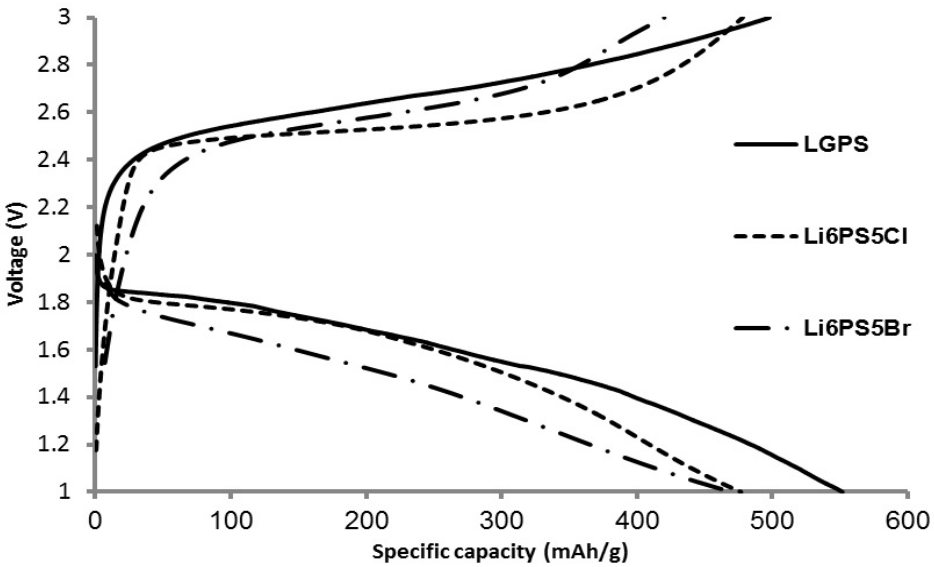


Figure 4. Initial charge discharge curves of all-solid-state Li/S cells using $Li_{10}GeP_2S_{12}$ (LGPS), Li_6PS_5Cl, Li_6PS_5Br as electrolyte. .

Figure 4 compares the charge-discharge curves obtained in all-solid-state Li/S cells using all the three solid electrolytes at 10 mA/g, which corresponds to C/60 (1 C = 1672 mA/g sulphur). The cells were charged to 3 V and discharged to 1 V (vs. Li). It should be noted that these cells use comparatively high content of

active material (60%S). Since sulphur is an isolator, addition of carbon and solid electrolyte is necessary to ensure electronic and ionic conductivity of the composite cathode. About 90% of first discharge specific capacity was retained for LGPS battery. Whereas, only about 75% of first discharge was retained for the batteries prepared from argyrodite electrolytes. The obtained capacity was normalized according to the weight of sulphur in the electrode. The batteries with $Li_{10}GeP_2S_{12}$, Li_6PS_5Cl and Li_6PS_5Br exhibited first discharge capacities of 538, 465 and 460 mAh/g, respectively.

The discharge plateau of the all-solid-state cell with the S electrode is ca. 1.9 V vs Li/Li^+. When compared to previous reports for all-solid-state Li-S batteries, the potential polarization (potential difference between discharge plateau and charge plateau) is relatively high in these batteries [14, 15, 16], which will be mostly caused by the relatively high sulphur and correspondingly low SE content and the thereby limited ionic conductivity of the composite. The specific capacity first charge is the same as the preceding discharge capacity in the case of LGPS, while for the two argryrodite electrolyte batteries a 2 and 11% decrease of the capacity is observed. We assume that the only a part of the sulphur is participating in discharge process for the formation of Li_2S in the electrode. This hypothesis has to be supported by the further ball milling the electrode materials or better coating of sulphur with carbon. In order to understand more about the mechanism of charge discharge procedure, various experiments are under progress in our lab.

4. Conclusions

Lithium ion conducting solid electrolytes were prepared using mechanical milling followed by annealing of the samples at 550°C for 6h. Among the prepared samples $Li_{10}GeP_2S_{12}$ exhibited high ionic conductivity above 10^{-3} S/cm at room temperature. All-solid-state rechargeable lithium sulphur batteries were prepared successfully with both argyrodite and LGPS solid electrolytes. Among the three batteries the battery prepared with $Li_{10}GeP_2S_{12}$ showed high first discharge capacity.

Acknowledgments

This research was supported by the National Research Foundation Singapore under its Competitive Research Programme (CRP award NRF-CRP102012-06).

References

1. J.M. Tarascon, M. Armand, *Nature*, **414**, 359 (2001).
2. M. Armand, J.M. Tarascon, *Nature*, **451**,652(2001).
3. P. G. Bruce, S. A. Freunberger, L. J. Hardwick, J.M. Tarascon, *Nature Mat.*, **11**, 19 (2012).
4. X. Ji, S. Evers, R. Black, L. F. Nazar, *Nature Comm.*, **2**, 325 (2011).
5. Y.S. Su, Y. Fu, T. Cochell, A. Manthiram, *Nature Comm.*,**4***,* 2985 (2013).
6. R. Prasada Rao, S. Adams, *Phys. Status Solidi A*, **208**, 1746(2011).
7. R. Prasada Rao, N. Sharma, V. K. Peterson, S. Adams, *Solid State Ionics* **230**, 72 (2013).
8. S .Adams, R. Prasada Rao, *J. Mater. Chem.*, **22**, 1426 (2012).
9. A. C. Larson and R. B. von Dreele, General Structure Analysis System (GSAS); Report LAUR 86-748; Los Alamos National Laboratory, Los Alamos, NM (2000).
10. B.J. Toby, *J. Appl Crystallogr* **34**, 210(2001).
11. H.-J. Deiseroth, S.-T. Kong, H. Eckert, J. Vannahme, C. Reiner, T. Zaiss, M. Schlosser, *Angewandte Chemie,* **47**, 755 (2008).
12. N. Kamaya, K. Homma, Y. Yamakawa, M. Hirayama, R. Kanno, M. Yonemura, T. Kamiyama, Y. Kato, S. Hama, K. Kawamoto, and A. Mitsui, *Nature Mat.,* **10**, 682 (2011).
13. J. Hassoun, R. Verrelli, P. Reale, S. Panero, G. Mariotto,S. Greenbaum, B. Scrosati, *J. Power Sources*, **229**, 117 (2013).
14. C. Maohua, R. Prasada Rao, S. Adams, *this issue*, (2014)
15. M. Nagao, A. Hayashi, M. Tatsumisago, *Electrochimica Acta*, **56**, 6055 (2011).
16. H. Nagata, Y. Chikusa, *J. Power Sources*, **263**, 141 (2014).

PERFOMANCES OF TiO_2 AS CATHODE MATERIAL IN RECHARGEBLE Mg BATTERIES WITH POLYETHYLENE OXIDE BASED GEL ELECTROLYTE

H.N.M. Sarangika[1, 2, 5]

[1)] *Department of Physical Sciences and Technology, Sabaragamuwa University of Sri Lanka, Belihuloya, Sri Lanka.*

W.A.R.B. Weerasekera[3], G.K.R. Senadeera[2, 3], M.A.K.L. Dissanayake[2,4,5], K.V.L. Amarasinghe[5], H.K.D.W.M.N. R. Divaratne[2,5], V.A. Seneviratne[4]

2. Institute of Fundamental Studies, Kandy, Sri Lanka.

[3)] *Department of Physics, The Open University of Sri Lanka, Nawala, Nugegoda, Sri Lanka.*

[4)] *Department of Physics, University of Peradeniya, Peradeniya, Sri Lanka*

[5)] *Postgraduate Institute of Science, University of Peradeniya, Sri Lanka*

In recent years there has been an increasing interest on research and development of solid state polymeric lithium batteries. Although Lithium ion battery technology is one of the most popular and evolving modern battery technologies, it also faces several difficulties such as the growth of a passivation layer on lithium anode, high reactivity of lithium metal, limited availability of lithium as a raw material etc.,. Therefore, it has been realized that Mg^{++} ion batteries would be among the best alternatives for solving the above problems. However, reported discharge capacities of the Mg batteries comprising with quasi solid Mg^{2+} ion conducting electrolytes are quite low due to the poor conductivity of the polymeric electrolyte and the mass and the properties of the cathode material used in these Mg batteries. In this study we have explored the possibilities of using low cost, highly abundant TiO_2 as the cathode martial in rechargeable magnesium batteries fabricated with Mg^{++} ion conducting, quasi solid (gel) polymeric electrolyte based on polyethylene oxide (PEO) as the host matrix. Electrolyte was characterized by AC impedance spectroscopy, cyclic voltammetry (CV) and DC polarization method. The best ionic conductivity of the electrolyte, determined by the complex impedance measurements was 2.52×10^{-3} S/cm at room temperature for the composition of PEO (12.20 wt%), $(CF_3SO_3)_2Mg$ (14.6 wt%), EC (36.6 wt%), PC (36.6 wt%). The conductivity appears to follow the Arrhenius behavior with increasing temperature. The estimated value of Mg^{+} ion transference number and total ionic transference number are found to be 0.10 and 0.98 respectively. Fabricated batteries with cell configuration $Mg/PEO:EC:PC:Mg(CF_3SO_3)_2/TiO_2$-C

Proceedings of the 14th Asian Conference on Solid State Ionics (ACSSI 2014)
Copyright © 2014 ACSSI 2014 Organizers. All rights reserved.
ISBN: 978-981-09-1137-9
doi:10.3850/978-981-09-1137-9_075

exhibited a discharge capacity of 270 mAh/g and 1.85 V open circuit voltage. The weight of the fabricated cathode material, TiO_2 used in these devices was approximately 1 mg.

Keywords: Mg Battery, Impedance spectroscopy, Polymeric electrolyte

1. Introduction

The energy demand is rapidly increasing with increasing global population. Therefore, the supply of energy has become the main challenge for maintaining a comfortable standard of living. Conventional energy sources derived from fossil fuels will soon be incapable of meeting the energy demand of the global population. Also, the use of fossil fuels will continue to enhance the current level of CO_2 in the atmosphere and environmental pollution. Therefore, finding alternative, environmental friendly, renewable energy sources such as solar and wind and storage devices such as batteries have become important in research and development work. Rechargeable battery technology is considered as a CO_2 emission free energy technology.

Majority of current rechargeable battery technologies are directed towards developing Li battery systems. In the view of the natural abundance of Magnesium, their low cost, low molecular weight and safety, Mg rechargeable battery system is considered to be one of the most suitable replacements for Li systems. A typical Mg battery consists of a metallic Mg anode, a Mg^{++} ion conducting electrolyte and a suitable cathode. During the charging process, Mg^{++} ions are released from the intercalation positive electrode (cathode) and metallic Mg^0 is deposited in the negative electrode (anode). Mg^{++} dissolution from the anode and intercalation into cathode happen during the discharging of the battery. Oxides are considered to be the most promising positive electrode materials for high energy density secondary Li batteries. The reason is the high degree of ionic character of metal oxygen bonds in oxides, which generally leads to high oxidizing power of the compound and hence to a high voltage of the battery. However for most Li batteries, $LiCoO_2$, V_2O_5 or MnO_2 or their derivatives have been used as the cathode material together with a liquid or gel electrolyte. The use of liquid electrolytes and rare earth materials for cathodes also limit their practical applications. Hence, developing solid or gel type electrolytes and low cost cathodic materials are still open problems with these batteries. Therefore, in this study we have explored the possibilities of developing a Mg^{++} ion battery using a PEO based gel electrolyte and low cost TiO_2 as the cathode martial. Possible Mg^{++} insertion and deinsertion into and out of TiO_2 occurs as follows:

$$\text{Positive electrode: } TiO_2 + x\,Mg^{++} + 2xe^- \longrightarrow Mg_xTiO_2$$

$$\text{Negative electrode: } x\,Mg \longrightarrow x\,Mg^{++} + 2xe^-$$

2. Experimental

2.1. Materials

Polyethylene oxide (PEO, Avg. Mw $4x10^6$), magnesium trifluoromethane sulfonate ($Mg(CF_3SO_3)_2$) were purchased from Sigma Aldrich and propylene carbonate (PC) ethylene carbonate (EC) with purity >98% were purchased from Fluka.

2.2. Electrolyte preparation and characterization

The electrolyte used for the Mg battery was prepared according to the following recepie: 0.12 g of magnesium trifluoromethanesulfonate ($Mg(CF_3SO_3)_2$) was dispersed in 0.3 g of propylene carbonate (PC) with 0.3 g of ethylene carbonate (EC) and the mixture was stirred well for complete dissolution. Then, 0.1 g of PEO was added to this solution and the mixture was heated up to 80°C under continuous stirring until a homogeneous viscous gel is formed. This viscous gel was then allowed to cool down to room temperature.

Total ionic conductivity of electrolyte samples was determined by using complex impedance analysis by a computer controlled Metrohm Autolab (PGATAT 128N) impedance analyzer in the frequency range between 0.1 Hz - 10 MHz. For these measurements appropriate amounts of polymer electrolytes were sandwiched between two polished stainless steel (SS) electrodes with the configuration SS/electrolyte/SS and the impedance measurements were taken from the room temperature up to 65 ^{0}C at 5^{o}C intervals.

Symmetrical cells, SS/electrolyte/SS and Mg/electrolyte/Mg were used for the DC polarization test by applying small dc voltage to estimate the total ionic transference number (t_{ion}) and the magnesium ion transference number (t_{Mg+2}) respectively. The ac complex impedance response of the Mg/electrolyte/Mg cell was also measured before and after dc polarization.

2.3. Preparation of the TiO_2 cathode

A powder mixture (0.2 g) of 89 wt% TiO_2, (0.025 g) of 11 wt% carbon powders, one drop of Triton-X and few drops of acetic acid were thoroughly ground with ethanol. This mixture was used to prepare the cathode pellet of 5 mm diameter and two tape thickness (24μm) pellet on Fluorine doped Tin Oxide (FTO) glass substrate and then sintered at 450 °C for 45 minutes. The weight of the prepared

TiO_2 electrode was 1 mg. The weight of the magnesium pellet used as the anode was 0.07 g.

2.4. Fabrication of the Mg/Electrolyte/TiO_2-C/FTO Cell.

A cleaned pellet of metallic magnesium was used as the anode. The Mg/PEO:EC:PC:$Mg(CF_3SO_3)_2$/TiO_2-C/FTO cell was assembled by sandwiching the gel electrolyte in between the magnesium anode and the TiO_2 cathode.

2.5. Characterization of the cell

In order to characterize the cells the discharge capacity of the Mg/Electrolyte/TiO_2-C/FTO cells was monitored by applying a constant load of 60 kΩ.

3. Results and discussion

3.1 Electrolyte characterization

The ionic conductivity of the gel polymer electrolyte was calculated using the relation

$$\sigma = l / R_b A \quad (1)$$

where l is the thickness of the electrolyte sample, A is the contact area between the electrolyte and the stainless steel electrode and R_b is the resistance determined from impedance spectra. Room temperature ionic conductivity is found to be 2.52×10^{-3} S/cm. As shown in Figure 1, the temperature dependence of the conductivity follows the classical Arrhenius equation,

$$\sigma = \sigma_o \exp(-E_a/RT). \quad (2)$$

Magnesium transference number (t_{Mg+2}) was measured using the dc and ac measurements suggested in the literature [1] by using the relation.

$$t_{Mg+2} = \frac{I_S(\Delta V - R_0 I_0)}{I_0(\Delta V - R_S I_S)} \quad (3)$$

Where I_0 and I_S are the initial and final steady state currents of Mg/electrolyte/Mg (Fig.2) and R_0 and R_S are the Mg/electrolyte/Mg cell resistance before and after the dc polarization respectively. Evaluated Mg^{++} ion transference number for the gel electrolyte is found to be 0.10 indicating the Mg^{++} contribution to the electrolyte.

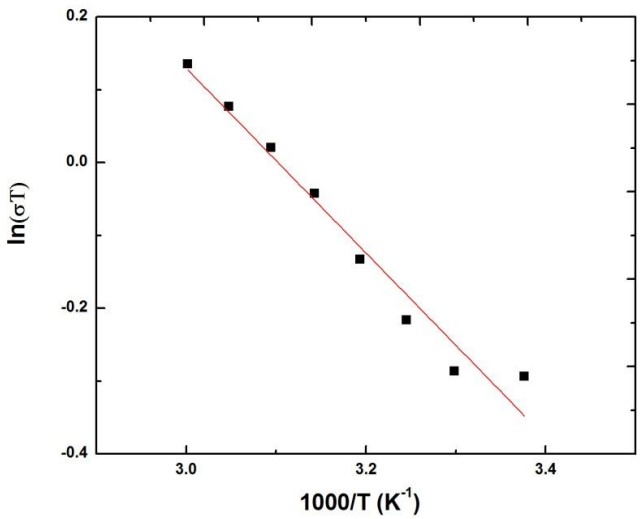


Figure 1. Temperature dependence of the ionic conductivity of the PEO based electrolyte PEO:EC:PC: $Mg(CF_3SO_3)_2$ in logarithm scale.

The results of the DC polarization test taken with Mg/Electrolyte/Mg symmetrical cell and applying a DC voltage of 1.5 V is shown in Figure 2.

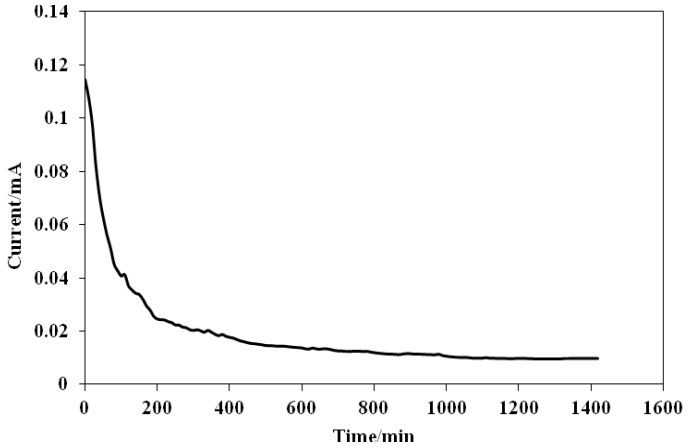


Figure 2. Variation of dc polarization current as a function of time for Mg/EC:PC:PEO:Mgtf/Mg

The total ionic transference number was determined by the DC polarization test using the symmetrical cell SS/electrolyte/SS and according to the equation

$$t_{ion} = I_i - I_f / I_i \quad (4)$$

where I_i is the initial current and I_f is the final residual current. In this method the dc polarization current was monitored as a function of time (Fig.3). Calculated value was found to be 0.985 showing that the ionic conductivity in the gel electrolyte is dominant and the electronic conductivity is negligible.

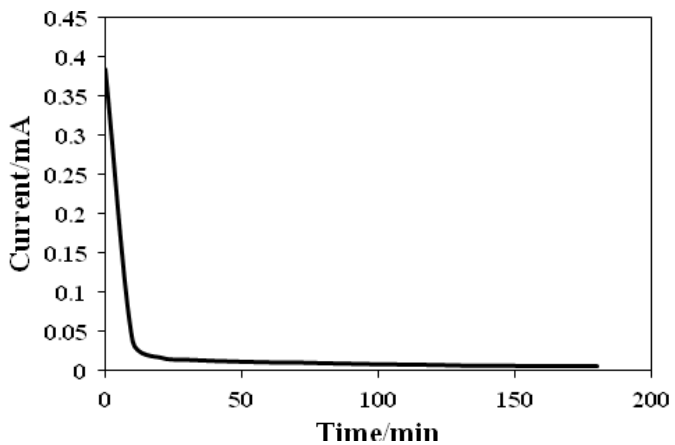


Figure 3. Variation of polarization current as a function of time for SS/EC:PC:PEO:Mgtf/SS

3.2. Mg/electrolyte/ TiO_2-C cell

The open circuit voltage of the Mg/Electrolyte/TiO_2-C battery was monitored for the first 24 hours until it became stabilized. Initial increase of voltage was observed during the first 2 hours after assembling the cell which was subsequently stabilized at 1.82 V. This value remained essentially constant up to nearly 30 hours (Figure 4)

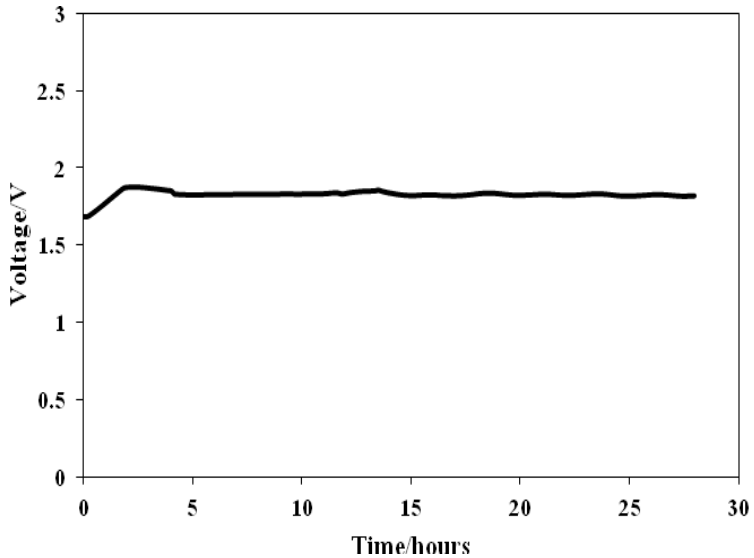


Figure 4. Open circuit voltage of Mg/ PEO:EC:PC: $Mg(CF_3SO_3)_2$/TiO_2-C/FTO cell during 24 hours of storage.

Fig.5. shows the discharge characteristics of the cell Mg/Electrolyte/TiO_2-C for a constant load of 60 kΩ. It shows that the discharge was sustained for nearly 25 hours for 60 kΩ. The value of the discharge capacity was evaluated by integrating the area under the curve of figure 5 according to

$$C = \frac{\int_0^t I(t)dt}{M} \tag{5}$$

where M is the mass of the active material (TiO_2) in the cathode. Estimated discharge capacity of the cell is 270 mAh/g.

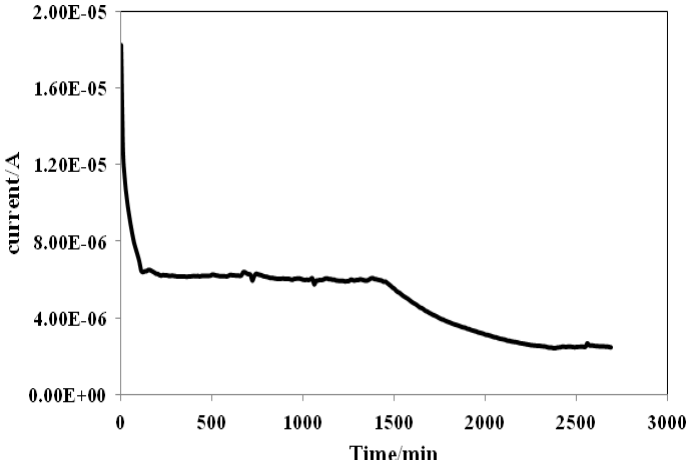


Figure 5. Constant load discharge characteristics of the cell Mg/PEO:EC:PC: $Mg(CF_3SO_3)_2/TiO_2$-C/FTO under 60 kΩ load.

Fig. 6 shows typical charge and discharge curves of the Mg/PEO:EC:PC: $Mg(CF_3SO_3)_2/TiO_2$-C cell under constant current. The data show stable charge-discharge cycles.

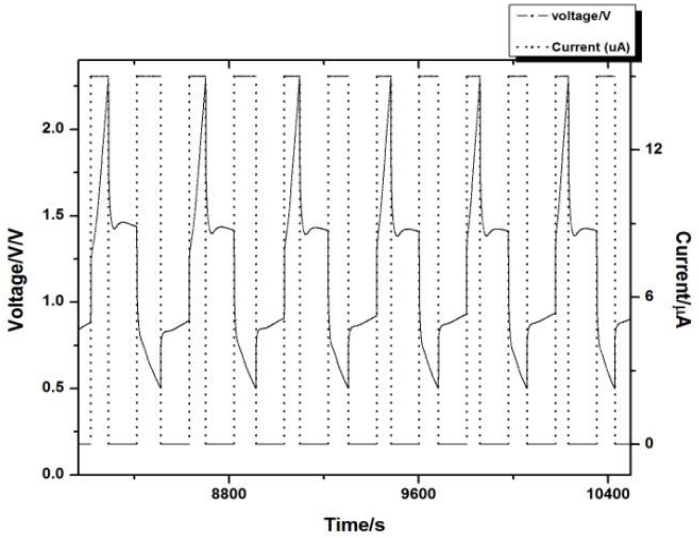


Figure 6. Charge - discharge curves of a Mg/PEO:EC:PC:$Mg(CF_3SO_3)_2/TiO_2$-C/FTO cell at room temperature.

4. Conclusion

PEO:EC:PC: $Mg(CF_3SO_3)_2$ gel polymer electrolyte was synthesized and characterized. It shows predominantly ionic nature with negligible electronic conductivity. Mg^{++} ionic transference number is about 0.10. Mg batteries were fabricated with this gel polymer electrolyte and low cost TiO_2 cathode. The discharge capacity of these Mg cells is 270 mA/g. These results show that magnesium polymeric electrolyte offers and interesting alternative to lithium systems for room temperature solid sate batteries. On the other hand the conventional cathode materials such as $LiCoO_2$, V_2O and MnO_2 used in lithium batteries can be substituted with low cost TiO_2 in Mg batteries can be done with the lost cost heavily available materials like TiO_2 effectively.

References

1. E. Sheha, *Solid State Ionics*, 1**80,** 1575-1579 (2009).
2. E. Sheha, *Int. J. Electrochem. Sci*. **8,** 3653 - 3663 (2013**).**
3. M. Inamoto, H. Kurihara and T. Yajima, *Materials*, **6**, 4514-4522 (2013).
4. S. K Deraman, N.S. Mohamed, and R.H.Y. Subban, *Int. J. Electrochem. Sci.* **8** 1459 – 1468 (2013).
5. Xin Su , Q. L. Wu , X. Zhan , Ji Wu , S. Wei and Z. Guo *J Mater Sci*. **47**, 2519–2534 (2012).
6. E. Sheha, M.K. El-Mansy, *Journal of Power Sources,* **185,** 1509–1513 (2008).
7. N. Yoshimoto, S. Yakushiji, M. Ishikawa, M. Morita, *Solid State Ionics* **152– 153**, 259– 266 (2002).
8. A. Ryu, M.-Sik Park, W. Cho, J.S. Kim and Young-Jun *Kim Korean Chem. Soc.* **34**, No. 10 3033 (2013).
9. R. C. Agrawal and D. K. Sahu, *Journal of Physical Science and Application* 3,**1**, 9-17 (2013).
10. H. D. Yoo, I. Shterenberg, Y. Gofer, G. Gershinsky, N. Pour and D. Aurbach, *Energy Environ. Sci*. **6**, 2265 (2013).

THE EFFECT OF ANNEALING TEMPERATURE ON MORPHOLOGY, STRUCTURE AND ELECTROCHEMICAL PERFORMANCE OF SPINEL- $LIMN_2O_4$

TEGUH YULIUS SURYA PANCA PUTRA

Center for Science and Technology of Advanced Materials, National Nuclear Energy Agency (BATAN), Kawasan Puspiptek Serpong, Tangerang Selatan 15314, Indonesia

EVVY KARTINI

Center for Science and Technology of Advanced Materials, National Nuclear Energy Agency (BATAN), Kawasan Puspiptek Serpong, Tangerang Selatan 15314, Indonesia

DESWITA

Center for Science and Technology of Advanced Materials, National Nuclear Energy Agency (BATAN), Kawasan Puspiptek Serpong, Tangerang Selatan 15314, Indonesia

MASAO YONEMURA

High Energy Accelerator Research Organization (KEK), 1-1 Oho, Tsukuba, Ibaraki 305-0801, Japan

SHUKI TORII

High Energy Accelerator Research Organization (KEK), 1-1 Oho, Tsukuba, Ibaraki 305-0801, Japan

TORU ISHIGAKI

Frontier Research Center for Applied Atomic Science, Ibaraki University (iFRC), IQBRC, Shirakata 162-1, Tokai Village, Naka-gun, Ibaraki 319-1106, Japan

TAKASHI KAMIYAMA

High Energy Accelerator Research Organization (KEK), 1-1 Oho, Tsukuba, Ibaraki 305-0801, Japan

The development of lithium ion battery technology is very important in its utilization as a new energy sources, for example in electrical vehicle (EV). One of the components that affect the performance of the battery is the cathode, such as spinel $LiMn_2O_4$. In an effort to obtain a good cathode material it is necessary to set the proper synthesis conditions. In this study, spinel $LiMn_2O_4$ powder was synthesized from $LiOH.H_2O$ and MnO_x by mechanical alloying (MA) method followed by heat treatment at 700°C, 800°C and 900°C. The influence of morphology and crystal structure of the spinel $LiMn_2O_4$ as a

Proceedings of the 14th Asian Conference on Solid State Ionics (ACSSI 2014)
Copyright © 2014 ACSSI 2014 Organizers. All rights reserved.
ISBN: 978-981-09-1137-9
doi:10.3850/978-981-09-1137-9_153

result of heat treatment on electrochemical performance was investigated. Observation by SEM showed that the higher the annealing temperature, the crystallinity of the powder particles of the spinel $LiMn_2O_4$ increased. Phase and crystal structure analysis by XRD showed that the purity and crystallinity of the spinel $LiMn_2O_4$ increased with annealing temperature, characterized by sharper peaks of the diffraction patterns. Crystal structure analysis by neutron powder diffraction (NPD) showed that $LiMn_2O_4$ synthesized has spinel structure with space group *Fd-3m* and lattice parameter of 8.233316(8) Å, 8.239790(5) Å and 8.244564(4) Å for annealing temperatures of 700°C, 800°C and 900°C. It is also found that the electrochemical performance of $LiMn_2O_4$ cathode in Li-ion battery increased with annealing temperature, shown by capacity of 248.95 $mAhg^{-1}$, 264.29 $mAhg^{-1}$and 277.24 $mAhg^{-1}$. These results show that increasing purity and crystallinity of the cathode material $LiMn_2O_4$ are significantly affect the electrochemical performance of Li-ion battery.

1. Introduction

In an effort to find new energy sources for wide applications, such as in electrical vehicle (EV), the development of Li-ion battery technology is very important. Cathode materials, such as spinel $LiMn_2O_4$, also affect the performance of the Li-ion battery. Spinel $LiMn_2O_4$ has attracted attention, both in terms of its structure and application, in an effort to find a suitable material for cathode in Li-ion battery system. $LiMn_2O_4$ has advantageous such as relatively low toxicity, cheaper, easiness in preparation, better electrochemical performance etc. $LiMn_2O_4$ is also known to have large rechargeable capacity of 120 mAh/g in the 4V region, which is slightly smaller than that of $LiCoO_2$ (150 mAh/g) and $LiNiO_2$ (200 mAh/g) [1-16].

The physical and electrochemical properties of the material are determined by some factors such as particle size, lattice parameter, stoichiometry, average Mn valence, surface morphology and homogeneity [4,12]. In practice, these factors are closely related to the synthesis condition, such as heating temperature, holding time as well as cooling rate. It will affect the cathodic properties of the lithium transition metal oxides. Another factors such as starting material and the content of lithium is also known to determine the properties of $LiMn_2O_4$ [17].

Various methods have been proposed in order to synthesize $LiMn_2O_4$ with best performance such as conventional solid-state reaction [18-21], sol-gel method [22-24], combustion technique [25], molten salt technique [26], melt impregnation technique [27-29], simple soft-chemical technique [30], co-doping anti-electricity ions [31]. Recently, mechanical alloying (MA) has become a popular method and widely used as an alternative to the solid-state reaction. MA is expected to be an easy, effective, low energy expenses and low-cost method, which offer alternative to conventional high temperature synthesis or solution

chemistry, giving a product of spinel with controllable properties. Many works have been done to study the spinel $LiMn_2O_4$ synthesized by MA method [2-11]. Related to structural study, an accurate and precise method supported by sophisticated facility and instrument, i.e. neutron powder diffraction (NPD), is indispensable.

In this paper, the relationship among synthesis condition by MA, the annealing temperature, and the crystal structure of the spinel $LiMn_2O_4$ will be studied by several methods, namely by Scanning Electron Microscope (SEM) and X-Ray Diffraction (XRD). In order to obtain the information of the occupancy of the atoms, it is important to perform high-resolution NPD. The highest capacity of Li-ion batteries using cathode $LiMn_2O_4$ will be determined by electrochemical measurement. It is expected that the optimum composition of the spinel $LiMn_2O_4$ will replace the existing cathode of Li-ion battery.

2. Experimental Method

Spinels $LiMn_2O_4$ were synthesized from mixtures of stoichiometric amount of $LiOH{\cdot}H_2O$ and MnO_x and milled by MA method in a stainless steel (SS) jar using a planetary ball mill (RETSCH PM 200) with SS balls (10 mm dia.) for 6 hrs. The mixtures were then pressed into pellet and heated at 700°C, 800°C and 900°C in oxygen for 4 hrs.

Morphology of the spinel $LiMn_2O_4$was studied by Scanning Electron Microscope (SEM) method at Center for Science and Technology of Advanced Materials (PSTBM), Puspiptek Serpong, Indonesia. Phase analyses were conducted by XRD method using Rigaku SmartLab XRD at KEK Tokai Campus, Japan. Crystal structure of the spinel samples at room temperature were studied by neutron diffraction on iMATERIA (BL-20), at Materials and Life Science Facility (MLF), Japan-Proton Accelerator Research Complex (J-PARC), Tokai, Japan. The structural parameters were refined with Z-Rietveld [32, 33]. Electrochemical study of the spinel as cathode material in Li-ion battery was performed at Kanno and Hirayama's Lab. of Tokyo Institute of Technology, Yokohama, Japan. Electrochemical testing was performed in 2032 coin type cells with lithium foil as negative electrode. The electrolyte used was 1 M $LiPF_6$ in EC:DEC (3:7v/v). The assembled cells were charged and discharged within a voltage range of 2.0 – 4.8 V at a constant current density of 10 mA g^{-1}.

3. Results and Discussion

3.1. *Morphology by SEM*

Figure 1.a and 1.b-d showed morphology of the spinel-type $LiMn_2O_4$ synthesized by MA for 6 hrs before and after annealed at temperature range of 700 - 900°C in oxygen, respectively. Before annealing, agglomerated particles of the mixture are observed. After annealing at 700°C (figure 1.b) the morphology shows agglomerates with roughness on the surface, while the spinel annealed at 800°C (figure 1.c) shows agglomeration contains more distinct particulates on its surface with an average particle size of about 250 nm and narrow particle size distribution. The crystalized shape was clearly observed at 900°C with an average size of about 550 nm as shown in figure 1.d.

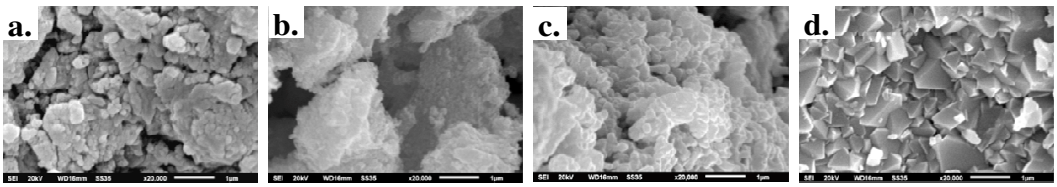


Figure 1. SEM micrograph of the spinel-type $LiMn_2O_4$ synthesized with an initial molar ratio of Li/Mn = 0.50 after MA for 6 hrs (a) before, and after annealing at (b) 700°C, (c) 800°C, and (d) 900°C for 4 hrs in oxygen.

3.2. *Phase and Crystal Structure by XRD*

Figure 2 shows XRD pattern for spinel $LiMn_2O_4$ after annealed at 700°C, 800°C and 900°C. The formation of spinel-type $LiMn_2O_4$ is shown for all annealed samples. However, the impurity from Mn_2O_3 and Li_2MnO_3 still appeared at 700°C. The crystal structure of the spinel $LiMn_2O_4$ belongs to space group *Fd-3m*. It is shown that the Bragg's peaks are getting sharper and higher with increasing temperature due to increasing crystallinity.

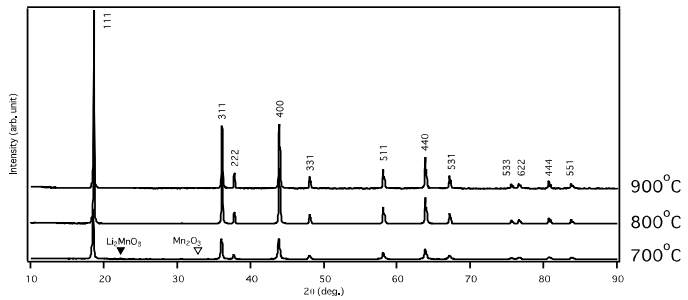


Figure 2. XRD patterns of the spinel-type $LiMn_2O_4$ synthesized with an initial molar ratio of Li/Mn = 0.50 by MA methods for 6 hrs and annealed at 700°C, 800°C and 900°C for 4 hrs in O_2.

3.3. *Crystal Structure by NPD*

In order to obtain detailed information on crystal structure and structural parameters, NPD is indispensable. Figure 3.a-c showed the Rietveld refinement patterns of neutron diffraction data of the spinel samples for various annealing temperatures with the interplanar spacings between 0.5 and 2.6 Å. All the patterns could be indexed using cubic spinel cell with space group *Fd-3m* and is consistent with the results of XRD.

The structural parameters were refined by adopting space group *Fd-3m* origin choice 2 using the model [12]: Li at 8*a* sites (1/8, 1/8, 1/8), Mn at 16*d* sites (1/2, 1/2, 1/2), and O at 32*e* sites (*x*, *x*, *x*) with $x \approx 0.26$. The refinement of the powder refinement data showing Fe and Cr that came from stainless steel jar and balls. Both atoms are positioned in Mn 16*d* sites with occupancies based on the chemical analysis using ICP-AAS [34]. The refinements result of neutron diffraction data at 700°C, 800°C and 900°C are listed in Tables 1, 2 and 3, respectively. The tables list the lattice constant and structural parameters with their estimated standard deviations in parentheses, and final *R* factors. The occupancy of Fe and Cr were fixed during the refinement of the neutron diffraction data for all $LiMn_2O_4$ samples, while the occupancy for Li, Mn, and O were varied. As the result, the occupancy of oxygen was found to be smaller than 1. The effect of annealing temperature to the content of oxygen is shown, where the occupancy of oxygen decreases with increasing annealing temperature. The occupancy of oxygen for the sample annealed at 700°C decreased to 0.9737 as shown in table 1. As the annealing temperature increased to 800°C, more oxygen was lost and the occupancy decreased further to 0.9705 as shown in table 2. Table 3 shows that the lost of oxygen is progressively increased and the occupancy of the oxygen for the sample annealed at 900°C is 0.9700.

The annealing temperature dependence of lattice constant, oxygen occupancy, manganese valence and lithium occupancy of the spinel samples are shown in figures 4.a-d. During refinement, vacancies were found in the oxygen 32*e* site and changed systematically with temperature and thus affected manganese valence in $LiMn_2O_4$ compound. Naturally, the existence of Fe in Mn 16*d* site will increase the Mn valence. The effect of oxygen lost, however, gives more impact and thus, resulted in decreasing of Mn valence. Therefore, it is clear that the oxygen occupancy decreased with increasing annealing temperatures. So that, the manganese valence decreased, while the lattice constant increased. It is related to Mn radius, whereas the radius of Mn^{3+} ion (0.0645 nm) is higher than Mn^{4+} (0.0530 nm). It is also found that lithium occupancy increases with increasing annealing temperature. Figure 4.e. showed the temperature

dependence of Li–O and Mn–O distances of the spinel samples, where both distances increased with temperature. Those can be related to the decreasing of oxygen occupancy and the average manganese valence as shown in figures 4.b-c. The Mn–O distances is related to Mn radius as previously explained. Figure 4.b and 4.e. show the relationship between oxygen occupancy and Li–O distances, where Li–O distances increases with decreasing oxygen occupancy.

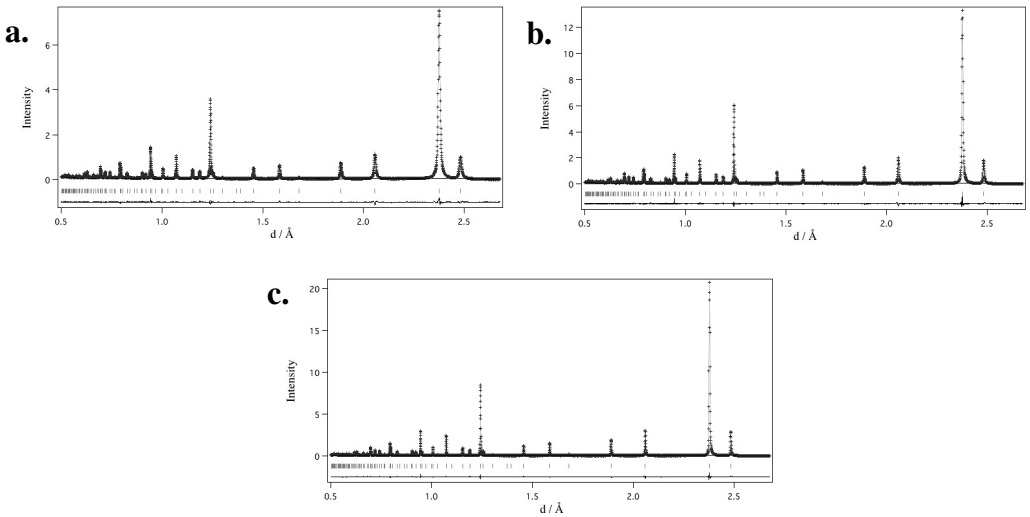


Figure 3. Rietveld refinement patterns of neutron diffraction data for spinel $LiMn_2O_4$ annealed at (a) 700°C, (b) 800°C, and (c) 900°C in O_2 from starting materials $LiOH.H_2O$ and MnO_x and a Li/Mn ratio of 1/2.

Table 1. Rietveld refinement results of spinel $LiMn_2O_4$ annealed at 700°C in O_2.

Atom	site	*g*	*x*	*y*	*z*	*B*/Å^2
Li(1)	8*a*	0.9536(41)	1/8	1/8	1/8	1.000(17)
Mn(1)	16*d*	0.9660	1/2	1/2	1/2	0.718(5)
O(1)	32*e*	0.9737(14)	0.26296(1)	= *x*(O1)	= *x*(O1)	1.153(5)
Fe	16*d*	0.0105	1/2	1/2	1/2	= *B*(Mn1)
Cr	16*d*	0.0017	1/2	1/2	1/2	= *B*(Mn1)
Atom	B_{11}/Å^2	B_{22}/Å^2	B_{33}/Å^2	B_{12}/Å^2	B_{13}/Å^2	B_{23}/Å^2
Li(1)	1.034(27)	= B_{11}(Li1)	= B_{11}(Li1)	0	0	0
Mn(1)	0.727(7)	= B_{11}(Mn1)	= B_{11}(Mn1)	-0.154(6)	= B_{12}(Mn1)	= B_{12}(Mn1)
O(1)	1.158(5)	= B_{11}(O1)	= B_{11}(O1)	-0.283(3)	= B_{12}(O1)	= B_{12}(O1)

Space group *Fd-3m*, a = 8.233316(8) Å, R_{wp} = 4.54, R_p = 3.78, R_e = 2.68, $S = R_{wp}/R_e$ = 1.69, R_B = 1.43, R_F = 3.15

Table 2. Rietveld refinement results of spinel $LiMn_2O_4$ annealed at 800°C in O_2.

Atom	site	*g*	*x*	*y*	*z*	*B*/Å^2
Li(1)	8*a*	0.9723(42)	1/8	1/8	1/8	1.050(17)
Mn(1)	16*d*	0.9627	1/2	1/2	1/2	0.700(5)
O(1)	32*e*	0.9705(14)	0.26296(1)	= *x*(O1)	= *x*(O1)	1.198(5)
Fe	16*d*	0.0139	1/2	1/2	1/2	= *B*(Mn1)
Cr	16*d*	0.0024	1/2	1/2	1/2	= *B*(Mn1)
Atom	B_{11}/Å^2	B_{22}/Å^2	B_{33}/Å^2	B_{12}/Å^2	B_{13}/Å^2	B_{23}/Å^2
Li(1)	1.090(27)	= B_{11}(Li1)	= B_{11}(Li1)	0	0	0
Mn(1)	0.711(7)	= B_{11}(Mn1)	= B_{11}(Mn1)	-0.162(5)	= B_{12}(Mn1)	= B_{12}(Mn1)
O(1)	1.198(5)	= B_{11}(O1)	= B_{11}(O1)	-0.277(3)	= B_{12}(O1)	= B_{12}(O1)

Space group *Fd-3m*, *a* = 8.239790(5) Å, R_{wp} = 4.74, R_p = 4.05, R_e = 3.10, $S = R_{wp}/R_e$ = 1.53, R_B = 1.32, R_F = 3.55

Table 3. Rietveld refinement results of spinel $LiMn_2O_4$ annealed at 900°C in O_2.

Atom	site	*g*	*x*	*y*	*z*	*B*/Å^2
Li(1)	8*a*	0.9845(40)	1/8	1/8	1/8	1.104(15)
Mn(1)	16*d*	0.9676	1/2	1/2	1/2	0.681(4)
O(1)	32*e*	0.9700(13)	0.26296(1)	= *x*(O1)	= *x*(O1)	1.195(4)
Fe	16*d*	0.0107	1/2	1/2	1/2	= *B*(Mn1)
Cr	16*d*	0.0017	1/2	1/2	1/2	= *B*(Mn1)
Atom	B_{11}/Å^2	B_{22}/Å^2	B_{33}/Å^2	B_{12}/Å^2	B_{13}/Å^2	B_{23}/Å^2
Li(1)	1.147(25)	= B_{11}(Li1)	= B_{11}(Li1)	0	0	0
Mn(1)	0.698(7)	= B_{11}(Mn1)	= B_{11}(Mn1)	-0.169(5)	= B_{12}(Mn1)	= B_{12}(Mn1)
O(1)	1.195(5)	= B_{11}(O1)	= B_{11}(O1)	-0.283(3)	= B_{12}(O1)	= B_{12}(O1)

Space group *Fd-3m*, *a* = 8.244564(4) Å, R_{wp} = 4.99, R_p = 4.21, R_e = 3.11, $S = R_{wp}/R_e$ = 1.60, R_B = 1.41, R_F = 4.06

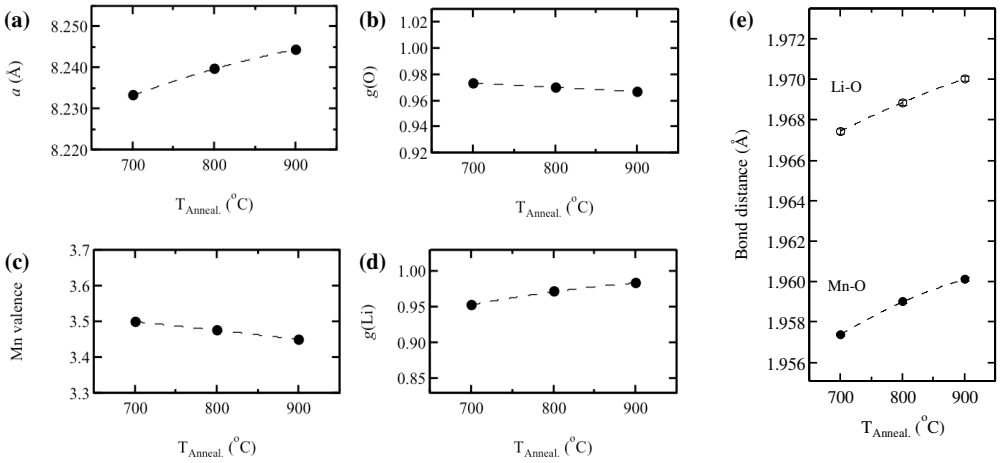


Figure 4. (a) Lattice constant, (b) oxygen occupancy, (c) manganese valence, (d) lithium occupancy, and (e) bond distances (Li–O, Mn–O) as a function of annealing temperature of the spinel-type $LiMn_2O_4$.

3.4. *Electrochemical Performance of the Spinel $LiMn_2O_4$*

The variation of first charge-discharge curves after cycled at 10 mA g^{-1} over the potential range of 2.0 – 4.8 V of the spinel $LiMn_2O_4$ synthesized by MA for 6 hrs and annealed in O_2 for 4 hrs at 700°C, 800°C and 900°C are shown in figure 5.

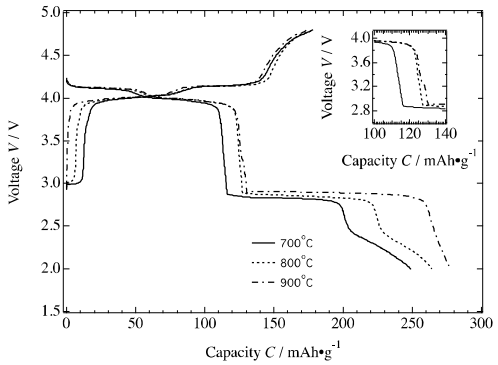


Figure 5. A continuous discharge curves over the potential range of 2.0 – 4.8 V at a constant current density of 10 mA g^{-1} for the Li/1M $LiPF_6$ – EC/DEC solution/porous $LiMn_2O_4$ cells using spinels $LiMn_2O_4$ powder annealed at 700–900°C in O_2.

The discharge capacities and voltage plateaus are increased with increasing temperature. The initial discharge capacity increases from 248.95 mAh g^{-1} to 264.29 mAh g^{-1} and finally to 277.24 mAh g^{-1} and the three voltage plateaus were shifted to higher voltages as the annealing temperature increases from 700°C to 800°C and to 900°C, respectively. In addition, the length of plateau increases with temperature. It is related to the crystallinity of the material and increasing lattice constant *a* with temperature. The lower crystallization of the sample annealed at lower temperature, i.e. 700°C, caused a small coulombic repulsive reaction [35]. In the material with low crystallinity, a number of cation defect is formed which results in disproportion occupancy of tetrahedral and octahedral cation. Therefore, the material annealed at lower temperature has lower discharge potential [36]. The initial discharge capacity increased at 800°C due to higher crystallinity and purity. The initial discharge capacity then increased further for the material annealed at 900°C. However, it is worth noting that a pseudo plateau was occurred at voltage around 3.27 V as shown in the inset of figure 5 related to further intercalation of Li in the stoichiometric $LiMn_2O_4$ spinel and lead to the transformation from cubic $Li[Mn_2]O_4$ to tetragonal $Li_2[Mn_2]O_4$.

4. Conclusion

Spinel $LiMn_2O_4$ powder for cathode material in Li-ion battery have been synthesized by MA method and subsequent annealing at different temperatures. It is found that the initial discharge capacity of the Li-ion battery increased with annealing temperature and reached the highest at 277.24 mAh g^{-1} after annealed at 900°C. It is related to the increasing crystallinity and purity of the spinel $LiMn_2O_4$ as shown by the results from SEM and XRD. The results from NPD showed that lattice constant increased with temperature, related to the increasing crystallinity. Characterization and analyses of the obtained spinel samples showed relationship between annealing temperature and characteristic of the spinel such as crystallinity, composition, structural parameters and electrochemical behavior.

Acknowledgement

T.Y.S.P.P. is grateful for all support kindly provided by MEXT Japan. Valuable discussion and suggestion from the members of Powder Diffraction Group in KEK and J-PARC, from the members of Kanno and Hirayama's Lab., and from Prof. T. Sakuma of Ibaraki University are greatly acknowledged.

References

1. A. Yamada and M. Tanaka, *Mat. Res. Bull.* **30(6)**, 715 (1995).
2. W. T. Jeong, J. H. Joo and K. S. Lee, *J. Alloys and Compounds* **358**, 294 (2003).
3. W. T. Jeong, J. H. Joo and K. S. Lee, *J. Power Sources* **119–121**, 690 (2003).
4. S. H. Ye, J. Y. Lv, X. P. Gao, F. Wu and D. Y. Song, *ElectrochimicaActa* **49**, 1623 (2004).
5. L. J. Ning, Y. P. Wu, S. B. Fang, E. Rahm and R. Holze, *J. Power Sources* **133**, 229 (2004).
6. J-M. Tarascon, M. Morcrette, J. Saint, L. Aymard and R. Janot, *C. R. Chimie* **8**, 17 (2005).
7. A. Yamada, *J. Solid State Chem.* **122**, 160 (1996).
8. A. Yamada, M. Tanaka, K. Tanaka and K. Sekai, *J. Power Sources* **81-82**, 73 (1999).
9. N. V. Kosova, I. P. Asanov, E. T. Devyatkina and E. G. Avvakumov, *J. Solid State Chem.* **146**, 184 (1999).
10. N. V. Kosova, N. F. Uvarov, E. T. Devyatkina and E. G. Avvakumov, *Solid State Ionics* **135**, 107 (2000).
11. N. V. Kosova, E. T. Devyatkina and S. G. Kozlova, *J. Power Sources*, **97-98**, 406 (2001).

12. M. Yonemura, *Synthesis, Crystal Structure, and Physical Properties of Lithium Containing Cathode Materials with the Spinel and Olivine Structure*, Doctoral Thesis, Kobe: Kobe University, (2004).
13. Y. -K. Sun, *Solid State Ionics* **100**, 115 (1997).
14. Y. -K. Sun, I. -H. Oh and K. Y. Kim, *Ind. Eng. Chem. Res.* **36**, 4839 (1997).
15. Y. -K. Sun and I. -H. Oh, *J. Power Sources* **94**, 132 (2001).
16. Y. -K. Sun, S. W. Oh, C. S. Yoon, H. J. Bang, and J. Prakash, *J. Power Sources* **161**, 19 (2006).
17. L. Tao, Q. Weihua, Z. Hailei and L. Jingjing, *Materials Letters* **60**, 1251 (2006).
18. A. S. Wills, N. P. Raju and J. E. Greedan, *Chem. Mater.* **11**, 1510 (1999).
19. X. Q. Yang, X. Sun, M. Balasubramanian, J. McBreen, Y. Xia, T. Sakai and M. Yoshio, *Electrochemical and Solid-State Letters* **4 (8)**, A117-A120 (2001).
20. J-M. Tarascon and D. Guyomard, *Electrochimica Acta* **38: 9**, 1221 (1993).
21. D. Guyomard and J-M. Tarascon, *Solid State Ionics* **69**, 222 (1994).
22. P. Barboux, J-M. Tarascon and F. K. Shokoohi, *J. Solid State Chem.* **94**, 185 (1991).
23. S-W. Jang, H-Y. Lee, K-C. Shin, S.M. Lee, J-K. Lee, S-J. Lee, H-K. Baik and D-S. Rhee, *J. Power Sources* **88**, 274 (2000).
24. X. He, L. Wang, W. Pu, G. Zhang, C. Jiang and C. Wan, *Int. J. Electrochem. Sci.* **1**, 12 (2006).
25. A. Lagashetty, V. Havanoor, S. Basavaraja and A. Venkataraman, *Indian Journal of Chemical Technology* **15**, 41 (2008).
26. M. Helan, L. J. Berchmans, and A. Z. Hussain, *Ionics* **16**, 227 (2010).
27. Y. Xia, H. Takeshige, H. Noguchi and M. Yoshio, *J. Power Sources* **56**, 61 (1995).
28. Y-S. Lee, N. Kumada and M. Yoshio, *J. Power Sources* **96**, 376 (2001).
29. Y-S. Lee, S-J. Cho and M. Yoshio, *Korean J. Chem. Eng.* **23(4)**, 566 (2006).
30. Y. Wei, K. B. Kim, G. Chen and C. W. Park, *Materials Characterization* **59**, 1196 (2008).
31. X. Jin, Z. Hua-li, C. Zhao-yong, P. Zhong-dong and H. Guo-rong, *Trans. Nonferrous Met. Soc. China* **16**, 467 (2006).
32. R. Oishi .et al., *Nuclear Instruments and Methods in Physics Research* A **600**, 94–96 (2009).
33. High Energy Accelerator Research Organization, *User's guide for Z-Rietveld*. Tsukuba: KEK. (2009).
34. Unpublished data.
35. Y. M. Hon, H. Y. Chung, K. Z. Fung and M. H. Hon *J. Solid State Chem.* **160**, 368 (2001).
36. T. F. Yi, C-L. Hao, C-B. Yue, R-S. Zhu and J. Shu, *Synthetic Metals* **159**, 1255 (2009).

Polymer Electrolytes I

OPTIMIZATION OF IODIDE ION CONDUCTIVITY IN ELECTROLYTES FOR DYE SENSITIZED SOLAR CELLS

M.A.K. LAKSHMAN DISSANAYAKE

Institute of Fundamental Studies, Kandy, Sri Lanka &
Department of Physics, University of Peradeniya, Peradeniya, Sri Lanka

Dye sensitized solar cells (DSSCs) based on nanostructured, dye-sensitized titanium dioxide (TiO_2) have attracted worldwide attention as a low cost alternative to conventional silicon cells. These solar cells generally employ an electrolyte with a I^-/I_3^- redox couple and have impressive energy conversion efficiencies reaching around 11% for solvent based cells and around 5% for gel based cells. The iodide ion conductivity contribution to the overall ionic conductivity of the electrolyte in a DSSC is a major factor which determines the short circuit current density (J_{SC}) and hence the efficiency. This is because, the iodide/tri-iodide (I^-/I_3^-) ions, while participating in the redox reaction, also shuttles between the photo-electrode and the counter electrode. Although iodide ion conductivity is an important parameter in determining the short circuit photocurrent and hence the efficiency of DSSCs, not much systematic research work has been reported on this aspect. In several DSSC systems employing polymer gel electrolytes, we have been able to measure the iodide ion transference number and establish a direct correlation between the iodide ion conductivity and the DSSC efficiency. The effect of using a mixed cation iodide having a large and small size cations such as Pr_4NI and KI in optimizing the iodide ion conductivity and the solar cell efficiency with polymer gel electrolytes based on PAN, PMMA, PVdF and PEO have also been established. In these DSSC systems, the variation of efficiency (η) with salt concentration ratio follows the same trend as the J_{SC} which appears to be governed by the iodide ion conductivity of the gel electrolyte.The efficiency has been enhanced by 10-25% due to the mixed cation effect, compared to the cells using only a single cation iodide salt.

1. Introduction

Dye sensitized solar cells (DSSCs) based on nanostructured titanium dioxide (TiO_2) are emerging as a low cost alternative to conventional silicon and thin film photovoltaic solar cells. DSSCs were first reported by Gratzel and co-workers in 1991[1,2,3]. These solar cells generally employ a solvent electrolyte based on acetonitrile and a I^-/I_2 redox couple and have impressive energy conversion efficiencies reaching around 11%. However, a major drawback of these solution based DSSCs is the lack of long-term stability due to liquid leakage, presence of volatile liquids such as acetonitrile, electrode degradation, and photodecomposition of the dye in the solvent medium. In order to overcome these problems, research efforts are being focused on developing quasi-solid state or gel polymer electrolytes [2,3,4] to replace the liquid electrolyte. Polyacrylonitrile (PAN), polymethylmethacrylate (PMMA), poly vinylidenefluoride (PVdF) and also polyethylene oxide (PEO) have been successfully used as host polymers to develop gel polymer electrolytes resulting reasonably high conversion efficiencies around 5 % [4,5,6,7,8,9]. There are many reports on lithium ion (Li^+) conducting quasi-solid state or gel polymer electrolytes based on these host polymers intended for applications in lithium ion

Proceedings of the 14th Asian Conference on Solid State Ionics (ACSSI 2014)
Copyright © 2014 ACSSI 2014 Organizers. All rights reserved.
ISBN: 978-981-09-1137-9
doi:10.3850/978-981-09-1137-9_080

rechargeable batteries [10, 11, 12]. In most of these gel electrolytes, except perhaps, those based on PEO, whether they are cationic (example, Li^+ for batteries) or anionic (example, I^- for DSSCs) conductors, it is generally accepted that the electrolytic solution formed by dissolving the ionic salt in a ethylenecarbonate/propylenecarbonate (EC/PC) co-solvent is "trapped" in cages formed by the PAN or PMMA or PVdF polymer matrix yielding almost liquid like ionic conductivities [8,9,10,13,14,15]. Quaternary ammonium salts such as Pr_4NI, Bu_4NI and Hex_4NI with bulky cations are widely used as iodide salts in these electrolytes because of high ionic dissociation leading to a large number of free iodide (I^-) ions. Although iodide ion conductivity is an important parameter in determining the short circuit photocurrent and the efficiency of DSSCs, not much work has been reported on this subject.

Depending on the ionic size, cations in the electrolyte play a dual role in determining overall efficiency of a DSSC. They influence the short circuit current density through iodide ion conductivity and also influence the charge injection mechanism at the semiconductor/electrolyte interface. Cation size and the charge density is an important factor influencing both these aspects. While bulky cations such as Pr_4N^+ and Hex_4N^+ are expected to contribute much less to the cationic conductivity but enhance the iodide ion conductivity in the electrolyte by providing free iodide ions through ionic dissociation, small size cations with high charge density, such as K^+ , Li^+ or Na^+ are expected to contribute towards better photo-generation of electrons at the dye and faster diffusion dynamics at the dye-semiconductor interface. Therefore, it would be interesting to explore the combined effect of using a binary mixture of two iodide salts consisting of a bulky cation and a small cation in the electrolyte in order to benefit from both above mentioned mechanisms. In this paper, several representative examples of DSSC systems fabricated with polymer gel electrolytes consisting of two iodide salts with two dissimilar cations are discussed.

2. Experimental

Polyacrylonitrile (PAN), polymethylmethacrylate (PMMA) or poly (vinylidenefluoride (PVdF), tetrapropylammonium iodide (Pr_4NI) and polyethylene oxide (PEO) all with purity greater than 98 % purchased from Aldrich and ethylene carbonate (EC), propylene carbonate (PC), iodine chips (I_2), potassium iodide (KI) with purity greater than 98 % purchased from Fluka were used as starting materials. Titanium dioxide powder (TiO_2) (P-25) was purchased from Degussa AG. Fluorine-doped tin oxide glass plates (FTO) (Nippon glass of sheet resistance 10^{-12} Ohm/cm^2) were used as a substrate for

coating TiO_2 paste. Ru dye was purchased from Solaronix SA. All the chemicals except I_2 and PC were vacuum dried at 60 ^oC for 24 hours prior to use.

2.1 Preparation and characterization of the polymer gel electrolytes

In order to prepare the polymer gel electrolyte samples, appropriate weights of the polymer, EC and PC plasticizers and the iodide salts (KI and Pr_4NI) were mixed under constant stirring at 80 ^oC for about 30 min until the components was fully dissolved. Finally the mixture was allowed to cool down to room temperature and I_2 chips were added and again continuously magnetically stirred in a closed bottle overnight (12 hours) to obtain a homogeneous gel electrolyte. The weight of iodine added was taken to be one-tenth of the total mole amount of the iodide salts.

The ionic conductivity of the gel polymer electrolyte samples was determined by the AC complex impedance method with a computer controlled Solatron SI–1260 impedance analyzer or Autolab (PGSTAT 128N) impedance analyzer in the frequency range 20 Hz – 10 MHz. In order to estimate the ionic nature of the gel electrolyte, the dc polarization test was carried out at room temperature by sandwiching the electrolyte sample between two stainless steel blocking electrodes in the SS/electrolyte/SS configuration and applying a small dc voltage of about 1 V and measuring the variation of the resulting current with time. This test was repeated for all the samples by sandwiching them between two iodine non-blocking electrode pellets in the SS/I_2/electrolyte/I_2/SS configuration in order to measure the iodide ion transference number and estimate the iodide ion contribution to ionic conductivity.

2.2 Preparation of the TiO_2 photoanode

TiO_2 paste was prepared by grinding 0.20 g of TiO_2 (Degussa P-25) with 12 drops (about 0.15 g) of glacial acetic acid, one drop (about 0.02 g) of triton X-100 and about 2 ml of ethanol. This paste was spread on a pre-cleaned, fluorine-doped conducting tin oxide (FTO) glass (Nippon sheet glass 10-12 Ω/sq). An active cell area of 0.25 cm^2 was obtained by spreading the paste using the doctor blade technique and sintering at 450 ^oC for 45 minutes. The resulting TiO_2nano-porous film was allowed to cool down to room temperature. Dye absorbance was carried out by immersing the above film in ethanolic dye solution containing Ruthenium dye N719 for 24 hours.

2.3 Fabrication of dye sensitized solar cells and their characterization

The gel polymer electrolyte based dye-sensitized solar cells (DSSCs) of configuration Glass/FTO/TiO_2/Dye/electrolyte/Pt/FTO/glass were fabricated by sandwiching the polymer electrolyte between the dye adsorbed TiO_2 electrode and a platinum (Pt) coated FTO glass. The photocurrent-voltage (*I-V*) characteristics of the cells were measured under the illumination of 100 mW cm^{-2} (AM 1.5) simulated sunlight.

3.0 Results and Discussion

3.1 PAN:EC:PC:$Pr_4N^+I^-$ + x wt% KI, I_2 electrolyte

The DSSCs fabricated with six different composition of this electrolyte with configuration Glass/FTO/TiO_2/Dye/electrolyte/Pt/FTO/glass has been characterized. As shown in Fig. 1, the DSSC with 16.6 % KI + 83.4% Pr_4NI salt ratio exhibits the maximum power conversion efficiency. In the electrolyte, at any given salt concentration, the dissociated K^+ and I^- ions from KI as well as I^- ions from Pr_4NI will make the dominant contribution to the ionic conductivity of the gel electrolyte. The DC polarization curves (not shown), taken with iodine non-blocking electrodes for the gel electrolyte samples with six different compositions clearly show the different iodide ion (I^-) contributions to the overall ionic conductivity in each sample. The dc polarization curves taken with iodine electrodes give an estimate of the contribution to ionic conductivity by I^- ions in the electrolyte, which essentially determines the short circuit photocurrent density of the solar cell. However, the net result of several competing factors, such as the number of dissociated I^- ions and their mobility, the number of K^+ ions and their mobility, the number of Pr_4N^+ ions and their mobility, the number of ionic aggregates and the variation of viscosity of the electrolyte solution with salt concentration ratio appear to give rise to the maximum seen in the short circuit current density (J_{sc}) of the solar cell around 16.6 wt% KI concentration (Fig.1). What is important to realize here is that it is the iodide ion conductivity which essentially determines the short circuit current density of the solar cell. It is interesting to see from Figure 1 that the efficiency variation follows essentially the same variation as J_{sc} and the solar cell fabricated with the binary iodide mixture with 16.6 % (w/w) KI concentration has shown the highest energy conversion efficiency of 5.36 % whereas the solar cells fabricated with the

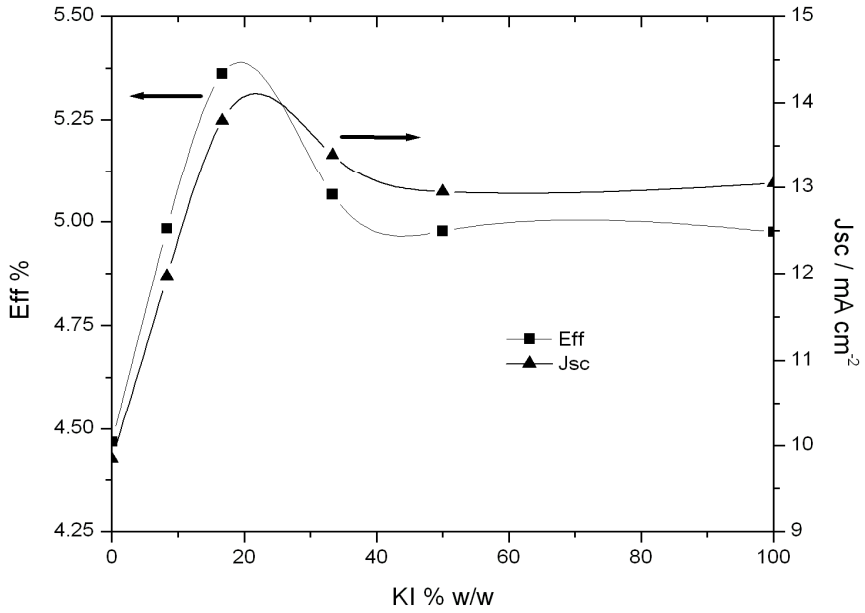


Figure 1. The variation of (a) the efficiency (η) and (b) the short circuit current density (J_{sc}) of all six solar cells as a function of the weight percentage of KI salt in the PAN:EC:PC:$Pr_4N^+I^-$ + x wt% KI, I_2 gel electrolyte

electrolyte having either only KI or only Pr_4NI have shown efficiencies of 4.98 % and 4.47 % respectively. The use of the binary iodide mixture has clearly enhanced the solar cell efficiency by a factor of about 8 %. The dominant contribution to the solar cell efficiency has evidently come from the J_{sc} which is determined essentially by the relative amount of iodide ion conductivity in the gel electrolyte [14].

3.2 PMMA:EC:PC:$Pr_4N^+I^-$ + x wt% KI, I_2 electrolyte

Dye sensitized solar cells made with PMMA based gel polymer electrolyte incorporating the binary iodide salt system consisting of KI and Pr_4NI have been fabricated and characterized similar to the procedure outlined in section 3.1. The variation of efficiency with wt% KI follows a similar variation as the J_{sc} which appears to be governed by the iodide ion conductivity in the electrolyte (Fig.2). This is further supported by the iodide ion transference number estimated from dc polarization data taken with iodine non-blocking electrodes. The dependence of the short circuit photocurrent and the open circuit photovoltage on the cation type of the two end member compositions generally agrees with reported data for

related systems. The maximum efficiency and the maximum in J_{sc} occurs at 22.2 wt% KI concentration. With identical electrolyte compositions, the solar cell with 100 wt% KI showed an efficiency of 3.39 % and the cell with 100 wt% Pr_4NI showed an efficiency of 3.21 %. However, the cell with the mixed iodide system with 22.2 wt% KI + 77.8 wt% Pr_4NI showed the highest efficiency of 3.99 % which corresponds to the maximum in J_{sc} of 10.70 mA cm^{-2}. This is an efficiency enhancement by about 18%.

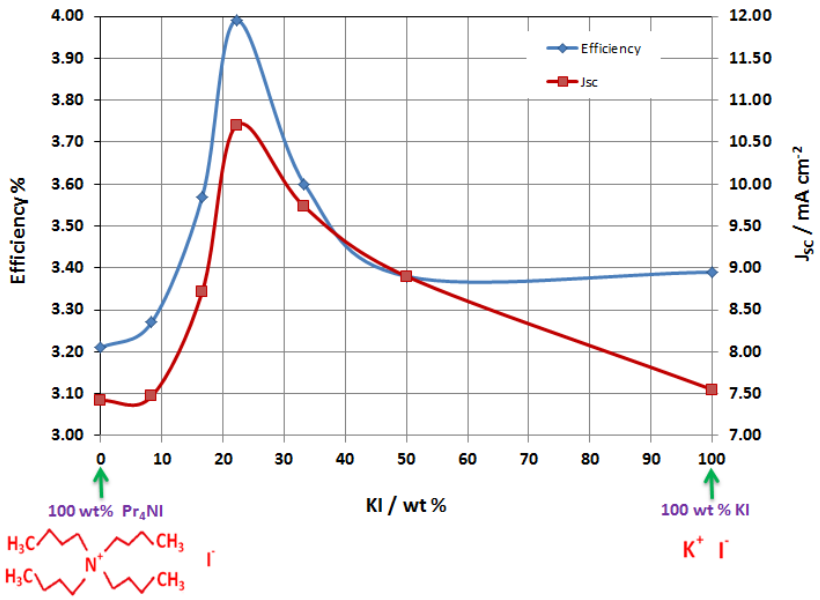


Figure 2: The variation of (a) the efficiency (η) and (b) the short circuit current density (J_{sc}) of all seven solar cells as a function of the wt% KI in the PMMA:EC:PC:$Pr_4N^+I^-$ + x wt% KI, I_2 electrolyte.

.

3.3 PVdF:EC:PC:$Pr_4N^+I^-$ + x wt % KI, I_2 electrolyte

DSSCs have been fabricated with gel polymer electrolytes PVdF:EC:PC:(1-x) $Pr_4N^+I^-$+ x wt% KI, I_2, where x = 0%, 8.3%, 16.6%, 33.3%, 50%, 100% according to the procedure described earlier in section 3.1. They have been characterized with I-V measurements and the results are shown in Fig.3. In this DSSC system, the maximum solar cell efficiency and the maximum J_{sc} occur at the salt ratio 16.6 wt % KI + 83.4 wt% Pr_4NI [15].

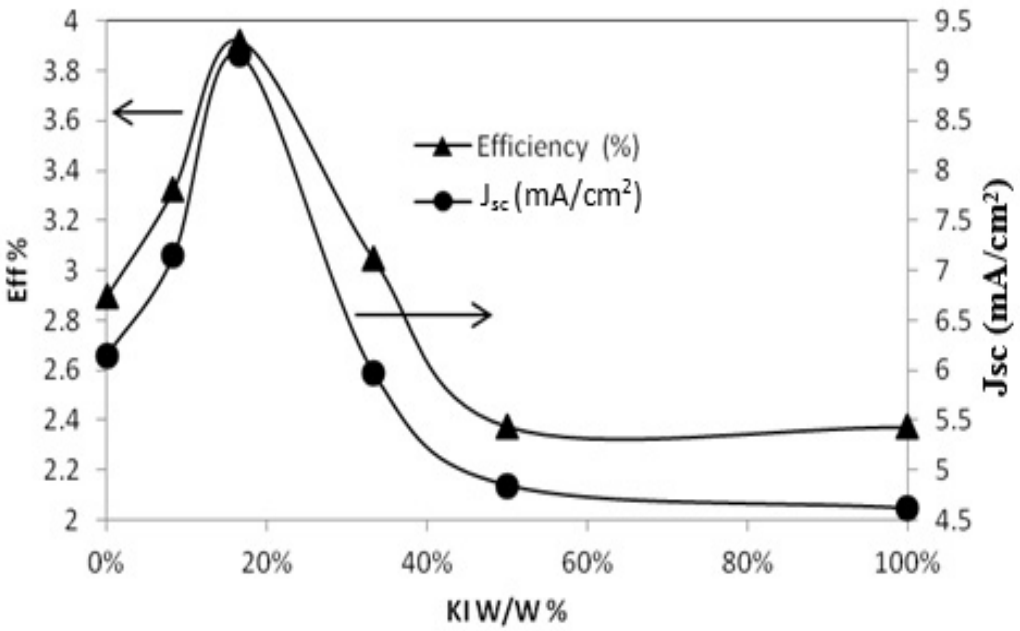


Figure 3. Variation of (a) Efficiency and (b) Short circuit current density of PVdF:EC:PC based dye sensitized solar cells with % wt ratio of KI/ Pr_4NI. The maximum solar cell efficiency and the maximum J_{sc} occurs at the optimum salt ratio 16.6 wt % KI + 83.4 wt% Pr_4NI.

3.4 PEO: PC: $Pr_4N^+I^-$ + x wt.% KI: I_2 gel electrolyte

DC polarization curves taken for the gel electrolyte samples PEO: PC: $Pr_4N^+I^-$ + *x* wt.% KI: I_2 are shown in Figure 4. Top six curves were obtained using I_2 non - blocking electrodes and the top most curve was taken for sample containing 2.5% TiO_2 as a nano filler. These DC polarization test results clearly show the variation of the anionic (iodide ions, I^-) transference number for different electrolyte compositions. Out of the filler free electrolytes, the sample with 75 wt% KI exhibits the highest iodide ion transference number of 0.49. Addition of 2.5 wt% of nano TiO_2 filler to this sample clearly shows a further enhancement in the iodide ion transference number resulting a value of 0.60. It is interesting to note that the variation of iodide ion transference number with salt weight ratio follows the same trend as the variation of the short circuit current density of the corresponding DSSC. Therefore the increase in short circuit current density can be attributed to the increase in iodide ion conductivity in the electrolyte.

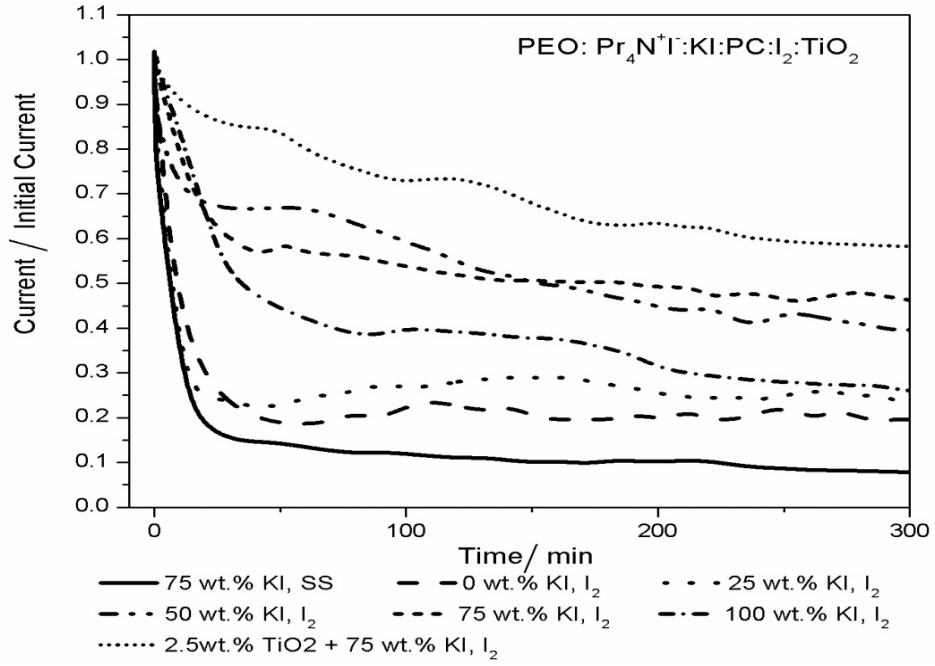


Figure 4: DC polarization curves taken for the gel electrolyte samples PEO: PC: $Pr_4N^+I^-$ + x wt.% KI: I_2. Top six curves were obtained using I_2 non-blocking electrodes. The top most curve was taken for sample H incorporating 2.5% TiO_2. The bottom curve (continuous line) was taken with stainless steel blocking electrodes for sample E.

Figure 5 shows the variation of short circuit photo current density and the efficiency of the solar cells with respect to the amount of KI% in the electrolyte. As can be clearly seen from this figure, the variation of the solar cell efficiency essentially follows the variation of the J_{sc} of the cells. The increase of the J_{sc} could be explained in terms of the enhancement of the iodide ion conductivity (or the iodide ion transference number) of the mixed salt electrolyte and the intercalation of cations into the dyed TiO_2 electrode. As it is well known, the velocity of the random walk of electrons through the nanoporous TiO_2 layer in the photoanode is mainly reduced by the traps in the layer. Small cations like K^+ and Li^+ can intercalate into these traps causing a positive shift in the conduction band leading to an increase in the J_{sc} by increasing the charge injection rate while decreasing the open circuit voltage of the cell. This positive shift caused by the intercalation of cations varies according to the type and the size of the cation used. It is greater for small cations and vice versa. On the other hand, though the positive conduction band shift is smaller for bulky cations, the ionic dissociation is greater and generates free iodide ions. The bulky cations can be considered to be essentially immobile compared to anions. Therefore, while the existence of the two salts with dissimilar cations gives rise to the enhancement in iodide ion conductivity of the electrolyte, it also increases the charge injection

rate and hence the enhancement in the short circuit photo current density and the efficiency of the solar cell.

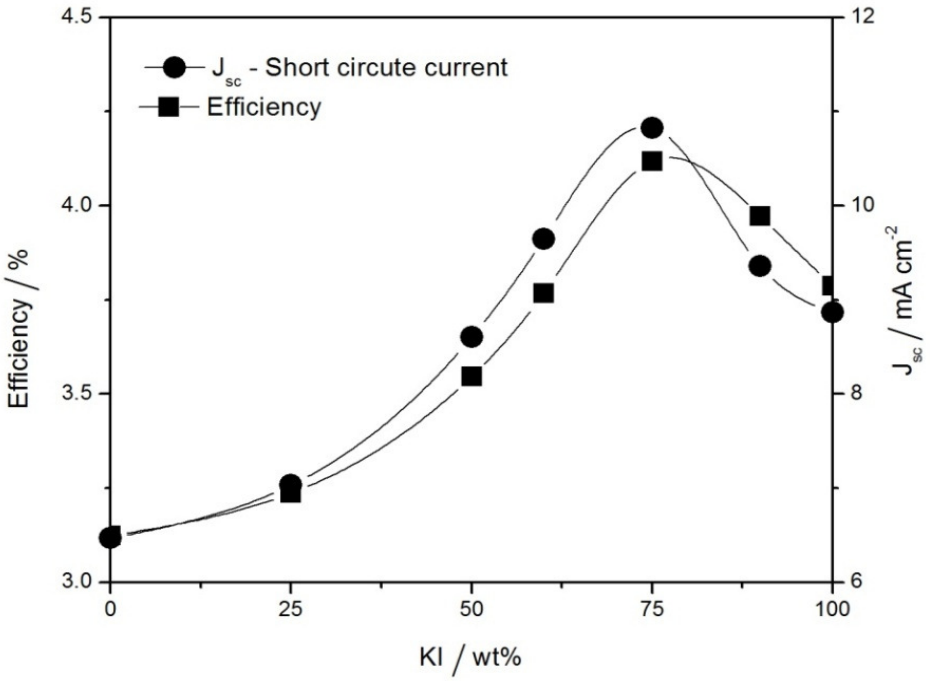


Figure 5: Variation of efficiency and short circuit current density, J_{sc} with respect to the KI wt.% in the electrolyte.

The existence of the two iodide salts with two dissimilar cations have given rise to the enhancement in iodide ion conductivity of the electrolyte at 75 wt% KI +25 wt% Pr_4NI composition. This is evidently caused by the increase in the charge injection rate and hence the short circuit photo current density, resulting an enhancement in the efficiency of the solar cell. On the other hand the reduction of the crystallinity (or enhancement of the amorphous phase content) of the PEO electrolyte with the addition of the TiO_2 nano filler facilitates the anion migration providing another factor contributing to a further enhancement of the J_{sc} and the efficiency.

Acknowledgements

Author wishes to acknowledge with thank the support provided by International Programmes in Physical Sciences (IPPS), Uppsala University, Sweden, Chalmers University of Technology, Gothenburg, Sweden, National Science Foundation (NSF), Sri Lanka, National Research Council (NRC), Sri Lanka, University of Peradeniya and Institute of Fundamental Studies, Sri Lanka.

References

1. B.O. Regan and M. Gratzel ,*Nature.* **353,** 737 (1991).
2. K. Tennakone, G.K.R. Senadeera, V.P.S. Perera, I.R.M. Kottegoda, L.A.A.D. Silva*J. Chem. Mater.* **11,** 2474 (1999).
3. T.M.W.J. Bandara, M.A.K.L. Dissanayake, B.-E.Mellander, *Electrochimica Acta.* **55**, 2044 (2010).
4. O. A. Ileperuma, M. A. K. L. Dissanayake, S. Somasunderam, L. R. A. K. Bandara, *Sol. Energy Mater. Sol. Cells.* **84**, 117 (2004).
5. O. A. Ileperuma, G.R. Asoka Kumara, Hong-Sheng Yang, Kenji Murakami, *J. Photochem and Photobio A: Chem.* **217**, 308 (2011).
6. T.M.W.J. Bandara, M.A.K.L. Dissanayake, I. Albinsson, B.-E.Mellander, *J. Power Sources.* **195**, 3730 (2010).
7. O.A. Ileperuma, M.A.K.L. Dissanayake, S. Somasunderam, *Electrochimica Acta.* **47,** 2801 (2002).
8. O.A. Ileperuma, M.A.K.L. Dissanayake, S. Somasunderam, L.R.A.K. Bandara*J. Sol. Energy Mater. Sol. Cells.* **84,** 117 (2004).
9. O.A. Ileperuma, G.R.A. Kumara, K. Murakami,*Chemistry Letters.* **37(1),** 36 (2008).
10.P.A.R.D. Jayathilaka, M.A.K.L. Dissanayake, I. Albinsson, B.-E.Mellander, *Solid State Ionics.* **156**, 179 (2003).
11. H.M.J.C. Pitawala, M.A.K.L. Dissanayake, V.A. Seneviratne, B.-E. Mellander and I. Albinson, *J Solid State Electrochemistry*. **12,** 783 (2008).
12. H.M.J.C. Pitawala, M.A.K.L. Dissanayake and V.A. Seneviratne, *Solid State Ionics*. **78,** 885 (2007).
13. M.A.K.L. Dissanayake, L.R.A.K. Bandara, R.S.P. Bokalawela, P.A.R.D. Jayathilaka, O.A. Ileperuma and S. Somasunadaram, *Materials Research Bulletin*. **37**, 867 (2002).
14. M.A.K.L. Dissanayake, C.A. Thotawatthage , G.K.R. Senadeera, T.M.W.J. Bandara, W.J.M.J.S.R. Jayasundera and B.-E. Mellander *J Photochemistry & Photobiology: A Chemistry*. **246,** 29 (2012).
15. A.K. Arof, M.F. Aziz, M.M. Noor, M.A. Careem, L.R.A.K. Bandara, C.A. Thotawatthage, W.N.S. Rupasinghe, M.A.K.L. Dissanayake, *Int J Hydrogen Energy.* **39**, 2929 (2014).

FABRICATION OF LITHIUM POLYMER BATTERY BASED ON PVA: PVP: LiX (X=CLO_4^-, NO_3^-) POLYMER BLEND ELECTROLYTE

N. RAJESWARI

Department of Physics, PSR Engineering College, Sivakasi, Tamilnadu – 626140, India

S. SELVASEKARAPANDIAN[1], S. ASATH BAHADUR[2], J. KAWAMURA[3], S. R. S. PRABAHARAN[4]

[1]Materials Research Centre, Coimbatore - 641045, Tamilnadu, India

[2]Department of Physics, Kalasalingam University, Krishnankoil-626126, Tamilnadu, India

[3]Institute of Multidisciplinary Research for Advanced Materials (IMRAM), Tohoku University, Sendai - 980-8577, Japan

[4]VIT University, Chennai - 600127, Tamilnadu, India

Due to the rapid increase in the use of portable devices, there is an increasing demand for larger capacity, small size, light weight and lower priced rechargeable Lithium based batteries such as Lithium Ion Battery (LIB) and Lithium Polymer Battery (LPB). The lithium salts (X) (X=$LiNO_3$ and $LiClO_4$) doped with 70PVA: 30PVP blend polymer electrolyte has been prepared by simple solution casting technique using DMSO as a solvent. XRD studies revealed that the crystallinity of polymer blend have been reduced due to the addition of lithium salts. The conductivity of polymer blend electrolyte is discussed using the results of AC impedance studies. The maximum conductivity has been observed in the order of 6.828×10^{-4} S cm^{-1} and 1.20×10^{-4} S cm^{-1} for the composition of 25Wt% of $LiNO_3$ and 25Wt% of $LiClO_4$ doped with 70PVA:30PVP blend. The temperature-dependent conductivity of the polymer electrolyte follows an Arrhenius relationship, which shows hopping of ions in the polymer matrix. Raman spectroscopy has been used to monitor polymer-salt complex formation, ion-ion and ion-polymer interactions as a function of salt concentration. Li-Polymer battery performance using the new polymer blend electrolyte has been assembled Li/[PVA-PVP+$LiClO_4$] / $LiCoO_2$ and tested. The galvanostatic charge/discharge performance is carried out from 3 to 4.6 V Vs Li^+/Li. The electrochemical stability of the polymer blend electrolyte membrane has been found to be stable up to ~ 4.6V versus Li/Li^+.

Proceedings of the 14th Asian Conference on Solid State Ionics (ACSSI 2014)
Copyright © 2014 ACSSI 2014 Organizers. All rights reserved.
ISBN: 978-981-09-1137-9
doi:10.3850/978-981-09-1137-9_087

1. Introduction

In recent years Li-ion battery is one of the most important power sources because of its higher energy density, shape and design, flexibility, lower-self discharge rate, no memory effect and long life span. Lithium polymer battery technology is regarded as advanced batteries due to their distinct properties like mouldability in various physical shapes, light weight, good electrode-electrolyte contact and favorable mechanical properties [1, 2]. Among the various types of polymer electrolyte systems used in lithium polymer batteries, solid polymer electrolytes (SPEs) have many advantages such as high ionic conductivity, high-energy density, leak proof, solvent-free condition, wide electrochemical stability windows, easy processability and light weight. Till now different polymers, such as PAN [3], PMMA and PVdF, were studied with these advantages in mind. Biodegradable polymers have received an upsurge of interest nowadays in replacing those environmentally unfriendly polymers. Among biodegradable synthetic polymers, Poly (Vinyl alcohol) and Poly (Vinyl pyrrolidone) offers good mechanical stability, environmental friendliness and easy film formation. Among the various lithium salts, $LiNO_3$, $LiClO_4$ possess high conductivity as well as high anodic stability, less hygroscopicity, stable to ambient moisture and low lattice energy which can result in better dissolution resulting in the generation of more free ions. In the present study, lithium ion conducting polymer blend electrolytes which is composed of PVA and PVP polymers has been prepared and also examined the structural, vibrational, electrolytic conductivity and electrochemical properties. Finally, Li-Polymer battery performance using the new polymer blend electrolyte has been assembled Li/[PVA-PVP+$LiClO_4$] / $LiCoO_2$ and tested.

2. Experimental Techniques

The polymer blend electrolyte comprising of Poly (Vinylalcohol) (PVA) -Poly (Vinylpyrrolidone) (PVP) as a host polymers and $LiNO_3$ & $LiClO_4$ as the salts has been prepared by solution casting technique using Dimethyl Sulphoxide (DMSO) as solvent. The X-ray diffraction patterns of polymer electrolytes have been recorded employing a PANalytical Xpert Pro. The Ionic conductivity study of the polymer electrolytes has been carried out in the temperature range of 303-373K over a frequency range of 42Hz- 1MHz using a computer interfaced HIOKI 3532 LCR meter. The complex formation between the polymer and salt was characterized using Nano finder 30 SOLAR TII Laser Raman spectroscopy. The Li polymer cells were assembled by sandwiching the polymer blend electrolyte membrane between the cathode $LiCoO_2$ and lithium metal anode. Cathode is prepared by spreading a mixture of active electrode material, $LiCoO_2$, 85Wt%, Conductive carbon (L6) 10Wt%, binder (PVdF) 5Wt% and coated onto a special Al foil. The galvanostatic charge/discharge performance is carried out from 3 to

4.6 V Vs Li^+/Li. (SP-150 Potentiostat/Galvanostat (BioLogic Science Instruments) equipped with EC-Lab® Express software, Japan).

3. Results and discussion

3.1. *X-ray diffraction analysis*

Fig 1 and 2 represents the XRD patterns for 70PVA-30PVP blend and 70PVA-30PVP: X $LiNO_3$ (X = 5Wt%, 10Wt%, 15Wt%, 20Wt%, 25Wt%, 30Wt% and 35Wt% $LiNO_3$) and 70PVA:30PVP: X $LiClO_4$ (X = 5Wt%, 15Wt%, 25Wt% and 35Wt % $LiClO_4$) polymer blend electrolytes. It is observed from the fig 1 and 2 that the diffraction peaks of 70PVA:30PVP blend decrease in intensity and their broadness increase with increase of lithium nitrate and lithium Perchlorate salts. This may be due to the increase of the amorphous nature of the 70PVA:30PVP blend with the addition of the $LiNO_3$ and $LiClO_4$ salt.

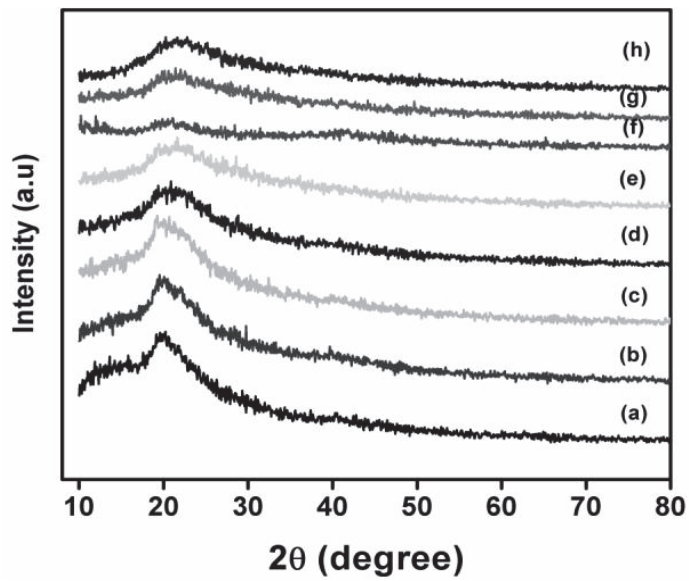


Figure 1 XRD pattern of (a) 70PVA:30PVP (b) 70PVA:30PVP:5Wt% $LiNO_3$ (c) 70PVA:30PVP:10Wt% $LiNO_3$ (d) 70PVA:30PVP:15Wt% $LiNO_3$ (e) 70PVA: 30PVP:20Wt% $LiNO_3$ (f) 70PVA:30PVP:25Wt% $LiNO_3$ (g) 70PVA:30PVP:30Wt% $LiNO_3$ (h) 70PVA:30PVP:35Wt% $LiNO_3$ polymer blend electrolyte

None of the peaks pertaining to $LiNO_3$ and $LiClO_4$ salt appear in the XRD pattern of polymer blend electrolyte, indicating the complete dissociation of the salts in the polymers matrix. The maximum amorphous nature has been observed for the sample 70PVA:30PVP: 25Wt% $LiClO_4$ and 70PVA:30PVP:25Wt% $LiNO_3$.

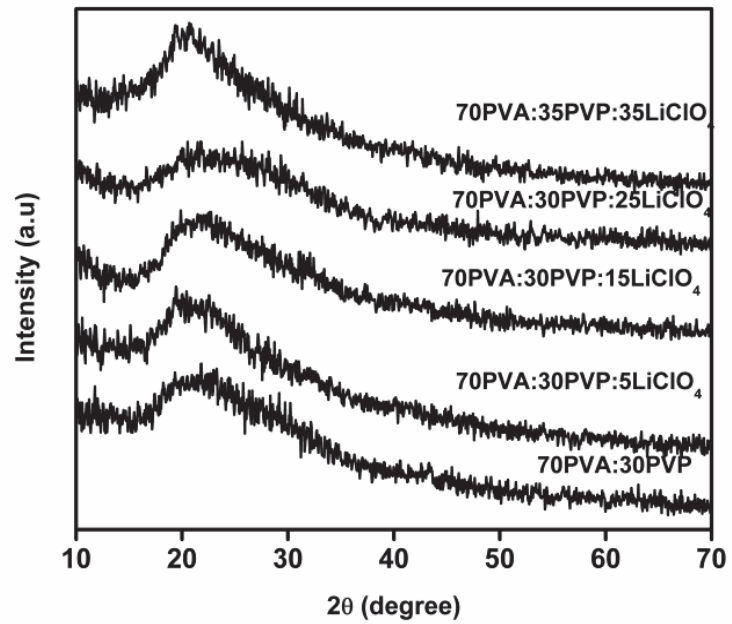


Figure 2.XRD pattern of 70PVA: 30PVP blend with different Wt% of $LiClO_4$ polymer blend electrolyte

3.2. *Ac Impedance Analysis*

The typical plots between log ω Vs log σ of the polymer blend electrolyte 70PVA:30PVP:X $LiNO_3$ (X = 5Wt%, 10Wt%, 15Wt%, 20 Wt%, 25 Wt%, 30Wt% and 35 Wt% $LiNO_3$) at 303K and 70PVA:30PVP:25Wt%$LiNO_3$ polymer blend electrolyte at different temperatures have been shown in Fig 3 and 4. The plots show three well defined regions, a low frequency dispersion region relating to the blocking of ions between the electrodes and the electrolyte, frequency independent plateau region in the mid frequency which is related to the bulk conductivity and dispersion at the high frequency obeying the power law $A\omega^n$. The conductivity σ (ω) obeys the jonscher's power law [4] and it is found to vary with angular frequency ω.

$$\sigma(\omega) = \sigma_{dc} + A\omega^n$$

Where σ_{dc} is the DC conductivity, A and n is temperature dependent parameters. The DC conductivity values have been calculated by the extrapolation of the plateau region to zero frequency. The highest conductivity 6.82×10^{-4} S cm^{-1} and 1.20×10^{-4}S cm^{-1} has been observed for the compositions of 70PVA:30PVP:25Wt % $LiNO_3$ and 70PVA:30PVP:25Wt % $LiClO_4$.

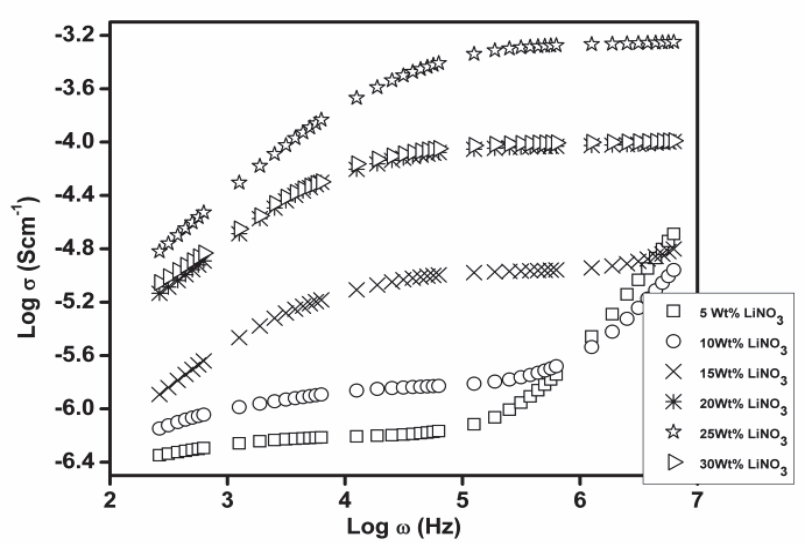


Figure 3.Conductance spectra of different Wt% of lithium nitrate doped with 70PVA:30PVP polymer blend electrolyte

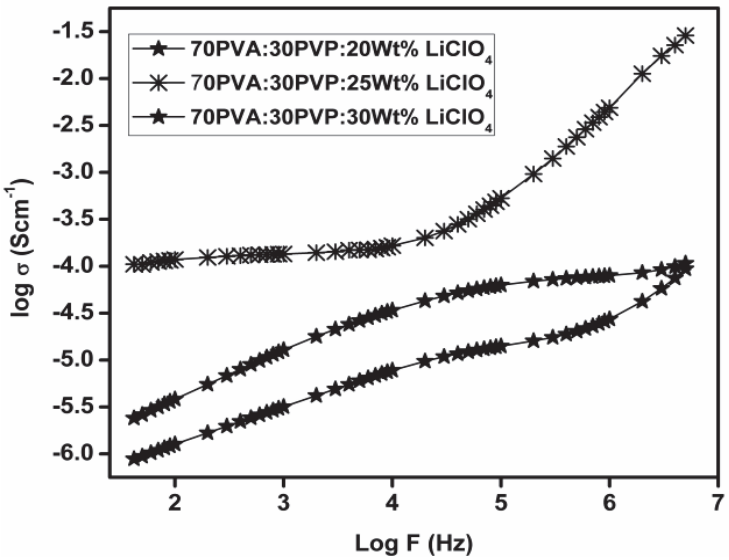


Figure 4.Conductance spectra of different Wt% $LiClO_4$ doped with 70PVA:30PVP polymer blend electrolyte

Fig 5 & 6 shows that the conductivity increases linearly with increases temperature for different Wt% $LiClO_4$ and $LiNO_3$ doped with 70PVA:30PVP blend. The regression values of the plots using a linear fit have been found to be close

to unity suggesting that the temperature dependence Ionic conductivity for all the composition obeys Arrhenius relation

$$\sigma = \sigma_o \exp(-E_a/KT)$$

Where σ_o is related to the number of charge carriers in the films and E_a is related to the activation energy of ion transport associated with the configurational entropy of the polymer chains and K is the Boltzmann constant. The low activation energy (0.38 eV) and (0.267 eV) has been observed in the high conductivity composition of 70PVA:30PVP:25Wt%$LiClO_4$ and 70PVA:30PVP:25Wt%$LiNO_3$.

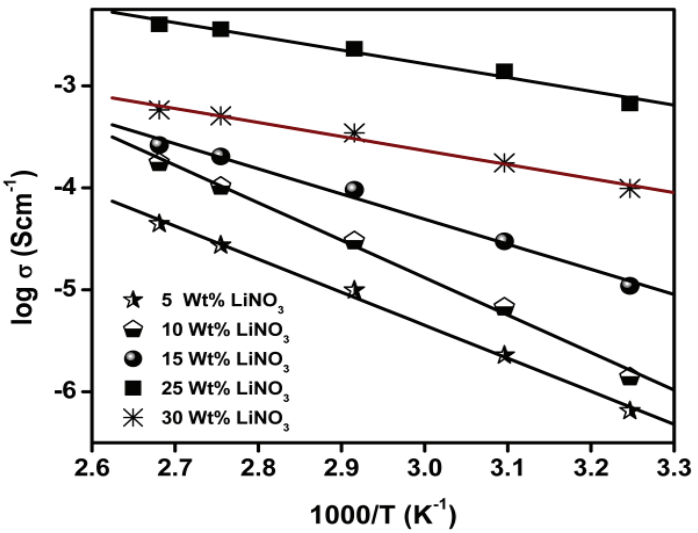


Figure 5. 1000/T Vs log σ for 70PVA:30PVP polymer blend with different concentration of $LiNO_3$

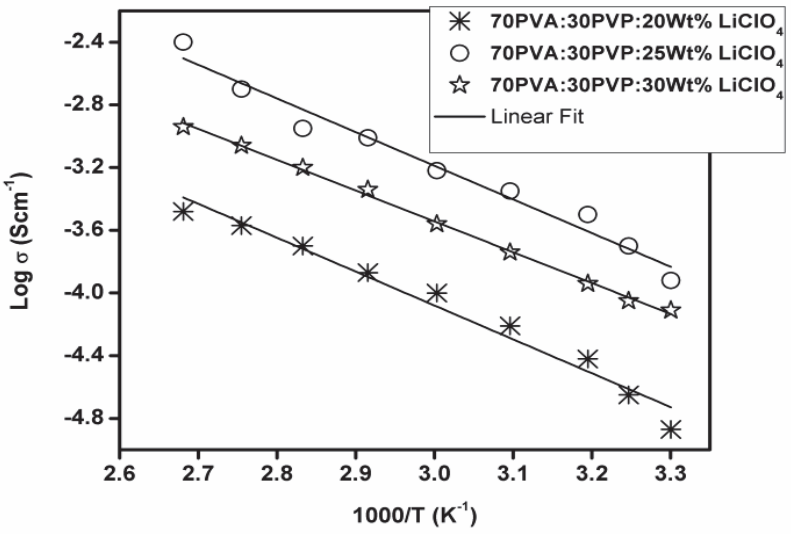


Figure 6. 1000/T Vs log σ for 70PVA:30PVP polymer blend with different concentration of $LiClO_4$

3.3. *Laser Raman Analysis*

Fig 7 and 8 represents the Raman spectra of 70PVA:30PVP blend and 70PVA:30PVP blend with different Wt% of $LiNO_3$ and $LiClO_4$ in the region 0-3500cm^{-1}. The bands at 923 cm^{-1}, 1289 cm^{-1}, 1421 cm^{-1} and 2923 cm^{-1} have been assigned to C-C stretching, C-H bending, OH bending and C-H stretching of pure PVA respectively. The bands at 748 cm^{-1}, 844 cm^{-1}, 1225 cm^{-1}, 1654 cm^{-1} and 2923 cm^{-1} of pure PVP respectively. The above mentioned PVA and PVP peaks get shifted when $LiNO_3$ salt doped in the 70PVA:30PVP polymer blend electrolyte.

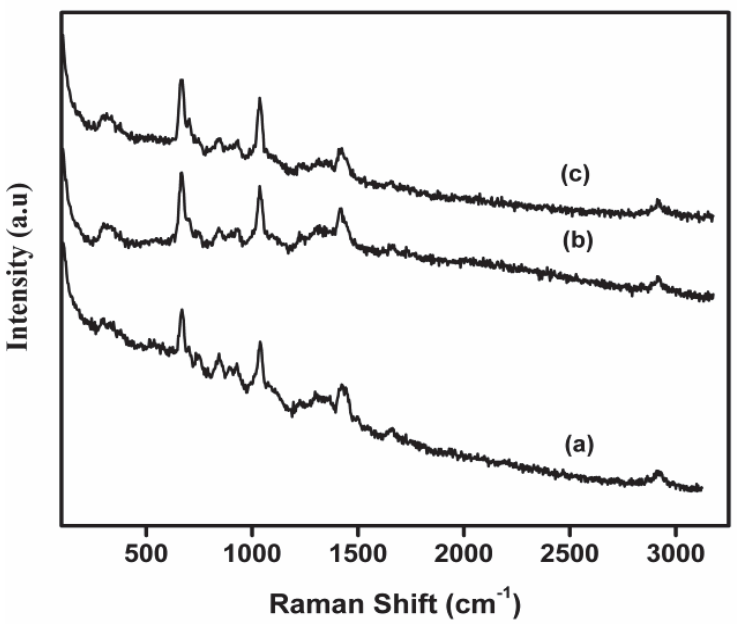


Fig.7 Raman spectra of (a) 70PVA:30PVP: 15Wt% $LiNO_3$ (b) 70PVA:30PVP: 25Wt% $LiNO_3$ (c) 70PVA:30PVP: 35Wt% $LiNO_3$ films

The four Raman Vibrational modes of Perchlorate anions have been clearly observed at around 449cm^{-1}, 663cm^{-1}, 922cm^{-1} and 1017cm^{-1} in the polymer blend electrolyte. These peaks correspond to the Vibrational modes of Perchlorate anions, assigned to the ν2 (ClO_4^-), ν4 (ClO_4^-), ν1 (ClO_4^-) and ν3 (ClO_4^-) respectively. The Raman spectra for the $LiClO_4$ doped with 70PVA:30PVP polymer blend electrolyte shows a most intense peak at 922cm^{-1} which corresponds to the symmetric stretching mode (ν1) of the (ClO_4^-) anion

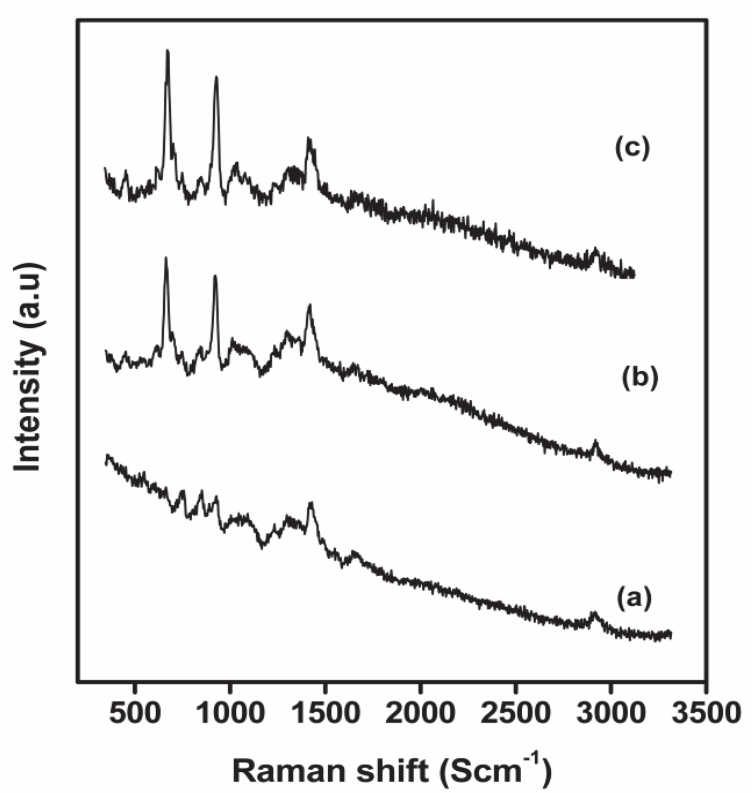


Fig. 8 Raman spectra of (a) 70PVA: 30PVP, (b) 70PVA: 30PVP: 25Wt%$LiClO_4$, (c) 70PVA: 30PVP: 35Wt%$LiClO_4$ polymer blend electrolyte

3.4. *Electrochemical Performance*

As-fabricated lithium polymer cell shown is allowed to equilibrate for 30 min and the OCV has been measured to be 3.01 V. The cell has been cycled galvanostatically at 10 μA and the electrochemical performance is shown in Fig 9. As depicted, the charging curve (plateau potential) indicates that Li^+ deintercalation occurs at the cathode side from the $LiCoO_2$ according to the below reaction:

$$Li_{1-x}CoO_2 + x\,Li^+ + xe^- \rightarrow xLi^+ + xe^- + Li^o$$

The removed Li^+ during the charging process is deposited/plated onto Li anode electrochemically. Similarly, on discharge, a charge plateau occurs near ~3.6 V vs. Li/Li^+ indicative of the intercalation of Li^+ into $LiCoO_2$. This process repeats as the cycle continues. This clearly indicates that the developed polymer blend electrolyte facilitates the Li^+ transport across it between the cathode and the anode.

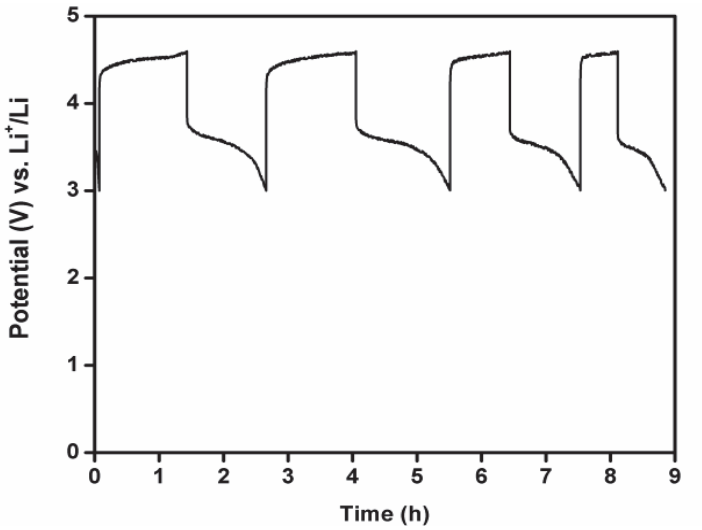


Fig 9 Typical galvanostatic cycling of the pouch type cell for 4 charge/discharge cycles.

4. Conclusion

Polymer blend electrolytes consisting of PVA and PVP blend with different Wt% of $LiNO_3$ and $LiClO_4$ have been prepared by solution casting method. The amorphous nature has been confirmed from the XRD. Raman spectroscopy has been used to monitor polymer-salt complex formation, ion-ion and ion-polymer interactions as a function of salt concentration. The room temperature electrolytic conductivity of the order of 10^{-4} S cm^{-1} with low activation energies for the composition of 70PVA:30PVP:25Wt%$LiClO_4$ and 70PVA:30PVP:25Wt%$LiNO_3$ has been observed from the Ac Impedance spectroscopy analysis. The temperature dependence of Ionic conductivity of these electrolytes exhibited Arrhenius behavior. 70PVA:30PVP:25Wt% $LiClO_4$ polymer blend electrolyte has been used in the fabrication of Lithium Polymer battery with the configuration of Li (metal foil) /SPE/$LiCoO_2$. The open circuit voltage (OCV) 3.01V has been observed and the cycling performance of the pouch cell has been studied.

References

1. F. M. Gray, VCH, New York (1991).
2. J. R. Maccallum, C. A. Vincent (Eds) Vol. 1 and 2, Elsevier, Applied Sciences Publisher, London, (1987 & 1989)

3. I. E. Kelly, J. R. Owen, B. C. H. Steele, *J. Power Sources* 14, 13 (1985).
4. A. K. Jonscher *Nature*, 267, 5613, 673-679 (1977).

EXPERIMENTAL STUDIES ON BLEND BASED POLYMER GEL ELECTROLYTE CONTAINING NANOFILLER (PVA: PVK): CH_3COONH_4: EC: SiO_2 SYSTEM

R.P. KUMHAR[ac]

[a]*Department of Physics, Govt. Maharaja College, Chhatarpur (M.P.) India*

NEELESH RAI[bc]

[b]*Department of Physics, AKS University, Satna (M.P.) India*

S.L. AGRAWAL[c]

[c]*SSI Laboratory Department of Physics, APS University, Rewa (M.P.) India*

The present work has been pursued with the aim to develop a proton conducting nanocompositepolymer gelelectrolyte namely,(PVA: PVK): CH_3COONH_4: EC: SiO_2system. All the electrolytes films have been characterized by structural, electrical and cyclic voltametric measurements. The XRD patterns affirm improvement in amorphous nature besides showing better compatibility among polymer components in the presence of salt.FTIR spectral studies have shown formation of blend and as well as their polymer gel electrolyte soaked with nano filler. The ionic conductivity of nanocomposite polymer gel electrolyte improves moderately (~5 times) at room temperature with an optimum of 5×10^{-3} S/cm for 6 wt% SiO_2. The temperature dependent conductivity analysis shows that ion conduction is controlled by combination of Arrhennious and VTF behavior.

1. Introduction

With the emergence of different electronic applications and technologies there is an exclusive demand for long life, environment friendly, low cost, reliable rechargeable batteries with specific energy power. Polymer electrolytes are materials of great importance for applications in such electro-chemical devices but relatively poor ionic conductivity limits their utility. The conductivity of these electrolytes is confined mostly in amorphous phase while the crystalline phases are considered as poor conductivity phase [1-3]. Thus over the years, attempts have been made to improve the amorphous phase of polymer electrolyte. Introduction of plasticizers in small amounts [2], polymer blending

Proceedings of the 14th Asian Conference on Solid State Ionics (ACSSI 2014)
Copyright © 2014 ACSSI 2014 Organizers. All rights reserved.
ISBN: 978-981-09-1137-9
doi:10.3850/978-981-09-1137-9_139

[4], use of comb- branched copolymer [5], cross- linking of polymer matrices [2] and incorporation of inorganic fillers [6] are some of the alternative ways that have been adopted to improve the ionic conductivity of polymer electrolytes in recent years. In addition, development of polymer gel electrolytes is yet another option which have been explored in the last two decades for various electrochemical devices [7-8]. Literature survey shows that most of the work on polymer gel electrolytes concerns development of lithium- based polymer batteries [8-10]. Among the different ionic conductors, proton conducting electrolytes have also attracted scientist a great deal because of their potential use in clean energy devices such as fuel cell, electrochromic devices (ECDs) and other smart devices [11]. However there are limited reports on proton conducting polymer gel electrolytes [8, 12-14]. Blending of polymers is yet another attractive approach that has been recently to develop blend based polymer gel electrolytes [15, 16]. Following this approach Agrawal and Kumhar [17] have recently reported a PVA: PVK blend based electrolytewith conductivities attainable to an extent of 10^{-3} S/cm using Ammonium Acetate salt. Despite improvement in electrical properties, all these polymer gel electrolyte system usually suffer from poor dimensional, mechanical stabilities and exudation of liquid from gel lump when retained for a long period. This has eluded their practical utility in devices. In recent times, dispersion of inorganic nano sized filler, in pristine polymer electrolytes [18] and in blend based solid polymer electrolytes [19] have been effectively tried to overcome these problems to a great extent leading to formation of nanocomposite polymer electrolytes. Prompted by these consideration, an attempt has been made in the present work to improve the performance of (PVA: PVK): CH_3COONH_4: EC gel electrolyte system through dispersal of sol gel derived nano- sized SiO_2. This system is expected to drastically impede crystallization process in polymer blend based nanocomposite electrolytes and thus improve ionic conductivity. To establish this view point, the synthesized electrolytes have been through XRD, FTIR, Optical Microscopy and electrical measurements.

2. Experimental

PVA (average molecular weight 124,000- 186,000 Aldrich make), PVK (average molecular weight 40,000 Aldrich make), ammonium acetate (CH_3COONH_4), AR grade sd fine chem.and aprotic solvent dimethyl sulphoxide (DMSO) merk limited, were used for the synthesis of nanocompositepolymer electrolyte. For the preparation of nanocomposite electrolytes firstly both polymers PVA and PVK were dissolved in DMSO in the ratio of {(PVA: PVK) 90:10} and stirred for 3 h at 50^0C to obtain homogeneous mixture. In the next step, an appropriate quantity of ammonium acetate (CH_3COONH_4) salt dissolved in EC (Aldrich

make) was added in stoichiometric proportion to the above mixture and stirred further for 2h. Finally, sol gel derived SiO_2nano filler was admixed in different wt% and stirred for another 2 to 3h. The final geletanous solution was poured in poly carbonate pettri dish to obtain thick films of nanocomposite electrolyte system. Silicon oxide (SiO_2) filler used in present work was synthesized by standard sol-gel technique described elsewhere [20, 21]. XRD patterns of nanofiller and gel electrolyte system were obtained on RIGAKU JAPAN MINIFLEX-II in the range $2\theta = 5^0$ to 70^0 ($\lambda = 1.5406$ Å). FTIR spectra were recorded on Nicolet iS10 spectrometer in the range 4000- 500 $cm^{-1}$to evaluate interaction among components. Morphological behavior of as synthesized composite films was studied using optical polarizing microscope (Carl Ziess-Germany model). C-V and I-t measurements were performed on a CH-electrochemical workstation (CH instruments model CH608) to determine electrochemical window and nature of charge transport. Electrical characterization of the material was carried out using impedance spectroscopy technique. Complex impedance parameters were measured with a Hioki impedance analyzer (model 3520) in the frequency range 40 Hz- 100 KHz using platinum electrodes for electrical contact at different temperatures.

3. Results & Discussion

3.1 XRD Study

Figure 1 depicts the XRD pattern of blend based polymer gel electrolyte films of (PVA: PVK): CH_3COONH_4: EC without and with SiO_2nanofillersalongwith pristine components. One peak around $2\theta = 19.6^0$ in XRD pattern of DMSO casted PVA (pattern a) is seen and it conforms to earlier reported values [15, 22]. Likewise a relatively sharp characteristic XRD peak at $2\theta = 22.1^0$ and a broad peak around 16.7^0(pattern b)closely matches with the peaks reported for PVK [23]. The slight deviations in characteristic reflection of PVK are possibly due to variation in solvent swollen nature of PVK in different organic solvents. XRD pattern of as synthesized SiO_2nanofiller particles showing prominent XRD peak at $2\theta = 26.6^0$ (pattern c)too conform to earlier reported results [21]. When the polymer components are admixed together to form PVA:PVK (90:10 ratio)blend the low intensity diffraction peaks appear at 2θ values 19.45^0, 19.76^0 and 20.6^0 while high intensity characteristic reflection is noticed around 24.23^0(pattern d). These diffraction maxima occur on account of interaction among components/ intercalation of PVK in PVA leading to formation of a new material viz polymer blend. It is worthwhile to mention here that few low intensity peaks are not clearly visible on account of merging of different pattern in a single figure. The presence of 19.45^0 and 19.76^0 can be correlated to

existence of unreacted PVA in the blend. The remaining peaks can be correlated to formation of PVA: PVK blend as they do not correspond to the reflection of pristine materials.Upon addition of salt CH_3COONH_4 (pattern e) the XRD peaks at 16.7^0related to PVK retraces towards lower 2θ value. On the other hand, the PVA related peak intensity diminishes. Also diffraction peak related to PVA: PVK: DMSO system at 24.2^0 intensifies owing to enhanced compatibility in the presence of added salt. Recently, PVA has been shown to complex with ammonium salts leading to formation of polymer gel electrolyte [13, 22& 24]. On the same lines it can be argued that ammonium acetate form complex with linkage at the OH group of PVA.

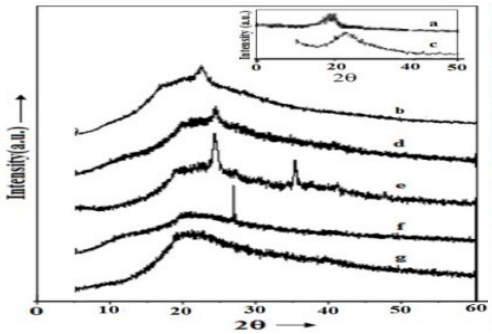


Figure 1. X- raydiffractograms of DMSO casted (b) PVK, (d) PVA: PVK and PVA: PVK: CH_3COONH_4:EC nanocomposite electrolyte containing (e) 0, (f) 6 and (g) 8 wt% SiO_2. Inset shows XRD of (a)DMSO casted PVA and (c) SiO_2.

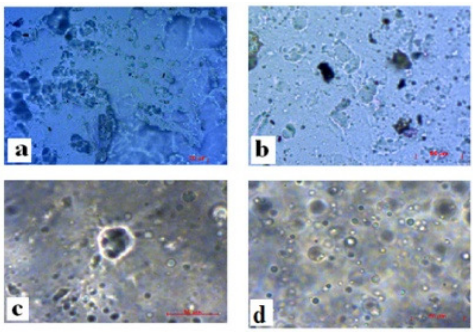


Figure 2. Optical Micrographs of DMSO casted (a) PVA: PVK, (b)PVA:PVK : CH_3COONH_4: EC electrolytes and its composite containing (c) 2 wt% and(d) 8 wt% SiO_2 filler.

In addition to the XRD peaks appearing at 16.7^0 and 24.2^0 few other peaks around 26.9^0, 27.2^0, 30.6^0, 35.2^0, 35.7^0, 41.1^0 and 47.6^0 appear in XRD pattern of polymer gel electrolyte. Since none of these peaks are assignable neither salt nor host polymers it is conjectured that complex formation takes place in electrolyte system.Upon addition of nanofillerSiO_2(pattern f) all the existing peaks are suppressed with increase in broadening of primary peak except the appearance of a strong sharp peak at 2θ= 26.6^0.This peak corresponds to characteristic peak of SiO_2 according to JCPDS data and also recorded in the experiment (pattern c). This observation supports the role of SiO_2 as that of passive filler in electrolyte with only improving the morphology of electrolyte system. Due to coverage of SiO_2 particles by matrix electrolyte at higher concentration of SiO_2 characteristic reflections of nanofiller could not be tracked.

3.2 Optical Microscopy

Optical micrographs of PVA: PVK, (PVA: PVK): CH_3COONH_4: EC electrolyte and composite system containing 2 and 8 wt% SiO_2 filler are shown in figure 2. In figure 2a the optical image of DMSO casted PVA: PVK film the dark regions indicate the presence of porous structure. Distribution in pore size reflects relatively poor solvent retention capability in PVA: PVK blend. Further rough surface morphology exhibits poor compatibility among polymers. The morphology of film seems to smoothen out upon introduction of salt to form blend based electrolyte. Also the pores of small dimension were observed in optical images with relatively homogeneous distribution of pores. This supports better solvent retention capability of electrolyte system. It seems that there exists better compatibility among polymer components in the presence of salt (figure 2b). Upon addition of SiO_2 filler the nanoparticles are trapped within the pores as reflected from bright regions within the pores (figure 2c). Due to nano size of filler particles, the porous region of electrolyte is capable of holding agglomerates of nanofillers. This enhances the possibility of trapping of liquid electrolyte and thus overall electrical conductivity.

3.1 FTIR studies

Figure 3 shows the FTIR spectra of PVA: PVK blend, blend based electrolyte and their nanocomposite polymer electrolyte loaded with different composition of nanofiller. In an earlier work on PVA: PVK: DMSO: CH_3COONH_4 system [17] it has been shown that PVA: PVK: DMSO blend show poor compatibility and which improves subsequent to salt addition. Comparison of IR data in the higher wave number regime do not show any significant shift in CH_3 symmetric and CH symmetric vibration upon addition of SiO_2 nanoparticles except change in intensity values.

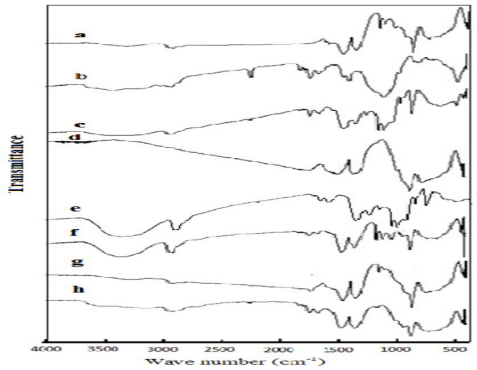


Figure 3.IR spectra of DMSO casted (a) PVA, (b) PVK, (c) PVA: PVK, and PVA: PVK: CH_3COONH_4: EC containing (d) 0, (e) 2, (f) 4, (g) 6 and (h) 8 wt% SiO_2 filler.

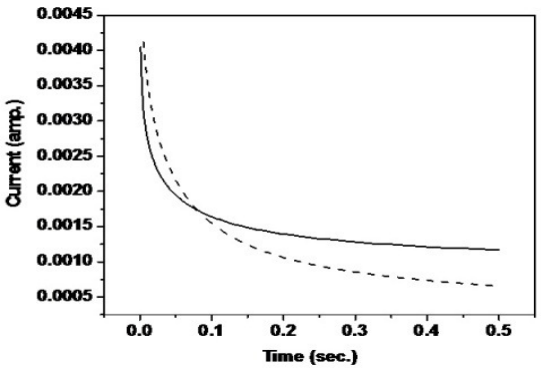


Figure 4. I-t Polarization curve of DMSO casted PVA: PVK: CH_3COONH_4: EC (solid line) 0 and (---) 6 wt% SiO_2.

The peak around 2241 cm^{-1} related to C-N stretch vibration in PVK shows a shift to higher wave number (2357 cm^{-1}) in blend based electrolyte system to indicate interaction in the presence of salt. This absorption peak is seen to decay in intensity and vanish before reimerging in electrolytes soaked with 6 wt% SiO_2. CH_3, $>CH_2$ deformation vibration observed in PVA at 1450 cm^{-1}, in PVK at 1456 cm^{-1} and in blended electrolyte at 1458 cm^{-1} shift to lower wave number upon addition of nano particles (1448 cm^{-1}, 1447 cm^{-1}) till 4 wt% SiO_2 and subsequently retraces to the vibration frequencies of blended electrolyte as a consequence of enhanced interaction among PVA, PVK and salt in the presence of dispersed nanoparticles. As synthesized SiO_2 nanoparticles show their presence in all thenanocomposite gel electrolyte (figure 3(e-h)) through appearance of bands at 1100 cm^{-1} (Si-O) asymmetric vibration) 1000 cm^{-1} (Si-OH asymmetric vibration) and 797 cm^{-1} (Si-O symmetric vibration) [25, 26]. CH in plane deformation of aromatic ring related to PVK at 1050 cm^{-1} is seen to vanish in pristine and composite system after addition of SiO_2 filler. Likewise CH rocking vibration in PVA (722 cm^{-1}), PVK (773 cm^{-1} and 700 cm^{-1}) PVA: PVK blend (759 $cm^{-1}$and 704 cm^{-1}) and blend electrolyte (745 cm^{-1}) appear in nanocomposite system around 706 cm^{-1} and 732 cm^{-1} respectively which gives signature of enhanced compatibility in blend in the presence of salt and nanofiller. In view of all these observations it is envisaged that strong interaction take place between polymer components in the presence of salt and nano filler leading to formation of nano composite electrolyte system. Further existence of SiO_2 related bands suggest its passive role in affecting electrolyte properties.

3.4 Wagner's polarization

Amperometric I-t technique was used to assess the nature of ion transport and evaluate total ionic transference number from current time plot with platinum electrodes. The variation of current with time for mixed conducting samples is shown in figure 4and used to evaluate total ionic transference number described elsewhere[21, 22].

Table 1. Ionic transference number and activation energy of DMSO casted composite electrolyte system (PVA: PVK: CH_3COONH_4: EC: SiO_2).

S.N.	Concentration of SiO_2 content in composite electrolyte (wt %)	Ionic Transference number t_{ion}	Activation energy E_a (ev)
1	0	0.70	0.47
2	2	0.93	0.30
3	4	0.82	0.20
4	6	0.90	0.086
5	8	0.46	0.40

The calculated values of t_{ion} for different composite films varies from 0.9 to 0.8 (table 1) with varying concentration of SiO_2 filler (till 6 wt% SiO_2 content) which ascertains dominance of ionic charge transport over electronic transport in nanocomposite electrolyte. For samples containing 8 wt% SiO_2 content t_{ion} significantly drops down due to loss of ionic conduction which results from filler segregation.

3.5 CV Studies

A stable potential window is of great practical importance for applications of electrolyte materials in batteries and super capacitor [22]. Figure 5 compares the cyclic voltagrams of blend based electrolyte and its nanocomposite loaded with different wt% of SiO_2nanofiller. It is apparent from this figure that electrochemical stability is moderately good in pristine blend based electrolyte with window range – 1.5 V to + 1.6 V. On addition of nanofiller, stability is seen to improve marginally (-1.54 V to +1.64V). Another effect of adding the nanofiller is the narrowing of faradic currents during oxidation and reduction cycles in the stable region. An interesting observation is the appearance of a single oxidation/reduction peak for all pristine and composite electrolytes, which is on account of NH_4^+ ions that contributes to ionic conduction. Comparison of C-V data indicates best cyclic reversibility for composite system containing 6 wt% SiO_2 filler.

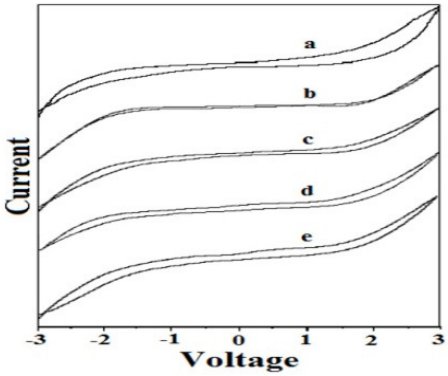


Figure 5. Cyclic votagrams of DMSO casted PVA: PVK: CH_3COONH_4: EC containing (a) 0, (b) 2, (c) 4, (d) 6 and (e) 8 wt% SiO_2 filler

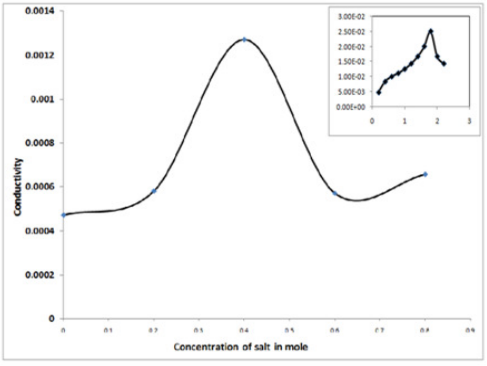


Figure 6. Ionic conductivity of (PVA: PVK): CH_3COONH_4: EC at different mole of Ammonium acetate salt. Inset shows the ionic conductivity of CH_3COONH_4: DMSO liquid electrolyte at different mole.

3.6 Electrical Conductivity

The variation of ionic conductivity of composite electrolyte (PVA: PVK): CH_3COONH_4: ECsystem as a function of salt concentration is shown in figure 6. The conductivity of blend based electrolyte is seen to rise with increasing salt concentration and reach an optimum at 1.27×10^{-3} S/cm for 0.4 M before decreasing again. Interaction among components has been noticed during FTIR investigation, which tend to raise the conductivity of the system through greater dissociation of salts (resulting in an increase in carrier concentration). In an earlier work on pristine system improvement in amorphous behavior was noticed which increases the mobility of the system. Both these factors thus cause significant improvement in ionic conductivity. For high salt concentration in excess of 0.4 M, dissociation of salt by polymer is restricted in contrast to liquid electrolyte where the optimum was observed around 1.8 M during experimental investigation [inset figure 6]. The fall in σ beyond 0.4 M is due to formation of ion agglomerates and presence of tortuous pathways.

Figure 7 depict the variation of ionic conductivity of nanocomposite polymer electrolyte with SiO_2 filler concentration. The ionic conductivity ofnanocomposite electrolyte is seen to improve moderately (~5 times) at room temperature for 6 wt% of SiO_2 filler.However, close observation of conductivity plotshows two maxima, one around 2 wt%and another around

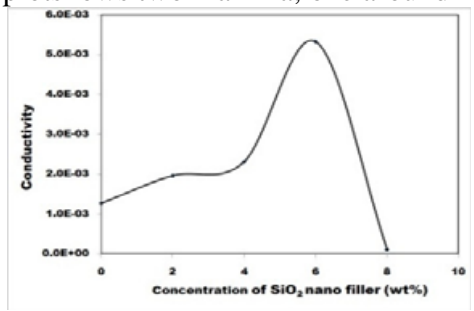


Figure 7. Variation of conductivity of polymer nanocomposite electrolytes with SiO_2 filler concentration (at room temperature).

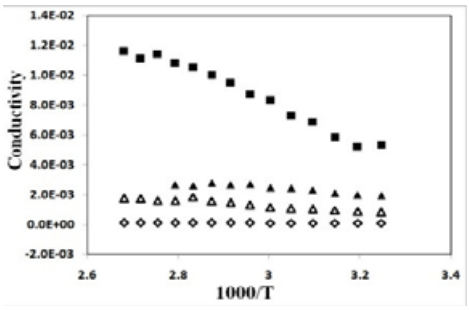


Figure 8. Temperature dependent conductivity of polymer nanocomposite electrolytes with (△) 0, (▲) 2, (■) 6 and (◇) 8 wt% SiO_2.

6 wt% filler concentration- a feature typical of nanocomposite polymer electrolyte [24, 25]. At low filler concentration (2 wt% SiO_2) enhancement in ionic conductivity is noticed to be of small magnitude. This feature can be associated to the fact that all the salt has been dissociated and so charge carrier concentration is limited. It is only the change in system morphology that tends to affect the conductivity as also evidenced in XRD studies. In situations, when

there is large quantity of nanoparticles in (excess of 3 wt% SiO_2) a sharp rise in room temperature conductivity takes place and attain an optimum for filler containing 6 wt% filler. This might be due to better compatibility among components leading to re-dissociation of salt into respective free ions giving rise to significant increase in ionic conductivity. Beyond 6 wt% of significant fall in ionic conductivity is seen. This results from agglomeration of these nanoparticles which leads to creation of tortuous pathways for mobile ions and thus conductivity drops. Another factor that can be associated with the fall in conductivity is the increase in the microscopic viscosity of composite system as envisaged in breathing chain model [3, 8].

3.7 Temperature Dependence of Conductivity

It is clear from Cole- Cole plots of PVA: PVK: CH_3COONH_4 system that there is a continuous drop in bulk resistance of composite system with increase of temperature. Hence temperature dependence of electrical conductivity of (PVA: PVK): CH_3COONH_4: EC: SiO_2 system at different filler concentration was studied and the result have been shown in figure 8.The variation of conductivity indicates that the conductivity increases with rise in temperature with two distinct straight lines separated by a region in which there appears a non- linear change in conductivity value. At low temperatures (around room temperature) the conductivity response is essentially dictated by the trapped liquid electrolyte within the polymer matrix and hence Arrhenious behavior is noticeable. However, as the temperature approaches the glass transition temperature of polymer blend (65^0 C) in polymer composite system, the matrix becomes flexible giving rise to conductivity response associated to that of blend based electrolyte. Therefore as the temperature is raised the conductivity enhancement is best described by VTF relationship. All the curve display similar behavior i.e. combination of Arrhenius and VTF with former being noticed in the low-temperature region and later at higher temperatures.

$$\sigma = \sigma_0 \exp(-E_a / KT) \qquad (1)$$

$$\sigma = \sigma_0 T^{-1/2} \exp(-E_a / T-T_0) \qquad (2)$$

where σ_0 is the pre-exponential factor, the activation energy and E_a is activation energy K is the Boltzmann constant and $T_0 = T_g - 60^0$C is quasi equilibrium glass transition temperature.

A low value of activation energy in low temperature region (table 1) has been observed with lowest value for samples containing 6 wt% filler.

4. Conclusion

Improvement in amorphous nature of PVA: PVK: CH_3COONH_4: EC: SiO_2 system has been confirmed through XRD, optical microscopy and FTIR studies. High ionic transference number (~ 0.9) observed in Wagner polarization studies indicate dominance of ionic charge transport over electronic counterpart. The ionic conductivity of nanocomposite electrolyte improves moderately (~5 times) at room temperature with an optimum of 5×10^{-3} S/cm for 6 wt%. The temperature dependent conductivity analysis shows that ion conduction is controlled by combination of Arrhennious and VTF behavior. Blend based nanocomposite polymer electrolyte for 6 wt% SiO_2 exhibit good conductivity and electrochemical window. This system can be used as electrolyte for batteries and other electrochemical devices.

References

1. J. R. MacCallum and C. A. Vincent (eds) *Polymer Electrolyte Reviews* Elsevier, London (1989).
2. F. M. Gray 1991 *Solid Polymer electrolytes- Fundamentals and Technological Application* VCH, New York (1991).
3. S. Chandra, S. S. Sekhon and N. Arora *Ionics***6,** 112 (2000).
4. S. Rajendran, M. Shivkumar and R. Subadevi*Materials Letters***58,** 641(2004).
5. D. W. Xia, D. Soltz and J. Samid*Solid State Ionics***14,** 221(1984).
6. J. E. Weston and B. C. Steele*Solid State Ionics***7,** 75(1982).
7. O. Bohnke, C. Rousselot, P. A. Gillet and C. J. Truche*Electochem. Soc.***40,** 139(1992).
8. S. S. Sekhon*Bull. Mater. Sci.***26,** 221(2003).
9. C. C. Caravanier, B. C. Montigny, D. Lemordant and G. Bosser*Solid State Ionics***156,** 113(2003).
10. T. Sato, K. Bonno, T. Maruo and R. Nozu*J Power Sources***152,** 264(2005).
11. P. Colomban (ed.) *Proton conductors: Solids, membranes and gels-materials and devices* Cambridge: Cambridge University Press (1992).
12. D. Radhucha, W. Wieczorek, Z. Florjanczyk and J. R. Stevens *J Phys. Chem***100,** 20126(1996).
13. S. L. Agrawal and A. Awadhia*Bull. Mater. Sci.***27,** 523(2004).
14. S. Pandey, S. K. Patel and S. L. Agrawal *Indian Journal of Physics***79,** 773(2005).
15. S. K. Patel, R. B. Patel, Awadhia A, Chand N and Agrawal S L *Pramana-Journal of physics***69,** 467(2007).
16. M. Sivakumar, R. Subadevi, S. Rajendran, N. L. Wu and J. Y. Lee *Materials Chemistry and Physics***97,** 330(2006).
17. S. L. Agrawal and R. P. Kumhar in National Conference: *Application of High Pressure Techniques & Novel Materials in the Frontiers of Science* (Eds) S. D. Dixit, M. M. Dwivedi and K. Pandey, National Centre of

Experimental Mineralogy and Petrology University of Allahabad, Allahabad (2013) pp 65.

18. S. L. Agrawal , M. Singh, M. M. Dwivedi, M. Tripathi and K. Pandey *J. Material Sci.***44,** 6068(2009).
19. K. Mishra, S. A. Hashmi and D. K. Rai*J.Solid State Electrochem***17,** 785(2013).
20. L.L. Hench and J. K. West *Chemical Review***90,** 33(1990).
21. K. Pandey, M. M. Dwivedi, M. Tripathi, M. Singh and S. L. Agrawal *Ionics***14,** 515(2008).
22. N. Chand, N. Rai, S. L. Agrawal and S. K. Patel *Bull. Mater. Sci.***34,** 1297(2011).
23. M. Ramrakhiani*International journal of Luminescence and Application***3,** 15(2013).
24. S. Selvasekarpandiana, G. Hirankumara, J. Kawamura, N. Kuwata, T. Hattori *Mater. Lett.***59,** 2741(2005).
25. A. Beganskiene, V. Sirutkaitis, M. Kurtinaitiene, R. Juskenas and A. Kareiva*Materials Science***10,** 287(2004).
26. N. D. Singho and M. R. Johan *Int. Electrochem. Sci.***7,** 5604(2012).

Fundamentals I

COMPARATIVE AB INITIO STUDY OF LITHIUM STORAGE IN AMORPHOUS AND CRYSTALLINE TiO_2*

FLEUR LEGRAIN, OLEKSANDR MALYI, SERGEI MANZHOS†

Department of Mechanical Engineering, National University of Singapore, Block EA #07-08, 9 Engineering Drive 1, Singapore 117576 Singapore

We present a density functional theory computational study of Li insertion into amorphous (*a*-)TiO_2 as well as the anatase, rutile, and bronze (B) phases. The computed defect formation energies in the crystalline phases are -1.38, -1.57, and -2.08 eV for anatase, rutile, and (B), respectively, vs. the reference state of *bcc* Li. Insertion sites in *a*-TiO_2 were identified with a clustering algorithm and further optimized by DFT. There is a distribution of insertion energies in *a*-TiO_2 ranging from -1.31 to -3.06 eV vs. Li metal. Amorphous TiO_2 is expected therefore to provide higher voltages at low Li concentrations than the crystalline phases.

1. Introduction

Titanium dioxide (TiO_2) is widely used in catalysis [1, 2], energy conversion [3-5] and electrochemical storage [6-12]. Most of these applications use crystalline TiO_2. The anatase phase is most thermodynamically stable at normal conditions and is widely used in the dye-sensitized technology [3-5], but rutile and (B) phases also find applications in catalysis and energy materials, as they are more reactive [9, 13-18]. Applications of these crystalline phases have also been supported by extensive theoretical and computational studies [19-23]. The use of amorphous TiO_2 (*a*-TiO_2) is, however, much less explored both experimentally and theoretically. The few studies that did explore *a*-TiO_2 suggest that it can be a promising material, especially for electrochemical storage [24-26], although applications in photocatalysis and solar energy conversion are also eyed [27, 28].

For applications in electrochemical storage, the interaction energy of metal ions such as Li^+ with the host structure is a critical parameter determining the suitability of the material as an electrode material as well as its voltage [29, 30]. While batteries operate by insertion-deinsertion of small to large amounts of lithium up to the theoretical capacity, insertion of small amounts of Li is also

* This work is supported by the Ministry of Education of Singapore via a Tier I AcRF grant.
† E-mail: mpemanzh@nus.edu.sg

Proceedings of the 14th Asian Conference on Solid State Ionics (ACSSI 2014)
Copyright © 2014 ACSSI 2014 Organizers. All rights reserved.
ISBN: 978-981-09-1137-9
doi:10.3850/978-981-09-1137-9_054

important for dye-sensitized solar cells, where Li salts are used in the electrolyte to control the energy of the conduction band minimum [31-35].

While several computational studies reported Li insertion energetics into various crystalline phases [36-40], there is to the best of our knowledge no study comparing with the same computational setup the insertion of Li into anatase, rutile and (B)-TiO_2 and, more importantly for this study, no ab initio study of Li insertion into *a*-TiO_2. Here, we report such a study at the DFT (density functional theory) level.

2. Methods

Structures were optimized using DFT [41] and the PBE functional [42]. Core electrons were replaced with Troullier-Martins pseudopotentials [43] (see Appendix). Calculations were done using the SIESTA code [44]. A DZP (double-ζ polarized) basis was used generated by SIESTA with the parameters PAO.EnergyShift of 0.001 Ry for Ti and O and 0.02 Ry for Li. The basis set reproduces the cohesive energies of Li (computed at 1.67 eV vs. the reference value of 1.66 eV) and TiO_2 (computed at 21.29 eV and 21.31 eV for anatase and rutile, respectively, vs. the reference value of 19.9 eV for rutile [45] and a cohesive energy of anatase 0.012-0.015 eV lower than that of rutile [46, 47], in agreement with the range of other reported (PBE) DFT values 18.77-21.44 eV [48, 49] and 21.54-21.60 eV [49, 50] for rutile and anatase, respectively). Structures were optimized until forces on all atoms were below 0.04 eV/ Å. All calculations were performed using unrestricted spin.

For *a*-TiO_2, a 192-atom supercell of size about 13x13x13 $Å^3$ was used. The initial structure was taken from Ref. [51] and re-optimized with the present setup. Due to the large cell size, the Brillouin zone was sampled at the Γ point, and the TiO_2 cell was first relaxed (until the stresses were below 0.1 GPa) and then held at fixed size during Li insertion. The energy cutoff for the Fourier expansion of the density was set to 100 Ry. The energy differences for the low energy insertion sites were about 0.01 eV when using 2 *k* points and the energy difference between two sites was found to be about 0.04 eV when increasing the density cutoff to 200 Ry.

For the crystalline phases, a 3×3×1 cell was used for anatase (~ 11×11×10 Å), 2×2×4 for rutile (~ 9×9×12 Å), and 1×3×2 for (B) (~ 12×11×13 Å). The Brillouin zone was sampled with a 3×3×3 Monkhorst-Pack point grid, and a 200 Ry cutoff was used for the expansion of the density.

To identify possible insertion sites in *a*-TiO_2, we covered the simulation cell with uniform grid of points spaced by 0.2 Å. We then performed a K-means

clustering [52, 53] analysis on points located farther than 1.5 Å from Ti and O atoms. The algorithm was made identify an increasing number of clusters. Up to 32 clusters were identified with the distance between the centers of the clusters larger than 2.5 Å. Those were used as initial guesses of insertion sites, further optimized by DFT.

3. Results

The lowest energy insertion site was found to be octahedral (octahedral coordination with respect to oxygen atoms) in anatase, rutile, and (B) TiO_2 (the lowest site in (B) TiO_2, called C site [54], being a distorted octahedral site). These sites are shown in Figure 1. We note that different studies suggested either the A2 [39] or the C [40] site as lowest-energy in (B)-TiO_2.

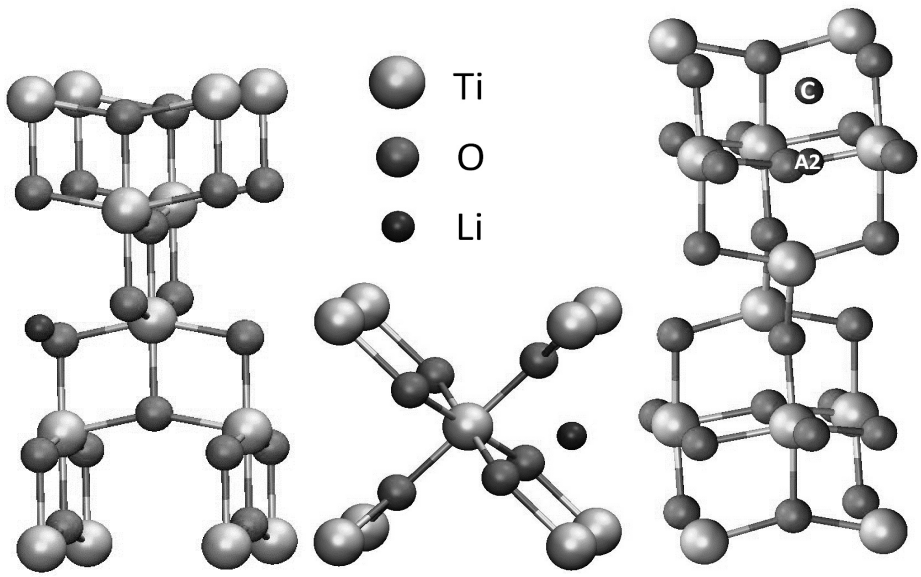


Figure 1. The lowest-energy Li insertion sites in (left to right) anatase, rutile, and (B)-TiO_2. The A2 site in (B) is also shown for comparison.

At the insertion sites, the defect formation energy was computed as

$$E_f = E(\mathrm{Li/TiO_2}) - E(\mathrm{TiO_2}) - E(bcc\ \mathrm{Li}), \quad (1)$$

where $E(\mathrm{Li/TiO_2})$, $E(\mathrm{TiO_2})$, and $E(bcc\ \mathrm{Li})$ are DFT energies of the TiO_2 cell with a Li atom inserted, of the pure TiO_2 cell, and of 1 Li atom in metallic Li, respectively. The E_f thus computed is therefore with respect to the Li metal reference state, and a negative value of E_f means that Li insertion is thermodynamically favored vs. Li plating.

Table 1. Defect formation energies (in eV) in crystalline and amorphous (min…max) TiO_2.

anatase	rutile	(B)	*a*-TiO_2
-1.38	-1.57	-2.08	-3.06…-1.31

The E_f values are listed in Table 1. Insertion is thermodynamically preferred in higher energy phases, as expected. (B)-TiO_2 is the most energetic (less stable) phase, which is therefore expected to provide the highest anode voltage at low states of charge.

The insertion sites found in *a*-TiO_2 are shown in Figure 2 (left) together with their E_f values compared to those of the crystalline phases (right). It is clear from Figure 2 that *a*-TiO_2 provides sites with a distribution of insertion energies, and many of those have lower E_f than in crystalline TiO_2. The minimum and maximum values of E_f are also listed in Table 1. The lowest-energy site in a-TiO_2 is stabilized by almost 1 eV vs. the lowest insertion energy crystalline structure, i.e. (B).

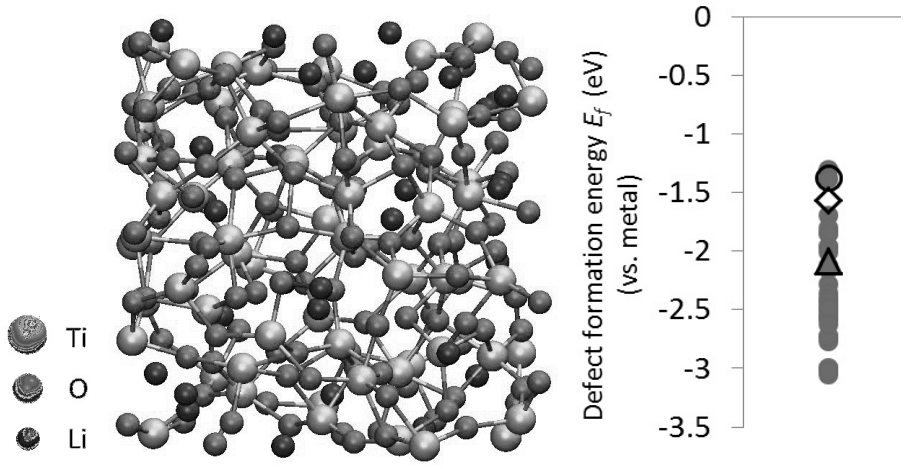


Figure 2. Insertion sites of Li in *a*-TiO_2 (left) and defect formation energies in *a*-TiO_2 (filled grey circles) as well as in the crystalline phases (empty black circle, rhombus, and triangle for anatase, rutile, and (B), respectively).

4. Conclusions

We compared computed Li insertion energetics in amorphous and crystalline phases (anatase, rutile, and (B)) of TiO_2. Among the crystalline phases, (B)-TiO_2 provides the lowest defect formation energy for Li, at -2.08 eV vs. metallic Li.

The corresponding values for anatase and rutile are -1.38 and -1.57 eV, respectively. Insertion sites in *a*-TiO_2 were found by K-means clustering. The lowest-energy site in *a*-TiO_2 is stabilized by almost 1 eV vs. the lowest insertion energy crystalline structure, i.e. (B). Amorphous TiO_2 is expected therefore to provide higher voltages at low Li concentrations than the crystalline phases.

Acknowledgments

The authors thank Prof. Drabold of Ohio University for sharing the initial structure of amorphous TiO_2.

Appendix

The pseudopotentials distributed with SIESTA are occasionally updated. To ensure reproducibility, we list here the headers of the pseudopotentials used in this work.

```
Ti pb nrl nc
ATM 3.2.2  9-APR-07 Troullier-Martins
4s 2.00  r= 2.71/4p 0.00  r= 2.71/3d 2.00  r= 2.48/4f 0.00  r= 2.48/
4  0 1111  1.126705534848E-04  1.250000000000E-02    4.000000000000
…
O pb nrl nc
ATM 3.2.2  9-APR-07 Troullier-Martins
2s 2.00  r= 1.47/2p 4.00  r= 1.47/3d 0.00  r= 1.47/4f 0.00  r= 1.47/
4  0 1030  3.098440220833E-04  1.250000000000E-02    6.000000000000
…
Li pb nrl pcec
ATM3      24-JUN-12 Troullier-Martins
2s 1.00  r= 2.26/2p 0.00  r= 2.26/3d 0.00  r= 2.59/4f 0.00  r= 2.59/
4  0  950  0.826250725555E-03  0.125000000000E-01    1.00000000000
…
```

References

1. D. C. Sorescu, S. Civiš, and K. D. Jordan, *The Journal of Physical Chemistry C* **118**, 1628 (2014).
2. K. Müller, D. Lu, S. D. Senanayake, and D. E. Starr, *The Journal of Physical Chemistry C* **118**, 1576 (2013).

3. M. Upadhyaya, S. Senthilarasu, M.-H. Hsu, and D. K. Kumar, *Solar Energy Materials and Solar Cells* **119**, 291 (2013).
4. Z. Ning, Y. Fu, and H. Tian, *Energy & Environmental Science* **3**, 1170 (2010).
5. H. S. Jung and J.-K. Lee, *The Journal of Physical Chemistry Letters* **4**, 1682 (2013).
6. D. Deng, M. G. Kim, J. Y. Lee, and J. Cho, *Energy & Environmental Science* **2**, 818 (2009).
7. Z. Yang, D. Choi, S. Kerisit, K. M. Rosso, D. Wang, J. Zhang, G. Graff, and J. Liu, *Journal of Power Sources* **192**, 588 (2009).
8. S. Liu, J. J. Hu, N. F. Yan, G. L. Pan, G. R. Li, and X. P. Gao, *Energy & Environmental Science* **5**, 9743 (2012).
9. A. G. Dylla, G. Henkelman, and K. J. Stevenson, *Accounts of Chemical Research* **46**, 1104 (2013).
10. S.-T. Myung, M. Kikuchi, C. S. Yoon, H. Yashiro, S.-J. Kim, Y.-K. Sun, and B. Scrosati, *Energy & Environmental Science* 6, 2609 (2013).
11. W. Li, et al., *Journal of the American Chemical Society* **135**, 18300 (2013).
12. K.-T. Kim, G. Ali, K. Y. Chung, C. S. Yoon, H. Yashiro, Y.-K. Sun, J. Lu, K. Amine, and S.-T. Myung, *Nano Letters* **14**, 416 (2014).
13. L. E. Walle, D. Ragazzon, A. Borg, P. Uvdal, and A. Sandell, *Surface Science* **621**, 77 (2014).
14. F. Yuan, S. Lu, W. Xu, and H. Zhang, *Surface Science* **621**, 88 (2014).
15. A. R. Armstrong, G. Armstrong, J. Canales, and P. G. Bruce, *Journal of Power Sources* **146**, 501 (2005).
16. H. Liu, Z. Bi, X.-G. Sun, R. R. Unocic, M. P. Paranthaman, S. Dai, and G. M. Brown, *Advanced Materials* **23**, 3450 (2011).
17. A. S. Dalton, A. A. Belak, and A. Van der Ven, *Chemistry of Materials* **24**, 1568 (2012).
18. H. Yildirim, J. Greeley, and S. K. R. S. Sankaranarayanan, *The Journal of Physical Chemistry C* **115**, 15661 (2011).
19. W. J. H. Borghols, M. Wagemaker, U. Lafont, E. M. Kelder, and F. M. Mulder, *Chemistry of Materials* **20**, 2949 (2008).
20. A. R. Armstrong, C. Arrouvel, V. Gentili, S. C. Parker, M. S. Islam, and P. G. Bruce*, Chemistry of Materials* **22**, 6426 (2010).
21. W. J. H. Borghols, D. Lutzenkirchen-Hecht, U. Haake, E. R. H. van Eck, F. M. Mulder, and M. Wagemaker, *Physical Chemistry Chemical Physics* **11**, 5742 (2009).
22. J. Kang, S.-H. Wei, K. Zhu, and Y.-H. Kim*, The Journal of Physical Chemistry C* **115**, 4909 (2011).
23. M. L. Sushko, K. M. Rosso, and J. Liu*, The Journal of Physical Chemistry C* **114**, 20277 (2010).

24. W. J. H. Borghols, et al., *Journal of The Electrochemical Society* **157**, A582 (2010).
25. M. Hibino, K. Abe, M. Mochizuki, and M. Miyayama, *Journal of Power Sources* **126**, 139 (2004).
26. X. Sun, M. Xie, J. J. Travis, G. Wang, H. Sun, J. Lian, and S. M. George, *The Journal of Physical Chemistry C* **117**, 22497 (2013).
27. R. D. Eithiraj and K. R. Geethalakshmi, *Chemical Physics Letters* **585**, 138 (2013).
28. K. Kaur and C. V. Singh, *Energy Procedia* **29**, 291 (2012).
29. M. K. Aydinol, A. F. Kohan, and G. Ceder, *Journal of Power Sources* **68**, 664 (1997).
30. M. S. Islam and C. A. J. Fisher, *Chemical Society Reviews* **43**, 185 (2014).
31. S. Manzhos and G. Giorgi, *Challenges* **4**, 116 (2013).
32. N. Kopidakis, K. D. Benkstein, J. van de Lagemaat, and A. J. Frank, *The Journal of Physical Chemistry B* **107**, 11307 (2003).
33. S. E. Koops, B. C. O'Regan, P. R. F. Barnes, and J. R. Durrant, *Journal of the American Chemical Society* **131**, 4808 (2009).
34. H. Wang and L. M. Peter, *The Journal of Physical Chemistry C* **116**, 10468 (2012).
35. Y. Shi, Y. Wang, M. Zhang, and X. Dong, *Physical Chemistry Chemical Physics* **13**, 14590 (2011).
36. C. L. Olson, J. Nelson, and M. S. Islam, *The Journal of Physical Chemistry B* **110**, 9995 (2006).
37. M. V. Koudriachova, N. M. Harrison, and S. W. de Leeuw, *Physical Review Letters* **86**, 1275 (2001).
38. M. A. Reddy, M. S. Kishore, V. Pralong, V. Caignaert, U. V. Varadaraju, and B. Raveau, *Electrochemistry Communications* **8**, 1299 (2006).
39. D. Panduwinata and J. D. Gale, *Journal of Materials Chemistry* **19**, 3931 (2009).
40. C. Arrouvel, S. C. Parker, and M. S. Islam, *Chemistry of Materials* **21**, 4778 (2009).
41. W. Kohn and L. J. Sham, *Physical Review* 140, A1133 (1965).
42. J. P. Perdew, K. Burke, and M. Ernzerhof, *Physical Review Letters* **77**, 3865 (1996).
43. N. Troullier and J. L. Martins, *Physical Review B* **43**, 1993 (1991).
44. M. S. José, A. Emilio, D. G. Julian, G. Alberto, J. Javier, O. Pablo, and S.-P. Daniel, *Journal of Physics: Condensed Matter* **14**, 2745 (2002).
45. *CRC Handbook of Chemistry and Physics* 64th ed. (CRC, Boca Raton, FL, 1983).
46. *Handbook of Chemistry and Physics*, edited by R.C. West (CRC, Cleveland, 1986).

47. M. W. Chase, C. A. Davies, J. R. Downey, D. J. Frurip, R. A. McDonald, and A. N. Syverud, *JANAF Thermodynamical Tables, Third Edition, Journal of Physical and Chemical Reference Data* **14**, 1680, Suppl.1 (1985)
48. B. A. Hamad, *The European Physical Journal B* **70**, 163 (2009).
49. M. Lazzeri, A. Vittadini, and A. Selloni, *Physical Review B* **63**, 155409 (2001).
50. H. G. Yang, C. H. Sun, S. Z. Qiao, J. Zou, G. Liu, S. C. Smith, H. M. Cheng, and G. Q. Lu, *Nature* **453**, 638 (2008).
51. B. Prasai, B. Cai, M. K. Underwood, J. Lewis, and D. A. Drabold, *Journal of Materials Science* **47**, 7515 (2012).
52. G. A. F. Seber, *Multivariate Observations* (John Wiley & Sons, Hoboken, NJ, 1984).
53. H. Spath, *Cluster Dissection and Analysis: Theory, FORTRAN Programs, Examples* (Halsted Press, New York, 1985).
54. L. Brohan and R. Marchand, *Solid State Ionics* **9–10**, Part 1, 419 (1983).

ELASTIC CONSTANTS OF IONIC CONDUCTORS: A THEORETICAL STUDY

HARUHITOSADAKUNI

and

MASARU ANIYA

Department of Physics, Graduate School of Science and Technology, Kumamoto University, Kurokami 2-39-1, Kumamoto 860-8555, Japan

The studies of elastic constants provide useful information to understand the physical properties of ionic conductors. In the present report, the close relationship between the temperature dependencies of the elastic constants and ionic conductivity in PbF_2 is shown as an example. Study on temperature dependence ofAnderson-Grüneisenparameter indicates that superionic materials exhibit anomalously large temperature effects. An expression that relates the bond stretching and bond bending force constant with the ionicity of the materials was obtained in the framework of the bond orbital model. The model permits to describe the chemical trend of elastic properties of superionic materials better than in previous studies.

1. Introduction

The physical properties of ionic conductors are intimately related with their elastic constants. However, few studies have been done to elucidate the background of that relation. In order to fill this gap and gain further understanding on fundamental properties of superionic materials, systematic studies of elastic properties in different materials are necessary. Based on this motivation, we have started a program to study the mechanical properties of superionic materials. Some of the results obtained were already reported [1-5]. Among these we can cite the temperature dependence of the elastic constants and the Cauchy relation in AgCl [1], the temperature dependence of the Anderson-Grüneisen parameter in ionic conductors [2], the comparative study of the elastic anisotropy in AgCl, AgBr and NaCl [3], and the study of bulk modulus in metal borohydrides [4].In the present report, after showing some examples that emphasize the intimate relation between mechanical and ionic transport properties in solids, new results that relates the bond stretching and bond bending force constant with the ionicity of the materials will be presented.The model permits us to consider the chemical trend of elastic

Proceedings of the 14th Asian Conference on Solid State Ionics (ACSSI 2014)
Copyright © 2014 ACSSI 2014 Organizers. All rights reserved.
ISBN: 978-981-09-1137-9
doi:10.3850/978-981-09-1137-9_074

constants of superionic materials which were not described appropriately in previous studies.

2. Mechanical Properties of Ionic conductors

2.1. *Elastic Constants and Ionic Conductivity*

In previous studies, we have shown that the second order elastic constants in AgCl [1] and AgBr [3] show strong deviation from the values predicted based on the Murnaghan model at high temperatures. In contrast, for the case of alkali halides, the same model reproduces well the observed temperature dependence of the elastic constants over wide temperature range [1]. As is well known, Ag halides exhibit high ionic conductivity at high temperature, whereas alkali halides are practically insulators. The results indicate that the elastic constants are intimately related with the ionic transport phenomena in solids. This observation is not new. Many researchers have observed large temperature dependencies of elastic properties in ionic conductors [6-13]. However, as far as the authors are informed, these observations were not exploited.

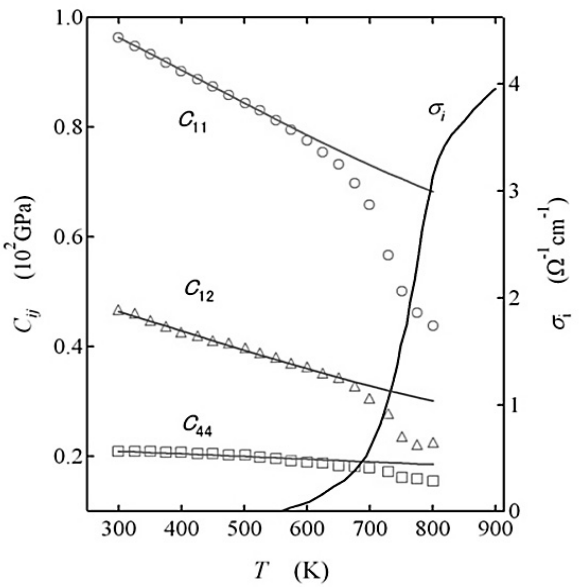


Figure 1.The temperature dependencies of the elastic constants C_{ij} and the ionic conductivity σ_i in PbF_2.

Fig. 1 shows an example of the interrelation between elastic constants and ionic conductivity in PbF_2 [5]. PbF_2 has a cubic structure. Therefore, it has three

independent elastic constants, C_{11}, C_{12} and C_{44}, which describe the longitudinal, transverse and shear stiffness, respectively. The solid line for each elastic constantare the theoretical values calculated from

$$M(T) = M_0\left(\frac{V(T)}{V_0}\right)^{-\delta_M^0}, \quad (1)$$

$$\delta_M = -\frac{V}{M}\left(\frac{\partial M}{\partial V}\right)_P, \quad (2)$$

where$M$ is any of the elastic moduli and the suffix 0 denotes that the quantity is taken at the temperature of reference. In the framework of Murnaghan equation, the quantity δ_M defined in Eq. (2) is assumed to take a constant value, i.e., $\delta_M = \delta_M^0 = \text{const}$[14]. From Fig. 1 we note that the agreement between the measured and calculated values is good at low temperature. In the high temperature part, large deviations from the theoretical prediction are apparent above 700 K. The theoretical curves start to overestimate the measured values at around 600 K. This means that there is a softening in the elastic constants of the crystals above this temperature. The experimental values of the elastic constants shown in Fig. 1 were obtained from [12].

PbF_2 exhibit a superionic phase transition at 705 K. The phase transition in PbF_2 is diffuse, that is, the ionic conductivity increases gradually with the increase of temperature as shown in Fig. 1[15]. From Fig. 1 we recognize clearly the existence of a correlation between ionic conductivity and elastic constants in PbF_2. The ionic conductivity starts to increase at around 600 K. At around the same temperature, the elastic constants start to deviate from the theoretical estimation based on Eq. (1). At around 700 K, an abrupt increase of the ionic conductivity and large change of elastic constants are discernible.Through the phase transition, the concentration of Frenkel defects increases dramatically [16]. Therefore, a part of the large deviations observed in the elastic constants at high temperatures is caused undoubtedly by these defects.

2.2. *Anderson Grüneisen Parameter*

The Anderson-Grüneisen(AG) parameter has been used widely in the description of the temperature dependence of elastic constants. It is defined as [17]

$$\delta = -\frac{1}{\alpha K}\left(\frac{\partial K}{\partial T}\right)_P, \tag{3}$$

whereα is the thermal expansion coefficient and K is the bulk modulus. In most compounds, the temperature dependence of the AG parameter can beignored. However, it has been shown recently that the AG parameter of superionic materials exhibit anomalously large temperature dependencies as shown in Fig. 2 [2]. From the figure we can see that the AG parameters of LiF, NaCl, KCl, KBr, MgO, CaO, Al_2O_3, Mg_2SiO_4, KCN, AlN, Si_3N_4, Ag and Al are almost constant or weakly temperature dependent as usually assumed. Concerning the ionic conducting materials, AgCl, AgBr, PbF_2, CaF_2, SrF_2 and BaF_2, large temperature dependences in the high temperature region are observed. We can recognize clearly that the behavior exhibited by AgCl and AgBr are sufficiently anomalous when compared with those of alkali halides, compounds that have the same crystal structure. The large difference arises from the high defect concentration that the Ag halides have. The high defect concentration also influences the ionic conductivity. This figure shows also the strong interrelation between elastic properties and ionic conduction.

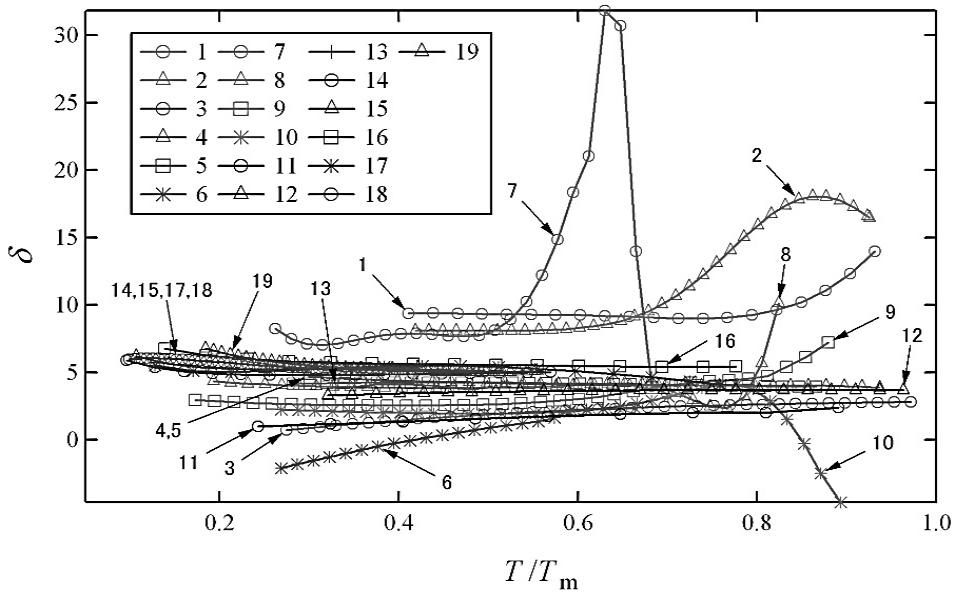


Figure 2.The Anderson-Grüneisen parameter δ of various materials as a function of normalized temperature T/T_m, where T_m is the melting temperature. The numbers after the compound names denote the melting temperature in K. The sources of the data are given in [2].1: AgCl(730), 2: AgBr(700), 3: NaCl(1091), 4: KBr(1063), 5: KCl(1003), 6: LiF(1115), 7: PbF_2(1143), 8: BaF_2(1553), 9: SrF_2(1733), 10: CaF_2(1673), 11: Ag (1235), 12: Al (934), 13: KCN (911), 14: MgO(3125), 15: CaO(2798), 16: Mg_2SiO_4(2163), 17: Al_2O_3(2345), 18: AlN(3023), 19: Si_3N_4(2173).

3. Bond Stretching,Bond Bending Force Constants and Ionicity

The results shown in the previous section indicate that for a deep understanding of ionic transport in solids, we need to understand the behavior of elastic constants. In this section, a semi-empirical expression developed under this objective is presented. The softening of the elastic constants of ionic conductors at high temperatures shown in previous studies [1, 3] and in section 2, are related with the relative magnitudes of the bond stretching (α) and bond bending (β) force constants. For the case of binary compounds, early work has considered that the ratio β/α decreases linearly with the increase of ionicity [18]. Following that work, it has been recognized that the relation is not linear [19].

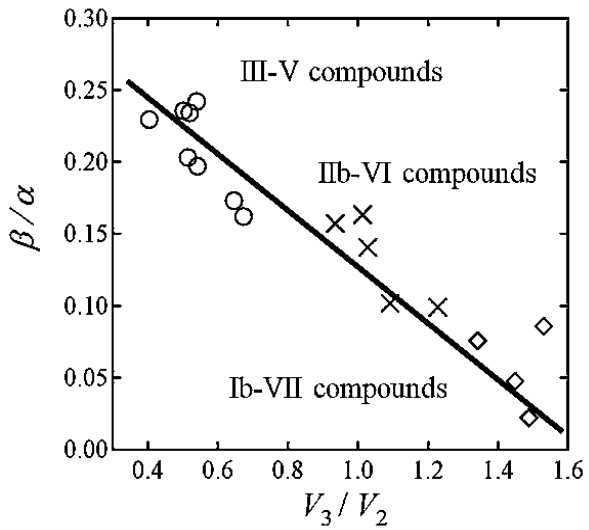


Figure 3.Relation between β/α and V_3/V_2 in binary compounds.

The relation between β/α and V_3/V_2 for binary compounds is shown in Fig. 3. Here, V_2 and V_3 denote respectively, the covalent and polar energy terms that are calculated based on the bond orbital theory [20, 21]. The figure indicates that the relation betweenβ/α and V_3/V_2 can be represented roughly by a straightline.

$$\frac{\beta}{\alpha} \approx m + n\frac{V_3}{V_2}, \tag{4}$$

where$m$ and$n$ are constants that characterize the straight line. The ionicityf_{i} can be written in terms of the polarityα_{p}as [22]

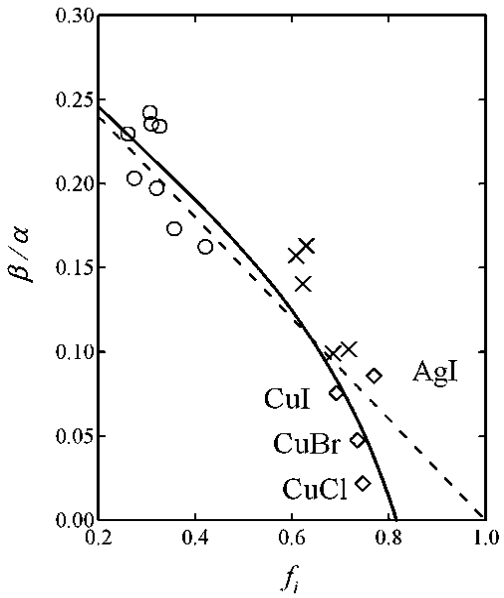


Figure 4.Relation between β/α andionicityf_i in binary compounds.
The solid line is described by Eq. (8).

$$f_i = 1 - (1 - \alpha_p^2)^{3/2}, \tag{5}$$

where

$$\alpha_p = \frac{V_3}{(V_2^2 + V_3^2)^{1/2}}. \tag{6}$$

From Eqs. (5) and (6), we have

$$\frac{V_3}{V_2} = [(1 - f_i)^{-2/3} - 1]^{1/2}. \tag{7}$$

Then, the Eq. (4) is rewritten as

$$\frac{\beta}{\alpha} \approx m + n[(1 - f_i)^{-2/3} - 1]^{1/2}. \tag{8}$$

The value of $m = 0.3$ is obtained from β/αof the materials characterized by $f_i = 0$, i.e., Si, Ge and Sn. The value of $n = -0.21$ is obtained from the slope shown in Fig. 3. The behavior of Eq. (8) is shown in Fig. 4. We can see that the relation describes relatively well the general trends of the behavior, including copper halides. These compounds and AgI are the compounds of interest from the ionic transport point of view.It should be also noted that β/α approaches

zero near the critical ionicity $f_c = 0.785$ .As have been discussed by some authors, the instability caused by the decrease of β/α is related with the high ionic mobility observed in copper halides and silver halides [23, 24].

4. Conclusion

The physical properties of ionic conductors are intimately related with their elastic constants. In the present report it was shown that the temperature dependencies of the elastic constants and the Anderson-Grüneisen parameter of ionic conductors exhibit a peculiar behavior. The analysis shows clearly that the large defect concentration which is a factor that controls the high ionic conductivity of these materials originates also the strong temperature dependence of elastic parameters.A new expression that relates the bond stretching and bond bending force constant with the ionicity of the materials was obtained in the framework of the bond orbital model. The new model permits to describe the chemical trend of elastic properties of superionic materials better than inprevious studies.

References

[1] M. Aniya and H. Sadakuni, *Thermochim. Acta***532**, 111 (2012).
[2] H. Sadakuni and M. Aniya, *Physica B***410**, 81 (2013).
[3] H. Sadakuni and M. Aniya, *Solid State Ionics, Ionics for Sustainable World, Eds. B. V. R. Chowdari et al.*, World Scientific, 705 (2012).
[4] Y. Noguchi and M. Aniya, *Solid State Ionics, Ionics for Sustainable World, Eds. B. V. R. Chowdari et al.*, World Scientific, 671 (2012).
[5] H. Sadakuni, M. Aniya, *Phys. Rep. Kumamoto Univ.***14**, 15 (2012).
[6] T. A. Fjeldly and R. C. Hanson, *Phys. Rev. B***10**, 3569 (1974).
[7] W. C. Hughes and L. S. Cain, *Phys. Rev. B***53**, 5174 (1996).
[8] L. S. Cain and G. Hu, *Phys. Rev. B***64**, 104104 (2001).
[9] T. Kanashiro, Y. Michihiro, J. Ozaki, T. Ohno and A. Kojima, *J. Phys. Soc. Jpn.***56**, 560 (1987).
[10] C. R. A. Catlow, J. D. Comins, F. A. Germano, R. T. Harley and W. Hayes, *J. Phys. C: Solid State Phys.***11**, 3197 (1978).
[11] M. H. Dickens, W. Hayes, M. T. Hutchings and W. G. Kleppmann, *J. Phys. C: Solid State Phys.***12**, 17 (1979).
[12] M. O. Manasreh and D. O. Pederson, *Phys. Rev. B***30**, 3482 (1984).
[13] R. K. Singh, S. S. Mitra and C. N. Rao, *Phys. Rev. B***44**, 838 (1991).
[14] A. Vijay and T. S. Verma, *Physica B***291**, 373 (2000).
[15] C. E. Derrington, A. Navrotsky and M. O.'Keeffe, *Solid State Commun.***18**, 47 (1976).
[16] J. Oberschmidt, *Phys. Rev. B***24**, 3584 (1981).

[17] O. L. Anderson, *Phys. Rev.***144**, 553 (1966).
[18] R. M. Martin, *Phys. Rev. B***1**, 4005 (1970).
[19]K. Kunc, M. Balkanski and M. A. Nusimovici, *Phys. Stat. Sol. (b)***72**,249 (1975)
[20] W. A. Harrison, *Electronic Structure and the Properties of Solids*, Freeman (1980).
[21] M. Aniya, *J. Chem. Phys.***96**, 2054 (1992).
[22] W. A. Harrison, *Phys. Rev. B***8**, 4487 (1973).
[23] J. C. Phillips, *J. Electrochem. Soc.***123**, 934 (1976).
[24] M. Aniya, *Solid State Ionics***50**, 125 (1992).

Electrode Materials II

SYNTHESIS AND ELECTROCHEMICAL PROPERTIES OF MOLYBDENUM DIOXIDE/GRAPHENE NANOMATERIAL

XUE YANG, YANG LI, YUELI LIU, WEN CHEN†

State Key Laboratory of Advanced Technology for Materials Synthesis and Processing, School of Material Science and Engineering, Wuhan University of Technology Wuhan, 430070, P. R. China

YANYUAN QI

Center for Materials Research and Analysis, Wuhan University of Technology Wuhan, 430070, P. R. China

In this study, molybdenum dioxide/graphene composites were prepared by a hydrothermal process. When the amount of graphene increased to 10 wt%, the molybdenum dioxide particles were uniformly deposited on the graphene sheets. And as the electrode material for lithium batteries, it exhibited high reversible specific capacities of 1267 $mAhg^{-1}$ at the second cycle and 629 $mAhg^{-1}$ after 60 cycles. The outstanding electrochemical performance of the composite can be attributed to the synergistic interaction between molybdenum dioxide and graphene. There were enough void spaces to buffer volume change in the structure. Furthermore, graphene nanosheets in hybrid material could act as not only lithium storage electrodes but also electronic conductive channels to improve the electrochemical performances.

1. Introduction

Rechargeable lithium ion batteries (LIBs) have become one of the most promising type of battery technology for electrochemical energy storage due to their high energy density, low maintenance, and relatively low self-discharge [1,2]. However, in the classical commercial LIBs, graphitic carbon was the most popular electrode material, which only delivers a theoretical specific capacity of 372 $mAhg^{-1}$ [3]. Developing new electrode materials with high energy densities has been an important way to satisfy the ever-growing demand for high performance LIBs. Nowadays, nanostructured transition-metal oxides have been regarded as high capacity anodes, due to the higher capacity than that of graphite [4-7]. Among them, molybdenum dioxide(MoO_2) has attracted much attention, owing to its appealing features, including low resistance, short diffusion path and

† Corresponding author, email: chenw@whut.edu.cn

Proceedings of the 14th Asian Conference on Solid State Ionics (ACSSI 2014)
Copyright © 2014 ACSSI 2014 Organizers. All rights reserved.
ISBN: 978-981-09-1137-9
doi:10.3850/978-981-09-1137-9_099

large surface area [8]. Although most pure MoO_2 nanostructures have the high specific capacity and mitigated pulverization, the cycling stability is still not satisfied [9]. Nano-structured MoO_2 hybridized with conductive and elastic carbon was an effective strategy to improve the structural integrity as well as the cycling performance [10]. Recently, a number of metal oxide/graphene hybrids have been reported, including Fe_3O_4, Mn_3O_4 and Co_3O_4 which can obtain better electrochemical properties than that counterpart [7, 11, 12].

In this work, MoO_2/graphene nanocomposites were prepared by the hydrothermal process from a precursor solution which was obtained by adding reducing agent and graphene turbid liquid into peroxo-polymolybdic acid. The effects of hydrothermal time and the mass ratios of MoO_2 to graphene on the growth of MoO_2 crystal and electrochemical properties have been studied.

2. Experimental

2.1. *Preparation of Graphene Oxide*

Graphene oxide (GO) was prepared by Hummers method [13]. Briefly, 2 g graphite powders and 1.5 g $NaNO_3$ were mixed in an ice bath, and then dropwise put into the 80 mL H_2SO_4. Under vigorous stirring, 10 g $KMnO_4$ was gradually added and the temperature of the mixture was kept below 20 ℃. Then, the mixture was stirred at 35 ℃ in a water bath for 3 h. After reaction, the mixture became pasty with a brownish color. 100 mL H_2O was slowly added into the pasty mixture with putting the mixture in an ice bath to keep the temperature below 35 ℃. 10 mL of 30% H_2O_2 solvent was added to the mixture, and the color of this solution became a brilliant yellow. Then, the mixture was washed with 10% HCl (aq.) and deionized water. The obtained suspension was sonicated for 30 min by ultrasonic cell disruptor. Finally, adding deionized water into the suspension until the concentration became 1 $mg \cdot mL^{-1}$.

2.2. *Preparation of MoO_2 Particles*

MoO_2 nanoparticles were prepared via hydrothermal method. 10 mL 30% H_2O_2 was added onto 1 g Mo with continually stirring until the clear orange sol was obtained. Then the sol was mixed with 20 mL ethanediol and 50 mL deionized water. Stirring the sol for about 30 min until the sol turned into clear and yellow mixture, which was directly transferred into a Teflon-lined autoclave and reacted at 180 ℃ for 72 h. Finally, the samples were centrifuged and washed by ethanol and distilled water for three times. After drying at 60 ℃ in vacuum condition for 24 h, the black powder were obtained.

2.3. *Preparation of MoO_2/Graphene Composites*

The composites were prepared by hydrothermal again. Firstly, 0.2 g as-prepared MoO_2 was dispersing in 30 mL ethanediol. Then various volumes of GO suspension were added sequentially under vigorously stirring. Then the L-ascorbic acid was added into the mixture. Afterwards, HCl aqueous solution was dropwise added with magnetic stirring until the pH value became 1. The mixture was transferred into a Teflon-lined autoclave after sonicated for 30 min and reacted at 180 ˚C for 10 h. Finally, the samples were centrifuged and washed by ethanol and distilled water for three times. After drying at 60 ˚C in vacuum condition for 24 h, the black powders were obtained.

2.4. *Characterization*

X-ray powder diffraction patterns of the prepared samples were recorded using a diffractometer (XRD; model X'pert PRO-PANalytical, Netherlands). The structure of samples was observed using field emission scanning electron microscopy (FESEM; model No. JSM-6700F, Japan). Raman spectroscopy equipped with a 633 nm laser (Raman; model Renishaw Invia, Britain) was employed to get the structural information.

2.5. *Electrochemical Measurements*

The electrochemical tests were performed via CR2025 coin-type test. To fabricate the working electrodes, 70 wt% active material(MoO_2 or MoO_2/Graphene), 25 wt% acetylene black and 5 wt% polytetrafluoroethylene (PTFE) were mixed, then compressed it into a lamella about 0.2 mm in thickness and cut it into a wafer about 1 cm^2 in area. Pure lithium foil was used as both counter and reference electrode. The electrolyte was 1 M $LiPF_6$ in EC/EMC/DMC (1:1:1 in volume). A Celgard 2300 membrane was used as the separator. The galvanostatic discharge/charge cycles were carried out on a XINWEI system over a voltage range of 0 to 3.00 V at room temperature. Cyclic voltammetry (CV) tests were performed on an Autolab Potentiostat 30 system. The specific capacities in this article were calculated based on the overall mass of the composite.

3. Results and Discussion

Figure 1 shows the X-ray diffraction (XRD) patterns for the as-prepared MoO_2/graphene. All the diffraction peaks are readily indexed to a pure monoclinic MoO_2 (JCPDS No. 78-1073, a=5.660 Å, b= 4.860 Å, β=120.94°).

The diffraction peaks from the graphene sheets are not clearly observed in the pattern due to their weak crystallinity and the overlap of the weak diffraction of the graphene sheets at 2θ of 26.6 degree with that of MoO_2 [14, 15]. The XRD patterns also show that the crystal structure of monoclinic MoO_2 is not changing with the increase of the graphene.

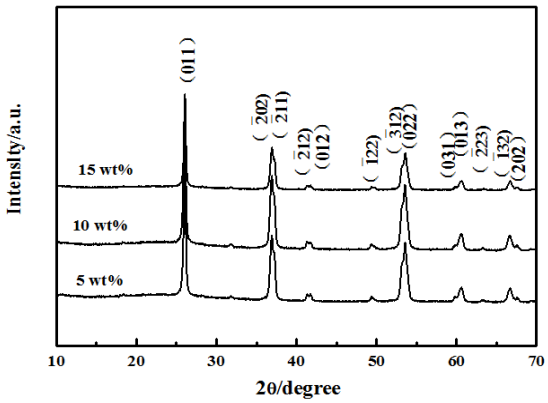


Figure 1. XRD patterns of MoO_2/graphene composites with different weight ratios

The structure of the composite was further characterized by Raman spectroscopy. As shown in Figure 2, the peaks appear at 992, 818, 662, 335 and 282 cm^{-1} refer to M=O stretch (A_g, υ_s), M=O stretch (A_g, υ_{as}), O-M-O stretch (B_{2g}, B_{3g}, υ_s), O-M-O bend (Ag, B_{1g}, δ), and O=M=O wagging (B_{2g}, δ) [16], respectively. The peaks at 1586 and 1344 cm^{-1} correspond to G band (E_{2g} symmetry, in-plane bond-stretching motion of pairs of sp^2 C atoms) and D band (defect-related) of graphene sheets [17, 18]. The characteristic peaks of MoO_2 particles and graphene appear at the same time, suggesting the formation of the MoO_2/graphene composite [19].

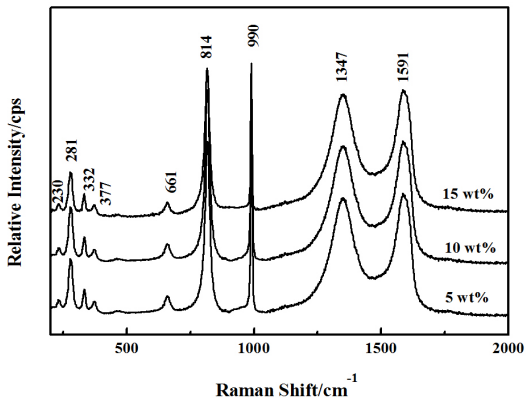


Figure 2. Raman spectra of MoO_2/graphene with different weight ratios

Figure 3 shows the FESEM images of the MoO_2/graphene with different amount of graphene. As seen from Figure 3(a), a curled morphology of graphene

sheets consisting of the thin wrinkled structures is observed. When the amount of graphene increases to 10 wt%, the molybdenum dioxide particles are uniformly deposited on the graphene sheets. However, both the graphene and MoO_2 particle have obvious agglomeration when the weight ratio of graphene sequentially increasing to 15 wt%.

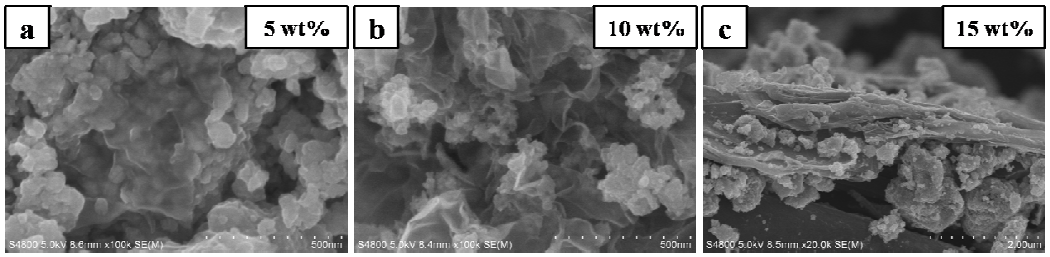


Figure 3. FESEM images of MoO_2/graphene with different weight ratios

The cycle performance of the composites with 5, 10 and 15 wt% is shown in Figure 4. The different capacities indicate the influence of graphene content in the composites on battery electrochemical performance. The capacity of the composite with less graphene (5 wt% graphene) shows capacities of 864 $mAhg^{-1}$ at second cycle and 461 $mAhg^{-1}$ after 60 cycles. When increasing the amount of graphene to 10 wt%, there is much higher capacity of 1267 $mAhg^{-1}$ at the second cycle and 629 $mAhg^{-1}$ after 60 cycles. The capacity of the composite with 15 wt% graphene is 621 $mAhg^{-1}$ at second cycle, but it decays to 95 $mAhg^{-1}$ after 60 cycles. In the other words, the capacity depends on the weight ratios of MoO_2 and graphene in the composites, and the capacity is highest when the amount of graphene is 10 wt%.

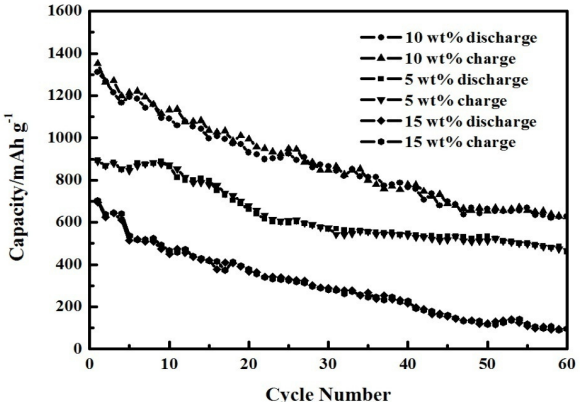


Figure 4. Cycling performance of MoO_2/graphene composites with 5 wt%, 10 wt%, and 15 wt%, at 0.1 $mA{\cdot}cm^{-2}$

Figure 5(a) shows the CV curves for the electrode made of the MoO_2/graphene composite (10 wt% GO in the composite) at a scan rate of 0.5 $mV{\cdot}s^{-1}$. In the first discharge cycle, there is a broad reduction peak at ~0.85 V

reflecting the irreversible reduction of electrolyte [20]. The CV curves remain almost the same from the second cycle onwards, indicating a highly reversible reduction and oxidation process of the as-prepared MoO_2/graphene composite [21]. The charge and discharge profiles for of the composite with 10 wt% GO for the 1st, 2nd, 20th, 40th, and 60th cycles at a voltage range of 0 V and 3.0 V versus Li^+/Li, and a current density of 0.1 mA·cm^{-2} are shown in Figure 5(b). In the first cycle, a short discharge plateaus at 0.85 V is observed and it is in agreement with the CV curves.

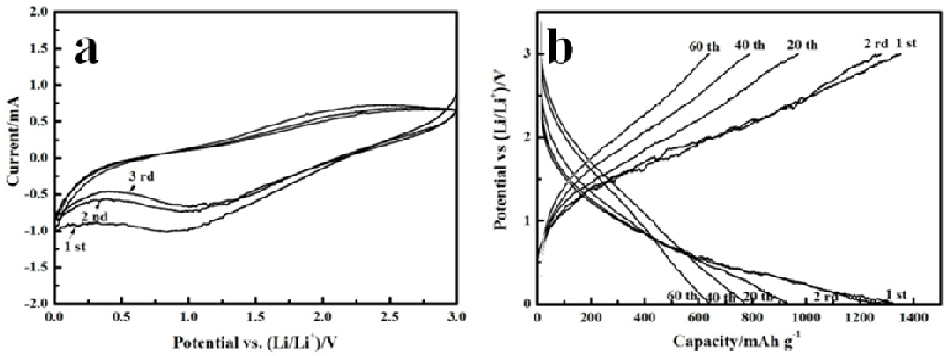


Figure 5. Electrochemical performance of the MoO_2/GO composites with 10 wt% graphene (a) cyclic voltammograms at a current density of 0.1 mA·cm^{-2} (b) the relation of the galvanostatic voltage versus the capacity

As shown in Figure 5(b), the discharge capacities of the electrode in the 1st, 2nd, 20th, 40th and 60th cycles are 1311, 1265, 931, 766 and 629 mAhg^{-1}, respectively, and the charge capacities of the electrode in the 2nd, 20th, 40th, and 60th cycles are 1271, 954, 778 and 626 mAhg^{-1}, respectively. From the first cycle onward, 49.7% discharge capacity and 49.25% charge capacity are retained up to the 60th cycle with a Coulombic efficiency of nearly 100%. According to previous research [22], the reaction between MoO_2 and Li^+ during the charge and discharge process is proposed to be as follows:

$$Mo + xLi^+ + xe \leftrightharpoons Li_xMoO_2 \quad (1)$$

In this paper, the x can be up to 3 at 60th cycle.

Theoretically, the capacity of MoO_2 is 838 mAhg^{-1}, and which of carbon material is 372 mAhg^{-1}. The theoretical capacity of composite could be calculated as MoO_2 wt% × 838 mAhg^{-1} + carbon wt% × 372 mAhg^{-1} [23], and the theoretical capacity of composites with 10 wt% graphene is 791.4 mAhg^{-1}. However, in the first cycle the discharge capacity is higher than the theoretical value. The extra capacity may arise from reversible reaction of lithium with the active surface groups of graphene (C-H and C-OOH bonds) [24]. After 35 cycles, the actual capacity approaches to the theoretical value.

The outstanding electrochemical performance of the composite can be attributed to two reasons. Firstly, a dimensional confinement of the MoO_2 particles by the surrounding graphene prevented the volume expansion upon lithium insertion. As pointed out before, the main reason for rapid fading of MoO_2 electrode was that a large volume expansion of the MoO_2 material occurs during the cycling [20, 22, 25]. In the above FESEM images, graphene nanosheets are homogeneously distributed between MoO_2 particles in the structure of the composite with 10 wt% graphene, so the stress formed during the process of lithium insertion was avoided. Even though the volume expansion has happened, the electrode was not pulverized because there were enough void spaces in MoO_2/graphene to buffer volume change. Secondly, the graphene also have made MoO_2 electrochemically active since charge carriers could be effectively and rapidly conducted back and forth from the MoO_2 nanoparticles to the current collector through the highly conducting the graphene network [26].

Acknowledgments

This work was supported by the National Nature Science Foundation of China (51202174), Science-Technology Chenguang Foundation for Young Scientist of Wuhan (201271031376), International S&T Cooperation Program of China (ISTCP) (2013DFR50710), Independent Innovation Project (2013-IV-030).

References

1. B. Luo, S. Liu and L. Zhi, *Small* **8**, 630 (2012).
2. D. Liu and G. Cao, *Energy Environ. Sci.* **3**, 1218 (2010).
3. W. Zhang, Y. Zeng, N. Xiao, H. H. Hng and Q. Yan, *J. Mater. Chem.* **22**, 8455 (2012).
4. D. Xie, W. Yuan, Z. Dong, Q. Su, J. Zhang and G. Du, *Electrochim. Acta* **92**, 87 (2013).
5. J. Wang, N. Yang, H. Tang, Z. Dong, Q. Jin, M. Yang, D. Kisailus, H. Zhao, Z. Tang and D. Wang, *Angew. Chem.* **125**, 6545 (2013).
6. A. Pan, H. B. Wu, L. Yu and X. W. D. Lou, *Angew. Chem.* **125**, 2282 (2013).
7. J. Luo, J. Liu, Z. Zeng, C. F. Ng, L. Ma, H. Zhang, J. Lin, Z. Shen and H. J. Fan, *Nano lett.* **13**, 6136 (2013).
8. Y. Liu, H. Zhang, P. Ouyang and Z. Li, *Electrochim. Acta* **102**, 429 (2013).
9. F. Gao, L. Zhang and S. Huang, *Mater. Lett.* **64**, 537 (2010).
10. W. Cho, J. H. Song, J. H. Kim, G. Jeong, E. Y. Lee and Y. J. Kim, *J. Appl. Electrochem.* **42**, 909 (2012).

11. Y. Yao, C. Xu, S. Yu, D. Zhang and S. Wang, *Ind. Eng. Chem. Res.* **52**, 3637 (2013).
12. Z.-S. Wu, W. Ren, L. Wen, L. Gao, J. Zhao, Z. Chen, G. Zhou, F. Li and H.M. Cheng, *ACS Nano* **4**, 3187 (2010).
13. V. Singh, D. Joung, L. Zhai, S. Das, S. I. Khondaker and S. Seal, *Prog. in Mater. Sci.* **56**, 1178 (2011).
14. H. Yu, T. Wang, B. Wen, M. Lu, Z. Xu, C. Zhu, Y. Chen, X. Xue, C. Sun and M. Cao, *J. Mater. Chem.* **22**, 21679 (2012).
15. Y. Chen, Q. Wang, C. Zhu, P. Gao, Q. Ouyang, T. Wang, Y. Ma and C. Sun, *J. Mater. Chem.* **22**, 5924 (2012).
16. M. Dieterle, G. Weinberg and G. Mestl, *Phys. Chem. Chem. Phys.* **4**, 812 (2002).
17. A. C. Ferrari, J. C. Meyer, V. Scardaci, C. Casiraghi, M. Lazzeri, F. Mauri, S. Piscanec, D. Jiang, K. S. Novoselov, S. Roth and A. K. Geim, *Phys. Rev. Lett.* **97**, 187401 (2006).
18. W. Shu, Y. Liu, Z. Peng, K. Chen, C. Zhang and W. Chen, *J. Alloys and Compd.* **563**, 229 (2013).
19. Q. Tang, Z. Shan, L. Wang and X. Qin, *Electrochim. Acta* **79**, 148 (2012).
20. Y. Shi, B. Guo, S. A. Corr, Q. Shi, Y. S. Hu, K. R. Heier, L. Chen,R. Seshadri and G. D. Stucky, *Nano Lett.* **9**, 4215 (2009).
21. Y. Sun, X. Hu, W. Luo and Y. Huang, *J. Mater. Chem.* **22**, 425 (2012).
22. L. C. Yang, Q. S. Gao, Y. H. Zhang, Y. Tang and Y. P. Wu, *Electrochem. Commun.* **10**, 118 (2008).
23. Y. Xu, R. Yi, B. Yuan, X. Wu, M. Dunwell, Q. Lin, L. Fei, S. Deng, P. Andersen, D. Wang, and H. Luo, *J. Phys. Chem. Lett.* **22** 309 (2012).
24. Q. Tang, Z. Shan, L. Wang and X. Qin, *Electrochim. Acta* **79**, 148 (2012).
25. H. Liu and J. Du, *Solid State Sci.* **8**, 526 (2006).
26. H. Wang, L. F. Cui, Y. Yang, H. S. Casalongue, J. T. Robinson, Y. Liang,Y. Cui and H. Dai, *J. Am. Chem. Soc.* **132**, 13978 (2010).

VC-$LiNO_3$:A HYBRID ADDITIVE IN CARBONIC ESTER ELECTROLYTESFOR SEI FORMATION ON LITHIUM METAL ELECTRODE

JING GUO, ZHAOYIN WEN*, MEIFEN WU, YU LIU

CAS Key Laboratory of Materials for Energy Conversion, Shanghai Institute of Ceramics,Chinese Academy of Sciences, Shanghai, China 200050

VC is considered as a desirable additive for the anode side in Li-ion batteries, while $LiNO_3$ is also supposed to be effective for improving the performance of Li-S batteries in ether-based electrolytes. Here we explored the modification effects of VC-$LiNO_3$ as an electrolyte additive in carbonic ester electrolytes. VC-$LiNO_3$ proves to perform quite well in enhancing the cycling performance of lithium metal anode. An efficiency of lithium plating/stripping as high as 98% was obtained. SEM images show a smooth lithium deposit obtained by the addition of VC-$LiNO_3$ indicating that a uniform solid electrolyte interphase(SEI) film is formed on the surface of lithium electrode. The electrochemical impedance spectroscopy (EIS) results demonstrate that the SEI layer, which can promptly accommodate to the change of lithium surface during cycling, is very stable. Given to the significant improvements in cycling performance and efficiency,VC-$LiNO_3$can be a promising candidate of electrolyte additive for lithium electrode in carbonate electrolyte.

1. Introduction

The lithium metal anode was used in primary batteries at the earliest and even realized commercially for a while due to its light weight and negative potential. But when it was employed in secondary cells, problems such as dendrite growth, low cycling efficiency, internal shorting etc. greatly hindered its application in rechargeable batteries[1-3]. Subsequently, other anode materials were studied to substitute lithium metal and carbon-based intercalation electrodes with safety performance and stable cycling capability have been successfully commercialized on a large scale in secondary batteries now.However, the theoretical capacity of C_6Li anode is only about 372 mAh/g[4]which is too limited to meet the demands for secondary lithium batteries with higher energy density. While Li metal possesses a specific capacity value as high as 3800 mAh/g that is 10 times of the one for carbon-based anodes[5]. Since today all kinds of communication equipments and digital electronic products are required to be lighter, thinner and

Proceedings of the 14th Asian Conference on Solid State Ionics (ACSSI 2014)
Copyright © 2014 ACSSI 2014 Organizers. All rights reserved.
ISBN: 978-981-09-1137-9
doi:10.3850/978-981-09-1137-9_151

smaller, researchers turn their attention to metallic lithium anode again expecting to solve the problematic issuesof it.

Despite of its attractive capacity, there exist two main problems when Li metal anodes being used in batteries. First, lithium reacts with solvent, electrolyte salts and trace of impurity in organic electrolytes generating a variety of complicated products[6]. These complex interface reactions lead to the increase of interface impedance and the deterioration of cycling capability. Second, heterogeneous deposition of lithium during cycling gives rise to the formation of dendrites and "dead" lithium, which lowers the coulombic efficiency and brings about safety concerns[1, 7].

Dendrite suppression has become an important issue in the research field of metallic lithium secondary batteries.It's urgent to find mechanisms of lithium dendrites growth and evolution so that the formation of dendrites could be prevented during the unintentional deposition of lithium[1].Researchers have been making great efforts to inhibit dendrites formation and realize the homogeneous electrochemical deposition of lithium. According to the previous study results, there are four categories of approaches for lithium metal modification. First, it's quite effective to conduct some pretreatments on lithium surface to form a protective layer. K. Chung et al. [8]deposited a thin, amorphous, smooth and dense protective solid electrolyte layer composed of lithium phosphorous oxynitride (LiPON)on the surface of the lithium electrode by RF magnetron sputtering. A stable solid electrolyte interface on the lithium anode was obtained which effectively limited the reaction between lithium and the electrolyte. Impedance measurements indicated that the LiPON layer was a more ionic conductor than the film formed by electrolyte decomposition. And cycling stability was also improved by the deposition of LiPON layer.Although this method seems to be of good controllability, itscost is too high to realize commercial application.Second, the common organic liquid electrolytes can be substituted by solid electrolytes[9], dry polymer electrolytes[10, 11] or other hybrid electrolytes[12-15], thus almost completely inhibiting the reaction between lithium metal and the liquid electrolyte. But the low ionic conductivity of non-liquid electrolytes and giant interfacial polarization limit their use in lithium metal batteries.Third, alloying of lithium metal with other elements could be adopted to inhibit the heterogeneous nucleation and growth of lithium electrodeposits.Johanna K. Stark et al. [16] studied the effect of alloying lithium metal with sodium to suppress dendritic growth. A small amount of sodium could disrupt lithium's dendritic growth and a smooth deposit was obtained, which was attributed to the change of the rate or mechanism of dendrite growth.However, this alloying approach goes against cycling performance of lithium anode. Fourth, some appropriate electrolyte additives, such as, hydrofluoric acid[17], acrylic

acid nitrile(AAN)[18], vinylene compound[19, 20] etc., can be added into liquid electrolytes to modify the solid electrolyte(SEI) film on lithium interface.Yet it's quite difficult and troublesome to seek out efficient additives among thousands of substance. In addition, some original methods were come up to deal with dendrite problems recently. Matthew Z. Mayers et al.[3] introduced a simulation model to describe lithium electrodeposition and dendrite growth in secondary lithium metal batteries, providing a powerful approach to addressing these questions.Liumin Suo et al.[21]showed a new class of 'Solvent-in-Salt' electrolyte in which salt holds a dominant position in the lithium-ion transport system. The cyclic and safety performance were remarkably enhanced via an effective suppression of lithium dendrite growth and shape change in the metallic lithium anode.

Among all the methods mentioned above, adding proper additives into electrolyte is the most widespread way to solve the dendrite problem.Vinylene carbonate(VC)was considered as a desirable additive for the anode side in Li-ion batteries[22], while $LiNO_3$was also supposed to be effective for improving the performance of Li-S batteries in ether-based electrolytes[23-25]. Considering that $LiNO_3$ has never been tested in carbonic ester electrolytes, here we explored the modification effects of VC-$LiNO_3$ as an electrolyte additive on SEI film in the most commonly used commercial electrolyte, namely1M $LiPF_6$in EC/DMC(1:1, vol%).

2. Experimental

Lithium battery grade ethylene carbonate (EC, Sigma), dimethyl carbonate (DMC, Sigma) and lithium hexafluorophosphate ($LiPF_6$, Aldrich) were used as received.In order to assess the electrochemical performance, Li/Cu coin cells of CR2025 type were assembled in an argon-filled glove box with oxygen and water contents less than 1 ppm. A solution of 1M $LiPF_6$ plus 0.1M $LiNO_3$ dissolved in EC/DMC with a volume ratio of 1:1 was employed as the electrolyte.2 vol% vinylenecarbonate(VC, anhydrous, ≥99%, Sigma) and 0.1 M $LiNO_3$ (≥99.99%, Sigma) were added together as the electrolyte additive. A glass fiber and lithium foil were used as the separator and as the anode, respectively.

Galvanostatic discharge/charge tests were performed on a LAND CT2001A battery test system by controlling discharge capacity in the plating process and charging voltage to 1.0V (vs. Li/Li^+) at a constant current of 0.5 mA/cm^2during the stripping process. AC impedance spectroscopy data were collected over a frequency range from 0.01 Hz to 1×10^6Hz with a potential amplitude of 10mV on an Autolab Electrochemical Workstation. All the electrochemical measurements were carried out at room temperature.

The samples for Scanning Electron Microscope(SEM, HITACHI S-3400)

measurements were prepared in the argon-filled glove box as follows.The cells were disassembled after 100 cycles and cycled lithium electrodes were washed with1,2-dimethoxyethane(DME, anhydrous, Sigma) and then dried for 2h.A special transfer system was employed to transfer lithium samples from the glove box to a SEM system without being exposed in the air.

3. Results and Discussion

3.1.*Cycling Efficiency*

Figure 1 compares the plating/stripping efficiency of Li/Cu cells cycled in electrolytes with and without VC-$LiNO_3$ additive. For the cell cycled in electrolyte without any additives,the efficiency is fluctuated around a low value of 85%, which indicates that the cycling process is rather instable. By contrast, the plating/strippingefficiency of the one cycled in electrolyte with VC-$LiNO_3$almost reaches 98% and maintains extremely stable after the first cycle.

The low efficiencyof the first cycle can be attributed to the electrochemical reaction between lithium and the components in electrolytes. It is corresponding to the formation of SEI film on lithium surface, similar to the process of electrochemical activation.When SEI film covers the whole surface of lithium, it will play a role in passivating lithium metal and prevents it from reacting with the electrolytes continuously[26]. The reason why cycling efficiency cannot reach exactly 100% is that part of SEI film cracks during the Li plating/stripping process.Then the exposed fresh lithium metal reacts constantly with the solvents and additives in electrolytes. So the charge(stripping) capacity is always less than the discharge(plating) capacity. This result indicates that VC-$LiNO_3$ indeed makes some positive modification on the interface between Li electrode and the organic electrolyte system.

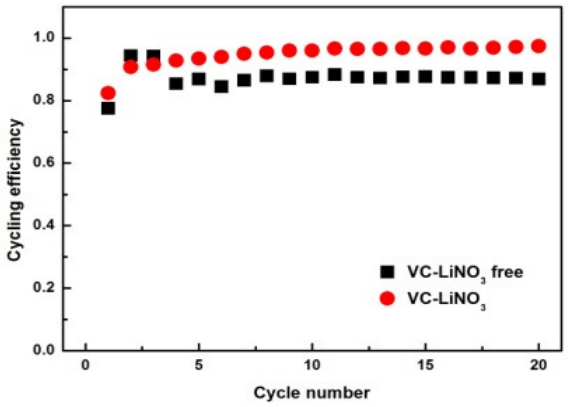


Figure 1.Cycling efficiencyof lithium electrode in electrolytes with or without VC-$LiNO_3$.

3.2. *SEM*

As previously mentioned, the SEI film with good properties can protect Li from reacting with electrolytes and suppress the formation of dendrites. Hence, to further investigate the SEI film and find more proof to explain the function of VC-$LiNO_3$ additive, the morphology of cycled lithium was examined by SEM as is shown in figure 2.

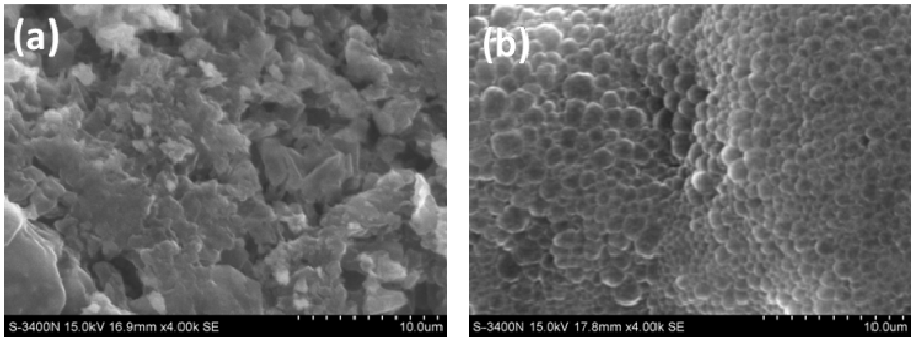


Figure 2.SEM images of lithium surface in electrolytesafter 20 cycles
a) without VC-$LiNO_3$ and b) with VC-$LiNO_3$.

Figure 2a and b show the difference of surface morphology of lithium after 20 cycles in two electrolytes. When VC-$LiNO_3$ is added, the coarse, uneven deposits(figure 2a) are substituted by a smooth deposition of lithium(figure 2b). Spherical particles with the diameter of 1-2μm are obtained due to the homogeneous SEI protective layer on the surface of them. This agrees with the difference of cycling efficiency in figure 1. This result provides powerful evidence for that VC-$LiNO_3$ is an additive conducive to the high plating/stripping efficiency when applied to carbonate electrolyte system.

3.3. *Electrochemical impedance spectroscopy*

Electrochemical impedance spectroscopy (EIS) of Li/Cu cells at various voltages provides further evidence for the superior cycling performance of lithium electrode in VC-$LiNO_3$ containing electrolyte, as figure 3 indicates. In view of the fact that formation and growth of SEI film is accompanied by change of the $R_{interface}$, we can use EIS as an in situ tool to study the property of the SEI[27].

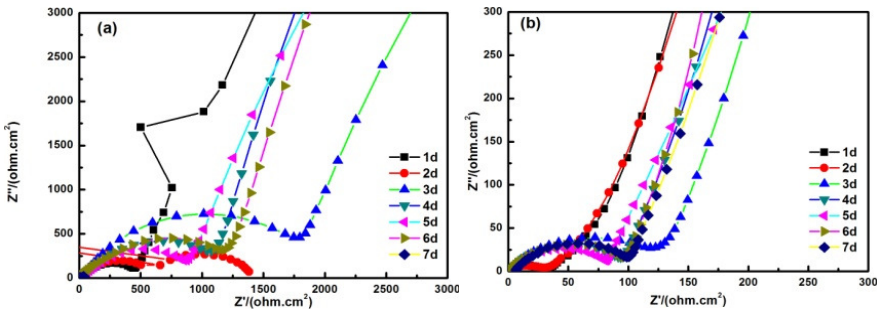


Figure 3.Nyquist plots of Li/Cu cells in electrolyte a) without additives and b) with VC-$LiNO_3$.

According to the change of Nyquist plot with time, it's reasonable to conclude that the interface in VC-$LiNO_3$ containing electrolyte system is relatively stable in 7 days, which can be clearly seen in figure 3b. In general, the resistance increases with the reactivity of solvents and salts[27]. However, this phenomenon is not observed for the cell with VC-$LiNO_3$ containing electrolyte, the resistance value of which is almost invariable with time. This suggests that addition of VC-$LiNO_3$ into electrolyte can significant enhance stability of the SEI since it participates into the formation of the SEI. It should also be noted that the value of resistancegreatly decreases when VC-$LiNO_3$ being added, demonstrating the formation of highly conductive SEI film.

4. Conclusion

VC-$LiNO_3$, as an effective electrolyte additive in the most common carbonate electrolyte system, which participates into the formation of the SEI, makes positive modifications on SEI film on the surface of lithium electrode. An efficiency of lithium plating/stripping as high as nearly 98% was obtained and maintains extremely stable after the first cycle.A very homogeneous morphology of cycled lithium indicates formation of uniform SEI film that can inhibit growth of dendrites to some extent. EIS results demonstrate that addition of VC-$LiNO_3$ into electrolyte can significant enhance stability of the SEI and electrochemical activity.We believe that VC-$LiNO_3$ is expected to become a fairly promising additive candidate for carbonate electrolytes.

Acknowledgement

This work was financially supported by the Natural Science Foundation of China (NSFC, Project No.51201177).

References

1. J. K. Stark, Y. Ding and P. A. Kohl, *Journal of the Electrochemical Society*. **160**, D337 (2013).
2. I. W. Seong, C. H. Hong, B. K. Kim and W. Y. Yoon, *Journal of Power Sources*. **178**, 769 (2008).
3. M. Z. Mayers, J. W. Kaminski and T. F. Miller, *The Journal of Physical Chemistry C*. **116**, 26214 (2012).
4. K. Nishikawa, T. Mori, T. Nishida, Y. Fukunaka and M. Rosso, *Journal of Electroanalytical Chemistry*. **661**, 84 (2011).
5. P. Suresh, A. K. Shukla, S. A. Shivashankar and N. Munichandraiah, *Journal of Power Sources*. **132**, 166 (2004).
6. D. Aurbach, *Journal of Power Sources*. **89**, 206 (2000).
7. D. R. Ely and R. E. Garcia, *Journal of the Electrochemical Society*. **160**, A662 (2013).
8. K. Chung, W. S. Kim and Y. K. Choi, *Journal of Electroanalytical Chemistry*. **566**, 263 (2004).
9. I. Gurevitch, R. Buonsanti, A. A. Teran, B. Gludovatz, R. O. Ritchie, J. Cabana and N. P. Balsara, *Journal of the Electrochemical Society*. **160**, A1611 (2013).
10. J. M. Tarascon and M. Armand, *Nature*. **414**, 359 (2001).
11. C. Monroe and J. Newman, *Journal of The Electrochemical Society*. **150**, A1377 (2003).
12. X.-W. Zhang, Y. Li, S. A. Khan and P. S. Fedkiw, *Journal of The Electrochemical Society*. **151**, A1257 (2004).
13. Y. Lu, S. S. Moganty, J. L. Schaefer and L. A. Archer, *Journal of Materials Chemistry*. **22**, 4066 (2012).
14. T. Tatsuma, M. Taguchi and N. Oyama, *Electrochimica Acta*. **46**, 1201 (2001).
15. T. Tatsuma, M. Taguchi, M. Iwaku, T. Sotomura and N. Oyama, *Journal of Electroanalytical Chemistry*. **472**, 142 (1999).
16. J. K. Stark, Y. Ding and P. A. Kohl, *Journal of The Electrochemical Society*. **158**, A1100 (2011).
17. K. Kanamura, *Journal of The Electrochemical Society*. **143**, 2187 (1996).
18. H. J. Santner, K. C. Möller, J. Ivančo, M. G. Ramsey, F. P. Netzer, S. Yamaguchi, J. O. Besenhard and M. Winter, *Journal of Power Sources*. **119-121**, 368 (2003).
19. C. Korepp, H. J. Santner, T. Fujii, M. Ue, J. O. Besenhard, K. C. Möller and M. Winter, *Journal of Power Sources*. **158**, 578 (2006).
20. K. C. Möller, H. J. Santner, W. Kern, S. Yamaguchi, J. O. Besenhard and M. Winter, *Journal of Power Sources*. **119-121**, 561 (2003).
21. L. Suo, Y. S. Hu, H. Li, M. Armand and L. Chen, *Nature communications*. **4**, 1481 (2013).
22. D. Aurbach, *Electrochimica Acta* (2002).
23. Z. W. Xiao Liang, *Journal of Power Sources* (2011).
24. S. Xiong, *Electrochimica Acta* (2012).
25. S. S. Zhang, *Electrochimica Acta*. **70**, 344 (2012).
26. P. Verma, P. Maire and P. Novák, *Electrochimica Acta*. **55**, 6332 (2010).
27. S. S. Zhang, K. Xu and T. R. Jow, *Electrochimica Acta*. **51**, 1636 (2006).

ELECTROCHEMICAL IMPEDANCE SPECTROSCOPY ANALYSIS OF V_2O_5 NANOWIRES ELECTRODE AS LITHIUM-ION BATTERIES

ZHAOLONG LI, SHANSHAN JIANG, QUANYAO ZHU, SHENGNAN HUANG, CHUNXIA ZHAO, WEN CHEN†

State Key Laboratory of Advanced Technology for Materials Synthesis and Processing, School of Material Science and Engineering, Wuhan University of Technology Wuhan 430070, P. R. China

GALINA S. ZAKHAROVA

Institute of Solid State Chemistry, Ural Branch of the Russian Academy of Sciences Ekaterinburg 620990, Russian Federation

Vanadium pentoxide (V_2O_5) nanowires were synthesized by a hydrothermal method. The electrode was synthesized by dispersal and filter process to form flexible shape. The structure and morphology of the V_2O_5 nanowires were characteristic by XRD and FESEM. The cyclic voltammetry (CV) curve revealed the three pairs of reduction/oxidation electrochemical reaction occurred during the lithium ions insertion/extraction process. The electrochemical impedance spectroscopy (EIS) was used to explore the interface changes at different discharge state for V_2O_5 nanowire electrode. The results indicated that the charge transfer resistance of V_2O_5 nanowire increased from 22.08 to 507.98 Ω when the discharge voltage decreased from 4.0 to 2.0 V.

1. Introduction

Recently, the applications of lithium-ion batteries (LIBs) to electrical vehicles are investigated for the demands of the high-power density and long cycle life [1]. As these performances are highly determined by the electrode/electrolyte interfacial effect, it is very importance to understand the reaction mechanisms and control the interfacial reactions [2, 3].

Electrochemical impedance spectroscopy (EIS) is widely used to gain a deep insight into internal interfaces and the changes that occur during charging-discharging process and degradation of the LIBs [4]. The EIS measurement possesses a wide frequency range, which offers the possibility to draw

†Corresponding author, email: chenw@whut.edu.cn

Proceedings of the 14th Asian Conference on Solid State Ionics (ACSSI 2014)
Copyright © 2014 ACSSI 2014 Organizers. All rights reserved.
ISBN: 978-981-09-1137-9
doi:10.3850/978-981-09-1137-9_102

conclusions about internal process with different time constants. These constants imply the interpretation and quantification of the changes in the impedance spectra depending on the determination of parameters related with state-of-charge and state-of-health [5].

In this work, V_2O_5 nanowires were synthesized by hydrothermal method. The internal interfaces and the influence of voltage state of V_2O_5 nanowire electrode based half-cells LIBs have been explored by EIS analyses. The equivalent-circuit model has been employed to interpret the EIS data. The value changes on the impedance spectra were measured in order to study the regular rules between the charge voltage and the internal interface resistance.

2. Experimental

2.1. *Synthesis of V_2O_5 Nanowires*

The vanadium oxide sol was synthesized by a chemical reaction between V_2O_5 powder and hydrogen peroxide (H_2O_2, 30%). Briefly, 0.364 mg V_2O_5 powder was added into 65 mL deionized water, and 5 mL H_2O_2 was slowly dissolved in the solution under vigorously stirring. Then, the orange solution was stand at 4 °C for 24 hours to form a dark orange V_2O_5 sol. The V_2O_5 nanowires were fabricated by a hydrothermal method. In brief, the prepared V_2O_5 sol was transferred to a 100 mL Teflon-lined autoclave with a stainless steel shell. Then the autoclave was kept at 240 °C in oven for 2 days. The obtained yellow floccule was vigorously stirring in deionized water to form a V_2O_5 nanowires suspension. During the stirring process, the carbon black (20% weight ratio compared to V_2O_5 nanowires) was added into the suspension. And then the mixture suspension followed filtration, dried process. At last, the flexible paper shape was obtained.

2.2. *Characterizations*

The structure of the samples was characterized by X-ray diffraction (XRD) with a CuK_α (λ=1.5418 Å) radiation and graphite monochrometer. Field emission scanning electron microscopy (FESEM) images were collected on a JSM-5610LV microscope operated at 20 kV.

2.3. *Coin Cell Assemble and Electrochemical Measurements*

The cathode materials were synthesized by punching the V_2O_5 nanowires paper to small circle pieces with diameters of 11 mm. The electrolyte was used of 1 M $LiPF_6$ dissolved in ethylene carbonate (EC)-dimethyl carbonate (DMC) (1:1, v/v).

Celgard 2500 was used as the separator, and lithium metal as the anode electrode. The 2032 coin cells were assembled in an argon-filled glove box with both moisture and oxygen levels were less than 1 ppm.

Galvanostatic charge-discharge tests were carried out using LAND cell-testing system in the voltage range from 2.0 to 4.0 V. All coin cells were cycled five times at the rate of 0.1 *C* before the electrochemical tests. Cyclic voltammetry (CV) was measured by a PGSTAT 30 Autolab with a potential range from 2.0 to 4.0 V at the scanning rate of 0.1 mVs^{-1}. Electrochemical impedance spectroscopy (EIS) measurements were collected in the frequency region between 0.01Hz and 100 kHz with a 5 mV amplitude voltage. Nyqusit plots were simulated and analyzed using NOVA software.

3. Results and Discussion

3.1. *Morphology and Structure*

Figure 1(a) shows the photo of the synthesized V_2O_5 nanowires. It shows a good flexibility property. Figure 1(b) and (c) show the FESEM images of the V_2O_5 nanowires paper. It can be seen that the V_2O_5 nanowires form a network morphology with length of several tens micrometers and width ranging from 50-150 nm. The small particles are the carbon black, which homogeneous dispersed in the V_2O_5 nanowires network.

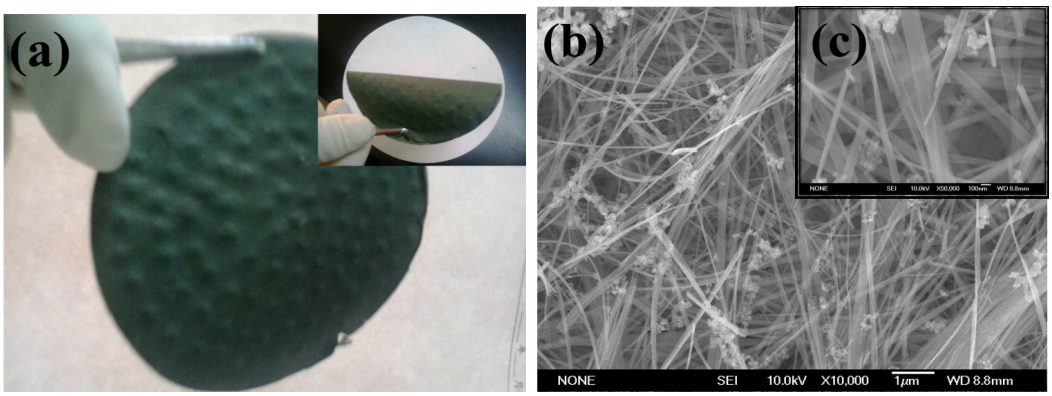


Figure 1. (a) Photo of V_2O_5 nanowires paper, (b) and (c) FESEM images of V_2O_5 nanowires.

Figure 2 shows the XRD pattern of V_2O_5 nanowires. A series of characteristics diffraction peaks (200), (010), (110), (210), (310), (311), (320), and (610) are ascribed to the reflections of orthorhombic V_2O_5 (JCPDS No. 01-086-2248).

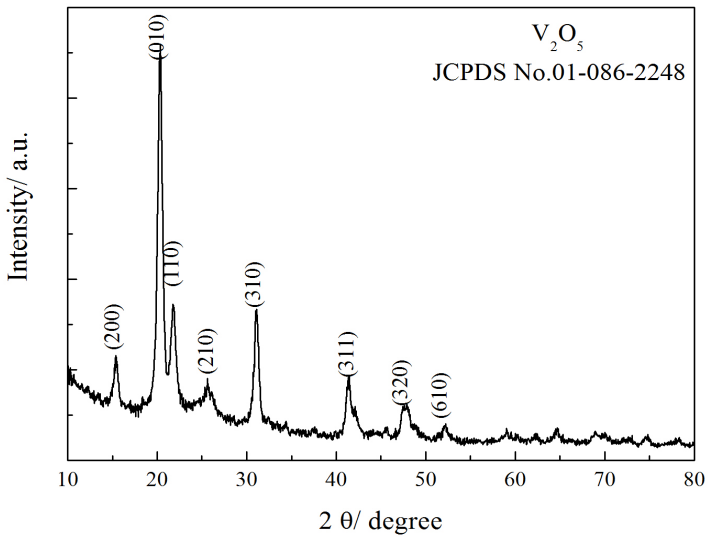


Figure 2. XRD pattern of the V_2O_5 nanowires.

3.2. *Electrochemical Performance*

Figure 3 shows the CV curve of V_2O_5 nanowires electrode at a scan rate of 0.1 mVs^{-1} within 4.0-2.0 V (vs. Li/Li^+). The three cathodic (reduction) peaks located at the potential of 3.4, 3.2, and 2.3 V indicate the multi-step lithium ions insertion process. While the obtained anodic (oxidation) peaks appeared at the potential of 2.6, 3.3, and 3.6 V correspond to the lithium ions extraction process.

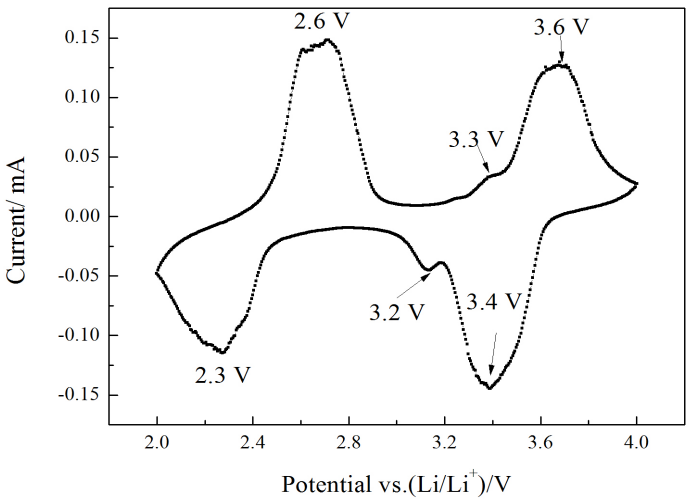


Figure 3. CV curve of the V_2O_5 nanowires at a scan rate of 0.1 mVs^{-1} between 2.0 and 4.0 V.

Figure 4(a) shows the discharge curve of V_2O_5 nanowires in the potential ranges of 4.0-2.0 V at 0.1 *C*. It can be seen that the V_2O_5 nanowires exhibit three discharge plateaus, which are corresponding to the three reduction peaks as shown in Figure 3. Due to the lithium ions insertion affection, the V_2O_5 nanowires display three phase transition process during the electrochemical reactions. To investigate the interface reaction process, we studied the EIS of V_2O_5 nanowires electrode. Figure 4(b)-(g) show the Nyquist plots for the impedance of the nanowires at different discharge state. The intercept at the *Z'* axis in the high frequency refers to the electrolyte solution resistance and electric contact resistance. The depressed semicircle in the high frequency corresponded to the lithium ions migration resistance through the solid-electrolyte interface (SEI) layer forms on the electrode. Second semicircle in the middle frequency range is related to the charge transfer resistance. The sloping line in the low frequency represents lithium-ion diffusion resistance in the electrode material, namely the Warburg impedance [6]. Figure 4(h) shows the fitting equivalent circuit result from the Nyquist plots. Herein, R_s stands for the electrolyte resistance and electric contact resistance in the coin battery, R_f and CPE_1 refer to the resistance and capacitance of the SEI layer, respectively. R_{ct} and CPE_2 describe as the charge transfer resistance and double-layer capacitance, respectively. And *W* is the Warburg impedance. Table 1 shows the impedance parameters calculated depending on the equivalent circuits. As the state charge to 4.0 V, the slop value of the Warburg diffusion curve is greater than that of fitting value. Generally, the standard slops value of the Warburg diffusion is $\pi/4$. The obviously large value of the measured date may ascribe to the ordered layer of lithium ions at high voltage state. The values of the R_s and R_f show a little change as the discharge state decreases from 4.0 to 2.3 V. While the R_{ct} increases from 22.08 to 120.78 Ω. The results indicate a sustained and stable electrochemical reaction for the insertion of lithium ions. However, there is a significant change in the impedance parameters when the electrode discharges to 2.0 V. The increases values of R_s may describe by series-connected and short-circuit terminated reaction after the V_2O_5 layer inserted by lithium ions. The presence of huge R_{ct} values implies diffusion of lithium ion inside a disordered layer of the V_2O_5 crystalline. And then the lithium ions follow subsequent transfer through a disordered layer/crystalline kernel interface and further diffusion inside the crystalline kernel [7]. On the other hand, the impedance parameters down back to the original values as the electrode recharge to 4.0 V, which means a stable and repeatable performance of the interface of V_2O_5 nanowires electrode. In addition, we note that the R_f for SEI layer keeps a minor changes as the discharge state changes. This highly stable SEI layer can be benefit for the stability capacity of V_2O_5 nanowires electrode during the charge/discharge process.

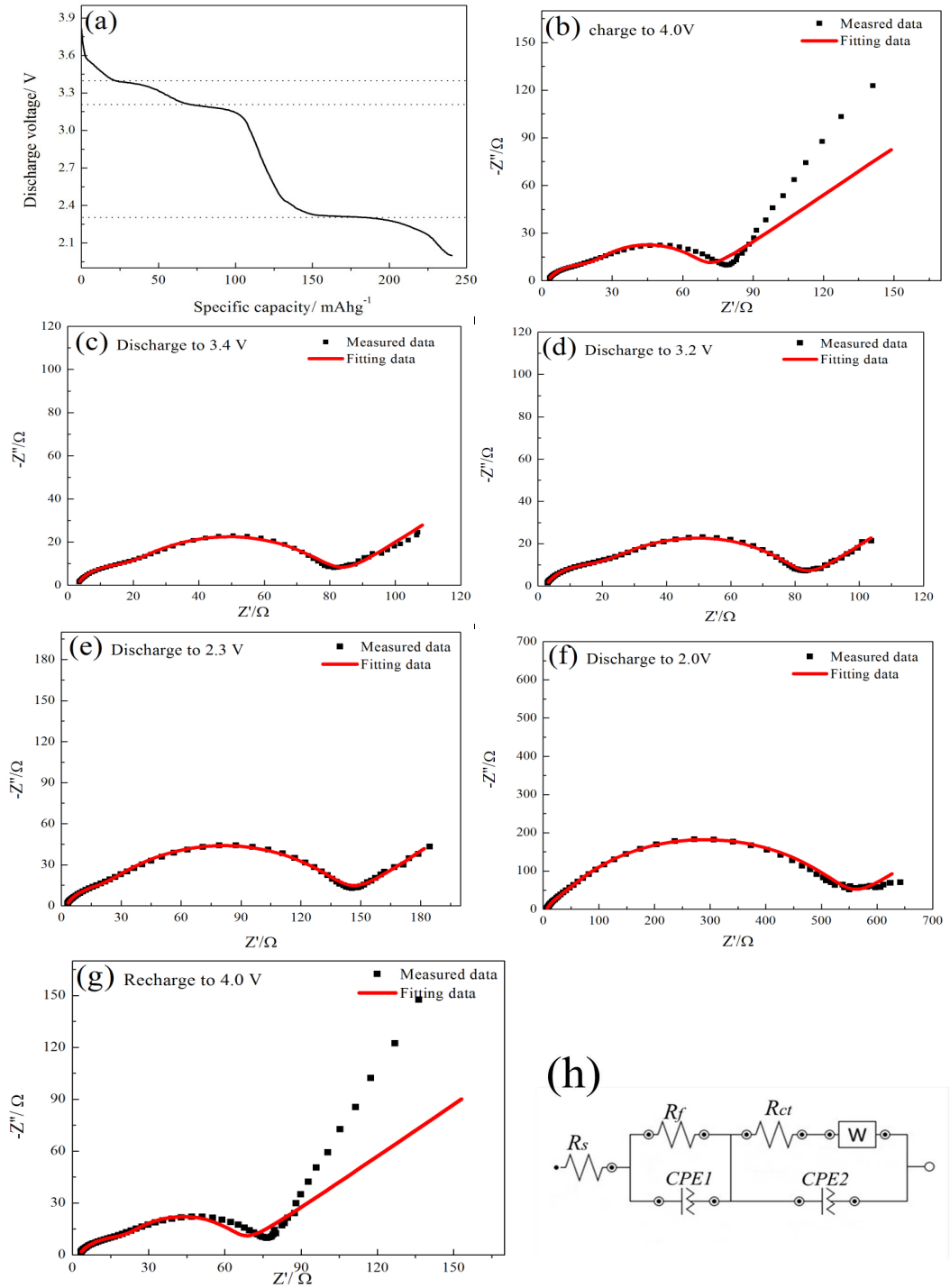


Figure 4. (a) Discharge curve of V_2O_5 nanowires, (b)-(g) Nyuist plots of V_2O_5 nanowires electrode at different discharge state with 5 mV amplitude, (h) the equivalent circuits used to model the impedance spectra.

Table 1. Impedance parameters calculated from equivalent circuits.

Voltage state	R_s/Ω	R_f/Ω	R_{ct}/Ω
Charge to 4.0 V	2.55	18.56	22.08
Discharge to 3.4 V	2.93	14.53	63.69
Discharge to 3.2 V	2.49	16.80	62.22
Discharge to 2.3 V	2.62	16.81	120.78
Discharge to 2.0 V	6.43	18.12	507.98
Re-charge to 4.0 V	2.55	19.92	37.55

4. Conclusions

In summary, the V_2O_5 nanowires were fabricated by hydrothermal method. The electrode was synthesized by a filter process. The CV curve indicates that the V_2O_5 nanowires show three pairs of redox peaks which indicate a three phase transition of V_2O_5 crystalline during the lithium ions insertion and extraction process. The EIS results indicate the SEI layer plays an important role during the batteries cycle process. The transfer resistance of V_2O_5 nanowires increases from 22.08 to 507.98 Ω when the discharge voltage decreases from 4.0 to 2.0 V.

Acknowledgments

This work is supported by the Fundamental Research Funds for the Central Universities (145101008, 20131049701001) and a joint project of National Nature Science Foundation of China and Russian Foundation for Basic Research (NSFC-RFBR 51011120252).

References

1. B. Dunn, H. Kamath and J.M. Tarascon, *Science* **334**, 928 (2011).
2. J.M. Tarascon and M. Armand, *Nature* **414**, 359 (2001).
3. N. Schweikert, R. Heinzmann, A. Eichhöfer, H. Hahn and S. Indris, *Solid State Ionics* **226**, 15 (2012).
4. M. Gaberscek, J. Moskon, E. Erjavec, R. Dominko and J. Jamnik, *Electrochem. Solid-State Lett.* **11,** A170 (2008).
5. D. Andre, M. Meiler, K. Steiner, C. Wimmer, T. Soczka-Guth and D.U. Sauer, *J. Power Sources* **196**, 5334 (2011).
6. S. Rodrigues, N. Munichandraiah and A.K. Shukla, *J. Solid State Electrochem.* **3**, 397 (1999).
7. O.Y. Posudievsky, O.A. Kozarenko, V.S. Dyadyun, S.W. Jorgensen, J.A. Spearot, V.G. Koshechko and V.D. Pokhodenko, *Electrochim. Acta* **58**, 442 (2011).

Solid Electrolytes II

ALL-SOLID-STATE LITHIUM BATTERIES USING Li_6PS_5Br SOLID ELECTROLYTE

CHEN MAOHUA, RAYAVARAPU PRASADA RAO, STEFAN ADAMS

Department of Materials Science and Engineering, National University of Singapore, 5 Engineering Drive 2, E2 05-22, Singapore, 117579, Singapore

Lithium argyrodites Li_6PS_5X (X= Cl, Br) are attractive candidates for all-solid-state lithium batteries with regard to their relatively high ionic conductivity, low cost and low temperature fabrication. Here we discuss the combination of the argyrodite Li_6PS_5Br with various cathode materials CuS, S and MoS_2 in such batteries. CuS/Li_6PS_5Br/In-Li batteries show an initial discharge capacity of 650 mAh/g, yet a reversible capacity of 90 mAh/g after 20 cycles. Ex-situ XRD data of the composite cathode yield a peculiar reaction mechanism of CuS in this battery involving the partial exchange of Cu^+ for Li^+ in the both argyrodites and active material at intermediate discharge state, yielding $Cu_xLi_{6-x}PS_5Br$ and $Cu_yLi_{2-x}S$. The resulting reduced ionic conductivity is one of the reasons for the poor capacity retention. Eliminating this detrimental effect of Cu^+, S/Li_6PS_5Br/In-Li batteries reach an initial discharge capacity of 1670 mAh/g and an enhanced cyclic performance with capacity of 1280 mAh/g after 5 cycles. In MoS_2/Li_6PS_5Br/In-Li batteries the initial discharge product metallic Mo no longer participates in the cycling, but acts as a well-dispersed conductivity enhancing component in the thereby formed Li/S battery further reducing the capacity fading but also somewhat reducing theoretically achievable capacity.

1. Introduction

By using ceramic solid electrolytes, all-solid-state lithium secondary batteries promise improved safety, cyclability and energy density when compared to batteries containing conventional liquid electrolyte batteries. Fast Li^+ conductors lithium argyrodites Li_6PS_5X (X= Cl, Br) are one of the most promising candidates as solid electrolyte, due to their high ionic conductivity (~7×10^{-4} S/cm) and wide electrochemical windows.[1,2,3] However, there are only a few preliminary studies on all-solid-state lithium secondary batteries using Li_6PS_5X solid electrolyte. Stadler et al. [4] prepared LTO/Li_6PS_5Br/Al-Li batteries, yet showing high overpotential and poor cyclic performance at room temperature. At non-ambient temperature, e.g. 75°C, the battery worked better with an initial discharge capacity of 150 mAh/g and reversible capacity of 90 mAh/g after 30 cycles at C/50. Later, our group also realized a LTO/Li_6PS_5Cl/Li battery with enhanced room temperature cyclic performance, reaching a reversible capacity of 57 mAh/g after 60 cycles.[3]

Proceedings of the 14th Asian Conference on Solid State Ionics (ACSSI 2014)
Copyright © 2014 ACSSI 2014 Organizers. All rights reserved.
ISBN: 978-981-09-1137-9
doi:10.3850/978-981-09-1137-9_154

Despite of decades of investigation on intercalation cathode materials, energy density of lithium-ion batteries has not been significantly improved yet, mainly due to the natural limitation of intercalation materials: typically only up to one Li^+ could be intercalated per 3d-metal atom. Therefore, sulfur-based conversion-type materials [5,6] have attracted considerable attention: two to four Li^+ could take part into the reaction per 3d-metal atom (or 2 Li^+ per S in Li/S batteries), leading to substantially higher specific capacity. In this study we report on all-solid-state lithium batteries combining argyrodite Li_6PS_5Br solid electrolyte with three types of sulfur-based conversion cathode materials, namely CuS, S and MoS_2.

CuS batteries show a high initial discharge capacity of 650 mAh/g of CuS but experience a fast fading to 90 mAh/g after 20 cycles. Our studies reveal that the mixed mobile ion effect caused by Cu^+ for Li^+ substitution in argyrodites as one of the factors causing this capacity fading. When we directly used elemental sulfur as the active cathode material (which requires the formation of a well-distributed carbon/S/solid electrolyte composite to ensure both electronic and cionic conductivity in the cathode), all-solid-state batteries achieved a high initial discharge capacity of 1670 mAh/g of S as well as less capacity fading (1280 mAh/g after 5 cycles). Similarly, fully discharging MoS_2 cathodes resulted in a Li/S battery, where electrochemically inactive metallic Mo particles were well-dispersed in the cathode and thereby increased the electronic conductivity of the composite cathode and further reduced the capacity fading.

2. Experimental

Argyrodite Li_6PS_5Br solid electrolyte was synthesized by ball milling and subsequent annealing.[7] Stoichiometric mixture of Li_2S, P_2S_5 and LiBr were ball milled under a rotating speed of 500 rpm for 20h using the planetary ball mill apparatus (Fritsch Pulverisette 7). The ball-milled precursor was then pelletized and annealed at 300°C for 5 h. The resulting pellet was ground into powder for further application. It is noted that the synthesis was conducted in a dry Ar atmosphere.

CuS and MoS_2 composite cathodes were prepared simply by one-step ball milling. The mixture of CuS/MoS_2, Li_6PS_5Br and carbon black in a weight ratio of 40: 56: 4 was ball milled at 500 rpm for 30 min. On the other hand, S composite cathode was fabricated by two-step ball milling. Sulfur and carbon black was ball milled in a weight ratio of 1: 1 at 500 rpm for 5 h. Li_6PS_5Br was added to the mixture, leading to a weight ratio of S: Li_6PS_5Br: C= 20: 60: 20, and ball milled again at 500 rpm for 30 min. These three kinds of composite cathode powders, combined with Li_6PS_5Br solid electrolyte, were used to design all-solid-state lithium secondary batteries. The solid electrolyte powder and

respective cathode mixture were pelletized in a 13 mm die under a pressure of 6000 kg/cm^2. An indium-lithium anode was then attached to the pellet and sealed in a Swagelok-type cell.

Room temperature cyclic performance of the all-solid-state lithium secondary batteries were studied at a rate of C/50 using a potentiostat/ galvanostat (Arbin BT2000). The voltage scale was 0.05 to 2.5 V for CuS battery and 0.4 to 2.4 V for S battery, while that for MoS_2 was -0.5 to 2.5 V in the first 5 cycles followed by 0.05 to 2.5 V in the subsequent cycles. Ex-situ X-ray diffraction (XRD) measurement was performed on CuS composited cathode before cycling and at a discharge state of 300 mAh/g. Rietveld refinement of the XRD patterns was conducted using the generalized structure analysis system (GSAS) [8] with the graphical user interface EXPGUI [9].

3. Results and Discussion

Room temperature cyclic performance of the all-solid-state CuS/Li_6PS_5Br/In-Li battery was investigated at C/50 rate between 0.05 and 2.5 V.[10] Discharge capacity and charge capacity of the battery during cycling is shown in Figure 1. A high discharge capacity of 650 mAh/g (with respect to the weight of CuS) could be obtained in the first cycle. While the theoretical specific capacity of CuS is 560 mAh/g, the excess capacity of 90 mAh/g could be attributed to pseudo-capacitive interfacial charge storage. During cycling, however, the capacity of the battery rapidly deceased, leaving only 90 mAh/g after 20 cycles.

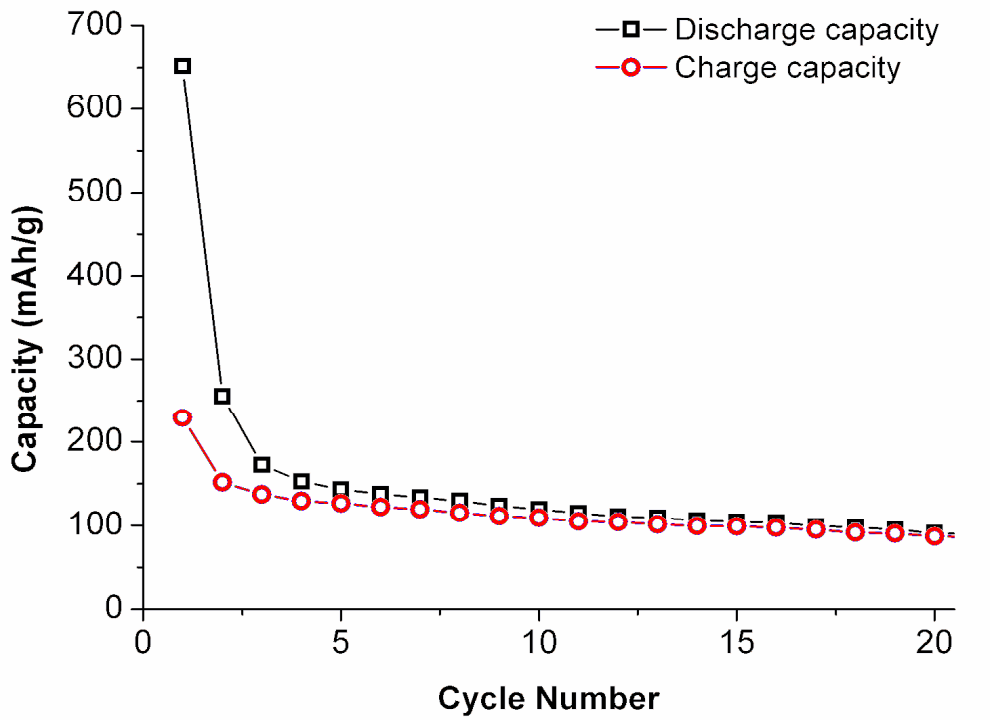


Figure 1. Room temperature cyclic performance of all-solid-state CuS/Li_6PS_5Br/In-Li batteries at C/50 rate in the voltage scale of 0.05 V and 2.5 V up to 20 cycles.

To figure out the reasons for this rapid capacity fading of CuS/Li_6PS_5Br/In-Li battery, ex-situ XRD was conducted on the composite cathode before cycling and at a discharge state of 300 mAh/g (around half discharge). The XRD patterns are shown in Figure 2. The composite cathode before cycling only showed the phases of argyrodite-type Li_6PS_5Br and CuS. When the composite cathode was discharged to 300 mAh/g, CuS disappeared completely, while a substantial amount of Li_2S occurred. However, no sign of crystalline phases containing Cu^{2+}/Cu^{+}/Cu or of a substantial amount of amorphous phases is discernible, suggesting that the Cu atoms should reside in argyrodite and/or Li_2S. A closer look at the peaks of argyrodites revealed that the individual peak positions and intensities significantly varied, suggesting formation of analogous argyrodite structure. Considering that copper argyrodite Cu_6PS_5Br is isostructural to Li_6PS_5Br [11,12] and Cu^{+} crystal-chemically behaves similar to Li^{+} [13], it should be plausible to propose that Cu^{+} ions reversibly replace Li^{+} in Li_6PS_5Br, leading to $Cu_xLi_{6-x}PS_5Br$. Detailed Rietveld refinement allowing for such Cu^{+} for Li^{+} exchange in both argyrodite and Li_2S led to considerably enhanced fit, which confirms the formation of $Cu_xLi_{6-x}PS_5Br$ and $Cu_yLi_{2-y}S$. Such partial cation exchange leads to a mixed mobile ion electrolyte with reduced conductivity, thus reducing the cyclic performance of the battery.

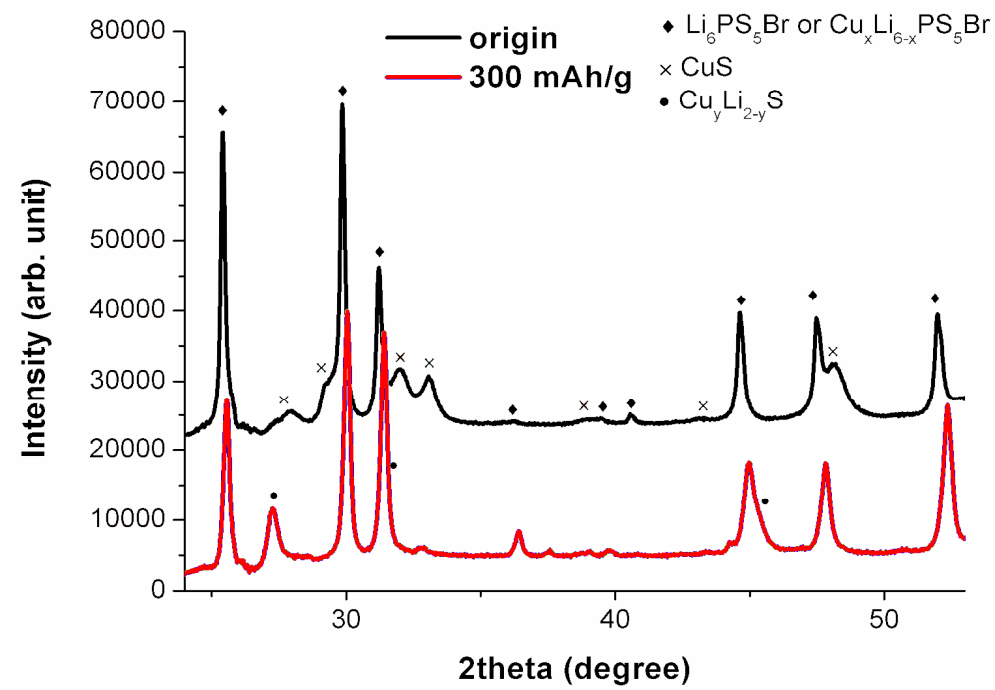


Figure 2. XRD patterns of the composite cathode of all-solid-state CuS/Li_6PS_5Br/In-Li battery before cycling and at a discharge state of 300 mAh/g.

Considering the negative role of Cu^+ in the cyclic performance of all-solid-state lithium batteries using Li_6PS_5Br solid electrolyte, copper compounds that can generate Cu^+ during cycling should be avoided as a constituent of the cathode materials in battery designs involving argyrodites (or related thiophosphate solid electrolytes). Therefore, as the next step we prepared an all-solid-state Li/S battery. The sulfur composite cathode powder was prepared by two-step ball milling. As a result, sulfur, super P carbon and argyrodite solid electrolyte were uniformly mixed, with a particle size smaller than 100 nm. Discharge/charge curves of the battery cycling at C/50 between 0.4 and 2.4 V up to 5 cycles at room temperature are shown in Figure 3. As seen an initial discharge capacity of 1670 mAh/g was achieved, which matches the theoretical capacity. When compared to the CuS-based batteries, the cyclability was significantly improved. After 5 cycles the reversible discharge capacity was still 1280 mAh/g. However, a continuous increase of overpotential with prolonged cycling could also be discerned. This may be tentatively traced back to the ca. 80% volume change of the active material during the electrode reaction $S+2Li \leftrightarrow Li_2S$. As a consequence the interface among S, carbon and argyrodites deteriorates progressively. Since both S and Li_2S are of poor electronic and ionic conductivity, such weakening contact to the conductive phases may be expected to play a dominant role for the capacity fading in these all-solid-state batteries.

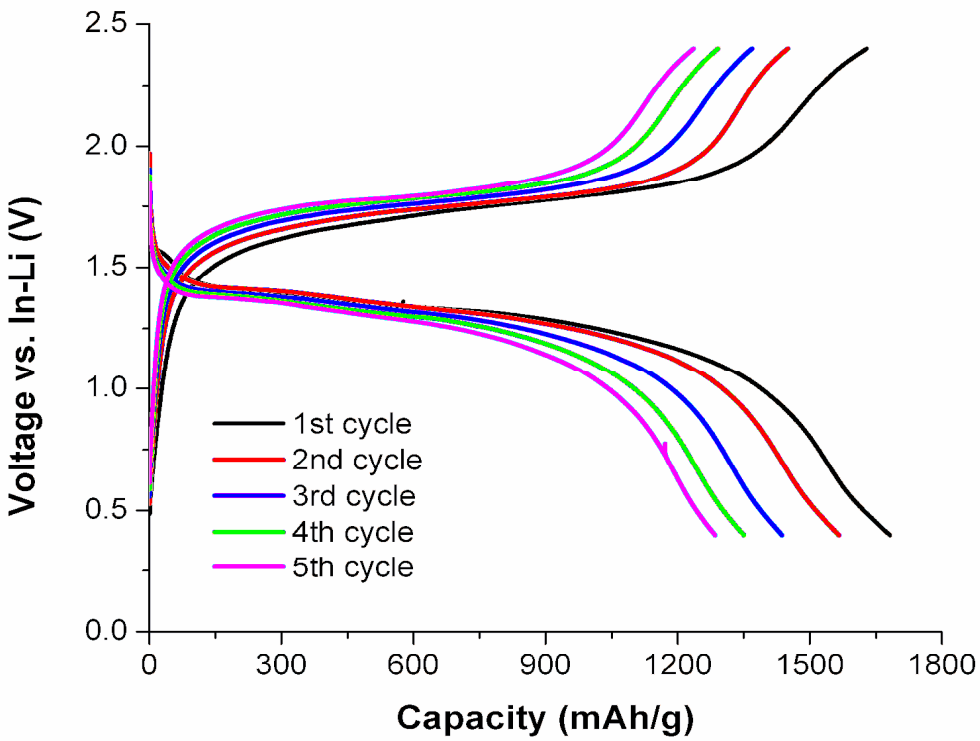


Figure 3. Discharge/Charge curves of all-solid-state S/Li_6PS_5Br/In-Li batteries at C/50 rate in the voltage scale of 0.4 V and 2.4 V up to 5 cycles.

When using MoS_2 (with a theoretical capacity of 670 mAh/g) as the active cathode material it has been reported that the conversion reaction occurring on full discharge is not reversible.[14,15] The thereby formed metallic Mo particles will no longer take part into the reaction and the battery will effectively become a Li/S battery with nano-sized Mo particles embedded in the active materials. This in turn will improve the electronic conductivity of the cathode. In our study we also prepared the first all-solid-state Li/MoS_2 battery using Li_6PS_5Br as the solid electrolyte. Figure 4 demonstrates the capacity of an all-solid-state Li/MoS_2 battery during cycling. In the first 5 cycles, the battery was cycled between -0.5 – 2.5 V (vs. In-Li) to activate the battery, i.e. to ensure a complete conversion of MoS_2 to Mo and Li_2S. An initial discharge capacity of 825 mAh/g was achieved, including the low-voltage contributions from pseudocapacitive effects. The formation of finely dispersed Mo and the different electrochemical reaction lead to an enhanced energy efficiency via an increased discharge voltage. After a steep drop of capacity at the second cycle, the capacity became relatively stable. In contrast to the Li/S battery discussed above, there is also no sign of a significant increase in overpotential during cycling. At the 5^{th} cycle, the discharge capacity was still reaching 610 mAh/g. Thereafter the voltage range was restricted to between 0.05 and 2.5 V vs In-Li. Still the battery showed an

improved capacity retention compared to that of the all-solid-state batteries using CuS or S as cathode, suggesting that the dispersed Mo particles in the cathode can significantly improve the cyclic performance of the battery. A reversible capacity of 260 mAh/g was obtained up to 25 cycles.

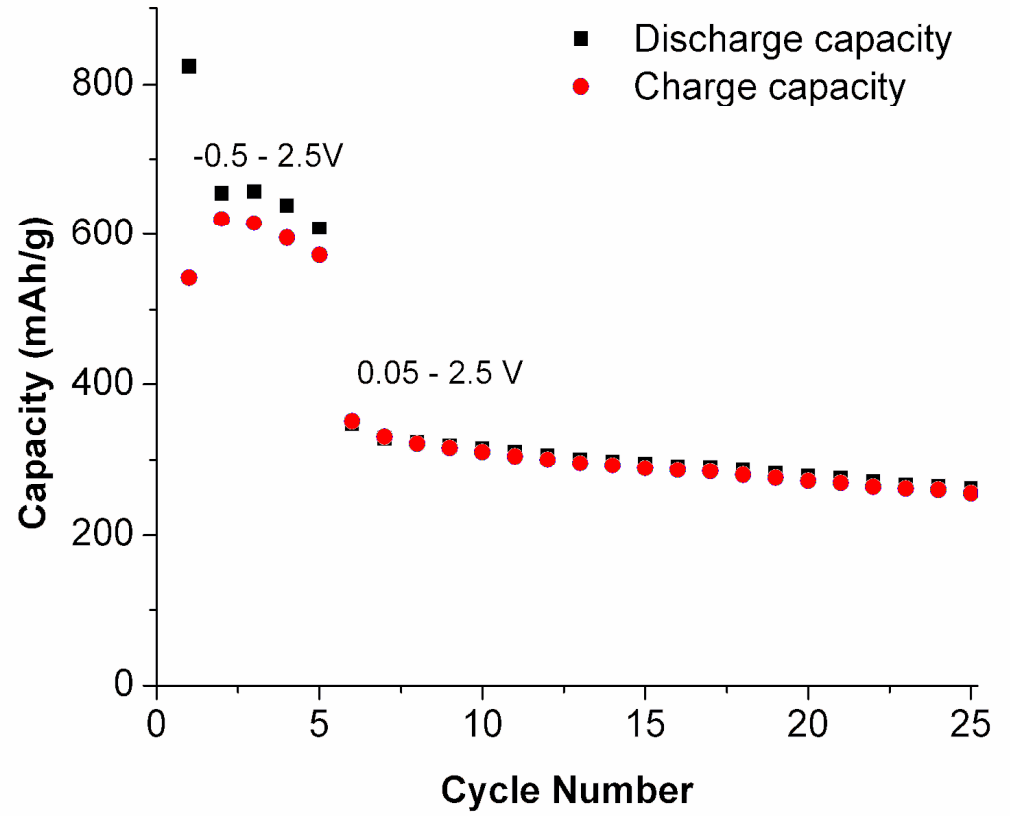


Figure 4. Cyclic performance of all-solid-state S/Li_6PS_5Br/In-Li batteries at C/50 rate. The voltage range was -0.5 – 2.5V in the first 5 cycles, and changed to 0.05 – 2.5 V from the 6th to 25th cycle.

4. Conclusions

All-solid-state lithium batteries combining argyrodite Li_6PS_5Br solid electrolyte with sulfur-based cathode materials of CuS, S and MoS_2 were investigated. Cu^+ for Li^+ exchange was found in the CuS composite cathode, resulting in poor capacity retention of the battery. By eliminating the usage of Cu, the all-solid-state Li/S battery showed an enhanced cyclic performance. After full discharge, Li/MoS_2 battery effectively becomes a Li/S battery with metallic Mo dispersed in the cathode, which among the argyrodite-based batteries studied so far showed the best cyclic performance. In the future, we plan to design nanostructured MoS_2 cathodes and explore their application in all-solid-state battery in combination with argyrodite solid electrolyte.

Acknowledgments

This research was supported by the National Research Foundation, Prime Minister's Office, Singapore under its Competitive Research Programmes NRF-CRP 10-2012-6 and NRF-CRP 8-2011-4.

References

1. H.-J. Deiseroth, S.-T. Kong, H. Eckert, J. Vannahme, C. Reiner, T. Zaiss and M. Schlosser, *Angew. Chem. Int. Ed.* **47**, 755 (2008).
2. R. P. Rao and S. Adams, *Phys. Stat. Sol. A* **208**, 1804 (2011).
3. R. P. Rao, N. Sharma, V. K. Peterson and S. Adams, *Solid State Ionics* **230**, 72 (2013).
4. F. Stadler and C. Fietzek, *ECS transactions* **25**, 177 (2010).
5. A. Hayashi, T. Ohtomo, F. Mizuno, K. Tadanaga and M. Tatsumisago, *Electrochem. Commun.* **5**, 701 (2003).
6. K. Aso, A. Sakuda, A. Hayashi and M. Tatsumisago, *Appl. Mater. Interfaces* **5**, 685 (2013).
7. M. Chen, R.P. Rao and S. Adams, *Solid State Ionics* (2013), in press, http://dx.doi.org/10.1016/j.ssi.2013.10.057.
8. A. C. Larson and R. B. von Dreele, Los Alamos National Laboratory Report LAUR 86 (1994).
9. B. H. Toby, *J. Appl. Cryst.* **34**, 210 (2001).
10. M. Chen, R.P. Rao and S. Adams, *Solid State Ionics* (2013), Accepted.
11. W.F. Kuhs, R. Nitsche and K. Scheunemann, *Acta Crystallogr. B* **34**, 64 (1978).
12. A. Haznar, A. Pietraszko and I. Studenyak, *Solid State Ionics* **119**, 31 (1999).
13. H.-J. Deiseroth, S.-T. Kong, H. Eckert, J. Vannahme, C. Reiner, T. Zaiss and M. Schlosser, *Angew. Chem. Int. Ed.* **47**, 755 (2008).
14. J. Xiao, X. Wang, X.-Q. Yang, S. Xun, G. Liu, P.K. Koech, J. Liu and J.P. Lemmon, *Adv. Funct. Mater.* **21**, 2840 (2011).
15. X. Fang, X. Guo, Y. Mao, C. Hua, L. Shen, Y. Hu, Z. Wang, F. Wu and L. Chen, *Chem. Asian J.* **7**, 1013 (2012).

TEMPERATURE - DEPENDENT DIELECTRIC AND ELECTRICAL CHARACTERISTICS OF UNDOPED AND SAMARIUM DOPED $SrBi_2Ta_2O_9$ FERROELECTRIC CERAMICS

B.RAJESH KANNAN

Department of Physics, Birla Institute of Technology and Science (BITS) - Pilani, Hyderabad Campus, Jawahar Nagar, Shameerpet Mandal, R. R. Dist - 500078 (AP), India

B. HARIHARA VENKATARAMAN

Department of Physics, Birla Institute of Technology and Science (BITS) - Pilani, Hyderabad Campus, Jawahar Nagar, Shameerpet Mandal, R. R. Dist - 500078(AP), India

The electrical conductivity and dielectric properties of undoped and 10 mol% samarium doped ferroelectric SBT ceramics have been investigated in detail in the frequency range of 20Hz - 1MHz at various temperatures (300 - 673K). The frequency dependence real and imaginary parts of dielectric constant of these ceramics showed a strong dispersion at low frequencies and higher temperatures. The predominance of the dc conductivity is also identified from the slope of the log ε_r'' vs log f curve. This noticeable dispersion in both the components of the complex dielectric constant appears to be a common feature in ferroelectrics associated with non - negligible ionic conductivity. The ac conductivity spectra of undoped and 10mol% samarium doped SBT ceramics exhibited power law (ω^n) behavior at higher temperatures.

1. Introduction

Strontium bismuth tantalate, $SrBi_2Ta_2O_9$ (SBT) is one of the excellent ferroelectric materials for the non-volatile random access memory (NVRAM) device application [1-2]. The structural formula of SBT is $(SrTa_2O_7)^{2-}$ $(Bi_2O_2)^{2+}$, consisting of two perovskite structure interleaved between the bismuth oxide layer [3]. Though the ferroelectric fatigue behavior is comparatively better than

Proceedings of the 14th Asian Conference on Solid State Ionics (ACSSI 2014)
Copyright © 2014 ACSSI 2014 Organizers. All rights reserved.
ISBN: 978-981-09-1137-9
doi:10.3850/978-981-09-1137-9_017

the $PbZr_{(1-x)}Ti_xO_3$(PZT) material, the SBT compound is associated with low remnant polarization and high processing temperature[4]. In order to reduce the processing temperature and also tailor the physical properties of the aforementioned compound, partial cationic substitutions were carried out in the Sr or Ta sites as well as in the Bi_2O_2 layer[5-7]. However, this class of material exhibit ionic conductivity arising out of oxygen ion vacancies especially at high temperatures. The existence of oxygen ion vacancy driven leakage current effects in these materials at high temperatures is an impediment for device applications. The isovalent rare earth ions doping (Sm^{3+}, La^{3+}, Nd^{3+}) on the Bi^{3+} site of SBT would enhance the polar property and also controls the transport of oxygen ion vacancies by suppressing the volatilization of bismuth[8] at high temperatures. Hence, a comparative study on the dielectric and conductivity properties of undoped SBT and 10mol% samarium doped SBT (SBSmT) ceramics synthesized by low temperature molten salt synthesis route is reported in this paper over a wide frequency range and temperatures.

2. Materials and Methods

Molten salt synthesis route had been employed to fabricate the undoped and 10mol% samarium doped SBT ceramics. The stoichiometric ratio of $SrCO_3$, Bi_2O_3, Ta_2O_5 and Sm_2O_3 powders were well mixed in the acetone medium with KCl flux in the molar ratio of 1:5. These mixed powders were calcined at 800°C for four hour followed by the sintering at 1050°C for 10h. The structural and microstructural characterization was carried out for these sintered samples by using X-ray diffractometer and Scanning electron microscopic technique. The dielectric and conductivity studies were done for SBT and SBSmT ceramic samples for various frequency range and temperatures by using Waynkerr LCR meter.

3. Results and discussion

3.1 *Structural Analyses*

The existence of monophasic formation of polycrystalline SBT and SBSmT ceramic samples was confirmed by X - ray powder diffraction studies. The calculated lattice parameters from the X-ray diffraction patterns of these sintered samples are depicted in Table 1, and the present data are in close agreement with the standard JCPDS pattern. It is observed that there is a slight influence on the lattice parameters by samarium doping in SBT lattice due to the ionic size difference between the bismuth and samarium ions.

Table 1. Unit-Cell Parameters Derived from X-ray Powder Diffraction Data

Composition	a(Å)	b(Å)	c(Å)	V(Å)
$SrBi_2Ta_2O_9$	5.512	5.543	24.966	762.73
$Sr(Bi_{0.9}Sm_{0.1})_2Ta_2O_9$	5.507	5.537	24.984	761.83

3.2 *Microstructural Analyses*

The scanning electron micrographs recorded for the undoped and 10mol% samarium doped SBT calcined samples are shown in Figure 1. The undoped SBT micrographs clearly reveal the presence of plate shaped morphology with crystallites of larger size compared to the 10 mol% samarium doped SBT polycrystalline samples. The reason for the reduction in the crystallite size could be due to the addition of samarium that suppresses the volatilization of the bismuth resulting in the reduction of ionic transport in the material [9].

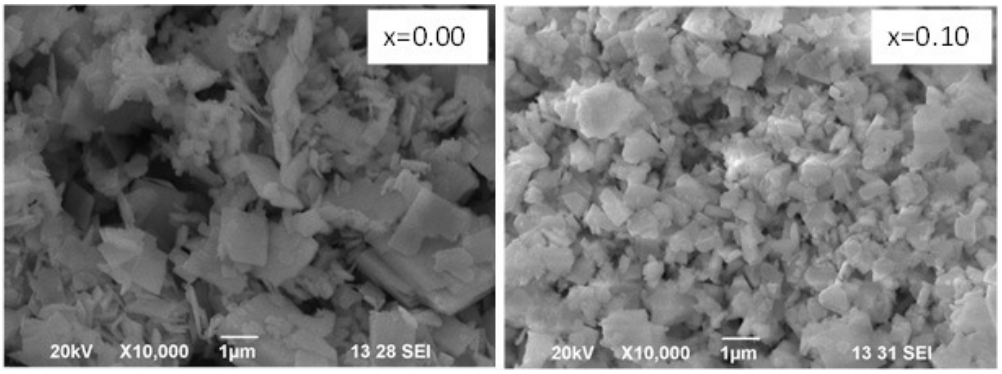


Figure 1. Scanning electron micrographs obtained for the polycrystalline $Sr(Bi_{1-x}Sm_x)_2Ta_2O_9$ powders calcined at 800°C for 4 hr.

3.3 *Dielectric properties*

The frequency dependence real part of dielectric constant (ε'_r) for SBT and SBSmT ceramics at various temperatures is shown in Figure 2(a and b). It is observed that there is an existence of low frequency dispersion and an almost plateau like region in the high frequency range for both the samples. In addition, the low frequency dispersion is also found to increase with the increase in temperature. Generally, this kind of behavior is encountered in lossy dielectric

materials and is referred as low frequency dielectric dispersion (LFDD)[10]. Interestingly, the frequency dispersion for SBSmT ceramics is lower than that of pure SBT indicating the suppression of oxygen ion vacancies due to samarium ion doping in the bismuth site.

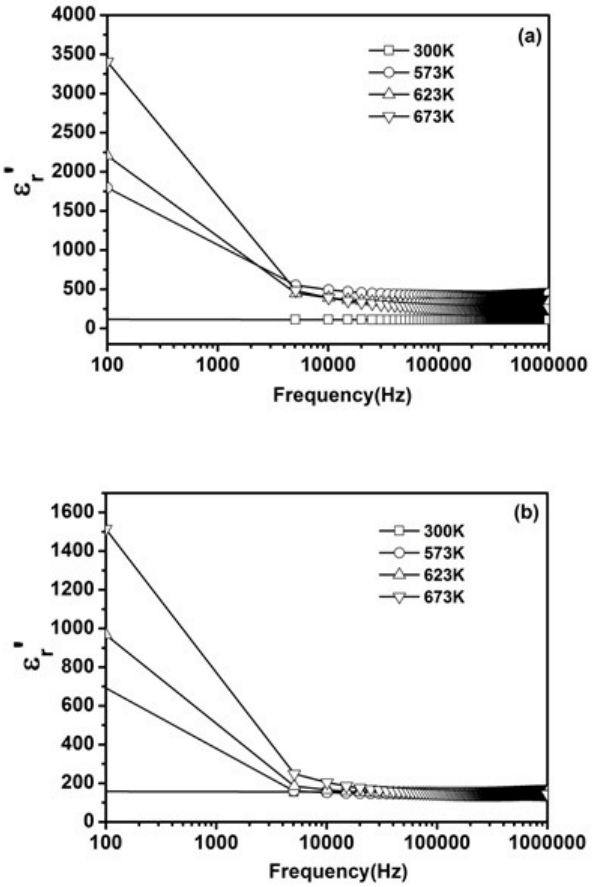


Figure 2. The frequency dependence of ε'_r on semi-log scale at various temperatures of (a)SBT (b)SBSmT ceramics.

Figure 3(a and b) shows the frequency dependence imaginary part of dielectric constant, ε''_r for SBT and SBSmT ceramics at few elevated temperatures. In both the samples, the frequency dispersion of the imaginary part of the dielectric constant is stronger than that of the real part, ε'_r. We could also predict the predominance of the dc conduction in the low frequency region from the imaginary part of the dielectric constant plot.

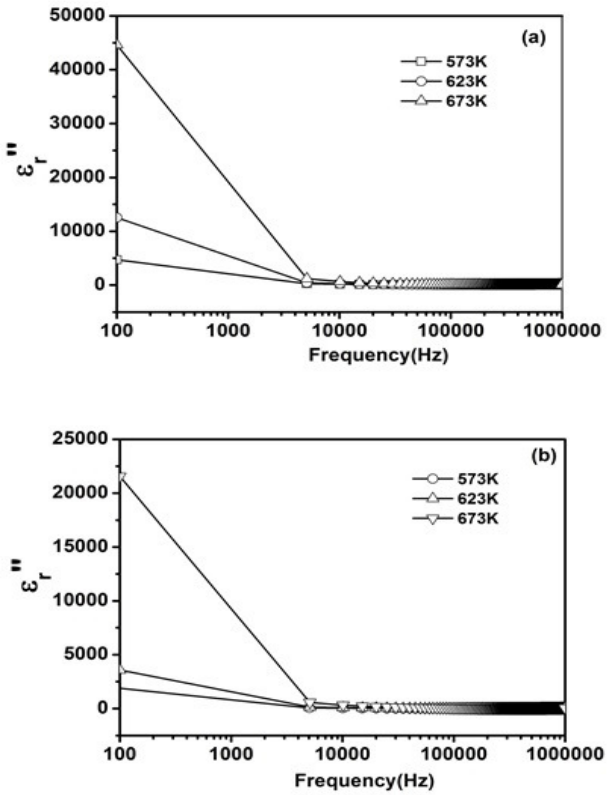


Figure 3. The frequency dependence of ε''_r on semi-log scale at various temperatures of (a) SBT (b)SBSmT ceramics.

3.4 *Conductivity studies*

Figure 4 (a and b) depicts the variation of the real part of the ac conductivity as a function of frequency at few elevated temperatures. Jonscher proposed the following power - law relation to correlate the frequency dependence of ac conductivity.

$$\sigma = \sigma_o + A\omega^n \quad (1)$$

where σ is the total conductivity, σ_o is the dc conductivity and the coefficient A and exponent n are temperature and material dependent parameters[11]. In the low frequency region, σ is almost independent of frequency and subsequently the conductivity increases with increase in frequency, varying approximately as a power of frequency (ω^n). It is also observed that the onset of the dispersion is shifted to higher frequencies as the temperature is increased. Interestingly, the conductivity value of the SBSmT ceramics is lower than that of the SBT sample

in all the temperatures under study and it could be attributed to the decreased concentration of the mobile charge carriers [12].

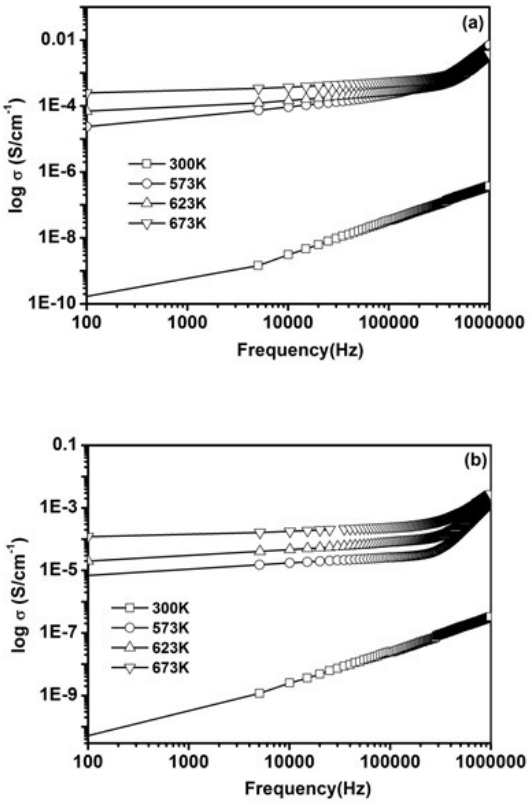


Figure 4. Double logarithmic plot of ac conductivity vs frequency at various temperatures for (a) SBT and (b) SBSmT ceramics.

4. Conclusions

Undoped and 10 mol% samarium doped $SrBi_2Ta_2O_9$ ceramics have been found to exhibit low frequency dielectric dispersion when the dielectric studies were conducted in the 20 Hz - 1 MHz frequency range at various temperatures. It was interesting to observe that the frequency dependence of conductivity of SBSmT ceramics is lower than that of the pure SBT for all the range of temperatures under study.

Acknowledgments

The authors thank Alagappa University, Karaikudi, India and Karunya University, Coimbatore, India for their assistance in characterization. This work was supported by Department of Science and Technology (Project No: SR/FT/CS-065/2009), India.

References

1. U.Chon, H.M.jang, M.G.Kim and C.H.Chang, *Phys. Rev. Lett.* **89**, 087601(2002).
2. Roy, A. Dhar and S. K. Ray, *J. Appl. Phys.* **104** , 064103 (2008).
3. Y. Shimakawa, Y. Kubo, Y. Nakagawa, S. Goto, T. Kamiyama, H. Asano and F. Izumi, *Phys. Rev.B* **61**,6559(2000).
4. K.Kato, C.Zheng, J.M.Finder and S.K.Dey, *J. Am. Ceram. Soc.* **81**,1869(1998).
5. Y.Wu, M.J.Forbess, S.Seraji, S.J.Limmer, T.P.Chou and G.Cao, *J. Appl. Phys.***89**,5647(2001).
6. C.H.Lu, D.P.Chang, *J. Phys. Chem. Solids* **69**,480(2008).
7. K.R.Whittle, N.C.Hyatt and I.M. Reaney, *Chem. Mater.***20**,6427(2008).
8. Y.M.Kan, G.J.Zhang, P.L.Wang and Y.B. Cheng , *J. Eur. Ceram. Soc.* **28**,1641(2008).
9. Y.Kan, X.Jin, G.Zhang, P.Wang, Y.B.Cheng and D.Yan, *J. Mater. Chem.* **14**, 3566(2004).
10. Z.Lu, J.P.Bonnet, J.Ravez and P.Hagenmuller, *Solid State Ionics* **57**,235(1992).
11. K. Jonscher, Dielectric Relaxation in Solids (Chelsea Dielectric Press, London, 1983).
12. T. C. Chen, C. L. Thio, and S. B. Desu, *J. Mater. Res.* **12**, 2628 (1997).

A MODEL FOR THE NON-ARRHENIUS IONIC CONDUCTIVITY OF SOLID ELECTROLYTES

YOHEI OKADA,[a] SAHARA,[a,b] MASAHIRO IKEDA,[c] and MASARU ANIYA[a]

[a]*Department of Physics, Graduate School of Science and Technology, Kumamoto University, Kurokami, 860-8555, Japan*

[b]*Department of Physics, Faculty of Science and Technology, State Islamic University (UIN) Alauddin, Makassar, Indonesia*

[c]*Course of General Education, Natural Science, Applied Physics, Fukui National College of Technology, Sabae 916-8507, Japan*

Some solid electrolytes exhibit non-Arrhenius, or Vogel-Fulcher-Tamman (VFT) type behavior in the ionic conductivity, whose origin is not still well understood. In the present study, a model for the non-Arrhenius ionic conductivity of solid electrolytes has been proposed by applying the formulation of the Bond Strength-Coordination Number Fluctuation model of the viscosity and the concepts gained from the bond fluctuation model of superionic conductors. Our study indicates that when the fluctuation of bonding energy and/or coordination number of the diffusing ion is large, it results in large deviation from the Arrhenius type behavior in the ionic conductivity. The model suggests that good ionic conductors should exhibit a non-Arrhenius type ionic conductivity.

1. Introduction

Superionic conductors or solid electrolytes are widely applied in fuel cells, electrolytic condensers, gas sensors, batteries, etc. Understanding the fundamental properties of these materials is of primordial importance to expand their applicability. Usually, the temperature dependence of the ionic conductivity of many solid electrolytes follows the Arrhenius type behavior. However, it has been discovered that some optimized superionic conductors exhibit a non-Arrhenius behavior at high temperature, whereas at low temperature, they follow the usual Arrhenius behavior[1]. In order to explain this behavior, some works have been done[2-6]. However, the behavior is not fully understood yet.

The non-Arrhenius temperature dependence is not a behavior specific for ionic conductivity. It has been observed frequently in the temperature dependence of the viscosity and relaxation time of supercooled liquids. For these cases, the empirical Vogel-Fulcher-Tamman (VFT) equation has been used quite frequently. Concerning the temperature dependence of the viscosity, the Bond Strength-Coordination Number Fluctuation (BSCNF) model has been developed[7]. It has been applied successfully to analyze the temperature

Proceedings of the 14th Asian Conference on Solid State Ionics (ACSSI 2014)
Copyright © 2014 ACSSI 2014 Organizers. All rights reserved.
ISBN: 978-981-09-1137-9
doi:10.3850/978-981-09-1137-9_106

dependence of the viscosity of different type of materials[8]. In a recent study, an interpretation for the empirical VFT parameters was given in terms of the BSCNF model[9]. In the present study, the formulation of the BSCNF model is applied to develop a model for the non-Arrhenius temperature dependence of ionic conductivity.

2. Model

The BSCNF model was introduced based on the physical picture that the viscous flow of the melt occurs by breaking or twisting the bonds between the structural units[7]. According to this model, the temperature dependence of the viscosity is described in terms of the mean bond strength E_0, the mean coordination number Z_0, and their fluctuations, ΔE, ΔZ, of the structural units that form the melt. It is expressed as

$$\ln\left(\frac{\eta}{\eta_0}\right)=\frac{Cx+Cx^2\left[\left\{\ln\left(\frac{\eta_{Tg}}{\eta_0}\right)+\frac{1}{2}\ln(1-B)\right\}\frac{(1-B)}{C}-1\right]}{1-Bx^2}-\frac{1}{2}\ln(1-Bx^2), \quad (1)$$

$$B=\frac{(\Delta E)^2(\Delta Z)^2}{R^2T_g^2},\ C=\frac{E_0Z_0}{RT_g},\quad x=\frac{T_g}{T}.$$

Here, T_g is the glass transition temperature and R is the gas constant. η_0 and η_{Tg} are the values of the viscosities at the high temperature limit and at T_g, respectively. In the case where the condition $|\Delta E|/E_0 = |\Delta Z|/Z_0$ is satisfied, Eq. (1) follows closely the behavior of the Vogel-Fulcher-Tammann (VFT) equation widely used in the literature[8]. Explicitly, it reduces to[9]

$$\eta=\frac{\eta_0 T}{\sqrt{T^2-(\Delta E\Delta Z/R)^2}}\exp\left(\frac{E_0Z_0/R}{T-\Delta E\Delta Z/R}\right). \quad (2)$$

The expression given in Eq. (1) reproduces well the temperature dependence of the viscosity observed experimentally. This fact leads us to apply the concept of the BSCNF model of the viscosity to treat ionic conduction in solids. However, in order to do that, it is necessary to modify some points. In the BSCNF model of the viscosity, the presence of structural units that form the melt is assumed[7]. The structural unit depends greatly on the type of the materials. For instance, in strong glass-formers such as SiO_2, the tetrahedral $SiO_{4/2}$ units are regarded as the structural unit. For the metallic glass-forming systems, the structural units might

be icosahedral clusters. For the cases of polymers and ionic liquids, each monomer and ions (e.g., cations and anions) are considered as structural units. A schematic representation of the structural unit is shown in Fig. 1 (a). The quantities E_0, Z_0, ΔE and ΔZ that appear in Eq. (1), describe the bond strength and the coordination number of these structural units. The viscous flow occurs by the movements of these structural units as illustrated by arrows in Fig. 1 (a).

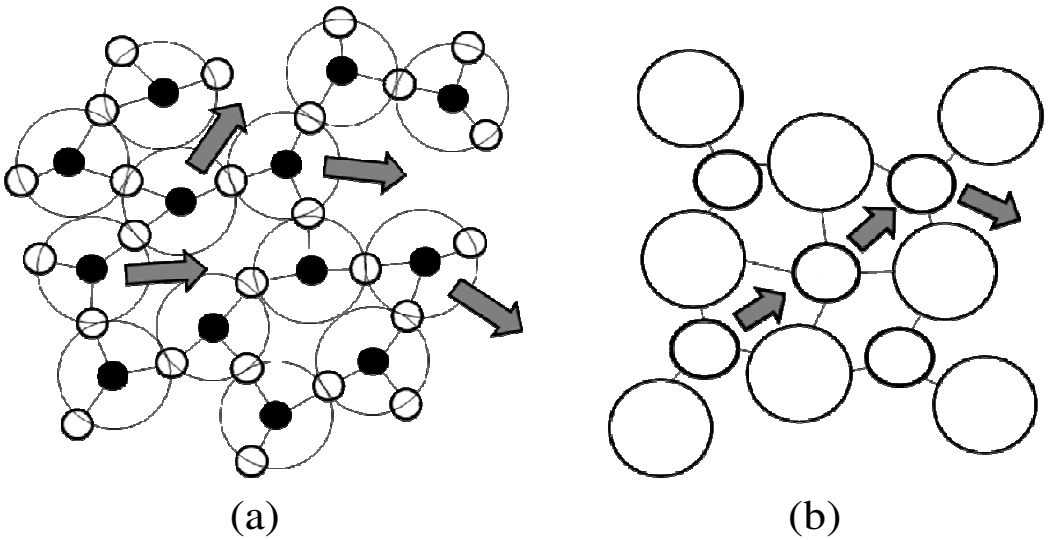


Figure 1. (a) A schematic representation of the structural units that form the melt. The small open and black circles represent atoms. Large circles represent the structural units. (b) Schematic illustration of vitreous solid electrolytes. The small and large circles represent mobile and non-mobile ions. The length of the sticks connecting the circles represents the magnitude of the interionic interactions.

In contrast with the viscous flow, where the movement of large number of atoms are involved, in the ionic transport in solids, the number of atoms (or ions) involved is restricted. As illustrated in Fig. 1 (b), only a part of the atoms contributes to mass transport. To avoid misunderstanding, it does not mean that the non-diffusing atoms are static in the strict sense. The dynamics of the non-diffusing atoms play important roles in the mass transport processes as has been discussed in the bond fluctuation model of superionic conductors[10].

The important point is the recognition that the ionic transport occurs by breaking or twisting the bonds that surrounds the mobile ion. This observation leads us to write the following expression for the ionic conductivity, in analogy with the expression for the viscosity given in Eq. (2),

$$\sigma = \frac{\sigma_0 T}{\sqrt{T^2 - (\Delta\tilde{E}\Delta\tilde{Z}/R)^2}} \exp\left(-\frac{\tilde{E}_0\tilde{Z}_0/R}{T - \Delta\tilde{E}\Delta\tilde{Z}/R}\right). \qquad (3)$$

Here $\tilde{E}_0$ and $\tilde{Z}_0$ denote the mean values of the bond energy and coordination number of the mobile ion, and $\Delta\tilde{E}$ and $\Delta\tilde{Z}$ are their fluctuations. In Eq. (3) it is assumed that $|\Delta\tilde{E}|/\tilde{E}_0 = |\Delta\tilde{Z}|/\tilde{Z}_0$. It should be noted that although Eq. (3) seems similar to Eq. (2), the parameters appearing in both equations represent different physical entities.

3. Result and discussion

Fig. 2 shows the temperature dependence of the conductivity of some solid electrolytes. The symbols denote the experimental data and the solid lines denote the theoretical curves described by Eq. (3). The values of the parameters for each material obtained by fitting procedure of Eq. (3) are given in Table 1. Although deviations at low temperature are observed for some materials, the result shown in Fig. 2 indicates that the model describes relatively well the temperature dependence of the non-Arrhenius ionic conductivity of solid electrolytes.

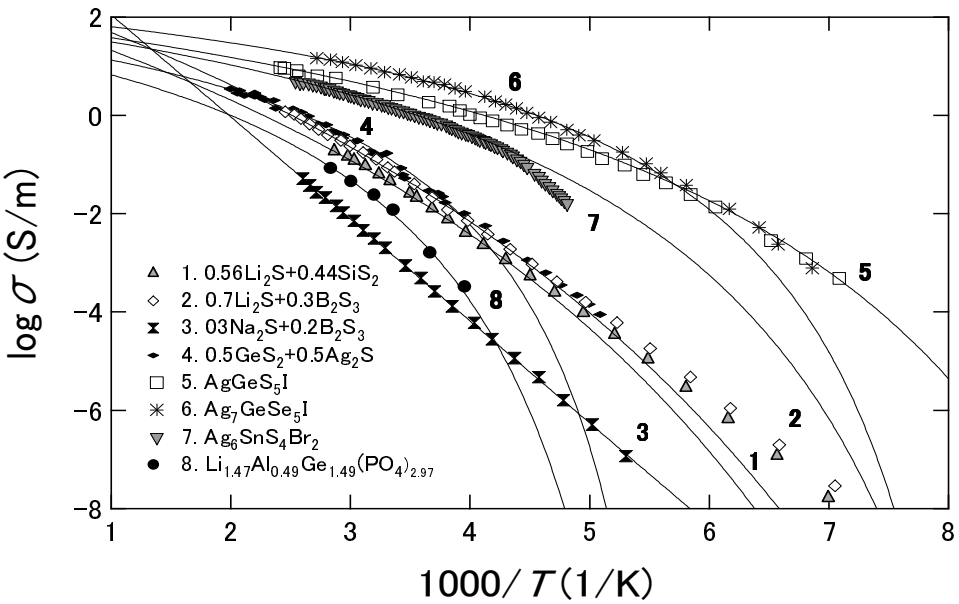


Figure 2. Temperature dependence of the ionic conductivity of some materials.

Table 1. The values of parameters for the materials shown in Fig. 2.

No.	Materials	$\tilde{E}_0\tilde{Z}_0/R$ (K)	$\Delta\tilde{E}\Delta\tilde{Z}/R$ (K)	σ_o (S/m)	Ref.
1	$0.56Li_2S+0.44SiS_2$	1810	80	150	1
2	$0.7Li_2S+0.3B_2S_3$	1960	72	400	1
3	$0.3Na_2S+0.2B_2S_3$	4780	0	13200	1
4	$0.5GeS_2$-$0.5Ag_2S$	822	158	35	11
5	Ag_7GeS_5I	716	83	83	11
6	Ag_7GeSe_5I	535	110	115	12
7	$Ag_6SnS_4Br_2$	790	101	75	13
8	$Li_{1.47}Al_{0.49}Ge_{1.49}(PO_4)_{2.97}$	1120	158	25	14

The expression given in Eq. (3) provides a means to understand the origin of the non-Arrhenius behavior of the ionic conductivity. Eq. (3) can be rewritten as

$$\sigma = \frac{\sigma_0 T}{\sqrt{T^2 - (\Delta\tilde{E}\Delta\tilde{Z}/R)^2}} \exp\left(-\frac{1}{RT/\tilde{E}_0\tilde{Z}_0 - \Delta\tilde{E}\Delta\tilde{Z}/\tilde{E}_0\tilde{Z}_0}\right). \quad (4)$$

From Eq. (4) we note that the condition for the observation of Arrhenius type conductivity is

$$\frac{RT}{\tilde{E}_0\tilde{Z}_0} \gg \frac{\Delta\tilde{E}\Delta\tilde{Z}}{\tilde{E}_0\tilde{Z}_0}. \quad (5)$$

The condition expressed in Eq. (5) indicates that large fluctuations of the bond strength (expressed effectively by $\Delta\tilde{E}\Delta\tilde{Z}$) of the mobile ion plays a key role in the appearance of the non-Arrhenius type ionic conductivity. This observation remind us the prediction of the bond fluctuation model of superionic conductors, which states that fast ion movements occurs accompanied by local change of the chemical bond[10]. For instance, in typical AB-type superionic conducting materials, the ionic bond emerges as fluctuations in a matrix governed by covalent bonds. In this regards, the experimental observation by Kincs and Martin[1] is interesting. They discovered that the ionic conductivity of optimized

ionic conductors, i.e., a material with optimized bond fluctuation process exhibit a non-Arrhenius behavior.

It is well known that typical superionic conductors exhibit intermediate behavior between ionic and covalent materials[15]. The bond fluctuation model mentioned above was proposed based on this observation[10]. In the following, an attempt to understand the condition of Eq. (5) from the bonding nature point of view will be presented. For such objective, we have used the following quantities.

$$r_\sigma = \left| \left(\frac{\sum_i n_i \left(r_{p,i} + r_{s,i} \right)}{\sum_i n_i} \right) - \left(\frac{\sum_j n_j \left(r_{p,j} + r_{s,j} \right)}{\sum_j n_j} \right) \right|, \tag{6}$$

$$r_\pi^{-1} = \left[\left(\frac{\sum_i n_i \left(r_{p,i} - r_{s,i} \right)}{\sum_i n_i} \right) + \left(\frac{\sum_j n_j \left(r_{p,j} - r_{s,j} \right)}{\sum_j n_j} \right) \right]^{-1}. \tag{7}$$

These quantities were introduced by St. John *et al.* for binary compounds[16], and extended recently for multicomponent systems[17]. Eq. (6) is a variation of such extension. In these equations, n_i is the number of cations of species i, and n_j is the number of anions of species j. $r_{l,i}$ and $r_{l,j}$ (l=s, p) are the valence radii of the l-orbital of atom i and j, respectively. Previous studies[16-18] have revealed that r_σ gives a measure for the ionicity of a compound, whereas r_π^{-1} gives a measure for the hybridization. These scales were used successfully to understand the trends of materials properties[16-18].

The quantities calculated through Eqs. (6) and (7) were used as scales to study the bonding characteristics of the materials that exhibit non-Arrhenius type ionic conductivity. The result is shown in Fig. 3. The solid line indicates the boundary between the four-fold and six-fold coordinated compounds[18]. The bond fluctuation process mentioned above occurs more frequently in systems located close to this boundary. From Fig. 3 we note that the compounds in consideration are located in the ionic bond dominated region in a plane defined by r_σ and r_π^{-1}. We also note that the deviation from the solid line depends on the material.

The relation between this deviation and $\Delta\tilde{E}\Delta\tilde{Z} / \tilde{E}_0\tilde{Z}_0$ is shown in Fig. 4. We recognize clearly that the degree of the fluctuation $\Delta\tilde{E}\Delta\tilde{Z} / \tilde{E}_0\tilde{Z}_0$ decreases with the increase of the deviation from the solid line that demarcates the six- and four-fold coordinated compounds. The result shown in Fig. 4 and the expression given in Eq. (4) indicate that when the bond fluctuation process occurs

frequently, large value of $\Delta\tilde{E}\Delta\tilde{Z}/\tilde{E}_0\tilde{Z}_0$ is obtained, which leads to a deviation from the Arrhenius type behavior in the ionic conductivity. Therefore, the model developed in the presented analysis suggests that good ionic conductors should exhibit a non-Arrhenius type ionic conductivity.

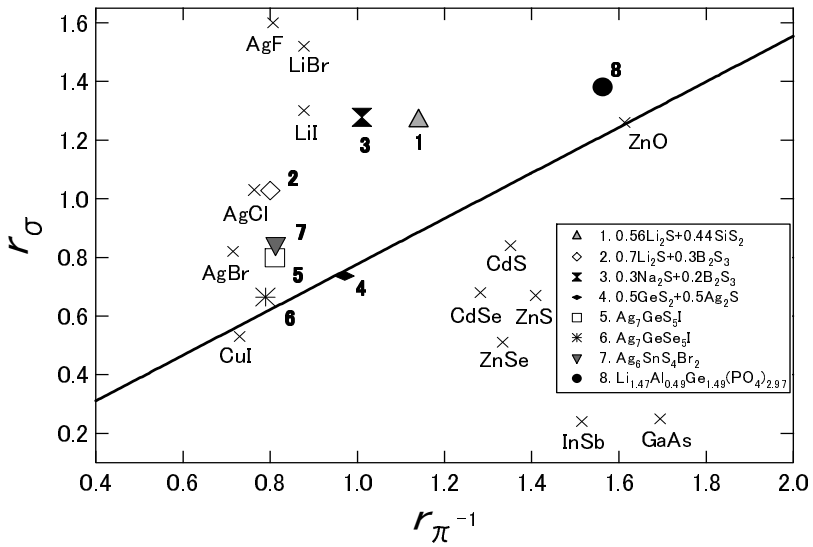


Figure 3. Characterization of the materials in terms of r_σ and r_π^{-1}.The solid line indicates the boundary between the four-fold and six-fold coordinated compounds[18].

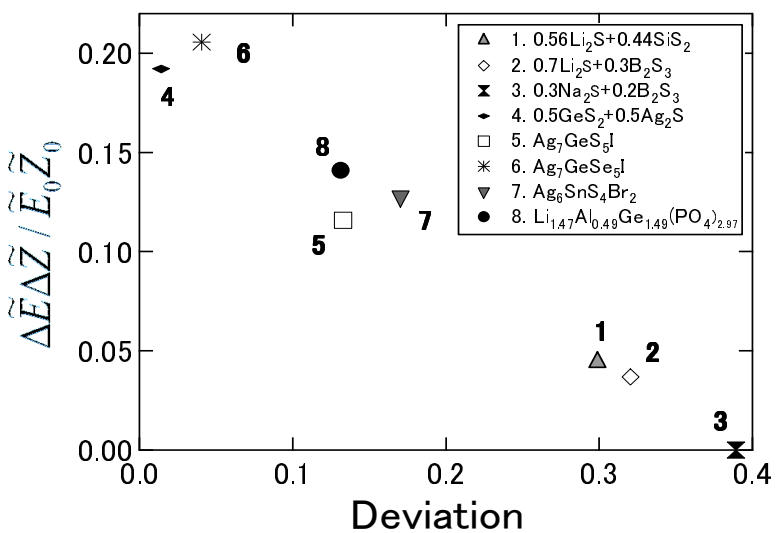


Figure 4. Relation between the magnitude of the fluctuation $\Delta\tilde{E}\Delta\tilde{Z}/\tilde{E}_0\tilde{Z}_0$ and the deviation from the boundary line that demarcates the six- and four-fold coordinated compounds.

4. Conclusion

The formulation of the BSCNF model of the viscosity has been applied to describe the non-Arrhenius type ionic conductivity of solids. The model indicates that the deviation from the Arrhenius behavior is controlled by the degree of the fluctuation of bonding energy and coordination number of the diffusing ion. By relating this finding with the bond fluctuation model of superionic conductors, it is suggested that good ionic conductors should exhibit a non-Arrhenius type ionic conductivity.

References

1. J. Kincs and S. W. Martin, *Phys. Rev. Lett*. **76**, 70 (1996).
2. K. L. Ngai and A. K. Rizos, *Phys. Rev. Lett.* **76**, 1296 (1996).
3. Q. Mei, B. Meyer, D. Martin and S. W. Martin, *Solid State Ionics* **168**, 75 (2004).
4. P. Maass, M. Meyer, A. Bunde and W. Dieterich, *Phys. Rev. Lett*. **77**, 1528 (1996).
5. T. Indoh and M. Aniya, *J. Phys. Soc. Jpn*. **79**, Suppl. A, 113 (2010).
6. T. Indoh and M. Aniya, *Adv. Mat. Res.* **123-125**, 1103 (2010).
7. M. Aniya, *J. Therm. Anal. Calorim*. **69**, 971 (2002).
8. M. Ikeda and M. Aniya, *Materials* **3**, 5246 (2010).
9. M. Ikeda and M. Aniya, *J. Non-Cryst. Solids* **371-372,** 53 (2013).
10. M. Aniya, *Solid State Ionics* **50,** 125 (1992).
11. M. Ribes, G. Taillades and A. Pradel, *Solid State Ionics* **105**, 159 (1998).
12. A. Zerouale, B. Cros, B. Deroide and M. Ribes, *Solid State Ionics* **28-30**, 1317 (1988).
13. O. G. Mykolaychuk, N. V. Moroz, P. Yu. Demchenko, L. G. Akselrud and R. E. Gladyshevskii, *Inorg. Mater.* **46**, 707 (2010).
14. H. S. Jadhav, M.-S. Cho, R. S. Kalubarme, J.-S. Lee, K.-N. Jung, K.-H. Shin and C.-J. Park, *J. Power Sources* **241**, 502 (2013).
15. J. C. Phillips, Bonds and Bands in Semiconductors (Academic Press, New York, 1973).
16. J. St. John and A. N. Bloch, *Phys. Rev. Lett.* **33**, 1095 (1974).
17. D. Lencer, M. Salinga, B. Grabowski, T. Hickel, J. Neugebauer and M. Wuttig, *Nature Mater.* **7**, 972 (2008).
18. J. R. Chelikowsky and J. C. Phillips, *Phys. Rev. B* **17**, 2453 (1978).

DIFFUSION COEFFICIENT MEASUREMENT OF LITHIUM ION IN β-ALUMINA SINGLE CRYSTAL BY PULSED FIELD GRADIENT NMR SPECTROSCOPY*

MOHAMMED TAREQUE CHOWDHURY*,

Institute of Multidisciplinary Research for Advanced Materials(IMRAM),Tohoku University, 2-1-1 Katahira, Aoba ku,Sendai 8577, Japan

REIJI TAKEKAWA, YOSHIKI IWAI, NAOAKI KUWATA, JUNICHI KAWAMURA

Institute of Multidisciplinary Research for Advanced Materials(IMRAM),Tohoku University ,2-1-1 Katahira, Aoba ku,Sendai 8577, Japan

Diffusion coefficient of ^{7}Li in 93% Liβ-alumina single crystal is measured by pulsed field gradient (PFG) NMR spectroscopy in the temperature range from 297K to 333K. The crystal *c* axis is oriented perpendicular with the static magnetic field. The room temperature diffusion coefficient was found 1.22×10^{-11}m^2/sec for ^{7}Li in 93%Liβ-alumina. The experimental data suggests that the macroscopic diffusion of Li ion in theβ-alumina crystal is mainly two dimensional. The PFG NMR diffusion data such as diffusion coefficient, activation energy and correlation time was compared with the diffusion data obtained from the impedance measurement. Activation energy from PFG NMR measurement (0.14eV) was found smaller than the impedance measurement (0.27eV) was explained interms of the defect formation energy.

1. Introduction

A solid electrolyte with high ionic conductivity is an attractive material in designing high performance and safe lithium ion batteries. Since thefirst report of high ionic conductivity of [1], Li ion contained β-alumina recognized as one of the best high Li ion conductors among the other Li ion contained solid electrolytes [2].Therefore, one of the fundamental research interests is to study the transport mechanisms of Li ion inβ-aluminasolid electrolyte. Diffusion in sold is most is most fundamental transport process characterized by diffusion coefficient. Diffusion coefficient of Li was first directly measured by Yao and Kummer*et al.* by Tracer diffusion process [1]. Since then there is no report of measuring diffusion coefficient of Liβ-alumina single crystal. Recently, PFG-NMR spectroscopy is used to measure the Li diffusion coefficient of Li_3N

* Corresponding author email : mtareque@mail.tagen.tohoku.ac.jp

Proceedings of the 14th Asian Conference on Solid State Ionics (ACSSI 2014)
Copyright © 2014 ACSSI 2014 Organizers. All rights reserved.
ISBN: 978-981-09-1137-9
doi:10.3850/978-981-09-1137-9_149

[3]and $(Li_2S)_7(P_2S_5)_3$[4]. Inthis paper we will report the ^{7}Li diffusion coefficient in β-alumina single crystal using Pulse field gradient NMR and compare our result with the previously reported result obtained by tracer diffusion method.

2. Theory

The NMR echo intensity as function of the magnetic gradient field is fitted to the following Eq (1) to extract the diffusion coefficient D.[5]

$$I = I(0)\exp\left\{-D(2.\pi.g_i.\gamma.\delta)^2(\Delta - \frac{\delta}{3})\right\} \qquad (1)$$

Where I is the echo intensity which is a function of gradient field, I(0) is the intensity without any gradient field,$g_i$is the 'i' th magnetic field gradient along z direction (unit is G/cm), γis gyromagnetic ratio (unit is Hz/G), Δ is the diffusion time and δis gradient pulse duration.
In the PFG method,the motion of the Li ion was probed by dephasing of the nuclear spin caused by the translational motion and the field gradient. The dephasing results in the attenuation of the NMR signal. The gradient dependent intensity was then used to estimate the diffusion coefficient using Eq. (1)

3. Experimental

3.1 *Ion exchange methods*

Single crystal of Liβ-alumina was prepared by ion exchange method from Naβ-alumina. The Naβ-alumina crystals were put in to alumina crucible with LiCl salt and ion exchange was completed with two steps having 700C for 24 hour in each step. The ion exchangedβ-alumina contained 93% Limeasured by ICP AES experiment.

3.2 *PFG NMR*

The NMR experiment was performed in the Bruker 400 Avance. The ^{7}Li 1D spectra were observed using $\frac{\pi}{2}$pulses with Larmour frequency 155.5MHz. The diffusion coefficient was measured by stimulated echo (STE) pulse sequence. The pulse sequence was shown in Figure 1. The δis 5 ms and Δ which is diffusion time is 10 ms,the maximum field gradient was 1492G/cm and the starting magnetic field gradient is 46.80 G/cm. We measured the diffusion coefficient in the temperature range of 297K-333K.The single crystal Li β alumina was oriented in such a way that the angle between the static magnetic

field and crystal *c* axis is 90°. It is expected that in this orientation the Li will show highest diffusion coefficient.

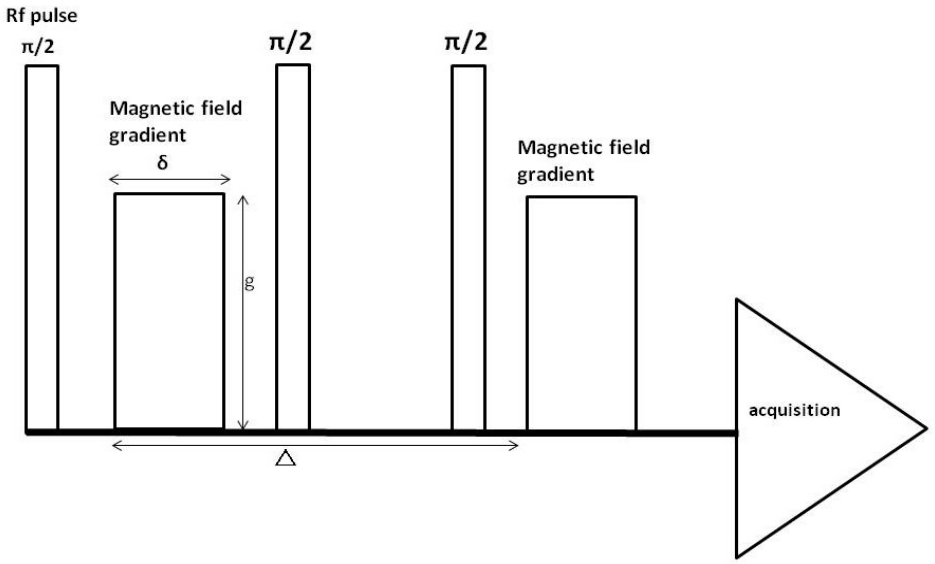


Figure1.Stimulated echo (STE) pulse sequenced used for the PFG NMR experiment.

4. Results and Discussion

4.1 Diffusion coefficient measurement

Figure 2 Shows the 1D ^{7}Li NMR spectra for parallel and perpendicular orientation of 93% Li β-alumina single crystal. The satellite transition peak is visible suggests small quadrupole moment of ^{7}Li. The room temperature T_1 relaxation time was measured by inversion recovery and the value of T_1 for parallel and perpendicular orientation is 0.11sec and 0.38sec respectively. The $T_2$for parallel and the perpendicular orientation was found 0.0025s and 0.0036s,respectively. Because of the small T_2 STE pulse sequence was used for the PFG NMR measurement.The diffusion coefficient along the ab plane and along the *c* direction of the single crystal was measured by rotating the *c* axis with an angle 90° and 0° with static magnetic field, respectively.A room temperature diffusion coefficient D_{PFG} of 1.22×10^{-11} m^2/s was obtained at perpendicular orientation. [6]In case of parallel orientation at room temperature, the diffusion signal intensity was very weak and the signal to noise ratio very low.Therefore the diffusion coefficient along C axis was measured at 333K which is 6.4×10^{-13} m^2/s or less.[6] For the perpendicular orientation of the

crystal, a diffusion coefficient D_{PFG} of 2.26×10^{-11} m^2/s was obtained at 333 K[6]. The diffusion spectra measured at 333K for perpendicular orientation as function of the magnetic field gradient are shown in Figure 3.It is appeared that as the gradient increased the amplitude of the spectra decreased as shown in Figure 4.

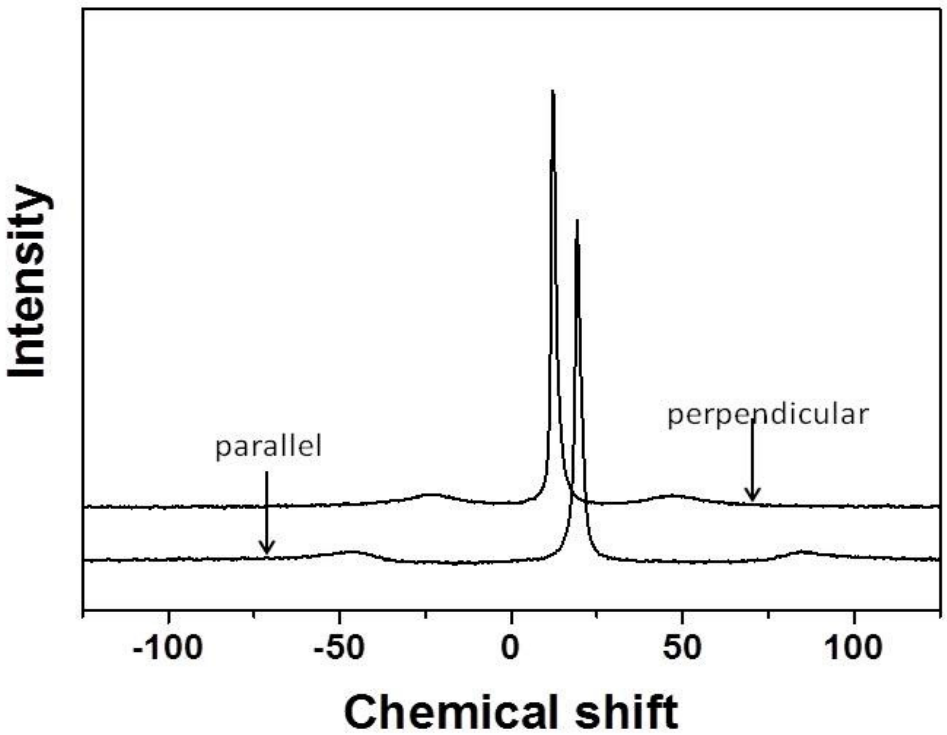


Figure 2. 1D ^{7}Li NMR spectra for parallel and perpendicular orientation of 93% Li β-alumina at 300K

The ^{7}Li echo signal intensity was obtained as a function of the magnetic field gradient. The diffusion coefficient was obtained by fitting the gradient dependent echo intensity to Eq. (1).Direct measurement of the diffusion coefficient in the parallel and perpendicular directions suggests that macroscopic motion of the cation in β–alumina single crystal is 2D in nature. Here it is also important to mentioned that the present authors measured the ionic conductivity along ab plane and parallel to *c* axis which are 1.19×10^{-3} $\Omega^{-1}cm^{-1}$ [7] and 1.85×10^{-15} $\Omega^{-1}cm^{-1}$, respectively at 303K. Furthermore the temperature dependent conductivity measurement show that the *ab* plane activation energy is

0.27eV and the parallel to the *c* axis the activation energy is 0.93eV.Therefore the anisotropic conductivity data is very much consistent with the PFG NMR results.

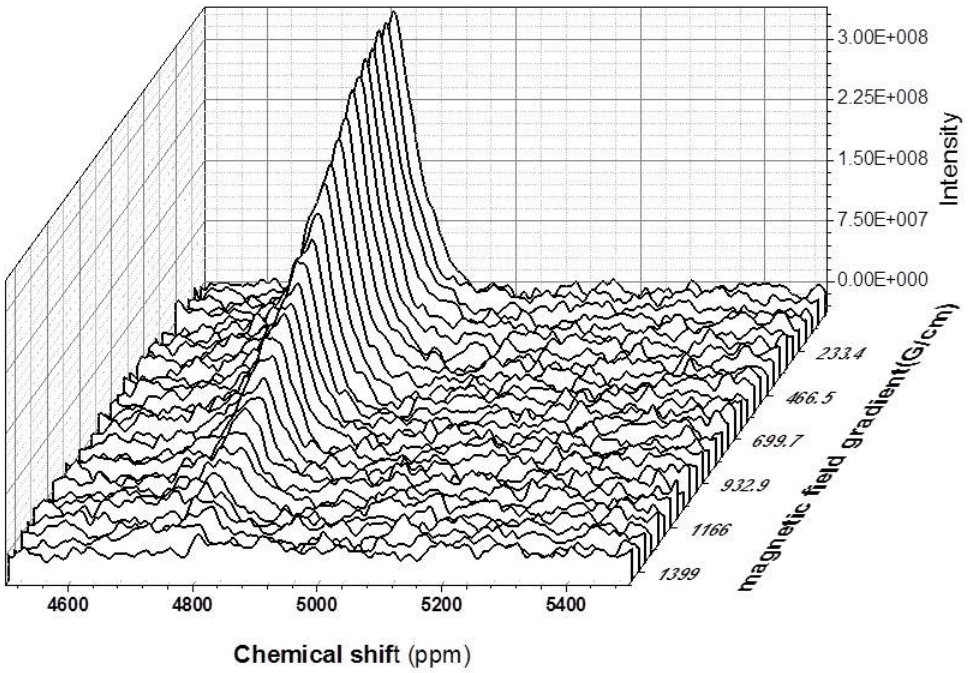


Figure 3. ^{7}Li NMR spectraof Li β-alumina single crystal as function of magnetic field gradient at 333K for parallel orientation

However, a small diffusion coefficient along the parallel direction does not rule out the possibility of local microscopic motion of the Li ion along the *c* axis since we previously obtained a small activation energy corresponding to the local motion of Li ions from the temperature dependent quadrupole interaction.[7].

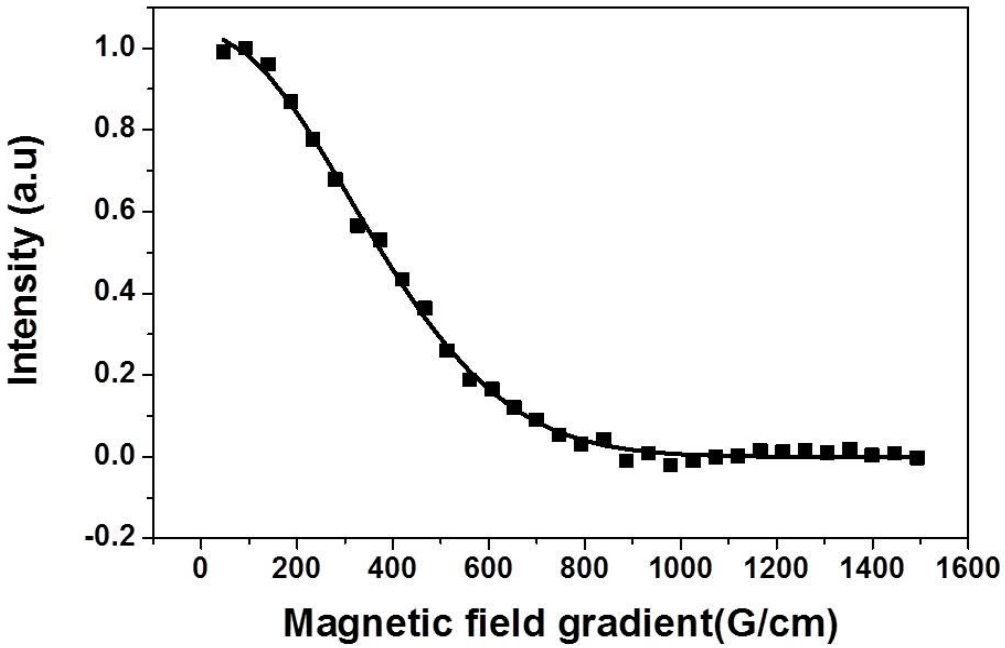


Figure4.[7]Li echo signal intensity as function of magnetic field gradient of Li β-alumina single crystal with the crystal c-axis perpendicular to the static magnetic field at 333K.[9]

4.2 *Activation energy*

The diffusion coefficient is estimated from the impedance measurement using Nernst -Einstein equation given below,

$$D_\sigma = \frac{\sigma(T)\ \ k_B T}{Nq^2}. \qquad (1)$$

Here σ is the ionic conductivity which is obtained previously published report [7].k_B is the Boltzmann constant, N is the charge carrier density, q is the charge of a carrier, and T is the temperature in Kelvin. The activation energy from the impedance measurement is found 0.27eV was estimated from Arrhenius relation, which is higher than the activation energy obtained from the PFG NMR 0.14eV.The temperature dependent Diffusion coefficient follows the Arrhenius relation given in Equation (3)

$$D = D_0 \exp\left(\frac{-E_a}{kT}\right) (3)$$

Here E_a is the activation energy for the diffusion process, k is the Boltzmann constant and D_0 is the pre exponential term. The difference between the

activation energy obtained from PFG NMR and impedance measurement is attributed to the defect formation energy. [6]

4.3 Jump rate estimation

The jump time of Li ion from one crystallographic position to other in the conduction plane of β-aluminacan be estimated using simple Jump model given in Eq.(4).

$$D = \frac{a^2}{4\tau} \quad (4)$$

Here *a* is the 1.5 Å or 3.2 Å. 1.5Å correspond to mo-BR or mo-aBR and 3.2 Å corresponds to BR-aBR or mO-mO distances in Naβ-alumina.[8] Because of the unavailability of the crystallographic data of 93% Liβ-alumina the data correspond to Na β-alumina is used as rough estimation. D is the diffusion coefficient.The jump time τcan be varying from $4.62\text{x}10^{-10}$s to $2.48\text{x}10^{-10}$s for mo-BR or mo-aBR depending on the temperature.A pre-exponential factor $6.4\text{x}10^{11}$ $s^{-1}$for mo-BR or mo-aBR was estimated from the PFG NMR data using the jump model (Eq.4) and Arrhenius relation (Eq.5)

$$\frac{1}{\tau} = \frac{1}{\tau_0} \exp \frac{-E_a}{kT} \quad (5)$$

From Eq. (2) and (4) the jump time/ jumprate can be estimated by Eq. (6) from the conductivity data obtained from the impedance spectroscopy

$$\tau^{-1} = \frac{\sigma \ 4k_B T}{Nq^2a^2} \quad (6)$$

Jump time τ was estimated from the temperature dependent line width data following the BPP relation as shown in below,[9]

$$\tau(T) = \frac{1}{2\pi\alpha\Delta\nu(T)} \tan\left[\frac{\pi}{2}\left(\frac{\Delta\nu(T)}{\Delta\nu_{RL}}\right)^2\right] \quad (7)$$

where $\Delta\nu_{RL}$ is the rigid lattice line width , α=1, Δν(T) is the spectral width at the temperature T and τ(T) is the jump rate at temperature. Additionally, the temperature dependent jump timeτ(or jump rate) which follow Arrhenius type relation given in Eq. (5) provide the activation energy which is 0.0631 eV and a very low estimation pre exponential factor ($\frac{1}{\tau_0} = 5.00 \times 10^6$/s). Figure 5 shows the

jump time estimated from the PFG NMR, impedance data. The low estimation of activation energy form NMR linewidth data is due to limitations of BPP model. There might be structural inhomogeniety inβ-alumina system which can cause activation energy distribution or jump rate distribution. In Table 1, we reported the pre exponential factor estimated using Eq. (6) fromdifferent experimental techniques. This pre exponential factor which is known as the 'attempt frequency' is related to the hopping motion of ion. This attempt frequency might be corresponds to the optical phonon frequency (vibration frequency) which can be measured directlyby Raman or infrared spectroscopy [10].Our PFG –NMR data and impedance data show reasonable agreement with previously reported data obtained from Raman measurement for Na β-alumina which is $2x10^{12}$ sec^{-1}[11] and T_1 relaxation measurement($\approx 10^{12} sec^{-1}$) for 85% Li β-alumina [12]. Since the Raman spectroscopy gives the direct measurement of vibrationfrequency, it is reasonable to compare our data with Raman data. However, the NMR line narrowing data show a very low estimation of the vibration frequency since the pre exponential factor appears10^6/sec.

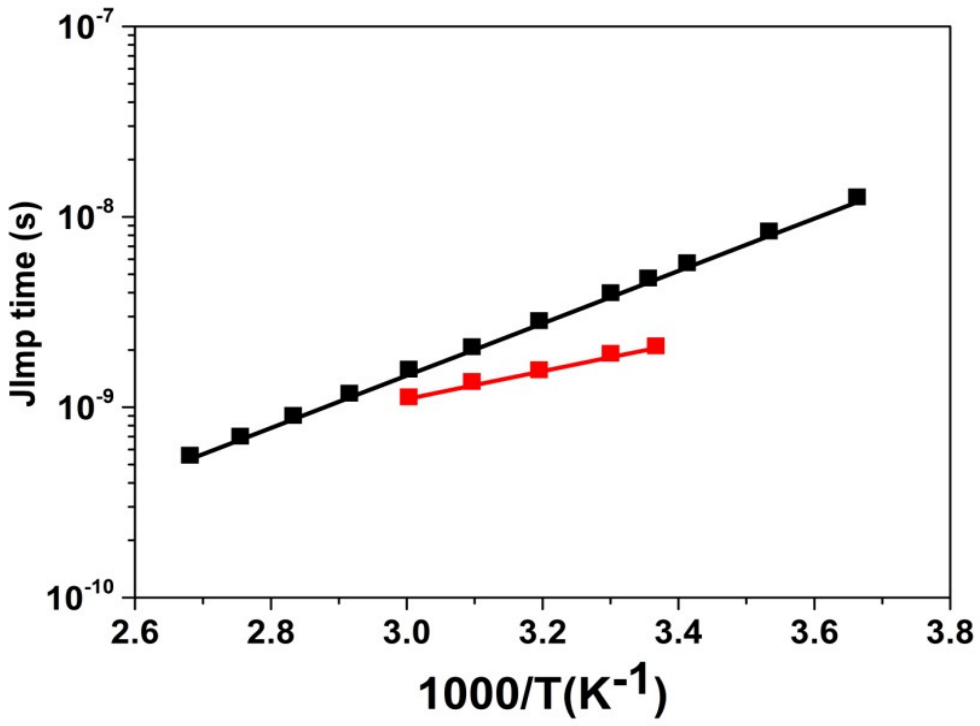


Figure 5. Jump time τas a function of inverse temperature estimated from PFG NMR data and the impedance data for 93% Liβ-alumina for perpendicular orientation. The redsquare data calculated using Eq. (5), the black solid square obtained using Eq. (7). The black and red solid line calculated using Eq(6). The jump distance is used as a=3.2$\dot{A}$ which is corresponds to BR-aBR or mO-mO distances.

This is known as 'prefactor anomaly' previouslyreported forβ-alumina[12]. The reason behind this low estimation is still not clear. However, it might be appearfor thelocal field distribution due to the structural disorder presence in the β-alumina crustal which is properlymodeled in the BPP relation.

Table1. Prefactor corresponds to attempt frequency or vibration frequency of ^{7}Li 93% Liβ-alumina estimated from NMR line narrowing, PFG NMR and impedance method. Raman and T_1 relaxation data obtained from the previous report.

NMR Line narrowing ^{7}Li 93% Li β alumina[6]	Raman (Na-β alumina) [11]	T_1 relaxation measurement [12] Liβ-alumina	PFG-NMR ^{7}Li 93% Li β alumina[6]		Impedance ^{7}Li 93% Li β alumina[6]	
			a=3.2 Å	a=1.5 Å	a=3.2 Å	a=1.5 Å
5.00×10^{6} /sec	2×10^{12} /sec	10^{12} /sec	1.41×10^{11} /sec	6.4×10^{11} /sec	9.09×10^{12} /sec	4.13×10^{13} /sec

5. Conclusion

We measured the anisotropic diffusion coefficient of ^{7}Li in 93% Liβ-aluminausing PFG NMR at two different crystal orientations. Diffusion coefficient was found $1.22\text{x}10^{-11}\text{m}^2$/sec at room temperature for ^{7}Li in 93%Liβ-alumina. Temperature dependent diffusion coefficient follows Arrhenius relation. The activation energy found by PFG NMR data is smaller than that of the impedance data.

Acknowledgments

The first author acknowledges MEXT, Japan for Monbukagakushoscholarship.

References

1 Yung-Fang Yu Yao and J.T Kummer,*J. Inorg. Nucl. Chem.*, **29** 2453. (1967)
2 J. L. Briant and G.C. Farrington, *J. Electrochem. Soc,***128** 1830(1981)
3. Zhongli Wang, Mallory Gobet, Vincent Sarou-Kanian, Dominique Massiot, Catherine Bessada, and Michael Deschamps, *Phys. Chem. Chem. Phys***14**, 13535 (2012).
4 Kikuko Hayamizu and Yuichi Aihara,*Solid State Ionics***238**, 7 (2013).
5 E. O. Stejskal and J. E. Tanner *J. Chem. Phys.***42**, 288 (1965).

6. Mohammed Tareque Chowdhury Reiji Takekawa, Yoshiki Iwai, Naoaki Kuwata, and Junichi Kawamura, *J. Chem. Phys.***140**, 124509 (2014); doi: 10.1063/1.4869347
7. MohammedTareque Chowdhury, Reiji Takekawa, Yoshiki Iwai, Naoaki Kuwata, and Junichi Kawamura,*Solid State Ionics*(2013),http://dx.doi.org/10.1016/j.ssi.2013.10.022
8R. Collongues, D. Gourier, A. Kahn, J. P. Boilot, PH. Colomban, and A. Wicker, *J. Phys. Chem. Solids* **45**, 981 (1984).
9 N. Bloembergen, E. M. Purcell, and R. V. Pound, *Phys. Rev. B***73**, 679 (1948)
10P. M. Richards, Topics in Current Physics: Physics of Superionic Conductors edited by M.B Salamon Springer–Verlag Berlin Heidelberg 1979.
11W. L Roth, F. Reidinger, S. La placa: In super Ionic conductors, Ed by G.DMahan, W. L Roth(Plenum Press , Newyork 1976
12 Marco Villa, John L. Bjorkstam, Gino Mariotto, Aldo Fontana, and Enzo Cazzanelli, *J. Chem.Phys.***76,** 2804 (1982).

Solid Electrolytes III

SYNTHESIS AND CHARACTERIZATION OF NEW SOLID ELECTROLYTE LAYER $(Li_2O)_x(P_2O_5)_y$ *

EVVY KARTINI, WAGIYO HONGGOWIRANTO, SUPARDI, HERI JODI, AZIS K.JAHYA, WAHYUDIANINGSIH

Center for Science and Technology of Advanced Materials,National Nuclear Energy Agency, Puspiptek Area, Serpong, South Tangerang 15314, Indonesia

The energy storage materials, such as lithium ion battery is very important for the application in the electric vehicles, electronic devices or home appliances. The battery contains electrodes (anode and cathode), separator and the electrolyte materials. The existing organic liquid electrolyte is a flammable material, when contact with open atmosphere. The use of a separator in between electrodes is also un-safety, due to low melting point and easily to get short. In an effort to overcome these problems, many researches have been focused to find new solid electrolytes for replacing the liquid electrolyte. In order to overcome this problem, mixtures of solid electrolytes $(Li_2O)x(P_2O_5)y$ with the ratio of x:y = 1:1, 2:1, 3:1, 4:1 and 5:1 has been synthesized by melt quenching method. The conductivities are increasing with various Lithium contents from 10^{-8} S/cm to 10^{-5} S/cm. The final products show that the conductivity maximum was observed for $(Li_2O)_2(P_2O_5)$. Furthermore, in order to obtain the solid electrolyte layer that is applicable for solid state battery, the addition of some polymer binders such as PVDF is recommended. The powders of 95% $(Li_2O)_2(P_2O_5)$ and 5% PVDF were mixed and dissolved in NMP. The new solid electrolyte layer based lithium phosphate oxide with the thickness of less than 0.5 mm was obtained and applied as a solid electrolyte in the solid state rechargeable battery. It is expected, that this layer will replace the existing separator and liquid polymer electrolyte, and it is promising for applications in high powers and energy density batteries with higher safety, stability, and reliability.

Keywords: Li_3PO_4, $LiPO_3$, $(Li_2O)_x(P_2O_5)_y$, solid electrolyte; electrochemical properties

* This work is supported by research Grant SINAS Consortium of Lithium Battery, Ministry Research and Technology, Indonesia.

Proceedings of the 14th Asian Conference on Solid State Ionics (ACSSI 2014)
Copyright © 2014 ACSSI 2014 Organizers. All rights reserved.
ISBN: 978-981-09-1137-9
doi:10.3850/978-981-09-1137-9_147

1. Introduction

1.1. *Scientific Background*

The energy storage materials, such as lithium ion batteries are very important for the application in the electric vehicles, electronic devices or home appliances. A rechargeable lithium-ion battery (LIB) consists of cathode, anode, electrolyte and separator, which are very important in producing very high energy density of battery [1]. There are many challenges to improve the existing lithium ion battery materials, in order to increase their life time, cyclic ability and also their stability and safety. Improvements for better electrode materials such as $LiCoO_2$, $LiMn_2O_4$ and $LiFePO_4$, and their corresponding systems are very crucial [2,3]. On the other hand, another important aspect of safety and friendly environment are still in the highest list of demand for the electrical energy storage. It has been tremendous issues, that the use of organic liquid electrolyte will give potential hazard on using current Lithium ion battery. A combustion of the electronic devices or cars, due to explosive materials in the separator or liquid-electrolyte is necessary to be resolved. In an effort to improve the safety of next-generation batteries, the research has been focused on finding new solid electrolytes with high ionic conductivity and electrochemical stability [4,5].

S*uperionic conducting glasses*, such as lithium phosphate glasses $LiPO_3$, is very important not only in the application as lithium-ion battery component, but also in the scientific point of view [5,6]. However, the ionic conductivity of this system is still low around 10^{-8} to 10^{-7} S/cm at room temperature. The lithium solid electrolyte Li_3PO_4 has become more interesting in the application of all solid state battery, and extremely suitable for the all thin film solid state battery, though the ionic conductivity of Li_3PO_4 is still low at 5.1×10^{-7} S cm^{-1} [7]. Due to this reason, our research focused on developing lithium phosphorous oxide superionic conductor, with the aim to obtain better solid electrolyte with higher ionic conductivity and better thermal and mechanical stability.

A previous work on Li_2O-P_2O_5 was performed by P.Dabas and K.Hariharan [8], but they focused on increasing the number glass former, P_2O_5. The former Li_2O acts as the glass modifier, while the later P_2O_5 as the glass former. So far there are no studies on Li_2O-P_2O_5, with highly containing lithium oxides, Li_2O. In order to improve performance of existing lithium phosphate solid electrolytes $LiPO_3$ and Li_3PO_4, our group developed new series of lithium-phosphorous

superionic conductor, $(Li_2O)_x(P_2O_5)_y$ by increasing a number of lithium contents [9]. Various $(Li_2O)_x(P_2O_5)_y$ glasses containing large amounts of Li_2O were synthesized by melt quenching method [9]. The conductivities are increasing with various Lithium contents from 10^{-8} S/cm to 10^{-5} S/cm. The final products show that the conductivity maximum was observed for $(Li_2O)_2(P_2O_5)$.

Furthermore, in order to obtain the solid electrolyte layer $(Li_2O)_2(P_2O_5)$ that is applicable for solid state battery, the addition of some polymer binders such as PVDF is recommended. It is expected, that this layer will replace the existing separator and liquid polymer electrolyte, and it is promising for applications in high powers and energy density batteries with higher safety, stability, and reliability

2. Experimental Methods

2.1.Synthesis

Mixtures of solid electrolytes $(Li_2O)_x(P_2O_5)_y$ with the ratio of x:y = 1:1, 2:1, 3:1,4:1 and 5:1 were prepared by melt quenching methods. The appropriate amounts of lithium carbonate, Li_2CO_3 (Aldrich, 99.99%) and ammonium-dihydrogen-phosphate, $NH_4H_2PO_4$ (Merck, 99.99%) were mixed and heated gradually up to 800^{o}C. The molten mixture was then quenched in the liquid nitrogen. Detail preparation has been described elsewhere [9].

The transparent bulk glass of $LiPO_3$ was obtained for the composition x:y=1:1.. A product of $(Li_2O)_2(P_2O_5)$ showed opaque bulk glass. A product of $(Li_2O)_3(P_2O_5)$ resulted a white granular powder corresponds to crystalline Li_3PO_4. Another mixture containing large number of Li_2O resulted white granular powder. All bulk glasses and granular powder were finely crushed and grinded by using an agate mortar and used for different characterizations.

Furthermore, in order to obtain the solid electrolyte layer that is applicable for solid state battery, the addition of some polymer binders such as poly vinylidene fluoride (PVDF, Aldrich) is recommended. The powders of 95% $(Li_2O)_2(P_2O_5)$ and 5% PVDF were mixed and dissolved in N-methyl pyrrolidinone (NMP, 99% Alrich). The electrolyte slurry was coated on the separator and dried in the vacuum. A new solid electrolyte layer $(Li_2O)_2(P_2O_5)$ with the thickness of less than 0.5 mm was obtained and applied as a solid electrolyte in the solid state rechargeable battery

2.2. Characterizations

In order to complete these features, several characterizations have been conducted of these materials. The crystalline phases present in the crystallized samples were identified by X-ray diffraction (XRD) analyses (CuKa radiation) at room temperature. The microstructures of these samples were measured by a Scanning Electron Microscope (SEM). Electrical conductivities of the glasses and glass–ceramics, were measured by an alternating current (AC) impedance method using an impedance analyzer (LCR meter Hioki) with the oscillation level of_1 V in the frequency range of 1 Hz–1kHz

2.3. Electrochemical Measurements

The electrochemical measurements were carried out using a CR-2032 type coin cell with a Celgard membrane separator (MTI), and 1 M $LiPF_6$-ethylene carbonate (EC)/diethyl carbonate (DEC) (1:1 in volume, Merck) as electrolyte. The composite cathode electrode was composed of 80 wt.% active material, 10.% conductive carbon black (MTI) and 10 wt.% PVDF, which were mixed in N-methyl pyrrolidinone (NMP) solvent to dissolve the binder and to obtain viscous slurry. The slurry was then coated on to an etched aluminum foil (20 μm thickness) using doctor Blade method. Cells were assembled in Argon-filled glove box (VYGOR, USA). Li-metal foil with thickness of 0.2 mm (MTI, USA) was used as counter (anode) and reference electrode. Galvanostatic cycling between 3.2-4.0 Volt vs Li at room temperature was carried out using 8 Channel Battery Analyzer (0.002-1mA, up to 5 V) with software program for Battery testing (Model BST8-WA, MTI USA).

3.Results and Discussions

3.1. X-ray Diffraction

The X-ray diffraction data for the composition 1:1 is showing only a halo pattern. This result confirms that $(Li_2O)(P_2O_5)$ an amorphous phase. The broad peak position is at $2\Theta \sim 28^o$, corresponding to the peak of crystalline $LiPO_3$. The composition of 2:1 is partial-crystalline phase. The diffraction contains background from the crystalline $LiPO_3$ and other unknown crystalline phase.

The composition of 3:1 gives the results of $(Li_2O)_3(P_2O_5)$ corresponding to the crystalline structure of Li_3PO_4. This result was confirmed by quick analysis using a fool proof refinement method on the X-ray data, that those majority of Bragg peaks are belong to the γ and β phases of Li_3PO_4. Further increasing Li_2O, for $(Li_2O)_4(P_2O_5)$ with composition 4:1, the samples show similar crystal structure of earlier phase Li_3PO_4 with unknown phase. But, more detail refinement is still needed. A different crystal structure was obtained for $(Li_2O)_5(P_2O_5)$ with the composition of 5:1.

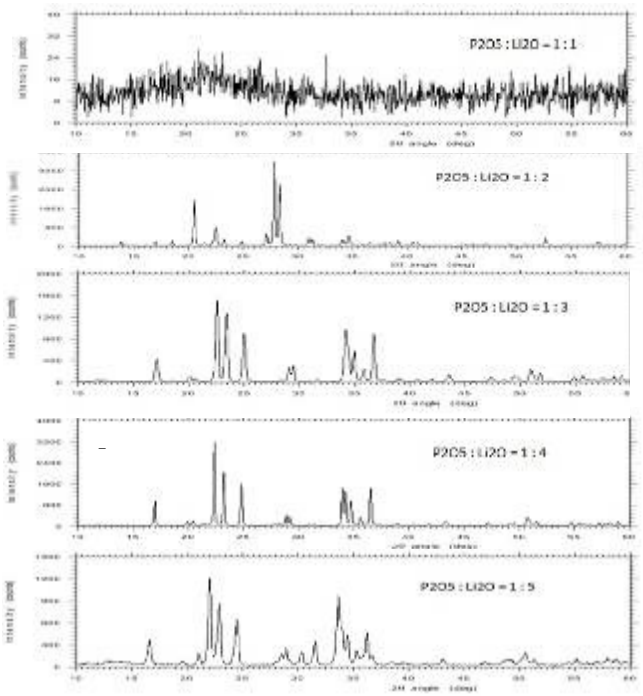


Figure 1. X-ray diffraction of the $(Li_2O)_x(P_2O_5)_y$ with various compositions (x:y=1:1, 2:1,3:1, 4:1 and 5:1) [9]

3.2. Conductivity

Figure 2 shows the ionic conductivity of the series sample $(Li_2O)_x(P_2O_5)_y$. The ionic conductivity is of $LiPO_3$ was around 10^{-8} S/cm, as previously reported [6]. The total conductivity consists of DC conductivity, which is frequency independent, σ_{DC}, and the AC conductivity $\sigma(\omega)$. The frequency dependent of conductivity data were fitted with the power law equation $\sigma(\omega) = A\, f(\omega)^n$, where

A is the pre-exponential factor and n is the exponent power. Table 1 shows the DC conductivity, A and n values for $(Li_2O)_x(P_2O_5)_y$ with various compositions.

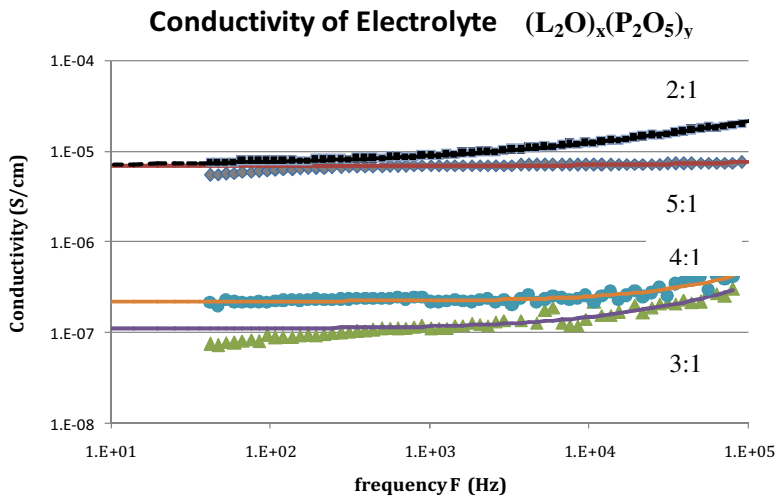


Figure 2. Conductivity of $(Li_2O)_x(P_2O_5)_y$ with (x:y=2:1,3:1,4:1 and 5:1) [9]

The conductivities are rather similar for $(Li_2O)_4(P_2O_5)$ and $(Li_2O)_3(P_2O_5)$. namely 10^{-7} S/cm. However, for $(Li_2O)_2(P_2O_5)$ and $(Li_2O)_5(P_2O_5)$., the conductivities are 100 times higher than those compositions, about 10^{-5} S/cm. The final products showed that the highest conductivity was about $6.78\ 10^{-6}$ S/cm for $(Li_2O)_2(P_2O_5)$. It is reflecting that this material is good for battery applications.

Table 1. Conductivity measurement for $(Li_2O)_x(P_2O_5)_y$ with various compositions.

No.	Ratio x:y	σ_{DC} (S/cm)	A	n
1.	2:1	6.7881 E-06	1.3019 E-09	0.55597
2.	3:1	1.1004 E-07	3.6307 E-11	0.7531
3.	4:1	2.2163 E-07	4.6341 E-12	0.9421
4.	5:1	6.8903 E-06	9.5558 E-08	0.4375

3.3. Scanning Electron Microscope (SEM)

The microstructures of bulk $(Li_2O)_2(P_2O_5)$ and $(Li_2O)_3(P_2O_5)$ are shown in the figure 3(a) and 3(b), respectively.

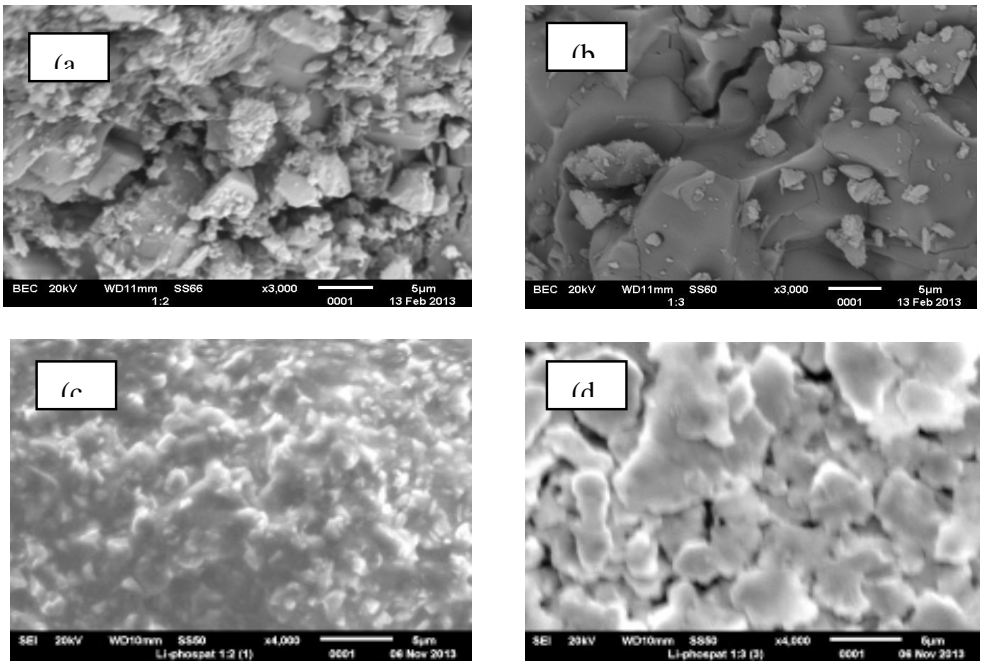


Figure 3. SEM photograph of (a) bulk $(Li_2O)_2(P_2O_5)$; (b) bulk $(Li_2O)_3(P_2O_5)$; (c) layer. $(Li_2O)_2(P_2O_5)$ and (d) layer $(Li_2O)_3(P_2O_5)$

The mixture of $(Li_2O)_2(P_2O_5)$ produced a partially crystalline sample, as shown in Fig.3(a). This is due to over the solubility limit of that $LiPO_3$ glass with the addition of Li_2O. However, the base glass $LiPO_3$ is still a major fraction of this sample, as confirmed by X-ray data. Further increasing amount of Li_2O, the sample crystalized with different crystal structures, as shown in Figures 3(b) for $(Li_2O)_3(P_2O_5)$ The results showed various shapes of crystallized samples with the grain boundaries around 10-100 µm corresponds to a crystalline Li_3PO4, a well-known solid electrolyte material for solid state battery.

The layers of $(Li_2O)_2(P_2O_5)$ and $(Li_2O)_3(P_2O_5)$ are shown in the figure 3(c) and 3(d), respectively. After mixing with polymer binder, both solid electrolyte layers showed more homogenous structures with less grain boundary and clusters. It is important to obtain a homogenous surface layer in order to have a better contact and to avoid the short circuit during application in the battery cell.

3.3. Coin Battery Cell

In order to check performance of the new solid electrolyte layer, several arrangements were made in the form of coin cell. The first and second cells consist of $LiMn_2O_4$/Separator+$LiTf_3$/Li and $LiMn_2O_4$/Separator+$LiPf_6$/Li, which can be used as references. Another two cells are using the solid electrolyte layers $(Li_2O)_2(P_2O_5)$ and $(Li_2O)_3(P_2O_5)$, with the arrangements $LiMn_2O_4$/ layers $(Li_2O)_2(P_2O_5)$ +$LiPF_6$/Li and $LiMn_2O_4$/ layers $(Li_2O)_2(P_2O_5)$ +$LiPF_6$/Li. In this case, a small amount (ppm) of $LiPF_6$ was used just to start contacting the interface between the solid electrolyte and the cathodes.

As the preliminary test, the conductivities of the coin cells were measured by impedance spectrometer. Those values of conductivities are shown in Table 3.
It is clear that the ionic conductivity of the cell using solid electrolyte layer have a higher conductivity compared with the other cells that using only the separator. The highest conductivity was achieved for the cell with the solid electrolyte layer $(Li_2O)_2(P_2O_5)$ which is about 2.318 10^{-2} S/cm, while the cell with commercial solid electrolyte layer Li_3PO_4 is around 8.974 10^{-3} S/cm.

Table 3. Conductivity of coin cells with various arrangements [10].

No	Sample	σ_{DC} (S/cm)	A	n
1.	Cell_0	1.469 E-03	4.5059e-013	1.258
2.	Cell_1	4.174 E-04	2.0583e-014	1.3878
3.	Cell_2	2.318 E-02	1.0514e-011	1.2358
4.	Cell_3	8.974 E-03	1.5101e-011	1.0674

3.4.Electrochemical Studies

The galvanostatic charge-discharge profiles from the initial, until the 50th of the cell-2 ($LiMn_2O_4$/$(Li_2O)_2(P_2O_5)$/Li and between 3.2-4.0 V are displayed in As shown in the figure, this all solid state battery exhibited low specific capacity. The initial cycle charge capacity and discharge capacity were 0.015mA/mg and 0.01 mAh/mg, respectively, hence the sample weight was 0.06 mg.

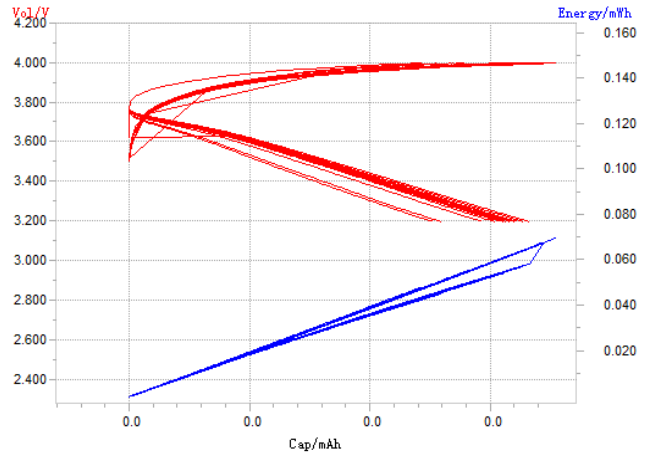


Figure 4. (a) Galvanostatic charge-discharge profiles from the initial, until the 50th of the cell-2 ($LiMn_2O_4$/$(Li_2O)_2(P_2O_5)$/Li and between 3.2-4.0 V, (b) Charge-discharge capacity at a current 0.01 mAh.

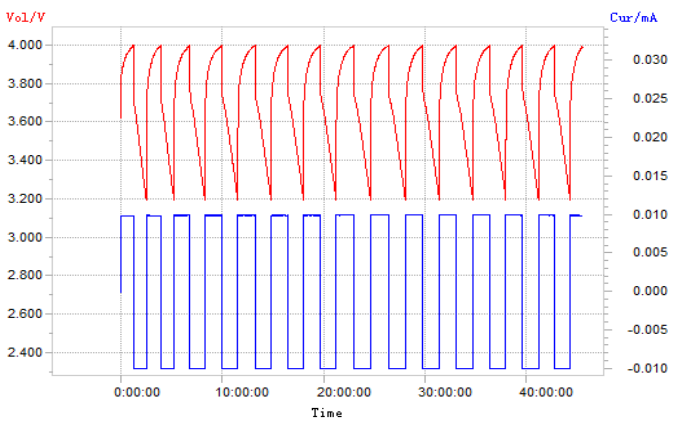


Figure 5. The charge and discharge process of the cell-2

The charge and discharge current vs time plot of the cell-2 from the initial until 14th is shown in figure 5. The charge and discharge process for one cycle took about 2.5 hours, and relatively stable until 14th cycle and 50th cycle. The charge and discharge capacity vs. cycle number plot of the cell-2 up to 14th cycles is shown in Fig.6 and up to 50th cycles, not shown here. The energy efficiencies up to 50th cycles of cell-2 are still stable from the initial discharge 99% to 98% and 95%, at the 14th and 50th cycles. Moreover, the charge and discharge plots stay close after the 50th cycle, which indicates a good electrochemical reversibility. The reason of the stability after the fifth cycle can be attributed to the 'formation cycle' of the electrode and solid electrolyte material during initial cycles.

.

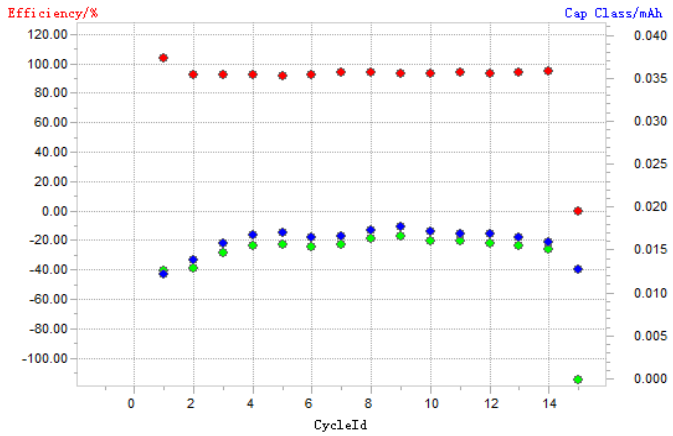


Figure 6. The charge and discharge efficiency of the cell-2 (Please noted that the 15th cycle was just interrupted during the cycle)

4. Conclusions

The new solid electrolyte based on lithium phosphorous oxide glass, $(Li_2O)_x(P_2O_5)_y$ have been synthesized and characterized. The maximum conductivity of about 10^{-5} S/cm was observed for the solid electrolyte with the composition of $(Li_2O)_2(P_2O_5)$. The solid electrolyte layer of $(Li_2O)_2(P_2O_5)$ with the thickness of 0.5mm was made by mixing with polymer binder and used for a battery. A coin battery cell with the arrangement of $LiMn_2O_4$/ $(Li_2O)_2(P_2O_5)$/Li showed a better ionic conductivity of about $2.3x10^{-2}$ S/cm in comparison with the conductivity of cell-3 with commercial Li_3PO_4 ($8.9x10^{-3}$ S/cm). Though the capacity of the battery is still low, at 25 mAh/g, but charge-discharge efficiencies are relatively stable even after 50th cycles. Further improvement of solid electrolyte is very important in order to obtain all solid state battery.

Acknowledgments

The Ministry Research and Technology, Indonesia, for funding though the Research Grant of SINAS Consortium on Lithium Ion Batteries.

References

1.Shi-Xi Zhao, Hao Ding, Yan-Chao Wang a,b, Bao-Hua Li, Ce-Wen Nan *Journal of Alloys and Compounds* **566** (2013) 206–211

2.X.Zhao, M.V. Redy, S.Ramakrishna, S.Mahishalkar, and B.V.R. Chowdari, in Proceeding of the 13th Asian Conference on Solid State Ionics: Ionics for Sustainable World, Sendai, Japan 17-20 July (2012) 3-9.

3.She-huang Wua, Je-Jang Shiua, Jeng-Yu Lin, *Journal of Power Sources* **196** (2011) 6676–6681

4.R.Prasada Rao, Maohua Chen, Stefan Adams, in Proceeding of the 13th Asian Conference on Solid State Ionics: Ionics for Sustainable World, Sendai, Japan 17-20 July (2012)18-26.

5.R. PrasadaRao, N. Sharma, V.K. Peterson, S. Adams, *Solid State Ionics* **230** (2013) 72–76

6. E.Kartini, T.Y.S. Panca Putra, I.Kuntoro, T.Sakuma, K.Basar, O. Kamishima and J.Kawamura, *J. Phys. Soc. Jpn*. **79** Suppl. A, 54 (2010)

7.E.Kartini, M.Nakamura, M.Arai, Y.Inamura, K.Nakajima, T.Maksum, W.Honggowiranto, T.Y.S.P. Putra, *Solid State Ionics* (2014) in press

8.P.Dabas and K.Hariharan, in Proceeding of the 13th Asian Conference on Solid State Ionics: Ionics for Sustainable World, Sendai, Japan 17-20 July 2012, p.679-688

9.E.Kartini, Azis K.Jahya, W.Honggowiranto, T.Y.S.S.Putra, H.Jodi, Supardi, presented at ICMAT2013, to be published

Polymer Electrolytes II

POLYVINYL ALCOHOL GEL POLYMER ELECTOLYTE BASED DYE SENSITIZED SOLAR CELLS

M.A. CAREEM, M.H. BURAIDAH, M.F. AZIZ, H.C. HASSAN, A.K. AROF

Center for Ionics University of Malaya, Department of Physics, Faculty of Science, University of Malaya, 50603, Kuala Lumpur Malaysia

Polyvinyl alcohol (PVA) based gel polymer electrolytes have been prepared with potassium iodide (KI) salt and with double salt containing KI and tetrapropylammonium iodide (TPAI) and optimized for application in dye sensitized soar cells. A ruthenium-N3 DSSC with the GPE containing only KI salt having the optimized composition 5.6 wt.% PVA-8.4 wt.% EC-11.1 wt.% PC-61.4 wt.% DMSO-11.7 wt.% KI(+1.8 wt.% I_2)showed a power conversion efficiency (PCE) of 2.64%. The same GPE in a DSSC sensitized withnatural chlorophyllobtained frommoss bryophyteproduced a PCE of 1. 4 %. When part of the KI in the GPE was replaced with the same amount of TPAI, the PCE of N3-DSSC increased to 3.12% and that of the chlorophyll-DSSC increased to 2.1 %. In the case of double salts, the smaller K^+ions facilitate more electron injection but the larger TPA^+ions enhance the iodide conductivity in the electrolyte and both processes contribute to higher current and efficiency. On incorporation of a newtype of compact layer to the photoanode the efficiency of the N3 dye with double salt electrolyte increased to an impressive 5.51% indicating the necessity of the compact layer to improve the performance of GPE based DSSCs.

1. Introduction

Dye-sensitized solar cells (DSSCs) with low productioncost have attracted considerable researchinterest since it was first reported by O'Regan and Grätzel[**1**] due to their potential as an alternative to conventional silicon solar cells.A DSSC consists of three main components (shown in Figure 1); (i) a photoanodecontaining a transparent conducting oxide (TCO), dye sensitizer and oxide wide semiconductor (usually nanocrystalline titanium dioxide,TiO_2, with thickness in the range 5-30 μm) (ii)an electrolyte containing a redox mediator (usually I/I_3^-) and (iii)a counter electrodecoated with Pt (as a catalyst). Unlike in a p-n junction silicon solar cell, the absorption and transportation processes in a DSSC occur in different materials. The absorption occursinthe dye sensitizer and transportation takes place in the

Proceedings of the 14th Asian Conference on Solid State Ionics (ACSSI 2014)
Copyright © 2014 ACSSI 2014 Organizers. All rights reserved.
ISBN: 978-981-09-1137-9
doi:10.3850/978-981-09-1137-9_117

TiO_2semiconductor and the electrolyte. On illumination with light, the dye will be excited by transferring an electron from the highest occupied molecular orbital to lowestor higher unoccupied molecular orbital. The excited dye will inject the electron to the conduction band of TiO_2 and the electron is transported to the counter electrode through the mesoporous TiO_2 and the external circuit. At the counter electrode, I_3^-reduces to I^-which diffuses to the photoanode to regenerate the oxidized dye to complete the circuit.The processes continue as long as the light is present resulting in continuous current from the DSSC.

Until now, the highest efficiency obtained for this type of solar cell is around 13 % [2] using a liquid electrolyte. Although capable of producing high efficiencies, liquid electrolyte based DSSCs exhibit poor long-term stability due to leakage, volatility and flammability of the solvent. These problems can be overcome by replacing the liquid electrolytewith quasi-solid state gel polymer electrolytes (GPEs). Typical GPEs for DSSC consist of a host polymer, ionic salts and plasticizers. Polymers such as polyacrylonitrile(PAN) [3], polyethylene oxide (PEO) [4] andpolyvinylidene fluoride (PVDF) [5] have been studied for application in DSSCs.
I^-/I_3^-redox mediator can be obtained by using iodide salts such as lithium iodide (LiI), potassium iodide (KI) and tetrapropylammonium iodide (TPAI). Ethylene carbonate (EC), propylene carbonate (PC) and dimethylformamide (DMF)are some examples of plasticizers that have been used in GPEs.

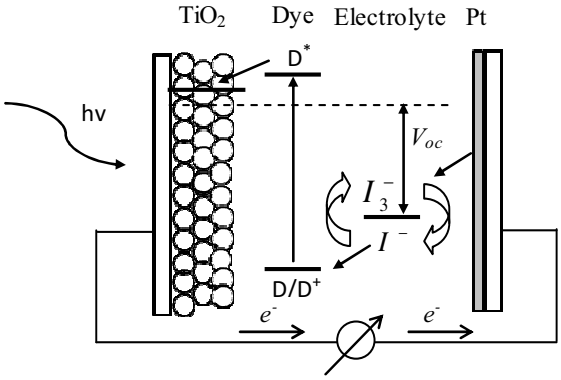


Figure 1. Schematic diagram of DSSC structure

The dye sensitizer can be either a synthetic or natural material. Usual synthetic sensitizersare ruthenium complexes[6] and indoline baseddyes [7]. Natural sensitizers such as anthocyanin, chlorophyll and carotenoid are readily available and cheap, and can reduce the cost of DSSC devices.In this paper we discuss some GPEs

based on polyvinyl alcohol (PVA) that have been optimized and tested in DSSCs. PVA has been chosen as the host polymer because it is cheap, non toxic and biodegradable and therefore the DSSCS based on it will be cheap and environment friendly. Both synthetic N3 dye and natural chlorophyll were used as sensitizers. Potassium iodide (KI) and tetrpropylammonium iodide (TPAI)salts were used as single and double salt to provide the iodide ions. The combination of double iodide salt containing smaller cation (K^+) and larger cation (TPA^+) was chosen as such double salts were found to enhance the efficiency of DSSCs with PAN and PVdFGPEs through mixed cationeffect [8, 9]. The smaller cationwith high charge density such as K^+ is expected to facilitate better electron injection and the bulky cation such as TPA^+leads to reduced cation conduction and increased iodide ion concentration and both these increases lead to a large current and thereby enhanced efficiency [8]. In the present work a similar study is reported using PVA as the polymer host in order to prove the general nature of the mixed cation effect in enhancing the efficiency of solar cells irrespective of the polymer host involved. Ethylene carbonate (EC), propylene carbonate (PC) and dimethyl sulfoxide(DMSO)were used as the plasticizers.

2. Experimental

2.1. *Electrolyte preparation*

Appropriate amountsof PVA, EC and PC were dissolved in DMSO. Different amounts of potassium iodide (KI) salt were added to the mixture of PVA, EC, PC and DMSO.The mixtures were stirred at 110 °C for 1 hour until gelpolymersare formed. When the gel is formed, the heater was immediately stopped and the gel was allowed to cool down. On reaching room temperature I_2 (10 mole % of KI) was added into the gel electrolyte. The homogenous gel polymer electrolyte was placed in desiccators overnight before being used in dye-sensitized solar cells. The gel electrolytes were characterized using electrochemical impedance spectroscopy (EIS) in the frequency range between 50 Hz and 1 MHz. The ionic conductivity, σ can be calculated from the equation given below:

$$\sigma = \frac{d}{R_b A} \qquad (1)$$

*A*and*d* are the area and thickness of the samples, respectively. R_b is the bulk resistance obtained from the complex impedance plot.

2.2. *DSSC assembly*

A fluorine dope tin-oxide (ITO) glass substrate was cleaned with distilled water and acetone. The TiO_2 paste was prepared by grinding 0.2 g TiO_2 powder (P25) with acetic acid, surfactant (Triton X 100) in ethanol. The paste was then deposited on FTO glass by doctor-blade technique. The TiO_2 layer was then sintered at 450 ^oC for 30 minutes and immersed in 3 mMcis-Ru(II) bis(2,2'-bipyridyl-4,4'-dicarboxylate)-$(NCS)_2$ red dye (or N3) solution for 24 hours. Platinum counter electrodes were prepared by brushing platinum solution on top of FTO glass. The electrodes were then heat treated at 450 ^oC for 30 minutes. The gel electrolyte was sandwiched between the TiO_2/dyephotoanode and platinum counter electrode.The photocurrent density-voltage (*J-V*) characteristics of the samples were obtained using the Keithley 2400 electrometer. The DSSCs were illuminated using a Xenon light source of intensity of100 mW/cm^2.In order to establish the importance of a blocking layer between the mesoporous layer and TCO a new type of thin dense layer containing smaller TiO_2nanoparticles was introduced in some DSSCs, This blocking layer was prepared by spin coating a TiO_2 paste made from Deggusa(P90) powder with 2 ml of HNO_3 (pH=1).The spin coating was done in two steps with different spinning rates and the layer was sintered at 450 $^{\circ}C$ for about 30 minutes in a furnace.

3. Results and discussions

3.1*Optimized gel polymer electrolytes*

The gel polymer electrolytes with PVA were prepared with various KI contents and optimized for conductivity. Then part of the KI in the optimized electrolyte was replaced with various amounts of the second salt TPAI ranging from 0 to100 % and the salt compositions giving the optimum conductivity was determined. The polymercompositions giving the maximum conductivities with KI and KI and TPAI salts are tabulated in Table 1.The KI single salt gives a maximum conductivity of 12.9 mS cm^{-1} whereas the double salt gives a lower conductivity of 9.8mS cm^{-1}. In the single salt system the conductivity is determined by both iodide anions and smaller K^+cations as both types of ions can be expected to be mobile. In polymer electrolytes cations are usually coordinated to the polymer chains and anions are free to move. When the cations are small they also can move via breaking and forming of bonds assisted by segmental motions of the polymer. However, in the double salt

system some of the K^+ ions are replaced with the TPA^+ ions which are bulky and less mobile and therefore the overall conductivity of the electrolyte becomes smaller.

Table 1: Compositions of the optimized single double salt electrolytes and their conductivities

GPEs	Conductivity,σ $mScm^{-1}$
5.6 wt.% PVA-8.4 wt.% EC-11.1 wt.% PC-61.4 wt.% DMSO-11.7 wt.% KI(+1.8 wt.% I_2) –Single salt	12.9
5.6 wt.% PVA-8.4 wt.% EC-11.2 wt.% PC-61.5 wt.% DMSO-8.2 wt.% KI-3.5 wt.% TPAI(+1.6 wt.% I_2)- Double salt	9.8

3.2*DSSC performance*

The fill factor*ff* and external light to electricity conversion efficiency$\eta$of DSSCswere calculated using the following equations:

$$ff = \frac{V_{max} \times J_{max}}{V_{oc} \times J_{sc}} \quad (2)$$

$$\eta\,(\%) = \frac{V_{oc} \cdot J_{sc} \cdot ff}{P_{in}} X\ 100\% \quad (3)$$

whereV_{oc} is open circuit voltage, J_{sc} is short circuit current density, J_{max} (mA/cm^2) and V_{max} (V) are the current density and voltage in the *J-V* curves, respectively, at the point of maximum power output. P_{in} is the incident light power.The working principal of DSSC can be summarized as follows:

Electrolyte;

$$I_2 + I^- \rightarrow 3I^- \quad (4)$$

Photoanode;

$$hv + D \rightarrow D^* \quad (5)$$

$$D^* + TiO_2 \rightarrow D^+ + e^-_{cb}(TiO_2) \quad (6)$$

$$2D^+ + 3I^- \rightarrow I_3^- + 2D \quad (7)$$

Counter electrode;

$$I_3^- + 2e^- \rightarrow 3I^- \quad (8)$$

where D represents the dye molecule and *hv* is the light energy

The redox mediator concentration in the gel polymer electrolyte plays an important role in DSSC as shown in equations (4), (7) and (8). The redox mediator concentration can be increased by increasing the iodide salt content in the

electrolyte. Fig. 2 (a) and (b) show the variations of J_{sc}, V_{oc} and efficiency of the DSSC with KI concentrations in electrolyte used in the DSSC. The results shown in the figures are for DSSCsfabricated with electrolytes having various KI concentrations up to the composition giving the maximum conductivity.

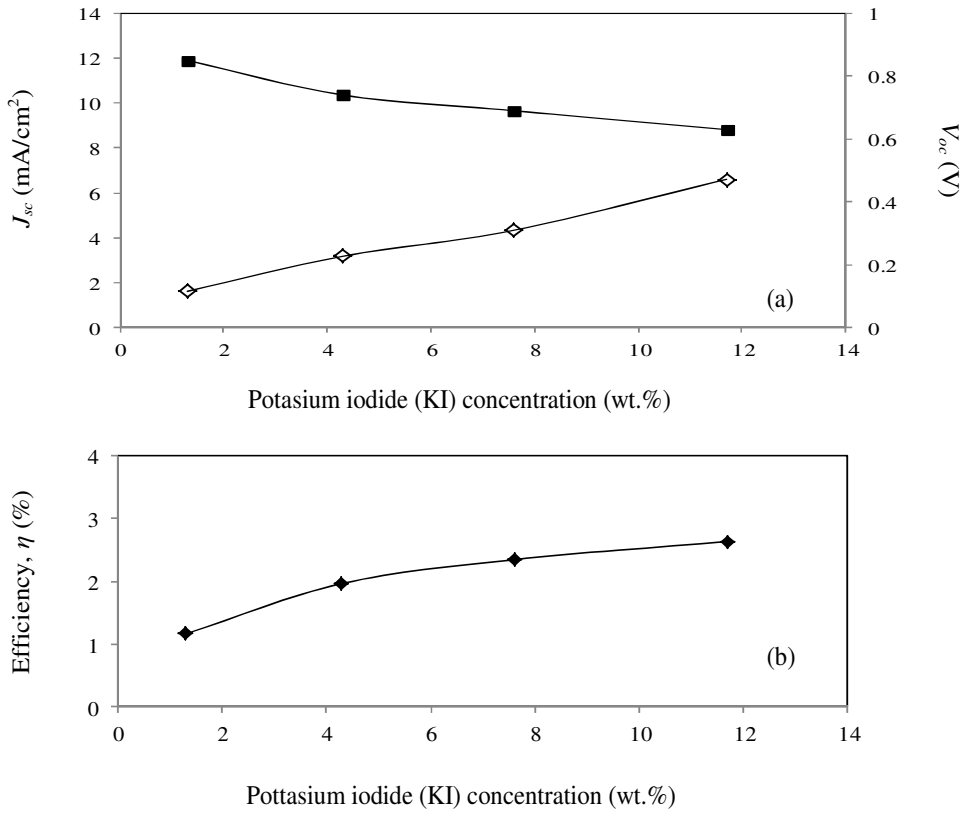


Figure 2.Variations of J_{sc}, V_{oc} and efficiency of the DSSC with KI concentration in the electrolyte

It can be seen from the Figure 2 that J_{sc} of the DSSC increases with increasing KI concentration. The increasing KI concentration leads to increasing number of iodide (I^-) ions and hence the regeneration of oxidized dyes becomes faster. At the same time, the small sizedK^+ ions get adsorbedon the surface ofthe mesoporous TiO_2surface and change the position of the Fermi level to low energy values[9].This shift facilitates increased electron injection from excited dye moleculesto conduction band of $TiO_2$and thus increasesJ_{sc} and decreases V_{oc} as shown in Figure 2.V_{oc} is the difference between Fermi level of TiO_2 semiconductor and redox potential in the electrolyte.The relationship between V_{oc} and iodide concentration in the electrolyte [I_3^-] is given in equation [10]:

$$V_{oc} = \frac{kT}{e} \ln\left(\frac{I_{inj}}{n_0 k_{et}[I_3^-]}\right) \quad (9)$$

where I_{inj} is the flux of charge resulting frominjection of electrons from excited dye molecules, $n_o$is the electron density in the conduction band of TiO_2 in the dark, k_{et} is the recombination reaction rate for a given iodide concentration [I_3^-], k is Boltzmann constant, T is absolute temperature and $e$is electron charge. The increase in salt concentration also leads to increase in the number of triiodide ions, and hence increase in the recombination rate. According to the equation (9) V_{oc} decreases with increasing number of triidide ions.As can be seen in Fig 2 (b) the power conversion efficiency of the cells follows the J_{sc} and increases with salt concentration. The highest efficiency of 2.64 % is obtained for DSSC with the electrolyte having single iodide salt (KI) of composition 5.6 wt.% PVA-8.4 wt.% EC-11.1 wt.% PC-61.4 wt.% DMSO-11.7 wt.% KI(+1.8 wt.% I_2) electrolyte. When part of the KI in this electrolyte is replaced with a larger iodide salt (TPAI) as in the second composition shown in Table 1, the DSSC performance improves with a better efficiency 3.12 % as shown in Figure 3.This corresponds to an efficiency enhancement of 18 % from that of the single salt DSSC.

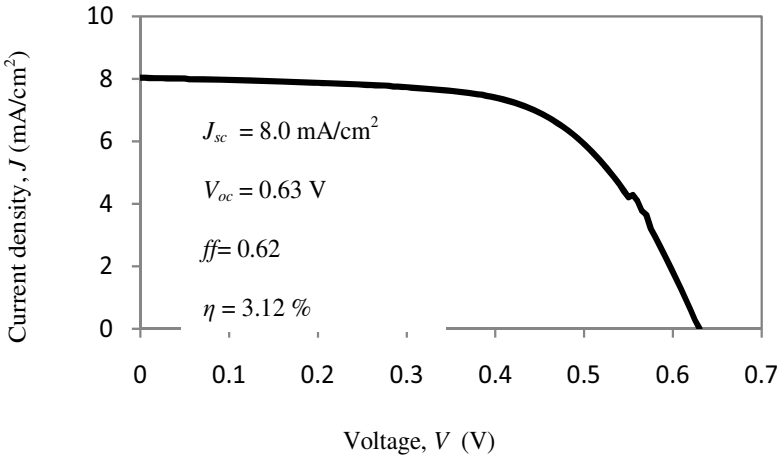


Figure 3.*J-V* curve of DSSC with the double salt electrolyte of composition 5.6 wt.% PVA-8.4 wt.% EC-11.2 wt.% PC-61.5 wt.% DMSO-8.2 wt.% KI-3.5 wt.% TPAI(+1.6 wt.% I_2)

As shown in Figure 3, the values of V_{oc} and *ff* for the DSSC with the double iodide saltare almost similar to those obtained with single iodide salt but J_{sc} increases to 8.0 mA/cm^2.The increase in J_{sc} is due to increasing in the number of iodide ions due to the addition of the second salt containing bigger sizedcations (TPA^+). The salts with bigger cationshave lower lattice energy and dissociate easily into constituent

ions. Therefore, the addition of larger TPAI results in larger number of iodide ionsand they give rise to increased current.V_{oc} does not change that much due to the addition of the second salt as it is controlled mainly by the smaller K^+ cations getting adsorbed to TiO_2 surface. The better performance with larger efficiency can be attributed to the mixed cation effect due to the presence smaller and larger cations in the GPE.

Other way to increase the efficiency is to suppress the recombination losses. Loss of injected electron occurs through the recombination with oxidized dyes and I_3^- in electrolyte as shown in following reactions:

$$D^+ + e_{cb}^- (TiO_2) \rightarrow D + TiO_2 \quad (10)$$

$$I_3^- + 2e_{cb}^- (TiO_2) \rightarrow 3I^- + TiO_2 \quad (11)$$

These losses have been prevented to some extent by faster regeneration of the oxidized dye (D^+) due to increased iodide ion concentration because of the presence of the double salt in the electrolyte. Loss of electrons to the electrolyte also takes place due to the porous nature of the TiO_2 layer.It is possible for the gel polymer electrolyte to flow through the TiO_2 layer and touch the conducting surface of the FTO glass. Hence, the recombination of electronsreaching the TCO and I_3^- in the electrolyte can take place. This can be prevented by depositing a blocking compact TiO_2 layer on top of TCO before the mesoporous TiO_2 layer is depositedas shown in Figure 4 (b).In this work a new type of thin layer of dense TiO_2prepared using smaller Degussa P90 particles was used. Fig. 4 (a) shows the J-V characteristics of the DSSC with the double salt electrolyte with the added compact layer.

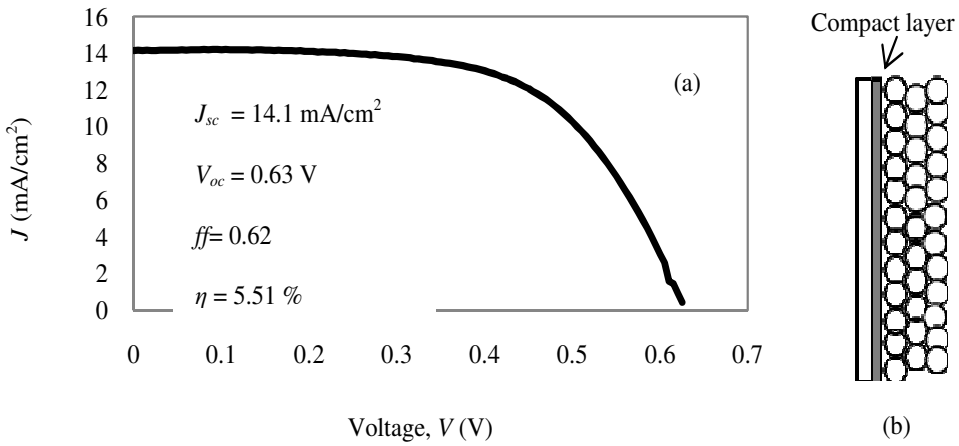


Figure 4.(a) *J-V* curve of DSSC containing a compact layer in the photoanode. (b) Diagram of TiO_2photoanode with the compact layer

As can be seen in Fig 4 (a), when the compact layer was introduced in the photo anode, both J_{sc} and efficiency were increasedto 14.1 mA/cm^2 and 5.51 % respectively while the V_{oc} and *ff* remain almost same as indicated in Fig 3. The increases in current and efficiency correspond to nearly 76 %. The compact layer helps to reduce the recombination from the TCO and reduces the dark current and thus increases the J_{sc} and efficiency.These results indicatethe necessity of the compact layer in improving the efficiency of gel polymer electrolyte based DSSCs especially with PVA based systems. The new type of compact layer used is very effective in preventing the recombination losses.

The PVA based gel single and double salt electrolytes also have been tested in DSSCssensitized with chlorophyll obtained from bryophyte moss. A small amount of ferulic acid (3 wt. %) was added to the chlorophyll as a stabilizer. The DSSCs were fabricated with photoanodes having both compact and porous layers. The performance parameters of the DSSCs are summarized in Table 2.

Table 2.Performance parameters of DSSC with chlorophyll sensitizer

Electrolyte	J_{sc} (mA/cm^2)	V_{oc} (V)	*ff*	η(%)
5.6 wt.% PVA-8.4 wt.% EC-11.1 wt.% PC-61.4 wt.% DMSO-11.7 wt.% KI(+1.8 wt.% I_2) Single salt	4.98	0.50	0.56	1.39
5.6 wt.% PVA-8.4 wt.% EC-11.2 wt.% PC-61.5 wt.% DMSO-8.2 wt.% KI-3.5 wt.% TPAI(+1.6 wt.% I_2) – Double salt	5.94	0.55	0.634	2.05

The efficiency increased from 1.39 % for the single salt electrolyte to 2.05 % when double salt was used. This corresponds to an efficiency enhancement of 47%. Hence the natural DSSCs also show the same performance trend as the synthetic dye based DSSCs with PVA gel electrolytes. However the efficiencies are lower in view of the poor absorption by the natural dyes.

4. Conclusions

PVA based gel electrolytes have been prepared with KI single salt and KI and TPAI double salt and optimized for application in dye sensitized solar cells. While the single salt electrolyte produced an efficiency of 2.64 % in a N3 based DSSC, the double salt resulted in an increased efficiency of 3.12 % corresponding to enhancement of nearly 18 %. However, the same electrolyte combinations in a stabilized chlorophyll sensitized solar cells produced efficiencies of 1.4% and 2.1%

respectively indicating an efficiency enhancement of nearly 47% when double cations are used in the electrolyte. The efficiency enhancement arising due to the use of double slat in the electrolyte can be attributed to the mixed cation effect. The efficiency of the N3 dye based DSSC with the double salt GPE jumped to 5.51% when a thin compact layer was introduced in the photoanode. This result indicates the importance of an additional denselayer to prevent electron recombination and enhance the performance of GPE based DSSCs.

Acknowledgments

Authors thank University of Malaya for the AFR Program grant No. RP003D-13AFR.

References

1. B. O'Regan and M. Grätzel, Nature 353 737(1991)
2. S. Mathew, A. Yella, P. Gao, R. Humphry-Baker, B.F. E. Curchod, N. Ashari-Astani, I. Tavernelli, U. Rothlisberger, Md.K. Nazeeruddin, M. Grätzel, *Nature Chemistry* 6242 (2014)
3. T.M.W.J. Bandara, W.J.M.J.S.R. Jayasundara, M.A.K.L. Dissanayake, M. Furlani, I. Albinsson, B.-E. Mellander, ElectrochimicaActa 109 609 (2013)
4. H. Yang, J. Liu, Y. Lin, J. Zhang, X. Zhou, ElectrochimicaActa, 56 6271 (2011)
5. S. Ganesan, B. Muthuraaman, Vinod Mathew, M. Kumara Vadivel, P. Maruthamuthu, M. Ashokkumar, S. Austin Suthanthiraraj, ElectrochimicaActa, 56 8811 (2011)
6. G. Yue, X. Zhang, L. Wang, F. Tan, J. Wu, Q. Jiang, J. Lin, M. Huang, Z.Lan, ElectrochimicaActa 129229 (2014)
7. L. Wang, M. Liang, Y. Zhang, F. Cheng, X. Wang, Z. Sun, S. Xue, Dyes and Pigments 101 270 (2014)
8. M.A.K.L. Dissanayake, C.A. Thotawatthage, G.K.R. Senadeera, T.M.W.J. Bandara, W.J.M.J.S.R. Jayasundera, B.-E. Mellander, Journal of Photochemistry and Photobiology A: Chemistry 246 29 (2012)
9. A.K. Arof, M.F. Aziz, M.M. Noor, M.A. Careem, L.R.A.K. Bandara, C.A. Thotawatthage, W.N.S. Rupasinghe, M.A.K.L. Dissanayake, International Journal of Hydrogen Energy 39 2929 (2014)
10. J. Gong, J. Liang, K. Sumathy, Renewable and Sustainable Energy Reviews 165848 (2012)

ELECTRICAL CHARACTERIZATION OF TETRABUTYLAMMONIUM IODIDE BASED POLYMER FREE GEL ELECTROLYTE

E.M.T.K.EKANAYAKA[1]

[1]*Department of Physics, University of Peradeniya, Peradeniya, Sri Lanka*

V.A.SENAVIRATHNE[1,2,3*], L.R.A.K.BANDARA[1,2], K.V.L.AMARASINGHE[2], C.A.THOTAWATHTHAGE[3], J.M.K.W.KUMARI[3], M.A.K.L.DISSANAYAKE[3]

[2]*Postgraduate institute of Science, University of Peradeniya, Peradeniya, SriLanka.*

[3]*Institute of Fundamental Studies(IFS), Kandy, Sri Lanka.*

**Corresponding author: sene7403@yahoo.com, dmvas@pdn.ac.lk*

Gel Electrolytes (GE) have been extensively studied due to their long term stability and durability and they have attracted worldwide attention due to the ability of use them in the practical applications like solar cells and rechargeable batteries. The most of the GE systems studied are polymer gel electrolytes. In this work, a polymer free GE system was fabricated by adding a innert filler, fumed silica, to tetrabutylammonium iodide ($Bu_4N^+I^-$) salt dissolved in a solvent mixture of ethylene carbonate (EC) and propylene carbonate (PC). A series of GEs, x% EC: x% PC ; y% Bu_4N+I^- , were prepared by varing the weight of salt as y=20,15,12,and 10. In every sample, EC to PC weight ratio was 1:1 and the amount of fumed silica added was 10% of the total weight of EC,PC and $Bu_4N^+I^-$. The ionic conductivities of fumed silica added GEs with different salt concentrations are in the order of ~10^{-3} S cm^{-1} at room temperature. The highest conductivity of 6.51×10^{-3} S cm^{-1} at 24 ^oC was obtained for the sample with composition 40% EC: 40% PC: 20% $Bu_4N^+I^-$. The DC polarization testa were carried out and the results verified that the prepared electrolytes were predominantly ionic conductors with negligible electronic conductivity. FT-IR studies were carried out to investigate the interactions of Bu_4N^+ ions with the ether oxygen of EC and PC. The vibrational modes of EC and PC do not show major changes with the addition of the salt to the EC + PC solvent. Dye sensitized splar cells of configuration Glass/FTO/TiO_2 working electrode/dye(N719)/gel electrolyte/ platinized FTO/ glass were fabricated using the optimized GE and it showed a maximum short circuit current density(J_{sc}) of 9.30 mA cm^{-2}, open circuit voltage (V_{oc}) of 651.4 mV and efficiency of 3.73% exhibiting the ability to use the proposed GE system in solar cells.

Proceedings of the 14th Asian Conference on Solid State Ionics (ACSSI 2014)
Copyright © 2014 ACSSI 2014 Organizers. All rights reserved.
ISBN: 978-981-09-1137-9
doi:10.3850/978-981-09-1137-9_084

1. Introduction

Dye sensitized solar cells (DSSC) are emerging as low cost alternative source to photovoltaic semiconductor junction devices. These solar cells conventionally used liquid electrolytes, which have several drawbacks like solvent eveporation and leakage, corrotion of the platinum electrode, desorption and photo degradation of the dye, and ineffective sealing of cells for long term applications. Therefore, to overcome the above problems, these liquid electrolytes have been replaced by solid and gel type electrolytes. Althouhg the solid electrolytes are used to replace the liquid electrolytes, they show lower energy conversion efficiency compared to liquids due to poor contact with the dye coated TiO_2 surface. However, the gel electrolytes show good device properties, while drastically reducing the above mentioned problems caused by liquid electrolytes. Therefore, in the past few decades, the most of the researches have been focused on synthesizing gel electrolytes incorporating a polymer. Due to numerous advantages of polymer gel electrolytes, lithium ion conducting polymer electrolytes are being developed for lithium rechargeable- batteries and iodide ion conducting polymer electrolytes for dye sensitized photo-electrochemical(PEC) solar cells. Conventionally, PGEs were formed by incorporating a host polymer, the ionic salt and the plastilizers such as ethylene carbonate(EC) and propylene carbonate(PC). For DSSCs, the gel electrolyte should be developed with iodide salts and many studies have been done incorporating alkaline metal iodides in PAN based and PEO based PGEs. There, the effect of changing the size of the cation on the performance of the electrolyte and the solar cell have also[1,2] been studied.

The photocurrent density (J_{sc}) is an important parameter of a solar cell and it depends on the mobility of the iodide ions. When the cation is large, the iodide ion mobility increases[2] and it enhances the J_{sc}. Therefore by incorporating a salt which contain a bulky cation compared to the iodide ion, such as quaternary ammonium iodide salts, the performance of DSSCs can be enhanced. These quaternary ammonium iodide salts are tetrapropylammonium iodide($Pr_4N^+I^-$), tetrabutylammonium iodide($Bu_4N^+I^-$), and tetrahexylammonium iodide ($Hex_4N^+I^-$) and the radius of the cation increases respectively. These three salts have been used with host polymers and reasonably good cell performance have been reported[3-7]. In this study, we have focused on a gel electrolyte incorporating quaternary ammonium iodide salt, $Bu_4N^+I^-$. This new gel system was prepared by using EC, PC and by adding an inner filler fumed silica, which create a network structure to form the gel electrolyte. The samples were characterized using complex impedence analyser and DC polarization test. Finally, DSSCs

were fabricated using the gel electrolyte with optimized conductivity and the fabricated cells were characterized.

2. Experiment

2.1. Materials

Ethylene carbonate (EC) (Aldrich,99%), propylene carbonate(PC) (Aldrich), fumed silica(Aldrich,7nm grain size, surface area 350-430 m^2 per g) and $Bu_4N^+I^-$ (tetrabutylammonium iodide) were used as starting materials. $Bu_4N^+I^-$ was vaccume dried for 24 hours at 80 ^oC and SiO_2 was heated at 500 ^oC for 24 hours. EC and PC were used as recieved. Titanum dioxide powder (TiO_2), iodine, glacial acetic acid, tetraisopropoxide (TIP) triton-X-100, ethanol were purchased from Aldrich. Fluorine doped tin oxide glass plates (FTO)(sheet resistance 16 ohms/cm^2) were used as a substrate for coating TiO_2 paste. Ruthenium dye (N719) [ditetrabutylammoniumcis-bis(isothiocyanato)bis(2,2α -bipyridyl-4.4α -dicarboxylato)ruthenium(II)] was purchased from Solatronics to use as the sensitizer.

2.2. Sample preparation

Different compositions of EC,PC,$Bu_4N^+I^-$ and fumed silica were used in order to obtain a polymer free gel electrolyte. For that the weight ratio between EC and PC was kept unchanged. That is, it was kept 1:1 ratio for all the samples. The total weight ratio of EC,PC and $Bu_4N^+I^-$ was always kept as 1g. Fumed silica was added as a percentage of the total weight. At first, appropiately weighted amounts of EC,PC and $Bu_4N^+I^-$ were magnetically stirred at room temperature for 24 hrs with constant amount of silica. A gel electrolyte sample with LiI was also prepared in the same manner for comparison. The compositions of the gel electrolytes are given in the table 1.

Table 2.1: Compositions of gel electrolytes prepared by varying EC,PC and $Bu_4N^+I^-$ or LiI. The total weight of EC,PC and the salt was 1g and amount of added fumed silica is 10% of total weight.

Electrolyte	EC(x %)	PC(x %)	$Bu_4N^+I^-$ (y %)	LiI(y%)
A	40	40	20	-
B	42.5	42.5	15	-
C	44	44	12	-
D	45	45	10	-
E	40	40	-	20

Solar cell characterization was done only for the electrolyte sample A, which gives the highest conductivity. For that the electrolyte samples were prepared by adding I_2 while keeping the I^-:I_2 molar ratio at afixed value of 10:1. The I_2 was added for the EC,PC and salt solvent, which has been stirred until I_2 dispersed well in the solvent and then fumed silica was added and stirred for 3 to 4 hours.

2.3. Fabrication of the DSSCs

Initially the TiO_2 colloidal particles were prepared in order to prepare the photo-electrode. For that, first 2.2 ml of acetic acid was added to 20 ml of tetraisopropoxide. Then 25 ml of ethanol was added to the mixture and a steam was passed through the solution until the mixture turn in to light blue colour. Then 50 ml of water was added (drop by drop) and it was stirred for 12 hrs. Finally the solution was autoclaved at 150 ^oC for 3 hrs. Afterthat 20 ml of the autoclaved TiO_2 colloidal was taken. Then 55 ml of acetic acid was added and it was ground well using a motor. Next 5 drops of triton-X-100 were added and was mixed well. Finally 20 ml of ethanol was added. This colloidal was sprayed on the FTO glass plate using hand spray method. Then the glass plates were sintered at 500 ^oC for 30 mins. Afterthat the glass plates were allowed to cool at about 80 ^oC. Then the plates were diped in the Ruthenium dye(N719) for 12 hrs. DSSCs were fabricated by sandwiching the gel electrolyte in between platinized electrode and dye absorbed TiO_2 electrode with configuration glass/FTO/TiO_2/dye/gel electrolyte/ counter electrode.

2.4. Solar cell and material characterization

2.4.1. Conductivity studies

The electrical conductivities of the prepared samples were measured using a schlumberger SI 1260 Impedence analyser (Solatron), in the frequency range from 20 Hz to 10 MHz. The gel electrolyte was sandwiched between two stainless steel electrodes in a homemade cell holder and the temperature was varied from 25 ^oC to 60 ^oC at approximately 5^oC intervals. The temperature of the sample was allowed to stabilize at each measuring temperature for about 30 minutes.

2.4.2. DC polarization measurements

In order to estimate the ionic nature of the GEs, the DC polarization test was carried out at room temperature. The samples were sandwiched between two

stainless steel blocking electrodes and a small voltage of about 1V was applied. The current was measured with time and this was repeated for all gel samples.

2.4.3. Solar cell characterization

Current voltage characteristics of the solar cells were measured under the irradiance of 100 mW cm^{-2} simulated sunlight using a homemade setup coupled with Keithley 2000 multimeter via computer controlled software. In order to get the simulated sunlight with above intensity, Xenon 500 lamp was used.

2.4.3 FT-IR Measurements

FT-IR spectra were obtained for the GE samples A,D and E, tetrabutylammonium iodide salt and a mixture of ethylene carbonate and propylene carbonate (EC+PC) using Thermo Nicolet 6700 FT-IR spectrometer in the range 600 to 4000 cm^{-1}.

3. Results and Discussion

The conductivity plots for gel electrolyte samples with different salt concentrations and constant amount of fumed silica are shown in figure1.

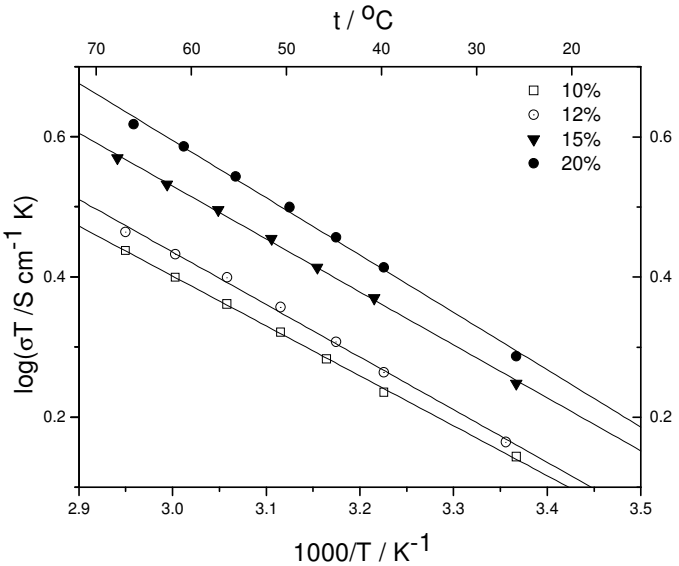


Figure 1. The ionic conductivities of GE samples with different salt concentrations

The conductivity variation of all GEs well obeys Arrhenius relationship:

$$\sigma T = \sigma_o \exp[-E_a / KT] \quad (2)$$

within the tested temperature range, where E_a is the activation energy, σ_o is the pre-exponential factor, *k* is the Boltzmann constant and T is the absolute temperature[8]. All curves have a linear behavior for log(σT) vs. 1000/T agreeing with the theory. The highest ionic conductivity of 6.51×10^{-3} S cm^{-1} was obtained at room temperature for the sample containing 20% of salt and 40% of each EC and PC. With the increase of the salt concentration the conductivity increases and can be attributed essentially to an increase of number of free ions.

However, further addition of salt (more than 20% salt) was not possible due to the difficulty of dissolving the salt in the EC and PC solvent mixture. We can speculate a decrease in the conductivity with the further increase of salt due to the formation of large number of ion pairs and higher ionic aggregates. Here silica acts as a gelling agent which immobilizes the liquid medium to produce a gel electrolyte. Fumed silica is an electrochemically inert material and because of the enormous surface area (50-400 m^2/g) of these particles, the surface functional groups (silanol, siloxane) play a major role in creating bonds with EC,PC and salt ions and forming a network.

Dc polarization tests were performed for all the gel electrolytes using stainless steel blocking electrodes. An abrupt current change was observed with the current dropping to 1/10 of the initial current within the first few minues. After about 60 minutes, current reached to a very low stable value. Hence, all these electrolytes show mainly the ionic nature and the electronic conductivity is negligible.

The electrolyte consists of EC and PC, where each molecule has three oxygen atoms for possible coordination of cation (figure 2). Also an anion may interact with the $–CH_3$ moity of PC. These ion- solvent interactions may lead to changes in several vibrational modes of EC and PC.



i ii

Figure 2. The chemical structures of (i) Ethylene Carbonate and (ii) Propylene Carbonate

The FT-IR spectra in the region 860 to 910 cm^{-1} of , pure $Bu_4N^+I^-$, EC+PC, gel electrolyte samples A,D, and E are shown in figure 3. The FT-IR spectrum of $Bu_4N^+I^-$ has two peaks at 870 and 880 cm^{-1} which belongs to the cation. The peak at 894cm^{-1} of spectrum (b) is attributed to the ring breathing mode of EC, which shows in the (c),(d), and (e) spectra of gel electrolytes as well[9]. However, in spectrum (e), which is belonging to the sample E, has an extra peak at 903 cm^{-1} . When oxygen atoms of EC molecules coordinate with cations present in the solution, there will be changes in the above mode. This has been observed by many researches. For example, a polymer gel electrolyte based on PAN, EC and $LiClO_4$ studied by Wang *et al.*[9] observe a peak growing at around 900cm^{-1}, other than the peak at 890cm^{-1} belonging to EC. However, in spectra (c) and (d) there is no corresponding peak or shoulder at around 900cm^{-1} showing that the cation of the $Bu_4N^+I^-$ has no strong interactions with the oxygen atoms of EC. Sample D, which has the highest $Bu_4N^+I^-$ concentration has a broad peak appearing at around 880cm^{-1} corresponding to the salt $Bu_4N^+I^-$.

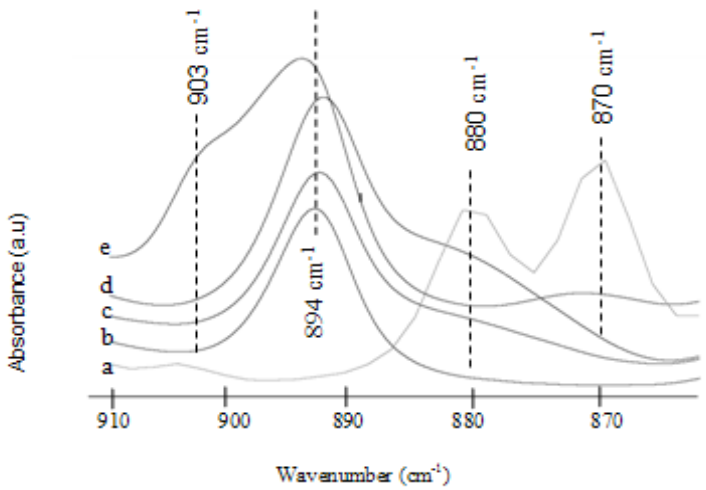


Figure 3. FT-IR spectra attributed to the ring breathing mode of EC in the region 860-910 cm^{-1}, (a) Pure $Bu_4N^+I^-$; (b)EC+PC; (c) EC+PC+10% $Bu_4N^+I^-$ salt+10% silica; (d) EC+PC+20% $Bu_4N^+I^-$ salt+10% silica; (e) EC+PC+20% LiI salt +10% silica.

This fact is evident from a few other modes, namely, ring bending of EC and symmetric ring deformation of PC situated at 714cm^{-1} and the C=O symmetric stretching mode of EC (~1800 cm^{-1} and 1770cm^{-1}) and PC(~1800cm^{-1})[9-11]. The symmetric stretching mode of EC (figure 4) is a very strong broad band which

has split into two with the peak positions at 1787 cm^{-1} and 1770 cm^{-1}. The same mode of PC has a very strong broad IR band peaked at 1787cm^{-1} (figure 4). In spectrum e, this band has broadened while it is not in spectra (c) and (d), again showing the absence of interactions between $Bu_4N^+I^-$ and solvent molecules.

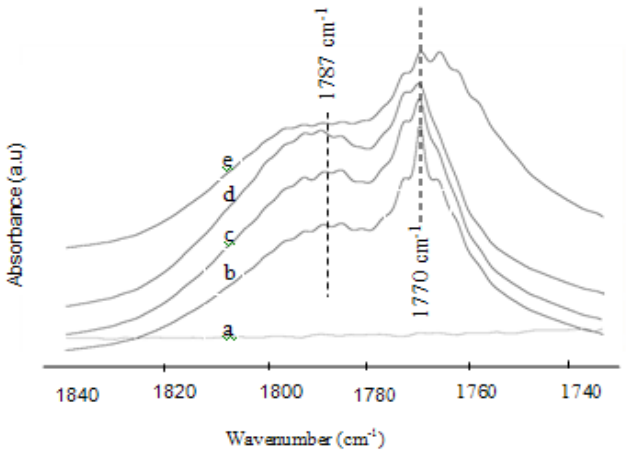


Figure 4. FT-IR spectrum of C=O streching band in EC and PC in the region 1700-1850$cm^{-1,}$ (a) Pure $Bu_4N^+I^-$; (b)EC+PC; (c) EC+PC+10% $Bu_4N^+I^-$ salt+10% silica; (d) EC+PC+20% $Bu_4N^+I^-$ salt+10% silica; (e) EC+PC+20% LiI salt +10% silica.

Ring bending mode of EC and symmetric ring deformation mode[10,11] of PC is centered at 714cm^{-1} and a growing shoulder can be observed at 729 cm^{-1} in FT-IR spectra of sample E, without such a shoulder for samples C and D, showing the presence of strong Li^+ interactions with EC and PC but no strong interactions with the cation of $Bu_4N^+I^-$.

The reason for Li^+ ion coordination with EC and PC is that Li^+ ions have a very high surface charge density and low-lying orbitals available for electron pair acceptance, is prone to get linear, tetrahedral or even octahedral coordination by these ligands, while such coordination is impossible for the $Bu_4N^+I^-$, which have no low –lying empty orbitals to get coordinated by the ligands. $Bu_4N^+I^-$ has a bulky cation and low surface charge density preventing interactions with solvent molecules.

The photocurrent- photovoltage(I-V) characteristics of three solar cells of configuration glass / FTO / TiO_2 /dye / gel electrolyte / counter electrode were measured using the gel electrolyte sample with the highest conductivity. Solar cell parameters such as open circuit voltage(V_{oc}) and the short circuit current density (J_{sc}) were measured and the fill factor (FF%) and effciency (η%) are

calculated. It showed a J_{sc} of 9.39 mA cm^{-2} , V_{oc} of 651.4 mV and efficiency of 3.73% exhibiting the ability to use the proposed GE system in solar cells. The short circuit current density, 9.39 mA cm^{-2} is rather a good value compared to quasi solid state solar cells reported using quaternary ammonium iodide salts and ruthenium dye complexes[3-6].

4. Conclusion

A polymer free gel electrolyte was prepared by incoporating the a bulk cation salt $Bu_4N^+I^-$, plastilizers EC and PC and a innert filler, fumed silica and the conductivity for these samples were studied. The gel electrolyte samples shows a highest conductivity for the sample with 20% (0.2g) salt (0.4g of EC and PC). Dc polarization tests were performed for all the gel electrolytes using blocking electrodes and all the electrolytes showed mainly the ionic nature and the electric conductivity is negligible. DSSCs were fabricated for the gel electrolyte with highest conductivity in order to see how much of efficiency could be obtained from this new system. This system, without using a polymer, incorporating $Bu_4N^+I^-$ shows efficiency of 3.73%. FT-IR spectrums give information about how efficiency the cation of the salt ($Bu_4N^+I^-$) coordinates with EC and PC in the gel electrolyte. The $Bu_4N^+I^-$ didnot show any coordination with EC and PC, because Bu_4N^+ ions have no low-lying empty orbitals. It was shown that a gel electrolyte can fabricate without using a polymer and can obtain reasonable efficiencies for DSSCs compared to polymer gel electrolytes.

References

1. Tennakone K., Senadeera G.K.R., Perera V.P.S., KottegodaI.R.M. & Silva L.A.A.D., *Journal of Materials Chemistry* **11**: 2474 – 2477, (1999).
2. Shen X., Xu W., Xu J., Liang G., Yang H. & Yao M., *Solid State Ionics* **179**: 2027 – 2030, (2008).
3. Dissanayake M.A.K.L., Bandara L.R.A.K., Bokalawala R.S.P., Jayathilaka P.A.R.D., Ileperuma O.A. &Somasunderam S., *Materials Research Bulletin* **37**(5): 867 – 874, (2002).
4. Ileperuma O.A., Dissanayake M.A.K.L., Somasunderam S. &Bandara L.R.A.K., *Solar Energy Materials and Solar Cells* **84**: 117 – 124, (2004),
5. Ileperuma O.A., Kumara G.R.A. & Murakami K.., *Chemistry Letters* **37**(1): 36 – 37, (2008).
6. Ileperuma O.A., Kumara G.R.A.,Yang H-S. &MurakamiK.. *Journal of Photochemistry and Photobiology A: Chemistry* **217**: 308 – 312, (2011).
7. T.M.W.J. Bandara, T. Svensson, M.A.K.L. Dissanayake, M. Furlani, W.J.M.J.S.R. Jayasundara, P.S.L. Fernando, I. Albinsson and B.E. Mellander, J.Natn.Sci.Foundation *Sri Lanka 41 (3): 175-184,*(2013).

8. Y.J.Song, C.L. Cheng, Y.Y.Wang and C.C.Wan; J. Electrochem. Soc., 149(9), A1230 (2002).
9. Wang. Z.,Huang. B .,Huang. H ., Chena. L., Xue. R .,Wang. F .,*Solid State Ionics*.85, 143-148, (1996).
10. Starkey. S. R ., Frech . R ., *Electrochimica Acta*, Vol. 42, No. 3, pp. 471-474, (1997).
11. Battisti. D ., Nazri. G. A., Klassen. B., Aroca. R.., *J. Phys. Chem*., 97, 5826-5830, (1993).

ELECTRICAL, STRUCTURAL, OPTICAL AND THERMAL PROPERTIES OF (1-*X*)BLEND: *X* Li[$(CF_3SO_2)_2N$] SOLID POLYMER ELECTROLYTE SYSTEM

RAVINDRA KUMAR GUPTA*

CRC, Department of Optometry, College of Applied Medical Sciences, King Saud University, Riyadh 11433, Saudi Arabia

HEE-WOO RHEE

Department of Chemical and Biomolecular Engineering, Sogang University Seoul 121-742, Korea

Effect of Li[$(CF_3SO_2)_2N$] content (x = 0 – 0.3 in weight fraction) on the electrical, structural, optical and thermal properties of (1-x)blend: xLi[$(CF_3SO_2)_2N$] solid polymer electrolyte system is reported for the first time. The blend consisted of a conventional polymer matrix, poly(ethylene oxide) and a plastic crystal, succinonitrile in equal weight fraction. Salt solvation and plasticization of the poly(ethylene oxide) and succinonitrile helped to improve electrical conductivity (σ_{25^oC}) via increasing ionic mobility and mobile ion concentration. An increase of x increased the σ_{25^oC}-value up to the optimum conducting composition (x = 0.25, OCC) with σ_{25^oC} ~3.9×10^{-4} S cm^{-1}. The log σ – 1/T curves showed a nearly Arrhenius type pattern for the OCC. The XRD pattern of the OCC was free from the reflection peaks of the constituents. In addition, no poly(ethylene oxide) spherulites was noticed in the polarized optical microscopic image. The differential scanning calorimetry showed significantly low value of the relative crystallinity for the OCC indicating plasticizing effect of the Li[$(CF_3SO_2)_2N$] salt.

1. Introduction

Lithium ion conducting solid polymer electrolytes (SPEs) with electrical conductivity (σ_{25^oC}) of ~10^{-3} S cm^{-1} exhibit potential industrial applications in all-solid-state electrochemical devices [1-3]. The SPE in a form of polymer matrix-LiX (X = I, BF_4, PF_6, ClO_4, CF_3SO_3, $(CF_3SO_2)_2N$, $(C_2F_5SO_2)_2N$, etc.) offers various advantageous properties, such as thin-film formation to act as a separator, easy processing, flexibility, chemical and mechanical stability, and a wide electrochemical voltage window. A coordinating polar polymer, poly(ethylene oxide), abbreviated as PEO is the most commonly used polymer matrix. The PEO shows self-standing film formation, thermal stability up to 200

* For correspondence. e-mail rgupta@ksu.edu.sa, Phone: +96611469 8623, Fax: +96611469 3536

Proceedings of the 14th Asian Conference on Solid State Ionics (ACSSI 2014)
Copyright © 2014 ACSSI 2014 Organizers. All rights reserved.
ISBN: 978-981-09-1137-9
doi:10.3850/978-981-09-1137-9_162

°C, eco- and bio-friendliness, low material cost, salt solvating and ion transport through ethereal oxygen. The optimal conducting composition of the PEO-LiX electrolyte exhibited σ_{25^oC}-value less than 10^{-5} S cm^{-1} due to the high PEO crystallinity, which makes the electrolyte inappropriate for the device application. Hence, in order to reduce the PEO crystallinity, new polymer electrolyte structures, based on the modified PEO main polymer chain with grafted polymers, block copolymers, cross-linked polymer networks, were attempted with σ_{25^oC} of ~10^{-4} S cm^{-1} [2, 3]. A simple blend consisting of PEO and a polymer, e.g., poly(vinylidene fluoride) [4], polydimethyl siloxane [5] showed very low PEO crystallinity and σ_{25^oC}-value as high as 5.6×10^{-5} S cm^{-1}.

In the past, plastic crystal succinonitrile (SCN)-based electrolytes were investigated due to high diffusivity, plasticity and solvating power of the SCN [6]. These electrolytes exhibited σ_{25^oC} as high as 3×10^{-3} S cm^{-1}, however, with the poor thermal and mechanical properties. The LiX content was also fixed to 5 mol%. Therefore, the PEO was added in a varying concentration to the SCN-LiX, while keeping [O]/[Li^+] ratio constant, in order to improve the thermal and mechanical properties [7-11]. We noticed that an addition of the PEO in equal weight proportion to the SCN is sufficient enough to inhibit the sublimation of the SCN up to 100 °C [12]. The blend also resulted in better conducting redox-couple solid polymer electrolytes with σ_{25^oC} ~$3–7\times10^{-4}$ S cm^{-1} [13, 14].

Since, salt concentration significantly controls the ionic conductivity via ionic mobility and mobile ion concentration [15, 16], it is necessary to vary the salt concentration for optimizing the electrical conductivity of a solid polymer electrolyte system. In fact, the salt acts as a plasticizer and improves the electrical conductivity [13]. In the present paper, we have varied the salt concentration (x) from 0 to 0.3 in weight fraction for obtaining the optimum conducting composition (OCC) of the (1-x)blend: xLi[$(CF_3SO_2)_2N$] solid polymer electrolyte system. The blend corresponds to equal weight fraction of the PEO and the SCN [12]. The Li$(CF_3SO_2)_2N$ (LiTFSI) is used as a salt due to the following reasons. (i) It has high thermal and electrochemical stability; (ii) its low lattice energy facilitates the ion solvation by the ether group; (iii) its large anionic size helps to decrease the anionic contribution in the total current, and (iv) the electrons in TFSI anion is highly delocalized, therefore salt acts as a plasticizer, hence, resulting in more flexible polymer chains in the polymer electrolytes [2, 3, 6]. An increase of σ_{25^oC}-value with increasing x is explored via investigating the structural, optical and thermal properties of solid polymer electrolyte system.

2. Experimental

Sigma-Aldrich chemicals with purity greater than 99% were used without further purification. The molecular weight of the PEO was 1 M g mol^{-1}. The precursors in anhydrous acetonitrile (99.8%, Aldrich) were dissolved through continuously stirring at 60°C for 24 h. The resulted homogeneous solution was then casted on a Teflon Petri dish. It was dried in nitrogen gas atmosphere at room temperature for a couple of weeks and further dried under vacuum at 28°C for a day leading to a thick SPE film.

The samples were characterized using a Solartron impedance analyzer (model 1252A) coupled with an SI 1287 electrochemical interface, a Rigaku x-ray diffractometer (XRD, model D-MAX 2500), a Nikon polarized optical microscope (model Optiphot-2 Pol), a Jasco UV-visible spectrophotometer (model V550), and a TA Instruments differential scanning calorimeter (DSC, model MDSC 2910). The details of characterization techniques are described elsewhere [12-14].

3. Results and discussion

Table 1 shows σ_{25^oC}-value of the (1-*x*)blend: *x*Li[$(CF_3SO_2)_2N$] SPE system with *x*. The [O]/[Li^+]-value is also shown for direct comparison. One can note that the σ_{25^oC}-value increased up to $x = 0.25$, though it is nearly flat from $x = 0.15$ to $x = 0.25$. It is then decreased for $x = 0.3$. Thus, the composition, $x = 0.25$ having the highest σ_{25^oC}-value (3.9×10^{-4} S cm^{-1}, more than 4 orders in magnitude higher than that of the pure blend), can be referred to as the OCC. It is also similar to the σ_{30^oC}-value, 5×10^{-4} S cm^{-1} observed by Fan et al. [8] for an identical SPE with the [O]/[Li^+] = 11.

Table 1. Electrical conductivity (σ_{25^oC}), melting temperature (T_m) and relative crystallinity (χ) of (1-*x*)blend: *x*Li[$(CF_3SO_2)_2N$] SPE system.

Composition (*x*)		σ_{25^oC}	T_m	χ
Wt. fraction	[O]/[Li^+]	(S cm^{-1})	(°C)	(%)
0	∞	1.0×10^{-8}	30.1	25.2
0.05	61.9	2.6×10^{-6}	28.7	11.1
0.10	29.3	8.0×10^{-5}	30.2	8.6
0.15	18.5	3.4×10^{-4}	19.8	0.3
0.20	13.0	3.5×10^{-4}	23.0	0.2
0.25	9.8	3.9×10^{-4}	20.4	0
0.30	7.6	1.7×10^{-4}	19.1	0

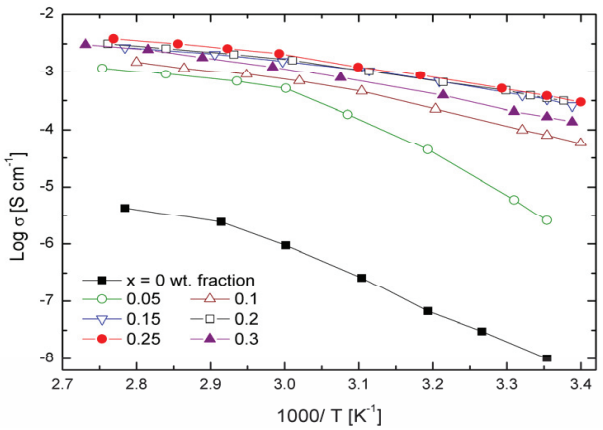


Figure 1. Log σ –1/T variations of the (1-*x*)blend: *x*Li[$(CF_3SO_2)_2N$] SPE system with $x = 0 - 0.3$.

An increase of σ up to the OCC followed by a decrease is a commonly observed phenomenon in the solid polymer electrolyte systems and composite electrolyte systems [1-3, 14-16]. It is associated with a general expression of electrical conductivity: $\sigma = n\, q\mu$, which asserts that an increase in σ is due to either an increase in mobile ion concentration (n) or ionic mobility (μ) or both, where q is a constant (the charge on the mobile ion). Thus, for the present system, the PEO helped to solvate ionic salt resulting in an increase in n with increasing x. It is also helped by the solvating property of the SCN. In addition, owing to an interaction between ethereal oxygen of the PEO and nitrogen of the SCN, there is a high probability for a competition between ethereal oxygen and nitrogen to bind Li^+ ions resulting in more free ions for conduction [14]. One can also expect an increase in μ with increasing x due to the combined effects of the (i) segmental motion of polymeric chains of the PEO, (ii) Li^+ ion transport through PEO's ethereal group, (iii) plasticizing property of the salt, and (iv) high diffusivity and plasticity of the SCN [1-3, 14-16]. For the electrolyte with $x = 0.3$, Coulombic interaction between ions starts to dominate resulting in formation of ionic pairs, ionic multiplets and/ or salt aggregation, and thus a decrease of n. It may also be associated with a decrease of μ *via* immobilization of polymeric chains due to the formation of cross-linking O–Li^+–O between oxygen atoms of different polymeric chains.

We also measured the σ-value of the (1-*x*)blend: *x*Li[$(CF_3SO_2)_2N$] SPE system with temperature for $x = 0$ to 0.3 and showed in Figure 1. The σ-value increased with increasing temperature and formed a concave-type shape for $x = 0.05$ to 0.3. This suggests that the ion transport is in the amorphous domains, coupled with the polymer segmental motion, and governed by the Vogel-Tamman-Fulcher type empirical relation [10, 13, 14]. A decrease of curvature

with increasing x up to 0.25 suggested a decrease of activation energy [14-16]. Investigations on structural, optical, and thermal properties of the (1-x)blend: xLi[$(CF_3SO_2)_2$N] SPE system, which have been discussed below, revealed a decrease of the PEO crystallinity with increasing x. The plasticizing property of the SCN and salt helped to decrease the PEO crystallinity with increasing x, which in turns enhanced the rate of transition from gauche to trans and thus increased the trans conformer concentration. The trans isomer acted as an impurity resulting in the enhancement of lattice defects and lowering of activation energy for ionic conduction.

Figure 2 shows XRD pattern of the (1-x)blend: xLi[$(CF_3SO_2)_2$N] SPE system with x = 0 – 0.3. The blend (x = 0) exhibited reflection peaks of the PEO and SCN indicating its composite nature [1, 2]. For a small fraction of salt concentration (x = 0.05 and 0.1), the electrolytes observed a significant reduction of the reflection peaks of the PEO and SCN, while no reflection peaks were noticed for the electrolytes with x = 0.15–0.3. A perfect salt solvation by the blend is clearly visualized by the absence of reflection peaks of the salt in the diffractograms of the SPEs (x = 0.05 – 0.3). This infers that an increase of x led to Li^+ ions complexation with the ethereal oxygen of PEO and hindrance of the PEO crystallization by the large TFSI anions. Plasticizing property of the SCN and salt, and a competition between the ethereal oxygen and the nitrogen to coordinate Li^+ ions, may also be responsible for a large decrease of PEO crystallinity and a large increase of free Li^+ concentration.

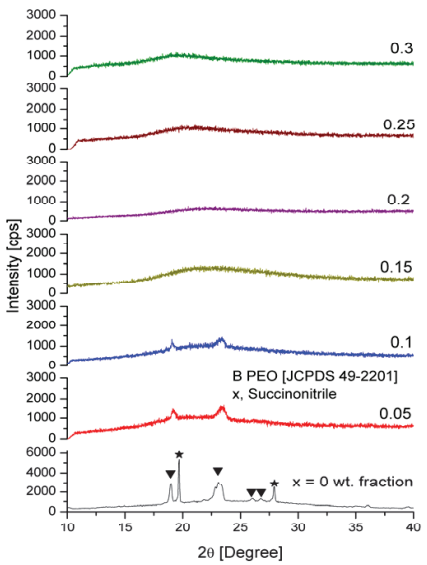


Figure 2. XRD patterns of the (1-x)blend: xLi[$(CF_3SO_2)_2$N] SPE system with x = 0 – 0.3.

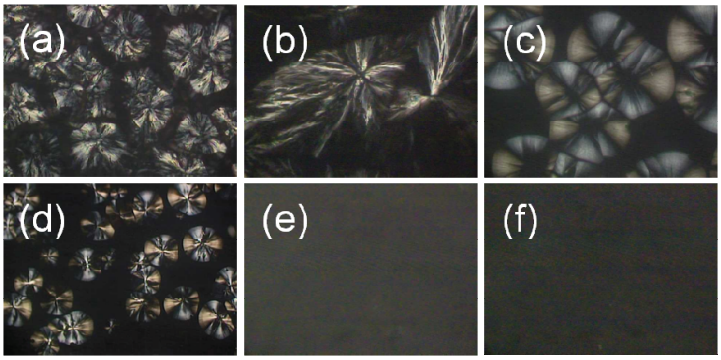


Figure 3. Polarized optical microscopic images of the (1-x)blend: xLi[$(CF_3SO_2)_2$N] SPE system with x = (a) 0, (b) 0.05, (c) 0.1, (d) 0.15, (e) 0.2, and (f) 0.25. Magnification, 400x.

Figure 3 shows polarized optical micrographs (POMs) of the (1-x)blend: xLi[$(CF_3SO_2)_2$N] SPE system with x = 0 – 0.25. The image of blend (x = 0) portrayed a large number of PEO spherulites in the dark region. The dark region corresponds to a highly conductive amorphous area [12-14]. At the low salt concentration (x = 0.05 and 0.1), the PEO lamellae are weakly and randomly oriented. At x = 0.15, the salt complexation resulted in only a few PEO spherulites with largely reduced size and extended dark region. The plasticizing effect of salt and SCN is prominent for x = 0.2 and 0.25, which resulted in completely weak and randomly oriented PEO chains as indicated by a complete dark region. This study indicates a decrease of the PEO crystallinity with increasing x.

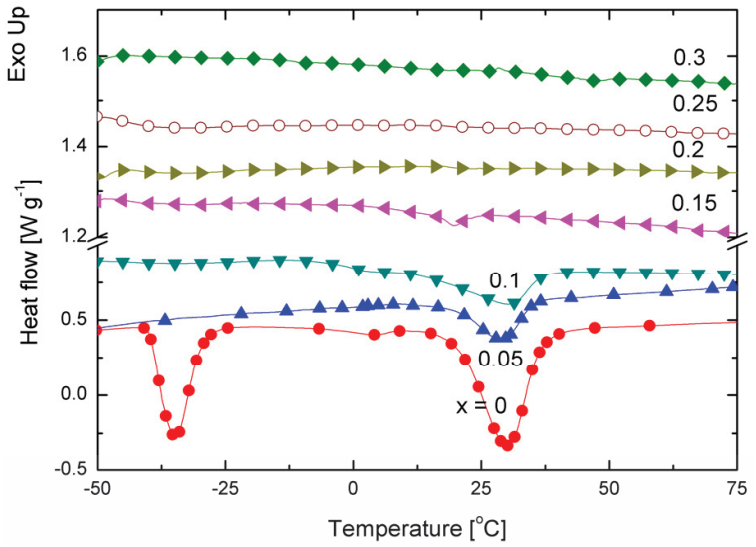


Figure 4. DSC curves of the (1-x)blend: xLi[$(CF_3SO_2)_2$N] SPE system with x = 0 – 0.3.

Figure 4 shows DSC curves for the (1-x)blend: xLi[$(CF_3SO_2)_2N$] SPE system with x = 0 – 0.3. The pure blend (x = 0) portrayed a strong endothermic peak due to its melting temperature (T_m) at 30°C. A relatively low intense T_m-peak was noticed at 29°C and 30°C for the electrolytes with x = 0.05 and 0.1, respectively. For the x = 0.15 – 0.3 the T_m-value was reduced to between 20°C and 23°C with significantly reduced peak intensity. It infers that an increase in x decreased the PEO crystallinity [14].We quantified the relative PEO crystallinity (χ) using the ratio of change in enthalpy (ΔH_m) of sample to that of the fully crystalline PEO (≈193 J g^{-1}) [12-14]. The χ-value of the SPE, shown in Table 1, largely decreased with increasing x indicating plasticizing effect of the salt. One can also note that the blend exhibited an intense plastic crystal phase transition temperature (T_{cp})-peak at −35°C, which was totally disappeared after the salt complexation. In general, presence of impurity, e.g. PEO and Li^+ reduces the trans-gauche energy barrier of the SCN, which leads to an enhanced trans concentration and existence of trans phase at temperature lower than the T_{cp} of the SCN. Consequently, it helps to increase the ion conduction [14].

4. Conclusions

Effect of Li[$(CF_3SO_2)_2N$] concentration (x) on the electrical, structural, optical and thermal properties of the [PEO–succinonitrile]–Li[$(CF_3SO_2)_2N$] solid polymer electrolyte system is investigated. An increase of the salt concentration increased the electrical conductivity up to the OCC (x = 0.25, σ_{25^oC} ~3.9×10^{-4} S cm^{-1}). It was explained by considering the role of mobile ion concentration and ionic mobility. The salt solvation property of the PEO and succinonitrile, and an interaction between the ethereal oxygen of the PEO and nitrogen of the succinonitrile were ascribed for an increase in mobile ion concentration with increasing x. An increase in ionic mobility with increasing x is explained through (i) segmental motion of polymeric chains of the PEO, (ii) Li^+ ion transport through PEO's ethereal group, (iii) plasticizing property of the salt, and (iv) high diffusivity and plasticity of the succinonitrile. The results of the XRD, POM, and DSC studies revealed a decrease of the PEO crystallinity with increasing x confirming a role of ionic mobility for the conductivity enhancement.

Acknowledgments

The authors extend their appreciation to the College of Applied Medical Sciences Research Center and the Deanship of Scientific Research at King Saud University for funding this research.

References

1. R. C. Agrawal and R. K. Gupta, *J. Mater. Sci.* **34**, 1131 (1999).
2. F. B. Dias, L. Plomp and J. B.J. Veldhuis, *J. Power Sources* **88**, 169 (2000).
3. R. C. Agrawal and G. P. Pandey, *J. Phys. D Appl. Phys.* **41**, 223001 (2008).
4. M.M.E. Jacob, S.R.S. Prabaharan and S. Radhakrishna, *Solid State Ionics* **104**, 267 (1997).
5. A. Das, A. K. Thakur and K. Kumar, *Ionics* **19**, 1811 (2013).
6. P.-J. Alarco, Y. Abu-Lebdeh, A. Abouimrane and M. Armand, *Nature Mater.* **3**, 476 (2004).
7. L.-Z. Fan and J. Maier, *Electrochem. Commun.* **8**, 1753 (2006).
8. L.-Z. Fan, Y.-S. Hu, A. J. Bhattacharyya and J. Maier, *Adv. Funct. Mater.* **17**, 2800 (2007).
9. L.-Z. Fan, X.-L. Wang, F. L. and X. Wang, *Solid State Ionics* **179**, 1772 (2008).
10. R. Yue, Y. Niu, Z. Wang, J. F. Douglas, X. Zhu and E. Chen, *Polymer* **50**, 1288 (2009).
11. Y.-H. Li, X.-L. Wu, J.-H. Kim, S. Xin, J. Su, Y. Yan, J.-S. Lee and Y.-G. Guo, *J. Power Sources* **244**, 234 (2013).
12. R.K. Gupta, H.-M. Kim and H.-W. Rhee, *J. Phys. D Appl. Phys.* **44**, 205106 (2011).
13. R.K. Gupta and H.-W. Rhee, *Electrochim. Acta* **76**, 159 (2012).
14. R.K. Gupta and H.-W. Rhee, *J. Phys. Chem. B* **117**, 7465 (2013).
15. R.K. Gupta, H.Y. Jung and C.M. Whang, *J. Mater. Chem.* **12**, 3779 (2002).
16. H.Y. Jung, R.K. Gupta, C.J. Wi and C.M. Whang, *J. Phys. D Appl. Phys.* **36**, 529 (2003).

ENHANCEMENT OF DIELECTRIC CONSTANT IN $LaFeO_3$-$NiFe_2O_4$ COMPOSITES *

V.M.GAIKWAD†

Department of Physics,Rashtrasant Tukadoji Maharaj Nagpur University Campus, Amravati Road, Nagpur, Maharashtra 440033, India.

S.A.ACHARYA

Department of Physics, Rashtrasant Tukadoji Maharaj Nagpur University Campus, Amravati Road, Nagpur, Maharashtra 440033, India.

Email:saha275@yahoo.com

Developments of composite materials have been fascinating under current research trend. Composites are the mixture of at least two chemically distinct materials with an interface separating constituent phases. Combination of two phases of composites can result in unique properties that neither of phases individually shows. Enhancement in the properties due to positive interaction between component phases. For composites, in addition to intrinsic physical properties of component phases, size of particles, their geometrical arrangement and interface play a key role for their functional performance. It gives a unique opportunity to explore new emerging properties of composites which are not present in single components. Perovskite-spinel composites are extensively studied because of their role in magnetoelectric coupling. It has been reported that elastic coupling between perovskite and spinel phase plays a major role in ME coupling in composites. The perovksite-spinel interface is also of great interest in complex oxide based magnetic tunnel junctions. With this motivation, perovskite-spinel (1-x)$LaFeO_3$-x$NiFe_2O_4$ composites are prepared by mixing individual phases of $LaFeO_3$(LFO) and $NiFe_2O_4$(NFO) in different proportions (x=20, 30, 40 wt%). Initially, LFO is synthesized by gel combustion route and NFO by hydrothermal route, respectively. Then, they mixed mechanically in different proportions. The crystallinity of prepared composites is checked by X-ray diffraction (XRD). The XRD data shows both the phases of $LaFeO_3$ and $NiFe_2O_4$ confirms composite formation. Rietveld refinement of XRD patterns is carried out by Fullprof suite. Dielectric analysis of prepared composites is studied by LCR meter (frequency range 100 Hz-200 kHz). Frequency dependence dielectric constant plots of composites shows higher dielectric constant (4-5 times) than $LaFeO_3$. Dielectric constant decreases with increase in frequency indicates dispersive behavior in low frequency region. Temperature versus dielectric constant plots for LFO and composites at 100 kHz gives dielectric anomaly around 450^{o}C. This anomaly attributed to antiferromagnetic transition (T_N) temperature of LFO. Dielectric constant increases with temperature up to T_N and then becomes lower for higher temperatures.

Proceedings of the 14th Asian Conference on Solid State Ionics (ACSSI 2014)
Copyright © 2014 ACSSI 2014 Organizers. All rights reserved.
ISBN: 978-981-09-1137-9
doi:10.3850/978-981-09-1137-9_044

1. Introduction

Materials having colossal values of the dielectric constant ($\varepsilon \geq 10^3$) are the intensely focused due to their ability to reduce the size of capacitive components, offering an opportunity to miniaturize electronic system. Ferroelectrics are well known for their high dielectrics constants in a narrow temperature range near T_c. High value of temperature dependence of dielectric constant near T_c limits their applications. Current research efforts are focused on non-ferroelectric materials possessing colossal values of the dielectric constant with weak temperature dependence or composite materials having combination of two phases; which can results into unique properties. Enhancement in the properties of composites due to positive interaction between component phases [1]. Combination of perovskite spinel phase is very prominent for multifunctional or multiferroic properties [2]. Perovskite-spinel interface is also of great interest in complex oxide based magnetic tunnel junctions [1]. Elastic coupling between perovskite spinel phase leads to magnetoelectric (ME) coupling. Combination of spinel phase with perovskite such as $BiFeO_3$ and $BaTiO_3$ has been well established, but with $LaFeO_3$ is rarely studied.

Very recently, an orthorhombically distorted pervoskite $LaFeO_3$ was found to be canted antiferromagnetic and ferroelectric multiferroic. In orthoferrites, a structure deformed from the ideal pervoskite result in a large value of dielectric constant (10^4-10^5) even well below the high curie temperature (Tc = 475 K). However, the origin of this high dielectric constant is still ambiguous [3-6].

$NiFe_2O_4$ (NFO) is well known soft ferrimagnetic insulator with inverse spinel structure. Its ferromagnetic ordering temperature around T_c ~ 850 K. Within inverse spinel structure, Fe^{3+} ions occupied at tetrahedral site in sublattice A. Ni^{2+} and Fe^{3+} ions are located at octahedral site in sublattice B. It means, Fe^{3+} ions are equally distributed in tetrahedral as well as octahedral site inside inverse spinel structure. Magnetic structure of NFO consists of antiferromagnetic coupling between two sublattices A and B. With this ordering, moment of Fe^{3+} ion at A and B site cancel out which leaves behind $2\mu_B$/f.u. magnetic moment arises only due to Ni^{2+} [7-12]. It exhibits interesting dielectric behavior.

With this background, in the present attempt, we developed composite LFO-NFO system with a view to enhance dielectric values as compared to individual phases. Soft chemical approach was used to developed fine scale particles of LFO and NFO individually. By mechanical mixing route LFO and NFO were mixed in different proportion to obtain composites. The systematic studies of dielectric behavior of the composites systems were done.

2. Experimental

Perovskite LFO and spinel NFO compounds were synthesized separately by gel combustion and hydrothermal route, respectively. Then, mechanically ground to form (1-x)$LaFeO_3$-x$NiFe_2O_4$ (x=20,30, & 40%) powder composites. Lanthanum nitrate [$La(NO_3)_3.6H_2O$, 99.9% pure, Sigma-Aldrich], Iron nitrate [$Fe(NO_3)_3.9H_2O$,99.9% pure, Sigma-Aldrich], Nickel nitrate [$Ni(NO_3)_2.6H_2O$, 99% pure, Sigma-Aldrich], Sodium hydroxide flakes [NaOH, 90%Merck], and Glycine were used as precursors. LFO was synthesized by microwave assisted sol gel combustion synthesis route. Lanthanum nitrate and Iron nitrate in stoichiometric (1:1) proportions were dissolved in double distilled water and stirred for 15 minutes. Then, 4 Moles of Glycine were added into the prepared solution. The resultant solution was evaporated in microwave synthesis assembly at 210 W power until gelification. The resultant gel was combusted at same power level. After combustion, yellowish powder was formed within few seconds. Synthesized powders were then calcined at 600^oC for 3 hours to get final product as polycrystalline LFO. NFO was synthesized by hydrothermal synthesis route. Stoichiometric amount of nickel nitrate and iron nitrate were dissolved in 100 ml double distilled water. This solution was stirred for 30 minutes. Then, pH of solution was adjusted to 13 by adding 2M NaOH solution dropwise into it. After adjusting pH, the solution was transferred into sealed Teflon stainless steel autoclave and then placed in hot air oven at 160^oC for 18 h (optimize condition). After the hydrothermal reaction, autoclave was allowed to cool naturally. The resultant precipitate (insoluble in water) was separated by centrifugation and washed with distilled water in sequence to remove water soluble salts. Then, precipitate was dried at 80^oC in oven to get final powder as polycrystalline NFO.After synthesis of LFO and NFO compounds separately, the appropriate proportion of both these compounds was mechanically ground to form (1-x)LFO-xNFO (x=20,30, & 40 wt%) powder composites.

3. Results and discussions

X-ray diffraction patterns for pure LFO, NFO and LFO-NFO composites are shown in Fig.1. XRD confirms crystalline phases of the samples. XRD pattern of pure LFO is indexed orthorhombic phase (JCPDS file no. 74-2203) while for NFO, it matches with cubic spinel phase (JCPDS file no.89-4927) without any traces of impurities. LFO and NFO retain their respective structure and phase in LFO-NFO composite form. This is as expected because both the phases synthesized separately. Peak corresponds to spinel phase along (311) direction appears stronger with the increasing concentration of NFO in composites. [Fig 1(b)]. This is the features of formation of perovskite-spinel mixed structure. Rietveld refinement of X-ray diffraction patterns revealed orthorhombic (space group :Pbnm) symmetry for LFO and inverse spinel cubic (space group: Fd3m)

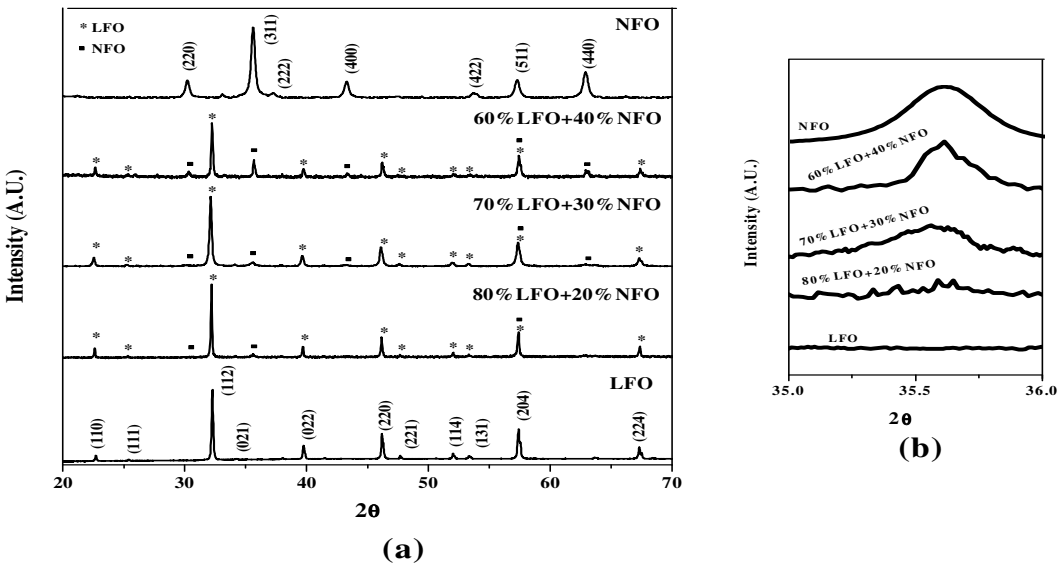


Fig. 1 (a) XRD patterns for LFO-NFO composites (b) Appearance of spinel phase with increase in percentage of NFO.

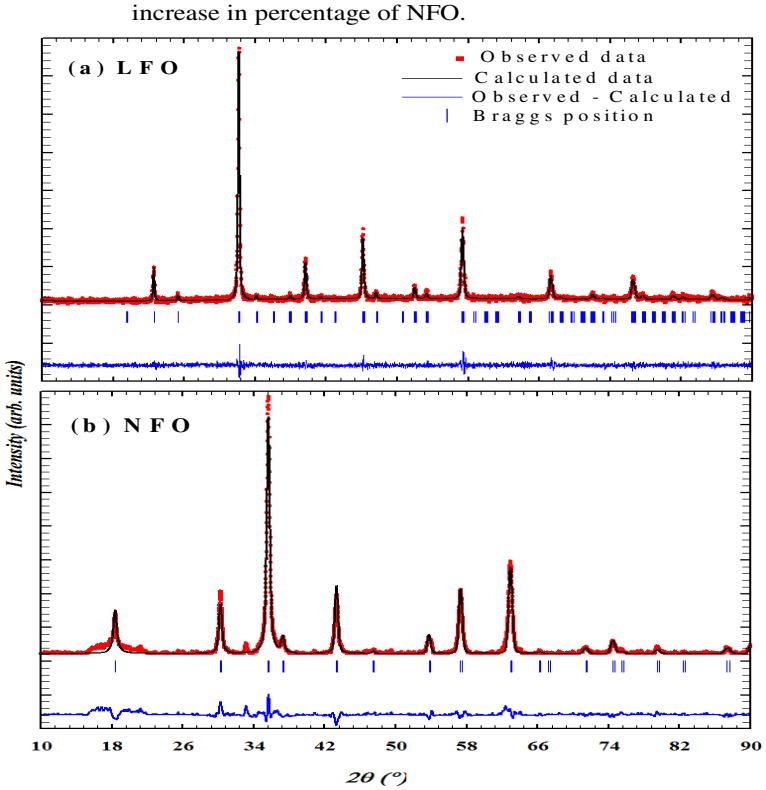


Fig. 2 Rietveld refinement of XRD patterns of (a) LFO and (b) NFO

symmetry for NFO [Fig.2]. Ritveld refined lattice parameters are a = 5.558A^o, b = 5.572 A^o and c = 7.860 A^o for LFO and a = b = c = 8.349A^o for NFO. Fig.4 shows combined FTIR spectra for pure LFO, NFO and LFO-NFO composites between 50-680cm^{-1}. According to symmetric calculations, orthorhombic Pbnm phase (for LFO) should possess 25 IR active optical phonon modes [$9B_{1u}+7B_{2u}+9B_{3u}$) fall in the range 115-645cm^{-1} [13,14]. But, in our case, due to line broadening we observed only 8 of them for LFO. Modes due to La^{3+} vibrations are observed below 200 cm^{-1}(ν_1 & ν_2). Strong absorption peak at 170 cm^{-1}(ν_2) assigned to 'external' phonon mode, it arises due to vibration of La^{3+} ions against FeO_6 octahedra [15] . Absorption bands between 200-300 cm^{-1} (ν_3 & ν_4) referred as oxygen octahedral tilting modes [18]. Broad absorption peak (ν_5) near at 350 cm^{-1} is correlated with Fe^{3+}-O^{2-} bending vibrations [17]. Transverse optic (TO) mode B_{1u} (ν_6) observed at 441cm^{-1} correspond to O-Fe-O deformation vibration of perovskite LFO and band (TO, B_{3u}) at 540 cm^{-1} (ν_7) gives iron to oxygen (Fe-O) stretching vibrations.[14,16-17] Small shoulder (ν_8) appears at 600 cm^{-1} which is the characteristic feature of rare earth orthoferrites. In spinel structure, lower energy bands corresponds to intrinsic stretching vibrations of metal-oxygen bond at tetrahedral site (ν_4',ν_5',ν_6') whereas higher energy bands correlated to metal-oxygen bond at octahedral site (ν_1', ν_2', ν_3') [18]. FTIR spectra of composites concludes that there is no structural modulation after mixing individual phases of LFO and NFO. LFO and NFO retained their identity in prepared composites. [Fig.4]

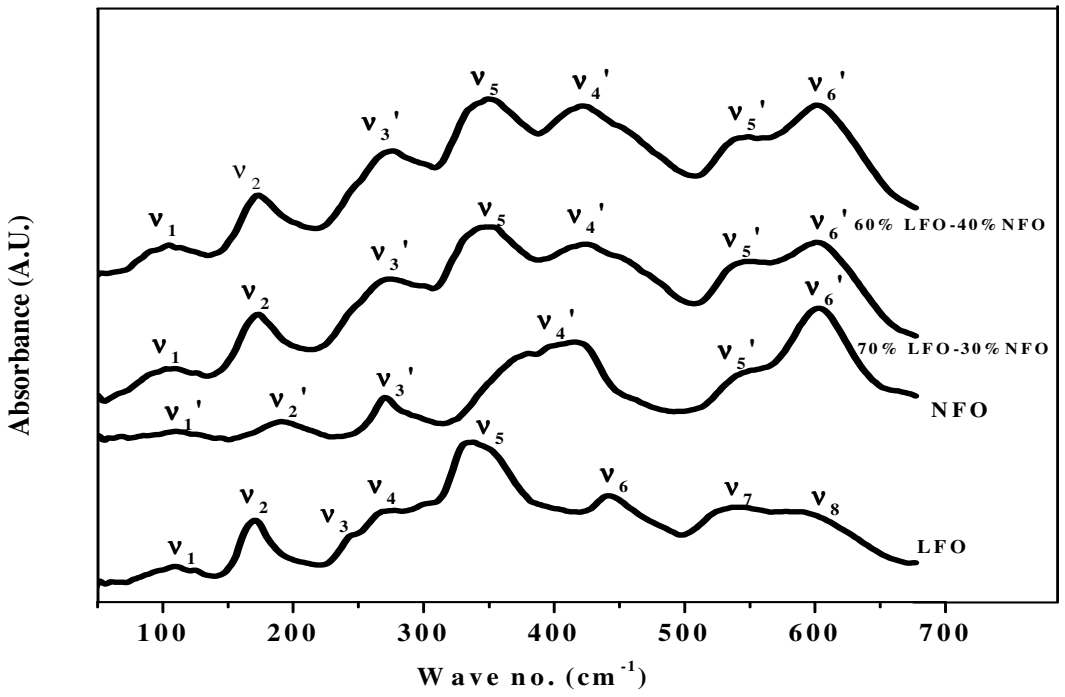


Fig. 3. Combined FTIR spectra of LFO-NFO composites at room temperature.

Fig. 4(a) shows frequency dependence dielectric constant for LFO, NFO and their composites at room temperature. Dielectric constant of all the samples decreases rapidly as frequency increases indicates dispersive behavior at low frequencies and then saturates at higher frequencies. The observed behavior is well explained with the help of Maxwell-Wagner polarization in agreement with Koop's theory [19-22]. High dielectric constant at low frequencies for composites than individual phases is due to large space charge polarization caused by inhomogeneous dielectric structure. This inhomogeneity arises from the fact that there are inhomogeneous distributions of LFO and NFO grains in composites. Space charge polarization is due to localized accumulation of charges at the LFO-NFO interfaces under the influence of an electric field. Assembly of space charge carriers are line up in such a way that their axes parallel to an alternating electric field at lower frequency. If the frequency of a.c. field increases, a point is reached when the space charge carriers unable to keep up with the field and the alternation of their direction lags behind that of the field; thus resulting in a reduction in the dielectric constant of the composite material [23]. In our case, we found greater composite effect for 70%LFO-30%NFO composition, dielectric constant increased about 10-12 times than individual phases at low frequency region at Room Temperature (T = 27^{o}C, RT). Despite from that dielectric constant of (80%LFO-20%NFO) composite found to be nearer to LFO since this composition has greater percentage of LFO phase whereas 60%LFO-40%NFO have dielectric constant value close to NFO, behaves as NFO rich phase at RT. Fig.4(b) shows variation of dissipation factor tan δ with frequency at RT. For LFO and composites, the value of tan δ drops rapidly at lower frequency and remains constant at high frequencies. High loss factor (tan δ) at low frequency region is due to interfacial effect caused by grain boundary defects in composites but, at higher frequencies space charge polarization no longer contributes to dielectric response (only dipolar, ionic and electronic contribution remains), hence dielectric loss decreases. For NFO, tan δ decreases initially and then increases upto critical frequency called resonance frequency at which frequency of localized charge carriers approximately equal to that of applied alternating electric field. Then, decrease in tan δ takes place because of the jumping frequency of electric charge carriers cannot follow the alternation of applied AC electric field beyond critical frequency [24]. Significant high loss is observed in 70%LFO-30%NFO composite than other composition. This associates with high space charge polarization and defect association with this composite. Fig.5(a) shows temperature dependent dielectric constant for LFO, NFO and their composites at f = 100 kHz. For LFO, dielectric constant increases with increase in temperature upto ~ 441^{o}C and then decreases. This change in dielectric behavior with respect to temperature may attribute to magnetic transition of Fe^{3+} cations. The transition of sample from ordered

antiferromagnetic state to disordered paramagnetic state. Change in magnetic ordering of Fe^{3+} causes change in polarization, affects dielectric constant of material [25-28]. With increase in temperature, dipole-dipole interaction reduces resulting into more dipoles aligning towards applied electric field. Thus, dielectric constant increases with temperature. Decrement in dielectric constant after magnetic transition is attributed to scattering of charge carriers which cause depletion in space charge layers [29]. Loss peak is observed in temperature versus tan δ plot for LFO, this corresponds to dielectric relaxation in the system. At high temperatures (>450, for LFO), conductivity begins to dominate which is responsible for further rise in tan δ. [30]. In case of $NiFe_2O_4$ (NFO), on increasing temperature electrical conductivity increases due to increase in thermally activated charge carriers according to conduction hopping mechanism ($Fe^{2+} \leftrightarrow Fe^{3+}$ exchange). So, dielectric polarization increases causing increase in dielectric constant with temperature for NFO. Anomaly is observed near 450^{o}C, due to ferrimagnetic to paramagnetic transition. Increase in dielectric loss with temperature for nickel ferrite is attributed to increase in number of thermally activated (Fe^{3+}-O^{2-}—Fe^{3+}) and (Ni^{2+}-O^{2-}—Ni^{2+}) linkages. We observe two relaxation peaks in Temperature versus tanδ plot for NFO, these relaxations are corresponding to cation-anion-cation interaction at octahedral B-site.[26, 29]. Same dielectric behavior also shown in LFO-NFO composites. Dielectric constant of 80%LFO-20%NFO, 70%LFO-30% NFO and 60%LFO-40% NFO samples found to be lower with respect to temperature than the individual phases of LFO and NFO. This may be due to the alteration of polarization causes by the interaction of LFOand NFO phases at higher temperature. In NFO, rotation of ($Fe^{2+} \leftrightarrow Fe^{3+}$) dipoles with temperature responsible for electron exchange which cause polarization. But, because of addition of LFO, it is responsible to alter the rotation of NFO molecules and thus, electron exchange becomes less. It leads to reduce the dielectric constant at higher temperature in composites. on the other hand, high dielectric loss is observed in composites as compared to pure samples. This is because of space charges and defects associated with interfaces [31]. The rate of increase in tan δ at low temperature is slow, while at high temperature is sharper because, there is presence of thermally activated charge carriers and defects (such as oxygen vacancies) at high temperatures. Most important reason is that conductivity begins to dominate at high temperature which is responsible for high losses in composites.

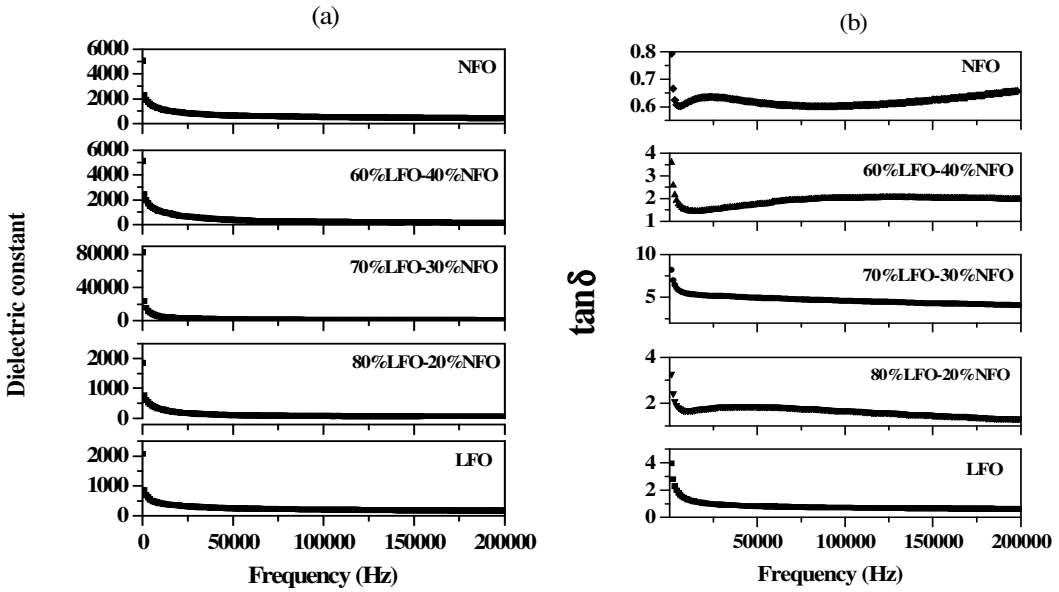


Fig. 4 Frequency dependence (a) dielectric constant (b) tanδ at RT for LFO, NFO and their composites.

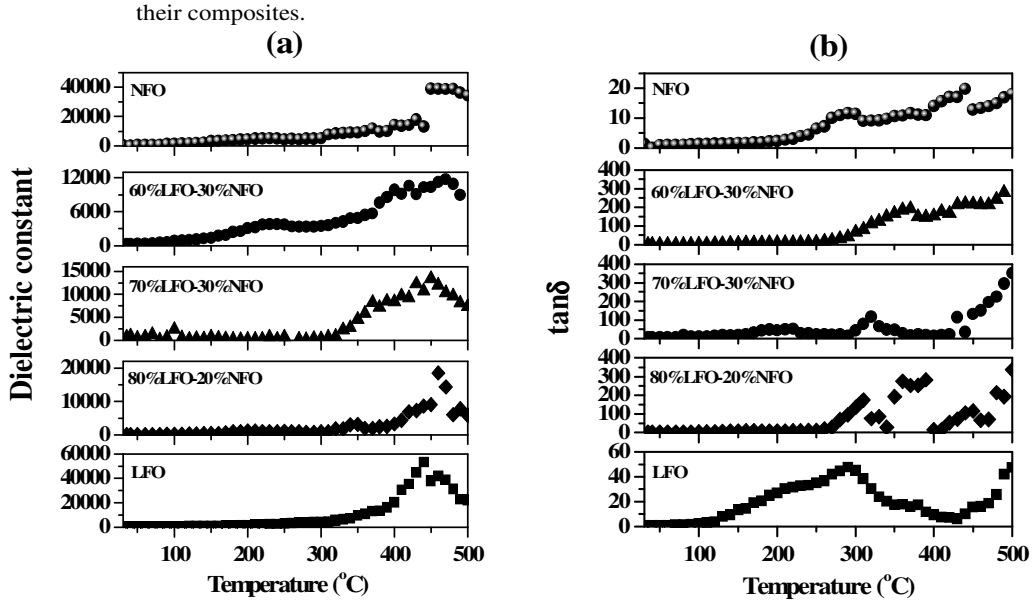


Fig. 5 Temperature dependence (a) dielectric constant (b) tanδ at f=100kHz for LFO, NFO and their composites.

4. Conclusion

Perovskite-spinel (1-x)$LaFeO_3$- x$NiFe_2O_4$ composites are prepared by mixing individual phases of $LaFeO_3$ (LFO) and $NiFe_2O_4$ (NFO) in different proportions (x=20, 30, 40 wt%). The crystallinity of prepared composites is checked by X-ray diffraction (XRD). The XRD data shows both the phases of $LaFeO_3$ and $NiFe_2O_4$ confirms composite formation. FTIR spectra of composites concludes that there is no structural modulation after mixing individual phases of LFO and NFO. LFO and NFO retained their identity in prepared composites. Frequency dependence dielectric constant plots of composites shows higher dielectric constant (4-5 times) than $LaFeO_3$. Dielectric constant decreases with increase in frequency indicates dispersive behavior in low frequency region. Temperature versus dielectric constant plots for LFO and composites (at 100 kHz) gives dielectric anomaly around 450^oC. This anomaly may be attributed to magnetic transition of prepared samples. Dielectric constant with respect to temperature found to be lower in composites than individual phases.

5. Acknowledgement

One of the author V.M.Gaikwad wants to acknowledge UGC, New Delhi, India for providing financial support through RGNF fellowship.

References

[1] Q.Zhan, R.Yu, S.P.Crane, H.Zheng, C.Kisielowski, and R.Ramesh, Appl. Phys. Lett. 89, 172902(2006).
[2] J.Hoffmann et al, J.Mater.Res. 27, No.11(2012).
[3] R.Koferstein, and S.G.Ebbinghaus, Solid State Ionics **231**, 43-48(2013).
[4] D.Wang, and M.Gong, J.Appl.Phys. **109**, 114304(2011).
[5] M.Idrees, M.Nadeem, M.Mehmood, M.Atif, K.H.Chae, and M.M.Hassan, J.Phys.D: Appl.Phys. **44**, 105401(2011).
[6] D.Wang, X.Chu, and M.Gong, Nanotechnology **17**, 5501-5505(2006).
[7] U.Luders, A.Barthelemy, M.Bibes et al, Adv.Mater. 18, 1733-1736(2006).
[8] S.E.Shirsath, S.S.Jadhav, B.G.Toksha, S.M.Patange, and K.M.Jadhav, J.Appl.Phys. 110, 013914(2011).
[9] M.Younas, M.Nadeem, M.Atif, and R.Grossinger, J.Appl.Phys. 109, 093704(2011).
[10] S.M.Patange, S.E.Shirsath, G.S.Jangam, K.S.Lohar, S.S.Jadhav, and K.M.Jadhav, J.Appl.Phys. 109, 053909(2011).

[11] K.V.P.M.Shafi, Y.Koltypin, A.Gedanken, R.Prozorov, J.Balogh, J.Lendvai, J.Felner, J.Phys.Chem.B 101, 6409-6414(1997).
[12] Y.Shi, J.Ding, Z.X.Shen, W.X.Sun, and L.Wang, Solid State Communication 115, 237-241(2000).
[13] I.S. Smirnova, A .V. Bazhenov, T.N. Fursova, A .F. Dubovitskii, L.S. Uspenskaya, M.Yu. Maksimuk, Physica B **403**, 3896-3902(2008).
[14] M.Romero, R.W.Gomez, V.Morquina, J.L.Perez-Mazariego, and R.Escamilla, Physica B **443**, 90-94(2014).
[15] R. A. Lewis, A. D. Martin, X. L. Wang and S. X. Dou, Aust. J. Phys. **52**, 197-203(1999).
[16] M. Sivakumar, A.Gedanken, W.Zhong, Y.H.Jiang, Y.W.Du, I.Brukental, D. Bhattacharya,Y. Yeshurun, and I. Nowik, J. Mater. Chem. **14**, 764–769(2004).
[17] M.A. Ahmed, R. Seoudi, and S.I. El-dek, Journal of Molecular Structure **754**, 41–44(2005).
[18]B. Senthilkumar, R. K. Selvan, P. Vinothbabu, I. Perelshtein, A. Gedanken, Materials Chemistry and Physics, Article in press (2011).
[19] K.K. Patankar, S.S. Joshi, B.K. Chougule, Physics Letters A **346**, 337–341 (2005).
[20] C. G. Koops,Phys. Rev.**83**, 121(1951)
[21] K. W. Wagner, Ann. Phys.**40**, 818 (1993).
[22] S. Narendra Babu, Jen-Hwa Hsu, Y. S. Chen, and J. G. Lin, J. Appl. Phys.**107**, 09D919(2010).
[23] B. P. Rao, and K. H. Rao, Journal of Materials Science **32,** 6049-6054 (1997)
[24] A.M. Abdeen, Journal of Magnetism and Magnetic Materials **192**, 121-129 (1999)
[25] G.Ranga Mohan et al, Mater.Lett. **40**, 39-45(1999).
[26] A.M.Bhavikatti, S.Kulkarni, and A.Lagashetty, Int. Journal of Engineering Science and Technology **3**, 687-695(2011)
[27] F. Yen, B. Lorenz, Y. Y. Sun, C. W. Chu, L. N. Bezmaternykh, and A. N. Vasiliev, Phys.Rev. B **73**, 054435(2006).
[28] P. Tirupathi, and A. Chandra, J.Alloys and compounds **564**, 151–157(2013).
[29] M.Younas, M.Nadeem, M.Atif, and R.Grossinger, J.Appl.Phys. **109**, 093704(2011).
[30] A.Mekap, P.R.Das, and R.N.P.Choudhary, J.Mater.Sci :Mater Electron **24**, 4757-4763(2013).
[31] R.Y.Zheng, J.Wang, and S.Ramakrishna, J.Appl.Phys. **104**, 034106(2006).

INFLUENCE OF ALIOVALENT DOPANTS ON THE STRUCTURE AND DEFECTS OF CERIA UNDER FUEL CELL OPERATING TEMPERATURE

S A ACHARYA*, V. M. GAIKWAD
[1]*Department of Physics, RTM Nagpur University, Nagpur-440033, M.S. India*

Ion transport mechanism in ceria based system is understood by correlating atomic positional shift, oxygen vacancy defects with oxide ion conductivity in doped ceria system. X-ray diffraction (XRD) and Raman spectroscopy study at operating temperature (300-600^{o}C) of Intermediate Temperature Solid Oxide Fuel Cell (IT-SOFC) are performed. High temperature XRD data is used to quantify atomic positional shifting from mean position with temperature. The Raman spectroscopy study shows additional vibration modes related to ordering of defect species $(M_{Ce}^{'} - V_o^{\bullet\bullet})^{*}$ and $(2M_{Ce}^{'} - V_o^{\bullet\bullet})^{x}$ generated due to association of extrinsic oxygen vacancies and dopant $M^{2+/3+}$, which disappear at 450^{o}C; indicating oxygen vacancies dissociation from the defect complex. The experimental evidences of cation-anion positional shifting and oxygen vacancies dissociation from defect complex in the IT-SOFC operating temperature are discussed to correlate with activation energy for ionic conductivity.

Keywords: Aliovalent doped ceria, intermediate temperature solid oxide fuel cell, Raman spectroscopy

1. Introduction

Ongoing attempts on the lowering of the operating temperature solid oxide fuel cell (SOFC), aliovalent doped ceria have been emerging out as promising electrolyte candidates. The higher ionic conductivity at intermediate temperature range (300-500^{o}C) is highly desired by electrolytes for lowering the working temperature of SOFC. The ionic conductivity is dependent on concentration of oxygen vacancies which are commonly induced by aliovalent dopants to compensate excess charges and maintain neutrality of the system [1-9]. The ion transport mechanism leads to ionic conductivity. The ion transport mechanism introduces local changes in the system. The close monitoring of local structural changes and their correlation with ionic conductivity at the working temperature

Proceedings of the 14th Asian Conference on Solid State Ionics (ACSSI 2014)
Copyright © 2014 ACSSI 2014 Organizers. All rights reserved.
ISBN: 978-981-09-1137-9
doi:10.3850/978-981-09-1137-9_100

of intermediate temperature solid oxide fuel cell (IT-SOFCs) is of utmost importance.

The oxy-ion transport mechanism occurs at high temperature; literature reveals many theortical aspects of ion transport mechanisms in doped ceria[10-19] [10-19]. In some experimental approaches, Omar and Nino et al have established the correlation between crystal structure and ionic conductivity in doped ceria by using lattice parameter mismatch between doped ceria and pure ceria (critical dopant ionic radius, r_c) at different temperatures [20]. Bishop et al have studied the chemical expansion of doped ceria as a function of oxygen non-stiochimetry in oxygen partial pressure at operating conditions of IT-SOFC [21-22]. In spite of many studies that have been carried out, there are no convicing explanation on structure-conductivity correlation in IT-SOFC operating temperature and found insufficient to elucidate ion transport mechanism in doped ceria system. The local structure under fuel cells operating conditions are found to differ from the ones observed at room temperature. In the present attempt we have performed X-Ray Diffraction and Raman spectroscopy studies of samarium (Sm) doped CeO_2 at IT-SOFC operating temperature (300-600^{o}C) to reveal changes in local structure, oxygen vacancies defect cluster and their correlation with ionic-conductivity.

2. Experimental

The nano-sized solid solution samples of $Ce_{1-x}Gd/Sm_xO_{2-x/2}$ (GDC and SDC, x = 0.05 – 0.30 at %) were prepared by a hydrothermal route. Cerium(III) nitrate hexahydrate $Ce(NO_3)_3{\cdot}6H_2O$, ≥ 99% (Sigma–Aldrich), samarium and gadolinium(III) nitrate hexahydrate $Gd(NO_3)_3{\cdot}6H_2O$, 99.9% (Sigma–Aldrich) and sodium hydroxide NaOH flakes, 90% (Merck, Germany) were used as precursors. The aqueous solutions of each composition were prepared by dissolving the nitrate salts to the desired concentrations in distilled water and dilution in 1.2 M of NaOH under constant stirring. Each solution was ultrasonicated for 2 min and hydrothermal reaction was carried out in an autoclave using teflon-lined steel vessel. The solutions were then sealed into steel vessel and placed in an oven, and heated to the soaking temperature of 200^{o}C for 24 h reaction time. After the hydrothermal treatment, the solution was centrifuged and washed with distilled water at 7000 rpm for 5 min. The powders were redispersed in water and centrifugation process was repeated five times to remove the unreacted chemicals and then dried in vacuum oven at 80^{o}C. The dry powders were compacted into pellets in a uni-axial 5 ton die press for 5 min followed by sintering to get high (gas-tight) density for electric characterization.

To obtain high-density with low growth rate of particle, nanostructured materials under pressureless sintering fast-firing procedure i.e. fast heating, short dwell-time and fast cooling is more favourable. A microwave heating mode is used to get more control on microstructure of sintered pellet. The gas-tight density (i.e. relative density ~94%) was obtained by sintering at 1100^{o}C for 1 hr.

X-ray powder diffraction measurments of the ceria system were performed using a Bruker AXS D8 Advance X-ray diffractometer equipped with a copper target (CuK_{α}= 1.5405 Å). The diffraction data was collected in the range of 20^{o} to 80^{o} in air temperature starting from 25^{o} to 600^{o}C with 50^{o} C interval. The diffraction data thus obtained was analyzed by Rietveld method with Full-proof software. Raman spectroscopy was carried out using Jobin YVON Horiba LABRAM-HR-Visible micro Raman system using a He-Ne laser operating at 632.8 nm as the source in the backscattering geometry. The scattered light was analyzed using a single stage spectrograph CCD detector. The laser was focused to a spot of ~2 μm and 50x objective lens was used for the collection of the scattered light. Ionic conductivity was measured by impedance spectroscopy using a Novocontrol Alpha-A high performance frequency Analyzer. Measurements were carried out in the range 300^{o}C – 600^{o}C at variable frequency from 5 μHz to 3 MHz. The transmission electron microscopy (TEM) images were obtained using Technai $20G^2$ operated at 200 KV. The samples were prepared by dispersing the powders in N, N dimethylformamide (DMF) and placing a drop of liquid on carbon coated formvar grids

3. Results and discussion

X-ray diffraction patterns of as-synthesized CeO_2, SDC15 and GDC15 shown in Fig 1a confirm that all the samples were crystallized in cubic phase. Additional peaks observed at 40.65^{o} and 47.08^{o} in every diffraction pattern are due to Pt substrate used to support the powder samples. The SEM and TEM images of the as-synthesized samples (see Fig 2) show that microstructure consist of very fine scale particles having size between 7 to 10 nm.

XRD patterns of as-synthesized SDC15 at IT-SOFC operating temperature during heating and cooling cycle are shown in Fig 1b. The crystal structure of all the samples were refined by the fluorite-type structure (space group: Fm-3m). The Ce/Gd atoms were put at (0, 0, 0) Wyckoff sites: 4a and O atoms were placed at 1/4,1/4,1/4 wyckoff position:8c. A Rietveld fitted data files is displayed in Fig 1c. The XRD data clearly shows (Fig 1d) that during heating, the peak shifted to lower 2θ position and during cooling, the peak shifted to higher 2θ position, which indicates thermal expansion during heating and

contraction during cooling. Normalized XRD patterns of SDC15 during heating cycle depict (Fig 1c: Inset-heating) that intensity of peaks is continuously increasing during heating. Generally, peak intensity reflects degree of crystallinity, which is found to be increasing during heating. However peak intensity (Fig 1c: Inset-cooling) is almost constant during cooling, indicating that crystallinity was completed and did not change. The observed trends of variation of lattice parameter as a function of temperatures are comparable with literature [20][24]. No structural changes are observed in the working temperature of SOFC.

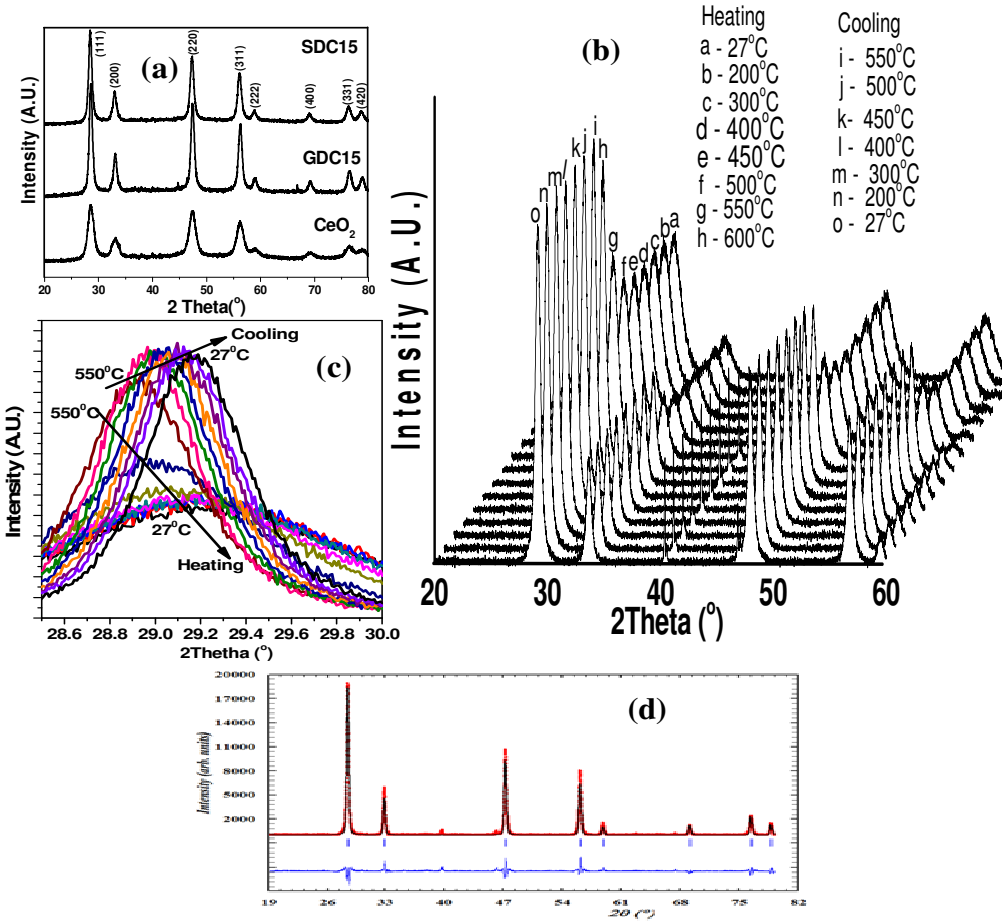


Fig 1. (a) XRD of as-synthesized samples CeO_2, GDC and SDC (b) XRD of SDC15 during heating and cooling cycle, (c) Thermal expansion and contraction of SDC15, (d) Rietveld fitted data file for SDC15.

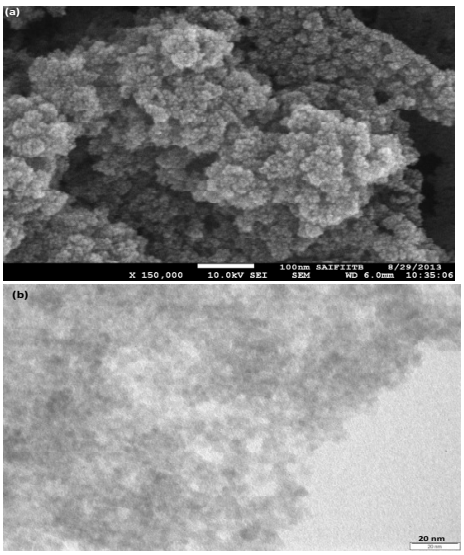


Fig 2. (a) SEM and (b) TEM image of SDC15

Raman spectroscopy is sufficiently powerful to analyze structural properties of materials at local level, owing to the strong sensitivity of the phonon characteristics to the crystalline nature of the materials. Raman spectroscopy study of doped ceria are systematically conducted in IT-SOFC operating temperature. Raman spectra of CeO_2, SDC15 and GDC15 at 25^{o}C are shown in Fig 3(a). Room temperature (25^{o}C) Raman spectra of SDC15 and GDC15 show four modes around 255, 461, 561 and 604 cm^{-1}. However, Raman spectrum of pure ceria exhibits only three modes around 252, 455, and 600 cm^{-1}. The Raman mode at 252 cm^{-1} can be assigned to doubly degenerated 2TA mode. The mode near 455 cm^{-1} corresponded to the only first order Raman active F2g mode of the CeO_2 fluorite structure and represents the symmetrical stretching vibration of the CeO_8 vibrational unit [23]. This mode is broad, asymmetric and shifted to lower wavenumbers as compared to the single-crystal value [24-26]. The other two modes are second order Raman modes attributed to the defect ordering due to oxygen vacancies. The mode near 600 cm^{-1} is related to intrinsic oxygen vacancies due to non-stoichiometry of ceria. The possible disorder reaction in pure ceria for intrinsic oxygen vacancies [27][35]

$$Ce_{Ce} + 2O_o \rightarrow V''''+2V_o^{\bullet\bullet} + CeO_2 \quad (1)$$

$$Ce_{Ce} \rightarrow V_{Ce}^{''''} + Ce_i^{\bullet\bullet\bullet\bullet} \quad (2)$$

$$O_o \rightarrow V_o^{\bullet\bullet} + O_i'' \quad (3)$$

In addition to that CeO_2 has been found to experience more loss of oxygen ions when its average particle size decreases down to nanoscale [28-29]. The mode near 550 cm^{-1} is assigned to extrinsic oxygen vacancies. The extrinsic oxygen

vacancies are originated due to charge compensating defects due to the substitution of Ce^{4+} ions by Sm^{3+}/Gd^{3+} ions which gives rise to loss of oxygen ions O^{2-} [30] . The probable reaction of extrinsic oxygen vacancies generation is:

$$(1-x)CeO_2 + \frac{x}{2}M_2O_3 \rightarrow (1-x)Ce_{Ce} + xM'_{Ce} + (2-\frac{x}{2})O_o + (2-\frac{x}{2})O_o + \frac{x}{2}V_o^{\bullet\bullet} \quad (4)$$

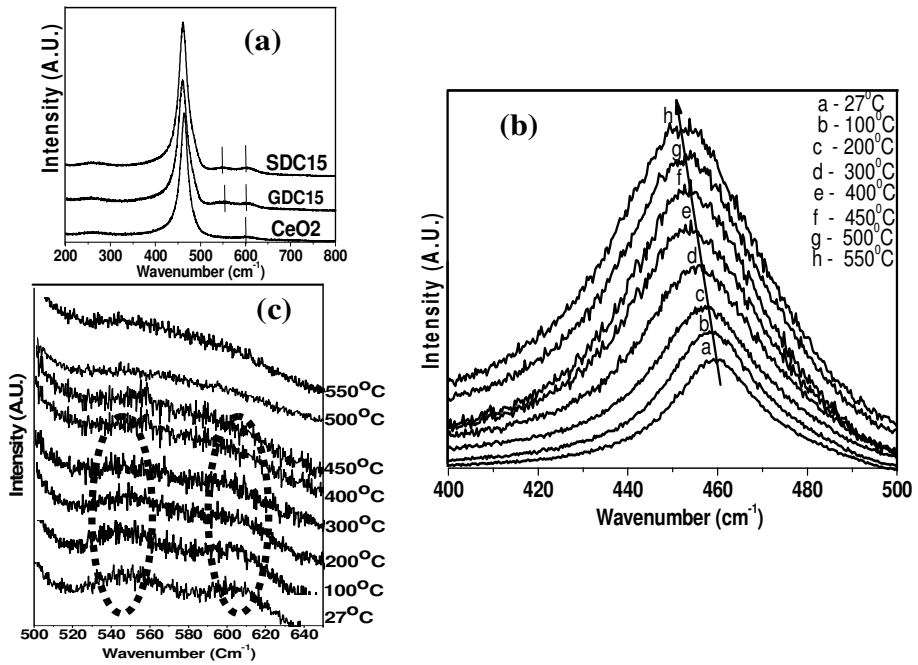


Fig 3: (a) Raman spectra of CeO_2, SDC15, GDC15 (b) Temperature dependent Raman spectra, (c) Defect associated Raman modes

Experimental Raman spectra are fitted using Lorentzian function. The best fit of the wavenumber values during the heating up to 400°C was obtained including the four-phonon anharmonic term, while at higher temperatures three-phonon decay processes became dominant. It reflects the change in phonon-phonon interaction at 450°C onwards. High temperature Raman spectra exhibit noteworthy changes. With increasing temperature, the F2g mode is found to shift towards lower wavenumber values and become asymmetric. However, half width of full maxima (FWHM) of F2g mode is observed to increase with rising temperature (as shown in inset Fig 3b). The dopant effect on redshift of F2g Raman mode is compensated by Gruneisen shift considering Gruneisen parameter $\gamma = 1.24$ as taken from ref [31]. In general there are several factors attributed to the changes. These include phonon confinement, strain, broadening associated with the size distribution and variation in phonon relaxation. In CeO_{2-x} system the combined effects of strain and phonon confinement are found to be

responsible for the red shift and band width increase with increasing temperature [32-33].

The next focus is on vibrational modes near 550 cm^{-1} and 600 cm^{-1}, which are assigned to defect spaces form by extrinsic and intrinsic oxygen vacancies, respectively. Raman spectrum displays the ordering of the defects. The intensity of the modes decreases with increase of temperature and totally disappears at 450°C in SDC15 and pure CeO_{2-x} (Fig 3c). The band near 550 cm^{-1} is attributed to vibration mode related to defect ordering formed by association of extrinsic oxygen vacancy with dopants cations viz $(M'_{Ce} - V_o^{\bullet\bullet})^{\bullet}$ and $(2M'_{Ce} - V_o^{\bullet\bullet})^{x}$. However the band at 600 cm^{-1} is assigned to defect spaces developed due to association of intrinsic oxygen vacancy with reduced host cations. The decrease in intensity of the vacancy mode with temperature and its disappearance at a particular higher temperature can be explained in terms of the dissociation of oxygen vacancies from $(M'_{Ce} - V_o^{\bullet\bullet})^{\bullet}$ and $(2M'_{Ce} - V_o^{\bullet\bullet})^{x}$ cluster (extrinsic vacancies). Isolation of defects leads to decrease in intensity of respective Raman mode. With increase in temperature, detectable decrease in intensity of the defects related vibrational mode (550 & 600 cm^{-1}) can be clearly visualized from the normalized Raman spectra as shown in Fig 4. In case of pure ceria, Raman mode related to intrinsic vacancy defects ordering observed near 600 cm^{-1} disappears at 400°C. For SDC15, both the modes disappear at 400°C onwards. It can be manifested as dissociation of oxygen vacancies from cations cluster and become mobile, in ITSOFCs operating temperature and pure ceria (Fig 3c). For all the samples, the vibrational mode related to intrinsic vacancies (600 cm^{-1}) disappears above 400°C.

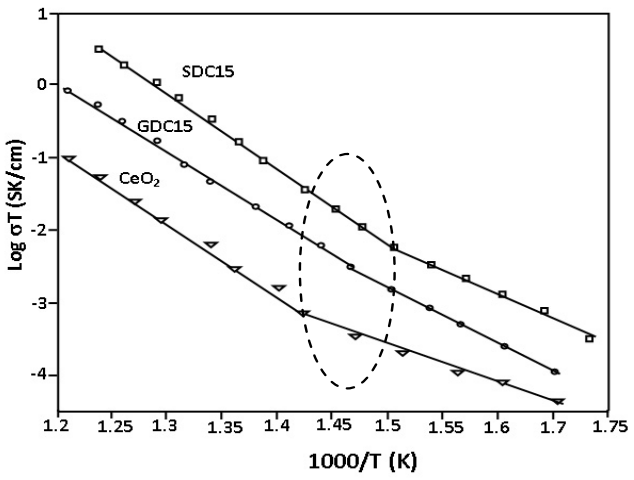


Fig 4. Arrhenius plot of pure ceria, GDC15 and SDC15

The Arrhenius plot of ionic conductivity for different dopant concentrations are shown in Fig 4. The plots clearly reveal increase of conductivity with temperature. There are changes in the slope around 400°C Conductivity for pure ceria is lowest and tends to increase with dopant.

Conductivity of SDC systems are found more than GDC systems. The activation energy of ionic conductivity calculated from Arrhenius plot are obtained as 0.85 eV, 0.93 eV and 1.2 eV for SDC15, GDC15 and for pure-ceria, respectively; the activation energy of the doped ceria is comparable with reported values[33-40].

In general, ionic conductivity in doped ceria is due to oxygen ions that are transported through oxygen vacancies. Ionic conductivity in ceria is closely related to oxygen-vacancy formation and migration properties. Ceria doped with lower valence cations introduces extrinsic oxygen vacancies to compensate charge imbalance, which improve the conductivity. However, because of interactions, the dopants and vacancies form associates with a certain binding or association energy (E_{ass}), which prevents the vacancies from being mobile. The number of mobile vacancies is determined by E_{ass}. Hence, for doped ceria, Activation energy E_a for ionic conductivity can be identified as the sum of E_{ass} and E_m . At sufficiently high temperature, most vacancies will be dissociated, and in this regime, the concentration of mobile vacancies is increased.

The corresponding oxygen vacancies dissociations from defect cluster results out mobile species which are capable to overcome energy barrier for hopping to a neighboring site. Thus site near defect cluster has lower energy barrier then neighboring ones; which induce non-equivalent defects sites surrounding to cluster defects. Therefore oxygen vacancies dissociations create low energetic path for oxygen ion migration. Raman spectra illustrate that vibrational mode related defect ordering due to extrinsic (550 cm^{-1}) and intrinsic (600 cm^{-1}) oxygen vacancies disappear at around 400^{o}C in SDC15, GDC15, Both these results provide evidences to speculate that the dissociation of oxygen vacancies from defect complex. The oxygen vacancies become mobile and more responsible for conductivity.

4. Conclusion

In summary, correlation between atomic positional shift, oxygen vacancies defects and oxide ion conducitivity in aliovalent doped ceria system has been established using XRD and Raman spectroscopy at Intermediate Temperature Solid Oxide Fuel Cell (IT-SOFC) operating temperature (300-600^{o}C). The thermal expansion and contraction of lattice parameter during heating and cooling cycle of GDC samples are used to quantify cation-anion positional shift. The Raman spectroscopy data are fitted by Lorentzian function and found best fit during the heating up to 400^{o}C was obtained the four-phonon anharmonic term, while at higher temperatures three-phonon decay processes became dominant. The additional phonon modes related to defect ordering

$(M_{Ce}^{'} - V_o^{\bullet\bullet})^{\bullet}$ and $(2M_{Ce}^{'} - V_o^{\bullet\bullet})^{x}$. The decay of phonon mode above 400°C is related to the dissociation of extrinsic oxygen vacancies from the defects cluster. The experimentally observed trend of cation-anion positional disorder and oxygen vacancies dissociation from defect complex in the IT-SOFC operating temperature range are correlated with energy of oxygen ion migration and association (i.e.activation energy), respectively.

Acknowledgments

The authors SAA want to acknowledge financial support from DST, New Delhi, India under project of SR/FTP/PS-106/2009 (G) and UGC under MRP F.N. 41-871/2012.

References

[1] D. Marrocchelli, P.A. Madden, S.T. Norberg, and S.Hull, Chem. Mater. **23**, 1365(2011).
[2] B.C.H. Steel, A. Heinezi, Nature **414**, 345(2001).
[3] B.C.H. Steel, Solid State Ionics **134**, 3(2000).
[4] X.M. Lin, L.P. Li, G.S. Li, and W.H. Su, Mater. Chem. Phys. **69**, 236 (2001).
[5] A. Sin, Y. Dubitsky, A. Zaopo, A.S. arico, L. Gulli, D.L.Rosa, S. Siracusano, V. antonucci, C. Oliva, and O. Ballabio, Solid State Ionics **175**, 361 (2004).
[6] H. Inaba and H. Tagawa, Solid State Ionics **83**, 1 (1996).
[7] S. Kuharuangrong, J. Pow. Sources **171**, 506 (2007).
[8] S. Omar, E. D. Wachsman, and J. C. Nino, Appl. Phy. Lett. **91**, 144106 (2007).
[9] K. Eguchi, H.Yahiro, and H.Arai, Solid State Ionics **36**, 71 (1989).
[10] Z.P.Li, T. Mori, G. J. Auchterlonie, J.Zou, and J.Drennan, Appl. Phys. Lett. **98**, 093104-3 (2011).
[11] J.A.Kilner, Chem. Letter **37**, 1012(2008).
[12] Z.P.Li, T.Mori, F.Ye, D.R. Ou, J.Zou, and J.Drennan, Microsc. Microanal. **17**, 49(2011).
[13] H.Yoshida, H.Deguchi, K.Miura, M.Horiuchi, and T.Inagaki, Solid State Ionics **140**, 191(2001).
[14] M.P. Anderson, D.E. Cox, K. Halperin, A.S. Nowick, Solid State Ionics **9–10**, 953(1983).
[15] D.R.Ou, T.Mori, F.Ye, J.Zou, G.Auchterlonie, J.Drennan, Phys.Rev. B **77**, 024108(2008).
[16] F.Ye, T.Mori, D.R.Ou, J.Zou, J.Drennan, Solid State Ionics **180**, 1414 (2009).
[17] H.Nitani, T.Nakagawa, M.Yamanouchi, T.Osuki, M.Yuya, and T. A. Yamamoto, Materials Letters **58**, 2076 (2004).
[18] H.Deguchi, H.Yoshida,T.Inagaki, M.Horiuchi, Solid State Ionics **176**,1817 (2005).
[19] A.Banerji, V.Grover, V.Sathe, S. K. Deb, and A.K. Tyagi, Solid State Ionics **149**, 1689(2009).

[20] S. Omar, E. D. Wachman, J. L. Jones and J.C. Nino, J. Am. Ceram Soc., **92[11]** 2674 (2009).
[21] S R Bishop, K.L. Duncan, E.D. Wachsman, *Acta Materialia*, 57 (2009) 3596.
[22] S R Bishop, K.L. Duncan, E.D. Wachsman, *Electrochimica Acta,* 54 (2009) 1436.
[23] J. Godinho, R.F. Gonçalves, L.P. S Santos, J.A. Varela, E. Longo, and E.R. Leite, Materials Letters **61**, 1904 (2007).
[24] T. Otake, H Yugami, K. Yashiro, Y. Nigara, T. Kawada, J. Mizusaki, Solid State Ionics, 161 (2003)181.
[25] S R Bishop, T S Stefanik and H L Tuler, Phys. Chem. Chem. Phys., 13 (2011), 10165.
[26] K L Duncan, Y Wang, S R Bishop, F Ebrahimi, and E D Wachsman, J Am Ceram. Soc., 89 [10] (2006) 3162.
[27] J. R. McBride, K. C. Hass, B. D. Poindexter, and W. H. Weber, J. Appl. Phys. **76**, 2435 (1994).
[28] I.Kosacki, T.Suzuki, H.U.Anderson,and P.Colomban, Solid State Ionics 149, 99(2002).
[29] J. E. Spanier, R.D. Robinson, F. Zhang, S.W. Chan, and I.P.Herman, Phys.Rev.B **64**, 245407(2001).
[30] L.Minervini, M.O.Zacate, and R.W.Grimes, Solid State Ionics **116**, 339(1999).
[31] S. Askrabic, Z. D. Dohcevic-Mitrovic, M. Radovic, M.Scepanovic, and
Z. V. Popovic, J. Raman Spectrosc. **40**, 650(2009).
[32] J.R. McBride, K.C. Hass, B.D. Poindexter, and W.H. Weber, J. Appl. Phys. **76**, 2435 (1994).
[33] Z.D. Dohcevic-Mitrovic, M. grujic-Brojcin, M. Scepanovic, Z.V. Popovic, S. Boskovic, B. Matovic, M. Zinkevich, and F. Aldinger, J.Phys.Condens. Matter **18**, S2061(2006).
[34] W.H. Weber, K.C. Hass, J.R. Mcbride, Phys Rev B 48 178 (1993).
[35] M. Balkanski, R.F. Wallis, and E. Hero, Phys. Rev. B **28**, 1928 (1983).
[36] Z.D. Dohcevic-Mitrovic, M. Radovic, M. Scepanovic, M. Grujic-Brojcin, Z.V. Popovic, Appl. Phys. Lett. **91**, 203118 (2007).
[37] M.G. Chourashiya, S.R. Bharadwaj, L.D. Jadhav, Thin Solid Films **519**, 650, 2010.
[38] S.L. Reis, E.C.C. Souza, E.N.S. Muccillo, Solid State Ionics **192,** 172, 2011.
[39] H. Duncan, A. Lasia, Solid State Ionics **176**, 1429, 2005.
[40] S. Kuharuangrong, J Power Sources **171**, 506, 2007.

IONIZATION CONDITION SCALED WITH MOLECULAR COOPERATIVITY IN IONIC LIQUIDS – LITHIUM SALT MIXTURES

MASAHIRO IKEDA[†]

Course of General Education, Natural Science, Applied Physics, Fukui National College of Technology, Geshi-chou, Sabae City, 916-8507, Japan

MASARU ANIYA

Department of Physics, Graduate School of Science and Technology, Kumamoto University, 2-40-1, Kurokami Chuo-ku, Kumamoto City, 860-8555, Japan

For practical applications of ionic liquids (ILs) to electrolytes, it is important to evaluate the degree of ionization or dissociation of the components in the electrolyte solutions. In the present contribution, the ionization condition of ionic liquids with lithium salt mixtures (ILs-Li) is discussed in terms of the molecular cooperativity (MC). According to Saito *et al.*, the ionization condition of ILs-Li is described by the ratio between the self-diffusion coefficients of cation and anion. We applied their method to the MC estimated by a model of the viscosity, the bond strength-coordination number fluctuation (BSCNF) model. It is shown that the diffusion coefficients of the ionic components are closely related with the quantity N_B that describes the MC involved in the thermally activated viscous flow. The present study shows that the ionization condition of the ILs-Li investigated can be scaled well with the MC based on N_B, which suggests that the diffusivity of cations and anions is promoted via the bond-formation and bond-breaking between the components in the ILs-Li solutions.

1. Introduction

The utilization of room temperature ionic liquids or simply called ionic liquids (ILs) as electrolytes in lithium ion battery has been proposed due to the excellent material properties of the ILs [1-4] such as non-flammability, negligible vapor pressure, thermal and chemical stability, and high ionic conductivity. In addition, the feasibility of a wide variety of combinations between cations and anions has strengthened the application of ILs. These properties motivated many researchers to find more desirable ILs and their applications [1, 2, 4, 5]. In recent decades, a large number of studies have been performed aiming for a better

[†]This work was supported by Grant-in-Aid for Young Scientists (B) of Japan (No. 25871035) and Research Foundation for the Electrotechnology of Chubu (REFEC).

Proceedings of the 14th Asian Conference on Solid State Ionics (ACSSI 2014)
Copyright © 2014 ACSSI 2014 Organizers. All rights reserved.
ISBN: 978-981-09-1137-9
doi:10.3850/978-981-09-1137-9_067

usage of ILs in the areas of electrochemistry, environmental chemistry, chemical engineering, etc [2-6]. However, some questions on fundamental properties of ILs still remain unsolved. For instance, detail on the degree of ionization or dissociations of the components in the electrolytes solutions is not clear. The problem of how one can relate the degree of ionization to the transport coefficients such as viscosity, diffusivity, ionic conductivity, and their mutual interrelations is also still an open question [7-12]. Although it is not easy to give answers to such questions, recently, some researchers have proposed promising ideas to solve these problems. For instance, Saito *et al.* [12] have presented a way to evaluate the "ionization condition" in ILs with lithium salt mixtures (ILs-Li). Specifically, they have provided a relation that evaluates the ionization condition in ILs-Li by using the self-diffusion coefficients measured by the pulse-gradient spin-echo (PGSE) NMR technique [12, 13].

In our previous studies [14-16], the relation between the transport coefficients and the molecular cooperativity (MC) was investigated for some ILs and ILs-Li. There, it was discussed that the MC can be estimated in terms of a model of the viscosity, the bond strength-coordination number fluctuation (BSCNF) model [17, 18]. It has been found [14] that the MC involved in the thermally activated viscous flow is correlated with the diffusion coefficient better than the ionic conductivity and the viscosity. This result prompts us to study the relation between the ionization condition and the MC for ILs-Li solutions. In what follows, we discuss on a possible link between them and their implications in the diffusivity of ILs-Li.

2. Correlation between the diffusivity and the MC

The present analysis focuses on the transport property of ILs-Li composed of *N*-methyl-*N*-propyl-pyrrolidinium (P_{13}^+) and 1-ethyl-3-methylimidazolium ($emim^+$) as cation, and bis(trifluoromethanesulfonyl)amide ($[(CF_3SO_2)_2N]^-$ or $TFSA^-$) and bis(fluorosulfonyle)amide ($[(FSO_2)_2N]^-$ or FSA^-) as anions [10, 11]. For these ions, the ionic conductivity of ILs-Li with $TFSA^-$ is lower than those in conventional organic solvents. This shortcoming of TFSA-type ILs-Li results from their high viscosity. On the other hand, the viscosity of ILs-Li based on FSA^- has been found to be lower than that based on $TFSA^-$ [2]. The transport property of ILs-Li with a different cation, tetrafluoroborate (BF_4^-), has been investigated in detail by others [19].

In the analysis of the temperature dependence of the viscosity, many studies have employed the Vogel-Fulcher-Tammann (VFT) equation. In the present work, we employ the BSCNF model instead of the VFT equation, because this

model has some merits. For instance, the parameters of the BSCNF model have clear physical meanings compared with those of the VFT equation which has been proposed empirically [20-22].

According to the BSCNF model, the temperature dependence of the viscosity is given by [17, 18]

$$\eta = \frac{\eta_0}{\sqrt{1-Bx^2}} \exp\left[\frac{Cx + Cx^2 \left\{ \left[\ln\left(\frac{\eta_{Tg}}{\eta_0}\right) + \frac{1}{2}\ln(1-B) \right] \frac{(1-B)}{C} - 1 \right\}}{1-Bx^2} \right], \tag{1}$$

where

$$B = \frac{(\Delta E)^2 (\Delta Z)^2}{R^2 T_g^2}, \qquad C = \frac{E_0 Z_0}{R T_g}, \qquad x = \frac{T_g}{T}. \tag{2}$$

Here, E_0 and Z_0 are the mean value of the bond strength and the coordination number, and ΔE and ΔZ are their fluctuation of the structural units that form the viscous liquid. η_0 and η_{Tg} are the viscosities at the high temperature limit and at the glass transition temperature, respectively, and R is the gas constant.

Figure 1 (a) shows that Eq. (1) reproduces well the measured viscosity data of ILs and ILs-Li investigated. By using the BSCNF model in place of the VFT equation, additional information on the MC is obtained, which is also one of the merits of the BSCNF model [14]. In the light of the BSCNF model, the MC is evaluated by

$$N_B(T) = \frac{1}{C}\frac{d}{dx}\ln\eta_{BSCNF}(B, C, T). \tag{3}$$

It has been found that the quantity N_B, which was defined originally as $N_B = E_\eta/(E_0 Z_0)$ [23] where E_η is the activation energy for the viscous flow, shows a good correlation with the self-diffusion coefficients compared with other transport coefficients [14]. The temperature dependence of the MC evaluated by Eq. (3) is shown in Figure 1 (b) for P_{13}-TFSA and P_{13}-FSA and their lithium salt mixtures. It is seen that the FSA-based systems are less cooperative than the TFSA-based one. This behavior is consistent with the observation of Figure 1 (a), that is, the value of the viscosity in FSA-type ILs is lower than that of the TFSA-type ILs. It means that the degree of the cooperativity in ILs and ILs-Li can be evaluated from the analysis of the viscosity through Eq. (3).

After finding the expression given in Eq. (3), the possibility whether a correlation between N_B and other transport coefficients exists or not, was discussed [14]. As a result

of the previous investigation, it was found that the following relationship holds over the measured temperature range for the ILs investigated [15],

$$D \propto \left(\frac{T}{\eta}\right)^{p} \propto (N_{\mathrm{B}}{}^{-1})^{\zeta}, \qquad \zeta = \frac{E_D}{E_{N\mathrm{B}}}. \tag{4}$$

The relation $D \propto (T/\eta)^p$ is called fractional Stokes-Einstein (FSE) law [10, 24, 25]. Here p gives the degree of deviation from the original Stokes-Einstein law. As shown in Figure 2, it should be noted that the relation $D \propto (N_{\mathrm{B}}{}^{-1})^{\zeta}$ follows the experimental data of the self-diffusion coefficients measured by PGSE NMR technique. Here, ζ is the ratio between the activation energies of the diffusion coefficient D and N_{B} [14, 15]. In order to relate N_{B} with D within the same scale, we assumed that the temperature dependence of N_{B} is represented by $N_{\mathrm{B}}=N_{\mathrm{B0}}\exp(E_{N\mathrm{B}}/RT)$ [14, 15]. The value of $E_{N\mathrm{B}}$ in Eq. (4) is obtained from this expression. In Figure 2, we can see that the slope in the relation between ln$D$ and ln($N_{\mathrm{B}}{}^{-1}$), that is the value of ζ, is almost temperature-independent.

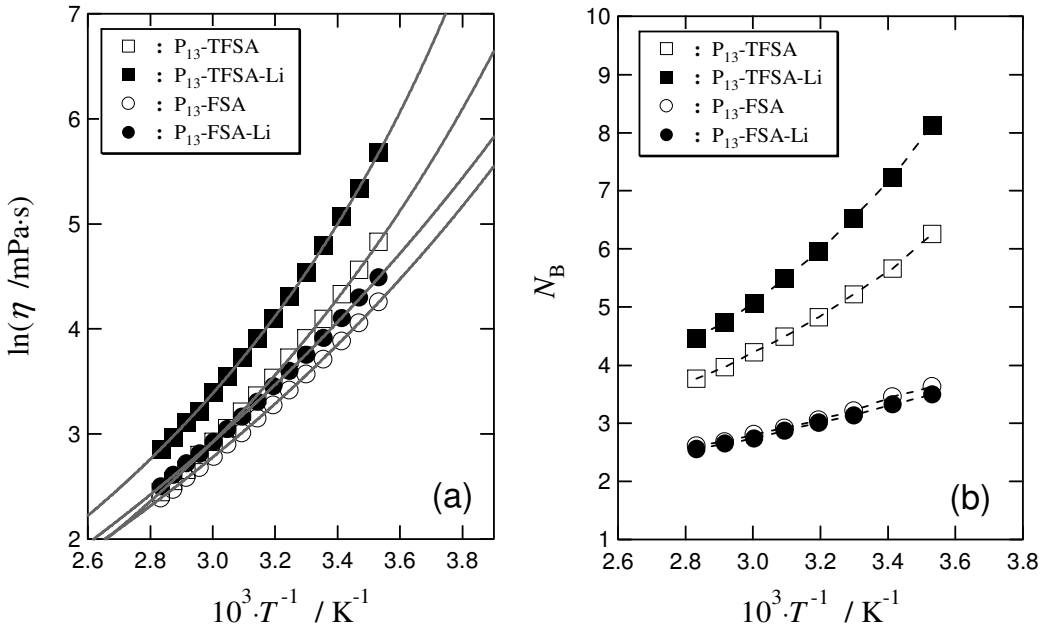


Figure 1. (a) Temperature dependence of the viscosity in ILs and ILs-Li. (b) Temperature dependence of the MC evaluated by N_{B} for the materials considered in (a). The parameters used in the analysis are given in Table 1.

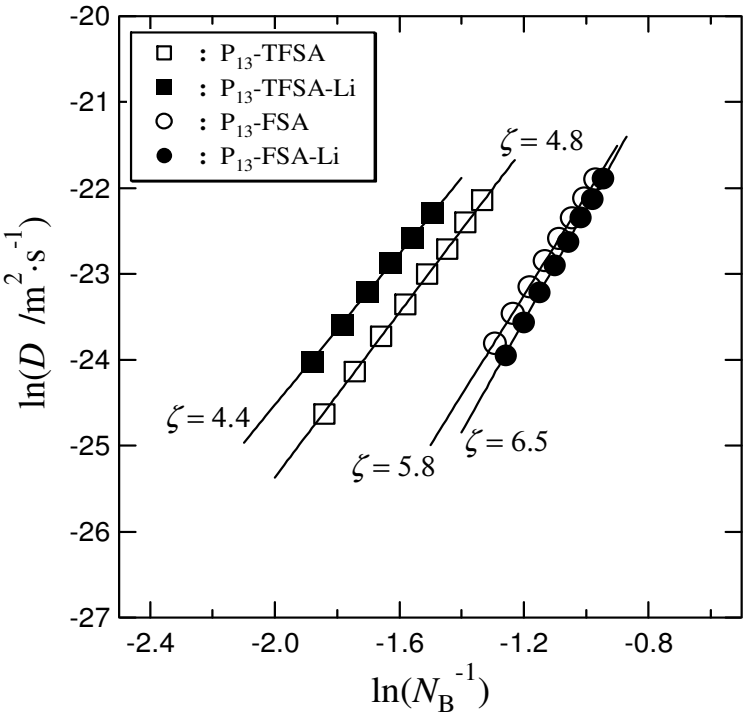


Figure 2. Relation between ln$D$ and ln(N_B^{-1}). Here, D is used as a sum of the self-diffusion coefficients of cation and anion, $D = D_{cation} + D_{anion}$. The experimental data are taken from Ref. [10]. The straight line used in the figure is described by $\ln(D\ /\mathrm{m}^2\cdot\mathrm{s}^{-1}) = \zeta \ln(N_B^{-1}) + b$, where the values of b are: –15.77 for P_{13}-TFSA, –15.73 for P_{13}-TFSA-Li, –16.29 for P_{13}-FSA and –15.75 for P_{13}-FSA-Li, respectively.

Table 1. Parameters of the BSCNF model used in the present analysis. The shift factor a_T is given by $a_T = \ln(\eta_{Tg}/\eta_0)$.

Materials	$\eta_0/10^{-1}$ mPa·s	a_T	B	C
P_{13}-TFSA	1.71	36.31	0.77	4.36
P_{13}-TFSA-Li	3.03	35.73	0.82	3.29
P_{13}-FSA	2.19	36.06	0.73	5.13
P_{13}-FSA-Li	1.51	36.43	0.68	6.19

Physically, this suggests that the diffusion process is highly cooperative in ILs and ILs-Li solutions. In other words, the diffusivity is expected to be promoted via the bond-switching between the ionic components. This picture does not contradict the result of the MD simulation [26]. There, it has been reported that the diffusion of Li^+ exhibits a random-walk-like motion and diffuses by exchanging the anionic species.

3. Ionization condition scaled with the MC

The diffusion process in ILs is reflected in the motions of individual ionic species that are ionized and counteract each other. Actually, the mobility of cations and anions in ILs are greatly influenced by the variations of the temperature. Such influence is observed in the temperature dependence of the diffusion coefficients as a non-Arrhenius behavior [7-10].

As demonstrated in many studies, the PGSE NMR technique provides us the details of the dynamics of the components through the self-diffusivity of each cations and anions. However, due to the formations of ion pairs or presumably higher-ordered aggregates, duplicated contributions from the isolated ions and the aggregates are included in the observed self-diffusion coefficients measured by the PGSE NMR method [7]. Moreover, the addition of lithium salt into the ILs solutions complicates the situation considered.

According to Saito *et al.* [12], the observed self-diffusion coefficients for the case of Li-TFSA/BMI-TFSA system can be represented as

$$\begin{aligned} D_{\mathrm{Li}}^{(\mathrm{obs.})} &= x_1 D_{\mathrm{Li}^+} + (1-x_1) D_{\text{Li-TFSA}} \\ D_{\mathrm{F1}}^{(\mathrm{obs.})} &= x_1 D_{\mathrm{TFSA}^-} + (1-x_1) D_{\text{Li-TFSA}} \\ D_{\mathrm{H}}^{(\mathrm{obs.})} &= x_2 D_{\mathrm{BMI}^+} + (1-x_2) D_{\text{BMI-TFSA}} \\ D_{\mathrm{F2}}^{(\mathrm{obs.})} &= x_2 D_{\mathrm{TFSA}^-} + (1-x_2) D_{\text{BMI-TFSA}} \end{aligned} \tag{5}$$

where x_1 and x_2 are the degrees of the dissociation of the lithium salt Li-TFSA and that of the ILs systems BMI-TFSA. Here, BMI represents 1-butyl-3-methylimidazolium. The subscripts Li, H, F_1 and F_2 represent the probed nuclei of ^{7}Li, ^{1}H and ^{19}F, respectively [12]. It has been noted that in the actual measurement by the PGSE NMR method, the contribution of D_{F1} and D_{F2} is indistinguishable due to the contribution from two factors, the isolated ions and the aggregates combined with $TFSA^-$. From Eq. (5), the diffusivity ratios are written in the extreme cases as

$$\frac{D_{\mathrm{Li}}^{(\mathrm{obs.})}}{D_{\mathrm{F1}}^{(\mathrm{obs.})}} = \begin{cases} \dfrac{D_{\mathrm{Li}^+}}{D_{\mathrm{TFSA}^-}} & (x_1 \approx 1) \\ 1 & (x_1 \approx 0) \end{cases} \qquad \frac{D_{\mathrm{H}}^{(\mathrm{obs.})}}{D_{\mathrm{F2}}^{(\mathrm{obs.})}} = \begin{cases} \dfrac{D_{\mathrm{BMI}^+}}{D_{\mathrm{TFSA}^-}} & (x_2 \approx 1) \\ 1 & (x_2 \approx 0) \end{cases} \tag{6}$$

As mentioned above, D_{F1} and D_{F2} are practically indistinguishable. Thus, Saito *et al.* have introduced the following expression, $D_F = (D_{F1} + RD_{F2})/(1+R)$, where R is the molar ratio between Li-TFSA and BMI-TFSA. This expression takes

simultaneously into consideration both, D_{F1} and D_{F2} by using the extra information of the concentration R. In the present analysis, we examine simply the ratio between the self-diffusion coefficients of cation and anion, that is, D_{cation}/D_{anion}. According to Eq. (6), the value of this ratio deviates from unity when the dissociation in the ILs-Li is highly promoted. This provides an effective way to evaluate the degree of the ionization condition in ILs-Li solutions.

In the previous section, we mentioned that the diffusion coefficient D is in harmony with the MC described by N_B, which was given in Eq. (4). From this relation, we note that it is possible to relate the ionization condition with N_B, and discuss the degree of the dissociation in ILs and ILs-IL solutions in terms of the MC.

4. Result and discussion

By applying Eq. (4) to each ionic component in the ILs-Li investigated in the present study, we obtain the following relations of proportionality,

$$\begin{aligned} D_+ &\propto (N_B^{-1})^{\zeta_+}, \quad (\zeta_+ = E_{D_+}/E_{N_B}) \\ D_- &\propto (N_B^{-1})^{\zeta_-}, \quad (\zeta_- = E_{D_-}/E_{N_B}) \\ D_{Li} &\propto (N_B^{-1})^{\zeta_{Li}}, \quad (\zeta_{Li} = E_{D_{Li}}/E_{N_B}) \end{aligned} \tag{7}$$

where D_+, D_- and D_{Li} are the self-diffusion coefficients of cation, anion and lithium ion, respectively. Furthermore, by using these relations, we obtain

$$\frac{D_+}{D_-} = \alpha \left(\frac{1}{N_B}\right)^{\zeta_+ - \zeta_-}, \qquad \frac{D_{Li}}{D_-} = \alpha \left(\frac{1}{N_B}\right)^{\zeta_{Li} - \zeta_-}. \tag{8}$$

Here, α is a constant related with the values of the self-diffusion coefficients at the high temperature limit. Figure 3 shows the temperature dependence of the ratio, D_{cation}/D_{anion}, for the solutions (a) Li-TFSA(FSA)/P_{13}-TFSA(FSA) and (b) Li-TFSA(FSA)/emim-TFSA(FSA), respectively. In these figures, the curves following the experimental data are given by Eq. (8). We can see that Eq. (8) reproduces roughly the trend of the ratio D_{cation}/D_{anion} over the measured temperature range. From Figure 3, it is observed that for the TFSA-based systems, D_{P13}/D_{TFSA} and D_{emim}/D_{TFSA} deviate more largely from unity than D_{Li}/D_{TFSA}. In addition, the result of the figures suggests that the diffusion mechanism of the ILs-Li based on $TFSA^-$ is different from that based on FSA^-.

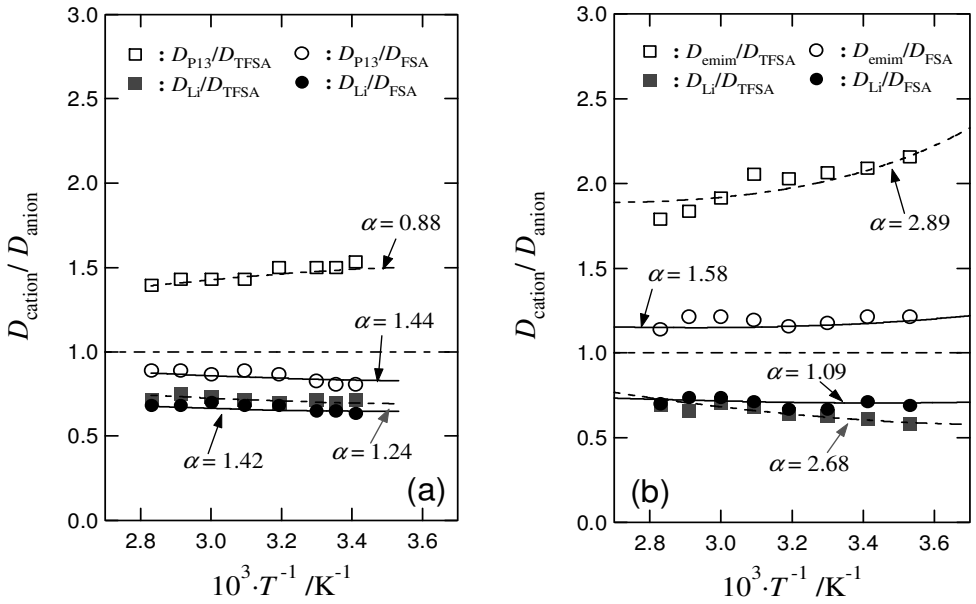


Figure 3. (a) Temperature dependence of the ratio, D_{cation}/D_{anion}, for Li-TFSA(FSA)/P_{13}-TFSA(FSA). (b) Temperature dependence of the ratio, D_{cation}/D_{anion}, for Li-TFSA(FSA)/emim-TFSA(FSA).

Saito *et al.* have pointed out [12] that solvated species, or aggregated species between Li^+ and $TFSA^-$ such as $Li(TFSA)_{n+1}^{n-}$ could exist in the Li-TFSA/BMI-TFSA systems. From the result of Figure 3, it is also speculated that aggregates combined with Li^+ and anions exist, since the deviation of D_{Li}/D_{TFSA} from unity is less than that in D_{P13}/D_{TFSA} and D_{emim}/D_{TFSA}. That is, lager deviation from unity means more dissociated, as described by Eqs. (5) and (6). In other words, the less the deviation from the unity is, the larger amounts of aggregates are included in the systems.

The result of Figure 3, or the validity of Eq. (8), is based on the correlation between the diffusivity and the cooperativity, $D \propto (N_B^{-1})^{\zeta}$. According to this relation, it is expected that the diffusivity increases when the cooperativity is lower. That is, less cooperative system exhibits lower viscosity, and accordingly, higher diffusivity and ionic conductivity. This picture is consistent with the experimental observations in the ILs systems investigated by other groups [9, 10]. Microscopically speaking, it suggests that the translational diffusivity and charge diffusivity could occur via the bond-formation and bond-breaking between the liquid components. This conjecture is expected to be closely related with the decoupling phenomena discussed by Videa and Angell [27].

In our recent work, we examined the relation between the ionic conductivity σ, the molar conductivity Λ, and the viscosity η for the same ILs-Li systems of the present study. Usually, the mechanism of charge transport responsible for the ionic conduction is discussed in the light of the Nernst–Einstein and the FSE laws, and the Walden rule [8].

With the results of the present study, we propose that the MC described by Eq. (3) provides a new point of view to study the transport property and the ionization condition of ILs and ILs-Li solutions.

5. Conclusion

In the present contribution, it was discussed that the ionization condition in ILs-Li is associated with the molecular cooperativity obtained by the BSCNF model. The ionization condition proposed by Saito *et al*. gives an effective way to evaluate the degree of the dissociation in ILs-Li. In this study, we applied these notions to Li-TFSA(FSA)/P_{13}-TFSA(FSA) and Li-TFSA(FSA)/emim-TFSA(FSA) systems. The present study suggests that the diffusion process is highly cooperative, and is promoted via the bond-formation and bond-breaking between the ionic components. We suggest that the MC described by the BSCNF model gives a new viewpoint to understand the transport property and the ionization condition of ILs and ILs-Li solutions.

References

1. K. R. Seddon, *J. Chem. Tech. Biotechnol.* **68**, 351 (1997).
2. H. Matsumoto, H. Sakaebe, K. Tatsumi, M. Kikuta, E. Ishiko and M. Kono, *J. Power Sources* **160**, 1308 (2006).
3. M. Galiński, A. Lewandowski and I. Stępniak, *Electrochim. Acta* **51**, 5567 (2006).
4. S. Nazari, S. Cameron, M. B. Johnson and K. Ghandi, *J. Mater. Chem. A* **1**, 11570 (2013).
5. X. Sun, Y. Ji, J. Chen and J. Ma, *J. Rare Earths* **27**, 932 (2009).
6. G.-c. Tian, J. Li and Y.-x. Hua, *Trans. Nonferrous. Met. Soc. China* **20**, 513 (2010).
7. N. A. Stolwijk and Sh. Obeidi, *Electrochim. Acta* **54**, 1645 (2009).
8. K. R. Harris, M. Kanakubo, N. Tsuchihashi, K. Ibuki and M. Ueno, *J. Phys. Chem. B* **112**, 9830 (2008).
9. H. Tokuda, K. Hayamizu, K. Ishii, Md. A. B. H. Susan and M. Watanabe, *J. Phys. Chem. B* **109**, 6103 (2005).
10. K. Hayamizu, S. Tsuzuki, S. Seki, K. Fujii, M. Suenaga and Y. Uemebayashi, *J. Chem. Phys.* **133**, 194505 (2010).
11. S. Tsuzuki, K. Hayamizu and S. Seki, *J. Phys. Chem. B* **114**, 16329 (2010).
12. Y. Saito, T. Umecky, J. Niwa, T. Sakai and S. Maeda, *J. Phys. Chem. B* **111**, 11794 (2007).
13. H. Kataoka and U. Saito, *J. Phys. Chem. B* **106**, 13064 (2002).
14. M. Ikeda and M. Aniya, *J. Phys. Soc. Jpn.* **79**, Suppl. A 150 (2010).

15. M. Ikeda and M. Aniya, *J. Rare Earths* **29**, Special issue 164 (2011).
16. M. Ikeda and M. Aniya, *Solid State Ionics,* in press (2014).
17. M. Aniya, *J. Therm. Anal. Calorim.* **69**, 971 (2002).
18. M. Ikeda and M. Aniya, *Materials* **3**, 5246 (2010).
19. K. Hayamizu, Y. Aihara, H. Nakagawa, T. Nukuda and W. S. Price, *J. Phys. Chem. B* **108**, 19527 (2004).
20. H. Vogel, *Phys. Z.* **22**, 645 (1921).
21. G. S. Fulcher, *J. Am. Ceram. Soc.* **8**, 339 (1925).
22. G. Tammann and W. Hesse, *Z. Anorg. Allg. Chem.* **156**, 245 (1926).
23. M. Aniya and T. Shinkawa, *Mater. Trans.* **48**, 1793 (2007).
24. A. Voronel, E. Veliyulin and V. Sh. Machavariani, *Phys. Rev. Lett.* **80**, 2630 (1998).
25. S. H. Chung, R. Lopato, S. G. Greenbaum. H. Shirota, E. W. Castner Jr. and J. F. Wishart, *J. Phys. Chem. B* **111**, 4885 (2007).
26. O. Borodin, G. D. Smith and W. Henderson, *J. Phys. Chem. B* **110**, 16879 (2006).
27. M. Videa and C. A. Angell, *J. Phys. Chem. B* **103**, 4185 (1999).

PGSE NMR STUDIES ON ROOM TEMPERATURE IONIC LIQUIDS C_NMIM TFSI

ARUNKUMAR DORAI †

Institute of Multidisciplinary Research for Advanced Materials, Tohoku University, Aoba-ku, Sendai, Miyagi, Japan

REIJI TAKEKAWA, NITHYA HELLAR, NAOAKI KUWATA, JUNICHI KAWAMURA*

Institute of Multidisciplinary Research for Advanced Materials, Tohoku University, Aoba-ku, Sendai, Miyagi, Japan

Room temperature ionic liquids consisting of anions and cations have attracted much attention on account of their physical properties such as viscosity, vapor pressure, conductivity and possible usages such as electrolytes and solvents. C_nMIM (n=1, 2..) is a popular and important cation that produces thermally stable ionic liquids with various cations. NMR is one of the most important techniques to study the molecular motion and translational diffusion coefficients. To study the translational and rotational motions of ionic liquids by NMR, the diffusion coefficient (D) and relaxation time (T_1) of the individual ion are important parameters in the temperature range for which ILs are in liquid state. In the present study, ion diffusion coefficients of the cation and anion for two types of ionic liquids with different cations (EMIM, HMIM) and common anion TFSI were investigated by multinuclear pulsed field gradient spin echo NMR spectroscopy. Spin lattice relaxation time (T_1) and self-diffusion coefficient (D) of the cations and anions were measured by ^{1}H and ^{19}F NMR spectroscopy respectively in the temperature range (293 K - 373 K). The results indicate that the cations diffuse slightly faster than the anion. The spin lattice relaxation time of the cations and anions is linear within the temperature range studied. The experimental results will be discussed in detail.

Keywords: Ionic Liquid, Diffusion, PGSE NMR

1. Introduction

Room temperature ionic liquids (RTILs) are finding great interest in the recent years due to their unique properties (low vapor pressure, high thermal stability, high electrochemical potential, etc). RTILs are stable in the liquid form in a wide range of temperature including room temperature. The physicochemical

† arunphysics@gmail.com
* kawajun@tagen.tohoku.ac.jp

Proceedings of the 14th Asian Conference on Solid State Ionics (ACSSI 2014)
Copyright © 2014 ACSSI 2014 Organizers. All rights reserved.
ISBN: 978-981-09-1137-9
doi:10.3850/978-981-09-1137-9_113

properties (e.g. nonvolatility, nonflammability, chemical and thermal stability, and ionic conductivity) of the RTILs can easily be tuned according to the nature of applications since RTILs are comprised entirely of ions, making them 'designer solvents' [1-3]. In the recent years several attempts are made to gain the fundamental understanding of the unique characteristics of the new RTILs by forming new combinations using new anions ($TFSI^-$, BF_4^-, PF_6^-, etc) and cations ($RMIm^+$, P_{13}^+, $TEPP^+$, etc) and study their physical properties such as thermal behavior, density, viscosity, and ionic conductivity, as well as on chemical properties, such as solubility of liquids and gases, and polarity [3]. A lot of work has been carried out on RTILs containing $TFSI^-$ as the anion. NMR is one of the important techniques for studying molecular motions and translational diffusion coefficients. Research has been carried out to study the microscopic information about the ion dynamics, self-diffusion coefficient which directly influence physicochemical properties of the ionic liquids using multinuclear NMR [3-8]. The diffusion coefficients of the cation and anion were determined using pulsed-gradient-spin-echo (PGSE) NMR measurements. Recent reports on the measurement of the spin-lattice relaxation time ($T1$) in imidazolium based ionic liquids [9, 10], and tetrafluoroborate based ionic liquids provides detailed information on the molecular motion related to a measuring nucleus [11]. The reports on the relaxation time of the ILs are scarce and the objective of the present work is to rectify it. In the present study, we have successfully applied the pulsed-field-gradient spin-echo (PGSE) NMR method for the determination of the cationic and anionic self-diffusion coefficients of two $TFSI^-$ based RTILs, 1-ethyl-3-methylimidazolium (EMIM) and 1-hexyl-3-methylimidazolium (HMIM) trifluorosulfonyl imide (TFSI), by ^1H NMR for the cations and ^{19}F NMR for the anion. The ion transport property, conductivity and the relaxation time depending on the alkyl chain length of the cation has been studied.

2. Experimental Details

2.1. *Sample preparation*

1-ethyl-3-methyl-imidazolium bis(trifluoro-methane sulfonyl)Imide [EMIM-TFSI] and 1-hexyl-3-methyl-imidazolium bis(trifluoro-methane sulfonyl)Imide [HMIM-TFSI] of high purity grade were purchased from Iolitec Chemical Co., Inc. (Germany) and used without further purification. The chemical structures of the ionic liquids are shown in figure 1. For the NMR measurements, the samples were placed into a 5 mm NMR microtube (BMS-005J, Shigemi, Tokyo) to a height of 3 mm.

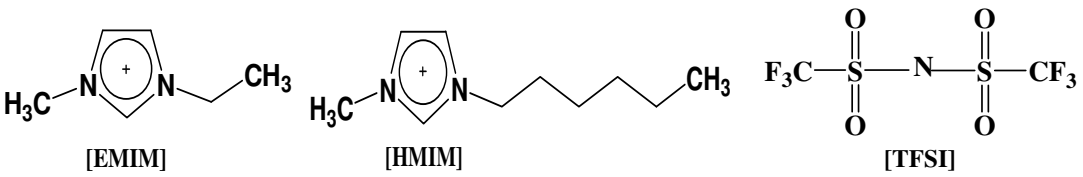


Figure 1 Structure of the ionic liquids under study

2.2. *Ionic Conductivity*

The bulk ionic conductivity of the samples was measured by complex impedance measurements, using Novocontrol alpha analyzer over the frequency range 0.1 Hz to 10 MHz. The measurement of the samples was carried out in a commercially available conductivity cell with gold interdigitated electrodes (BDS 1410) at controlled temperatures with cooling from 100 to 20 °C.

2.3. *NMR measurement*

All NMR spectra were measured on a JEOL ECA 300 spectrometer equipped with a PFG probe controlled by a JEOL console. The T_1 measurements were performed using the inversion recovery (180°-τ-90°-Acq.) sequence. The ^{1}H and ^{19}F NMR spectra were measured at frequencies of 300.5 and 282.8 respectively. All measurements were performed without sample spinning to prevent disturbance from sample motion.

A modified Hahn spin-echo based sequence incorporating a gradient pulse in each period (PGSE) was used to measure the diffusion coefficient. The echo attenuation E is related to the experimental variables and the diffusion coefficient D by

$$E = \exp[-\gamma^2 g^2 \delta^2 D(\Delta - \delta/3)] \quad (1)$$

where g is the strength of the gradient pulse of duration δ and Δ is the interval between the leading edges of the gradient pulses [12, 13]. Δ defines the time scale in the diffusion measurement, and in a homogenous system, D should be independent of Δ. A single exponential diffusion plot following equation 1 indicates free diffusion. The measurements of the ^{1}H and ^{19}F NMR frequencies for the individual nuclei have been made simultaneously at a set temperature.

3. Results and Discussion

The ^{1}H NMR spectra of the RTILs obtained by collecting the free induction decay following a 90° pulse is shown in figure 2 with the spectral assignments. The ^{19}F spectra for all the samples show a single peak.

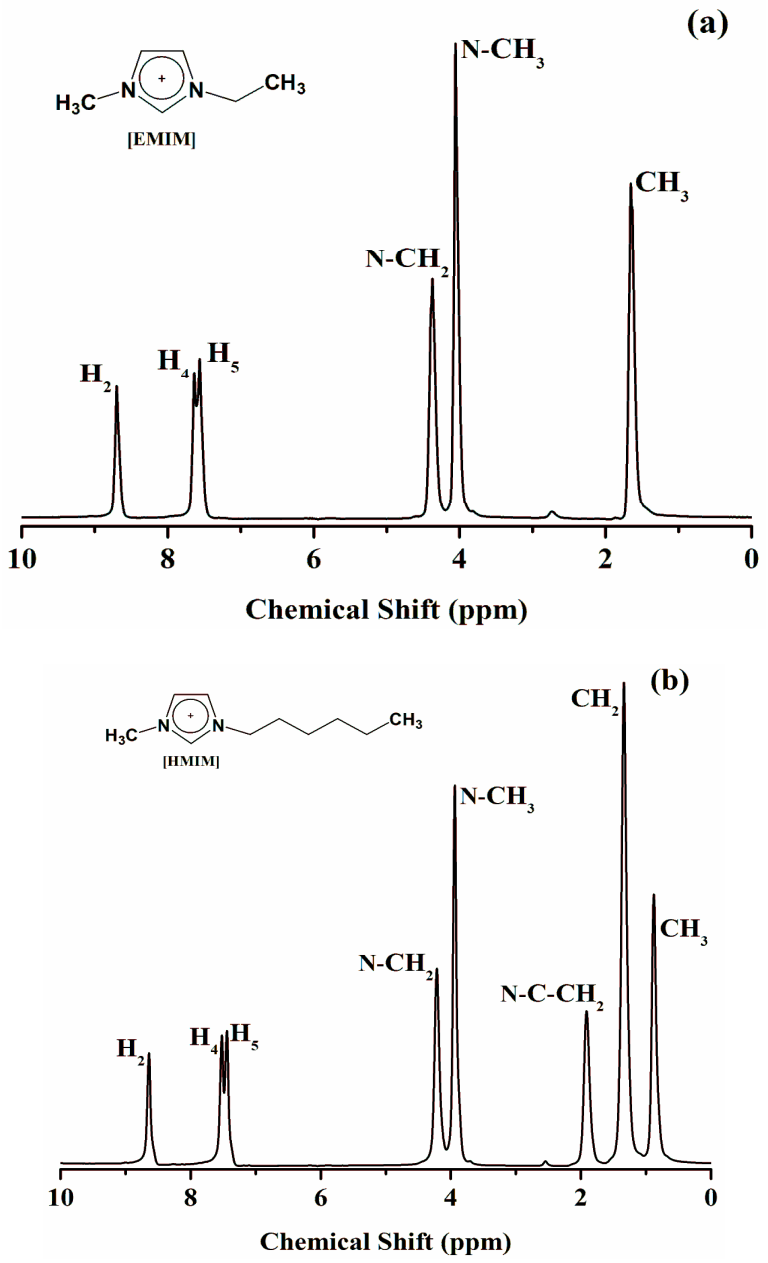


Figure 2 ^{1}H spectra of (a) [EMIM] and (b) [HMIM] measured with single pulse

Figure 3 illustrates the temperature dependent ionic conductivity for the RTILs. The ionic conductivity follows the Vogel-Fulcher-Tamman (VFT) behavior. The VFT equation for conductivity is

$$\sigma = \sigma_0 \exp[-B/(T - T_0)] \cdot \tag{2}$$

where σ_0 (Scm^{-1}), B (K), and T_0 (K) are constants. Table 1 tabulates the best-fit parameters for conductivity. EMIM-TFSI is found to exhibit high conductivity.

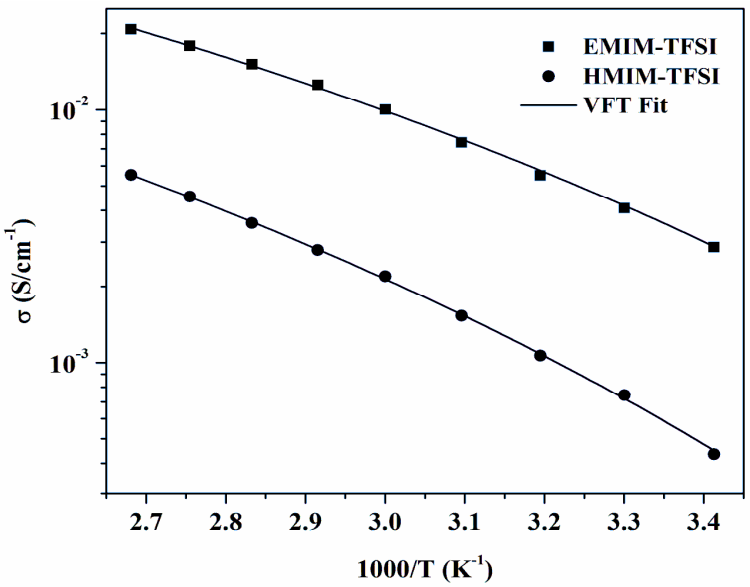


Figure 3 Temperature dependence of ionic conductivity for [EMIM] and [HMIM]-TFSI

Table 1. VFT Equation parameters of Ionic conductivity data

$\sigma = \sigma_0 \exp[-B/(T - T_0)]$			
	$\sigma_0/10^{-1}$ Scm^{-1}	$B/10^{-1}$ K	T_0/K
[EMIM-TFSI]	4.411±0.5	2.73±0.18	160±2
[HMIM-TFSI]	5.716±0.6	3.16±0.2	164±1

Figure 4 illustrates the temperature dependence of self-diffusion coefficients of the cations (D_{cation}) and (D_{anion}) for the RTILs. The simple summation of the cationic and anionic self-diffusion coefficients for the RTILs is also shown in the figure. The temperature dependency of diffusion coefficients exhibit curved profile, suggesting VFT behavior [14-16]. The VFT equation for diffusivity is

$$D = D_0 \exp[-B/(T - T_0)] \cdot \quad (3)$$

where the constants D_0 (m^2s^{-1}), B (K), and T_0 (K) are adjustable parameters. Table 2 presents the best fit of the self-diffusion coefficients. The curves calculated using the best-fit parameters and equation 3 is shown as solid lines in Figure 4. The summation of the cationic and anionic diffusion coefficients shows that the diffusion coefficient of EMIM > HMIM in the measured temperature range.

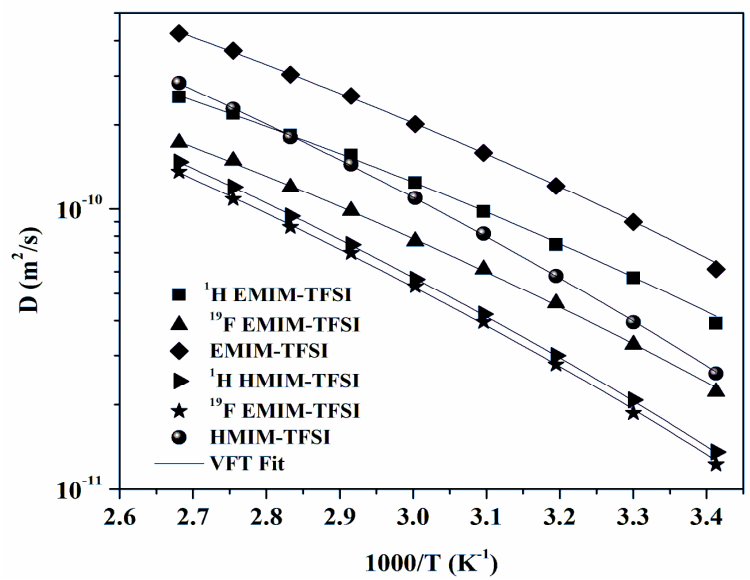


Figure 4 Temperature dependent self-diffusion coefficients of the cation, anion and the summation of cation+anion for [EMIM] and [HMIM]-TFSI.

Table 2. VFT Equation parameters of self-diffusion coefficient data

$D = D_0 \exp[-B/(T - T_0)]$				
IL	Nuclei	$D_0/10^{-6}$ Scm^{-1}	$B/10^{-1}$ K	T_0/K
EMIM-TFSI	^1H	3.382±0.10	4.33±0.11	138±1
	^{19}F	6.849±0.12	4.83±0.12	138±1
	$^1H+^{19}F$	8.664±0.12	4.52±0.10	138±1
EMIM-TFSI	^1H	0.979±0.15	6.49±0.11	133±2
	^{19}F	0.792±0.2	6.43±0.10	133±2
	$^1H+^{19}F$	1.818±0.12	6.49±0.31	133±2

Figure 5 shows the apparent transference number of the cations for the RTILs. From the figure, EMIm having smaller alkyl chain length is found to be inversely dependent on the temperature. On the other hand HMIM having comparably a longer alkyl chain length shows mostly undisturbed nature with respect to temperature indicating the influence of alkyl chain length in the cations of the RTILs on the apparent transference number. The apparent transference number value of above 0.5 for HMIM indicates that the cations diffuse faster than the anions even though the cationic radius is larger than the anion. The results are identical to the previous reports with same anion [3]. The high transference number value (0.65) for EMIM may be due to the planar structure of the cationic backbone [3].

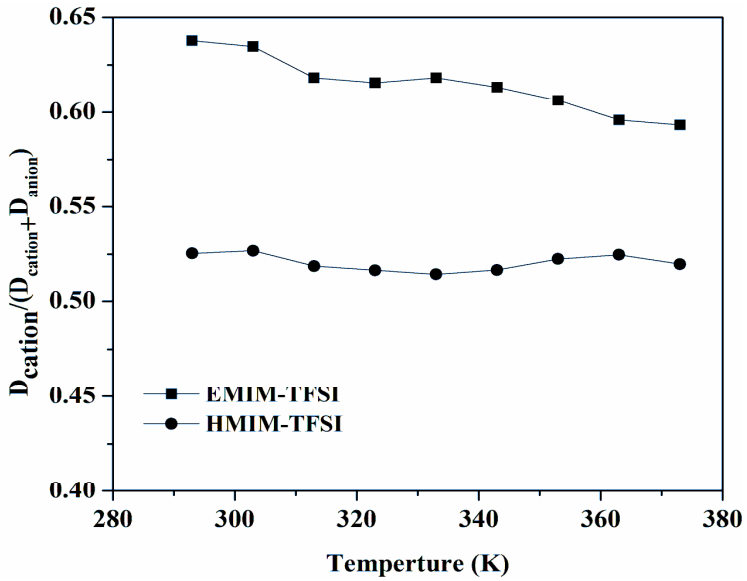


Figure 5 Apparent cationic transference numbers for the RTILs

The spin-lattice relaxation times (T_1) measured using ^1H and ^{19}F NMR for the RTILs are plotted against temperature and shown in figure 6. T_1 was measured for the all the components observed in the ^1H NMR spectra. Even though a non-linear behavior is observed for T_1 for the components, a well-defined minimum is not observed in any of the RTILs in the present temperature range. Similar behavior is also observed for ^{19}F relaxation measurement. Since no minimum is observed within the temperature range measured, T_1 measurements will be carried out in the low temperature range.

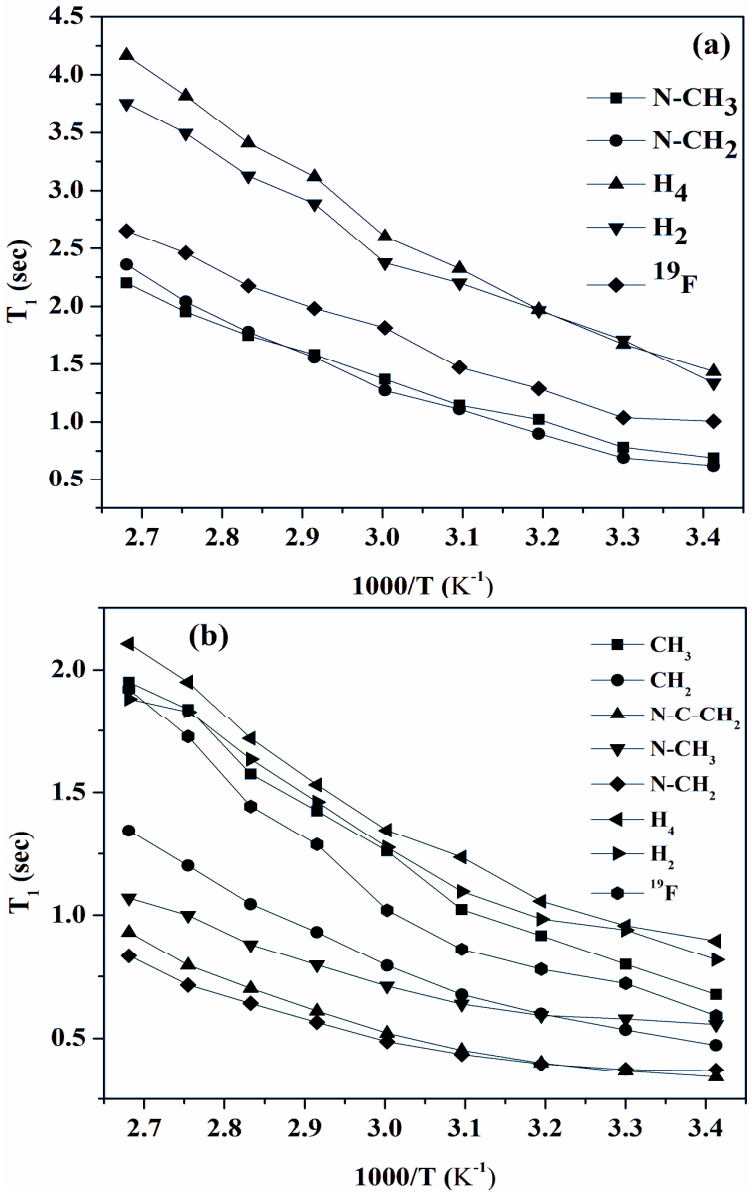


Figure 6 Arrhenius plots of T_1 of ^1H and ^{19}F NMR for (a) EMIM-TFSI and (b) HMIM-TFSI

4. Conclusion

Ionic liquids composing of cations with different alkyl chain length and a common cation were studied by measuring the self-diffusion coefficients and spin lattice relaxation time T_1 by ^1H and ^{19}F NMR spectroscopy in the

temperature range 293-273 K. Arrhenius plots for self-diffusion coefficient for both nuclear species exhibit VTF-type curvature. The apparent self-diffusion coefficient indicates that irrespective of the cationic size, the cationic diffusion coefficient is higher than the anion. Arrhenius plots for the spin-lattice relaxation T_1 does not exhibit any minima within the temperature range measured irrespective of the nuclei.

Acknowledgments

This research was performed under the project "High-efficiency rare element extraction technology" supported by the Ministry of Education, Culture, Sports, Science and Technology (MEXT).

References

1. J. D. Holbrey, K.R. Seddon, Ionic Liquids. Clean Prod. Proc. 1 (4), 223 (1999)
2. A. Muhammad, M.I. Abdul Mutalib, T. Murugesan, Z. Man and A.Bustam, Journal of Applied Sciences, 11 (13): 2452 (2011).
3. Hiroyuki Tokuda, Kikuko Hayamizu, Kunikazu Ishii, Md. Abu Bin Hasan Susan, and Masayoshi Watanabe, J. Phys. Chem. B 109 6103 (2005).
4. Hayamizu, K.; Aihara, Y.; Nakagawa, H.; Nukuda, T.; Price, W. S. J. Phys. Chem. B 108, 19527 (2004)
5. Hayamizu, K.; Tsuzuki, S.; Seki, S.; Ohno, Y.; Miyashiro, H.; Kobayashi, Y. J. Phys. Chem. B, 112, 1189 (2008)
6. V. Baran, M. Colonna, M. Di Toro and V. Greco, Phys. Rev. Lett. **86**, 4492 (2001)
7. Hiroyuki Tokuda, Kikuko Hayamizu, Kunikazu Ishii, Md. Abu Bin Hasan Susan, and Masayoshi Watanabe J. Phys. Chem. B 108, 16593 (2004)
8. Azita Ahosseini, Laurence R. Weatherley, and Aaron M. Scurto, J. Chem. Eng. Data, 56, 3715 (2011)
9. Song H. C, Richard L, Greenbaum S.G, Shirota H, Castner E. W. Jr., and James F. Wishart J. Phys. Chem. B 111, 4885 (2007)
10. Kikuko Hayamizu, Seiji Tsuzuki, Shiro Seki, and Yasuhiro Umebayashi, J Chem Phys 135, 84505 (2011)
11. Kikuko Hayamizu, Seiji Tsuzuki, Shiro Seki, and Yasuhiro Umebayashi J. Phys. Chem. B, 116, 11284 (2012)
12. Stejskal, E. O.; Tanner, J. E. J. Chem. Phys., 42, 288 (1965)
13. Tanner, J. E. J. Chem. Phys. 52, 2523 (1970)
14. Vogel, H. Phys. Z. 22, 645 (1921)
15. Tammann, G.; Hesse, W. Z. Anorg. Allg. Chem. 156, 245 (1926)
16. Fulcher, G. S. J. Am. Ceram. Soc. 8, 339 (1925)

POLYVINYLIDENE FLUORIDE AND COBALT BASED NANOCOMPOSITES EXHIBITING HIGH DIELECTRIC CONSTANT

K. VASUNDHARA, B. P. MANDAL, A. K. TYAGI
Chemistry Division, Bhabha Atomic Research Centre, Mumbai-400085, India
Email id: bpmandal@barc.gov.in, aktyagi@barc.gov.in

Polymer dielectrics have been drawing ever increasing interest due to their easy processing, flexibility, mechanical strength and high dielectric break down field. Among the various polymers, β-PVDF (polyvinylidene fluoride) has better technological importance due to its comparatively high dielectric constant. In this work, β phase of PVDF has been stabilized by using cobalt nanoparticle. Additionally the dielectric constant of the composite has been improved due to presence of cobalt nanoparticle. Cobalt nanoparticle was synthesized in alcoholic medium by using $NaBH_4$ as reducing agent. The obtained cobalt nanoparticle was combined with PVDF to fabricate a dielectric composite with high dielectric constant. FTIR spectra, X-ray diffraction were used to characterize the studied sample. An increase in the amount of β-phase in Co containing composites has been observed by the X-ray diffraction study. In order to study the effect of Co nanoparticle on dielectric properties of PVDF, the complex dielectric properties were investigated. The relative dielectric constant observed for unloaded PVDF at ambient temperature observed is about 4 at 1 kHz and it increases with the loading of Co nanoparticle. The dielectric constant of the composite with 20 vol% of Co at 1 kHz increased to 23. The dielectric loss tangent is significantly low in the frequency 10^3 to 10^5 Hz. The higher dielectric loss at low frequency and the decreasing trend with increasing thickness of polymer insulation layer confirm the existence of an interfacial relaxation. The electrical conductivities of all samples are in the range of 10^{-10} to 10^{-9} S/cm which indicate that cobalt has not reached the percolation system.

Introduction:

The continuous increase of energy requirement and decrease in the natural sources causes the demand for the energy storage capacitors. As the requirement for the development of new energy storage materials.one should focus on materials which have the high dielectric constant and high dielectric break down strength[1,2], because the energy density of ideal dielectric materials is

Proceedings of the 14th Asian Conference on Solid State Ionics (ACSSI 2014)
Copyright © 2014 ACSSI 2014 Organizers. All rights reserved.
ISBN: 978-981-09-1137-9
doi:10.3850/978-981-09-1137-9_010

proportional to the dielectric constant and square of the breakdown field (UE α ε_r E_b^2). Both the ceramics and polymers are traditionally used as capacitors. Even though, the ceramic dielectric materials have the high dielectric constant with relatively low dielectric loss, but their higher sintering temperature and poor flexibility limits their usage. On the other hand the polymeric dielectrics have been getting more attention due to their high flexibility, low cost and high dielectric breakdown strength [3,4]. Polyvinylidene fluoride (PVDF) is one of the promising candidates due to their relatively high dielectric constant and non-toxicity compared to the other polymers. The dielectric constant of PVDF has been improved by blending with other fillers. Two types of fillers are reported in literatures. First, the introduction of the high dielectric constant ceramic materials with higher dielectric constant such as $BaTiO_3$, CCTO($CaCu_3Ti_4O_{12}$), $PbZrTiO_3$ etc [5-7] in to the polymer to form 0-3 type composites. Second, the conductive filler like metal nanoparticle, graphene, conductive carbon etc have also been added to improve the dielectric constant of PVDF [8].

Due to difference in the surface characteristics of the ceramic filler and polymer, uniform dispersion of the ceramic filler was found to be difficult. As a result of the electric field within the film becomes inhomogeneous. These types of composites exhibit lower dielectric constant [9]. On the other hand, more than 50% of ceramics filler is required to achieve the high dielectric constant. At such high concentration of the ceramics, pores, voids, and imperfections are developed in the matrix results lowering of the break down voltage. By surface modification amount of ceramic filler in the matrix can be increased to get the higher dielectric permittivity. Dopamine modified $BaTiO_3$-PVDF nano composite is found to have higher breakdown strength because dopamine facilitate the homogenous dispersion of $BaTiO_3$ in PVDF. It also increases the interfacial polarization which causes the increase in the dielectric constant of the composites[10].

The dielectric constant of the polymer can also be increased by the conductive filler approach. Large enhancement of the dielectric permittivity of composite observed even at the lower concentration of the conductive filler. This low concentration of filler is helpful to preserve the mechanical flexibility of polymer. Commonly used metal nanoparticle for these type of composites are Ni, Zn, Al, Ag, Cu and carbon based particles such as carbon black (CB), graphite carbon nanotubes etc.[8,11-16]. Though the conductive filler polymer composites have higher dielectric constant still they are limited by the higher dielectric loss with low breakdown field due to conductive paths formed by the

conductive fillers the percolation limit. This dielectric loss can be minimized by the introducing insulating layer between the conductive fillers, which can acts as a potentials barrier for the transport of electrons. Xie et al synthesized the core shell type of Ag@$BaTiO_3$ exhibiting remarkably improved energy density and energy storage efficiency in comparison with the nanocomposite with $BaTiO_3$ nanoparticle [17].

In this work, we report the design of flexible, self-standing and mechanically stable dielectric films, composed of ferroelectric PVDF and ferromagnetic Co nanoparticle. Co metal nanoparticle was synthesized in alcoholic medium. PVDF was used as polymer matrix because of its high dielectric constant. A significant improvement in dielectric permittivity is observed in the PVDF-Co composites.

Experimental Materials

Cobalt acetate from sigma Aldrich, polyvinylidene fluoride (PVDF) obtained from sigma Aldrich, N-N dimethylformamide(DMF), sodium borohydride ($NaBH_4$), ethylene glycol(OH-CH_2-CH_2-OH) and sodium hydroxide(NaOH) were obtained from local commercial sources.

Synthesis of Cobalt nanoparticle:

All the chemicals used in this process are reagent grade and used without any further purification. Calculated amount of cobalt acetate has been dissolved in ethylene glycol at 100^{o}C. 1g of NaOH is added to this solution, after that round bottom flask was removed from the oil bath, and solution was cooled to room temperature and 0.5g of $NaBH_4$ is added. At a temperature of 140^{o}C black color cobalt nanoparticle were formed after about 2 h stirring. Black color precipitate obtained by this method was separated by permanent magnet and washing was performed with distilled water for three times and finally once with methanol.

Preparation of PVDF-Co composites:

The ferroelectric PVDF/Co composites were prepared by grinding the PVDF powder and cobalt nanoparticle. The mixed powder then dispersed in 10ml DMF at room temperature and the mixer was sonicated for 1 hr. After sonication the mixture was poured on cleaned glass slide and then thermally treated at 80^{o}C in static air atmosphere to ensure the evaporation of DMF.

Finally dried self sustained PVDF and PVDF-Co composite polymer films were obtained.

Characterization

The phase purities of the studied samples were investigated by powder X ray diffraction (XRD) studies. The powder XRD patters of the samples were recorded on Philips X-Pert Pro diffractometer using monochromatic CuKα radiation (λ= 1.54 Å) obtained from copper target using an in-built Ni filter.

FTIR spectra of PVDF and PVDF-Co composites were recorded using a Bomem MB102FTIR (model 610) equipped with DTGS detector.

Both the sides of the thick films were coated by Electrolube's conductive silver paint and dried at room temperature The dielectric properties of the samples has been measured using Novacontrols Alpha–A high performance frequency analyser. All the samples measurements were done over a frequency range of 5MHz to 10Hz at room temperatures

Results and Discussion

X-ray Diffraction study

Fig(1) shows the XRD pattern of the as synthesized Co nanoparticle and PVDF-Co nano composites. All the diffraction peaks of the Co metal are matching with the PCPDF data with card number 15-0806 indicating formation of phase pure cobalt nanoparticles. No other characteristics peaks corresponding to impurities are observed. As it is know, PVDF has four different crystalline phases, peaks corresponding to the both α and β phase are observed From the XRD plots, the peak for β phase at 20.7 ± 0.2^{o} corresponding to the (110) and (200) planes has been observed. The peak observed at 26.5 ± 0.2^{o} corresponding to the (021) of α plane .After incorporation of Co metal nano particle in to the polymer matrix, the intensity of the PVDF peaks reduced. The peak corresponding to the Co metal is clearly visible due to high Z of Co metal than the polymer PVDF. This indicates the existence of the Co nanoparticle in the polymer matrix. The amount of the β phase increases with the Co concentration in the composites.

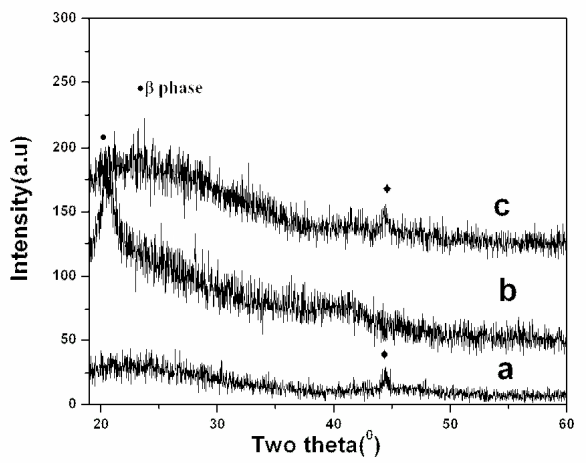


Fig 1**:** Typical XRD pattern of (a) Cobalt nanoparticle (b) PVDF (c) Co-PVDF composite

FTIR studies:

Fig (2) shows the FTIR spectra of PVDF and PVDF-Co nano composites. It was observed that composite films and polymer film consist of α, β and γ phases. The characteristic bands at 612, 763, 796, 853 and 975 cm^{-1} corresponding to the α phase. The band at 612cm^{-1} was assigned to mixed modes of CF_2 bending and C-C-C skeletal vibration. Another characteristic band of α phase at 763 cm^{-1} corresponds to the rocking vibration of the PVDF chain [18]. The β phase present in the composite characterized by the peaks at 840, 511, 878 and 472 cm^{-1}. The absorbance band at 878 obtained from CH_2 rocking and CF_2 stretching. The 510 cm^{-1} band related to CF_2 bending mode perpendicular to the chain axis and parallel to the polar b axis [19, 20].

While the bands observed at 1070, 1231 and 1406 cm^{-1} are attributed to bending vibration of C-C-C , waging and rocking vibration of CH_2 and in plane bending or scissoring vibration of CH_2 respectively. From the both XRD and IR data it was inferred that with the addition of Co metal nanoparticle β phase of PVDF increases.

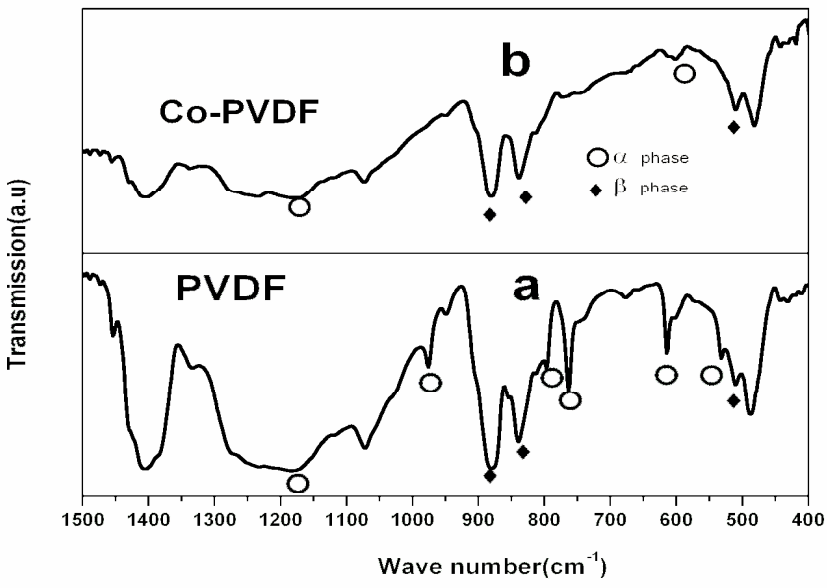


Fig 2: FTIR spectra of (a) PVDF (b) Co-PVDF composite

Dielectric properties:

Variation of the dielectric properties of the pure PVDF and PVDF/Co composite at room temperature is shown in the Fig(3a,b). The dielectric permittivity of both pure PVDF and composites increases with decrease in frequency because of increase in the dipolar contribution. Introduction of the Co metal nanoparticle in the PVDF significantly increases the dielectric permittivity. For example the dielectric permittivity of PVDF/Co composite at 100 Hz is one order higher than the pure PVDF. In case of these types of composites, charge accumulation takes place at the interfaces of the components causing Maxwell-Wagner-Sillar polarization. Hence dielectric constant increases with the cobalt concentration. At the same time the dielectric loss of the composite films can also higher than the PVDF. The tanδ observed in our sample is low. The low dielectric loss can be explained because our sample is made in polyol medium and ethylene glycol moiety is coated on the surface of the Co metal nanoparticle which serves as a insulating interface among Co nanoparticles. The coated cobalt nanoparticles prevent the leakage current. The conductivity of the composites also measured and it is observed that the PVDF/Co composite films at low frequency are around 10^{-10}S/cm. It increases with increase in the frequency. Although from earlier reports the conductivity of the conductive metal-composite increases rapidly near percolation limit due to insulator-conductor transition. Such

dramatic increase in the conductivity has not been observed in our PVDF-Co composites. From our experimental results, the behavior of increase in conductivity with frequency as well as lower conductivity value indicates the PVDF-Co composite materials are electrically insulating. It indicates that our samples have not reached the percolative limit. Similar results are observed in the PVDF-GO-PANI composites. In these composites sudden increase in the conductivity is not observed and dielectric loss are also very low (0.05) [21]. This is due to dielectric PANI acts as an isolated barrier to prevent the direct contact of the graphene nanosheets. If the system has reached the percolation threshold a sudden increase in the dielectric permittivity as well as a very higher conductivity could be obtained. Yuan et al successfully prepared a PANI/PVDF composite films when the volume fraction of the PANI around at 0.05 a very high conductivity value (10^{-2})is obtained and this does not changes in the whole region of frequency which indicates the percolation limit of f_c=0.05[22] .

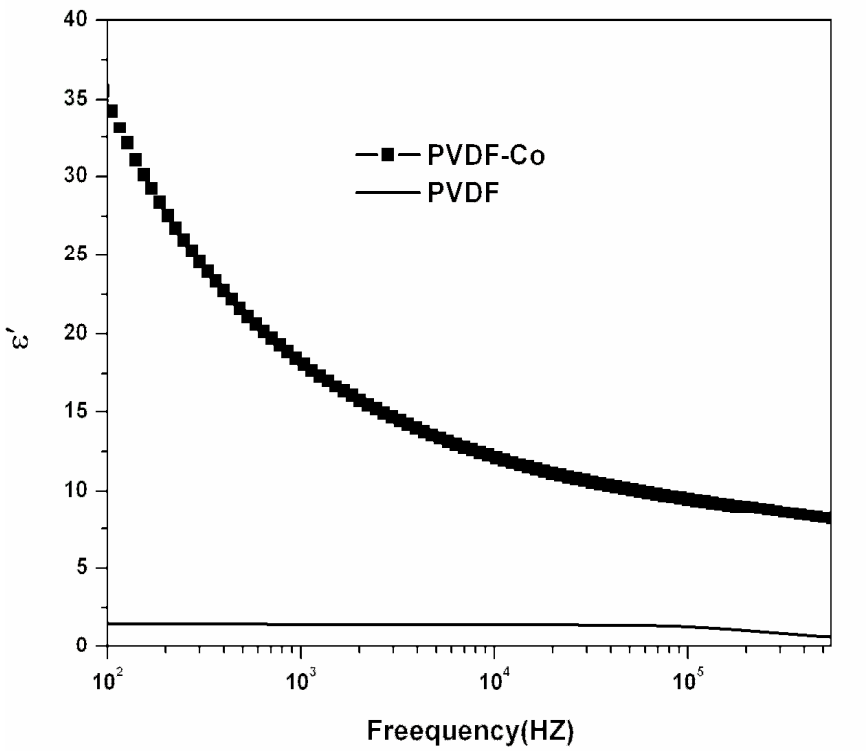


Fig 3a Variation of dielectric permittivity of PVDF and PVDF-Co composite as a function of frequency at room temperature

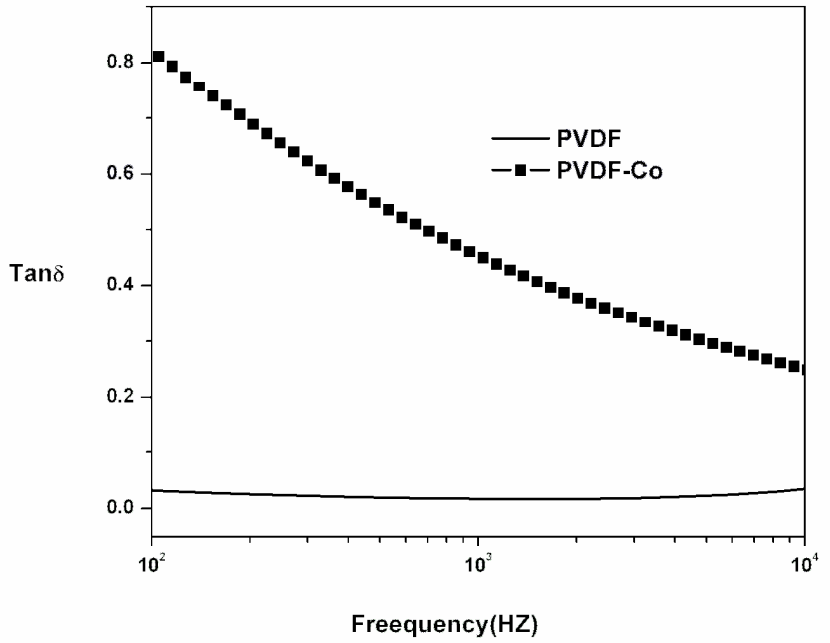


Fig 3b Variation of dielectric loss of PVDF and PVDF-Co composite as a function of frequency at room temperature

Conclusion:

In summary cobalt nanoparticle were prepared by the polyol method and PVDF-Co nanocomposite prepared by the cast method. The resulting PVDF-Co nanocomposite films were used for the characterization and dielectric measurements. XRD results show the phase purity of the sample. From the FTIR studies different types of phases present in the PVDF are identified. The experimental result of this work shows that polymer nanocomposite with PVDF-Co exhibits high dielectric permittivity than pure PVDF. The achieved high dielectric permittivity achieved can be explained by the interfacial polarization

Acknowledgements: This project is financially supported by Department of Atomic Energy's Science Research Council (DAE-SRC) sanction number no. 2010/21/9-BRNS/2025 dated 7-12-2010

References:

1. W. Sarjeant, J. Zirnheld and F. MacDougall, *IEEE Trans. Plasma Sci.* **26**, 1368(1998).

2. Y. Rao and C. P. Wong, *J. Appl. Polym. Sci*. **92,** 2228(2004).
3. M. Zhang, H. F. Li, M. Poh, F. Xia, Z. Y. Cheng, H. S. Xu and C. Huang, *Nature*.**419,** 284(2002).
4. S. Das and J. Appenzeller, *Nano Lett.* **11**, 4003(2011).
5. Z. M. Dang, Y. Q. Lin, H. P. Xu, C. Y. Shi and J. Bai, *Adv. Funct. Mater***. 18,** 1509(2008).
6. M. Arbatti, X. B. Shan and Z. Y. Chong, *Adv. Mater*. **19**,1369(2007).
7. J. Yao, C. Xiong, L. Dong, C. Chen, Y. Lei, L. Chen, R. Li, Q. Zhu and X. Liu, *J. Mater. Chem*., **19**,2817(2009).
8. M. Panda, V. Srinivas and A. K. Thakur, *Appl. Phys. Lett*. **92**,132905(2008).
9. Y. Bai, Z. Y. Cheng, V. Bharti, H. S. Xu and Q. M. Zhang, *Appl. Phys. Lett.* **76**, 3804(2000).
10. Yu Song, Yang Shen, Haiyang Liu, Yuanhua Lin, Ming Li and Ce-Wen Nan *J. Mater. Chem*. **22,**8063(2012).
11. Y. Zhang, Y. Wang, Y. Deng, M. Li and J. Bai, *Mater. Lett.* **72,**9(2012).
12. J. W. Xu and C. P. Wong, *Appl. Phys. Lett*. **87,** 082907(2005).
13. X. Y. Huang, P. K. Jiang and L. Y. Xie, *Appl. Phys. Lett*. **95**, 242901(2009).
14. J. K. Yuan, W. L. Li, S. H. Yao, Y. Q. Lin, A. Sylvestre and J. Bai, *Appl. Phys. Lett.* **98,** 032901(2011).
15. F. He, S. Lau, H. L. Chan and J. Fan, *Adv. Mater*. **21**, 710(2009).
16. H. P. Xu, Z. M. Dang, M. J. Jiang, S. H. Yao and J. Bai, *J. Mater. Chem.* **18**, 229(2008).
17. Liyuan Xie,Xingyi Huang, Bao-Wen Li, Chunyi Zhi,Toshikatsu Tanaka and Pingkai Jiang, *Phys. Chem. Chem. Phys.* **15**, 17560(2013).
18. A. K. Zak, W. C. Gan, W. H. A. Majid, M. Darroudi and T. S. Velayutham, *Ceram. Int*. **37**, 1653(2011).
19. Chi Chen, G.; Su, J.; Fina, L.J. FTIR-ATR Studies of Drawing and Poling in Polymer Bilaminate Films. *J. Polym. Sci., Polym. Phys.* **32,** 2065(1994).
20. B.Mattsson, H.Ericson, L.M.Torell, F.Sundholm, *Micro-Raman Investigations of PVDF-Based Proton-Conducting Membranes. J. Polym. Sci., Part A: Polym.Chem*. **37,**3317(1999).
21 He. Linxiang and Sie Chin Tjong, *RSC Adv*. **3**,22981(2013).
22. Jin-Kai Yuan, Zhi-Min Dang, Sheng-Hong Yao, Jun-Wei Zha,Tao Zhou,a Sheng-Tao Li and Jinbo Bai, *J. Mater. Chem.*,**20,** 2441(2010).

A NEW STYLE FIELD EFFECT TRANSISTOR BASED ON IONIC-ELECTRONIC CONDUCTOR COMPOSITE NANOSTRUCTURES

GUOWEI ZHANG

State Key Lab of Low-Dimensional Quantum Physics, Department of Physics, Tsinghua University, Beijing, 100084, China

ZHANMIN DONG

Department of Physics, Tsinghua University, Beijing, 100084, China

JINQUAN WEI

Key Lab for Advanced Materials Processing Technology of Education Ministry, School of Materials Science and Engineering, Tsinghua University, Beijing, 100084, China

JIA-LIN SUN†

State Key Lab of Low-Dimensional Quantum Physics, Department of Physics, Tsinghua University, Beijing, 100084, China

Collaborative Innovation Center of Quantum Matter, Beijing, China

JIA-LIN ZHU†

State Key Lab of Low-Dimensional Quantum Physics, Department of Physics, Tsinghua University, Beijing, 100084, China

We have fabricated and characterized a new style field effect transistor (FET) based on ionic-electronic conductor composite nanostructures, made of superionic conductor $RbAg_4I_5$ films and carbon nanotube (CNT) bundles. Electrical measurements reveal that the formation of ion-electron bound states (IEBSs) leads to about 76% conductance drop of CNT after the deposition of $RbAg_4I_5$ films. With increasing gate voltage V_{gb}, the drain-source current I_{ds} increases rapidly and linearly, which is ascribed to the dissociation of IEBSs under the effect of external electric fields. Our results are expected to provide potential applications in the field of nano-FET based on ion-electron interactions.

† Corresponding author: jlsun@tsinghua.edu.cn.
† Corresponding author: zjl-dmp@tsinghua.edu.cn.

Proceedings of the 14th Asian Conference on Solid State Ionics (ACSSI 2014)
Copyright © 2014 ACSSI 2014 Organizers. All rights reserved.
ISBN: 978-981-09-1137-9
doi:10.3850/978-981-09-1137-9_035

1. Introduction

Superionic conductors are materials with high ionic conductivity, which primarily use ions as charge carriers for electric currents similar to liquid electrolytes. For many years, superionic conductors have drawn considerable attention in the fields of solid-state batteries [1] and memory switches [2-4]. $RbAg_4I_5$ is a typical silver ion conductor material, which can be prepared by vacuum thermal evaporation technique [5] or pulsed laser deposition [6]. At room temperature, the ionic conductivity σ_i of $RbAg_4I_5$ is up to ~ 0.2 $\Omega^{-1}\,cm^{-1}$ [7, 8], much larger than its electronic conductivity σ_e of ~ $2.5 \times 10^{-9}\,\Omega^{-1}\,cm^{-1}$ [9]. Mixed ionic-electronic conductors (MIECs), conducting both ions and electrons, supply us an ideal medium to study the basic science of ion-electron interactions (IEIs).

Carbon nanotubes (CNTs) have been widely employed as transport channels for electrons or holes in field effect transistors (FETs) [10-12], owing to their excellent electrical properties. In Ref. [13], interesting phenomena of ion-modulated electron transport in CNTs have been observed, related to the formation/dissociation of ion-electron bound states (IEBSs). In this paper, we report the fabrication and characterization of a new style FET based on ionic-electronic conductor composite nanostructures, made of superionic conductor $RbAg_4I_5$ films and CNT bundles. Electronic transport properties of CNTs under modulation of different gate voltages were explored.

2. Experimental details

For fabrication of the FET device, as seen in Figure 1(a), we chose a SiO_2/Si wafer as the insulating substrate, on the bottom surface of which Al film was deposited to serve as back electrode. CNT films were synthesized by an improved catalytic chemical vapor deposition method [14], consisting of thousands of CNT bundles. The as-prepared CNT film with width of ~ 1 cm was spread on the insulating substrate, then two silver film electrodes at ~ 2 cm intervals were deposited on its two ends used as source and drain electrodes, respectively. Finally, $RbAg_4I_5$ films were deposited on the CNT film to partially cover it, thus the composite nanostructure sample made of CNT film and $RbAg_4I_5$ film was obtained. After that, Au film was defined as gate electrode on the top of $RbAg_4I_5$ film. Figure 1(b) is the scanning electron microscope (SEM) image of CNT films, showing that CNT bundles in the film were arbitrarily oriented and tangled together into a porous net. After the deposition of $RbAg_4I_5$, CNT bundles were coaxially wrapped by the superionic conductor film, as seen in Figure 1(c).

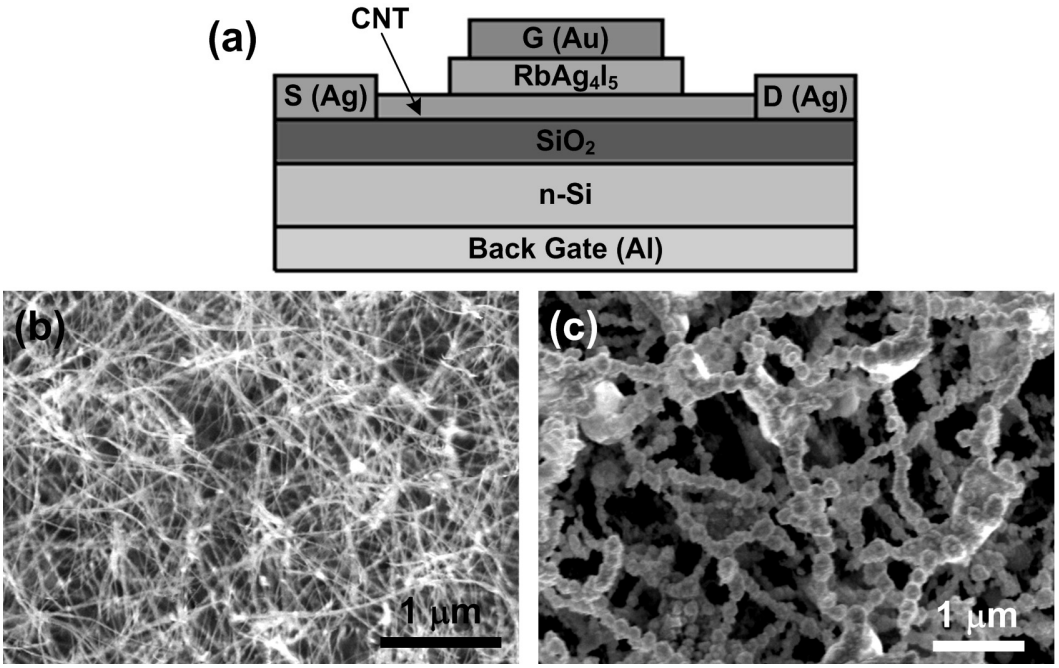


Figure 1. (a) Schematic diagram of the as-fabricated device: CNT film with width of 1 cm, the space between two silver film electrodes is 2 cm. SEM images of (b) CNT film and (c) CNT bundle/$RbAg_4I_5$ film composite nanostructures.

3. Results and discussion

Figure 2(a) shows the I-V characteristics of CNT films before and after the deposition of $RbAg_4I_5$ films within the bias voltage range of ±10 V. All the measurements were performed under vacuum conditions at room temperature and currents were recorded with a SourceMeter (Keithley 2400). Clearly, the total conductance of CNT/$RbAg_4I_5$ composite nanostructures σ_{total} decreased gradually, relative to the conductance of pure CNT σ_{CNT}, as seen in Figure 2(b). The last two I-V curves (23.5 h and 27.5 h) appeared as one, indicating that the composite nanostructure sample stabilized. After the deposition of the superionic conductor film, the conductance of CNT dropped by ~ 76%, resulted from the formation of IEBSs as proved by experiment and theory in Ref. 13. At the interface between CNT bundle and $RbAg_4I_5$ film, some of conducting electrons in CNT were confined by mobile silver ions in $RbAg_4I_5$ due to Coulomb interactions and became localized, thus the density of free carriers decreased, leading to the decrease of conductance.

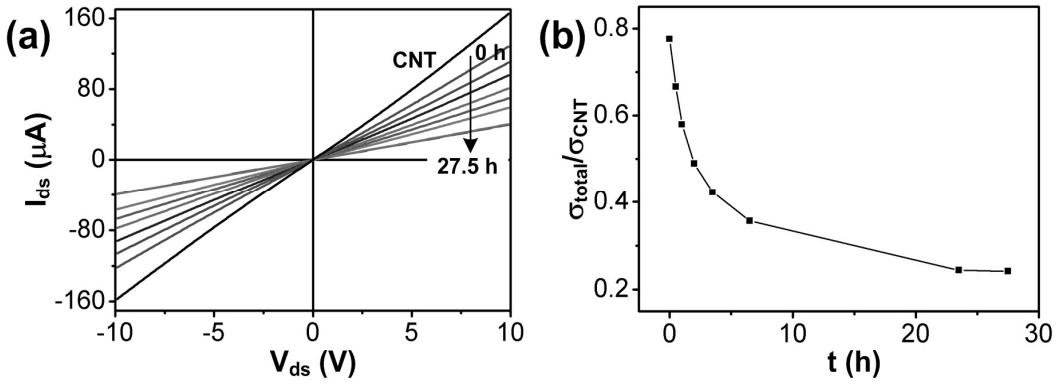


Figure 2. (a) I-V characteristics of CNT film and CNT/$RbAg_4I_5$ composite nanostructures measured at different hours after the deposition of $RbAg_4I_5$ film: 0 h, 0.5 h, 1 h, 2 h, 3.5 h, 6.5 h, 23.5 h, and 27.5 h. The two I-V cures (23.5 h and 27.5 h) overlapped. (b) Relative conductance $\sigma_{total}/\sigma_{CNT}$ calculated from Figure 2(a).

To investigate the impact of gate voltage V_{gb} on drain-source current I_{ds}, pulsed gate voltage was applied to the sample, with periods of "on" and "off" cycles both maintaining 5 s. Figures 3(a)-3(e) show the dynamic responses of CNT/$RbAg_4I_5$ composite nanostructures under modulation of different gate voltages, with drain-source voltage V_{ds} fixed at 10 V. Obviously, when V_{gb} was turned on, I_{ds} immediately increased to its maximum, and then gradually decreased. We propose that field-induced dissociation of IEBSs plays the dominant role in current increase. Under the effect of external electric fields, part of the IEBSs was dissociated, therefore these confined electrons were set free to transport to external electrodes, leading to the rapid increase of I_{ds}. On the other hand, these dissociated IEBSs formed built-in electric fields, which were in the opposite direction of external electric fields. Consequently, external electric fields were weakened, resulting in the gradual decrease in current. When V_{gb} was turned off, I_{ds} decreased immediately, attributed to the reformation of IEBSs. The response time of the sample to external electric fields is as quick as tens of milliseconds, providing possible applications in the field of high frequency electronic devices. From Figures 3(a)-3(e), it can be seen clearly that a current jump was observed just at the moment when V_{gb} was turned on, we define this current jump as ΔI_{ds}, with the exclusion of several singular points. ΔI_{ds} versus V_{gb} is plotted in Figure 3(f) and demonstrates a perfect linear relationship, indicating that I_{ds} can be modulated linearly by V_{gb}.

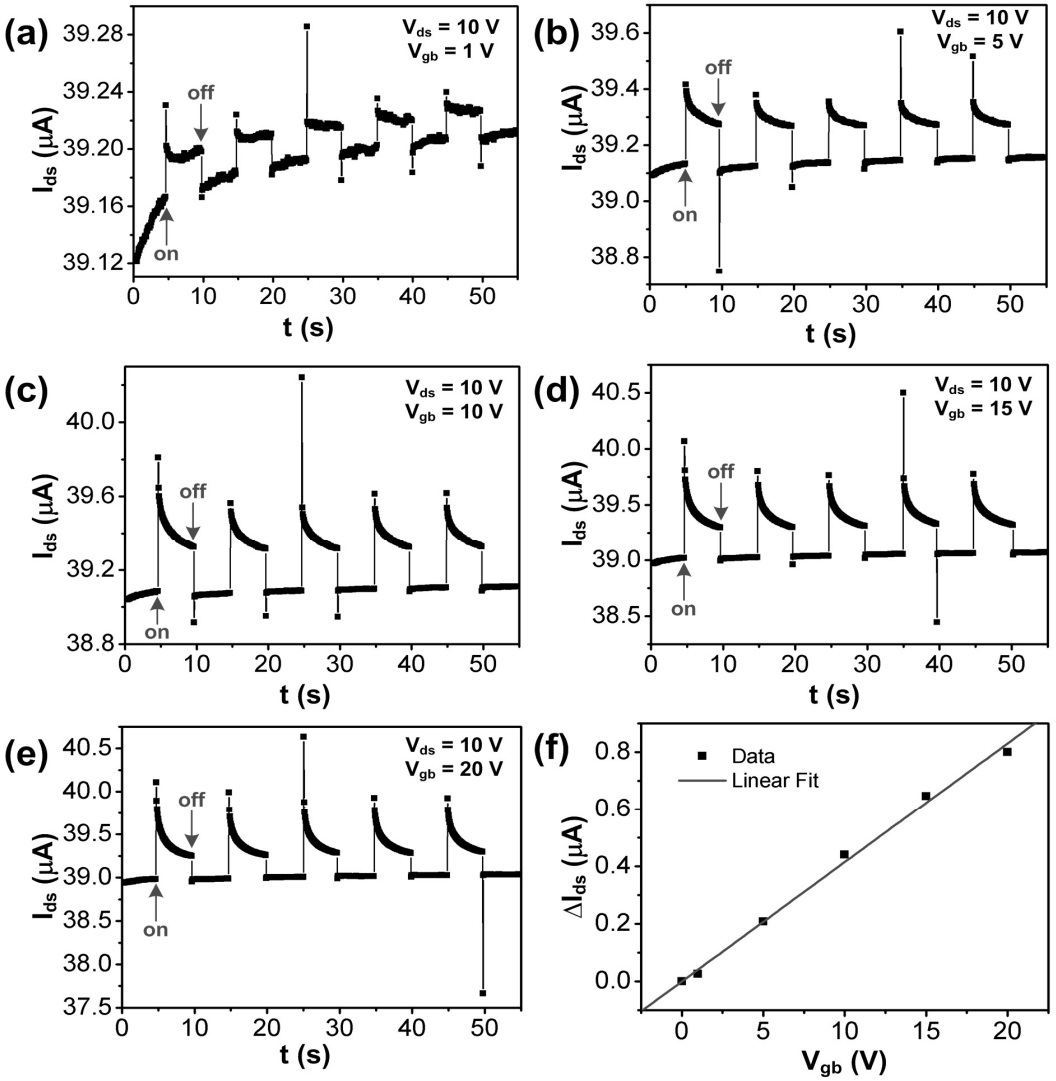


Figure 3. (a)-(e) Dynamic responses of CNT/$RbAg_4I_5$ composite nanostructures at 10 V drain-source voltage under modulation of different gate voltages with a period of 5 s. (f) Relationship of drain-source current jump ΔI_{ds} versus gate voltage V_{gb}, fitted by a linear function: $\Delta I_{ds} = 0.04152 V_{gb}$.

4. Conclusions

A new style FET based on CNT film and $RbAg_4I_5$ film has been skillfully designed, in which IEI effect has a strong impact on electron transport. The formation of IEBSs leads to a remarkable conductance decrease. Under the modulation of V_{gb}, a rapid and linear increase of I_{ds} is observed, ascribed to the dissociation of IEBSs. Our results may open up new possibilities in the field of high frequency FET.

Acknowledgments

This work was partially supported by the National Natural Science Foundations of China (Nos. 11374172, 11174172 and 11174170) and National Basic Research Program of China (2011CB921901).

References

1. J. M. Tarascon and M. Armand, *Nature* **414**, 359 (2001).
2. T. Sakamoto, H. Sunamura and H. Kawaura, *Appl. Phys. Lett.* **82**, 3032 (2003).
3. K. Terabe, T. Hasegawa, T. Nakayama and M. Aono, *Nature* **433**, 47 (2005).
4. X. F. Liang, Y. Chen, L. Chen, J. Yin and Z. G. Liu, *Appl. Phys. Lett.* **90**, 022508 (2007).
5. Y. Cao, H. S. Sun, J. L. Sun, G. Y. Tian, Z. Xing and J. H. Guo, *Chin. Phys. Lett.* **20**, 756 (2003).
6. B. Yang, X. F. Liang, H. X. Guo, K. B. Yin, J. Yin and Z G Liu, *J. Phys. D: Appl. Phys.* **41**, 115304 (2008).
7. B. B. Owens and G. R. Argue, *Science* **157**, 308 (1967).
8. S. Hull, D. A. Keen, D. S. Sivia and P. Berastegui, *J. Solid State Chem.* **165**, 363 (2002).
9. A. V. Boris and S. I. Bredikhin, *Solid State Ionics* **40-41**, 269 (1990).
10. S. J. Tans, A. R. M. Verschueren and C. Dekker, *Nature* **393**, 49 (1998).
11. R. Martel, T. Schmidt, H. R. Shea, T. Hertel and Ph. Avouris, *Appl. Phys. Lett.* **73**, 2447 (1998).
12. S. J. Wind, J. Appenzeller, R. Martel, V. Derycke and Ph. Avouris, *Appl. Phys. Lett.* **80**, 3817 (2002).
13. J. L. Sun, W. Zhang, J. Q. Wei and B. F. Gu, *J. Appl. Phys.* **115**, 044302 (2014).
14. J. Q. Wei, B. Jiang, D. H. Wu and B. Q. Wei, *J. Phys. Chem. B* **108**, 8844 (2004).

ELECTROCHEMICAL STUDIES OF 'EXFOLIATED GRAPHENE OXIDE-MOO_2' COMPOSITE SYNTHESIZED BY NOVEL GRAPHENOTHERMAL REDUCTION

SHAIKSHAVALI PETNIKOTA[a,b], KEEFE WAYNE TEO [b,d], LUO CHEN[b,d], M. V. REDDY[c,*], SANDEEP KUMAR MARKA [a,b], VADALI V. S. S. SRIKANTH[a], B. V. R. CHOWDARI[b]

[a]*School of Engineering Sciences and Technology (SEST), University of Hyderabad, Gachibowli, Hyderabad 500046, India*

[b]*Advanced Batteries Lab, Department of Physics, National University of Singapore, Singapore 117542, Singapore*

[c]*Department of Materials Science and Engineering, National University of Singapore, Singapore 117576, Singapore*

[d]*NUS High School of Mathematics and Science, 20 Clementi Avenue 1, Singapore 129957*

Exfoliated Graphene Oxide-MoO_2 (EG-MoO_2) composite material was synthesized in scalable amounts by a novel Graphenothermal Reduction (GTR) method which is analogous to carbothermal reduction in which Graphene Oxide (GO) acts as reducing agent by giving up some of its free carbons and other various gas species like CO that are released upon heating. Mechanically grinded 2:1 molar mixture of GO and MoO_3 dry powder was heated at 750ºC for 8 hours in Argon so that simultaneous reduction of both reagents takes place, producing EG-MoO_2 powder. X-ray diffraction pattern (XRD) of as-prepared composite contains only strong peaks of MoO_2 and this pattern matches with monoclinic crystal structure. Morphology was observed with FESEM and various shapes like spherical, rods, needles, etc. of MoO_2 are observed on a continuous EG matrix. Synthesised EG-MoO_2 powder was then used to prepare electrodes, which are used as anodes to fabricate LIBs coin cells. Electrochemical studies of these LIBs were done by using galvanostatic cycling (GC), cyclic voltammetry (CV) and Electrochemical Impedance Spectroscopy (EIS). As an anode, EG-MoO_2 shows a reversible capacity between 600 and 380 $mAhg^{-1}$ for current densities between 0.25 and 1.0 C respectively. High Coulombic efficiency (QE) was found in-between 96-98% after few initial cycles despite of 52% during first cycle. Thus, EG-MoO_2 was found to be suitable for anodic application in LIBs.

Key words: Graphenothermal Reduction, Graphene Oxide, MoO_3, EG-MoO_2, Lithium Ion Battery, Anode.

* Corresponding author. Tel: +65 6516 2605; E-mail address: phymvvr@nus.edu.sg; msemvvr@nus.edu.sg; reddymvvr@gmail.com (M. V. Reddy)

Proceedings of the 14th Asian Conference on Solid State Ionics (ACSSI 2014)
Copyright © 2014 ACSSI 2014 Organizers. All rights reserved.
ISBN: 978-981-09-1137-9
doi:10.3850/978-981-09-1137-9_101

1. Introduction

Li-ion batteries are increasingly popular and constitute a vital part in today's world. Not only do these batteries have higher capacity than traditional alkaline batteries, it is also rechargeable and cheap to manufacture. This enables them to be a good choice in powering various gadgets like mobile phones and laptops. In view of the increasing demands needs of newer battery applications, the current technology of the conventional Li-ion batteries would not be able to meet up. Firstly, they use graphite as the anode that results in low capacity and easily allows formation of potentially dangerous dendrites when cycled at high current rates. However for anodic application nothing can be dearer than the commercial graphite as it offers maximum discharging and charging capacities lies around 0.15-0.25 V with least hysteresis, but it shows lower practical capacities 330-360 mAh/g that too at lower current rates out of its theoretical capacity of 372 mAh/g. As more and more new devices require more power, especially in electrical cars, it is necessary to explore other anode materials that could better address the disadvantages of the commercial Li-ion batteries as mentioned above, while being economical at the same time[1]. As a layered structured metal oxide, MoO_2 has recently received much attention, and has been considered as a promising anode material in lithium ion batteries because of its low electrical resistivity, high electrochemical activity, and high stability[2]. Even though MoO_2 alone undergoes severe irreversible volume changes upon lithiation that leads pulverization which causes continuous capacity loss[2]. To overcome this loss, several synthetic approaches have been reported for preparing MoO_2 nanostructures like carbon coated MoO_2[3] or graphene-MoO_2[2, 4-6], still facile green synthesis methodologies are lacking in producing them in bulk amounts. In this regard we are reporting our effort in the synthesis of Exfoliated Graphene Oxide-MoO_2 (EG-MoO_2) composite in scalable amounts by a novel facile route, Graphenothermal Reduction (GTR) method. This method is simple solid state, one pot, eco-friendly, no separate chemical reducing agent required, simultaneous reduction of both reagents as well as exfoliation of GO happens during heating by releasing only non toxic gaseous by-products (except for gases like CO, CO_2). Furthermore, no post production treatment like purification is required, as prepared material can be directly used for applications like anodes of Lithium Ion Battery (LIB). Most importantly, product yield can be easily manipulated from several grams to kilograms. In this method materials used i.e. GO and MoO_3 are cheap and less toxic in nature and there is no requirement for separate reducing agent.

2. Experimental Methods

2.1. *Materials and Methods*

Graphene Oxide (GO) was synthesized from natural graphite by a modified Hummers method[7]. In brief, each 1 g of graphite was dispersed in 25 mL of 95-98% H_2SO_4 and stirred about 5-10 minutes to ensure that the mixture is uniform then the beaker is transferred in to ice bath in order to remove excess heat generated by exothermic reactions during the addition of oxidizers. Then 0.5 g of $NaNO_3$ followed by 3 g of $KMnO_4$ were added gradually and after thorough mixing the reaction mixture was removed from ice bath and stirred at 45 °C for half an hour. Subsequently, 25 mL of Distilled H_2O was added into the solution and the temperature is raised to 98°C for an hour. Then, the beaker is filled with distilled H_2O to the brim and 1 mL of 30% H_2O_2 was added and stirred for 5 minutes. The synthesized GO suspended in the solution (yellowish solution) is then left to settle down for a few hours before decanting the supernant solution away and sediment is washed several times until the pH of the solution becomes approximately 7. After the final decant, the suspended GO solution is then poured into a filter and the excess water removed. The residue (GO) on the filter funnel is then left in an oven to dry for over 12 hours to remove all water content until layered sheets of GO has been obtained. The GO is then grinded into fine powders, ready to be added into the final reaction mixture in its appropriate amounts. EG-MoO_2 composite material was synthesized by GTR method in which 2:1 molar mixture of GO and MoO_3 powders mechanically grinded for 30 min and then this dry powder mixture was heated at 750ºC for 8 hours in Argon environment so that simultaneous reduction of both reagents happens along with exfoliation of GO, producing 2EG-MoO_2 fine powder. For every gram of reaction mixture we approximately got half gram of 2EG-MoO_2 fine powder and this high yield method can be easily translated to industry level production.

Electrode slurry is prepared by taking as-synthesized EG-MoO2, PVDF and Super-P carbon in the weight ratio of 70:15:15 which were dissolved in N-Methyl-2-pyrrolidone (NMP) solvent. The slurry was then coated onto etched copper foil up to a thickness of 25μm. The foil was then placed in an oven at 80°C overnight and then foil was then punched into discs with a 16 mm diameter. The electrodes along with separator, bottom and top stainless steel caps with plastic ohring were then placed in a vacuum oven overnight to make completely dry and then they were transferred inside a glove box filled with argon gas. In accordance to coin cells (CR2016), the assembly of a battery was done by taking Li metal counter, glass microfiber filter paper as separator. The

electrolyte used was 1M $LiPF_6$ in ethylene carbonate (EC) and dimethyl carbonate (DMC) in a 1:1 volume ratio.

2.2. *Characterisation Techniques*

XRD (Empyrean Pananlytical) was performed on EG-MoO_2 by using CuK_α radiation (wavelength 1.5418Å) and results were analysed using Rietveld refinement via TOPAS(v2.1). Morphological studies were carried out by using FESEM (Model Ultra 55 of Carls Zeiss-Germany). The Brunauer–Emmett–Teller (BET) surface method [Micromeritics TriStar, USA] was used to investigate the surface area. The Bitrode multi-channel tester [MCV16-05/001-5, Bitrode, USA] was used for charge-discharge cycling of the batteries. Raman spectra (Renishaw Raman system 2000) were recorded with auto excitation wavelength and auto confocality. Cyclic voltammetry (CV) was performed at room temperature using a multi-potentiostat (Macpile II, Biologic, France). EIS was performed with Solartron Impedance/gain-phase analyser (SI 1255) at room temperature.

3. Results and Discussion

3.1. *Structure and Morphology*

3.1.1. *Scanning Electron Microscopy (SEM)*

The morphology of as-prepared EG-MoO_2 powder is observed by FESEM images as shown in Fig.1. EG surfaces contains randomly dispersed varying shape and sized MoO_2 particles. Submicron sized MoO_2 spherical particles are scattered densely across the edge surfaces of the EG where exfoliation seems to be more as shown in Fig.1(a) and 1(b). This indicates that during the exfoliation of GO freshly formed individual MoO_2 nanoparticles are pushed away along with partitioning graphene layers and eventually the chance of agglomeration ceased. But the scenario as shown in the Fig.1(c) and 1(d) is totally different than earlier case by thickly populated and agglomerated MoO_2 particles. This situation might have arised due to presence of high amounts of MoO_3 and lesser GO platelets prior to exfoliation and reduction process. In these two images MoO_2 particles are found in quasi spherical, needles and rod shapes and micron sized rod shapes might be evolved as result of prolonged agglomeration.

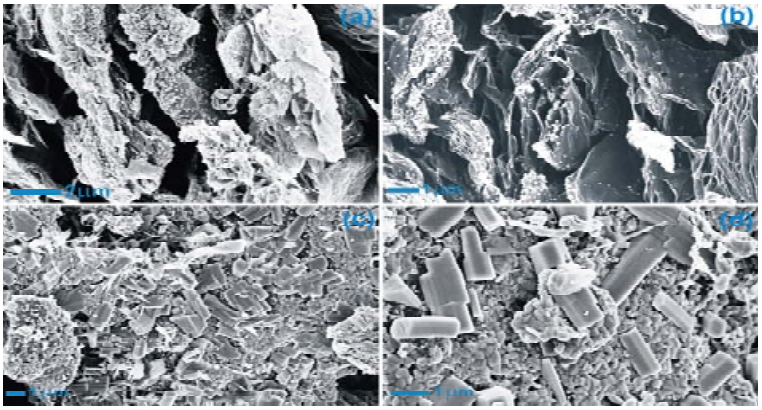


Figure 1. SEM images of MoO_2 nanoparticles at edges of EG (a),(b); freestanding and agglomerated MoO_2 particles (c),(d).

3.1.2. *X-ray Diffraction and BET Surface Area*

The X-ray diffraction (XRD) pattern of as-prepared EG-MoO_2 (Fig.2(a)) is matched with monoclinic crystal structure (JCPDS#78-1069). After Rietveld refinement with space group P21/c, lattice parameters are found to be a = 5.613 Å, b = 4.860 Å, c = 5.627 Å and beta = 120.88°. The average crystallite size is found approximately equal to 42.2 nm. There are no graphitic peaks from EG observed and these XRD results indicates that MoO_2 particles are crystallized well that too they belongs to single lattice system despite of their different shapes and sizes as observed in SEM images.

BET and Langmuir surface areas of EG-MoO_2 are found to be 3.15 and 4.4 m^2/g respectively. This small surface area might be resulted from high synthesis temperature, inert nature of MoO_2 surfaces and also they covered active surfaces of EG. The average pore volume is around 0.0121 cm^3/g with average pore diameter of 15.36 nm. The moderate hysteresis as shown in Fig.2(b) between nitrogen adsorption and desorption isotherms of EG-MoO_2 indicates that it possess mesoporosity which might be due to cavities and gaps formed between exfoliated individual graphene layers.

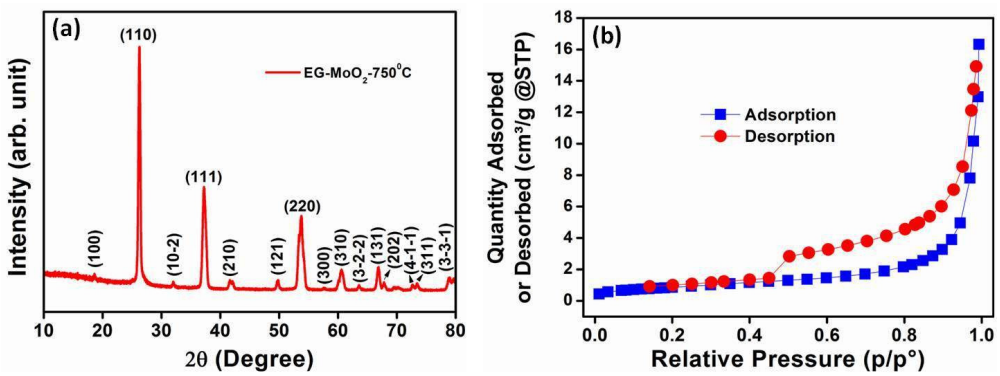


Figure 2. (a) XRD pattern and (b) N_2 adsorption and desorption isotherms of EG-MoO_2

3.1.2. *Raman Spectroscopy*

The extent of exfoliation of EG in comparison with GO and type of molybdenum oxide existed after thermal reduction is pursued with Raman spectroscopy as shown in Fig.3. There are only weak and broad D and G-bands

are observed in GO with no 2D-band except continuous broad region in its place which might resulted due to attachment of various functional groups covalently onto it. But after exfoliation the distinct and strong D, G-bands are appeared in EG that are centered around 1345 and 1585 cm^{-1} respectively. There is also weak and slightly broadened 2D-band around 2710 cm^{-1} is observed which might be appeared due to increased disorder imposed upon exfoliation. The sharp and strong peaks observed at 990, 817, 732, 567, 494 and 355 cm^{-1} are corresponds to various modes of vibrations between O and Mo atoms in MoO_2 and the extra peak appeared at 900 cm^{-1} is may be related to higher oxide of Mo[8]. These various MoO_2 peaks observed are closely commensurate with MoO_2 that is coated by carbon[3] or anchored on graphene[2]. Thus Raman study of EG-MoO_2 proven that thermal annealing at temperature chosen by us yielded good exfoliation to GO as well as complete reduction of MoO_3 to MoO_2 in good agreement with XRD results.

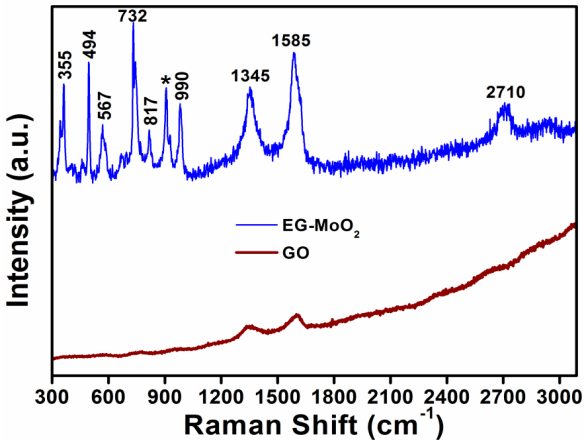


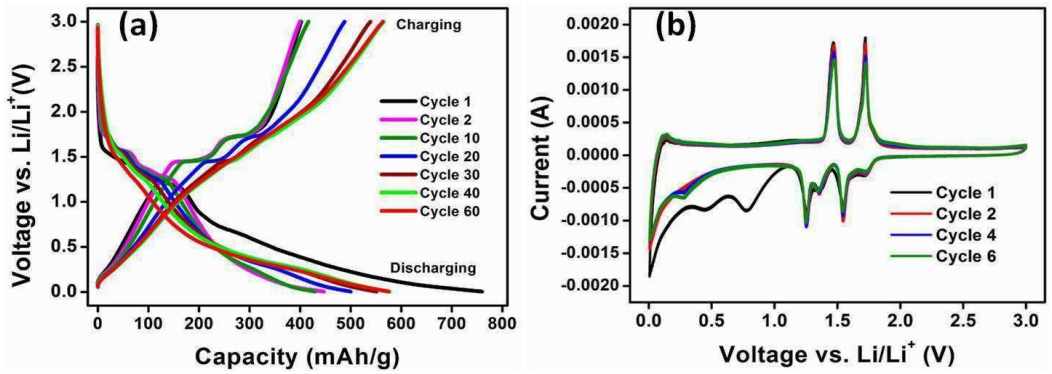
Figure 3. Raman scattering results of EG-MoO_2.

3.2. *Electrochemical characteristics*

3.2.1. *Galvanostatic Cycling*

Galvanostatic charge-discharge cycling response of EG-MoO_2 in the voltage window 0.005V-3.0V and at the current rate 210 mA/g (0.25C) is shown in Fig.4(a). The first discharge curve is appeared very steeper starting from OCV to 1.6 V where first change in slope is observed; further curve declined gently up to 1.25 V where second change in slope visualized and beyond this continuous decline is observed up to 0.005 V as discharge progressed. Thus a net capacity of 760 mAh/g is observed for first discharging to 0.005V. The second and few subsequent discharges curves are found similar to first discharge curve but there

are distinct ramps are observed in between 1.55 and 1.25 V but they are disappeared as cycling continued and final discharging curve found similar to pristine graphene. Here during the each discharge, capacity values dramatically first decreased for first few cycles (say 5) and then increased for remaining cycles. The first charging curve is observed to incline gently uninterruptedly up to 1.4 V at which first change in slope followed by second change at 1.72 V and at each of this change curve became flat like ramp which are each lasted for about 100 mAh/g; beyond these changes finally curve became steeper as charging progressed to 3.0V where final charging capacity is found to be 402 mAh/g. Here in charging case also same trend of decrease followed by increase of capacity values are observed during second and subsequent charging as like discharging curves. The ramps around 1.4 and 1.72 V are moved to higher capacity values as cycling progressed but they disappeared soon and final charging curves are also resembled pristine graphene. Thus overall voltage vs. capacity profile features are in tune with various redox current peaks found in



CV characteristics. The significant undesired voltage hysteresis i.e. voltage polarization between discharging and charging curves is observed to come down as number of cycles increased.

Figure 4. Charge-discharging profile at 210 mA/g (a) and CV results of EG-MoO_2.

The capacity vs. cycle number plots along with Coulombic efficiencies (QEs%) of EG-MoO_2 at 0.25, 0.5 and 1 C (=838 mA/g) current rates are shown in Fig.5. At 0.25C during first cycle reversible capacity is found to be 402 mAh/g which is decreased to 410 mAh/g at 5th cycle from then it increased continuously up to 50th discharge where it became 584 mAh/g followed by slight decrease to 564 mAh/g at the end of the test which secured capacity retention of 140%. Similar trend is observed in 0.5 and 1.0 C current densities applied and capacity decrease at the end is not observed as shown Fig.5 and respective values are furnished in Table1. This type of initial decrease and increase in

capacity might be collectively originated from cycle formation effect which enhances proper percolation of electrolyte[9] and activation process of the electrode material which improves the Li^+ to and fro shuttling by improving its diffusion kinetics[2]. The observed QEs during first cycle are around 53% but an increase to 90-91% is visualized in second cycle and further soon they varied in between 97 and 98% as cycling progressed. The present capacity values are found superior than the bare MoO_2[10-12], carbon coated MoO_2[3] and graphene-MoO_2[2, 4] composites.

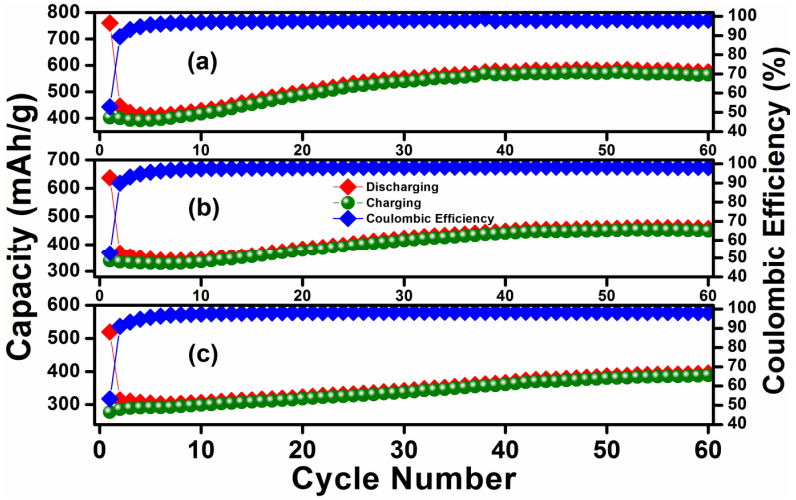


Figure 5. Cyclic performance of EG α MoO_2 at 210 (a), 420 (b) and 840 mA/g (c)

Table 1. Cycling performance of EG-MoO_2 at 1st, 2nd, 60th cycles (DC=Discharge Capacity and CC=Charge Capacity in $mAhg^{-1}$).

Current Rate	1st DC	1stCC	1stQE	60th DC	60th CC	60thQE
0.25 C	760	402	52.91	575	564	97.96
0.5 C	637	337	52.92	458	449	98.06
1.0 C	519	277	53.35	396	388	98.15

3.2.2. *Cyclic voltammetry*

Cyclic voltammetry (CV) whose results obtained at a scan rate of 58 μV/s and in the voltage range of 0.005-3.0V are shown in Fig.4(b). During first anodic scan there are two distinct reduction current peaks centred around 1.55 and 1.25 are observed along with two broad peaks around 0.77 and 0.45 V and finally a steep peak found nearby 0.005V. The first two big peaks whose current slightly increased followed by decrease in later reduction sweeps are corresponds to

crystalline phase transformations of MoO_2 upon lithiation to form $LixMoO_2$, but second cycle onwards these peaks belongs to lithiation by conversion reaction of MoO_2 to form metallic Mo and Li_2O[2, 3]. The latter two small and broad reduction peaks at 0.77 and 0.45 V might be resulted from formation of SEI as they disappeared in second sweep onwards and final steeper peak might be belongs to lithiation by intercalation into graphene sheets of EG. There is another small reduction peak with increasing current observed at 0.27V which plausibly corresponds to lithiation by intercalation into EG as like in graphite. Apart from earlier said major reduction peaks there are two small humps noticed around 1.35 and 1.72 V which corresponds to intermediate compounds formed during lithiation by either crystal phase transitions or conversion reaction of MoO_2[2, 3]. On the other hand during first cathodic scan there are three current peaks observed at 0.15, 1.46 and 1.72 V. Among these three oxidation peaks first one shown increasing current corresponds to lithium deintercalation from EG[9] while later two big peaks are due to de-lithiation by either crystal phase transformations or conversion reactions which leads to form MoO_2[2, 3]. The remaining small current seen at all voltages might be due to electrochemical absorption and desorption of lithium by EG (capacitance behaviour). Here in CV results the positions of redox couples related to MoO_2 are commensurate with positions of ramps observed in GC discharge-charge curves. Thus overall lithium insertion and extraction by EG-MoO_2 is due to mixed contribution from its individual phases.

3.2.3. *Electrochemical Impedance Spectroscopy*

The frequency dependent AC impedance of EG-MoO_2 at various states are shown in Fig.6 as Nyquist plots along with their equivalent circuit that is comprised of a R_e (electrolyte resistance), R_{ct} (resistance to charge transfer), CPE_{dl} (double layer capacitance), R_{ct} (bulk resistance) W_s (Warburg impedance) and C_i (lithium intercalation capacitance) whose values furnished in Table II[13]. The value of R_e varied in between 4-5.5 Ω as shown in Table 2. The charge transfer resistance R_{ct} is found ~88 Ω at OCV which is reduced to ~49 and ~4.8 Ω after first discharge and charge respectively. The tenfold decrease in resistance while first charging than discharging signifies that material readily allows lithium to leave it. The constant phase element CPE_{dl} values are around ~5.6-39 μF in tune with R_{ct} values. The values of R_b those are larger than R_e or R_{ct} as shown in Table2 are indicative for fast faradic reactions and might be accounted for high reversible capacities observed in GC results. The Warburg element W_s which represents the resistance to lithium ion diffusion is found

relatively very high than R_e or R_{ct}. The observed values of C_i <1F confirming that lithium intercalation mechanism through EG is contributing very less to overall lithium insertion and extraction capacities in agreement with CV results in which apart from redox couple due to conversion reactions between lithium and MoO_2, electrochemical absorption and desorption of lithium onto EG is observed rather than intercalation.

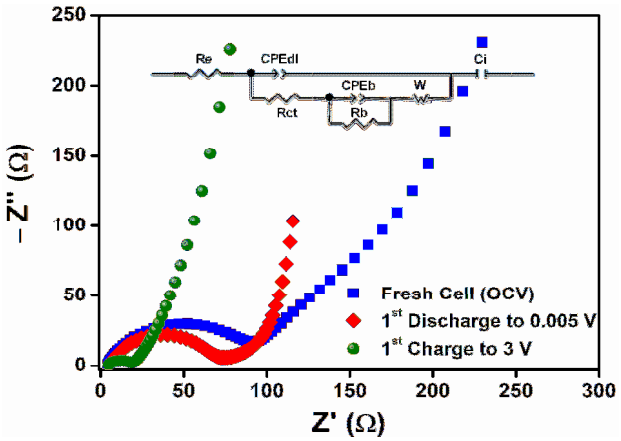


Figure 6. Nyquist plots of EG-MoO_2 at various states.

Table 2. EIS results of EG-MoO_2 at OCV, fully discharged and charged states.

Battery state	R_e (Ω) (±0.1)	R_{ct} (Ω) (±1)	CPE_{dl} (μF) (±0.2)	R_b (Ω) (±1)
Fresh Cell (OCV)	4.06	88.62	32.31	61.07±9.8
1st Discharge (0.005 V)	5.47	49.5	38.9	---
1st Charge (3V)	4.72	4.8	5.6	9.06±0.99

4. Conclusion

EG-MoO_2 nano-composite material was synthesized via GTR method and it was characterized through XRD, SEM, BET and Raman Spectroscopy. galvanostatic cycling, CV and EIS were carried out to understand physical and chemical-electrochemical properties. In galvanostatic cycling at current rate of 210 mAg^{-1}, EG-MoO_2 shown reversible capacity of 402 mAh g^{-1} during first cycle which increased to 565 mAh g^{-1} at the end of 60th cycle. In contrast to commercial graphite anode which undergoes capacity fading and shows lower reversible capacity, EG-MoO_2 shown an increase in capacity of 28.6%. At higher current rates of 420 and 840 mAg^{-1}, it showed an increase in capacity as well, with 23.8% and 26.1% respectively. Such a significant increase in capacity is

extremely interesting and it would be useful for us to study the reason for such an increase in future so as to be able to optimise our compounds for better performances. Given that our compounds are cheap and eco-friendly, and it undergoes a fast and versatile method of preparation, GTR. Furthermore, it could produce our materials in bulk and it is a simple process leaving no harmful by-products. Thus, our research product found suitability as anode for LIBs and potential material for real industrial applications.

Acknowledgments

PSS is grateful to Government of India for providing financial support through MANF (F1-17.1/2011/MANF-MUS-AND-213/(SA-III/Website)) to pursue research studies at the University of Hyderabad. PSS and SKM (SIPIS-2013) are thankful to NUS for financial support through India research initiative (NUS-IRI) fund. MVR thank to National Research Foundation, Prime Minister's Office, Singapore under its Competitive Research Programme (CRP Award No. NRF-CRP 10-2012-6) for research support.

References

1. M. V. Reddy, G. V. Subba Rao, B. V. R. Chowdari, *Chemical Reviews* **2013**, *113*, 5364.
2. Q. Tang, Z. Shan, L. Wang, X. Qin, *Electrochimica Acta* **2012**, *79*, 148.
3. L. Yang, L. Liu, Y. Zhu, X. Wang, Y. Wu, *Journal of Materials Chemistry* **2012**, *22*, 13148.
4. Y. Xu, R. Yi, B. Yuan, X. Wu, M. Dunwell, Q. Lin, L. Fei, S. Deng, P. Andersen, D. Wang, H. Luo, *The Journal of Physical Chemistry Letters* **2012**, *3*, 309.
5. Y. Sun, X. Hu, W. Luo, Y. Huang, *ACS Nano* **2011**, *5*, 7100.
6. Z. Yufei, Z. Yuxia, Y. Zhiyu, Y. Yiming, S. Kening, *Science and Technology of Advanced Materials* **2013**, *14*, 043501.
7. W. S. Hummers, R. E. Offeman, *Journal of the American Chemical Society* **1958**, *80*, 1339.
8. M. Dieterle, G. Mestl, *Physical Chemistry Chemical Physics* **2002**, *4*, 822.
9. S. Petnikota, N. Rotte, V. S. S. Srikanth, B. R. Kota, M. V. Reddy, K. Loh, B. V. R. Chowdari, *Journal of Solid State Electrochemistry* **2013**, *18*, 941.
10. Y. Liang, S. Yang, Z. Yi, X. Lei, J. Sun, Y. Zhou, *Materials Science and Engineering: B* **2005**, *121*, 152.
11. L. C. Yang, Q. S. Gao, Y. Tang, Y. P. Wu, R. Holze, *Journal of Power Sources* **2008**, *179*, 357.
12. L. C. Yang, Q. S. Gao, Y. H. Zhang, Y. Tang, Y. P. Wu, *Electrochemistry Communications* **2008**, *10*, 118.
13. M. V. Reddy, B. L. Wei Wen, K. P. Loh, B. V. R. Chowdari, *ACS Applied Materials & Interfaces* **2013**, *5*, 7777.

DEVELOPMENT OF SRI LANKAN NATURAL VEIN GRAPHITE AS ANODE MATERIAL FOR LITHIUM-ION RECHARGEABLE BATTERIES

T.H.N.G. AMARAWEERA[1,2]
[1]*Institute of Fundamental Studies, Kandy, Sri Lanka*
[2]*Department of Science and Technology, Uva Wellassa University Badulla, Sri Lanka*

N.W.B. BALASOORIYA
Faculty of Applied Sciences, South Eastern University of Sri Lanka Sammanthurai, Sri Lanka

H.W.M.A.C. WIJAYASINGHE
Institute of Fundamental Studies, Kandy, Sri Lanka

A.N.B.ATTANAYAKA
Department of Science and Technology, Uva Wellassa University Badulla, Sri lanka

M.A.K.L. DISSANAYAKE
Institute of Fundamental Studies, Kandy, Sri Lanka

B.-E. MELLANDER
Department of Applied Physics, Chalmers University of Technology Göteborg, Sweden

Natural graphite has been identified as a cost effective source to produce anode material in rechargeable lithium ion batteries (LIB). Sri Lankan vein graphite is renowned for high purity and crystallinity. However, high anisotropy of vein graphite surface and impurities present in trace levels cause profound alteration of chemical and electrochemical activities in LIBs. Therefore, a low cost chemical process to purify highly crystalline Sri Lankan natural vein graphite for the LIB anode was investigated in this study. This involved treating graphite with aqueous HCl solutions of 5 to 25 vol. % at 60 ^{0}C. The purified graphite was characterized by measurement of its carbon content, d.c electrical conductivity, X-ray diffraction and scanning electron microscopy analysis. Our process effectively eliminated the impurities in sulfate and carbonate forms after with low HCl concentrations. Further, the effectiveness of the purification process appears to depend on the structural type and initial purity of raw graphite. Moreover, this purified graphite posesses sufficient electrical conductivity of 0.7 S/cm at room

Proceedings of the 14th Asian Conference on Solid State Ionics (ACSSI 2014)
Copyright © 2014 ACSSI 2014 Organizers. All rights reserved.
ISBN: 978-981-09-1137-9
doi:10.3850/978-981-09-1137-9_039

temperature adequate for the anode application in LIBs. The electrochemical properties of the graphite electrode were studied with CR2032 coin cells using lithium metal foil as the counter and reference electrodes with 1M $LiPF_6$ in EC:DEC:DMC (1:1:1 wt %). The charge-discharge study of the cell with purified vein graphite presented an initial charge-discharge coulombic efficiency of 87 % and discharge capacity of 327 $mAhg^{1}$ in the voltage range of 0.002 - 1.5 V at C/5 rate. Hence, this study revealed the possibility of preparing natural Sri Lankan vein graphite as anode material suitable for LIBs.

1. Introduction

The upcoming demand for portable energy sources with the rapid growth of electrical vehicles and portable electrical items cannot be met with conventional batteries. This is presently addressed with the introduction of rechargeable batteries, specially the LIBs. However, the high unit cost, particularly due to expensive electrode materials, obstructs the development of LIB as a cheaper portable power source [1]. Moreover, LIB anode is the second largest component by weight in the battery. Still, expensive porous carbon material and synthetic graphite are the most commonly used anode materials in commercial LIBs. The rising price of synthetic graphite has resulted in an increased use of natural graphite as alternative electrode material. .

Sri Lankan vein graphite with high purity and crystallinity has been categorized into four structurally distinct graphite varieties, shiny-slippery-fibrous graphite (SSF), needle-platy graphite (NPG), coarse striated-flaky graphite (CSF) and coarse flakes of radial graphite (CFR) [2]. Each structural type consists of 95-99% of carbon with impurities in sulphate and carbonates forms [2]. These impurities are either mechanically attached to the graphite surface or intercalated between graphene layers [2]. However, the impurities present in trace levels and high anisotropy of natural vein graphite surface leads to profound alteration of chemical and electrochemical activities [1]. Therefore, further enhancement of purity is necessary before it is used for rechargeable battery applications [3,4]. Consequently a low cost chemical process to purify highly crystalline Sri Lankan natural vein graphite for the LIB anode was investigated in this study.

2. Materials and Methods

Different structural types of vein graphite, from Bogala and Kahatagaha mines in Sri Lanka with particle size < 53 μm and carbon content 95-99% were used for this study. Raw graphite was leached in aqueous solution containing 5, 10, 15, 20 and 25 vol. % HCl (250 ml each) separately and heated to 60 ^{0}C for 75

minutes. The acid-leached materials were washed to neutral and dried. The treated graphite was further leached by repeating the same process.

The purified graphite was characterized by carbon content measurements, d.c electrical conductivity, X-ray diffraction (Siemens D5000 Diffractometer) and scanning electron microscopy (FEI Quanta 200 FEG-ESEM). The concentration of Fe, Mg, Ca and Cu ions released from graphite during the process of acid leaching into acid waste water were measured by atomic absorption spectral analysis (GEC 933AA). Electrodes were prepared by tape casting the slurry of developed electrode materials onto a copper-foil by the doctor blade method. The slurry for the electrode was prepared using 90 wt. % active material with 10 wt. % PVdF in Acetone. Subsequently, the electrodes were allowed to dry overnight at room temperature (25^0C) and for 24 hours at 120 ^{0}C under vacuum.. After that, coin cells (CR 2032) were assembled in an argon-filled glove-box (< 1 ppm O_2 and H_2O) with prepared circular disks of graphite as anode, Li- foil (Sigma Aldrich) as the reference and counter electrode with a porous polypropylene separator (Cellgard 2400) in an non-aqueous electrolyte containing 1M $LiPF_6$ in ethylene carbonate, diethyl carbonate and dimethyl carbonate (1:1:1 ratio in weight) (LP71, BASF, USA). Finally, the charge discharge cycling of assembled cells were carried out at C/5 rate with a cut-off voltage of 0.002 - 1.5 V at room temperature using Metrohm Auto lab (PGSTAT302N) controlled by Nova 1.1 programm.

3. Results and Discussion

Graphs presented in Figure 1 show the effect of HCl concentration on upgrading the carbon content of different structural types of vein graphite. These results suggest a strong dependence of final purity on HCl concentration and the initial purity. Different structural types of graphite with initial carbon content greater than 98% carbon were upgraded into its maximum by the repeated treatment with 5 vol. % HCl. Graphite with 97 to 98 % and 95 to 97% of carbon reached its maximum level when repeatedly treated with 10 vol. % and 20 vol. % HCl, respectively. The treatments with HCl concentrations above these values did not show any significant effect on the carbon percentage.

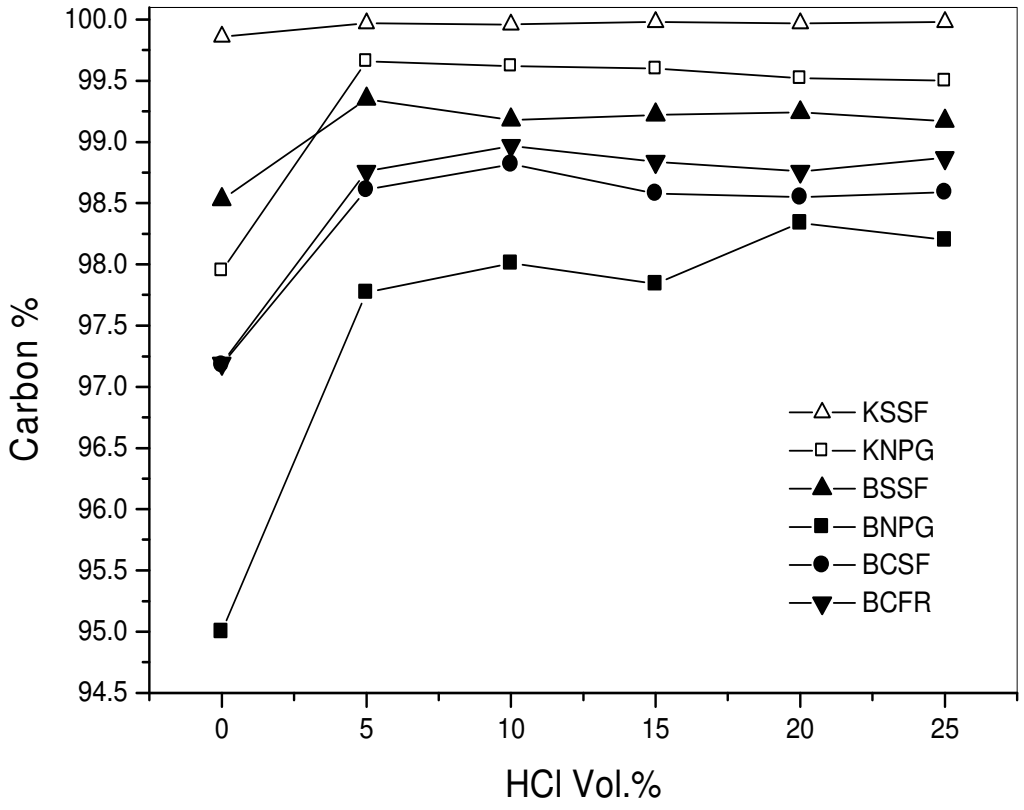


Figure 1 Effect of HCl vol.% on upgrading the carbon percentage of vein graphite. (SSF - shiny-slippery-fibrous graphite, NPG – needle-platy graphite, CSF- coarse striated-flaky graphite and CFR coarse-flake of radial graphite. K and B refers to samples from Kahatagaha and Bogala mines in Sri Lanka.

Table 1 gives the concentrations of Fe, Mg, Ca and Cu in the filtered solution after first and second acid leaching where higher enhancements of carbon percentages were observed. Generally, the concentration of Fe, Ca, Mg and Cu in the acid waste water depends on the structural type. Gangue minerals bearing sulphates and carbonates, which are physically attached to the graphite surface may react with HCl releasing Fe, Mg, Ca and Cu ions into the solutions. Concentrations of impurities in the filtered solution after second round of treatment were significantly reduced compared to those of the first round of treatment, indicating the effectiveness of purification process.

Table 1. Concentration of impurities in the filtered solution after the first and the second rounds of acid leaching, K and B refers to samples from Kahatagaha and Bogala mines in Sri Lanka.

Structural Type	HCl vol. %	Concentration of impurities in the filtered solution (ppm)							
		After first round of treatment				After second round of treatment			
		Fe	Cu	Mg	Ca	Fe	Cu	Mg	Ca
BSSF	5	328.0	7.2	256.9	125.4	16.6	3.9	2.4	2.2
BNPG	20	1920.7	33.0	34.2	15.3	110.2	18.4	4.3	5.8
BCSF	10	166.3	0.5	225.1	251.7	135.1	1.7	0.8	10.6
BCFR	10	511.4	7.2	135.6	76.4	11.9	1.9	0.7	10.7
KSSF	5	1843.4	45.7	16.6	3.8	57.6	1.7	7.2	4.3
KNPG	5	72.9	2.9	15.1	3.5	44.2	0.1	8.0	6.0
KCSF	5	61.9	0.3	19.2	4.6	15.1	0.4	6.6	3.6
KCFR	5	160.3	8.9	10.9	6.8	25.2	1.9	8.3	3.9

The XRD patterns of raw and purified vein graphite of SSF structural type are depicted in Figure 2. The XRD spectrum of raw and purified graphite samples shows the characteristic peak pattern of highly crystalline graphite. Further, it indicates that the purification process did not damage the crystal structure, which is preferred for LIB anode. Pyrite and dolomite are the major impurities present in raw graphite. The corresponding peaks of these impurities are marked as dots in the diffractogram. The major peaks corresponding to these impurities are absent in the purified graphite indicating their removal.

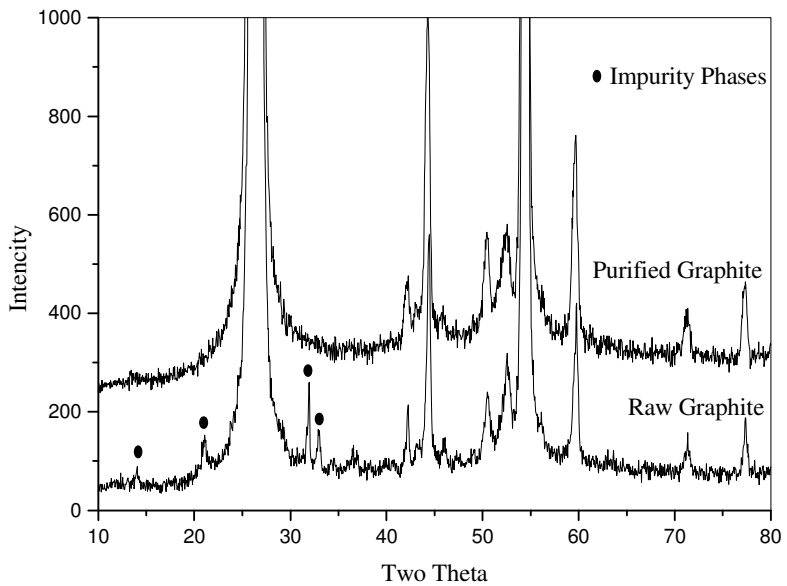
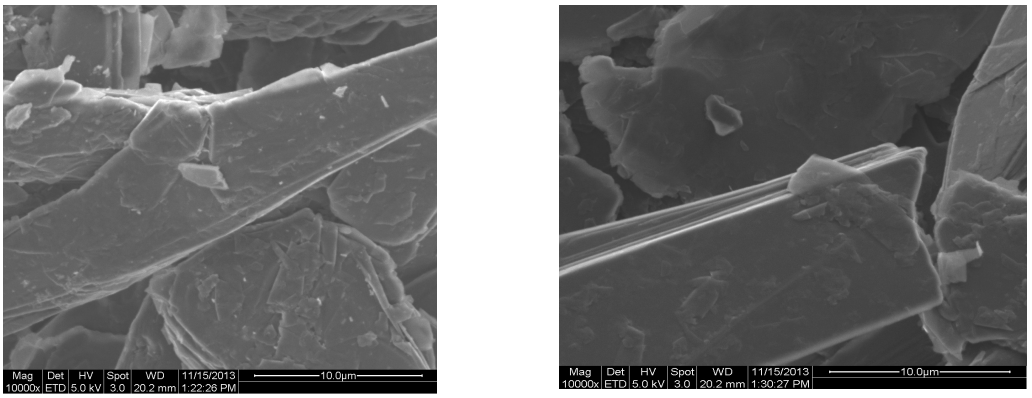


Figure 2 XRD patterns of raw SSF and purified SSF graphite

Figure 3 compares representative SEM image of raw and purified vein graphite of SSF structural type. Vein graphite exists as flat, planer structure with irregular surface. The raw graphite provides a surface morphology with a large degree of surface heterogeneity (Figure 3, panel a). The basal plane surface of graphite shows a large number of "defects" or disordered arrangements leading to a certain degree of "surface-roughness". This kind of surface-roughness is also observed at the edge surface of the raw graphite (Figure 3.3, panel a). The SEM image for the purified graphite clearly indicates change in the surface morphology (Figure 3, panel b). The basal and edge plane surface of purified graphite provide decreased surface roughness and seems to be "cleaned" by the purification process.



a b

Figure 3 SEM image of (a) raw SSF and (b) purified SSF graphite

Figure 4 displays the initial charge-discharge profile of raw and purified vein graphite of SSF structural type. Table 2 shows the charge discharge capacity and columbic efficiency as well as the irreversible capacity of investigated samples. The initial discharge capacity of raw graphite is 317 $mAhg^{-1}$. It has increased to 327.18 $mAhg^{-1}$ after purification. Further, raw graphite provides a first cycle columbic efficiency of 84.3 %, whereas the purified graphite exhibits an increased efficiency of 87.8 %.

This enhancement of the electrochemical performance of the purified graphite could be due to two reasons. Firstly, the removal of sulphite and metallic impurities, which may react with the electrolyte resulting in its decomposition and alter electronic properties [2]. Secondly, due to modification

of surface structure as evidence by the SEM images may also contribute to performance enhancement [5,6].

Table 2. First charge discharge cycle test results

Sample	Discharge Capacity $mAhg^{-1}$	Charge Capacity $mAhg^{-1}$	Irreversible Capacity $mAhg^{-1}$	Coulombic Efficiency (%)
Raw Graphite	317.65	267.84	49.8	84.3
Purified Graphite	327.18	287.47	39.7	87.8

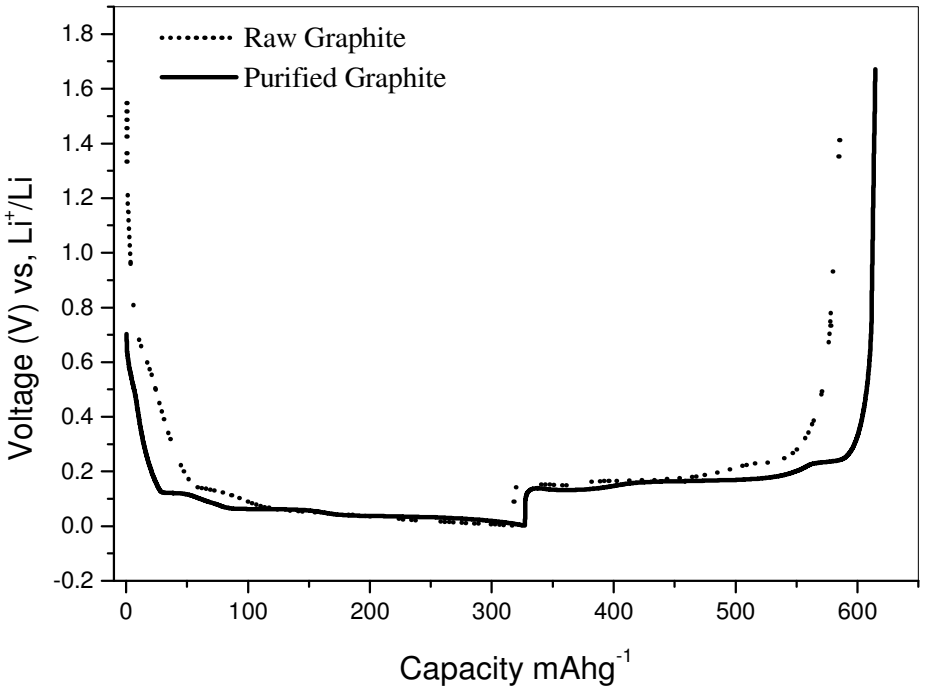


Figure 4 Initial charge-discharge profiles for raw SSF and purified SSF graphite

4. Conclusions

It has been found that the acid leaching purification process is an effective method both for the removal of sulphide and for carbonate impurities from natural graphite at low temperature of 60 ^{0}C.

The purified vein graphite shows higher reversible capacity and lower irreversible capacity than un-purified vein graphite. The charge-discharge

characteristics of the purified vein graphite shows an initial charge-discharge coulombic efficiency of 87 % and discharge capacity of 327 $mAhg^{-1}$ in a voltage range of 0.002- 1.5 V at 0.2 C rate. Hence, present study confirms that purified Sri Lankan natural vein graphite is promising as anode material in lithium ion rechargeable batteries due to its unique morphology, low cost and high purity.

Acknowledgments

The Financial support provided by Higher Education for Twenty First Century (HETC) Project, Ministry of Higher Education, Sri Lanka is greatfully acknowledged.

References

1. J.Vetter, P. Novák, M.R. Wagner, C. Veit, K.C. Möller. J.O. Besenhard, M.Winter, M.Wohlfahrt-Mahrens, C.Vogler and A. Hammouche, *J. Power Sources* **147**, 862 (2005).
2. N. Balasooriya, K. Bandaranayake and C. Descolas-Gros, *Can.Mineral*. **48,** 1373 (2010).
3. K. Zaghib, X. Song, A. Guerfi, R. Rioux, and K. Kinoshita, *J. Power Sources* **119-121**, 8 (2003).
4. Jihui-Li, Huifang-Da, Qian-Liu and Shufen-Liu, *Materials Letters* **60**, 3927(2006).
5. T. Placke, V. Siozios, R. Schmitz, S.F. Lux, P.Bieker, C.Colle, H.-W. Meyer, S. Passerini and M, Winter, *J. Power Sources* **200**, 83 (2012).
6. W.-H. Zhang, L. Fang, M. Yue and Z.-L. Yu, *J. Power Sources* **174**, 766 (2007).

HIERARCHICAL MESOPOROUS NANOSTRUCTURED $NiCo_2O_4$ SPINEL: FACILE PREPARATION AND APPLICATION AS ANODES FOR RECHARGEABLE SODIUM BATTERIES

KUN RUI, YAN LU, CHEN SHEN AND ZHAOYIN WEN

CAS Key Laboratory of Materials for Energy Conversion, Shanghai Institute of Ceramics, Chinese Academy of Sciences, Shanghai, China 200050.

Hierarchical mesoporous nanostructured $NiCo_2O_4$ spinel has been successfully synthesized via a facile solvothermal routine and subsequent annealing in air atmosphere with $Ni(NO_3)_2 \cdot 6H_2O$ and $Co(NO_3)_2 \cdot 6H_2O$ as the nickel and cobalt sources. Self-assembled nanosheets and urchin-like nanostructured $NiCo_2O_4$ were obtained respectively by using hexamethylenetetramine and urea to facilitate the hydrolysis and precipitation of both Ni^{2+} and Co^{2+}. The obtained material is explored as anodes for rechargeable sodium ion batteries. A first discharge capacity of 899 mAh/g at 0.1 C between 0.01-3 V is achieved. The irreversible capacity loss of the first cycle can be ascribed to the typical conversion reaction mechanism of transition metal oxides as electrode materials for both lithium and sodium batteries. The electrochemical impedance spectroscopy (EIS) technique has also been involved to investigate charge transfer and Na^+ diffusion kinetics for $NiCo_2O_4$ electrode before and after cycling. The increase of charge transfer resistance illustrates the deterioration of $NiCo_2O_4$/Na cell in some way.

1. Introduction

Since their commercialization two decades ago, lithium ion batteries have been the power sources of choices for popular portable electronics applications [1, 2]. In addition, there are concrete possibilities that high energy density lithium batteries such as Li-air and Li-sulfur batteries can also aggressively enter strategically important markets of automotive and grid storage[3]. However, for large-scale electrical energy storage (EES) application, there have been growing concerns about cost and limitation of lithium abundance in earth's crust for its uneven geographic distribution and recycling difficulties[4, 5]. Sodium ion batteries are now revisited as a potential alternative to lithium ion batteries for large scale electric storage because of its natural abundance, low cost and environmental benignity of Na resources [6, 7]. Furthermore, Na has similar physical and chemical properties compared with Li. A major challenge in

Proceedings of the 14th Asian Conference on Solid State Ionics (ACSSI 2014)
Copyright © 2014 ACSSI 2014 Organizers. All rights reserved.
ISBN: 978-981-09-1137-9
doi:10.3850/978-981-09-1137-9_081

developing room temperature sodium ion batteries is to find appropriate Na storage electrode materials that are capable of hosting larger Na^+ ions with sufficient capacity and diffusion kinetics [8].

Previous work in sodium ion batteries were mostly focused on cathode materials[9], by investigating many mature electrode materials for lithium ion chemistry as counterparts, some of which demonstrated considerable Na-storage capacity, rate capability and cyclability by tailoring the morphology, size and tunnelling structure[10-13].

However, the development of suitable anode materials for sodium ion batteries remains a considerable challenge. It has been evidenced that graphite, whose reversible electrochemical mechanism of lithium has been widely studied for anodes in lithium ion batteries, did not allow significant sodium insertion into graphite layers. Thus, numerous modified carbon materials have been proposed and display improved Na-storage performance and kinetics [14-16]. However, the sodium insertion potential in carbon materials is very close to the deposition potential of sodium, which easily leads to a safety issue when a slight polarization occurs. A number of alloys have also attracted increasing interests because of their high storage capacity investigated in lithium batteries [17, 18], but the large volume changes and rapid deterioration in cycling stability severely hinder their application for sodium ion batteries.

Most oxides can accommodate Li as anode materials with high storage capacity [19], however, the case is not optimistic in sodium ion batteries, which may be due to the large size of Na^+ ion [20]. $Na_2Ti_3O_7$ was reported to possess the lowest voltage among oxide insertion electrodes by uptaking 2 Na in a formula unit at 0.3 V vs. Na^+/Na by Palacín in 2011[21]. Further studies of other research groups have been done to improve the morphology of $Na_2Ti_3O_7$ [22, 23] and explore the Na storage properties for the unsatisfied performance [24]. Transitional metal oxides with conversion reaction mechanism have also been calculated to show high capacities for Na-storage. However, only very few materials, such as Fe_3O_4 [25], Fe_2O_3 [26], have been investigated as Na-storage hosts with a rechargeable capacity of 160-189 mAh/g.

Spinel $NiCo_2O_4$ was used as anode material for sodium ion batteries for the first time in 2002 with a first discharge capacity of 618 mAh/g and reversible capacity of about 200 mAh/g [27], which confirmed the Na-storage property of $NiCo_2O_4$ with a typical conversion reaction. However, the initial coulombic efficiency of 35% was rather low and no cycling performance was given for $NiCo_2O_4$ synthesized by a precipitation method. With better electrical conductivity and higher electrochemical activity compared with binary nickel oxide (NiO) and cobalt oxide (Co_3O_4), ternary nickel cobaltite ($NiCo_2O_4$) has recently been studied as a high-performance material for electrochemical

applications such as supercapacitors, lithium ion batteries, lithium-air batteries and so on[28-30]. Moreover, nano-decoration technology has been widely applied for fabrication of nanostructured electrode materials for both lithium and sodium ion batteries in order to enlarge the contact area with the electrolyte, increase the surface reactivity and shorten both electronic and ionic pathway within particles [9, 31, 32]. Therefore, hierarchical mesoporous nanostructured $NiCo_2O_4$ spinel has been successfully prepared in this study and investigated in sodium ion batteries.

2. Experimental

2.1 *Material Preparation*

All the chemicals were directly used after purchase without further purification. Hierarchical mesoporous nanostructured $NiCo_2O_4$ spinel has been successfully synthesized using $Ni(NO_3)_2 \cdot 6H_2O$ and $Co(NO_3)_2 \cdot 6H_2O$ as the nickel and cobalt sources, respectively. In a typical synthesis, 1 mmol of $Ni(NO_3)_2 \cdot 6H_2O$ and 2 mmol of $Co(NO_3)_2 \cdot 6H_2O$ were dissolved into 60 mL of DI water at room temperature to form a clear pink solution, followed by the addition of 6 mmol of hexamethylene-tetramine or 12 mmol of urea to facilitate the hydrolysis and precipitation of both Ni^{2+} and Co^{2+}. After stirred for 1 h, the solution was then transferred to a Teflon autoclave, sealed and heated to 100 °C for 10 h. When the solution was cooled to room temperature, the precipitates were washed with distilled water and ethanol and centrifuged at 10000 rpm five times to remove remaining impurities before dried in a vacuum oven at 65 °C for 12 h. In order to get crystallized mesoporous $NiCo_2O_4$ spinel, the collected precursors were annealed in air at a temperature of 300 °C for 6 h with a heating rate of 2 °C/min.

2.2 *Material characterization*

Both products were characterized by X-ray diffractometry (XRD) on a Rigaku Ultima IV (40 KV/30 mA) diffractometer with Cu-Kα radiation at a scanning rate of 6 degrees/min. The morphology of the as-prepared materials was investigated using a scanning electron microscope (SEM, S-3400N, Hitachi). The specific surface area was measured by the Brunauer-Emmett-Teller (BET) method using nitrogen adsorption-desorption isotherms on a Micromeritics Tristar 3000 analyzer, and the pore size distribution was obtained from the desorption branch of the isotherm by the Barrett-Joyner-Halenda (BJH) method.

2.3 *Electrochemical measurements*

The electrochemical performances of $NiCo_2O_4$ as anodes for rechargeable sodium ion batteries were examined in coin type cells with sodium foil (Aldrich) as both counter and reference electrodes. The working electrodes were prepared by mixing $NiCo_2O_4$, acetylene black and poly(vinyldifluoride) (PVDF) dissolved in n-methyl pyrrolidinone (NMP) with a weight ratio of 80:10:10, which were then pasted onto a copper foil substrate followed by drying in vacuum at 80 °C for 24 h. Glass fiber (GF/D) from Whatman was employed as the separator. The electrolyte involves 1 M NaClO4 in propylene carbonate (PC). The cells were assembled in an Ar-filled glove box with oxygen and water contents less than 1 ppm. Galvanostatic charge-discharge measurements of $NiCo_2O_4$ anodes vs Na/Na^+ were performed at room temperature under different rates (0.05 to 2 C) in a voltage range of 0.01-3.0 V on a LANDCT2001A battery test system. The AC impedance spectrum was measured using Autolab Electrochemical Workstation in a frequency range of 0.1-10^6 Hz.

3. Results and discussion

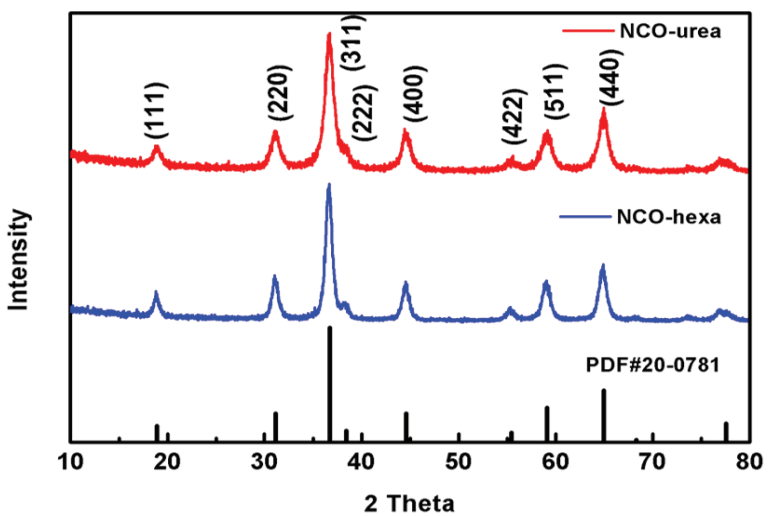


Figure 1. XRD patterns of the as-prepared $NiCo_2O_4$ spinel after annealing

Figure 1 shows the XRD patterns of the as-prepared products after thermal annealing at 300 °C. No peaks from other crystallized phases were observed, indicating the formation of the pure spinel $NiCo_2O_4$ after low-temperature thermal treatment. All the well-defined diffraction peaks of both samples could be indexed as the cubic structured $NiCo_2O_4$ with a space group of Fd3m (JCPDS No. 20-0781), which shows that the use of hexamethylenetetramine and urea for the hydrolysis-precipitation process has no influence on the phase formation.

Broadened reflections were observed in both samples, demonstrating the existence of nanocrystalline phase and their small size.

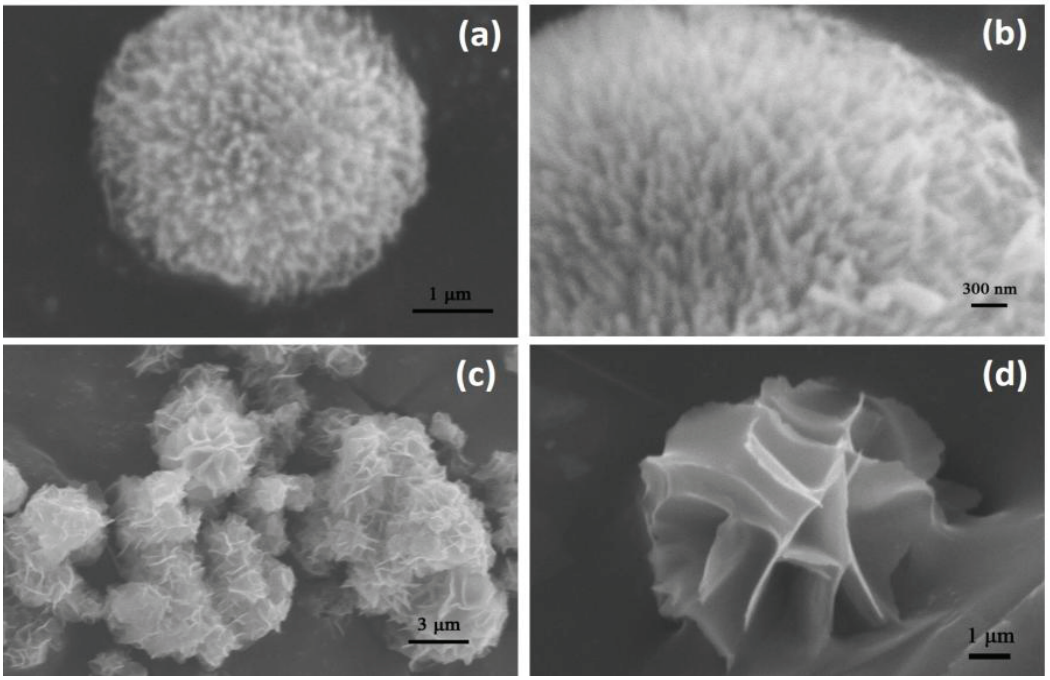


Figure 2. SEM images of the as-prepared nanostructured $NiCo_2O_4$ spinel

Figure 2 shows SEM images of the produced $NiCo_2O_4$ samples using hexamethylenetetramine and urea to facilitate the hydrolysis and precipitation process, respectively. As can be seen from Figure 2(a) and (b), spherical urchin-like $NiCo_2O_4$ nanostructures with diameters of about 3 μm can be obtained with the addition of urea. Typically, the $NiCo_2O_4$ urchins are composed of numerous small nanorods radially grown from the center. It was expected that this unique structure might provide a high surface area due to the hierarchical nanorods together with high morphology stability, thus contributing to enhanced electrochemical performances resulting from the easy access of the active materials in the redox process to their interface as well as the enlarged contact area between the active materials and the electrolyte. However, with the use of hexamethylenetetramine, different morphologies can be obtained as shown in Figure 2(c) and (d). Irregular nanosheets assembly with diameters of about 5 μm exhibits folding flower-like morphology composed of ultrathin nanosheets. Due to the much larger lateral size than the thickness, the assembly of bending, curling and crumpling can be easily observed. Both morphologies display hierarchical micro-architectures composed of self-assembled nanorods or nanosheets under the condition of different hydrolysis-precipitation additives.

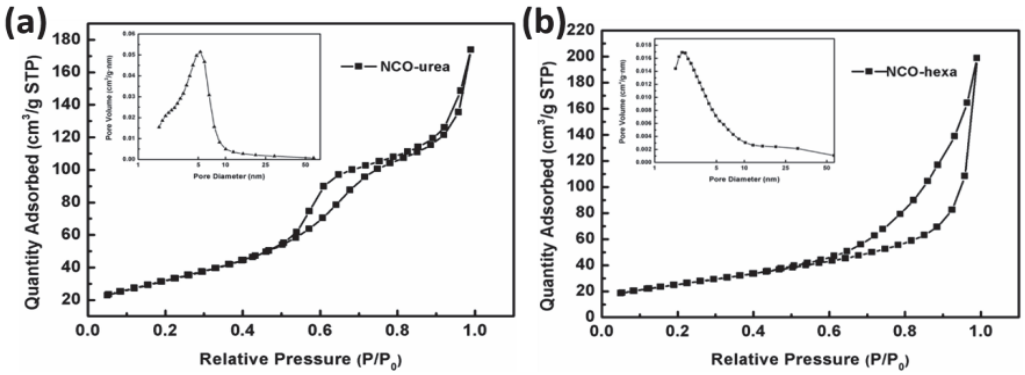


Figure 3. Nitrogen adsorption-desorption isotherms and BJH pore size distributions (insets) of the as-prepared $NiCo_2O_4$

The specific surface areas and hierarchical porous nature of the as-prepared self-assembled $NiCo_2O_4$ nanostructures were further investigated by nitrogen adsorption-desorption measurements, as indicated in Figure 3. We can see that the curves exhibited a typical type IV characteristic according to the IUPAC classification with an obvious hysteresis loop, indicating the presence of mesopores in the as-prepared material. The mesoporous structure was further supported by the Barrett-Joyner-Halenda (BJH) pore size distribution data shown in the insets of Fig. the Brunauer-Emmett-Teller (BET) surface area of the urchin-like nanostructured $NiCo_2O_4$ is thus calculated to be around 117.4633 m^2/g, while the BET surface area value of the self-assembled nanosheets is 92.1784 m^2/g. With a large surface area and mesoporous structures, the as-prepared spinel $NiCo_2O_4$ nanostructures may have potential application in sodium ion batteries, since these features are of huge benefits for the transport and diffusion for both the Na^+ ions and electrons during the charge-discharge process.

The electrochemical performances of the hierarchical mesoporous nanostructured $NiCo_2O_4$ spinel as anodes for rechargeable sodium ion batteries have been investigated. The galvanostatic charge-discharge process was performed at 25 °C in a voltage range of 0.01-3.0 V. Generally, the first charge and discharge cycle is critical to represent the electrochemical performance as the formation of SEI. As Figure 4(a) shows, the total discharge capacity of the first cycle at a current density of 0.1 C is 898 mAh/g, which is a little bit higher than the theoretical value for a complete reduction to the transition metals and formation of 4 Na_2O per formula (890 mAh/g), according to

$$NiCo_2O_4 + 8Na \rightarrow Ni + 2Co + 4Na_2O \quad (1)$$

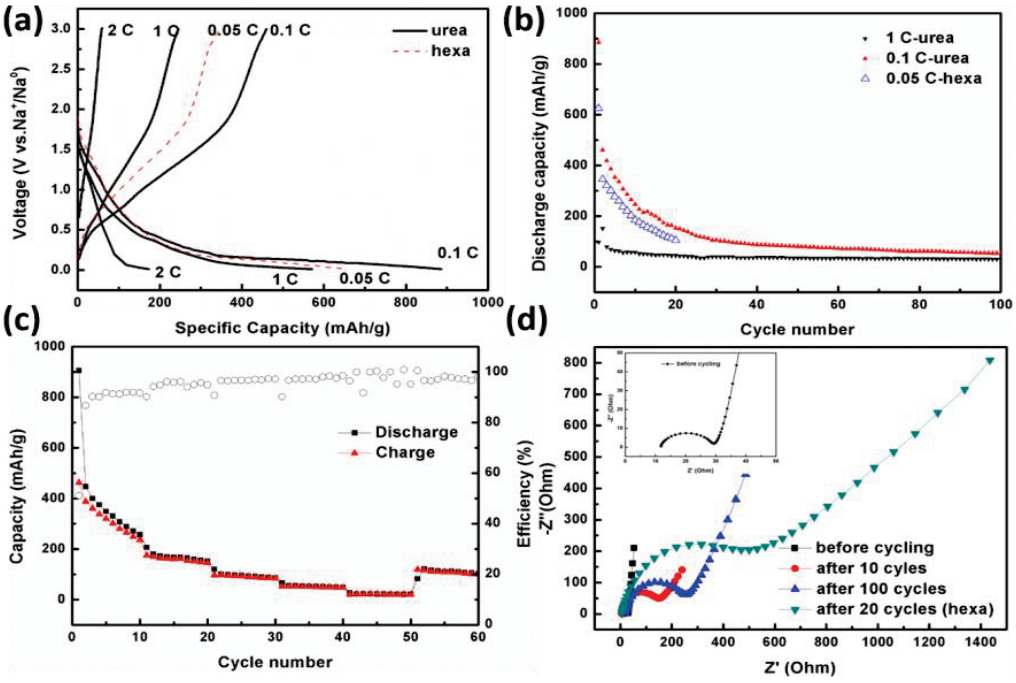


Figure 4. (a) Discharge-charge curves of the first cycle at various rates between a voltage range of 0.01-3.0 V, (b) Discharge capacity as a function of cycle numbers at different rates, (c) Rate performance at different rates and the corresponding coulombic efficiency, (d) Nyquist plots in the frequency range from 1000 kHz to 0.1 Hz of the electrodes before and after cycling.

The extra Na storage capacity of the first cycle may be caused by an interfacial interaction of sodium within the transition metal/ Na_2O matrix and thus a distinct local charging along with the formation of a solid/electrolyte interphase (SEI) film on the electrode surface, as proposed by Tarascon's group. On the other hand, the charge capacity of the first cycle is 460 mAh/g, leading to a large capacity loss during the initial discharge-charge process, which is one of the typical drawbacks of conversion reaction electrodes. Similar phenomena can also be discovered in transition metal oxides used as electrode materials in lithium ion batteries [33]. The reversible reaction of sodium with a metal oxide in which Na_2O and the metallic Ni and Co are formed has been confirmed by Tirado in 2002 with an ex-situ XRD characterization of the discharged electrodes [27].

Galvanostatic discharge-charge curves of the first cycle for different current rates are also presented in Figure 4(a). It is noteworthy that the first discharge capacity of $NiCo_2O_4$ obtained by using hexamethylenetetramine at 0.05 C is lower than that of $NiCo_2O_4$ obtained with urea tested at a higher rate of 0.1 C. What's more, the discharge capacity is reported to be 618 mAh/g and a reversible capacity of 200 mAh/g was obtained by Tirado's group. The

enhanced electrochemical performances of the hierarchical mesoporous urchin-like $NiCo_2O_4$ could be attributed to the improved electrochemical activity derived from the optimized morphology and nanostructure.

The cycling stability of the $NiCo_2O_4$ electrode for sodium ion batteries is characterized for the first time and discharge capacities obtained at different discharge-charge rates are presented in Figure 4(b). For the urchin-like $NiCo_2O_4$ electrode, a large capacity loss between the first two cycles can be observed owing to the irreversible reaction of the metallic Ni and Co with inert Na_2O to form $NiCo_2O_4$ again. Capacity fading also obviously exists in the following 20 cycles and after that, a reversible capacity as high as mAh/g is maintained throughout the rest cycles. Furthermore, the urchin-like $NiCo_2O_4$ shows higher capacities at 0.1 C than the one obtained by using hexamethylenetetramine with self-assembled nanosheets morphology at an even lower rate of 0.05 C, demonstrating the significant influences of different morphologies on electrochemical performances of $NiCo_2O_4$. In this way, we can infer that hierarchical mesoporous nanostructured $NiCo_2O_4$ with urchin-like nanostructures can achieve better electrochemical properties since the microspheres composed of 1D nanorods possess better structural stability and endure volume changes during the discharge-charge cycles than the irregular flower-like assembly of 2D nanosheets.

Rate performances of the urchin-like $NiCo_2O_4$ electrode have been further examined by first cycling the cell at 0.1 C for ten cycles with a stepwise increase of the discharge/charge rates to as high as 2 C, demonstrating the reversibility of the electrode deduced from the overlapping of the discharge and charge capacity in each cycle as shown in Figure 4(c). Reversible capacities of about 400 mAh/g at a discharge-charge rate of 0.1C, 170 mAh/g at 0.2 C, 90 mAh/g at 0.5 C, 50 mAh/g at 1C, 20 mAh/g at 2C are achieved respectively.

The electrochemical impedance spectroscopy (EIS) technique has been widely used to investigate charge transfer and ion diffusion kinetics in various electrode materials. To better understand the difference of electrochemical performances between two $NiCo_2O_4$ anodes with different morphologies, an EIS measurement has been performed with both of them. Figure 4(d) shows the Nyquist plots in the frequency range from 1000 kHz to 0.1 Hz. These plots clearly show that after discharge-charge cycling, the diameter of the semicircle of the electrode is much larger than that of the original electrode before cycling, indicating the increase in the charge transfer resistance after the cycling process and thus illustrating the capacity deterioration of $NiCo_2O_4$/Na cell in some way. What's more, larger charge-transfer resistance can be observed for the $NiCo_2O_4$ electrode with the morphology of self-assembled nanosheets. In the case of the low frequency region, the slope of Warburg impedance represents the electrolyte

ion diffusion behavior. The urchin-like $NiCo_2O_4$ electrode shows a more vertical line than the flower-like one with self-assembled nanosheets because of the lower ion diffusion resistance in the microspheres composed of 1D nanorods. The enhanced electrode kinetics must be associated with higher surface area and better accommodation for volume change during the charge-discharge process, ensuring better electrochemical performances for the urchin-like $NiCo_2O_4$ electrode.

4. Conclusions

In summary, by using urea and hexamethylenetetramine to facilitate the hydrolysis and precipitation process of transition metal ions, hierarchical mesoporous nanostructured $NiCo_2O_4$ spinel with two different morphologies have been successfully synthesized. The mesoporous urchin-like $NiCo_2O_4$ shows better electrochemical performances as anodes for sodium ion batteries with an initial discharge capacity of 899mAh/g at 0.1 C corresponding to 8 Na uptake with a typical conversion reaction mechanism. The irreversible capacity loss of the first cycle can be ascribed to the incomplete reversibility of the reaction of decomposition of inert Na_2O. The increase of charge transfer resistance illustrates the deterioration of $NiCo_2O_4$/Na cell in some way. Therefore, it is believed that the electrochemical performance of $NiCo_2O_4$ spinel anodes for sodium ion batteries can be further improved by varying synthesis conditions to optimize the morphology and nanostructure of $NiCo_2O_4$ in the future.

References

1. Z. Yang, J. Zhang, M. C. W. Kintner-Meyer, X. Lu, D. Choi, J. P. Lemmon and J. Liu, *Chemical reviews*. **111**, 3577 (2011).
2. B. Dunn, H. Kamath and J.-M. Tarascon, *Science*. **334**, 928 (2011).
3. P. G. Bruce, S. A. Freunberger, L. J. Hardwick and J. M. Tarascon, *Nature materials*. **11**, 19 (2012).
4. M. D. Slater, D. Kim, E. Lee and C. S. Johnson, *Advanced Functional Materials*, n/a (2012).
5. V. Palomares, P. Serras, I. Villaluenga, K. B. Hueso, J. Carretero-González and T. Rojo, *Energy & Environmental Science*. **5**, 5884 (2012).
6. B. L. Ellis and L. F. Nazar, *Current Opinion in Solid State and Materials Science*. **16**, 168 (2012).
7. H. Pan, Y.-S. Hu and L. Chen, *Energy & Environmental Science*. **6**, 2338 (2013).
8. S.-W. Kim, D.-H. Seo, X. Ma, G. Ceder and K. Kang, *Advanced Energy Materials*. **2**, 710 (2012).
9. M. S. Islam and C. A. Fisher, *Chemical Society reviews*. **43**, 185 (2014).
10. N. Yabuuchi, M. Kajiyama, J. Iwatate, and H. Nishikawa, *Nature materials*. **11**, 512 (2012).

11. C. D. Wessells, R. A. Huggins and Y. Cui, *Nature communications*. **2**, 550 (2011).
12. H. Kim, I. Park, D. H. Seo, S. Lee, S. W. Kim, W. J. Kwon, Y. U. Park, and K. Kang, *Journal of the American Chemical Society*. **134**, 10369 (2012).
13. Y. Cao, L. Xiao, Z. Yang and J. Liu, *Adv Mater*. **23**, 3155 (2011).
14. D. A. Stevens and J. R. Dahn, *Journal of The Electrochemical Society*. **147**, 1271 (2000).
15. R. Alcantara, J. M. Jimenez-Mateos, P. Lavela and J. L. Tirado, *Electrochemistry Communications*. **3**, 639 (2001).
16. P. Thomas and D. Billaud, *Electrochimica Acta*. **46**, 3359 (2001).
17. J. Qian, Y. Chen , X. Ai and H. Yang, *Chem Commun*. **48**, 7070 (2012).
18. L. Xiao, Y. Cao , Z. Nie and J. Liu, *Chem Commun*. **48**, 3321 (2012).
19. J. Cabana, L. Monconduit, D. Larcher and M. R. Palacin, *Adv Mater*. **22**, E170 (2010).
20. F. Klein, B. Jache, A. Bhide and P. Adelhelm, *Physical chemistry chemical physics : PCCP*. **15**, 15876 (2013).
21. P. Senguttuvan, G. Rousse, V. Seznec, J.-M. Tarascon and M. Rosa Palacin, *Chemistry of Materials*. **23**, 4109 (2011).
22. W. Wang, C. Yu, Z. Lin, J. Hou, H. Zhu and S. Jiao, *Nanoscale* (2012).
23. W. Wang, C. Yu, H. Zhu and S. Jiao, *RSC Advances*. **3**, 1041 (2013).
24. A. Rudola, K. Saravanan, C. W. Mason and P. Balaya, *Journal of Materials Chemistry A*. **1**, 2653 (2013).
25. S. Komaba, T. Mikumo, N. Yabuuchi, A. Ogata, H. Yoshida and Y. Yamada, *Journal of The Electrochemical Society*. **157**, A60 (2010).
26. S. Komaba, T. Mikumo and A. Ogata, *Electrochemistry Communications*. **10**, 1276 (2008).
27. R. Alcantara, M. Jaraba, P. Lavela and J. L. Tirado, *Chemistry of Materials*. **14**, 2847 (2002).
28. C. Yuan, J. Li, L. Hou, X. Zhang, L. Shen and X. W. D. Lou, *Advanced Functional Materials*. **22**, 4592 (2012).
29. L. X. Zhang, S. L. Zhang, K. J. Zhang, G. J. Xu, X. He, S. M. Dong, Z. H. Liu, C. S. Huang, L. Gu and G. L. Cui, *Chemical Communications*. **49**, 3540 (2013).
30. J. Liu, C. P. Liu, Y. L. Wan, W. Liu, Z. S. Ma, S. M. Ji, J. B. Wang, Y. C. Zhou, P. Hodgson and Y. C. Li, *Crystengcomm*. **15**, 1578 (2013).
31. F. Cheng, J. Liang, Z. Tao and J. Chen, *Advanced Materials*. **23**, 1695 (2011).
32. Y. G. Guo, J. S. Hu and L. J. Wan, *Advanced Materials*. **20**, 2878 (2008).
33. B. Zhang, Y. Zhang, Z. Miao, T. Wu, Z. Zhang and X. Yang, *Journal of Power Sources*. **248**, 289 (2014).

SYNTHESIS AND ELECTROCHEMICAL PROPERTIES OF MESOPOROUS CARBON SUPPORTED WELL-DISPERSED COBALT OXIDES NANOPARTICLES

CHUNXIA ZHAO, JUNSHEN LI, WEN CHEN†

State Key Laboratory of Advanced Technology for Materials Synthesis and Processing, School of Materials Science and Engineering, Wuhan University of Technology Wuhan 430070, China

YUNXIA YANG, KEN CHIANG, NICK BURKE

CSIRO Earth Science and Resource Engineering VIC 3168, Australia

Well-dispersed cobalt oxide nanoparticles supported on mesoporous carbon (CMK-3) have been synthesized in the current work. By carefully controlling the impregnation conditions, a good control of the cobalt particle size and dispersion has been achieved. The composites are characterized by field emission scanning electron microscopy, transmission electron microscopy, nitrogen adsorption-desorption analysis, X-ray diffraction and thermogravimetric analysis. The results have confirmed that, at a cobalt loading of 15 wt%, the composites have not only retained mesoporous structure of the support but also shown a good control of dispersed cobalt oxide nanoparticles with size of ~4 nm. The electrochemical property tests for the synthesized samples have shown significant improvement compared to the blank carbon (CMK-3) without cobalt oxide incorporation.

1. Introduction

The recent advances in nanoscience and nanotechnology have provided an impetus for the development of new hybrid porous nanostructures, especially metal oxide nanoparticles (NPs) confined in porous carbons. Hybrid porous nanocomposites have received much attention because of their unique properties including well-controlled pore structures, high surface areas, and large and tunable pore sizes [1]. The small metal oxide particles and porous structure can significantly enhance the utilization of active materials and shorten the transport/diffusion path of ions and molecular entities. Thus, porous carbon-based nanocomposites have many potential applications including electrodes [2], catalysts [3, 4] and adsorbents [5]. The use of mesoporous carbon incorporated

Proceedings of the 14th Asian Conference on Solid State Ionics (ACSSI 2014)
Copyright © 2014 ACSSI 2014 Organizers. All rights reserved.
ISBN: 978-981-09-1137-9
doi:10.3850/978-981-09-1137-9_085

nanosized metal oxide materials have attracted huge attention as they have demonstrated many unique advantages for supercapacitor and secondary lithium battery applications.

Cobalt metal and its oxides have been heavily studied for applications such as supercapacitors [6-8], anode materials in Li-ion rechargeable batteries [9], solid-state sensor [10], heterogeneous catalysts [11], solar energy absorbers [12], and electrochromic devices [13]. In strategies for enhancement of performance in applied catalysis or in energy conversion based on cobalt oxides, the utilization of carbon-based materials such as activated carbon, carbon nanotubes (CNTs) and graphene nanosheet (GNS) can be meaningful and useful method [9, 14-16]. Consider the unique physicochemical properties offered by these carbon materials, in particular ordered mesoporous carbons (OMCs), are regarded as ideal hosts for host-guest hybrid porous nanocomposites due to the more favorable mass transfer processes within the pores [2, 17] . Hu and co-workers [18] developed silica-supported porous carbon nanomembrane (SS-CNM) as a conductive support for the electroactive Co_3O_4. Their aim was to fabricate regularly packed nanorods in the mesochannels. This type of SS-CNM was prepared from a self-assembled monolayer of an enediyne compound on the surface of mesoporous silica followed by Bergman cyclization and carbonization. Meanwhile, in situ combination of carbon and guest precursors was considered as an alternative because of the relative simple and controllable synthesis protocols. Zhao's group used an in-situ route to synthesize ZSM-5 microspheres composed of well-dispersed uniformly sized Fe_3O_4 NPs [19] and ordered mesoporous Pt@graphitic carbon hybrids [20]. This approach shows clear advantages to control the guest size and dispersion. One limitation is that a reduced utilization and activity of guests may be resulted because they usually situate inside the walls of hosts

In order to achieve better control of metal oxide NPs, mesoporous carbon supported well-dispersed cobalt oxides NPs have been synthesized with ordered mesoporous carbon CMK-3 as the matrix and cobalt nitrate hexahydrate as the cobalt oxides precursor through ammonia post-treated impermanent route. The particle size and dispersion of cobalt oxides were investigated. The electrochemical properties of the prepared composites were also discussed.

2. Experimental Methods

2.1. *Material Synthesis*

Mesoporous ordered carbon, CMK-3, was purchased from XFnano (China) and used without further purification. Cobalt nitrate hexahydrate was purchased from Sigma-Aldrich.

A predetermined amount of CMK-3 was first dispersed in ethanol, followed by the addition of a 20 wt% ethanolic solution containing cobalt nitrate hexahydrate. The mixture was continuously stirred at room temperature until the solvent was fully evaporated. After drying the impregnated sample in the vacuum oven overnight, it was brought into contact with ammonia vapor that was generated by heating a ~14 wt% ammonia solution at 60 °C for 3 h. This procedure hydrolyzes the adsorbed cobalt nitrate in a controlled manner prior to high temperature calcination. After this step, the sample was washed with ethanol, dried at 45 °C under vacuum overnight, and finally calcined under an argon atmosphere at 400~500 °C for 2 h. The obtained sample was denoted as *x*Co@C_*T*, where *x* and *T* stand for the loading of cobalt in wt% and the calcination temperature, respectively. The cobalt loading in this work was calculated based on the Co in its zero valent form.

2.2. *Characterization*

Field emission scanning electron microscopy (SEM) was carried out on an FEI Nova NanoSEM 450 FEGSEM and an FEI Magellan 400 high resolution SEM. Both SEMs are equipped with in-lens detectors and directional concentric backscattered detectors. Selected backscattered electron (BSE) images were analyzed by Image-Pro Plus 5.0 software to provide particle size information. Transmission electron microscope (TEM) images were acquired with an FEI Tecnai F20 transmission electron microscope. Powder X-ray Diffraction (XRD) analysis was performed on a Philips PW1130 powder diffractometer with CuKα radiation (λ = 1.5405 Å) at 40 kV and 25 mA. Nitrogen sorption data was collected at 77 K by using a Micromeritics Tri-star sorption analyzer.

The electrochemical experiments were performed on Autolab PGSTAT30 (Eco Echemie B.V. company) with a three-electrode electrochemical cell system that consisted of a working electrode, a platinum counter electrode and an Ag/AgCl reference electrode. The distance between the working electrode and the counter electrode was 2.5 cm. The working electrode was prepared firstly by mixing the powder composite and polytetrafluoroethylene (PTFE, 10 wt%) at a weight percent ratio of 9:1 in isopropyl alcohol. The resultant slurry was then

coated onto the 1 cm^2 nickel foam which was used as the current collector. The coated nickel foam was finally pressed at a pressure of 10 MPa for 5 minutes and subsequently dried at 80 °C under vacuum for 12 h. Cyclic voltammetry was carried out in the potential range (-0.4 V, 0.4 V) in a 6 M KOH electrolyte at room temperature.

3. Results and Discussion

Figure 1(a) shows the secondary electron (SE) image of 10Co@C sample calcined at 400 °C. A clean surface and channel structure similar to the CMK-3 template was observed which indicated the well-preserved porous carbon structure after the impregnation and the calcination processes. Figure 1(b) shows the corresponding TEM image of 10Co@C_400. The fact that only continuous stripes with no aggregated particles were observed, suggested a uniform distribution of the precursor inside the channels of carbon. The BET specific surface area and total pore volume of CMK-3 are 1250 m^2g^{-1} and 1.36 cm^3g^{-1}, respectively (Table 1). After Co was loaded, the BET specific surface area and total pore volume of 10Co@C_400 reduce to 1080 m^2g^{-1} and 1.09 cm^3g^{-1}, respectively. It suggests that the cobalt precursors likely consume the space in the micro and mesopore, causing the reduction of the surface area and pore volume.

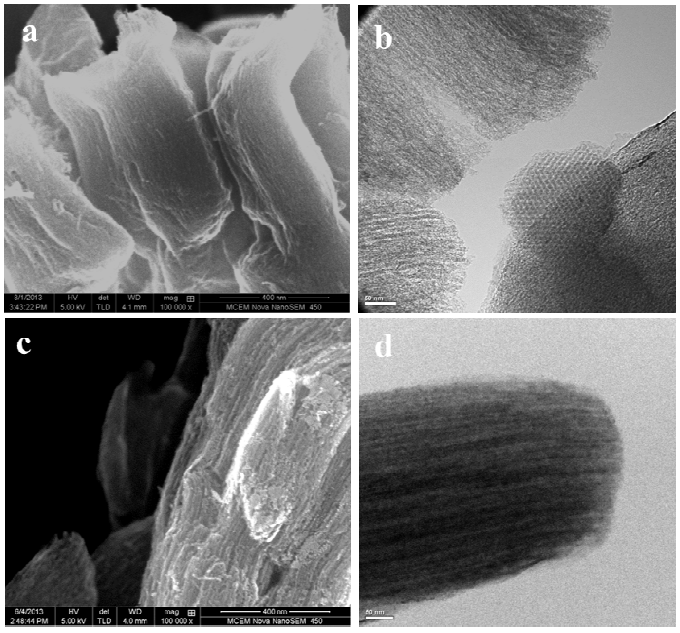


Figure 1. Secondary electron (a) and transmission electron (b) images of 10Co@C_400, secondary electron (c) and transmission electron (d) images of 15Co@C_400

Based on the total pore volume of CMK-3 and the theoretical assumption of using the cobalt precursor solution to completely fill all the pores, the maximum possible amount of cobalt was calculated. This corresponded to a final structure with a cobalt loading of 15 wt%. However, even after the cobalt loading was increased to 15 wt%, apart from the carbon channel stripes, no clear particles was observed in the SE image (Figure 1(c)), suggesting uniform distribution of cobalt oxide particles and well-retained carbon structure. Figure 1(d) shows its TEM image. Channel-like structures can be easily observed having tiny particles present, revealing that the increment of cobalt loading has boosted particle development. 15Co@C_400 showed a BET specific surface area of 1000 m^2g^{-1} which was lower than 10Co@C_400 (Table 1). It was noteworthy from the nitrogen sorption analysis data that both 10Co@C_400 and 15Co@C_400 show significant reductions of pore volume both in the meso and microrange compared to CMK-3. This suggests that the cobalt precursors were likely occupying the space in meso and micropore.

Table 1. Porosity parameters of carbon support and *x*Co@C_*T* composites.

Sample name	BET specific surface area (m^2g^{-1})	Micropore volume (cm^3g^{-1})	Mesopore volume (cm^3g^{-1})	Total pore volume (cm^3g^{-1})	Pore size (nm)
CMK-3	1250	0.52	0.84	1.36	3.50
10Co@C_400	1080	0.45	0.64	1.09	3.48
15Co@C_400	1000	0.41	0.56	0.97	3.35
15Co@C_500	1160	0.48	0.66	1.14	3.52

As the calcination temperature was increased to 500 °C, NPs of cobalt oxides could be identified in the SE image of 15Co@C_500 (Figure 2(a)). To further investigate the NPs dispersion, concentric backscattered electron analysis was performed. Figure 2(b) shows the corresponding BSE image of 15Co@C_500. The observation of continuous stripes with well-dispersed bright spots suggests the uniform distribution of NPs inside the carbon channels. Cobalt oxide particles are identified as bright spots in the BSE images. Figure 2(c) shows the TEM image of 15Co@C_500. The NPs were observed well-dispersed with uniform size of ~4 nm. These results demonstrate that our synthesis approach has successfully and uniformly incorporated the cobalt oxide NPs into the meso-channels of the CMK-3 carbon. Moreover, 15Co@C_500 sample shows higher specific surface area of 1160 m^2g^{-1} than that of 15Co@C_400. Considering of the temperature adopted for calcination, we believe that at the temperature of 400 °C, most of the cobalt precursors have not been fully

decomposed. But at the temperature of 500 °C, the decomposition is almost complete, releasing more surface area and pore volume for gas adsorption. With the TEM result (Figure 2(c)) for this sample, it is also clear that metal oxide particles in this sample are bigger than those in 15Co@C_400.

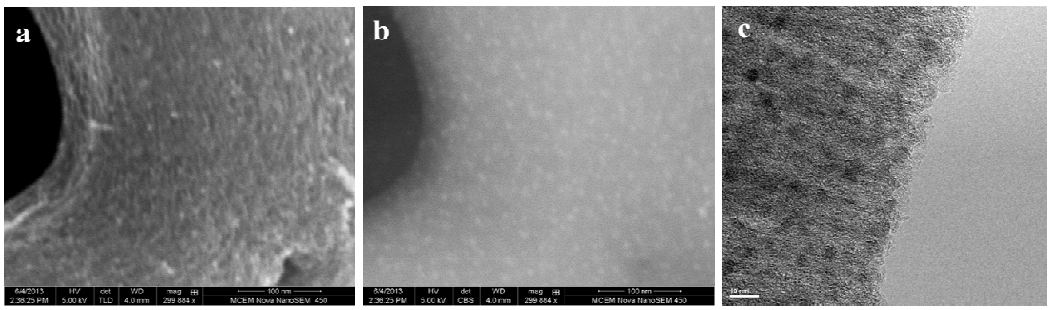


Figure 2. Secondary electron (a), backscattered electron (b) and transmission electron (c) images of 15Co@C_500.

The XRD patterns of CMK-3 and 15Co@C_500 are shown in Figure 3. Only two broad peaks emerged at 23.4 and 43.5° were detected for CMK-3, and confirmed the amorphous nature of this material. For 15Co@C_500, broad and weak diffraction peaks observed at 36.62 and 42.20° can be indexed to CoO (72-1474). The weak intensity of the diffraction peaks suggested that CoO was not very crystalline and was not fully developed upon the decomposition of the cobalt precursor in argon atmosphere.

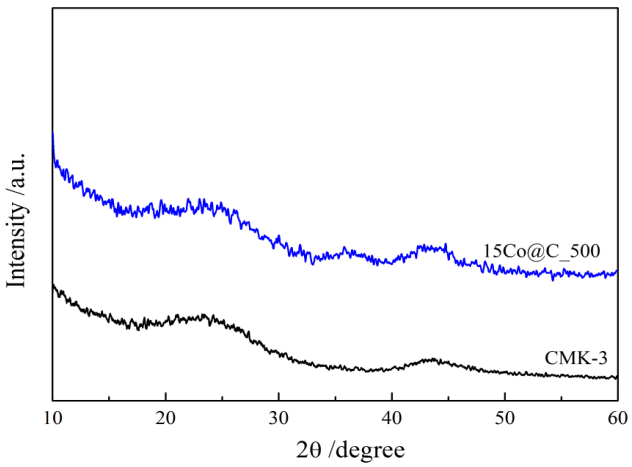


Figure 3. Powder X-ray diffraction patterns of CMK-3 and 15Co@C _500.

The results obtained from cyclic voltammetry (CV) tests for the electrodes prepared using CMK-3 and 15Co@C_500 are presented in Figure 4. The CV

curve of CMK-3 electrode exhibited a rectangular shape in the potential range from -0.40 to 0.10 V, at a voltage sweep rate of 10 mVs^{-1} (Figure 4(a)), indicating the typical electric double-layer capacitive (EDLC) behavior. However, with a 15 wt% cobalt loading, electrode 15Co@C_500' CV curve shows clear redox peaks in (-0.1 V, 0.4 V), suggesting typical pseudo capacitance (Figure 4(b)). The shape represents response of cobalt oxides active sites, showing the pseudo capacitance caused by electrochemical reactions. Two redox reaction peaks are visible in its CV curve. The oxidation peaks at 0.30 V is assigned to the processes of Co^{2+}/Co^{3+} transition [16]. And, the reduction peaks at 0.13 V is corresponded to the reverse processes. The overall electrochemical processes could be expressed as follows:

$$CoO+OH^- \rightleftharpoons CoOOH + e^-$$

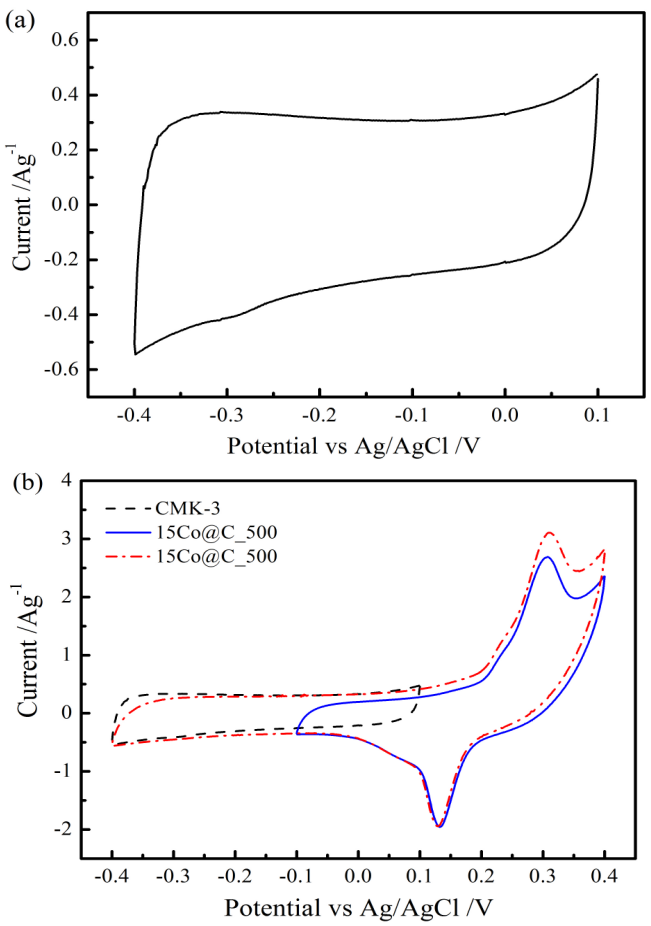


Figure 4. Cyclic voltammograms of CMK-3 and 15Co@C_500.

Since the areas of CV curves are proportional to the capacitance, the result suggests that 15Co@C_500 electrode possesses increased capacitance. However, 15Co@C_500 has lower specific surface area than CMK-3, which means lower double layer capacitance. It is likely that the increased capacitance originated from the redox reaction in the material. By extending the potential range to (-0.4 V, 0.4 V), the CV curve of 15Co@C_500 electrode exhibited significant shape in which the CV curve of CMK-3 was included. It clearly reveals that 15Co@C_500 possessed both EDLC and pseudo capacitance in a wide range. Moreover, at (-0.4, 0.1 V), the CV curve of 15Co@C_500 covers that of CMK-3 very well. It suggests that the EDLC characteristic maintains very well after loading cobalt oxide NPs into carbon channels. Thus, the well-retained mesoporous structure of carbon support can also facilitate electrolyte filtration and increase ion diffusion, which both retains EDLC and promotes the electrochemical reaction to achieve important pseudo capacitance. Thus, the CMK-3 supported well-dispersed cobalt oxide NPs show significant improvement of electrochemical properties.

4. Conclusion

Well-dispersed cobalt oxide nanoparticles supported on mesoporous carbon CMK-3 have been synthesized successfully. The prepared composites can have as high as 15 wt% cobalt. The sample possesses a good dispersion of cobalt particles (~4 nm) and a surface area of up to 1160 m^2g^{-1}. The electrochemical testing results suggest that the mesoporous structure of the composites could facilitate the ion diffusion in the rich porous structure and then possess important double layer capacitance. More importantly, cobalt oxides clearly enhanced the pseudo capacitance of the materials, due to the faradic reaction generated from cobalt oxide nanoparticles.

Acknowledgments

This work was financially supported by the National Basic Research Program of China (2013CB934103) and the collaboration fund provided by CSIRO. The first author gratefully acknowledges financial support from China Scholarship Council. The authors acknowledge use of facilities within the Monash Centre for Electron Microscopy.

References

1. Y. Wan, H. Wang, Q. Zhao, M. Klingstedt, O. Terasaki and D. Zhao, *J. Am. Chem. Soc.* **131**, 4541 (2009).
2. H. Jiang, J. Ma and C. Li, *Adv. Mater.* **24**, 4197 (2012).
3. Q. Zhang, J. Kang and Y. Wang, *ChemCatChem.* **2**, 1030 (2010).
4. H. Zhang, C. Lancelot, W. Chu, J. Hong, A.Y. Khodakov, P.A. Chernavskii, J. Zheng and D. Tong, *J. Mater. Chem.* **19**, 9241 (2009).
5. Z. Wu, N. Hao, G. Xiao, L. Liu, P. Webley and D. Zhao, *Phys. Chem. Chem. Phys.* **13**, 2495 (2011).
6. T. Battumur, S.B. Ambade, R.B. Ambade, P. Pokharel, D.S. Lee, S.-H. Han, W. Lee and S.-H. Lee, *Curr. Appl. Phys.* **13**, 196 (2013).
7. E.M. Garcia, H.A. Tarôco, T. Matencio, R.Z. Domingues, J.A.F.d. Santos, R.V. Ferreira, E. Lorençon, D.Q. Lima and M.B.J.G.d. Freitas, *J. Appl. Electrochem.* **42**, 361 (2012).
8. C. Zhou, Y. Zhang, Y. Li and J. Liu, *Nano Lett.* **13**, 2078 (2013).
9. X. Wang, X.Y. Chen, L.S. Gao, H.G. Zheng, Z.D. Zhang and Y.T. Qian, *J. Phys. Chem. B* **108**, 16401 (2004).
10. A.M. Cao, J.S. Hu and H.P. Liang, *J. Phys. Chem. B* **110**, 15858 (2006).
11. K.-S. Ha, G. Kwak, K.W. Jun, J. Hwang and J. Lee, *Chem. Commun.* **49**, 5141 (2013).
12. E. Barrera, T. Viveros, A. Montoya and M. Ruiz, *J. Sol. Energy Mater. Sol. Cells* **57**, 127 (1999).
13. J. Feng and H.C. Zeng, *Chem. Mater.* **15**, 2829 (2003).
14. X. Song, Y. Ding, W. Chen, W. Dong, Y. Pei, J. Zang, L. Yan and Y. Lu, *Appl. Catal. A: General* **452**, 155 (2013).
15. Y. Shan and L. Gao, *Mater. Chem. Phys.* **103**, 206 (2007).
16. S. Park and S. Kim, *Electrochim. Acta* **89**, 516 (2013).
17. G. Wang, L. Zhang and J. Zhang, *Chem. Soc. Rev.* **41**, 797 (2012).
18. J. Zhi, S. Deng, Y. Zhang, Y. Wang and A. Hu, *J. Mater. Chem. A* **1**, 3171 (2013).
19. B. Li, B. Sun, X. Qian, W. Li, Z. Wu, Z. Sun, M. Qiao, M. Duke and D. Zhao, *J. Am. Chem. Soc.* **135**, 1181 (2013).
20. Z.X. Wu, Y.Y. Lv, Y.Y. Xia, P. Webley and D. Zhao, *J. Am. Chem. Soc.* **134**, 2236 (2012).

SYNTHESIS OF EG S Ge COMPOSITE BY NOVEL GRAPHENOTHERMAL REDUCTION AND ITS ANODIC STUDIES FOR LITHIUM ION BATTERIES

SHAIKSHAVALI PETNIKOTA[a,b], SANDEEP KUMAR MARKA[a,b], M. V. REDDY [*,c], VADALI, V.S.S. SRIKANTH[a] and B. V. R. CHOWDARI[b]

[a]*School of Engineering Sciences and Technology (SEST), University of Hyderabad, Gachibowli, Hyderabad 500046, India*

[b]*Advanced Batteries Lab, Department of Physics, National University of Singapore, Singapore 117542, Singapore*

[c]*Department of Materials Science and Engineering, National University of Singapore, Singapore 117576, Singapore*

Exfoliated Graphene Oxide-Germanium (EG-Ge) is prepared by following simple solid state and eco-friendly graphenothermal reduction (GTR) method. 2:1 molar dry mixture of graphene oxide (GO) and GeO_2 is heated at 900 °C for 2 hours with 5 °C/min heating and cooling rate in Argon environment to obtain EG-Ge. The existence of Ge nanoparticles with cubic crystal structure on EG surfaces is confirmed by XRD, SAED and Raman spectroscopy. Specific surface area (BET) of the as-synthesized powder is found to be ~115 m^2/g. As-synthesized EG-Ge powder is used as an active material to prepare electrodes which are subsequently used as anodes for Lithium Ion Batteries (LIBs). EG-Ge as an anode of LIB shown reversible capacity 947 mAh/g at a current rate of 400 mA/g during first cycle. Coulombic efficiency at end of first cycle is 60.5% which increased to 90% and then soon it fluctuated in between 96-98% during remaining cycles. The mechanism of lithium insertion and extraction by alloying and de-alloying with germanium along with electrochemical absorption and desorption onto EG is understood with cyclic voltammetry (CV). The relatively low impedance values are observed from EIS measurements. Finally, EG-Ge is found to be suitable for anodic application in LIBs but still deserving pre or post synthesis modifications for improved cycling performance.

Key words: Graphenothermal Reduction, Graphene Oxide, GeO_2, EG-Ge, Lithium Ion Battery, Anode.

1. Introduction

Lithium Ion Batteries (LIBs) are most promising and fruitful energy storage devices for portable electronics to electromobile automotives. LIBs are in great

Proceedings of the 14th Asian Conference on Solid State Ionics (ACSSI 2014)
Copyright © 2014 ACSSI 2014 Organizers. All rights reserved.
ISBN: 978-981-09-1137-9
doi:10.3850/978-981-09-1137-9_125

need of high capacity anode materials that possess maximum capacities with least voltage hysteresis in the range 0-0.5 V like graphite. Silicon (4200 mAh/g) and Germanium (1623 mAh/g) are considered as most promising prospective anode materials but their commercial usage have been hindering by their early stage failure due to huge volume expansion and pulverization of material upon lithiation that causes rapid capacity decay (poor cycle stability).[1, 2] Making composite of Si and Ge with graphene effectively stops the volume changes and retains the reversible lithiation reactions for longer time. But to meet cost effective issues there is a need to develop bulk synthesis methodologies. Here in our study, Ge was chosen for the reasons that it possess superior electronic conductivity than Si and easy scope for thermal reduction of GeO_2 at relatively low temperature than SiO_2. In this regards here we reports synthesis of 'Exfoliated Graphene Oxide-Germanium (EG-Ge)' in bulk amounts by following novel Graphenothermal reduction (GTR) which is analogous to Carbothermal reduction (CTR). In this new method Graphene Oxide (GO) and GeO_2 are mixed in specific molar ratio in mechanical grinder and heated in Argon environment at temperature 900ºC for 2 hours. During heating reduction of both reagents and exfoliation to GO takes place simultaneously. Here GO acts as reducing agent by sacrificing some of its free carbons as well as gas species like CO released from it upon heating which are capable of reducing GeO_2. The merits of GTR method are it is simple solid state, one pot, eco-friendly, no separate reducing agent required, only non toxic gaseous by-products like CO, CO_2, post production treatment like purification etc not required, as prepared material can be directly used for final application like anode of LIBs and most importantly yield can be several grams to kilograms achievable. The physical and chemical characterization of as prepared EG-Ge is carried out with XRD, TEM, Raman Spectroscopy etc. Coin cell LIBs fabricated by using EG-Ge as anode are tested for their performance with galvanostatic cycling (GC), cyclic voltammetry (CV) and Electrochemical Impedance Spectroscopy (EIS) techniques and more details of instrumentation are reported elsewhere.[3-5]

2. Experimental Details

2.1. *Synthesis of GO and EG-Ge*

Graphene Oxide (GO) was prepared from natural graphite by a modified Hummers method[6]. In brief 150 mL of 95-98% H_2SO_4 was taken in a clean beaker that kept in an ice bath in order to remove excess heat generated by exothermic reactions during the addition of oxidizers. Next 6 g of graphite was

dispersed into H_2SO_4 and stirred about few minutes till the mixture became uniform. Then 0.5 g of $NaNO_3$ followed by 3 g of $KMnO_4$ were added slowly pinch by pinch in order to avoid excessive heat generation and after thorough mixing the reaction mixture was transferred to stirrer whose hotplate maintained at 45 °C for half an hour. Next, 150 mL of distilled water was added to the reaction mixture and eventually mixture is stirred at its raised temperature of 98°C for an hour. Then, the beaker is filled with distilled H_2O up to the neck and after cooling to room temperature, 5 mL of 30% H_2O_2 was added prior to stirring stopped. Then the synthesized GO suspension was allowed to settle down for a few hours before decanting the supernant solution. After discarding supernant away sediment is washed several times with warm distilled water until the pH of the solution becomes neutral (7). After the final decant, the GO is then filtered and placed in an oven to dry for over 12 hours. Then the dried GO directly added into the final reaction mixture that mage with GeO_2 in its appropriate amounts. In order to synthesize EG-Ge composite powder, GO and GeO_2 dry powders were taken in 2:1 molar ratio (6 g) and mechanically grinded for 30 min. Next this dry powder mixture was heated at 900 ºC for 2 hours in continuous argon gas flow with same heating and cooling rates of 5 ºC/min. As result of heating fine black powder of EG-Ge (3g) was produced and this powder is directly used for further characterizations without any post synthesis treatment.

2.2. *Coin cell LIBs Fabrication*

Prior to fabricating coin cell LIBs, electrodes (anodes) of EG-Ge were prepared by as follows. Electrode slurry was made by taking as-synthesized EG-Ge powder as the active material, polyvinylidene fluoride (PVDF) in N-Methyl-2-pyrrolidone (NMP) solvent as a polymer binder, and Super-P carbon (230 m^2g^{-1}) as a conductive additive in the weight ratio of 70:15:15. The coin cells (CR2016) were fabricated by using Li metal serving as counter (cathode) electrode, polymer separator (Celgard) followed by the prepared EG-Ge electrode. The 1M $LiPF_6$ dissolved in ethylene carbonate (EC) and dimethyl carbonate (DMC) in a 1:1 volume ratio was used as electrolyte. More details about coin cell battery fabrication are reported in our previous work. [3-5]

2.3. *Characterisation Techniques*

Morphological studies were carried out by using Transmission electron microscope (TEM) (Model FEI Technai G^2 S-Twin). Electron micrographs recorded with accelerating voltages of 200 kV at various magnifications. XRD (Empyrean Panalytical) was performed on EG-Ge powder using CuK_α radiation

(wavelength 1.5418Å), and the technique used to investigate the crystallinity, lattice parameters and average crystallite size etc of the powder specimen, which can be derived after using Rietveld refinement via TOPAS(v2.1). XRD patterns were taken at 40 kV, 30 mA and at step size 0.02°/s. Raman spectra (Renishaw Raman system 2000) were recorded with auto excitation wavelength and auto confocality focussed by 100X objective lens (spot diameter ~1 μm) in open atmosphere at room temperature in order to detect extent of exfoliation to GO by recording various carbon hexagon breathings in both GO and EG. Specific surface area and porosity (pore size and pore diameter) were measured from the analysis of N_2 physisorption at 77 K with Micromeritics (Tristar 3000, USA) using Brunauer–Emmett–Teller (BET) and Barrett-Joyner-Halenda (BJH) multipoint methods. Samples were preheated under N_2 flow at 200 °C for 1 hour. To record isotherms of N_2 adsorption and desorption, NTP conditions were maintained around sample holder while mixture of He and N_2 gases flowed in according to The Dynamic (Flowing Gas) Technique.

The electrochemical analysis of the coin cell batteries was carried out at room temperature of 25 ^{o}C as follows. The Bitrode multi-channel tester [MCV16-05/001-5, Bitrode, USA] was used for measuring charge-discharge capacity values at a current density of 400 mA g^{-1} over a 100 cycles (galvanostatic cycling, GC). Cyclic voltammetry (CV) was performed at the scan rate of 58 μV s^{-1} by using a multi-potentiostat (Mac-pile II system, Biologic, France). Electrochemical Impedance Spectroscopic (EIS) measurements of the coin cell were done with a Solartron impedance/gain-phase analyzer (model SI 1255) coupled with a potentiostat (SI 1268) in the frequency range 0.18 MHz to 3 mHz with an AC signal amplitude of 10 mV. Both GC and CV testing were conducted in the range of 0.005-3.0 V while impedance was measured in a state of fresh (OCV), discharged to 0.005V and charged to 3.0 V. The impedance data were analyzed using Z-view software (version 2.2, Scribner Assoc., Inc., U.S.A.) in order to model equivalent circuits.

3. Results and Discussions

Fig.1(a) and 1(b) shows TEM images of EG-Ge in which germanium nanoparticles are found to be distributed all over the graphene sheet in a tightly physisorbed manner and there are no free standing particles found. Bright field imaging (Fig.1(c)) clearly visualizes how sparingly germanium nanoparticles (dark grayish spots) scattered across the semitransparent graphene sheets. The corresponding SAED ring pattern depicted in Fig.1(d) also evident for germanium and graphenes are well stickered together. The observed SAED ring

pattern mainly contains atomic projections of various facets of graphene and germanium. The ring pattern of germanium that corresponds to (111) facet is confirmed partially that germanium nanoparticles are well crystallized. Further microstructural features of as-prepared EG-Ge powder are investigated with XRD technique and resulted diffraction pattern is strongly dominated by germanium peaks only as shown in Fig.2. In contrast, pattern of GO contains only a sharp peak nearby 10º which is considered as a (002) graphitic peak that shifted from 26.5º as result of increased d-spacing due to oxidation of graphite to form GO. The absence of graphitic peaks in EG-Ge pattern suggesting that either full exfoliation of GO happened to form two dimensional EG or intense peaks of Ge made them negligible in agreement with TEM results.

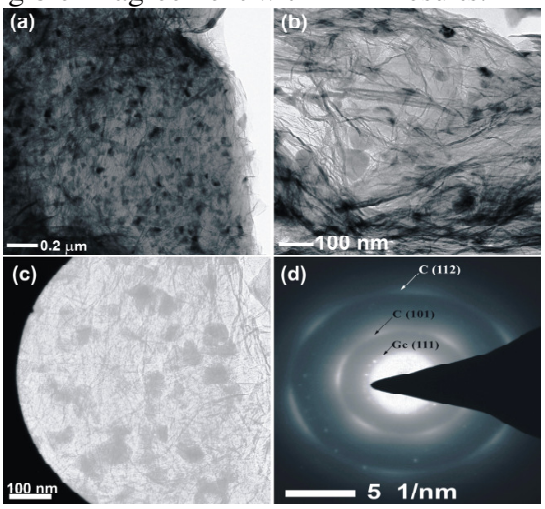


Figure 1. TEM images of EG-Ge (a), (b), (c) and corresponding SAED pattern (d).

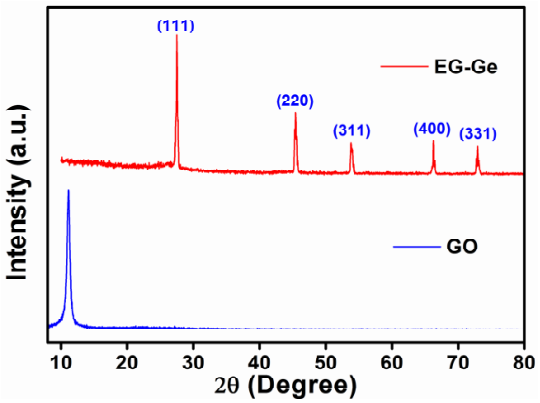


Figure 2. XRD patterns of EG-Ge (red) and GO (blue).

BET specific surface area of EG-Ge powder is found to be ~115.45 m^2g^{-1} with average pore volume of ~0.405 cm^3g^{-1} and the corresponding average pore

size is found to be ~14.04 nm. The small hysteresis is found between nitrogen adsorption and desorption isotherms as shown in Fig.3(a). which also determines materials porosity in tune with average pore size and diameters calculated. The observed isotherms of nitrogen gas adsorption and desorption are matched to the type III isotherm among the BET classification types I-VI.[5] This specific surface area of EG-Ge is moderately low when compared with pristine graphene prepared under similar conditions. This might be happened due germanium nanoparticles that covered active sites of EG and they may not be effectively allows N_2 molecules to be adsorbed onto them.[5]

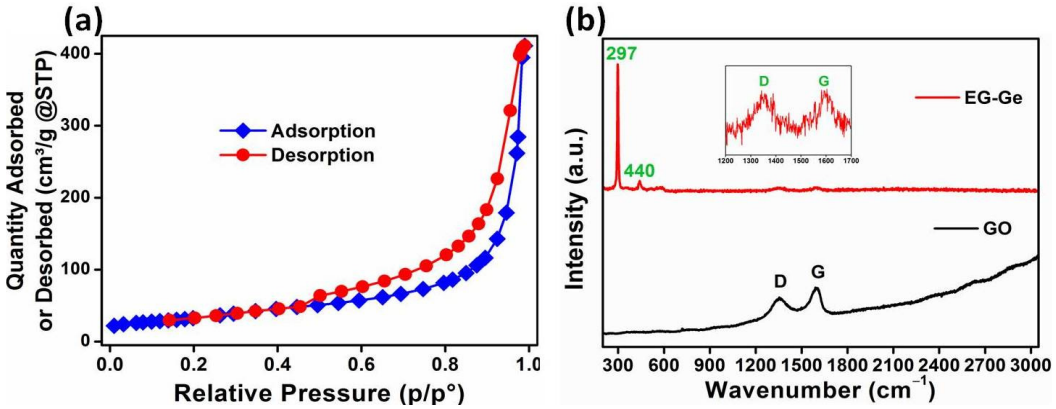


Figure 3. N_2 adsorption and desorption isotherms of EG-Ge powder (a), Raman spectra of EG-Ge (red) and GO (black) (b).

The Raman scattering results of EG-Ge and GO are shown in Fig.3(b). The Raman spectra of EG-Ge is dominated by sharp peaks from germanium whilst common peaks of EG (D, G and 2D-bands) are found to be very weak.[5] The strong peaks found at 297 and 440 cm^{-1} are corresponds to Ge-Ge and Ge-Si (impurities) vibrations respectively.[7] The D and G-bands of EG are found to be centered around 1350 and 1595 cm^{-1} respectively. The positions of D and G-bands in GO are found almost same as in EG but their intensity seems to be higher. In both cases there is no sign of 2D-band that might be resulted from higher degree of disorder imposed due to chemical oxidation to form GO and thermal reduction to form EG.

Galvanostatic cyclic results of EG-Ge for first 100 cycles are shown in Fig.4. The first discharge curve is very steeper and voltage dropped down to below 1.0 V without any slope change. The first change in slope is observed around 0.9-0.7 V which corresponds to typical electrolyte decomposition to form solid electrolyte interphase (SEI). The second change in slope is noticed around 0.5V which secured approximately 350 mAh/g capacity is majorly due to

lithiation by Li alloying with Ge to form $Li_{4.4}Ge$. [1, 2] The third change in slope of is happened at 0.25V corresponding to discharging capacity of 1100 mAh/g which might be contributed by lithium intercalation into EG as like in graphite (ref of ur J. Solid state electrochemistry vali etal.). Further this curve is declined gently with same slope till the voltage drops to 0.005V by securing total discharge capacity of ~1566 mAh/g. The first charging curve is inclined steeply up to 0.5V from where curve is quite horizontally extended up to 0.6 V by bagging net charging capacity of ~500 mAh/g and this capacity is mainly due to de-alloying of lithium from $Li_{4.4}Ge$. [1, 2] Above 0.6 V slope of the charging curve has changed continually up to 1.5 V from whereby once again it shown steer inclination up to 3.0V for which total charging capacity of ~947 mAh/g is observed. Thus more than 60% discharge capacity is reversed while charging by leaving a difference of 619 mAh/g which is also known as irreversible capacity loss (ICL). The observed ICL is majorly considered to be originates from lithium loss that covalently trapped inside SEI constituent compounds like Li_2O and Li_2CO_3 etc. [5] The second and subsequent discharging and charging curves are found similar to first cycle curves but their capacity is gradually decreased. This gradual decay plausibly due to continuous ceasing of lithium's reversibility via alloying and de-alloying reactions with Ge as like in bare Ge anode. Here great amount of capacity loss is occurred only due to continuous shortening of horizontal portion around 0.5V that indicates Ge is becoming more and more inactive as cycling progressed and eventually its contribution to total capacities goes on decreased. Finally there is no sign of alloying and de-alloying of lithium with Ge and whatever capacity shown by composites seems to be only contributed by EG as curves above 40^{th} cycle are found similar to pristine graphene. Here by anchoring Ge nanoparticles onto good conducting type EG, good electrical contacts are expected during pulverization of Ge crystals upon de-lithiation unlike bare Ge anode in which pulverization causes electrical insulation. But decay in capacity due to Ge might be evolved from competition for lithiation between EG and Ge in which EG dominates Ge at current densities >C/10 and present case testing rate (C/4) is well beyond this limit.[1, 2] Also continuous formation of SEI might also be other reasoning for this decay which might isolated Ge phase from interacting with Li- ion coupling with its native pulverization effect. However EG-Ge shown stable reversible capacity of 250-260 mAh/g after 50^{th} cycle onwards with QEs 96-98% despite of 60.48 % during first cycle.

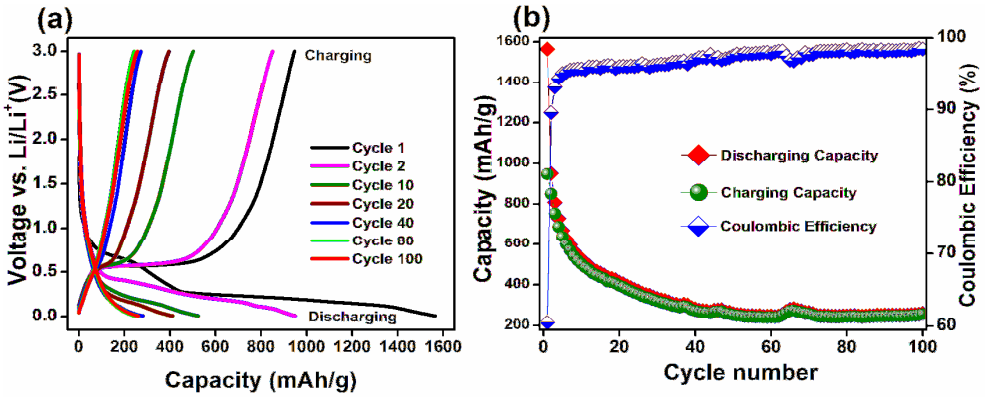


Figure 4. Discharge-charge vs. voltage profile (a) and cyclic performance (b) of EG-Ge at 0.25C.

Cyclic voltammetry results of EG-Ge for first six reduction and oxidation sweeps are shown in Fig.5(a). During the first reduction scan, starting from OCV there is no change in current until voltage becomes 0.9V. Beyond this voltage reduction current is increased gradually till voltage drops to 0.25V from whereby increase is found huge and continuous until voltages drops to it final set value of 0.005V. On the other hand, during the first oxidation scan a sudden jump in current value to zero is observed when voltage reaches 0.2 V and beyond this voltage current is negligible till 0.45V from where current is once again increased largely followed by same amount of decrease (up to 1.0V) to form peak centered around 0.6V. Further oxidation curve is appeared very flat with negligible current up to final voltage of 3.0V. From the second reduction scan onwards there is one broad peak with small intensity is observed around 0.15V and its current is continuously decreased with increasing cycle number. This small and broad reduction peak in between 0.6 and 0.005V might be resulted from insertion of lithium into EG-Ge by alloying with Ge to form $Li_{4.4}Ge$ and intercalation/electrochemically absorbed onto EG. [1, 2, 5] The large current difference found between first and second reduction curves can be ascribed to SEI and ICL formation. From the second oxidation sweep onwards also there is only one peak around 0.6V is observed as like in first sweep but current of this peak goes down continuously as number of sweeps wears on. This oxidation peaks is attributed mainly to removal of lithium from EG-Ge by de-alloying from $Li_{4.4}Ge$ to form individual Li and Ge phases. [1, 2] The remaining entire oxidation current is either due to de-intercalation or electrochemical desorption of Li from EG. Thus overall CV results are completely in tune with GC results where role of Ge to hold or release lithium decreases and became negligible at the end of the test and finally EG is alone active for (de)lithiation. Thus overall less impedance values during charging than OCV and discharge signifies lithium will

be extracted easily from EG-Ge and this might appeared high reversible capacity observed in GC results.

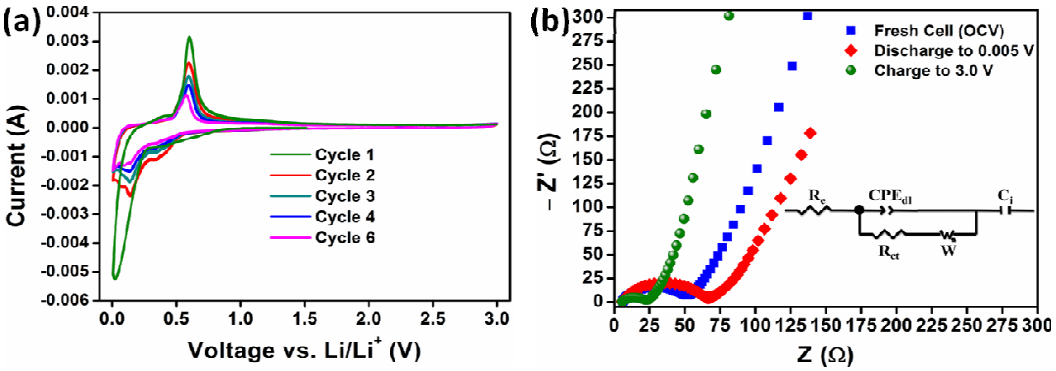


Figure 5. Cyclic voltammetry results of EG-Ge (a) and EIS spectra (after fitting) of EG-Ge at OCV, fully discharged and charged states (b).

EIS spectra of EG-Ge as Nyquist plots are shown in Fig.5(b) for its fresh, fully discharged (to 0.005V) and fully charged (to 3.0V) states. Fig.7 also shows model equivalent electrical circuit into which raw impedance data fitted best. The first circuit element R_e is known as electrolyte/contact resistance[8, 9] and its value is found to be ~5.7 Ω for OCV and after first discharge but this value slightly decreased to ~5.0 Ω after first charge. The other circuit element R_{ct} is charge transfer resistance[8, 9] is observed to be ~46.2, ~58.3 and ~18.1 Ω at OCV, discharge and charge respectively. The constant phase element, CPE_{dl} that corresponds to capacitance of double layer formation due to charge transfer[8, 9] is found ~49, 52 μF at OCV and first discharge respectively, but this value increased enormously to ~283 μF after first charge. The Warburg element that equivalent to resistance experienced by diffusing lithium ions found relatively very high than R_e or R_{ct}. The last element C_i corresponds to lithium's (de)intercalation capacity found less than 0.5F in all three states of coin cell. [8, 9]

4. Conclusion

In conclusion, we successfully demonstrated the synthesis of EG-Ge composite material by following navel GTR method. In this method, simultaneous reduction of GO and GeO_2 takes place along with exfoliation of GO to form EG-Ge upon heating in an inert environment. The GTR method is very advantageous for the sake of its ecofriendly nature and being simple solid state yield in bulk amounts can be simply tailored by varying initial reagents. The formation of EG-Ge is confirmed by XRD, TEM and Raman spectroscopy to As-synthesised EG-Ge powder is used to make anodes which are subsequently used to fabricate coin cell LIBs. As an anode of LIBs, EG-Ge shown high reversible capacity with

good QEs but deserving appropriate pre or post-synthesis modification in order to attain improved capacity retention. At 400 mA/g current EG-Ge has shown reversible capacity 947 mAh/g and found to be suitable for anodic application in LIBs. Both CV and GC results indicated that lithiation by germanium enormously decreased upon cycling and EG-Ge needs modification to retain germaniums initial contribution to total reversible capacity.

Acknowledgments

PSS is grateful to Government of India for providing financial support through MANF (F1-17.1/2011/MANF-MUS-AND-213/(SA-III/Website)) to pursue research studies at the University of Hyderabad. PSS and SKM (SIPIS-2013) are thankful to NUS for financial support through India research initiative (NUS-IRI) fund. MVR thank to National Research Foundation, Prime Minister's Office, Singapore under its Competitive Research Programme (CRP Award No. NRF-CRP 10-2012-6) for research support.

References

1. K. H. Seng, M.-h. Park, Z. P. Guo, H. K. Liu and J. Cho, *Nano Letters*, 2013, **13**, 1230-1236.
2. A. M. Chockla, M. G. Panthani, V. C. Holmberg, C. M. Hessel, D. K. Reid, T. D. Bogart, J. T. Harris, C. B. Mullins and B. A. Korgel, *The Journal of Physical Chemistry C*, 2012, **116**, 11917-11923.
3. M. V. Reddy, G. V. Subba Rao and B. V. R. Chowdari, *Journal of Materials Chemistry*, 2011, **21**, 10003-10011.
4. B. Das, M. V. Reddy, G. V. Subba Rao and B. V. R. Chowdari, *Journal of Materials Chemistry*, 2011, **21**, 1171-1180.
5. S. Petnikota, N. Rotte, V. S. S. Srikanth, B. R. Kota, M. V. Reddy, K. Loh and B. V. R. Chowdari, *Journal of Solid State Electrochemistry*, 2014, **18**, 941-949.
6. W. S. Hummers and R. E. Offeman, *Journal of the American Chemical Society*, 1958, **80**, 1339-1339.
7. P. H. Tan, K. Brunner, D. Bougeard and G. Abstreiter, *Physical Review B*, 2003, **68**, 125302.
8. M. V. Reddy, B. L. Wei Wen, K. P. Loh and B. V. R. Chowdari, *ACS Applied Materials & Interfaces*, 2013, **5**, 7777-7785.
9. M. V. Reddy, T. Yu, C. H. Sow, Z. X. Shen, C. T. Lim, G. V. Subba Rao and B. V. R. Chowdari, *Advanced Functional Materials*, 2007, **17**, 2792-2799.

SYNTHESIS OF CARBON-ENCAPSULATED SNO_2 NANOPARTICLES AS ANODE MATERIAL WITH SUPERIOR CYCLABILITY FOR LITHIUM ION BATTERIES *

PENG PENG, ZHAOYIN WEN†, YU LIU

CAS Key Laboratory of Materials for Energy Conversion, Shanghai Institute of Ceramics, Chinese Academy of Sciences,1295 Ding Xi Road, Shanghai, 200050, China

A designed carbon-encapsulated SnO_2 composite was synthesized by a reduction process with subsequent carbonization. X-ray diffraction, scanning electron microscopy and transmission electron microscopy were conducted to characterize the product. SnO_2 nanoparticles were uniformly encapsulated into the carbon matrix. Taking advantage of the special microstructure, the composite revealed an excellent cycling stability with a good high-rate performance.

1. Introduction

In recent years, lithium alloy anodes with high theoretical capacity become a main development trend, but their serious volumetric effect causes sharp capacity fading, resulting in the poor electrochemical performance [1]. Among these alloy anodes, Sn-based anode is a special one due to the generation of inert lithium oxide acting as a buffer material [2], leading to a favorable cycling stability. Of particular note is that a nanoparticle-based system is expected to improve the electrochemical performance of SnO_2-based anode, but these active nanoparticles would aggregate during cycling, resulting in a poor capacity retention [3]. Dispersing active particles into a matrix is an effective method to deal with this problem, which can prevent the particles from electrical disconnection [4]. Carbonaceous materials with the good conductivity and chemical and mechanical stability [3], like graphite and carbon, have been studied to improve the performance of cathode and anode materials in lithium-ion batteries [5, 6]. As reported by Guo et al, carbon-coated SnO_2 hollow microspheres were fabricated by the hydrothermal reaction followed with the heat treatment and displayed a reversible capacity well over the theoretical capacity of carbon-free SnO_2 [7]. Chen reported a core-shell structure composed

* This work is supported by the National Natural Science Foundation of China No. 51373195.

†Corresponding author. Tel.: +86 21 52411704; fax: +86 21 52413903. E-mail address: zywen@mail.sic.ac.cn

Proceedings of the 14th Asian Conference on Solid State Ionics (ACSSI 2014)
Copyright © 2014 ACSSI 2014 Organizers. All rights reserved.
ISBN: 978-981-09-1137-9
doi:10.3850/978-981-09-1137-9_130

of SnO_2 nanoparticles confined in mesoporous hollow carbon spheres with a superior cycling performance, whose capacity reached 450 $mA•g^{-1}$ at 1/5 C after 50 cycles [8]. Carbonizing organic precursors is a common method to obtain carbon and the core-shell structure. In this paper, we combined SnO_2 nanoparticles with carbon by pyrolyzing glucose in an attempt to reduce capacity fading. And the electrochemical behaviors and morphology were also discussed.

2. Experimental

2.1. *Material preparation*

Glucose, $SnCl_4•5H_2O$ and sodium borohydride were purchased from Sinopharm Chemical Reagent Co., Ltd. $SnCl_4•5H_2O$ and glucose was dissolved under constant stirring. Afterwards sodium borohydride ($NaBH_4$, $NaBH_4$:$SnCl_2$=1:2 in mole) dissolved in deionized water was drop wise added under constant stirring at 273K. Until the precipitates became white, the solvent, deionized water, was evaporated gradually along with the stirring to get a solid blend. Then the blend precursor was heated at 973K under a flowing argon atmosphere for 2 hours. The final product was obtained after grinding and sieving.

2.2. *Physical characterization and electrochemical tests*

The crystalline phase and structure were characterized by X-ray diffraction (XRD, D/max 2550V) and infrared spectroscopy (IR; Bruker TENSOR27) of the powder samples diluted with KBr. The constitution was analyzed by thermogravimetric-differential scanning calorimetry (TG-DSC; Netzsch 409PC). The morphology was analyzed by scanning electron microscopy (SEM, JSM-6700F, S-3400N) and transmission electron microscopy (TEM, JEM-2010).

The electrodes were prepared by ball-milling the mixture of the composites, acetylene black and sodium alginate binder (8:1:1 in mass). The electrochemical tests were carried out with 2025 coin type cells. The cells were assembled in an Ar-filled glove box with oxygen and water contents less than 1 ppm. The electrolyte was $1mol•L^{-1}$ $LiPF_6$ in a mixture of ethylene carbonate (EC) and dimethyl carbonate (DEC) (1:1 volume) with 2wt% vinylene carbonate (VC). Lithium foil was used as the counter and reference anode. The cells were cycled under different current densities in the voltage range of 0.05-1.5V using a CT2001A Land (Wuhan, China) battery test system. Impedance measurements in the frequency range of 0.01Hz-10M Hz with AC

amplitude of 10 mV were carried out on Autolab PGSTAT302 potentiostat-galvanostata electrochemical work station (Metrohm).

3. Results and discussion

3.1. *Phase and structure characterization of SnO_2@C composite*

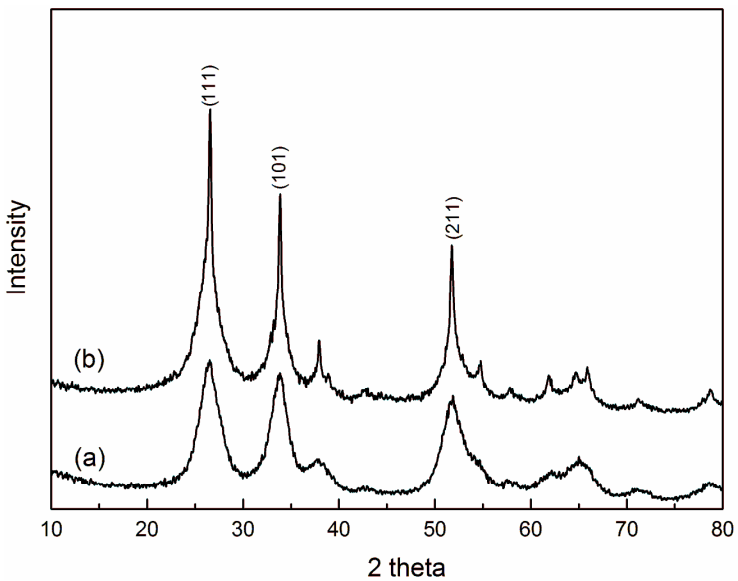


Figure 1. XRD patterns of (a) SnO_2@C composite and (b) SnO_2 nanoparticles

The crystal structures of SnO_2 nanoparticles and as-synthesized SnO_2@C composite are characterized by XRD measurement as shown in Figure 1. The two samples display a similar crystalline phase. The main dominant peaks identified at $2\theta = 26.61^o$, 33.89^o and 51.78^o are assigned to (110), (101) and (211) planes of a typical tetragonal SnO_2 (a=b=4.738 Å and c=3.187 Å, JCPDS 77-0450) [9]. No obvious peaks attributed to carbon appear in the pattern of SnO_2@C composite, demonstrating that the carbon composited with SnO_2@C is amorphous. The characteristic peaks of SnO_2 are wider in the pattern of SnO_2@C composite, which means that the crystallinity decreases and the crystal size increases after introducing carbon.

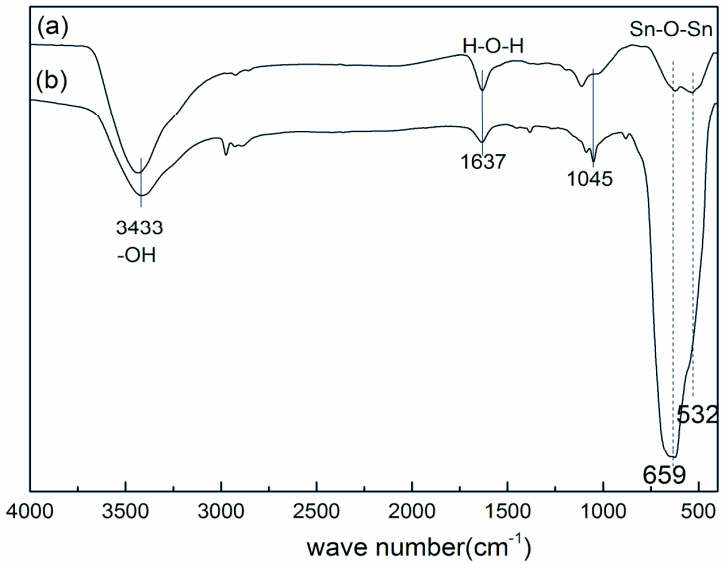


Figure 2. IR spectra of (a)SnO_2@C composite and (b) SnO_2 nanoparticles

To further understand the effect of the amorphous carbon, IR spectroscopy was also taken to characterize the structure as shown in Figure 2. The peaks at 3442 cm^{-1} and 1630 cm^{-1} correspond to the vibration of hydroxyl and H–O–H bands, due to the unavoidable absorption of water on the surface of powders [10]. The peak at 1045 cm^{-1} is attributed to the vibration of surface hydroxyl groups' bands [11]. The bands at 532 cm^{-1} and 659 cm^{-1} are ascribed to the anti-symmetric mode of Sn–O–Sn [12]. There're no obvious differences between the two spectra, demonstrating no chemical bonds between the amorphous carbon and SnO_2 nanoparticles.

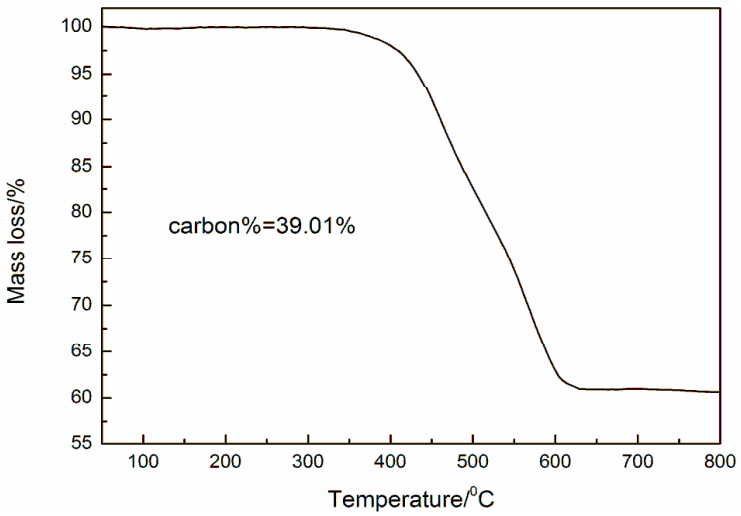


Figure 3 TG curve of SnO_2@C composite

TG analysis was carried out to calculate the chemical composition of SnO_2@C composite as shown in Figure 3. An obvious weight loss occurred in the range from 400℃ to 600℃ when the composite was heated to 800℃ in air atmosphere, which was mainly ascribed to the oxidization of carbon to generate escaping CO_2 [13]. So the mass fraction of carbon in SnO_2@C composite is calculated as 39.01%.

3.2. *Morphology analysis of SnO_2@C composite*

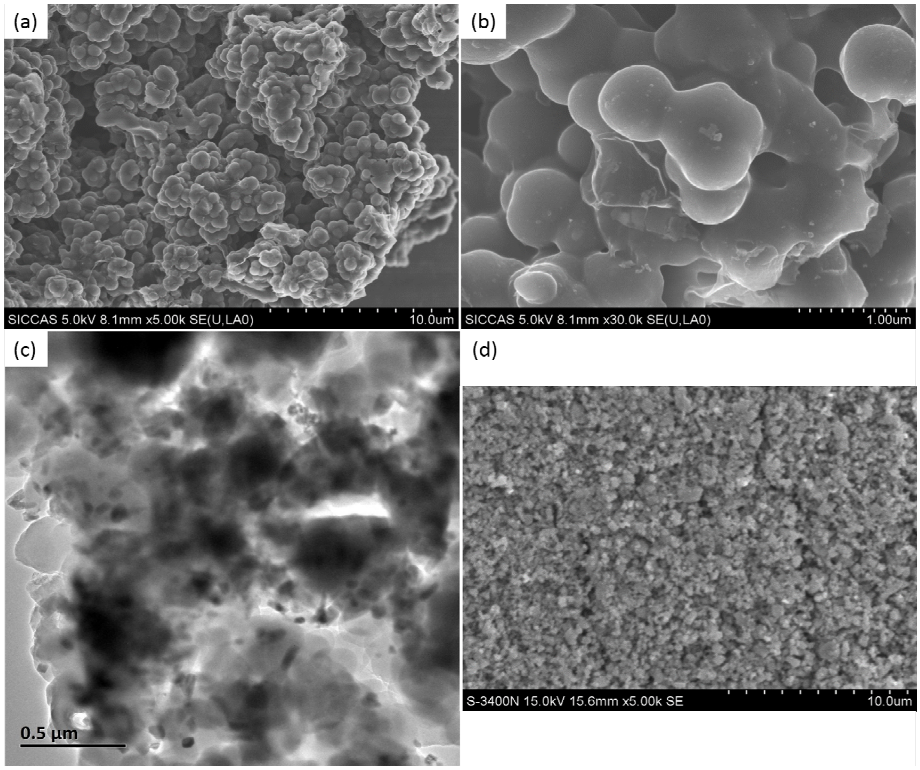


Figure 4. (a) Low- and (b) high-magnification SEM images of SnO_2@C composite; (c) TEM image of SnO_2@C composite; (d)low-magnification SEM image of SnO_2 nanoparticle

The morphology of SnO_2 nanoparticles and SnO_2@C composite was analyzed by SEM and TEM measurement as shown in Figure 4. The low-magnification SEM image in Figure 4(a) shows that SnO_2@C composite displays a pear-liked appearance, while SnO_2 nanoparticles disperse uniformly with an approximate diameter lower than 0.5 μm as shown in Figure 4(d) [14], the high-magnification SEM image in Figure 4(b) reveals that SnO_2@C composite interconnects to form a larger cluster. TEM measurement was further taken to detect the microstructure of the composite. The appearance of clusters are shown in Figure 4(c). Various SnO_2 nanoparticles are encapsulated into the amorphous carbon which acts as the matrix and connects with each other. The

base material, carbon by pyrolyzing glucose, can both prevent SnO_2 nanoparticles from the aggregation, and mitigate the pulverization of SnO_2 nanoparticles during the lithiation/delithiation, leading to the superior cycling performance.

3.3. *Cycling performance of SnO_2@C composite*

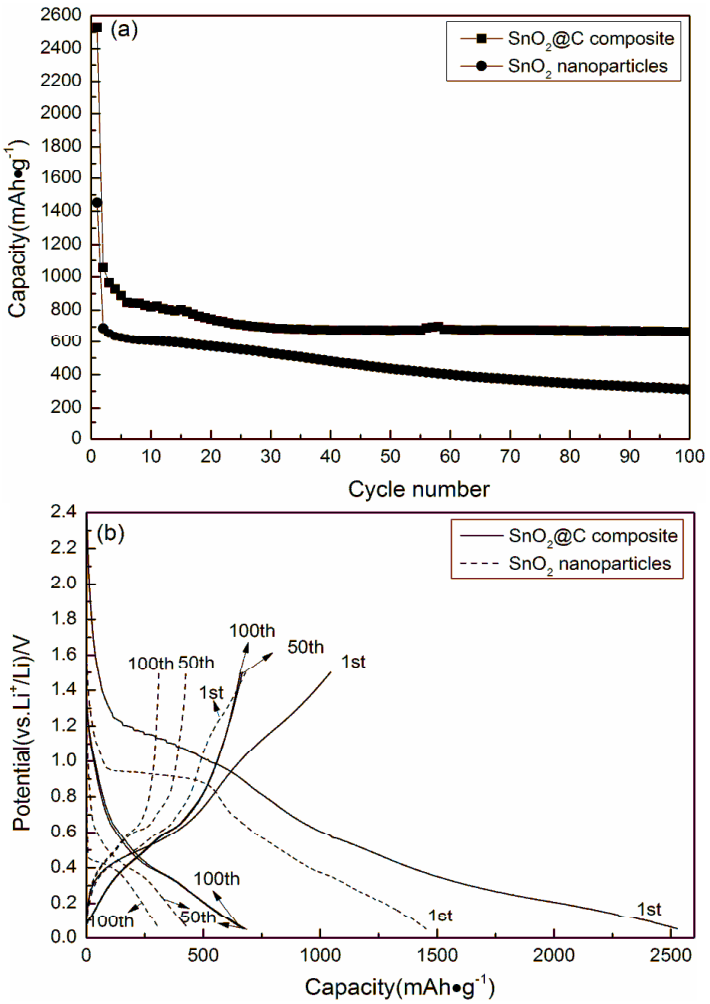


Figure 5. (a) Delithiation capacity of SnO_2@C composite and SnO_2 nanoparticle anodes at the rate of C/10 for 100 cycles; (b) Charging-discharging voltage profiles of SnO_2@C composite and SnO_2 nanoparticle anodes at C/10

Figure 5(a) shows the cycling performance of SnO_2@C composite and SnO_2 nanoparticle anodes, and the specific delithiation capacity as a function of cycling number was tested at the rate of C/10 for 100 cycles. Obviously SnO_2@C composite anode delivers a better cycling stability than SnO_2 nanoparticle anode. The reversible capacity of modified SnO_2-based anode

stayed at about 700 $mAhg^{-1}$ after 40 cycles, which is almost 300 $mAhg^{-1}$ higher than that of SnO_2 nanoparticle anode. The superior cycling performance of SnO_2@C composite anode is benefited from the carbon matrix which does a favor to prevent the particles from electrical disconnection and keep the integrity of the electrode.

Figure 5(b) shows the 1st, 50th, 100th charging-discharging voltage profiles of SnO_2@C composite and SnO_2 nanoparticle anodes at C/10. Both SnO_2-based anodes exhibit a wide steady plateau around 1.0V (vs Li^+/Li) during the first lithiation but then disappear in the following curves, which is assigned to the main specific capacity loss [15]. The subsequent 50th and 100th charging-discharging profiles of SnO_2@C composite anodes are almost coincide, demonstrating the outstanding cycling stability of our product.

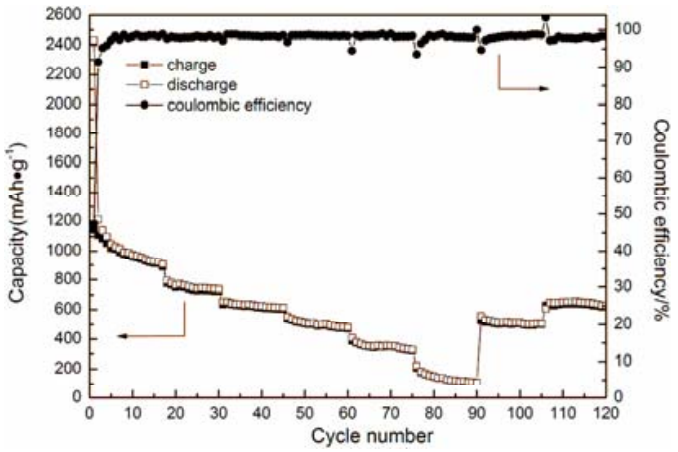


Figure 6. The cycling performance of SnO_2@C composite anode at different rates

To confirm the high-rate performance of SnO_2@C composite anode, the electrochemical behavior was tested at different current rates and 15 cycles were measured for each step as shown in Figure 6. As expected, SnO_2@C composite anode exhibits a stable cycling performance along with the rate increasing. When the current rate returns back to its initial value of C/10, the retention capacity is recovered to about 700 $mAh•g^{-1}$. Thanks to the microstructure for SnO_2 nanoparticles encapsulated into the amorphous carbon, an optimal high-rate performance is achieved.

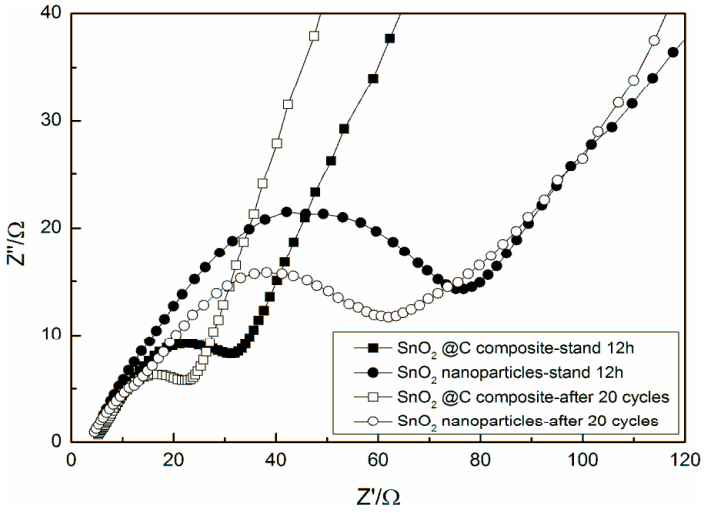


Figure 7. EIS of SnO_2@C composite and SnO_2 nanoparticle anodes after 20 cycles

To distinguish the better cycling performance of SnO_2@C composite anode, EIS (electrochemical impedance spectroscopy) was conducted to analyze the impedance of SnO_2@C composite and SnO_2 nanoparticle anodes. The impedance spectra of the initial and 20th cycles were tested at the rate of C/10 in Figure 7. All plots are composed of a semicircle at high-middle frequency whose diameter corresponds to the charge transfer resistance for lithium, and a nearly 45° line at low frequency which represents Warburg diffusion impedance [16-18]. Whether before or after 20 cycles, SnO_2@C composite anode possesses less charge transfer resistance than SnO_2 nanoparticle anode, demonstrating a better cycling performance and stability.

4. Conclusions

SnO_2@C composite was fabricated *via* the reduction and subsequent carbonization. SnO_2 nanoparticles were encapsulated into the amorphous carbon acting as the matrix. The as-designed microstructure made a contribution to improve the electrochemical performance and the composite delivered an excellent cycling stability and a good high-rate performance.

References

1. Z. Du, S. Zhang, T. Jiang, X. Wu, L. Zhang, H. Fang, *J. Power Sources* **219**, 199 (2012).
2. H. Park, T. Song, H. Han, A. Devadoss, J. Yuh, C. Choi, U. Paik., *Electrochem. Commun.* **22**, 81 (2012).
3. Y. Wang, J. Y. Lee, B. H. Chen, *Electrochem. Solid State Lett.* **6**, A19 (2003).
4. L. Yuan, J. Wang, S. Y. Chew, J. Chen, Z. P. Guo, L. Zhao, K. Konstantinov, H. K. Liu, *J. Power Sources* **174**, 1183 (2007).

5. J. Y. Lee, R. Zhang, Z. Liu, *Electrochem. Solid State Lett.* **3**, 167 (2000).
6. J. Read, D. Foster, J. Wolfenstine, W. Behl, *J. Power Sources* **96**, 277 (2001).
7. X. W. Guo, X. P. Fang, Y. Sun, L. Y. Shen, Z. X. Wang, L. Q. Chen, *J. Power Sources* **226**, 75 (2013).
8. X. W. Guo, X. P. Fang, Y. Sun, L. Y. Shen, Z. X. Wang and L. Q. Chen, *J. Power Sources* **226**, 75 (2013).
9. X. W. Lou, Y. Wang, C. L. Yuan, J. Y. Lee and L. A. Archer, *Adv. Mater.* **18**, 2325 (2006).
10. M.A. Gondal, Q.A. Drmosh, T.A. Saleh, *Appl. Surf. Sci.* **23**, 7067 (2010).
11. L. M. Fang, X. T. Zu, Z. J. Li, S. Zhu, C. M. Liu, W. L. Zhou, L. M. Wang, *J. Alloys Compd.* **454**, 261 (2008).
12. Z. M. Sun, Z. Q. Bai, H. L. Shen, S. L. Zheng, R. L. Frost, *Mater. Res. Bull.* **48**, 1013 (2013).
13. Y. N. Jo, Y. Kim, J. S. Kim, J. H. Song, K. J. Kim, C. Y. Kwag, D. J. Lee, C. W. Park and Y. J. Kim, *J. Power Sources* **195**, 6031 (2010).
14. J. Yang, Y. Takeda, N. Imanishi, and O. Yamamoto, *J. Electrochem. Soc.* **146(11)**, 4009 (1999).
15. Z. Wang, G. Chen and D. Xia, *J. Power Sources* **184**, 432 (2008).
16. S. L. Chou, X. W. Gao, J. Z. Wang, D. Wexler, Z. X. Wang, L. Q. Chen, H. K. Liu, *Dalton Trans.* **40**, 12801 (2011).
17. S. Yang, H. Song, H. Yi, W. Liu, H. Zhang, X. Chen, *Electrochim. Acta* **55**, 521 (2009).
18. H. Zhang, H. Song, X. Chen, J. Zhou, H. Zhang, *Electrochim. Acta* **59**, 160 (2012).

Li-CYCLING STUDIES OF MFe_2O_4 (M=Ni, $(Ni_{0.5}Zn_{0.5})$ & Zn)

M .V. REDDY[1,2*], CHU YAO QUAN[2,3], KEEFE WAYNE TEO[2,3], LIM JI HO[2,3], S. ADAMS[1], B.V.R. CHOWDARI[2]

[1]*Departments of Materials Science & Engineering, National University of Singapore, Singapore 117546*

[2]*Department of Physics, National University of Singapore, Singapore 117542*

[3]*NUS High School of Math and Science, 20 Clementi Avenue 1, Singapore 129957*

$NiFe_2O_4$, $Ni_{0.5}Zn_{0.5}Fe_2O_4$, $ZnFe_2O_4$ compounds were synthesized using molten salt method with KCl as the molten salt. They were characterized by Scanning Electron Microscopy (SEM), X-Ray Diffraction (XRD), Brunauer-Emmett-Teller (BET) surface and density methods. Li-cycling studies Cyclic Voltammetry (CV) and Galvanostatic Cycling tests. Li-cycling profiles show average potentials of ~1.0V and ~1.5V vs. Li respectively for discharge and charge cycle. The electrochemical storage properties of prepared compounds showed a reversible capacity (mAh/g) of 706, 536, 637 for M= Ni, $(Ni_{0.5}Zn_{0.5})$ and Zn, respectively, at the end of the 50^{th} cycle.

Key words: Molten salt method; $NiFe_2O_4$, $Ni_{0.5}Zn_{0.5}Fe_2O_4$, $ZnFe_2O_4$; Electrochemical properties

1. Introduction

After early work on conversion oxides by the group of Tarascon [1], there was great interest on oxide anodes based on conversion and alloying–de-alloying reactions[2]. Some of the well studied conversion and alloying-de-alloying reaction mechanism anodes materials are $ZnCo_2O_4$[3, 4], $ZnFe_2O_4$[5, 6], $CdFe_2O_4$[7] etc. Among them includes $ZnFe_2O_4$, which undergoes conversion reaction due to Fe and alloying-de-alloying reaction because Zn and $NiFe_2O_4$[2, 8, 9] undergoes only conversion (redox) reaction due to Ni and Fe. It will great to understand the structure and electrochemical properties of $NiFe_2O_4$, $(Zn_{0.5}Ni_{0.5})Fe_2O_4$ and $ZnFe_2O_4$, since these materials are cheap and less toxic in nature, and its theoretical capacity (720-900 mAh/g) is higher than graphite (372

Proceedings of the 14th Asian Conference on Solid State Ionics (ACSSI 2014)
Copyright © 2014 ACSSI 2014 Organizers. All rights reserved.
ISBN: 978-981-09-1137-9
doi:10.3850/978-981-09-1137-9_132

mAh/g). Christie et al.[10] reported anodic properties of $Ni_{1-x}Zn_xFe_2O_4$ using Sol–gel auto-combustion method to prepare solid solutions of nano-crystalline spinel oxides. The electrochemical results clearly shows huge capacity fading (40-67%) and they showed a reversible capacity of 200-570 mAh/g at the end of 50^{th} cycle.

Here, we adopted molten salt method (MSM) to prepare our compounds. In molten media, reactions are usually controlled by chemical equilibria and proceed much faster than diffusion controlled solid-state reactions[11]. Presently, we prepared three compounds which are MFe_2O_4 (M=Ni, $(Ni_{0.5}Zn_{0.5})$ Zn) thus studying how the effect of solid solutions would have an effect on the electrochemical properties.

2. Experimental

2.1 *Preparation*

$NiFe_2O_4$, $Ni_{0.5}Zn_{0.5}Fe_2O_4$, and $ZnFe_2O_4$ were prepared using materials high purity (99%) metal salts from its suppliers, namely KCl (Merck), FeC_2O_4(Aldrich), $ZnSO_4$ (Merck), $NiCO_3$(Aldrich). The raw materials are weighed according to the stoichiometric and then mixed well in an alumina crucible. KCl was used as the molten salt. 30g of initial reactants is used in accordance to their molecular weight and stoichiometric ratios, and heated to 900^oC for 3hours (excludes heating and cooling time) in a box furnace (Carbolyte box furnace), at 3^oC/min. Eventually, all products will be washed with distilled water to remove excess Li-salts and filtered and then dried in a vacuum oven.

2.2 *Electrode Fabrication*

Electrodes were fabricated using the synthesized compounds as the active material, polyvinylidene fluoride (PVDF) as a polymer binder (Kynar 2801), and Super-P carbon (ENSACO, MMM Super P, 230 m^2g^{-1}) as a conductive additive in the weight ratio of 70:15:15, and *N*-Methyl-2-pyrrolidone (NMP) as an organic solvent (Alfa Aesar). Slurry was coated on an etched copper foil (Shenzhen Vanlead Tech. Co. Ltd, China), which will serve as a current collector. The doctor blade technique was used to coat the electrode uniformly with a slurry thickness of 20 mm. The foil was then placed in an oven at 80°C overnight. The foil was then punched into discs with a 16mm diameter (2.0cm^2 geometric area) using an electrode cutter and dried in on oven. The steel discs were then crimped using a press (Schmidt, Germany) to make it like spring-like, which would compress the contents of the completed cell, ensuring that the components were in contact with each other. The crimped disc was then spot welded (Avio, Japan) to the cell casing. In accordance to coin cells (CR2016),

the assembly of a battery is as follows, from top to bottom: the upper lid, a plastic ring, a metal spring, Li metal serving as counter and reference electrode, glass microfiber (Whatman) paper as a separator (Sigma-Aldrich), followed by the prepared electrode MFe_2O_4 , and lastly the coin cell cap. The electrolyte used was 1M $LiPF_6$ dissolved in ethylene carbonate (EC) and dimethyl carbonate (DMC) in a 1:1 volume ratio. Fabrication of the battery was carried out in the glove box filled with argon gas.

2.3 *Characterisation Techniques*

X-ray diffraction (XRD) (Empyrean Pananlytical) was performed using CuK_α radiation (wavelength 1.5418Å), lattice parameters can be derived after using Rietveld refinement via TOPAS (v2.1). Scanning electron microscopy (SEM) compounds were taken to determine the surface morphology. The Brunauer-Emmett-Teller (BET) surface method (Micromeritics TriStar, USA) was used to investigate the surface area of the compounds. The Bitrode multi-channel tester (MCV16-05/001-5, Bitrode, USA) was used study charge-discharge cycling. Information about density is also collected using an AccuPyc 1330 (Micromeritics, USA) pycnometer at ambient temperature. CV was also performed at room temperature of 25^{o}C using a multi-potentiostat (Macpile II, Biologic, France) at potentials of 0.005V – 3.0V, which gives information about redox couples. Galvanostatic charge-discharge cycling was conducted in the range of 0.005-3.0V vs Li at low current rate of 60 mAg^{-1}. To ensure percolation of the electrolyte to the electrodes, the cells were left to rest for 12 h before measurements.

3. Results and Discussions

3.1. *Structure and morphology*

All synthesized compounds are either black or brown. The powder XRD patterns are shown in Fig. 1. Lattice parameter values are obtained via the Rietveld refinement using reported spinel structure with reported space group (Fd3m). The lattice values of $NiFe_2O_4$, $Ni_{0.5}Zn_{0.5}Fe_2O_4$ and $ZnFe_2O_4$ are a = 8.3656(4)Å, 8.3590(6) Å, 8.4375(2) Å. The reported lattice parameter values are in between $NiFe_2O_4$ (JCPDS 86-2267) and $ZnFe_2O_4$ (JCDPS 82-1049). The slight differences in the lattice parameter values are due to differences in the ionic radius of the metal ions[12].

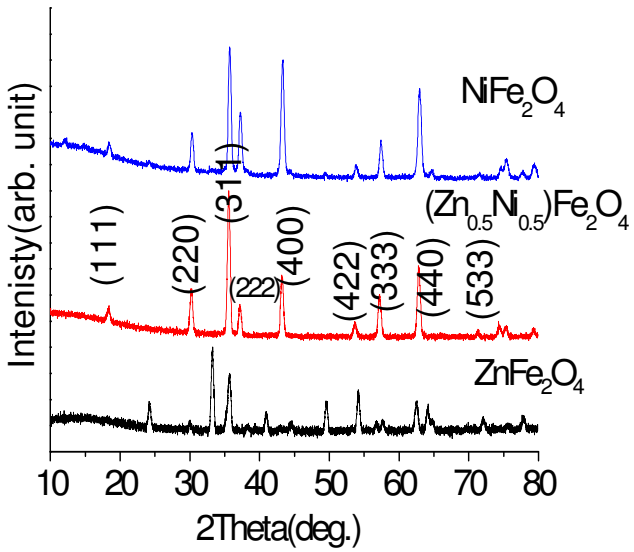


Figure 1. Powder X-ray diffraction patterns of $(Ni_{1-x}Zn_x)\ Fe_2O_4$ (x=0, 0.5, 1)

The SEM images of three compounds are shown in Fig. 2. From the images, we can see that all the compounds have quite similar morphology, which are all agglomerated and porous. The morphology and porosity of the particles are found to have a profound effect on the first cycle of discharge and charge cycling profiles and long-term cyclability of the spinel oxides compounds. Primary nanoparticles in the form of aggregates with spherical or flaky morphology to give rise to secondary particles with a macroporous structure are found to give high and stable reversible capacities with number of cycles. Present compounds are able to have good capacity retention; this can also be ascribed to the optimal particle size and macroporous structure, in comparison to those prepared at other temperatures, discussed in the later section. The average crystallite size obtained using XRD for $NiFe_2O_4$, $Ni_{0.5}Zn_{0.5}Fe_2O_4$, $ZnFe_2O_4$ are 25.7, 29.1, 25.8 nm and these values are close to SEM results. The observed density and surface area of $NiFe_2O_4$, $Ni_{0.5}Zn_{0.5}Fe_2O_4$, $ZnFe_2O_4$ are :5.71415 g/cm^3;6.88 m^2/g, 8.005 g/cm^3;2.25 m^2/g, 6.8338 g/cm^3;0.79 m^2/g, respectively.

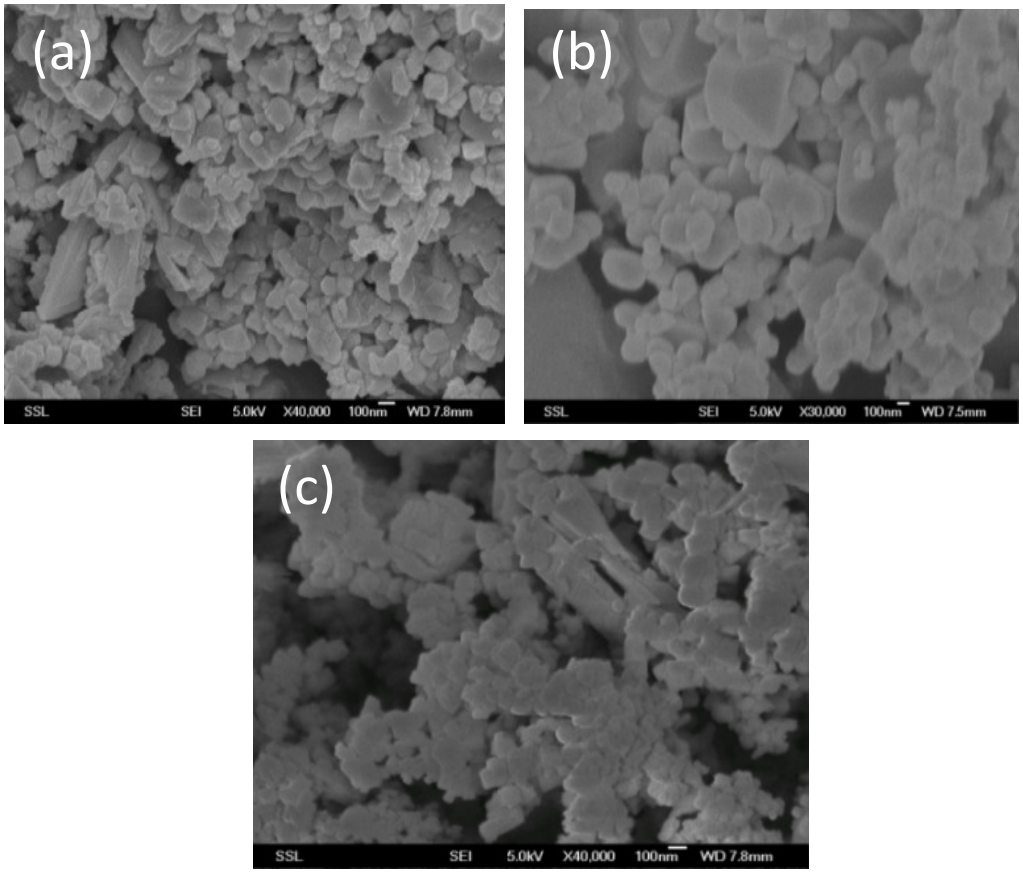


Figure 2. Scanning electron microscopy (SEM) images of (a) $ZnFe_2O_4$, (b) $Zn_{0.5}Ni_{0.5}Fe_2O_4$ and (c) $NiFe_2O_4$, Scale bar: 100 nm

3.2. Electrochemical studies

Galvanostatic charge-discharge cycling carried at a constant current rate of 60mA/g and a voltage range, 0.005V-3.0V. For select materials two duplicate cells were used in these tests to ensure consistent result. The voltage vs. capacity profiles are shown in Fig.3. Selected cycles are chosen for clarity, as these important cycles show the structural phase transformation during charge and discharge cycles. Graph 3(a) shows the 1st charge and discharge cycles of $NiFe_2O_4$. During the first discharge cycle, the voltage drops sharply from the open-circuit voltage (OCV) of about 2.8V to about 0.85V. This corresponds to the beginning of the single-phase Li-intercalation to the MFe_2O_4 structure, as shown in reaction 1. At this point, the corresponding capacity observed is about 60mAh/g. The discharge profile describes a voltage plateau at about 0.85V for

all compounds, except for $NiFe_2O_4$, which had two abrupt voltage plateaus of 0.75V and 0.7V. At about 0.75V, the voltage starts to slope downwards gently for the compounds, spanning over a capacity of about 650mAh/g. On the other hand, 1st cycle experiences a downward gentle slope that spans over 550mAh/g at 0.65V, which is evident of the Li-intercalation undergoing a two-step reaction mechanism. Reaction 2 represents this portion of the graph. As the discharge voltage decreases to 0.005V, resulting in the crystalline structure destruction, amorphisation of the crystalline structure, and reduction of metal ions (equation 2), and subsequently the formation of metal nanoparticles embedded in an amorphous matrix of Li_2O[2]. The first cycle discharge capacity of the compounds are of the following: $NiFe_2O_4$ at 1416 mAh/g, $Ni_{0.5}Zn_{0.5}Fe_2O_4$ at 1350 and $ZnFe_2O_4$ at 1515 mAh/g.

$$Ni_xZn_{1-x}Fe_2O_4 + bLi^+ + be^- \rightarrow Li_bNi_xZn_{1-x}Fe_2O_4 \quad (1)$$

$$Li_bNi_xZn_{1-x}Fe_2O_4 + (8-b)Li^+ + (8-b)e^- \rightarrow 2Fe + xNi + (1-x)Zn + 4Li_2O \quad (2)$$

$$xZn + Li^+ + e^- \rightleftharpoons LiZn_x \quad (3)$$

$$xNi + (1-x)Zn + Li_2O \rightleftharpoons Ni_xO + Zn_{1-x}O + 2Li^+ + 2e^- \quad (4)$$

$$2Fe + 3Li_2O \rightleftharpoons Fe_2O_3 + 6Li^+ + 6e \quad (5)$$

(where x=0,0.5, 1), $(0.4 \leq b \leq 0.6)$

The overall capacity at the end of the first charge cycles ranges between (923, 842, 863) mAh/g for M= Ni, ($Ni_{0.5}Zn_{0.5}$) and Zn, respectively, which houses an irreversible capacity loss (ICL) of about 500mAh/g. This loss is due to the formation of the solid electrolyte interface (SEI) and partially due to the reduction of the solvent and the electrolytes. Consumed in the formation of the organic polymeric layer on the metal nanoparticles forms when the electrode potential dips to 0.005V, which also contributes to ICL. Similar ICL is commonly observed in many other metal oxides[13, 14] and reports on $Ni_xZn_{1-x}Fe_2O_4$ [10]. In the charging process (Li-extraction), the initial spinel ferrite phase was not recovered, but simpler oxides were formed after reactions take place in reaction 4. The first charge cycle has no voltage plateau, but has a sloping profile between 1.5-2.0V spanning a capacity of about 550 mAh/g. During these charge cycles, the Li-intercalated MFe_2O_4 cells are gradually reforming through reaction 5.

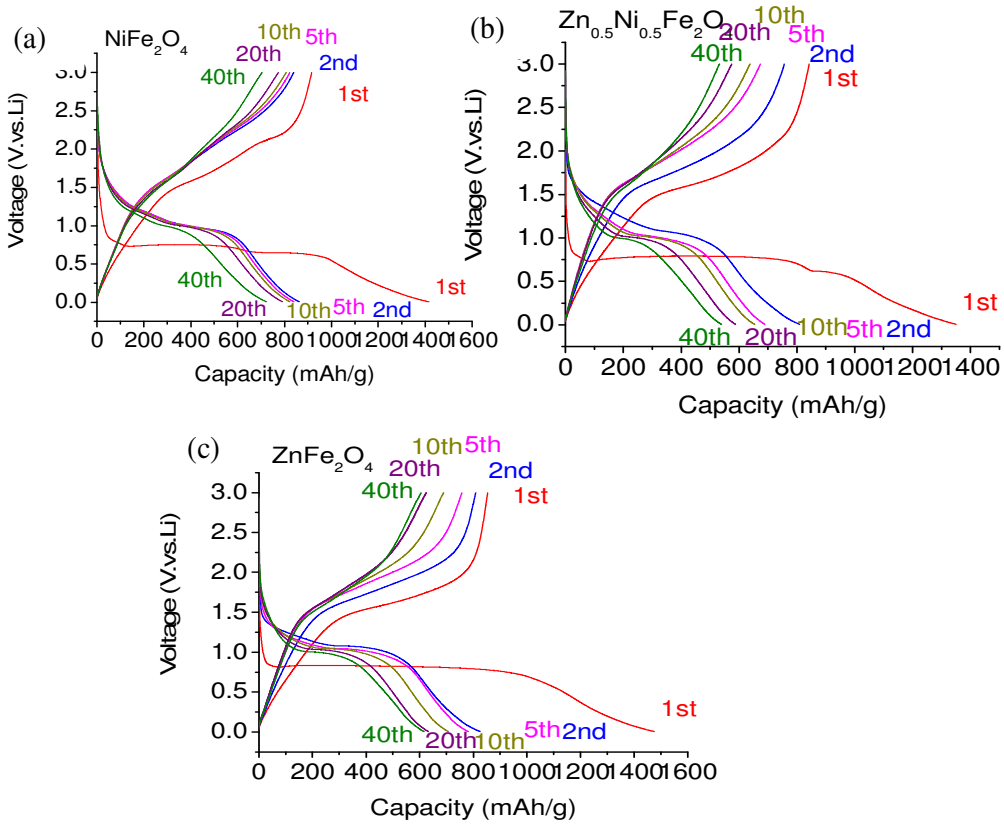


Figure 3. Voltage vs. Capacity plots of $NiFe_2O_4$, $Ni_{0.5}Zn_{0.5}Fe_2O_4$, $ZnFe_2O_4$, current rate, 60 mA/g, voltage range, 0.005-3.0V.

The second and subsequent discharge cycle has a different profile from the first discharge cycle. The voltage plateau at 0.85V is no longer seen. Instead, the sloping profile changes at 1.0V, and varies until 0.005V. This results in a final discharge capacity of (895, 809, 817) mAh/g for M= Ni, ($Ni_{0.5}Zn_{0.5}$) and Zn, respectively, which differs from the first cycle. Despite so, the second charge cycle is analogous to the first charge cycle, which indicates that similar electrochemical reactions are taking place in both cycles. However, it is necessary for the cells to be subjected at above 2.0V, in order to achieve a stable capacity because dissolution of the polymeric layer (formed during discharge) occurs above 2.0V[2, 3].

The capacity vs. cycle number plots are shown in Fig. 4. All cells displayed good capacity retention and columbic efficiency over 50 cycles, which values are 706, 536 and 637 mAh/g for M= Ni, ($Ni_{0.5}Zn_{0.5}$) and Zn, respectively. The present capacity values are greater than the other reported values via the Sol-gel auto

combustion method, which is 2-3 times greater at the 50th cycle[10]. Furthermore, capacity fading has also improved to 21.1%, 33.3% and 22.0%.

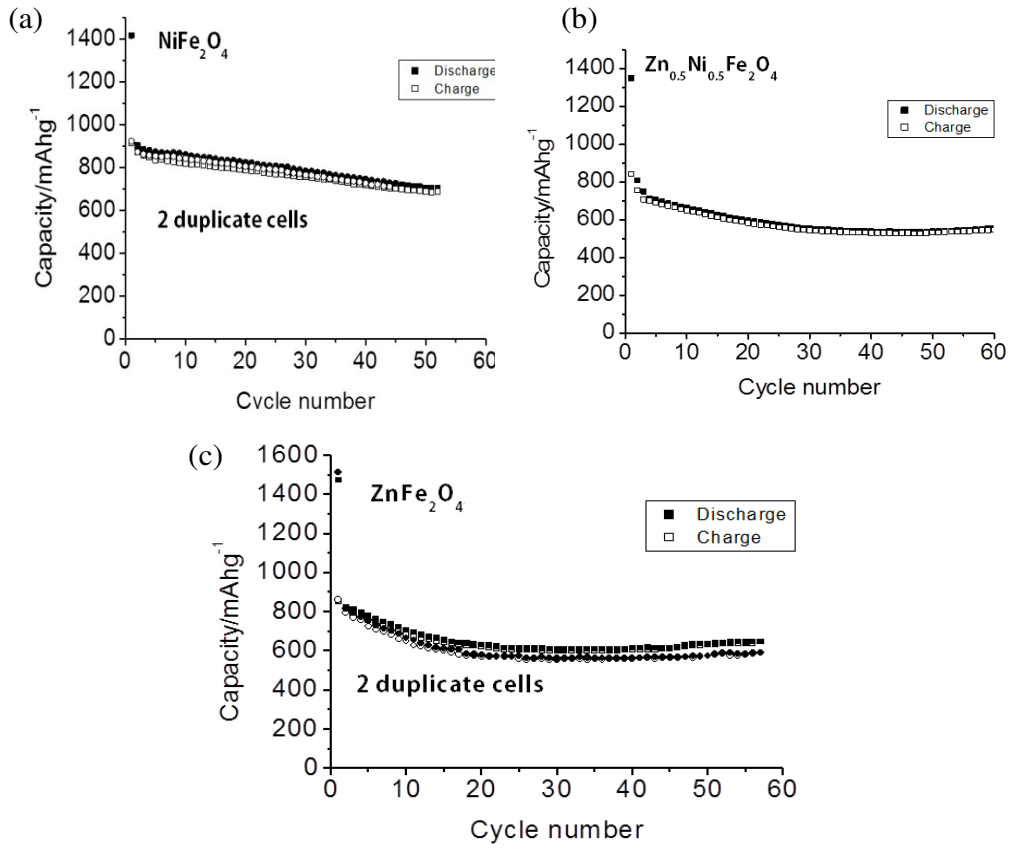


Figure 4. Capacity vs. cycle number plots of MFe_2O_4, voltage range, 0.005-3.0V, Current rate: 60 mA/g

Cyclic voltammetry studies (CV) are used to complement the galvanostatic cycling tests. CV was carried at a scan rate of 0.058mV/s at a voltage range of 0.005-3.0V and Li as the counter electrode. The voltammograms of three compounds are shown in Fig.5. Our first cathodic scan differs from the subsequent cathodic scans in all three compounds. Not only do they exhibit a cathodic peak of 0.6($\pm$0.1) V vs. Li, a continuous reduction in potential from the OCV ranges from about 2.8V to 0.8V is observed, which is similar to that of the galvanostatic scans. Such cathodic peaks occur due to crystal structure destruction, which is caused by the reduction of the Ni(II), Zn(II) and Fe(III) to corresponding metallic particles[15]. Formation of SEI also contributed for the peak, which is caused by the reduction of solvents in the electrolyte. $NiFe_2O_4$

showed two cathodic peaks, with the smaller peak arising before a larger peak, which is not seen in $ZnFe_2O_4$ and $Zn_{0.5}Ni_{0.5}Fe_2O_4$ was noted. However, the second cathodic scan does not experience a huge dip in its scans. These dips occur at about 1.0(±0.1) V.

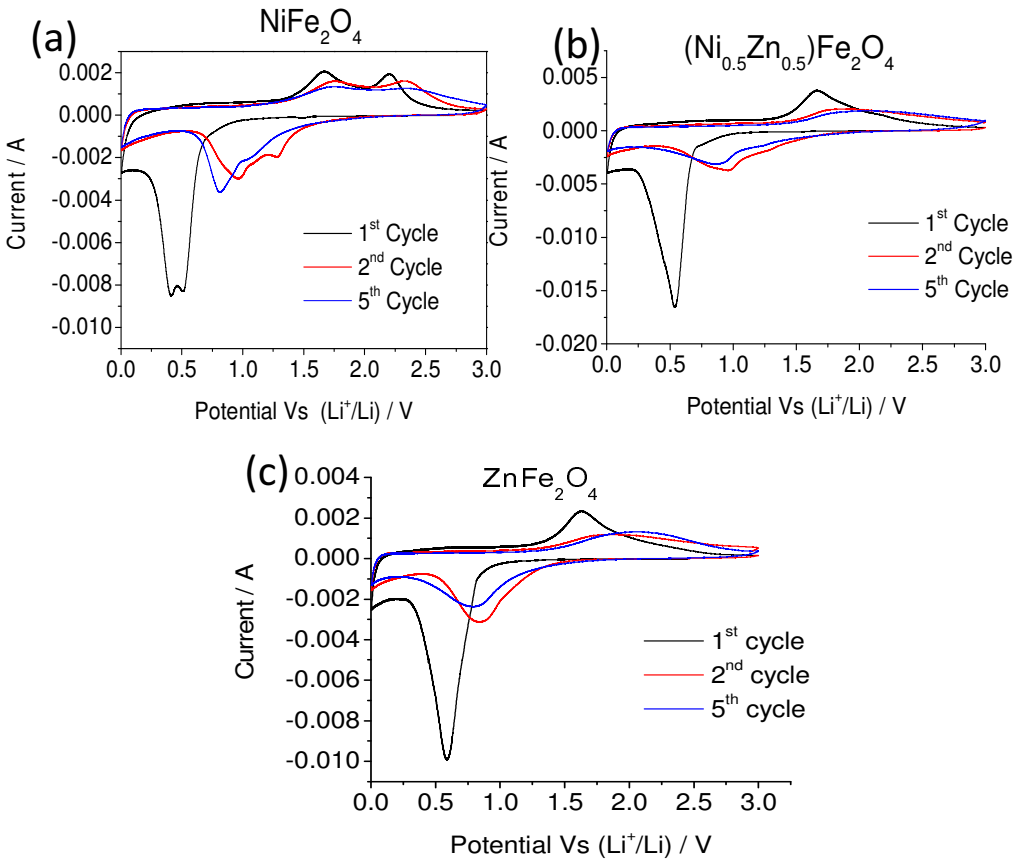


Figure 5. The cyclic voltammetry curves of (a) $NiFe_2O_4$; (b) $Zn_{0.5}Ni_{0.5}Fe_2O_4$ and (c) $ZnFe_2O_4$. Voltage range, 0.005-3.0V, Scan rate, 0.058mV/sec.

The first anodic scan generally occurs at 1.7(±0.1) V. In subsequent cycles, the anodic peak becomes flat and shifts towards a higher voltage value of 2.0(±0.2) V. This effect may account for the oxidation of Fe, Ni and Zn nanoparticles to the respective metal oxides. $NiFe_2O_4$ showed two distinct peaks at 1.8 was oxidation of Fe to Fe oxides[16, 17], anodic peak noted at higher voltage at 2.2V is due to reformation of NiO[18]. A decreasing trend of potentials is consistent through the subsequent cycles, as the peaks began to become flat and gentler. The observed board lines in CV are due to amorphization of crystal lattice structure and capacity fading at initial cycles.

4. Conclusion

Nano-sized materials, MFe_2O_4 (where x=Ni, Zn, ($Zn_{0.5}Ni_{0.5}$)) were synthesized via MSM and were characterized through XRD, SEM, BET and density methods. Galvanostatic cycling and CV carried out to understand physical and chemical-electrochemical properties. $Ni_{0.5}Zn_{0.5}Fe_2O_4$ showed greater capacity fading (34% at the end of 50^{th} cycle) possibly due to differences in surface area, morphology and crystalline structure. $ZnFe_2O_4$ and $NiFe_2O_4$, showed better Li-storage performances. All compounds showed higher reversible capacity than the commercial graphite anode. Furthermore, our compounds have lower capacity fading, which then allow our compounds to have an even greater (est. ~5 times on average) 50^{th} discharge capacity as the commercial graphite anode. Our compounds are cheap and eco-friendly, and versatile method of preparation. Furthermore, it could produce in anode our materials bulk and it is a simple process. For practical applications further reduction of discharge –charge voltage values or search for high voltage cathodes are needed.

Acknowledgments

MVR and ASN thanks to National Research Foundation, for the grant R-284-00-115-281). MVR and NUS HS students thank to Gifted Education Branch, Ministry of Education, Singapore to participate in the Science Mentorship Program and Dr Teh Yun Ling, NUSHS.

References

1. P. Poizot, S. Laruelle, S. Grugeon, L. Dupont, J.M. Tarascon, Nature 407 (2000) (6803) 496.
2. M.V. Reddy, G.V. Subba Rao, B.V.R. Chowdari, Chem. Rev. 113 (2013) 5364.
3. Y. Sharma, N. Sharma, G.V. Subba Rao, B.V.R. Chowdari, Adv. Funct. Mater. 17 (2007) (15) 2855.
4. M.V. Reddy, K.Y.H. Kenrick, T.Y. Wei, G.Y. Chong, G.H. Leong, B.V.R. Chowdari, J. Electrochem. Soc. 158 (2011) (12) A1423[5]
5. X.W. Guo, X. Lu, X.P. Fang, Y. Mao, Z.X. Wang, L.Q. Chen, X.X. Xu, H. Yang, Y.N. Liu, Electrochem. Commun. 12 (2010) (6) 847.
6. Y. Sharma, N. Sharma, G.V. Subba Rao, B.V.R. Chowdari, Bull. Mater. Sci. 32 (2009) (3) 295.
7. R. Alcantara, M. Jaraba, P. Lavela, J.L. Tirado, J.C. Jumas, J. Olivier-Fourcade, Electrochem. Commun. 5 (2003) (1) 16.

8. C.T. Cherian, J. Sundaramurthy, M.V. Reddy, P.S. Kumar, K. Mani, D. Pliszka, C.H. Sow, S. Ramakrishna, B.V.R. Chowdari, ACS Appl. Mater. Interfaces 5 (2013) (20) 9957.
9. C.T. Cherian, M.V. Reddy, G.V. Subba Rao, C.H. Sow, B.V.R. Chowdari, J. Solid State Electrochem. 16 (2012) (5) 1823.
10. P. Afanasiev, C. Geantet, Coord. Chem. Rev. 178 (1998) 1725.
11. R.D. Shannon, Acta Crystallographica A32 (1976) 751.
12. M.V. Reddy, B.L.W. Wen, K.P. Loh, B.V.R. Chowdari, ACS Appl. Mater. Interfaces 5 (2013) (16) 7777.
13. C.T. Cherian, M.V. Reddy, S.C. Haur, B.V.R. Chowdari, ACS Applied Materials and Interfaces 5 (2013) (3) 918.
14. C. Vidal-Abarca, P. Lavela, J.L. Tirado, J. Phys. Chem. C 114 (2010) (29) 12828.
15. C.T. Cherian, J. Sundaramurthy, M. Kalaivani, P. Ragupathy, P.S. Kumar, V. Thavasi, M.V. Reddy, C.H. Sow, S.G. Mhaisalkar, S. Ramakrishna, B.V.R. Chowdari, J. Mater. Chem. 22 (2012) (24) 12198.
16. M.V. Reddy, C.T. Cherian, K. Ramanathan, K.C.W. Jie, T.Y.W. Daryl, T.Y. Hao, S. Adams, K.P. Loh, B.V.R. Chowdari, Electrochim. Acta 118 (2014) 75.
17. B. Varghese, M.V. Reddy, Z. Yanwu, C.S. Lit, T.C. Hoong, G.V. Subba Rao, B.V.R. Chowdari, A.T.S. Wee, C.T. Lim, C.H. Sow, Chem. Mater. 20 (2008) (10) 3360.

LI-AIR BATTERIES WITH LAGP-POLYMER COMPOSITE MEMBRANES

DORSASADAT SAFANAMA
Department of Materials Science and Engineering, National University of Singapore, 117574, Singapore

RAYAVARAPU PRASADA RAO
Department of Materials Science and Engineering, National University of Singapore, 117574, Singapore

STEFAN ADAMS
Department of Materials Science and Engineering, National University of Singapore, 117574, Singapore

The high theoretical capacities and gravimetric energy densities of Li-air batteries have inspired intensive research. Still, limited energy efficiency and power performance have impeded practical use. With the progress in fast Li^+ ion conducting solids suitable for protecting Li anodes from chemical reaction with polar solvents, aqueous Li-air batteries have been reconsidered. In these systems catholytes with high solubility for the discharge product enhance the cycle efficiency, power performance and volumetric energy density. Here, a composite membrane consisting of NASICON-type LAGP (conductivity 5×10^{-4} Scm^{-1}) dispersed in a polymer matrix of PVDF: PEO: $LiBF_4$ is prepared and Li-air cells employing this composite membrane and 1M lithium hydroxide or H_3PO_4/LiH_2PO_4 (pH~4) buffer catholyte solutions are tested in ambient air.

1. Introduction

The need to minimize the dependence on fossil fuels has forced battery researcher to seek for high performance batteries. Since rechargeable lithium ion battery chemistries have almost reached their theoretical limits and the achievable energy densities and cost-efficiencies do not meet the demand of future technologies especially in the area of support for sustainable power grids, the pursuit of new rechargeable high energy density batteries has come into the scene [1].

Proceedings of the 14th Asian Conference on Solid State Ionics (ACSSI 2014)
Copyright © 2014 ACSSI 2014 Organizers. All rights reserved.
ISBN: 978-981-09-1137-9
doi:10.3850/978-981-09-1137-9_157

The interest in Li-air batteries was first started in the late 1970s due to their extreme theoretical energy density of 3458 Wh/kg for non-aqueous systems or 2249 Wh/kg for aqueous systems (see e.g. [2, 3]). A deeper understanding the working principle of rechargeable Li-air batteries started much later in 1990s when Abraham et al. presented a design based on a polymer electrolyte for non-aqueous Li-air batteries which showed a specific capacity between 250 to 350 $Whkg^{-1}$ [4]. Even though organic Li-air batteries offer the highest energy density due to the low specific weigh of Li_2O_2, with the progress of research on organic Li-air batteries [5, 6], high polarization during the charge and discharge process with gradual decomposition of the organic (polycarbonate) electrolytes and contamination with moisture in the air turned out to be a challenge [7, 8]. In aqueous Li-air batteries, unlike organic type, the discharge products are soluble in the catholyte, hence improving the cycle efficiency, power performance and volumetric energy density [9, 10]. The main issue in this type of batteries is the parasitic reaction of the lithium anode with the catholyte giving rise to safety concerns. One approach to address this problem is to protect the lithium anode from the aqueous catholyte using anode protecting membrane having high ionic conductivity and wide electrochemical window [11].

Herein, the applicability of hybrid inorganic-organic membranes consisting of NASICON-type $Li_{1.5}Al_{0.5}Ge_{1.5}(PO_4)_3$ (LAGP) as the fast ion conducting ceramic (with conductivities > 10^{-4} S cm^{-1}) and the polymer electrolyte of polyvinylidene fluoride (PVDF) : polyethylene oxide (PEO): $LiBF_4$ is investigated as an anode protecting membrane in Li-air cell.

2. Experimental

2.1. *Preparation of $Li_{1+x}Al_xGe_{2-x}(PO_4)_3$ (LAGP) glass ceramics*

LAGP glasses are prepared by melt quenching. Lithium carbonate (Li_2CO_3) and germanium oxide (GeO_2) were obtained from Alfa Aesar, Ward Hill, MA. Aluminium oxide (Al_2O_3) and ammonium dihydrogen phosphate ($NH_4H_2PO_4$) were purchased from Sigma Aldrich and Merck, respectively. Precursors were ball milled using zirconia ball for 5 hours prior to a two-step heat treatment. All volatile components are removed by heating at 700 ^oC for 2 hours and the melt is produced by further heating at 1450 ^oC. The melt is further quenched using copper plate yielding to transparent glass. The powdered glass was shaped into pellets and annealed at the optimum temperature to achieve the highest ionic conductivity.

2.2. *Preparation of hybrid inorganic-organic (composite) membranes*

Hybrid inorganic-organic (composite) membranes were prepared using tape casting. Polyvinylidene fluoride (PVDF) was obtained from Alfa Aesar, Ward Hill, MA and polyethylene oxide (PEO), lithium tetrafluoroborate ($LiBF_4$) and N-methyl-2-pyrrolidinone (NMP) were purchased from Sigma Aldrich. Mixtures of PEO (6 wt%), PVDF (18 wt%) and $LiBF_4$ (6 wt%) were dispersed in NMP and stirred for 6 hours at 100 ^oC. Powdered crystalline LAGP (70 wt%) was further introduced into the slurry and the resulting slurry was stirred for further 6 hours. The slurry was tape cast using a film coater (MTI-*MSK-AFA-III-110*) and dried at 80ºC for 24 hours. The membrane is flexible enough to be cut into desired shape for further characterization.

2.3. *Characterization*

The chemical stability of the composite membrane was tested by immersing the membrane into 1M lithium hydroxide or H_3PO_4/LiH_2PO_4 (pH~4) buffer catholyte solutions. X-ray powder diffractometer (Bruker D8) employing Cu Kα radiation (λ=1.5406 Å) in the 2θ range of 10-100º was utilized for structural characterization of the membrane before and after immersion. AC impedance measurement was performed on gold coated composite membranes using impedance spectroscopy (IS) (Solartron SI1260) in the frequency range of 100 Hz – 5 MHz. Impedance spectra were fitted using the FRA software applying the equivalent circuit R(RQ)(Q). Conductivities are calculated using the geometrical dimensions of the sample. Microscopic structure of samples was examined using scanning electron microscope (SEM, Zeiss Supra 40 VP).

In the simple cell design, the composite membrane is sandwiched between lithium anode and air cathode and the catholyte is impregnated on glass fiber separator. The charge/discharge performance of the Li anode/composite membrane/catholyte/air cathode cell was measured in the voltage range of 1.0-3.8 V (*vs.* Li) using Abrin battery tester (BT2000).

3. Results and Discussion

Figure 1(a) and (b) show the XRD patterns of the composite membrane before and after immersion for up to 1 month at room temperature in 1M lithium hydroxide (LiOH) and H_3PO_4/LiH_2PO_4 (pH~4) buffer catholyte solutions, respectively. According to the Rietveld-refinement of the XRD data for the membrane before immersion, NASICON-type LAGP (space group *R*-3*c* with lattice parameters of a = 8.2539(1) Å, c=20.6843(3) Å is the dominant crystalline phase present along with peaks indicating slight impurities of 8%

GeO_2 and 0.4% $AlPO_4$ [12]. As can be seen in Figure 1(a), more pronounced impurity peaks of GeO_2 are observed after immersion in LiOH, while LAGP peaks almost vanish and a broad peak suggests the formation of a new amorphous phase. For H_3PO_4/LiH_2PO_4 (pH~4) buffer solution, after 10 days immersion new impurity peaks of lithium hydrogen phosphate (LiH_2PO_4) precipitated from the buffer solution are observed in the XRD. The XRD patterns after 10 days immersion and 1 month immersion are almost identical and no indications of a decomposition of LAGP are observed.

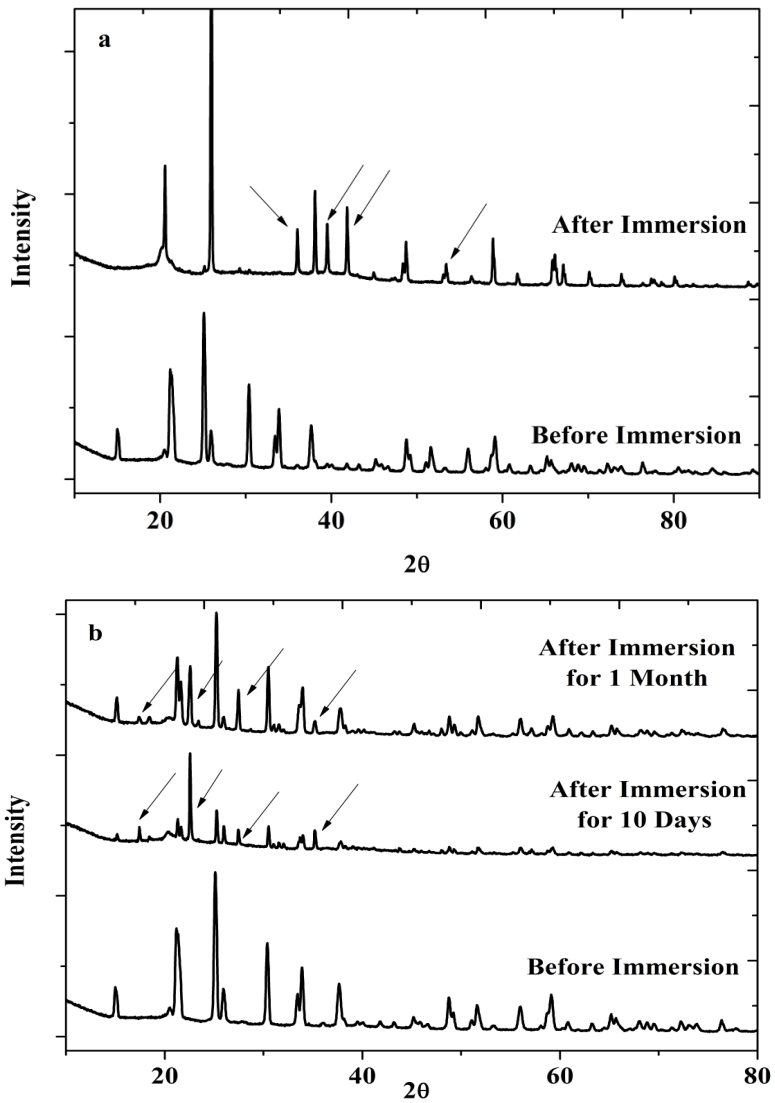


Figure 1. XRD pattern of composite membrane before and after immersion in (a) 1M lithium hydroxide (b) H_3PO_4/LiH_2PO_4 (pH~4) buffer catholyte solutions

Nyquist plots of conductivity for the composite membrane before and after immersion in LiOH for 1 month are plotted in Figure 2. Accordingly, by immersing in LiOH, both bulk and grain boundary resistances are decreased and the total conductivity value is increased by a factor of 1.5. As there is little crystalline LAGP left and GeO_2 is not ionically conducting, the observed conductivity has however to be ascribed to the amorphous phase that should be an $AlPO_4$-rich glass. The relatively high total conductivity might be affected by the space charge effect induced by GeO_2 in the glassy conductor [13]. For the case of phosphate buffer, there is no change in the value of conductivity after 10 days immersion. But after immersion for 1 month, the conductivity drastically decreased by two orders of magnitude. According to SEM images shown in Figure 3, the polymer component of the composite membrane is attacked by the solution leaving large holes in the structure.

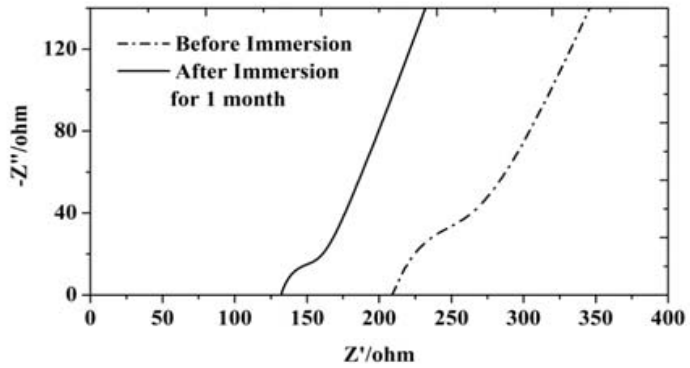


Figure 2. Nyquist plots of room temperature impedance spectra before and after immersion for 1 month in LiOH

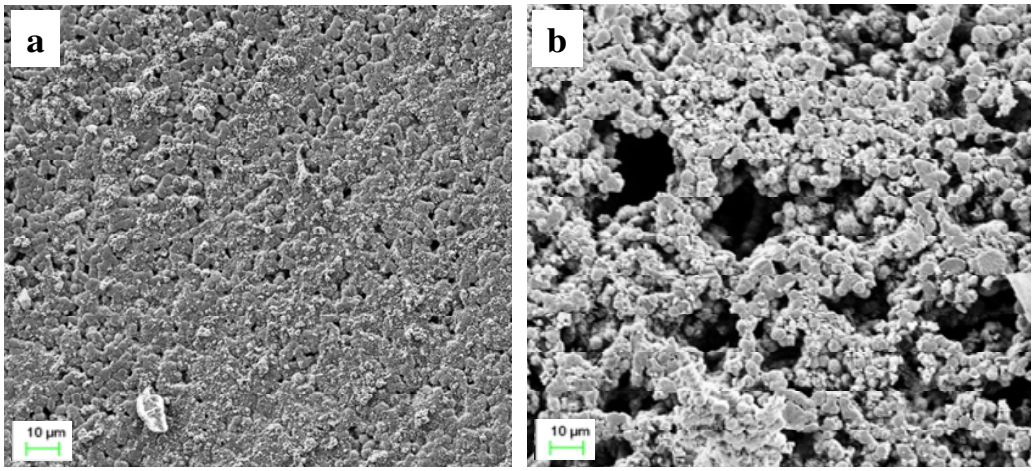


Figure 3. SEM images of composite membrane (a) before immersion and (b) after immersion in H_3PO_4/LiH_2PO_4 (pH~4) buffer solution for 1 month.

Li-air cells consisting of lithium metal anode, composite electrolyte membrane, 1M lithium hydroxide or H_3PO_4/LiH_2PO_4 (pH~4) buffer catholyte solutions and air carbon-based cathode are tested in ambient air. Figure 4 is the schematic illustration of the cell design employing the composite membrane. The air cathode consisted of Pt particles deposited on multi-walled carbon nanotube (CNT) arrays on carbon fibers.

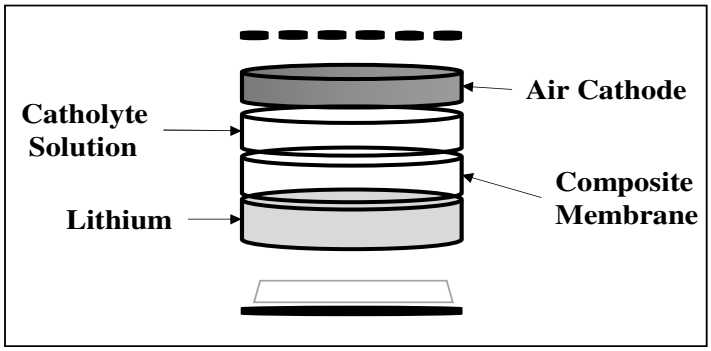


Figure 4. Schematic illustration of the Li-O_2 cell design

In the simple coin cell design, an open circuit voltage of ca. 3.0 V is observed. In the voltage range of 1.0-3.8 vs. Li/Li^+ the cell with LiOH catholyte shows a capacity of 300 mAh per g of carbon, respectively under constant current density of 0.6 $mAcm^{-2}$ (Figure 5). Under this relatively low current density the polarization between charge and discharge curves is considerably lower than for organic liquid electrolytes. As shown in Figure 6 cells containing a concentrated phosphate buffer catholyte reach a capacity of 990 mAh per g of carbon.

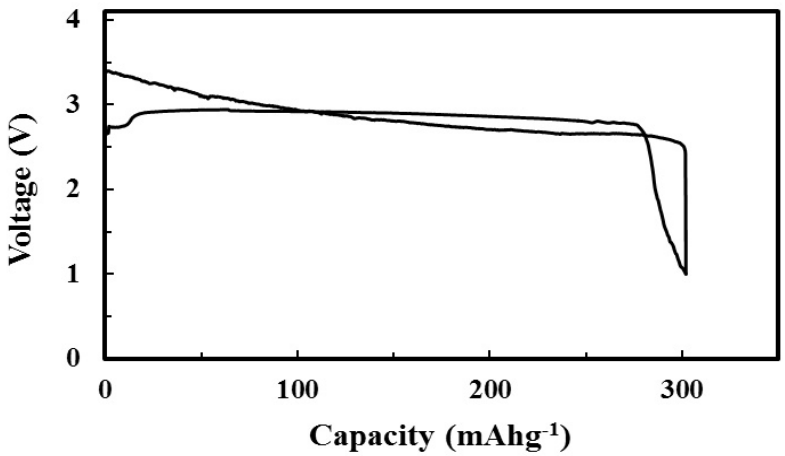


Figure 5. Room temperature charge-discharge curve of a lithium air cell as a function of time at constant current density of 0.6 $mAcm^{-2}$ for the cell with LiOH catholyte.

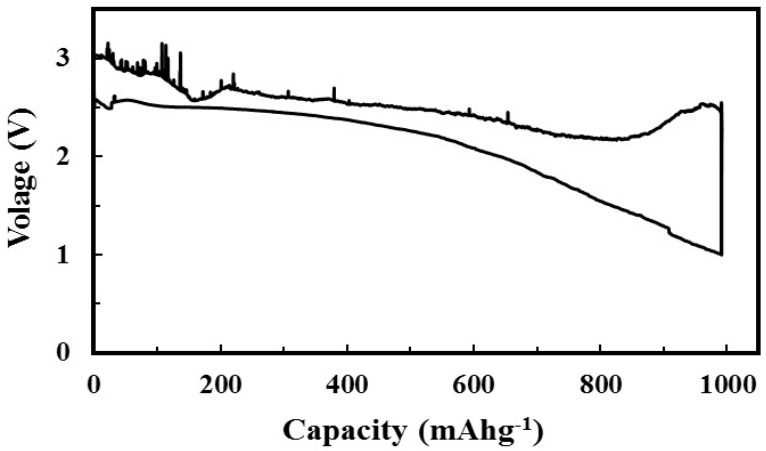


Figure 6. Room temperature charge-discharge curve of a lithium air cell as a function of time at constant current density of 0.6 $mAcm^{-2}$ for the cell with phosphate buffer catholyte.

4. Conclusion

LAGP-based composite membrane is fabricated and the performance of the membrane in Li-air cell using LiOH or phosphate buffer catholyte is assessed. Immersion in both catholytes results in the formation of new peaks in the XRD pattern hence further studies are needed to improve the stability of the membrane in these solutions. The cell shows relatively low polarization between charge and discharge curves. Evaporation of the catholyte or the formation of by-products during discharge may be the reason behind the poor cycleability of the cell and need to be further addressed.

Acknowledgments

This research is supported by the National Research Foundation, Prime Minister's Office, Singapore under its Competitive Research Programme (CRP Award No. NRF-CRP 10-2012-6 and NRF-CRP8-2011-04).

References

[1]M. Balaish, A. Kraytsberg, Y. Ein-Eli, *Physical Chemistry Chemical Physics* **16** (2014) (7) 2801.
[2]J.P. Zheng, R.Y. Liang, M. Hendrickson, E.J. Plichta, *Journal of Electrochemical Society* **155** (2008) A432.
[3]J.P. Zheng, Z.P. Andrei, M. Hendrickson, E.J. Plichta, *Journal of Electrochemical Society* **158** (2011) A34.

[4] K.M. Abraham, Z. Jiang, *Journal of Electrochemical Society* **143** (1996) (1).
[5] S.A. Freunberger, Y. Chen, Z. Peng, J.M. Griffin, L.J. Hardwick, F. Bardé, P. Novák, P.G. Bruce, *Journal of the American Chemical Society* **133** (2011) (20) 8040.
[6] V.S. Bryantsev, M. Blanco, *J. Phys. Chem. Lett.* **2** (2011) 379.
[7] T. Ogasawara, A. Debart, M. Holzapfel, P. Novak, P.G. Bruce, *J. Am. Chem. Soc.* **128** (2006) 1390.
[8] A. Debart, J. Bao, G. Armstrong, P.G. Bruce, *Journal of Power Sources* **174** (2007).
[9] T. Zhang, N. Imanishi, S. Hasegawa, A. Hirano, J. Xie, Y. Takeda, O. Yamamoto, N. Sammes, *Electrochemical and Solid-State Letters* **12** (2009) (7) A132.
[10] N. Imanishi, Y. Takeda, O. Yamamoto, *Electrochemistry* **80** (2012) (10) 706.
[11] Y. Shimonishi, T. Zhang, N. Imanishi, D. Im, D.J. Lee, A. Hirano, Y. Takeda, O. Yamamoto, N. Sammes, *Journal of Power Sources* **196** (2011) (11) 5128.
[12] D. Safanama, D. Damiano, R.P. Rao, S. Adams, *Solid State Ionics* (0).
[13] B. Kumar, D. Thomas, J. Kumar, *Journal of The Electrochemical Society* **156** (2009) (7) A506.

SYNTHESISAND CHARACTERIZATION OF LIMNO$_2$ NANOSTRUCTURE AT VARIOUS TEMPERATURES*

WAGIYO HONGGOWIRANTO[1,*], EVVY KARTINI[1],
AZIZ KHAN JAHJA[1], MARDIYANTO[1†]

*Center for Science and Technology of Advance Material National Nuclear Energy Agency (BATAN)Kawasan PUSPIPTEKSerpong,,Ged.71, Tangerang 15314, Indonesia*wagiyo@batan.go.id*

Abstract. Synthesis of positive electrode materials $LiMnO_2$ for solid state rechargeable-battery has been carried out by a reaction process of $MnSO_4$ and LiOH mixture in the 7.5% hydrogen peroxide media inside a self-designed stainless steel autoclave. After steering, the mixtures were put into a closed *teflon*-tube and placed in the stainless steels autoclave, then it was sealed off tightly followed by heating in an electric oven of various temperatures at160°C, 180°C, 200°C and 220°C each for 12 hours. The nanostructure the crystal structure and the conductivity of the material products were characterized by using a Scanning Electron Microscope (SEM), an X-ray diffraction (XRD) and conductivity LCR-meter methods, respectively. The SEM results showed the microstructure of the nano-particles with diameters in the range of 105 to 265 nm was obtained from thesample synthesized at 180 °C.Comparison with the XRD pattern of commercial $LiMnO_2$shows that the characteristic signature peaks, i.e. [010], [110], [011], [120], [200], are clearly identifiable in the synthesized nanoparticle sample prepared at 220 °C, therefore confirming the formation of the orthorhombic $LiMnO_2$structure belonging to the *P m n m* space group. The X-ray diffraction patterns of the synthesized nano-$LiMnO_2$prepared at 180 °Cand 200 °Ceither shows that some reflection peaks have experienced angular shift, or that these reflection peaks are still very weak in comparison with the X-ray diffraction patterns of commercial $LiMnO_2$, which iscaused by different processes of synthesizing.On the other hand, the peak at 2θ~19° belonging to the $LiMn_2O_3$ 'impurity'phase,appears to be still very prominent at all preparation temperatures. The highiest conductivity of nano-$LiMnO_2$is2.34×10^{-3} S/cm was obtained from thesample synthesized at 180 °C and charge discharge energy efficienciesat 100thcyclewas 90 %

Keywords: *Nanostructure, $LiMnO_2$, hydrothermal, SEM, XRD,LCR-meter.*

1. Introduction

The secondary battery which consists of light weight components has been widely used as an energy source which has revolutionized the portable electronics industry, such as mobile phones, laptop computers, digital music players, and other lightweight devices, since the early 1990s. The fast growth of the light weight secondary battery was initiated in 1990, when Sony announced

*This work is supported bytheMinistry Research and Technolgy of Indonesia.

Proceedings of the 14th Asian Conference on Solid State Ionics (ACSSI 2014)
Copyright © 2014 ACSSI 2014 Organizers. All rights reserved.
ISBN: 978-981-09-1137-9
doi:10.3850/978-981-09-1137-9_164

the first commercial batteries based on the use of $LiCoO_2$ cathode[1]. However, due to its high cost and toxicity, it has pushed the extensive research pursuing alternative cathodes. The three most expensive components of a Li-ion battery, no matter what the configuration, are the cathode, the separator, and the electrolyte. Reduction of cost has been one of the primary driving forces for the investigation of new cathode materials to replace expensive $LiCoO_2$. Research efforts should be done for having ideal materials that can meet requirements for all applications, especially a high energy source for vehicular applications which is designed with multiple cells wired in series arrays. Premature failure of one cell in a string may cause others to go into overcharge during the passage of current. Moreover, low cost materials should be obtained to replace the expensive ones. The lithium based transition metal oxides such as $LiMnO_2$ have recently become attractive base materials in the manufacture of cathodes in lithium-ion secondary rechargeable batteries, because of their relative low cost and high capacity [2].

$LiMnO_2$ is of high fundamental and technological interestas a cathode material for rechargeable lithium batteries. It has been chosen as the cathode material in lithium batteries due to their good chemical and physical stability. Recently, however, there is a growing indication that battery electrode materials having nanosize microstructure morphology show better performance.

Furthermore, it was found that $LiMnO_2$ nano-particles exhibited higher charge storage capacity and better cycle stability than the regular one [3]. To synthesize the $LiMnO_2$ nano-particles, a new method called the hydrothermal process has been utilized by several authors [4]. In order to obtain better mechanical stability, the nano particles $LiMnO_2$ was mixed with 10% PVDF. In this paper, the authors report the synthesis of nano-particles $LiMnO_2$ using a hydrothermal method. The mixtures of the raw materials were put into a closed teflon-tube and placed in the stainless steels autoclave, then it was sealed off tightly followed by heating in an electric oven of various temperatures at 160°C, 180°C, 200°C and 220°C each for 12 hours. The crystal structure, micro structure and the electrochemical performance of the synthesized $LiMnO_2$ nano-particles will be characterized by XRD, SEM/TEM and LCR meter, respectively and the results discussed.

2. Experimental

The appropriate amounts of raw materials H_2O_2, $MnSO_4$ and $LiOH.H_2O$ were mixed in a glass beaker and slowly stirred. The mixed reactants were then transferred into a teflon container and put in a specially designed SS304 stainless steel autoclave vessel, and the vessel's lid was then sealed off tightly. The autoclave is heated in a furnace, which is set at 400°C, and it took30-40

minutes for the reactants to reach 180-200 °C. Subsequently, the autoclave was transferred into the electric oven and the heating process is continued at 180°C, 200 °C and 220°C for 12 h. The system was then allowed to cool to room temperature. The resulting powder was washed with distilled water several times and subsequently dried at 60 °C. The end product, powder sample of $LiMnO_2$, was characterized,the crystal structureusingXRD,the micro structure using SEM JEOL JSM 6510LA, the conductivity using Impedance Spectrometer methods and electrochemical usingBattery Analyzer.Electrochemical tests were carried out in liquid electrolyte using Cell (Swagelok-type from MTI) batteries. Cathode slurry was a composite mixture of active oxide, artificial carbon (10 wt. %) and PVDF binder (10 wt.%). The electrolyte was a commercial solution of LiPF6 in diethyl carbonate (DEC) (1:1 in volume, Merck). Anode electrodes were 0.2 mm thick lithium foil. Electrochemical cells were assembled in a glove box (Vygor) under argon with ≤ 1 ppm O_2.Galvanostatic cycling between 3.2-4.0 Volt vs Li at room temperature was carried out using 8 Channel Battery Analyzer (0.002-1mA, up to 5 V) with software program for Battery testing (Model BST8-WA, MTI USA).

3. Result and Discussion

The reaction of nanoparticle formation is estimated to take place in three stages. First, $MnSO_4$reacts withLiOH to form thecompound $Mn(OH)_2$ in a solution, which is immediately oxidized to $Mn(OH)_3$ by H_2O_2 and air. Finally, $Mn(OH)_2$ is converted into $LiMnO_2$ by heating in a solution of LiOH [4].

3.1. *XRD Analysis*

The orthorhombic crystal symmetry of the synthesized $LiMnO_2$ was verified using XRD method. Figure.1 shows the XRD patterns of *o*-$LiMnO_2$ synthesized by the one-step HDT method with different heating temperatures,160, 180, 200 and 220 °C respectively. For comparison, the XRD spectrum of spinel $LiMn_2O_4$ and the simulated pattern of orthorhombic *o*-$LiMnO_2$ are also shown. The simulated pattern is obtained based upon The *P m m n* orthorhombic symmetry, with lattice parameters a = 4.5750 Å, b = 5.7510 Å, c = 2.8060 Å [5].

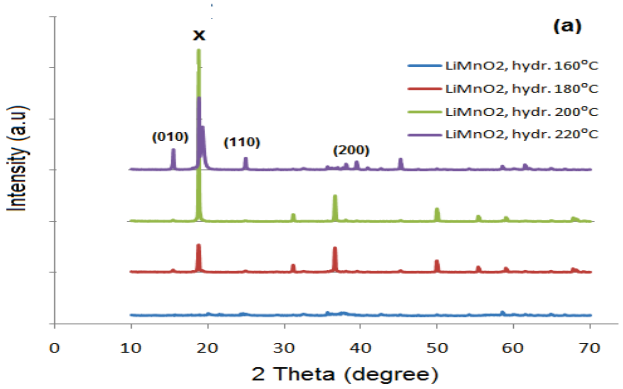


Figure 1.a. The XRD patterns of *o*-$LiMnO_2$ synthesized by the one-step HDT method with different heating temperatures, 160°C, 180°C, 200°C and 220 °C, respectively.

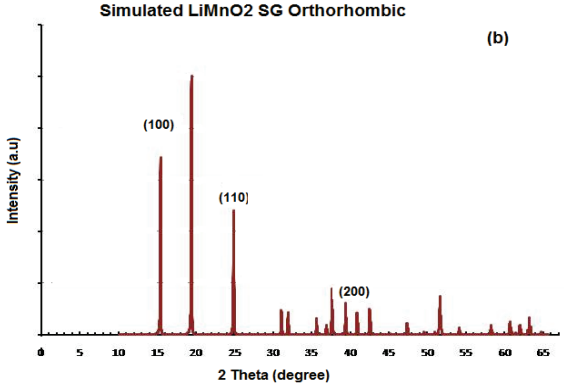


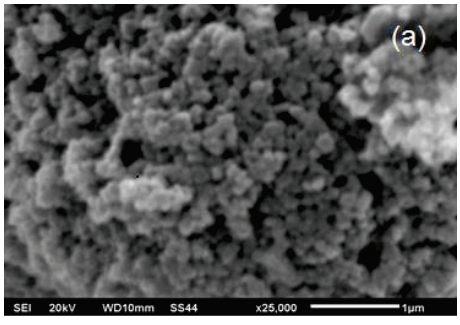
Figure 1.b. The XRD patterns of the simulated pattern of orthorhombic *o*-$LiMnO_2$ are also shown.

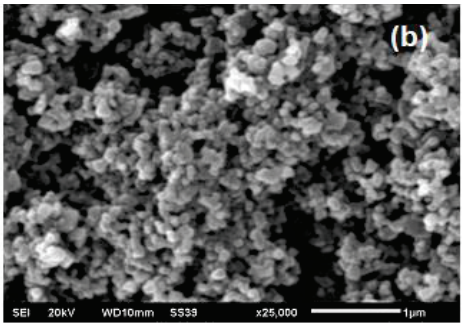
After comparison with the simulated pattern, it is evident that only the diffraction peaks of the 220°C heated *o*-$LiMnO_2$ could be indexed according to the space group *Pmmn* of the orthorhombic structure. It could be directly verified that the XRD pattern of the 220 °C heated *o*-$LiMnO_2$ (Fig. 1) agreed well with the reported pattern for orthorhombic o-$LiMnO_2$ (JCPDS 86-0356) except for the peak at 2θ = 18.6° (marked "×"), which in this case is attributed to $LiMn_2O_3$. Only the 220 °C heating temperature HDT method yields the primary phase of *o*-$LiMnO_2$. The three major reflection peaks [100], [110] and [200] appear at their respective diffraction angles 2θ and seem to match the peaks' positions shown in the simulated pattern. The first two reflection peaks do not yet appear in the samples synthesized with 180°C and 200 °C heating temperatures. However, a second phase appeared, showing a relatively strong peak at 2θ = 18.3°, which was assignable to Li_2MnO_3 [5]. This second phase

originated from the oxidation decomposition reaction, and does not seem to appear in the XRD patterns of the samples heated at 180- and 200 °C. The stability of lithium-manganese oxides had been studied using density functional theory in the local density and generalized gradient approximation [6], and it was found that orthorhombic *o*-$LiMnO_2$ is structurally more stable compared to the other phases (layered monoclinic and cubic spinel) of $LiMnO_2$.

3.2. Scanning Electron Microscope (SEM)

The size and morphology of the SEM image of the samples which weresynthesizedby hydrothermal methods at temperatureof 160 °C, 180 °C, 200°C and 220 °C for 12 hours are shown in Figures. 2(a),2(b),2(c) and 2(d), respectively. Figure2(a) shows $LiMnO_2$which was prepared at temperatures160 °C. Itis composed of nanoparticles where the size ranging between130-525 nm with themajoritybeing beingsmaller than 250 nm. TheSEM image of $LiMnO_2$ (Fig. 2(b)) of the sample which wassynthesized at temperature of 180 °C shows that the material consisted mainly of relatively uniform nanoparticles having diameters of 105-260 nm with themajority being smaller than 155 nm. It is the minimum size of the nanoparticles $LiMnO_2$ being sythesized. Fig. 2 (c) shows the $LiMnO_2$ prepared at temperatures of 200 °C. It is illustrated that the particle sizeis irregular and some aglomerations are shown which may be caused by cleaning after hydrothermal process. $LiMnO_2$which was prepared at temperatures of 220 °Cis shown in Fig. 2(d). The material consists of mainly relativly uniform nanoparticles having diameters of 115-250 nm with the majority of size being smaller than160 nm. It is predicted that the smaller theparticle size the better the ionic conductivity will be, becausethe Li ion candecalates easily in a short pathway, although italso still depends onother variablessuch aspurityandcrystalinity of the sample.





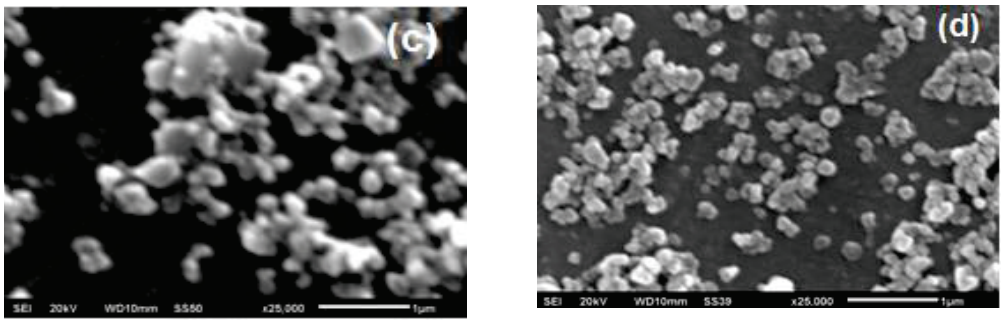


Figure.2. The SEM image*o*-LiMnO_2 synthesized by the one-step HDT method with heating temperatures (a) 160°C, (b) 180°C, (c)200°C and (d)220°C.

3.3. Conductivity

The results of conductivity measurements are illustrated in Fig.3. It is shown that nanoparticle LiMnO_2compounds each prepared at 160-, 180 - and 220 °C heating temperatures will turn out to have each a different conductivity value. The highest conductivity value is obtained when the material was heatedat 180°C namely in the order of 10^{-3} S/cm. Moreover, based on the XRD results, the fine nanoparticle LiMnO_2 was obtained, when it was heated at that same temperature. The high conductivity value may due to intimatestructure among the fine nanoparticles which ensures a better intergrain conductivity and a higher tolerance to changes in manganese valence. It may improve the electrochemical performances when it is used for the battery positive electrode. To be able to identify the charge transport processes in the grains and grain boundaries of ceramics over a wide temperature range, an impedance investigation of the LiMnO_2 ionic conductors over a wide frequency range has ben carried out [7]

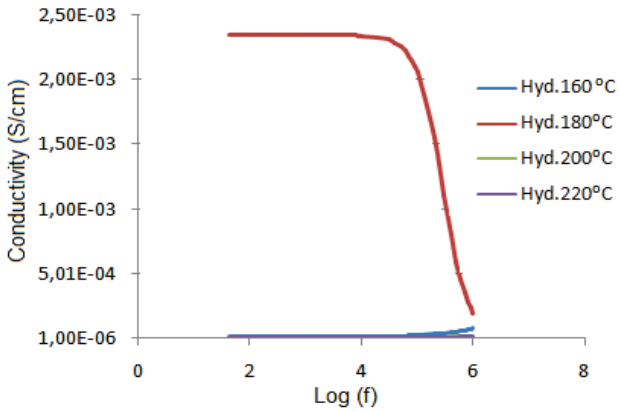


Figure.3.Conductivityc of *o*-LiMnO_2 synthesized by the one-step HDT method with heating temperatures160°C, 180°C,200°C and 220 °C

3.4.Electrochemical Studies

The galvanostatic charge-discharge profiles from the initial, until the 100thof the cell battery used cathode of *o*-$LiMnO_2$by the one-step HDT method synthesized with heating temperatures 180^{o}C($LiMnO_2$/(LiPF6)/Li and between 3.2-4.0 V as shown Figure 4. (cycle 68-87). The initial cycle charge capacity and discharge capacity were 0.015mAh/mg and 0.015mAh/mg, respectively, hence the sample weight was 0.05 mg. The charge and discharge process for one cycle took about 1hours 5 minute, and the cycles are relatively stable until 87th. The energy efficiency up to 89th(Figure 5.) cycles of cell are still stable with efficiencies of 91%, and from cycle 88th to 100th relatively is not stable butthe cycling performance efficiency is still largely 90%.

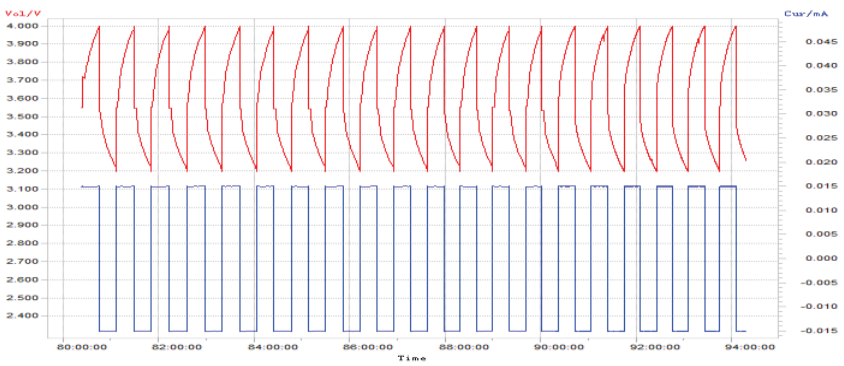


Figure 4. The charge and discharge process of the cellbatteryused cathode of *o*-$LiMnO_2$by the one-step HDT method synthesized with heating temperature180^{o}C, cycle 68th-87th

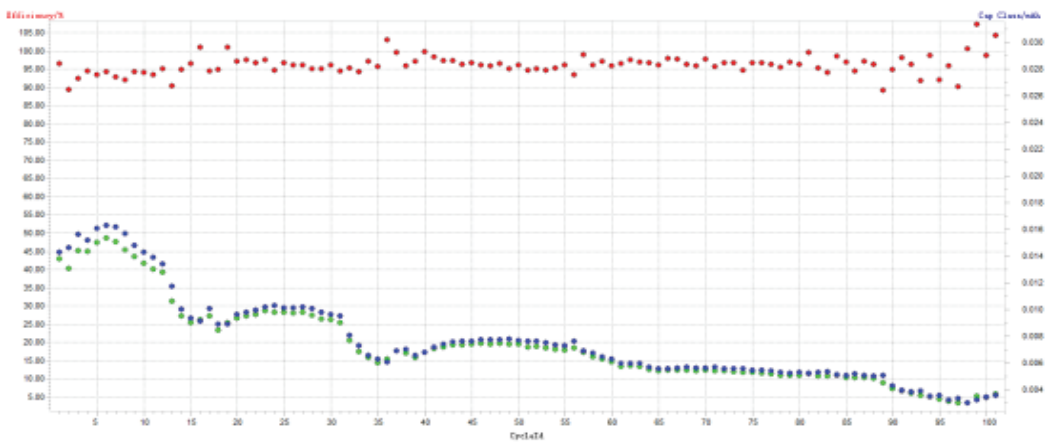


Figure 5. The charge and discharge efficiency of the the cellbatteryused cathode of *o*-$LiMnO_2$by the one-step HDT method synthesized with heating temperatures180^{o}C, cycle from 1st-100th

Conclusions

The X-ray diffraction patterns of the synthesized nano-$LiMnO_2$preparedat 180 °Cand 200 °Ceither shows that some reflection peaks have experienced angular shift, or that these reflection peaks are still very weak in comparison with the X-ray diffraction patterns of commercial $LiMnO_2$, which iscaused by different processes of synthesizing.On the other hand, the peak at 2θ~19° belonging to the $LiMn_2O_3$ 'impurity'phase,appears to be still very prominent at all preparation temperatures. The SEM results showed the microstructure of the nano-particlesof $LiMnO_2$ with diameters in the range of 105 to 265 nm,the higherst conductivity ofis2.34×10^{-3} S/cmwas obtained from thesample synthesized at 180 °C. was obtained from thesample synthesized at 180 °C and efficiency energy at the 100^{th}cycle was 90 %

References

1. Nagaura T, Tozawa K (1990) Lithium ion rechargeable battery. Progress in Batteries & Solar Cells 9:209–219.
2. Haisheng Tao, Zhizhong Feng, Hao Liu, Xianwen Kan and P. Chen, *The Open Materials Science Journal,* 2011, *5,* 204-2141874-088
3. CG. Hu, X. Yi, L.Hong, and LW. Zhong, J. Mater. Chem. 19, 858 (2009)
4. X. Xiao, L. Wang, D. Wang, X. He, Q. Peng, and Y. L, Nano Res 2, 923(2009)
5. Y. Idemoto, T. Mochizuki, K. Ui and N. Koura, *J. Electrochem. Soc.*, **153** _2 A418-A424 (2006)
6. S. K. Mishra and G. Ceder, *Phys. Rev.* **B59**, 6120 (1999).
7. T. Savitha, S. Selvasekarapandian, C.S. Ramya, M.S. Bhuvaneswari, G. Hirankumar, R. Baskaran, P.C. Angelo,*Journal of Power Sources***157** 533–536(2006)

FACILE SYNTHESIS OF ELECTROSPUN HIERARCHICAL α-Fe_2O_3–SiO_2 BINARY NANOTUBES FOR LIBS

Y.Z. WU†*
NUS Graduate School for Integrative Sciences and Engineering, 117456, Singapore

R. MURUGAN†
Department of Mechanical Engineering, National University of Singapore, 117574, Singapore

M. V. REDDY, B. V. R. CHOWDARI
Department of physics, NUS, 117542, Singapore

S. RAMAKRISHNA
Department of Mechanical Engineering, National University of Singapore, 117574, Singapore

In this work, a new magnetically recoverable α-Fe2O3-SiO2 nanotube was fabricated by electrospinning of polyvinylpyrrolidone (PVP), ferric acetylacetonate, tetraethyl-orthosilicate sol gel composite. As-spun nanobibres were sintered at 500°C for 5h to form interconnected tubes of α-Fe2O3−SiO2 nanofibers. We have tried to develop hybrid α-Fe2O3−SiO2 nanotube morphology which exhibits interesting electrochemical performance in the application of lithium ion battery (LIB). FESEM, TEM, XRD and FTIR were employed to analyse α-Fe2O3-SiO2 nanotube.

1. Introduction

Nanoscale magnetic materials are scientifically and technologically important area of research with many potential applications in environmental, biomedicine, magnetic recording and spin electronics. Among the nanomaterials, design and synthesis of nanotubes have been the subject of considerable research in the

* R. Murugan and Y.Z. Wu contributed equally to this work. Authors thank M3TC, National University of Singapore for financial support (Electrospun nanomaterials for environmental remediation, Grant number: R-261-501-018-414).

Proceedings of the 14th Asian Conference on Solid State Ionics (ACSSI 2014)
Copyright © 2014 ACSSI 2014 Organizers. All rights reserved.
ISBN: 978-981-09-1137-9
doi:10.3850/978-981-09-1137-9_175

recent years because of their potential utility in a wide variety of chemical, biological, and materials science applications [1-4].

Recently, nanomaterial metal oxides have been widely investigated as high-capacity anode for Li ion batteries in view their high theoretical capacity (400-100mA h/g), because of their ability to reversibly react with more than one Li ion through the conversion reaction [5]. Combination of more than one metal oxide has attracted significant attention and its shown good capacity values on cycling in LIB applications [6, 7]. Iron based binary metal oxides has much attention due to their physiochemical properties. Xiao et al. reported Fe based $MnFe_2O_4$-GO nanocomposite with enhanced performance as anode materials for LIBs [8]. $ZnFe_2O_4$ electrospun nanoweb anode 1-D material and its LIB performance reported by Teh et al. [9]. $ZnFe_2O_4$-MWCNT binary oxide nanocomposites and their LIB application has reported by Sui et al. [10]. Besides, Fe-Ni and Fe-Co binary oxide materials have also been found with high Li storage performance [11, 12].

Metal oxide nanotubes lie at the heart of 1-D nanostructures and have attracted great scientific interest because of their unique physicochemical properties [13]. These properties are directly related to their structural features such as the high surface area, large porosity and availability of a hollow cavity. In the application of LIBs, nanostructure is well known to shorten the diffusion path for both ions and electrons, accommodate unfavorable strains during lithium insertion/extraction [14,15], and change the reaction pathway affording high capacities and rechargeability5. For the hollow nanotube morphology, extensive studies have been done on different inorganic oxides, including TiO_2, [16], SnO_2 [17], and Fe_2O_3 [18]. They demonstrate great improvement than conventional bulk materials to some extent, respectively. Among the various metal oxide nanotubular materials, Iron oxide is one of the most investigated nanomaterials for biological and industrial applications [19]. α-Fe_2O_3 the most stable phase of iron oxide has broad technological potential application in catalysis, gas sensor, field emission, energy storage and pigments [20]. Various approaches including ALD [21], electrospinning [22], hydrothermal [23], potentiostatic anodization [24], solvothermal [25], sonoelectro- chemical [26], template synthesis [27] and STAH methods [28] have been developed for the preparation of α-Fe_2O_3 based nanotubes. However, bare nanotube morphology generally increases the risk of secondary reactions involving electrolyte decomposition with a high surface area [14]. Therefore it would be of great interest to control the unnecessary contact of electrolyte with the nanotube surface. Iron based binary oxides such as Fe-Fe-

Mn, Fe-Zr and Fe-Si has potential application in arsenic removal from water [29,30]. Fe-Si and Fe-Al binary oxides used as catalyst for direct coal liquefaction [31] Fe-Mn and Fe-Ce based binary oxides utilized for Fischer-Tropsch synthesis [32, 33]. Fe-Mo mixed oxides used for selective oxidation34 and Fe-Zr binary oxides have been used for phosphate removal from aqueous solution [35]. Coating the nanotube outer surface with "buffer", like SiO_2, would protect the electrolyte from the unwanted oxidation or reduction by the electrode materials. In this paper, we introduce a facile and scalable way to produce such hierarchical nanotube morphology with a binary composition of α-Fe_2O_3 and SiO_2.

2. Experimental

2.1 *Materials and methods*

Ferric acetylacetonate, tetraethyl orthosilicate (TEOS), acetic acid, ethanol and polyvinylpyrrolidone (PVP 1,300,000) were purchased from Aldrich. They were used without further purification.

2.2 *Electrospinning*

The electrospinning sol gel was prepared from PVP, ethanol acetic acid, ferric acetylacetonate and TEOS using a typical procedure. 0.5 g of ferric acetylacetante and 0.1 g TEOS were dissolved in 10 mL of ethanol. 1 g of PVP and 1 mL acetic acid were then added into the solution. The solution was kept under stirring at room temperature for overnight when the red colour viscous solution became homogeneous. The obtained red composite sol was taken in a 10 mL plastic syringe attached with a 22 G needle. The sol gel was then subjected to electrospinning using the applied voltage was 15 KV (Gamma high-voltage, FL) was applied between the needle and the ground at a distance of 10 cm and a flow rate 1 mL/h. The nanofibers were collected on an aluminum foil and the electrospun membranes were dried in a vacuum pump. Then as-spun nanofibers were sintered at 500 °C for 5h in air at a rate 5 °C/min.

2.3 *Characterization*

The morphology of the as-spun nanofibers and the sintered tubular mesostructures were characterized by field-emission scanning electron microscope (FE-SEM JEOL JSM-6700F). High resolution transmission electron microscopy (HR-TEM) images were

collected suing (JEOL 3010) microscope. Surface morphology of $Fe(acac)_3$-TEOS polymer nanofibres sintered at 500°C were characterized by FESEM and HRTEM. Fig.1a. shows the morphology of the as-spun $Fe(acac)_3$-TEOS polymer nanofibres. It was observed that the nanofibers were randomly oriented and interconnected. The calcinated nanofibers were uniform, continuous and amorphous.

The as-prepared α-Fe_2O_3-SiO_2 nanofibers were mixed with super carbon black and binder (polyvinylidene difluoride, PVDF) in the weight ratio at 70 : 15 : 15 using N-methyl pyrrolidinone (NMP) as the solvent. The mixture was uniformly spread on etched copper foil with a thickness of 15 µm as the current collector by using a doctor-blade technique and dried at 80 °C under vacuum. Then, it was cut into circular disks with geometrical area of 2.0 cm^2. Lithium metal foil (Kyokuto metal Co., Japan), 1M $LiPF_6$ in ethylene carbonate (EC)/ diethyl carbonate (DEC) (1 : 1 by volume) (Merck) and a Celgard 2502 membrane were used as the counter electrode, electrolyte and separator respectively to assemble a 2016 coin-type cell in an argon-filled glove box. The cells were aged for 12 hours before measurement. Charge–discharge cycling tests and cyclic voltammetry were investigated at a constant current mode using a computer controlled Bitrode battery tester (Model SCN-12-4-5/18, USA). Typical procedures can be found in our previous reports.[36-38]

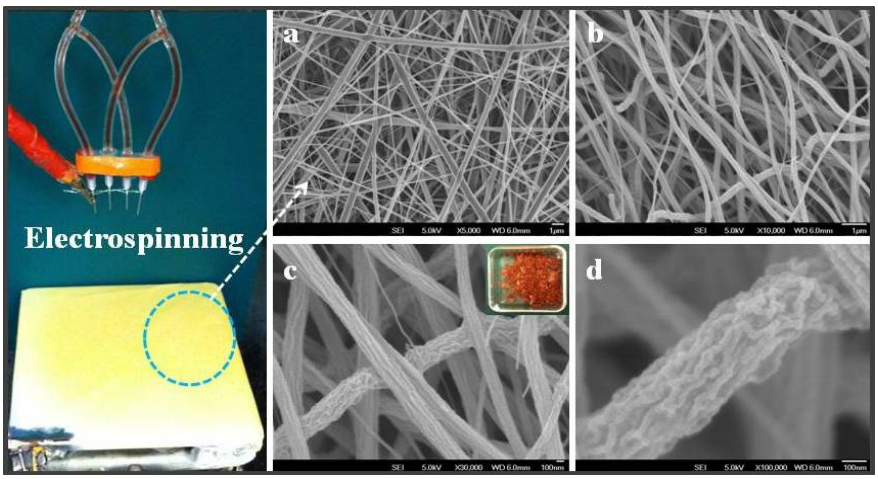


Fig.1. FESEM images of the (a) as-spun $Fe(acac)_3$-TEOS polymer nanofibres (b & C) Fe_2O_3-SiO_2 tubular nanofibres obtained after sintering; (c) the inset shows the photo image Fe_2O_3-SiO_2 nanofibres (d) High magnification images of the Fe_2O_3-SiO_2 nanotube.

3. Results and discussions

The morphology of the as-spun Fe_2O_3-SiO_2 polymer nanofibres is shown in the Figure 1(a). It can be seen that these randomly aligned as-spun nanofibres have a uniform

diameter of nearly 200 nm and are continuous and interconnected. The sintering of the α-Fe_2O_3-SiO_2 nanofibers was performed at a temperature of 500 ºC for 5 h. After being sintered the fiber network transformed into a hollow tubular morphology. Figure 1(b-d) shows the low and SiO_2 mesohollow tubes. As shown in Figure 2 the fibre morphology is retained after decomposition of the polymer but the cross-section of a α-Fe_2O_3-SiO_2 nanofibre shown in the inset reveals a hollow morphology. The inner diameter of the hollow nanofibres measures nearly 160 nm. It can be seen that the surface of the nanofibres are porous with a certain degree of roughness. To further confirm the tubular nature of the α-Fe_2O_3-SiO_2 nanofibres, a TEM study was performed. The Figure 3 shows the TEM image of the nanofibres and a contrast between the darker periphery of the nanofibres and the lighter core confirms the tubular nature of the α-Fe_2O_3-SiO_2 nanofibres. The tubular structure was further examined by HRTEM and Figure 3(b) shows selected area electron diffraction (SAED) pattern of the α-Fe_2O_3-SiO_2 nanotubes.

An EDX was performed after sintering of the α-Fe_2O_3-SiO_2 nanofibres to determine the constituting elements in the hollow nanofibres (Figure 4). As shown in the Figure 4, prominent peaks of Si, O and Fe were detected confirming the constituents of the α-Fe_2O_3-SiO_2 nanofibres. Study of the crystal structure of α-Fe_2O_3-SiO_2 nanotubes was performed by analyzing the XRD pattern of the nanostructures. Figure 6 shows XRD pattern of the post-sintered α-Fe_2O_3-SiO_2 hollow nanofibres. The diffraction peaks at 24.22°, 33.15°, 35.71°, 40.83°, 49.44°, 54.07°, 57.29°, 62.39° and 64.00° correspond to the (012), (104), (110), (113), (024), (116), (018), (214) and (300) planes. It is observed that these peaks are sharp and well defined which is indicative of crystalline nature of the sample.

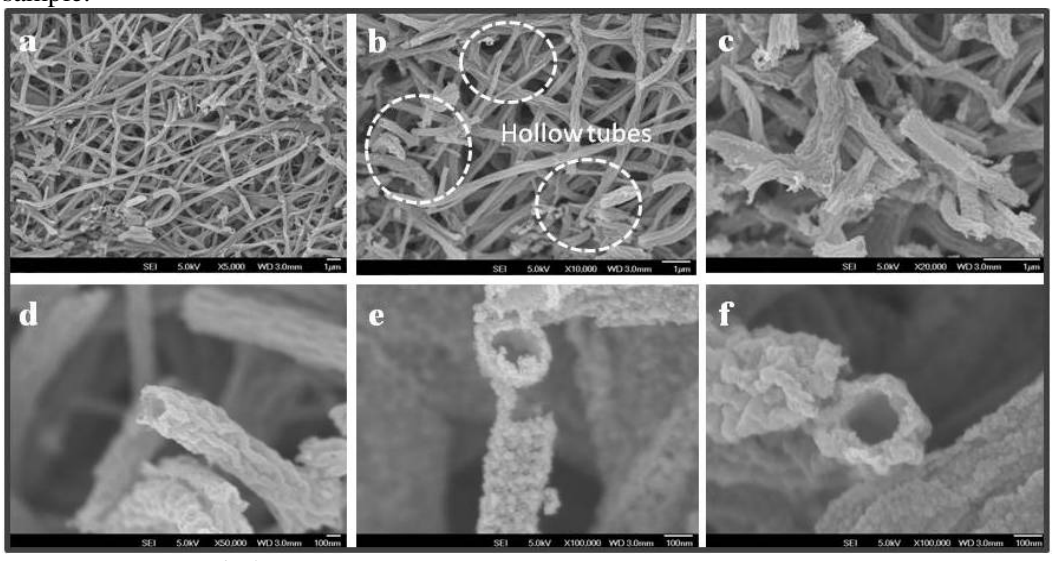


Fig.2. FESEM images of the Fe_2O_3-SiO_2 polymer nanotubes.

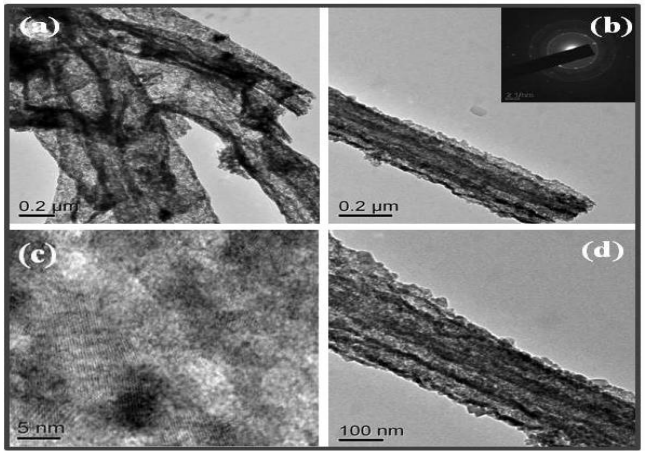


Fig.3. TEM images of Fe_2O_3-SiO_2 nanotubes.

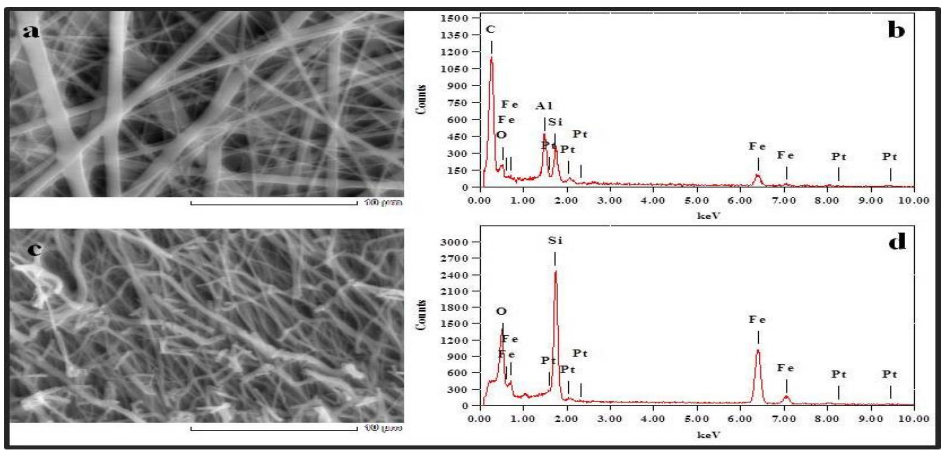


Fig.4. EDX analysis of polymer $Fe(acac)_3$-TEOS nanofibers (a,b) and calcinated Fe_2O_3-SiO_2 nanotubes (c, d).

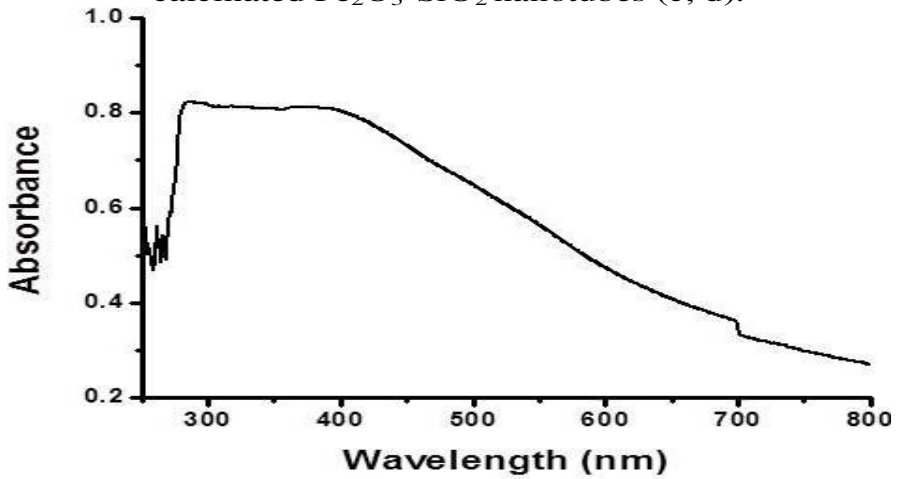


Fig.5. UV-Vis spectrum of Fe_2O_3-SiO_2 hollow nanotubes.

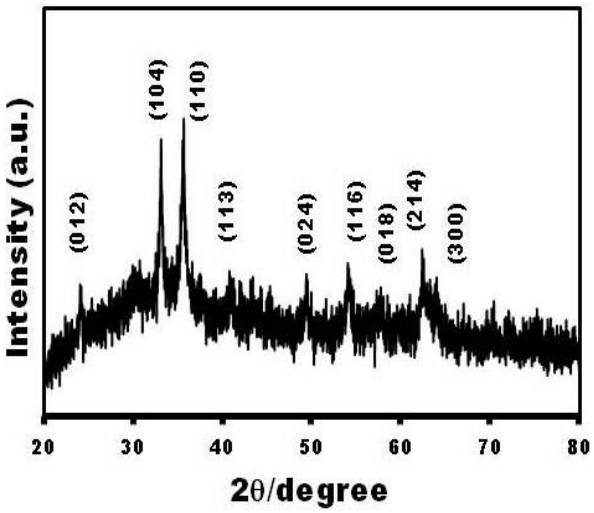


Fig.6. XRD spectrum Fe_2O_3-SiO_2 hollow fibers.

Cyclic voltammetry (CV) of the electrode made from α-Fe_2O_3-SiO_2 hollow nanotube electrode was shown in Fig. 7. The scan starts from open circuit voltage (OCV=2.95 V) at a rate of 58 mVs^{-1} in the voltage window from 0.005 V to 3.0 V, and curves at first, second, fifth and tenth cycle are presented as comparison to demonstrate its electrochemical performance. Substantial differences can clearly be observed between the first and the subsequent cycles. During the first cathodic scan, four peaks ae located at 1.37 V, 0.96 V, 0.70 V and 0.44 V, respectively. The sharp high-intensity peak at 0.70 V corresponds to the complete reduction of $Fe^{2+/3+}$ to Fe^0, the beginning of irreversible decomposition of electrolyte, and forming the solid electrolyte interface (SEI) layer. In consistent with the previous studies on electrospun α-Fe_2O_3 hollow fibers[39], small cathodic peak at 0.96 V occurs indicating the phase transformation of α-$Li_xFe_2O_3$ to cubic $Li_2Fe_2O_3$ during the initial cycle. However, two broad peaks at 1.37 V and 0.44 V are different, which might be due to the effects of existing nano-SiO_2 on the surface of α-Fe_2O_3 hollow nanotubes. Although the mechanism is still unclear to us, such result indicates some interaction between α-Fe_2O_3 hollow nanotube and nanosized-SiO_2 on its outer shell. In the first anodic polarization process, at 1.6 V appears a distinguished peak while around 1.97 V and 2.11 V broad peaks can be observed overlapping each other. They corresponds to the oxidation of Fe^0 to $Fe^{2+/3+}$ and the delithiation from lithium silicon oxides compounds.[40-42]

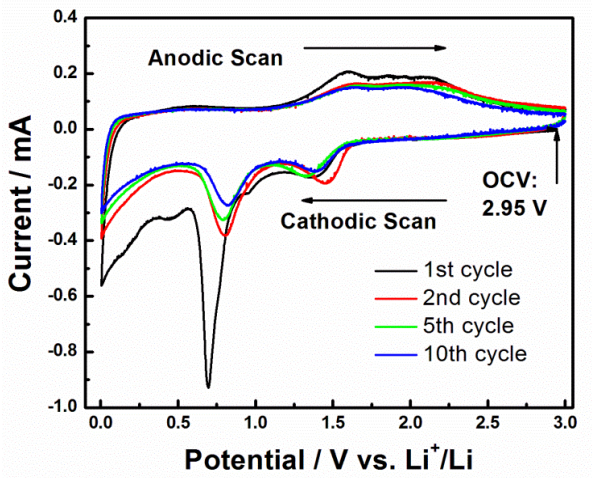


Fig. 7. CV of α-Fe_2O_3-SiO_2 hollow nanotube electrode/Li cells (scan rate: 58 mVs^{-1} in the voltage window from 0.005 V to 3.0 V).

For the second cycle, cathodic peaks sharpens at two main locations, 0.8 V and 1.45 V, while broad anodic bump forms from 1.64 V to 2.18 V. The peak ~0.8 V demonstrates the reversible Li reaction with α-Fe_2O_3 and the one at 1.45 V corresponds to that with nanostructured SiO_2 similar to the result shown in the previous study[42]. The anodic bump observed here is due to the composite electrode of α-Fe_2O_3 nanotube and nano-SiO_2. From the second cycle onwards, the intensity of peaks decreases with the cycle number indicating that capacity is decreased during cycling and slight shifts in potential are due to the minor structural rearrangement for active materials and "conditioning" of the electrode to have better electrical contact with current collector and liquid electrolyte.[43] All CV curves matches well with the galvanostatic cycling data shown below.

The cycle stability of α-Fe_2O_3-SiO_2 hollow nanotubes was investigated at a low current rate of 100 mAg^{-1} and is shown in Fig. 8, which demonstrates an interesting cycling performance after a long term running up to 150 cycles. In Fig. 8a, the galvanostatic discharge-charge curves for 1^{st}, 2^{nd}, 5^{th}, 10^{th}, 50^{th} and 150^{th} cycles are presented. During discharge, an initial capacity was found at 1265 $mAhg^{-1}$ and the value dropped dramatically to 712 $mAhg^{-1}$ at the second cycle due to the electrolyte decomposition and the SEI layer formation[44]. In the voltage profiles of selected galvanostatic cycles, a distinguished plateau around 0.8 V can be observed echoing well with the sharp high-intensity peak bringing in during the first cycle and is kept for the next few cycles. However, such plateau almost diminishes after 40^{th} cycles presenting a decreased capacity till 381 $mAhg^{-1}$, as shown in the graph of capacity vs. cycle number (Fig. 8b). Although the capacity value at 40^{th} cycle is only 54% of the second cycle, it is

still higher than the theoretical capacity of graphite (372 $mAhg^{-1}$) and the decreasing rate is similar to the bare α-Fe_2O_3 nanotubes in previous report[18]. More interestingly, the capacity value recovers considerably to 582 $mAhg^{-1}$ at the end of the 150th cycle. The charge/discharge voltage profile of the 150th cycle also demonstrates that most capacity recovery during discharge comes from the region below the original 0.8 V plateau, which enlarges the working voltage for the whole cell, thus enhancing the overall energy density as well. The recovery is possibly due to the outer shell layer of nano-SiO_2, which is usually used to coat cathodes for the enhancement of stability and cycle life. The SiO_2 on the surface helps to enable lithium ions to intercalate into active material through the coating layer and prevents the direct contact of active material with electrolyte media.[45]

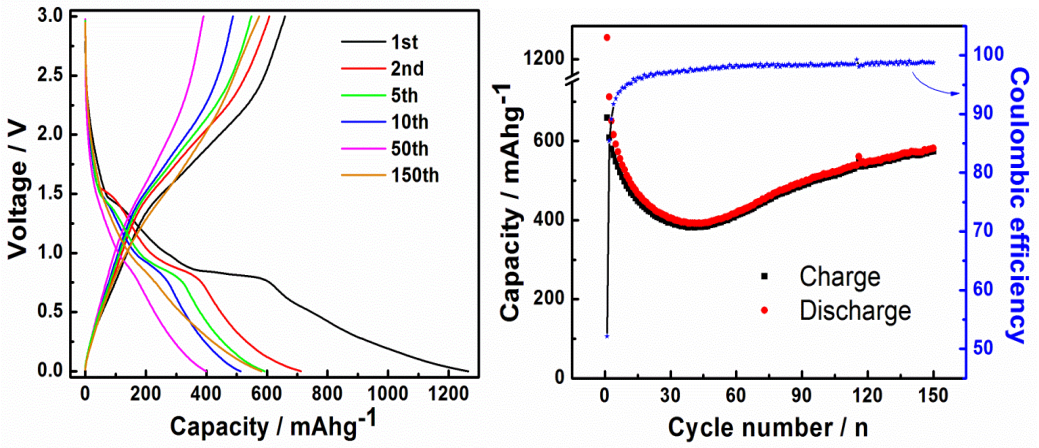


Fig. 8. Capacity vs. cycle number profile of α-Fe_2O_3-SiO_2 hollow nanotube electrode/Li cells. Current rate; 100 mAg^{-1}.

When the electrode was charged towards 3 V, a sloping rise can always be observed from 1.5 V to 2.1 V during cycling while rises in other regions are relatively steeper. For the first charge capacity at 660 $mAhg^{-1}$, the initial irreversible capacity loss is as high as 47.8%. Thus, the Coulombic efficiency is low at 52.2% initially, rises over 90% quickly after few cycles and retains >96% for most 150 cycles. (shown in Fig. 8b, right axis) The results demonstrate that the reversible capacity achieved by α-Fe_2O_3-SiO_2 hollow nanotubes can reach 712 $mAhg^{-1}$ at a low current rate of 100 mAg^{-1}, drop to ~ 400 $mAhg^{-1}$ within 40 cycles and then stabilize itself back toward 600 $mAhg^{-1}$ after 150 cycles.

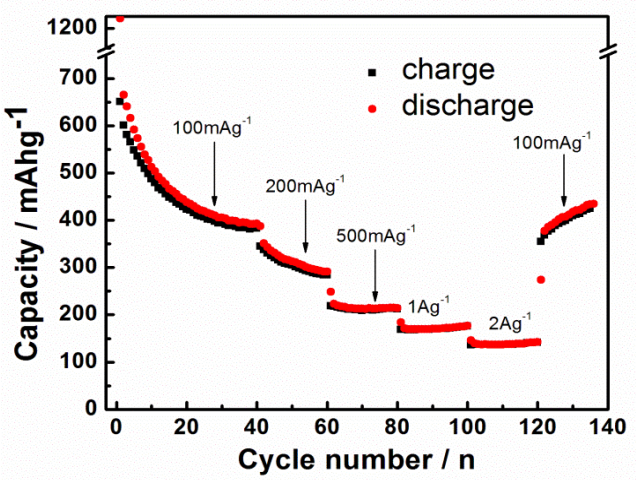


Fig. 9. Rate capacity performance of α-Fe_2O_3-SiO_2 hollow nanotube electrode/Li cells.

The rate capacity test was carried out on a duplicate cell with α-Fe_2O_3-SiO_2 hollow nanotubes in the voltage range, 0.005-3 V, at different current rates and results are shown in Fig. 9. The specific cycling current is increased in steps from 100 mAg^{-1} to 2Ag^{-1}. The capacity can stabilize ~400 $mAhg^{-1}$ at 100 mAg^{-1} for 40 cycles. Although decreases in capacity are observed at higher rates of 200 mAg^{-1}, 500 mAg^{-1}, 1 Ag^{-1}, and 2 Ag^{-1}, the battery stability has been enhanced to a large extent at higher rates. At a charging-discharging rate of 2 Ag^{-1}, a consistent capacity around 170 mAg^{-1} can be retained over 20 cycles and a slight increase in capacity during cycling can be noticed, which coincides with the capacity recovery trend after 120 cycles and results discussed above at low rate of 100 mAg^{-1}.

4. Conclusions

We report that, we have fabricated interconnected nanotubes of α-Fe_2O_3-SiO_2 nanofibers by direct calcination of as-spun $Fe(acac)_3$-TEOS-PVP nanofibers. The as-prepared material demonstrates interesting electrochemical properties in the application of lithium ion battery. It shows a recoverable capacity ~582 $mAhg^{-1}$ after 150 cycles at a current rate of 100 mAg^{-1}.

References

1. S. Iijima, Nature, 1991, **354,** 56.
2. H. Nakamura, Y. Matsui, *Adv. Mater.*, 1995, **7,** 871.
3. G. W. Orr, L. J. Barbour, J. L. Atwood, *Science,* 1999, **285,** 1049.
4. D. Yan, Y. Zhou, J. Hou, *Science,* 2004, **303,** 65.

5. P. Poizot, S. Laruelle, S. Grugeon, L. Dupont, J.-M. Tarascon, *Nature,* 2000, **407,** 496.
6. M. V. Reddy, T. Yu, C. H. Sow, Z. X. Shen, C. T. Lim, G. V. Subba Rao, B. V. R. Chowdari, *Adv. Funct. Mater.,* 2007, **17,** 2792.
7. M. V. Reddy, G. V. Subba Rao, B. V. R. Chowdari, Chem. Rev., 2013, **in press**.
8. Y. Xiao, J. Zai, L. Tao, B. Li, Q. Han, C. Yu, X. Qian, Phys. Chem. Chem. Phys., 2013 DOI: 10.1039/C3CP50220A
9. P. F. Teh, Y. Sharma, S. S. Pramana, M. Srinivasan, *J. Mater.* Chem*.,* 2011, **21,** 14999.
10. J. Sui, C. Zhang, D. Hong, J. Li, Q. Cheng, Z. Li, W. Cai, *J. Mater. Chem.,* 2012, **22,** 13674.
11. Y. Zhao, J. Li, Y. Ding, L. Guan, *J.* Mater *Chem.,* 2011, **21,** 19101.
12. T. C. Christie, M. V. Reddy, G. V. Subba Rao, C. H. Sow, B. V. R. Chowdari, *J. Solid State Electr.*, 2012, **16,**1823.
13. J. B. Lian, X. C. Duan, J. M. Ma, P. Peng, T. Kim, W. J. Zheng, *ACS Nano,* 2009, **3,** 3749.
14. M. Armand and J.-M. Tarascon, *Nature,* 2008, **451,** 652.
15. P. G. Bruce, B. Scrosati, J.-M. Tarascon, *Angew. Chem. Int. Edit.,* 2008, 47, 2930.
16. T. Yuan, B. T. Zhao, R. Cai, Y. K. Zhou, Z. P. Shao, *J. Mater. Chem.*, 2011, 21, 15041.
17. L. M. Li, X. M. Yin, S. Liu, Y. G. Wang, L. B. Chen, T. H. Wang, *Electrochem. Commun.,* 2010, 12, 1383.
18. J. Chen, L. N. Xu, W. Y. Li, et al. *Adv. Mater.,* 2005, 17, 582.
19. W. N. Li, J. Yuan, X. F. Shen, S. Gomez-Mower, L. P. Xu, S. Sithambaram, M. Aindow, S. L. Suib, *Adv. Funct. Mater.,* 2006, 16, 1247.
20. J. Y. Zhong, C. B. Cao, Y. Y. Liu, Y. N. Li, W. S. Khan, Chem. Commun., 2010, 46, 3869; J.X. Yu, B. B. Huang, Z. Y. Wang, X. Y. Qin, X. Y. Zhang, P. Wang, *Inorg. Chem.,* 2009, 48, 10548.
21. J. Bachmann, J. Jing, M. Knez, S. Barth, H. Shen, S. Mathur, U. Gosele, K. Nielsch, *J. Am. Chem. Soc.,* 2007, 129, 9554.
22. H. Shao, X. Zhang, F. Chen, S. Liu, Y. Ji, Y. Zhu, Y. Feng, *Appl. Phys. A.* 2012, 108, 961.
23. S. Hafmann, R. Sharma, C. Ducati, G. Du, C. Mattevi, C. Cepek, M. Cantoro, S. Pisana, A. Parvez, F. C. Sodi, A. C. Ferrari, R. D. Borkowski, S. Lizzit, L. Petaccia, A. Goldoni, J. Robertson, *Nano Lett.,* 2007, 7, 602.
24. T. J. Latempa, X. Peng, M. Paulose, C. A. Grimes, *J. Phys. Chem. C*, 2009, 113, 16293.
25. J. Y. Raty, F. Gygi, G. Galli, *Phys. Rev. Lett.,* 2005, 95, 096103.
26. S. K. Mohapatra, S. E. John, S. Banerjee, M. Misra, *Chem. Mater.,* 2009, 21, 3048.
27. Z. Wang, D. Luan, S. Madhavi, C. M. Li, X. W. Lou, *Chem. Commun.,* 2011, 47, 8061.
28. J. Liu, Y. Li, H. Fan, Z. Zhu, J. Jiang, R. Ding, Y. Hu, X. Huang*, Chem. Mater.,* 2010, 22, 212.
29. Z. Ren, G. Zhang, J. P. Chen, *J Colloid & Interface Science,* 2011, 358, 230.
30. L. Zeng, Water Res. 2003, 37, 4351.
31. J. Zhao, Z. Feng, F. E. Huggins, G. P. Huffman, *Energy & Fuels,* 1994, 8, 38.

32. T. Herranz, S. Rojas, M. Ojeda, F. J. Perez-Alonso, P. Terreros, K. Pirota, and J. L. G. Fierro *Chem. Mater.* 2006, 18, 2364.
33. Alonso FJ P., Granados ML., Ojeda M., Herranz T., Rojas S., Terreros P., Fierro JLG., Gracia M and Gancedo JR., *J. Phys. Chem. B,* 2006, 110, 23870.
34. K. T. Li, C. H. Huang, The Canadian *J Chemical Engineering,* 1999, 77, 1141.
35. F. Long, J. L. Gong, G. M. Zeng, L. Chen, X. Y. Wang, J. H. Deng, Q. Y. Niu, H. Y. Zhang, X. R. Zhang, *Chem. Eng. J.,* 2011, 171, 448.
36. Y. Z. Wu, P. N. Zhu, X. Zhao, M. V. Reddy, S. J. Peng, B. V. R. Chowdari, S. Ramakrishna, *J. Mater. Chem. A.,* 2013, 1, 852.
37. P. N. Zhu, Y. Z. Wu, M. V. Reddy, A. S. Nair, B. V. R. Chowdari, S. Ramakrishna, *RSC Adv.,* 2012, 2, 531.
38. Y. Z. Wu, M. V. Reddy, B. V. R. Chowdari, S. Ramakrishna*, Electrochim. Acta,* 2012, 67, 33.
39. S. Chaudhari, M. Srinivasan, *J. Mater. Chem.,* 2012, 22, 23049.
40. T. C. Christie, J. Sundaramurthy, M. Kalaivani, P. Ragupathy, P. S. Kumar, V. Thavasi, M. V. Reddy, C. H. Sow, S. G. Mhaisalkar, S. Ramakrishna, B. V. R. Chowdari, *J. Mater. Chem.,* 2012, 22, 12198.
41. B. K. Guo, J. Shu, Z. X. Wang, H. Yang, L. H. Shi, Y. N. Liu, L. Q. Chen, *Electrochem. Commun.,* 2008, 10, 1876.
42. Q. Sun, B. Zhang, Z. W. Fu, Appl. Surf. Sci., 2008, 254, 3774.
43. M.V. Reddy, G.V. Subba Rao, B.V.R. Chowdari, *J. Power Sources,* 2010, 195, 5768.
44. P. Poizot, S. Laruelle, S. Grugeon, L. Dupont, J.-M. Tarascon*, J. Power Sources,* 2001, 97, 235.
45. H. Omanda, T. Brousse, C. Marhic, D.M. Schleicha, J. Electrochem. Soc., 2004, 151, A922; J. Cho*, J. Power Sources,* 2004, 126, 186.

METHODS OF PREPARATION-MOLTEN SALT AND MIXED HYDROXIDES AND CATHODIC STUDIES ON LAYERED-STRUCTURE MATERIALS $Li(Ni_{1/3}Co_{1/3}Mn_{1/3})O_2$ FOR Li-ION BATTERIES

M V REDDY[1,2*], NGUYEN NGOC MINH UYEN[3,2], TOH WEI QI[3,2], WU XIAO YUE[3,2], S ADAMS[1], B.V.R.CHOWDARI[2]

[1]*Department of Materials Science & Engineering, National University of Singapore, Singapore 117576*

[2]*Department of Physics, National University of Singapore, Singapore 117542*

[3]*NUS High School of Math and Science, 20 Clementi Avenue 1, Singapore 129957*

In our project, we prepared layered compound, $Li(Ni_{1/3}Co_{1/3}Mn_{1/3})O_2$ (LNCMO) by molten-salt method (MSM) and mixed-hydroxides method. The prepared samples are then characterized by X-ray diffraction (XRD), scanning electron microscopy (SEM) and Brunauer, Emmett and Teller (BET) tests. Electro-analytical studies such as cyclic voltammetry (CV), galvanostatic cycling and electrochemical impedance studies (EIS) were conducted to investigate the materials' performance for energy storage in cells. Results from our studies showed that LNCMO prepared by MSM from LiCl, $Ni(OH)_2$, $Co(OH)_2$, $MnCO_3$ salts at 950°C, 8 hours, showed an average capacity of 105mAhg^{-1} over 50 cycles and a relatively stable cycling ability between 2.7V and 4.3V. It showed a 3.9V redox couple. LNCMO prepared by MSM from a eutectic mixture of LiCl and $LiNO_3$ in a mole ratio of 0.12:0.88 and $NiSO_4$, $CoSO_4$, $MnSO_4$ salts showed lower capacity of 65 mAhg^{-1} over 50 cycles. LNCMO prepared using the mixed-hydroxides method and heated at 950°C, 6 hours, displayed promising results with a reversible capacity of 110-130mAhg^{-1}. Although slight capacity fading of ~11% was initially observed, stable cycling with negligible capacity fading occurred at a reversible capacity of 110mAhg^{-1} from cycle 26 to cycle 50. In general, preparation of LNCMO using different methods and starting materials significantly affects its electrochemical properties.

1. Introduction

As an energy source, Lithium-ion batteries (LIB) are essential to portable electrical devices in the present day. Their pre-eminence over their counterparts can be ascribed to their small size, relatively inexpensive production cost and high charge densities. Commercial LIBs are made of $LiCoO_2$ cathode[1], Gel polymer as electrolyte and graphite anode[2]. An extensive amount of research

Proceedings of the 14th Asian Conference on Solid State Ionics (ACSSI 2014)
Copyright © 2014 ACSSI 2014 Organizers. All rights reserved.
ISBN: 978-981-09-1137-9
doi:10.3850/978-981-09-1137-9_178

has been carried out to further enhance the electrochemical performance of LIB. One such approach is to find alternative materials for cathode and anode.

$LiCoO_2$ is commercially used as cathode material due to its high capacity and good redox potential, but it has poor thermal stability, low practical capacity, is toxic and costly. Hence, there is a pressing need to research for an alternative that is safer and more efficient. The toxicity of $LiCoO_2$ can be reduced by lowering the proportion of Cobalt by transition metal ions like Mn, Ni. Research has shown that $Li(Ni_{1/3}Co_{1/3}Mn_{1/3})O_2$ layered compound can be a high potential candidate due to its relatively high capacity and thermal stability. Moreover, the cobalt concentration is reduced to 1/3. Various synthesis and characterization of $Li(Ni_{1/3}Co_{1/3}Mn_{1/3})O_2$ are reported[3-5]. In general, electrochemical properties will depend on method of preparation and reaction conditions such as temperature and time. In this paper we prepared $Li(Ni_{1/3}Co_{1/3}Mn_{1/3})O_2$ by different preparation methods and electrochemical performance as a cathode. .

2. Experiment

2.1. *Synthesis of materials*

2.1.1. *Molten salt method*

The compound, $Li(Mn_{1/3}Co_{1/3}Ni_{1/3})O_2$ (LNCMO), was first prepared by MSM with highly purified LiCl-$LiNO_3$ salts (Alfar Aesar) in the mole ratio of 0.88:0.12 (eutectic mixture) and $NiSO_4$ (Merck), $CoSO_4$ (Fisher Scientific UK), $MnSO_4$ (Fluka) salts. The ratio of eutectic to transition metal sulphates is 10:1. LNCMO was then prepared with varying starting materials, one with only LiCl and a mixture of the above mentioned transition metal sulfates, and another with LiCl and $Co(OH)_2$ (Aldrich), $Ni(OH)_2$ (Jiangmon,China) and $MnCO_3$ (Merck) salts. All three samples were well mixed, placed in high purity alumina crucibles and heated to 950^{o}C in air in a box furnace (Carbolite, UK) at a heating rate of 3^{o}C min^{-1}, kept for 8 hours then cooled to room temperature (RT = 25^{o}C). The compounds were washed with de-ionized (DI) water and filtered using a vacuum pump. The residues were dried in air oven at 80^{o}C for 24h. Black powder samples were obtained. Some of the samples obtained were reheated to further investigate their electrochemical properties.

2.1.2. *Mixed hydroxides method*

LNCMO was again prepared by mixed hydroxides method. LiOH and transition metal nitrate hexahydrates in a mass ratio of 2:1 and dissolved to form two separate solutions. The solution (200ml) of 1/3M $Ni(NO_3)_2.6H_2O$ (Fluka),1/3M $Co(NO_3)_2.6H_2O$ (Sigma-Aldrich), 1/3M $Mn(NO_3)_2.6H_2O$ (Afa) was added drop-by-

drop into a solution (400ml) of 1.5M LiOH (Merck), forming black precipitate. The mixture was then filtered and the residue was subsequently dried in air oven at 80°C for 24h to obtain $(Ni_{1/3}Co_{1/3}Mn_{1/3})(OH)_2$. 1.03M of LiOH (Merck) was mixed with 1M of the mixed-metal hydroxide and pressed into a pellet before it was heated to 950°C in a box furnace (Carbolite, UK) at a heating rate of 3°C min^{-1}. It was soaked for 6 hours, then cooled to room temperature (25°C). The pellet was ground to obtain a black powder sample.

2.2. Characterization and electrochemical techniques

The powder X-ray diffraction (XRD) patterns were taken with Bruker axs D8 diffractometer using Cu Kα radiation. TOPAS R (version 3) software was used to carry out Rietveld refinement of XRD data. The compounds morphology and surface area were studied by scanning electron microscope (SEM) (JEOL JSM-67500F), and Brunauer, Emmett and Teller (BET) (Micromeritics Tristar 3000 (USA)) techniques. For electrochemical studies, the composite cathodes were fabricated with active material, super P carbon black and binder (Kynar 2801) in the weight ratio 70:15:15, using N-methyl pyrrolidone (NMP) as solvent. The mixtures were coated on aluminum foil (current collector) using doctor blade technique and cut into circular disks. The coin-type cells (size 2016) were assembled in an Ar-filled glove-box (MBraun, Germany) using Lithium metal foil (Kyokuto Metal Co., Japan) as anode, 1M $LiPF_6$ ethylene carbonate (EC) + diethyl carbonate (DEC) (1:1 V/V) (Merck) as the electrolyte, and Whatman glass paper as a separator. The cells were aged for 24h before the electrochemical tests at RT. Cyclic voltammetry and charge-discharge cycling at a constant current were carried out using computer controlled Mac-pile II system (Bio-logic, France) and Bitrode multiple tester (Model SCN, Bitrode, USA) and more details are given in our previous studies[6] .

3. Results and Discussion

3.1. Structure and Morphology

Rietveld refined XRD pattern of LNCMO are shown in fig .1. The Rietveld refinement patterns are refined using the space group R-3m, with α-$NaFeO_2$ type structure and transition metals (Ni,Co,Mn) occupying at 3a site (0,0,0), Li at 3b site (0,0,½), O at 6a site (0,0,0.25). Refined parameter values are summarized in Table 1. lattice parameter values of LNCMO synthesized by mixed hydroxide method display closer values (c=14.25Å) to those reported in literature[7] (c=14.24Å) than samples prepared by MSM (c=14.198Å) [8]. The distinct peaks (2θ ranges 37°–40° and 64°–67° in Figure 1) of the XRD diffraction pattern of

LNCMO and a nice ratio of (003/104) lines (I≥1.5) as well as well-defined splitting indicate a well-ordered layered structure. The MSM samples with LiCl showed a minor peaks of LiOH line at 2theta 30° .

Table 1. Lattice parameters, density and BET surface area values of LNCMO samples.

Compound	a (Å)	c (Å)	c/a
LNCMO (MSM LiCl, $Ni(OH)_2$, $Co(OH)_2$, $MnCO_3$ 950°C 8hrs)	2.948(0)	14.566(5)	4.941
LNCMO (MSM $LiNO_3$-LiCl, $NiSO_4$, $CoSO_4$, $MnSO_4$ 950°C 8hrs)	2.861(3)	14.226(6)	4.972
LNCMO (MSM LiCl, $Ni(OH)_2$, $Co(OH)_2$, $MnCO_3$ 950oC 8hrs, reheated at 950°C 6hrs)	2.959(7)	14.12(3)	4.937
LNCMO (MSM LiCl, $NiSO_4$, $CoSO_4$, $MnSO_4$ 950°C 8hrs, reheated at 950°C 6hrs)	2.861(5)	14.241(9)	4.977
LNCMO (Mixed hydroxides method, 950+C 6hrs)	2.864(3)	14.255(0)	4.976

Compound	Density (g/cm^3)	BET Surface Area (m^2/g)	Average Pore Volume (cm^3/g)	Average Pore Diameter (nm)
LNCMO (MSM LiCl, $Ni(OH)_2$, $Co(OH)_2$, $MnCO_3$ 950°C 8hrs)	6.1499 ± 0.0231	0.5131 ± 0.00021	0.001239	9.661
LNCMO (MSM $LiNO_3$-LiCl, $NiSO_4$, $CoSO_4$, $MnSO_4$ 950°C 8hrs)	4.4559 ± 0.0165	0.7179 ± 0.00056	0.013847	7.6702

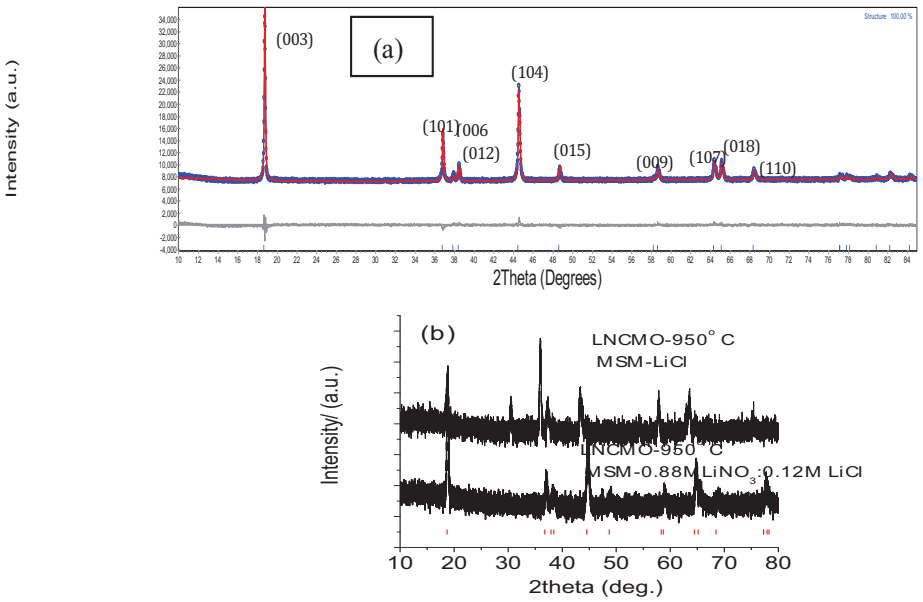


Fig.1 X-Ray Diffraction pattern of LNCMO prepared using (a) mixed hydroxide method at 950oC for 6 hours and (b) MSM method. Fitted refinement and difference pattern (a), bottom vertical (hkl) lines are also shown.

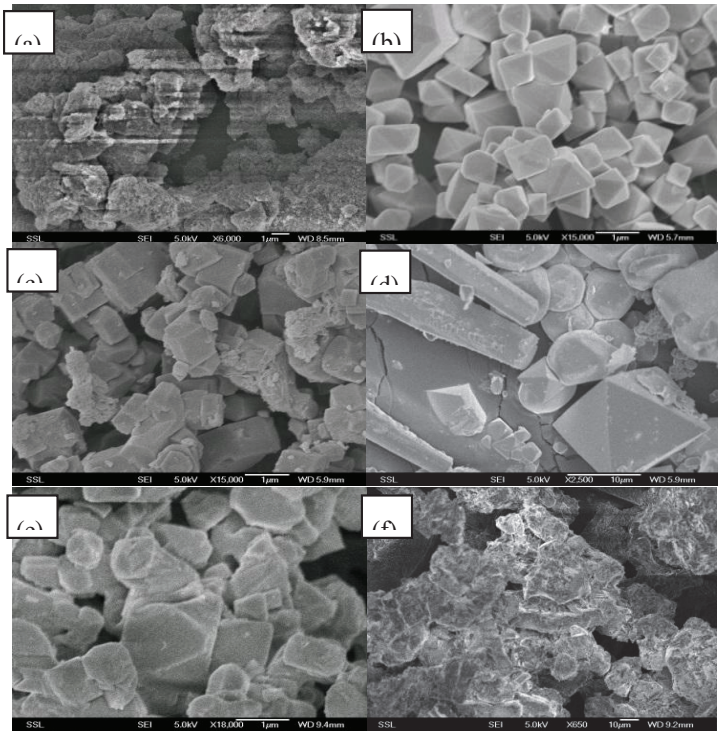


Fig. 2. SEM photographs of LNCMO samples prepared with: (a) mixed hydroxides method, 950°C for 6hrs (X6,000); (b) MSM, LiCl-$LiNO_3$, with $NiSO_4$, $CoSO_4$, $MnSO_4$, 950°C for 8hrs

(X15,000); (c) MSM LiCl, with $Ni(OH)_2$, $Co(OH)_2$, $MnCo_3$, 950°C for 8hrs (X15,000); (d) MSM LiCl, with $NiSO_4$, $CoSO_4$, $MnSO_4$, 950°C for 8hrs (X2,500); (e) Sample in (b) reheated at 950°C for 6hrs (X18,000); (f) Sample in (c) reheated at 950°C for 6hrs (X650).

The SEM images of LNCMO are shown in Figure 2. The particles are submicron particles with platelet-like morphology and their sizes vary with different methods of preparation. Interestingly, the particles of LNCMO-mixed hydroxides method synthesized display the smallest particle size (<1 μm), are flatter and more spherical while those of LNCMO-MSM synthesized have a variegated range (from 1μm to over 10 μm), suggest greater volume per particle and more crystal-like surface. The effects of particle size and surface will be manifested in the electrochemical performance. Due to high temperature preparation decreases.

2.2. *Electrochemical studies*

Cathodic studies of LNCMO are cycled at room temperature (25°C) in the voltage range of 2.5-4.3V versus Li at a current density of 30mAg^{-1}. Profiles of voltage against capacity for selected cycles of LNCMO prepared at different method are shown in Figure 3. The process of Li-deintercalation (charge) is indicated by the curve where voltage increases with capacity, while Li-intercalation (discharge) is observed from the curve where voltage decreases against increase in capacity. As seen from the voltage against capacity profile of LNCMO prepared using the mixed hydroxides method heated at 950°C for 6 hours, in the first charge process, the voltage of the cell increased steeply from the open circuit voltage (OCV) of 2.5V to ~3.75V. This is followed by a plateau before voltage increases gradually to the cut off voltage of 4.3V. No plateau is observed from the Li-intercalation curves. In subsequent cycles the charging curve also increased steeply but to a lower voltage of ~3.7V. The lack of a plateau in these subsequent cycles also serves as an indication that the 'formation' of the electrode is complete.

Capacity against cycle number profiles are obtained from the results of the charge-discharge cycling for each compound over 50 cycles, shown in Figure 4. The decrease in charge and discharge capacity for the first cycle of each compound prepared displays the irreversible capacity loss (ICL). ICL ranges from 20 to 32 mAhg^{-1} in the LNCMO compounds. The difference decreases significantly after around 5 cycles, showing high columbic efficiency. LNCMO synthesized by the mixed hydroxides method displays promising results, with an initial discharge capacity of 130 mAhg^{-1}. A discharge capacity of 124 mAhg^{-1} is observed in the 4th cycle, which degrades to 110 mAhg^{-1} in cycle 26 indicating

~11% of capacity fading. From cycle 26 to the end of 50 cycles, the reversible capacity of LNCMO prepared by mixed hydroxides method remains stable at 110 (±2) $mAhg^{-1}$ with negligible capacity fading. The observed capacity of 110-130 $mAhg^{-1}$ is hence a moderately good result, showing ~43.2% of the theoretical capacity. LNCMO prepared by MSM using $Ni(OH)_2$, $Co(OH)_2$, $MnCO_3$ salts displays a moderate reversible capacity of 105 (±6) $mAhg^{-1}$ with relatively stable cycling over 50 cycles. LNCMO prepared by MSM using a eutectic mixture ($0.12LiCl:0.88LiNO_3$) and $NiSO_4$, $CoSO_4$, $MnSO_4$ salts has a lower discharge capacity of 65 $mAhg^{-1}$ that is stable over 50 cycles with low capacity fading. With its higher reversible capacity, LNCMO synthesized by mixed hydroxides method is able to store more charge and proves the best performance as a cathode material in batteries out of the samples of LNCMO we prepared by MSM. It is likely that a more homogeneous surface and small particle size resulting from preparation using the mixed hydroxides method contribute to the higher capacity observed.

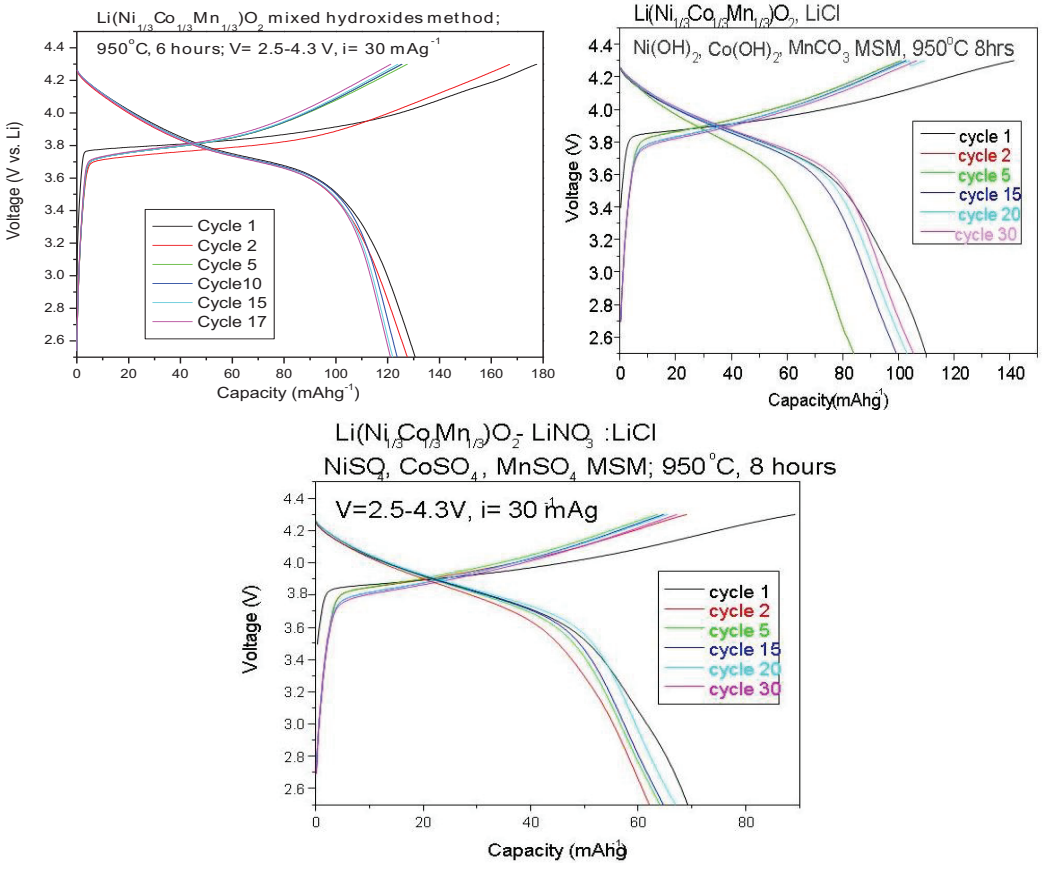


Fig. 3. Voltage against capacity profile for selected charge-discharge cycles of LNCMO prepared by mixed hydroxide and molten salt method. Voltage range, 2.5-4.3V, current rate: 30 mA/g.

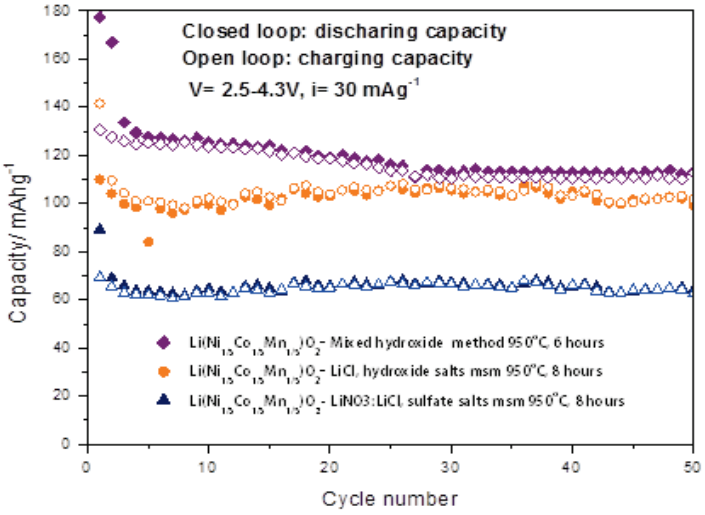


Fig. 4. Capacity against cycle number profiles for LNCMO samples over 50 cycles

Cyclic voltammetry using LNCMO prepared with the mixed hydroxide method, the test was run the voltage range of 2.5-4.3V at room temperature (25°C) with a scan rate of 0.058mVs^{-1}, up to the 6th cycle. The CV profile for all 6 cycles are shown in Figure 5.

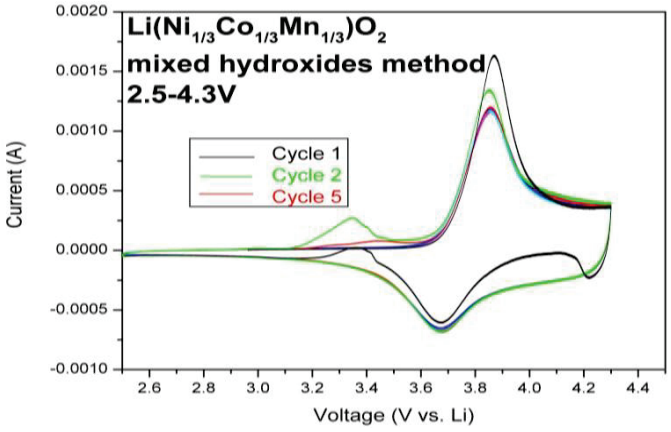


Fig. 5. CV profile of 6 cycles for LNCMO prepared by the mixed hydroxides method, scan rate, 0.058mV/sec.

The electrode material displayed the anodic peak at ~3.87V vs. Li and corresponding cathodic peak of ~3.67V vs. Li in the first cycle. A minor cathodic peak is also observed at ~4.2V in the first cycle this is due hexagonal structural transition. The anodic peak indicates the occurrence of the de-intercalation reaction while the cathodic peak indicates the occurrence of the intercalation reaction. In the subsequent cycles, the anodic peak shifted slightly to the left to a voltage of ~3.83V, while the cathodic peak remained its position at ~3.67V. The slightly lower voltage of the anodic peak voltage indicates the 'formation' of the electrode in the first cycle, a process in which the active material makes good electrical contact with the liquid electrolyte, current collector and the conducting carbon particles in the composite electrode. Potentials determined in the CV profile at which the Li intercalation-de-intercalation reactions occur agree with voltage values obtained from the corresponding plateaus in the graphs obtained from galvanostatic cycling studies conducted. The anodic and cathodic peak voltages are corresponds to $Ni^{2+/3+/4+}$ redox couple[8].

Nyquist plots ($Z^{'}$ vs. –Z'') are shown in Fig.6a, fitted using reported equivalent electrical circuit are shown Fig.6b. Impedance values are very sensitive to voltages at de-intercalation or charge cycle. After changing above 3.7V in addition to charge transfer resistance (Rct), the contribution of bulk resistance (R_b) was noted (fig.6a), which arises due to electronic conductivity of active material and ionic conductivity of electrolyte filled in the composite electrode[6] and surface (R_{sf}) due to solid electrolyte interface was noted with high frequency region.

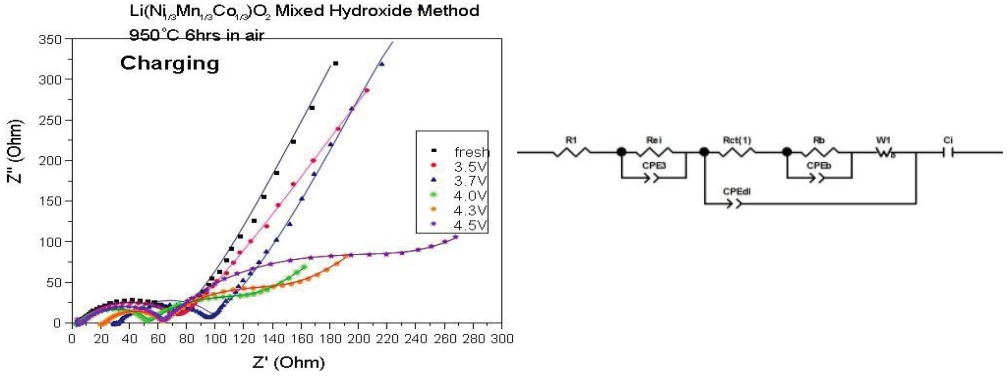


Fig. 6. Nyquist plots for (a) charging and (b) discharging of LNCMO prepared with mixed hydroxides method. (b) Equivalent circuit for cell fabricated with LNCMO prepared by the mixed hydroxides method.

4. Conclusion

We successfully prepared LNCMO by MSM and mixed hydroxides method. The LNCMO samples prepared were characterised with XRD, Rietveld refinement, SEM, BET test and density measurements. Galvanostatic cycling studies and cyclic voltammetry revealed that Li-ion intercalation and deintercalation occurs at ~3.87V and ~3.67V respectively. From our studies, LNCMO prepared by the mixed hydroxide method suggests the most promising result, with a good reversible capacity of 130 mAh/g comparable to the capacity in commercial $LiCoO_2$ (~120 mAh/g). However, slight capacity fading of ~11% is initially observed before stable cycling with no capacity fading occurs at a reversible capacity of 110 $mAhg^{-1}$ from cycle 26 to the end of cycle 50. LNCMO prepared by MSM using LiCl and $Ni(OH)_2$, $Co(OH)_2$, $MnCO_3$ at 950°C for 8hrs, on the other hand, displays a moderate capacity of 105 mAh/g and has relatively good capacity retention over 50 cycles. LNCMO material prepared by MSM from a eutectic mixture of LiCl and $LiNO_3$ and $NiSO_4$, $CoSO_4$, $MnSO_4$ salts shows lower capacity of 65 mAh/g with no capacity fading over 50 cycles

Acknowledgements

MVR and SA thank to National Research Foundation, Prime Minister's Office, Singapore under its Competitive Research Programme (CRP Award No. NRF-CRP 10-2012-6) for research support. NUSHS students thank to Dr Teh Yun Ling, NUS High school for her assistance.

References

[1] M.S. Whittingham, *Chem. Rev.* **104** (2004) (10) 4271.

[2] G.-A. Nazri, G. Pistoia, *(eds.), Lithium Batteries: Science and Technology, Kluwer Acad Publ., New York, USA.* (2003).

[3] J.W. Fergus, *J. Power Sources* **195** (2010) (4) 939.

[4] J.B. Goodenough, Y. Kim, *Chem. Mater.* **22** (2010) (3) 587.

[5] M.V. Reddy, G.V. Subba Rao, B.V.R. Chowdari, *"Future generation electrode materials for Lithium batteries" Solid State Ionics: Fundamental Researches and Technological applications, In proceedings of the 12th Asian Conf. on Solid State Ionics, B. V. R. Chowdari, et al. (eds.), Wuhan Univ. of Tech. Press, Wuhan, China* (2010) 497.

[6] M.V. Reddy, G.V. Subba Rao, B.V.R. Chowdari, *J. Phys. Chem. C* **111** (2007) (31) 11712.

[7] T. Ohzuku, Y. Makimura, *Chem. Lett.* (2001) (7) 642.

[8] M.V. Reddy, G.V. Subba Rao, B.V.R. Chowdari, *J. Power Sources* **159** (2006) (1) 263.

IMPROVEMENT OF ELECTROCHEMICAL PERFORMANCE OF Li_2MNO_3 CATHODE MATERIALS BY BISMUTH SUBSTITUBION

SHA WU[†1,2], ZHIYONG YU[*1], HANXING LIU[1,2]

[1]*School of Materials Science and Engineering, Wuhan University of technology, Wuhan, 40070, China*

[2]*State Key Laboratory of Advanced Technology for Materials Synthesis and Processing, Wuhan University of technology, Wuhan, 40070, China*

**Corresponding author: yuzhiyong@whut.edu.cn*

Bi^{3+} doped layed lithium manganese oxides $Li_2Mn_{1-x}Bi_xO_3$ (x=0,0.03,0.06) were successfully synthesized using a facile sol-gel method followed by a fast combustion method and heat treatment. The as-prepared $Li_2Mn_{1-x}Bi_xO_3$ powders were characterized by X-ray diffraction(XRD) and scanning electron microscopy (SEM).Their electrochemical performances were also investigated and compared in detail. The results indicated that Bi^{3+} doped $Li_2Mn_{1-x}Bi_xO_3$ initial discharge capacity is somewhat smaller as the increase of x. However, it has a much better cycle performance than the pure Li_2MnO_3. Among the materials prepared in this work, $Li_2Mn_{0.97}Bi_{0.03}O_3$ exhibits the best electrochemical properties in terms of capacity 110mAh/g at the current of 10mA/g and excellent cycleability, almost no capacity fading up to 30 cycles. In comparation, the undoped sample only remains 44.5% capacity after 30 times of cycling. Even the current doubles, the capacity of $Li_2Mn_{0.97}Bi_{0.03}O_3$ has no obvious fading and also exhibits excellent cycle performance. Its excellent cycle performance may have a relationship with the more stable structure with the doping of Bi in the Li_2MnO_3.

1. Introduction

Lithium ion batteries have been widely used to portable electronic equipments in our daily life, and have been considered as a promising power source for electric or hybrid vehicles[1]. Cathode materials play a very important role in the performance of lithium ion battery. In the past decades, much attention has been paid on layered lithium transition metal oxide cathode materials of Li-ion battery[2,3]. Compared with the widely applied Co- or Ni-based oxide cathode

† This work was supported by the Fundamental Research Funds for the Central Universities (WUT: 2013-IV-052)".

Proceedings of the 14th Asian Conference on Solid State Ionics (ACSSI 2014)
Copyright © 2014 ACSSI 2014 Organizers. All rights reserved.
ISBN: 978-981-09-1137-9
doi:10.3850/978-981-09-1137-9_186

materials, Mn-based cathode materials have some specific advantages such as lower cost, less toxic and environmental friendly, which are very important factors especially for the commercial application[2,4].

In recent years, Li-rich layered manganese oxide ($(1-x)LiMO_2$-xLi_2MnO_3, $0<x<1$,M=Mn,Co,Ni, or their mixture) are potencial candidates which show specific capacity higher than 300 mAh/g within the wider voltage range from 2.0 to 4.8 V[5]. However, many problems (complex synthetic method, high sintering temperature, serious capacity fading with cycle number, poor rate performance etc.) have been revealed in relation to practical appliation[6]. As the host material and the simplest system of Li-rich materials, monoclinic Li_2MnO_3 with the tetravalent Mn-ion can be represented as $Li[Li_{1/3}Mn_{2/3}]O_2$ and has a similar layered structure to $LiMO_2$, possessing high potential of Li extraction (>4.5 V), and a high theoretical capacity of 458 mAh/g for total Li extraction[7].

However, Li_2MnO_3 is electrochemically inactive once within normal voltage range (<4.4 V vs. Li+/Li) since all of Mn atoms in Li_2MnO_3 are existed in +4 valence state, and hence it usually needs a higher cut-off voltage (4.8 V vs. Li+/Li) to activate Li_2MnO_3 during the initial charge process[8,9]. Unfortunately, serious capacity decay of the activated Li_2MnO_3 would happen when cycling is performed at such high cut-off voltage[10].

It has been reported that with the bismuth modification, the performance of $LiMn_2O_4$ as cathode materials of Li ion battery can be improved. The modified sample has better cycling stability, quicker charge-transfer process and better chemical stability than the unmodified sample[11]. Here, Bi^{3+} doped layed lithium manganese oxides $Li_2Mn_{1-x}Bi_xO_3$(x=0,0.03,0.06) is successfully synthesized using a facile sol-gel method followed by a fast combustion method and heat treatment. As a result, bismuth modification was proposed to improve the Li_2MnO_3 stability in this paper.

2. Experimental

2.1. *Preparation of electrode materials*

All samples ($Li_2Mn_{1-x}Bi_xO_3$, x=0, 0.03, 0.06) were synthesized by a facile sol-gel method. First, stoichiometric lithium nitrate, manganese nitrate and bismuth nitrate were dissolved in deionized water. After vigorously stirring, the above solution was poured into a citric acid aqueous solution, yielding a gel-like mixture. Adjust pH of the solution to about 8, then put the mixture solution on the thermostatic water bath heating 80 ^oC for 8 hours to generate uniform gel.

The gel mixture was dried in the drying oven at 80 °C for 16h to evaporate water and then dried at 150 °C to form dry gel. Then we conduct a fast combustion synthesis of the dry gel in 5 minutes at 500 °Cin a furnace. The resulting powder is grinding and calcined for 12h at 600 °C in air. In convenience, we call the sample B3 and B6 for the above two doping samples respectively. All the regents used in the experiment were analytical grade.

2.2. *Characterization*

XRD analysis was performed using Cu Kα radiation (X'Pert PRO, PANalytical, Holland). XRD measurements were collected in the 2θ range 10-80° at 1.6 kW(40kV, 40mA). Microstructure and grain size were observed by field-emission scanning electron microscope (FE-SEM) (S-4800, Hitachi, Japan).

2.3. *Electrochemical measurements*

The $Li_2Mn_{1-x}Bi_xO_3$(x=0,0.03,0.06) electrodes were prepared according to the following steps. The mixture containing 80% cathode active materials, 12% carbon black and 8% poly(vinylidence fluoride)(PVDF) was well mixed and then dispersed in N-methylpyrrolidone(NMP) and stirred for 12h.The resultant slurry, pasted on stainless steel, was dried at 80 °C for 12h in the vacuum oven to remove the solvent. The electrochemical tests were taken on a coin-type cell (CR-2025) assembled with a positive electrode/a separator/and a negative electrode (Li metal) in an argon-filled glove box. The electrolyte was 1.0M $LiPF_6$ in 1:1:1 volume ratio of ethylene carbonate(EC):diethyl carbonate (DEC):dimethyl carbonate (DMC). The charge/discharge performance of the CR2025 coin cell was performed between 2.0-4.8V at room temperature on a battery evaluation system (Land,CT2001A). For the impedance measurement, the frequency range was 0.01Hz to 100kHz over the voltage ranging from 2.0-4.8V by CHI660B (Chenhua, Shanghai). All electrochemical measurements were carried out at room temperature.

3. Results anf discussion

3.1. *Structural study*

The XRD patterns of the pristine and doped samples are showed in Fig.1. It can be seen that all the diffraction peaks of the sample are indexed by the layered rock-salt structure with space group C2/m(PDF: 84-1634). But some diffraction peaks of impurity Bi_2O_3 is found in the sample B6. However, the absence of any

other impurity phase in B3 reveals that bismuth may incorporat into the structural lattice or the content of the impurity is too small to be detected.

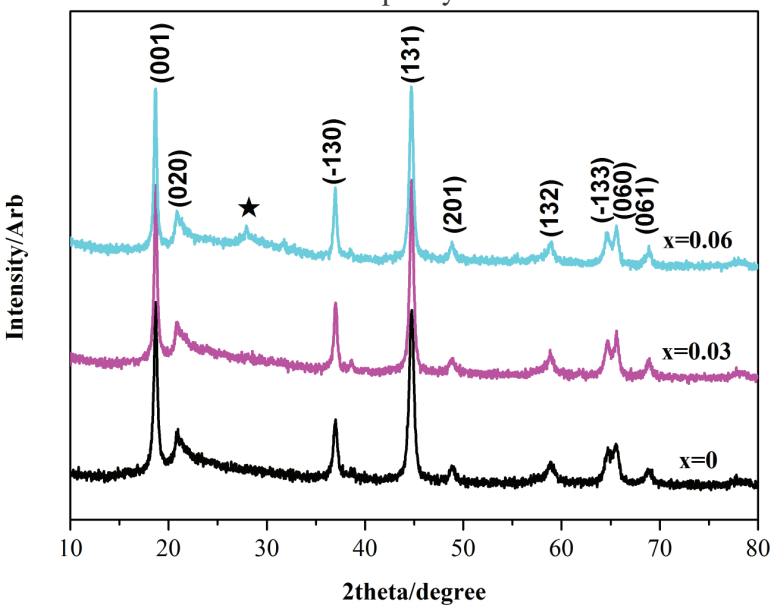


Figure 1.XRD patterns of the $Li_2Mn_{1-x}Bi_xO_3$(x=0,0.03,0.06)

3.2. *Morphology characterization*

SEM images of the $Li_2Mn_{1-x}Bi_xO_3$(x=0, 0.03, 0.06) are given in Fig.2. Fig. 2a-c displays the morphologies of the bismuth free Li_2MnO_3, B3 and B6, respectively. It can be seen that the pure Li_2MnO_3 is composed of relatively small particles about 100nm, and the particles size increase with increasing bismuth amount. The distribution of particle size becomes more nonuniform with the increasing bismuth amount.

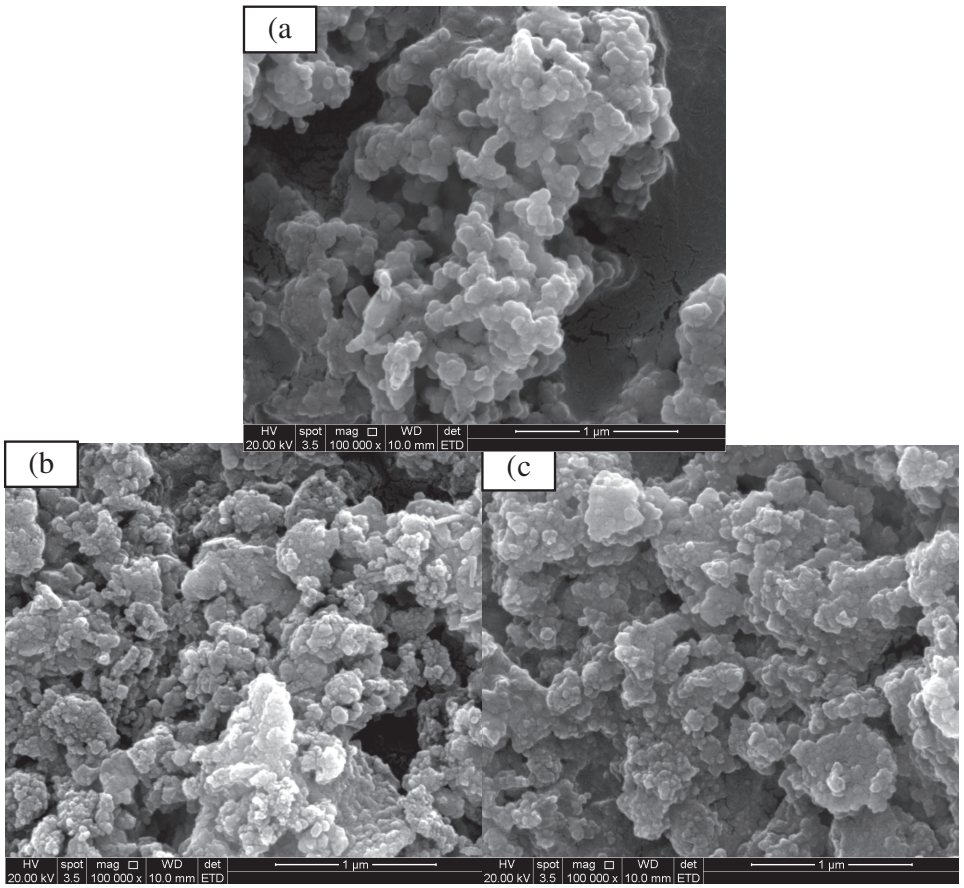


Figure 2. SEM images of Li2Mn1-xBixO3 with (a) x = 0, (b) x = 0.03 and (c) x = 0.06

3.3. *Electrochemical characterization*

Fig.3 shows initial discharge profiles of the synthesized cathodes materials in the voltage range of 2.0-4.8V at a current rate of 10mAh/g. It is seen that the specific discharge capacity of the Li_2MnO_3, B3 and B6 is 148.4mAh/g , 114.6mAh/g, 95.8mAh/g, respectively .It means that the initical capacity of the Li_2MnO_3 has a little loss with bismuth doping. It consistent with that reported for other cathode materials with bismuth modification[11].

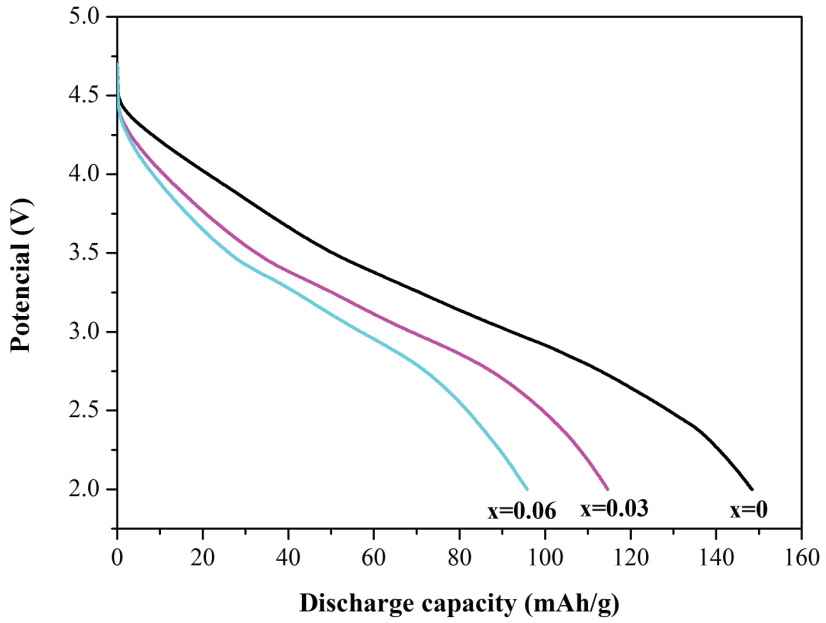


Figure 3. Initial discharge profiles of the $Li_2Mn_{1-x}Bi_xO_3$(x=0,0.03,0.06)

Fig.4 shows the cycling ability of doped and undoped samples. It is performed in the voltage range of 2.0-4.8V at a current rate of 10mAh/g for 30 cycles. As shown in Fig.4, the cycling stability of the Li_2MnO_3 has been improved by bismuth doping. It can be seen that the cycling stability of pure Li_2MnO_3 is bad. After 30 cycles, it only possesses a capacity of 66 mAh/g, which is only 44.5% of its initial capacity. However, bismuth doped sample has a better capacity stability with the increasing of the cycling times. For B3, it has a specific capacity of 98.8mAh/g after 30 times of cycling, which is 86.2% of its first diacharge capacity. For B6, with the increasing of the cycling times, its discharge capacity has a little increase first, then slowly come to stabilize. As a result, it owns a capacity of 101.2 mAh/g, which is even higher than its first discharge capacity. It may have something to do with the impurity Bi_2O_3 for the cycling stability improvement of the doped samples. When the current doubles to 20mA/g, it finds that the initial capacity of B3 only dicreasees slightly to a specific capacity of 100.4 mAh/g. After 30 times of cycling, it stills remains 95.4 mAh/g, which suggests that Li_2MnO_3 has a better rate performance by doping bismuth.

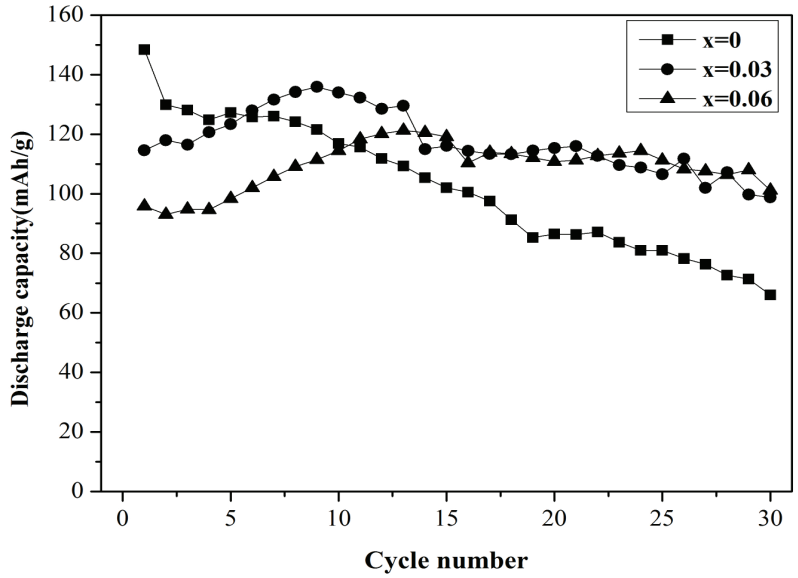


Figure 4.Cycle performance of the $Li_2Mn_{1-x}Bi_xO_3$(x=0,0.03,0.06)

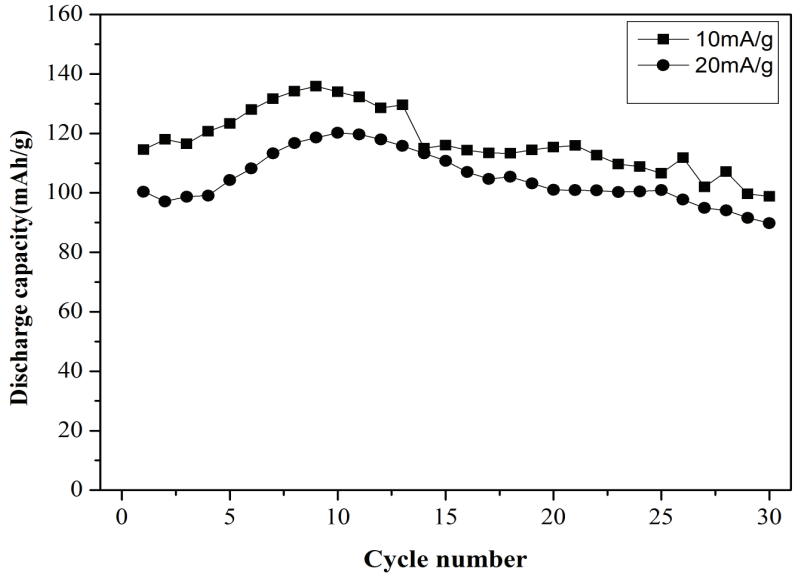


Figure 5.Cycle performance of $Li_2Mn_{1-x}Bi_xO_3$(x=0.03) at different current

Electrochemical impedance of Li_2MnO_3 and Bi-doped samples were also investigated, as showed in Fig.6. It can be clearly seen that the EIS Spectra are composed of a quasi-semicircle at the range from high to middle frequency and a straight slopping line at the low frequency range. Generally, it should possess a semicircle in the high-frequency, which is related to the passivation surface film, the so-called solid electrolyte interface resistance (R_{SEI}). The intermediate-frequency semicircle is ascribed to the charge transfer resistance(R_{ct}) in the

electrode/electrolyte interface. The low-frequency tail is associated with the Li^+ ion diffusion process in the solid electrode[13]. So the most obvious difference is observed when comparing the solid electrolyte interface resistance and the charge transfer resistances of pristine and Bi-doped sample. According to the Ziew curve fitting calculation, the R_{SEI} value of the pristine material is 69.94Ω at the 30nd cycle, which is much larger than the 0.03Bi-doped sample, which is 11.85Ω. What's more, the R_{ct} value of the 0.03Bi-doped sample is 93.85Ω, which is also much smaller than the pristine of 278.3Ω. The results suggests that bismuth doping facilitates to suppress increase of the solid electrolyte interface resistance and the charge transfer resistance, thus improve the electrochemical performance.

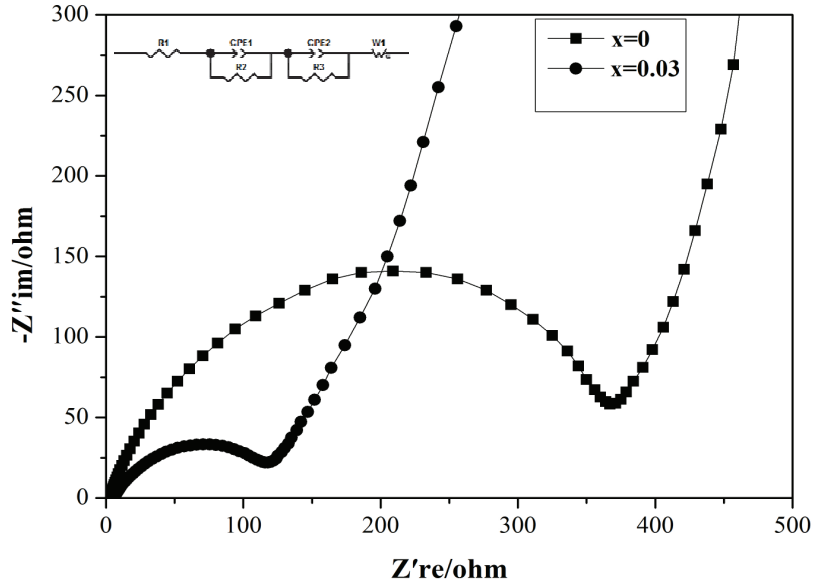


Figure 6.Impedance spectra of the $Li_2Mn_{1-x}Bi_xO_3$(x=0,0.03,0.06) after 30 cycles.

4. Conclusions

Bi^{3+} doped lithium manganese oxides $Li_2Mn_{1-x}Bi_xO_3$ (x=0,0.03,0.06) is successfully synthesized using a facile sol-gel method followed by a fast combustion method and heat treatment. The Bi-doped $Li_2Mn_{1-x}Bi_xO_3$ materials show better cycling performance in comparison with the pristine one at room temperature in spite of a little lower discharge capacity. Even if the current doubles, its capacity has no obvious fading and also exhibits excellent cycle performance. The improved cycling performance could be attributed to bismuth doping, which may stabilize the structure of the Li_2MnO_3.

References

1. A.M.A.Hashem, A.E.Abdel-Ghany, Ae.Eid and J.Trottier, K.Zaghib, A.Mauger, C.M.Julien. *J. Power Sources.* **196**, 8632 (2011).
2. P. He, H. Yu, D. Li, H. Zhou, *J. Mater. Chem.* **22,** 3680 (2012).
3. Y.K. Sun, Z.H. Chen, H.J. Noh, D.J. Lee, H.G. Jung, Y. Ren, S. Wang, C.S. Yoon, S.T.Myung, K. Amine, *Nat. Mater.* **11**, 942 (2012).
4. N.S. Choi, Z.H. Chen, S.A. Freunberger, X.L. Ji, Y.K. Sun, K. Amine, G. Yushin, L.F. Nazar, J. Cho, P.G. Bruce, *Chem. Int. Ed*. **51,** 9994 (2012) .
5. D. Wang, I. Belharouak, G. Zhou, K. Amine, *Adv. Funct. Mater*. **23**, 1070 (2013).
6. Mitsuharu Tabuchi, Yoko Nabeshima, Tomonari Takeuchi, Hiroyuki Kageyama, Junichi Imaizumi, Hideka Shibuya, Junji Akimoto, *J. Power Sources.* **221,** 427 (2013).
7. M.M. Thackeray, S.H. Kang, C.S. Johnson, J.T. Vaughey, R. Benedek, S.A. Hackney, *J. Mater. Chem.* **17,** 3112 (2007).
8. A.D. Robertson, P.G. Bruce,*Chem. Commun*. 2790 (2002) .
9. A.D. Robertson, P.G. Bruce,*Chem. Mater*. **15**, 1984 (2003) .
10. D.Y.W. Yu, K. Yanagida, Y. Kato, H. Nakamura, *J. Electrochem. Soc*. **A417**, 156 (2009).
11. C.L. Tan, H.J. Zhou, W.S. Li, X.H. Hou, D.S. Lu, M.Q. Xu, Q.M. Huang, *J. Power Sources.* **184,** 408 (2008).
12. H. Chiba, T. Atou, Y. Syono, *J. Solid State Chem.* **132**, 139 (1997).
13. Jianming Zheng, Xiaobiao Wu, Yong Yang, *Electrochim. Acta.* **105**, 200 (2013).

Li AND Na STORAGE ON TCNE: A COMPUTATIONAL STUDY

YING Q. CHEN, SERGEI MANZHOS*

Department of Mechanical Engineering, National University of Singapore, Block EA #07-08, 9 Engineering Drive 1, Singapore 117575, Singapore

Li and Na attachment to free tetracyanoethylene (TCNE) molecules is studied using density functional theory. Up to four Li and Na atoms can be stored on one TCNE molecule with binding energies stronger than cohesive energies of the Li and Na metals. TCNE could therefore become an efficient anode material for organic Li and Na ion batteries.

1. Introduction

With the growing use of renewable but intermittent sources of electricity (such as wind and solar) and with the unrelenting advance of all-electric vehicles, demands for energy storage and, specifically, electrochemical storage are growing [1]. Li ion batteries provide today the highest energy density and cycle rate and life among commercial battery technologies [2]. Those, however, still require improvements [3]. Especially for efficient grid storage, to achieve load balancing and possibly price arbitrage, storage on massive scale, allowing for very rapid (within minutes) charge and discharge, is needed [4, 5]. Such rates of charge-discharge are beyond those of present commercial Li ion batteries [3]. Electrode materials of available Li ion batteries also include expensive or poisonous components like Co (30% of global Co production is consumed by Li ion batteries [6]). Na ion batteries, on the other hand, are the most promising candidate technology for bulk electrochemical storage. Lithium deposits are geographically concentrated, and Li might become too expensive to use Li ion batteries on a large scale [7, 8], while sodium is abundant and cheap. It appears that it is more difficult to make (inorganic) electrode materials with suitable electrodynamics and kinetics compared to materials for Li storage [9-12].

Organic electrodes are a way to achieve high rate (high power) and environment-friendly batteries. In recent years, exciting progress in the

* E-mail: mpemanzh@nus.edu.sg

Proceedings of the 14th Asian Conference on Solid State Ionics (ACSSI 2014)
Copyright © 2014 ACSSI 2014 Organizers. All rights reserved.
ISBN: 978-981-09-1137-9
doi:10.3850/978-981-09-1137-9_197

development of organic electrodes has been made [13]. Capacities of up to 900 mAh/g (i.e. competitive with inorganic electrodes) and rates of up to 1000C (unprecedented for inorganic electrodes) have been reported [13]. Moreover, organic electrodes are also promising for post-Li storage [14, 15], which will have to be developed for making massive deployment of electrochemical batteries feasible [16]. Organic electrodes can be made from common feedstock (e.g. biomass) and are therefore sustainable.

To develop practical (commercial) organic batteries, many issues still need to be resolved. Specifically, voltage control is needed to realize organic cathodes and anodes and to maximize power and energy density. To maximize specific capacity, multiple Li or Na atoms need to be stored per formula unit. Search for organic molecules suitable to work as electrodes for Li and Na batteries is still on.

Here, we present a density functional theory (DFT) computational study of the possibilities of Li and Na storage on tetracyanoethylene (TCNE). This is a light molecule which is expected to attach up to 4 Li atoms [17], which would result in a theoretical capacity of about 840 mAh/g. We find that up to four Li and Na atoms can be stored on free TCNE with binding energies stronger than cohesive energies of the Li and Na metals. Therefore, we conclude that TCNE could become an efficient anode material for organic Li and Na ion batteries.

2. Methods

Molecular and electronic structures were optimized with DFT [18] using the SIESTA code [19]. The PBE exchange-correlation functional [20] and a DZP (double-ζ polarized) basis were used. The basis was optimized to reproduce cohesive energies of C, Li and Na. For other elements, the basis was generated with the setting "PAO.EnergyShift = 0.01 Ry". Geometries were optimized until forces on all atoms were below 0.02 eV/Å. A cutoff of 100 Ry was used for the Fourier expansion of the density, and grid cell sampling was used to minimize the eggbox effect. An electronic temperature of 500 K was used to speed up the convergence. Spin polarization was used. A ~15x17 x20 Å supercell was used. Charge transfer between Li/Na atoms and TCNE was analyzed using Voronoi charges as well as charge density difference maps.

The binding energy (E_b) per Li/Na atom was computed as

$$E_b=(E_{nX/TCNE}-E_{TCNE}-nE_X)/n, \quad (1)$$

where $E_{nX/TCNE}$ is the total energy of n X atoms attached to TCNE, and X = Li/Na; E_{TCNE} is the total energy of a stand-alone TCNE molecule, and E_X is the total energy of a X atom in a vacuum box (of the same size as the supercell). The

binding energies were corrected for the BSSE (basis set superposition error) by using a counterpoise correction [21].

We also computed binding energies including the vdW correction by Grimme [22] (DFT-D) with parameters taken from Ref. [22]. While GGA DFT is known to underestimate vdW bonding, DFT-D, as a semi-empirical approach, makes the calculation non- ab initio and may overestimate vdW bonding. We therefore provide numbers computed by both DFT and DFT-D for Li/Na-TCNE complexes to show that both approaches lead to similar conclusions. The same amount of BSSE correction as in DFT was used for DFT-D calculations.

Bond formation between Li/Na atoms and TCNE was analyzed using charge density difference which was computed as

$$\Delta\rho = \rho_{nX/TCNE} - \rho_{TCNE} - \rho_{nX}, \quad (2)$$

where all charge densities ρ are computed at the atomic positions of *n*X/*TCNE* comlexes.

3. Results

For all systems, we studied all combinations of adsorption sites of one to four Li/Na atoms. Only stable non-equivalent configurations are showed below. Figure 1 shows Li/Na complexes with a TCNE molecule and lists corresponding binding energies. The computed cohesive energy of Li metal is E_{coh}^{Li} = -1.67 (-1.78) eV (here and below, the numbers in parentheses are for DFT-D) and E_{coh}^{Na} = -1.14 (-1.31) eV (Non-BSSE corrected values are used for E_{coh}, as the basis sets of Na and Li were tuned to reproduce their respective E_{coh}). Therefore an isolated TCNE molecule can operate as an anode with "voltages" ($V = E_{coh} - E_b$) in the range of 0.29-1.58 (0.23-1.66) V for Li storage and 0.37-1.60 (0.36-1.60) V for Na storage.

In Figure 2, we plot the expected voltage profiles for Li/Na storage on the TCNE molecule. It can be seen that the inclusion of the Grimme potential changes the voltage by up to 0.3 V but does not change the curve qualitatively, so that both of DFT and DFT-D predict feasibility of Li/Na storage. Significantly, the computed voltage, at least for up to 2 Li/Na atoms per TCNE molecule, is higher than the reduction potential of common liquid organic electrolytes, such as $LiPF_6$ in EC:DEC/DMC at around 1.3 V [23] and $NaClO_4$ in EC:DMC at around 1.2 V [24]. This anode could therefore avoid the formation of the SEI and associated kinetic hindrance and loss of Li/Na.

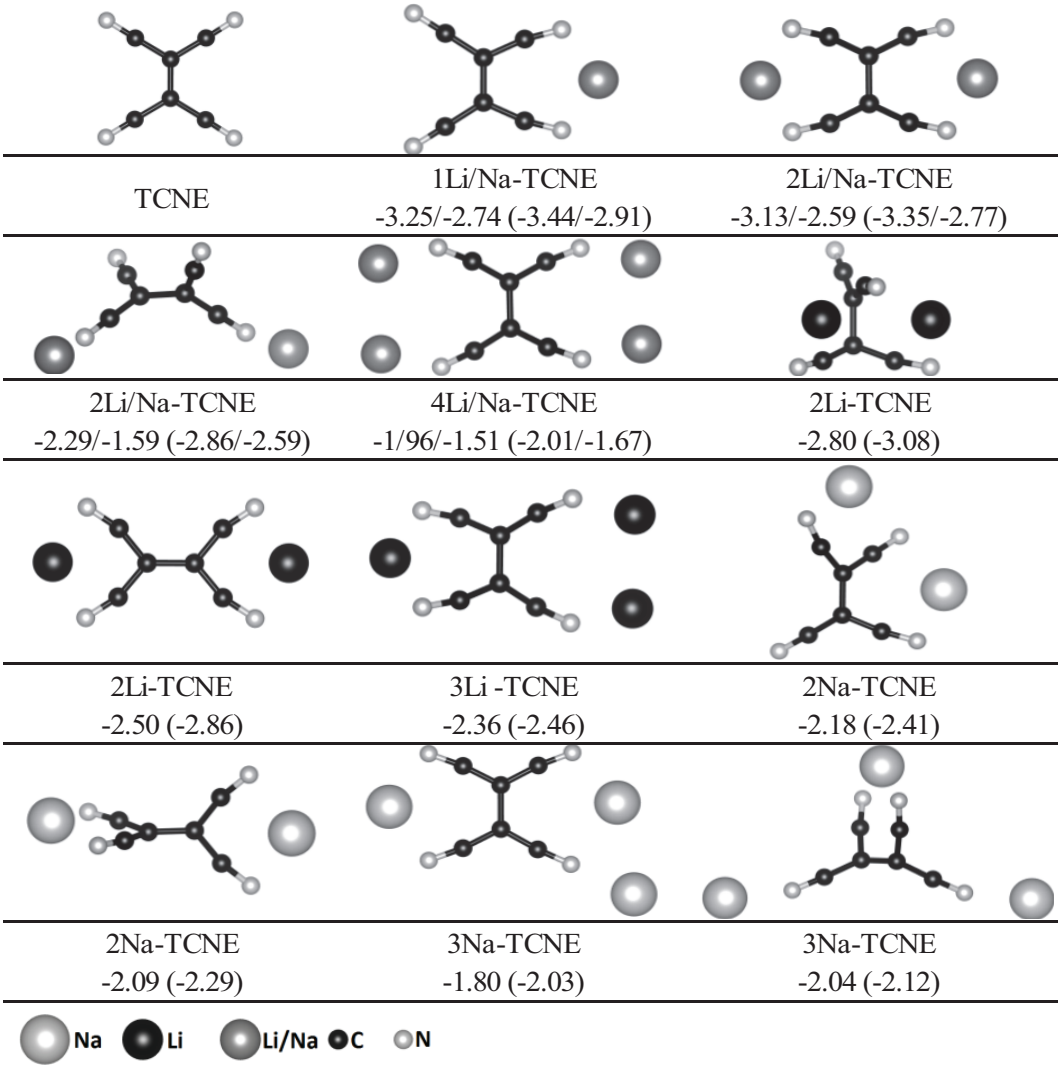


Figure 1. Complexes of 1-4 Li/Na atoms with a free TCNE molecule and corresponding binding energies (per Li/Na atom) E_b, in eV. Here and elsewhere, DFT-D values are given in parentheses. Configurations identical for Li and Na are shown with grey atoms labelled "Li/Na".

Also in Figure 2 (right scale) shown is the average charge donation per Li or Na atom to the molecule, based on Voronoi charges. The charge donation is significant, reaching about half an electron in 1Li/Na-TCNE complexes. It, however, becomes progressively smaller as the number of attached Li/Na atoms increases. This decrease in charge donation also tracks well the dependence of

E_b or voltage on the number of attached atoms. Interestingly, Na donates more charge to TCNE than Li.

Figure 3 shows an example of a charge density difference map $\Delta\rho$ (Eq. 2), where the formation of Li/Na-TCNE bonds can be identified as accumulation of charge density between Li/Na and N atoms. In some configurations, Li or Na atoms are near each other. The analysis of $\Delta\rho$ allows one to identify bond formation also between Li/Na atoms.

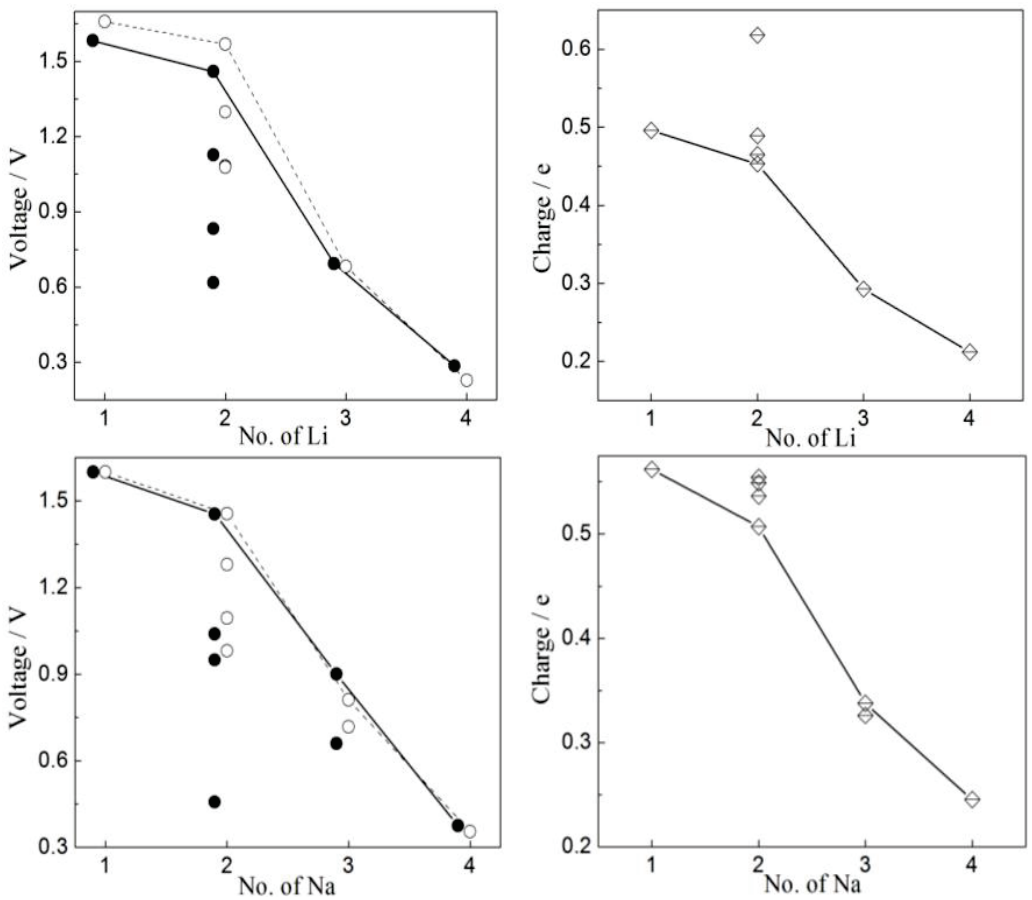


Figure 2. Left: DFT (filled circles and solid lines) and DFT-D (empty circles and dashed lines) values for voltages (E_b-$E_{coh}^{Li/Na}$) of different Li/Na-TCNE complexes. Right: average charge donation (per Li/Na atom) in different Li/Na-TCNE complexes. The lines connect lowest-energy configurations. Top panels are for Li and bottom for Na.

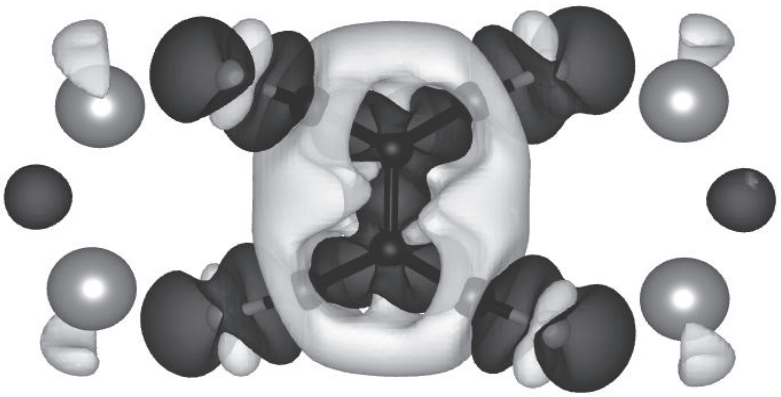


Figure 3. Example of charge density difference (Eq. 2) for 4Li/Na-TCNE (cf. the image in Figure 1). Black color corresponds to density accumulation, grey to depletion. Atom shading scheme is same with Figure 1.

4. Conclusions

We studied computationally Li/Na storage at TCNE molecules as prospective organic anodes suitable for Li as well as Na ion batteries. We used both GGA DFT and DFT-D and both methods lead to similar conclusions. A TCNE molecule can store up to 4 Li/Na atoms. The Li/Na-TCNE binding energy decreases with the number of attached atoms increasing, and this correlates with the average amount or charge donation to the molecule. The voltage of such an anode molecule is predicted to be 0.29-1.58 (0.23-1.66) V for Li storage and 0.37-1.60 (0.36-1.60) V for Na storage with DFT (DFT-D), i.e. SEI formation could be avoided. This indicates that TCNE could become an efficient anode material for organic Li and Na ion batteries, but further studies are required of its performance in adsorbed or solid [17] state.

Acknowledgments

This work was supported by Tier 1 AcRF grant R-265-000-430-133 by the Ministry of Education of Singapore.

References

1. T. Kousksou, P. Bruel, A. Jamil, T. El Rhafiki and Y. Zeraouli, *Sol. Energy Mater. Sol. Cells* **120, Part A**, 59 (2014).
2. M.M. Thackeray, C. Wolverton and E.D. Isaacs, *Energy Environ. Sci.* **5**, 7854 (2012).

3. J.B. Goodenough, *Energy Environ. Sci.* **7**, 14 (2014).
4. E. Barbour, I.A.G. Wilson, I.G. Bryden, P.G. McGregor, P.A. Mulheran and P.J. Hall, *Energy Environ. Sci.* **5**, 5425 (2012).
5. C.J. Barnhart, M. Dale, A.R. Brandt and S.M. Benson, *Energy Environ. Sci.* **6**, 2804 (2013).
6. C. Lupi and M. Pasquali, *Miner. Eng.* **16**, 537 (2003).
7. V. Palomares, P. Serras, I. Villaluenga, K.B. Hueso, J. Carretero-Gonzalez and T. Rojo, *Energy Environ. Sci.* **5**, 5884 (2012).
8. J.M. Tarascon, *Nature Chem.* **2**, 510 (2010).
9. O.I. Malyi, T.L. Tan and S. Manzhos, *Appl. Phys. Express* **6** (2013).
10. O.I. Malyi, T.L. Tan and S. Manzhos, *J. Power Sources* **233**, 341 (2013).
11. O. Malyi, V.V. Kulish, T.L. Tan and S. Manzhos, *Nano Energy* **2**, 1149 (2013).
12. F. Legrain, O.I. Malyi and S. Manzhos, *Solid State Ionics* **253**, 157 (2013).
13. Y.L. Liang, Z.L. Tao and J. Chen, *Adv. Energy Mater.* **2**, 742 (2012).
14. A. Abouimrane, W. Weng, H. Eltayeb, Y. Cui, J. Niklas, O. Poluektov and K. Amine, *Energy Environ. Sci.* **5**, 9632 (2012).
15. Y. NuLi, Z. Guo, H. Liu and J. Yang, *Electrochem. Commun.* **9**, 1913 (2007).
16. A.K. Shukla and T.P. Kumar, *J. Phys. Chem. Lett.* **4**, 551 (2013).
17. J.H. Her, P.W. Stephens, R.A. Davidson, K.S. Min, J.D. Bagnato, K. van Schooten, C. Boehme and J.S. Miller, *J. Am. Chem. Soc.* **135**, 18060 (2013).
18. W. Kohn and L.J. Sham, *Phys. Rev.* **140**, A1133 (1965).
19. M.S. José, A. Emilio, D.G. Julian, G. Alberto, J. Javier, O. Pablo and S.-P. Daniel, *J. Phys.: Condens. Matter* **14**, 2745 (2002).
20. J.P. Perdew, K. Burke and M. Ernzerhof, *Phys. Rev. Lett.* **77**, 3865 (1996).
21. S.F. Boys and F. Bernardi, *Mol. Phys.* **100**, 65 (2002).
22. S. Grimme, *J. Comput. Chem.* **27**, 1787 (2006).
23. J.B. Goodenough and Y. Kim, *Chem. Mater.* **22**, 587 (2009).
24. S. Komaba, W. Murata, T. Ishikawa, N. Yabuuchi, T. Ozeki, T. Nakayama, A. Ogata, K. Gotoh and K. Fujiwara, *Adv. Funct. Mater.* **21**, 3859 (2011).

EFFECTS OF MESOPOROUS Co_3O_4 ON ELECTROCHEMICAL PROPERTIES OF LITHIUM/SULFUR BATTERY*

GUOQIANG MA, ZHAOYIN WEN, JUN JIN, PENG PENG, QINGSONG WANG

CAS Key Laboratory of Materials for Energy Conversion, Shanghai Institute of Ceramics, Chinese Academy of Sciences, Shanghai 200050, P.R. China

Mesoporous Co_3O_4 has been prepared using mesoporous silica KIT-6 as the template and added into sulfur cathode to enhance the electrochemical performance of Li-S battery. The adsoption effect of mesoporous Co_3O_4 to sulfur particles is observed by SEM image. FTIR shows that there is Co-S bond generated during charge/discharge process, improving the adsorption effect between mesoporous Co_3O_4 and lithium polysulfides, which can further enhance the cycling performance of Li-S battery. Particularly, the initial discharge capacity of the cell with 5wt% mesoporous Co_3O_4 reaches at 692mAh.g^{-1} after 80 cycles, which is much higher than the cell without mesoporous Co_3O_4 in the cathode (243mAh.g^{-1}). Furthermore, the average coulombic efficiency reaches 99.7% after 30 cycles, and the impedance values of the Li-S battery are no longer improved rapidly during charge/discharge process.

1. Introduction

The rapid growth of portable electronic devices such as notebook computers, camcorders, and cellular phones have required the development of rechargeable Lithium ion battery with higher energy density and capacity[1-3]. The cathode material is one of the major factors to improve the energy density and capacity. Sulfur is an attractive cathode due to its high theoretical specific capacity of 1672mAh/g and theoretical energy density of 2600Wh/Kg[4-6], in combination with the natural abundance, low cost and environmental friendliness of sulfur, Li-S battery becomes a promising candidate for the next generation power source.

Although Li-S battery has many advantages, low active material utilization rate, poor cycle life and low coulombic efficiency limit its practical applications [4,

* This work was financially supported by NSFC Project No.51373195 No.51372262 and No. 51272267; research projects from the Science and Technology Commission of Shanghai Municipality No. 08DZ2210900.

Proceedings of the 14th Asian Conference on Solid State Ionics (ACSSI 2014)
Copyright © 2014 ACSSI 2014 Organizers. All rights reserved.
ISBN: 978-981-09-1137-9
doi:10.3850/978-981-09-1137-9_120

7]. The insulating sulfur decreases the utilization rate of active material, and the high solubility of lithium polysulfides (Li_2S_x) generated during the electrochemical-reduction reaction process will dissolve in the liquid electrolyte, then they migrate in the liquid electrolyte and pass through the separator and directly react with metallic-lithium anode, which is known as shuttle mechanism and has been considered as the major reason for capacity fading and low coulombic efficiency of Li-S battery. Moreover, because of the dissolution of Li_2S_x in the electrolyte, the final product of the insulating Li_2S will deposit and gradually aggregate on the cathode's surface, resulting in a poor rate performance and cycle stability.

Therefore, the dissolution and migration of Li_2S_x should be overcome to enhance the electrochemical performance of Li-S battery. Various kinds of approaches have been studied, such as the modification of electrolyte [8], the application of mesoporous carbon[9], carbon nanotubes[10], and GO[11] as the matrix of sulfur, and the additives to the sulfur cathode. In the previous reports, vanadium oxide[12], silicates[13], nano-Al_2O_3[14], $Mg_{0.6}Ni_{0.4}O$[15], $Mg_{0.8}Cu_{0.2}O$[16] and mesoporous titania[17] have been added into sulfur cathode to adsorb Li_2S_x. It seems that the additives with large surface or mesopores such as nanosized Al_2O_3, mesoporous silica and mesoporous titania had better effects on the performance of Li-S battery. Mesoporous Co_3O_4 has been widely studied as the anode of lithium battery and catalyst, ceramic pigment. However, to the best of our knowledge, there are few reports on mesoporous Co_3O_4 used as the additive of sulfur cathode.

Herein, two kinds of mesoporous Co_3O_4 were prepared and added into the sulfur cathode in order to enhance the electrochemical performance of Li-S battery. The high surface area and porous structure are beneficial to the adsorption of Li_2S_x, and offer high electrochemical activity with synergistic effect to enhance the battery performance.

2. Experimental

2.1 Preparation of mesoporous Co_3O_4

Cubic ordered mesoporous silica (KIT-6) was synthesized according to the literature with some modification[18]. The resulting mesoporous silica templates aged at 130°C and 400°C were denoted as KIT-6-130 and KIT-6-40, respectively. Synthesis of mesoporous Co_3O_4 was performed by the "bisolvent" impregnation method reported previously by Davidson[19]. Mesoporous Co_3O_4

prepared by using KIT-6-130 and KIT-6-40 was denoted as $Co_3O_4^{-1}$ and $Co_3O_4^{-2}$, respectively.

2.2 Preparation of the sulfur cathode and coin-type cell

Sulfur cathode slurry was prepared by mixing with 55% elemental sulfur, 30wt% acetylene black (AB), 5wt% mesoporous Co_3O_4 as additive through ball milling, and then 10wt% poly(vinylidene difluoride) (PVDF) binder dissolved in N-methyl-2-pyrrolidene (NMP) solution to the mixture. For the comparison study, sulfur cathode slurry without mesoporous Co_3O_4 additives (55wt% sulfur, 35wt% AB, and 10wt% PVDF in NMP solution) was also prepared in the same way. The slurry of the cathode was cast onto aluminum foil substrate. After the organic solvent evaporated, the coated electrodes were cut into circles with 14 mm in diameter and then dried at 60°C under vacuum for 12 h. CR2025 type coin cells were assembled in a glove box with oxygen and water contents less than 1 ppm. A solution of 1 M LiTFSI dissolved in DOL/DME (v/v, 1/1) was employed as the electrolyte. The cells contained Celgard 2400 as the separator and lithium foils as the counter and reference electrodes.

2.3 Characterization and electrochemical measurement

FTIR spectra were carried out on the Thermo Nicolet 7000-C Fourier Transform Spectrometer with $\pm 2cm^{-1}$ resolution between 4000 and $400cm^{-1}$ using KBr disk method. SEM images were measured by field emission scanning electron microscope (FESEM JSM-6700) and scanning electron microscope (Hitachi S-3400N). Transmission electron microscopy (TEM) images were measured on a JEOL JEM-2010 transmission electron microscope.

AC impedance measurement was carried out by Frequency Response Analyzer (FRA) technique on an Autolab Electrochemical Workstation over the frequency range from 0.01 Hz to 10 MHz with the amplitude of 10 mV. Cyclic-voltammetry (CV) measurements were also conducted using the Autolab Electrochemical Workstation. The galvanostatic charge and discharge tests were conducted on a LAND CT2001A battery test system in a voltage range of 1.3-3.0 V (vs. Li/Li+) at a current density of 0.1 mA cm^{-2}.

3. Results and discussion

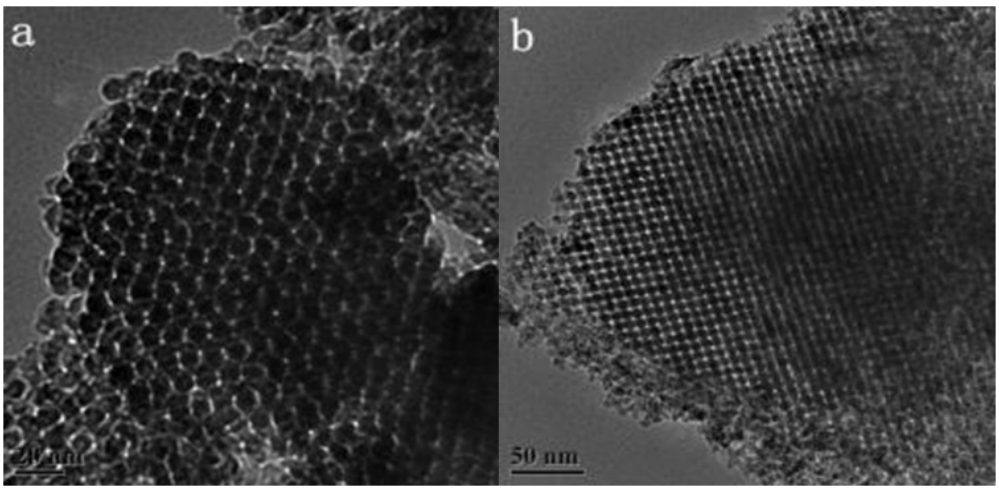


Fig.1. TEM images of mesoporous $Co_3O_4^{-1}$ (a) and $Co_3O_4^{-2}$ (b).

The TEM images of mesoporous $Co_3O_4^{-1}$ and $Co_3O_4^{-2}$ are shown in Fig.1. Since the mesoporous Co_3O_4 is exactly an inverse replica of KIT-6, which consists of 3D cubic (Ia3d symmetry) mesoporous tubes, it exhibits a long-range-ordered mesostructure in the whole domain. Owing to the difference between the templates used for each syntheses, the $Co_3O_4^{-1}$ displays a very narrow pore size distribution centered at 3.89nm with a very high surface area ($105 m^2/g$), while $Co_3O_4^{-2}$ has a significantly higher specific surface area (69.1 m^2/g) with much larger pore size (5.26nm)[18].

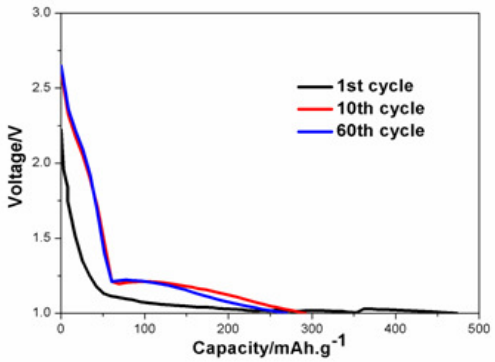


Fig.2. The discharge profiles of pure mesoporous Co_3O_4 at a current density of 0.1 mA cm^{-2}

The charge/discharge profiles of the cells for pure mesoporous Co_3O_4 are shown in Fig.2. The plateau corresponding to the discharging of Co_3O_4 is less than 1.3V [20, 21], therefore, to separate the contribution of Co_3O_4 and sulfur to

the overall capacity, the discharge cut-off voltage of Li-S battery is improved to 1.3V.

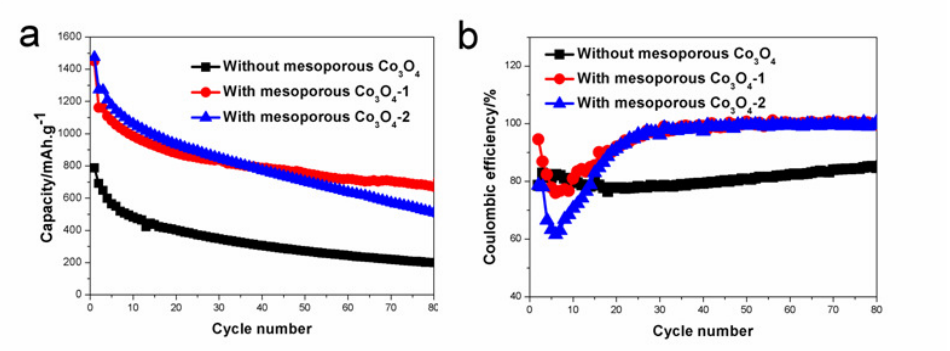


Fig.3 Cycle performance (a) Coulombic efficiency (b) of the cell with and without mesoporous Co_3O_4

Fig.3 shows the cycle performance and coulombic efficiency of the cells with and without mesoporous Co_3O_4. The cell with mesoporous Co_3O_4 shows much higher initial discharge specific capacity 1448 mAh/g with 86.4% utilization rate of sulfur, and between the 30th and 80th cycles, the capacity retaining rate of the cell with Co_3O_4-1 reaches 80.7%, which is higher than that of the cell without mesoporous Co_3O_4 (56%). Otherwise, the average coulombic efficiency with Co_3O_4-1 reaches 99.7% after 30 cycles, which are much higher than that of the cell without mesoporous Co_3O_4. To figure out the reasons for the enhancement of the cell performance with the addition of mesoporous Co_3O_4, different tests are carried out as follows.

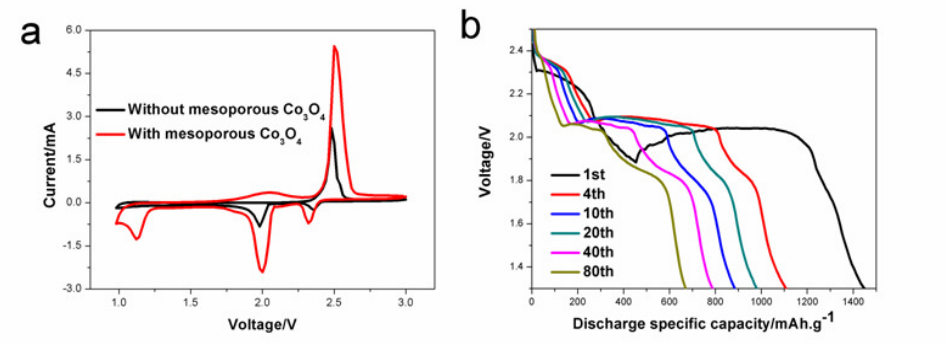


Fig.4. (a) CV curves of the cells with and without mesoporous Co_3O_4-1 at a scan rate of 0.5mV/s, (b) The charge/discharge profiles of Li-S battery with mesoporous Co_3O_4 at different cycles.

Firstly, cyclic voltammograms of the cells with and without mesoporous Co_3O_4 are tested as shown in Fig.4 (a). The cell with mesoporous Co_3O_4 shows three reduction peaks respectively at 2.3V, 2.0V and 1.1V. The first two peaks are

considered corresponding to reduction of sulfur to Li_2S_x and Li_2S_2/Li_2S, respectively, and the third peak corresponding to the reduction of Co_3O_4. In addition, the cell with mesoporous Co_3O_4 shows a larger reaction area than that of the cell without mesoporous Co_3O_4, meaning a higher capacity. The charge/discharge profiles of Li-S battery with mesoporous $Co_3O_4^{-1}$ are shown in Fig.4b. Similar to the other Li-S battery, there are two voltage plateaux of the initial discharging profiles at 2.3V and 2.1V. However, the voltage plateaux at 2.3V and 2.1V become shorter and shorter with circulation, with a sloping plateau between 1.7V and 1.9V appeared at the 4th cycle which becomes more obvious in the following cycles. In previous references [22, 23], similar plateaus were also observed and were attributed to the reduction of CoS_x.

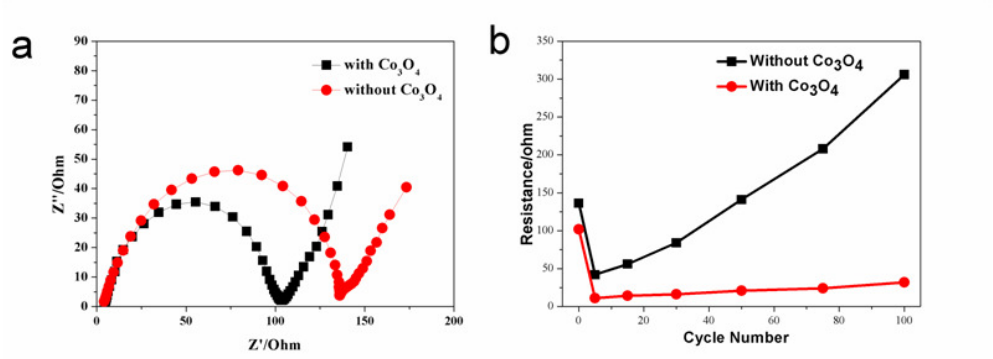


Fig.5 (a) Electrochemical impedance spectroscopy plots of Li-S cells with and without mesoporous CO_3O_4 (b) the AC impedance of the cell with and without mesoporous Co_3O_4 changes at different cycles.

Electrochemical impedance spectroscopy (EIS) studies are performed on the full cells at fully charged state, and the Nyquist plots are shown in Fig.5 (a). The very high frequency region corresponds to the electrolyte resistance, which is similar to different cathodes. The semi-circle in the high frequency domain corresponding to the charge transfer resistance and interfacial resistance is the most noticeable difference among different cathodes. As seen, the resistance decreased evidently with the addition of mesoporous Co_3O_4.

At the same time, the resistance at different cycles of sulfur cathodes with and without mesoporous Co_3O_4 was shown in Fig.5b. The two sulfur cathodes show the similar trend with the resistance decreases as the 5th cycles to a minimum value (41.9Ω and 11Ω, respectively) [24]. Then the resistance increases in the following 100 cycles. It has been shown in previous reports that the redistribution of insulating sulfur and Li_2S/Li_2S_2 during the charge/discharge process results in a poor conductivity. However, as shown in Fig.5 (b), the resistance of the cells with mesoporous Co_3O_4 increases much more slowly than those of the sulfur cathodes without mesoporous Co_3O_4. After 100 cycles, the

resistance of cell without mesoporous Co_3O_4 reaches 306Ω, which is much higher than that of the cell with mesoporous Co_3O_4 (32Ω).

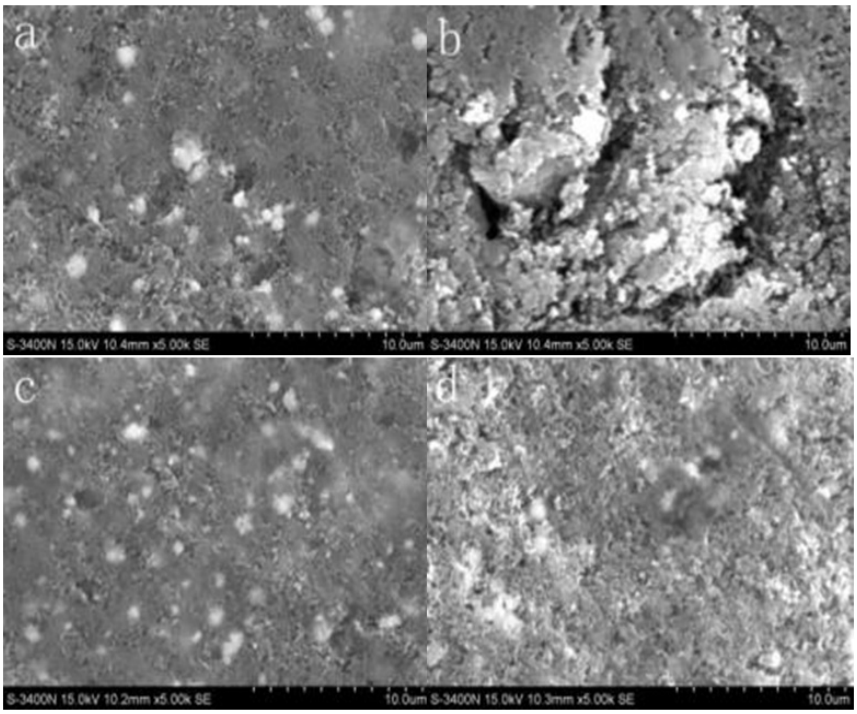


Fig.6. SEM morphologies of sulfur electrodes (a) without mesoporous Co_3O_4 before cycling (b) without mesoporous Co_3O_4 after 20 cycles (c) with mesoporous Co_3O_4 before cycling (d) with mesoporous Co_3O_4 after 20 cycles.

Morphology changes of cathode before and after 20 cycles are observed by SEM, and the cathode materials are collected after being fully charged to 3V. As shown in Fig.6 (a) and (c), the initial cathodes with and without mesoporous Co_3O_4 are similar. However, after 20 cycles, the morphology of the cathode without mesoporous Co_3O_x changed greatly. Serious agglomeration in the whole electrode was observed with big vacant formed by the loss of active material, suggesting a serious shuttle mechanism in the charge/discharge process. When mesoporous Co_3O_4 is added, as shown in Fig.6 (d), the sulfur cathode shows small pores and relatively dense surface due to Li_2S_x absorbed by mesoporous Co_3O_4, which inhibits the dissolution of Li_2S_x into the liquid electrolyte, then the active material loss is suppressed. As expected, the small pores in the cathode is beneficial to the contact between cathode and electrolyte, which will be helpful to the improvement of the utilization rate of active materials.

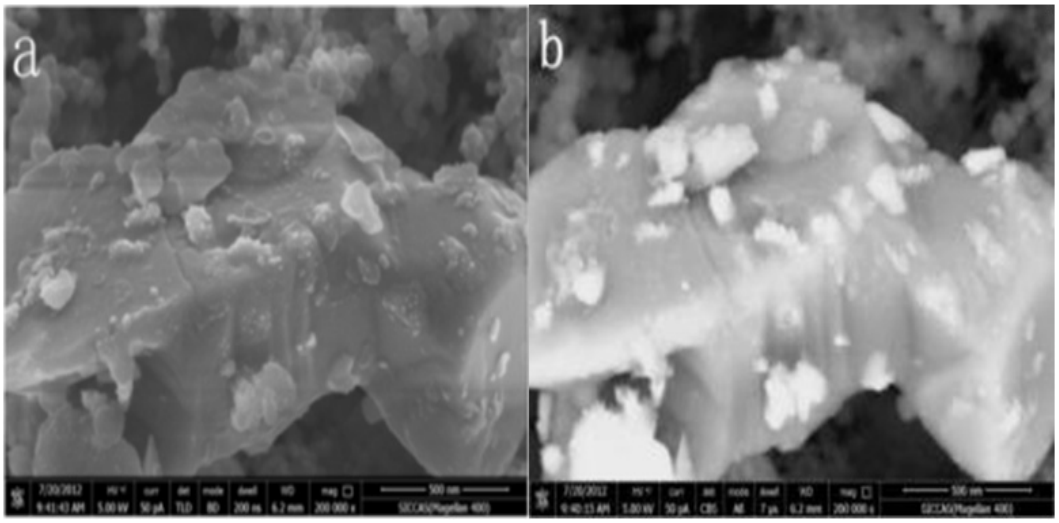


Fig.7. SEM images of the sulfur, AB, and mesoporous Co_3O_4 composites, the secondary electron image (a) and the back scattered image (b).

Afterwards, to observe the morphology of S, AB and mesoporous Co_3O_4 composite, SEM is used and the images are shown in Fig.7. The big particle in the images indicates sulfur in the composite, while the small and lighter particles on the surface of sulfur particle in Fig.7b are correspond to mesoporous Co_3O_4. Since the content of Co_3O_4 in the composite is only 5%, the SEM morphology of the composite demonstrate nonuniformity of the components.

It is reasonable to suggest weak adsorption between mesoporous Co_3O_4 and sulfur or Li_2S_x which makes it easy to explain the EIS change trends of the cell and the morphology changes of the cathode. As known, the Co_3O_4 conducts badly, however, the nano-sized mesoporous Co_3O_4 is adsorbed easily on the surface of sulfur, which improves the dispersion of non-conductive sulfur among AB, which could shorten the length of electron transport and decrease the charge transfer resistance. The mesoporous Co_3O_4 can absorb Li_2S_x and prohibit them to be dissolved in the liquid electrolyte, then, the redistribution of S and lithium sulfide in the cathode will be suppressed, inhibiting the aggregation of insulating sulfur or Li_2S/Li_2S_2 on the surface of the electrodes, so the charge transport resistances increase slowly. The vacant area is generated by the loss of active material, which is the indication of shuttle phenomenon. With the addition of mesoporous Co_3O_4, the shuttle phenomenon is suppressed owing to the adsorption effect of Li_2S_x by mesoporous Co_3O_4.

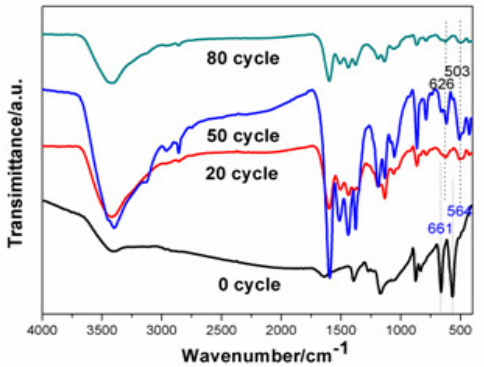


Fig.8. FTIR spectra of the sulfur cathode with mesoporous Co_3O_4 before and after different cycles.

Furthermore, FTIR spectra of sulfur cathode with mesoporous Co_3O_4 before and after different cycles are tested as shown in Fig.8. The characteristic peaks ($564cm^{-1}$, $661cm^{-1}$) can be ascribed to the existence of Co-O band in the mesoporous Co_3O_4 in the sulfur cathode before cycling[18]. However, after cycling, the characteristic peaks corresponding to Co-O bond disappear, replaced by the characteristic peaks ($503cm^{-1}$, $626cm^{-1}$) corresponding to Co-S band, indicating reactions between Co element and S element[25] and the generation of CoS_x. The discharge sloping plateau between 1.7V and 1.9V in Fig.4b can be ascribed to the generation of CoS_x. Since no shuttle effect is proposed for CoS_x as cathode active material, the electrochemical performance, especially the coulombic efficiency can be enhanced with the addition of CoS_x.

4. Conclusions

In summary, with the addition of mesoporous Co_3O_4, the electrochemical performance of Li-S battery is enhanced. The Li-S battery with mesoporous Co_3O_4 displays an initial discharge capacity of 1475mAh/g and maintains a discharge capacity above 692mAh/g after 80 cycles. The average coulombic efficiency reaches 99.7% at the 30th cycle. The existence of mesoporous Co_3O_4 effectively inhibits the loss of Li_2S_x into the liquid electrolyte. Besides, the generation of CoS_x in the charge/discharge process further enhances the electrochemical performance of the cell.

Acknowledgements

This work was financially supported by NSFC Project No.51373195, No. 51272267 and No.51372262; research projects from the Science and Technology Commission of Shanghai Municipality No. 08DZ2210900.

References

[1] Dunn B, Kamath H, Tarascon J M. Science, **334(6058)**, 928 (2011).
[2] Bruce P G, Freunberger S A, Hardwick L J, J. M. Tarascon. Nature Material, **11(1)**, 19 (2012).
[3] Y. Yang, G. Zheng, Y. Cui, Chem Soc Rev, **42**, 3018 (2013).
[4] Evers S, Nazar L F. [J]. *Accounts Chem Res*, **46(5)**, 1135 (2012).
[5] S. E. Cheon, K.-S. Ko, J.-H. Cho, S.-W. Kim, E.-Y. Chin, H.-T. Kim, Journal of the Electrochemical Society, **150**, A796 (2003).
[6] Yin, Y. X., Xin, S., Guo, Y. G., Wan, L. J. Angew. Chem. Int. Ed. **52(50)** , 13186 (2013).
[7] Manthiram, A., Fu, Y., Su, Y. S. *Accounts Chem Res*, **46(5)**, 1125 (2012).
[8] Liang, X., Wen, Z., Liu, Y., Wu, M., Jin, J., Zhang, H., & Wu, X.. *Journal of Power Sources*, **196** (22), 9839 (2011).
[9] S. R. Chen, Y. P. Zhai, G. L. Xu, Y. X. Jiang, D. Y. Zhao, J. T. Li, L. Huang, S. G. Sun, Electrochim Acta, **56**, 9549 (2011).
[10] W. Ahn, K.B. Kim, K.N. Jung, K.H. Shin, C.S. Jin, J Power Sources, **202**, 394 (2012).
[11] L. Yin, J. Wang, F. Lin, J. Yang, Y. Nuli, Energ Environ Sci, **5**, 6966 (2012).
[12] Y. Zhang, L. Wang, A. Zhang, Y. Song, X. Li, H. Feng, X. Wu, P. Du, Solid State Ionics, **181**, 835 (2010).
[13] K.T. Lee, R. Black, T. Yim, X. Ji, L.F. Nazar, Adv Energy Mater, **2**, 1490 (2012).
[14] Y.J. Choi, B.S. Jung, D.J. Lee, J.H. Jeong, K.W. Kim, H.J. Ahn, K.K. Cho, H.B. Gu, Phys Scripta, **T129**, 62 (2007).
[15] M.S. Song, S.C. Han, H.S. Kim, J.H. Kim, K.T. Kim, Y.M. Kang, H.J. Ahn, S.X. Dou, J.Y. Lee, Journal of the Electrochemical Society, **151**, A791 (2004).
[16] Y. Zhang, X. Wu, H. Feng, L. Wang, A. Zhang, T. Xia, H. Dong, Int J Hydrogen Energ, **34**, 1556 (2009).
[17] S. Evers, T. Yim, L.F. Nazar, The Journal of Physical Chemistry C, **116**, 19653 (2012).
[18] S. Sun, Q. Gao, H. Wang, J. Zhu, H. Guo, Applied Catalysis B: Environmental, **97** ,284 (2010).
[19] M. Imperor-Clerc, D. Bazin, M.D. Appay, P. Beaunier, A. Davidson, Chemistry of Materials, **16**, 1813 (2004).
[20] X. Rui, H. Tan, D. Sim, W. Liu, C. Xu, H.H. Hng, R. Yazami, T.M. Lim, Q. Yan, J Power Sources, **222**, 97 (2013).
[21] N. Jayaprakash, W.D. Jones, S.S. Moganty, L.A. Archer, J Power Sources, **200**, 53 (2012).
[22] Luo, W., Xie, Y., Wu, C., & Zheng, F.. *Nanotechnology*, ***19*(7)**, 075602 (2008).
[23] Y. Wang, J. Wu, Y. Tang, X. Lü, C. Yang, M. Qin, F. Huang, X. Li, X. Zhang, Acs Appl Mater Inter, **4**, 4246 (2012).
[24] G.-C. Li, G.-R. Li, S.-H. Ye, X.-P. Gao, Adv Energy Mater, **2**, 1238 (2012).
[25] X.D. Daxi Wang, Shujun Wang, JOURNAL OF MOLECULAR SCIENCE, **6**, 129 (2007).

PREPARATION AND ELECTROCHEMICAL STUDIES OF MnO_2 FOR LI-ION AND LI-AIR BATTERIES

Y.H. LEE, M.V. REDDY, S. ADAMS*

Department of Materials Science and Engineering, National University of Singapore, Singapore117546

Mn-based oxides have various advantages like less toxicity and low cost and they can also be used as the electrode material for both Li-ion and Li-air batteries. While α-MnO_2 is usually prepared by a hydrothermal method, here we attempted to prepare it by a one pot molten salt method and studied the effect of different polymers Polyvinylpyrrolidone (PVP), and Polyvinyl Alcohol (PVA). Rod type morphology was noted using SEM, and XRD patterns showed lattice parameters of a = 9.85Å, c = 2.87Å. The BET surface areas are in range, 31.9 – 15.7 m^2/g for bare and polymer assisted MnO_2 compounds. Electrochemical properties were characterized using galvanostatic cycling (GC) and cyclic voltammetry. Li-cycling studies showed average discharge and charge potentials of 0.47, 1.14 V, respectively vs. Li/Li^+ close to CV redox potentials. Reversible capacity values obtained were in the range 934 – 1050 mAh/g. Preliminary studies on Li-air batteries were studied using GC and impedance spectroscopy.

1. Introduction

In this technologically advanced age, electrical consumer products play a big part in our daily lives. Ranging from mobile phones, laptops to mp3, Lithium-ion batteries (LIBs) are often the most popular choice as the energy supply in these devices[1, 2]. Our concern for environmental issues like global warming and the depletion of fossil fuels have allowed us to seek for solutions that reduce resources usage. As compared to single-use batteries, LIBs are more environmental friendly since they are rechargeable and have long cycle life[2] Other benefits also include no memory effect, high capacity and low self-discharge rate. Although many advantages can be stated for LIBs, there are limitations as well, including fire hazard when overheated and the high cost involved during manufacturing.

* Corresponding author e-mail: mseasn@nus.edu.sg

Proceedings of the 14th Asian Conference on Solid State Ionics (ACSSI 2014)
Copyright © 2014 ACSSI 2014 Organizers. All rights reserved.
ISBN: 978-981-09-1137-9
doi:10.3850/978-981-09-1137-9_156

To improve the performance and capability of LIBs, a variety of metal oxides have been researched on as the anode material of the batteries[3], including tin dioxide (SnO_2)[4], titanium dioxide (TiO_2)[5], nickel oxides, and cobalt oxides etc.[3]., each has their own benefits and limitations. Among these, the abundance on Earth, low cost and toxicity of manganese dioxide (MnO_2) gives it an advantage over the other metal oxides. Hence, this paper will focus on the study of MnO_2 as the anode material for both LIBs and Li-air batteries[3, 6-8].

According to various literature reviews, there are many different ways to synthesize MnO_2. Su, et al.[9] synthesized α- MnO_2 nanorods through a hydrothermal method, by heating the solution of $KMnO_4$ and concentrated HCl at 140^{o}C for 12 hours in an autoclave. Hashemzadeh et al.[10] used sol-gel method instead, where manganese acetate and acid were first dissolved in distilled water and then heated to 80^{o}C for a few hours to obtain wet gel which was later dried. Calcination takes place before acid treatment to get the resulting MnO_2. Hydrothermal synthesis is often the choice commercially for large scale production of nanostructured materials[11]. MnO_2 /carbon composites by expensive Chemical Vapour Deposition (CVD) method[12]. However, high cost of the equipment needed in hydrothermal synthesis/CVD technique and the long heating time often complicate the whole process. In this research, one-pot molten salt method will be used for MnO_2 synthesis as it is a simpler and lower cost alternative to produce metal oxides[8].

During the synthesis process, the addition of sacrificial polymers serves as a template to guide the growth of metal oxide in order to have a better control of size and shapes of the metal oxides nanoparticles [13]. There have also been other structure directing agents like the mesoporous silica and other surfactants under research, but polymers are commonly used [14, 15]. The use of polyvinylpyrrolidone (PVP) as well as polyvinyl alcohol (PVA) as structure directing agents will be featured because they are water soluble polymers, which can be dissolved in water and easily filtered off from the MnO_2 obtained.

The main objectives of this experiment are: 1. To prepare α-MnO_2 from one-pot molten salt method (MSM) instead of the conventional hydrothermal method, since MSM is an easier method to prepare various metal oxides. 2. To study and understand the effect of different polymers on the morphology, crystal structure and also the electrochemical properties of MnO_2 for Li-ion batteries.

2. Experimental Method

2.1. *Preparation of MnO_2*

To obtain MnO_2 powders by MSM, three different samples are prepared. Sample 1 mentioned as a control, sample 2 has PVP added in it while sample 3 has PVA added. 2 grams of PVA and PVP are used respectively, with the ratio of manganese containing salt to molten salts as 1:10. The molten salts $0.5MLiNO_3$ and $0.5M$ KNO_3 are put in all three alumina crucibles together with $MnSO_4.H_2O$, with the polymers added in into their respectively samples as stated before. They are mixed thoroughly before placing them into the furnace at 310^oC for 3 hours, in air. After cooling, the resulting products are washed with distilled water to remove excess salts, then filtered to get rid of the polymers and any other excess Li and K-salts present. MnO_2 powders are obtained after drying the residues.

2.2. *Fabrication of electrodes for batteries*

MnO_2, polyvinylidene fluoride (PVDF) and Super P carbon are mixed together in the ratio of 70:15:15. A small amount of N-methyl-2-pyrrolidone is added to form thick viscous black slurry. It is stirred continuously for at least overnight before being spread evenly onto a copper foil. After drying in an air oven, the foil is being cut into small circular shape to form the electrode. The MnO_2 electrode is first placed on a cell cap, and then a polymeric separator is placed on top of it. 1M $LiPF_6$ (in EC:DMC) is added as the electrolyte before putting in a small layer of lithium metal. CR2016 coin cells were fabricated using coin cell crimper.

2.3. *Battery performance characterization*

To study the electrochemical properties of the electrodes, Cyclic Voltammetry (CV) and Galvanostatic cycling tests were carried in the voltage range, 0.005-3.0V vs. Li at scan rate of 0.058 mV/s at current rate of 30 mA/g with half-cell configuration.

2.4. *Li-air battery*

Bare MnO_2 (control sample), PVDF and Super P Carbon in the ratio of 40:15:45 are mixed and coated onto a Ni-mesh cut into circular shape and dried in air oven. A lab made cylindrical stainless steel test cell was used for the Li-air battery, where the contents are placed in the following order: Ni-mesh with the

MnO_2 electrode on top, glass separator, LiTFSI in 1:1 Dioxolane Dimethoxyethane electrolyte, lithium metal.

3. Results and Discussions

3.1. *Structure and morphology*

The structures are first characterized by X-ray Diffraction (XRD) to understand the phases and materials formed. The XRD data obtained from MnO_2 control sample fits perfectly with α-MnO_2 tetragonal structure. As observed from Figure 1, when PVA and PVP are added in, there are some additional peaks that resulted, which shows that additional phases have been formed. In the PVA sample, the intense and considerably sharper additional peaks match those from Mn_2O_3, whereas for the PVP sample, some of the peaks can be traced back to Mn_3O_4.

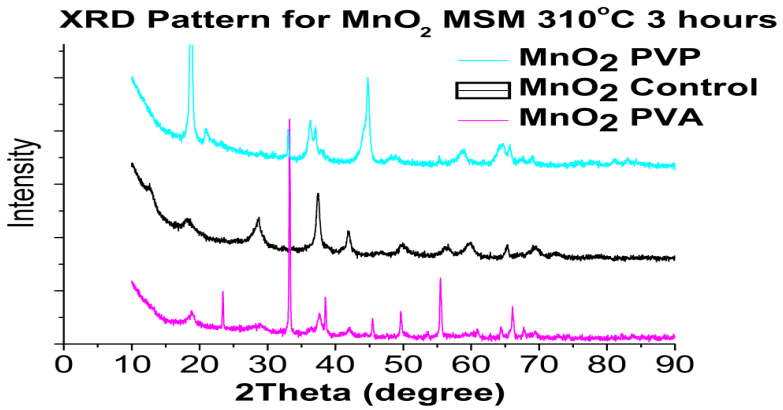


Figure 1. XRD pattern of various MnO_2 samples prepared from MSM 310°C for 3 hours.

As seen in Table 1, the use of polymers affects the lattice parameters of the MnO_2 phase formed. Moreover, MnO_2 control sample has much higher surface area than the other two, which affects the electrochemical properties as discussed in the later section.

Table 1. Lattice parameter, density and BET surface area of MnO_2 samples prepared with MSM 310°C for 3 hours

Compound	Lattice Parameter		Experimental Density (g/cm^3)	BET Surface Area (m^2/g)
	a (Å)	c (Å)		
MnO_2 - Control	9.816(3)	2.866(0)	4.15	31.9
MnO_2 - PVA	10.037(9)	2.844(9)	4.03	15.7
MnO_2 - PVP	10.139(0)	3.095(1)	4.93	19.1
Literature report [16]	9.82	2.84	-	-

Samples are analyzed by scanning electron microscopy (SEM) to further study the morphology of these samples and the resulting micrographs (shown in Fig. 2) demonstrate the change in morphologies, which in turn provides a clue to understand the changes in the performance of the battery cells. All three samples are in the nanometer scale. From Figure 2, the SEM image of MnO_2 control shows the typical long and thin α-MnO_2 nanowire shape. This morphology is preferred as it shows good electrochemical properties for applications like battery and supercapacitors [17]. However, with the inclusion of PVA, the nanoparticles change into cylindrical shape. The addition of PVP causes the particles to be even rounder and spherical. These results conclude that polymers will direct the particles to grow in such a way that they lose their original nanowire shape and become more isometric.

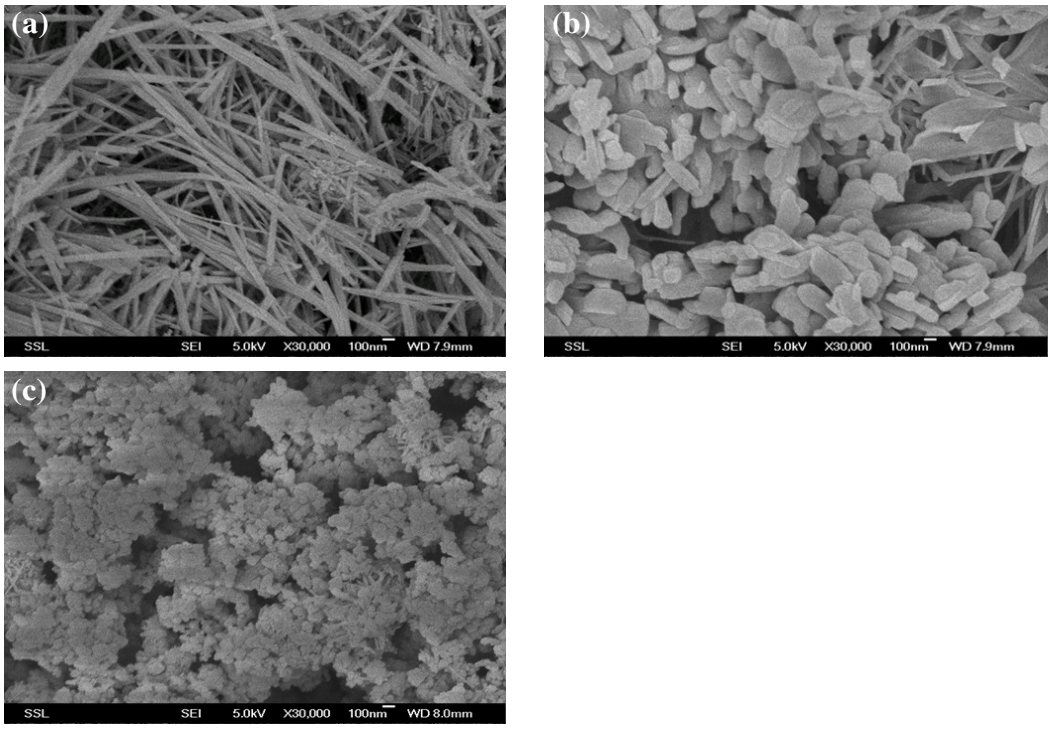


Figure 2. SEM images of MSM 310^{o}C 3 hours
(a) MnO_2-Control (b) MnO_2 – PVA (c) MnO_2 – PVP, scale bar 100nm

3.2. Electrochemical studies on Li-ion Batteries

Cyclic voltammetry is carried out using Li-metal used as counter and reference electrode. The observed cyclic voltammograms are shown in Figure. 3, the average discharge potential of the control sample is 0.47 V vs. Li while average

charge potential is 1.14 V vs. Li. For PVA sample, average discharge potential is around 0.48 V vs. Li whereas average charge potential is 1.19 V vs. Li. The discharge and charge potentials are 0.43 and 1.12 V vs. Li respectively for PVP sample. It can be observed that from all three samples, the resulting potentials during charging and discharging remain almost the same between samples. The first cycle of each electrode used also tend to be different form the rest because as the battery undergoes cycling, it undergoes structural modifications, a slight reactions take place in the electrolyte which greatly decrease the electrochemical property after the half-cell went through the first discharge and charge cycle.

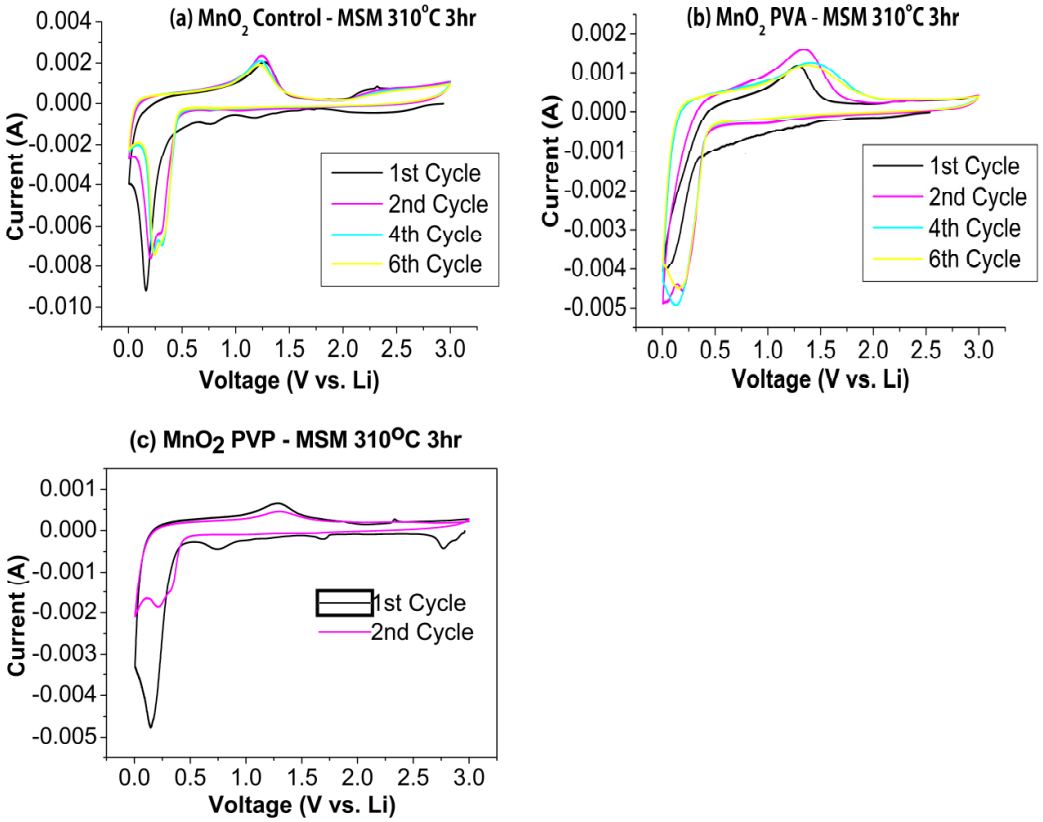


Figure 3. Current vs. Voltage plot of MSM 310°C 3 hours (a) MnO_2-Control (b) MnO_2 – PVA (c) MnO_2 – PVP, Voltage range, 0.005-3.0V, Scan rate, 0.058mV/sec.

Galvanostatic cycling was carried out in the voltage range 0.005-3.0V at a current rate of 30mA/g. Figure 4 shows the voltage vs. capacity of selected cycles of MnO_2 control and MnO_2-PVA sample. During the 1st discharge cycle a minor high voltage plateau (ca. 1.5 V) is followed by a major plateau at 0.45V; while during charging the occurs at ca. 1.0V. In the second and subsequent

cycles the high voltage discharge plateau is vanishing. As seen from Fig. 4 the value of reversible capacity is 1050 mAh/g. Based on Figure 5, the reversible capacity is 548 and 478 mAh/g for PVA and PVP samples respectively. As noted from these graphs, capacity decreases during initial cycles and stabilizes after 15 cycles.

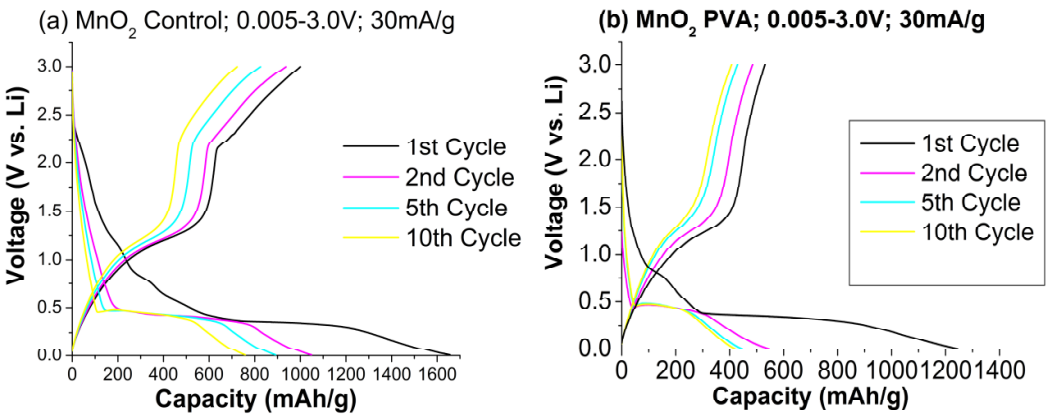


Figure 4. For clarity voltage vs. capacity plot of MnO_2-Control (b) MnO_2-PVA are shown, Current rate, 30 mA/g, Voltage range, 30 mA/g.

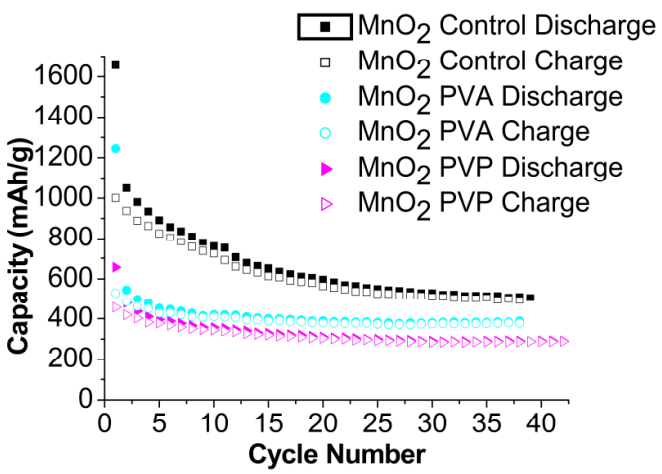


Figure 5. Capacity vs. cycle number plots of Mn-oxides, voltage range, 0.005-3.0V, Current rate: 30 mA/g

It can be easily observed that the capacity in decreasing order is as follows: Control, PVA, PVP. After approximately 20 cycles, the capacity stabilized, almost keeping constant for all three samples. From the results, MnO_2 control sample has the highest capacity among all, and it also retains most of the

capacity, whereas PVP sample has the least capacity. This phenomenon can be explained mainly due to the morphology and differences in the crystal structure of the sample. According to Li et al.[18], nanowire morphology is the best for electrode material because of the very high aspect ratio that gives it good electrical conductivity[19]. However, when polymers are added into the sample during the synthesis process, they act as structure directing agents that change the structure and morphology of the final product. The smaller the aspect ratio, the lower the electrochemical performance of the battery. The spherical nanoparticles have lower aspect ratio than cylindrical shaped particles; hence PVA has a capacity value higher than PVP sample. The formation of other phases like Mn_2O_3 and Mn_3O_4 etc. is another factor that affects the performance of the battery as they will hinder the transportation of ions and electrons. Having a higher surface area also increases the area where the electrolyte can be covered, allowing the Li ions to be transported efficiently between electrodes for intercalation to happen.

The proposed reaction mechanism in the half cell is given as $Mn^{4+}O_2 + xLi + xe^- \rightarrow Li_xMn^{3+}O_2 \rightarrow Li_2O + Mn^{4+/0}$, where Li ions are first intercalated into the layered structure of MnO_2 at the voltage of approximately 1 V, forming $Li_xMn^{3+}O_2$. This compound can be further converted into Li_2O and $Mn^{4+/0}$ at the voltage of 0.005 V.

3.3. Electrochemical studies on Li-air Batteries

Preliminary electrochemical studies were conducted on MnO_2 rods (MnO_2 control). The discharge and charge profiles are shown in the Figure 7, during discharge it showed major plateau around 2.84V and it showed a high discharge capacity value of 1200 mAh/g. However, a big drop in capacity from 1200 to 40 mAh/g is seen during the second cycle. To understand the reasons for degradation of capacity with cycle number impedance spectroscopy studies were conducted in the 0.18Mz to 5 mHz range, with an AC amplitude of 10 mV.

Nyquist plots of Li-air cell before and after cycling are shown in Figure 7. The fresh cell showed around 35 ohms resistance, whereas cycled electrode showed a large variation of resistance around 25000 Ohms. The possible reasons for the rise of impedance is due formation of insulating layer at the interface, which leads to drastic capacity fading. Hence, it can be concluded that impedance will increase to a high value after the Li-air battery has undergo many cycles, which greatly affect the battery performance.

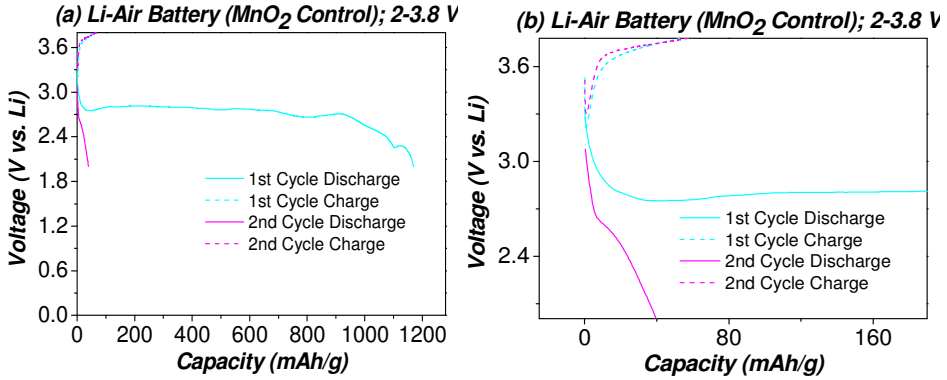


Figure 7: (a) Voltage vs. capacity plot of MnO_2-Control MSM 310^oC for Li-air battery. (b) same as (a), expanded graphs are shown for clarity. Current 0.4mA

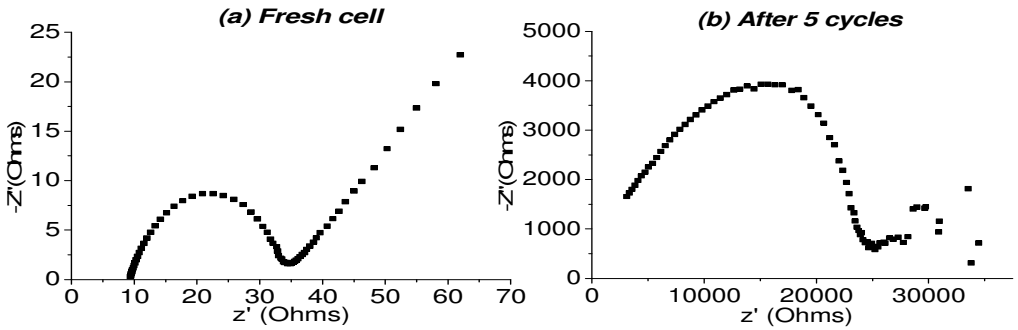


Figure 8: Nyquist plots of (Z' vs. –Z") of Li-air cell prepared using MnO_2-control sample (a) Fresh cell, (b) after 5 cycles.

1. Conclusion

MnO_2 can be prepared by a variety of method, from co-precipitation to sol-gel method. Among the, hydrothermal method is the most commonly used, with expensive equipment needed. Molten salt method provides a simpler alternative to produce metal oxides and it is being studied in this paper. Polymers act as structure-directing agents that modify the overall structure and morphology. The overall structure becomes more spherical and aspect ratio decreased. Surface area of nanoparticles as well as additional phases formed will also affect the electrochemical properties.

Acknowledgments

This research is supported by the National Research Foundation, Prime Minister's Office, Singapore under its Competitive Research Programme (CRP Award No. NRF-CRP 10-2012-6). We would like to acknowledge the support from Prof. Chowdari, Dept. of Physics, Faculty of Science, NUS

Award No. NRF-CRP 10-2012-6). We would like to acknowledge the support from Prof. Chowdari, Dept. of Physics, Faculty of Science, NUS.

References

1. M. Winter, J.O. Besenhard, M.E. Spahr, P. Novak, Advanced Materials, 10 (1998) 725-763.
2. K.E. Alifantis, S.A. Hackney, R. Vasant Kumar, (eds.), 'High Energy density Lithium batteries: Materials, Engineering, Applications' Wiley VCH, 2010.
3. M.V. Reddy, G.V. Subba Rao, B.V.R. Chowdari, Chem. Rev., 113 (2013) 5364-5457.
4. M.V. Reddy, L.Y.T. Andreea, A.Y. Ling, J.N.C. Hwee, C.A. Lin, S. Adams, K.P. Loh, M.K. Mathe, K.I. Ozoemena B.V.R. Chowdari, Electrochim. Acta, 106 (2013) 143-148.
5. M.V. Reddy, S. Adams, G.T.J. Liang, I.F. Mingze, H. Van Tu An, B.V.R. Chowdari, Solid State Ionics, (2014) (in press).
6. D. Capsoni, M. Bini, S. Ferrari, E. Quartarone, P. Mustarelli, J. Power Sources, 220 (2012) 253-263.
7. Y. Yu, B. Zhang, Y.-B. He, Z.-D. Huang, S.-W. Oh, J.-K. Kim, Journal of Materials Chemistry A, 1 (2013) 1163-1170.
8. Y. Chen, Z. Zhang, W. Zhang, C. Shu, L. Liu, Kuei Suan Jen Hsueh Pao/ Journal of the Chinese Ceramic Society, 36 (2008) 1053-1056.
9. D. Su, H.-J. Ahn, G. Wang, Journal of Materials Chemistry A, 1 (2013) 4845-4850.
10. F. Hashemzadeh, M. Mehdi Kashani Motlagh, A. Maghsoudipour, J. Sol-Gel Sci. Technol., 51 (2009) 169-174.
11. B. Lan, M. Sun, T. Lin, G. Cheng, L. Yu, S. Peng, J. Xu, Mater. Lett., 121 (2014) 234-237.
12. A.L.M. Reddy, M.M. Shaijumon, S.R. Gowda, P.M. Ajayan, Nano Lett., 9 (2009) 1002-1006.
13. Y. Mai, F. Zhang, X. Feng, Nanoscale, 6 (2014) 106-121.
14. M. Lashanizadegan, H. Mirzazadeh, Asian J. Chem., 25 (2013) 1425-1428.
15. F. Cheng, Z. Tao, J. Liang, J. Chen, Chem. Mat., 20 (2008) 667-681.
16. Y. Qin, J. Lu, P. Du, Z. Chen, Y. Ren, T. Wu, J.T. Miller, J. Wen, D.J. Miller, Z. Zhang, K. Amine, Energy & Environmental Science, 6 (2013) 519-531.
17. Y. Li, H. Xie, J. Wang, L. Chen, Mater. Lett., 65 (2011) 403-405.
18. W. Li, Q. Liu, Y. Sun, J. Sun, R. Zou, G. Li, X. Hu, G. Song, G. Ma, J. Yang, Z. Chen, J. Hu, J. Mater. Chem., 22 (2012) 14864-14867.
19. K. Song, J. Jung, Y.U. Heo, Y.C. Lee, K. Cho, Y.M. Kang, PCCP, 15 (2013) 20075-20079.

DEVELOPMENT AND CHARACTERIZATION OF PVA: CELLOBIOSE - NH_4NO_3 POLYMER MEMBRANE

VINITHRA GURUNARAYANAN[1], S. SELVASEKARAPANDIAN[1*], SINDHUJA MANOHARAN[1],VINOTH PANDI. D[1], VEERAMANIKANDAN C[1], ARUN ARAICHIMANI[2]

[1]*Materials Research Centre, Coimbatore, Tamilnadu, India.*

*sekarapandian@rediffmail.com

[2]*Department of Chemistry, Government arts college, Tiruvannamalai.*

The Polymer blend electrolytes based on Polyvinylalcohol (PVA), Cellobiose with various ratio of Ammonium Nitrate (NH_4NO_3) has been prepared by solution casting technique using double distilled water as solvent. Synthesized polymer membrane's structure and properties were characterized by XRD, FTIR and Ac impedance. From the XRD spectra we confirmed that the amorphous nature of PVA: Cellobiose increase with addition of different amounts of NH_4NO_3. The amorphous nature is found to be higher for PVA-Cellobiose blend with 0.321g of NH_4NO_3. Ac impedance studies show that ionic conductivity for the same ratio is $5.4x10^{-6}$ S/cm. The ionic conductivity of PVA: Cellobiose membrane on addition of NH_4NO_3 has increased by one order of magnitude when compared with pure PVA-Cellobiose membrane. Dielectric and modulus behavior has been studied further.

1. Introduction

Commercial interests in new portable and renewable energy sources across the board has been the driving force for the development of rechargeable Lithium-based polymer-batteries. Ionically conducting polymers has potential application as solid polymer electrolyte. Polymer electrolytes has many advantages such as flexibility, high energy density, electrochemical stability and easy in handling.[1] Hence an effort has been made to develop a blend polymer membrane.

Polymer membrane has been developed by blending Polyvinyl Alcohol (PVA), Cellobiose which contains eight –OH group which gives rise to strong inter and intra molecular hydrogen bonds through its acetal and semi hemiacetal linkage. The electrical and conductivity and charge –storage capacity of PVA can be effectively used by doping some suitable impurities. Already membrane of PVA

Proceedings of the 14th Asian Conference on Solid State Ionics (ACSSI 2014)
Copyright © 2014 ACSSI 2014 Organizers. All rights reserved.
ISBN: 978-981-09-1137-9
doi:10.3850/978-981-09-1137-9_027

and Cellulobiose has been prepared in our group which shows conductivity of $1.36x10^{-7}$ S/cm.[2] So an effort has been made to blend ammonium salt with Cellobiose and PVA, since Ammonium salts could act as proton donor, with a motive to use this material as proton conducting solid electrolyte membrane in fuel cells by replacing Nafion, as Nafion is a costly and has some disadvantages.

2. Experimental details

The polymer PVA (Polyvinyl Alcohol) of average molecular weight 1,25,000 Cellobiose (Cb) and the NH_4NO_3 were used as the raw materials for the preparation of the membrane . The membranes were prepared by solution casting technique using double distilled water as solvent. 1,3,4,5 mol percentage of NH_4NO_3 were added incrementally with fixed amount of PVA (1g) and Cellobiose (.4g). The mixture of PVA, Cellobiose and NH_4NO_3 are stirred continuously with a magnetic stirrer for several hours at temperature 60^0C to obtain a homogenous solution. The solution was then poured into petri dishes and allowed to evaporate in vacuum oven at 65^0C. After 48 hours, free standing transparent films were obtained. X-ray diffraction patterns of the prepared samples are recorded at room temperature on a Philips X'Pert PRO diffractometer using Cukα radiation. FTIR spectra are recorded for the polymer electrolyte films using a SHIMADZU – IR Affinity -1Spectrometer in the range of 400 - 4000 cm^{-1} at room temperature. Conductivity measurements were carried out by using a HIOKI 3532 LCZ meter in the frequency range of 42 Hz – 1 MHz over the temperature range of 303 – 443K.

3. Results and discussion

3.1. *X-ray diffraction analysis*

Fig 1. represents the XRD pattern of PVA(1g) : Cb (.4g) (pure) and the XRD pattern obtained on incremental addition. It is clear from this fig 1 that the peak around 20^{o} which is ascribed to the PVA: Cb blend started broadening with decrease in the intensity of the peak on each addition of NH_4NO_3. This reveals that the amorphous nature of the system increases with incremental addition. It is known that as amorphous nature increases conductivity also increases[3]. Also, the change in the nature of PVA:Cb peak on incremental addition indicate complete dissociation of ammonium salt in to the polymer matrix. Thus the X-ray diffraction analysis confirms the complex formation between the blend polymer and the salt.

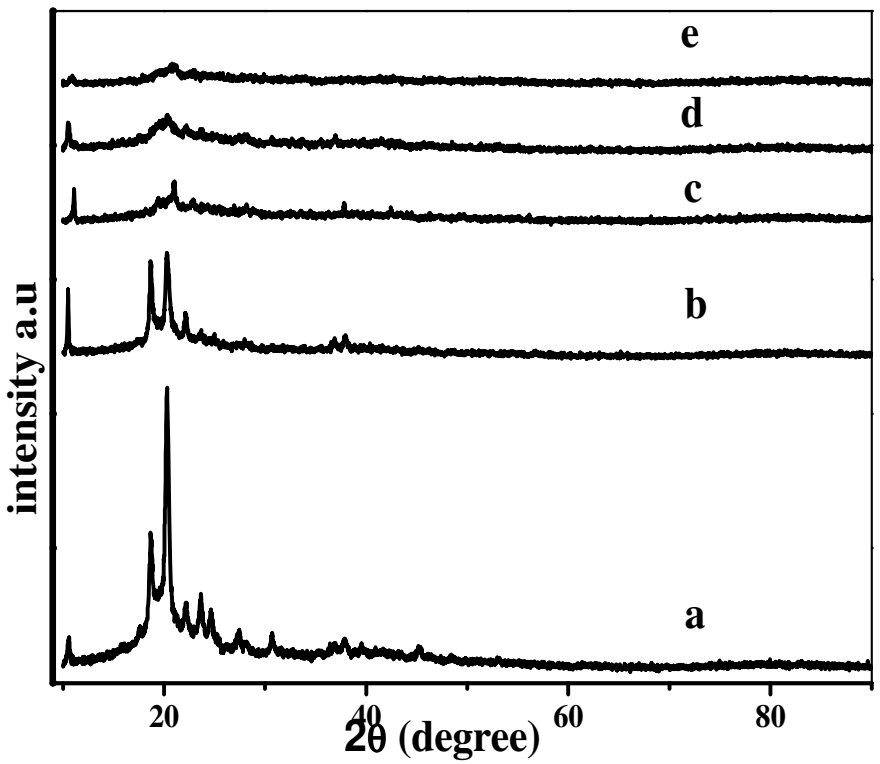


Figure: 1 XRD spectrum of PVA: Cb (a), PVA:Cb with 1 mol % NH_4NO_3 (b), PVA:Cb with 3 mol % NH_4NO_3 (c), PVA:Cb with 4 mol % NH_4NO_3 (d), PVA:Cb with 5 mol % NH_4NO_3 (e).

3.2. *FTIR analysis*

Interaction among the atoms or ions in the electrolyte system during complex formation induces change in the vibrational modes of the blend polymer; this has been studied using FTIR spectrum. Figure 2 shows the FTIR spectrum of polymer before and after addition of ammonium salt. In (fig 2.a) The broad peak in the region around 3400 cm^{-1}, 1417 cm^{-1} and 2051 cm^{-1} corresponds to the O-H stretching, H-O-H bending and C=O stretching respectively. With ammonium salts the OH stretching band started decreasing and for the (e) system the OH band reappears. In the same way the peak at 2051cm^{-1} disappears completely with 1mol percentage of NH_4NO_3 itself which indicates the complex formation of NH_4NO_3 with PVA:Cb.

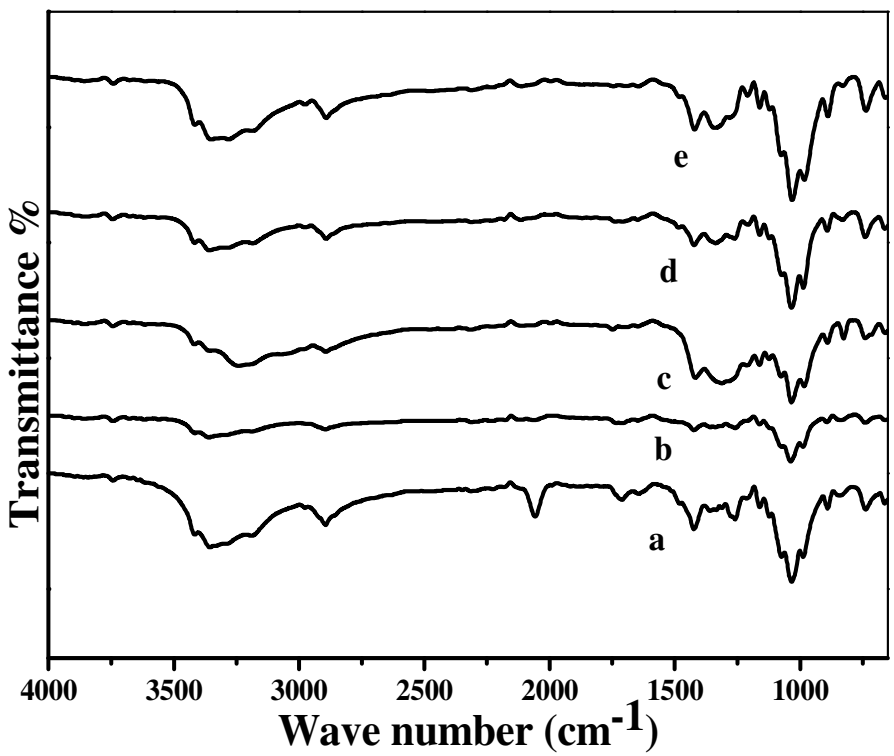


Figure: 2 Vibrational spectrum of PVA: Cb (a), PVA:Cb with 1 mol % NH_4NO_3 (b), PVA:Cb with 3 mol % NH_4NO_3 (c), PVA:Cb with 4 mol % NH_4NO_3 (d), PVA:Cb with 5 mol % NH_4NO_3 (e).

3.3. *AC Impedance analysis*

3.3.1 Conductance spectra Analysis

The logarithmic plot of the conductivity as a function of angular frequency for all doped blend polymer electrolytes at room temperature is shown in Figure 3.The plots consist of two distinct regions[4] a low frequency dispersion region and a frequency independent plateau region. The low frequency dispersion region is due to electrode polarization effect and the plateau region corresponds to dc conductivity (σdc) of the blend polymer electrolyte. The dc conductivity of the blend polymer electrolyte has been obtained by extrapolating the plateau region on the logσ – axis. Highest conductivity $5.4x10^{-6}$ S/cm is observed for PVA:Cb: 4 mol% NH_4NO_3.

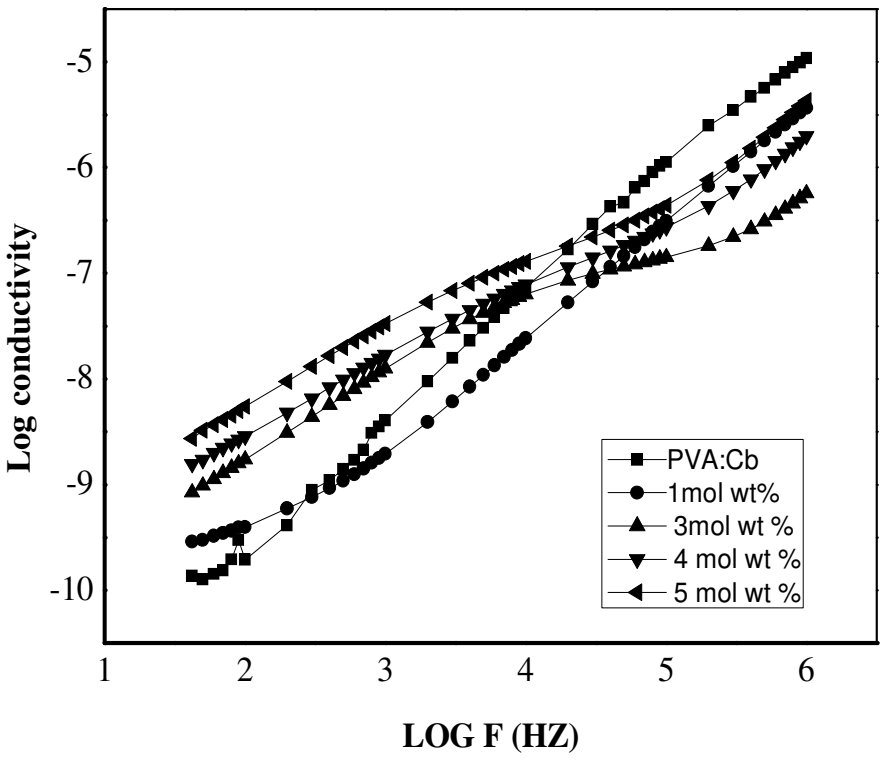


Figure 3: conduction spectra for all compositions of PVA:Cb with NH_4NO_3 at room temperature.

3.3.2 Dielectric Analysis

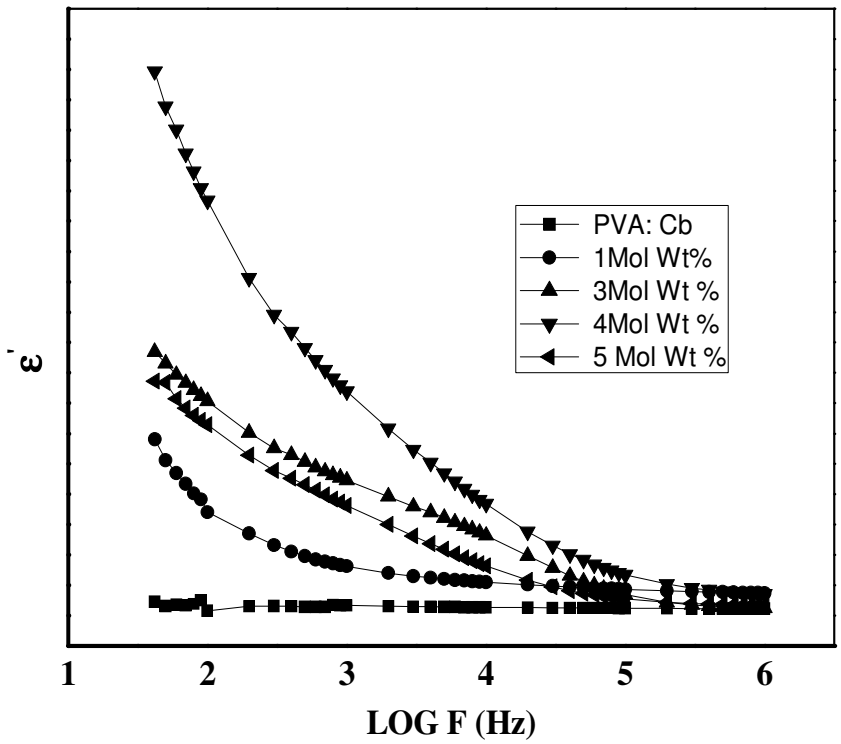


Figure 4: Dielectric spectra for all compositions of PVA:Cb NH_4NO_3 at room temperature.

The dielectric behaviour of the polymer electrolyte system is described by using the dielectric function ε and is defined by,

$$\varepsilon^* = \varepsilon'(\omega) - i\,\varepsilon''(\omega)$$

Where real $\varepsilon'(\omega)$ and imaginary $\varepsilon''(\omega)$ components are the storage and the loss of energy in each cycle of the applied electric field[5]. It is clear from the fig (4), that the values of $\varepsilon'(\omega)$ are very high at low frequency and decrease with increase of frequency and become constant at higher frequencies. Such high value of dielectric permittivity at low frequencies has been explained by the presence of space charge effects, which is contributed by the accumulation of charge carriers near the electrodes[6]. At higher frequencies, periodic reversal of the field takes place so rapidly that the charge carriers will hardly to be able to orient themselves in the decrease of dielectric constant[7]. High dielectric constant is found for 4 mol% NH_4NO_3 blended PVA:Cb.

4. Conclusion

PolyvinylAlcohol (PVA): cellobiose (Cb) based proton conducting polymer electrolytes blended with various weight percentage of NH_4NO_3 has been prepared by solution casting technique. The amorphous nature of the polymer electrolyte has been revealed by XRD analysis. Complexation of NH_4NO_3 with blend PVA: Cb was confirmed by vibrational spectroscopic studies. From the conductivity analysis the highest conductivity at room temperature has been found to be $5.4x10^{-6}$ S/cm. for PVA:Cb: 4 wt% NH_4NO_3 polymer electrolyte.

Acknowledgement

One of the authors (Vinithra Gurunarayanan), acknowledges Dr. S. Selvasekarapandian, Materials Research Centre for carrying out the research work.

References

1. G.C Farrington and J.LBriant Science 4 (1979) 1371; 'Solid eleectrolytes and their application'(edited by E.C.Subbrao), plenum press, NY (1980).
2. S.Karthikeyan *et al* , International conference on polymers :Vision & innovations, 2014.
3. Hodge RM,Edward GH,Simon GP, Polymer **37**, 1371 (1996).
4. N.Vijaya, Subramanian Selvasekarapandian, G Hirankumar, S.Karthikeyan, H.Nithya, C.S.Ramya, M.Prabu, Ionics **18**, 91 (2012).
5. Dutta P, Biswas S, (2002) Mater Res Bull **37**: 193-200.
6. Armstrong RD,Dickman Twills PW, J.*Electronal Chem* **53**, 389(1974).
7. Adachi K,urakawa O, J.*Non-cryst Solids* **307**, 667(2002).

CHARACETRIZATION OF PVA:CELLOBIOSE - NH_4SCN POLYMER ELECTROLYTE

SINDHUJA MANOHARAN[1], S. SELVASEKARAPANDIAN[1*], VINITHRA GURUNARAYANAN[1], VINOTH PANDI. D[1], VEERAMANIKANDAN C[1], ARUN ARAICHIMANI[2]

[1]*Materials Research Centre, Coimbatore, Tamilnadu, India.*

*sekarapandian@rediffmail.com

[2]*Department of Chemistry, Government arts college, Tiruvannamalai*

The polymer electrolytes are solid membranous electrolytes with the applications ranging from batteries, fuel cells, supercapacitors, sensors, filtrations to solid chromic displays. The blend polymers electrolyte of Poly(vinyl alcohol) PVA and Cellobiose with the ammonium thiocyanate salt addition has been prepared using solution casting technique. The interaction of blends with salt addition could be evinced by X-Ray diffraction and Fourier Transform Infrared analysis. The XRD gives details about the increase in amorphous nature with the increment in addition of salts and FTIR spectrum shows the intricate interaction of blend and salt at various concentrations. The highest conductivity is measured as 1.11 x 10^{-04} S/cm with the NH_4SCN addition of 0.304g with the AC impedance spectroscopy. Modulus and dielectric behavior has also been studied and presented in this paper.

1. Introduction

Solid polymer electrolytes or fast ion conducting solids are materials with conductivity ranging from 10^{-5} to 10^{-1} S cm^{-1}. These polymer electrolytes are widely used in batteries, fuel cells, supercapcatiors applications[1-3]. Hence for making an efficient and environmental friendly conducting membrane, proton conducting membranes are widely being prepared as the hydrogen intercalation is more because of its smaller size. Hence novel approach is being employed in preparing the proton conducting membrane for obtaining the highest conductivity. The main merit of using polymer electrolytes are their mechanical properties, adaptable size for various preferred products and to lead a contact between electrode-electrolyte[4]. Blending of two polymers is very much useful in enhancing the electrical, mechanical and electrochemical properties of the

Proceedings of the 14th Asian Conference on Solid State Ionics (ACSSI 2014)
Copyright © 2014 ACSSI 2014 Organizers. All rights reserved.
ISBN: 978-981-09-1137-9
doi:10.3850/978-981-09-1137-9_028

polymer electrolytes. These blend helps in altering the molecular chains of two individual polymers and our required product will be obtained when uniform miscibility of the polymers is reached.

Poly(vinyl alcohol) (PVA) is an amorphous, bio compatible polymer with immense inherent characteristics and cost effective. Hence an attempt has been made to increase its conductivity for our applications in batteries and fuel cell. Cellobiose is a bio polymer, disaccharide and its presence is abundant in nature. The blending of PVA with cellobiose was very much effective, as cellobiose has eight alcohol groups. We have successfully prepared film with the blend of PVA with cellobiose gave conductivity of 1.36 X 10^{-07} S/cm^{-1}[5] from our group. Hence for making it an efficient proton conducting membrane, it is necessary to dope with appropriate impurity which will increase the electrical conductivity and charge storage capacity. In the proton conducting membrane NH_4SCN is used, as ammonium salts are good proton donors because of weakly bonded hydrogen .

2. Experimental Technique

The Polyvinyl alcohol (PVA), Cellobiose and ammoniumthiocyanate of analytical quality are taken and dissolved in dimethyl formamide. 1 gram of PVA : 0.428g of Cellobiose with ammonium thiocyanate of 1,2,3,4,5% of its molecular weight are prepared using the solution casting technique. The blend of polymers and salts are obtained after 48hours of mixing at 70-75°C for obtaining homogeneity and the solution is casted in the petri dishes and kept in a vacuum oven at 60°C for 24 hours. A free standing and transparent film is obtained. The obtained films are characterized by X-Ray Diffractometer of Philip X'pert PRO using CuK_α radiation, Fourier Transform Infrared spectroscopy with SHIMADZU-8000 spectrophotometer in the range of 400-4000 cm^{-1} and AC impedance spectroscopy of HIOKI 3532 LCZ meter with the frequency range of 42Hz - 1MHz.

The X-Ray Diffraction pattern gives the evidences for the complex formation between blend polymer and also the interactions with NH_4SCN salt

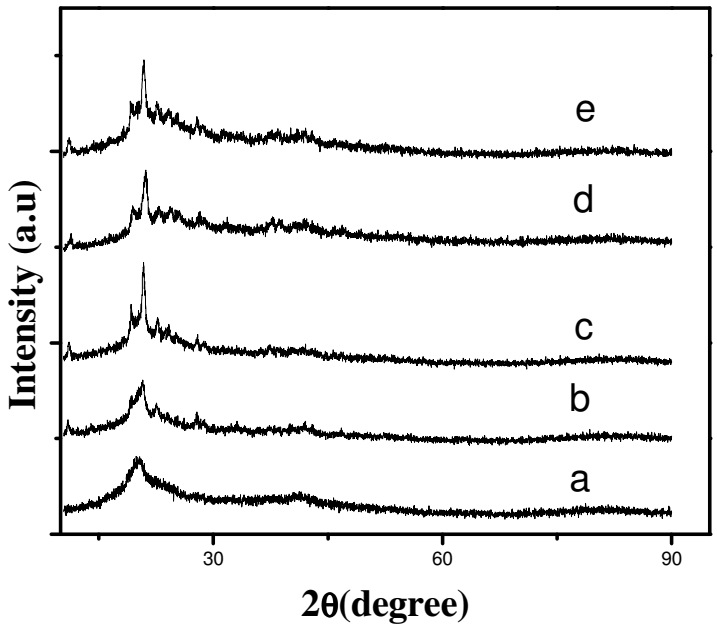


Figure 1. XRD pattern of (a) PVA+CA(blend), (b) Blend with 1% m.w of NH_4SCN, (c) Blend with 3% m.w of NH_4SCN, (d) Blend with 4% m.w of NH_4SCN, (e) Blend with 5% m.w of NH_4SCN.

The observed XRD pattern of the prepared samples are shown in the figure 1. PVA orthorhombic crystalline peak at 19.7° is observed[6]. In our case as we have tried the blend of PVA and Cellobiose, there is shift in the peak to 21.4° and also there is a reduction in the intensity of the peak. As the concentration of NH_4SCN increases, we are obtaining a semi-crystalline material. The full width half maximum is highest in the (1-d) with the 4% molecular weight addition in the blend. Hence the amorphous nature is maximum in this concentration. The peak for NH_4SCN is completely absent because the salt is totally dissociated with the polymer matrix.

The FTIR analysis shows the intricate interaction of atoms, the vibrations of atoms and bonding nature could also be studied. The blending of PVA and cellobiose shows the change in shift of the peak. When the salt addition is increased we could also see the interaction with the increase of intensity in C=O stretching at 2046 cm^{-1} .

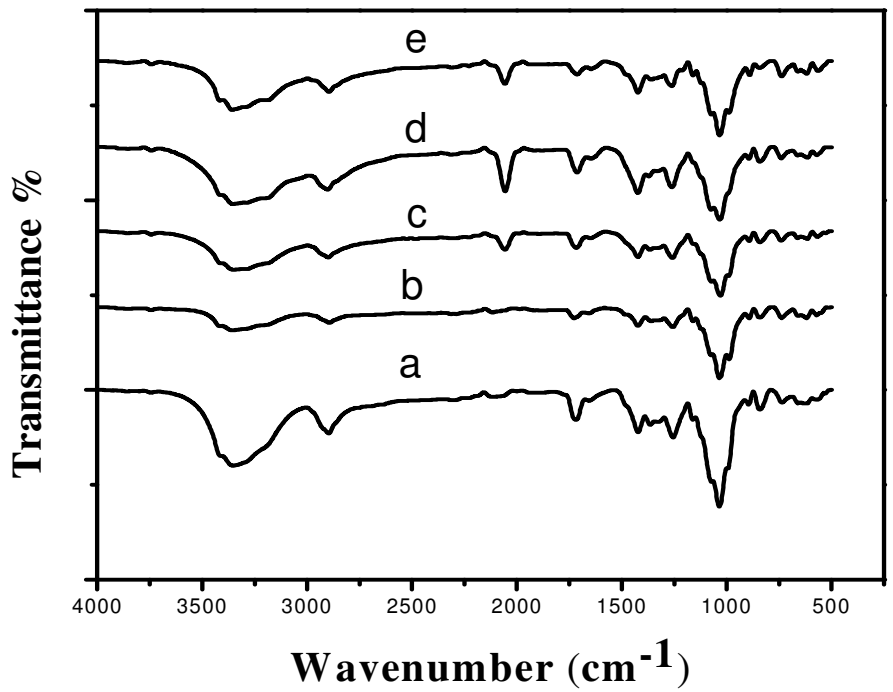


Figure 2. FTIR spectrum of (a) PVA+CA(blend), (b) Blend with 1% m.w of NH_4SCN (c) Blend with 3% m.w of NH_4SCN, (d) Blend with 4% m.w of NH_4SCN, (e) Blend with 5% m.w of NH_4SCN.

The FTIR spectrum is given in the figure 2. The bands of 3344, 1421, 1031 cm^{-1} are O-H stretching, O-H bending C-H bending corresponding to Polyvinyl alcohol (2-a) and the rest of the peaks are similar to the cellobiose. The blend shows C-O stretching with high intensity. When the salt is added, intensity of the peak of C-O stretching is decreased and the band at 2046 cm^{-1} intensity increases (2-d). In the peak in (2-e) the peak of C-O stretching starts to decrease. Thus the salt addition reaches its saturation and then the number of C-O stretching is

decreased. The shift in peaks is seen because of the intricate interaction of NH_4SCN salt and blend.

3.3 AC Impedance analysis

3.3.1 Conduction spectra analysis

The impedance spectroscopy is used in measuring the electrical and electrochemical properties in batteries, corrosion and semiconductors.

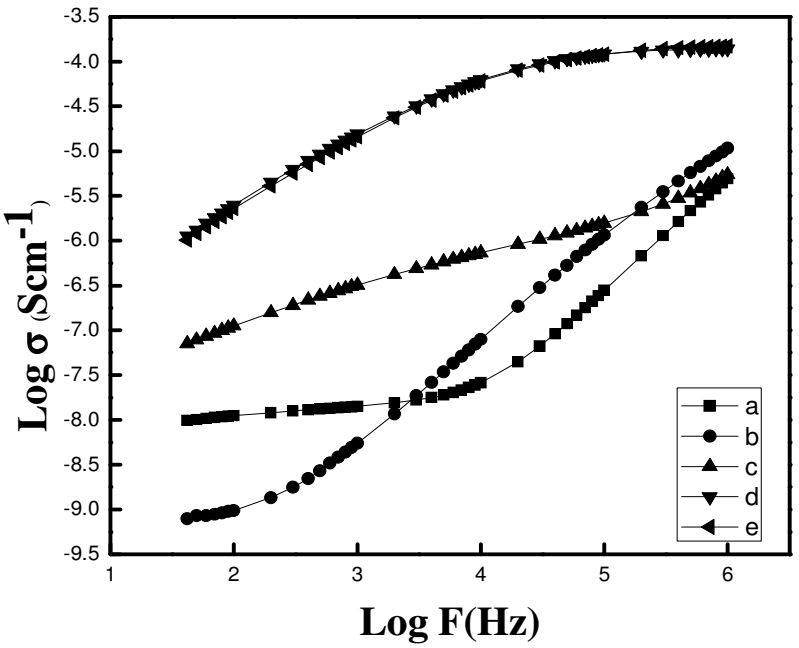


Figure 3. Conduction spectra at room temperature of (a) PVA+CA(blend), (b) Blend with 1% m.w of NH_4SCN (c) Blend with 3% m.w of NH_4SCN, (d) Blend with 4% m.w of NH_4SCN, (e) Blend with 5% m.w of NH_4SCN.

The conduction spectra has three frequency regions of low frequency dispersion, frequency independent region and high frequency dispersion region. The frequency independent plateau region gives us the conduction caused due to the hopping movement of the mobile ions. The logarithmic scales are taken and the point in the plateau region gives the logσ with the extrapolation and dc conductivity is obtained with the corresponding σ value. The high frequency behavior is attributed to the relaxation of the mobile ion hopping, which is due to the columbic interactions of the charge carrier and the disorder with the

structure. The plateau region is obtained with the salt addition and the highest conductivity is measured in the (3-d) blend with 4% molecular weight of NH_4SCN with the conductivity of 1.111 x 10^{-4} S cm^{-1} .

3.3.2. Dielectric analysis

The dielectric constant or permittivity is given by $\varepsilon^* = \varepsilon' - \varepsilon''$, where ε' and ε'' are the real and imaginary part of dielectric constant of the material.

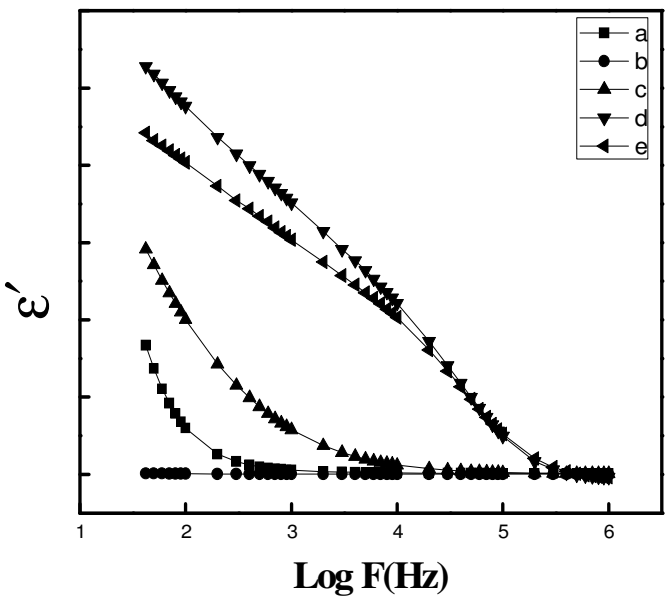


Figure 4. Dielectric behavior with dependence of frequency at room temperature of (a) PVA+CA(blend), (b) Blend with 1% m.w of NH_4SCN (c) Blend with 3% m.w of NH_4SCN, (d) Blend with 4% m.w of NH_4SCN, (e) Blend with 5% m.w of NH_4SCN.

Figure 4, explains the dielectric behavior of the system with frequency dependence. This value increases with the increase in salt addition at room temperature. The low frequency dispersion region is due to the contribution of charge accumulation at the electrode-electrolyte interfaces. The high value is due to the enhanced charge carrier density at the space charge accumulation region resulting in an increase in the equivalent capacitance. At higher frequency there is high periodic reversal of the field at the interface. At high frequencies, due to high periodic reversal of the electric field at the interface, the contribution of charge carriers towards the dielectric constant decreases with increase in frequency. The contribution of charge carriers (ions) towards the dielectric

constant has decreased with increase in frequency.(R.Mishra, K.J.Rao, Solid State Ionics,106(1998)113).

3.3.3. Modulus spectra analysis

The modulus behavior aids to investigate the bulk dielectric response by suppressing the effect of electrode polarization. The figure 5 explains the modulus behavior of frequency dependence.

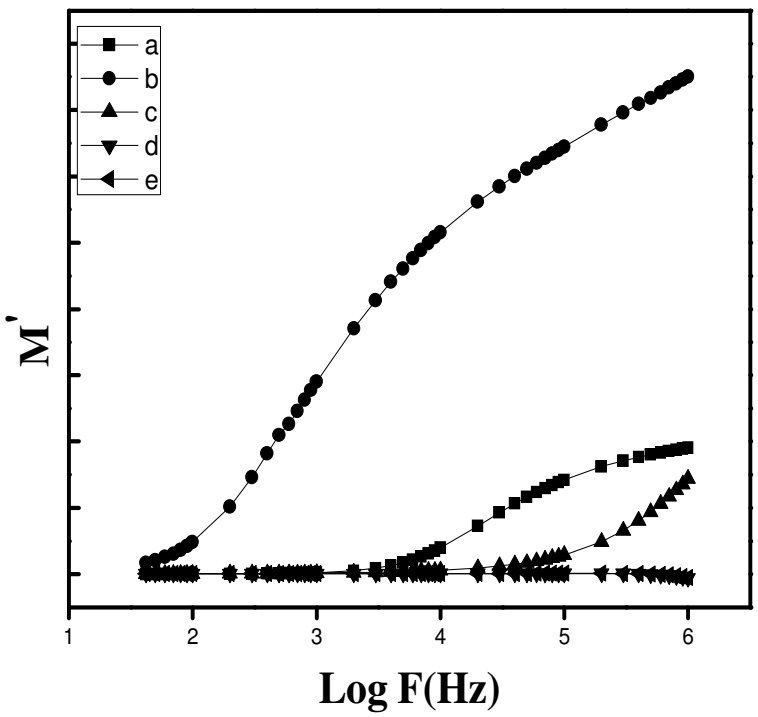


Figure 5. Modulus behavior with dependence of frequency at room temperature of (a) PVA+CA(blend), (b) Blend with 1% m.w of NH_4SCN (c) Blend with 3% m.w of NH_4SCN, (d) Blend with 4% m.w of NH_4SCN, (e) Blend with 5% m.w of NH_4SCN.

The lower frequency approaches to zero indicating that electrode polarization phenomena make a negligible contribution. The value of M' increase in high frequency end which might be due to bulk effect of the polymer electrolyte. The observed long tail at low frequencies is due to large capacitance associated with the electrode.

4. Conclusion

Polyvinyl alcohol (PVA) and Cellobiose blend proton conducting polymer electrolytes with the addition of ammonium thiocyanate in different molecular weight percentage have been synthesized through solution casting technique. The XRD analysis shows the increase in amorphous nature of the polymer electrolytes. The FTIR provides evidences for the intricate complexation of salt (NH_4SCN) with the blend polymer. From the conductivity measurements the highest conductivity at room temperature obtained as 1.111×10^{-4} S cm^{-1} for the blend polymer with 4% molecular weight of NH_4SCN. The low frequency dispersion of dielectric constant reveals the space charge effect arising from the electrodes.

Acknowledgement

One of the authors (Sindhuja Manoharan), acknowledges Dr. S. Selvasekarapandian, Materials Research Centre for carrying out the research work.

References

1. Maccullum JR, Vincent CA (eds) (1987) Polymer electrolyte reviews. Elsevier, London
2. Bruce PG, Campbell SA, Lightfoot P, Mehta MA (1995) Polymer electrolytes: structure and electrode processes. *Solid State Ion* 78:191–198
3. Blonsky PM, Clancy S, Hardy LC, Harris CS, Spindler R, Tonge JS, Shriver DF (1989) *Polymeric Electrolytes*. Chem Tech 758
4. Subba Reddy ChV, Sharmanad AK, NarasimhaRao VVR (2004) Characterization of a solid state battery based on polyblend of (PVP + PVA + KBr O_3) electrolyte. *Ionics* 10:142–147
5. S.Karthikeyan *et al.*, International conference on polymers :Vision & innovations, 2014.
6. R.Schellekens,C.J.Bastiaansed, *J.Appl.Polym.Sci* 43(1991)2311.
7. Selvasekarapandian S, Hirankumar G, Kawamura J, Kuwata N, Hattori T (2005) 1H solid state NMR studies on the proton conducting polymer electrolytes. *Mater Lett* 59:2741–2745
8. Varnell DF, Cole man MM (1981) FT I.R. Studies of polymer blends: V. Further observations on polyester-poly(vinyl chloride) blends. *Polymer* 22:1324–1328

9. N. Rajeswari, S. Selvasekarapandian,C. Sanjeeviraja, J. Kawamura & S. Asath Bahadur, *polym.bull* 71:1061-1080 (2014).
10 N.Vijaya, Subramanian Selvasekarapandian, G Hirankumar, S.Karthikeyan, H.Nithya, C.S.Ramya, M.Prabu Ionics **18**, 91 (2012).

AC CONDUCTIVITY STUDIES OF PAN- NH_4Cl POLYMER ELECTROLYTE SYSTEM

S.SIKKANTHAR

Research and Development Centre, Bharathiar University, Coimbatore, Tamilnadu, India, Materials Research Centre, Coimbatore, Tamil Nadu, India

Arignar Anna Government Arts College, Cheyyar, Tamilnadu, India

S. KARTHIKEYAN

Department of Physics, Ramco institute of technology, Rajapalayam, Tamilnadu, India

S. SELVASEKARAPANDIAN*, D.VINOTH PANDI

Materials Research Centre, Coimbatore, Tamil Nadu, India

S.NITHYA

Department of Physics, SRNM College for women, Sivakasi, Tamilnadu, India

C. SANJEEVIRAJA

Department of Physics, Alagappa Chettiar College of Engineering & Technology, Karaikudi, Tamilnadu, India

G.MANI

PG & Research department of physics, Arignar Anna Government Arts College, Cheyyar, Tamilnadu, India

Polymer electrolytes are electrolytic materials that are widely used in batteries, fuel cells and other applications such as supercapacitors, photoelectrochemical and electrochromic devices. PAN based polymer electrolyte films doped with ammonium chloride (NH_4Cl) has been prepared by the solution casting method. The prepared polymer electrolytes have been investigated by different techniques such as XRD, FTIR and AC impedance spectroscopy. XRD and FTIR analysis indicate complexation of ammonium chloride with PAN polymer electrolyte. From the AC impedance spectroscopy, the maximum proton conductivity at room temperature has been found to be 6.4×10^{-3} Scm^{-1} for 25 mol% NH_4Cl doped PAN polymer electrolyte. Dielectric and modulus behavior of the polymer electrolyte have also been studied and the results are presented in this paper.

Proceedings of the 14th Asian Conference on Solid State Ionics (ACSSI 2014)
Copyright © 2014 ACSSI 2014 Organizers. All rights reserved.
ISBN: 978-981-09-1137-9
doi:10.3850/978-981-09-1137-9_036

1. Introduction

Ionically conducting polymers have been considerable interest because of their potential application as a solid polymer electrolyte. Polymer electrolytes are electrolytic materials that are widely used in batteries, fuel cells and other applications such as super capacitors, photo electrochemical and electro chromic devices (1). Polymer electrolytes have many advantages, such as flexibility, high energy density, electrochemical stability and easy handling [2].ease of processing into thin films of large surface area, electrochemical stability and leak-proof nature. Polyacrylonitrile (PAN) is an important engineering polymer material that has been widely used to produce a variety of synthetic fibers. Polyacrylonitrile (PAN) polymer has been extensively studied due to their good chemical and flame resistance and electrochemical stability [3]. The ionic conductivity of the gelled electrolyte based on PAN -propylene carbonate (PC) and $LiBF_4$ was studied by Nagasubramanian et al.[4]. PAN/Ag nano particle composites were synthesized by ultraviolet irradiation of a mixture of silver nitrate (AgNO3) and acrylonitrile (AN) monomers (Zhongping Zhang) [5]. Research works on PAN with ammonium salt based polymer electrolyte are rare. The present work is to prepare and characterize PAN based polymer electrolyte with different molWt% of NH_4Cl. Ammonium salts are very good proton donor for developing membrane with highest proton conductivity [6].

2. Experimental Technique

PAN (M.W= 1, 50,000 from Sigma Aldrich) along with NH_4Cl(Merck) have been used in the present study. To prepare polymer membrane by solution casting technique, DMF is used as solvent. The X-ray diffraction pattern has been recorded using CuK_α (λ=1,54060Å). The FTIR measurements have been made with Perkin-Elmer 5771R spectrometer. Impedance measurements have been made using HIOKI 3532 LCR meter in the temperature range 303K to 343K over a frequency range 42Hz-1MHz.

3. Results and discussion

3.1.XRD analysis

From the Fig 1 (a) for pure PAN film shows that the films are semicrystallline in nature having a peak at 2θ=17°, it corresponding to orthorhombic PAN (110) reflection [7]. This peak intensity gets reduced with increasing salt concentration. The high amorphous nature has been observed for the composition of 75PAN:25NH_4Cl. Small peaks corresponding to NH_4Cl have been observed for 30molWt% of NH_4Cl doped PAN film. It may be due to the incomplete dissolution of the salt in the polymer matrix. Thus the XRD study confirms that complexation has occurred between PAN polymer and ammonium chloride.

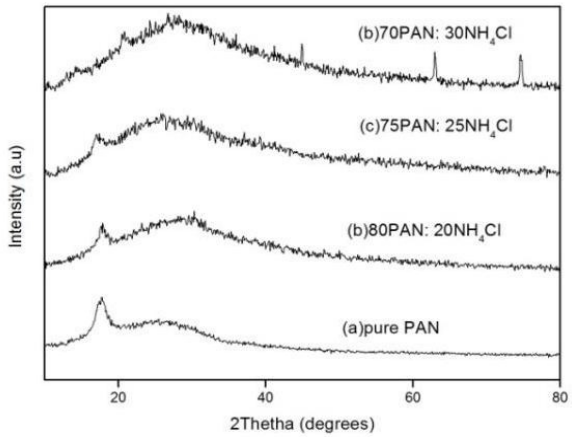


Figure.1 XRD Pattern of Pure PAN and PAN doped with different molWt% of NH_4Cl

3.2. FTIR analysis

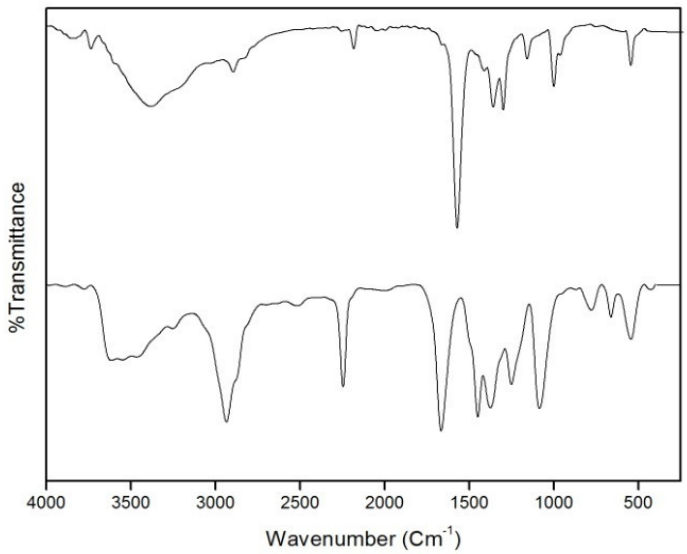


Figure.2 FTIR Spectrum of Pure PAN and 75 PAN: 25 mol% NH_4Cl

FTIR (Fourier Transform Infrared) Spectroscopy provides information regarding various nature of chemical bonding. Fig 2 shows the FTIR spectra of Pure PAN and 75PAN:25NH_4Cl polymer electrolyte. The peak at 2245cm^{-1} is attributed to the C≡N stretching vibration of acrylonitrile unit in the polymer chain. The

band at 2926 cm-1 is attributed to ν C-H in CH_2. The δ C-H in CH_2 is assigned at 1451 cm^{-1}. The weak absorption at 1655 cm^{-1} may be attributed to C=C (νC=C) [8, 9, 10, 11]. The intensity of above peaks has either decreased or increased and the peak positions get shifted due to the interaction of the salt with the polymer matrix. The above results confirm the complex formation between polymer and salt.

3.3. AC Impedance analysis

The a.c impedance technique is a powerful method for characterizing the electrical properties of materials. Fig 3 shows the cole-cole plot of PAN doped with NH_4Cl of different concentration at 303K. The plots consist of a high frequency depressed semicircle represented by a frequency dependent capacitor C_g parallel to a bulk resistor (R_b) and a low frequency spike represented by a constant phase element CPE. The disappearance of semicircle in the impedance plot leads to a conclusion that the current carriers are ions mainly due to the ion conduction [12].

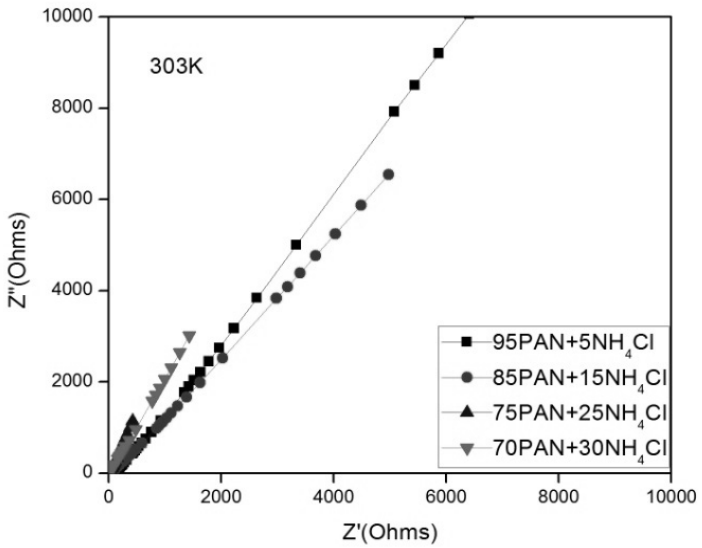


Figure 3. Cole-Cole plot of all composition of polymer electrolyte at room temperature

.

The ionic conductivity is calculated using the relation,

$$\sigma = l/(R_b.A)$$

where l is the thickness of the film, R_b is the bulk resistance, and A is contact area of the electrolyte film.

The EQ software program developed by B.A. Boukamp et al [13] has been used to extract the bulk electrical resistance (R_b) of the polymer electrolytes from the impedance plot of the low frequency side intercept on the Z' axis. The highest room temperature conductivity value is found to be $6.4X10^{-3}Scm^{-1}$ for the system $75PAN:25NH_4Cl$.

3.4. Conductance Spectra

The logarithmic plots of the conductivity as a function of angular frequency for all the polymer electrolytes at ambient temperature is shown in Fig. 4 can be divided into a frequency-independent plateau region in the low frequency range and high frequency dispersion region. The frequency-independent plateau region is connected with the σ_{dc} of the complexed polymer electrolyte. The extrapolation of the plateau region to zero frequency gives the value of dc conductivity at all temperatures. In the higher frequency domain, the conductivity increases as the frequency increases. However, at high frequencies, the conductivity is observed to be much less temperature-dependent than the dc conductivity.

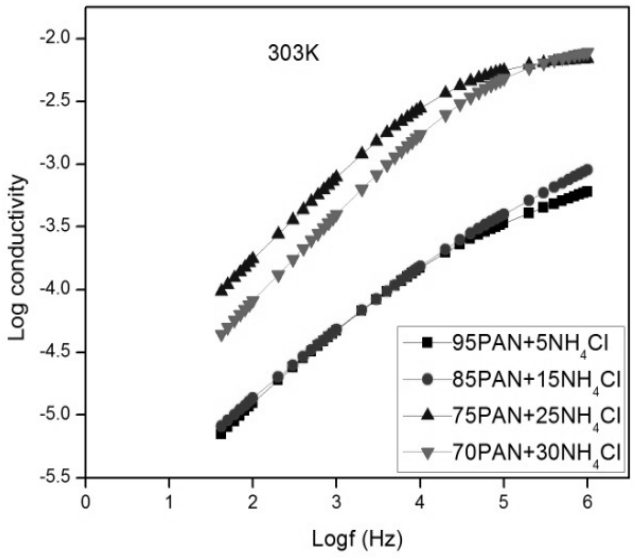


Figure 4 Conductance spectra for different composition of PAN: NH_4Cl at room temperature

3.5. Dielectric analysis

The dielectric behaviour of the polymer electrolyte brings about important insights in to ionic transport phenomenon [14]. The measured impedance data are used to calculate the real and imaginary parts of the complex permittivity using the relation

$$\varepsilon^* = \varepsilon'(\omega) - \varepsilon''(\omega) = 1/j\omega c_0 z^*$$

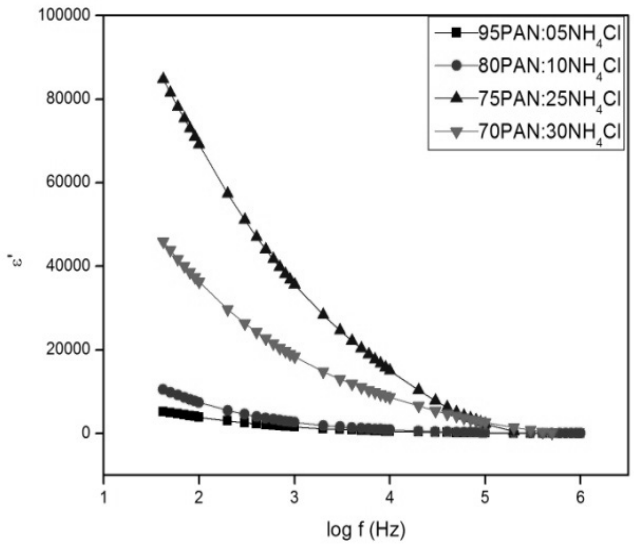


Figure. 5 Dielectric spectra for different composition of PAN: NH_4Cl at room temperature

Real ε' and imaginary ε'' components are the storage and loss of energy in each cycle of the applied electric field [15]. Fig 5 represents frequency dependence of ε' (ω) for room temperature. The increase in the dielectric constant represents a fractional increase in charges within the polymer electrolyte. It is clear that the values of ε' (ω) very high at a very low frequency region. It has been explained by the presence of space charge effects which is contributed by the accumulation of charge carriers near the electrode [16]. At high frequencies, ε' (ω) have been found to be relatively constant with frequency. This is because periodic reversal of the field takes place so rapidly that the charge carriers will be able to orient themselves in the field direction resulting in decrease of dielectric constant [17]. A high dielectric constant has been found for 25mol % NH_4Cl doped polymer electrolyte.

3.6 Modulus spectra studies

Fig 6 represents the frequency dependence of M' (ω) for room temperature. Modulus spectra show an increase at the high frequency end, but well defined dispersion peaks are not observed. This increase of modulus value in the plot at higher frequencies may be due to the bulk effect. With the increase of temperature, the height of the peak decreases suggesting a plurality of relaxation mechanism [18].

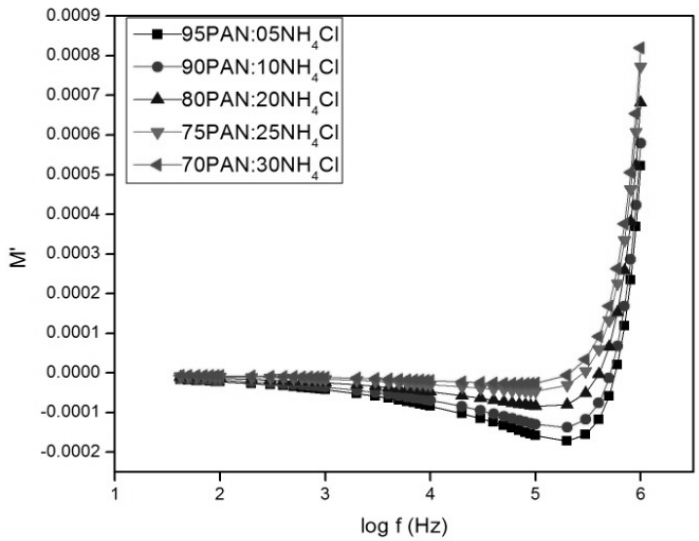


Figure 6. Modulus spectra for different composition of PAN: NH_4Cl at room temperature

4. Conclusion

Polyacrylonitrile (PAN) based proton conducting polymer electrolytes with ammonium chloride (NH_4Cl) in different mole percentage have been prepared by solution casting technique. The XRD analysis reveals the increase in amorphous nature of the polymer electrolytes. The FTIR provides evident for complexation of salt (NH_4Cl) with polymer (PAN). From the conductivity analysis the highest conductivity at room temperature have been found to be $6.4x10^{-3}Scm^{-1}$ for $75PAN:25NH_4Cl$ polymer electrolyte. The low frequency dispersion of dielectric constant reveals the space charge effects arising from the electrodes.

References

1. C. Farrington and J.L. Briant science **4** (1979) 1371; 'solid electrolytes and their applications' (edited by E.C. Subba Rao), plenum press, NY (1980)
2. Wagner JB, Wagner C (1957) J Chem Phys **26**:1597
3. Song J.Y, Wang Y.Y, and Wan C.C, J.Power Sources, **77**:183, (1999)
4. G. Nagasubramanian, A. I. Attia, G. Halpert, J. Appl. Elec. Chem. **24** 298-302, (1994)
5. Zhongping Zhang, Lide Zhang, Shixing Wang, Wei Chen, Yong Lei, Polymer **42** 8315-8318 (2001)
6. C.S. Ramya etal J. Non Crys Solids **354**, 1494-1502, (2008)
7. A.Ahmad, K.B.Md.Isa and Z.Osman, Malaysia Polymer International Conference (MPIC 2009)
8. .S. Dalton, F. Heatley, P. M. Budd, Polymer, **40**, 5531, (1999)
9. Xue T J, Mckinney M A, Wilkie C A. The thermal degradation of Polyacrylonitrile. Polymer Degradation and Stability, **58**,193-202, (1997)
10. Q. Ouyang, L. Cheng, H. Wang, K. Li, Polymer Degradation and stability **93**, 1415-1421, (2008)
11. M Ji, C Wang, Y Bai, M Yu, Y Wang. Polymer Bulletin **59**, 527-536(2007)
12. Izuchi S, Ochiai S, Takeuchi K J Power sources 1987, 68, **37**
13. B. A. Boukamp, Solid State Ionics, **20** (1986) 301
14. Mac Callum JR, Vincent CA, (1989) Polymer electrolyte reviews. Elsevier, London
15. Dutta P, Biswas S, (2002) Mater Res Bull**37**:193-200
16. Amstrong RD, Dickinson T, Wills PM (1974) J Electro anal chem. **53** (3): 389-405
17. Adachi K, Urakawa O, (2002) J Non-Cryst solids 307-310; 667-670
18. Ramesh S, Arof AK (3001) Mater.Sc.Eng B 2001 **85**:11-15.

STUDY OF BIO – DEGRADABLE POLYMER PCL WITH NH_4SCN

D.VINOTH PANDI
Materials Research Centre, Coimbatore, Tamil Nadu, India

S. SELVASEKARAPANDIAN*
Materials research centre, Coimbatore, Tamilnadu, India

N. VIJAYA
Department of Physics, SFR College for women, Sivakasi, Tamilnadu, India

C.SANJEEVIRAJA
Department of Physics,Alagappa ChettiarCollege of Engineering & Technology, Karaikudi,Tamilnadu, India

Abstract

Membrane of PCL doped with NH_4SCN of different concentration (0.1 – 0.6 mol. Wt. %) have been prepared by solution casting technique using DMF as solvent. XRD, FTIR and Ac Impedance studies have been undertaken for the above mentioned film. XRD pattern of pure PCL shows peak at (21^O, 24^O). Above two peak decreases in intensity as the concentration of NH_4SCN increases. Complex formation between PCL and NH_4SCN has been confirmed by FTIR analysis. The ionic conductivity is $1.24x10^{-05}$ S/cm for PCL 1g : NH_4SCN 0.6 mol. Wt. % membrane. Dielectric and Modulus results have been discussed.

1. Introduction

Research on bio degradable polymers has received increasing attention in recent years because of their wide application in environmentally friendly packaging biomedical materials but also in various industrial applications such as computer and mobile phone industry. The most popular biodegradable polymers are aliphatic polyester such as PCL, Polylactic acid, Poly (butylenes adipate teraph thalate), poly hydroxy butyrale.

Among biodegradable Polymer PCL, a semicrystalline linear aliphatic polyester known for the compatibility and bio degradability which make it useful material resorbable surfaces, drug delivery systems, etc. PCL is one of more hydrophobic of the commercially available. It has a good mechanical property with low melting point and low Tg around -60^0C [1-3]. Study of proton conducting polymer electrolyte based on PCL is rare in the literature. Ammonium salts are found to be good proton donor. So proton conducting polymer electrolyte based on PCL and NH_4SCN has been developed and various characterization such as

Proceedings of the 14th Asian Conference on Solid State Ionics (ACSSI 2014)
Copyright © 2014 ACSSI 2014 Organizers. All rights reserved.
ISBN: 978-981-09-1137-9
doi:10.3850/978-981-09-1137-9_041

XRD, FTIR AC Impedance have been made and the results are presented in this paper.

2. Experimental Technique

Biodegradable Polymer electrolyte based on PCL and NH_4SCN have been prepared by solution casting technique using DMF as solvent. The required amount of PCL and NH_4SCN dissolved in DMF and stirred continuously to get homogeneous solution and solution is transferred to petri dishes for evaporation of solvent at 50^0C to free standing films of composition pure PCL, PCL : 0.1 to 0.6 mol wt % polymer electrolyte of NH_4SCN. XRD measurements are made with Philips X' pert PRO diffractometer using CuK_α radiation. FTIR measurements are made with Bruker spectrophotometer. Impedance measurements are made using HIOKI 3532 LCR impedance analyser in the frequency range 42 Hz to 1 MHz.

3. Results and discussion

3.1XRD analysis

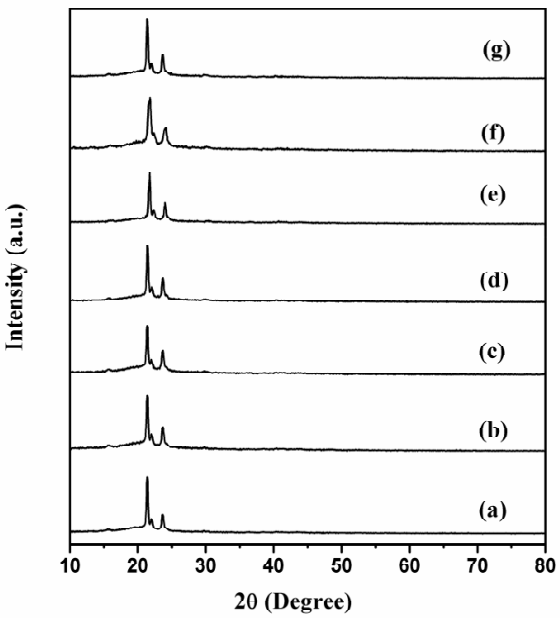


Figure.1 XRD pattern of (a) Pure PCL, (b)PCL1g : 0.1mol.wt. % NH_4SCN,(c) PCL1g : 0.2mol.wt. % (d) PCL1g: 0.3mol.wt. % (e) PCL1g : 0.4mol.wt. % NH_4SCN (f) PCL1g : 0.5mol.wt. % NH_4SCN (g) PCL1g: 0.6mol.wt. % NH_4SCN polymer electrolytes.

XRD measurements for polymer electrolyte based on PCL and PCL doped with NH_4SCN is shown in figure 1. Three sharp peaks at $2\theta = 21.2^0$, 22^0, 23.7^0 corresponding to (110), (111) and (200) orientations respectively of the orthorhombic crystal (4) structure are observed for pure PCL (curve c). The intensity of above mentioned peak decreases for polymer electrolyte 1 gm PCL with different concentration of NH_4SCN (0.1 to 0.6 mol. wt. %) curve (b-g). Peaks at 22^0 get reduced to shoulder as the concentration of NH_4SCN is increased from 0.1 to 0.6 mol. wt. %. It is observed that as the concentration of NH_4SCN increases in the polymer matrix the amorphous nature also increases which is obtained from the increase in broadness and decrease in intensity of the peaks with respect to that of pure polymer which can be interpreted in terms of the criterion of Hodge et. al. (5) which establishes a correlation between the height of the peak and the degree of crystallinity. It is also observed that in the XRD pattern of PCL: NH_4SCN complexes there are no peaks corresponding to pure NH_4SCN which indicates the complete dissociation of salt in the copolymer matrix.

3.2 FTIR analysis

FTIR spectroscopy has been a powerful tool for identifying the nature of bonding and different functional groups present in a sample by monitoring the vibrational energy levels of the molecules which are essentially the fingerprint of different molecules. FTIR spectra of pure PCL (curve a) and 1gm of PCL doped with different concentration (0.1 to 0.6 mol. wt. %) of NH_4SCN are shown in figure 2 (curve b-g). Various assignment of FTIR peaks of pure PCL and 1 gm of PCL with different concentration of NH_4SCN (0.1 to 0.6 mol. wt. %) are provided in table 1.

Change in intensity and shifts in the frequency of PCL doped NH_4SCN of different concentration when compared to pure PCL confirms the complex formation between PCL and NH_4SCN.

Table 1. FTIR band assignments for PCL and PCL doped NH_4SCN polymer complexes

Pure PCL	PCL 1g : X mol. wt. %						ASSIGNMENT
	X=0.1	X=0.2	X=0.3	X=0.4	X=0.5	X=0.6	
1167	1175	1172	1170	1169	1173	1171	symmetric C-O stretching
1237	1238	1236	1237	1232	1238	1237	Asymmetric C-O stretching
1722	1719	1717	1720	1723	1716	1719	Carbonyl stretching
2902	2909	2907	2912	2913	2910	2911	Asymmetric CH_2 stretching

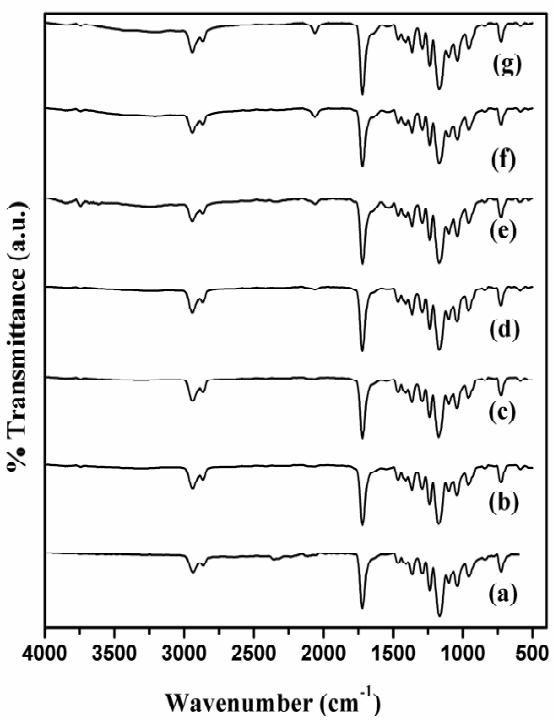


Figure.2 FTIR pattern of (a) Pure PCL, (b)PCL1g : 0.1mol.wt. % NH_4SCN,(c) PCL1g : 0.2mol.wt. % (d) PCL1g : 0.3mol.wt. % (e) PCL1g : 0.4mol.wt. % NH_4SCN (f) PCL1g : 0.5mol.wt. % NH_4SCN (g) PCL1g : 0.6mol.wt. % NH_4SCN polymer electrolytes.

3.3 Ac Impedance Analysis

Impedance spectroscopy is a powerful technique of characterization of many of the electrical properties of electrolyte materials and their interfaces with electronically conducting electrodes. Figure 3 and 4 shows the cole-cole plot for pure PCL, 1g PCL: 0.1 mol. wt. % of NH_4SCN, 1g PCL: 0.2 mol. wt. % of NH_4SCN, 1g PCL: 0.3 mol. wt. % of NH_4SCN, 1g PCL: 0.4 to 0.6 mol. wt. % of NH_4SCN respectively. The plot consists of a high frequency semi circle which yields information about the properties of the electrolyte and the low frequency spike carriers information on the electrode electrolyte interfacial properties. High frequency semicircle yields the bulk resistance (R_b), intensity R_b and ω_{max}, the bulk capacitance C_b can be calculated using the relation $R_b C_b \omega_{max} = 1$. Spikes inclined at an angle of less than 90^0 to the real axis and this is due to roughness of the electrode/electrolyte (6).

The 'EQ' software programme developed by Boukamp has been used to find bulk resistance of the polymer electrolytes. The ionic conductivity (σ) of the polymer electrolytes can be calculated using the equation

$$\sigma = \frac{l}{AR_b} \quad \text{---------- (1)}$$

Where l and A are the thickness and area of the polymer electrolyte and it is given in the table 2. It is observed that maximum ionic conductivity, $\sigma = 1.3044 \times 10^{-5}$ S/cm for PCL : 0.6 mol wt% NH_4SCN.

Table.2 Ionic conductivity values of pure PCL, different mol. wt. % of NH_4SCN doped PCL at room temperature

Sample	**Conductivity σ (Scm^{-1})**
Pure PCL	2.16042×10^{-08}
PCL 1g : 0.1 (mol. Wt. %) NH_4SCN	1.29627×10^{-07}
PCL 1g : 0.2 (mol. Wt. %) NH_4SCN	1.44119×10^{-07}
PCL 1g : 0.3 (mol. Wt. %) NH_4SCN	2.0598×10^{-07}
PCL 1g : 0.4 (mol. Wt. %) NH_4SCN	7.7198×10^{-07}
PCL 1g : 0.5 (mol. Wt. %) NH_4SCN	1.2421×10^{-06}
PCL 1g : 0.6 (mol. Wt. %) NH_4SCN	1.3044×10^{-05}

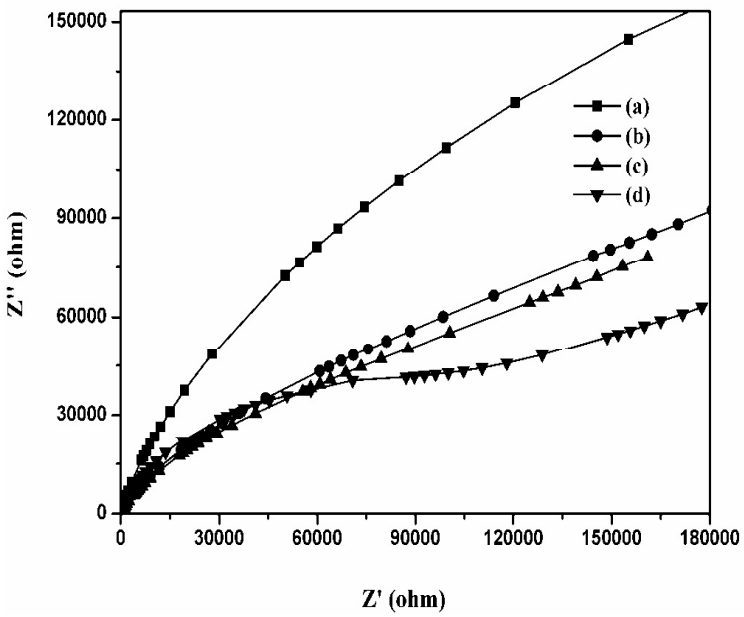


Figure.3 Impedance plot of (a) Pure PCL, (b)PCL1g : 0.1mol.wt. % NH_4SCN,(c) PCL1g : 0.2mol.wt. % (d) PCL1g : 0.3mol.wt. % CN polymer electrolytes at 303K

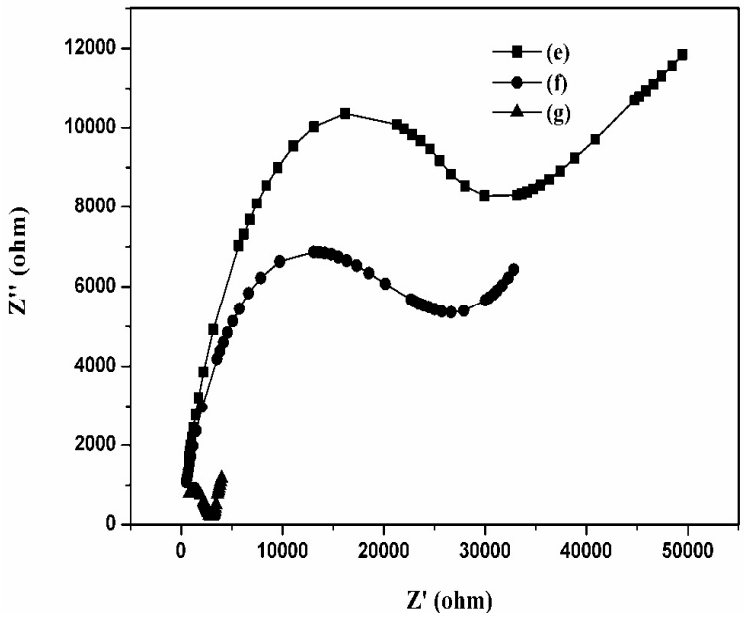


Figure.4 Impedance plot of (b)PCL1g : 0.4mol.wt. % NH_4SCN,(c) PCL1g : 0.5mol.wt. % (d) PCL1g : 0.6mol.wt. % CN polymer electrolytes at 303K

3.4 Conductance Spectra

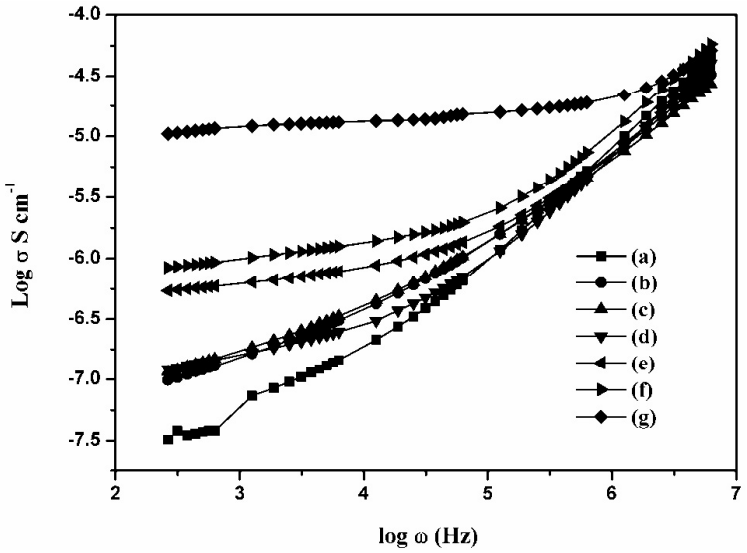


Figure 5. Conductance spectra for (a) Pure PCL, (b)PCL1g : 0.1mol.wt. % NH_4SCN,(c) PCL1g : 0.2mol.wt. % (d) PCL1g : 0.3mol.wt. % (e) PCL1g : 0.4mol.wt. % NH_4SCN (f) PCL1g : 0.5mol.wt. % NH_4SCN (g) PCL1g : 0.6mol.wt. % NH_4SCN polymer electrolytes at 303K

The dc conductivity of the mobile species in the polymer electrolyte has been determined from conductance spectra. The logarithmic plots of the variation of ionic conductivity with of angular frequency for all polymer electrolytes at room temperature have been shown in Fig. 5 At low frequency the ionic conductivity is high enough to produce significant buildup charges at the electrodes which reduces the effective applied field and hence the conductivity. At high frequencies range the period of the applied field is too short for charging to occur and the Ac conductivity is generally taken to assure the frequencies independent value which is equal to the dc conductance. The extrapolation of the dc plateau on the log σ axis use the dc conductivity value which agrees with the values calculated from cole – cole plot.

3.5 Dielectric analysis

The complex permittivity or dielectric constant of a system has been defined by

$$\varepsilon^* = \varepsilon' - j\,\varepsilon''$$

where ε', ε'' are the real and imaginary part of dielectric constant of the material. The fig 6 & fig 7 show the variation of ε' *vs.* log f and ε'' *vs.* log f plots respectively for the polymer electrolyte. As seen from Fig. 6, the dielectric

permittivity has risen sharply towards low frequencies which is due to the electrode polarization effects (7).

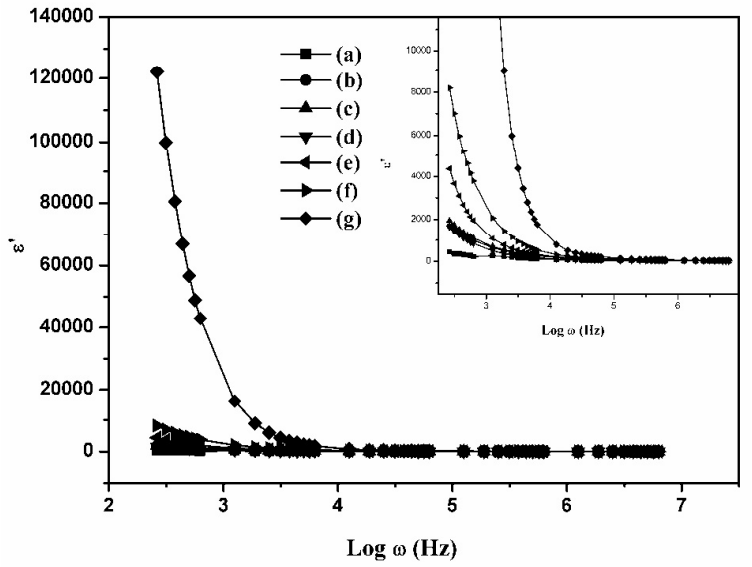


Figure 6 Variation of ε′ as a function of frequency of (a) Pure CA, (b)PCL1g : 0.1mol.wt. % NH_4SCN,(c) PCL1g : 0.2mol.wt. % (d) PCL1g : 0.3mol.wt. % (e) PCL1g : 0.4mol.wt. % NH_4SCN (f) PCL1g : 0.5mol.wt. % NH_4SCN (g) PCL1g : 0.6mol.wt. % NH_4SCN polymer electrolytes at 303K.

At high frequencies, due to high periodic reversal of the field at the interface, the contribution of charge carriers towards the dielectric constant has decreased with increased frequencies. Hence ε′ has decreased with increased frequency. From fig 7 it is observed that dielectric loss (ε″) has become very large at lower frequencies due to the recharge motion with in the material (8). This values does not corresponds to bulk dielectric processes but are due to free charges build up at the interface between the material and the electrode. At very low frequencies there is time for charges to build up at the interfaces before the field charges the direction and this has contributed to very large apparent values for ε″ (9).

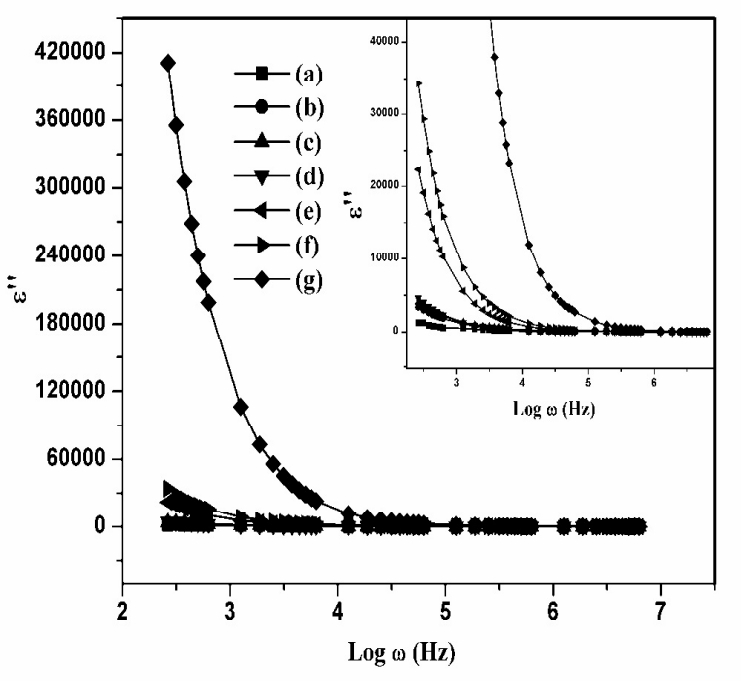


Figure 7 Variation of ε″ as a function of frequency of (a) Pure CA, (b)PCL1g : 0.1mol.wt. % NH_4SCN,(c) PCL1g : 0.2mol.wt. % (d) PCL1g : 0.3mol.wt. % (e) PCL1g : 0.4mol.wt. % NH_4SCN (f) PCL1g : 0.5mol.wt. % NH_4SCN (g) PCL1g : 0.6mol.wt. % NH_4SCN polymer electrolytes at 303K.

3.6 Modulus Spectra analysis

The complex electric modulus was first applied to the study of glasses by Macedo et.al. in studies of dielectric properties of alkali silicate glass and is given by the equation

$M^* = M'+jM''=j\omega C_O Z$

The real and imaginary parts of the modulus are plotted against log f for pure PCL and PCl doped with different concentration of NH_4SCN for all the polymer electrodes as seen from fig 8 & fig 9 the value of M' and M" show an increase at high frequency and which might be due to the bulk effect of the polymer electrolyte. At low frequencies M' & M" approaches zero indicating that the electrode polarization phenomena made a negligible contribution (10).

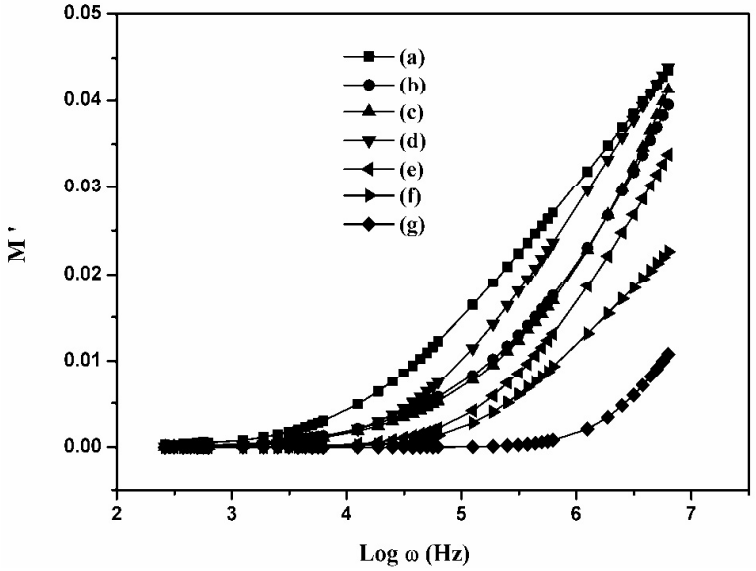


Figure 8 Variation of M′ as a function of frequency of (a) Pure CA, (b)PCL1g : 0.1mol.wt. % NH_4SCN,(c) PCL1g : 0.2mol.wt. % (d) PCL1g : 0.3mol.wt. % (e) PCL1g : 0.4mol.wt. % NH_4SCN (f) PCL1g : 0.5mol.wt. % NH_4SCN (g) PCL1g : 0.6mol.wt. % NH_4SCN polymer electrolytes at 303K.

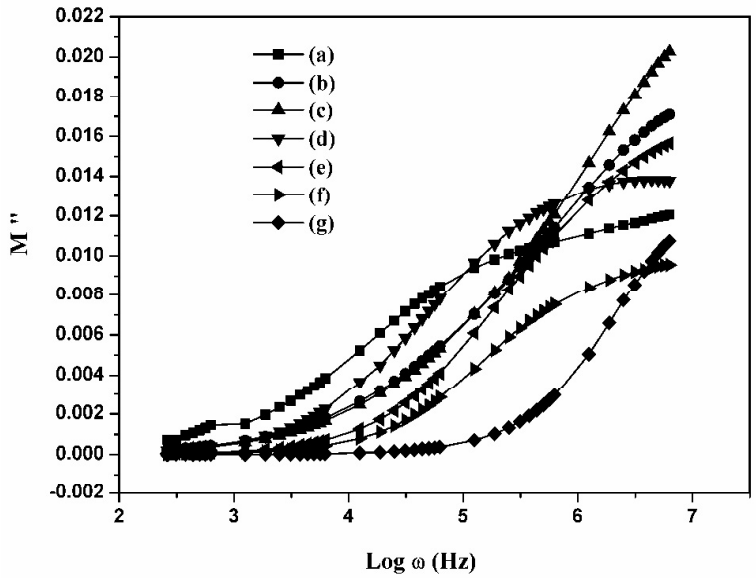


Figure 9 Variation of M″ as a function of frequency of (a) Pure CA, (b)PCL1g : 0.1mol.wt. % NH_4SCN,(c) PCL1g : 0.2mol.wt. % (d) PCL1g : 0.3mol.wt. % (e) PCL1g : 0.4mol.wt. % NH_4SCN (f) PCL1g : 0.5mol.wt. % NH_4SCN (g) PCL1g : 0.6mol.wt. % NH_4SCN polymer electrolytes at 303K.

4. Conclusion

Bio – degradable proton conducting polymer electrolyte based on PCL and NH_4SCN have been developed. The maximum ionic conductivity $\sigma = 1.3044 \times 10^{-05}$ S/cm for 1g of PCL doped with 0.6 mol. Wt. % of NH^4SCN

References

1. JeriSperacek, Jiri Brus , European Polymer Journal 43 (2007) 1866-1875

2. Abdellathif Mohamed, Sherald H. Gorden Polymer Degradable and Stability 92 (2007)1177-1185

3. Hae young Kween, m, Kyang Yoo Biomaterials 24 (2003) 801-808

4. Tamava Elzer , Mohamed Nasser –Eddine, Journal of Coolid and Interface Science 273 (2004) 381-383

5. R.M. Hodge, G.H.Edward, G.P. Simon (1996) Polymer **37**:1371-1376.

6. Manuel Stephen A, J.Power sources 81-82 (1998) 752-758

7. K.J. Rao, Solid State Ionics 106 (1998) 113

8. F.S.Howell, R.A.Bose, J.Phys.Chem 78 (1974) 639

9. J.C.Dyre J.Non Crystalline Solids 135 (1991) 219

10. G. Hirankumar, characterization of solid state polymer electrolyte based on PVA, Ph.D thesis Bharathiar university 2005.

BIO – POLYMER PECTIN BASED PROTON CONDUCTING POLYMER ELECTROLYTE

N. VIJAYA
Department of Physics, S.F.R. College for Women, Sivakasi--626123, Tamil Nadu, India

S. SELVASEKARAPANDIAN*
*Materials Research Center, Coimbatore-641*045, Tamil Nadu, India*

D. VINOTH PANDI
Materials Research Center, Coimbatore-641045, Tamil Nadu, India

A.ARUN
Department of Chemistry, Government Arts College, Thiruvannamalai-606603, Tamil Nadu, India

S. KARTHIKEYAN
Department of Physics, Ramco Institute of Technology, Rajapalayam-626117, Tamil Nadu, India

M. SINDHUJA
Materials Research Center, Coimbatore-641045, Tamil Nadu, Indi

Proton conducting polymer electrolyte based on Bio polymer pectin doped with different concentration of NH_4SCN have been prepared by solution casting technique using double distilled water as solvent. XRD, FTIR and Ac Impedance studies have been undertaken for the above Bio polymer films. XRD Pattern indicates that the amorphous nature of the pure pectin increases on addition of different concentration of NH_4SCN. The amorphous nature is maximum for 50 mol% Pectin doped with 50 mol% NH_4SCN. Complex formation between the polymer and the salt has been confirmed by FTIR spectroscopy analysis. Ac Impedance study shows that ionic conductivity of pure pectin film is 5.64×10^{-8} S/cm. The ionic conductivity of the pectin film doped with NH_4SCN increases as the concentration of the NH_4SCN increases. The ionic conductivity is 4.505×10^{-4} S/cm for 50 mol% pectin-50 mol% NH_4SCN. Dielectric and modulus behavior have been undertaken further.

* Corresponding author: sekarapandian@rediffmail.com

Proceedings of the 14th Asian Conference on Solid State Ionics (ACSSI 2014)
Copyright © 2014 ACSSI 2014 Organizers. All rights reserved.
ISBN: 978-981-09-1137-9
doi:10.3850/978-981-09-1137-9_043

1. Introduction

Much effort has been focused in recent years to develop environmentally compatible bio-plastic products from naturally renewable materials as an alternative to synthetic polymers. Films made from natural products are of increasing scientific and commercial interest. They are not only biodegradable but may be recyclable as well as acceptable for various electrochemical devices. Pectin, a biodegradable polysaccharide found in higher plant cells is a naturally occurring bio polymer. Pectin is a complex mixture of polysaccharides that contain methylated ester of poly (galacturonic acid), which consists of chains of 300–1000 galacturonic acid units **[1].** At present, commercial pectins are almost exclusively derived from citrus peel or apple pomace, which are by-products from juice (or cider) manufacturing processes [2]. Pectin is water soluble polymer with fairly good biodegradable nature which can be exploited for designing pectin films **[3]**.

The pectin derived films have shown potential applications in coating, encapsulating and thickening for food and pharmaceutical uses [**4**]. Several reports on various biomedical applications of pectin-based materials are found in literature. Liu et al **[5]** developed pectin/poly (lactide-co-glycolide) (PLGA) composite matrices for the delivery of bioactive substances for tissue regeneration. R.K.Mishra et al **[6-9]** have studied pectin-based blend films for applications. Ammonium salts are found to be proton donor to polymer matrix. The study of proton conducting polymer electrolytes based on pectin doped with ammonium salts is rare. The aim of this work is to develop a proton conducting membrane from bio polymer pectin doped with ammonium thiocyanate.

2. Materials and Methods

Pectin (Chemical Grade, M_W ~30000–100000 and degree of esterification (DE = 63-66%) has been purchased from Loba-chemie Pvt. Ltd. Mumbai, India. Ammonium thiocyanate has been obtained from Spectrum, India. Double distilled water is used as the solvent. The technique adopted to prepare the polymer electrolytes is the conventional solution casting technique.

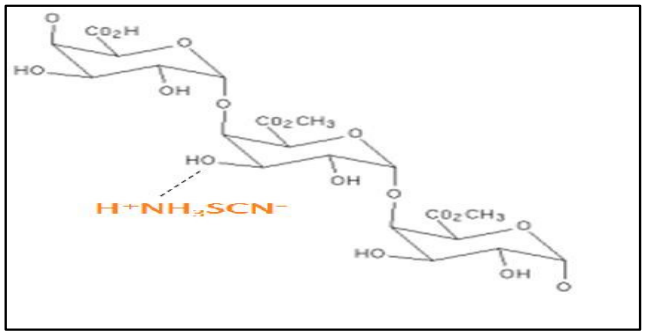
To prepare the proton conducting polymer electrolytes based on pectin doped with ammonium thiocyanate (NH_4SCN), aqueous solutions of pectin and NH_4SCN with different compositions (in mol%) have been prepared and stirred continuously with magnetic stirrer for several hours until the solutions become homogeneous. After complete dissolution of Pectin and NH_4SCN, the solutions are cast into plastic petri dishes and left to dry at room temperature for 24 hours

under vacuum. Then the films are peeled from plastic dishes and subjected to various experimental techniques for characterization.

Philip's X'Pert PRO diffractometer with CuKα radiation has been used to record the X-ray Diffraction (XRD) patterns of the films at room temperature in the range of 2θ from 10º to 80º. Fourier Transform- Infra-red (FT-IR) spectroscopy measurements are carried out at room temperature using a Bruker Spectrophotometer in the wavenumber range 400–4000 cm^{-1}. The AC impedance measurements are carried out on the films with aluminium blocking electrodes using a HIOKI 3532 LCZ meter of frequency range 42 Hz–1MHz at room temperature.

3. Results and Discussion

3.1. The possible interaction of the NH_4SCN salt with the pectin biopolymer is shown in scheme 1. The proton from the cation (NH_4^+) of the dissociated salt may interact with the hydroxyl group of the pectin.



Scheme 1 Possible interaction between NH_4SCN and pectin

3.2. *XRD Analysis*

Figure 1 shows X-ray diffraction pattern of pure pectin and different compositions of pectin-NH_4SCN polymer electrolyte. The X-ray diffractogram of pure pectin shows one broad peak and relatively two narrow peaks at 2θ equals to 13.5º, 18º and 20º indicating the amorphous nature of pure pectin. On addition of NH_4SCN salt to the pectin, the intensity of the diffraction peak of pure pectin at 13.5º decreases and becomes minimum for the composition of 50 mol% pectin-50 mol% NH_4SCN while the other two peaks of pure pectin combine to form a single peak at around 20.8º in the case of pectin doped with different concentration of the salt.

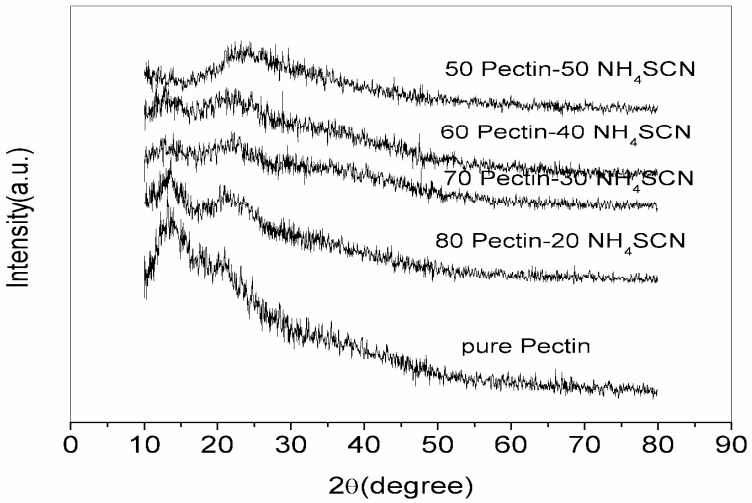


Figure 1 X-ray diffraction pattern of pure pectin and different compositions of pectin-NH_4SCN polymer electrolyte

It is observed from the diffractograms of the pectin-NH_4SCN electrolyte films that the broadness of this single peak increases with the increase of NH_4SCN content in the concentration range studied in this work. A shift in this peak is also observed as the concentration of the NH_4SCN is increased. These changes may be due to the interaction of the NH_4SCN with the pectin. From the XRD analysis, it is observed that the amorphous nature of the pectin film increases with increasing salt concentration and the electrolyte film 50 mol% pectin- 50 mol% NH_4SCN is found to be more amorphous.

3.3. *FTIR Analysis*

The FTIR spectra of various compositions of Pectin-NH_4SCN electrolyte films are shown in figure 2 which show a band around 3200 cm^{-1} due to the stretching of –OH groups. The peaks around 2922 cm^{-1} and 1734 cm^{-1} indicate –C–H stretching vibration and C = O stretching vibrations due to the presence of $–COOCH_3$ group, respectively [6]. The peaks at 1428 cm^{-1} and 1326 cm^{-1} could be assigned to $–CH_2$ scissoring and –OH bending vibration, respectively. The peak at 1068 cm^{-1} suggests –CH–O–CH– stretching. The peak positions and their assignments are listed in Table 1.

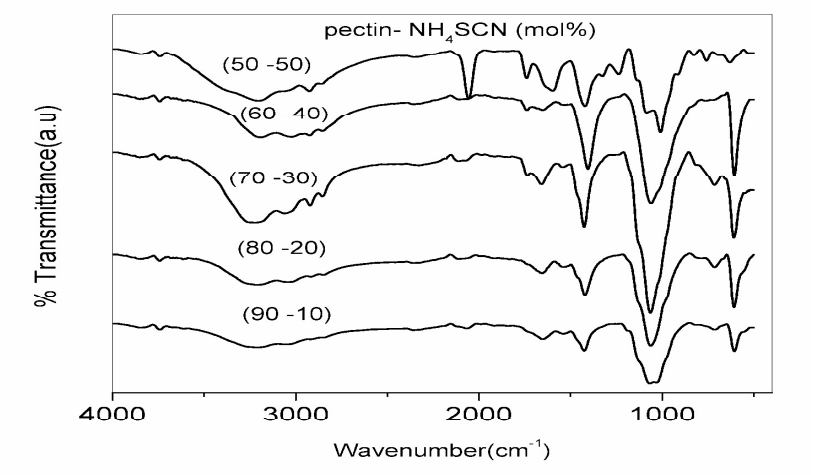


Figure 2 FT-IR spectra of Pectin-NH_4SCN polymer membrane

Table 1 Absorption peaks of Pectin-NH_4SCN (mol%) polymer Electrolyte

Absorption peaks of Pectin-NH_4SCN (mol%) polymer Electrolyte (cm^{-1})					Peak Assignment
90 -10	80-20	70-30	60-40	50-50	
1068	1063	1064	1060	1085	-CH-O-CH- Stretching
-	-	-	-	1326	-OH Bending
1428	1422	1426	1405	1421	CH_2 Bending
1730	1732	1734	1736	1740	-$COOCH_3$ (Carboxy methyl group)
2918	2920	2922	2924	2926	-CH Stretching
3210	3209	3223	3192	3205	-OH Stretching

The characteristic absorption peaks of the pectin are found to be shifted in the pectin-NH_4SCN complexes. New peaks are also observed in the 50 mol% Pectin-50 mol% NH_4SCN film. In addition, the intensity of all the peaks changes as the concentration of NH_4SCN salt changes. This reveals the complex formation between the polymer and the salt**.**

3.3. *AC impedance Analysis*

The Complex impedance (Cole-Cole) plots for pure pectin and different compositions of pectin-NH_4SCN complexes have been presented in figure 3(a) &(b).

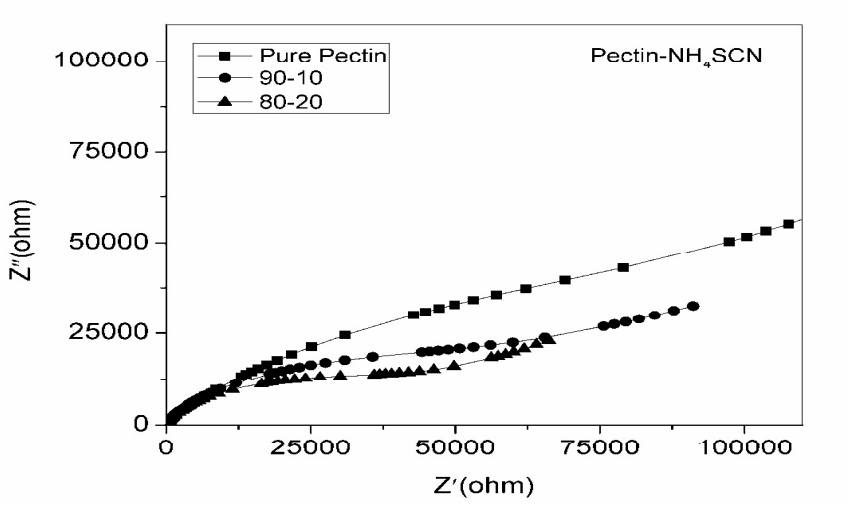


Fig. 3 (a) Cole – Cole plots for different compositions of Pectin-NH_4SCN (in mol%) at room temperature

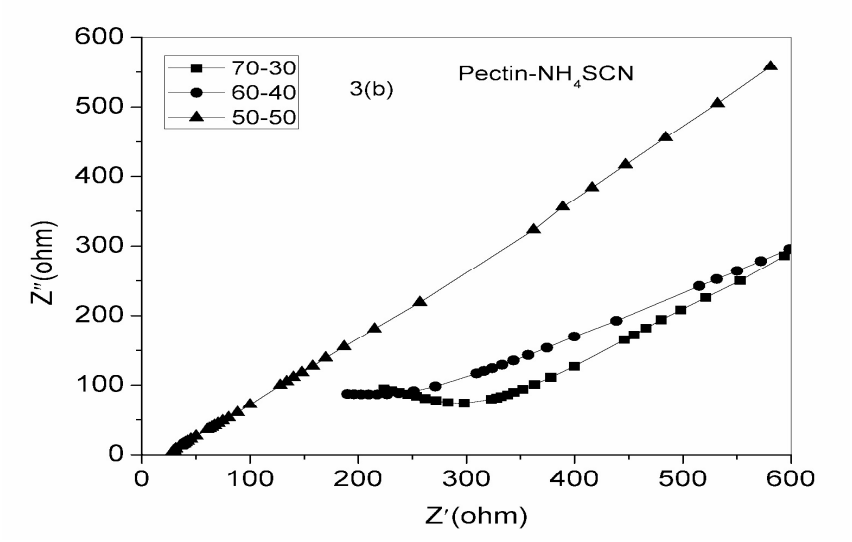


Fig. 3(b) Cole – Cole plots for different compositions of Pectin-NH_4SCN (in mol%) at room temperature

The plot consists of a high-frequency semicircle representing the parallel combination of bulk resistance and capacitance which is due to the bulk effect of the electrolytes and a low frequency spike which may be due to the effect of the blocking electrodes [10]. The intercept of the semicircle or spike with the real impedance (Z') axis gives the bulk resistance (R_b) of the polymer-salt complexes. The EQ software program developed by Boukamp [11] is used to extract the bulk electrical resistance (R_b) of the polymer electrolytes. The radius of the semicircle decreases with increasing concentration of NH_4SCN indicating the decrease in bulk resistance of the electrolyte films. The ionic conductivity has been calculated by the equation $r_b = l/(R_bA)$, where l is the thickness of the film and A, the surface area of the film. The conductivity values are tabulated in Table 2. The highest conductivity is found to be 4.505×10^{-4} S/cm at 303 K for 50 mol% pectin-50 mol% NH_4SCN.

Table 1 Ionic conductivity values for different compositions of Pectin-NH_4SCN Polymer Electrolytes at 303 K

S. No.	Composition of Pectin and NH_4SCN	Ionic Conductivity, σ (S cm^{-1})
1	100 mol% Pectin-0 mol% NH_4SCN	5.640×10^{-8}
2	90 mol% Pectin-10 mol% NH_4SCN	1.949×10^{-7}
3	80 mol% Pectin-20 mol% NH_4SCN	3.243×10^{-7}
4	70 mol% Pectin-30 mol% NH_4SCN	3.602×10^{-5}
5	60 mol% Pectin-40 mol% NH_4SCN	3.891×10^{-5}
6	50 mol% Pectin-50 mol% NH_4SCN	4.505×10^{-4}

3.4. Conductance spectra Analysis

The logarithmic plots of the conductivity as a function of angular frequency for Pectin-NH_4SCN complexes are depicted in figure 4.

As seen from the figure 4, the conductance spectra show three regions, a low frequency dispersion region due to the space charge polarization at the blocking electrodes [12], frequency independent

plateau region in the mid frequency range representing the dc conductivity and dispersive region at high frequencies corresponding to

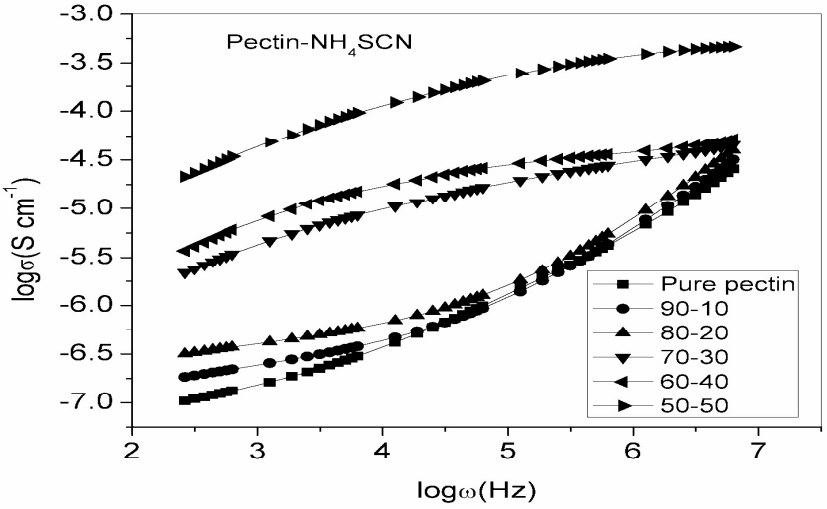


Figure 4 Conductance Spectra for different compositions of Pectin : NH_4SCN (in mol%) at room temperature

the bulk relaxation phenomena. The extrapolation of the plateau to zero frequency gives the value of dc ionic conductivity. It is seen that the conductivity values obtained from the Cole-Cole plots and Conductance spectra are in good agreement with each other.

3.5. Dielectric spectra Analysis

The complex permittivity (ε') or dielectric constant of a system has been defined by $\varepsilon^* = \varepsilon' - j\,\varepsilon'' = \varepsilon' - j(\sigma/\omega\varepsilon_0)$ where ε', ε'', σ, ω and ε_0 represent the real part of dielectric constant of the material, imaginary part of dielectric constant of the material, conductivity, angular frequency and permittivity of free space respectively.

Figure 5 shows ε' vs. logω plot for Pectin-NH_4SCN from which it is inferred that the dielectric permittivity rises sharply towards low frequency which is due to the electrode polarization effects [13]. The low frequency dispersion region has been attributed to the contribution of charge accumulation at the electrode-electrolyte interface. At high frequencies, due to high periodic reversal of the field at the electrode–electrolyte interface, the contribution of

charge carriers (ions) towards the dielectric constant decreases with increasing frequency. Hence ε' decreases with increasing frequency.

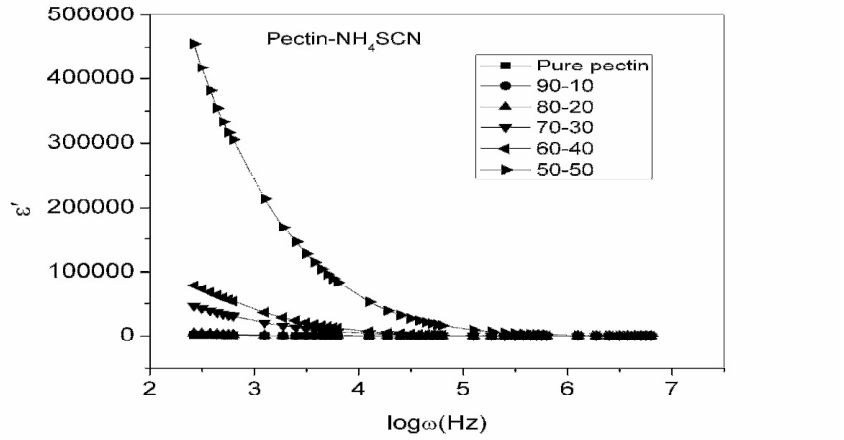


Figure 5 Dielectric constant vs logω plot for Pectin- NH_4SCN polymer electrolytes at room temperature

3.5. Modulus spectra Analysis

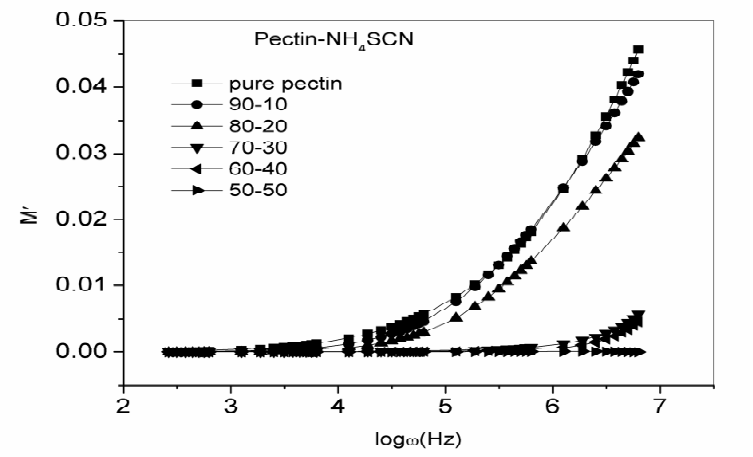


Figure 6 Variation of real value of modulus constant M' as a function of frequency at 303 K

The complex electric modulus is described by the equation, $M^* = M' + jM'' = j\omega C_0 Z^*$ where M' and M'' are the real and imaginary parts of the modulus. Figure 6 represents the variation of M' for pure Pectin and for different compositions of Pectin-NH_4SCN electrolyte films.

The value of M' shows an increase at the high frequency end which may be due to the bulk effect of the polymer electrolyte. At low frequencies, M' approaches zero indicating that the electrode polarization is negligible. The presence of long tail in the low frequency region confirms a large equivalent capacitance associated with the electrodes [14].

4. Conclusion

Various compositions of proton conducting polymer electrolytes based on the bio-polymer Pectin and the ammonium salt NH_4SCN have been prepared by solution casting technique. The amorphous nature of the polymer–salt complexes has been confirmed by the XRD study. FTIR study reveals the complex formation between the Pectin and the salt. It has been observed from the Ac Impedance analysis that the ionic conductivity of the pectin film doped with NH_4SCN increases with increasing concentration of the NH_4SCN in the concentration range studied and it is found to be 4.505×10^{-4} S/cm for 50 mol% pectin-50 mol% NH_4SCN. The dielectric spectra of the polymer-salt complexes reveal the space charge effects arising from the electrodes.

References

[1] U. Kalapathy and A. Proctor, *Food Chem.* 73(1), 393 (2001).
[2] M.A. Salam , N. Jahan, M.A. Islam and M.M. Hoque, *Journal of Chemical Engineering, IEB.* 27(2) (2012).
[3] R. K. Mishra, A. K. Banthia and A. B. A. Majeed, Asian Journal of Pharmaceutical and Clinical Research, 5(4) (2012).
[4] L.S. Liu, V.L. Finkenstadt, Liu, C.-K.; Jin, T.; Fishman, M. L.; Hicks, K. B. J Applied Polym. Sci., 106, 801 (2007).
[5] L.S. Liu, Y.J. Won and P.H. Cooke, D.R. Coffin, M.L. Fishman, K.B. Hicks, P.X. Ma, P. X. Biomaterials, 25, 3201 (2004).
[6] R.K. Mishra, M. Datt, A.K. Banthia, AAPS PharmSciTech. 9, 395 (2008).
[7] R.K. Mishra, A.B.A. Majeed, A.K. Banthia, Int. J. Plast. Tech., 15, 82 (2011).
[8] Juliana R. Andrade, Ellen Raphael and Agnieszka Pawlicka ELECTROCHIM ACTA , 54(26), 6479 (2009).
[9] R.K. Mishra, A. Anis, S. Mondal, M. Dutt and A.K. Banthia, Chinese Journal of Polymer Science 27(5), 639 (2009).
[10]K. Karthikeyan, P. Vinatier, A. Levasseur, Bull. Materials Science, 23, 179 (2000).
[11] B.A. Boukamp, Solid State Ionics 20, 301 (1986)
[12] J.R. Macdonald, Impedance Spectroscopy, Johnwiley & sons, Newyork, pp. 12–13.
[13] R. Mishra, K.J. Rao, Solid State Ionics, 106, 113 (1998).
[14] S.Ramesh and A.K.Arof, Mater. Sci. Eng., 85, 11 (2001).

STUDY OF NATURAL POLYMER CELLULOSE ACETATAE WITH NH_4BF_4

S.KARTHIKEYAN
Department of Physics, Ramco Institute of Technology, Rajapalayam, Tamilnadu, India

S. SELVASEKARAPANDIAN*
Materials research centre, Coimbatore, Tamilnadu, India

D.VINOTH PANDI
Materials Research Centre, Coimbatore, Tamil Nadu, India

N. VIJAYA
Department of Physics, SFR College for women, Sivakasi, Tamilnadu, India

SINDHUJA MANOHARAN
Materials Research Centre, Coimbatore, Tamilnadu, India

ARUN ARAICHIMANI
Department of Chemistry, Government Arts College, Tiruvannamalai, Tamilnadu, India

Cellulose acetate is one of the natural polymer with very good film forming capacity. It also has a important advantage of neutral character. It is nontoxic in nature and low cast. It has been widely used in producing fibers, selective membrane, bio-active and bio-compatible material. Ammonium salts are found to be good proton donor. An attempt is made to be develop membrane from natural polymer with NH_4BF_4. 1g of natural polymer CA doped with different concentration of NH_4BF_4 has been prepared by solution casting technique using DMF as solvent. XRD, FTIR, AC impedance studies have been undertaken for the above natural membrane. XRD pattern indicates that amorphous nature of pure CA increases on addition of different concentration of NH_4BF_4. The amorphous nature is maximum for 1g of CA doped with 315 mg of different concentration of NH_4BF_4 .complex formation has been confirmed by FTIR spectroscopic Analysis. Impedance shows that ionic conductivity $2.6602x10^{-06}$ for 1g of CA:315mg NH_4BF_4. This paper also includes dielectric and modulus behavior.

1. Introduction

Proceedings of the 14th Asian Conference on Solid State Ionics (ACSSI 2014)
Copyright © 2014 ACSSI 2014 Organizers. All rights reserved.
ISBN: 978-981-09-1137-9
doi:10.3850/978-981-09-1137-9_046

Polymer electrolyte membrane or proton exchange membrane fuel cell (PEMFC) uses a thin sheet of polymer as the solid electrolyte which allows only protons to pass through. PEMFC has high power density, low operating temperature, low weight, low volume and efficiency of value 40 to 60 percent. Grubb first demonstrated the usage of polymer electrolyte in fuel cell. PEMFC uses an expensive perfluorinated sulfonic acid type membrane called Nafion as electrolyte. Developing a low cost proton conducting membrane is very important for the commercialization of fuel cell. A good proton conducting polymer should have chemical stability, chemical compatibility to form a clean electrode-electrolyte interface, mechanical strength, mechanical stability, low permeability, to reactant gases, high proton conductivity, low resistive loss, zero electrical conductivity, high water transport and a low production cost. Most of the work is reported on ionic conductivity based on synthetic polymers such as polyvinyl alcohol, PEG, PAN, PVAc, and other blend polymers. Efforts have been undertaken to develop membrane using natural polymers. One important polymer among nature polymer is cellulose acetate. Cellulose acetate is the acetate ester of cellulose and is a biodegradable polymer which is very attractive for its abundance in nature, low cast, simple membrane preparation method, non-toxic nature and easy disposal [1-3]. It is used widely in textiles and plastic industries. It is also used in drug delivery system and in the manufacture of cigarette filters. It has higher water permeability for low acetyl content [4]. Ammonium salts are considered to be great proton donor. The study of cellulose acetate based proton conducting polymer electrolyte is rare in literature. Proton conducting polymer electrolyte cellulose acetate with different concentration of NH_4BF_4 has been studied and their results are presented in this paper.

2. Experimental Technique

Polymer electrolyte CA and CA doped with different amounts of NH_4BF_4 (315mg, 420mg) have been prepared by solution casting technique using DMF as solvent. 315mg and 420mg of NH_4BF_4 are with 1 gm of CA are dissolved in 50ml of DMF. The resultant solution is stirred well until a homogeneous solution is obtained and then poured into propylene dishes and allowed to evaporate at 60^{o}C to get free standing films. Prepared CA and CA with two concentrations of NH_4BF_4 (315,420mg) are subjected to XRD, FTIR and AC impedance characterization. X ray diffraction patterns are recorded at room temperature on Philips X' pert PRO diffractometer using CuK_{α} radiation. FTIR measurements are made with Bruker spectrophotometer. Impedance measurements are made using HIOKI 3532 LCR impedance analyser.

3. Results and discussion

3.1XRD analysis

Figure 1 represents XRD patterns for pure CA, CA-315mg NH_4BF_4 and CA-420mg NH_4BF_4. It is clear from Figure 1a that both crystalline and amorphous phase of the membrane. The crystalline peaks observed are at 2θ=18°, 23° and 27° and amorphous nature increases for 315mg NH_4BF_4. When the concentration of NH_4BF_4 is increased to 420mg, the crystalline peaks due to CA appear again. XRD peaks due to NH_4BF_4 are absent in all polymer membranes. This result is interpreted in terms of Hodge etal.,[5] criterion which establishes a correlation between the intensity and the decrease of crystallinity.

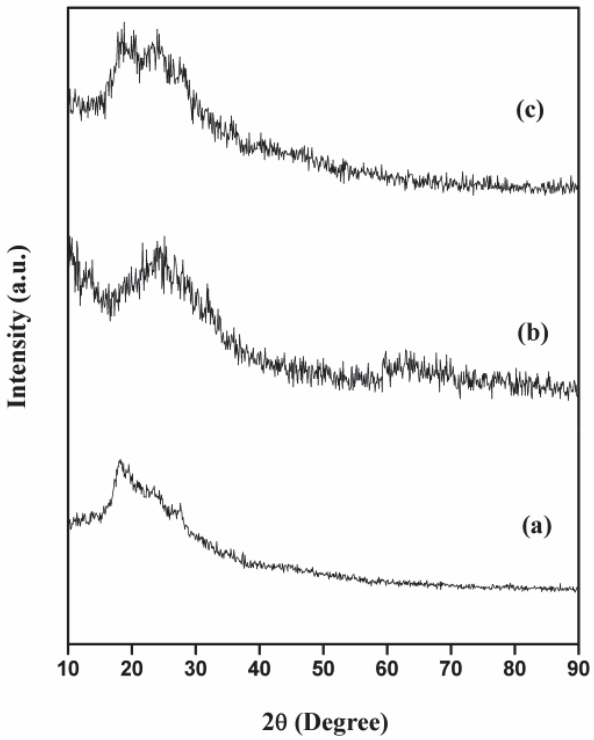


Figure 1. XRD pattern of (a) Pure CA, (b) CA 1g:315mg NH_4BF_4,(c) CA 1g:420mg NH_4BF_4 polymer electrolytes

3.2. FTIR analysis

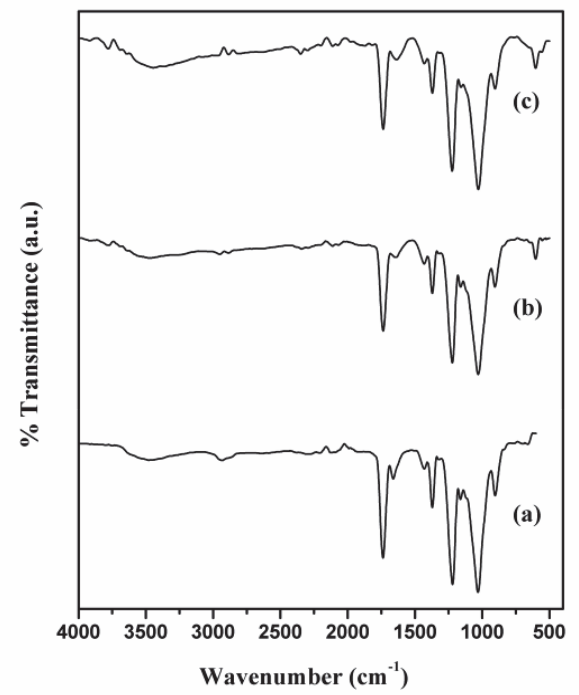


Figure 2. FTIR spectra of XRD pattern of (a) Pure CA, (b) CA1g:315mgNH_4BF_4, (c) CA1g:420mgNH_4BF_4 polymer electrolytes

FTIR spectroscopy has been used to study the interaction between the polymer CA and ammonium salt NH_4BF_4. Figure 2 shows the FTIR spectrum of pure CA (Curve a), 1gm of CA:315mg NH_4BF_4 (Curve b) and 1gm of CA:420 NH_4BF_4 (Curve c). Peak assignments are provided in the Table 1. Increase/decrease of intensity of peaks have been observed for CA doped with NH_4BF_4 when compared to pure CA peaks. FTIR results confirm the complex formation between polymer CA and ammonium salt NH_4BF_4.

Table.1 Vibrational peaks and assignments of CA/NH_4BF_4 polymer electrolytes

Pure CA	CA:350mg	CA:420mg	Assignment
1031	1029	1028	C-O-C Stretching of pyrose ring
1371	1371	1371	δCH bending
1737	1735	1735	C=O Symmetric Stretching
2900	2951	2952	CH Stretching (CH_2)
3500	3445	3448	OH Stretching

3.3. AC Impedance analysis

Electrical properties of polymer membrane could be studied by Impedance technique. Figure 3 shows the cole-cole plot for pure CA, CA: 315mg NH_4BF_4 and CA: 420mg NH_4BF_4. The plot consists of a high frequency semi circle and a constant phase element. The high frequency part of the impedance plot has been related to bulk relaxation processes according to Armstrong's model of solid electrolyte [6]. The low frequency spike resulted from the electrode-electrolyte interfacial properties. It is also observed that radius of the semicircle decreases as the concentration of NH_4BF_4 increases.

The 'EQ' software programme developed by Boukamp [7] has been used to find bulk resistance of the polymer electrolytes. The ionic conductivity (ζ) of the polymer electrolytes can be calculated using the equation

$$\zeta = \frac{l}{AR_b} \quad \text{---------- (1)}$$

Where l and A are the thickness and area of the polymer electrolyte. The highest conductivity at ambient temperature has been found to be 2.6602 x 10^{-6} S cm^{-1} for CA: 315mg NH_4BF_4. This value is one order of magnitude higher than the pure CA (3.731x10^{-7}S/cm). When the concentration of NH_4BF_4 is increased to 420mg, the conductivity decreases to a value 6.643x10^{-8} S/cm.

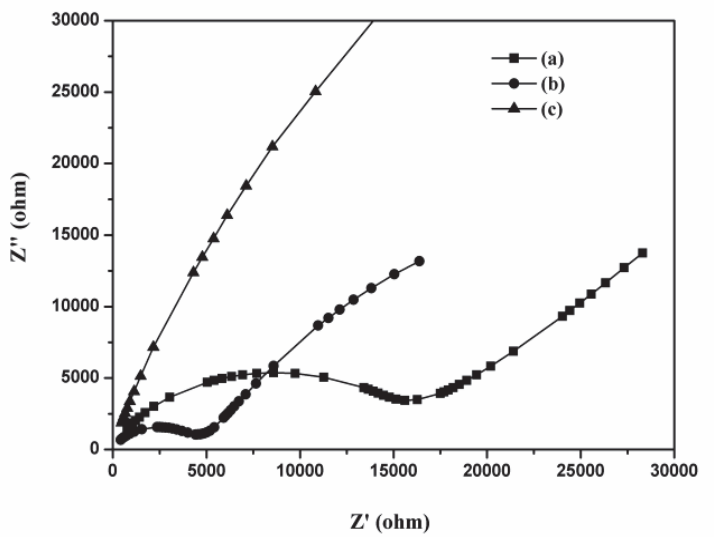


Figure 3. Complex impedance plots of (a) Pure CA, (b) CA 1g:315mg NH_4BF_4, (c) CA 1g:420mg NH_4BF_4 polymer electrolytes at 303K.

3.4. Conductance Spectra

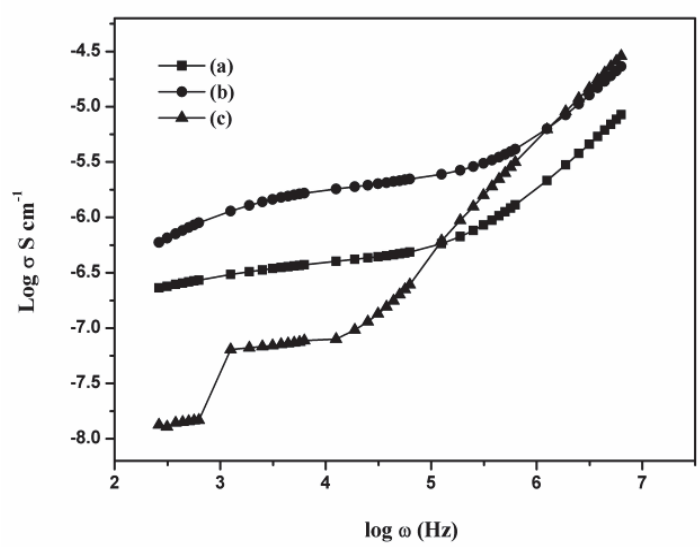


Figure 4. Conductance spectra for (a) Pure CA, (b) CA 1g:315mg NH_4BF_4, (c) CA 1g:420mg NH_4BF_4 polymer electrolytes at 303K.

The logarithmic plots of the conductivity as a function of angular frequency for pure CA and CA: 315mg NH_4BF_4 and CA: 420mg NH_4BF_4 at room temperature have been shown in Figure 4. The conduction spectra can be divided into three regions, low frequency dispersion region, frequency-independent plateau region in the intermediate frequency and a high frequency dispersion region. The plateau characterizes the conduction which is caused mainly by the hopping motion of the mobile ion and the extrapolation of the plateau region on the logζ axis gives dc conductivity. The dc conductivity values obtained from the conductance spectra have been found to coincide with the bulk conductivity values obtained from Nyquist plot.

3.5. Dielectric analysis

The Figure 5 and 6 show ε' versus log f and ε'' versus log f plots for pure CA, CA: 315mg NH_4BF_4, CA:420mg NH_4BF_4 respectively. The complex permittivity or dielectric constant of a system has been defined by $\varepsilon^* = \varepsilon' - j\,\varepsilon''$ where ε', ε'' are the real and imaginary part of dielectric constant of the material. It is observed from the figure 5 that the dielectric permittivity raises sharply towards low frequencies which is contributed surface polarization capacitance which is much larger than the sample capacitance. The high positive dielectric permittivity is obtained for CA: 315mg NH_4BF_4. At high frequency, due to high periodic reversal

of the field at the interface, the contribution of charge carriers (ions) towards the dielectric constant decreases with increasing frequency [8].

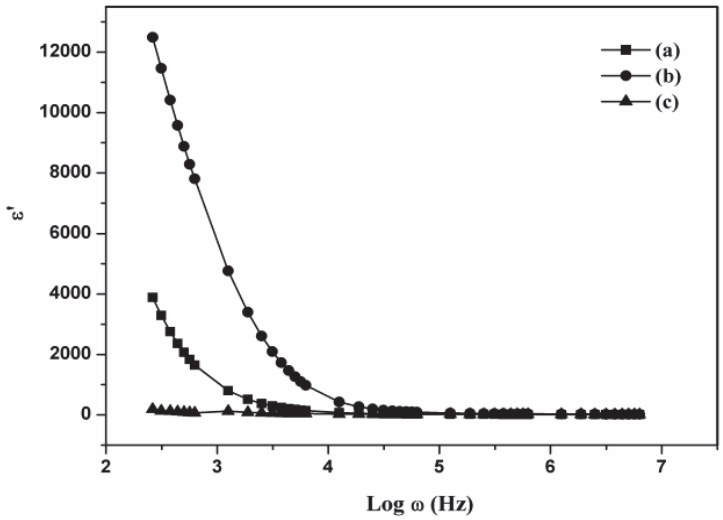


Figure 5. Variation of ε′ as a function of frequency of (a) Pure CA, (b) CA1g:315mgNH_4BF_4, (c) CA1g:420mgNH_4BF_4 polymer electrolytes at 303K.

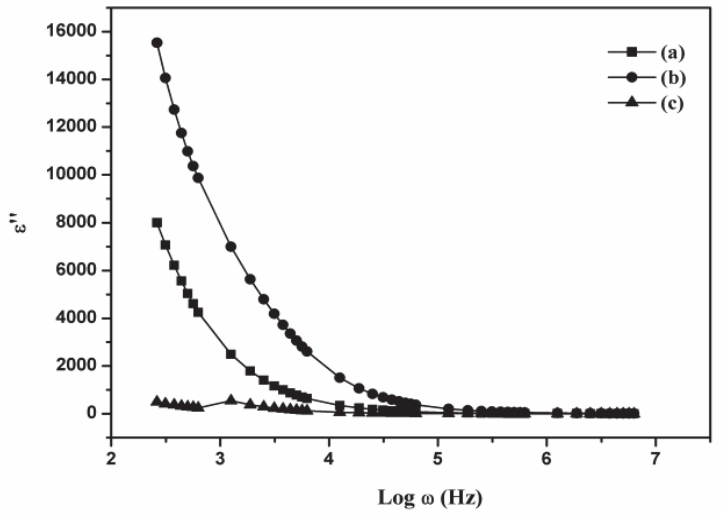
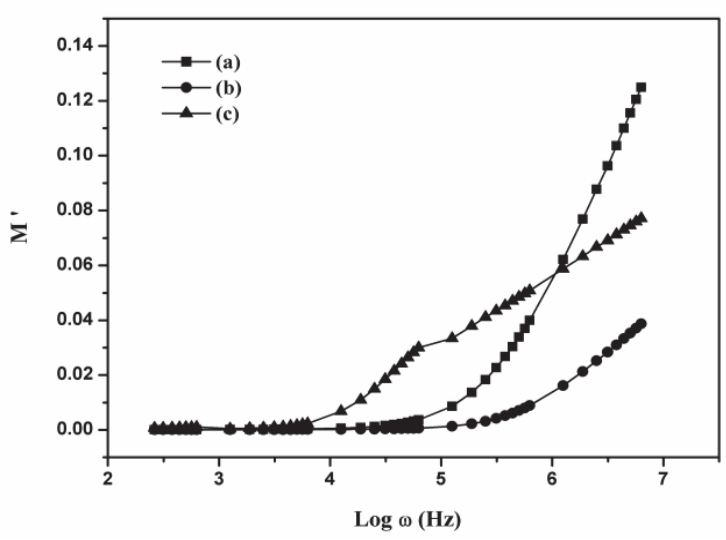


Figure 6. Variation of ε′ as a function of frequency of (a) Pure CA, (b) CA1g:315mgNH_4BF_4, (c) CA1g:420mgNH_4BF_4 polymer electrolytes at 303K.

Dielectric loss (ε”) is the direct measure of the energy dissipated and is generally composed of the contribution from the ionic transport and from the polarization of charge of a dipole [9]. From the Figure 6, it is observed that the dielectric loss has become very large for CA:315mg NH_4BF_4 at lower frequencies due to free charge motion within the material. At low frequencies there is time for charges to

build up at the interfaces before the field changes the direction and this has contributed to very large apparent values of ε".

3.6 Modulus Spectra analysis



.**Figure 7**. Variation of M' as function of frequency of (a) Pure CA, (b) CA1g:315mgNH_4BF_4, (c) CA1g:420mgNH_4BF_4 polymer electrolytes at 303K.

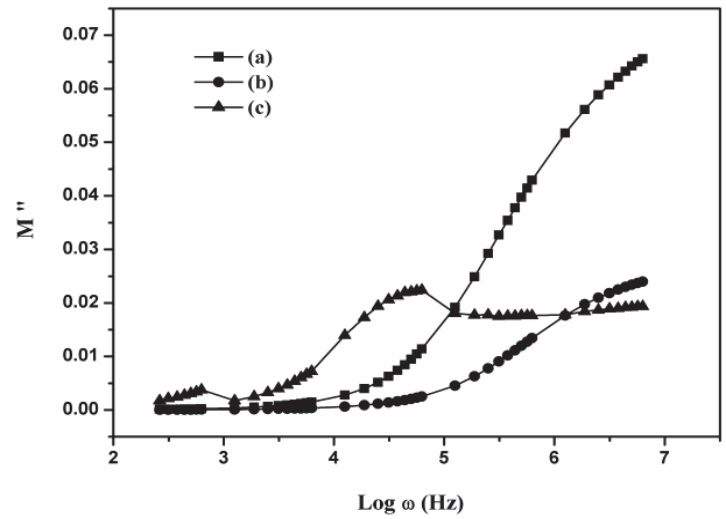


Figure 8. Variation of M'' as function of frequency of (a) Pure CA, (b) CA 1g:315mg NH_4BF_4, (c) CA 1g:420mg NH_4BF_4 polymer electrolytes at 303K.

In the field of solid electrolytes, the complex electric modulus formalism has been used because it discriminates against electro polarization and other interfacial

effects [10]. Figure 7 and 8 show the real and imaginary parts of the modulus are plotted against log w for pure CA, CA: 315mg NH_4BF_4 and CA: 420mg NH_4BF_4. The values of M' and M" show an increase at high frequency end which may be due to the bulk effect of the polymer electrolyte. At low frequency, M' and M" approach zero indicating that the electrode polarization phenomenon makes a negligible contribution.

3.7 Loss Tangent Spectra analysis

The variation of tanδ with frequency have been represented in Figure 9 for pure CA, CA: 315mg NH_4BF_4 and CA:420mg NH_4BF_4. It has been observed that for all the three polymer electrolytes, tan δ increases with increasing frequency. The maximum of the peak shifts towards high frequency for 315mg NH_4BF_4 and for 420 mg NH_4BF_4 towards low frequency. The absorption peak is described by the relation $\omega\eta=1$

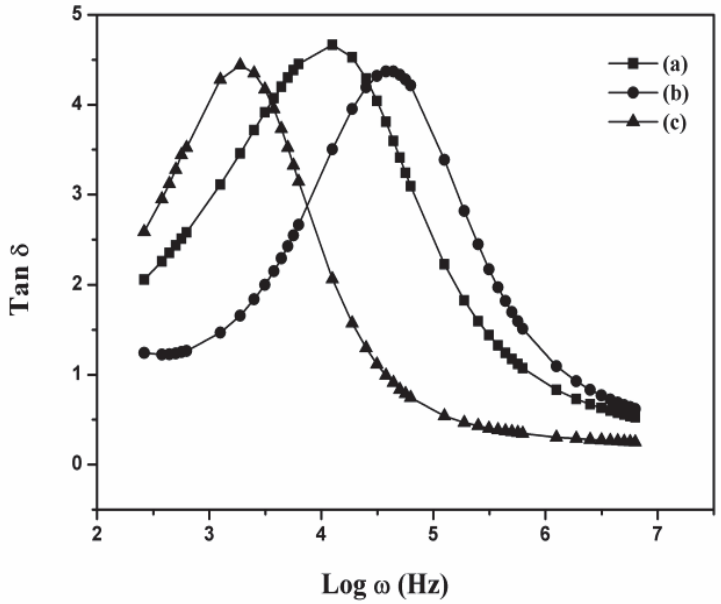


Figure 9. Tangent loss spectra of (a) Pure CA, (b) CA1g:315mgNH_4BF_4, (c) CA1g:420mgNH_4BF_4 polymer electrolytes at 303K.

where η and ω are the relaxation time of hopping process and angular frequency of the electric field[11].The relaxation parameters for pure CA, CA:315mg NH_4BF_4 and CA:420mg NH_4BF_4 polymer electrolytes have been calculated and tabulated in Table 2

Table.2 Hopping frequency (ω_p) and relaxation time (η) of pure CA and different composition

sample	Log ω_p (Hz)	ω_p (Hz)	Relaxation time η(s)
Pure CA	4.6293	42589.25	$7.3x10^{-05}$
CA: 350mgNH_4BH_4	4.1007	12609.6	$2.348x10^{-05}$
CA: 420mgNH_4BH_4	3.2870	1936.42	$5.164x10^{-04}$

4. Conclusion

Natural polymer electrolyte based on CA and NH_4BF_4 have been prepared. XRD, FTIR and AC impedance properties of the membrane have been studied. The maximum conductivity ζ=$2.662x10^{-6}$ S/cm has been observed for CA: 315mg NH_4BF_4. This membrane has low relaxation of $2.38x10^{-5}$ seconds.

References

1. Vinod Kumar Gupta, Deepak Rathania, Pardeep Singh, Bhim Singh Rathore, Priyanka Chauvan, Carbohydrate Polymers **95** (2013) 434-440
2. S. Ramesh, R. Shanthi, Ezra Morris Carbohydrate Polymers **91** (2013) 14-21
3. S. Ramesh, R. Shanthi, Ezra Morris Carbohydrate Polymers **87** (2012) 2624-2629
4. R. K. Verma et al Forulation aspects in the development of osmotically controlled oral drug delivery systems, Journal of Controlled Release **79** (2002) 7-27
5. R.M. Hodge, G.H.Edward, G.P. Simon (1996) Polymer **37**:1371-1376.
6. Amstrong et al J.Electro anal.chem.**52**(1974) 413
7. B.A. Boukamp, Solid State Ionics **20** (1986) 31-44
8. R. Mishra, K. J. Rao, Solid State Ionics, **106** (1998)113
9. K A Maurtz, Macromolecules 22(1989)4483, F S Howell, J.Phys.Chem. **78**(1974)639
10. S.Ramesh, A.K.Arof, Mat Sci.Eng.**85**(2011)11
11. N.Vijaya, Ionics **18** (2012) 91-99

AC CONDUCTIVITY,VIBRATIONAL AND STRUCTURAL BEHAVIOUR OF PROTON CONDUCTING GEL POLYMEF ELECTROLYTE BASED ON POLY(VINYL ALCOHOL)

K.P. RADHA

Department of Physics, S.F.R. College for Women, Sivakasi,Tamil Nadu, India, Research and Development Centre, Bharathiar University, Coimbatore, Tamil Nadu, India

Materials Research Centre, Coimbatore, Tamil Nadu, India

S. SELVASEKARAPANDIAN*, D.VINOTH PANDI

Materials Research Centre, Coimbatore, Tamil Nadu, India

S. KARTHIKEYAN

Department of Physics, Ramco institute of technology, Rajapalayam, Tamilnadu, Indic

M. HEMA

Kamaraj College of Engineering and Technology, Viruthunagar, Tamil Nadu, India

C. SANJEEVIRAJA

Department of Physics, Alagappa Chettiar College of Engineering & Technology, Karaikudi, Tamilnadu, India

Solid Polymer Electrolytes plays a vital role in all electrochemical devices like batteries, Fuel cell etc. The recent attention to polymer electrolytes is focused on high ionic conductivity as well as good mechanical properties. One method of improving the ionic conductivity of polymer electrolytes is the incorporation of a low molecular weight plasticizer like EC,PC, DEF, etc. Eventually plasticizer may serve to promote both the number of available charge carriers and their mobility through the polymer network. The proton ion conducting gel polymer electrolytes based on PVA-NH_4PF_6-DMF of various compositions using DMSO as solvent have been prepared by solution casting technique. The amorphous nature of the plasticized polymer electrolyte has been confirmed by XRD analysis. The complex formation among the polymer PVA, the salt NH_4PF_6 and the plasticizers DMF have been confirmed by FTIR analysis. The maximum ionic conductivity for 70 PVA: 30 NH_4PF_6 has been found to be 2.1 x 10^{-4} Scm^{-1} at ambient temperature. In the present work, the addition of 20 mol% of the plasticizer DMF to the

Proceedings of the 14th Asian Conference on Solid State Ionics (ACSSI 2014)
Copyright © 2014 ACSSI 2014 Organizers. All rights reserved.
ISBN: 978-981-09-1137-9
doi:10.3850/978-981-09-1137-9_047

electrolyte 70 PVA: 30 NH_4PF_6 enhances the conductivity to 2.3 x 10^{-3} Scm^{-1}. The temperature dependence of the conductivity of plasticized polymer electrolytes obeys Arrhenius relation. In the high frequency region, $\epsilon'(\omega)$ value saturates and giving rise to the dielectric constant of the material. In the modulus spectra, there is a long tail at low frequencies which is an evidence for large capacitance associated with the electrodes.

1. Introduction

Polymers with enhanced ionic conductivities at ambient temperatures are being investigated for their use in electrochemical devices as solid polymeric electrolytes. Several methods have been adopted to modify the ionic conductivity of the polymer electrolytes. Plasticization is one of the most significant contemporary ways to enhance the ionic conductivity of the polymer electrolytes. Kelly et.al [1] reported already that the addition of plasticizer enhances the amorphous phases present in the polymeric electrolytes and thus the ionic conductivity. Among the plasticizers Propylene carbonate PC, Ethylene carbonate (EC) polyethylene glycol (PEG), the low molecular weight 73.09 g/mol, low melting point, dielectric constant 36.1 at 250C, low viscosity 0.8 at 25°C and co-ordinating ability of N,N-Dimethyl formamide [2] plays a vital role to select as plasticizer in the present work. R.H.Y.Subban et.al has reported already the ionic conductivity of PVC-$LiCF_3SO3$ increases with the addition of the plasticizer DMF [3]. M.M.E.Jacob et.al has investigated DMF plasticized poly (vinyledene fluoride) based polymer electrolytes [4].

The polymer Poly (vinyl alcohol) PVA has been investigated by many researchers for its applications in electrochemical devices due to its properties such as a very high dielectric strength, good film forming ability, mechanical strength, dopant dependent optical and electrical properties, low cost, electrochemical stability etc.,. Vargas et.al [5] has investigated Poly (vinyl alcohol) for the phase behavior. Ionically conducting polymer electrolytes based on PVA has been developed by Fritz and Breitosomer [6].

Only limited number of polymer electrolyte systems doped with ammonium salts has been reported so far. G.Hirankumar et. al reported that the ammonium salts are very good proton donor to the polymer matrix like ploy (vinyl alcohol) [7]. In such systems, protons or NH_4 cations can act as mobile species. The present work is to develop PVA based plasticized polymer electrolyte by incorporating ammonium hexafluorophosphate (NH_4PF_6) as proton donor and N, N- Dimethyl Formamide (DMF) as plasticizer to the polymer host PVA.

2. Experimental Technique

PVA with an average molecular weight 125,000 (Sd. Fine. Chem. make), Inorganic salt NH_4PF_6 (Merck) and DMF (Merck) have been used as raw materials in this study. Plasticized proton conducting polymer electrolyte containing DMF in molar ratios 10, 20 and 30 complexes with 70PVA:30 NH_4PF_6 have been prepared by Solution Casting Technique. Appropriate weight of the ammonium hexafluoroposphate and PVA are dissolved in the solvent Dimethyl Sulphoxide (DMSO, Merck). The mixture is stirred for several hours to obtain homogeneous mixtures. The plasticizer DMF is then added to the mixture and again stirred well to obtain homogeneous mixtures. Finally the mixture has been poured into glass Petri dish and is allowed to evaporate the solvent DMSO in the vacuum oven at 70°C for 5 days. Finally the film is visually examined for its dryness and free standing nature.

Characterization of a material plays a vital role in the field of solid electrolytes. The prepared polymer electrolytes have been subjected to structural and electrical analysis The XRD measurements have been carried out using XPERT – PRO diffiractometer system with radiation in the range of $2\theta=0°$-90°. FTIR spectra have been recorded in the range of 4000 – 400 cm^{-1} using SHIMADZU IR Affinity -1 spectrophotometer. The electrical conductivity studies of the polymer electrolytes has been carried out in the temperature range of 303 K – 373 K over a frequency range of 42 Hz – 1 MHz using a computer controlled HIOKI 3532 LCR meter with a cell having stainless steel electrodes.

3. Results and discussion

3.1. *XRD analysis*

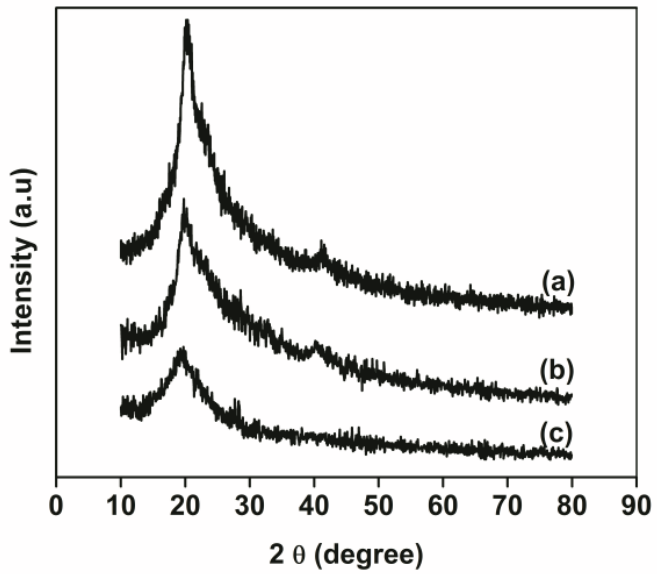


Figure 1 XRD pattern of (a) pure PVA (b) 70 PVA: 30NH_4PF_6(C) 70 PVA: 30NH_4PF_6:20DMF

Figure 1 shows XRD pattern of (a) pure PVA (b) 70 PVA: 30 NH_4PF_6 (C) 70 PVA: 30NH_4PF_6:20DMF. The characteristic diffraction peak of pure PVA has been observed at 20° and it has been slightly shifted in the complexes. The height of this peak decreases with the addition of the salt NH_4PF_6 and the plasticizer N, N-Dimethyl formamide DMF. A correlation between the height of the peak and the degree of crystallinity has been established by Hodge et.al [8]. No peaks corresponding to NH_4PF_6 appeared in the complexes. It reveals the complete dissociation of ammonium salt in the polymer matrix. A higher degree of amorphous nature has been observed for 70PVA:30NH_4PF_6:20DMF polymer electrolyte. The amorphous phase is responsible for higher ionic conductivity. Thus XRD studies confirm the amorphous nature of the complexes.

3.2. *FTIR analysis*

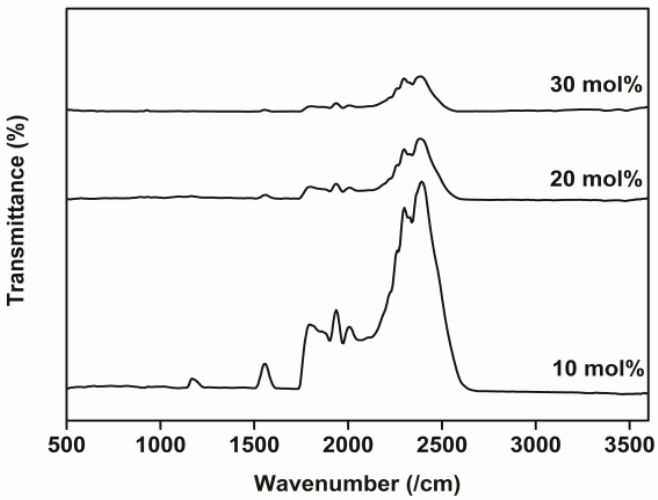


Figure 2 FTIR spectra of 70PVA:30NH_4PF_6:X DMF (X= 10,20,30 mol%) polymer electrolytes

Figure 2 shows FTIR spectra of 70 PVA: 30 NH_4PF_6 : XDMF (X= 10, 20, 30 in mol %). The absorption peak at 2911cm^{-1} corresponding to C–H asymmetric stretching of CH_2 becomes broadened in the complexes. It is due to the impact of Hydrogen bonding in PVA. The vibrational peaks at 1732cm^{-1}, 1644cm^{-1} and 944cm^{-1} attributed to C=0 stretching, CH_2 bending and C–O stretching of PVA get shifted in the complexes (Table 1). The absorption peaks at 2145cm^{-1} and 701cm^{-1} ascribed to C-S stretching of DMSO. It indicates that a trace of the solvent DMSO present in the 70 PVA: 30 NH_4PF_6 polymer electrolyte. These peaks have been found to be absent in the complexes. FTIR studies reveal the complex formation among the components of the polymer electrolytes.

Table 1 Vibrational peaks and its assignments

Composition of Electrolytes 70PVA:30NH_4PF_6:X DMF in mol% (cm^{-1})				Assignments
X = 0	X = 10	X =20	X =30	
2911	broad	broad	broad	C – H (asy. S)
2145	2344	2329	2329	C -S
1732	1725	1739	1732	C = O
1644	1614	1622	1617	C H_2 (B)

944	930	943	944	C – O (S)

3.3. *Impedance analysis*

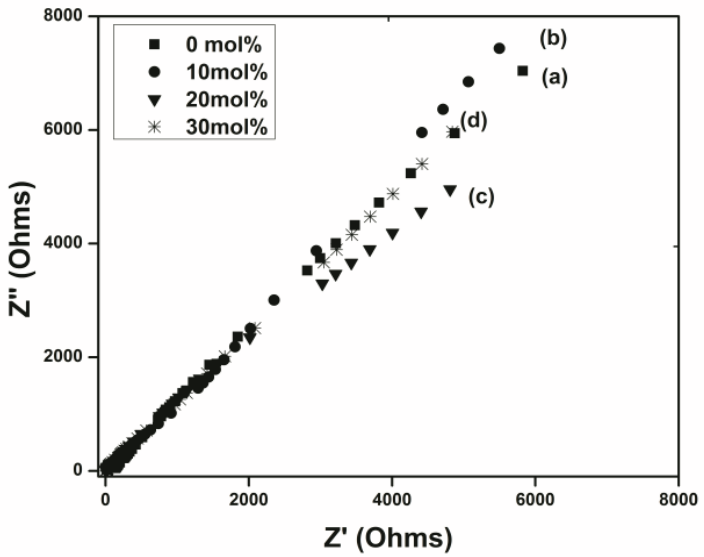


Figure 3 Cole-Cole plot of the polymer electrolytes a) 70 PVA: 30 NH_4PF_6 b) 70PVA: 30NH_4PF_6: 10DMF c) 70PVA: 30NH_4PF_6: 20 DMF d) 70PVA: 30NH_4PF_6: 30DMF at 303K

Figure 3 shows the complex impedance plot of all plasticized polymer electrolytes at ambient temperature. The low frequency response of impedance appears as an inclined spike. The bulk resistance has been obtained from the intercept of the spike with the Z' axis. Conductivities of the polymer electrolytes have been calculated using the relation

$$\sigma = l/R_b A \quad (1)$$

where R_b-bulk resistance, A-area and l-thickness of the electrolytes. The disappearance of the semicircular portion in the high frequency region of the impedance plot reveals that the current carriers are ions. It leads to the conclusion that the total conductivity is mainly due to ion conduction as many authors reported already [9, 10]. The addition of 20 mol% of N-N Dimethyl formamide (DMF) to the polymer electrolyte 70 PVA: 30NH_4PF_6 enhances the ionic conductivity from 2.1 X 10^{-4} S/cm to 2.3 x 10^{-3} S/cm at ambient temperature (Table 2).

Table 2 Conductivity and Dielectric constant of the plasticized polymer electrolytes at 303K

Composition (mol %)	Conductivity S/cm	LOG ξ ' at 1KHz
70PVA:30NH_4PF_6	2.1 x 10^{-4}	4.272942
70PVA:30NH_4PF_6:10DMF	1.1 x 10^{-3}	4.355545
70PVA:30NH_4PF_6:20DMF	2.3 x 10^{-3}	4.697059
70PVA:30NH_4PF_6:30DMF	1.4 x 10^{-3}	4.555942

3.4. *Concentration dependent conductivity*

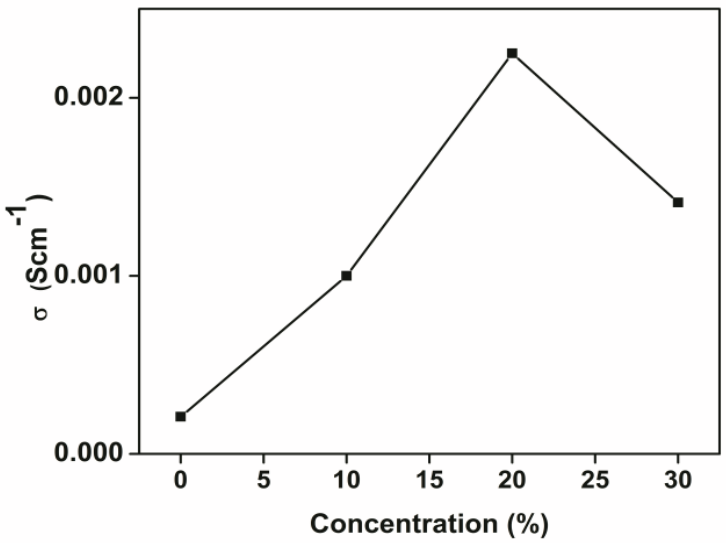


Figure 4 Conductivity vs concentration of DMF of the plasticized polymer electrolytes

Figure 4 shows ionic conductivity of the polymer electrolyte 70PVA: 30NH_4PF_6 as a function of the concentration of DMF as 0 mol%, 10mol%, 20mol% and 30mol%. Ionic conductivity of the polymer electrolytes is given by the relation

$$\sigma (T) = \Sigma n_i q_i \mu_i \quad (2)$$

where ni is the number of charge carrier of type I, qi is the charge on each carrier and μi is the mobility of charge carriers. The ionic conductivity of the plasticized polymer electrolytes increases upto 20mol% of DMF and then it decreases. The reason may be due to dielectric constant associated with the plasticizer. One of the advantages of the plasticizer is to increase the degree of dissociation of the salt. Similar results have been reported by many authors [11,12]. Further the low

viscosity of the plasticizer DMF lead to the high ionic mobility thereby maximizing the conductivity [13]. The decrease in the ionic conductivity after 20mol% may be attributed to ion aggregation leading to the formation of ion pairs. Thus it decreases the number of mobile charge carriers and hence the mobility [14]. The plasticized polymer electrolyte 70PVA: 30NH_4PF_6: 20DMF has the maximum ionic conductivity among the prepared polymer electrolytes.

3.5. *Dielectric analysis*

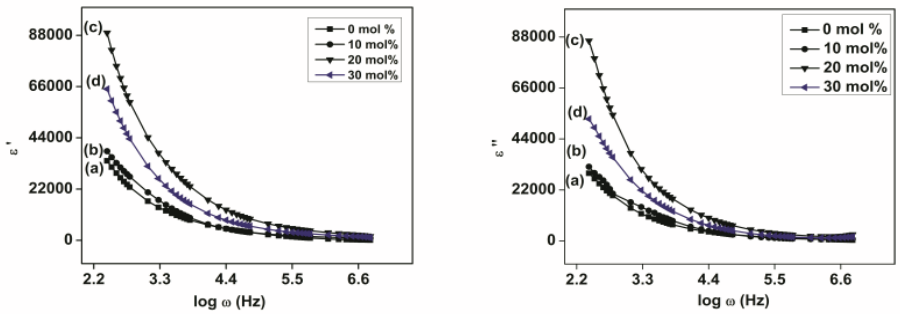


Figure 5 Real and Imaginary parts of Dielectric permittivity of a) 70 PVA: 30 NH_4PF_6 b) 70PVA: 30 NH_4PF_6: 10DMF c) 70PVA: 30 NH_4PF_6: 20 DMF d) 70PVA: 30 NH_4PF_6:30DMF at 303K

The frequency dependence of real and imaginary parts of the dielectric constant of polymer electrolytes a) 70PVA:30 NH_4PF_6 b) 70PVA: 30 NH_4PF_6; 10DMF c) 70PVA: 30 NH_4PF_6: 20 DMF d) 70PVA: 30 NH_4PF_6:30DMF have been shown in Figure 5. The sharp rise in the dielectric constant towards low frequencies is due to the electrode polarization effects. The dielectric constant for plasticized systems are higher than that of the unplasticized system(70 PVA: 30 NH_4PF_6). It may be attributed to the enhanced charge carrier density at the space charge accumulation region, resulting in an increase in equivalent capacitance. The dispersion in the low frequency region is owing to charge accumulation at the electrode-electrolyte interface. At high frequencies, the dipoles are not able to follow the periodic reversal of the electric field since it occurs very fast. As a result, there is no excess ion diffusion in the direction of electric filed. Weaker ion interaction of dipoles with the electric field causes the observed decrease in dielectric constant.

It has been observed that the log of dielectric constant for plasticized polymer electrolytes are higher compared to non-plasticized system (70PVA: 30 NH_4PF_6) as shown in Table 2. The dielectric constant of DMF (36.7) is higher than the dielectric constant of the host polymer PVA. Hence the addition of the

plasticizer DMF enhances the permittivity of the mixture as reported by the Author G. Andrea et.al [15].

3.6. *Modulus analysis*

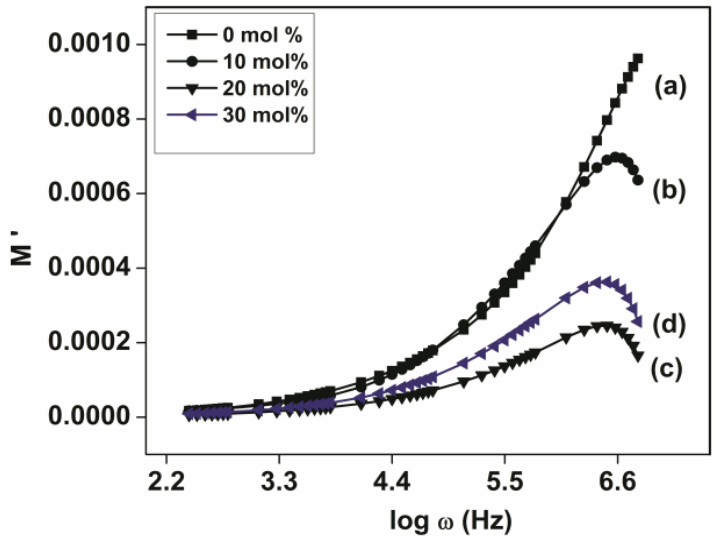


Figure 6 Real part of Dielectric permittivity of a) 70PVA:30 NH_4PF_6 b) 70PVA:30 NH_4PF_6: 10DMF c) 70PVA: 30 NH_4PF_6: 20 DMF d) 70PVA: 30 NH_4PF_6: 30DMF at 303K

A complex electric modulus is different approach to study the conductivity relaxation phenomena. In the dielectric modulus the electrode polarization effects are suppressed. Variation of real (M') part of electric modulus as a function of frequency for all plasticized polymer electrolytes has been depicted in Figure 6. Both M' show an increase at high frequency end. The occurrences of peaks at high frequencies are pertained to the bulk effect [16]. At low frequencies, it has been observed that the value of M' and M'' is in the vicinity of zero showing the fact the effect of electrode polarization is negligible and ignored. The long tail in the low frequency is probably the consequence of the large capacitance associated with the electrode. Similar results have been reported by many authors [17,18]. The possible presence of peaks in the modulus formalism at higher frequencies for all plasticized polymer electrolytes reveals that the plasticized polymer electrolytes are ionic conductors as reported by S.Ramesh et.al [19]. Overall, it is clear that the heights of the peaks decrease in plasticized system compared to non-plasticized system (70PVA: 30NH_4PF_6). It indicates a plurality of relaxation mechanism.

4. Conclusion

The new plasticized polymer electrolyte comprising of Poly (vinyl alcohol), Ammonium hexafluorophosphate and N, N-Dimethyl formamide have been prepared by solution costing technique. The conductivity, dielectric and modulus analysis of the samples have been studied for different temperature and frequencies. From XRD analysis, the amorphous nature of the investigated sample has been confirmed. The maximum ionic conductivity has been found to be 2.3 x 10^{-3} S/cm at ambient temperature for 70PVA: 30NH_4PF_6:20DMF polymer electrolyte. The low frequency dispersion in the dielectric constant is due to space charge accumulation near the electrode/ electrolyte contact. Higher values of dielectric constant at low frequencies indicate that the sample is super ionic one. The dielectric permittivity decreases with increase in frequencies. It is verifying the fact the dielectric permittivity is dependent on temperature and frequency for polar polymers.

References

1. I.E.Kelly, J.R.Owen and B.C.H.Steele , *J. Power Sources,* **14,** 13 **(**1985).
2. D.R. MacFarlane and J.Sun, *Electrochim. Acta***, 40**, 2131 (1995).
3. R.H..Y.Subban and A.K.Arof, *European Polymer Journal* **40**, 1841 (2004).
4. M.M.E,Jacob and A.K.Arof, *Electrochimica Acta*,**45,** 1701 (2000).
5. R.A.Vargas, A.Garcia and M.A.Vargas, *Electrochim Acta,* **43**,1271 (1998).
6. H.P. Fritz and M.Breitsamer, *Solid State Ionics,* **45,** 255 (1991).
7. G.Hirankumar, S.Selvasekarapandian, J.Kazamura, N.Kuwata and T.Hattori, *J. Power Sources,* **144**, 262 (2005).
8. R.M.Hodge, G.H.Edward and G.P.Simon, *Polymer,* **37**, 1371 (1996).
9. M.Watnabe, K. Sanui, N. Ogata, T. Kobayashi and Z. Ohbaki, *J. Appl.phys.,* **57 (1),** 123 (1985).
10. M.M.E. Jacob, S.R.S. Prabaharan and S.Radhakrishna, *Solid State Ionics,* **104,** 267 (1997).
11. J.C.W. Walker and M. Salomon, *J. Electrochem. Soc*.,**140**, 3409 (1993).
12. M. Ratner, *Mater. Forum***, 15**, 1 (1991).
13. J.P. Southall, H.V.St.A. Hubbard, S.F. Johnston, V.Rogers, G.R. Davies, J. E. McIntyre and I.M. Ward, *Solid State Ionics*, **85**, 51 (1996).
14. C.S.Ramya, S.selvasekarapandian, T.Savitha and G.Hirankumar, *Physica B,* **393**,11 (2007).
15. G.Andrea, Bishop, R.Douglas, MacFarlane and Maria Forsyth, *Electrochimica Acta,* **43**, 1153.
16. S.Ramesh, A.H.Yahaya and A.K.Arof, *Solid State Ion,* **152**, 291 (2002).
17. S.Ramesh, and M.F.Chai, *Mater. Sci. Eng B.,***139**, 240 (2007).

18. N.Gokulamurali, S.A. Suthanthiraj and P.Maruthamuthu, *Proc. Solid State Ionics: Mater. Appl* ., **373** (1992) .
19. S.Ramesh and A.K.Arof, *Mater Sci Eng B,* **85,** 11 (2001).

CELLULOSE ACETATAE BASED PROTON CONDUCTING POLYMER ELECTROLYTE

S. SELVASEKARAPANDIAN*
Materials research centre, Coimbatore, Tamilnadu, India

N. RUBIYA EVANGELIN
Department of Physics, NMSSVN College, Madurai, Tamilnadu, India

D.VINOTH PANDI
Materials Research Centre, Coimbatore, Tamil Nadu, India

ARUN ARAICHIMANI
Department of Chemistry,Government ArtsCollege, Tiruvannamalai, Tamilnadu, India

N. VIJAYA
Department of Physics, SFR College for women, Sivakasi, Tamilnadu, India

SINDHUJA MANOHARAN
Materials Research Centre,Coimbatore,Tamilnadu, India

S.KARTHIKEYAN
Department of Physics , Ramco Institute of Technology, Rajapalayam, Tamilnadu, India

T. MATHAVAN
Department of Physics, NMSSVN College, Madurai, Tamilnadu, India

Abstract

Research has been undertaken to prevent environmental degradation, to develop membranes from natural polymers. The natural polymer that gains interest is cellulose acetate. The widespread use of CA is attributed to the availability of renewable resources, non- toxic nature, low cost and also due to its bio degradable in nature. It has a lot of industrial application such as membrane using cellulose acetate. So proton conducting membranes CA with NH_4SCN which is known to be a good proton donor have been prepared by solution casting technique using DMF as solvent. XRD, FTIR nad AC Impedance studies have been undertaken for the above membranes. XRD pattern indicates that the amorphous nature of membrane increases addition of different

Proceedings of the 14th Asian Conference on Solid State Ionics (ACSSI 2014)
Copyright © 2014 ACSSI 2014 Organizers. All rights reserved.
ISBN: 978-981-09-1137-9
doi:10.3850/978-981-09-1137-9_048

concentration of salt. Complex formation has been confirmed by FTIR spectroscopic studies. The ionic conductivity of CA membrane increases as the concentration of NH_4SCN increases. The maximum ionic conductivity value is $4.202x10^{-03}Scm^{-1}$ for $50CA:50NH_4SCN$. Dielectric and modulus behavior have also been studied.

1. Introduction

Research has been undertaken to prevent environmental degradation, to develop membranes from natural polymers. The natural polymer that gains interest is cellulose acetate.

Cellulose acetate has number of outstanding properties such as film forming nature, non- toxic nature, availability of renewable resources, low cost and bio degradable in nature. Another advantage is presented functional group in its polymer. But, its high glass transition temperature, rigidity or its highly crystalline nature and relative hydrophobic character can be limited drawbacks for some application [1-3].

To overcome above drawbacks are approach is to incorporate suitable additives to convert the highly crystalline region in CA matrix to amorphous for better ion conduction. Suitable additive could be ionic salt into the CA matrix. For development of proton conducting membrane with CA, ammonium salts such as NH_4SCN, NH_4NO_3. Such as ammonium salts are well known proton donor to the polymer matrix. In this paper proton conducting membrane CA with NH_4SCN has been studied and the results are presented.

2. Experimental Technique

The polymer cellulose acetate (Sigma Aldrich, product code 1001345528) and salt NH_4SCN are used to raw material in this study. Dimethyl formamide has been used as a solvent. The polymer electrolytes CA doped with NH_4SCN in different composition such as 100:0; 90:10; 80:20; 70:30;60;40 and 50:50 have been prepared by solution casting technique. The mixture of CA and NH_4SCN has been stirred continuously with magnetic stirrer for several hours to obtain homogenious solution. The solution is then cast in petri dishes and samples are vacuum dried. After 24 hours free standing transparent films are obtained. X ray diffraction pattern of the prepared samples are recorded at room temperature on a Philips X' pert PRO diffractometer using CuK_α radiation. Electrical measurements are performed on the polymer electrolyte film in the frequency range 42Hz- 1MHz at room temperature by sandwiching them between aluminum blocking electrode using HIOKI 3532 LCZ meter interfaced with a computer. FTIR spectrum has been recorded for samples using BRUCKER spectrophotometer in the range 400-4000 cm^{-1}.

3. Results and discussion

3.1 XRD analysis

X ray diffraction (XRD) studies have been carried out to investigate the occurance of the complex formation between the polymer and the salt and the degree of crystallanity of the polymer complex. **Figure.1(a)** and **Figure.1(b-f)** show the XRD pattern of pure CA and CA doped with NH_4SCN respectively. The observation of both crystalline and amorphous phase on the film makes it to perfect in semicrystalline nature. It is clear that first structural disorder images occur when CA powder is dissolved in DMF solvent to process in to thin films. The crystalline peaks observed are at $2\theta = 9°$, 13°, 18°, 23° and 27°. Similarly XRD peaks have been observed by Ramesh et.al [2].

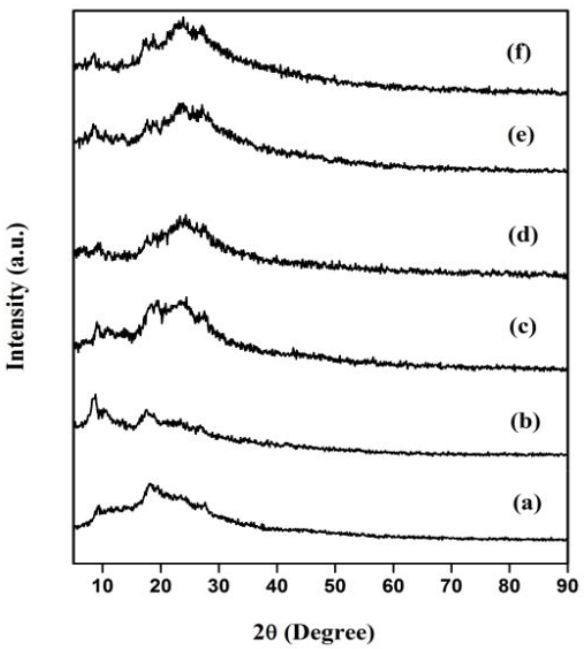


Figure.1 XRD pattern of (a) Pure CA, (b)90CA:10NH_4SCN,(c)80CA:20NH_4SCN,(d) 70CA:30NH_4SCN, (e) 60CA:40NH_4SCN, (f) 50CA:50NH_4SCN polymer electrolytes

It is also observed that as concentration of NH_4SCN is increased, the intensity of above mentioned peaks decreases and amorphous nature increases. Maximum amorphous nature has been observed for 50CA: 50NH_4SCN. This result is interpreted in terms of Hodge et.al [4] criterian which establishes a correlation

between the intensity of the peak and the decrease of crystallanity. The peaks corresponding to pure NH4SCN have been found to be absent in the salt doped polymer complex indicating the complete dissociation of the salt in the polymer matrix.

3.2.FTIR analysis

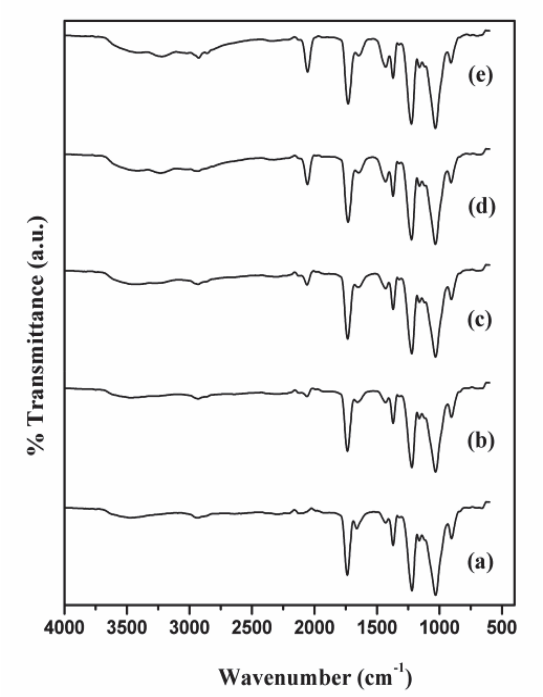


Figure.2 FTIR pattern of (a) Pure CA, (b)90CA:10NH_4SCN,(c)80CA:20NH_4SCN, (d) 70CA:30NH_4SCN, (e) 60CA:40NH_4SCN, (f) 50CA:50NH_4SCN polymer electrolytes

FTIR spectroscopy has been used to study the interaction between the polymer CA and NH_4SCN. Figure 2 shows the spectrum of pure CA and CA doped with different concentrations of NH_4SCN. The peak assignments of the various FTIR peaks of pure CA and CA doped with different concentration of NH_4SCN are provided in the table 1. Increase/decrease of intensity of peaks have been observed for CA doped with NH_4SCN when compared to pure CA peaks. FTIR results confirm the complex formation between the polymer CA and NH_4SCN.

Table 1. FTIR band assignments for CA and CA doped NH_4SCN polymer complexes

Pure CA	80CA:20 NH_4SCN	60CA:40 NH_4SCN	50CA:50 NH_4SCN	ASSIGNMENT
1031	1031	1032	1033	C-O-C stretching of pyrose ring
1371	1372	1374	1375	δ C –H bending
1734	1737	1738	1730	C=O symmetric stretching
2900	2904	2904	2932	C-H stretching (CH_3)
3445	3450	3420	3440	OH stretching

3.3. AC Impedance analysis

Impedance Spectroscopy is a powerful method of characterizing many of the electrical properties of electrolyte materials and their interfaces with electronically conducting electrodes.

The complex impedance plane plot for pure cellulose acetate is shown in **Fig 3(a).** curves (b-f) in fig 3 show cole - cole plot for 90CA:10NH_4SCN; 80CA:20 NH_4SCN; 70CA:30 NH_4SCN;60CA:40 NH_4SCN and 50CA:50 NH_4SCN polymer membrane respectively.

Curve (a) in fig.3 consists of a high frequency depressed semicircle represented by a frequency dependent capacitor (C_g) parallel to a bulk resistor (R_b) and a low frequency spike represented by a constant phase element (CPE). In this case the migration of ions may occur through the free volume of polymer matrix, which can be represented by a resistor. The immobile polymer chains become polarized in the alternating field, which can be represented by a capacitor. The ionic migration and bulk polarization are physically in parallel and therefore gives a semi circle at high frequency can be observed. The inclined straight line at the low frequency region could be the effect of electrode and electrolyte interface [5].

It is also observed that curves (b-f) of fig3 the radius of the semicircle decreases as the concentration of NH_4SCN is increased. For 50mol% of NH_4SCN only spike is observed.

The 'EQ' software programme developed by Boukamp [6] has been used to find bulk resistance of the polymer electrolytes. The ionic conductivity (ζ) of the polymer electrolytes can be calculated using the equation

$$\zeta = \frac{l}{AR_b} \quad \text{---------- (1)}$$

Where l and A are the thickness and area of the polymer electrolyte. The highest conductivity at ambient temperature has been found to 4.202 x 10^{-3} S cm^{-1} for 50 mol% salt doped polymer electrolyte. The enhancement in ionic conductivity may be due to 1) the transition from semicrystalline phase to an amorphous phase of the polymer complex 2) the increase of charge carrier concentration [7]. The conductivity values for all compositions at ambient temperature are presented in **table. 2**.

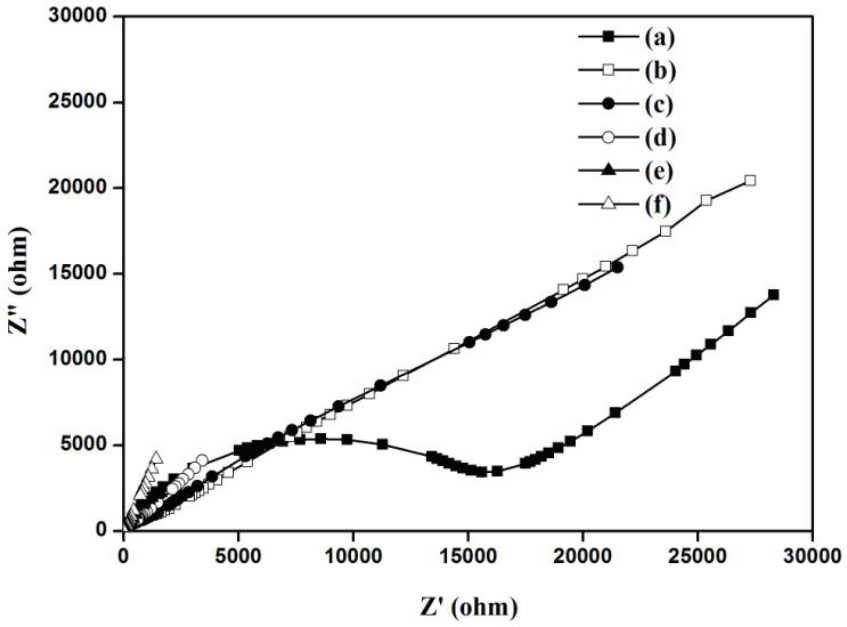


Figure 3. Impedance plots of (a) Pure CA, (b)90CA:10NH_4SCN,(c)80CA:20NH_4SCN, (d)70CA:30NH_4SCN, (e) 60CA:40NH_4SCN, (f) 50CA:50NH_4SCN polymer electrolytes

Table.2 Ionic conductivity values of pure CA, different mol% of NH_4SCN doped CA at room temperature

Sample	Conductivity σ (Scm^{-1})
Pure CA	$3.731X10^{-07}$
90CA:40NH_4SCN	$1.274X10^{-06}$
80CA:20NH_4SCN	$2.026X10^{-06}$
70CA:30NH_4SCN	$1.5967X10^{-04}$
60CA:40NH_4SCN	$2.131X10^{-03}$

3.4.Conductance Spectra

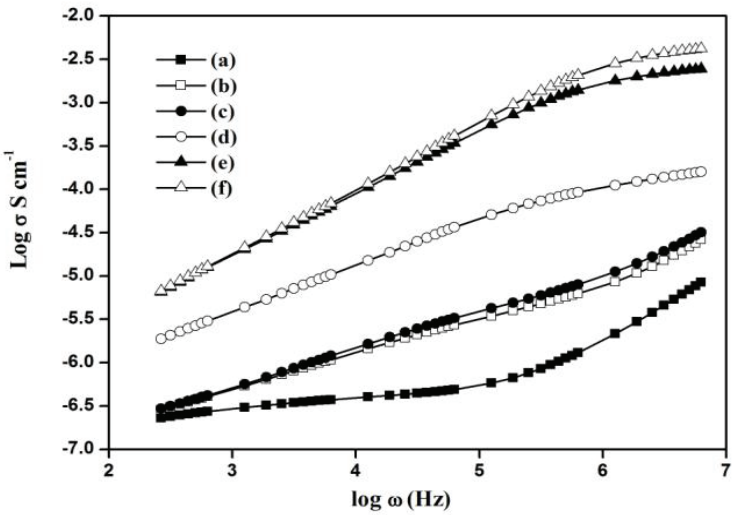


Figure 4 Conductance spectra of (a) Pure CA, (b) 90CA:10NH4SCN, (c) 80CA:20NH4SCN, (d) 70CA:30NH4SCN, (e) 60CA:40NH_4SCN, (f) 50CA:50NH_4SCN polymer electrolytes

The logarithmic plots of the conductivity as a function of angular frequency for pure CA and CA doped with different concentration of NH_4SCN at room temperature have been shown in Fig. 4. The conduction spectra can be divided into three regions, low frequency dispersion region, frequency-independent plateau region in the intermediate frequency and a high frequency dispersion region. The plateau characterizes the conduction which is caused mainly by the hopping motion of the mobile ion and the extrapolation of the plateau region on

the logζ axis gives dc conductivity. The high frequency behavior is attributed to the relaxation of mobile ion hopping which is due to the coulombic interaction of the charge carrier and disorder within the structure [8]. The dc conductivity values obtained from the conductance spectra have been found to coincide with the bulk conductivity values obtained from Nyquist plot..

3.5.Dielectric analysis

The complex permittivity or dielectric constant of a system has been defined by $\varepsilon^* = \varepsilon' - j\,\varepsilon''$

Where ε', ε'' are the real and imaginary part of dielectric constant of the material. Fig 5 shows ε' Vs log f plots for pure CA and CA doped different concentration of NH_4SCN. It is seen from the fig that values of ε' is very at low frequency. This value increases as the concentration of NH_4SCN increases. The low frequency dispersion region has been attributed to the presence of space charge effects which is contributed by the accumulation of charge carriers near electrodes. At high frequency due to high periodic reversal of the field at the interface. The contribution of charge carriers (ions) towards the dielectric constant has decreased with increasing frequency[9].

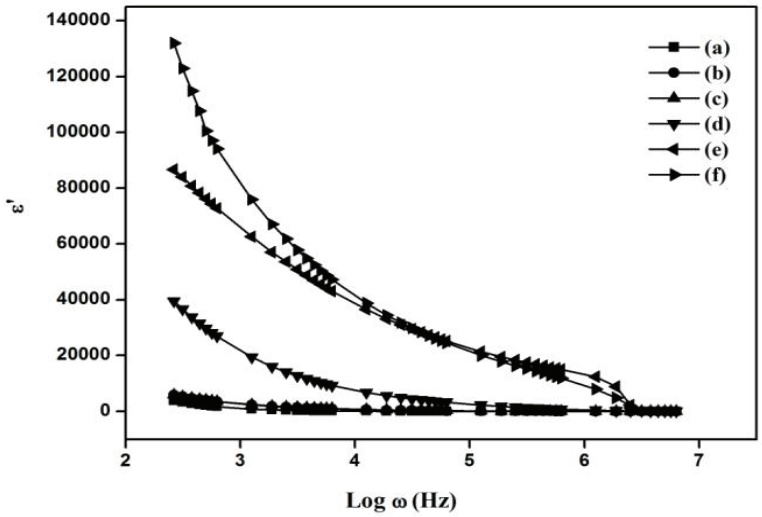


Figure. 5 Variation of ε' as a function of frequency of (a) Pure CA, (b) 90CA:10NH_4SCN, (c)80CA:20NH_4SCN, (d)70CA:30NH_4SCN, (e) 60CA:40NH_4SCN, (f) 50CA:50NH_4SCN polymer electrolytes

3.6 Modulus Spectra analysis

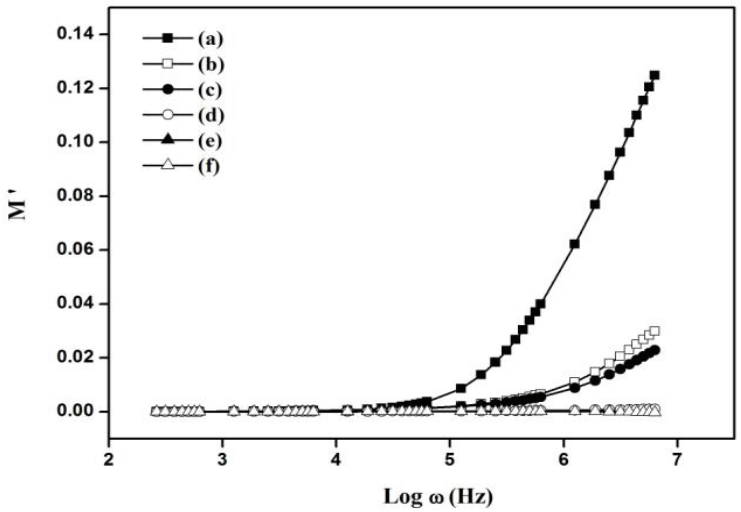


Figure 6a. Variation of M' as function of frequency for (a) Pure CA, (b) 90CA:10NH4SCN, (c)80CA:20NH_4SCN, (d)70CA:30NH_4SCN, (e) 60CA:40NH_4SCN, (f) 50CA:50NH_4SCN polymer electrolytes

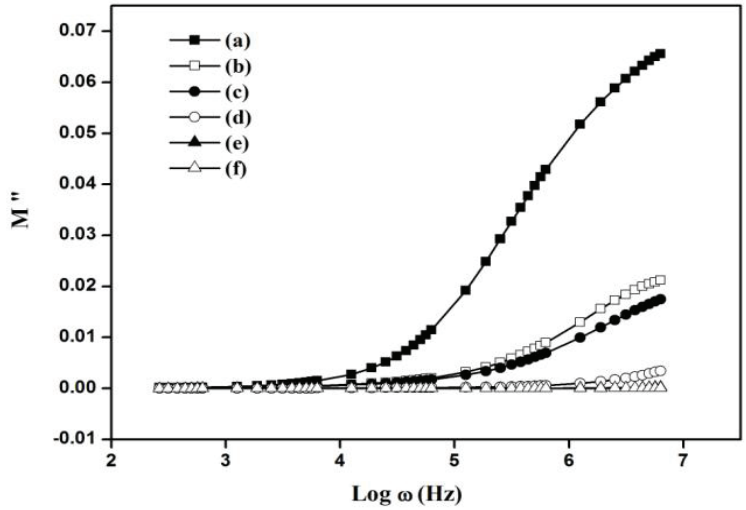


Figure 6b. Variation M" as function of frequency for (a) Pure CA, (b)90CA:10NH_4SCN, (c)80CA:20NH_4SCN, (d)70CA:30NH_4SCN, (e) 60CA:40NH_4SCN, (f) 50CA:50NH_4SCN polymer electrolytes

The dielectric modulus analysis is a tool to investigate the bulk dielectric response by suppressing the effect of electrode polarization. Fig 5 and Fig6 represent the variation of log f with M' and log f with M" respectively for pure CA and CA doped with different concentration of NH_4SCN. From the plot it is observed that both M' and M" approaches to zero at low frequency region. This suggests that suppression of electrical double layer at the electrode. This is because of high capacitance values associated with the electrode in the polymer electrolyte. It has been show that values of dielectric modulus increases with increasing frequency. The long tail at lower frequencies is due to the large capacitance associated with the electrode.

4. Conclusion

CA-based polymer electrolytes with different concentrations of NH_4SCN have been prepared using the solution casting technique. From XRD analysis, the amorphous nature of the polymer electrolyte films increases on the addition of NH_4SCN. FTIR studies reveal the complex formation between the CA and NH_4SCN. The highest ionic conductivity has been found to be 4.202 X 10^{-3} Scm^{-1} for 50Mwt%CA: 50Mwt% NH_4SCN polymer electrolyte from the Cole-Cole plot and also confirmed from conductance spectra. The low frequency dispersion of dielectric constant reveals the space charge effects arising from the electrode.

References

1. Vinod Kumar Gupta, Deepak Rathania, Pardeep Singh, Bhim Singh Rathore, Priyanka Chauvan, Carbohydrate Polymers **95** (2013) 434-440
2. S. Ramesh, R. Shanthi, Ezra Morris Carbohydrate Polymers **91** (2013) 14-21
3. S. Ramesh, R. Shanthi, Ezra Morris Carbohydrate Polymers **87** (2012) 2624-2629
4. R.M. Hodge, G.H.Edward, G.P. Simon (1996) Polymer **37**:1371-1376.
5. J. R. Macdonald (Ed), Impedance spectroscopy, John wiley & sons, Newyork, 1987, P. **12-23**.
6. R.M. Hodge, G.H.Edward, G.P. Simon (1996) Polymer 37:1371-1376.
7. Seong Hun Kim, Jun Young Kim, Han Sang Kim, Hyun Nam Cho, Solid State Ionics **116** (1999) 63-71
8. C. K im, G. Lee, K. Leo, K S Ryu , SH Chang, Solid State Ionics, **123** (1999) 251
9. R. Mishra, K. J. Rao, Solid State Ionics, **106** (1998)113

PREPARATION AND CHARACTERIZATION OF PVA COMPLEXED WITH AMINO ACID, ARGININE

R.BHUVANESWARI
Research and Development Centre, Bharathiar University, Coimbatore, Tamilnadu, India, Materials Research Centre, Coimbatore, Tamil Nadu, India

S. KARTHIKEYAN
Department of Physics, Ramco institute of technology, Rajapalayam, Tamilnadu, India

S. SELVASEKARAPANDIAN*, D.VINOTH PANDI
Materials Research Centre, Coimbatore, Tamil Nadu, India

N. VIJAYA
Department of Physics, SFR College for women, Sivakasi, Tamilnadu, India

ARUN ARAICHIMANI
Department of Chemistry, Government Arts College,Tiruvannamalai, Tamilnadu, India

C. SANJEEVIRAJA
Department of Physics, Alagappa Chettiar College of Engineering & Technology, Karaikudi, Tamilnadu, India

Abstract

Polymers have been used for drug delivery for patients. Polymer to be used for drug delivery should be bio degradable in nature. Among bio degradable polymers PVA is bio compatible, non-toxic and protein absorption as desired in bio medical applications and having properties such as good charge storage capacity, very high dielectric strength and dopant dependent electrical and optical properties [1]. Bio degradable polymers such as PVA have to be studied complexed with different types of drugs such as enzymes and other types of drugs. To use polymer PVA for drug delivery, one has to understand the interaction between PVA and the drug to be used. The drug, amino acids are essentials for human health. An attempt is made to study the interaction between PVA and one of the amino acid Ariginine. Ariginine is a type of amino acid that may play an important role in the treatment of heart disease due to its block arterial plaque buildup, blood clots and platelets clumping and to increase blood flow through the coronary artery. PVA along with Arginine with different concentration have been used to prepare polymer membrane by solution casting technique using distilled water as solvent. In this paper, characterization of a PVA complexed with Arginine has been studied using XRD, FTIR and Impedance analysis and the result are reported. It is observed from the powder XRD, amorphous nature of membrane increases as the concentration of Arginine is increased upto to a particular concentration. FTIR spectrum confirms the complex formation between the PVA and Arginine. From the AC impedance analysis, the maximum conductivity has been found to be 1.97×10^{-6} S cm^{-1} for 75Mwt%PVA:25Mwt%Arginine sample at room temperature. The dielectric permittivity (ε') and Tangent loss spectra have been calculated from the ac impedance spectroscopy in the frequency range 42Hz – 1 MHz.

Proceedings of the 14th Asian Conference on Solid State Ionics (ACSSI 2014)
Copyright © 2014 ACSSI 2014 Organizers. All rights reserved.
ISBN: 978-981-09-1137-9
doi:10.3850/978-981-09-1137-9_049

1. Introduction

Polymers play a vital role in technological applications such as drug delivery, Fuel cells, Sensors and electro chromic display. Polymers are used for drug delivery which is bio-degradable in nature. Among bio-degradable polymers, PVA has been chosen as polymer host for the present study because of its high mechanical strength, excellent film-forming ability, dopant-dependent electrical and optical properties, low cost, and high tensile strength. PVA is a semi-crystalline material, and it is highly biocompatible and non-toxic. PVA is a water-soluble polymer that readily reacts with different cross-linking agents to form a gel [2]. These properties have led to the use of PVA in a wide range of applications in medical, cosmetic, food, pharmaceutical and packaging industries. The PVA protects the active ingredients from moisture, oxygen and other environmental components, while simultaneously masking their taste and odor. Amino acids are interesting organic materials. They exist as Zwitterions as they contain a proton donor carbonyl acid group (COOH) and Proton acceptor (NH_2) group [3,4]. In the amino acid group, Arginine is the non-essential amino acid that can be synthesized in the body by healthy individuals. Arginine is involved in many metabolic processes and important in the treatment of heart diseases and high blood pressure. Ariginine improves the circulation, strengthens the immune system of the human body. Research suggests that the amino acid accelerates the rate of healing of wounds, improves the burning of excess of fats and can be used in weight –reducing diets. In the literature, no work has been reported using PVA and Arginine. The present work is to synthesis and characterize PVA based polymer electrolyte with different Mwt% of Arginine This study has led to know the interaction between the PVA and Arginine for further research in drug delivery system.

2. Experimental Technique

The polymer PVA (Sigma Aldrich) of average molecular weight of 1,25,000 and the Amino acid, Arginine (LOBO Chemie) are used as raw materials in this study. Water is used as solvent. Separate solutions of PVA and Arginine in water are prepared and subsequently mixed with incremental proportions in steps of five resulting in series of transparent solutions ranging in PVA/Arginine ratios of 95:5 to 75:25 by Mwt%. The solution is then cased in poly propylene petridishes, and the samples are subjected to an extended drying period in a Vacuum chamber before analysis until complete solvent removal takes place. The thickness of the samples has been found to be in the range of 0.0084-.0136 cm. FTIR spectroscopy studies are carried out using SHIMADZU-8000

spectrophotometer in the range 400-4000 cm^{-1}. The Cu-Kα line has been used for XRD measurements by the usual θ-2θ scan. Conductivity measurements are carried out using a HOIOKI-3532 LCZ meter in the frequency range of 42Hz-5MHz at room temperature using stainless steel as blocking electrodes.

3. Results and discussion

3.1. *XRD analysis*

Figure.1 depicts the XRD patterns of pure PVA and PVA complexes with Arginine with different molar ratios. A broad peak around 19.7^0 [5] ascribed to the Pure PVA has been found in **figure 1a**. The XRD peaks due to Arginine at 18.2^0, 19.4^0, 23.1^0, 27.4^0 **[JCPDS File Number 30-1527]** have been observed as in **Figure 1c.** The intensity of these peaks increases as we increase the concentration up to 20Mwt% Arginine.

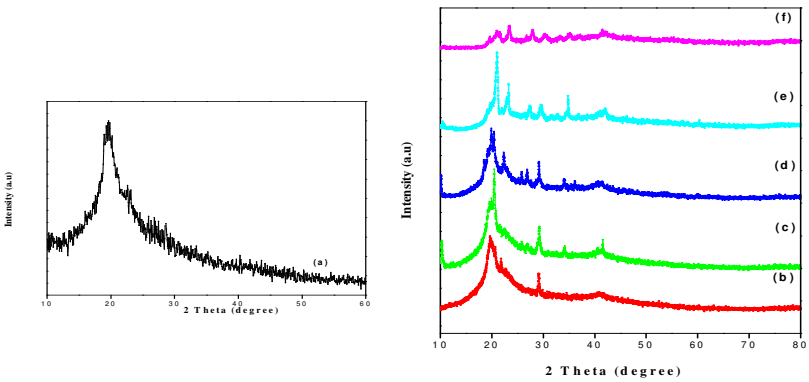


Figure.1 XRD pattern of (a) Pure PVA (b)95Mwt%PVA:5Mwt%Arginine (c) 90Mwt% PVA :10Mwt% Arginine (d) 85Mwt%PVA:15Mwt% Arginine (e) 80Mwt%PVA:20Mwt% Arginine (f) 75Mwt% PVA :25Mwt% Arginine polymer electrolytes at 303K

On further increase of concentration of Arginine to 25Mwt%, it is observed that the intensity of above peaks get drastically reduced and amorphous nature increases. This result can be interpreted in terms of the Hodge et al [6] criterion which has established a correlation between the height of the peak and the degree of crystallinity. In the present study, 75Mwt%PVA: 25Mwt%Arginine polymer electrolyte has high amorphous nature when compared with other electrolytes. Thus, the X-ray diffraction analysis reveals complex formation in

the polymer matrices and also the increased amorphous nature of the polymer electrolyte films on the addition of Arginine.

3.2. *FTIR analysis*

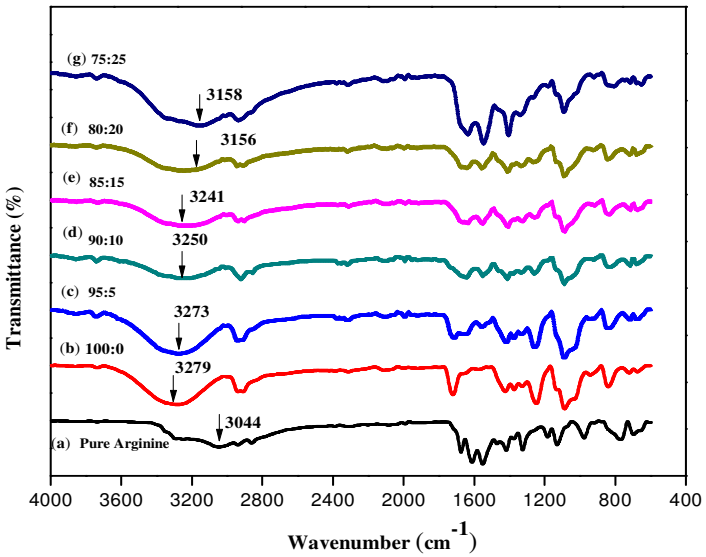


Figure.2 FTIR spectra of (100-x)PVA : xArginine (x= 0,5,10,15,20,25 MWt%) polymer electrolytes

FTIR spectroscopy has been used to analyze the interaction among atoms or ions in electrolyte systems. The IR spectra of Pure PVA, PVA complexed with Arginine concentration recorded at room temperature in the region 400-4000 cm^{-1} are shown in **figure 2**. From the **figure 2 (a)**, it has been observed that the peak at 3279 cm^{-1} in pure PVA is ascribed to hydroxyl group (O-H) stretching, and it is not due to absorbed water content. The hydroxyl band is shifted towards higher wave number in the complexes. It gives strong indication of specific interaction of Arginine and host polymer PVA in the polymer electrolytes [7]. The band corresponding to methylene (CH_2) group asymmetric stretching and aliphatic C-H stretching vibration of pure PVA occurs at about 2938 cm^{-1} [8, 9]. The bands at 1,462 cm^{-1} are assigned to C-H stretching vibration of CH2 of pure PVA. The bands at 1,196 and 1,115cm^{-1} are corresponding to C-O bending and stretching vibration of acetyl group present on the PVA backbone. It is observed that all the peaks of pure PVA get shifted, and their intensity also gets changed for complexed polymer electrolytes of different concentrations shown in

Table 1. The increase of amorphous nature, the shift and changes in the intensity of peaks position of FTIR spectra for different Arginine concentration confirm the complex formation between the polymer PVA and Arginine.

Table.1 Vibrational peaks and assignments of PVA/Arginine polymer electrolytes

Vibrational peaks of the electrolytes (cm^{-1})							Assignments
Pure PVA	Arginine	95PVA: 5Arginine	90PVA: 10Arginine	85PVA: 15Arginine	80PVA: 20Arginine	75PVA: 25Arginine	
3279	3288	3273	3250	3241	3156	3158	N-H stretching and O-H stretching
2938	2941	2938	2921	2940	2921	2936	C-H asymmetric stretching of CH_2
1654	1675	1653	1640	1668	1636	1643	C=O stretching and C=C stretching
1422	1471	1416	1411	1408	1404	1405	O-H bending and C-H bending of CH_2

3.3. *AC Impedance analysis*

Electrical characterization of all the prepared polymer samples has been performed using AC impedance spectroscopy technique. **Figure 3** shows the complex impedance plots of PVA/Arginine polymer electrolyte with different concentrations of Arginine at 303 K. Each plot consists of a high frequency depressed semicircle represented by a frequency dependent bulk capacitor C_b parallel to bulk resistor R_b. The low frequency capacitive spike is due to typical of blocking electrode.

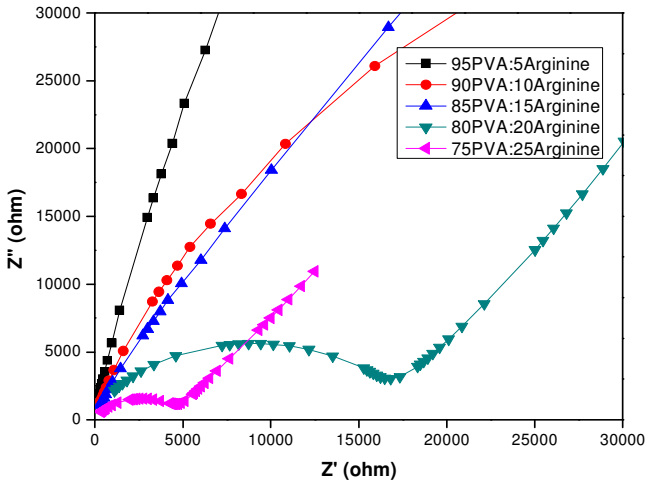


Figure 3. Complex impedance plots of PVA : Arginine polymer electrolytes with different concentrations at 303K.

The EQ software program developed by B.A. Boukamp et al. [10] has been used to extract the bulk electrical resistance (R_b) of the polymer electrolyte from the low frequency intercept of the semicircle on the Z' axis.
The ionic conductivity is calculated by using the equation as

$$\sigma = \frac{l}{AR_b} \text{---------- (1)}$$

where *l* and *A* are the thickness and area of the polymer electrolyte, respectively. From the **figure 3**, it is found that 75Mwt% PVA complexed with 25Mwt% Arginine has the highest conductivity at ambient temperature (303K) of 1.97 x 10^{-6} S cm^{-1}[11]. The conductivity values for all compositions of PVA-Arginine complexes at different temperatures are presented in **Table 2**.

Table.2 Ionic conductivity values of PVA:Arginine (Mwt%) polymer electrolytes from the impedance plots at different temperature

Temp. (K)	Conductivity σ (Scm^{-1})				
	95:5	**90:10**	**85:15**	**80:20**	**75:25**
303	2.14 X 10^{-9}	7.76 X 10^{-8}	2.15 X 10^{-8}	9.61 X 10^{-7}	1.97 X 10^{-6}
313	5.02 X 10^{-8}	2.78 X 10^{-7}	2.32 X 10^{-8}	2.01 X 10^{-6}	4.27X 10^{-6}
323	6.98 X 10^{-7}	6.68 X 10^{-7}	5.86 X 10^{-8}	3.73 X 10^{-6}	9.36 X 10^{-6}
333	2.33 X 10^{-6}	1.24 X 10^{-6}	8.79 X 10^{-8}	4.59 X 10^{-6}	1.74 X 10^{-5}
343	2.02 X 10^{-6}	2.52 X 10^{-6}	1.41 X 10^{-7}	1.01 X 10^{-5}	3.29 X 10^{-5}

3.4. *Conductance Spectra*

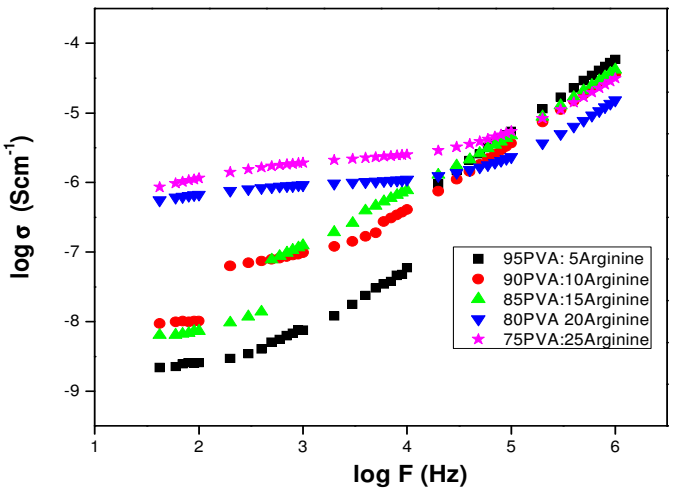


Figure 4 Conductance spectra for all compositions of PVA/Arginine polymer electrolytes at 303K.

The frequency dependence of the conductivity for all compositions of PVA/Arginine polymer electrolytes at 303K is depicted in **Figure 4**. Each plot shows three regions - low frequency dispersion region due to the space charge polarization at the blocking electrode, frequency- independent plateau region representing the dc conductivity (σ_{dc}) of the polymer complex and high frequency dispersion region corresponding to bulk relaxation phenomenon. The σ_{dc} values can be calculated by extrapolating the plateau region to logσ axis. Calculated value of conductivity is shown in the **Table-2.**

3.5. *Dielectric analysis*

The dielectric property indicates the amount of charge that can be stored by material and it can be used as an indicator to prove that the increase in conductivity is due to an increase in the charge carriers or free mobile ions. If dielectric property of the material increases, the amount of charge stored by the materials will also increase. The variation of ε' and ε'' as a function of frequency for different compositions of PVA:Arginine polymer electrolyte at 303K is shown in **figure 5(a) and figure 5(b)** respectively.

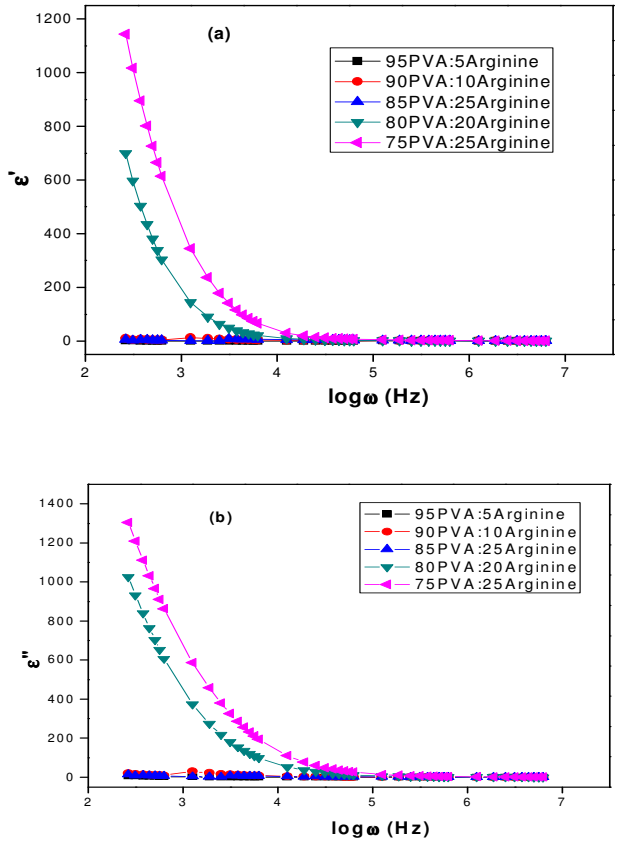


Figure. 5 (a) and (b) Variation of ε′ and ε″ as a function of frequency for all PVA:Arginine polymer electrolytes at 303K

The values of ε′ and ε″ are very high at low frequencies and relatively constant at higher frequencies. These values are found to be increased with the Arginine content in polymer complexes. The highest conducting polymer electrolyte, 75Mwt%PVA:25Mwt% Arginine exhibits the high ε′ and ε″ values at room temperature. The high values of ε′ and ε″ attributed to the localization of the charge carriers. The low frequency dispersion region is attributed to the contribution of charge accumulation at the electrode-electrolyte interface [12]. At higher frequency, due to the high periodical reversal of the electric field, there is no excess ion diffusion in the field direction. The polarization due to the charge accumulation decreases leading to decrease in the values of ε′ and ε″ [13]. The large value of ε″ is also due to the free charge motion within the material .

3.6 Loss Tangent Spectra analysis

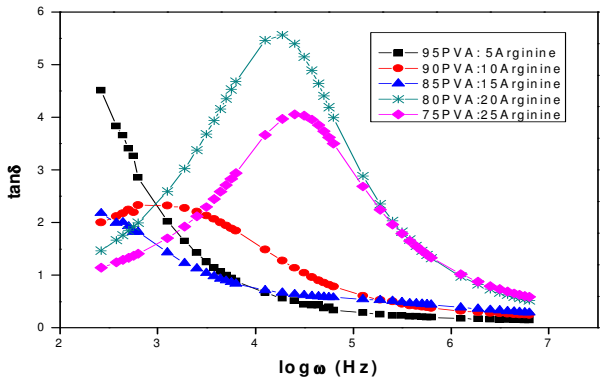


Figure 6. Variation of Tanδ as function of frequency for all compositions of PVA/Arginine polymer electrolytes.

The dielectric relaxation parameter of the polymer electrolytes can be obtained from the study of Tanδ as a function of frequency. The dielectric loss tangent, Tanδ can be defined by the equation Tanδ = ε″/ ε′. The variation of Tanδ with frequency for all the prepared PVA/Arginine complexes at 303K is presented in **Figure 6**. It has been observed, that Tan δ increases with increasing frequency and reaches a maximum. Then it decreases for further increase of frequency. The dispersion observed at low frequencies could be attributed to the interfacial polarization mechanism [14]. The dispersion observed at high frequency could be attributed to the dipolar relaxation. The loss tangent peak is described by the relation ωτ = 1, where τ is the relaxation time and ω is the angular frequency of the applied electric filed. The relaxation parameters are calculated for all the prepared polymer electrolytes at 303K and are tabulated in **Table 3.** A low relaxation time τ = 3.12 X 10^{-5} s is obtained for 75Mwt%PVA:25Mwt%Arginine of polymer electrolyte.

Table 3. Dielectric relaxation parameters for all compositions of PVA/Arginine polymer electrolytes

PVA-Arginine (Mwt%)	Relaxation frequency Log ω_n (Hz)	ω_n (Hz)	Relaxation time τ (s)
95PVA:5Arginine	2.43	2.67×10^{2}	3.75×10^{-3}
90PVA:10 Arginine	2.84	6.88×10^{2}	1.45×10^{-3}
85PVA:15 Arginine	2.42	2.60×10^{2}	3.85×10^{-3}
80PVA:20 Arginine	4.24	1.74×10^{4}	5.75×10^{-5}
75PVA:25 Arginine	**4.51**	**3.23×10^{4}**	**3.12×10^{-5}**

4. Conclusion

PVA-based polymer electrolytes with different concentrations of Arginine have been prepared using the solution casting technique. From XRD analysis, the amorphous nature of the investigated sample has been confirmed Amorphous nature of the polymer electrolyte films increases on the addition of Arginine. FTIR studies reveal the complex formation between the PVA and Arginine. The highest ionic conductivity has been found to be 1.97 X 10^{-6} Scm^{-1} for 75Mwt%PVA: 25Mwt%Arginine polymer electrolyte from the Cole-Cole plot and also confirmed from conductance spectra. From Loss Tangent spectra, low relaxation time 3.12 x 10^{-5} seconds has been observed for the electrolyte having highest ionic conductivity. The polymer electrolyte 75Mwt%PVA: 25Mwt% Arginine has the highest dielectric constant indicating the high storage capacity.

References

1.C.Shao, H.. Kim, J.Gong, B. Ding, D. Lee, S. Park, Materials Letters 57 (2003) 1579

2.M. Krumova, D. López, R. Benavente, C. Mijangos, J.M. Pereña, Polymer 41 (2000) 9265.

3.M.-H. Jiang, Q. Frang, Adv. Mater. 11 (1999) 1147.

4.S. Dhanuskodi, K. Vasantha, P.A Angeli Mary, Spectrochim. Acta A 66 (2007)

5.S. Rajendran, M. Sivakumar, R. Subadevi (2003) J Power Sources 124:225-230.

6.R.M. Hodge, G.H.Edward, G.P. Simon (1996) Polymer 37:1371-1376.

7.E.M. Abdelrazek, I.S. Elashmawi, S. Labeeb (2010) Physica B 405:2021–2027

8.S. Rajendran, M. Sivakumar, R. Subadevi (2003) J Appl Polym Sci 90:2794

9. S.Rajendran, M. Sivakumar, R. Subadevi, Wu NL, Lee JY (2007) J Appl Polym Sci 103:3950
10. B.A. Boukamp, Solid State Ionids 20(1986) 301.
11. C.S. Sunandana, P. Sentil Kumar (2004) Bull Mater Sci 27:1.
12. F.S. Howell, R.A. Bose, P.B. Macedo, C.T. Moynihan, J. Phys. Chem.78 (1974) 639
13. J.A. Campbell, A.A. Goodwin, G.P. Simon, Polymer 42 (2001) 4731
14. N.K. Singh, A. Panigrahi, R.N.P. Choudhary, Mater. Lett. 50 (2001) 1-5.

THE EFFECT OF DOPANT CONCENTRATION ON THE IONIC CONDUCTIVITY OF LIQUID PMMA OLIGOMER

NORASHIMA KAMALUDDIN[†]

Faculty of Applied Sciences, Universiti Teknologi MARA, 40450 Shah Alam, Selangor, Malaysia

FAMIZA ABDUL LATIF

Faculty of Applied Sciences, Universiti Teknologi MARA, 40450 Shah Alam, Selangor, Malaysia

CHAN CHIN HAN

Faculty of Applied Sciences, Universiti Teknologi MARA, 40450 Shah Alam, Selangor, Malaysia

RUHANI IBRAHIM

Faculty of Applied Sciences, Universiti Teknologi MARA, 40450 Shah Alam, Selangor, Malaysia

SHARIL FADLI MOHAMAD ZAMRI

Faculty of Applied Sciences, Universiti Teknologi MARA, 40450 Shah Alam, Selangor, Malaysia

FITRAH HADIP

Faculty of Applied Sciences, Universiti Teknologi MARA, 40450 Shah Alam, Selangor, Malaysia

To date gel and film type polymer electrolytes have been widely synthesized due to their wide range of electrical properties. However these types of polymer electrolytes exhibit poor mechanical stability and poor electrode-electrolyte contact hence deprive the overall performance of a battery system. Therefore, in order to indulge the advantages of polymer as electrolyte, a new class of polymer electrolyte was synthesized and investigated. In this study, liquid poly (methyl methacrylate) (PMMA) electrolyte was synthesized using the simplest free radical polymerization technique using benzoyl peroxide as the initiator. At this stage, it was found that this liquid PMMA oligomer (Mw=3000 g/mole) has a potential as electrolyte in electrochemical devices. It was found that an ionic conductivity of ~10^{-7} S/cm at room temperature can be achieved when only

[†] Core Frontier Materials and Industry Application, Research Management Institute, Universiti Teknologi MARA, 40450 Shah Alam, Selangor, Malaysia.

Proceedings of the 14th Asian Conference on Solid State Ionics (ACSSI 2014)
Copyright © 2014 ACSSI 2014 Organizers. All rights reserved.
ISBN: 978-981-09-1137-9
doi:10.3850/978-981-09-1137-9_057

small volume of high molarity of sulfuric acid (H_2SO_4) was doped in the liquid PMMA oligomer. The properties of this liquid PMMA oligomer were further investigated using Fourier Transform Infrared Spectroscopy (FTIR).

1. Introduction

The need of having smaller batteries with high energy and power density are becoming crucial due to the advancement in the communications and information technology such as smart phones and Tablet PCs. Polymeric materials have became the most extensively studied electrolyte host due to its flexible characteristic that make them possible to be fabricated into thin films and exhibit wide range of electrical properties. To date gel-type [1-3] and film-type [4-5] polymer electrolytes have been widely investigated. Unfortunately, these types of polymer electrolytes exhibited poor electrode-electrolyte contact or poor mechanical stability hence deprived the overall performance [6-7].

Therefore, in this study, a new type of liquid polymer electrolyte base on PMMA has been investigated. To the best of our knowledge, this liquid type polymer electrolyte has not been extensively explored. PMMA is chosen because of its unique properties that showed stability towards electrode [8]. In addition, it is a non-explosive and nonflammable material and when it leaks it will not harm the users like the common aqueous based electrolytes do. Since this liquid PMMA is not commercially available, it needs to be synthesized. Therefore, this liquid PMMA electrolyte was prepared by free radical polymerization technique because it is the easiest method that requires no stringent conditions.

Note that the importance of this study is to identify the potential of this liquid polymer electrolyte as a conducting host. Therefore, at this stage meticulous polymer synthesizing technique and further purification of the polymer obtained were not implemented though a pure liquid polymer can be obtained. To ensure that all electrolyte systems are in liquid condition, therefore, H_2SO_4 acid was used to provide proton for the conducting ions. Note that only 1 mL of the doping acid was used to study the potential of this liquid polymer electrolyte. This study will introduce a new class of conducting material to fit the need of growing portable electronic devices. The outcome of this study will be the starting point of the development of a new liquid type polymer electrolyte.

2. Experimental

2.1. *Synthesis of Liquid-based PMMA Oligomer Electrolyte*

5 mL of MMA monomer (ACROS) (Mw=100.12 g/mole) was added with 10% of benzoyl peroxide (MERCK) of the monomer mass. The test tubes were then soaked in a hot water bath for a few minutes to accelerate the polymerization process. The polymerization of PMMA was then allowed to continue at room temperature for another 24 hours. After 24 hours, only test tubes containing polymer in liquid form were doped with 1 mL of 1,3,5,7 and 9 M of H_2SO_4 acid (FLUKA) and was characterized immediately.

2.2. *Measurements*

2.2.1. *FT-IR Analysis*

The polymer-ion complexation was determined by PERKIN ELMER Fourier transform infra red spectrophotometer in the frequency range of 4000-600 cm^{-1} at a resolution of 16 cm^{-1}.

2.2.2. *Impedance Spectroscopy*

To measure the impedance of this liquid PMMA oligomer electrolyte, a Hioki LCR HiTester was used to perform the impedance (Z) measurement for each sample over the frequency range of 100 Hz-1 MHz. From the Cole-Cole plots obtained, the bulk resistance, R_b of each sample was determined and hence the conductivity (σ) of the samples were then calculated using Eq. (1): where l is the distance of the electrodes (cm), A is the effective contact area of the electrodes and the electrolyte (cm^2) and R_b is the bulk resistance (Ω) of the samples.

$$\sigma = l / R_b A \quad (1)$$

3. Results and Discussion

3.1. *The Formation of Doped Liquid PMMA Oligomer Electrolyte*

The molecular weight of this prepared undoped liquid PMMA oligomer was 3000 g/mole. This liquid PMMA oligomer has able to be sustained as liquid for 48 hours. Interestingly, the addition of H_2SO_4 helped to further sustain its condition in liquid form for 96 hours (4 days). It can be suggested that this acid also played the role as an inhibitor to slower down the polymerization rate.

3.2. *Characterization of Liquid PMMA Oligomer Electrolyte*

3.2.1. *FT-IR Analysis*

Figure 1 exhibits the FTIR spectra for H_2SO_4 doped PMMA oligomers. It was noted that a new peak was observed at 3500-3000 cm^{-1} when H_2SO_4 was added into the system. This peak can be suggested as hydrogen bond that formed between the carbonyl (C=O) group of PMMA and the H^+ ion from the acid [9]. This can be further confirmed by the decreasing of the intensity area ratio of the C=O band at ~1730 cm^{-1} as the concentration of the acid increased. It was also found that this C=O band shifted to higher frequency suggesting that the interaction between the oligomer and the doping acid is weak.

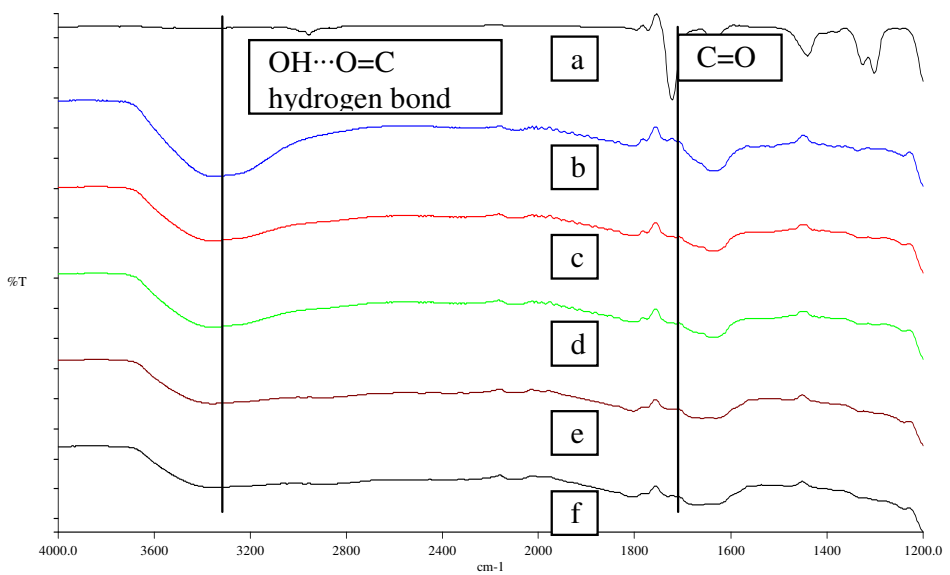


Figure 1. FTIR spectra for (a) undoped liquid PMMA oligomer and liquid PMMA oligomer doped with (b) 1 M, (c) 3 M, (d) 5 M, (e) 7 M and (f) 9 M of H_2SO_4 respectively.

3.2.2. *Electrical Studies*

Since FTIR analyses indicated that the interaction between the oligomer and the doping acid was weak, therefore the H^+ ion can be easily detached from the carbonyl group and free to move. Therefore, it explains why this PMMA oligomer was able to become ionic conductor. Table 1 summarized the ionic conductivity of the PMMA oligomer electrolyte at room temperature. It was found that the ionic conductivity increased as the concentration of H_2SO_4 acid increased. As the molarity of acid increased, the number of free H^+ ion also increased which was supported by the decreased in the intensity area ratio of the C=O band at higher concentration of acid.

Table 1. Average conductivity of liquid PMMA oligomer/H_2SO_4 at room temperature.

Molarity of H_2SO_4 (M)	Conductivity (S/cm)
1	4.167×10^{-9}
3	8.333×10^{-9}
5	2.609×10^{-8}
7	7.895×10^{-8}
9	1.744×10^{-7}

This can be further supported from the dielectric plot (Figure 2) in which PMMA oligomer doped with 9 M of acid exhibited the highest dielectric value at room temperature. Interestingly, it was noted that the dielectric constant plot of this system does not reach zero value at higher frequency like other gel or film PMMA electrolyte sytems. This may indicates that full charge dissipation does not occur at higher frequency in a liquid polymer system probably because contact area between the liquid polymer electrolyte and the electrode is better than in gel or film PMMA electrolyte systems [10-11].

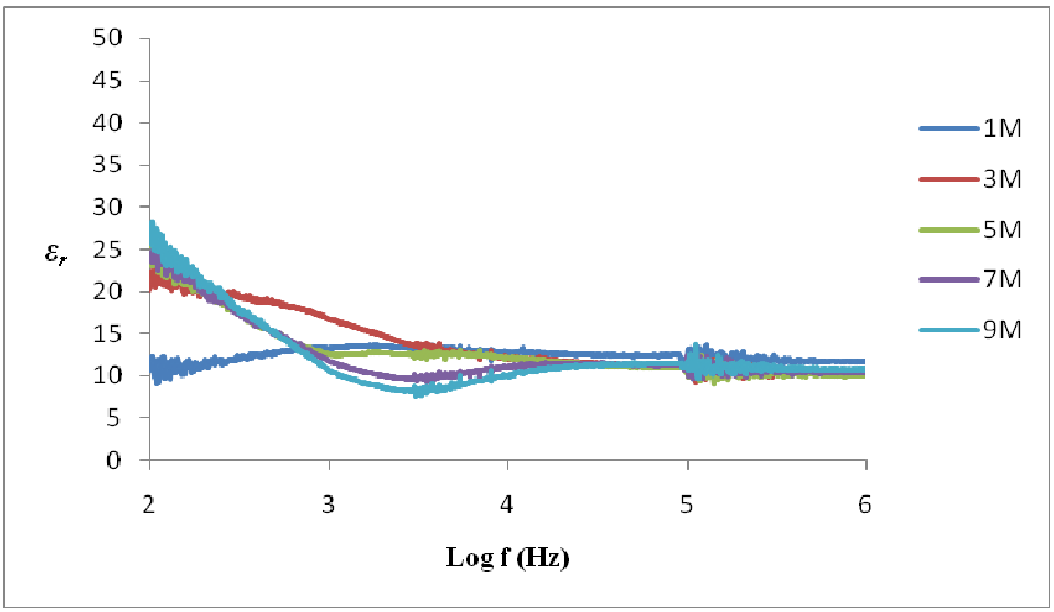


Figure 2. Variation of the dielectric constant with frequency for liquid PMMA oligomer doped with 1 M, 3 M, 5 M, 7 M and 9 M of H_2SO_4 at room temperature respectively.

4. Conclusion

This liquid PMMA oligomer exhibited similar characteristic as gel or film type of PMMA electrolyte but with better interfacial contact. Therefore, this new type of liquid PMMA oligomer can be considered as a new class of polymer electrolyte for various electrochemical applications.

Acknowledgement

Financial support and technical support from Malaysia Toray Science Foundation (MTSF), The Ministry of Higher Education (FRGS grant) and UiTM are highly acknowledged.

References

1. D. Saikia and A. Kumar, *European Polymer Journal,* **41**, 563-568 (2005).
2. R. Kumar, J. P. Sharma and S. S. Sekhon, *European Polymer Journal*, **41**, 2718-2725 (2005).
3. S. Rajendran, V.S. Bama and M.R. Prabhu, *Ionics,* **16**, 27-32 (2010).

4. R. Idris, M. D. Glasse, R. J. Latham, R.G. Linford and W. S. Schlindwein, *Journal of Power Sources*, **94**, 206-211 (2001).
5. R. Idris, N. H. N. Mohd and N. M. Arjan, *Ionics*, **13**, 227-230 (2007).
6. X. Hou and S. S. Kok, *Polymer*, **41**, 8689-8696 (2000).
7. S. Zhou and S. Fang, *European Polymer Journal*, **43**, 3695-3700 (2007).
8. G. B. Appetecchi, F. Croce and B. Scrosati, *Electrochimia Acta*, **40(8)**, 991-997 (1995).
9. H. Pu and D. Wang, *Electrochimia Acta*, **51**, 5612-5617 (2006).
10. F. Latif, M. Aziz, N. Kartun, A. M. M. Ali and M. Z. Yahya, *Journal of Power Sources*, **159**, 1401-1404 (2006).
11. T. Uma, T. Mahalingam and U. Stimming, *Materials Chemistry and Physics*, **90**, 245-249 (2005).

ELECTRICAL PROPERTIES OF RARE EARTH SALT DOPED IRRADIATED MH-PPV

FAMIZA ABD LATIF

Faculty Of Applied Science, Universiti Teknologi MARA, 40450, Shah Alam, Selangor, Malaysia

FITRAH BT HADIP, KAMARIAH BT MUDA

Faculty Of Applied Science, Universiti Teknologi MARA, 40450, Shah Alam, Selangor, Malaysia

It was noted that synthesizing poly[2-(heptyloxy)-5-methoxy-*p*-phenylenevinylene, MH-PPV can be expedited when synthesized via Microwave irradiation technique *i* MH-PPV. Lesser solvent was also used in the whole process. Though the conductivity of *i*-MH-PPV was higher than the MH-PPV synthesized via the conventional modified Gilch route (MH-PPV), its band gap was larger than the MH-PPV due to lattice imperfection. Therefore, in this study, this *i*-MH-PPV was doped with Terbium salt to reduce the energy band gap as well as increased its conductivity. Unfortunately, it was found that the addition of this rare earth salt slightly increased the energy gap of *i*-MH-PPV. In addition, the conductivity of this doped *i*-MH-PPV was also found to be decreased. Interestingly, the UV absorption peak shifted to the blue region. The physical properties of this doped MH-PPV was further investigated under FTIR spectrophotometer.

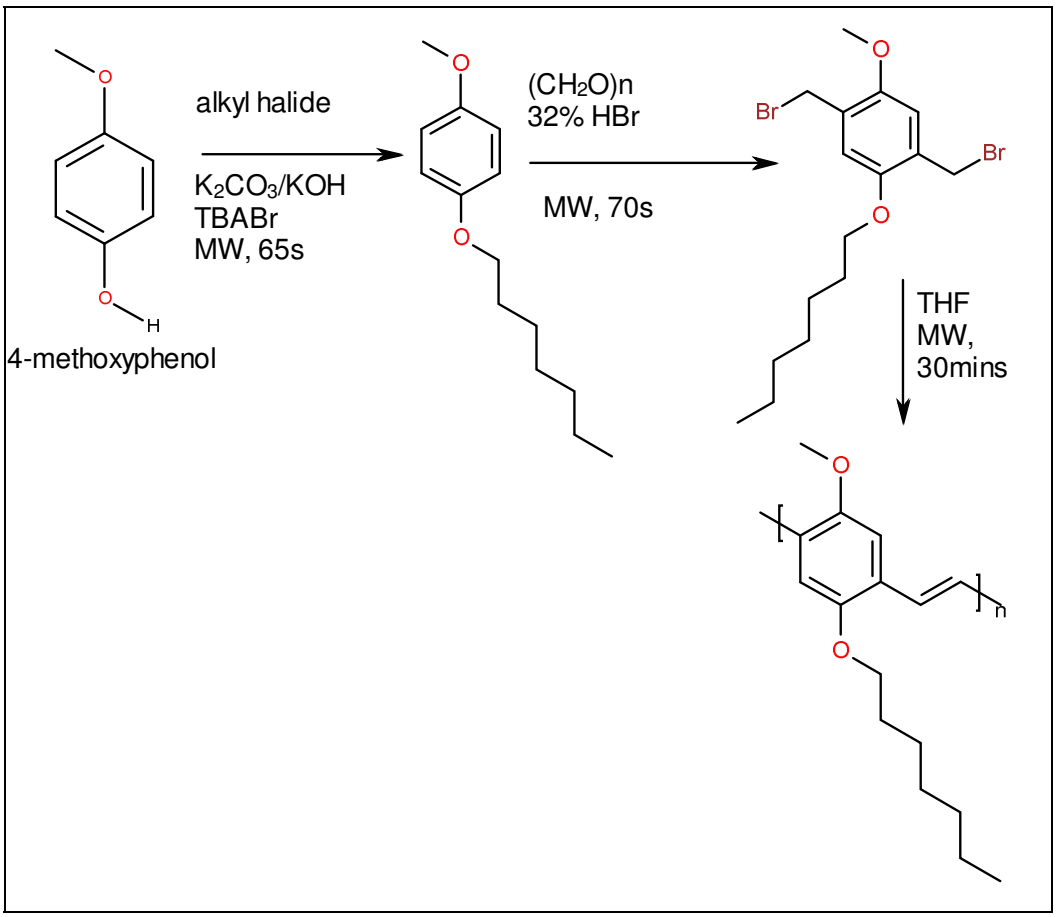
1. Introduction

Conjugated polymers are generally has the ability to conduct polymer by delocalization of electrons in its conjugated back bonds **[1].** To date over 100 conducting polymers **[2]** have been synthesized. Amongst them, poly(p-phenylenevinylene) (PPV) **[3]** has received much attentions due to its good mechanical properties and broad geometry possibilities **[4].** Due to the unique properties, it has been widely used in optical and electronic devices. However, PPV is insoluble in most organic solvents hence limits its application. Therefore, the structure of PPV is modified by substituting alkoxy or phenyl group at the second and fifth position of the phenylene unit of PPV.

These soluble PPV derivatives can be synthesized via Wessling route **[5],** Heck's coupling **[6],** Wittig-condensation route **[7]** and Gilch route **[8].** Amongst them, Gilch route is widely adopted in synthesizing high yield molecular weight PPV derivatives **[9].** However, this route required long reaction time and meticulous purification technique and required a lot of solvents in each step. Therefore, in our initial study we have synthesized MH-PPV (scheme 1) via microwave irradiation technique *i*-MH-PPV and compare it

Proceedings of the 14th Asian Conference on Solid State Ionics (ACSSI 2014)
Copyright © 2014 ACSSI 2014 Organizers. All rights reserved.
ISBN: 978-981-09-1137-9
doi:10.3850/978-981-09-1137-9_058

properties with MH-PPV that has been synthesized via Gilch route. We found that *i*-MH-PPV can be obtained within 32 minutes only. In addition this *i*-MH-PPV exhibited similar molecular structure with that MH-PPV obtained via Glch route (Figure 1). However, this *i*-MH-PPV exhibited higher ionic conductivity with higher band gap than MH-PPV.



Scheme 1 Synthesis of MH-PPV

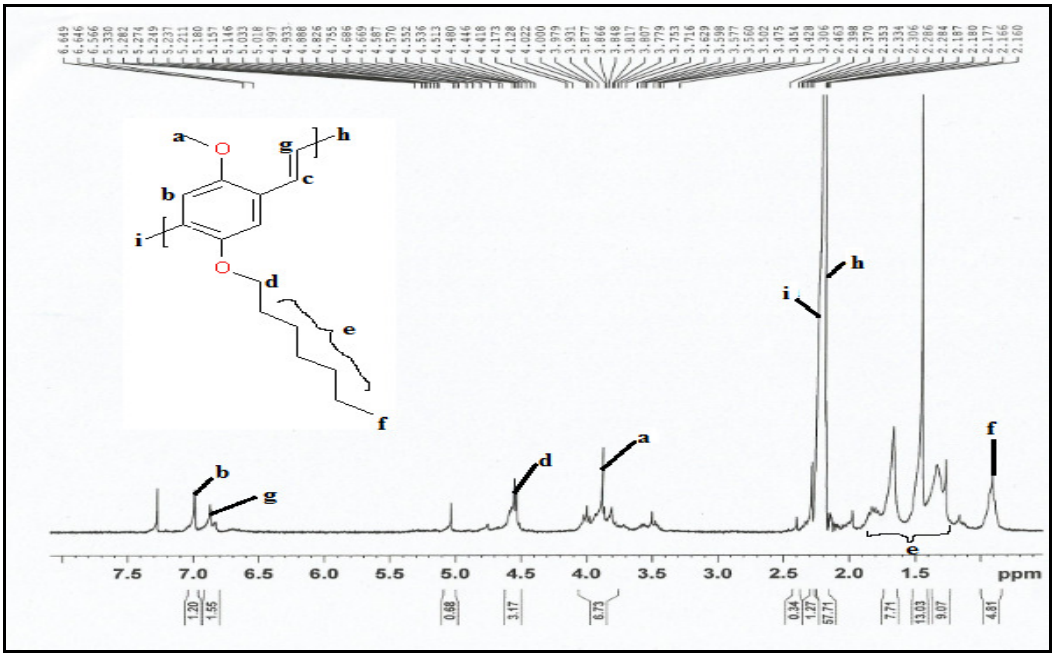


Figure 1 ^{1}H NMR spectra for *i*- MH-PPV

Therefore, in this study, this *i*-MH-PPV was doped with rare earth salt, i.e. terbium acetate hydrate, *d-i*MH-PPV to improve both electrical and optical properties of this *i*-MH-PPV. Doping material such as lithium salt **[10],** ZnO salt **[11],** titanium oxide (TiO_2) **[12]** have improved the conductivity or optical properties of a polymer electrolyte system. To the best of our knowledge, the use of rare earth salts as doping material have not been extensively studied. Therefore, these studies also contribute new knowledge on the effects of rare earth salts on the electrical and optical properties of a conducting polymer.

2. Experimental

2.1. Doping of *i*-MH-PPV

3% of terbium acetate (lll) hydrate was added into i-MH-PPV solution. The mixture was then stirred and casted into a teflon petridish. The *d-i*MH-PPV film was then dried in an oven at 50˚C for conductivity testing.

2.2. *Physical characterization*

The effect of doping material on the melting point and the solubility of *d-i*MH-PPV in tetrahydrofuran, dichloromethane and chloroform were investigated.

2.3. *FTIR analysis*

The FTIR analysis for *d-i*MH-PPV was carried out using SHIMADZU FTIR 8300 Fourier Transform Infra Red spectrophotometer at a frequency range of 4000-400cm^{-1}.

2.4. UV-VIS analysis

The UV-visible absorption spectrum of *d-i*MH-PPV was obtained using Perkin Elmer lambda spectrophotometer in the wavelength range of 300-800nm.

2.5. *Conductivity Studies*

The conductivity of *d-i*MH-PPV was calculated from the bulk resistance that was determined from the Cole-Cole plot obtained from HIOKI 3532-01 LCR High Tester. The instrument was interfaced to a computer and set to measure the impedance in a frequency range of 100 Hz – 1 MHz at room temperature.

3. Results and discussion

3.1. Physical properties of *d-i*MH-PPV

It was found that *d-i*MH-PPV exhibited higher boiling point (87°C) then the *i*-MH-PPV (55°C) indicating that the stability of *i*-MH-PPV has been improved without jeopardizing its solubility in all the common organic solvents used in this study. The increased in the stability of *d-i*MH-PPV was probably due to the formation polymer network that formed via hydrogen bonding between the polymer side chain and the hydroxyl group or the acetate group of the terbium salt.

3.2. FTIR analysis

Figure 3 exhibited the FTIR spectra for both *i*-MH-PPV and *d-i*MH-PPV. It was noted that both characteristic peaks of terbium salt at ~ 3000 cm^{-1} (-OH band) and ~1700 cm^{-1} (C=O band from the acetate group) were almost diminishing in the FTIR spectrum of *d-i*MH-PPV. These confirmed the formation of polymer network via hydrogen bonding between the polymer and salt that increased its stability.

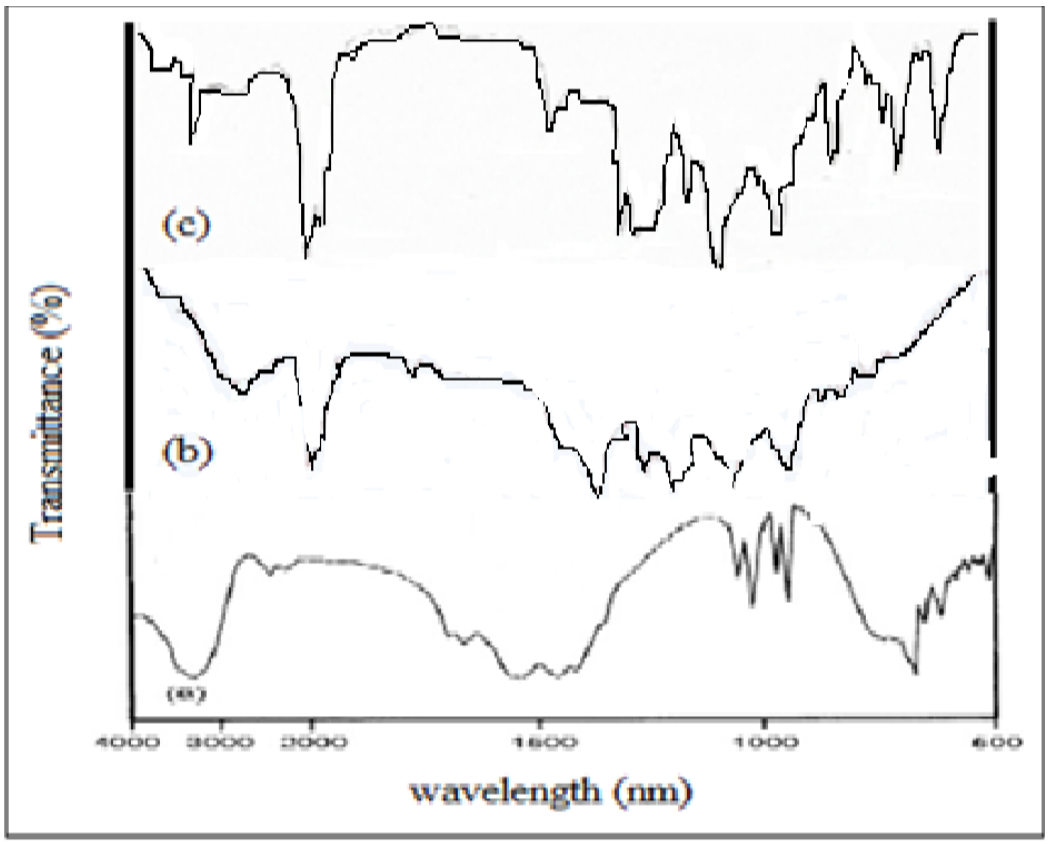


Figure 2 FTIR spectra for (a) terbium acetate hydrate (b) *i*-MH-PPV and (c) *d-i*MH-PPV

3.2. UV analysis

The UV-VIS absorption spectra for *i*-MH-PPV and *d-i*MH-PPV were presented in Figure 3. Interestingly, it was noted that after doping, the absorption peak of *i*-MH-PPV at 466 nm shifted to shorter wavelength that falls in the blue region. This shifting also indicates that the energy gap of *d-i*MH-PPV was slightly increased from 2.42 eV to 2.48 eV. This slight increase in the energy gap of *d-i*MH-PPV was probably due to the presence of terbium salt located in between the HOMO-LUMO that hinder the excitation of electron from HOMO to LUMO. This can be supported by the appearance of shoulder peak at 461 nm in the UV-VIS absorption spectra of *d-i*MH-PPV due to excitation of lone pair electron from the oxygen atoms of the salt's acetate group. The increased in the absoption peak of the *d-i*MH-PPV indicated that the excitation of electron in this system required higher amount of energy as compared in the *i*-MH-PPV system.

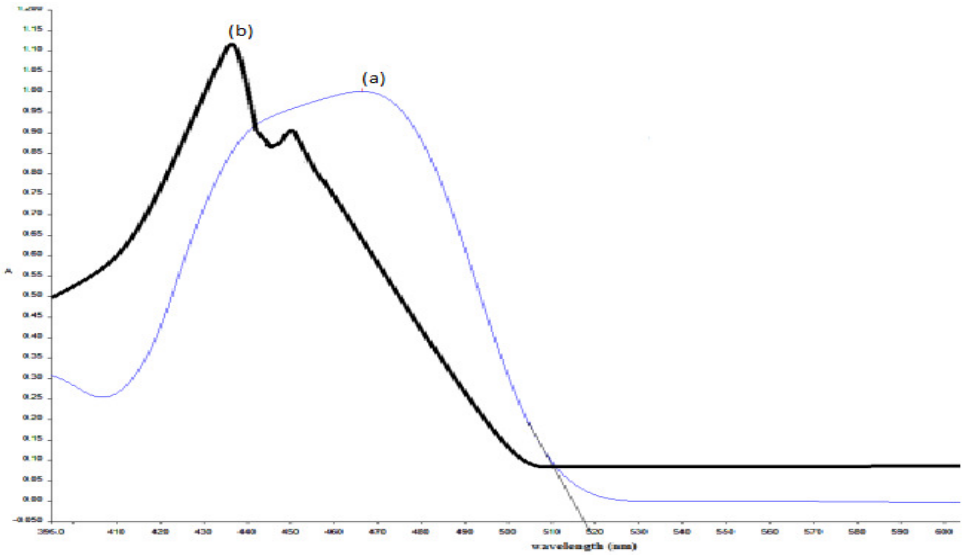
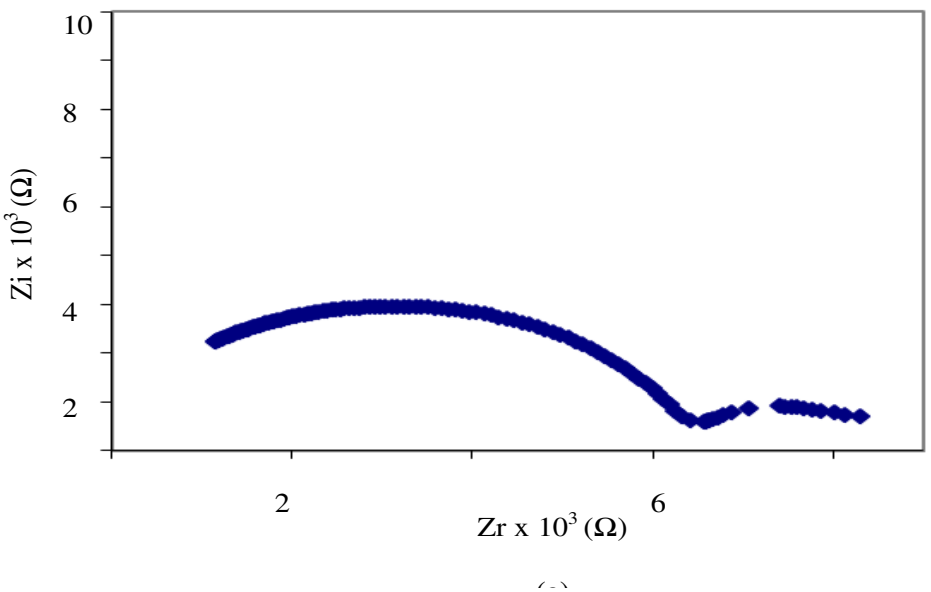
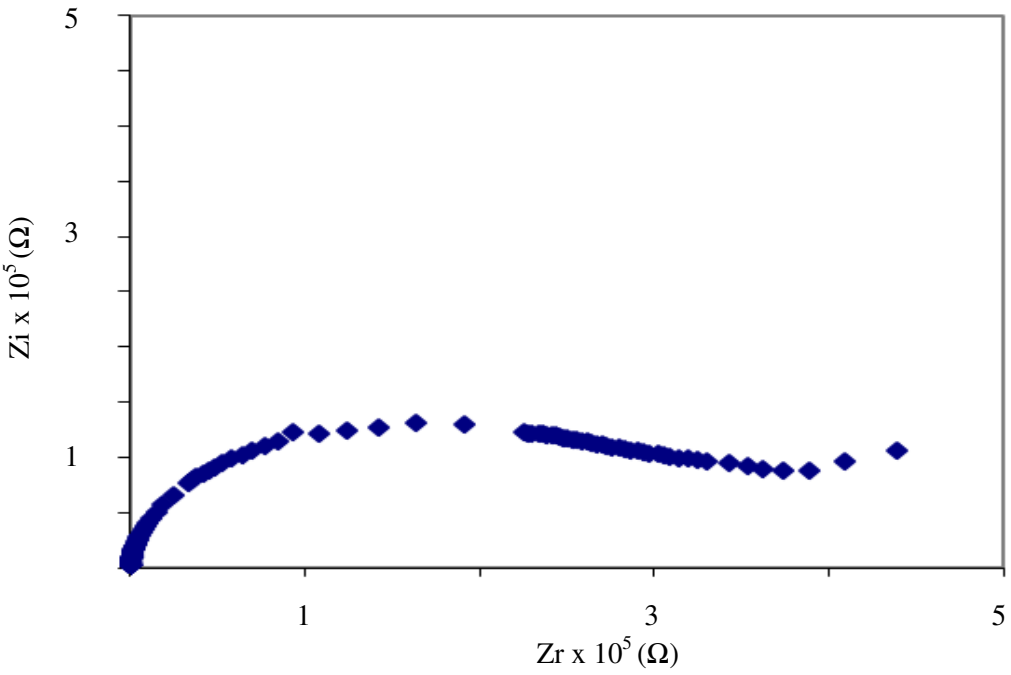


Figure 3 UV VIS spectra for for (a) *i*-MH-PPV and (b) *d*-*i*MH-PPV

3.3. Conductivity studies

Figure 4 displayed the Cole-Cole plots for both *i*-MH-PPV and *d*-*i*MH-PPV where showed two well resolved semicircles. It was found that *d*-*i*MH-PPV exhibited lower conductivity (1.17 x 10^{-8} S/cm) than the *i*MH-PPV (7.01 x 10^{-7} S/cm) at room temperature. This may be due to the presence of large terbium salt structure that hinder the transportation of electron along the polymer backbone.





(b)

Figure 4 Cole-cole plot for (a) *i*-MH-PPV and (b) *d-i*MH-PPV

4. Conclusion

Doping of *i*-MH-PPV with terbium salt was found to decreased the conductivity of the irradiated polymer with higher energy gap due to the present of large structure of the terbium acetate salt

Acknowledgement

Financial support and technical support from FRGS grant and UiTM are highly acknowledged.

References

[1] Davenas, J., Chouiki, M., Besbes, S., Ltaief, A., Ouada, H., Bouazizi, A., Trad, H., et al. (2003). Influence of the molecular structure on the optical absorption and emission of PPV derivatives, *139*, 617–620. doi:10.1016/S0379-6779(03)00266-2

[2] Unsworth, J., Costa, C., Zheshi, J., Kaynak, A., Ediriweera, R., Innis, P. and Booth, N.J., (**1994**). Conducting Polymers: Properties and Applications. *Journal of Intelligent Material Systems and Structures*. 5. 5. 595-604.

[3] Scotheim, R.L., Elsenbaumer, and Reynolds, J.R., (**1988**). *Handbook of Conducting Polymer.* Marcel Dekker Inc. New York.

[4] Jing, C., Chen , L., Shi, Y. and Jin, X. (2005). *Synthesis and characterization of exfoliated MEH-PPV/clay nanocomposites by in situ polymerization*. 41. 2388–2394

[5] Wessling, R.A. (1970). The solubility of poly(vinylidene chloride). *Journal of Applied Polymer Science*. 14. 6. 1531-1545.

[6] Shim, H.K. and Jin, J.I. (2002). Light-emitting Characteristics of Conjugated Polymer. *Advances in Polymer Science*. 158. 193-243.

[7]] Zou, Y., Xia, A., Yuan, Z., Tan, S., Tan, Z., Yang, Y. and Li, Y. (**2007**). Synthesis and optical properties of fluorene and p-phenylenevinylene copolymers containing non-conjugated spacer. *European Polymer Journal*. 43 . 4. 1394-140

[8] Gilch, H.G. and Wheelwright, W.L. (**1966**). Polymerization of α-halogenated p-xylenes with base. *Journal of Polymer Science Part a: Polymer Chemistry*. 4. 6. 1337-1349.

[9] Neef, C.J. and Ferraris, J.P., (**2000**). MEH-PPV: Improved synthetic procedure and molecular weight control. *Macromolecule.* 33. 2311-2314.

[10] Birgerson, J., Janssen, F. J. J., & Gon, A. W. D. Van Der. (2002). Doped polymeric cathodes for PPV / Al based LEDs, *132*, 57–61.

[11] Lira-cantu, M., & Krebs, F. C. (2006). Hybrid solar cells based on MEH-PPV and thin film semiconductor oxides (TiO 2 , Nb 2 O 5 , ZnO , CeO 2 and CeO 2 – TiO 2): Performance improvement during long-time irradiation, *90*, 2076–2086. doi:10.1016/j.solmat.2006.02.007

[12] Bi, D., Wu, F., Yue, W., Qu, Q., Cui, Q., Qiu, Z., Liu, C., et al. (2011). Improved performance of MEH-PPV / ZnO solar cells by addition of lithium salt. *Solar Energy*, *85*(11), 2819–2825. doi:10.1016/j.solener.2011.08.016

ELECTRICAL PROPERTIES OF PPV DERIVATIVES SYNTHESIZED VIA MICROWAVE IRRADIATION TECHNIQUE

FITRAH BT HADIP[†]

Faculty Of Applied Science, UniversitiTeknologi MARA, 40450, Shah Alam, Selangor, Malaysia

FAMIZA BT ABD LATIF, KAMARIAH BT MUDA

Faculty Of Applied Science, UniversitiTeknologi MARA, 40450, Shah Alam, Selangor, Malaysia

Poly[*p*-phenylenevinylene] (PPV) derivatives are a new class of conducting polymer that have potential application in optical and various electrical devices. To date they have been synthesized via modified Gilch route. Unfoetunately, this polymerization technique required long reaction time, meticulous purification technique and required a lot of solvents. Therefore, in this study, new PPV derivatives were synthesized using Microwave Irradiation Technique.. Overall, it was found that these PPV derivatives were obtained in less than 45 minutes. Only a small amount of solvent was used in the whole process of synthesizing each PPV derivatives. Interestingly, all PPV derivatives that were synthesized were soluble in common organic solvents. A high conductivity of 7.01 x 10^{-7} and 2.69 x 10^{-8} Scm^{-1} were obtained from these PPV derivatives with band gap ranging from 2.42 to 2.45 eV. It were also found that the polymers appeared to be in colour of dark brown with different melting point.

1. Introduction

Conjugated polymer have been a potential material for its fabrication in optoelectronic devices such as polymer light emitting diode (PLED), sensors and organic solar cells **[1].** One of the unique property of π-conjugated systems is the electron delocalization which have huge influence on the selective optical absorption and electronic conductivity. Poly(*p*-phenylenevinylene) and its derivatives had gained much interest for its ability to serve as an active material in polymer electroluminescent devices. There have been considerable research progress for better understanding of the influence of the modification of the PPV molecular structure induced by the side chain substitution on the phenyl ring

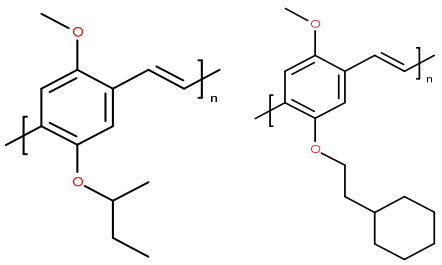
[†]Core Frontier Materials and Industry Application, Research Management Institute, UniversitiTeknologi MARA, 40450 Shah Alam, Selangor, Malaysia.

Proceedings of the 14th Asian Conference on Solid State Ionics (ACSSI 2014)
Copyright © 2014 ACSSI 2014 Organizers. All rights reserved.
ISBN: 978-981-09-1137-9
doi:10.3850/978-981-09-1137-9_059

which has a marked effect on the optical absorption and photoemission of the PPV derivatives.

The use of microwave irradiation as another approach compared to conventional heating (reflux) which has been employed in Gilch route for the synthesis of PPV derivatives represent a more simple yet fast reaction towards green chemistry as the excessive use of solvent was reduced **[2].**

In this study, poly[2-(methoxy)-5-(ethylcyclohexoxy)-*p*-phenylenevinylene] (MEC-PPV), Poly[2-(methoxy)-5-(sec-butoxy)-*p*-phenylenevinylene] (MSB-PPV) were synthesized via Gilch route using microwave irradiation technique. The chemical structure of PPV derivatives were shown in Figure 1. The length of the alkyl side chain was controlled to be more than 3 carbon**[3]** for complete solubility of PPV derivatives in common organic solvents. By modifying the alkyl side chain, the optical absorption and photoemission wavelength showed a different data for each PPV derivatives as well as their conductivity. The sensitivity of these polymer's optical spectra to slight changes suggest that it is necessary to take the effect of length of side chain into account as well as the influenced of microwave irradiation into the final product.



P1 **P2**

Figure 1 Schematic chemical structure of MSB-PPV (**P1**) and MCE-PPV (**P2**)

2. Experimental

2.1. *Synthesis of PPV derivatives*

2.1.1. O-alklation reaction reaction

0.6 mL of 4 methoxyphenol (ACROS) (Mw=124.14 g/mole), 0.6 mL of alkyl halide (ALDRICH), 0.17g of tetrabutylammonium bromide (ACROS) (Mw=322.36 g/mole) and the premixed 2.8g of potassium carbonate (R&M) and 1.1g of potassium hydroxide (R&M) (Mw=56.11 g/mole) were added in a closed glass vessel. The mixture was then irradiated under microwave irradiation until a product that gave one spot under TLC analysis was obtained. After the reaction completed, the sample was extracted twice with 25 mL tetrahydrofuran (SYSTERM) (Mw=72.11). Then 1g of anhydrous magnesium

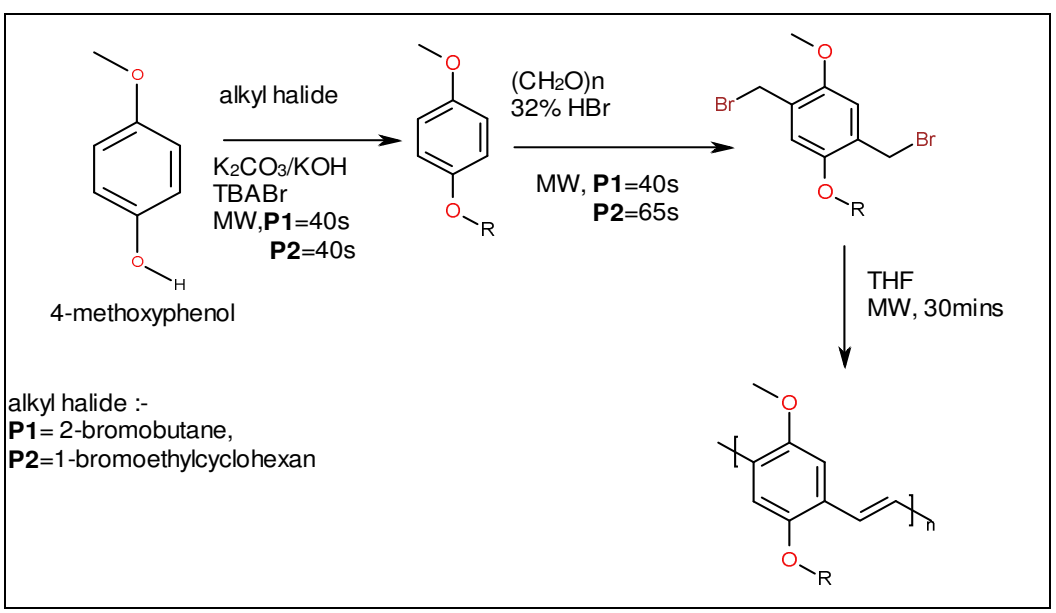
sulphate (SYSTERM) (Mw=120.37 g/mole) was added to the sample and filtered. The product was then purified by using recrystallization technique with the appropriate solvent mixture of hexane:dichloromethane in the ratio of 8:2 to produce the precursor. The structure was confirmed by FTIR and ^{1}H NMR.

2.1.2. *Hydrohalogenation reaction*

The precursor obtained was dissolved in 5mL acetic acid. Then the mixture, 3mL of 32% of HBR in acetic acid (MERCK) and 3g of paraformaldehyde (R&M). The mixture was then irradiated in microwave oven until the product that shown one sport under thin layer chromatography analysis was obtained. The product then was extracted with sodium hydrogen carbonate solution that made beforehand and THF. Then 1g of anhydrous magnesium sulphate was added to remove the water and filtered. The sample was recrystallized with appropriate solvent mixture of hexane:dichloromethane in the ratio 7:3 to obtained the monomer. The confirmation of structure was done using FTIR and ^{1}H NMR.

2.1.3. *Polymerization reaction*

The monomer obtained was then dissolved in 1mL of THF and irradiated in microwave oven until polymerization completed. The overall reaction was shown in Scheme 1.



Scheme 1 Synthesis of **P1** and **P2**via microwave irradiation technique

2.2. *Confirmation of polymer structure*

In this study, Perkin Elmer Spectrum One Fourier Transform Infrared Spectroscopy (FTIR) and Nuclear Magnetic Resonance (NMR)were used to confirm the structure of the **P1** and **P2**.

2.3. *Physical characterization*

The physical properties of the polymers were determined using solubility test in tetrahydrofuran, dichloromethane and chloroform and also (Fischer Scientific) melting point apparatus.

2.4. *UV-VIS analysis*

UV-visible absorption spectra of the polymers were obtained using Perkin Elmer lambda spectrophotometer in the wavelength range of 300-800nm.

2.5. *Conductivity analysis*

The conductivity of the polymers were determined using cole-cole plot obatained from (HIOKI) impendance spectroscopy.

3. Results and discussion

3.1. *Confirmation of polymer structure*

It was found that PPV derivatives can be successfully synthesized using microwave irradiation technique within 32 minutes for overall reaction which gave satisfied infrared spectra and clean NMR spectra for both polymers. The characteristic peaks from FTIR spectra were tabulated in Table 1and the NMR spectra were shown in Figure 2(a) and 2(b).

Table 1 The characteristic peaks of PPV derivatives

Types of Vibrations	Frequency observed (cm^{-1})		References
	P1	**P2**	
C-H sp^2 (stretch)	2861.01	2920.28	Chen et al., 2003
C=C (aromatic)	1493.41	1486.94	Chen et al., 2003
C-O-C (ethers)	1069.30	1226.80	Chen et al., 2003
Vinyl C=C	1602.21	1643.45	Chen et al., 2003

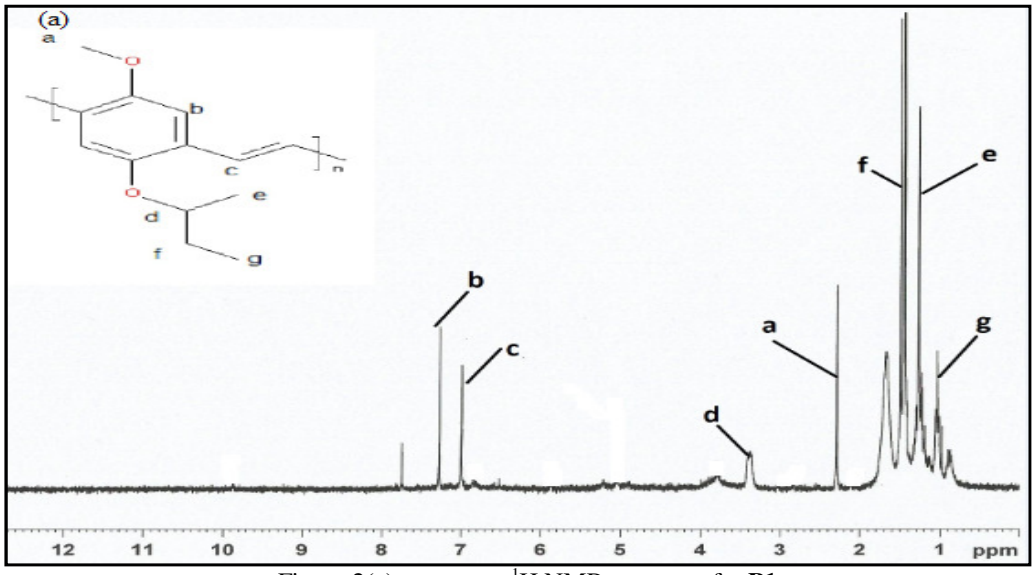


Figure 2(a) ^{1}H NMR spectrum for **P1**

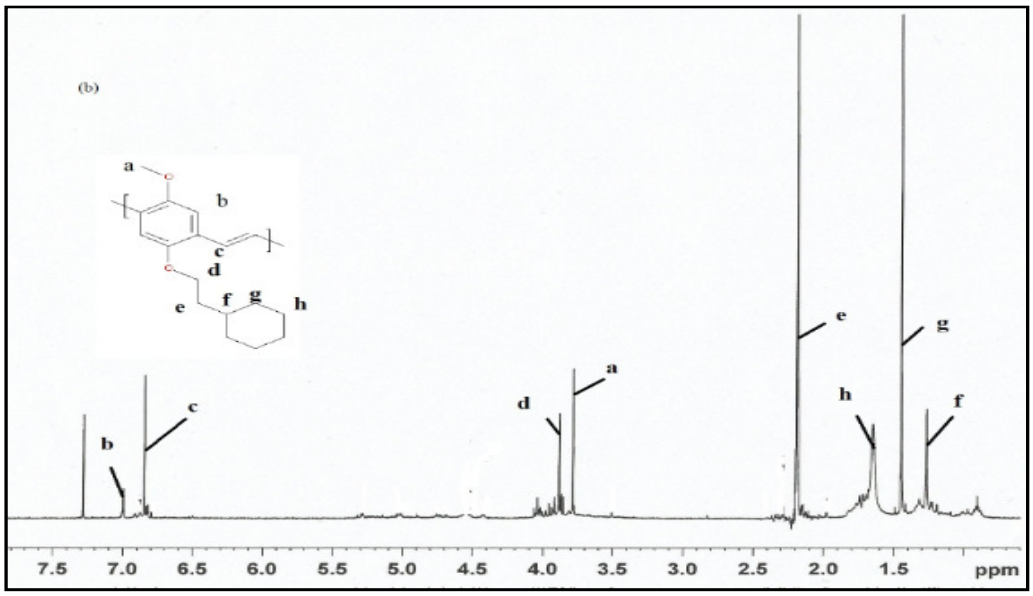


Figure 2(b) ^{1}H NMR spectrum for P**2**

3.3. *Physical properties of PPV derivatives*

Eventually, both PPV derivatives exhibits slightly different properties with their melting point of 99.4˚C and 89 ˚C for **P1** and **P2.** Furthermore, both polymers were completely soluble in common organic solvents such as tetrahydrofuran, dichloromethane, ethanol and etc. For the formation of thin films, the polymers form a brittle film which may due to the lattice imperfection formed during microwave heating**[4].**

3.4 *Band gap energy analysis*

The UV-VIS absorption spectra for both polymer were presented in Figure 3 where the maximum absorption peaks were 469 nm and 470 nm respectively.

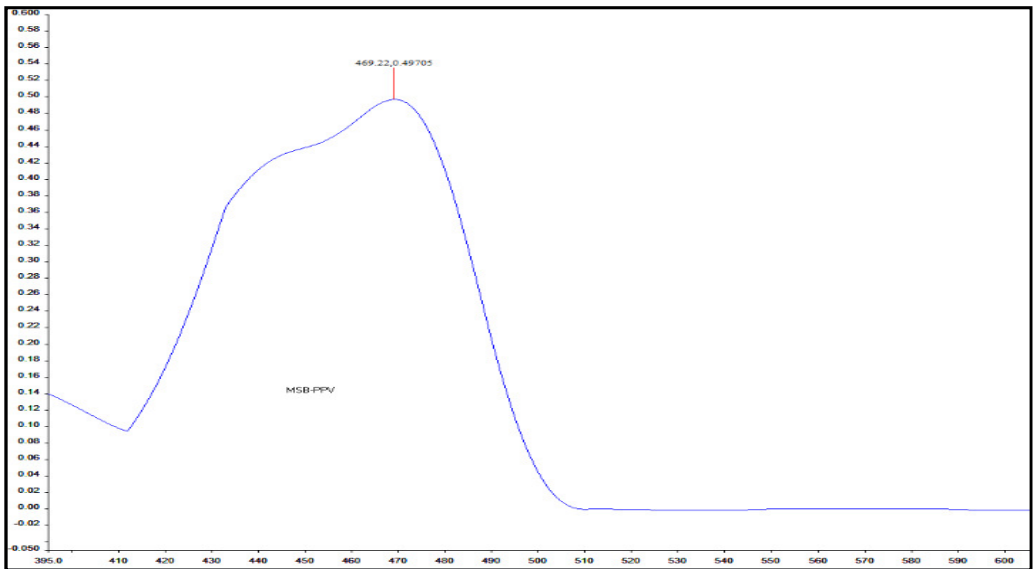


Figure 3(a) UV VIS spectra of **P1**

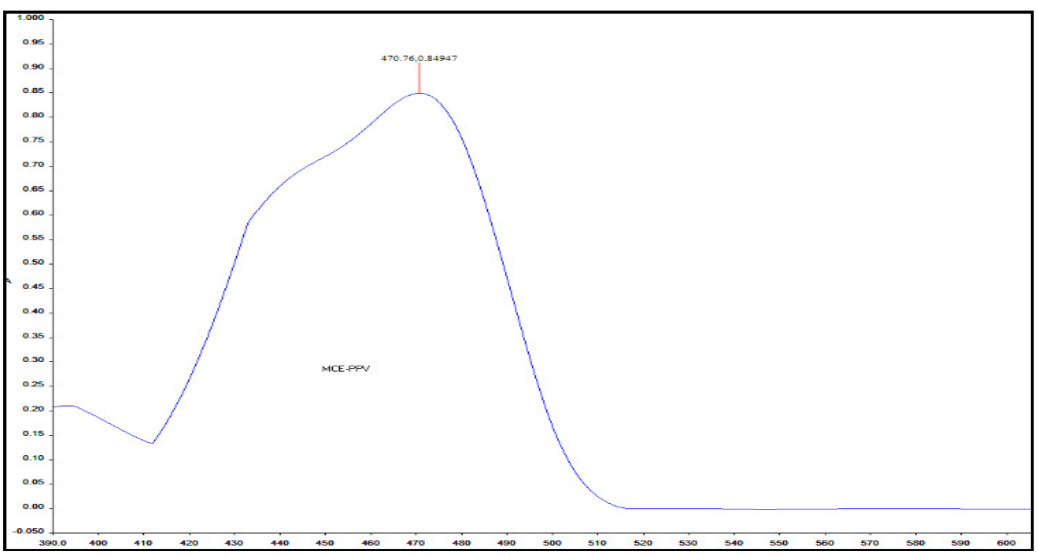


Figure 3(b) UV VIS spectra of **P2**

From the spectra above, it were observed that both peaks appeared to be broad with similar maximum absorption on the blue region from the broad band absorption filter spectra in Figure 4. The calculated band gap for P1 was 2.46 eV and P2 was 2.45 eVrespectively which is desirable for photovoltaic

application. The observed absorption spectrumwas broad due to the distribution of **P1** and **P2** chain length over the wide range and the vibration of polymer system during absorption process**[1].**

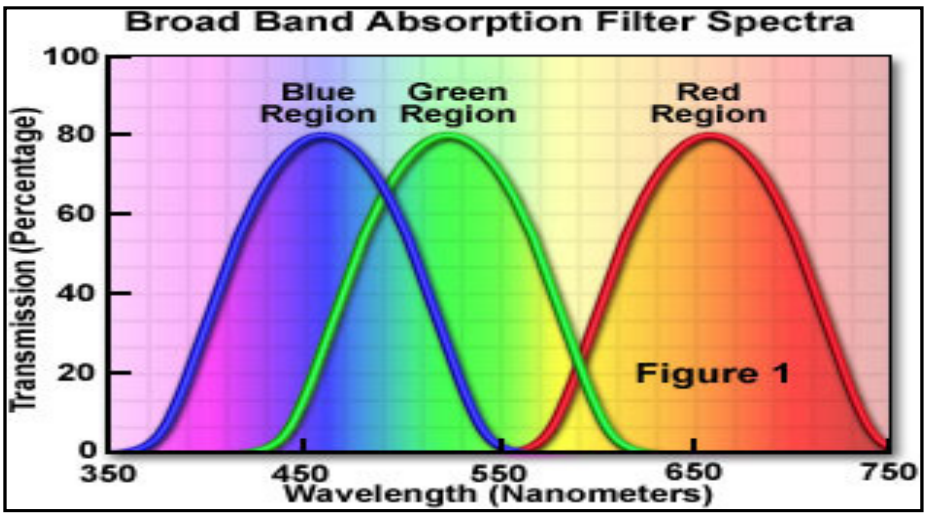


Figure 4 Broad band absorption filter spectra based on the colour of polymer

3.5 *Electrical conductivity analysis*

The electrical conductivity of P1 and P2 were investigated by using cole-cole plot presented in Figure 5(a) and 5(b).

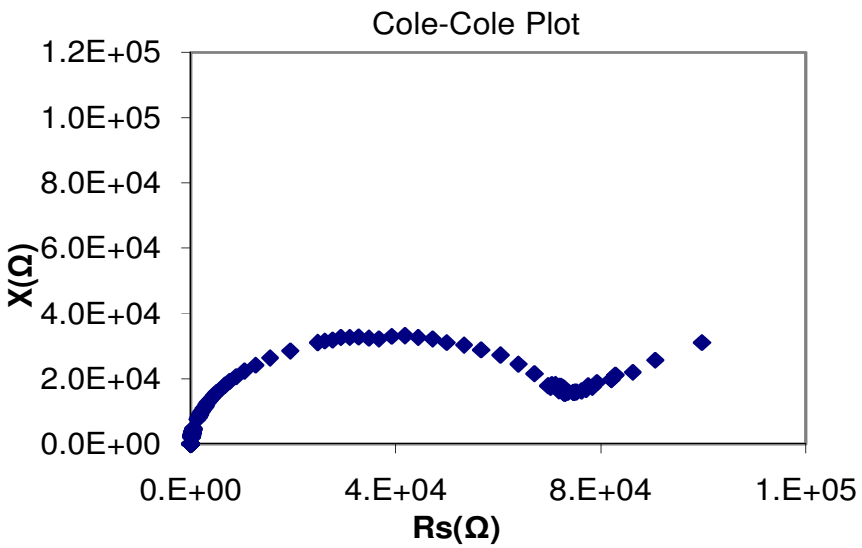


Figure 5(a) Cole-cole plot of **P1**

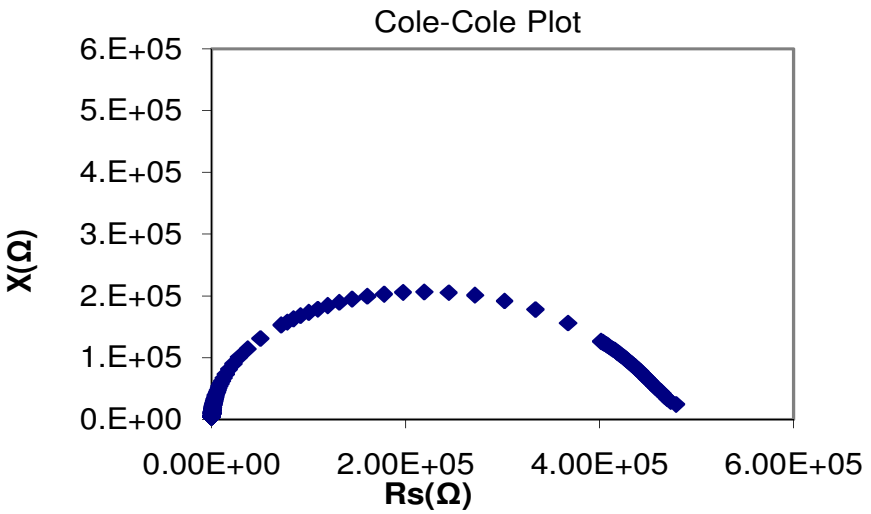


Figure 5(b) Cole-cole plot of **P2**

The calculated conductivity were 1.84 x 10^{-8} S/cm for **P1**and 9.82 x 10-^{9} S/cm for **P2** respectively. The difference in conductivity may due to the more bond breaking in **P1**from the alkyl side chain during microwave irradiation which cause an indirect excitation at the polymer chainof free electrons where in **P2** the bond interaction within substituted alkyl side chain is more stronger from the intermolecular chain exist in the molecular structure **[5].**
Since **P1**contained more electrons, more electrons will be excited to the conduction band from the valence band despite both polymer had similar energy band gap which give rise to the electrical conductivity of **P1 [6]**.

4. Conclusion

MSB-PPV and MCE-PPV were successfully synthesized via Gilch route with microwave irradiation technique adopted within 32 minutes of reaction time and gave satisfied FTIR and NMR spectrum. Both polymer absorb UV radiation at the wavelength of 469 nm respectively thus having similar energy band gap of 2.46 and 2.45 eV. This results can be concluded that the gap between HOMO and LUMO energy level was the same. However, MSB-PPV reported to gained higher conductivity of 1.84 x 10^{-8} S/cm than MCE-PPV of 9.82 x 10-^{9} S/cm which due to the more bond breaking in the alkyl side chain on the polymer structure from weaker intermolecular interaction between the bond.

Acknowledgement

Financial support and technical support from FRGS gran and UiTM are highly acknowledged.

References

[1]Kazim, S., Zulfequar, M., Haq, M. M., Bhatnagar, P. K., & Husain, M, *Solar Energy Materials & Solar Cells*, **91**, 1462–1466 (2007)
[2]Madhzi. A.S, Smita. J, K. R. Desai, *Archives of Applied Science Research,* **4(1),** 645-661 (2012)
[3]Chen, Z.K., Chua, S.J. Pan, J.Q., Xiao, Y., Lee, N.H.S., and Huang, W,*Thin Solid Films*,**363**. 98-101 (2000)
[4]Fulya. L, MICROWAVE INITIATED POLYMERIZATION OF. (2011)
[**5**] Davenas, J., Chouiki, M., Besbes, S., Ltaief, A., Ouada, H., Bouazizi, A., Trad, H, *Synthetic Metals*, **139**, 617–620 (2003)
[6]Basic UV-Vis Theory , Concepts and Applications Basic UV-Vis Theory , Concepts and Applications. (n.d.)., 1–28.

STRUCTURAL, IMPEDANCE AND MOISTURE ABSORPTION STUDIES ON POLYMER ELECTROLYTIC FILMS BASED ON PVA AND PAN

S. SIVA DEVI[1, 2, 3]
[1]*Research and Development Centre, Bharathiar University, Coimbatore, Tamilnadu, India*
[2]*Department of Physics, The S.F.R. College for Women, Sivakasi, Tamilnadu, India.*
[3]*Materials research Centre, Coimbatore, Tamilnadu, India.*

S.SELVASEKARAPANDIAN[3]
[3]*Materials research Centre, Coimbatore, Tamilnadu, India*

C.KARTHIKEYAN[4]
[4]*Department of Physics, Ramco Institute of Technology, Rajapalayam, Tamilnadu, India*

F.KINGSLIN MARY GENOVA[1,2,3]
[1]*Research and Development Centre, Bharathiar University, Coimbatore, Tamilnadu, India*
[2]*Department of Physics, The S.F.R. College for Women, Sivakasi, Tamilnadu, India.*
[3]*Materials research Centre, Coimbatore, Tamilnadu, India.*

N. VIJAYA[2]
[2]*Department of Physics, The S.F.R. College for Women, Sivakasi, Tamilnadu, India*

**Corresponding Author:sekarapandian@rediffmail.com*

Moisture absorption into the proton conducting polymer electrolytes used in electrochemical devices leads to a dramatic increase of the ionic conductivity. In the present work, PVA-PAN blend polymer is chosen for the study owing to its hydrophobic properties. Two sets of PVA-PAN blend polymer electrolytic films with different composition of ammonium salts are prepared using solution casting technique:- one set doped with ammonium hexaflourophosphate and another set doped with ammonium nitrate. The films are characterized by XRD technique and AC impedance measurement technique. XRD studies reveal the amorphous nature of the electrolytes. The highest conductivity at room temperature has been found to be 3.63 x10^{-5} S cm^{-1} for 30 mole % NH_4PF_6 doped PVA-PAN system and 1.34 x 10^{-3} S cm^{-1} for 15 mole % NH_4NO_3 doped PVA-PAN system. Moisture absorption studies reveal that the moisture acts as a plasticizer and increases the conductivity of the electrolytic films. It has been found that moisture absorption is more for the highest conducting electrolytic film. The conductivity of PVA:PAN: NH_4PF_6 film is increased to

Proceedings of the 14th Asian Conference on Solid State Ionics (ACSSI 2014)
Copyright © 2014 ACSSI 2014 Organizers. All rights reserved.
ISBN: 978-981-09-1137-9
doi:10.3850/978-981-09-1137-9_068

$1.45x10^{-3}$ S cm^{-1} per 2mg of water vapor absorbed. The conductivity of PVA:PAN:NH_4NO_3 electrolytic film is increased to $2.6x10^{-3}$ S cm^{-1} per 2mg of water vapor absorbed. The dependence of conductivity on the time of exposure of the film to moisture is found to be an exponential growth. The enhancement of conductivity of PVA:PAN:NH_4PF_6 electrolytic film is more than that of PVA:PAN:NH_4NO_3 electrolytic film which paves way for a possible application of moisture monitoring device using NH_4PF_6 doped system.

1.Introduction

Water diffusion into the polymer electrolytes leads to a dramatic increase of the ionic conductivity. Water is absorbed mainly by the amorphous regions, and is accompanied by a rapid destruction of crystalline region [1]. Since the ionic conductivity of the electrolytic film used in any electrochemical device is expected to be high, the effect of moisture absorption in polymeric films of different compositions becomes essential. At present, polymer blends have become commercially and technologically more important than homopolymers because of the possibility of getting new material with specific properties for the designed applications[2-4]. In the present work, PVA-PAN blend polymer is chosen owing to its hydrophobic properties. PVA is used in biomedical and pharmaceutical applications due to its nontoxic, noncarcinogenic and bioadhesive characteristics. PAN is used in textile industry, having interactions with plasticizers [5,6]. The conductivity of PVA film is found to be ~10^{-8}S/cm. The conductivity of PAN is <10^{-14} S/cm. However, when PVA is blended with PAN, the conductivity is increased to ~10^{-7} S/cm[7]. When an ammonium salt is added with this polymer matrix, the conductivity is further increased. It has been found that 92.5PVA:7.5PAN:15% NH_4NO_3 has the maximum conductivity which is 1.34 x 10^{-3} S cm^{-1} [8], and 92.5PVA:7.5PAN:30% NH_4PF_6 has the maximum conductivity which is 3.63 $x10^{-5}$ S cm^{-1}. In the present study, the effect of moisture on the conductivity of the 92.5PVA:7.5PAN:x% NH_4PF_6 (with x=15,20,25,30,35) electrolytic films are studied and a comparative analysis is done for 92.5PVA:7.5PAN:15% NH_4NO_3 with 92.5PVA:7.5PAN:30% NH_4PF_6 electrolytic films.

2.Experimental Technique

PVA (M_W =1,25,000), PAN (M_W =1,40,000) and Ammonium salts has been used to prepare blend polymer electrolyte of various compositions using Di Methyl Formamide (DMF) as solvent by solution casting technique. 92.5% by weight of PVA is stirred in DMF at 60^{o}C for 3 hours and after its complete dissociation, 7.5% by weight of PAN is added and stirred for 2 hours after which the ammonium salt is added. The mixture is stirred till it becomes homogeneous.

Then it is poured in the Petri dish and evaporated at 60°C in vacuum oven. Free standing film is obtained after 48 hours. Films obtained with 5%,10%,15%,20%,25% by weight of ammonium nitrate and films obtained with 15%,20%,25%,30%,35% by weight of ammonium hexafluorophosphate are characterized using XRD, and impedance techniques. XRD patterns are recorded with XPERT-PRO Diffractometer system using Cu Kα radiation in the range of $2\theta=10^0$ to 80^0. The impedance studies are made using a computer controlled HIOKI 3532 LCR meter over a frequency range of 42 Hz to 5 MHz with a cell having aluminium electrodes. Moisture absorption of films is studied by exposing the films to moisture contained in a closed container and measuring the mass of water vapors absorbed.

3.Result and discussion

3.1 X-Ray Diffraction Analysis

XRD analysis is used to study the complexation of the conducting polymer electrolyte films. The XRD patterns of the undoped blend polymer electrolyte 92.5PVA:7.5PAN and doped blend polymer electrolytes with different compositions of ammonium nitrate (ammonium hexaflour phosphate) are shown in **Figure 1 (Figure 2)**. It is observed from **Figure 1 and 2**, undoped blend polymer electrolyte 92.5PVA:7.5PAN exhibits peaks at 20.1° and 40.9° (which are ascribed to pure PVA [9] at 19.6° and 40.8° respectively) and as the concentration of ammonium salt is increased, the intensity of the peak at 20.1° decreases and the broadness increases up to 92.5PVA:7.5PAN:15% NH_4NO_3 (92.5PVA:7.5PAN:30% NH_4PF_6) doped blend polymer which indicates an increase in the amorphous nature of 92.5PVA:7.5PAN:15% NH_4NO_3 (92.5PVA:7.5PAN:30% NH_4PF_6) blend polymer. There is a slight shift in the peak at 20.1° in the complexes with respect to the 92.5PVA:7.5PAN blend polymer. Blend polymer electrolyte 92.5PVA:7.5PAN:15%NH_4NO_3 (92.5PVA:7.5PAN:30% NH_4PF_6), is found to be more amorphous. No peaks corresponding to NH_4NO_3 (NH_4PF_6) are observed in the blend polymer complexes indicating the complete dissociation of salt in the blend polymer 92.5PVA:7.5PAN. Also it has been observed from Figure 1 and 2 that 15%ammonium nitrate doped sample is more amorphous than 30%ammonium hexaflourophosphate doped sample.

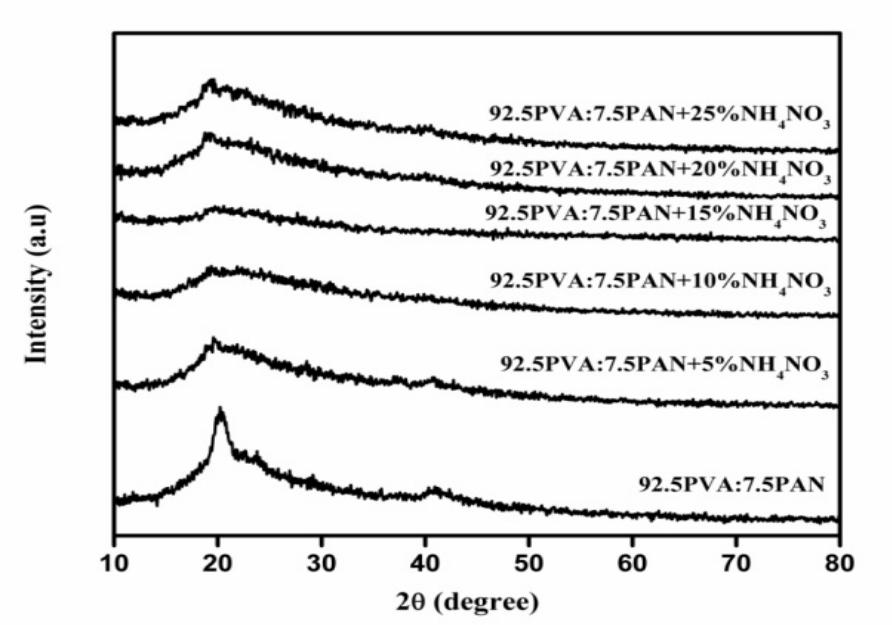


Figure 1 XRD patterns of NH_4NO_3doped blend polymer electrolytes.

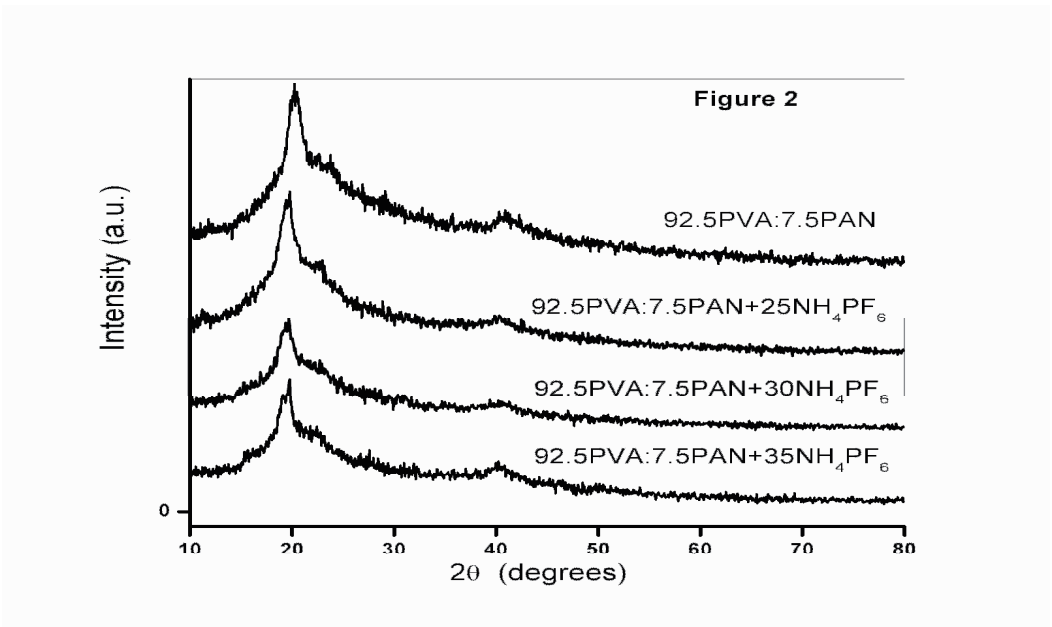


Figure 2. XRD patterns of NH_4PF_6 doped blend polymer electrolytes

The amorphous nature of the blend system which can be interpreted in terms of the Hodge et al. [10] criterion, which has established a correlation between the height of the peak and the degree of crystallanity. The crystallite size (D) for electrolytes shown in the figure 3 have been calculated by Debye Scherer's equation [11]

$$D=0.89\lambda/\beta\cos\theta$$

where λ is the wavelength of X-ray radiation, β is the full width at half maximum and θ is the diffraction angle. Table.1 shows the crystallites size and relative intensities of the samples. The low relative intensity for 92.5PVA: 7.5PAN:15NH_4NO_3 blend polymer electrolyte reveals that it is more amorphous than PVA92.5:PAN7.5:30NH_4PF_6 blend polymer electrolyte.

Table 1 Crystallite size for blend polymer electrolytes

Sample	2θ (degrees)	FWHM	Crystallite size	Height of peak
PVA92.5:PAN7.5:15NH_4NO_3	19.48	2.02	0.69	178
PVA92.5:PAN7.5:30NH_4PF_6	19.5	1.6	0.87	380

3.2 Conductance Spectra Analysis

The conductance spectra of NH_4NO_3 doped blend polymer systems is shown in **Figure 3** and NH_4PF_6 doped blend polymer systems is shown in **Figure 4**.The plots consist of two distinct regions [12]; a low frequency dispersion region and a frequency independent plateau region. The low frequency dispersion region is due to space charge polarization at the blocking electrode and the plateau region corresponds to DC conductivity (σ_{dc}) of the blend polymer electrolyte. The ionic conductivity of NH_4NO_3 doped blend polymer electrolytes is maximum for 92.5PVA:7.5PAN:15% NH_4NO_3 system and 92.5PVA:7.5PAN +30% NH_4PF_6 system. It is observed that the ionic conductivity decreases at higher salt contents. The increase in the ionic conductivity up to 92.5PVA:7.5PAN:15% NH_4NO_3 doped blend polymer system and 92.5PVA:7.5PAN:30%NH_4PF_6 blend polymer system can be related to an increase in the number of mobile charge carriers. The possible decrease in the ionic conductivity for 92.5PVA:7.5PAN:/20% NH_4NO_3 doped blend polymer system and 92.5PVA:7.5PAN +30%NH_4PF_6 blend polymer system can be attributed to

either incomplete dissociation of the salt or to the formation of ion multiples [13].

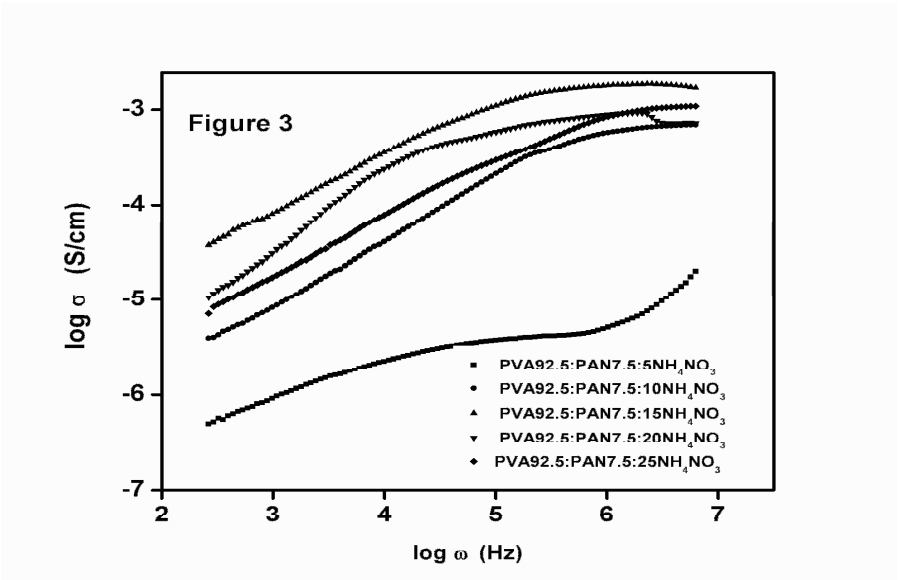


Figure 3 Conductance spectra of NH_4NO_3 doped blend polymer electrolytes.

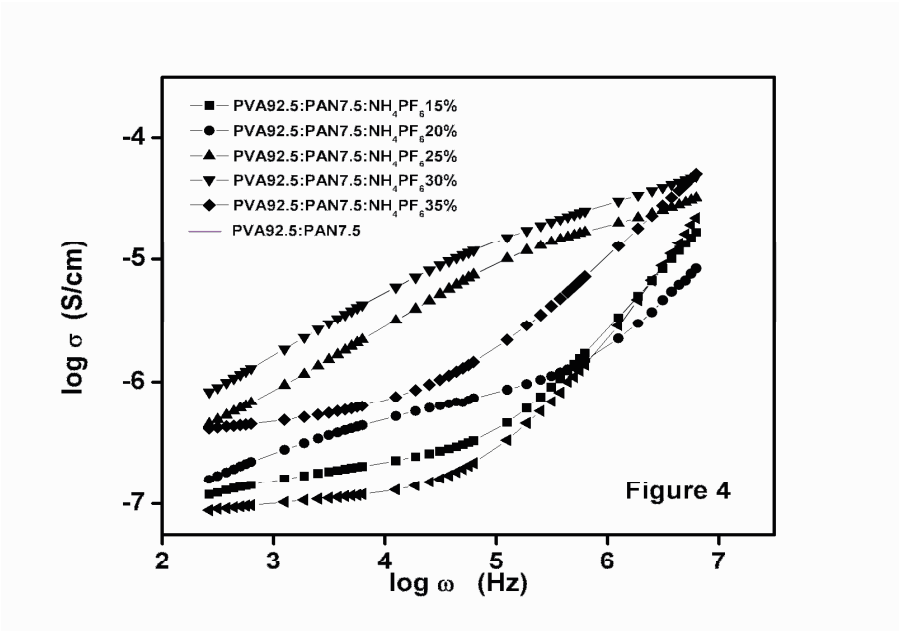


Figure 4 Conductance spectra of NH_4PF_6 doped blend polymer electrolytes.

3.3 Moisture absorption studies

Moisture absorption capacity of the polymeric film was determined by placing previously weighed films (W_1) into the moisture chamber for t seconds and then again weighed (W_2). The difference in masses (W_2 - W_1) gives the mass of moisture absorbed by the film. The percentage of relative change in the absorption of moisture in the film is measured at different times [14] using the formula

$$\text{Percentage of relative change in absorption} = \frac{[W_2 - W_1]}{W_1} * 100$$

and its variation with time is shown in the **Figure.5** for 92.5PVA:7.5PAN blend polymer films with different molar concentrations of ammonium hexaflourophosphate.

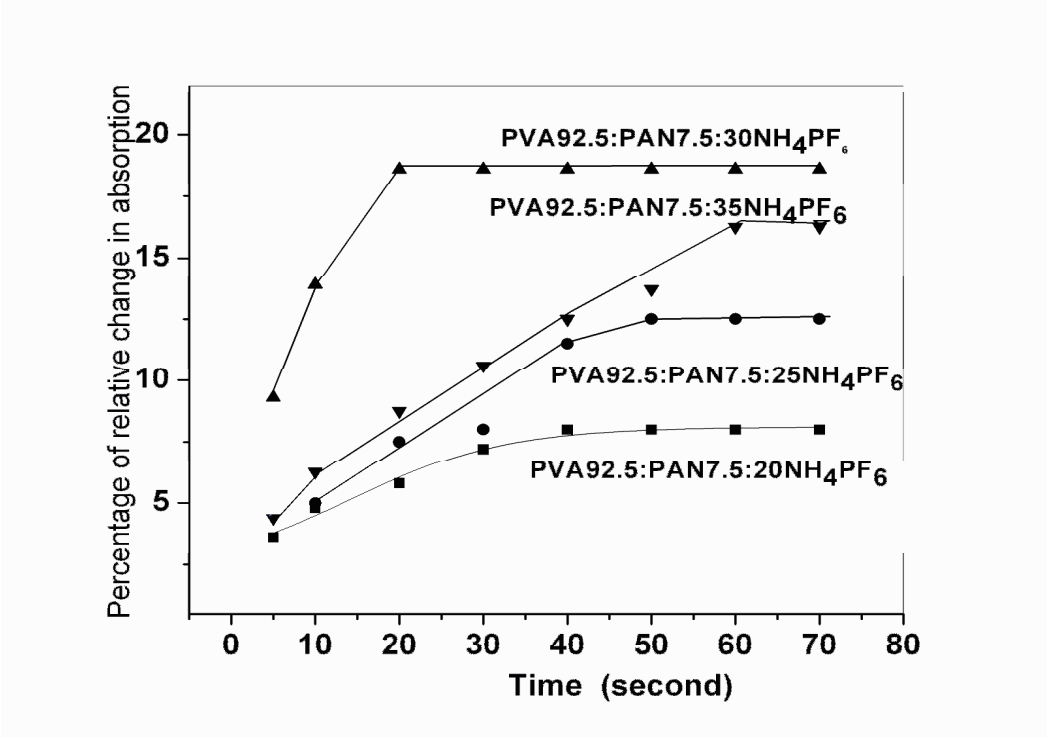


Figure 5. Moisture absorption of films with different concentrations

From **Figure.5**, it is observed that, the film which showed highest conductivity (92.5PVA: 7.5PAN +30 mol.%NH_4PF_6) absorbs more water vapors and attains saturation absorption in a short time than the other samples which may be due to the presence of more free volume in this sample. Moisture absorption attains

saturation value for all films which is due to complete occupation of free volume by vapors. The conductivities of 92.5PVA:7.5PAN:15% NH_4NO_3 and 92.5PVA: 7.5PAN: 30mol%NH_4PF_6 samples before and after absorption of moisture are shown in **Figure 6** and **Figure 7** respectively. It is seen from **Table 2** that moisture increases the conductivity of the polymer electrolyte which is due to plasticizing effect of moisture.

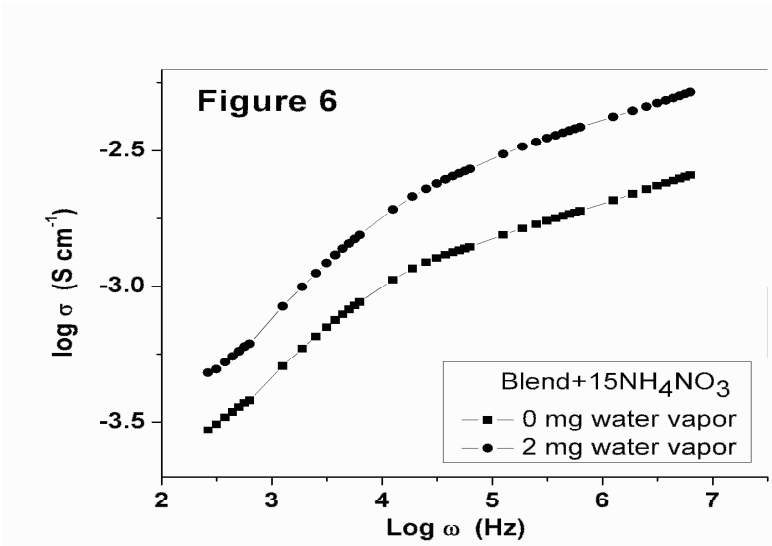


Figure 6 Effect of moisture on the conductance spectra of 92.5PVA:7.5PAN:15NH_4NO_3

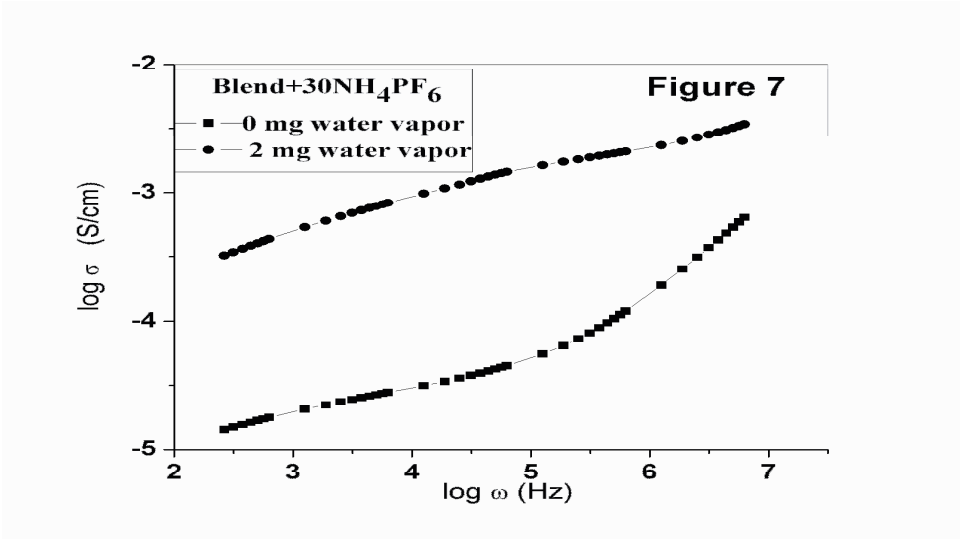


Figure 7 Effect of moisture on the conductance spectra of 92.5PVA:7.5PAN: 35NH_4PF_6

Table 2. Effect of moisture absorption on Conductivities of the samples

Sample	Conductivity (S/cm) before moisture absorption	Conductivity (S/cm) after moisture absorption
92.5PVA:7.5PAN:15% NH_4NO_3	1.34×10^{-3}	2.6×10^{-3}
92.5PVA: 7.5PAN: 30%NH_4PF_6	3.63×10^{-5}	1.45×10^{-3}

Figure 8 shows the dependence of the mass of water vapour absorbed on the time of exposure of the films 92.5PVA:7.5PAN:15% NH_4NO_3 and 92.5PVA: 7.5PAN: 30%NH_4PF_6 to moisture. It is seen from **Figure 8** that the mass of water vapour absorbed increases with time up to ~10 minutes after which there is very low absorption of vapor for NH_4NO_3 doped blend polymer film. But for NH_4PF_6 doped blend polymer film, the mass of water vapour absorbed increases with time up to ~60 minutes after which there is low absorption of vapor.

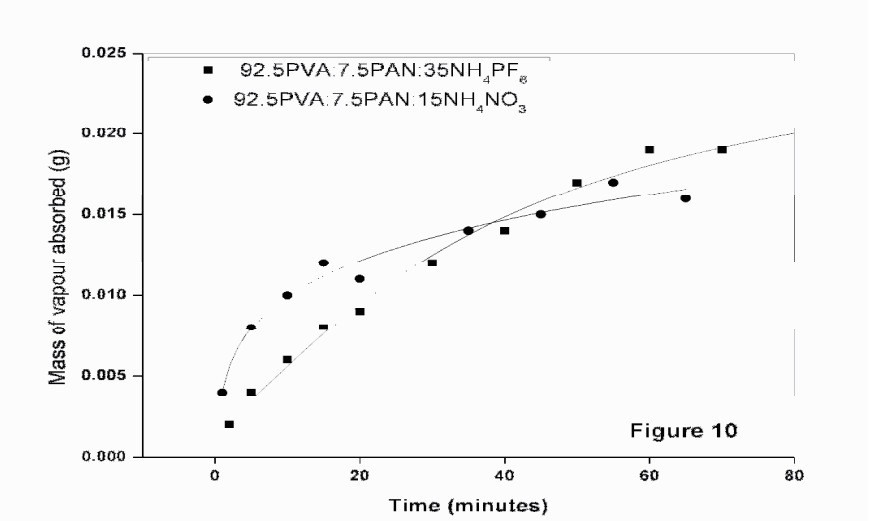


Figure 8 Variation of mass of vapour absorbed with time of exposure.

4. *Conclusions*

Polymer electrolyte of blend polymer with PVA and PAN in the ratio 92.5:7.5, complexed with ammonium nitrate and ammonium hexaflouro phosphate has been prepared by the solution casting technique. XRD pattern of the polymer electrolyte confirms the amorphous nature of polymer electrolyte for 15 molecular weight percentage of Ammonium Nitrate and for 30% molecular weight percentage of NH_4PF_6. The conductance spectra of doped blend polymer electrolyte for different compositions shows that 92.5 PVA: 7.5 PAN : 15 molecular weight of NH4NO3 polymer electrolyte exhibit conductivity (of the

order) 1.8 x 10^{-3} S cm^{-1} and PVA:PAN:30NH_4PF_6 has conductivity 3.63 x10^{-5} S cm^{-1} at room temperature. Moisture absorption studies reveal that the moisture acts as a plasticizer and increases the conductivity of the electrolytic films. It has been found that moisture absorption is more for the highest conducting electrolytic film. The conductivity of PVA:PAN:30NH_4PF_6 film is increased to 1.45x10^{-3} S cm^{-1} per 2mg of water vapor absorbed. The conductivity of PVA:PAN:NH_4NO_3 electrolytic film is increased to 2.6x10^{-3} S cm^{-1} per 2mg of water vapor absorbed. The dependence of conductivity on the time of exposure of the film to moisture is found to be an exponential growth. The enhancement of conductivity of PVA:PAN:NH_4PF_6 electrolytic film is more than that of PVA:PAN:NH_4NO_3 electrolytic film which paves way for a possible application of moisture monitoring device using NH_4PF_6 doped system.

References

1. Macromolecules,1998,31(12), pp 3886-3894
2. B.K.Choi, Y.W.Kim, H.K.Shin, Electrochemica Acta 45 (2000) 1371,
3. R.Baskararan, T.Hattori, Solid State Ionics 177(2006) 2679-2682,
4. S.Ramesh, A.H.Yahaya, A.K.Arof, Solid State Ionics 52-153(2002) 291
5. B.Huang,Z.Wang,G.LiHoltuang,R.Xae, L.Chen, F.Wang, Solid State Ionics 85 (1996) 79-84,
6. C.R.Yang, J.T.Perng, Y.Y.Wang, C.C.Wan, J.Power Sources 62 (1996) 89-93
7. S. Sivadevi, S. Selvasekarapandian, S. Karthikeyan, N.Vijaya, F. Kingslin Mary Genova, C. Sanjeeviraja,International Journal of Scientific Research 2 (2013) Issue 10.
8. S. Sivadevi, S. Selvasekarapandian, S. Karthikeyan, N. Vijaya, F. Kingslin Mary Genova, C. Sanjeeviraja, H. Nithya, Iwai, Junichi Kawamura, *Int. J. Electroact. Mater.* 1 (2013) 64-70
9. G. Hirankumar, S. Selvasekarapandian, M.S., Bhuvaneswwari, R. Baskaran, M.Vijayakumar, J., Solid State Electrochem. 10 (2006) 193.
10. Hodge RM, Edward GH, Simon GP(1996) Polymer 37; 1371-1376
11. D.Sridevi, K.V.Rajendran,Bull.Mater.Sci.,32(2) (2009) 165
12. S. Ramesh, A.K. Arof, Mater. Sci. Eng. B. 85 (2001)
13. R. Baskaran, S.Selvasekarapandian, Kuwata, N.J.Kawamwa, T. Hattori, Solid State Ionics 177 (2006) 2679.
14. Tekade A.R. & Gattani S.G., Investigation on Physical-Mechanical Properties of Natural Polymer Films, International Journal of PharmTech Research Vol.2, No.1, pp 106-112, Jan-Mar 2010.

ELECTRICAL PROPERTIES INVESTIGATION OF NEWLY SYNTHESIZED PEMA IONOGELS COMPOSITE

FAMIZA ABD. LATIF, RUHANI IBRAHIM, YUSAIRIE MOHD, MOHD AZRI AB RANI, NORASHIMA KAMALUDDIN, SHARIL FADLI MOHAMAD ZAMRI

Faculty of Applied Sciences, Universiti Teknologi MARA, 40450 Shah Alam, Selangor, Malaysia.

ruhani463@salam.uitm.edu.my

Ionic liquid (ILs) is a strong green solvent that is able to replace current volatile organic solvents such as N,N-dimethyl formamide (DMF), acetonitrile and γ-butyrolactone. Recently, ILs has been used in polymer electrolyte systems to provide ion for the ionic conduction, plastisizers etcs. However, most of polymer electrolyte system that has been fabricated were in the form of film or gel in which ILs used were not the major component of the polymer electrolyte system. Therefore, in this study 1-Ethyl-3-methylimidazolium bis (trifluoromethylsulfonyl) imide ([EMIM][NTf_2]) has been used as a major component in the formation of ionogels electrolyte to entrap poly(ethyl merthacrylate) (PEMA) and SiO_2 used as a cross-linking networks. In this study, the challange is to obtain the right composition of PEMA and SiO_2 to form the most stable ionogels with high ionic conductivity. It was found that the best ionogel with highest ionic conductivity of 10^{-3} Scm^{-1} at room temperature was obtained in system containing 40% PEMA and 40% SiO_2. The properties of this new ionogels were further investigated by Fourier Transform Infrared Spectroscopy (FTIR), UV- Vis and photoluminesence spectroscopy.

Keywords: Ionic liquids; PEMA; 1- Ethyl-3-methylimdazolium bis (trifluoromethylsulfonyl) imide; Ionogels; FT-IR;

Proceedings of the 14th Asian Conference on Solid State Ionics (ACSSI 2014)
Copyright © 2014 ACSSI 2014 Organizers. All rights reserved.
ISBN: 978-981-09-1137-9
doi:10.3850/978-981-09-1137-9_071

1. Introduction

Recently ionogels are being extensively investigated due to their special characteristic to overcome problems related to liquid and solid electrolyte. Ionogel exhibits high ionic conductivity, high performance and a safer electrolyte due to their nonvolatility and non leakage characteristic[2-4].. In addition it can be easily prepared by one-pot sol-gel method.

To date there are several ionogel system that have been studied [4]. The challange is to obtain a mechanically and dimensionaly strength ionogel [7] with high ionic conductivity. The average of ionic conductivity value obtained for an ionogel was about $\approx 10^{-5}$ Scm^{-1} above room temperature. In addition these ionic conductivity values were achieved with the addition salt [4]. Hence the objevtive of this study is to obtain new ionogel based on PEMA- ionic liquid system that is can exhibit high ionic conductivity at room temperature.

Therefore in this study ionogel comprising of only PEMA and ionic liquid was developed using SiO_2 as gelling agent. PEMA was chosen because it has the ability to encapsulate ionic liquid in its vicinity by temporary intermolecular bonding due to the presence of lone pair electron in its carbonyl group[1,2]. This concept similar with coordination bonding that occurred between a polymer and a salt in polymer electrolyte (PE) system. PEMA owing large pendant group that make it more flexible polymer backbone which is needed to strengthen mechanical and thermal stability[1]. On the other hand, 1-ethyl-3-methylimidazolium bis(trifluorosulfonyl) imide [EMIM][NTf_2] ionic liquid was used as ion sources due its high ionic conductivity, low viscocity, negligible vapour pressure and non-volatility characteristic. This PEMA ionogel was synthesized using sol- gel method. The effect of SiO_2 as gelling agent in the formation of PEMA ionogel and their conductivity at room temperature were further investigate.

The prepared ionogels are characterized using impedance spectroscopy and fourier transform infrared (FTIR)

2. Experimental

Materials

1-ethyl-3-methyl-imidazolium bis(perfluoroethylsulfonyl) imide [EMIPFSI] Aldrich high purity, SiO_2 15 nm size, tetrahydrofuran THF from Merck, Poly(ethyl methacrylate) PEMA (MW = 515,000, CAS = 9003-42-3, Aldrich) in powder form,

Preparation of Ionogels

PEMA ionogels were prepared by sol-gel technique in which the amount of PEMA and IL was fixed at 40 wt% of ionic liquid. Various amount(10 – 50%) of SiO_2 was added ti obtain a stable ionogel at room temperature.

Characterization

Fourier Transform Infrared Spectrscopy FTIR

FTIR was carried out to investigate the interactions that occur in the ionogels using Perkim Elmer FTIR Spectrometer; Spectrum One. Measurements were made in the range 4000 - 450 cm^{-1} with a resolution of 4 cm^{-1}.

Impedance Spectroscopy

The ionic conductivity measurements were carried out with the aim to observe the effect of silica addition on the electrical properties of the ionogels. Ionic conductivity of the ionogels obtained was measured with a computer controlled HIOKI 3532-50 LCR HITESTER frequency respond analyzer from 10 – 10^6 Hz at room temperature.

3. Results and Discussion

Formation of PEMA ionogel composite

The ionic conductivity measurements were carried out with the aim of observing the effect of silica addition on the electrical properties of the ionogel electrolyte systems. High conductivity value reveals that ions travel fastest in the sample. Figure 1 represents the cole-cole plot for one of the PEMA ionogels composite formed. It was noted that ionogel was successfully obtained when more than 40 wt% of SiO_2 was added (Table 1).

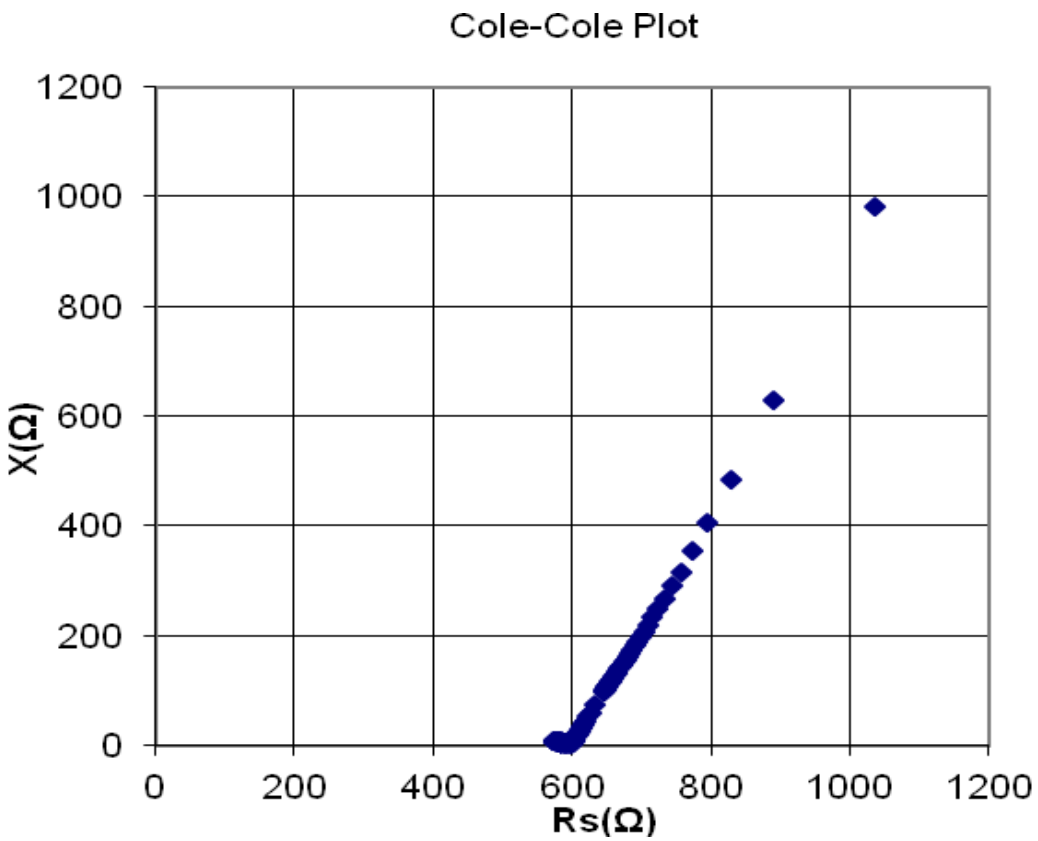


Figure 1: Cole-cole plot of PEMA ionogel composite

Table1: Conductivity values of PEMA-ionogels at room temperature

Sample	Conductivity value	Ionogel
ILPEMA40%	1.406 x10^{-3}	no
ILPEMASiO_2 10%	1.311 x10^{-3}	no
ILPEMASiO_2 20%	1.1.05 x10^{-3}	no
ILP ILPEMASiO_2 30%	0.921 x10^{-3}	no
ILPEMASiO_2 40%	1.1.07 x10^{-3}	yes
ILPEMASiO_2 50%	1. 150 x10^{-3}	yes

Interestingly the ionogel remains stable even after 4 months at room temperature. Both PEMA ionogel composite containing 40% and 50% exhibited incomplete semicircle indicating that both system were ionic conductor [2].

Interestingly it was noted that the addition of SiO_2 does not effect significantly the ionic conductivity value of the PEMA ionogel composite system (table 1). Therefore it can be concluded that the addition of SiO_2 is only to form a network between the polymer and the ionic liquid. These explain why there is no significant changes in the FTIR spectra of PEMA ionogel composite obtained.

4. Conclusion

PEMA ionogel composite were successfully obtained when more than 40 wt% SiO_2 were added to the system by sol–gel method. In addition the ionic conductivity of these new PEMA ionogel were more than $\approx 10^{-5}$ Scm^{-1} at room temperature which is better than previous ionogel system obtained. Due to these findings, PEMA ionogel composite can be considered as potential candidates as solid state electrolytes in electrochemical devices[5,6]. However these newly synthesized PEMA ionogel composite deserves further investigation.

Acknowledgement:
Financial support and technical support from Ministry of Higher Education (FRGS grant) and UiTM are highly acknowledged.

References

1) L.N. Sim, S.R. Majid, A.K. Arof ., (2012) . Characteristics of PEMA/PVdF-HFP blend polymeric gel films incorporated with lithium triflate salt in electrochromic device. *Solid State Ionics*, 209–210, 15–23

2) Amir S. N, Othman R., Subban R. H. Y. ,& Mohamed N. S., (2011). Ionic Conductivity of PEMA-$LiClO_4$ Polymer Electrolytes, *Sains Malaysiana* ,40, 701–705

3) Mecerreyes D, Marcilla R, Ochoteco E, Grande H, Pomposo J, Vergaz R, Sanchez Pena J,(2004). A simplified all-polymer flexible electrochromic device. Electrochimica Acta, ; 49 : 3555 -3559

4) Yun-Sheng Ye, John Rick, Bing-Joe Hwang, (2012). Ionic liquid polymer electrolyte. Journal of Materials Chemistry A,1, 2719 – 2743.

5) Kucharski M.,Ukaszewicz T., Mrozek p., (2004). New electrolyte for electrochromic devices. *Opto Electronics Review*, **12**(2), 175–180 .

6) S.A.M. Noor, P.M. Bayley, M. Fortysh, D.R.Macfarlane . (2013). Ionnogels based on ionic liquid as potential highly conductive solid state. Electrochimica Acta, ; 91: 219 – 226

7) Marie- Alexandra Neouze, Jean Le Bediau, Philippe Gaveau, Severine Bellayer, Andre Vioux.,(2006). Ionogels, new materials arising from the confinement of ionic liquids within silica-derived networks. Chem. Matter.;18: 3931 – 3936.

ELECTRICAL AND FT-IR STUDY OF FUMED SILICA BASED GEL ELECTROLYTES; $(TETRAGLYME)_nKI$AND $(ETHYLENE\ GLYCOL)_nKI$

K.V.L. AMARASINGHE[1]

[1]*Postgraduate Institute of Science, University of Peradeniya, Peradeniya, Sri Lanka.*

V. A. SENAVIRATNE[1,2,3*],L. R. A. K. BANDARA[1,2], M. A. K. L. DISSANAYAKE[3]

[2]*Department of Physics, University of Peradeniya, Peradeniya, Sri Lanka*
[3]*Institute of Fundamental Studies (IFS), Kandy, Sri Lanka*
**Corresponding author: sene7403@yahoo.com, dmvas@pdn.ac.lk*

Gel Electrolytes (GEs) are a newest generation of electrolytes, which exhibit high ionic conductivities at room temperature (RT) compared to solid electrolytes and good mechanical properties and long term stability compared to liquid electrolytes. Present days GEs have been identified as more promising electrolyte materials for various practical applications such as dye sensitized solar cells (DSSCs) and lithium ion rechargeable batteries. The emphasis of this work is on tetraethylene glycol dimethyl ether (tetraglyme), ethylene glycol (EG) and fumed silica based composite GE systems with potassium iodide (KI) as the salt. First, a series of liquid electrolytes were prepared by dissolving appropriate amounts of KI in EG and tetraglyme to obtain samples, $(tetraglyme)_nKI$ and $(EG)_nKI$, with different O:I ratios (n = 12, 15, 20, 25, 30, 40, 50, 60 and 80). Then the GEswere formed by adding 10 wt. % of fumed silica. The highest ionic conductivity of 2.80×10^{-3} S cm^{-1} at RT, was observed for the gel electrolyte $(tetraglyme)_{15}KI$with 10 wt. % fumed silica. The maximum conductivity of 1.50×10^{-2} S cm^{-1}at RT, was obtained for $(EG)_{12}KI$ gel electrolyte system. The conductivity values of both gel systems studied are in the same order as the conductivities of corresponding liquid electrolytes. The data obtained from DC polarization tests verify that the prepared electrolytes are predominantly ionic conductors. The FT-IR spectra of both liquid and gel electrolyte systems based on tetraglymeindicate strong interactions present between K^+ ions and the ether oxygens of tetraglyme. The addition of the salt to EG shifts the O-H stretching mode to a higher wavenumber showing the strong interactions between EG and KI in both liquid and gel electrolyte systems.

1. Introduction

The ever increasing energy demand requires more efficient, low cost, renewable energy sources. Alkaline batteries and solar cells play a major role in fulfilling the above need. Liquid electrolytes show high ionic conductivities and

Proceedings of the 14th Asian Conference on Solid State Ionics (ACSSI 2014)
Copyright © 2014 ACSSI 2014 Organizers. All rights reserved.
ISBN: 978-981-09-1137-9
doi:10.3850/978-981-09-1137-9_076

good performance in the above electrochromic devices compared to the solid electrolytes. However, there are a few inherit problems such assolvent vaporization, electrochemical corrosion and leakage with the use of liquid electrolytes. Gel electrolytes (GEs) have become promising materials for practical applications due to their valuable advantages over solid and liquid electrolytes. GEs exhibit comparably high ionic conductivities (> 10^{-3} S cm^{-1}) at room temperature compared to solid electrolytes[1, 2].

The present work focused on a gel electrolyte (GE) system formed by mixing low molecular weight organic solvents with fumed silica (SiO_2). Fumed silica has the ability to construct network structure in an organic media[3]. Fumed silica is formed by burning silicon tetrachloride ($SiCl_4$) in a flame of H_2 and $O_2$and as a result molten spheres of silicon dioxide are produced. Then these molten spheres are colliding and fuse with one another to form branched, three dimensional chains like aggregates. During the production process, hydroxyl groups tend to attach with the silicon atoms on the surface of the silica particles. These surface hydroxyl groups, called silanol groups (Si-OH), are able to make hydrogen bonds with suitable molecules. In the present study tetraethylene glycol dimethyl ether (or tetraglyme) and ethylene glycol (EG) were used as the organic solvents and potassium iodide (KI) was used as the salt to prepare GEs. The prepared electrolytes were characterized using AC impedance technique, DC polarization technique and FT-IR spectroscopy.

2. Experimental

Tetraglyme (Aldrich, 99%), ethylene glycol (99%), potassium iodide (KI) and fumed silica (SiO_2) (Aldrich, particle size 0.007 μ, surface area 390± 40 m^2 per gram) were used as the starting materials. Prior to use, SiO_2 was heated at 500 ^oC for 24 hours and KI was heated at 80 ^oC under vacuum for 24 hours. Tetraglyme and ethylene glycol was used as received.

2.1. Sample Preparation

A series of liquid electrolytes were prepared by dissolving appropriate amounts of KI in EG and tetraglyme to obtain samples, $(tetraglyme)_nKI$ and $(EG)_nKI$, with different O:I ratios (n = 12, 15, 20, 25, 30, 40, 50, 60 and 80). The mixtures of KI in EG and tetraglyme were stirred for 24 hours at room temperature and obtainedhomogeneous liquids.Then the composite gel was formed by adding the appropriate amount of fumed silica to achieve a filler concentration of 10 wt. %(*i.e.* 10% of the total weight of solvent (tetraglyme or EG) and KI).

2.2.Complex Impedance Spectroscopy

The ionic conductivity of the liquid electrolytes and GE samples were determined by the AC complex impedance technique with a computer controlled Solatron SI–1260 impedance analyzer in the frequency range 20 Hz –10 MHz.Impedance data of GEs weremeasured in the temperature range of 26^{o}C to 65^{o}C. For this gel electrolytes were smeared and sandwiched between two polished stainless steel blocking electrodes. For liquid electrolytes, a homemade glass holder was used with two polished stainless steel electrodes.
The ionic conductivity (σ) of the electrolyte samples were calculated using the Eq.(1):

$$\sigma = \frac{l}{R_b A} \tag{1}$$

where, $R_b$is the bulk resistance of the sample which was obtained from the graph of Z" (imaginary part of the impedance) vs. Z' (real part of the impedance), '*l*' is the thickness of the sample and '*A*' is the area of the sample.

2.3. DC Polarizing Technique

In order to determine the ionic nature of the prepared electrolyte samples, the DC polarizing technique was carried out. In this technique a small DC voltage ~1 V was applied across the sample and the DC current through the sample was noted down as a function of time. Stainless steel (SS) electrodes were used as blocking electrodes in the SS/GE/SS configuration; allowing only electrons to flow through an external circuit.

2.4 Fourier Transform Infrared (FT-IR) Spectroscopy

FT-IR studies were performed by using the Thermo Nicolet 6700 FTIR spectrometerin the wavenumber range from 600 cm^{-1}- 4000 cm^{-1} in order to determine the existence of the interactions between K^+ ion with the solvent (tetraglyme or EG) and fumed silica.

3. Results and discussion

3.1. DCPolarizing Technique

The Wagner's DC polarization test was performed for both liquid and gel polymer electrolytes[4]. This method was used to analyze the mobile species in the electrolyte. The DC current showed an abrupt drop within a short period of time for both liquid and gel samples due to the ion migration at the electrode electrolyte interface. After some time the current became constant which wasnegligible in magnitude, corresponding to the current due to electrons. According to our data it can be concluded that both liquid and gel electrolyte samples are predominantly ionic conductors with negligibly small electronic conductivity.

3.2. Complex Impedance Spectroscopy

The ionic conductivities of the liquid electrolytes with different O:I molar ratios at room temperature for both systems,$(Tetraglyme)_nKI$ and $(EG)_nKI$,are depicted in Figure 1 (a) and Figure 1(b) respectively.The highest ionic conductivity of 3.78×10^{-3} S $cm^{-1}$for $(Tetraglyme)_nKI$liquid electrolyte system was obtained at room temperature for the electrolyte sample with O:I molar ratio of 20:1. Further increase of salt {i.e. in $(Tetraglyme)_{15}KI$ and $(Tetraglyme)_{12}KI$ samples} reduces the ionic conductivities, presumably due to formation of large aggregate ions. The ionic conductivities of the liquid electrolytes of $(EG)_nKI$ system, with different O:I molar ratios at room temperature are depicted in the Figure 1(b). The highest ionic conductivity of 2.01×10^{-2} S cm^{-1} was obtained at room temperature for the electrolyte sample with O:I molar ratio of 12:1.

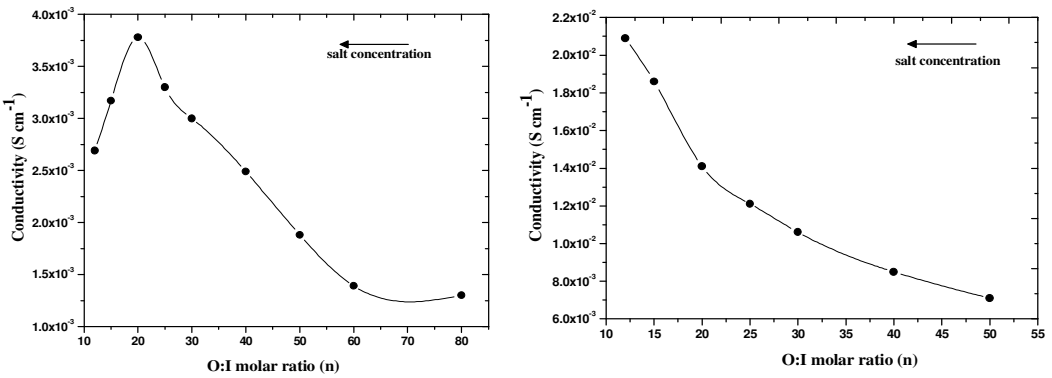


Figure 1: The ionic conductivities of the liquid electrolytes with different O:I molar ratios (a) $(Tetraglyme)_nKI$ system (b) $(EG)_nKI$ system.

Then preheated fumed silica was added as 10 wt. %of the total weight of tetraglyme or ethylene glycol and KI to the liquid electrolytes with different molar ratios to form GEs. Figure 2 shows the temperature dependence of the ionic conductivities of prepared GEs.

Within the tested temperature range, the conductivity variation of all GEs well obeys the Arrhenius relationship[5].

$$\sigma T = \sigma_0 \exp\left[\frac{-E_a}{kT}\right] \quad (2)$$

where E_a is the activation energy, σ_0 is the pre-exponential factor, k is the Boltzmann constant and T is the absolute temperature.

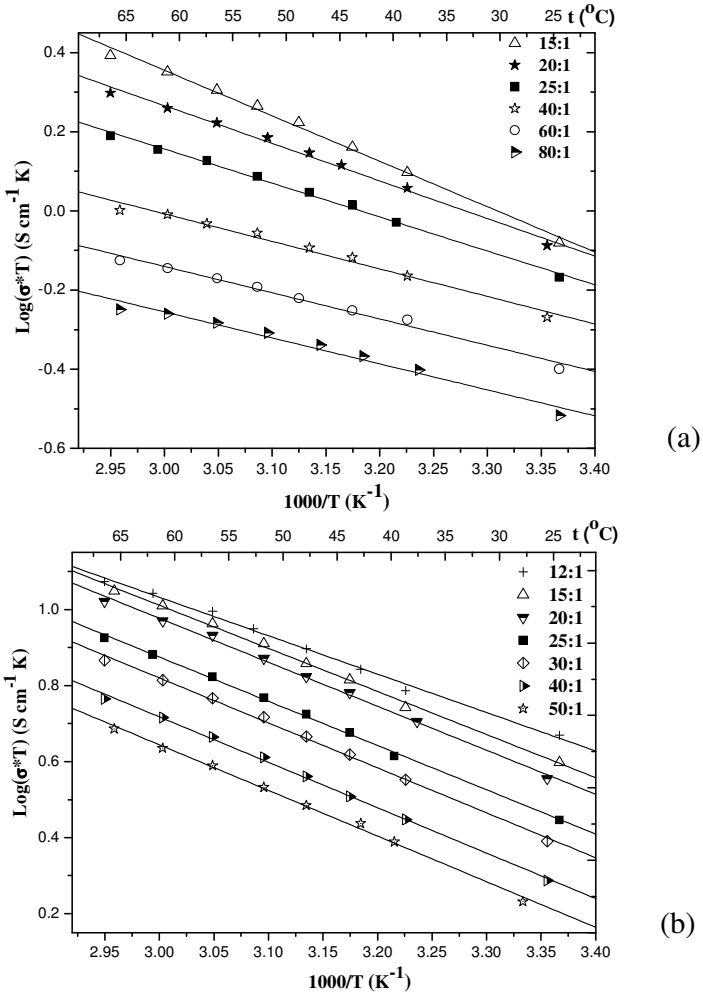


Figure 2. The ionic conductivities of the GEs with 10wt. % SiO_2 with different O:I molar ratios (a) $(Tetraglyme)_nKI$system (b) $(EG)_nKI$ system

As shown in Figure 2(a), after addition of fumed silica to $(Tetraglyme)_nKI$ liquid electrolytes to form gels, GE with 15:1 molar ratio exhibits the highest ionic conductivity of 2.80×10^{-3} S cm^{-1}, which is higher than the ionic conductivity of the 20:1 gel electrolyte sample. In the 15:1 gel electrolyte sample, the aggregate formation may be hindered by the addition of fumed silica.

For $(EG)_nKIGE$ system, 12:1 molar ratio exhibits the highest ionic conductivity of 2.01×10^{-2} S cm^{-1}. However, the ionic conductivity has been slightly reduced after the addition of silica in both GE systems. This may occur due to the blocking of the motion of salt ions.

In these systems fumed silica with surface silanol groups (Si-OH) was used as the gelation agent. The main driving force to form a gel is believed to be the hydrogen bond between silanol groups on adjacent silica molecules or hydrogen bonds between silanol groups of silica molecules and ether oxygen of tetraglyme molecules. Raghavan*et.al* has discussed in detail about three factors to interpret the possible mechanisms responsible for the stability of these silica gel systems. They are electrostatic interactions, van der Waals forces and solvation phenomenon. According to the findings of Raghavan*et.al,* electrostatic interactions and van der Walls forces play a negligible role and have no correlation for the network formation of these GE systems. So they suggest that a different mechanism, i.e. solvation phenomena due to hydrogen bonding, is affecting the gel formation of these systems[6].

In solvation phenomena, if the solvent possess high hydrogen bonding capacity, there will be hydrogen bonds formed between solvent molecules and surface silanol groups of silica particles. As a result, a solvation layer is formed around the silica particles. If the solvent possess low hydrogen bonding capacity, hydrogen bonding between surface silanol groups of neighbor silica particles can be more prominent to form a "gel"[6].

Among the two systems studied, ethylene glycol has high hydrogen bonding capacity than tetraglyme. Therefore, we believe that the interactions between silica surface groups is the most dominant driving force for the gelation process for $(Tetraglyme)_nKI$system and the interactions between silica surface groups and ethylene glycol is the most dominant driving force for the gelation process for $(EG)_nKI$system.

3.3. FT-IR Measurements

In the present paper the vibrational spectroscopy has been used to study the interactions between the cation and the solvent.Considering the cation interactions with other possible species in this GE, there can be two possibilities. First, the K^+ ion can form direct links with the ether oxygens from separate solventmolecules which restrict the motion of the solventmolecules or K^+ ion can attach to the ether oxygen of a single solvent molecule. In the second possibility, K^+ ions may bridge the surface silanols of the fumed silica and ether oxygens of the solvent molecules. In our study, evidence for the interactions between K^+ ion and the solvent molecules could be found.

3.3.1. Tetraglyme based GE system

In the FT-IR spectra in Figure 3 (a), bands between 800 cm^{-1} and 900 cm^{-1} have been assigned to modes of CH_2 wagging and C-O-C stretching motions[7]. FT-IR spectra of tetraglyme gel without KI and liquid tetraglyme show a band centered at wavenumber 850 cm^{-1} and with the increasing salt concentration a weak shoulder is appearing at around 862 cm^{-1}. This weak shoulder is assumed to be due to the CH_2 wagging and CH_2 twisting motions of C-O-C-C-O-C units which are interacting with the K^+ ions.

In Figure 3(b), the band appearing at the wavenumber 1098 cm^{-1} of liquid and gel tetraglymeis assigned to the vibrational mode of CH_2 wagging[7]. With the addition of the KI salt this peak is showing a downshift to wavenumber 1085 cm^{-1} for the gel electrolytewith 15:1 molar ratio. This indicates the K^+ interactions with ether oxygens of tetraglyme.

FT-IR spectra of gel and liquidtetraglyme and $(Tetraglyme)_nKI$ (n = 80, 20 and 15)gel electrolytes with different O:I molar ratios at room temperature in the range of wavenumbers 1310 cm^{-1} – 1410 cm^{-1} spectral region is shown in Figure 3(c). As seen in the spectrum of pure tetraglyme and $(Tetraglyme)_nKI$gel electrolytes, a weak shoulder is appearing in the range of wavenumbers 1310 cm^{-1} – 1410 cm^{-1}spectral region with the addition of salt. The band appearing at 1350 cm^{-1} in tetraglyme has been assigned for CH_2 rocking[8]. With the addition of the salt to the tetraglyme, the band has split further to give an additional component at around ~1359 cm^{-1}.

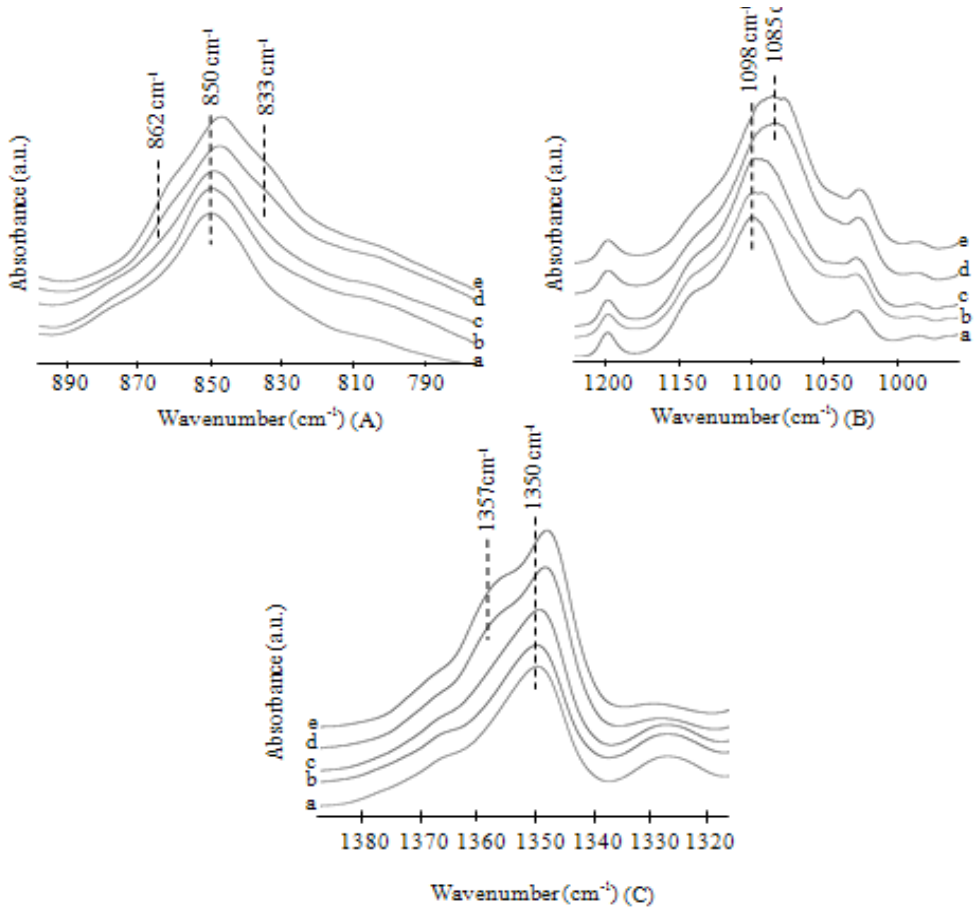


Figure 3: FT-IR spectra of a-liquid tetraglyme, b-gel tetraglyme (tetraglyme+ fumed SiO_2), c-$(Tetraglyme)_{80}KI$ GE, d- $(Tetraglyme)_{20}KI$ GE and e- $(Tetraglyme)_{15}KI$ GE at room temperature in the (A) 780 cm^{-1} – 890 cm^{-1} spectral region (B) 950 cm^{-1} – 1220 cm^{-1} spectral region (C) 1320 cm^{-1} – 1390 cm^{-1} spectral region.

3.3.2. Ethylene glycol based GE system

The Table 1 gives the vibrational frequencies of CH_2 rocking,CH_2 wagging, CH_2 twisting and C-O stretching modes of liquid and gel ethylene glycol without KI and gel electrolyte, $(EG)_{12}KI$, (i.e. n = 12). Coordination of K^+ions with the oxygen atoms of EG molecules has influenced the peak positions of the above modes of EG. Each peak is shifting by about 5 to 7 cm^{-1}. The C-C stretching vibration mode of pure ethylene glycol is located at 861 cm^{-1} wavenumber[9]. Its position remains unchanged with the addition of the salt. This indicates that the K^+ ions are interacting with both oxygen atoms of ethylene glycol, without disturbing to the symmetry of the EG molecule.

Table 1: FT-IR assignments of ethylene glycol[9].

Assignment	Wavenumber (cm^{-1})	
	Peak positions of pure EG	When interact with K^+ ion
C-C Stretching	861 *m*	861
CH_2 Rocking	882 *s*	877
C-O Stretching	1084 *vs*	1079
CH_2 Twisting	1205 *mb*	1198
CH_2 Wagging	1257 *wb*	1251

b= broad, *vs*= very strong, *s*= strong, *w*= weak, *m*= medium

As shown in the Figure 5, the interaction of K^+ ion and oxygen atoms of ethylene glycol has been influenced to O-H stretching mode causing a shift of the peak position. O-H stretching mode of pure EG (liquid and gel) is a broad band centered at around 3300 cm^{-1}wavenumber[9]. As the salt concentration is increased, the centre of the peak is shifted towards higher wavenumbers as shown in Figure 5.

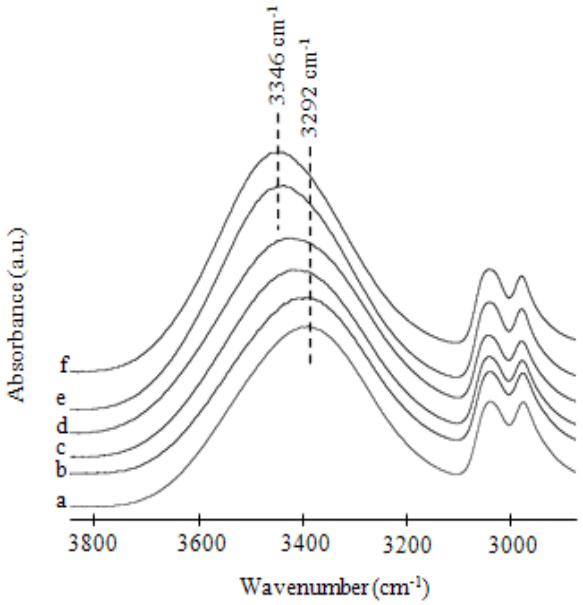


Figure 5: O-H stretching mode of,a-liquid EG, b-gel EG (EG+ fumed SiO_2), c- $(EG)_{50}KI$ GE, d- $(EG)_{30}KI$ GE, e- $(EG)_{15}KI$ GE and f- $(EG)_{12}KI$ GE systems at roomtemperature.

4. Conclusions

By mixing low molecular weight tetraglyme or ethylene glycol and KI based liquid electrolyte, with fumed silica, gel electrolytes has more stability compare to liquid electrolytes successfully fabricated. The prepared GEs were predominantly ionic conductors. The addition of fumed silica to liquid electrolyte forms a gel without a significant drop of ionic conductivity. The highest ionic conductivity of 2.80×10^{-3} S cm^{-1} was observed for the tetraglyme based GE of O: I molar ratio of 15:1 with 10 wt. % fumed silica. For ethylene glycol based GE system, the highest ionic conductivity 2.01×10^{-2} S $cm^{-1}$was observed for the electrolyte at 12:1 molar ratio. According to the FT-IR spectra of liquid electrolytes, the changes in the band shape and vibrational frequencies indicated that there are strong interactions of K^+ ions of dissociated KI with the ether oxygen of tetraglyme and ethylene glycol chains.

Acknowledgements

The authors would like to thank the National Science Foundation, Sri Lanka (Grant No. RG/2011/BS/03), Postgraduate Institute of Science (PGIS), University of Peradeniya and Institute of Fundamental Studies (IFS), Kandy.

References

1. A.M. Stephan,*European Polymer Journal*, 42, 21 (2006).
2. O.A. Ileperuma, M.A.K.L. Dissanayake, S. Somasunderam, L.R.A.K. Bandara, *Sol Energy Mater. and Sol. Cells*, **84**, 117 (2004).
3. S.R. Raghavan, M.W. Riley, P.S. Fedkiw, S.A. Khan, *Chem. Mater.*, **10,** 244 (1998).
4. J.B. Wagner Jr., C. Wagner, *J ChemPhys*, **26**, 1597 (1957).
5. Y.J. Song, C.L. Cheng, Y.Y. Wang, C.C. Wan, *J Electrochem. Soc.*, **149(9)**, A1230 (2002).
6. S.R. Raghavan, *Langmuir*,**1**6, 7920 (2000).
7. J.K. Hyun, Haitao Dong, C.P. Rhodes, R. Frech, R.A. Wheeler, *J. Phys. Chem. B*, **105**, 3329 (2001).
8. T.V. Kaulgud, N.R. Dhumal, S.P. Gejji, *J. Phys. Chem. A*, **110**, 9231 (2006).
9. K. Krishnan, R.S. Krishnan, *Proceedings of the Indian Academy of Sciences - Section A,***64**, 111 (1996).

INVESTIGATIONS ON INFLUENCE OF TITANIA CONTENT ON THE PROPERTIES OF (PVDF-CO-HFP) BASED POLYMER ELECTROLYTES *

P.ISSAC NELSON

Department of Physics, Karunya University
Coimbatore 641114, Tamilnadu, India

P.SENTHIL KUMAR

Department of Physics, Karunya University
Coimbatore 641114, Tamilnadu, India

A.SAKUNTHALA #

Department of Physics, Karunya University
Coimbatore 641114, Tamilnadu, India

M.PRABU

Department of Energy Systems Engineering, Daegu Gyeongbuk Institute of Science & Technology, South Korea

M.V.REDDY

Department of Physics, National University of Singapore
Singapore 117542

K.GOVINDAN

Water Institute, Karunya University
Coimbatore 641114, Tamilnadu, India

Lithium ion conducting plasticized polymer electrolytes based on poly (vinylidenefluoride-co-hexafluoropropylene), (PVdF-co-HFP), Ethylene carbonate and lithium perchlorate ($LiClO_4$) have been prepared in the weight ratio 50:35:15 using acetone as solvent by facile solution casting technique. Three different inert fillers Al_2O_3, SiO_2 and TiO_2 were prepared by simple hydrothermal route. The

* This work is supported by Department of Science and Technology (DST), New Delhi, India (Project No: SR/FTP/PS-192/2011).

Corresponding author: meetsaku@gmail.com

Proceedings of the 14th Asian Conference on Solid State Ionics (ACSSI 2014)
Copyright © 2014 ACSSI 2014 Organizers. All rights reserved.
ISBN: 978-981-09-1137-9
doi:10.3850/978-981-09-1137-9_093

prepared fillers were characterized by XRD and SEM. The composite electrolytes were prepared by the incorporation of 5 wt % of inert fillers Al_2O_3, SiO_2 and TiO_2 respectively. The sample 45 wt % PVdF-co-HFP: 5 wt % TiO_2: 35 wt % EC: 15 wt % $LiClO_4$ exhibits highest ionic conductivity of 1.11×10^{-2} S/cm at room temperature. The increase in amorphous nature of films in XRD measurements after the addition of inert fillers reflects in the enhancement of conductivity values.

1. Introduction

In recent year's plasticized polymer electrolytes have great attentions in Li-ion battery (LIB) due to their exhibition of high ionic conductivity as compared to solid polymer electrolytes [1-2]. Among different polymer electrolytes for LIB, the fluoro polymers had been of great interest due to their good electrochemical stability and mechanical stability [3-4]. Among them, PVdF-HFP copolymer has a significant attention because of its high dielectric constant, low crystallinity and low glass transition temperature which helps to provide the high dissolution of salt content in the polymer matrix. Moreover PVdF-HFP with both crystalline and amorphous phases exhibits good mechanical strength and provides high conductivity [5-9]. Many reports are seen on plasticized electrolytes based on PVdF-HFP [10-15]. Nanoparticles filled polymer electrolyte has been studied extensively to improve mechanical strength and to enhance the lithium ionic transport properties, such as ionic conductivity, the cation transference number, and interfacial compatibility with lithium electrodes. Here we chosen three different inert fillers Al_2O_3, SiO_2 and TiO_2.The lithium perchlorate ($LiClO_4$) was used as the salt because of its low lattice energy and less coordination between the cation and the anion. The ethylene carbonate (EC) was used as the plasticizer as it has excellent properties such as high dielectric constant, low molecular weight, high donor number and high boiling point compared to other plasticizers [16].

2. Experimental

The polymer electrolytes were prepared by the simple solution casting technique. Poly (vinylidene fluoride-co-hexafluoropropylene) (PVdF-HFP) [Mw=400000] and lithium perchlorate ($LiClO_4$) were purchased from Sigma-Aldrich. Ethylene carbonate (EC) and the solvent acetone were purchased from Himedia. Three different fillers Al_2O_3, SiO_2 and TiO_2 were synthesized by the procedures reported in the literature [17-19]. The 50 wt % of PVdF-HFP, 35 wt % EC and 15 wt % of $LiClO_4$ was dissolved in acetone and stirred well for 24 hrs. The obtained solution was poured in a petri dish and evaporated at room temperature for about 48 hrs.

Then the electrolyte film was further heated at 50°C for 5 hrs in vacuum oven. The composite polymer films were prepared by adding 5 wt % of Al_2O_3/ SiO_2/TiO_2 fillers respectively along with PVdF-co-HFP, EC and $LiClO_4$. X-ray diffraction patterns of the samples were obtained using a SHIMADZU-XRD-6000 diffractometer with Cu-Kα radiation (wavelength = 0.1541 nm) as the source at 40 kV with a scanning range of between 5◦ and 80◦. Morphology analysis was studied using JEOL-JSM 6000 scanning electron microscope. The AC impedance studies were carried out on the polymer electrolyte films with stainless steel as the blocking electrodes. The impedance studies were made using a computer-controlled CH-Instrument (CHI-600E) in the frequency range of 40 Hz– 1MHz at room temperature.

3. Results and discussion

3.1. XRD analysis

Figure 1(a) shows the XRD pattern of the as prepared Al_2O_3, SiO_2 and TiO_2. The high intensity (110) plane of the Al_2O_3 indicates the formation of well crystallined sample (JCPDS: 02-0921). In the SiO_2 XRD pattern the broad peak at $2\theta = 23^o$ corresponds to the characteristic (101) plane (JCPDS: 89-3606). The XRD pattern of the TiO_2 displays the single crystalline nature. It indicates that formation of anatase phase TiO_2 with high crystalline, in which the strongest peaks are at 2θ = 25.15, 37.73, 47.89, 54.00, 54.90, and 62.46° corresponds to the anatase (1 0 1), (0 0 4), (2 0 0), (1 0 5), (2 1 1) and (2 0 4) crystal planes (JCPDS: 21-1272).

Figure 1(b) shows the XRD diffractograms of pure PVdF-HFP, plasticized polymer electrolyte (PVDF-HFP: $LiClO_4$: EC) with 5 wt % of different inert fillers contents. The XRD pattern of pure PVdF-HFP film shows the characteristic peaks at $2\theta \sim 18^o$ and 21^o. This belongs to the planes (020) and (110) respectively, of the VdF γ-phase crystals. The peaks at $2\theta \sim 27^o$ and 39^o belongs to planes (021) and (131) respectively, of the VdF α-phase crystals [20].With addition of 35 wt % of plasticizer, EC, the (021) plane corresponding to the VdF γ-phase of PVdF-HFP was found to be completely suppressed, suggesting the decrease in crystalline nature of the film. From fig. 1(b), the XRD pattern of the composite electrolytes shows that there was no change in the structural aspects except for increase in broad nature of the diffraction peaks when compared to the pure and 50 wt% PVdF-HFP:35 wt % EC: 15 wt% $LiClO_4$ film. The composite electrolyte comprising TiO_2 exhibits the characteristic peaks of TiO_2 and some new peaks also appeared. Also, the (021) plane corresponding to the VdF γ-phase of PVdF-HFP was found to be completely suppressed in all composite electrolytes, suggesting the decrease in crystalline nature of the film.

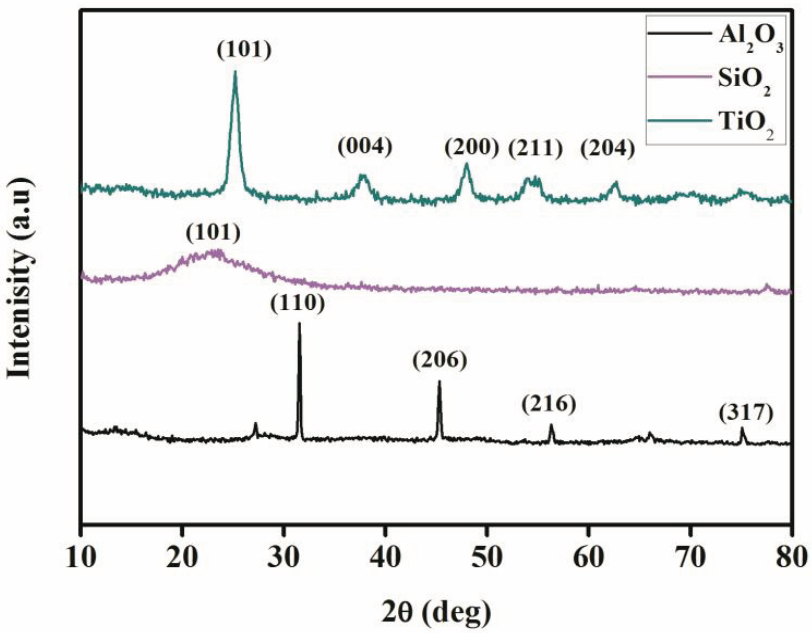


Figure 1(a). XRD pattern of prepared fillers

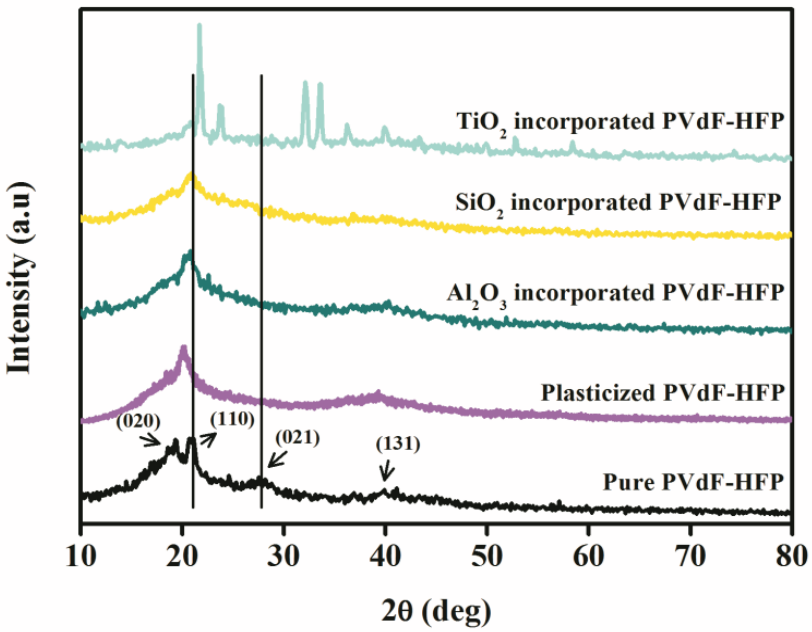
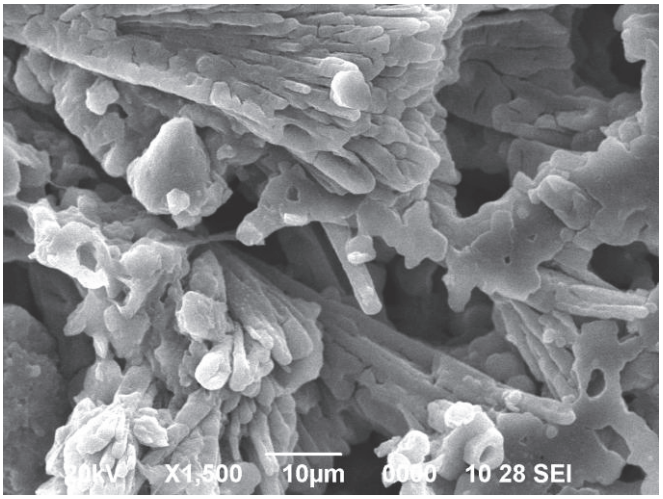


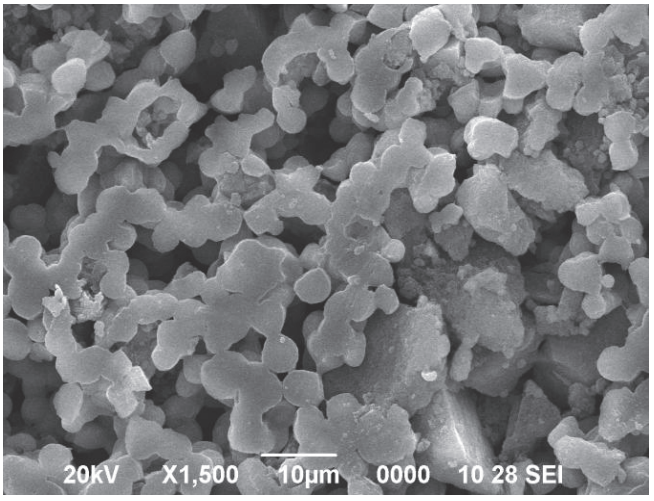
Figure 1(b) XRD pattern of filers incorporated polymer electrolyte

3.2. SEM analysis

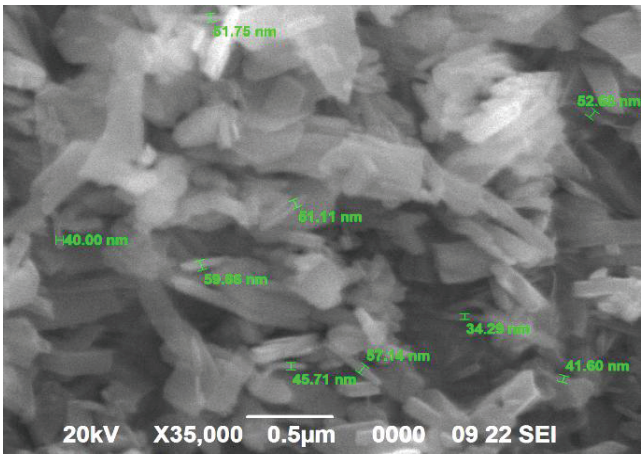
Figure 2 (a, b & c) shows SEM images of prepared Al_2O_3, SiO_2 and TiO_2 fillers respectively. The SEM image of Al_2O_3 shows that the high crystallinity of the prepared Al_2O_3 was reflected by the formation of rod shaped particles which were bundled together due to the agglomeration of micron particles. The SEM image of the SiO_2 shows that the particles were agglomerated and in sub-micron range. The SEM images of prepared TiO_2 illustrates that the nanorods of TiO_2 materials were uniformly distributed and the average particle size is about 30-60 nm.



(a)



(b)



(c)

Fig. 2 SEM images of prepared fillers

3.3 Electrical studies

3.3.1 Impedance analysis

The electrical conductivity of all the prepared filler incorporated polymer membranes have been characterized by using AC impedance spectroscopic technique. The Nyquist plot and conductance spectra for the polymer electrolyte (50- x) wt% PVdF-HFP: M(x) wt%: 35 wt% EC: 15 wt% $LiClO_4$ (x= 0 (WOF), 5 wt% and M = Al_2O_3 (WFA), SiO_2 (WFS) and TiO_2 (WFT)) for the frequency range 40 Hz to 1 MHz at 303 K is shown in fig. 3 a & b. The Nyquist plot consists of spike region with absence of semi-circle for all the polymer membrane system indicates that only the resistive component of the membrane prevails [21]. The bulk resistance of all the samples has been calculated from the intercept of the spike on the real axis. The addition of filler to the plasticized polymer membrane may increase the mobility of charge carriers which leads to the decrease in bulk resistance, as observed. The electrical conductivity of the sample was calculated by using the conductivity formula given in Eq. (1).

$$\sigma = l / R_b A \qquad (1)$$

where l and A are the thickness and area of specimen, respectively. The calculated electrical conductivity at ambient temperature is shown in Table 1. Within the measured frequency range the observed conductivity spectra have two well defined regions. The low frequency dispersive region due to the electrode-electrolyte interface at blocking electrodes and the mid frequency plateau region connected with the dc conductivity [22]. As the frequency decreases more and more the charge accumulation occurs at the electrode

electrolyte interface, which leads to a decrease in the number of mobile ions and eventually results in decrease in conductivity values at low frequency. In mid frequency region, the mobility of charge carriers was high and hence the conductivity increases with frequency. The observed conductivity values were coinciding with the one obtained from Nyquist plot.

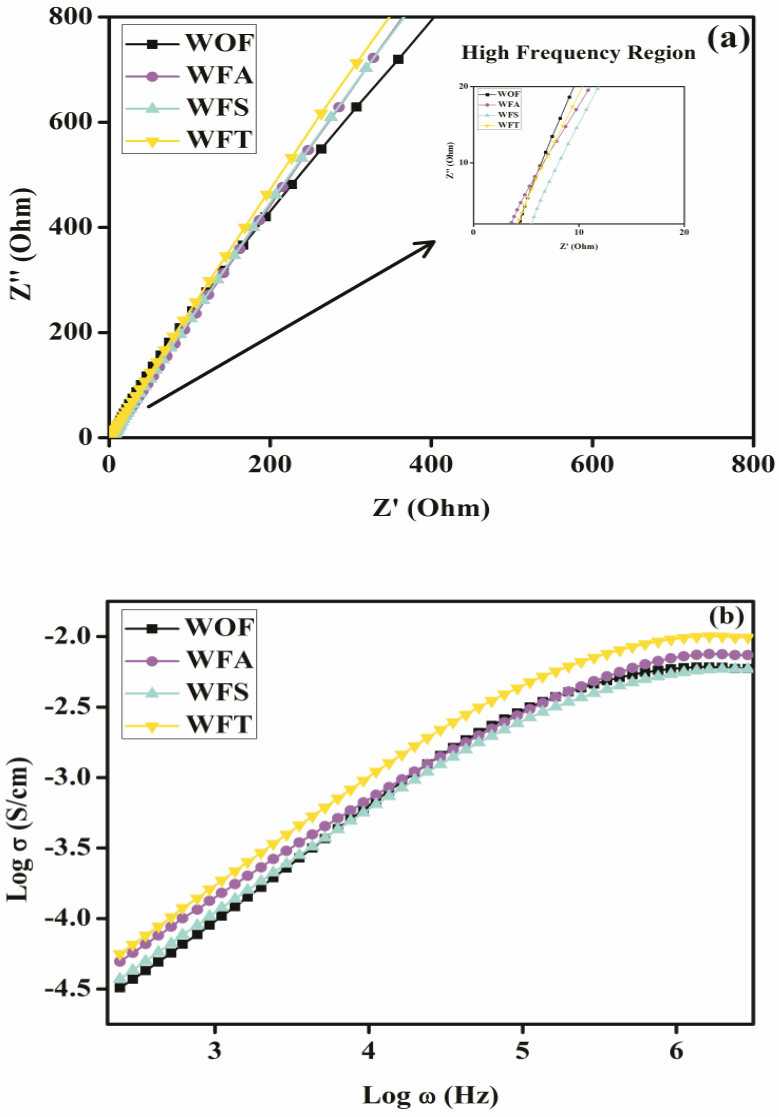


Fig. 3 a) Nyquist plot b) conductance spectra

3.3.2 Comparison of C-TiO_2 and N-TiO_2

Since among the fillers discussed above, TiO_2 nanorod doped polymer composite showed best electrical properties, it was compared with the commercial TiO_2 incorporated PVdF-HFP. As seen in Table .1, the commercial TiO_2 incorporated electrolyte was found to have poor electrical properties (impedance plot is not shown) than all the fillers discussed above. Based on the results, it was observed that the enhanced properties of nano TiO_2 + PVdF-HFP nanocomposites were solely due to the one dimensional TiO_2 nanorods. The present work shows that there is more scope on fillers with different morphology to tune the properties of chosen polymer electrolyte.

Table. 1 Conductivity values of prepared polymer electrolyte at room temperature

Polymer electrolyte	Conductivity (S/cm)
Without filler (WOF)	**3.15×10^{-3}**
With filler Al_2O_3 (WFA)	0.65×10^{-2}
With filler SiO_2 (WFS)	0.71×10^{-2}
With filler TiO_2 (WFT)	**1.11×10^{-2}**
Commercial TiO_2	1.72×10^{-4}

4. Conclusion

The inert fillers incorporated plasticized polymer electrolytes (50- x) wt% PVdF-HFP: M(x) wt%: 35 wt% EC: 15 wt% $LiClO_4$ (x= 0, 5 wt% and M = Al_2O_3, SiO_2 and TiO_2) have been prepared by simple solvent casting technique. The complex formation between plasticized polymer electrolytes with inert fillers has been confirmed by XRD analysis. Impedance spectroscopy exhibits that the electrical

conductivity of the filler incorporated polymer electrolyte increased by one order. A notable change with respect to structural and electrical properties of the films signifies the need for a systematic study on the compositional effect of different wt % of TiO_2 nanorods. The thermal, vibrational, mechanical and temperature dependent conductivity studies on different wt % of TiO_2 nanorod doped PVdF-HFP is underway.

Acknowledgements

The authors would like to thank Karunya University, Coimbatore- 641114 for the Central research facilities. The authors are very much grateful to the Department of Science and Technology, New Delhi (DST Project. No: SR/FTP/PS-192/2011) for providing fund for this research work.

References

1. M. Armand, *Solid State Ionics*, **69**, 309-319, (1994).
2. I. Kelly, J. Owen, B.C.H. Steele, *J. Power Sources,* **14**, 13-21, (1985).
3. N.T.Kalyana Sundaram, A. Subramania, *Electrochimica Acta,* **52**, 4987, (2007).
4. K.M. Kim, N.G. Park, K.S. Ryu, S.H. Chang, *Electrochimica Acta,* **51**, 5636, (2006).
5. J. Xi, X. Qiu, L. Chen, *Solid State Ionics,* **177**, 709, (2006).
6. M. Wachtler, D. Ostrovskii, P. Jacobsson, B. Scrosati, *Electrochimica Acta*, **50**, 357, (2004).
7. H.P. Zhang, P. Zhang, Z.H. Li, M. Sun, Y.P. Wu, H.Q. Wu, *Electrochemistry Communications*, **9**, 1700, (2007).
8. A. Subramania, N.T. Kalyana Sundaram, A.R. Sathiya Priya, G. Vijaya Kumar, *Journal of Membrane Science*, **8**, 2941, (2007).
9. Y.X. Jiang, Z.F. Chen, Q.C. Zhuang, J.M. Xu, Q.F. Dong, L. Huang, et al., *Journal of Power Sources,* **160**, 1320, (2006).
10. M. Usha Rani, Ravishanker Babu, S. Rajendran, *International Journal of ChemTech Research*, **5**, 1724-1732, (2013).
11. Rajendran, S., Usha Rani, M., Ravi Shanker Babu. *MSAIJ*. **7**, 3 (2011).
12. N.S. Choi, Y.G. Lee, J.K. Park and J.M. Ko, *Electrochimica Acta*, **46,** 1581-1586, (2001).
13. C. Lee, J.H. Kim and J.Y. Bae, *Polymer*, **44**, 7143-7155, (2003).
14. M. Ulaganathan & S. Rajendran, *Ionics,* **16**, 667–672, (2010).
15. M. Ulaganathan & S. Rajendran, *J. Appl. Electrochem*, **41**, 83–88, (2011).
16. S. Ramesh, O. Ling, *Polymer Chemistry*, (2010).
17. J.Zhang, Z.Xin, X.Meng, Y.Lv, M.Tao, *Ind. Eng. Chem. Res*, **52**, 14533-14544, (2013).
18. Goldberg et al., *Soil. Sci. Soc. Am. J,* **65**, 78-86, (2001).
19. Y.Yu and D.Xu, *Applied Catalysis B: Environmental*, **73**, 166-171, (2007).
20. V.Aravindhan et al, *Current applied physics*, **9**, 1106-1111, (2009).

21. T.Yammato, M.Inami, T.Kanbara, *Chem. Mater*, **6**, 44, (1994).
22. S.Ramesh, A.K.Arof, *Materials science and engineering*, **B85**, 11, (2001).

INVESTIGATIONS ON PURE AND CU DOPED NANOCRYSTALLINE LLTO FOR LITHIUM ION BATTERIES

CHRISTOPHER SELVIN.P[*] [a], ABHILASH.K.P [a], NALINI.B [b], SOMASUNDARAM.K [a]

[a] *Department of Physics, N.G.M.College, Pollachi, Coimbatore -642 001, India.*
[b] *Department of Physics, Avinashilingam Institute for Home Science and Higher Education for Women, Coimbatore -641 017, India.*

The nano-crystalline $Li_{0.5}La_{0.5}TiO_3$ (LLTO) was prepared as an electrolyte material for lithium-ion batteries. The effect of Cu ion doping in four different concentrations was investigated: $Cu_{0.2}Li_{0.3}La_{0.5}TiO_3$, $Cu_{0.3}Li_{0.2}La_{0.5}TiO_3$, $Cu_{0.4}Li_{0.1}La_{0.5}TiO_3$ and $Cu_{0.5}La_{0.5}TiO_3$ along with $Li_{0.5}La_{0.5}TiO_3$. The prepared pure and Cu doped LLTO were subjected for structural, morphological, electrical and optical characterizations. The cubic superlattice structure of LLTO nano-powder was altered due to the Cu substitution tending towards a tetragonal phase. The average crystallite size of the prepared ceramic electrolyte is found to be 40nm. The conductivity of the sample is decreased with increase in concentration of copper ion.

1 Introduction

Portable power applications continue to drive research and development of advanced battery systems. Due to the rapid increase in the use of portable computers, mobile phones, camera, electrical vehicles etc. there is an increasing demand for larger capacity, smaller size, less weight and lower priced rechargeable batteries. Among them, the Lithium ion batteries (LIBs) have become the predominant technology for electrical applications in the recent decade due to their energy, high voltage, good cycle life and excellent storage characteristics. The electrolyte forms the basic component of all batteries and fuel cells [1]. Recently the Lithium lanthanum titanate (LLTO) has been preferred as one of the important solid state electrolyte for lithium ion batteries, owing to several advantages such as higher safety and better capacity. More over

[*] Corresponding Author e-mail: pcsphyngmc@rediffmail.com or chris_sel@lycosmail.com. Permanent Address: Dr.P.Christopher Selvin, Associate Professor of Physics, N G M College, Pollachi-642 001, Coimbatore, India.

Proceedings of the 14th Asian Conference on Solid State Ionics (ACSSI 2014)
Copyright © 2014 ACSSI 2014 Organizers. All rights reserved.
ISBN: 978-981-09-1137-9
doi:10.3850/978-981-09-1137-9_095

the LLTO displays excellent ionic conductivity at room temperature typically 10^{-3}-10^{-4} Scm^{-1} [2] with the composition $Li_{3x}La_{(2/3-x)}TiO_3$ where (x=0.1).

The LLTO forms cubic perovskite (ABO_3) structure in which the vacancies at A-sites provide favorable transport tunnels [4, 5]. More importantly the overall grain boundary conductivity of LLTO ceramic is reported to be quite low of the order of 10^{-5}-10^{-7} Scm^{-1} The LLTO based compounds have perovskite structure in which Li^+ and La^+ occupies the A site and Ti occupies the B site [6]. The major impediment in developing LLTO electrolyte as the backbone for lithium ion batteries is its higher grain boundary resistance. Attempts had been made [7,8] to increase the ionic conductivity of LLTO by the substitution of ions on either the A site or the B site of the perovskite structure. In 2002, Nalini et.al [7] had reported the Eu^{2+} substitution on the 'B' sites of LLTO Perovskite, trace amount of Aluminium replacing the Titanium increases the total conductivity. The addition of silica during the preparation of LLTO leads to higher conductivity. But the replacement of some Oxygen with fluorine does not significantly affect the conductivity [8]. In 2010 Mei-Yu Chen et.al [9] had reported the structural and morphological changes that occur in 'Na' and 'Nd' substituted LLTO ceramics. Further recent studies have shown that the specific capacity corresponding to the charge stored in the bulk of the active material and cyclability which is the retention capacity during successive charge/discharge cycles depends on the synthetic route employed for its preparation. One effective way to improve the cyclability and storage capacity of LLTO is to reduce the particle size to a few nanometers [10].The reports on nanocrystalline LLTO is very scare in the literature. 2

The present study makes an attempt to substitute divalent Cu^{2+} ions in the LLTO 'nano'crystalline host trying to maintain the perovskite structure. The studies also include the effect of Cu^{2+} doping in the structural, morphological and electrical characteristics of the LLTO cubic perovskite cage.

2 Experimental details

The present work aims to synthesize LLTO and Cu doped LLTO nanoelectrolytes by modified sol-gel method. The $Li_{0.5}La_{0.5}TiO_3$ (Sample A) has been synthesized by using Lithium nitrate ($LiNO_3$-AR-99.5%, Aldrich), Lanthanum nitrate hexahydrate ($LiNO_3.6H_2O$- AR-99%, Himedia), Tetra butyl titanate ($C_{16}H_{36}O_4Ti$- AR 99%, Aldrich) and Acetyl acetone ($C_5H_8O_2$-AR-(99%, Himedia) as raw materials. The $LiNO_3$ and $LaNO_3.6H_2O$ were weighed in terms of the stochiometric composition $Li_{0.5}La_{0.5}TiO_3$ and dissolved in ethylene glycol monomethyl ether. Afterwards they were mixed with the mixture solution of Tetra butyl Titanate and Acetyl acetone. The precursor sol-gel was calcined at

900°C for 6 hours to yield pure LLTO white powder. The powder after grinding is further fired at 900°C for one hour in a muffle furnace, resulting in a white pure LLTO sample. The LLTO sample is doped with copper (Cu^{2+}) ion in four different ratios. They are indicated as

Sample B: $Cu_{0.2}Li_{0.4}La_{0.5}TiO_3$; (Cu:Li=2:4)
Sample C: $Cu_{0.3}Li_{0.2}La_{0.5}TiO_3$; (Cu:Li=3:2)
Sample D: $Cu_{0.4}Li_{0.1}La_{0.5}TiO_3$; (Cu:Li=4:1)
Sample E: $Cu_{0.5}La_{0.5}TiO_3$; (Cu:Li=5:0)

The copper doped LLTO samples were prepared by taking copper nitrate, Lithium nitrate, Lanthanum nitrate hexa hydrate, tetra butyl titanate and acetyl acetone in the above mentioned stochiometric ratios. The Cu^{2+} ions are expected to occupy the A sites of the perovskite cage replacing Li^{+}/La^{2+} ions.

The Powder X-ray Diffraction pattern of synthesized samples were recorded using Schimadzu-XRD-6000 X-ray diffractometer instrument with a scan speed of 3°/min. in the range of 10°- 80° using monochromatic Cu-Kα (1.5406 Å) radiation source. The Morphological studies of the samples were carried out using SEM (JEOL Model JSM-6390) instrument. The optical characterization is done using FTIR (SHIMAZDU 220-93270-55 IRTracer-100) spectrometer. The electrical characterizations of the samples were analyzed by Complex Impedance Analyzer (SHIMADZU LCR METER 35260) using silver paste as the contact electrode on either side of the sintered pellets.

3. Results and Discussion

3.1 *Structural analysis*

The figure 3.1 shows the XRD patterns of pure and copper doped LLTO samples. The electrolyte $Li_{0.5}La_{0.5}TiO_3$ (LLTO) shows a cubic perovskite structure is a class of compounds having same type of crystal structure as $CaTiO_3$ ($^{XII}A^{2+VI}B^{4+}X^{2-}{}_3$) [9].

The observed XRD pattern was compared with the standard JCPDS data (card no: 89-7506) and found that the cubic perovskite structure prevails in the prepared samples. The XRD peaks assigned to the cubic perovskite and found that a few of the peaks were due to super lattice structure. The super lattice lines are indicated by using (*) in the XRD pattern.

The substitutions of Cu^{2+} ions in LLTO introduce a distortion in the unit cell. From the XRD pattern, it is evident that the crystal structure gradually changes with the increase in copper ion concentrations. The $Cu_{0.2}Li_{0.3}La_{0.5}TiO_3$

shows a considerable shift from cubic structure to tetragonal. The intensity of the peak due to (101) plane decreases with Cu^{2+} substitution and the peak due to (105) plane starts emerging in the $Cu_{0.2}Li_{0.3}La_{0.5}TiO_3$, $Cu_{0.3}Li_{0.2}La_{0.5}TiO_3$ samples which is specific to tetragonal $CuLaTiO_3$. The $Cu_{0.4}Li_{0.1}La_{0.5}TiO_3$ sample clearly exhibits a mixed phase of cubic and tetragonal structure. The peak due to (105) and (008) planes became more prominent in this sample which ensures the formation of tetragonal structure. In this sample the LLTO major peak (101) at $2\theta=33.81^{\circ}$ splits into two and emerges as a new peak at (112) which is also specific to tetragonal phase. The $Cu_{0.5}La_{0.5}TiO_3$ which does not contain any Lithium content forms a perfect tetragonal structure. This indicates that the expansion of unit cell in the "c" axis due to the substitution of Cu^{2+} and reaches a complete tetragonal structure when Cu^{2+} occupies all the Li^{+} sites. The value of lattice constant for LLTO cubic crystal is a=3.887Å and got increased for $Cu_{0.5}La_{0.5}TiO_3$ as a=3.824 Å and c=26.329 Å which clearly shows that the volume of the unit cell is bigger than the pure LLTO sample. This increment may be caused due to the bigger ionic radi 4 Cu^{2+} ion compared with Li^{+} ion.

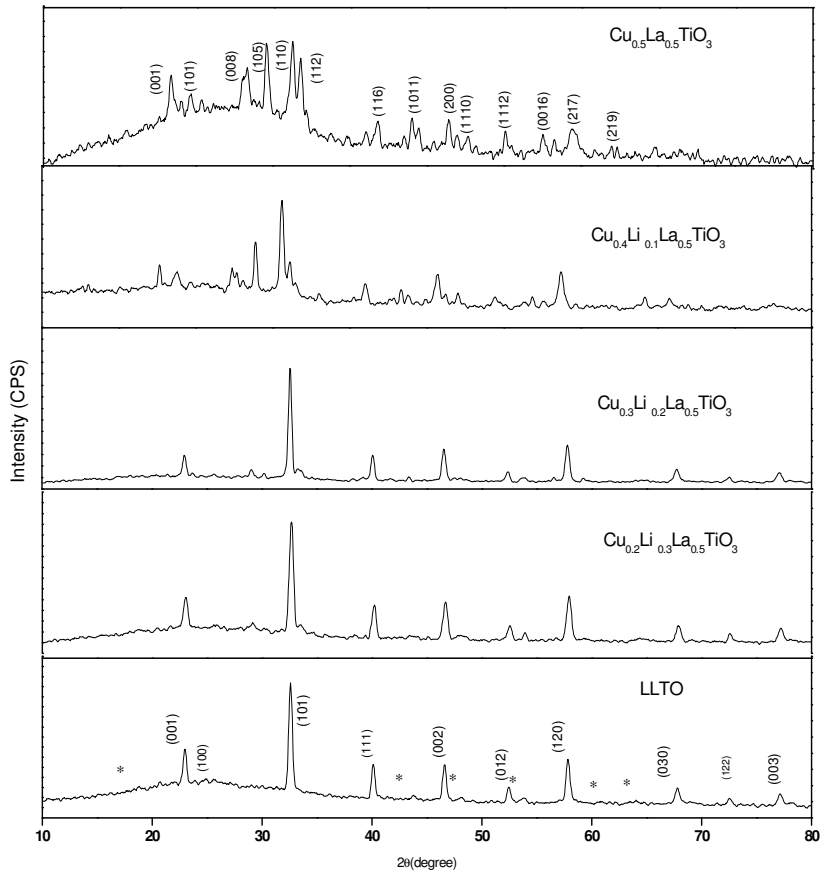


Figure.1 The XRD pattern of pure LLTO and Copper substituted LLTO samples

The average crystallite size calculated for LLTO powder using Debye Scherrer's formula is found to be 33 nm. With the Cu^{2+} substitution the crystallite size is found to increase to 45 nm for $Cu_{0.5}La_{0.5}TiO_3$ sample. From the XRD data it is also evident that the structural transformation of cubic perovskite to tetragonal phase occurs due to the Cu^{2+} substitution at different concentrations in the LLTO matrix.

3.2 Fourier Transform infrared (FTIR) spectroscopy

The Fourier Transform Infra Red Spectroscopy (FTIR) is known to be one of the good means of investigation for the structure and functional groups at a local scale. The FTIR spectra for all the samples are shown in figure 3.2.

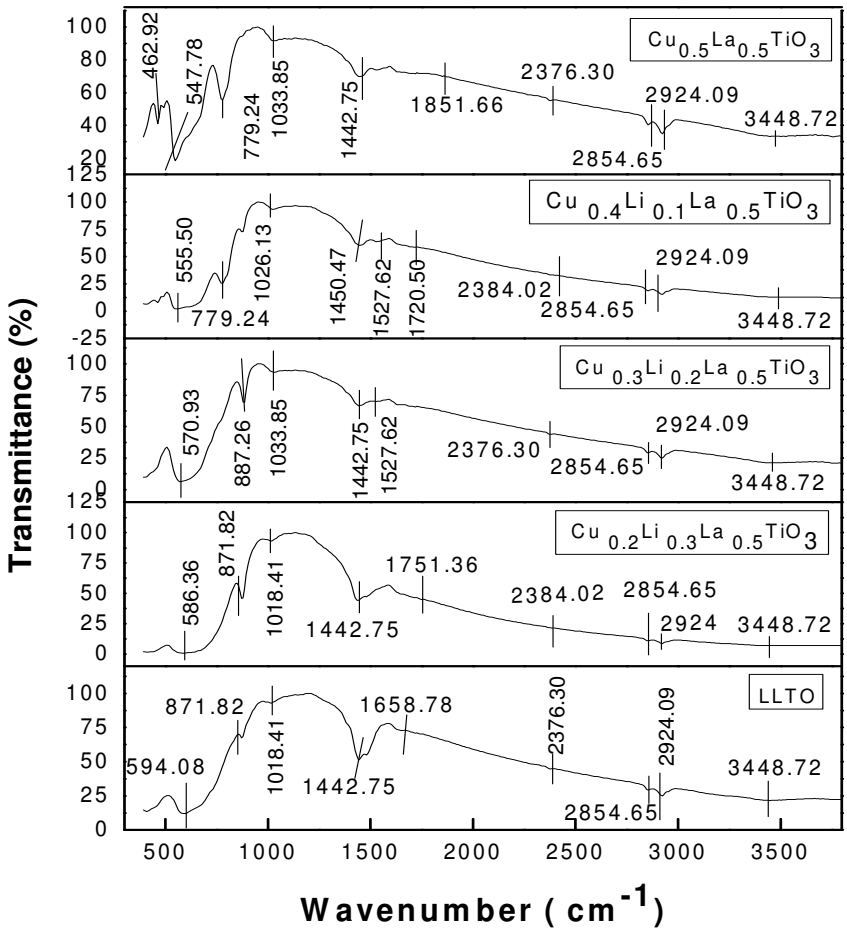


Fig 3.2 FTIR spectra of LLTO and Copper doped LLTO samples

.

The absorption peak centered at 594.08 cm^{-1} (in LLTO) is due to the vibration of the Ti-O_6 octahedra and it is found to shift to lower wave number due to the deformation in the Ti-O bond in the Cu^{2+} doped samples. The frequency of the peak due to the vibration of Ti-O_6 octahedra decreased to 547 cm^{-1} in $Cu_{0.5}La_{0.5}TiO_3$ [12]. The band that occurred at 3448 cm^{-1} can be ascribed to the stretching of OH group of water molecule which gives an indication of the surface adsorbed water content. The bands detected at 887 cm^{-1} is due to the vibrations of La-O bond. The peak at 1034 cm^{-1} is due to the vibration of Titanium oxide [13]. The peak around 1443 cm^{-1} is associated with the degeneracy of asymmetric stretching vibration mode of CO which is not much prominent in the doped sample when compared to the LLTO sample. The weak peaks in the range 1628-1721 cm^{-1} and around 1018 cm^{-1} originated from

the bending vibration of C-C bond [14] due to the acetone related impurities that occur in the sample

Doping of Cu^{2+} in LLTO shifts some of the peaks to higher or lower frequencies and some of the new peaks are also generated with the increase in concentration of Copper. The peak due to the presence of carbon, water and acetone impurities are common for the copper doped samples. A new peak due to the weak Ti-O-La bond at the frequency of 463 cm^{-1} can be observed in $Cu_{0.3}Li_{0.2}La_{0.5}TiO_3$, $Cu_{0.4}Li_{0.1}La_{0.5}TiO_3$ and $Cu_{0.5}La_{0.5}TiO_3$ sample. Another peak centered at 779 cm^{-1} also originates in $Cu_{0.4}Li_{0.1}La_{0.5}TiO_3$, $Cu_{0.5}La_{0.5}TiO_3$ samples by the deformed Ti-O bond due to structural change from cubic to tetragonal structure [15].

3.3 Morphological analysis

The SEM micrograph (JEOL JSM 6390) of pure $Li_{0.5}La_{0.5}TiO_3$ (LLTO) and Cu^{2+} doped LLTO samples were shown in Figure.3.3 (a, b, c, d & e). The SEM micrograph of pure LLTO shows the uniform formation of LLTO phase with the aggregation of nanosphere. The SEM micrograph of Cu^{2+} doped LLTO sample shows an increase in particle size with the increase in Copper ion concentration. The surface uniformity of the LLTO sample is found to be disturbed in $Cu_{0.2}$ $Li_{0.3}La_{0.5}TiO_3$ sample. This became more prominent in the $Cu_{0.3}$ $Li_{0.2}La_{0.5}TiO_3$ samples and this is in accordance with the XRD results of the doped sample showing a mixed phase. The $Cu_{0.4}$ $Li_{0.1}La_{0.5}TiO_3$ and $Cu_{0.5}La_{0.5}TiO_3$ samples showed a different morphology with increase in particle size. The XRD result shows that the phase transition (cubic perovskite – tetragonal) due to Cu^{2+} substitution end-up with a complete tetragonal phase in

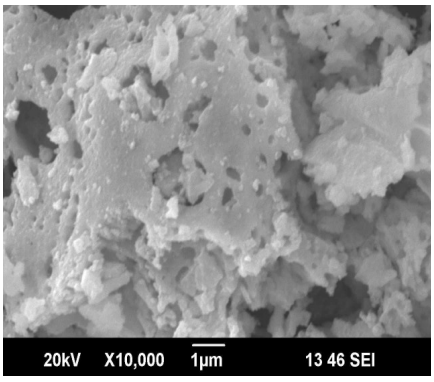


Fig. 3 (a) SEM image for $Li_{0.5}La_{0.5}TiO_3$

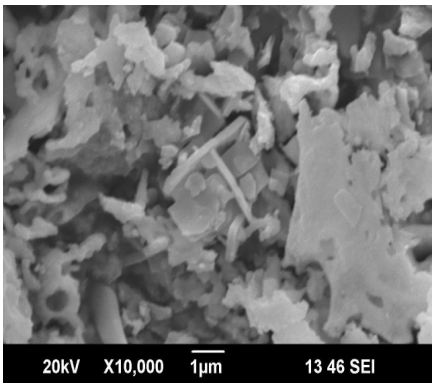


Fig. 3 (b) SEM image for $Cu_{0.2}Li_{0.3}La_{0.5}TiO_3$

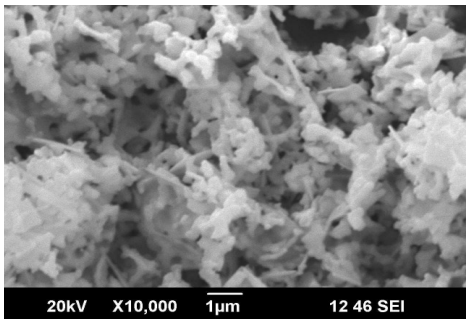


Fig.3 (c) SEM image for $Cu_{0.3}Li_{0.2}La_{0.5}TiO_3$

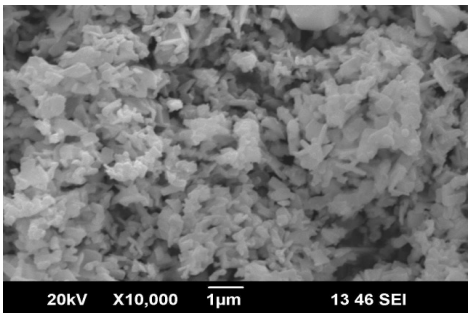


Fig. 3 (d) SEM image for $Cu_{0.4}Li_{0.1}La_{0.5}TiO_3$

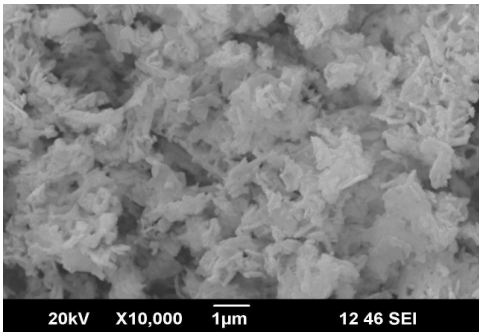


Fig. 3 (e) SEM image for $Cu_{0.5}La_{0.5}TiO_3$

$Cu_{0.5}La_{0.5}TiO_3$ sample. This is also evident from the SEM micrographs, in which a gradual transformation from a uniform morphology of LLTO to entirely different morphology occurs in $Cu_{0.5}La_{0.5}TiO_3$ samples.

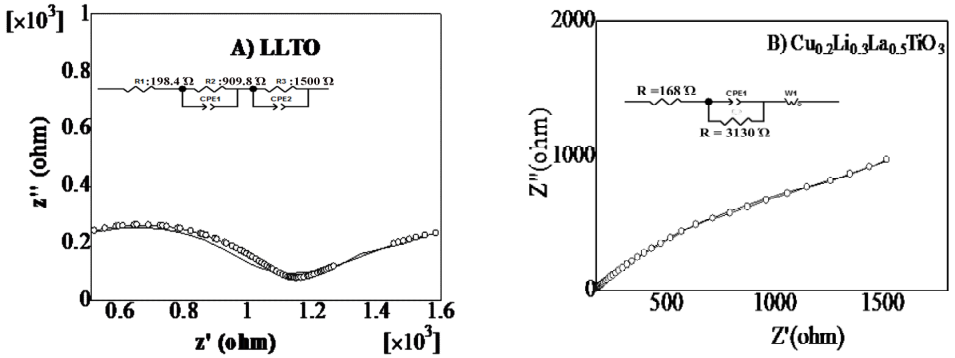
4 Conductivity studies

Figure 4 shows the Nyquist plots [Z' (real) Vs Z'' (imaginary) plots] at room temperature (301 K). The equivalent circuits for all the four samples fitted (inset figure) using Z-view software shows the best fit results.

The LLTO powder shows high frequency semicircle and low frequency spike. The bulk resistance is very low around 198.4 Ω. The XRD and SEM result shows that the particle size is in the nano level which substantiates the present result. The bulk conductivity of LLTO nano powder is 1.41×10^{-3} Scm^{-1} which is one of the highest conductivity reported in the literature [4, 5, 16]. The total conductivity of the present sample is 3.094×10^{-4} Scm^{-1} at room temperature, which includes the grain boundary effects of the LLTO nano particles.

The Cu^{2+} substituted samples show an increase in the total resistance. In $Cu_{0.2}Li_{0.3}La_{0.5}TiO_3$ sample, the total conductivity is reduced by one order of

magnitude than LLTO nanoparticles. The grain conductivity of the sample is 2.2 X 10^{-4} Scm^{-1} which is reduced by one order of magnitude than LLTO nano particles. The equivalent circuit contains high frequency semi circle, constant phase element (CPE) and low frequency Warburg impedance due to the space charge polarization effect. The grain and grain boundary conductivity could not be differentiated in $Cu_{0.3}Li_{0.2}La_{0.5}TiO_3$, $Cu_{0.4}Li_{0.1}La_{0.5}TiO_3$ samples. This samples shows further reduction in total conductivity and its total conductivity was reduced to $1.07x10^{-6}$ Scm^{-1}, 8.6×10^{-7} Scm^{-1} at room temperature. The $Cu_{0.5}La_{0.5}TiO_3$ which did not contain any lithium ion shows a conductivity of 9.02 x 10^{-8} Scm^{-1} which is lesser than the doped samples. As there is no lithium ion in the matrix, the Cu^{2+} ions alone contribute to the conductivity in this sample. The conductivities of the samples are tabulated in table.3.1. The result shows that the lithium ions diffuse faster in the grain and grain boundaries of the LLTO nano particles than that of the Cu^{2+} substituted samples. There is no significant diffusion effect observed in the Cu^{2+} substituted samples. The Cu^{2+} substitution not only changes the structure but reduces the available space for the mobility of Li^+ ion. The Cu^{2+} ions which are being bulkier in size than the Li^+ ions substitute some of the Li^+ ion A sites of the perovskite cage and do not allow the ions to move freely which explains the low conductivity of the Cu^{2+} ion substituted LLTO samples.



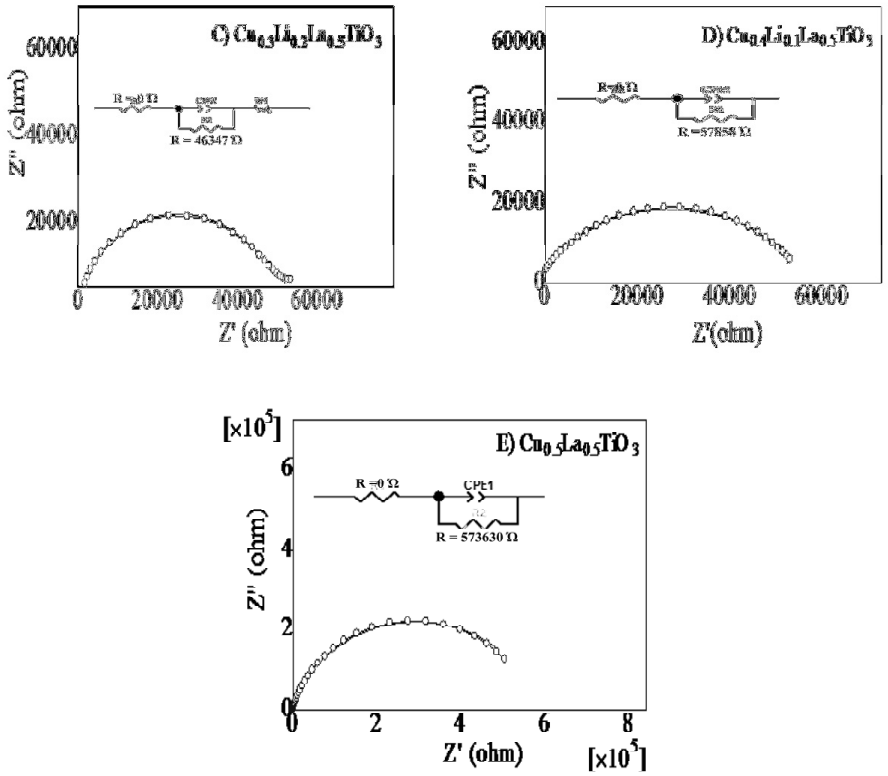


Fig. 4. (A,B,C,D,E) Conductivity spectra of LLTO and Cu^{2+} doped LLTO samples

Table : 3.1 Conductivity of pure and doped LLTO samples

Name of the sample	Thickness of the pellet (cm)	Total conductivity (Scm^{-1})
$Li_{0.5}La_{0.5}TiO_3$	0.197	3.094×10^{-4}
$Cu_{0.2}Li_{0.3}La_{0.5}TiO_3$	0.186	1.21×10^{-5}
$Cu_{0.3}Li_{0.2}La_{0.5}TiO_3$	0.153	1.07×10^{-6}
$Cu_{0.4}Li_{0.1}La_{0.5}TiO_3$	0.155	8.60×10^{-7}
$Cu_{0.5}La_{0.5}TiO_3$	0.197	9.02×10^{-8}

.5. Conclusion

The LLTO nanopowder shows cubic perovskite structure with highly ordered superlattice diffraction pattern. The grain resistance and interface effects were minimized in the nanocrystalline LLTO particles. The Cu^{2+} substitution disturbs

the cubic perovskite (Superlattice) structure of LLTO with the formation of tetragonal phase as the content of Cu^{2+} increases. As evidenced by the results, the transformation ends up as all the Lithium content of the samples have been replaced by Copper ions. The FTIR studies show the emergence of two new peaks at higher Cu^{2+} concentrations at 436 cm^{-1} and 779 cm^{-1} respectively due to the deformation of Ti-O bond by the tetrahedral deformation of the perovskite cage. The structural changes also reflect on the morphology of the samples which shows a transformation from uniform morphology of LLTO sample to a completely different morphology of $CuLaTiO_3$ Samples. The conductivity of Cu^{2+} substituted samples were reduced due to the non availability of free space for transportation of ions.

Acknowledgements

The authors sincerely thank University Grants Commission, New Delhi, for the financial assistance in the form of Major Research Project (F. No. 41-842/2012 (SR). One of the author Mr.Abhilash K P thanks to UGC for providing the fellowship.

References

[1] Nagai.R, Proceedings of 24th Battery symposium, Japan, (1983) 221.

[2] C.HChen, K.Amsine, Ionic conductivity of lithium insertion and extraction of lanthanum lithium titanate, Solid State Ionics 144 (2001) 51.

[3] AoMei, Xiao-Liang Wang, Jin-Le Lan, Yu-Chuan Feng, Hong-Xia Geng, Yuan-Hua, Ce-Wen Nan, Role of amorphous boundary layer in enhancing ionic conductivity of lithium lanthanum titanate electrolyte, Electrochemica Acta 55(2010) 2958.

[4] Ferreira J.D & Martin, peason, Prentice Hall, Upper saddle River (2008) 1.

[5] Megaw, Helen D, crystal structure of Barium Titanate, Nature 155 (1945) 484.

[6] C.H.Chen, K.Amine, Solid State Ionics, 144 (200) 51.

[7] B. Nalini, T. Takeuchi , H. Kageyama, Solid State Ionics 154-155 (2002) 629.

[8] Jeffrey W. Fergus, Journal of Power Sources 195 (2010) 4554.

[9] Mei-Yu Chen, Ching Yu Chiu, Chia-Ta Chia, J.F.Lee, J.J.Bian, Journal of the European Ceramic Society 30 (2010) 335.

[10] B.Antoniassi, A.H.M.Gonzalez, S.L.Fernades, C.F.O.Graeff, Microstructural and Electrochemical study of $Li_{0.5}$ $La_{0.5}TiO_3$, Material Chemistry and Physics 127 (2011) 51.

[11] O.Bohnke, C.Bohnke, J.Ould Sid'Ahmed, M.P.Crosnier-Lopez, H.Duroy, F.Le Berre, J.L. Forquet, Chemistry of Materials 13 (2001) 1593.
[12] [14] El-Mallawany R.A, Infrared Physics, 29 (1989) 781.
[13] Shalini.K, Shivashankar.S.A, Material Science, 28 (2005) 49.
[14] Bohnke.O, Pham.Q.N, Boulant.A, Emery.J, Salkus.T, Barre.M, Solid State Ionics, 188 (2011) 144.
[15] Thang-Dinh Nguyen, Cao-Thang Dinh and Trong-On Do, Langmuir, 25(18) (2009) 11142.
[16] Deer, Howie, Zussman, An Introduction to the Rock Forming Minerals Mineralogical Society of America, 90 (1966) 774.

PERMEABILITY STUDIES OF CELLULOSE ACETATE DOPED WITH NH_4NO_3 AND NH_4PF_6

T. CHIDAMBARAM
Water Research laboratory, Water Institute, Karunya University, Coimbatore-641114 Tamilnadu, India

S. SELVASEKARAPANDIAN
Material Research center, Coimbatore-641045, Tamilnadu, India

K. GOVINDAN
Water Research laboratory, Water Institute, Karunya University, Coimbatore-641114 Tamilnadu, India

ARUN ARAICHIMANI
Department of Chemistry, Government Arts College, Tiruvannamalai, Tamilnadu, India

Cellulose acetate is one of the most suitable semi permeable membrane for osmotic drug delivery system. In general as the acetyl content in cellulose acetate (CA) increases, the CA film permeability decreases, solvent resistance increases and the glass transition temperature increases. (Pharmaceutical technology Vol-33, pp-88-100 2009). It has been observed from literature that while preparing cellulose acetate membrane additives such as polyethylene glycol (PEG), Polyvinyl pyrolidone (PVP), lithium chloride ($LiCl_2$), egg albumin etc.. have been added. But addition of ammonium salt to the CA membrane is rare in the literature. Hence, CA membrane has been prepared with different concentration of ammonium salt ammonium nitrate (NH_4NO_3) and ammonium hexafluoro phosphate (NH_4PF_6) by solution casting technique using dimethyl formamide (DMF) as solvent. XRD, FTIR, SEM and water permeability have been undertaken. XRD patterns of the Cellulose acetate membrane doped with NH_4NO_3 and NH_4PF_6 confirm that complex formation. Pure water permeability studies have been carried out for the CA membrane doped with different concentration of NH_4NO_3 and NH_4PF_6 salts using dead end filtration (Stirred cell) technique at 5 bar pressure. Pure CA membrane does not allow water to pass through it. As the concentration of NH_4NO_3 and NH_4PF_6 from 0 to 30 M wt%, it is observed the membrane does not allow water to pass through it. As the NH_4NO_3 and NH_4PF_6 concentration is increased to 40 and 50 M wt %, the membrane allows 2.7 and 102 Liter/hr respectively in the case of NH_4NO_3. And 6.8 and 13.6 Liter/hr for NH_4PF_6 doped Cellulose acetate membrane. SEM measurement indicates that pores get started to form only when CA is doped with 40 and 50 M wt % of NH_4NO_3 and NH_4PF_6.

Proceedings of the 14th Asian Conference on Solid State Ionics (ACSSI 2014)
Copyright © 2014 ACSSI 2014 Organizers. All rights reserved.
ISBN: 978-981-09-1137-9
doi:10.3850/978-981-09-1137-9_126

1. Introduction

Recently membrane technology plays a vital role in wide variety of industrial applications i.e water and wastewater treatment, gas separation, and fuel cell applications. Commercially available and modified materials (organic and biopolymers) are being used so far. Since, cellulose is the most abundant natural organic biomaterials in earth; researchers started working with cellulose acetate for industrial applications such as water treatment from 1964 onwards as an ultrafiltration membrane. In 1970's asymmetric cellulose acetate (CA) membranes brought evolutions in nanofiltration and ultratfiltration in the field of water treatment [1]. In recent years many studies towards on improving the performance of cellulose acetate membranes by blending with other polymers, nanoparticles and carbon nanotubes etc.

Cellulose acetate (CA) was blended with multi walled carbon nanotubes (MWCNT's) for gas separation, which increases the mechanical properties when increasing MWCNT's composition [2, 5]. Addition of TiO_2 [3] and silica [9] nano particles increases the pore sizes of the CA membranes which leads to significant increase in pure water permeability. Recently Soyekwo et al., carried out the study with CA composite membrane fabrication with CA nanofiber via freeze extraction. In this studies 71% porosity were reported it leads to high water permeability [4]. CA blended with carboxymethyl cellulose acetate (CMCA) shows better performances for permeability studies. And cellulose triacetate/cellulose acetate was used for forward osmosis membrane preparation [7]. Microbial studies also carried out with thin film composite CA membranes [8]. Poly ethylene glycohol (PEG) 600 blended CA was used for the municipal sewage waste treatment [10]. Performance of proton conducting membranes prepared by CA with mixture of organic ionic plastic crystal (OIPC), chlorine dihydrogen phosphate and various acids were studied [12]. In addition to this dielectric constant, dielectric loss and a.c conductivity of poly blends of CA hydrogen phthalate (CAP) and Poly methylene metha acrylate (PMMA) of different composition have been studied [13].

Very limited studies on the addition of electrolyte salts in to the membrane have been reported until now. In the present work CA-NH_4NO_3 and CA-NH_4PF_6 proton conducting polymer have been prepared by solution casting technique. The results are discussed n the basis of water permeability and electrical conductivity, mainly as a function of the salt addition (NH_4NO_3 and NH_4PF_6) in to the polymeric membranes.

2. Materials and methods

2.1 Materials

Cellulose acetate (average M_n ~30,000 by GPC), Ammonium nitrate (≥98%) and ammonium hexafluoro phosphate (NH_4PF_6) (99.99% trace metals basis) analytical grade chemicals were purchased from sigma Aldrich chemicals. The analytical grade solvent dimethyl formamide was purchased from the merck India.

2.2 Membrane synthesis

Polymer doped solutions were prepared with CA with ammonium nitrate and ammonium hexafluoro phosphate of various compositions presented in Table. 1 using dimethyl formamide (DMF) as solvent by solution casting technique. Required amount of CA was dissolved in DMF at 60^{o}C for 3 hours with addition of ammonium salts for 2 hours with constant stirring. The mixture is stirred till it becomes homogeneous. Then it is poured in the petri dish and evaporated at 60^{o}C in vacuum oven. Free standing film is obtained after 48 hours. Films obtained with 10 %, 20 %, 30 %, 40 % and 50 % by weight of ammonium nitrate are characterized using SEM, XRD and FTIR. FTIR spectrum has been recorded in the range of 400-4000 cm-1 at room temperature using BRUKER Spectrophotometer.

Table 1. Composition of membranes

Membranes	Materials	Composition
M0	CA	(100:0)
M1	CA: NH_4NO_3	(90:10)
M2	CA: NH_4NO_3	(80:20)
M3	CA: NH_4NO_3	(70:30)
M4	CA: NH_4NO_3	(60:40)
M5	CA: NH_4NO_3	(50:50)
M6	CA: NH_4PF_6	(90:10)
M7	CA: NH_4PF_6	(80:20)
M8	CA: NH_4PF_6	(70:30)
M9	CA: NH_4PF_6	(60:40)
M10	CA: NH_4PF_6	(50:50)

2.3 Experimental set up (Pure water flux analysis)

The schematic diagram of the experimental setup with stirred cell (STERLITECH- HP4750) for the laboratory study is shown in Fig.1. The membrane used in the stirred cell had an effective area of (14.6×10^{-4} m^2). The stirred cell was connected to nitrogen cylinder through a regulator. The pure water flux analyses were carried at an operating pressure of 5 bars and at room temperature (25±1°C).The pure water flux rate was determined using the formula

Pure water flux (J) =Q/(A×t) Lh^{-1} m^{-2} Eq. (1)

where Q is the volume of permeate in Liter, A is the effective membrane area in m^{-2} and t is the Period of time in hours.

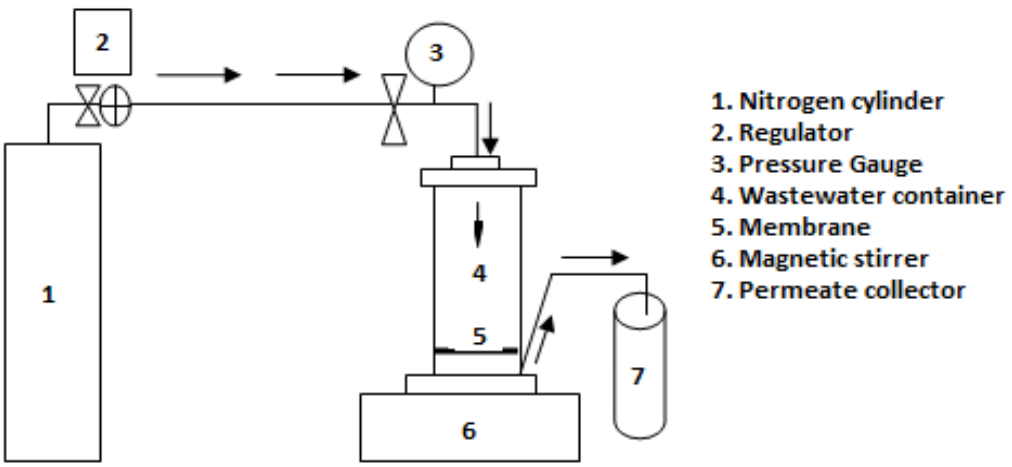


Figure 1. Schematic diagram of membrane separation set up (Stirred cell)

3. Results and discussions

3.1 *X-ray Diffraction (*XRD)

X-ray diffraction patterns of pure CA, CA with NH_4NO_3 and NH_4PF_6 with two different compositions are shown in Fig.2. It can be seen that the XRD patterns of pure CA shows semi crystalline nature. Peaks at 18°, 23° and 27° are observed for pure CA. The amorphous nature has increased for NH_4NO_3 and NH_4PF_6doped CA membrane along with presence of peaks observed for pure CA. XRD peaks due to NH_4NO_3 and NH_4PF_6 are absent.

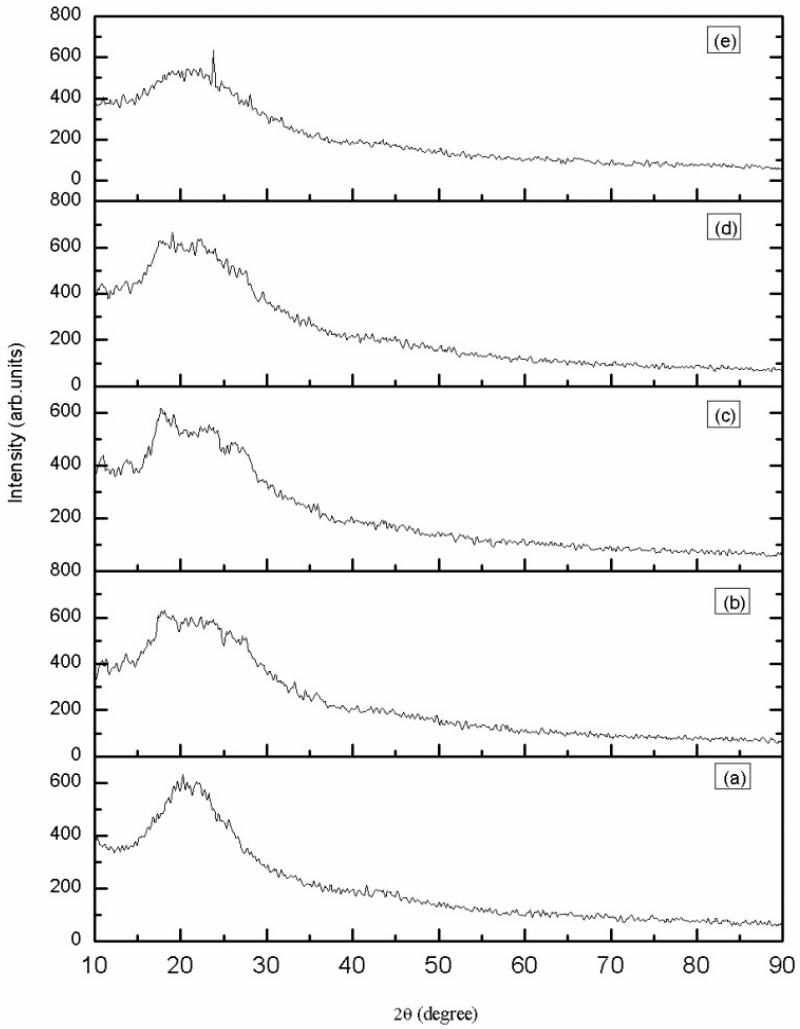


Fig.2 XRD patterns for the a) M0 b) M2 c) M5 d) M7 d) 10

3.2 Attenuated total reflectance Infrared spectroscopy (ATR-FTIR)

ATR-FTIR spectra are recorded on a BRUKERspectrometer. ATR-FTIR spectroscopy is used to analyze the interactions among atoms or ions in membranes systems. The FTIR spectra of pure CA, NH_4NO_3 and NH_4PF_6salts of 80:20 and 50:50 two compositions are shown in Fig.3. The bands at 1027 cm^{-1} and 1216 cm^{-1} have been assigned to C-O stretching. The bands at 897 cm^{-1} in Fig. 2 have been assigned to aromatic C–H bends which is presented in the Cellulose acetate. Increase/decrease of intensity of FTIR peaks of NH_4NO_3 and NH_4PF_6doped CA compared to pure CA has been observed. This confirms the complex formation between the polymer CA and NH_4NO_3 and NH_4PF_6salts.

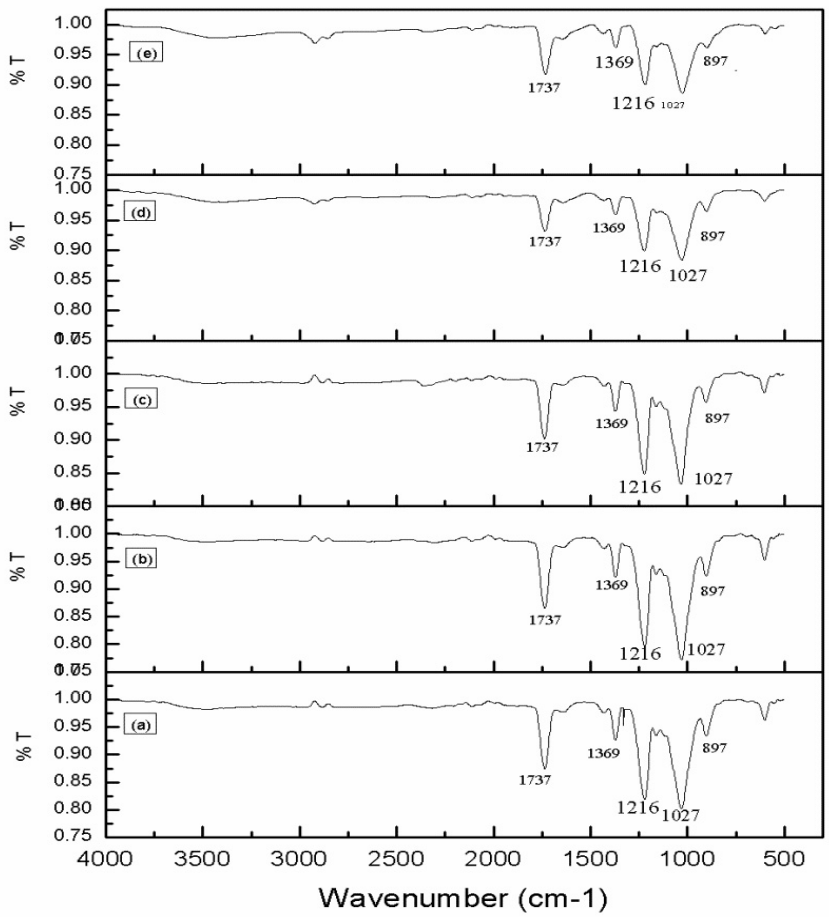


Fig.3 FT-IR spectra for the a) M0 b) M2 c) M5 d) M7 d) 10

3.3 Scanning electron microscopy (SEM)

Fig. 4a shows the pure cellulose acetate membrane which indicates that there is no pores formation in the membrane surface. Hence, it does not allow water to penetrate through the membranes. When adding the ammonium nitrate salts in to the CA polymer, the pores started to form (Fig.4b). The high porosity was noticed for the M5, which contains 50% of the ammonium nitrate. The size of the pores formed by the addition of ammonium salt is 80-250nm (Fig.4c). While adding ammonium hexafluoro phosphate in to the cellulose acetate membrane the same behavior was noticed. There was no porosity for the M0 and M7 membranes (Fig. 4d and 4e). But while the percentage of ammonium hexafluoro phosphate increases to the 50, the significant pore formation was noticed for M10 membrane (Fig.4f). The porosity of M10 membrane was in the range of 300-600nm, which leads to higher penetration of water through the membrane.

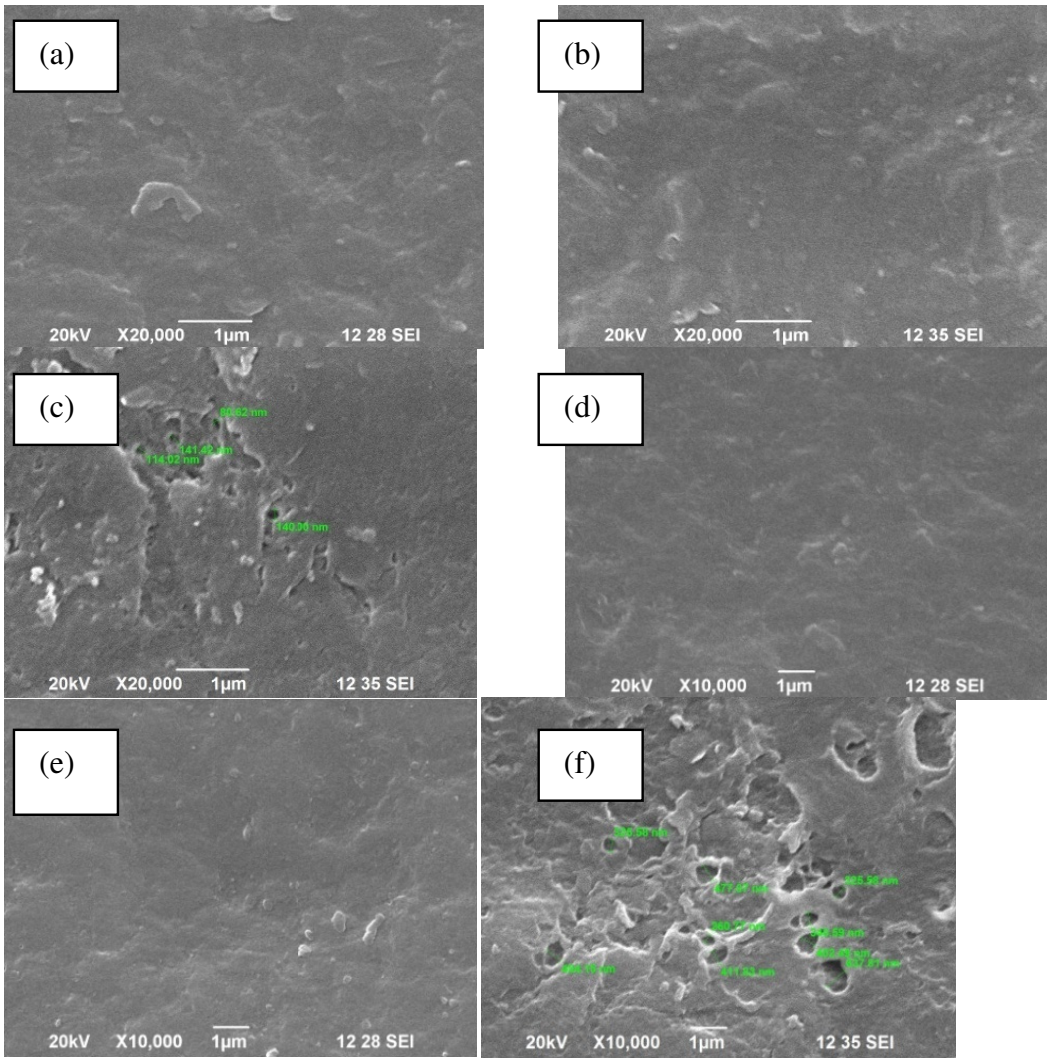


Figure 4. SEM images for a) M0 b) M2 c) M5 d) M0 e)M7 f)M10

3.4 Pure water flux (PWF)

Pure water fluxes were calculated by using the Eq. (1). No water permeability for the M0, M1, M2, M3 membranes which are doped by up to 30% NH_4NO_3 withcellulose acetate (CA) was noticed, because it does not contains pores in the membrane. But, the pore gets started to form for the 40% ammonium nitrate doping, hence about 2.7 L/h/m^2 was noticed for this membrane. Beyond increasing the NH_4NO_3 percentage to 50%, the water flux increases significantly. About 102 L/h/m^2 flux was noticed for this membrane at 5 bar (Figure.5).

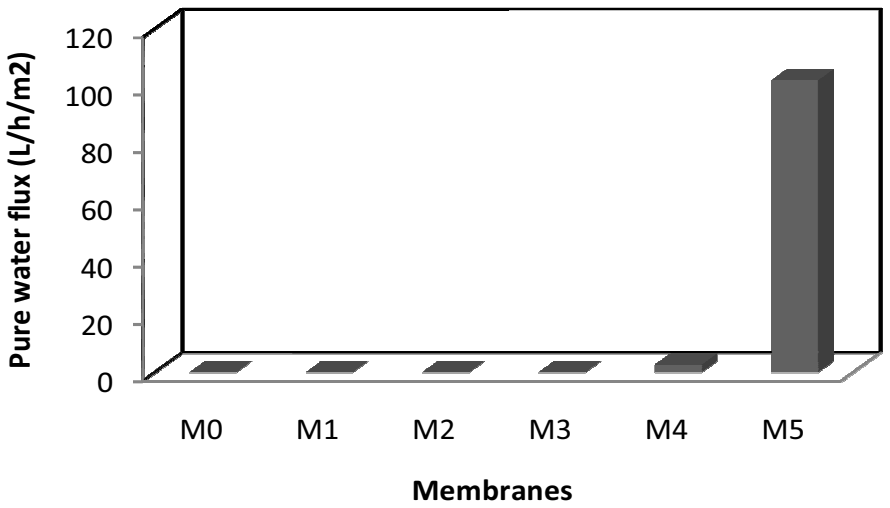


Figure 5. Pure water flux rate for the different composition NH_4NO_3 doped CA membranes

No water permeability for the 0%, 10%, 20%, 30% NH_3PF_6 doped cellulose acetate (CA) was noticed, similar to ammonium nitrate because itdoes not contains pores in the membrane. But, in the 40% doping the pore gets started to form, hence about 6.8 L/h/m^2 was noticed for this membrane. Eventhough increasing the NH_4PH_6 percentage to 50%, the water permeability not increases significantly. About 13.6 L/h/m^2 flux only was noticed for this membrane at 5 bar (Figure.6).

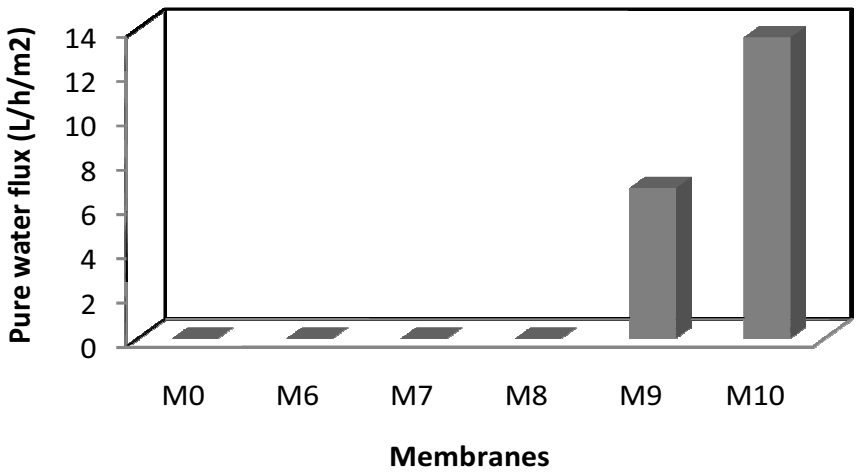


Figure 6. Pure water flux rate for the different composition NH_4PF_6 doped CA membranes.

4. Conclusion

XRD and FTIR confirm the structure and composition of the membranes. SEM analysis shows the pore formation while adding the ammonium salts. Addition of ammonium salts increases the pore size of the membranes which leads to higher water flux rate.

Acknowledgements

The authors would like to thank Karunya University for providing the facilities for water permeability studies. We would also like to offer our special thanks to material research centre for providing financial support for the synthesis and characterizations.

References

1. A.I Schafer, A.G Fane, and T.D Waite, Nanofiltration Principle and application, (2005).
2. A.R. Moghadassi , Z. Rajabi, S.M. Hosseini, and M. Mohammadi, J. of Indust. and Eng. Chem. 201050-1060 (2014).
3. Reza Abedini, Seyed Mahmoud Mousavi, Reza Aminzadeh, Desalination 277 (2011) 40–45
4. Faizal Soyekwo, Qiu Gen Zhang, ChaoDeng,Yi Gong, Ai Mei Zhu, Qing Lin Liu Journal ofMembraneScience454(2014)339–345
5. Nouran El Badawi, Adham R. Ramadan, Amal M.K. Esawi, Mohamed El-Morsi Desalination 344 (2014) 79–85
6. Baixin Han, Dalun Zhang, Ziqiang Shao, Linlin Kong, ShaoyiLv Desalination 311 (2013) 80–89
7. Thi-PhuongNgaNguyen, Eun-TaeYun, In-ChulKim, Young-NamKwon, Journal of Membrane Science 433 (2013) 49–59
8. D.H.N. Perera, S.K.Nataraj, N.M.Thomson, A.Sepe, S.Hüttner, U.Steiner, H. Qiblawey, E.Sivaniah, Journal ofMembraneScience453(2014)212–220
9. Mahdi Naghsh , MortezaSadeghi, AhmadMoheb, Mahdi PourafshariChenar, Mohammad Mohagheghian, Journal of Membrane Science 423–424 (2012) 97–106
10. Haolong Bai, Yitong Zhou, Xuan Wang, Liping Zhang Procedia Environmental Sciences 16 (2012) 346 - 351
11. ElodieGuilminot, Florent Fischer, Marian Chatenet, Arnaud Rigacci, Sandrine Berthon-Fabry, Patrick Achard, Eric Chainet Journal of Power Sources 166 (2007) 104–111
12. Usman Ali Rana, Imran Shakir, R. Vijayraghavan, Douglas R. MacFarlane, Masayoshi Watanabe, Maria Forsyth ElectrochimicaActa 111 (2013) 41– 48
13. Vijayalakshmi Rao, P.V. Ashokan, M.H. Shridhar Materials Science and Engineering A281 (2000) 213–220.

STUDIES ON BLEND BASED NANOCOMPOSITE POLYMER GEL ELECTROLYTE: {(PVA:PEG):NH_4SCN:Al_2O_3} SYSTEM

S. L. AGRAWAL*

**SSI Laboratory, Department of Physics, APS University, Rewa (M.P.) India*

NEELESH RAI#*

 # Department of Physics, AKS University, Satna (M.P.) India

The present work has been aimed to study the role of Alumina nanofiller (Al_2O_3) on the performance of a blend based polymer electrolyte gel films, namely, {(PVA:PEG):NH_4SCN:DMSO} for electrochemical devices. These blended polymer nanocomposite electrolyte films, prepared by solution cast technique have been characterized by structural, electrical and cyclic voltametry measurements. SEM images show reduction in porosity of PVA:PEG composite electrolyte after introducing Al_2O_3. Broadening of diffraction peaks in XRD patterns reaffirm change in morphology of composite electrolyte upon dispersion of filler. Incorporation of 4wt% filler in 50:50 ratio PVA:PEG blend based electrolyte showed maximum conductivity enhancement {$\sigma_{RT} = 1.02\times10^{-02}$ Scm^{-1}}. Composite system exhibits combination of Arrhenius and VTF behavior in temperature dependent conductivity studies. The a.c. conductivity seems to follow the universal power law. Maximum current stability during oxidation and reduction cycle is noticed for PVA:PEG (50:50) composite electrolyte viz. ±1.56V.

1. Introduction:

In recent times, polymer electrolytes have drawn special attention due to certain distinct advantages like high ionic conductivity, better mechanical stability and large electrochemical window [1-3]. Within this framework, polymer gel electrolytes possess soft morphology and porous structure which limit their in utility electrochemical devices like polymer batteries and fuel cells [3-4]. Variety of nano fillers like SiO_2, TiO_2, $BaTiO_3$, Al-Zn ferrite etc. have been tried to overcome the problems of gel electrolyte like liquid exudation and better mechanical integrity and it has led to emergence of nanocomposite polymer electrolytes [5-7]. Agrawal and Rai [8] have recently reported polyvinyl alcohol (PVA) based proton conducting nanocomposite gel electrolyte with high ionic conductivity. It has been shown that ionic mobility occurs in the amorphous phase and ion diffusion occurs through a complex mechanism involving PVA segmental mobility giving rise to ionic conduction. Addition of Al_2O_3 filler in

Proceedings of the 14th Asian Conference on Solid State Ionics (ACSSI 2014)
Copyright © 2014 ACSSI 2014 Organizers. All rights reserved.
ISBN: 978-981-09-1137-9
doi:10.3850/978-981-09-1137-9_015

PVA matrix has been shown to enhance the polar characteristics of polymer making it ionically more conductive [8-9]. Besides heterogeneous doping of fillers, use of blends and formation of their composites is one of the effective methods to improve the conductivity and stability of polymer electrolytes [8-9]. Blending of PVA with high molecular weight polyethylene glycol (PEG) has been shown to improve the morphology of the system (amorphous phase) leading to improvement in ionic conductivity [10]. Keeping these facts in mind, the present work has been pursued to understand the role of Alumina nanofiller on the performance of PVA:PEG blend based nanocomposite polymer electrolyte films, namely, {(PVA:PEG):NH_4SCN:DMSO}.

2. Experimental

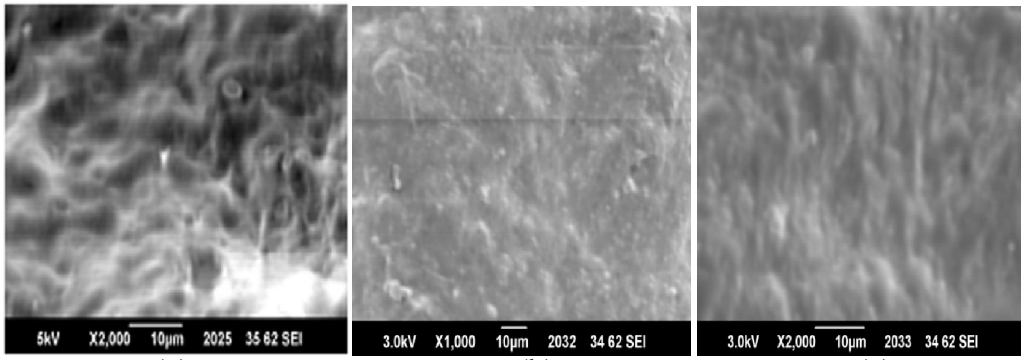
In the present investigation, PVA (average molecular weight 124, 000–186, 000, Aldrich make), PEG (Mw: 4000, Aldrich make), Ammonium thiocyanate (NH_4SCN), AR grade, sd fine chem make and aprotic solvent dimethyl sulphoxide (DMSO) Merck limited Mumbai were used for synthesis of blend based composite gel electrolyte system. Al_2O_3 nanofiller having particle size range 40-50nm was obtained from Alfa Aesar, CAS Number: 1344-28-1. Polymer PVA & PEG in different stoichiometric ratios were dispersed in 1 M NH_4SCN solution in DMSO to form pristine blend electrolyte (PVA:PEG:NH_4SCN) system. Composite polymer electrolytes were prepared by adding Al_2O_3 nano particle in different weight ratios of PVA:PEG blend electrolyte solution followed by thorough mixing at slightly elevated temperature on a magnetic stirrer. The so formed gel solutions were poured in PC pettridishes and covered with Al-foils to avoid contamination. After synersis, gels in the form of thick films were taken out and kept at room temperature for few days to obtain their stable gel films. SEM images of different nanocomposite polymer electrolyte system were recorded with JEOL JSM-6390A instrument. Diffraction patterns of as synthesized nanocomposite polymer electrolytes were recorded on X-ray Diffractometer (model no. RIGAKU JAPAN MINIFLEX-II). For recording of XRD pattern, Bragg angles (2θ) varied from 2˚ to 90˚ with the scan speed of $2^{\circ}min^{-1}$. The complex-impedance measurements were carried out with help of a computer controlled Hioki (Japan) make LCR meter (Model 3520) to assess electrical conductivity. The blend composite gel electrolyte films were sandwiched between two platinum electrodes and electrical measurements were performed in the frequency range 40Hz–100kHz at different temperatures varying in between 25° and 100ºC. Cyclic Voltammetry (CV) measurements were carried out at room temperature in ambient using an Electrochemical

workstation (CH Instruments, USA model no. CHI608D) in the voltage sweep range ±3V, keeping scan rate at $0.1Vs^{-1}$ to check electrochemical response.

3. Results and Discussion:

3.1. Morphological Studies

Figure 1 (a-c) depicts the surface morphology of {PVA:NH_4SCN:DMSO:Al_2O_3} electrolyte films with and without PEG contents. Pristine composite PVA gel electrolyte film shows a closed pore structure made up of PVA chains. Addition of 4 wt% Al_2O_3 nano particles distinctly shows porous structure of PVA composite electrolyte but with smaller pore size (figure 1a) on account of entrapment of Al_2O_3 nano particles between chains in the pores [9]. On addition of PEG as a form of blend with PVA (ratio PVA:PEG/70:30) (figure 1b), chains of PVA are fully covered with PEG thereby reducing pore size remarkably. On further raising PEG contents in the system so as to form 50:50 ratio PVA:PEG blend based electrolyte (figure 1c), chains of PVA are fully covered with PEG contents which indicate change in morphology of system in the presence of PEG.



(a) (b) (c)

Figure 1. SEM Images of: (a) PVA:NH_4SCN:DMSO:4wt% Al_2O_3 gel electrolyte and DMSO:NH_4SCN:4wt%Al_2O_3 blend based composite polymer electrolyte with (b) 70:30 & (c) 50:50 ratios of PVA:PEG contents.

3.2 XRD Studies:

The XRD patterns of composite polymer electrolyte gel films of {PVA:NH_4SCN:DMSO:Al_2O_3} with and without PEG along with pristine components are shown in figure 2(a-f). These patterns show an increase in amorphousness of polymer electrolyte after addition of Al_2O_3 nanofiller and blending with PEG. The intense XRD patterns for PVA:NH_4SCN:DMSO gel film (pattern b) exhibit a moderately intense peak around 18.9º, which shifts to

lower 2θ value in PVA:NH_4SCN:DMSO:Al_2O_3 (pattern c) composite electrolyte. Recently, this shifting of PVA related peak has been correlated to interaction among pristine components leading to formation of nanocomposite polymer gel electrolyte [8, 9].

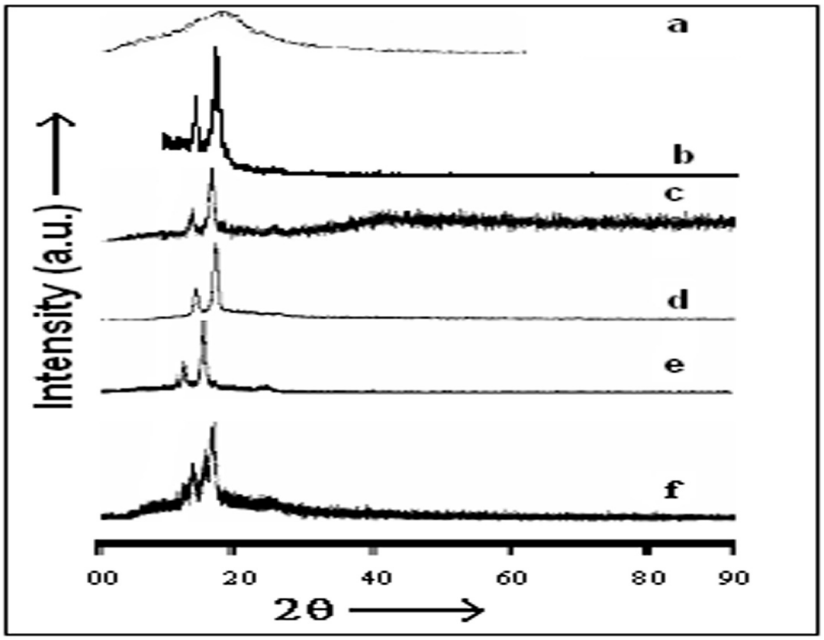


Figure 2. X-ray diffractograms of (a) pure PEG, (b) DMSO:PVA:NH_4SCN, (c) DMSO:PVA:NH_4SCN:4wt%Al_2O_3 and DMSO:NH_4SCN:4wt%Al_2O_3 blend composite polymer electrolyte with (d) 90:10, (e) 70:30 & (f) 50:50 ratios of PVA:PEG.

Table 1 Average crystallites size of nancomposite polymer gel electrolyte system {(PVA:PEG):NH_4SCN:DMSO:Al_2O_3}.

S/N	Concentration of PVA:PEG ratios in Nanocomposite polymer gel electrolyte	Average crystallites size (nm)
1	100:00	~ 49
2	90:10	~47
3	70:30	~ 39
4	50:50	~ 23

Upon addition of PEG to form a blend with PVA, the peak intensity decreases besides disappearance of PEG related peak (pattern a). On increasing PEG content {pattern e&f}, the peaks intensity is seen to further suppress down. This feature ascertains improvement in morphology (increase in amorphousness) of films and this provides sufficient free space for transportation of charge carriers within electrolyte matrix. This is also evident from crystallite size calculations using well known Debye Scherrer's relation [9]. Table 1 clearly shows improvement in system morphology with increase of PEG content.

3.3 Conductivity Studies:

Figure 3 shows the effect of blending on the ion conduction properties of composite polymer gel electrolytes. It is apparent from this figure that the conductivity of blend based composite electrolyte improves gradually in magnitude till 50:50 blend ratio where it tends to saturate. This behavior can be understood with the help of basic relation for the conductivity of electrolyte,

$$\sigma = n.q.\mu \qquad \ldots\ldots\ldots\ldots\ldots (i)$$

where q is the charge of mobile carrier, μ the carrier mobility and n the charge carrier concentration.

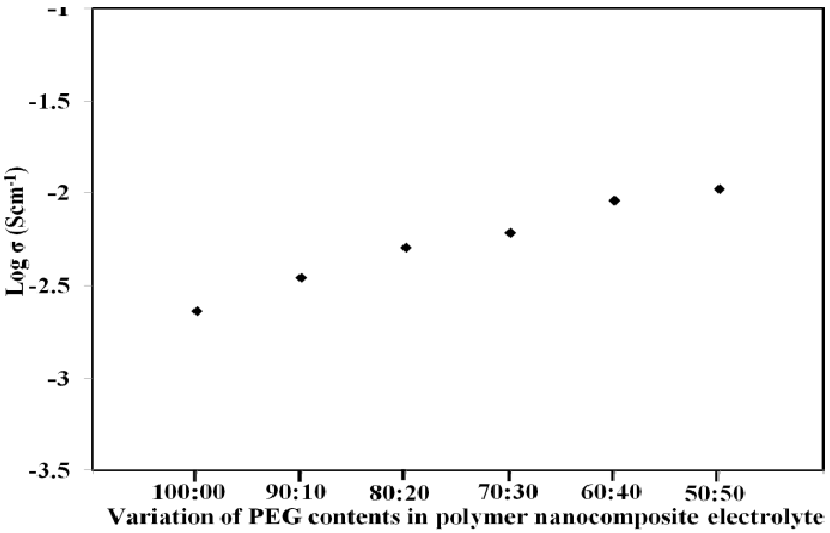


Figure 3. Variation of conductivity of DMSO:NH_4SCN:4wt%Al_2O_3 blend nanocomposite polymer electrolyte with different ratios of PVA:PEG contents.

Increase in amorphousness of blended electrolyte as seen in XRD studies causes a rise in mobility of charge carriers coercing conductivity to rise. Contribution of charge carrier concentration seems to be insignificant as it has been decided on the basis of earlier study [9]. Thus over all conductivity

behavior is seen to be dictated essentially by mobility of charge carriers in accordance with equation (i).

3.4 Temperature dependent conductivity:

Ionic conductivity of polymer electrolytes is known to augment with rise of temperature and it can be rationalized by recognizing free volume model [11]. According to this model, when the temperature increases, the vibration energy of a chain segment is sufficient to push against the hydrostatic pressure imposed by its neighbours and create a small amount of space surrounding its own volume in which vibration motion can occur [12]. This in turn positively affects the mobility of ion and polymer segments resulting in rise of bulk conductivity. The amount of increase in conductivity thus depends upon the free volume around the polymer chain. Present investigations too show an enhancement in bulk conductivity of composite system with increase of temperature (figure 4). Vogel-Tammam-Fulcher (VTF) relation [13] has been successfully used to describe temperature dependence of ionic conductivity of polymeric system.

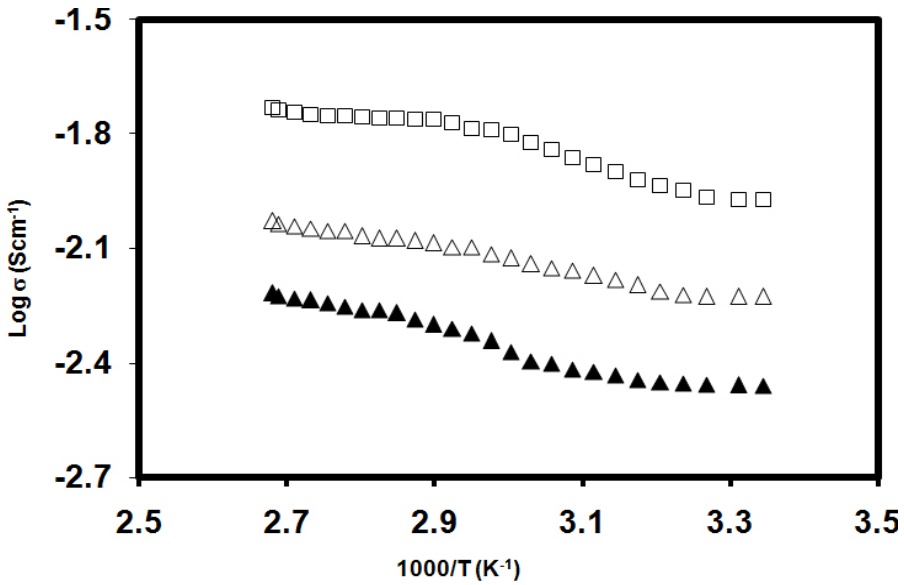


Figure 4. Temperature dependence conductivity of DMSO:NH_4SCN:4wt%Al_2O_3 blend nanocomposite with (▲) 100:00, (Δ) 70:30 & (□) 50:50 ratios of PVA:PEG contents.

Upon blending the composite system with PEG, over all temperature behavior of conductivity does not change in the present investigation i.e. two Arrhenius regions separated by a non-linear regime exists (figure 4). Similar behavior has been reported earlier for PVA:PMMA blend based composite polymer electrolytes [14]. The low temperature Arrhenius behavior is on account

of the presence of liquid electrolyte encapsulated in the blend matrix i.e. effect of temperature on conductivity of liquid electrolyte. As the temperature of system approaches the glass transition temperature of blend (PVA:PEG) conductivity increases significantly with temperature. Thus conductivity behavior would be dictated by well known VTF type behavior [13].

3.5 A.C. Conductivity

Figure 5 shows the variation of a.c. conductivity of blend based nanocomposite electrolyte films with frequency for different ratios of PVA:PEG compositions. It is apparent from the figure that a.c. conductivity increases with frequency in the low frequency regime followed by a nearly frequency independent behavior. The increasing conductivity behavior is connected to the electrode-electrolyte phenomena i.e. it results from electrode polarization effects [15], while saturation like behaviour results from the failure of hopping of ions from one site to another with increasing frequency. The over all a.c. conductivity can be best described by Jonscher's power law relation:

$$\sigma_{ac}(\omega) = \sigma_{dc} + A\omega^{p} \quad \text{..... (ii)}$$

Where σ_{dc} is bulk d.c. conductivity, A the pre-exponential factor, p the fraction exponent and ω the angular frequency. This kind of behaviour has been reported for wide range of nanocomposite polymer electrolytes [16].

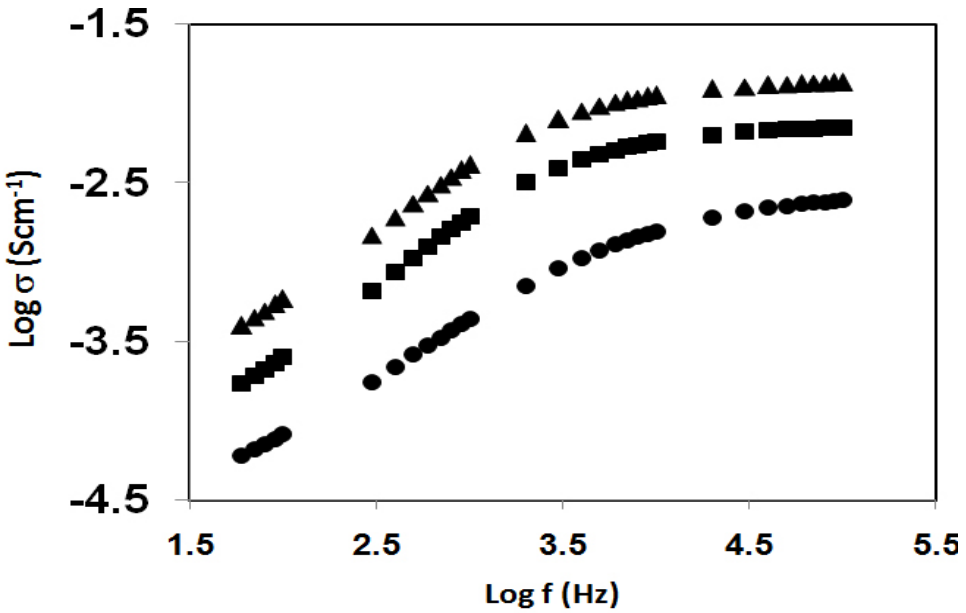


Figure 5. Variation of $\sigma_{ac}(\omega)$ for DMSO:NH_4SCN:4wt%Al_2O_3 blend based nanocomposite electrolytes with (●) 100:00, (■) 70:30, & (▲) 50:50 ratios of PVA:PEG contents.

Over all behavior of a.c. conductivity does not change with increasing PEG content in present study rather it only enhances the conductivity values. Such a behavior is possibly due to dilution effect of PEG in promoting charge transport.

3.6. CV Studies

Study of cyclic voltammograms of the Al_2O_3 loaded composite electrolyte systems having 50:50 ratio of PVA:PEG blend show an improvement in electrochemical stability {stability range from (-1.2V to +1.4V) to (-1.3V to +1.6V)} (figure 6). Another important observation is the narrowing of faradic currents during oxidation and reduction cycles upon increasing PEG content in the stable region. Further, appearance of a single oxidation/reduction peak for composite electrolytes has been noticed in voltagrams which is possibly on account of NH_4^+ ion that contributes to ionic conduction [9]. Optimum electrochemical window was observed to be ±1.56V for 4 wt% Al_2O_3 loaded composite electrolytes containing 50:50 ratio of PVA:PEG content (figure 6).

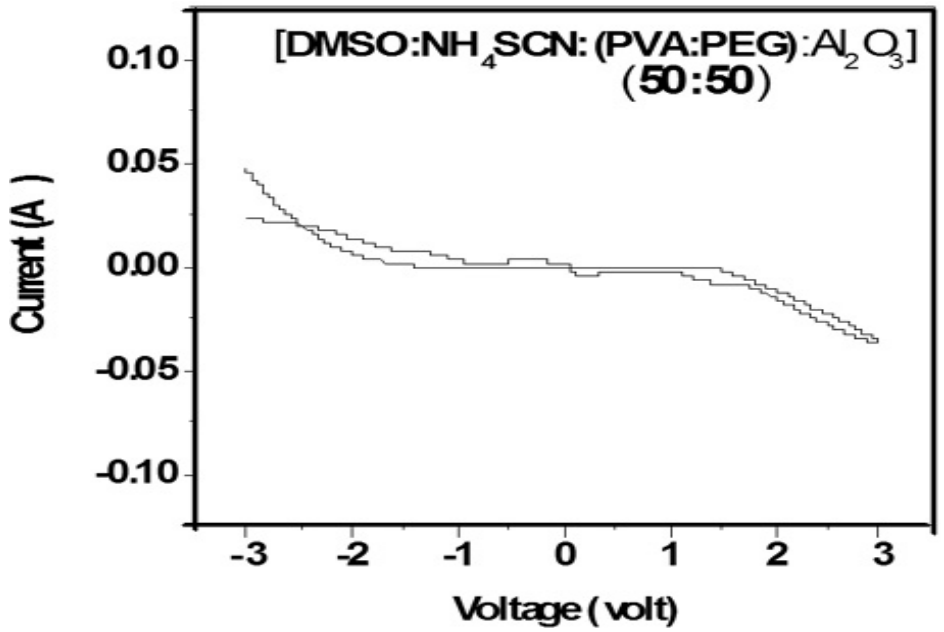


Figure 6. Cyclic Voltagram for DMSO:NH_4SCN:4wt%Al_2O_3 blend based nanocomposite electrolyte containing 50:50 ratio of PVA:PEG contents.

4. Conclusions:

Al_2O_3 nano particles filled PVA:PEG blended polymer composite electrolytes have been successfully synthesized by solution cast technique. XRD patterns exhibit decreasing trend in intensity of diffraction patterns of composite on

increase of PEG content in blend ratio up to 50:50 (PVA:PEG) suggesting improved amorphousness. Bulk conductivity of synthesised samples also increases gradually with increasing amount of PEG content. Temperature dependent conductivity study has been described by combination of Arrhenius and VTF nature. Jonscher power law best describes the a.c. conductivity response. Addition of PEG content provides better electrochemical current stability to nanocomposite electrolyte. All these results indicate possible application of this system in solid-state electrochemical devices particularly solid state batteries.

References:

1. D. Kumar and S. A. Hashmi, *J. Power Sources* **195,** 5101 (2010).
2. P. Colomban, "Proton conductors: Solid, membrane and gels-materials and devices", *Cambridge Univ. Press, Cambridge*, (1992).
3. F. M. Gray, Solid Polymer Electrolytes-Fundamental and Technological Applications, (VCH, New York) (1991).
4. A. Awadhia and S. L. Agrawal, *Solid State Ionics* **178**, 951 (2007).
5. J. Adebahr, N. Byrne, M. Forsyth, D. R. MacFarlane and P. Jacobsson, *Electrochim. Acta* **48**, 2099 (2003).
6. V. Aravindan and P. Vickraman *J. Appl. Polym. Sci.* **108**, 1314 (2008).
7. K. Pandey, M. M. Dwivedi, M. Singh and S. L. Agrawal, *J. Polym. Res.* **17**, 127 (2010).
8. S. L. Agrawal, N. Rai and N. Chand, *Int. J. Polym. Mater.* **62**, 61 (2013).
9. N. Chand, N. Rai, S. L. Agrawal and S. K. Patel, *Bull. Mater. Sci.* **34**, 1297 (2011).
10. S. K. Patel, A. Awadhia and S. L. Agrawal, *Phase Transitions* **82**, 421 (2009).
11. T. Miyamoto and K. Shibayama, *J. Appl. Phys.* **44**, 5372 (1973).
12. R. G. Linford, *Electrochemical Science and Technology of Polymers* vol 1 (*Elsevier:*Applied Science, London) Chapter 3, (1987).
13. H. Vogel, *Phys. Z.* **22**, 645 (1922).
14. M. Sivakumar, R. Subadevi, S. Rajendran, N. L. Wu and J. Y. Lee, *Mater. Chem. and Phys.* **97**, 330 (2006).
15. S. L. Agrawal, M. Singh, M. M. Dwivedi, M. Tripathi and K. Pandey, *J. Materials Sci.* **44**, 6068 (2009).
16. M. Abdullah, W. Lenggoro and K. Okuyama, Polymer Electrolyte Nanocomposites (H. S. Nalwa Ed.), *Encyclopedia of Nanosci. and Nanotech.*, *American Scientific Publishers* **8**, 731 (2004).

THIN FILM SOLID ELECTROLYTE OF GARNET-RELATED $Li_7La_3Zr_2O_{12}$ BY TAPE CASTING

ZHEN FENG YOW, WENYI GU, STEFAN ADAMS

Department of Materials Science and Engineering, National University of Singapore, 117575 Singapore.

In order to combine high energy density with practical power densities, various large scale energy storage systems including aqueous Lithium air batteries and Lithium-ion redox flow batteries require solid electrolyte membranes that combine high conductance with high stability against the active materials of the respective battery. Among the fast ion conducting solids, aliovalently doped garnet-type solid electrolytes exhibit a particularly high chemical stability with a wide electrochemical window and good thermal stability. However the processing of dense garnet ceramics that preserve both the high stability and fast ionic conductivity is challenging. Here we discuss the elaboration of a process for preparing garnet solid electrolyte membranes by tape casting employing cubic Ta- and Ga-co-doped $Li_7La_3Zr_2O_{12}$ (LLZ) as the garnet phase. A stable suspension of the solid electrolyte was prepared by wet ball milling to stabilize LLZ particles in water-alcohol systems containing a polymeric hyperdispersant. LLZ thin films were then tape-cast in a layer-by-layer sequence to achieve desired thickness. Membranes on Al substrates of ca. 150 µm thickness (as a precursor for Li-Al alloy anodes) were successfully produced. The thin films were characterized by SEM, EDX, XRD and impedance spectroscopy (IS). X-ray diffraction confirms that the cubic LLZ phase is preserved in the membrane. Scanning electron microscopy show a relatively dense and homogeneous distribution of LLZ. The solvent evaporation is optimized to minimize microscopic defects such as cracks and voids and to enhance the mechanical stability of the membrane.

Keywords: Garnet-related solid electrolytes, high stability solid electrolytes, solid electrolyte membrane

1. Introduction

The employment of solid electrolyte in a lithium ion battery (LiB) is generally considered safer than those of conventional liquid organic electrolyte by removing the issue of high flammability and high volatility. Ceramic solid electrolytes are believed to have potential advantages in terms of handling and chemical stability over liquid organic electrolyte [1]. Therefore, all-solid-state

Proceedings of the 14th Asian Conference on Solid State Ionics (ACSSI 2014)
Copyright © 2014 ACSSI 2014 Organizers. All rights reserved.
ISBN: 978-981-09-1137-9
doi:10.3850/978-981-09-1137-9_159

LiBs and related all-solid state lithium batteries (ASSLBs) have attracted significant attention in recent years.

Meanwhile, the increasing demand in microscale devices for various microsystem applications requires power sources of proportionate form factor [6-8]. Lithium-based all-solid-state thin film microbatteries can become a promising contributor in this area while using fast Li^+ ion conducting solids could extend the application range to higher power systems.

As one particularly promising class of such fast ion conducting solids, aliovalently doped garnet-related $Li_7La_3Zr_2O_{12}$ (LLZ) has been studied extensively due to its combination of high lithium ionic conductivity and electrochemical stability against lithium metal [1-3]. LLZ is also investigated for a wider range of energy storage systems beyond ASSLBs, especially in large scale flow batteries (as separating membrane in lithium redox flow batteries; and as anode protecting membrane in lithium-air batteries with polar catholytes etc.). Pure LLZ is stable at room temperature in tetragonal phase with a fully ordered lithium arrangement but consequentially low ionic conductivity, while cubic LLZ can be stabilized at room temperature by trivalent (e.g. $Al_{Li}^{\bullet\bullet}$) or pentavalent ($Nb_{Zr}^{\bullet\bullet}$, $Ta_{Zr}^{\bullet\bullet}$) doping [3-4]. The total ionic conductivity of tetragonal phase LLZ is approximately three orders of magnitude lower than that of cubic phase LLZ ($\sigma_{total} > 10^{-4}$ S cm^{-1}) [4-5].

However, the fabrication of a dense thin film garnet ceramic that conserves both high ionic conductivity and stability is challenging. In this paper, we discuss the fabrication process and the drying profile for preparing cubic $Li_{6.75}La_{2.95}Ga_{0.05}Zr_{1.75}Ta_{0.25}O_{12}$ (LLZ-TG) as thin film solid electrolyte membrane by tape casting technique. Here the gallium ($Ga_{La}^{\bullet\bullet}$) doping is included to reduce the sintering temperature. A solid state battery is then produced and tested with the tape-cast LLZ-TG solid electrolyte and a composite cathode consisting of LLZ-TG, $Li_4Ti_5O_{12}$ and acetylene black.

2. Experimental

2.1. *LLZ-TG powder synthesis*

The compound $Li_{6.75}La_{2.95}Ga_{0.05}Zr_{1.75}Ta_{0.25}O_{12}$ (LLZ-TG) is prepared by a solid-state method for which the powders Li_2CO_3, La_2O_3, ZrO_2, Ta_2O_5 and Ga_2O_3 are

used as starting materials. They are mixed and ball milled for 5 hours using zirconia balls and subsequent calcinated at 950°C for 18 hours. The milling process is repeated for 6 hours to break down the particle size of the calcinated LLZ-TG powder.

2.2. *Preparation of LLZ-TG colloidal ink*

A colloidal ink is prepared by first dispersing 1g of LLZ-TG and 0.05g of polymeric hyperdispersant (Solsperse 20000, Lubrizol) in 10ml of a solvent mixture of 70wt.% deionized water, 22.5wt.% absolute ethanol, 6.25wt.% diethylene glycol and 1.25wt.% triethanolamine. The suspension is ball milled for 6 hours to achieve a stable LLZ-TG colloidal suspension. The stable suspension is then mixed with an appropriate amount of water soluble carboxymethyl cellulose sodium salt (CMC) for 12 hours to achieve the targeted viscosity.

2.3. *Tape casting*

The LLZ-TG colloidal ink is deposited on aluminium foil and subsequently tape cast into a ca. 30 µm thin film using a MTI film coater at a speed of 15mm/s and a temperature of 70°C to assist the drying of the ink. The tape casting process is repeated four times for subsequent layers until a desirable coverage and thickness of ca. 150 µm is achieved. The film is further dried at 100°C for 2 hours and a disc-shaped film with a diameter of 12.7 mm is cut with a precision disc cutter for subsequent characterization.

2.4. *Battery testing*

A prototype Li-Al/LLZ-TG/$Li_4Ti_5O_{12}$ cell is prepared by tape casting $Li_4Ti_5O_{12}$ (LTO) colloidal ink on the surface of LLZ-TG thin film. The LTO colloidal ink is prepared by ball milling 56wt.% LLZ-TG, 40wt.% LTO and 4wt.% acetylene black via the same procedure mentioned in 2.2. The prototype cell is assembled in a swagelok cell in argon environment by using lithium metal foil as anode. The assembled cell is tested with battery tester (Arbin DT2000) at 60°C.

2.5. *Characterization*

Microstructure and element distribution of the LLZ-TG thin film are characterized with a scanning electron microscope (SEM, Zeiss) and energy dispersive X-ray analysis (EDX), respectively. The crystal structure of the thin film is confirmed by X-ray powder diffractometer (XRD, Bruker D8) using Cu

K_α radiation. Rietveld refinements of XRD patterns are performed with Generalized Structure Analysis System (GSAS), along with the graphical user interface (EXPGUI) [6]. Ionic conductivity measurements are determined by the electrochemical impedance spectroscopy (IS, Solartron SI 1260) in the frequency range of 1 Hz to 10 MHz. For this measurement, a 20 nm thin layer of Au is sputtered on the surface of LLZ-TG thin films without aluminum substrate to ensure a well-defined electrical contact area for ionic conductivity determination.

3. Results and discussion

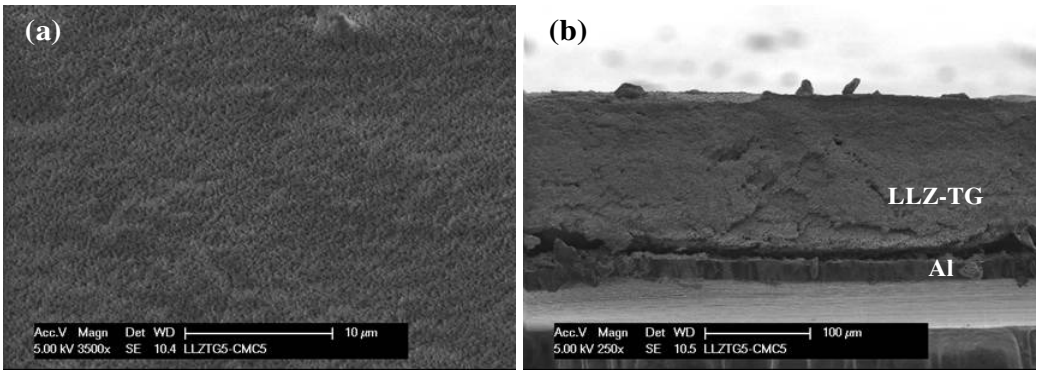


Figure 1. SEM images of $Li_{6.75}La_{2.95}Ga_{0.05}Zr_{1.75}Ta_{0.25}O_{12}$ thin film. (a) surface morphology, (b) cross sectional view.

Figure 1a and 1b show the surface and cross-sectional morphology of LLZ-TG thin film respectively. A dense morphology is observed for both images. The distribution of LLZ-TG particles is uniform throughout the surface of the thin film and no agglomeration of particles is observed. The cross sectional image revealed the thickness of the thin film is about 150 µm. The aluminium substrate seen under the LLZ-TG was used as a precursor to Li-Al alloy anodes in solid state batteries. The aluminium substrate also provides a suitable platform of low wettability for thin film formation during ink deposition and acts as a mechanical support for handling of the membrane [7-8]. Two step solvent evaporation is employed during the drying process, first removal of ethanol at 70°C and later removal of water at 100°C. The viscosity of the deposited ink increased by solvent evaporation thus restricting the ink flow under surface tension to heal any voids [9]. Ethanol removal at 70°C increases the viscosity of the deposited ink so as to provide a structural integrity to the thin film while the

remaining water allows the particles to sink down for void healing under the influence of surface tension [7, 10]. Under this condition, the microscopic defects are minimized as shown in the SEM images.

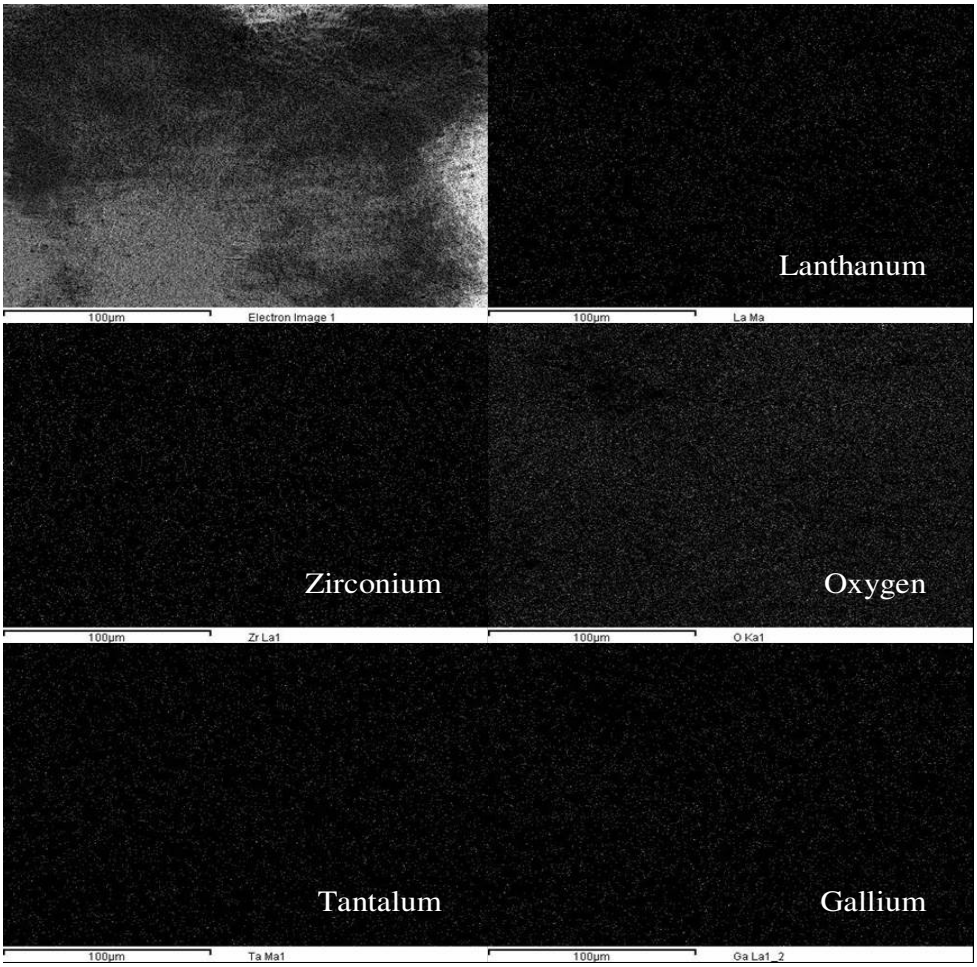


Figure 2. EDX mapping of $Li_{6.75}La_{2.95}Ga_{0.05}Zr_{1.75}Ta_{0.25}O_{12}$ thin film.

The elementary mapping of La, Zr, O, Ta and Ga is presented in Figure 2. Elementary mapping via EDX on LLZ-TG thin film confirmed that each element is evenly distributed throughout the surface, indicating the effectiveness of polymeric hyperdispersant in the colloidal ink [7-9].

Pure LLZ crystallizes at room temperature in the tetragonal space group $I4_1/acd$. On heating it undergoes diffusion-less phase transition [11-12] to the cubic aristotype structure (space group $Ia\text{-}3d$). This phase transition can essentially be

understood as an order-disorder transition primarily affecting the Li sites [4], so that the cubic phase might be obtainable as a metastable phase by synthesis routes that prevent Li ordering, but normally the Li ordering is suppressed by aliovalent doping enhancing that lithium vacancy concentration such as here the $Ta_{Zr}^{\bullet\bullet}$-doping. The ionic conductivity of sintered pellets (of ca. 2.1 mm thick) of cubic LLZ was reported to reach 1.67×10^{-4} S cm^{-1} at 25°C, while the room temperature conductivity of the Li-ordered tetragonal phase is three orders of magnitude lower [4-5]. Shimonishi et al. reported LLZ to be stable in an aqueous electrolyte and a water stable lithium electrode could be produced using LLZ without a polymer electrolyte interface, because LLZ is stable with lithium metal [13].

XRD patterns (see e.g. Fig. 3) demonstrate the preservation of cubic LLZ even after the fabrication of LLZ-TG thin film as shown in Figure 3. Due to the use of

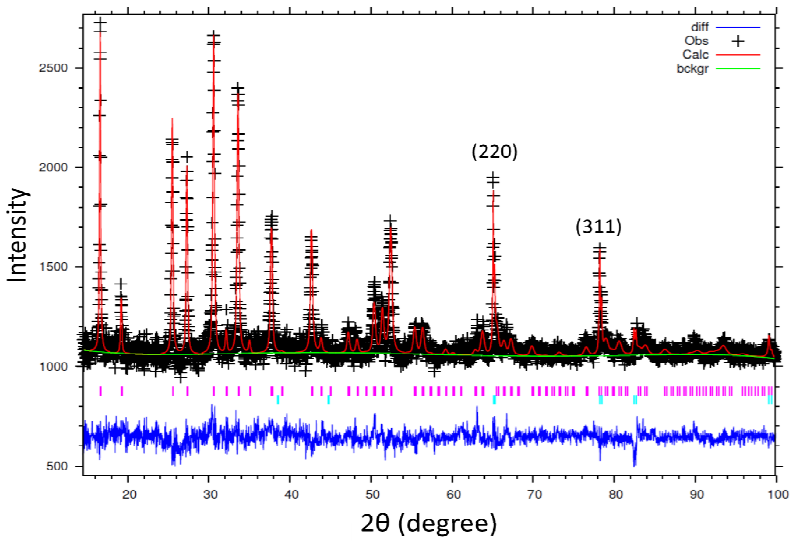


Figure 3. Rietveld refinement of $Li_{6.75}La_{2.95}Ga_{0.05}Zr_{1.75}Ta_{0.25}O_{12}$ thin film with aluminium peaks (220) and (311) fitted by the Le-Bail method (R_{wp} =3.5%).

CMC as binder in the ink, there is an amorphous peak visible in the XRD pattern. In Fig. 3, this CMC peak has been subtracted to facilitate the Rietveld refinement. The prominent peaks caused by the aluminium foil substrate are marked by their Miller indices. The resulting cubic lattice parameter a = 13.047(1) Å for the tape-cast LLZ-TG is found to significantly deviate from the value a = 12.964(1) Å refined for the LLZ-TG powder after dry ball milling (which is consistent with literature values [2, 4, 14]), most probably due to ion exchange reactions (e.g. H^+ for Li^+) of the LLZ-TG during ink preparation.

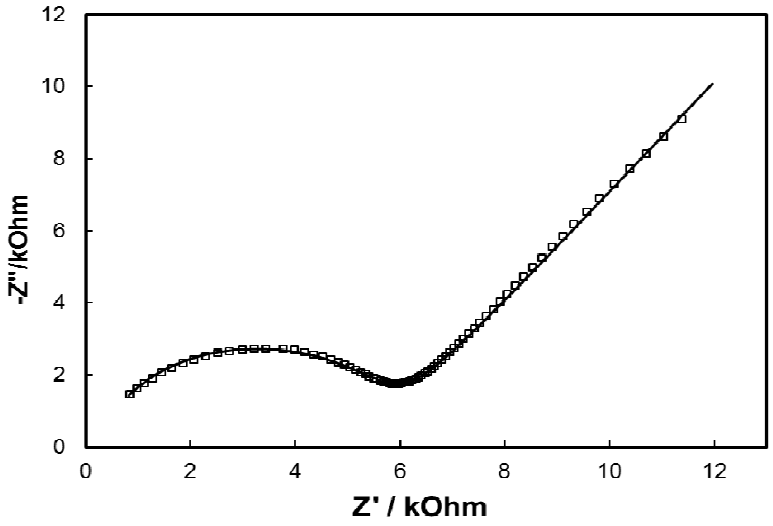


Figure 4. Nyquist impedance plot of $Li_{6.75}La_{2.95}Ga_{0.05}Zr_{1.75}Ta_{0.25}O_{12}$ thin film at room temperature.

A typical Nyquist plot of the impedance spectrum for a LLZ-TG thin film is shown in Figure 4. The high frequency semicircle is understood to comprise both bulk and grain boundary contributions whereas the low frequency tail represents the capacitive behavior of the ionically blocking electrode. The impedance data are fitted to an equivalent circuit model consisting of $(R_{total}Q_{total})Q_d$, where R_{total} represents the total resistance, Q_{total} is the constant phase element [5] and Q_d here represents a Warburg-type impedance. The total ionic conductivity of the LLZ-TG thin film at room temperature is 2.2×10^{-6} S cm^{-1}, approximately two orders of magnitude lower than the value for bulk LLZ-TG [4-5]. This is mainly due to the porous nature and the remaining organic thin film components, namely CMC and remaining diethylene glycol. The former acts as a binder whereas the latter as a humectants to promote bonding between individual layer and prevent cracks due to rapid drying [7].

Figure 5 shows the first discharge cycle of the prototype Li-Al/LLZ-TG/LTO cell with a current density of 1.5 mA g^{-1} at 60°C. The discharge capacity of the cell is only about 12 mAh g^{-1} which is 7% of the theoretical capacity of LTO (175 mAh g^{-1}), implying that while LLZ-TG thin films are potential candidate for lithium-based all-solid-state thin film microbatteries, the ink preparation has to be optimized to prevent compositional (and bulk conductivity) changes to the solid electrolyte. Moreover, the densification of tape-cast membranes and cathode have to be further improved to minimize the interfacial resistance within the membrane and the charge transfer resistance to the electrode materials. In this regard, further research is in progress.

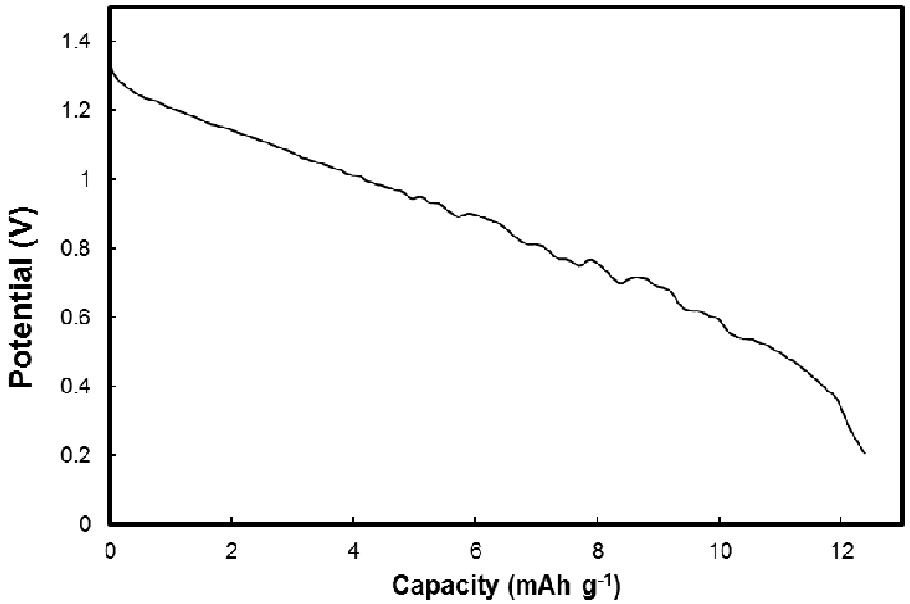


Figure 5. Discharge curve of Li-Al/ $Li_{6.75}La_{2.95}Ga_{0.05}Zr_{1.75}Ta_{0.25}O_{12}$ /$Li_4Ti_5O_{12}$ prototype battery at T= 60°C.

4. Conclusion

Relatively dense LLZ-TG thin film solid electrolyte with thickness of 150µm was successfully fabricated via a multilayer tape cast technique. LLZ-TG was homogenously distributed throughout the membrane with minimum microscopic defect as reported in this paper. The cubic structure of LLZ-TG was preserved after the conversion to colloidal ink with no additional impurities observed, but a significant lattice constant change suggesting compositional changes. CMC and diethylene glycol in the membrane itself might contribute to the lower total ionic conductivity of LLZ-TG thin film (2.2×10^{-6} S cm^{-1}), which is lower than the reported LLZ ($\sigma_{total} > 10^{-4}$ S cm^{-1}) but still comparable to those of dense lithium phosphorus oxynitride, $Li_xPO_yN_{(5 + x2y)/3}$ membranes. A further increase of the conductivity will require the densification of the ceramic membrane, enhanced compositional control and the minimization of the content of organic components by either varying the tape casting recipe or an optimized post-annealing.

Acknowledgments

This research is supported by the National Research Foundation, Prime Minister's Office, Singapore under its Competitive Research Programme (CRP Award No. NRF-CRP 10-2012-6 and NRF-CRP8-2011-04).

References

1. S. Ohta, T. Kobayashi, J. Seki, and T. Asaoka, *J. Pow. Sources,* **202**, 332 (2012).
2. M. Huang, T. Liu, Y. Deng, H. Geng, Y. Shen, Y. Lin, and W. Nan, *Solid State Ionics,* **204**, 41 (2011).
3. R. Murugan, V. Thangadurai, and W. Weppner, *Angew. Chem. Int. Ed.,* **46**, 7778 (2007).
4. S. Adams, and R. P. Rao, *J. Mater. Chem.,* **202**, 1426 (2012).
5. J. Tan, and A. Tiwari, *Elect. Sol. State Letters,* **15**, A37 (2012).
6. B. Toby, *J. Appl. Crystallogr.,* **34**, 210 (2001).
7. K. Sun, T. Wei, B. Y. Ahn, J. Y. Seo, S. J. Dillon, and J. A. Lewis. *Adv. Mater.,* (2013).
8. Y. Zhao, Q. Zhou, L. Liu, J. Xu, M. Yan, and Z. Jiang, *Elect. Acta,* **51**, 2639 (2006).
9. Y. Zhao, G. Liu, L. Liu, and Z. Jiang, *J. Solid State Elect.,* **13**, 705 (2009).
10. J. H. Song, and H. M. Nur, *J. Mater. Proc. Tech.,* **155**, 1286 (2004).
11. L. J. Miara, S. P. Ong, Y. Mo, W. D. Richards, Y. Park, J. M. Lee, H. S. Lee, and G. Ceder, *Chem. Mater.,* **25**, 3048 (2013).
12. R. Jalem, Y. Yamamoto, H. Shiiba, M. Nakayama, H. Munakata, T. Kasuga, and K. Kanamura, *Chem. Mater.,* **25**, 425 (2013).
13. Y. Shimonishi, A. Toda, T. Zhang, A. Hirano, N. Imanishi, O. Yamamoto, and Y. Takeda, *Solid State Ionics,* **183**, 48 (2011).
14. A. Kuhn, S. Narayanan, L. Spencer, G. Goward, V. Thangadurai, and M. Wilkening, *Phys. Rev. B,* **83**, 94302 (2011).
15. J. A. Lewis, *J. Am. Ceram. Soc.,* **83**, 2341 (2000).

CHARACTERIZATION OF LITHIUM BORATE AND LITHIUM SILICATE THINFILMS AS A SOLID ELECTROLYTE FOR THIN-FILM BATTERY

HARUKA ITABASHI,NAOAKI KUWATA, DAICHI FUJIMOTO,
YASUTAKA MATSUDA, JUNICHI KAWAMURA

Institute of Multidisciplinary Research for Advanced Materials, Tohoku University, Katahira2-1-1, Sendai 980-8577, Japan

The lithium borate glass (LBO), the lithium silicate glass (LSO), and their mixed lithium borosilicate glass (LBSO) thin-films were prepared by pulsed laser deposition method using ArFexcimer laser. The ionic conductivityandcompositions of thin-films were examined. The ionic conductivityvaluesof the thin-films were8.9×10^{-8} Scm^{-1}, 2.9×10^{-7} Scm^{-1} and 5.0×10^{-7} Scm^{-1}at room temperaturefor the LBO,the LBSO and the LSO, respectively. The activation energy of the thin-filmwas0.60 eV, 0.58 eV and 0.55 eV for the LBO, the LBSO andthe LSO, respectively.The electrochemical window ofthe LBO thin-film was from 0 to 6.5 V vs. Li/Li^{+}. All-solid-state thin-film battery (TFB) was successfully fabricatedusing LBO thin-film as an electrolyte with $LiCoO_2$ cathode and Li metal anode, whose charge-discharge voltage is around 4.0V.

1. Introduction

All-solid-state thin-film lithium-ion battery (TFB) is a promising energy device for microelectronics in future. Solid electrolyte with high ionic conductivity is the most important component for the TFB, where lithium oxide glasses are often used because of their high ionic conductivity and stability. Lithium phosphate [1] and lithium silicate [2] glasses are known to be successful for this purpose, which have been prepared by pulsed laser deposition(PLD) method.The lithium borate thin film fabricated bythermalevaporation method also has high ionic conductivity at room temperature [3].

However, no reports have been known on the thin filmof lithium borate glass preparedby PLD. Lithium borate, Li_3BO_3, is known as a lithium ion conductor in bulk glasses, and it shows an increase in conductivity whenit is mixed with Li_4SiO_4 [4]. The purpose of this study is toprepare thethin-films of thelithium borate glass(LBO), lithium silicate glass(LSO) and their mixed glass (LBSO)by PLD method and to characterize them. Based on the result, aTFB is fabricated using the LBO thin-film as a solid electrolyte.

Proceedings of the 14th Asian Conference on Solid State Ionics (ACSSI 2014)
Copyright © 2014 ACSSI 2014 Organizers. All rights reserved.
ISBN: 978-981-09-1137-9
doi:10.3850/978-981-09-1137-9_166

2. Experimental

2.1. *Preparation of thin-film and characterization*

Thin-films were deposited by PLD using an ArFExcimer laser at room temperature. Theenergy and repetition of ArFExcimer laser was 150 mJ and 10 Hz. The energy fluence was about 1 Jcm^{-2}. Thin films were grown in a vacuum chamber with continuous flow of oxygen gas at 0.2 Pa. The distance of target from substrate was 40 mm. The deposition rate of thin-films was about 1 μm/h.LBO and LSO thin films were deposited using a Li_3BO_3(Toshima) and Li_4SiO_4 target (Toshima), respectively. The LBSO thin-film was obtained by alternative laser irradiation on two targetsof Li_3BO_3 and Li_4SiO_4.

The thickness of thin-films was measured byprofilometer (Dektak).The ionic conductivity was measured as a function of frequency and temperature by impedance spectroscopy usingsolatron 1260 impedance analyzer. The range of parameters was 0°C to 100°C for temperature and 10^6 Hz to 10^{-1} Hz for frequency. For impedance measurements the thin-films were deposited on SiO_2 substrate with Pt comb-type electrodes. Impedance spectroscopy was measured by applying an ac voltage of 0.1 V according to frequency in a homemade cell under vacuum condition.The Li/Si and Li/B ratio was determined by inductively coupled plasma atomic emission spectroscopy (ICP-AES). The sample for ICP-AES was prepared by dissolving the thin-film using aqua regia.

2.2. *Thin-film-battery (TFB) fabrication*

TFB was constructed with the cell structure of $Li/Li_3BO_3/LiCoO_2$.$LiCoO_2$ thin-film was deposited on Pt-coated SiO_2substrate by PLD using Nd:YAG laser (λ=266 nm) at 500 °C in oxygen atmosphere at 20 Pa. The LBO thin-film was deposited on $LiCoO_2$ by using ArFexcimer laser (λ=193 nm) at room temperature in oxygen atmosphere at 0.2 Pa. Li metal was deposited on the LBO thin-film using a vacuum thermal evaporation (VTE) method. The area of TFB was 0.09 cm^2 (3mm×3mm)

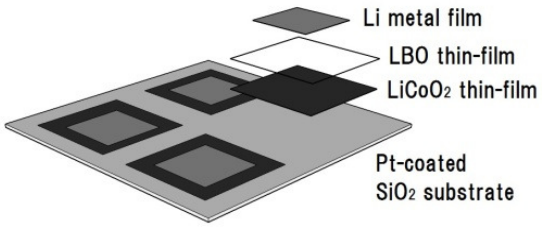


Figure1.Illustration of Li/LBO/$LiCoO_2$ cell.

2.3. *Electrochemical measurements*

The electrochemical property of the fabricated TFB was evaluated by cyclic voltammetry (CV) using Biologic SP-150, in a home-made vacuum cell at room temperature. The potential and scan rate were adjusted from 3.0 to 4.4 V and 6 mV/min to 60 mV/min respectively.

The electrochemical stability window of the LBO thin-film was estimated by Li/LBO/Pt half cell at room temperature. The sample for this measurement was prepared by two steps. First, the LBO thin-film was deposited on Pt/Cr/SiO_2 substrate, followed by Li metal deposition on them using a VTE technique. The sample was kept in vacuum and the electrochemical stability window was analyzed by CVbetween -0.1 to 6.5 V using BioLogic VMP3.

3. Results and Discussion

3.1. *Ionic conductivity of thin-films*

The ionic conductivity of the prepared thin films was calculated using

$$\sigma = \left(\frac{d}{S}\right)\frac{1}{R}\ \text{Scm}^{-1}, \tag{1}$$

where σ is total conductivity, d is the distance between the electrodes, S is the sectional area of samples and R is theresistance calculated from the real part of impedance. S is calculated by the product of thickness of electrolyte and width of electrode (Pt).

The ionic conductivity was measured using comb-type electrodes. Comb-type Pt electrodes were deposited on SiO_2 substrate at intervals of 2~5 μm.The LBO thin-film was deposited onto comb-type electrodes, and the ionic conductivity of the LBO thin-film was measured parallel to the substrate. Fig.2 shows the temperature dependence of ac impedance for the LBO thin-film.The plateau region corresponds to the ionic conductivity of Li, while in low frequency region, Li ion was blocked by Pt electrode.As increasing the temperature, the impedance of the LBO thin-film was decreased due to the increasing of ionic conductivity. The ionic conductivity σ was obtained by using (1) formula, where the resistance R was estimated from plateau of ac impedance plot using equivalent circuit fitting.

The ionic conductivity of the thin-films follows the Arrhenius relation and the plot is shown in Fig.3. The activation energy (E_a) was calculated using the Arrhenius equation.

$$\sigma = \sigma_0 \exp\left(-\frac{E_a}{kT}\right) \tag{2}$$

whereσ_0 isthe pre-exponential factor. The summary of ionic conductivity and activation energy were shown in Table.2.

Table1. Summary of film thickness and comb-type electrode parameters.

Thin-film	LBO	LBSO	LSO
Thickness of thin-film (h)	1.23μm	0.57 μm	0.72 μm
Width of electrode (l)	2 mm	2.4 mm	2.4 mm
Number of electrode set	65	65	65
Sectional area (S)	3.17×10^{-3} cm^2	1.76×10^{-3} cm^2	2.23×10^{-3} cm^2
Distance between electrodes (d)	2μm	5μm	5μm

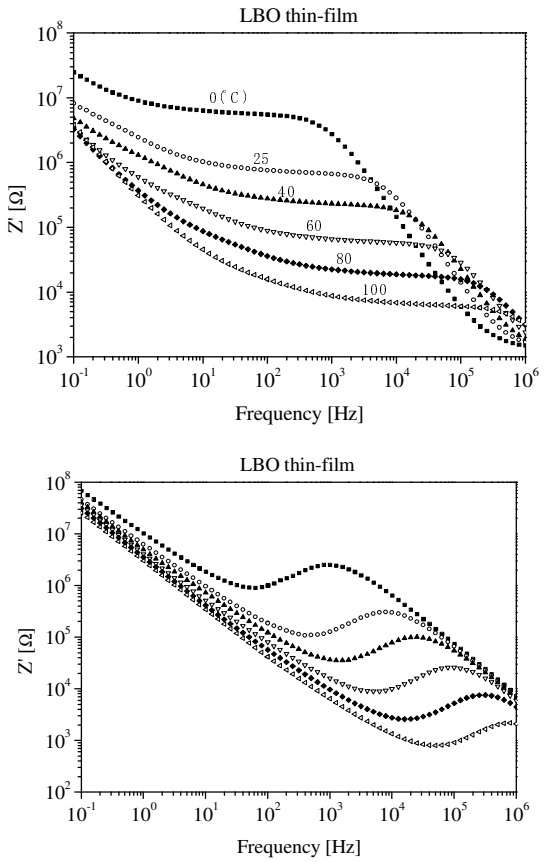


Figure2.ac impedance spectra of the LBO thin-film. LBSO and LSO thin-films also show similar spectra (not shown).

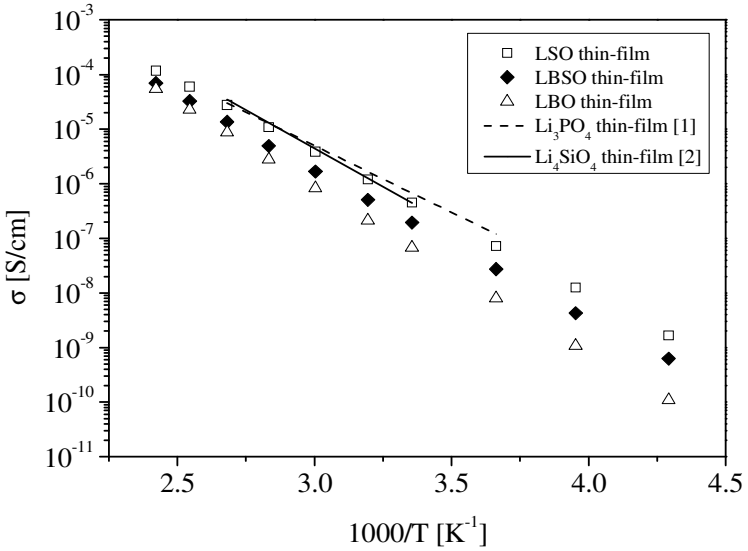


Figure3.Temperature dependent ionic conductivity of LBO, LBSO and LSO thin-films.

Table2.Summary of ionic conductivity and activation energy of the thin films

Thin-film	Ionic conductivity (at 25 °C) σ Scm^{-1}	Activation energy E_aeV
LBO	8.9×10^{-8}	0.60
LBSO	2.9×10^{-7}	0.58
LSO	5.0×10^{-7}	0.55

The ionic conductivity of the LBO thin-film was 8.9×10^{-8} Scm^{-1} at 25 °C. This value agrees with the reference data [3], $1\times10^{-7}Scm^{-1}$at room temperature, where the LBO thin-film was deposited by thermal evaporation.The ionic conductivity of the LBO thin-film was smaller than that of the LSO thin-film, because the Li composition ratio of the LBO thin-film was smaller than that of the LSO thin-films. The ratio of Li in composition are Li/(B+O)=3/4 for the LBO and Li/(Si+O)=4/5 for the LSO. In the oxide glasses, there is a tendency that the Li ion conductivity becomes higher and activation energy was lower.

It is known that the mixing of glass former such as borate and silicate will increase the ionic conductivity, which is called “mixed glass former effect (MGFE) [3]”.In this study, the MGFE was not observed. The possible reason for itis the loss oflithium during the deposition of thin-films as confirmed by the ICP analysis. The other reason is partial mixing of the borate and silicate thin-film.

3.2. *The ICP-AES analysis*

The results of the ICP-AES analysis weresummarized in Table.3. From Table 3the lithium concentration in the thin-films was lesser than the concentration inthe target. The lithium retention between the target and the thin-film during deposition of thin-films was 81.7% for LBO, 73.4% for LBSO and 68.8% for LSO thin-films.

Table.3Summary of components of thin-films by ICP-AES

Sample		
LBO thin-film	Ratio of Li/B	2.45
LBSO thin-film	Ratio of Li/(Si+B)	2.57
LSO thin-film	Ratio of Li/Si	2.75

3.3. *Electrochemical stability of the LBO thin-film*

The electrochemical stability of the LBO thin-film was examined by Li/LBO/Pt half cell. The cyclic voltammogram of Li/LBO/Pt half cell at the scanning rate of 1 mV/sec and scan range from -0.1 V to 6.5 V was shown in Fig.4. No remarkable peak is observed in the high potential range up to 6.5 V. The two peaks at 0.59 V and 1.35 V were due to the lithium dealloying reactions, which means the stability of direct contact to the metallic lithium. The electrochemical stability of the LBO thin-film was in range from 0 V to 6.5 V vs. Li/Li^+.

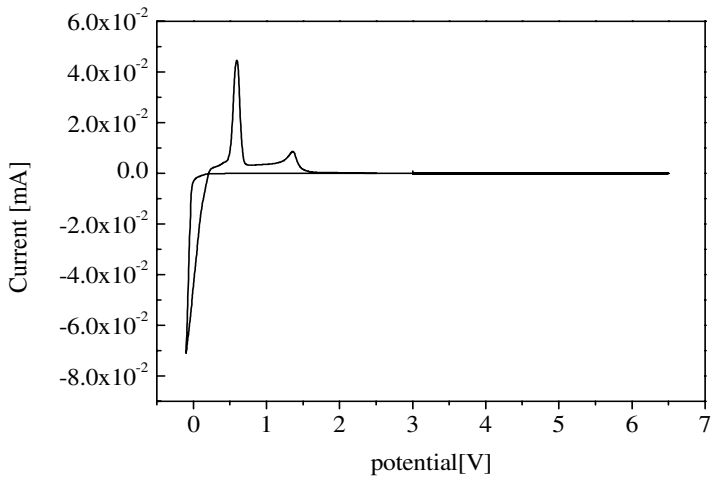


Figure4. Cyclic voltammetry of Li/LBO thin-film/Pt half cell at room temperature

3.4. *Characterization of TFB*

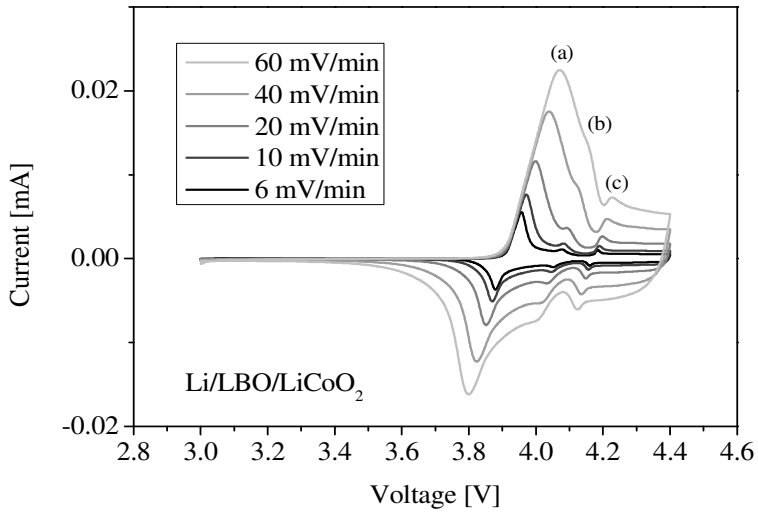


Figure5.Cyclic voltammogram of TFB consisted of Li/LBO/$LiCoO_2$

TFB was fabricated using the LBO as electrolyte, $LiCoO_2$ as cathode and Li as anode. Fig.5. shows the cyclic voltammogram of TFB between 3.0 and 4.4 V in different scan rates in vacuum cell at room temperature. Scanning rates were from 6 mV/min to 60mV/min. The LBO thin-film shows good contact between $LiCoO_2$ cathode, and the TFB shows reversible lithium intercalation/deintercalation cycles between 3.0 and 4.4 V. Several peaks are observed in Fig.5 is attributed to the layered structure of $LiCoO_2$. The peaks were marked as (a), (b) and (c). The peaks at (a) are the two-phase region of the hexagonal 1(H1) and hexagonal 2 (H2) phases. The peaks at(b) were two-phase region of the H2 and monoclinic (M) phases. The peaks of (c) were the two-phase region of M and second H2 phases. [5,6]

4. Conclusions

LBO, LBSO and LSO thin-films were successfully deposited by PLD using ArFExcimer laser. The X-ray diffraction results showed that the thin-films to be in amorphous state. The ionic conductivity at room temperature was8.9×10^{-8} Scm^{-1}, 2.9×10^{-7} $Scm^{-1}$and 5.0×10^{-7} $Scm^{-1}$for the LBO, theLBSO and theLSO thin-film respectively. The ionic conductivity of the LSO thin-film was lower than previous study [4]. The lithium loss from thin-films during deposition is the reason for the decrease in ionic conductivity in the present study. The lithium loss in the prepared thin-films was confirmed by ICP-AES. The results of CV showed that the LBO thin-film has high electrochemical stability in the range

-0.1 to 6.5 V range.The TFB with the LBO electrolyte showed good lithium intercalation property on CV measurement. Therefore the LBO glass is expected as an electrolyte of all-solid-state thin-film battery.

References

[1] NaoakiKuwata, NaoyaIwagami, YoshinariTanji, Yasutaka Matsuda and Junichi Kawamura, *J. Electrochem. Soc,* **157**, (4) (2010) A521.
[2] AtsuyoshiNakagawa, NaoakiKuwata, Yasutaka Matsuda and Junichi Kawamura, *J.Phys. Soc. JPN.***79**, Suppl.A, (2010) 98.
[3] Yukio ITO, KatsukiMiyauchi and Tetsu OI, *Journal of Non-Crystalline Solid*, **57** (1983) 389.
[4] Masahiro Tatsumisago, Nobuya Machida and Tsutomu Minami, *Yogyo-Kyokai-Shi*,**95** (1987) 197.
[5] Young Jang, Nancy J. Dudney, Douglas A. Blom and Lawrence F. Allard, *J. Electrochem. Soc.***149**, (11) (2002) A1442.
[6] Jan N. Reimers and J.R. Dahn, *J Electrochem. Soc*. **139** (8) (1992) 2091.

TOWARDS HYDROLYSIS-STABLE THIOPHOSPHATE SOLID ELECTROLYTES

CHEN HAOMIN, RAYAVARAPU PRASADA RAO, STEFAN ADAMS

Department of Materials Science and Engineering, National University of Singapore, 117574, Singapore

Thiophosphates and related compounds show high promise as fast ion conducting solids for bulk all-solid state batteries and a variety of rechargeable all-solid state batteries with high energy density and/or competitive power performance have been demonstrated. Still, industrial uptake of these materials is impeded by their sensitivity to hydrolysis in humid air. Here we compare the structural, electrochemical and hydrolysis stability for a range of known and predicted thiophosphate-related compounds by density functional studies. For selected compounds low energy ion conduction pathways are analysed based on bond valence pathway models. Therefrom, general trends for the optimization of hydrolysis stability in such thiophosphates and the balancing of (thermodynamic and kinetic) structural stability with fast ionic conductivity are derived.

1. Introduction

Among the known fast lithium ion conductors thiophosphates (e.g. $Li_7P_3S_{11}$), [1] related compounds where sulphur is partially replaced by halide ions (e.g. the Argyrodite $Li_{7-x}PS_{6-x}Cl_x$) [2,3] and compositional analogues where phosphorous is partly or completely replaced by other tetra- or pentavalent main group cations (e.g. $Li_{9+x}Ge_xP_{3-x}S_{12}$, $Li_{4-x}Sn_{1-x}As_xS_4$, etc.) [4,5] exhibit outstanding conductivities in combination with satisfactory electrochemical stability and low grain boundary resistances. The high polarisability of sulphur also favourably affects the mechanical properties of electrolyte:electrode composites for use in all-solid state batteries and mitigates capacity fading in case of pronounced volume changes in conversion-type active electrode materials during charge-discharge cycles. Most of the practically relevant fast ion-conducting thiophosphates are still neither thermodynamically stable nor stable against hydrolysis. While the lack of thermodynamic stability essentially requires (low temperature) synthesis routes with kinetic reaction control, the lack of hydrolysis stability represents a major challenge for the industrial application. Here we systematically compare, based on density functional theory (DFT) ab initio simulations, the structural and

Proceedings of the 14th Asian Conference on Solid State Ionics (ACSSI 2014)
Copyright © 2014 ACSSI 2014 Organizers. All rights reserved.
ISBN: 978-981-09-1137-9
doi:10.3850/978-981-09-1137-9_169

hydrolysis stability for a wide range of such lithium thiophosphates and related compounds in order to identify compounds with low-lying metastable or even thermodynamically stable structures and comparatively low tendency to hydrolyse. In the focus of our study are the lithium argyrodites first reported by the Deiseroth group [2], named after natural mineral Ag_8GeS_6. Argyrodites are a large family of compounds with the general chemical formula $A^{a+}_{(12-m-x)/a}(M^{m+}Y_4^{2-})Y^{2-}_{2-x}X^{-}_{x}$ (where $A^{a+} = Li^+, Cu^+, Ag^+, Cd^{2+}, \ldots$; $\boldsymbol{M^{m+}} = Ga^{3+}, Si^{4+}, Ge^{4+}, Sn^{4+}, P^{5+}, As^{5+}$; $\boldsymbol{Y^{2-}} = O, S, Se, Te$; $\boldsymbol{X^{-}} = Cl, Br, I$; $0 \leq x < 2$) that share a common high-temperature (aristotype) structure in cubic space group $F\text{-}43m$, while partial or complete A-site ordering leads to various lower symmetry phases. In some compounds e.g. $Ag_6(GeS_4)Br_2$ [6] the Argyrodite structure competes to a structurally distinct orthorhombic phase. For a subset of the compositions identified by structural and hydrolysis screening, ion transport pathways are determined using the bond valence analysis tools developed in our group. Thereby the suitability of the geometry-optimized structures for fast ion conductivity can be compared.

2. Experimental

2.1. *Computational details*

Structure relaxations and the calculation of formation or dissociation energies are performed by DFT methods using the Vienna ab initio simulation package (VASP) [7] employing GGA exchange-correlation potential [8]. Structures are relaxed with a cutoff frequency of 400 eV, an electronic convergence threshold of 10^{-4} eV and a force convergence threshold of 0.03 eV/Å. Given a typical size of argyrodite unit cells of ca. 10×10×10Å^3, a 3×3×3 k-mesh is used for argyrodites and k-meshes of similar k-point density are used for the other compounds included in the discussion for comparison.

As commonly observed for fast ion conductors some of the argyrodite structures are known to be disordered not only in terms of their cation distribution, but also with respect to the distribution of halide and sulphur ions, except those in the MS_4^{3-} tetrahedrons [2,3]. Each unit cell contains four pairs of exchangeable ions so stability against disordering is evaluated at an interval of 25% disordering for all lithium argyrodites in this overview study. To illustrate more in detail how stability and ion mobility can be affected by disorder in the immobile anion sub-structure, a 4-fold supercell of Li_6PS_5Br is constructed redefining the cell parameters to be (-1, 1, 1), (1, -1. 1), (1, 1, -1) which yields a 4-fold supercell with 16 pairs of exchangeable ions. Relaxation is performed by choosing the number of pairs exchanged and then randomly selecting the ions to be swapped. In view

of enhancing the chemical stability, the M-site cation P^{5+} can be completely replaced by tetravalent Si, Ge or Sn, and the halide to sulphide ratio can be varied, while a corresponding variation of the Li content maintains charge neutrality. Li^+ ion migration conduction pathways and associated activation energies of selected compounds are estimated using the bond valence site energy method discussed in detail in our previous work [6].

3. Results and Discussion

3.1. *Structural stability of Argyrodite phases and related compounds*

Structural stabilities are compared based on the calculated dissociation energies derived from the DFT geometry-optimised structure models considering the following reaction equations (1) to (6) where X = Cl, Br, I; and in equations (4) to (6) M = Si, Ge, Sn:

$$Li_5PS_4X_2 \leftrightarrow Li_3PS_4 + 2\ LiX \quad \text{(Eq. 1)}$$

$$Li_6PS_5X \leftrightarrow Li_3PS_4 + LiX + Li_2S \quad \text{(Eq. 2)}$$

$$Li_7PS_6 \leftrightarrow Li_3PS_4 + 2\ Li_2S \quad \text{(Eq. 3)}$$

$$Li_6MS_4X_2 \leftrightarrow Li_4MS_4 + 2\ LiX \quad \text{(Eq. 4)}$$

$$Li_7MS_5X \leftrightarrow Li_4MS_4 + Li_2S + LiX \quad \text{(Eq. 5)}$$

$$Li_8MS_6 \leftrightarrow Li_4MS_4 + 2\ Li_2S \quad \text{(Eq. 6)}$$

Table 1 lists the dissociation energies for a range of argyrodites in order to find out the most stable structures in this series of compounds. Higher (less negative) dissociation energy indicates a more stable compound as more energy has to be supplied to dissociate the compound. As mentioned above besides the argyrodite phases distinct orthorhombic competing phases of the same composition exist, here simulated starting from the configuration observed for $Ag_6(GeS_4)Br_2$ (space group *Pnma*) [5]. For each composition the two structure types are compared in Table 1. In addition, dissociation energies of the phases $Li_{9+x}Ge_xP_{3-x}S_{12}$, and $Li_{22-3n}M_3S_{11}$ (with n = 5 for M = P, or n=4 for M=Si, Ge, Sn) have been determined using the same approach and are listed in in Table 2 for comparison.

As seen from Tables 1 and 2 almost all of the Li_nMS_5X phases are only meta-stable, and when comparing compounds with different M cations, their stability increases in the order Sn < P < Ge < Si. As seen from table 2 the same systematic trend with respect to the M cation replacement applies also to thiophosphates with $Li_7P_3S_{11}$ and LGPS-type structures, where again stability increases in the sequence Sn < P < Ge < Si. When comparing in table 1 structures with different halide anions X^-, the structural stability of Li_nMS_5X argyrodites increases in the

sequence Cl < Br < I. Consequently, among the Li_nMS_5X phases studied Li_6SiS_5I is found to be the most stable (effectively the

Table 1: Comparison of dissociation energies (in eV) of $Li_nMS_{6-x}X_x$ in the argyrodite structure (A) or in the competing orthorhombic structure (O). For Li_nMS_5X argyrodites the value listed here is the one for the most stable configuration with respect to S^{2-}/Y^- site occupancy disorder (cf. table 3). Dissociation energies for the most stable phases of each composition are marked in bold (if the total dissociation energy is above -0.5 eV). If the dissociation energies of A and O phases differ only marginally, both are marked.

M	*X*	*phase*	Li_nMS_6	Li_nMS_5X	$Li_nMS_4X_2$
P	**Cl**	A	**-0.365**	**-0.344**	**-0.390**
		O	-1.006	-0.425	**-0.392**
P	**Br**	A	**-0.365**	**-0.387**	**-0.372**
		O	-1.006	**-0.404**	**-0.390**
P	**I**	A	**-0.365**	**-0.239**	-0.521
		O	-1.006	-0.531	-0.534
Si	**Cl**	A	**-0.326**	**-0.178**	-1.328
		O	-1.109	-0.781	**-0.098**
Si	**Br**	A	**-0.326**	**-0.014**	-0.868
		O	-1.109	-0.662	**-0.109**
Si	**I**	A	**-0.326**	**0.033**	-0.626
		O	-1.109	-0.845	**-0.451**
Ge	**Cl**	A	**-0.437**	**-0.325**	-1.491
		O	-1.176	-1.042	**-0.186**
Ge	**Br**	A	**-0.437**	**-0.206**	-0.984
		O	-1.176	-0.639	**-0.168**
Ge	**I**	A	**-0.437**	**-0.077**	-0.681
		O	-1.176	-0.900	**-0.462**
Sn	**Cl**	A	-0.875	-0.607	-1.861
		O	-1.008	-1.144	**-0.372**
Sn	**Br**	A	-0.875	**-0.488**	-1.215
		O	-1.008	-0.930	**-0.310**
Sn	**I**	A	-0.875	**-0.418**	-0.750
		O	-1.008	-1.174	**-0.415**

Table 2: Dissociation energies (in eV) of lithium thiophosphates and related compounds.

Dissociation reaction	Dissociation energy (eV)
$Li_9P_3S_{12} \leftrightarrow 3\ Li_3PS_4$	-0.794
$Li_{10}GeP_2S_{12} \leftrightarrow 2\ Li_3PS_4 + Li_4GeS_4$	-0.297
$Li_{11}Ge_2PS_{12} \leftrightarrow Li_3PS_4 + 2\ Li_4GeS_4$	-0.020
$Li_{12}Ge_3S_{12} \leftrightarrow 3\ Li_4GeS_4$	0.120
$Li_7P_3S_{11} \leftrightarrow Li_3PS_4 + Li_4P_2S_6 + S$	-0.394

$Li_{10}Si_3S_{11} \leftrightarrow 2.5\ Li_4SiS_4 + 0.5\ SiS_2$	0.020
$Li_{10}Ge_3S_{11} \leftrightarrow 2.5\ Li_4GeS_4 + 0.5\ GeS_2$	-0.188
$Li_{10}Sn_3S_{11} \leftrightarrow 2.5\ Li_4SnS_4 + 0.5\ SnS_2$	-0.545

only thermodynamically stable) compound. When compared to the halide-free compositions Li_nMS_6 an uptake of halide ions to form Li_nMS_5X argyrodites enhances the structural stability (except for Li_6PS_5Br), while further increase of the halide concentration destabilizes the argyrodite phase, and comparatively favour the orthorhombic structure for the same chemical composition for halide-rich compositions $Li_nMS_4X_2$, while for Li_nMS_5X and Li_nMS_6 compositions the argyrodite structure is thermodynamically preferred. For the studied P-containing solid electrolytes the structural stability decreases in the sequence

$Li_{11}Ge_2PS_{12} > Li_{10}GeP_2S_{12} > Li_6PS_5I > Li_6PS_5Cl > Li_6PS_5Br > Li_7P_3S_{11} >> Li_9P_3S_{12}$

Among these, the phosphorus containing argyrodites show a significant tendency to form anion disordered structures that was already observed in our earlier experimental structure determinations. Therefore we systematically studied the influence of S^{2-}/X^- anion disorder on structural stability. Results are summarized in table 3 and Fig. 1. While a stabilization by anion disorder is clearly observed in simulations for P-based argyrodites, results for compounds based on other M cations exhibit relatively flat energy curves as a function of anion distribution and in most cases the fully ordered structures with either all X^- ("0% inversion") or all S^{2-} on the 0,0,0 site (100% inversion) are found to be the most stable ones. It should be noted that due to limited computational resources, here ions are swapped within a single unit cell. Such a setup will introduce an artificial periodicity, whereas in practice the disordering should be fully random. Hence values reported here should only be used as an upper limit and the reference and we expect the true structures to be slightly more stable.

Table 3: Dissociation energy of Li_nMS_5X argyrodites as a function of X^-/S^{2-} site occupancy inversion. Percentage refers to the ratio of S^{2-} and X^- pairs that are swapped within a unit cell: 0% corresponds to the structure with all X^- on 0,0,0 while 100% is the fully inverted structure with all S^{2-} on 0,0,0. The lowest energy in the respective row (or the two lowest values if they differ only marginally) are marked in bold, unless they are below -0.5 eV.

M	*X*	*0%*	*25%*	*50%*	*75%*	*100%*
P	**Cl**	-1.052	**-0.344**	-0.412	-0.614	-3.450
P	**Br**	-0.631	**-0.387**	**-0.387**	-0.669	-3.613
P	**I**	-0.265	**-0.239**	-0.439	-0.766	-4.085
Si	**Cl**	**-0.178**	-0.292	-0.328	-0.246	**-0.178**
Si	**Br**	**-0.014**	-0.161	-0.277	-0.214	-0.140
Si	**I**	**0.033**	-0.152	-0.247	-0.228	-0.182

Ge	**Cl**	**-0.325**	-0.431	-0.507	-0.368	**-0.339**
Ge	**Br**	-0.639	-0.300	-0.354	-0.354	**-0.206**
Ge	**I**	**-0.077**	-0.269	-0.342	-0.323	-0.268
Sn	**Cl**	-0.751	-0.832	-0.649	-0.717	-0.607
Sn	**Br**	-0.533	-0.634	**-0.488**	-0.539	-0.512
Sn	**I**	**-0.418**	-0.577	-0.603	-0.580	**-0.432**

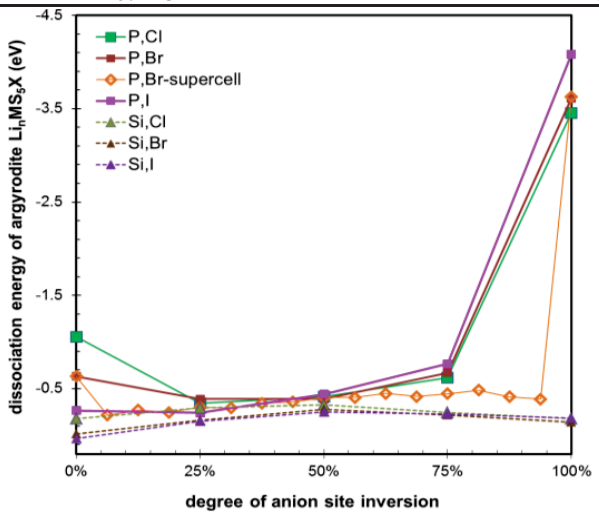


Figure 1: Dissociation energy of Li_nMS_5X argyrodites with M=P or Si as a function of the degree of S^{2-}/X^- anion site occupancy inversion. Solid lines (for P-based argyrodites) and broken lines (for Si-based argyrodites) serve as guides to the eye only. For Li_6PS_5Br results of more calculations in a fourfold supercell that allow for the variation of anion site inversion in finer steps are also shown.

For Li_6PS_5Br additional optimisations of a 4-fold supercell have been conducted to estimate the extent of model-size dependence and to analyze the dependence of the dissociation energy on the anion distribution for independently chosen more complex anion distribution patterns. Moreover the supercell allows for a finer resolution of the degree of anion site inversion and thus should reveal more details of the dependence. In accordance to the single unit cell simulations the fully ordered structures with 0% or 100% inversion show higher energy, but the system is stabilized significantly when a slight disordering occurs. As more bromide ions swap their sites with sulphide ions, the energy rises minutely.

3.2. *Electrochemical stability*

Argyrodites are insulators or wide band-gap semiconductors. To illustrate this we calculated the band-structure of Li_6PS_5Br. As can be seen from Fig. 2, Li_6PS_5Br exhibits a calculated bandgap of 2.12 eV. The GGA potentials employed in the DFT calculations are known to underestimate the bandgap, so that the

experimental bandgap should be substantially larger, which should result in negligible electronic conductivity as required for the use as solid electrolytes. Electrochemical stability is closely related to the dissociation energies of both the argyrodites and their competing phases. Thus we analysed the dissociation reactions for a range of conceivable decomposition products.Results are summarized in Table 4. A potential concern for using

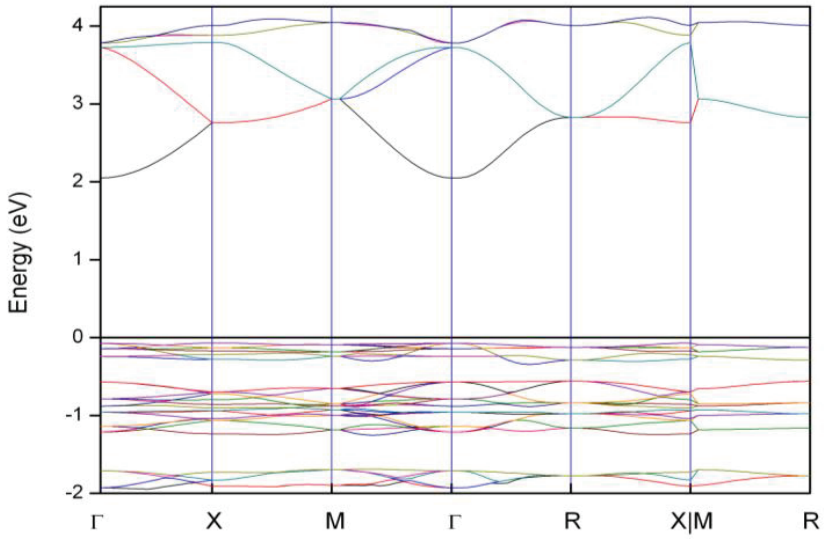


Figure 2: bandstructure of fully ordered Li_6PS_5Br.

Table 4: dissociation energy of considered decomposition products.

Dissociation reaction	Dissociation energy (eV)
$Li_3PS_4 \leftrightarrow 0.5\ P_2S_5 + 1.5\ Li_2S$	0.913
$Li_4GeS_4 \leftrightarrow GeS_2 + 2\ Li_2S$	0.329
$Li_4SnS_4 \leftrightarrow SnS_2 + 2\ Li_2S$	0.205
$Li_3BS_3 \leftrightarrow 0.5\ B_2S_3 + 1.5\ Li_2S$	0.200
$Li_2S \leftrightarrow 2\ Li + S$	4.103
$LiCl \leftrightarrow Li + 0.5\ Cl_2$	3.731
$LiBr \leftrightarrow Li + 0.5\ Br_2$	3.281
$LiI \leftrightarrow Li + 0.5\ I_2$	2.703
$P_2S_5 \leftrightarrow 2\ P + 5\ S$	1.231
$SiS_2 \leftrightarrow Si + 2\ S$	2.041
$GeS_2 \leftrightarrow Ge + 2S$	0.990
$SnS_2 \leftrightarrow Sn + 2S$	1.123
$B_2S_3 \leftrightarrow 2\ B + 3\ S$	2.155

halogenated thiophosphates such as the argyrodites is also the release of dihalogen gases, but this should only be possible for very high voltages that would also dissociate Li_2S. Unlike the oxidation of Li_2S, the production of dihalogen gases has to take place in one step hence a much higher activation

barrier should be expected, so that for the practical use of argyrodites in lithium-based batteries the hazard of dihalogen gases should not play any role. With respect to the electrochemical stability of phosphorus-containing argyrodites the high stability and significant ionic conductivity of the competing phase Li_3PS_4 (that limits the structural stability of the P-based argyrodites) may also be understood as an advantage compared to the less stable and often less conductive decomposition products of other Li_nMS_y solid electrolytes.

3.3. *Hydrolysis stability*

Estimating hydrolysis stability is a complex issue and predictions in principle should take into account both the kinetics and thermodynamics of the hydrolysis reactions into accounts. As the relevant transition state configurations required to analyse hydrolysis kinetics are generally not known, here we restrict ourselves to the thermodynamics of the hydolysis. The thermodynamic hydrolysis stability is estimated as the dissociation energy of the reaction in which the compound reacts with water to products known to be stable in aqueous environment. In this approach the hydrolysis stability of a compound is largely determined by its own structural stability and the reactivity of the potential decomposition products Li_3PS_4, Li_4SiS_4, Li_4GeS_4 and Li_4SnS_4 with water. Since the compounds contain different number of atoms per formula unit, hydrolysis stability is expressed as energy per atom in the respective sulphide compound.

According to the results in tables 5 and 6, Ge and Sn-containing argyrodites exhibit good hydrolysis stability (though it should be noted that the Sn-containing argyrodite phases have limited structural stability). Argyrodites containing phosphorus are actually the least stable against hydrolysis. Replacing some phosphorus by other elements should thus mitigate hydrolysis tendency, but possibly at the cost of further reduced structural stability. From a thermodynamic point of view argyrodites are more hydrolysis-resistant than $Li_7P_3S_{11}$ but less resistant than $Li_{10}GeP_2S_{12}$. As mentioned above it should be kept in mind that this allows for only rough predictions about hydrolysis rates, as the kinetics of the processes will be different (and in this respect it might have to be expected that compounds containing only ionically bonded S^{2-} such as most argyrodites should – for comparable thermodynamics - tend to promote faster hydrolysis kinetics than compounds that contain sulphur only in MS_4^{3-} groups).

Table 5: Hydrolysis stability of argyrodite decomposition products and selected other thiophosphate solid electrolytes.

Reaction of sulphide with water	Energy per atom (eV)
$Li_3PS_4 + 4\ H_2O \leftrightarrow Li_3PO_4 + 4\ H_2S$	-0.377

$Li_4SiS_4 + 4\ H_2O \leftrightarrow Li_4SiO_4 + 4\ H_2S$	-0.245
$Li_4GeS_4 + 4\ H_2O \leftrightarrow Li_4GeO_4 + 4H_2S$	0.022
$Li_4SnS_4 + 4\ H_2O \leftrightarrow 2/3\ Li_2SnO_3 + 1/3\ Li_8SnO_6 + 4\ H_2S$	0.146
$Li_3BS_3 + 3\ H_2O \leftrightarrow Li_3BO_3 + 3\ H_2S$	-0.282
$Li_2S + 2\ H_2O \leftrightarrow 2\ LiOH + H_2S$	-0.192
$Li_7P_3S_{11} + 12\ H_2O \leftrightarrow 7/3\ Li_3PO_4 + 2/3\ H_3PO_4 + 11\ H_2S$	-0.423
$Li_9P_3S_{12} + 12\ H_2O \leftrightarrow 3\ Li_3PO_4 + 12\ H_2S$	-0.411
$Li_{10}GeP_2S_{12} + 12\ H_2O \leftrightarrow 2\ Li_3PO_4 + Li_4GeO_4 + 12\ H_2S$	-0.246
$Li_{11}Ge_2PS_{12} + 12\ H_2O \leftrightarrow Li_3PO_4 + 2\ Li_4GeO_4 + 12\ H_2S$	-0.102
$Li_{12}Ge_3S_{12} + 12\ H_2O \leftrightarrow 3\ Li_4GeO_4 + 12\ H_2S$	0.026

Table 6: Comparison of hydrolysis stability of argyrodites (A) and orthorhombic phases (O).

Hydrolysis reaction	A	O
$Li_6PS_5Cl + 6\ H_2O \leftrightarrow Li_3PO_4 + LiCl + 2\ LiOH + 5\ H_2S$	-0.303	-0.309
$Li_5PS_4Cl_2 + 4\ H_2O \leftrightarrow Li_3PO_4 + 2\ LiCl + 4\ H_2S$	-0.284	-0.284
$Li_6PS_5Br + 6\ H_2O \leftrightarrow Li_3PO_4 + LiBr + 2\ LiOH + 5\ H_2S$	-0.307	-0.308
$Li_5PS_4Br_2 + 4\ H_2O \leftrightarrow Li_3PO_4 + 2\ LiBr + 4\ H_2S$	-0.353	-0.355
$Li_6PS_5I + 6\ H_2O \leftrightarrow Li_3PO_4 + LiI + 2\ LiOH + 5\ H_2S$	-0.295	-0.317
$Li_5PS_4I_2 + 4\ H_2O \leftrightarrow Li_3PO_4 + 2\ LiI + 4\ H_2S$	-0.295	-0.296
$Li_7PS_6 + 8\ H_2O \leftrightarrow Li_3PO_4 + 4\ LiOH + 6\ H_2S$	-0.324	-0.370
$Li_7SiS_5Cl + 6\ H_2O \leftrightarrow Li_4SiO_4 + LiCl + 2\ LiOH + 5\ H_2S$	-0.211	-0.254
$Li_6SiS_4Cl_2 + 4\ H_2O \leftrightarrow Li_4SiO_4 + 2\ LiCl + 4\ H_2S$	-0.271	-0.177
$Li_7SiS_5Br + 6\ H_2O \leftrightarrow Li_4SiO_4 + LiBr + 2\ LiOH + 5\ H_2S$	-0.200	-0.246
$Li_6SiS_4Br_2 + 4\ H_2O \leftrightarrow Li_4SiO_4 + 2\ LiBr + 4\ H_2S$	-0.236	-0.178
$Li_7SiS_5I + 6\ H_2O \leftrightarrow Li_4SiO_4 + LiI + 2\ LiOH + 5\ H_2S$	-0.196	-0.259
$Li_6SiS_4I_2 + 4\ H_2O \leftrightarrow Li_4SiO_4 + 2\ LiI + 4\ H_2S$	-0.218	-0.204
$Li_8SiS_6 + 8\ H_2O \leftrightarrow Li_4SiO_4 + 4\ LiOH + 6\ H_2S$	-0.246	-0.298
$Li_7GeS_5Cl + 6\ H_2O \leftrightarrow Li_4GeO_4 + LiCl + 2\ LiOH + 5\ H_2S$	**-0.051**	-0.102
$Li_6GeS_4Cl_2 + 4\ H_2O \leftrightarrow Li_4GeO_4 + 2\ LiCl + 4\ H_2S$	-0.100	**0.001**
$Li_7GeS_5Br + 6\ H_2O \leftrightarrow Li_4GeO_4 + LiBr + 2\ LiOH + 5\ H_2S$	**-0.038**	-0.073
$Li_6GeS_4Br_2 + 4\ H_2O \leftrightarrow Li_4GeO_4 + 2\ LiBr + 4\ H_2S$	-0.061	**0.002**
$Li_7GeS_5I + 6\ H_2O \leftrightarrow Li_4GeO_4 + LiI + 2\ LiOH + 5\ H_2S$	**-0.033**	-0.092
$Li_6GeS_4I_2 + 4\ H_2O \leftrightarrow Li_4GeO_4 + 2\ LiI + 4\ H_2S$	-0.038	**-0.021**
$Li_8GeS_6 + 8\ H_2O \leftrightarrow Li_4GeO_4 + 4\ LiOH + 6\ H_2S$	**-0.093**	-0.142
$Li_7SnS_5Cl + 6\ H_2O \leftrightarrow {}^2/_3\ Li_2SnO_3 + {}^1/_3\ Li_8SnO_6 + LiCl + 2\ LiOH + 5\ H_2S$	**0.006**	-0.029
$Li_6SnS_4Cl_2 + 4\ H_2O \leftrightarrow {}^2/_3\ Li_2SnO_3 + {}^1/_3\ Li_8SnO_6 + 2\ LiCl + 4\ H_2S$	-0.042	**0.072**
$Li_7SnS_5Br + 6\ H_2O \leftrightarrow {}^2/\ Li_2SnO_3 + {}^1/_3\ Li_8SnO_6 + LiBr + 2\ LiOH + 5\ H_2S$	**0.018**	-0.014
$Li_6SnS_4Br_2 + 4\ H_2O \leftrightarrow {}^2/_3\ Li_2SnO_3 + {}^1/_3\ Li_8SnO_6 + 2\ LiBr + 4\ H_2S$	0.008	**0.077**
$Li_7SnS_5I + 6\ H_2O \leftrightarrow {}^2/_3\ Li_2SnO_3 + {}^1/_3\ Li_8SnO_6 + LiI + 2\ LiOH + 5\ H_2S$	**0.010**	-0.031
$Li_6SnS_4I_2 + 4\ H_2O \leftrightarrow {}^2/_3\ Li_2SnO_3 + {}^1/_3\ Li_8SnO_6 + 2\ LiI + 4\ H_2S$	0.043	**0.069**
	-0.048	-
$Li_8SiS_6 + 8\ H_2O \leftrightarrow {}^2/_3\ Li_2SnO_3 + {}^1/_3\ Li_8SnO_6 + 4\ LiOH + 6\ H_2S$		0.056

3.4. *Ion transport pathways and migration energies*

Here we can only briefly summarize the bond valence site-energy pathway studies for our ab-initio geometry-optimized structure models. When comparing migration energies of $Li_{7-x}PS_{6-x}X_x$ phases, where experimental reference data are available, an increase in the sequence Cl < Br < I is observed in line with experimental findings. For a given halide X the activation energy for 3D Li^+ ion migration is 30% (for I) - 60% (for Cl) higher in the orthorhombic modification than for argyrodites. Among the orthorhombic phases the activation energies also increase substantially when raising the halide content from Li_6PS_5X to $Li_5PS_4X_2$. The predicted activation energies in Li_6PS_5Br argyrodites varies as a function of the degree of anion disorder by up to 50% with the lowest activation energies observed for models with >50% S^{2-}/X^- site occupancy inversion. Thus controlling anion disorder in argyrodites by thermal treatment (cf. [3]) also has a substantial influence on the activation energy in harmony to our experimental data. When substituting the M^{m+} cation in $Li_{11-m}MS_5Cl$ argyrodites the activation energy for Li^+ ion migration increases in the sequence Ge < Sn < P, so that doping P-argyrodites with Ge or Sn should be beneficial also from this point of view. Accordingly, increasing the Ge/P ratio in LGPS compounds slightly decreases the activation energy for 3D Li^+ migration from 0.23eV for $Li_{10}GeP_2S_{12}$ to 0.20 eV for $Li_{11}Ge_2PS_{12}$. In a comparison of argyrodites, LGPS and $Li_7P_3S_{11}$ the activation energy for (higher-dimensional) migration rises in the sequence

$$Li_6PS_5Cl < Li_{11}Ge_2PS_{12} < Li_6PS_5Br < Li_{10}GeP_2S_{12} < Li_7P_3S_{11} << Li_6PS_5I < Li_5PS_4X_2 \text{ (orh.)}$$

underlining the potential of argyrodites as fast ion conductors. It may also be noted that the predicted activation energy for 3D Li^+ migration in stoichiometric $Li_7P_3S_{11}$ is slightly higher than for LGPS, which seems to be in contrast to the reported lower activation energies (but in line with literature ab initio studies).

4. Concluding remarks

With respect to the properties studied in this work results for argyrodites are similar to and typically fall in-between the corresponding values for LGPS and $Li_7P_3S_{11}$-type solid electrolytes, the two currently leading classes of compounds in the search for the optimum compromise between fast room temperature conductivity and electrochemical stability for the use in batteries. Within each class of compounds the study also showed significant room for optimization of structural stability and ionic conductivity, as well as the mitigation of hydrolysis tendency. This should particularly be true for argyrodites that among the compounds screened here are probably the ones least explored so far.

Acknowledgments

This research is supported by the National Research Foundation, Prime Minister's Office, Singapore under its Competitive Research Programme (CRP Awards No. NRF-CRP 10-2012-6 and NRF-CRP8-2011-04).

References

1. H. Yamane, M. Shibata, Y. Shimane et al. (2007). *Solid State Ionics* 178:1163.
2. H.J. Deiseroth, S.T. Kong, et al. (2008). *Angew. Chem. Int. Ed.* 47:755.
3. R. Prasada Rao, N. Sharma, et al. (2013). *Solid State Ionics* 230 :72.
4. N.Kamaya, K. Homma, Y. Yamakawa et al. (2011), *Nature Materials* 10:682.
5. S. Adams, R. Prasada Rao (2012). *J. Mater. Chem.* 22:1426.
6. M. Wagener, H.J. Deiseroth, C. Reiner (2006). *Z. Kristallogr.* 221:533.
7. G. Kresse, J. Furthmüller, J. (1996). *Phys. Rev. B*, 54:11169.
8. J.P. Perdew, K. Burke, M. Ernzerhof (1996). *Phys. Rev. Lett.*, 77:3865.
9. S. Adams, R.P. Rao. (2011) *Phys. Status Solidi A*, 208, 8, 1746-1753.

THE EFFECT OF PLASTICIZER ADDITION TO SOLID POLYMER ELECTROLYTE BASED ON CHITOSAN MONMORILLONITE NANOCOMPOSITE

EVI YULIANTI*

Center for Science and Technology of Advance Materials, National NuclearEnergy Agency (BATAN), Kawasan Puspiptek Serpong, Tangerang, 15314,

SUDARYANTO

Center for Science and Technology of Advance Materials, National NuclearEnergy Agency (BATAN), Kawasan Puspiptek Serpong, Tangerang, 15314,

The effects of plasticizer addition to solid polymer electrolyte based on chitosan monmorillonite nanocomposite containing lithium salt have been studied. Ethylene glycol as plasticizer is an additive with low molecular weight expected to influence intrinsic polymer properties. A plasticizer also tends to dissociate ion pairs into free cation and anion which leads to an overall enhancement conductivity. The purpose of the research is to determine optimal composition of plasticizer addition to obtain good solid polymer electrolyte. The plasticizer within the range of $0 \leq x \leq 75\%$ w/w was added into chitosan monmorillonite nanocomposite. The mixture then was casted by slow evaporation in order to obtain thick film of solid electrolyte. The sample characterizations involve ionic conductivity measurement by LCR meter, crystal structure by an X-ray Diffraction, thermal analysis by a Differential Scanning Calorimetric and mechanical properties by a Universal Testing Machine. The results show that the addition of 50% w/w plasticizer could increase the ionic conductivity from ~10^{-9} S/cm until 2.26 x 10^{-4} S/cm and the polymer elasticity increase from 11.2% until 77.5% elongation break. The x-ray diffraction analysis showed that plasticizer addition make polymer more amorphous. It is concluded that the addition of plasticizer has improved the electrical and mechanical properties of the solid polymer electrolyte.

Keywords : nanocomposite, polymer electrolyte, chitosan, plasticizer

1. Introduction

Nowdays solid polymer electrolytes (SPEs) have attracted considerable attention because of their technological aspects which is widely used in energy storage components such as batteries, fuel cells, supercapacitor and a hybrid energy source [1,2]. SPEs is formed by dissolving salt in a macromolecule, typically such as poly(ethylene oxide) PEO, poly methyl metacrylate (PMMA), chitosan,

Proceedings of the 14th Asian Conference on Solid State Ionics (ACSSI 2014)
Copyright © 2014 ACSSI 2014 Organizers. All rights reserved.
ISBN: 978-981-09-1137-9
doi:10.3850/978-981-09-1137-9_183

etc. The solid polymer electrolyte membrane is the key component of polymer battery that has to fulfill a series requirement, including good mechanical properties (to assure easy battery fabrication, high ionic conductivity, high lithium ion transport, wide electrochemical stability, low cost and benign chemical composition (to be environmentally friendly). Unfortunately, it is not an easy task to achieve those requirements and until now SPEs still have low ionic conductivity at ambient temperature that acts as barrier to their utility [3,4]. To overcome these problems, the realization of single ion conduction is good alternative and development of polymer nanocomposite electrolyte (PNCEs) by using layered silicate clay meets these criteria. Polymer nanocomposite electrolyte was prepared by dispersing the ceramic material such as : SiO_2, Al_2O_3, and clay (bentonite , monmorillonite) into a complex matrix of polymers and salts [5-8] . The idea of composite formation by dispersing the ceramic or clay materials is an attractive approach to improve stability properties by modifying (i) the local structure / morphology (ii) crystallinity degree (iii) the glass transition temperature (iv) the flexibility of the polymeric segment (v) the chemical properties of the filler particles and (vi) the interaction between heterogeneous systems of filler, salt and polymers [9].

Generally, the ionic conductivity of PNCE usually lies in the range 10^{-7} to 10^{-5} S/cm at ambient temperature. Almost all composites polymer electrolyte posses inherent obstacle which come up of their partial crystalline nature that impedes their overall ionic conductivity and in that way impose limitation on their application [3, 9-13].

In order to overcome these limitations and to increase the ionic conductivity of PNCE without affecting their stability is plasticizing the composite polymer electrolyte with small organic molecules such as ethylene carbonate (EC), propylene carbonate (PC), ethylene glycol (EG), glycerol, etc. which have high dielectric constant and low vapour pressure [14]. These plasticizers helps in improving the ionic conductivity of PNCE by (i) increasing the amorphous content of polymer electrolytes, (ii) dissociating ion pairs into free cations and anions which leads to an overall enhancement conductivity, (iii) increasing the flexibility in the polymeric segment, (iv) significant change in local structure/microstructure, (iv) lowering the glass transition temperature, Tg [9].

The plasticizer addition can increase in the ionic conductivity of 1-2 orders of magnitude and a decrease of T_g values by 40°C of plasticized polymer electrolytes samples as reported by MacFarlane et al., and Forsyth et al. [15,16]. In these works, they investigated the PEO samples plasticized with 50 wt% of propylene carbonate and 50% of dimethyl formamide. Samples of plasticized chitosan-based polymer electrolytes were also reported by Aroof et. al., and

obtained that chitosan plasticized with 50 wt% of ethylene carbonate and 10 wt% of oleic acid showed the ionic conductivity of 10^{-5} S/cm. [17,18].
In this work, new composite polymer electrolyte based on chitosan are presented. The samples of PNCEs film based on chitosan containing monmorillonite and $LiClO_4$ were plasticized with ethylene glycol, and the influence of this additive to the properties of PNCEs films is investigated.

2. Methodology

2.1. *Materials*

Chitosan (CS) from crab shells with low molecular weight used in this work was purchased from Bogor Agricultural Institute Laboratory. This chitosan was obtained by deacetylation of chitin and it had a degree deacetylation of 86%. Glacial acetic acid (HAc) obtained from Merck was used as the solvent of chitosan, monmorillonite K 10 (MMT) as a filler, and LiClO4 as lithium salt source, both of them purchased from Sigma Aldrich and Ethylene glycol (EG) as plasticizer purchased from Merck.

2.2. *Preparation of Composite*

Chitosan solution was prepared by dissolving chitosan (CS) in a 1% (v/v) aqueous acetic acid solution at a concentration of 4 wt% . The mixture was stirred continuously with a magnetic stirrer until chitosan powder has completely dissolved in the acetic acid solution. Monmorillonit (MMT) was first swelled by 10% (w/v) $LiClO_4$ solution, then the plasticizer ethylene glycol was added with composition 10 wt%, 25 wt%, 50 wt% and 75 wt% and stirred for 1 hour. After that, each mixed solution is added to 100 ml chitosan solution and stirred for 10 hours. Then, MMT/CS/LiClO4/plasticizer solution was casted on a petri dish at 50°C for 48 hours until solvent free film were obtained. The films were kept in the desiccator for further drying.

2.3. *Materials Characterization*

Ionic conductivity measurement were performed with a computer controlled impedance analyzer (HIOKI LCR Hi-Tester Model 3532, Japan) in the frequency range 42 Hz to 5 MHz.. Mechanical properties of different plasticized composite polymer electrolyte film were studied by Universal Testing Machine (UTM) strograph VGS S-E Toyoseiki based on ASTM D-1822 L. The X-ray diffraction (XRD) pattern of plasticized polymer film was recorded at room temperature using an X-ray diffractometer (Shimadzu XD-610) with Cu

K_α radiation (λ= 1.5418 Å) in the 2θ (Bragg angles) range $5 \leq 2\theta \leq 65$ at scan speed 3° per minute. Differential Scanning Calorimetry (DSC) studies of different plasticized polymer films were carried out with a DSC unit (Perkin Elmer).

3. Result and Discussion

3.1. *Ionic Conductivity*

Figure 1 shows the variation of ionic conductivity (σ_{ac}) with frequency for different concentration of ethylene glycol at room temperature for CS + 2wt.% MMT + 40 wt.% LiClO4 + x wt.% EG. The ac conductivity patterns show a frequency independent plateau in the medium frequency region. From the graph it can be seen that the conductivity of polymer films undergo significant changes. The ionic conductivity of plasticized composite polymer film is higher than unplasticized polymer film (CS). The ionic conductivity starts increase at EG (x = 10%) until x = 50%. But at x = 75% the ionic conductivity values is not increase anymore, but tends to decrease significantly. It can be concluded that the optimum addition of plasticizer is 50 wt% for the CS/MMT/LiClO4 composite polymer system(PNCE). Referring to previous research by Yulianti, E. et. al [19] the ionic conductivity value of unplasticized CS/MMT/LiClO4 was 2.38 x 10^{-5} S/cm and in this work is obtained the ionic conductivity of plasticized composite polymer is 2.26 x10^{-4} S/cm increased by 1 orde, with 50 wt.% plasticizer addition.

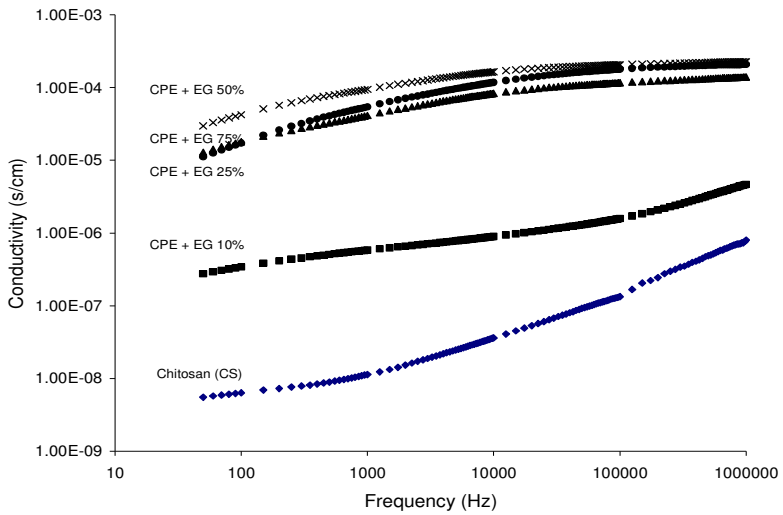


Figure 1. Variation of a.c conductivity with frequency CS + 5 wt.%MMT + 40% wt% LiClO4 (PNCE) + *x* wt.% EG

Plasticizer tends to dissociate ion pairs into free anions and cations, so the amount of moving ion into the system is increased. Therefore the ionic conductivity for plasticized composite polymers were higher than unplasticized ones. Plasticizer addition also increased the flexibility of composite polymer so that ions movement in the polymer matrix become more freely [9]. The plasticizer addition also made polymer more amorphous, and this phenomena can be seen from the X-ray diffraction pattern of CS/MMT composite film in Figure 2.

3.2. *X-ray diffraction*

The XRD patterns for composite polymer electrolyte based on chitosan with different plasticizer concentrationare shown in Figure 2. The XRD pattern has typical features namely a background hump followed by several characteristic peaks that are attributed to the host polymer (i.e., chitosan). This agrees with the result of Agnieska et al. [9,14] and indicates that the solid polymeric films are composed of a combination of crystalline and amorphous phases. Crystalline phase is characterized by the peak at position 2 θ angle of 11.97 ° and 18.52 °, not sharp but wide peak which indicates the presence of amorphous phase. Further, the appearance of small peak at at 2 θ angles ~° 27.05 may possibly be related to the existence of SnO2 that is contained in monmorillonite [19]. This suggests that the diffraction peaks of composite polymer electrolyte (PNCE) films are of composite nature.

The addition of ethylene glycol plasticizer brings substantial changes in the diffraction pattern of the composite polymer electrolyte with the increasing concentration of the plasticizer as observed in Fig 2(c) – (d). The main XRD peaks (due to chitosan) at 11.97 ° and 18.52 ° almost disappear and significant broadening with plasticizer addition. On the addition of ethylene glykol (EG) plasticizers up to 50% only one peak of chitosan at 18.52 ° is visible, whereas the addition of 75% plasticizer, the peak had disappeared and have maximum broadening, that suggest that the sample with EG = 75% has maximum disorder, shows the increasing amorphous phase in the polymer composite systems. Peak SnO2 of monmorillonite at ~° 27.05 at EG = 10% and 25% is still visible, while the addition of plasticizer at 50% and 75% the peak does not appear anymore.

The addition of plasticizers into the nanocomposite polymer systems have resulted in an enhancement in the amorphous fraction in polymer film. This is due to that a plasticizer which is a small molecular weight can increase the free volume or molecular mobility of the polymer by reducing the hydrogen bonds between the polymer chains. The composition, size, and shape of the plasticizer

affects its ability to disrupt hydrogen bonding of chitosan chains. Plasticizer reduces the intermolecular force of polymer chains, therefore there is a larger space for the ions (i.e. lithium ions) to move, thereby the ionic conductivity of the PNCE system will be increase as shown in Figure 1.

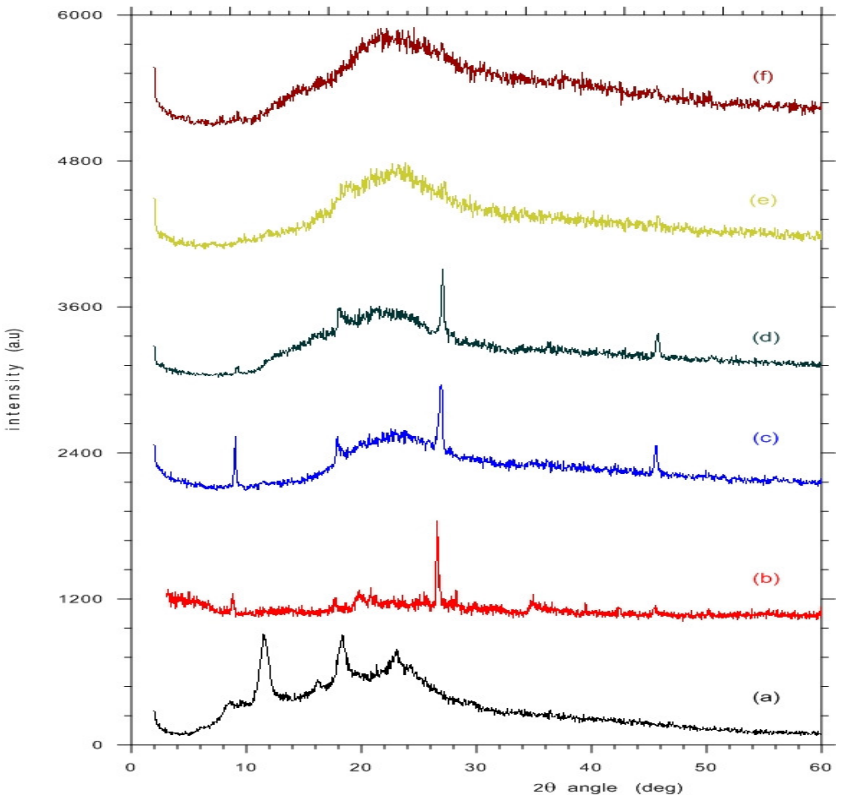


Figure 2. X-ray diffraction pattern of PNCE thin film with different concentration (x) of EG (a) chitosan, (b) monmorillonite, (c) x = 10% (d) x = 25% (e) x= 50% and (f) x= 75%.

3.3. *Differential Scanning calorimetry*

The thermal properties curves for of the composite polymer electrolyte (PNCE) system at various plasticizer concentrations measured by DSC are shown in Figure 3 over a wide range of temperature i.e., 30 to 450°C. In Figure 3 shows an endothermic peak which is melting temperature of PNCE crystalline fraction containing plasticizers which starts at onset temperature around 120°C. The more concentration of plasticizer added, the endothermic peaks become broader and shifted toward lower temperature and onset temperature also decreases. This is due to the addition of the plasticizer causes increasing the flexibility in the

polymeric segment, that is also convinced by the mechanical properties data of the PNCE film (i.e., the elongation break curve) that shows the PNCE films become more elastic with the higher concentration of plasticizer. These results are also consistent with measurements of X-ray diffraction pattern which shows the broadening of the peak which means higher amorphous fraction in PNCE with increasing concentration of plasticizer.

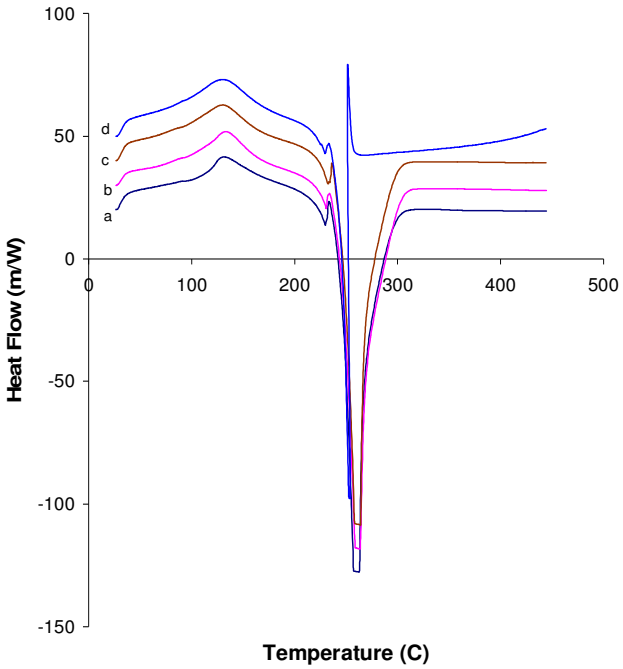


Figure 3. DSC curve of PNCE in temperature range 30 to 450°C with different concentration of EG (a) x = 10%, (b) x = 25% (c) x= 50% and (d) x= 75%

From the DSC curve, it is clear the effect of plasticizer addition on the thermal properties of PNCE. Further, it is revealed that that melting temperature of plasticized PNCE film decrease with increasing plasticizer concentration. Exothermic peak that appears at the onset temperature around 240 °C is a decomposition temperature of ethylene glycol. From the DSC curves it can be seen that the more concentration of ethylene glycol plasticizer is added, the exothermic peak become narrower, that means that decomposition process occurs slower. It can be concluded that PNCE films have better heat resistance and thermal properties with the increasing plasticizer concentration.

3.4. *Mechanical Properties*

Tensile strength and elongation break percentage were very important to explain how the mechanical characteristics of the material. Tensile strength values measured to determine the extent to which the membrane reacts to the pull force. Plasticizer is a material that can make polymer material becomes more elastic if it was added. The addition of this plasticizer is needed to overcome the stiffness properties of chitosan-based films. With the addition of the plasticizer in the polymer chains of chitosan causes inter-polymer bond can be damaged and made polymer more plasticity and flexibly. Mechanical properties data of PNCE added plasticizers ethylene glycol are shown in Figure 4 and Figure 5.

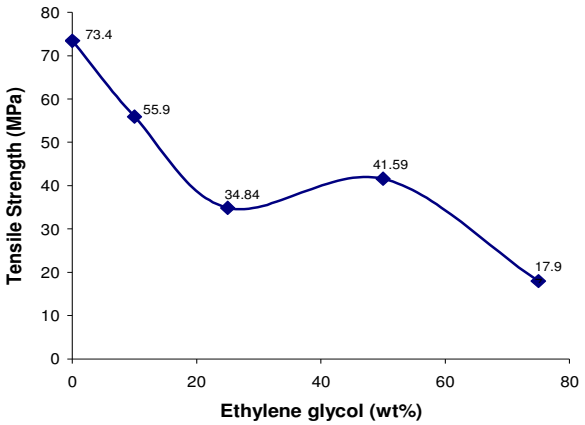


Figure 4. Tensile Strength curve of PNCE with different plasticizer concentration (x) (x= 0, 10%, 25%, 50% and 75%)

In Figure 4 it can be seen that the tensile strength of PNCE decreased with the increasing of plasticizer concentration. The unplasticized PNCE have tensile strength value 73.4 MPa, while the plasticized film with x = 10% is decreased to 55.94 MPa, and with x = 25% also decrease to 34.84 MPa. However, the plasticizer addition of 50% caused the tensile strength increased to 41.59 MPa, but at x = 75% PNCE the strength decreased again to 17.97 MPa.

Tensile measurements are usually performed in conjunction with elongation break measurement. Elongation break percentage determines the elasticity of a PNCE film. The higher the value of the elongation break, the more elastic the

PNCE film. The addition of plasticizer ethylene glycol was increase the elongation break of the PNCE films. The unplasticized PNCE film is inflexible and only has elongation break percentage 11.2%. The addition of plasticizer at composition 10 wt% has increased elongation break significantly until 60.7%, but at plasticizer concentration 25% little bit decrease to 50.7%. The highest elongation break value 77.5% is achieved at plasticizer concentration 50%. From the Figure 4 and 5 it can be seen that the optimum mechanical properties of PNCE films is achieved at plasticizer concentration of 50 wt%.

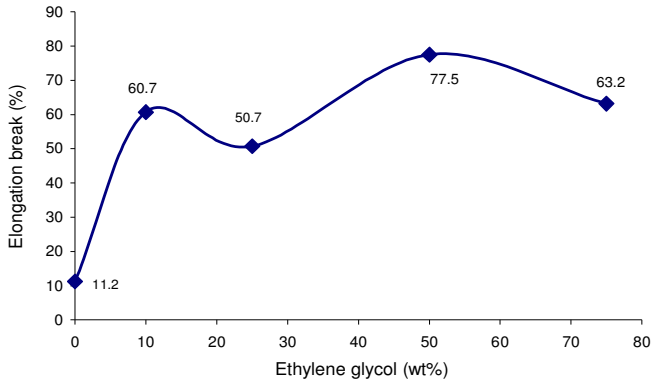


Figure 5. Elongation break curve of PNCE films with different plasticizer concentration (x) (x= 0, 10, 25, 50, and 75 wt%)

4. Conclusion

The effect of plasticizer ethylene glycol on properties of chitosan nanocomposite polymer electrolyte (PNCE) has been studied. Addition of plasticizer at concentration 50 wt% can increase the PNCE film conductivity until 2.25 x 10^{-4} S/cm. The plasticizer addition also influence the intrinsic properties PNCE films where the XRD pattern and thermal curves showed the PNCE films become amorphous with lower melting points. In addition to the higher plasticizer addition concentration, the PNCE films become more flexible and optimum condition is achieved at plasticizer concentration 50 wt% with elongation break 77.5%.

References

1. Yuan, X.Z., Wang, H., Song, C., Zang, J., Electrochemical Impedance Spectroscopy in PEM fuel cells. Springer London Dordrecth Heidelberg, New York. 2009
2. C. Polo Fonseca, S. Neves, Journal of Power Sources 159 (2006) 712-716
3. W.A.V. Schalkwijk, B. Scrosati, Advances in Lithium –Ion batteries, Kluwer Academic Publishers, New York, 2002
4. C. Sequeira and D. Santos, Polymer Electrolytes, fundamentals and Applications, Woodhead Publishing, Philadelphia (2010)
5. A. Usuki, Y. Kojima, M. Kawasumi, A. Okoda, Y. Fukushima, T. Kurauchi, J. Materials Research, 8, 1179, (1993)
6. J.E. Weston, B.C.H. Steele, Solid State Ionics, 7, 81, (1982)
7. Z. Shen, G.P. Simon, Y.B. Cheng, Poly. Engi. Sci., 42, 2369 (2002)
8. M. Kurian, M.E. Galvin, P.E. Trapa. D.R. Sadoway, A.M. Meyes, Electrochimica Acta, 50, 2125 (2005)
9. D.K. Pradan, B.K. Samantaray, R.N.P. Choudary, A.K. Thakur, Journal of Power Sources 139 (2005) 384-393
10. D.K. Pradhan, R.N.P. Choudary, B.K. Samantaray, Int. J. of Electrochem. Sci., 3 (2008) 597-608
11. Brinkmann, D., Gang, W., Croce, F., Scrosati, B., *Solid State Ionics* 53-56 (1992) 1202
12. Krawiec, L.W., Scanlon, L.G., Fellner, J.P., Vaia, R.A., Vasudevan, S., Giannelis, E.P., *J. Power Sources* 54 (2) (1995) 310
13. Leo, C.J., Subba Rao, G.V., Chowdari, B.V.R., *Solid State Ionics* 148 (2002) 159
14. A. Pawlicka, M. Danczuk, W. Wieczorek, E.Z. Monikowska, , *J. Phys. Chem. A*. 2008, 112, 8888-8895.
15. MacFarlane, D.R., Sun, J., Meakin, P., Fasoupoulos, P., Hey, J., Forsyth, M., *Electrochim. Acta* 1995, 40, 2131
16. Forsyth, M., Meakin, P.M., MacFarane, D.R., *Electrochim. Acta* 1995, 40 2339
17. Yahya, M.Z.A., Arof, A.K. *Eur Polym J*. 2003, 39, 897
18. Khiar, A.S.A., Puteh, P., Arof, A.K. Physica B 2006 373
19. E. Yulianti, R.D. Saputri, Sudaryanto, H. Jodi, R. Salam, J. Kimia dan Kemasan, 35, 2 (2013) 77-8

Fuel Cell Materials I

DESIGNING MIXED CONDUCTING ANODES FOR SOLID OXIDE FUEL CELLS (SOFCS)*

WANG HAY KAN, BEHZAD MIRFAKHRAEI, KALPANA SINGH, HALA T HANDAL, AND VENKATARAMAN THANGADURAI†

Department of Chemistry, University of Calgary, 2500 University Dr. NW, Calgary, AB, Canada

A solid oxide fuel cell (SOFC) is an electrochemical device, which directly converts chemical energy of fuel into electrical energy with high efficiency. Current SOFCs based on Y-doped zirconia suffer due to interface reaction products at the cathode due to high operating temperature, and poisoning at the anode due to fuel impurities, especially under hydrocarbons. In this paper, we give a short review of mixed ion-electronic conducting negative (anode) electrodes for SOFCs that were developed in the Thangadurai group over the last half-decade. The investigated inorganic metal oxide structures include perovskite (ABO_3), B-site ordered double perovskite-type ($A_2B_2O_6$), fluorite (CeO_2), Sr_2PbO_4-type and Nd_2WO_6-type. Various in-situ techniques such as powder X-ray diffraction (PXRD), electrochemical impedance spectroscopy (EIS) and thermogravimetric analysis (TGA) were used to characterize the structural and electrical properties. A total conductivity of 1 x 10^{-2} Scm-1 with activation energy of 0.43 eV was found for $Ba_2Ca_{0.79}Fe_{0.5}Nb_{0.71}O_{6-\delta}$ in wet N_2 at 600 ^oC. Fluorite-type $Ce_{0.7}Sm_{0.2}Mo_{0.1}O_2$ exhibits the total conductivity of about 8 x 10^{-2} Scm^{-1} at 450 ^oC, while Nd_2WO_6-type $Sm_{1.8}Ca_{0.2}MoO_{6-\delta}$ exhibits ~ 0.1 Scm^{-1} at 450 ^oC, with activation energy of 0.06 eV.

1. Introduction

Solid oxide fuel cells (SOFCs) are promising energy devices to convert chemical reaction energy into electricity and heat with high efficiency (combined electricity and heat up to 90%). Ideally, hydrocarbons can be used as fuels for SOFCs as they are abundant and less expensive compared to pure hydrogen. However, the state-of-the-art anode, i.e., Ni-YSZ cermet is limited to work in pure H_2 at elevated temperatures. Coke and S-poisoning at the anode are observed when H_2S-containing hydrocarbons are used. The electrochemical reaction zone is also restricted to the triple-phase boundary (TPB).[1] Recent reports have shown that mixed ion (H^+, O^{2-}) and electron conducting (MIECs) anodes have specific advantages of high chemical stability in H_2S (ppm level) contaminated fuels,[2-8] and a well-extended electrochemically active TPB.[8]

* This work is supported by SOFC Canada NSERC Strategic Research Network and other sponsors listed at www.sofccanada.com.

† For correspondence; Email: vthangad@ucalgary.ca Phone: 001 403 210 8649.

Proceedings of the 14th Asian Conference on Solid State Ionics (ACSSI 2014)
Copyright © 2014 ACSSI 2014 Organizers. All rights reserved.
ISBN: 978-981-09-1137-9
doi:10.3850/978-981-09-1137-9_011

MIECs exhibit appreciably high conductivities and show lower polarization resistances that are desirable for high power demand (≥1 W/cm^2) applications. To meet these requirements, we have worked intensively on various novel inorganic structure MIECs over the years. Here, we report our recent progress in the development of MIECs based on perovskite-type (ABO_3), ordered double perovskite-type ($A_2B_2O_6$), fluorites (CeO_2), Sr_2PbO_4-type Sr_2CeO_4, and Nd_2WO_6-type as SOFC anodes for advanced SOFCs (Figure 1).

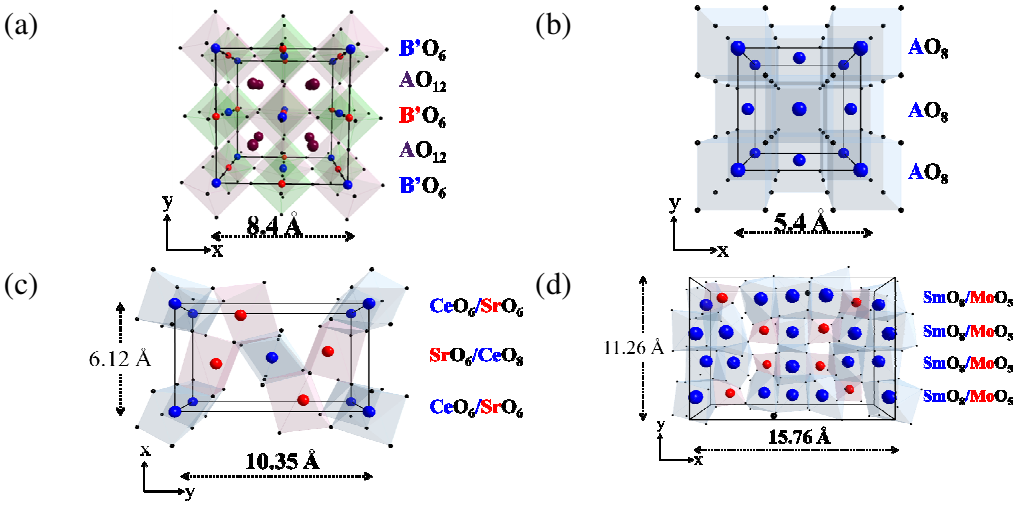


Figure 1. Idealized crystal structures of mixed ion and electron conducting (a) ordered-double perovskite ($A_2B_2O_6$), (b) fluorite-type CeO_2, (c) Sr_2PbO_4-type Sr_2CeO_4 and (d) Nd_2WO_6-type $Sm_2MoO_{6-\delta}$ (SMO).

2. Acceptor-doped perovskite and ordered perovskite-type MIECs for SOFCs

Acceptor-doped perovskites are of great interest due to their intrinsic structural stabilities under a wide range of oxygen partial pressures (pO_2) at elevated temperatures and they exhibit MIEC under low and high pO_2.[9] Electronic carriers can be generated under reducing atmosphere when early transition metals are doped in the crystal structure. Liu *et al.* demonstrated that Ni-$BaZr_{0.1}Ce_{0.7}Y_{0.1}Yb_{0.1}O_{3-\delta}$ anodes are highly active in 20 ppm H_2S/H_2 and achieved an impressive power performance of about 1 Wcm^{-2} at 750 ^oC.[7] However, the material requires a high sintering temperature of 1600^{o}C, where BaO might be partially vaporized. Consequently, it will decrease the electrical conductivity of the compound due to inter-diffusion of B-site dopant into the A-site vacancy, and increase difficulties in understanding the structure-functional property relationship. A possible solution is to use transition metal dopants in the perovskite structure, as those dopants generally require lower sintering temperatures.

Our recent results have indicated that perovskite-type $BaZr_{0.1}Ce_{0.7}Y_{0.1}M_{0.1}O_{3-\delta}$ (M = Mn, Fe, Co and Ni) shows substantial chemical stability in 30 ppm H_2S containing H_2 at elevated temperature. No S containing phases were detected for Fe-doped $BaZr_{0.1}Ce_{0.7}Y_{0.1}Fe_{0.1}O_{3-\delta}$ after it was exposed to 30 ppm H_2S at 600 ^oC for 24 h (Figure 2). The structural solutions from PXRD Rietveld refinement of the as-prepared perovskite-type $BaZr_{0.1}Ce_{0.7}Y_{0.1}Fe_{0.1}O_{3-\delta}$ and B-site ordered double perovskite-type $Ba_2Ca_{0.67}Fe_{0.33}NbO_{6-\delta}$ samples after reacting in 30 ppm H_2S at 600 ^oC for 24 h are summarized in Table 1. In the double perovskite-type structure (Figure 2a), both *4a* (Ca-site) and *4b* (Nb-site) sites are accessible for dopants to alter the electrochemical properties, which is an additional parameter over the simple perovskite-type.[10-12] The conductivities increase in the order of Mn < Fe < Co for the same composition of $Ba_2Ca_{1-x-y}M_{x+z}Nb_{1+y-z}O_{6-\delta}$ (M = Mn, Fe, Co) in air. The highest total conductivity of 3.7 x 10^{-2} Scm^{-1} was observed for $Ba_2Ca_{0.79}Co_{0.5}Nb_{0.71}O_{6-\delta}$ about 810 ^oC in air.[13] The electrical transport mechanism is correlated to the reduction of the dopants and the loss of oxide ions at elevated temperatures, as confirmed by TGA and *in-situ* PXRD. The thermal expansion coefficient of the $Ba_2Ca_{1-x-y}M_{x+z}Nb_{1+y-z}O_{6-\delta}$ (M = Mn, Fe, Co) samples matched well with the state-of-the-art YSZ electrolyte (11 × 10^{-6} $^oC^{-1}$ at 25–900 ^oC), suggesting that YSZ could be physically compatible with doped $Ba_2Ca_{1-x-y}M_{x+z}Nb_{1+y-z}O_{6-\delta}$ (M = Mn, Fe, Co) up to 900 ^oC.

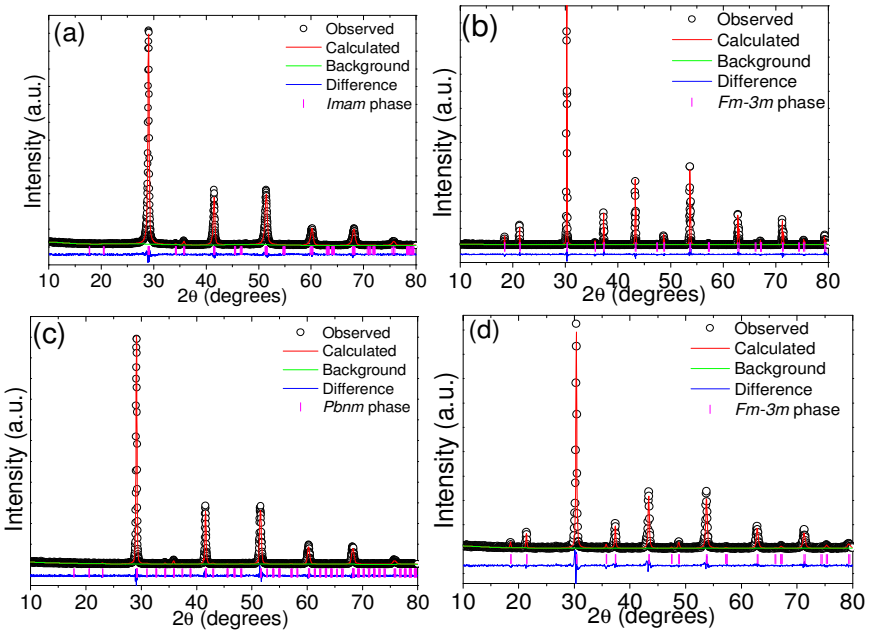


Figure 2. PXRD Rietveld refinement of the as-prepared (a) $BaZr_{0.1}Ce_{0.7}Y_{0.1}Fe_{0.1}O_{3-\delta}$ and (b) $Ba_2Ca_{0.67}Fe_{0.33}NbO_{6-\delta}$. The refinement of samples (a) and (b) after reacting in 30 ppm H_2S at 600^oC for 24 h are shown in (c) and (d), respectively. The detailed structural solution for the Rietveld refinement is summarized in Table 1.

Table 1. Structural solution of the Rietveld refinement of the as-prepared and H_2S treated B-site disordered $BaZr_{0.1}Ce_{0.7}Y_{0.1}Fe_{0.1}O_{2.9}$ and B-site ordered $Ba_2Ca_{0.67}Fe_{0.33}NbO_{6-\delta}$ samples.[11, 12, 17]

Compound	Atom	Wyckoff notation	x, y, z	U_{iso} ($100Å^2$)	Fraction
as-prepared	Ba	4e	0,0.25,-0.0033	1.0(1)	1
$BaZr_{0.1}Ce_{0.7}Y_{0.1}Fe_{0.1}O_{2.9}$	Ce/Zr/Y/Fe	4b	0,0,0.5	0.6(1)	0.7/0.1/0.1/0.1
Imma (74), a = 6.1836(9) Å,	O1	4e	0.5,0.25,0.06(1)	2.0(1)	0.97
b = 8.7050(6) Å, c = 6.1545(5) Å	O2	8g	0.25,0.038(2),0.75	1.0(1)	0.97
R_p: 5.84 χ^2: 1.390					
as-prepared	Ba	*8c*	0.25,0.25,0.25	0.53(5)	1
B-site ordered perovskite	Ca/Fe/Nb	*4a*	0,0,0	2.6(2)	0.67/0.08/0.25
$Ba_2Ca_{0.67}Fe_{0.33}NbO_{5.66}$	Fe/Nb	*4b*	0.5,0.5,0.5	0.3(1)	0.25/0.75
Fm-3m (225), *a* = 8.3750(2) Å	O	*24e*	0.2612(8),0,0	2.8(2)	0.94
R_p: 6.93 χ^2: 1.608					
30 ppm H_2S treated	Ba	4c	0.001,0.023,0.25	0.3(1)	1
$BaZr_{0.1}Ce_{0.7}Y_{0.1}Fe_{0.1}O_{2.9}$	Ce/Zr/Y/Fe	4b	0,0.5,0	0.4(2)	0.7/0.1/0.1/0.1
Pbnm (62), a = 6.1604(3) Å, b =	O1	4c	0.082(9),0.525(6),0.25	2(2)	0.97
6.1531(8) Å, c = 8.7110(4) Å	O2	8d	-0.263(7),0.230(8),	1(1)	0.97
R_p: 10.82 χ^2: 1.552			0.028(4)		
5000 ppm H_2S treated	Ba	*8c*	0.25,0.25,0.25	0.6(2)	1
B-site ordered perovskite	Ca/Fe/Nb	*4a*	0,0,0	0.5(5)	0.67/0.08/0.25
$Ba_2Ca_{0.67}Fe_{0.33}NbO_{5.66}$	Fe/Nb	*4b*	0.5,0.5,0.5	0.2(2)	0.25/0.75
Fm-3m (225), *a* = 8.3957(8) Å	O	*24e*	0.253(3),0,0	1.4(6)	0.94
R_p: 15.59 χ^2: 1.711					

Complex oxides $AZn_{0.33+x}Nb_{0.67-x}O_{3-\delta}$ (A = Sr, Ba; $0 \leq x \leq 0.08$) could be crystallized in a disordered perovskite-type structure, and they showed negligible grain-boundary impedance to total conductivity at low temperatures.[14] The highest total conductivity of 7.2×10^{-3} Scm^{-1} was observed for $BaZn_{0.33}Nb_{0.67}O_3$ at 800 °C in dry H_2 and the investigated compounds were chemically stable under CO_2 at 800 °C and H_2O at 100 °C. $SrZn_{0.33+x}Nb_{0.67-x}O_{3-\delta}$ maintained perovskite structure in 30 ppm H_2S at 800 °C, while the corresponding Ba analog decomposed into BaS_x under the same condition.[14]

3. Donor- and acceptor- doped fluorite-type MIECs for SOFCs

Donor-doped ceria (Figure 1b) was less studied compared to acceptor-doped as SOFC electrolyte materials due to their electronic conductivity under high oxygen partial pressure (pO_2). However, under reducing atmosphere, oxide vacancies are generated when dopants are partially reduced. The electrical properties of the Mo- doped CeO_2 have been explored as potential anode for SOFCs.[15-17] Interestingly, the nano-CMO enhanced the chemical stability under H_2S and H_2 (Figure 3a). Recently, our group has explored catalytic activity of the nano-sized CMO (10-15nm) made from plasma spray technique. The polarization resistance of the nano-CMO infiltrated in Gd doped ceria (GDC) in 10 ppm H_2S/H_2 was measured in a three-electrode half-cell measurement at 700°C. The nano-CMO has a positive impact in reducing the cell degradation at various temperatures from electrochemical impedance spectroscopy and galvanostatic measurements (Figure 4). Similarly, CMO impregnated Ni-YSZ

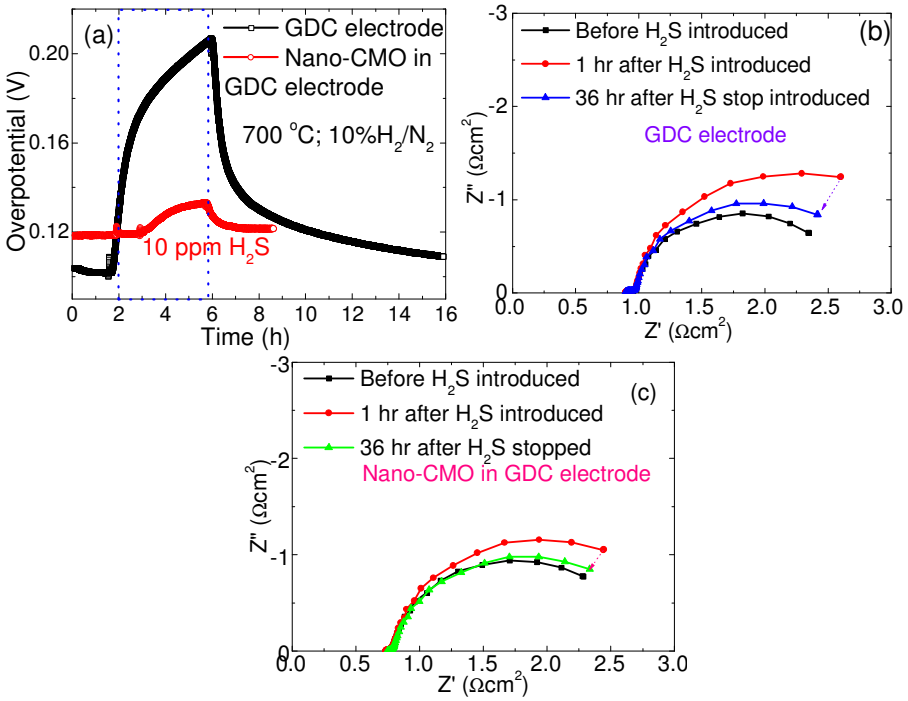
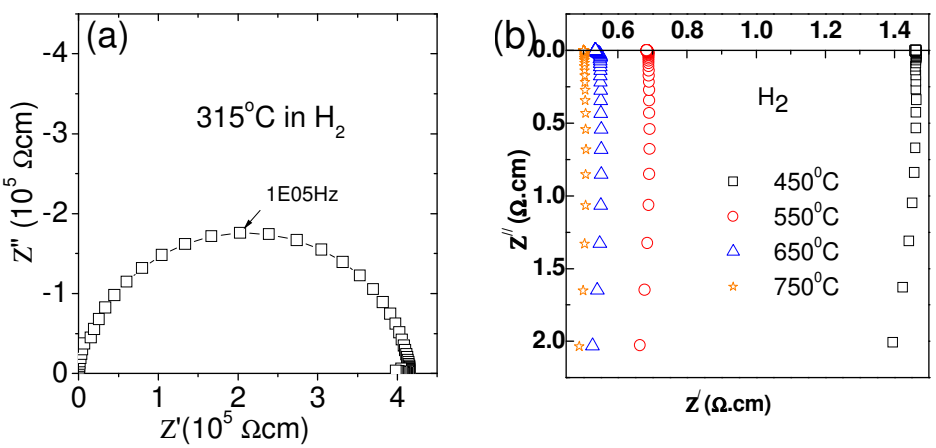


Figure 3. (a) Effect of 10 ppm H_2S on 33 mA/cm^2 galvanostatic measurement of 3-electrode YSZ electrolyte supported cell of GDC (black) and nano-CMO infiltrated GDC (red), and also area-corrected EIS spectra of the GDC (b) and nano-CMO infiltrated GDC (c) working electrodes.[17]



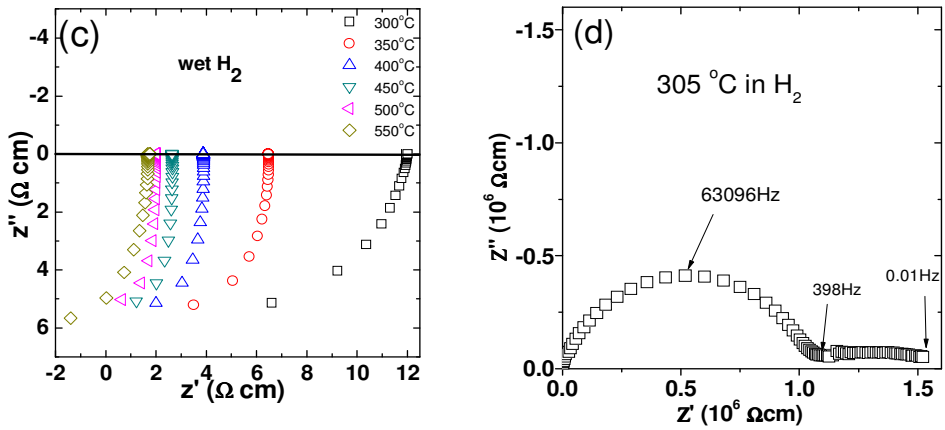


Figure 4. Typical AC impedance data obtained in hydrogen for (a) $Ba_2Ca_{0.79}Fe_{0.16}Nb_{1.05}O_{6-\delta}$; (b) $Ce_{0.85}Y_{0.1}Mn_{0.05}O_2$, (c) $Ce_{0.43}Zr_{0.4}Y_{0.12}Mo_{0.05}O_2$ and (d) $Sr_2Pr_{0.2}Ce_{0.8}O_4$.[11, 12, 19, 21-24]

The Mn-doped CeO_2 was recently investigated to further understand the impact of Mn on electrical properties. Co-doped $Ce_{0.9-x}Y_{0.1}Mn_xO_{2-\delta}$ (x = 0-15 mol %) (CYMO) was prepared by solid state and co-precipitation method and their structural, physical and chemical properties were investigated.[19] X-ray diffraction of Mn and Y-doped CeO_2 showed the formation of a fluorite-type structure with space group *Fm3-m*; however, minor impurity peaks due to a Mn_3O_4 phase was detected in some samples. Solubility of Mn in ceria appears to be less than 10 mol % under the investigated conditions. Among the Y- and Mn-codoped ceria, $Ce_{0.8}Y_{0.1}Mn_{0.1}O_{2-\delta}$ exhibited the highest conductivity of ca. 6×10^{-2} Scm^{-1} and 0.15 Scm^{-1} at 700 °C in air and H_2, respectively.[19]

Mo and rare-earth -codoped $Ce_{0.9-x}RE_xMo_{0.1}O_{2.1-0.5x}$ (x = 0.2, 0.3) (CRMO) fluorites can retain their structures under H_2 at elevated temperatures, while change in mass is explained using the reduction of both Ce^{IV} and Mo^{VI}.[20-22] For comparison, we also show the impedance data for, doped ceria, perovskite-type $Ba_2Ca_{0.79}Fe_{0.16}Nb_{1.05}O_{6-\delta}$ and other Ce-based compound $Sr_2Pr_{0.2}Ce_{0.8}O_4$ in H_2 in Figure 4. Fluorite-type ceria compounds show low impedances compared to other investigated compounds. The total electrical conductivity obtained using 2-probe AC and DC methods were consistent. Among the CRMO samples, $Ce_{0.7}Sm_{0.2}Mo_{0.1}O_2$ exhibits the highest conductivity of about 8×10^{-2} S cm^{-1} at 450 °C in wet H_2. The substitution of Mo in RE-doped ceria further increases the electronic conductivity. The oxide ion transference number determined using blocking electrodes increases with increasing temperature and pO_2.[20-22]

4. Sr_2PbO_4-type Sr_2CeO_4 MIECs for SOFCs

We explored an un-conventional "solid state and CO_2 mediated gas phase" synthesis for acceptor-doped CeO_2 to control the homogeneity and microstructure of the particles.[23] The homogenous and phase-pure Y_2O_3-doped

CeO_2 was obtained by conversion of Sr_2PbO_4-type Sr_2CeO_4 (Figure 1c) under CO_2 at elevated temperatures. The Y-doped CeO_2 prepared by CO_2 capture method exhibited one and half orders higher electrical conductivity than that of parent CeO_2.[23] Sr_2CeO_4 shows a Ce^{3+}/Ce^{4+} redox couple when is excited by UV-light at ambient conditions. Such valence couple could facilitate the oxidation reaction of H_2 and hydrocarbons on the anodic side.[24] However, we found experimentally that Sr_2CeO_4 can be thermally decomposed into SrO and CeO_2 at 1400 ^oC or above in air, although the reverse reaction occurs *in-situ* at 800 ^oC in air. This thermal instability requires special techniques (e.g., PLD, combustion method) to lower the sintering temperature and could increase the production costs.

Surprisingly, the substitution of Pr for Ce in Sr_2CeO_4 improved the thermal stability and samples can be sintered at 1400 ^oC. We further demonstrated that a M^{3+}/M^{4+} couple where M = Pr and Ce, can also be stabilized thermally under SOFC operation temperatures (< 1000 ^oC). The weight loss TGA was attributed to the loss of oxygen atoms due to the reduction of M^{4+} to M^{3+}. The crystal structure was found to be unchanged while the cell parameters increased linearly with temperature from *in-situ* PXRD measurement, as shown in Figure 5. We further examined the reducibility of the compounds upon the substitution of Ce^{4+} with Pr^{4+}. Interestingly, the conductivity of the compound increases with Pr-content, as the Pr ion has a lower reduction potential than Ce ions. The highest total electrical conductivity is 0.1 Scm^{-1} for the Pr rich compound at 700 ^oC in air.[24]

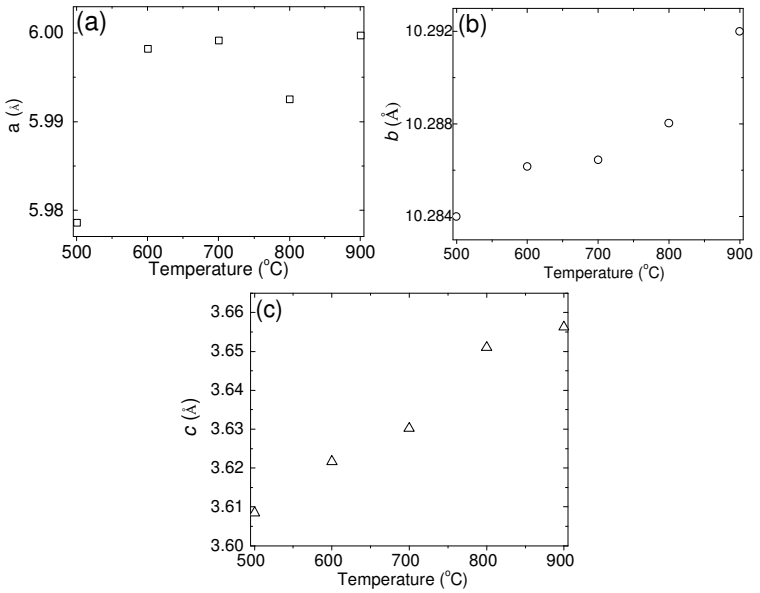


Figure 5. Variation of cell constant as a function of temperature for $Sr_2Ce_{0.2}Pr_{0.8}O_4$ in 10% H_2 in N_2.

5. Nd_2WO_6-type MIECs for SOFCs

Besides the investigations on the conventional perovskite and fluorite phases, for the first time, we have reported a family of fluorite-related structure materials with a chemical composition of Sm_2MoO_6 (SMO, in Figure 1d) and $Sm_2WO_{6-\delta}$ (SWO).[25] The former can be prepared from the Nd_2WO_6-related structure, Sm_2MoO_5 by H_2 reduction at 850 °C. The Nd_2WO_6-type structure contains oxygen rich dense layers of face and edge-shared $M'O_6/M'O_8$ (M' = Ln^{3+}) polyhedra, and oxygen deficient layers of edge and corner shared $M''O_5/M'O_7$ polyhedra (M'' = TM^{6+}; M' = Ln^{3+}) along the b-c plane in *I2/a* (Figure 1d).[25] The unique layered type structure suggests that electrons and oxides can move readily along the b-c plane. Experimental results showed that small divalent cations (e.g., Ca^{2+}) are susceptible to substitute for the trivalent cations in the structure, while tetravalent ions (e.g., Ce^{4+}) cannot substitute for hexavalent ions (e.g., Mo^{6+}), which may relate to the size/charge mismatch.

Sm_2MoO_6 showed a structural transformation from Nd_2WO_6-type structure to Sm_2MoO_5 as Mo^{6+} was reduced to lower valences in wet H_2. Both DC and AC methods confirmed that Sm_2MoO_5 (SMO) and $Sm_2WO_{6-\delta}$ (SWO) are very conductive in H_2 even at a low temperature and $Sm_{1.9}Ca_{0.1}MoO_{6-\delta}$ exhibited resistivity of ~10 Ωcm at 275 °C. The highest total conductivity of ~ 0.12 Scm^{-1} at 550 °C was obtained for SMO in dry H_2 as shown in Figure 6.[25] Interestingly, the activation energies of the same samples in wet H_2 are quite significantly lower and are in the range of 0.07-0.52 eV, except for CMO.

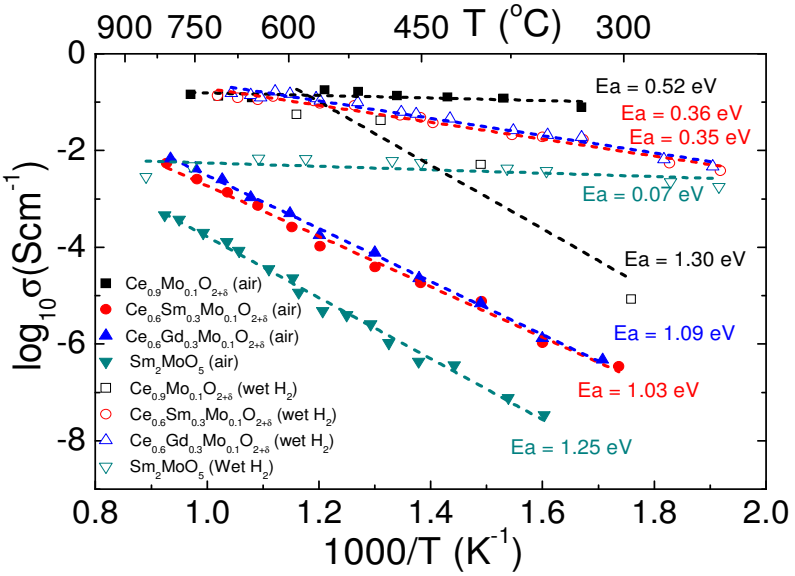


Figure 6. Comparison of the electrical conductivity of $Ce_{0.9}Mo_{0.1}O_{2+\delta}$ (air), $Ce_{0.6}Sm_{0.3}MoO_{2+\delta}$ (air), $Ce_{0.6}Gd_{0.3}Mo_{0.1}O_{2+\delta}$ (air), Sm_2MoO_5 (air), $Ce_{0.9}Mo_{0.1}O_{2+\delta}$ (wet H_2), $Ce_{0.6}Sm_{0.3}Mo_{0.1}O_{2+\delta}$ (wet H_2), $Ce_{0.6}Gd_{0.3}Mo_{0.1}O_{2+\delta}$ (wet H_2) and Sm_2MoO_5 (wet H_2).[15,20-22]

6. Conclusions

In summary, we have investigated four new families of inorganic structures, including perovskites, fluorites, Sr_2PbO_4-type Sr_2CeO_4, and Nd_2WO_6-type Sm_2MoO_5 (SMO) and $Sm_2WO_{6-\delta}$ (SWO) as potential MIECs for advanced SOFCs. The early transition metal-doped $Ba_3CaNb_2O_9$ can be sintered at a relatively low temperature of 1400 ^oC and showed mixed conductive properties in wet H_2 atmosphere in the intermediate temperature of 400-600 ^oC. The nano-CMO samples were found to be tolerant to H_2S (ppm level) in fuels at 700 ^oC. The roles of Pr in $Sr_2Ce_{1-x}Pr_xO_4$ were to improve the thermal stability and increase the reducibility of Ce/Pr ions in reducing atmospheres. Among the investigated MIECs, SMO showed the total conductivity of ~ 0.12 Scm^{-1} at 550 ^oC in dry H_2.

Acknowledgements

This research was financially supported by SOFC Canada NSERC Strategic Research Network and other sponsors listed at www.sofccanada.com. W. H. K. thanks for AITF scholarship. B. M. thanks for NSERC PGSD scholarship. H. T. H. thanks the Arab Republic of Egypt Fellowship scholarship program. We thank the Canada Foundation for Innovation (CFI) for providing funding for the X-ray facility.

References

1. A. Atkinson, S. Barnett, R. J. Gorte, J. T. S. Irvine, A. J. McEvoy, M. Mogensen, S. C. Singhal, J. Vohs, *Nat. Mater.* 3, 17(2004).
2. E. Perry Murray, T. Tsai, S. A. Barnett, *Nature* 400, 649(1999).
3. S. Park, J. M. Vohs, R. J. Gorte, *Nature* 404, 265(1999).
4. Z.-L. Zhan, S. A. Barnett, *Nature* 308, 844(2005).
5. S. Tao, J. T. S. Irvine, *Nature Mater.* 2, 320(2003).
6. Y.-H. Huang, R. I. Dass, Z.-L. Xing, J. B. Goodenough, *Science* 312, 254(2006).
7. L. Yang, S. Wang, K. Blinn, M. Liu, Z. Liu, Z. Cheng, M. Liu, *Science* 326, 126(2009).
8. W. C. Chueh, Y. Hao, W. Jung, S. M. Haile, *Nat. Mater.* 11, 155(2012).
9.V. Thangadurai, W. H. Kan, B. Mirfakhraei, S. Bhella, T. T. Trinh, *ECS Trans.* 35, 483(2011).
10. K. C. Liang, Y. Du, A. S. Nowick, *Solid State Ionics* 69, 117(1994).
11. W. H. Kan, T. T. Trinh, T. Fürstenhaupt, V. Thangadurai, *ECS Trans.* 35, 1259(2011).
12. W. H. Kan, T. T. Trinh, T. Fürstenhaupt, V. Thangadurai, *Can. J. Chem.* 89, 688(2011).
13. W. H. Kan, V. Thangadurai, *RSC Adv.* 3, 23824 (2013)

14. T. Pannu, K. G. S. Pannu, V. Thangadurai, *Inorg. Chem.* 50, 647(2011).
15. Q. Li, V. Thangadurai, *Fuel Cells* 9, 684(2009).
16. Q. Li, V. Thangadurai, *ECS Trans.* 28, 213(2010).
17. B. Mirfakhraei, V. I. Birss, V. Thangadurai, S. Paulson, K. E. Béré, F. Gitzhofer, *ECS Trans.* 35, 1727(2011).
18. Y. Chen, J. Bunch, C. Jin, C. Yang, F. Chen, *J. Power Sources* 204, 40(2012).
19. H. T. Handal, K. Singh, Q. Li and V. Thangadurai, *ECS Trans.* 45, 453(2012).
20. Q. Li, V. Thangadurai, J. Mater. Chem. 20 (2010) 7970.
21. H. T. Handal, V. Thangadruai, Solid State Ionics (2013) (in-press).
22. K. Singh, V. Thangadurai, Solid State Ionics (2013) (in-press).
23. R. G. Gerlach, S. S. Bhella, V. Thangadurai, *Inorg. Chem.* 48, 257(2009).
24. W. H. Kan, V. Thangadurai, *Inorg. Chem.* 51, 8973(2012).
25. Q. Li, V. Thangadurai, *J. Power Sources* 196, 169(2011).

Fuel Cell Materials II

PERFORMANCE OF IT-SOFC USING NOVEL NANOSTRUCTURED: $DY_{1-X}BA_XSR_{0.5}CO_{0.8}FE_{0.2}O_{3-\delta}$ (DBSCF) AND DBSCF-DOPED CERIA COMPOSITE AS CATHODE

S. A. Acharya

Department of Physics, Functional Materials Research Laboratory,
RTM Nagpur University, Nagpur-440033, M.S., India
Email :saha275@yahoo.com

Nanostructured novel system of cathode material $Dy_{1-x}Ba_xSr_{0.5}Co_{0.8}Fe_{0.2}O_{3-\delta}$ (x=0, 0.05, 0.10, 0.15, 0.20, DBSCF-x) are synthesized by hydrothermal route. The pervoskite structure with orthorhombic symmetry are confirmed for all the compositions by X-ray diffraction of as-synthesized powders. Transmission electron microscopy (TEM) images of as-synthesized DBSCF indicates nanoscale particles having size varying between 10-20 nm. Nanocomposite cathodes DBSCF(x)-SDC ($Ce_{0.80}Sm_{0.20}O_{2-\delta}$) are prepared by mechanical mixing of individually obtained DBSCF and SDC nanopowders. Electrolyte-supported Intermediate temperature Solid Oxide Fuel Cells NiO-SDC/SDC/DBSCF and NiO-SDC/SDC/DBSCF-SDC are prepared using spin coating method. SDC are used as the electrolytes with a thickness of about 500 μm each; on one side layer of DBSCF/DBSCF(x)-SDC as cathode and on another side layer of NiO-SDC as anode are deposited and sintered at 1100°C for 2 h. The area specific resistance of DBSCF(x)-SDC and DBSCF(x) with SDC as electrolyte are all lower than 0.185 Ωcm^2 and 0.038 Ωcm^2 at 600°C, respectively. The maximum power density of single cell with composite cathode achieve as 1100 $mWcm^{-2}$ at 600°C with the change of x= 0 – 0.1; however for pure cathode the maximum power density of single cell are obtained as 456-521 $mWcm^{-2}$. These result indiçâte that 50DBSCF0.1-50SDC composites are promising cathode material for IT-SOFCs.

1. Introduction

Development of novel oxides structure with high mixed ionic and electronic conductivity is the current need in order to reduce the operating temperature and enhance the performance of solid oxide fuel cell (SOFC). The considerable decrease of polarization resistance of cathode enables to reduce the operation temperature of SOFC to the intermediate range (400-600°C). Mixed conducting oxide and pervoskite and pervoskite-related intergrowth structure such as $Ln_{1-x}Sr_xMO_3$ (M = Mn, Fe, Ni and Co) [1-3], $Ln_2NiO_{4+\delta}$ [4-5], $LnBaCO_2O_{5+\delta}$ [6-9], $NdBaCo_{2-x}Cu_xO_{5+\delta}$ [10-13], $GdBaCo_{1.0}Cu_{1.0}O_{5+\delta}$ [14-17], $La_{1-x}Sr_xCo_{1-y}Fe_yO_{3-\delta}$ have been widely investigated as cathode candidates [18-24]. Despite the large improvement in the area-specific resistance (ASR) these materials do not

Proceedings of the 14th Asian Conference on Solid State Ionics (ACSSI 2014)
Copyright © 2014 ACSSI 2014 Organizers. All rights reserved.
ISBN: 978-981-09-1137-9
doi:10.3850/978-981-09-1137-9_045

perform well in the temperature range of 400-600^{0}C. Amongst this cobalt based pervoskite type oxide exhibit excellent electrochemical properties in combination with doped ceria electrolytes. The cobalt containing cathodes studied most in literature seem to be composition of $Sm_{0.5}Sr_{0.5}CoO_{3-\delta}$ or $La_{0.6}Sr_{0.4}Fe_{0.8}Co_{0.2}O_{3-\delta}$ with ceria based electrolytes [25-26]. With this background, in the present attempt we develop novel mixed pervoskite based system $Dy_{1-x}Ba_xSr_{0.5}Co_{0.8}Fe_{0.2}O_{3-\delta}$ with Sm-doped ceria.

One of the interesting features of ABO_3 pervoskite is that their physicochemical properties can be influenced by partial substitution of A and / or B sites with minimal changes in structure. The intrinsic properties of cathode materials depend on the material composition and lattice structure. Generally, A site cation responsible to tune the physiochemical properties and B site cations association with the redox catalytic mechanism. If A-site cation is partially substituted by larger cations results in the expansion in the cell volume and the reduction in binding energy of system, which facilitate the oxygen exchange kinetics on the surface of oxide, consequently leads to an improvement in the cathode performance. In the present work, Ba^{2+} is selected as dopant to partial substitute Dy^{3+} in DSCFO system. The corresponding change in electrical conductivity and electrochemical performance were systematically investigated. To enhance electrochemical performance electrode-electrolyte composite DBSCF-SDC are also developed and studied.

2. Experimental

2.1 Sample synthesis

$Dy_{0.5-x}Ba_xSr_{0.5}Co_{0.8}Fe_{0.2}O_{3-\delta}$ (DBSCF, x = 0, 0.02, 0.04, 0.08, 0.1) powders were synthesized by ethylene glycol-citrate combined sol-gel process. $Dy(NO_3)$, $Sr(NO_3)_2$, $Fe(NO_3)_2.9H_2O$ and $Co(NO_3)_2.6H_2O$ were used as raw materials. Stoichiometric amounts of these raw materials were dissolved into distilled water to form a solution. Into which ethylene-glycol and $NH_3.H_2O$ and citric acid were added in sequence at a molar ratio of 1:1:2 for total metal ions:ethylene glycol:citric acid, under heating and stirring. The solution was introduced into Teflon cup and placed in autoclave for heat treatment 180^{0}C for 18 hrs. The colloidal particles are separated from liquid by centrifugation. To remove unreacted residues the samples were washed three times by double distilled water. To develop electrolyte-electrodes composite cathode Sm-doped ceria $Ce_{0.85}Sm_{0.15}O_{2-\delta}$ (SDC) was synthesized as per reported elsewhere [27]. The DBSCF and SDC are mixed together in different proportion by mechanical

mixing to obtained composites (1-x)DBSCF-xSDC for (x = 0, 0.20, 0.30, 0.40 and 0.50).

2.2 Cell fabrication

For electrical conductivity measurement the powders were uniaxially pressed and sintered at 1200°C for 5 h. to fabricate the symmetric cells, the SDC powder was pressed into disk-shaped pellets under a pressure of 7 tons, followed by sintering at 1200°C for 5 hr in air. The resulted dense pellets having relative density 94%, diameter 12.8 mm and thickness 1 mm. To prepare the electrode layers DBSCF/ DBSCF-SDC suspension dispersed in mixed solution of ethylene glycol, ethanol and isopropyl alcohol was symmetrically deposited onto both surfaces of the electrolyte by spin-coating, followed by calcinations at 1000°C for 2 h. Both electrodes surfaces of symmetric cells were painted with thin layers of silver to acts as current collectors.

To fabricate the electrolyte-supported single cell for the measurement of power density of NiO_2 and SDC in the weight ratio of 40:60 was spin coated on one side of SDC pellet. The pellet was sintered at 1200°C in air to get good contact of electrolyte-anode. The DBSCF/ DBSCF-SDC suspension was spin coated over the other surface of the electrolyte followed by calcinations at 1000°C for 2 hrs in air.

3. Characterization

The phase of the synthesized powders were studied using Bruker AXS D8 Advance X-ray diffractometer equipped with a copper target (CuKα = 1.5405 Ao). The microstructure were viewed by JEOL, JSM, 6380 Analytical SEM. The transmission electron microscopy (TEM) images were obtained using a Technai 20 G^2 operated at 200 kV. The samples were prepared by dispersing the samples in N,N dimethylformamide (DNF) and placing a drop of liquid on carbon-coated Formvar grids. Electrical conductivity was measured by the four-probe D.C. technique. The electrical conductivity measurements were performed from 300 to 800°C at

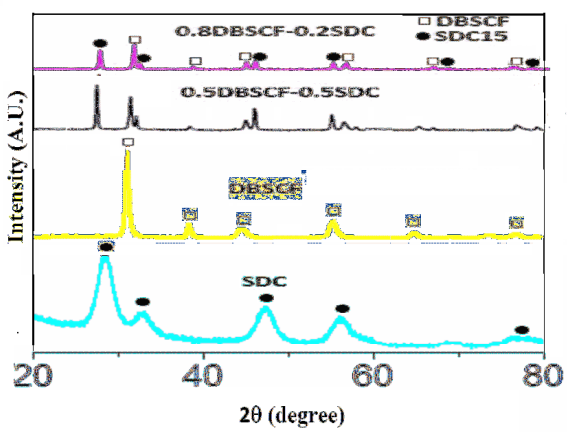


Fig 1: XRD pattern of SDC, DBSCF individual phases and composite phases

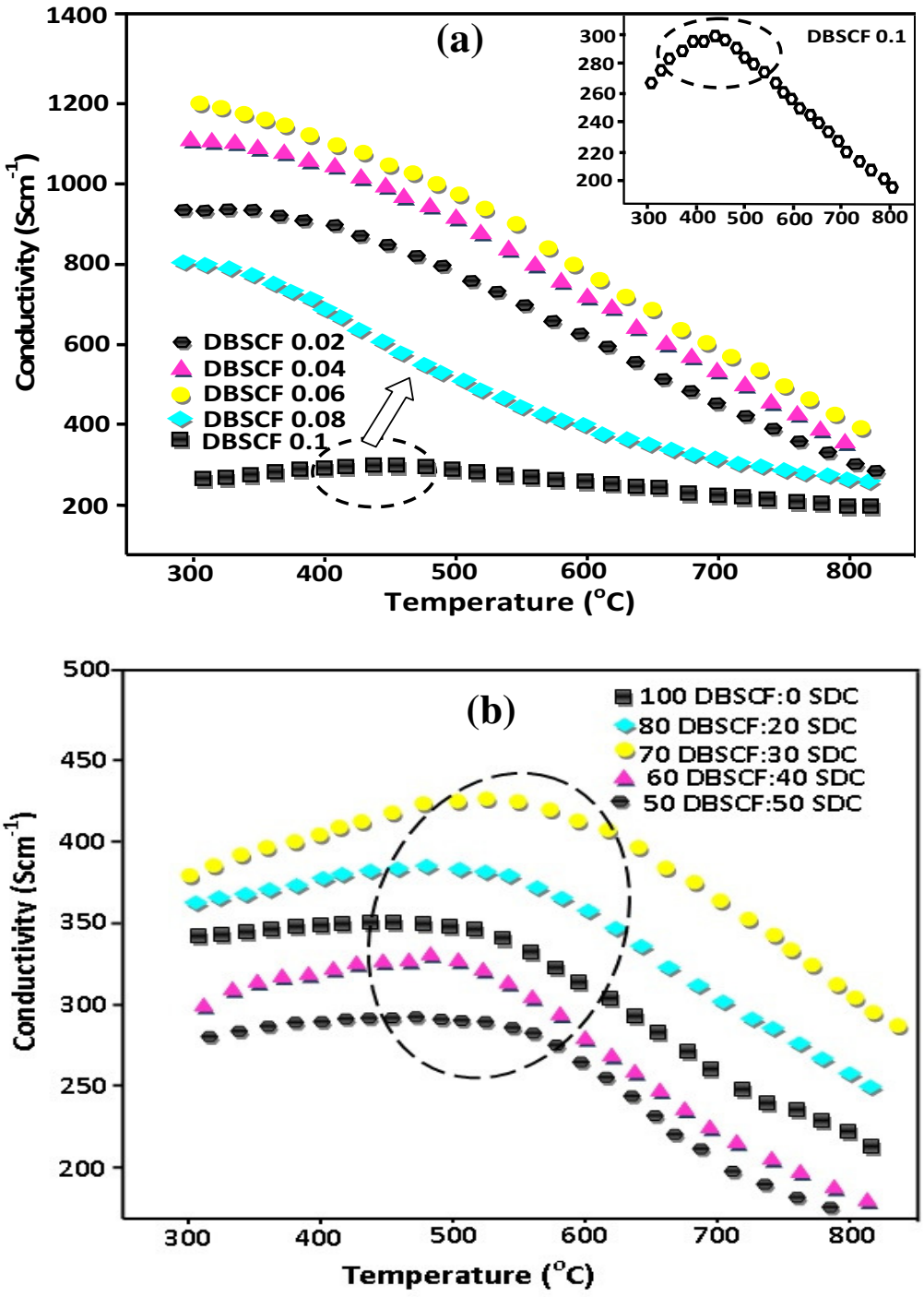


Fig 2: Electrical conductivity of (a) DBSCF for different Ba^{2+} percentage and (b) DBSCF-SDC for different composition

the intervals of 10°C in air. The current and voltage were detected by a keithley 2420 source meter.

Indigenously developed fuel cell test station was used to study the electrochemical performance of the fabricated fuel cell. The fuel cell was sealed into a quartz tube using silver paste to form an anode chamber, which was then heated at 650°C at the rate of 2°C/min and held for 5 h to set the seal. Hydrogen at a flow rate of 20 ml/min was introduced into an anode chamber to begin in situ reduction of anodic NiO_2 to metallic nickel. After about 5 h, the hydrogen flow rate was increased to 80 ml/min and bubbled through water at 25°C for IV cell polarization test. During the test, the cathode was exposed to the ambient atmosphere, I-V curves were collected at 50°C intervals over a temperature range of 400 – 550°C using digital source meter.

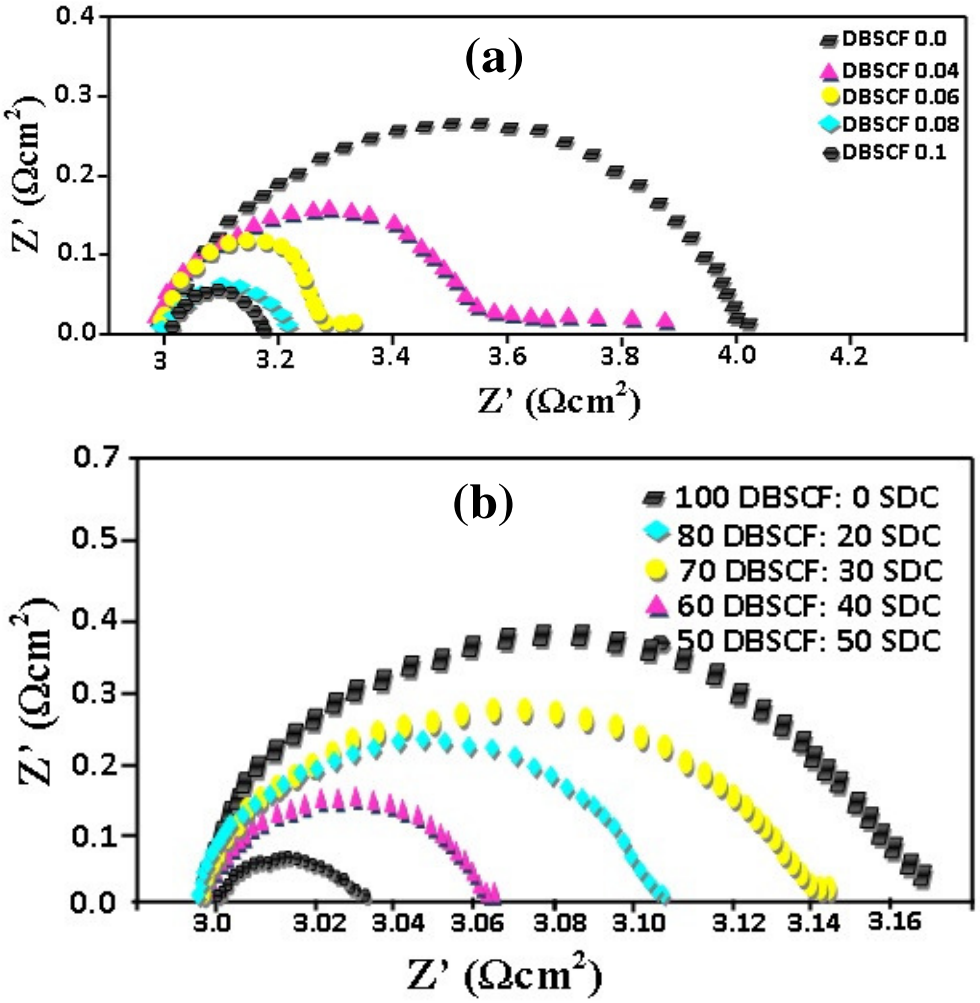


Fig 3: Impedance spectra (a) DBSCF-x (b) DBSCF-SDC composites

4. Results and discussion

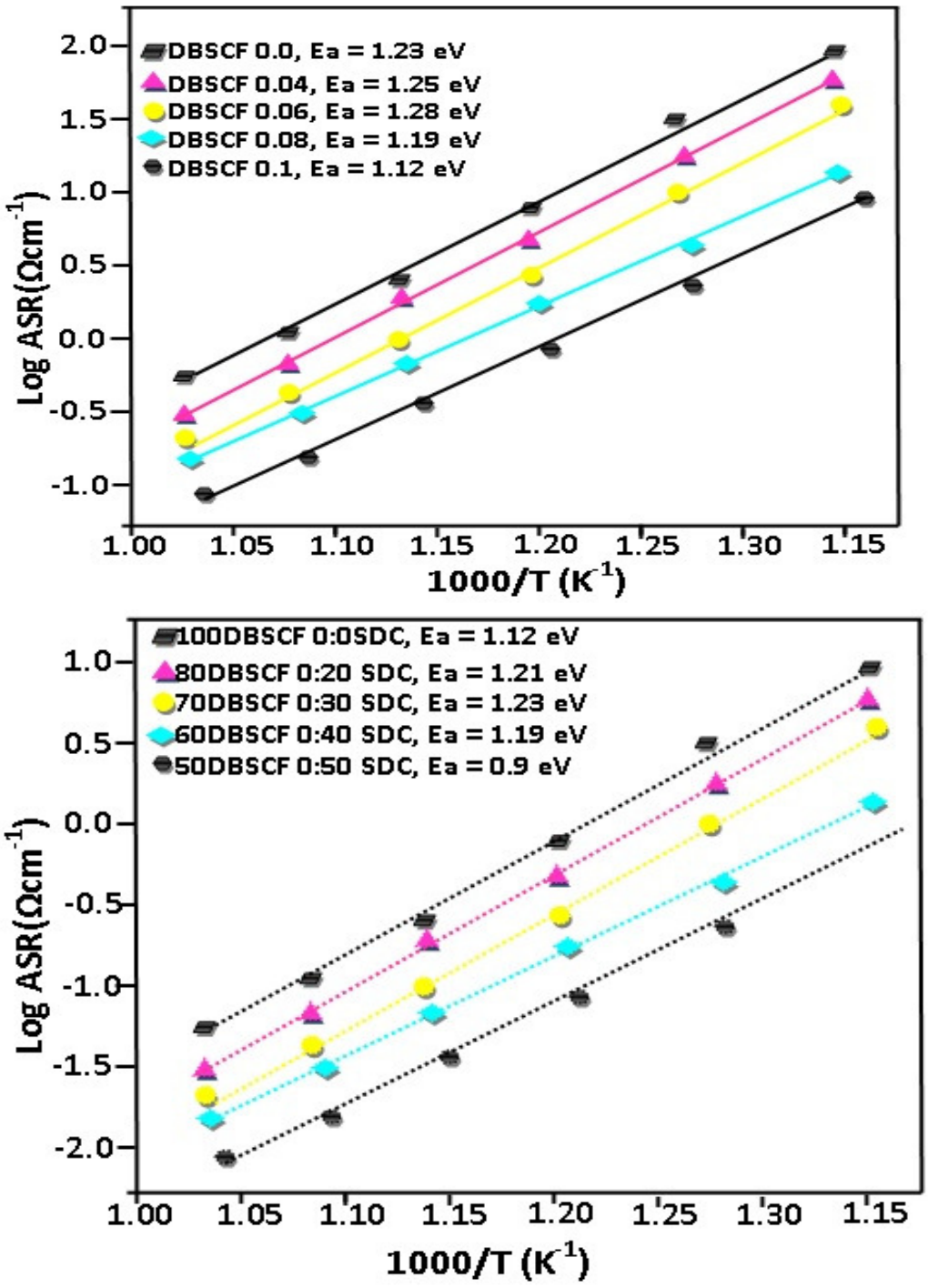


Fig 4: Arrhenius plot (a) DBSCF-x and (b) DBSCF-SDC

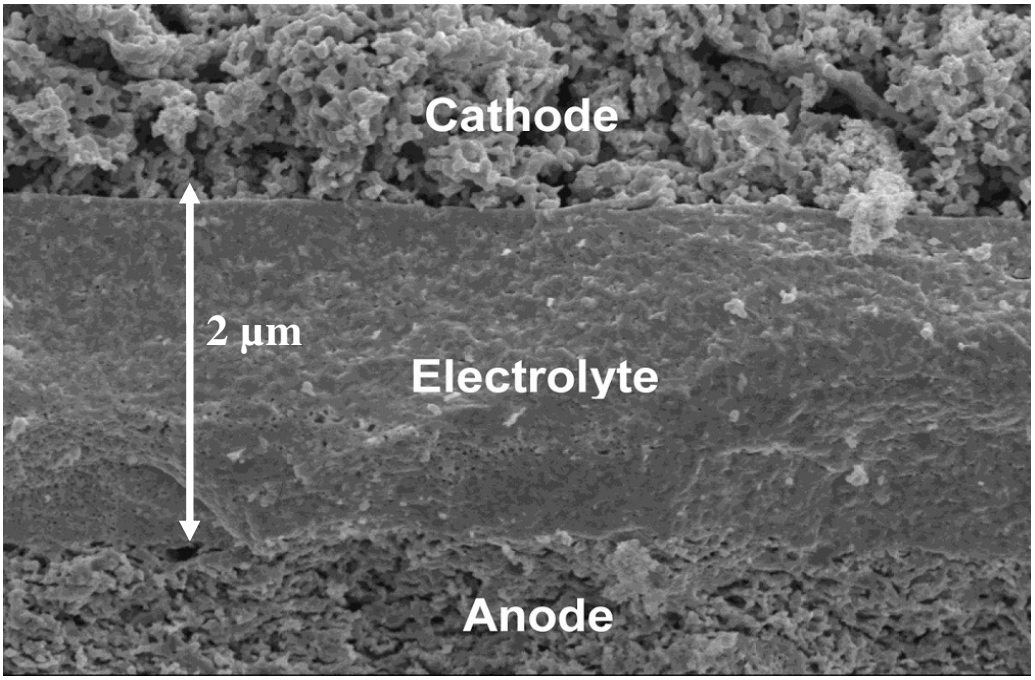


Fig 5: SEM images of Ni-SDC/SDC/50DBSCF-50SDC

The XRD patterns of SDC, DBSCF individual phase and DBSCF-SDC composite phases are shown in Fig 1. All XRD patterns of DBSCF indicate single phase structure and match with perovskite structure with orthorhombic symmetry (JCPDS file no 53-0112). SDC match with fluorite structure of cubic symmetry. For electrodes-electrolytes composite two phases related to SDC as well as DBSCF are observed indicate formation of composite.

5. Electrical conductivity

The Ba^{2+} concentration dependent electrical conductivity of DBSCF is shown in Fig 2. It is obvious that the substitution of Ba^{2+} for Dy^{3+} has significant effect on the electrical conductivity. The electrical conductivity of the composition with x = 0.04 and 0.06 are higher than that of the barium free composition. However increase of Ba^{2+} concentration above 0.06 results in decrease of electrical conductivity DBSCF. As the cation of Dy^{3+} in the A site is replaced by the lower valence cation Ba^{+}, according to the principle of the electron neutrality, the –ve charge is balanced by the formation of higher oxidation state ion at B-site or by the formation of oxygen vacancies. Electrical conductivities are consistently decreases with increasing temperature which is in accordance with metallic like conductivity behavior. For 0.1 Ba^{2+} concentrations, a lowest trend of electrical

conductivity is observed. It can be considered as optimized Ba^{2+} percentage for further study. The functionality of this system is improved by developing electrode-electrolyte composites (100-x)DBSCF0.1 – xSDC, (x = 10 - 50). Electrical conductivity is also found varying with changing the proportion of DBSCF to SDC. Comparative electrical conductivity is lowest for 50DBSCF-50SDC.

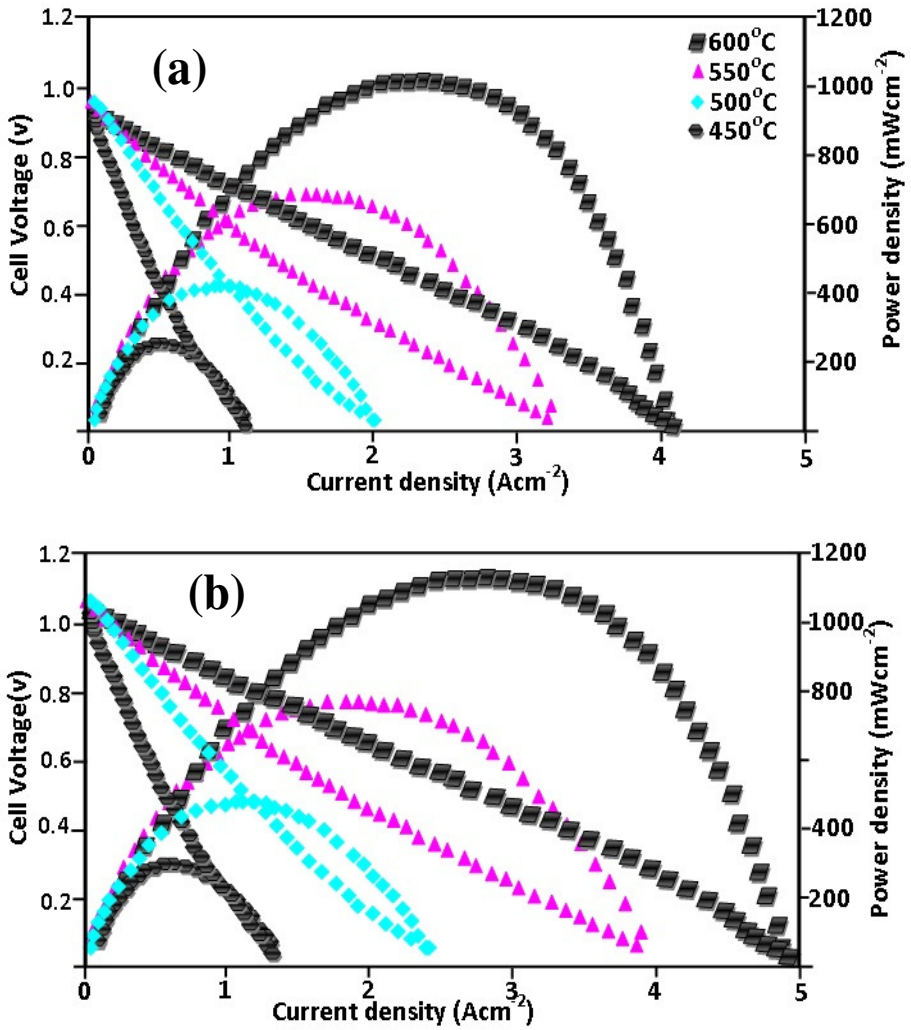


Fig 6: Cell voltage (left) and power density (right) as a function of current density of (a)DBSCF0.1 composition and (b) 50DBSCF0.1-50SDC composites

6. Impedance analysis

The variation of the impedance spectra of DBSCF with Ba^{2+} concentration and DBSCF-SDC at 550°C is shown in Fig 3 a and b, respectively. Impedance spectra of symmetric cell DBSCF/SDC/DBSCF and DBSCF-SDC/SDC/ DBSCF-SDC are tested in air under zero dc bias condition. It can be clearly observed from Fig 3a that the intercept of the impedance arc on the real axis decreases with increasing Ba^{2+} concentration, which indicates that the partial substitution of Ba^{2+} for Dy^{3+} results in a significant decrease in the interfacial polarization resistance Rp. Whereas in composite system, decrease in interfacial polarization resistance with increase in SDC composition in DBSCF-SDC composites are also observed (see Fig 3b). The interfacial polarization resistance of DBSCF for the composition x = 0.10 is found to be 0.185 Ωcm^2 and in composite for the composition of 50DBSCF-50SDC, it is found to be 0.038 Ωcm^2 at 600°C. All these system are found to be less than DSCF (1 Ωcm^2). The electrode-electrolyte composites are showing better performance than the single electrode system. These improvements are attributed to increase of oxygen vacancy concentration due to SDC electrolyte material composition which leads to oxygen reactivity.

The area specific resistance can be calculated using the following equation : $ASR = R_p S/2$, where S is the cathode surface, Rp is the difference between two intercepts at high and low frequencies at the real axis. The coefficient 2 of the denominator accounts for the fact that the cell is symmetrical.

The Arrhenius plots of the area specific resistance of DBSCF and DBSCF-SDC systems are shown in Fig 4a and b, respectively. From Fig 4a, it can be clearly observed that the area specific resistance is consistently decreases with Ba content, specifically from 0.63 Ωcm^2 for DSCF to 0.35 Ωcm^2 for composition with x = 0.1 at 550°C. However for 50DBSCF-50SDC composites, it is found 0.08 Ωcm^2 (see Fig 4b). The activation energy is in range of 1.23 to 1.12 eV for DBSCF and 1.12 to 0.91 eV for DBSCF-SDC composites.

Oxygen reduction at a porous cathode include a sequence of steps: (i) adsorption of oxygen from the gas phase to the surface of the porous cathode, (ii) dissociation of adsorbed oxygen molecules into atomic oxygen at the active sites, (iii) diffusion of O^{2-} ion through the cathode across the cathode/electrolyte interface and into the electrolyte. Cathode polarization resistance is closely related not adsorption/dissociation of oxygen but also to the transport speed of oxide ions through the cathode bulk and across the cathode/electrolyte interface. Therefore, the kinetics of the oxygen exchange and diffusion of oxide ions in the cathode as well as the electronic conductivity play a critical role on the oxygen

reduction reaction. Hence composite cathode exhibits more reaction activity than individual electrode system. Similarly Ba^{2+} as dopants to substitutes Dy^{3+} also is found enhancing electrode activity as compared to dopant free system.

7. Performance of single cell of SOFC with DBSCF and DBSCF-SDC as cathode

The SEM images of Ni-SDC/SDC/DBSCF0.1 and Ni-SDC/SDC/50DBSCF-50SDC as shown in Fig 5 demonstrates that all cathodes are well adhere to all electrolyte surface. Fig 6 shows the power density (right) and voltage (left) as a function of current density for the cells using H_2 as fuel and static air as oxidant in the temperature range 400-600^{o}C, respectively. The maximum power density (Pmax) at 600^{o}C reaches 1000 mwcm^{-2} and 1100 mwsm^{-2} for DBSCF0.1 and 50DBSCF0.1-50SDC, respectively. This means that composites cathode materials delivers remarkable power output at intermediate temperature range.

8. Conclusion

In this work DBSCF pervoskite with an orthorhombic structure is prepared by a hydrothermal route. The effect of Ba^{2+} substituent for Dy^{3+} on the structure and electrochemical properties on $Dy_{0.5}Sr_{0.5}Co_{0.8}Fe_{0.2}O_{3-\delta}$ are investigated. The functionality of DBSCF as cathode is optimized by developing electrode-electrolytes (DBSCF-SDC) composite systems. The studied 10 different cathode systems, the area specific resistance and power density for 50DBSCF-50SDC0.1 the cathode system is found to be highest. The system exhibits high potential to use as cathode for intermediate temperature solid oxide fuel cell.

Acknowledgments

The authors SAA want to acknowledge financial support from DST, New Delhi, India under project of SR/FTP/PS-106/2009 (G) and UGC under MRP F.N. 41-871/2012.

References

1. J.M. Ralph, C. Rossignol, R. Kumar, J. Electrochem. Soc. **150 (11)**, A1518 (2003).
2. B. Wei, Z. Lü, X. Huang, M. Liu, N. Li, W. Su, J. Power Sources **176** (1), 1 (2008).
3. H.E. Shinawi, C. Greaves, J. Solid State Chem **181**, 2705 (2008).
4. Q. Li, Y. Fan, H. Zhao, L.P. Sun, L.H. Huo, J. Power Sources **167**, 64 (2007).
5. Y.N. Kim, J.H. Kim, A. Manthiram, J. Power Sources **195**, 6411 (2010).

6. S.M. Haile, Acta Mater. 51, 5981 (2003).
7. J.H. Kim, Y. Kim, P.A. Connor, JT.S. Irvine, J. Bae, W. Zhou, J. Power Sources 194, 704 (2009)
8. D. Chen, R. Ran, K. Zhang, J. Wang, Z. Shao, J. Power Sources **188**, 96 (2009)
9. J.H. Kim, M. Cassidy, T.S. John, J. IrvineBae, J. Mater. Chem. **22**, 883 (2010).
10. Y.F. Cheng, H.L. Zhao, D.Q. Teng, F.L. Li, J. Membr. Sci. **322**, 484 (2008).
11. K.T. Lee, A. Manthiram, J. Electrochem. Soc. **152**, A197 (2005).
13. K.T. Lee, A. Manthiram, Solid State Ionics **176**, 1521 (2005).
14. A.A. Taskin, A.N. Lavrov, Y. Ando, Physical Reviews B **71**, 28 (2005).
15. A.A. Taskin, A.N. Lavrov, Y. Ando, Applied Physics Letters **86**, 3 (2005).
16. A.A. Taskin, A.N. Lavrov, Y. Ando, Progress in Solid State Chemistry **35** 481 (2007).
17. C.R. Xia, W. Rauch, F.L. Chen, M.L. Liu, Solid State Ionics **149**, 11 (2002).
18. M. Rieu, R. Sayers, M.A. Laguna-Bercero, S.J. Skinner, P. Lenormand, F. Ansart, Electrochem. Soc. Trans. **25**, 2565 (2009).
19. A. Esquirol, J. Kilner, N. Brandon, Solid State Ionics 175, 63 (2004).
20. F. Zhao, X. Wang, Zh. Wang, R. Peng, Ch. Xia, Solid State Ionics **179**, 1450 (2008).
21. H.-G. Jung, Y.-K. Sun, H.Y. Jung, J.S. Park, H.-R. Kim, G.-H. Kim, H.-W. Lee, J.-H. Lee, Solid State Ionics **179**, 1535 (2008).
22. S. Bebelis, N. Kotsionopoulos, A. Mai, D. Rutenbeck, F. Tietz, Solid State Ionics **177**, 1843 (2006).
23. V. Sadykov, S. Pavlova, V. Zarubina, A. Bobin, G. Alikina, A. Lukashevich, V. Muzykantov, V. Usoltsev, T. Kharlamova, A. Boronin, S. Koscheev, T. Krieger, A. Ishchenko, N. Mezentseva, A. Salanov, A. Smirnova, O. Bobrenok, N. Uvarov, Electrochem. Soc. Trans. **25**, 2403 (2009).
24. V. Sadykov, T. Kharlamova, L. Batuev, N. Mezentseva, G. Alikina, V. Muzykantov, T. Krieger, S. Pavlova, V. Zaikovskii, A. Ishchenko, V. Zarubina, V. Rogov, O. Bobrenok, N. Uvarov, J. Kilner, J. Druce, A. Smirnova, Mater. Res. Soc. Symp. Proc. **1098**, 1-1098-HH07-06 (2008).
25. M. Sahibzada, B.C.H. Steele, K. Zheng, R.A. Rudkin, J.M. Bae, N. Kiratzis, I.S. Metcalfe, in: Proc. 2nd European Solid Oxide Fuel Cell Forum, Oslo. **687**, (1996).
26. E.P. Murray, M.J. Sever, S.A. Barnett, Solid State Ionics 148, 27 (2002).
27. S.A. Acharya, Journal of Power Sources 198, **105** (2012).

PROCESS FOR MASS PRODUCTION AND CHARACTERIZATION OF ZIRCONATES BY AN OPTIMIZED SOLID-STATE REACTION METHOD

JINDUO HAN, ZHAOYIN WEN,* JINGCHAO ZHANG,
XIAOWEI CHI, HENG LIU, GUOQIANG MA

Shanghai Institute of Ceramics, Chinese Academy of Sciences

1295 Dingxi Road, Shanghai, China, Tel: +86 21 5241 2054, Fax: +86 21 5241 3903

Taking the formation mechanism of zirconate based on the reaction between the decomposed carbonate precursor and ZrO2 of the raw material as a guide, an optimized solid state reaction process was applied to prepare various carbonate powders and their ceramics. The size of the final particles was mainly dependent on the size of the starting ZrO2 powders. The fast, cheap, reproducible solid-state reaction process was practically easy to adjust the particles size in the range from nano to micro scale. The optimized process offers a route for mass production of the zirconate powder and high quality ceramics.

Keywords: Zirconate, Solid-state reaction, ZrO2, Mass production, Proton conductor

Keywords: Solid Polymer Electrolytes, High-energy Ball Milling, Nano-ionic Effect, Ionic Conductivity.

1. Introduction

Due to the excellent dielectric, electrochemical and thermal properties, zirconates are of great interests for many applications as electronic systems [1], fuel cells [2-6], hydrogen sensors [7] and buffer layer for coated conductors [8]. Moreover, the zirconate powders can be used in the manufacturing process of passive crucibles [9] suitable for the synthesis of single crystals, growth of electroceramic oxides, such as high-critical temperature superconducting materials. For such practical applications, the relative density of the ceramics is a key factor that would greatly influence their overall performance. To fabricate dense ceramics, well-distributed and highly reactive powders should be prepared first. Therefore, a lot of studies have been concentrated on the preparation and characterization of zirconate materials.

* E-mail address: zywen@mail.sic.ac.cn, Tel: +86 21 5241 2054, Fax: +86 21 5241 3903,

Proceedings of the 14th Asian Conference on Solid State Ionics (ACSSI 2014)
Copyright © 2014 ACSSI 2014 Organizers. All rights reserved.
ISBN: 978-981-09-1137-9
doi:10.3850/978-981-09-1137-9_079

Solid-state reaction method has been the most traditional way for the synthesis of zirconate powders [10]. However, its main disadvantages, such as large structural and compositional inhomogeneities, high calcining and sintering temperatures, prohibited its practical application. Several processes have been investigated to obtain high activity powders suitable for sintering dense ceramics at lower temperature. For example, a co-precipitation method was applied to synthesis sub-micron $CaZrO_3$ powders (200nm) at 1000°C [11]. A molten salt synthesis method was used to prepare 0.5-1.0μm sized $CaZrO_3$ powders at 1050°C by heating a mixture of $CaCl_2$, $NaCO_3$ and ZrO_2 [12]. High-energy ball milling method was applied to activate reactants and subsequently obtain nanocrystalline $CaZrO_3$ powders by heating the activated precursors at 1000°C for 2h [13]. Although the powders prepared by these methods exhibited small particle size and good homogeneity features, the disadvantages, such as the complex procedures, long soaking time, high energy-consumption and low yield, prohibited their practical applications [14-16].

In order to actually implement the application of zirconates, the synthesis method should scale-up from the research lab to mass production firstly. Our earlier studies on the formation mechanism and kinetics of $CaZrO_3$ from $CaCO_3$ and ZrO_2 showed that the formation of the zirconate was based on the reaction of CaO decomposed from $CaCO_3$ with ZrO_2, and the formation kinetics was well described by the Ginstling-Brounshtein model [17]. In the present study, in addition to the above calcium zirconate, the preparation of barium zirconates as well as strontium zirconate by the optimized solid-state reaction method are studied, characterization and comparison of their properties with the zirconates synthesized by the traditional solid-state reaction method are also carried out.

2. Experimental

Fig.1 showed the flowchart of the optimized solid state reaction process to prepare zirconates with mass production capacity, By which stoichiometric amounts of more than 1000mol of the mixture of $CaCO_3$, (or $BaCO_3$, $SrCO_3$, 99.5%) and ZrO_2 powders (99.9%), In_2O_3 (99.99%) were ball-milled for 4h with ethanol as medium, as shown in Table 1, to get a narrowly distributed raw materials. Then the mixtures were dried, pulverised and sieved before calcining in a pusher kiln (Fig. 1(a)) at 1000°C for 6h to obtain $CaZr_{0.95}In_{0.05}O_{3-\delta}$ (denoted as O-CZIO-5), $BaZr_{0.95}In_{0.05}O_{3-\delta}$ (denoted as O-BZIO-5), $SrZr_{0.95}In_{0.05}O_{3-\delta}$ (denoted as O-SZIO-5) in several hundred kilogrammes, respectively. For comparison, zirconates were also prepared by the traditional solid-state reaction method by ball-milling the raw materials for 1h and then heat at 1200°C for 6h.

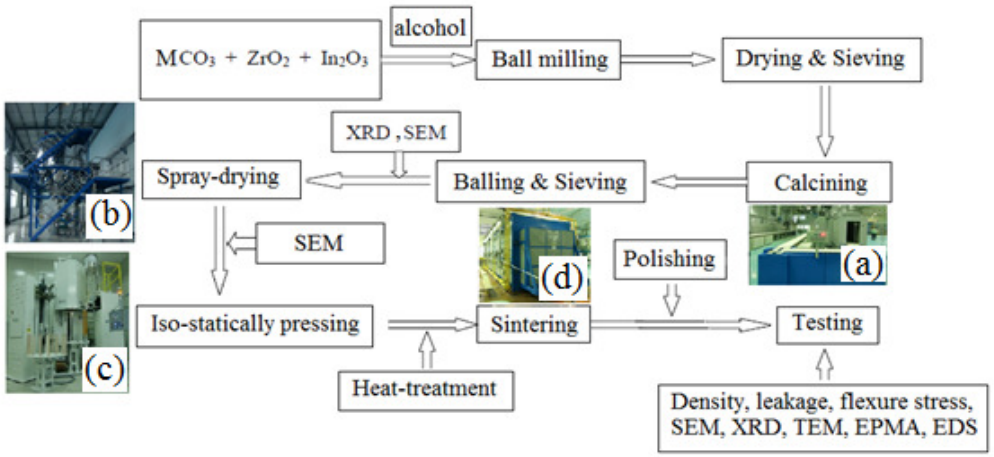


Fig.1. Flowchart of the optimized solid-state reaction method

To fabricate ceramics, the calcined powders were sieved and spray-dried with 2 wt% of PVB binder in the spray drying equipment (Fig.1 (b)) firstly. Then they were pressed into pellets at 4MPa, and cold iso-statically pressed at 200MPa (Fig.1 (c)). Afterwards, the pellets were undergone a heat-treatment at 600 ^{o}C for 2h to burn off the binders and finally sintered in the gas burning furnace (Fig.1 (d)) at the temperature of 1400 ^{o}C for 10h.

Formation of compounds and solid solubility were confirmed by an X-ray diffractometer (Rigaku RAD-C, CuKα, λ=1.54056Å). Morphology of them was characterized by field emission scanning electron microscopy (FESEM JSM-6700) and transmission electron microscopy (TEM, JEOL JEM-2010). Relative density of the ceramics was measured by Archimedes' principle with alcohol as medium. Leakage test was performed with the helium leak detector (ULVAC HELIOT 710). Flexure strength of the ceramics at room temperature was determined by the three point bending method (INSTRON-5500R) with rectangular bars (36×4×3mm) with a span length of 30mm and a crosshead speed of 0.5mm/min.

Platinum was used as block electrode for electrical conductivity measurements. The measurements were carried out by complex impedance method from 600 to 1000^{o}C in the 5% H_2 + 95% Ar atmosphere ($\log P(O_2)=10^{-6}$ and $\log P(H_2O)=10^{-6}$) on a Solartron 1260 impedance analyzer over the frequency range of 0.1Hz and 1MHz. The error of temperature control for the test was smaller than 1^{o}C.

Table 1. Influence of milling duration on the distribution of MCO_3/ZrO_2

Raw material	Milling time / min	Distribution of raw materials / μm
MCO_3	0	2.0~8.5
	30	1.5~6.5
	60	1.2~4
	120	1~2.5
	180	0.7~1.1
	240	0.5~0.7
	300	0.6~1.0
ZrO_2	0	0.4~1.0
	30	0.3~0.8
	60	0.25~0.6
	120	0.2~0.4
	180	0.15~0.2
	240	0.13~0.18
	300	0.16-0.2

3. Results and Discussion

As we have reported earlier, the formation mechanism of zirconates could be described by the following reactions:

$$MCO_3 \rightarrow MO + CO_2 \quad (1)$$

$$MO + 4ZrO_2 \rightarrow MZr_4O_9 \quad (2)$$

$$MZr_4O_9 + 3MO \rightarrow 4MZrO_3 \quad (3)$$

$$MO + ZrO_2 \rightarrow MZrO_3 \quad (4)$$

It was also found from the earlier report and Table 1 that the size and shape of the final particles were determined by the treating temperature and morphology of the starting ZrO_2 particles rather than MCO_3, because it would decompose into nano MO before the formation of $MZrO_3$.

The kinetics of the formation of $MZrO_3$ investigated by the thermal quench method could be well described by the Ginstling-Brounshtein model, and the reaction occurred in two stages as shown in Fig.2. During the first step, about 60% conversion was characterized by a high reaction rate with the formation of

MZr_4O_9 and $MZrO_3$. The second was characterized by a decrease of the reaction rate, and much longer time was required for complete transformation. The slower rate with the increase of time was ascribed to the product layer that would slow down the reaction between MO and ZrO_2.

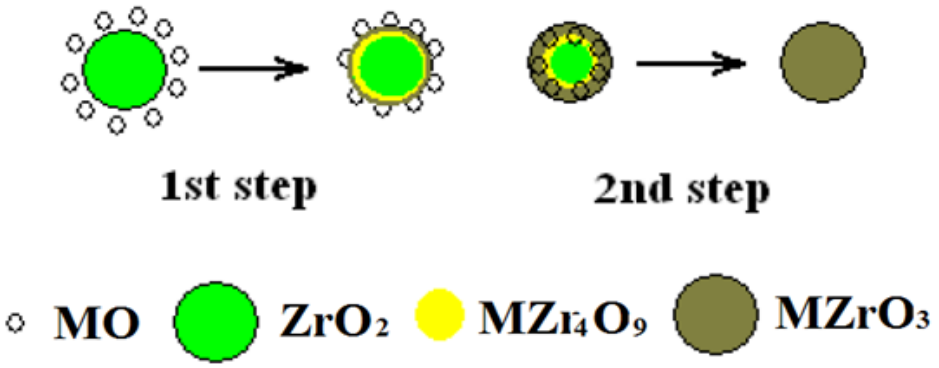


Fig.2. Kinetic model of the formation of $MZrO_3$

Fig.3 showed the green and sintered zirconate ceramics with different shapes as components used in fuel cells, hydrogen sensor, etc. The optimized solid-state reaction method provide a fast, cheap, reproducible, and easily scaled up method for obtaining different powders from nano to micron that can be used for sintering different ceramics.

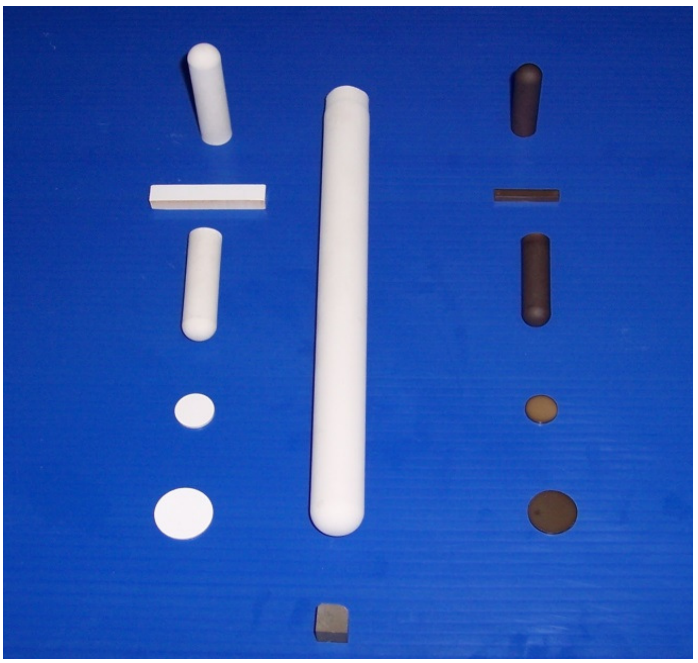


Fig.3. Various zirconate products

Table 2. Relative density, helium leakage rate and flexure stress of zirconates produced by the optimized and traditional solid-state reaction method

Method	Ceramics	Grain size (μm)	Relative density (%)
Optimized	O-CZIO-5	1.0~2.8	97.8±0.4
solid-state	O-BZIO-5	1.1~3.0	96.8±0.7
reaction	O-SZIO-5	1.0~3.0	97.3±0.7
Traditional	T-CZIO-5	2.5~6.8	92.3±1.6
solid-state	T-BZIO-5	3.1~8.0	90.7±2.7
reaction	T-SZIO-5	3.0~7.0	92.3±1.7

Method	Ceramics	Helium leak detection($Pa \cdot m^3 \cdot S^{-1}$)	Flexure stress (MPa)
Optimized	O-CZIO-5	$\leq 1.2\times10^{-9}$	203.5±8.2
solid-state	O-BZIO-5	$\leq 8.6\times10^{-9}$	190.8±16.9
reaction	O-SZIO-5	$\leq 3.8\times10^{-9}$	196.3±10.6
Traditional	T-CZIO-5	$\leq 7.9\times10^{-8}$	153.5±16.6
solid-state	T-BZIO-5	$\leq 5.6\times10^{-7}$	120.8±29.5
reaction	T-SZIO-5	$\leq 9.8\times10^{-8}$	146.3±18.6

Table 2 showed the relative density, helium leakage rate and the flexure stress of In-doped zirconates sintered at 1400°C for 6h. The results showed better properties that of the zirconates produced by the optimized solid-state reaction method than those synthesized by the traditional solid-state reaction method (denoted as T-CZIO-5, T-BZIO-5, T-SZIO-5 in the following). These results could be explained by the Hall-Petch equation.

$$\sigma_f = (\sigma_0 + K_1 d^{-1/2}) \exp(-nP) \qquad (5)$$

where σ_f and σ_0 are the mechanical strength with and without porosity, respectively, K_1 and n are the experimentally constants, d is the grain diameter and p is the porosity of the ceramics [18-19]. The above equation indicated that a smaller d and lower P could result in a higher σ_f of the ceramics.

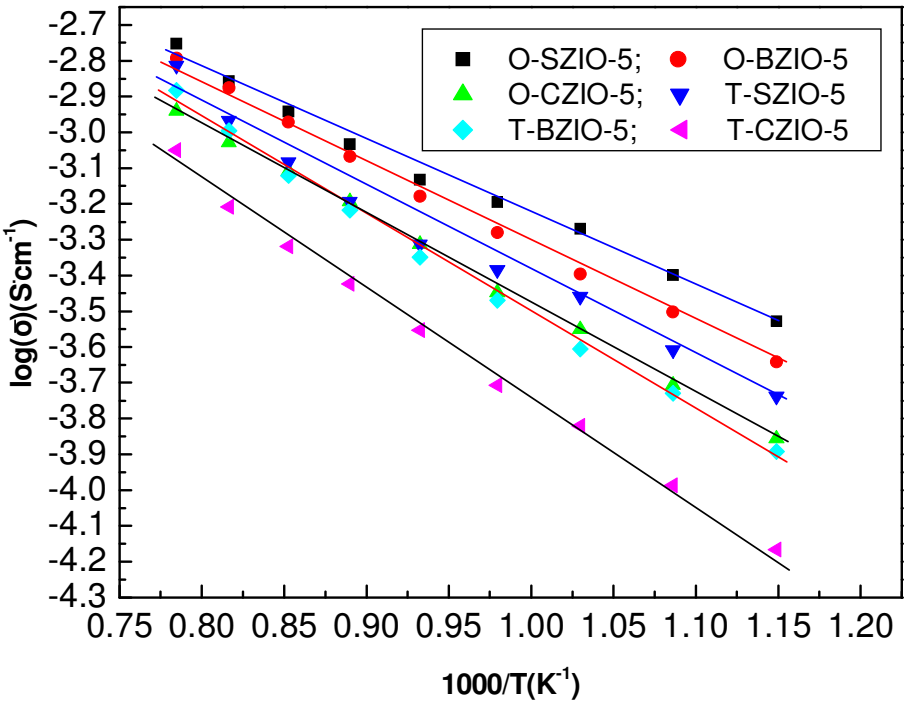


Fig.4. Conductivities of zirconates produced by the optimized and traditional solid-state reaction method

Fig.4 showed the conductivities of zirconates produced by the optimized and traditional solid-state reaction method under hydrogen atmosphere. According to Fig.4 and Table 3, the proton conductivity of zirconates, produced by the optimized solid-state reaction method were higher than those synthesized by the traditional solid-state reaction method, which could be ascribed to their higher relative density and more satisfactory grain boundary that was more effective to improve ionic transport properties.

Table 3. Conductivities at 1000°C of zirconates produced by the optimized and traditional solid-state reaction method

Method	Ceramics	Conductivities at 1000°C/10^{-3}S·cm^{-1}
Optimized solid-state reaction	O-CZIO-5	1.15
	O-BZIO-5	1.61
	O-SZIO-5	1.77
Traditional solid-state reaction	T-CZIO-5	0.89
	T-BZIO-5	1.31
	T-SZIO-5	1.54

4. Conclusions

Based on the mechanism and kinetics analysis, homogeneously distributed zirconate powders were mass produced by the optimized solid-state reaction method, which was cheaper, faster, easier and more effective than that of the wet-chemical method and traditional solid-state reaction method. The good performances like relative density, helium leak detection, higher flexure stress and conductivities afforded the zirconates wider range of technological applications in fuel cells, batteries, gas sensors, hydrogenation/dehydrogenation of hydrocarbons, electrolytes, refractory materials and corrosion resistance materials etc.

Acknowledgements

This work was financially supported by Natural Science Foundation of China (NSFC project nos. 51072211 and 51102269) and Science and Technology Commission of Shanghai Municipality (08DZ2210900).

References:

[1] Y. B. Huang, R. Flükiger, Reducing ac losses of Bi-2223 Multifilamentary tapes by oxide barriers, Physica C, 294 (1998) 71-82.

[2] H. Iwahara, T. Yajima, T. Hibino, K. Ozaki, H. Suzuki, Protonic conduction in calcium, strontium and barium zirconates, Solid State Ionics, 61(1993) 65-69.

[3] R.A. Davies, M.S. Islam, A.V. Chadwick, G.E. Rush, Cation dopant sites in the $CaZrO_3$ proton conductor: a combined EXAFS and computer simulation study, Solid State Ionics 130 (2000) 115–122.

[4] Yusuke Okumura,a Yoshitaro Nose,a Junichi Katayama,b and Tetsuya Uda, High Performance Protonic Ceramic Fuel Cells with Acid-Etched Surfaces, Journal of The Electrochemical Society, 158 (2011) B1067-B1071.

[5] K. Yashiro, S. Akoshima, T. Kudo, M. Oishi, H. Matsumoto, K. Sato, T. Kawada, J. Mizusaki, Electrical conductivity and chemical diffusion in perovskite-type proton conductors in H_2-H_2O gas mixtures, Solid State Ionics, 192 (2011) 76-82.

[6] F. Iguchi, N. Sata, H. Yugami, Proton transport properties at the grain boundary of barium zirconate based proton conductors for intermediate temperature operating SOFC, Journal of Materials Chemistry, 20 (2010) 6265-6270.

[7] Young-Chang Yang, Jinsu Park, Junwoong Kim, Angi Choi, C.O. Park, The study of the voltage drift in high-temperature proton conductor-based hydrogen sensors adopting the solid reference electrode, Sensors and Actuators B, 140 (2009) 273-277.

[8] Macmanus- Driscoll, J. L., Foltyn, S. R., Jia, Q. X., Wang. H., Serquis A., Civale L., Maiorov B., Hawley M. E., Maley M. P., Peterson D. E. Strongly enhance current densities in superconducting coated conductors of $YBa_2Cu_3O_{7-x}$ + $BaZrO_3$, Nature Materials, 3 (2004) 439-443.

[9] A. Sin, B. E. Montaser, P. Odier, Synthesis and sintering of large batches of barium zirconate nanopowders, Journal of American Ceramic Society, 85(2002) 1928-1932.

[10] F. Boschini, B. Guillaume, A. Rulmont, R. Cloots, R. Moreno, Slip casting of barium zirconate aqueous concentrated suspensions, Journal of the European Ceramic Society 26(2006) 1591-1598.

[11] L. Rij, L. Winnubst, L. Jun, J. Schoonman, Analysis of the preparation of In-doped $CaZrO_3$ using a peroxo-oxalate complexation method, Journal of Materials Chemistry, 10(2000) 2515-2521.

[12] Z. Li, W. Lee, Low-temperature synthesis of $CaZrO_3$ powder from molten salts, Journal of American Ceramic Society, 90 (2007) 364-368.

[13] S. Manik, S. Pradhan, X-ray microstructure characterization of ball-milled nanocrystalline microwave dielectric CaZrO3 by Rietveld method, Journal of applied crystallography, 38 (2005) 291-298.

[14] A.Sin, B. E. Montaser, P. Odier, E. Weiss, Synthesis and sintering of large batches of barium zirconate nanopowders, Journal of American Ceramic Society, 85 (2002) 1928-1932.

[15] T. Yu, W. Zhu, C. Chen, X. Chen, R. Krishinan, Preparation and characterization of sol-gel derived CaZrO3 dielectric thin films for high-*k* applications, Physica B 348 (2004) 440-445.

[16] J. Han, Z. Wen, J. Zhang, X. Wu, B. Lin, Electrical conductivity of fully densified nano CaZr0.90In0.10O2.95 ceramics prepared by a water-based gel precipitation method, Solid State Ionics, 180 (2009) 154-159.

[17] J. Han, Z. Wen, J. Zhang, Z. Gu, X. Xu, Fabrication of dense $CaZr_{0.90}In_{0.10}O_{3-\delta}$ ceramics from the fine powders prepared by an optimized solid-state reaction method, Solid State Ionics, 179 (2008) 1108-1111.

[18] E.O. Hall, The deformation and ageing of mild steel: III discussion of results, Proc. Phys. Soc. B, 64(1951) 747-753.

[19] N. Petch, The cleavage strength of polycrystals, J. Iron Steel Inst., 174(1953) 25.

SYNTHESIS AND CHARACTERIZATION OF $La_{0.6}Sr_{0.4}Co_{0.2}Fe_{0.8}O_{3-\alpha}$ COMPOUND PREPARED BY AN ACTIVATED CARBON-ASSISTED SOL GEL METHOD*

ISMARIZA ISMAIL

Faculty of Applied Sciences, Universiti Teknologi MARA, 40450 Shah Alam, Selangor, Malaysia

NAFISAH OSMAN, ABDUL MUTALIB MD JANI

Faculty of Applied Sciences, Universiti Teknologi MARA, 02600 Arau, Perlis, Malaysia

The deterioration of the electrochemical performance of cathode materials at intermediate temperature solid oxide fuel cell (IT-SOFC) has urged the development of new and improved of related materials. One of the most studied cathode material at intermediate temperatures (500-750 ^{o}C) is lanthanum strontium cobaltite ferrite (LSCF) due to their high electronic and ionic conductivities. In this study, the effect of activated carbon (AC) and calcination temperature on the formation of the LSCF phase and microstructure of the powders following the sol-gel synthesis method is investigated. Three cathode samples with different weight ratios of AC namely 0%, 20% and 40% were prepared and respectively denoted as C1, C2 and C3. The phase formation and morphology of the calcined powder ware examined by X-Ray diffractometer (XRD) and field emission scanning electron microscopy (FESEM), respectively. The specific surface area of the powder was measured by BET method. The characteristic peaks for LSCF phase appears in the X-ray diffractogram for all samples after calcined at 600 ^{o}C. SEM micrographs showed the presence of spherical particles of the powders with approximate particle size between 10 to 60 nm along with agglomerate morphologies. Well dispersed particles and fewer aggregates were observed for samples prepared with activated carbon as the synthesizing aid. The surface areas measured for sample C1, C2 and C3 is 7.39, 10.05 and 11.02 m^2/g respectively. The SEM observation is in accordance with BET results obtained in which higher surface areas were measured for sample C3 and C2 as compared to C1. It is found that the used of different weight ratios of AC in the synthesizing route gave significant effect on the microstructure of the LSCF but not to the phase formation of the compound.

* This work is supported by The Ministry of Higher Education for the Grant 600-RMI/RACE 16/6/2(3/2012) and 600-RMI/RAGS 5/3 (6/2013).

Proceedings of the 14th Asian Conference on Solid State Ionics (ACSSI 2014)
Copyright © 2014 ACSSI 2014 Organizers. All rights reserved.
ISBN: 978-981-09-1137-9
doi:10.3850/978-981-09-1137-9_063

1. Introduction

Solid oxide fuel cell (SOFC) is the cleanest and most efficient option for direct conversion of a wide variety of fuels to electricity. The operation of SOFC at high temperature (800-1000 ^{o}C), however required high construction and maintenance costs due to the physical and chemical degradation of the cell at such temperature [1, 2]. In order to make SOFC technology affordable, the reduction of the operating temperature to the intermediate temperature range is perquisite as this implies the use of low cost fabrication materials for construction and balance of plant [3, 4]. Unfortunately, lowering the operation temperature associated with the deterioration of cathode electrochemical activity predominantly for the typical perovskite-type manganite-based material such as LSM ($La_{1-x}Sr_xMnO_{3-\delta}$) which is primarily due to the electrode polarization losses [5, 6]. Therefore, extensive efforts have been devoted to the search for alternative cathode materials for intermediate temperature SOFC (ITSOFC) application. Among the most studied materials, LSCF compound have been reported as one of the most promising candidates for ITSOFC cathode materials due to their high electronic and ionic conductivity [7]. In this study, LSCF-based cathode powders are prepared by a complexing method using ethylene diamine tetra-acetic acid and citric acid as chelants assisted with addition of activated carbon as the dispersant. The dispersant is used in the synthesizing process as an effort to control the distribution and particle size of the cathode powders. The control of microstructure of the cathode materials is important because small particle size and high surface area are favorable for enhancement of the electrocatalytic reduction of oxidant which eventually yields higher catalytic activity [8, 9]. The LSCF powders synthesized with the assistance of dispersant are characterized for morphology and structural properties and subsequently compared with the sample synthesized without dispersant.

2. Methodology

The precursor solution were prepared by dissolving the stoichiometric composition of $La(NO_3)_3.6H_2O$ (99.9%, ACROS), $Sr(NO_3)_2$ (99%, ACROS), $Co(NO_3)_2.6H_2O$ (99%, ACROS) and $Fe(NO_3)_3.9H_2O$ (99%, ACROS) in 100 ml of deionized water. After complete dissolution of salts, citric acid monohydrate (CA) (99.5%, MERCK) was introduced to the nitrate solution, followed by ethylene diamine tetra-acetic acid (EDTA)

(99%, ACROS) powder. The solution was then heated in 70 ^{o}C water bath under continuous stirring. CA and EDTA powder served as the raw materials for chelation process. The molar ratio of CA and EDTA added to the mixture solution with respect to the overall metal cations content was 2:1:1 (CA:EDTA:Metal cation). After obtaining a clear solution, charcoal activated carbon (HmbG) was added as a dispersant. Three batch cathode samples with different weight ratios of activated carbon namely 0%, 20% and 40% were prepared and respectively denoted as C1, C2 and C3. The mixture was continuously stirred and heated on a hotplate to evaporate the water. The resulting viscous gel was dried at 100 ^{o}C in a vacuum oven overnight and the solidified precursor was then crushed and calcined at 700 ^{o}C for 5 hours. Phase formation of the oxide compound was verified by X-ray diffraction (XRD) (PANalytical X'Pert PRO MRD PW3040), employing Cu K_{α} radiation from 20^{o} to 80^{o} in step of 0.05^{o} at 2θ. Field emission scanning electron microscopy (FESEM) (Carl Zeiss SMT Supra 40VP) was employed to observe the microstructures and morphologies of the LSCF powders. The micrographs obtained were used to estimate the particle size and the morphology of the sample using an image analysis system (ImageJ 1.45p). Finally, the specific surface area of the LSCF powder was obtained using BET analyzer (Quantachrome Autosorb AS1C).

3. Results and Discussion

3.1 XRD Analysis

The X-ray diffractogram for C1, C2 and C3 cathode samples after calcined at 600 ^{o}C and 700 ^{o}C are respectively shown in Figure 1 (a) and (b). Almost all the characteristic peaks of the perovskite LSCF phase appears in the XRD spectra for all batches of cathode samples after calcined at 600 ^{o}C, which is at a relatively lower temperature compared with combustion process or other powder processes [5, 10, 11]. No secondary phases are observed, except a small peak at 2θ ≈ 26.5^{o} which correspond to the presence of La_2O_3. However, the impurity peak disappears as the calcination temperature increased to 700 ^{o}C and a single-phase perovskite structure is obtained. All the peaks are matched to the JCPDS Card no. 98-011-1667. No significant changes in the peak position of the cathode materials as a function of activated carbon implies that the addition of this dispersant agent does not influence the phase formation of the sample. These results are in agreement with other reported work published elsewhere [7, 9].

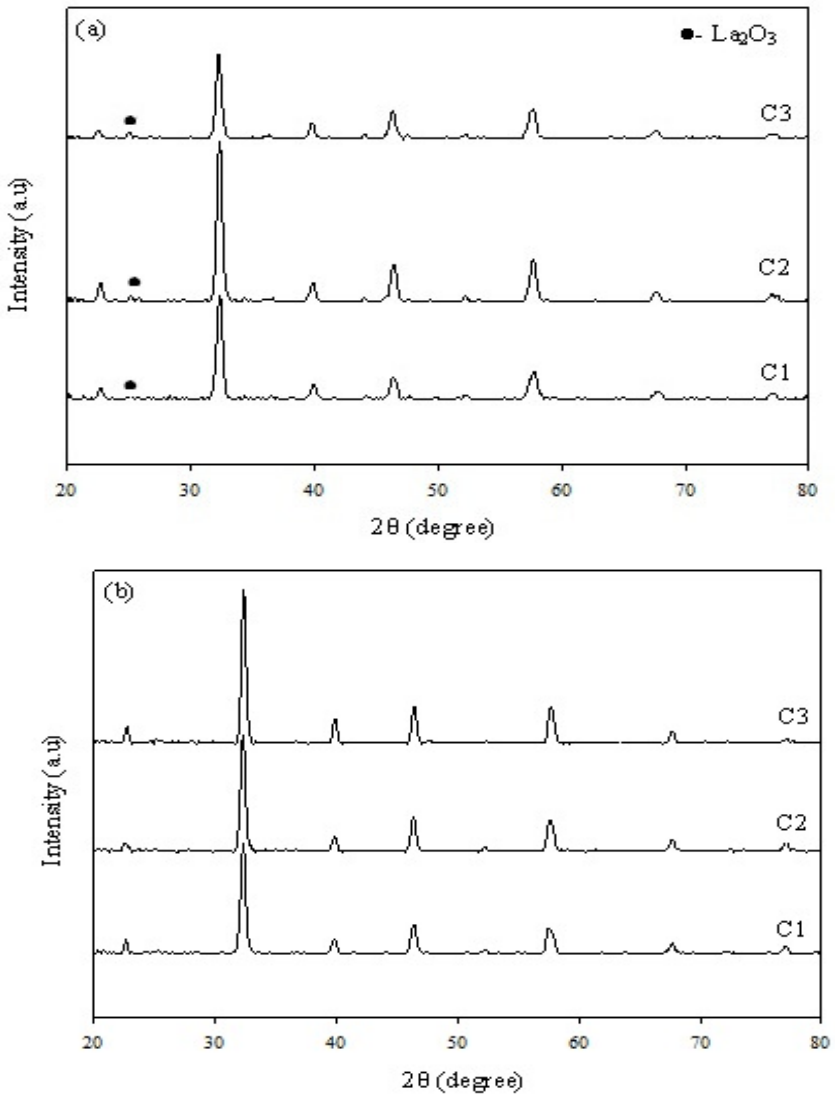


Figure 1. XRD diffraction patterns for LSCF cathodes after calcined at (a) 600 °C and (b) 700 °C.

3.2 Morphology Analysis

The FESEM micrographs of LSCF powder after calcined at 700 °C are presented in Figure 2. The morphology of the primary powders was almost spherical in shape with a diameter in the range of 10 to 60 nm. Agglomerated morphologies are also seen in all sample batches and most

prominent for sample C1, which is prepared without the help of the dispersant. The size of agglomerated particles measured for C2 and C3 sample powders is in the range of 40 to 200 nm whereas for C1 sample, the cluster size is around 90 to 800 nm. With the addition of activated carbon as the dispersant in C2 and C3 samples, it is noticeable that the particles are well dispersed and fewer aggregates were observed. In summary, activated carbon served as a good synthesizing aid in preventing agglomeration and these observations is in accordance with previous work [9].

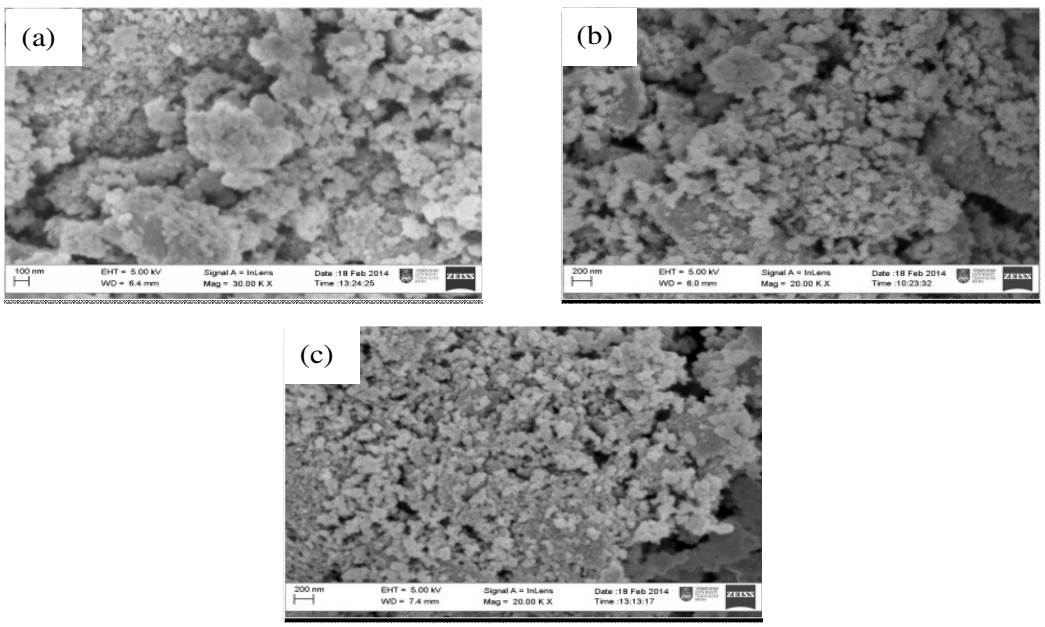


Figure 2.FESEM images of (a) C1, (b) C2 and (c) C3 after calcined at 700 ^{o}C.

3.3 BET Surface Area Analysis

The surface area characterized by BET measurement demonstrates an increasing trend with the addition of activated carbon as the dispersant during synthesizing process as shown in Table 1. The surface area measured for the sample prepared with the aid of the dispersant, C2 and C3, are relatively higher as compared to C1. The BET results are in accordance with the morphologies obtained from SEM images which are discussed in previous section. The surface area obtained is comparatively higher than those reported for powders prepared by other synthesizing route [5, 12].

This is particularly due to the well dispersed particles produced by the dispersant aid synthesizing route which prevent the agglomeration and eventually provide more site of the particle's surface for the reaction.

Table 1 Surface area of LSCF powder calcined at 700 ^{o}C

Sample	BET surface area (m^2g^{-1})
C1	7.39
C2	10.05
C3	11.02

4. Conclusion

Three batches of LSCF cathode powders were prepared with different weight ratios of activated carbon that serve as the dispersant for synthesizing aid. No significant differences observed in the X-ray diffractogram of all samples suggesting that the addition of dispersant not affecting the phase formation of the compound. In addition, SEM images reveal the effectiveness of activated carbon for preventing agglomeration and assist the production of well dispersed powders. The observation from SEM analysis is in accordance with the BET results in which higher surface area was obtained for the sample prepared with the addition of activated carbon. Therefore, addition of dispersant during the synthesizing process of cathode powders is believed to be one of the critical parameters in producing a small particle size and a high surface area of nanocrystalline materials that are favored for the cathode electrode of SOFCs.

Acknowledgments

The authors would like to acknowledge the Ministry of Higher Education for the financial support via Grant 600-RMI/RACE 16/6/2(3/2012) and 600-RMI/RAGS 5/3 (6/2013) awarded.

References

1 N. Ortiz-Vitoriano, C. Bernuy-López, I. Ruiz de Larramendi, R. Knibbe, K. Thydén, A. Hauch, P. Holtappels, and T. Rojo, Applied Energy **104**, 984 (2013).

2 Z. Ding, Z. Yang, D. Zhao, X. Deng, and G. Ma, Journal of Alloys and Compounds **550**, 204 (2013).
3 S. Ricote, N. Bonanos, P. M. Rørvik, and C. Haavik, Journal of Power Sources **209**, 172 (2012).
4 R. Peng, T. Wu, W. Liu, X. Liu, and G. Meng, Journal of Materials Chemistry **20**, 6218 (2010).
5 L. M. P. Garcia, D. A. Macedo, G. L. Souza, F. V. Motta, C. A. Paskocimas, and R. M. Nascimento, Ceramics International (2013).
6 L. Wu, Z. Jiang, S. Wang, and C. Xia, International Journal of Hydrogen Energy **38**, 2398 (2013).
7 H. W. Jin, J. H. Kim, Y. M. Park, C. Choi, H.-J. Kim, and H. Kim, JOURNAL OF CERAMIC PROCESSING RESEARCH **13**, S286 (2012).
8 W. Zhou, Z. Shao, and W. Jin, Journal of Alloys and Compounds **426**, 368 (2006).
9 J. H. Kim, Y. M. Park, and H. Kim, Journal of Power Sources **196**, 3544 (2011).
10 L. Baqué, A. Caneiro, M. S. Moreno, and A. Serquis, Electrochemistry Communications **10**, 1905 (2008).
11 S. Lee, H. S. Song, S. H. Hyun, J. Kim, and J. Moon, Journal of Power Sources **187**, 74 (2009).
12 K. Murata, T. Fukui, H. Abe, M. Naito, and K. Nogi, Journal of Power Sources **145**, 257 (2005).

Batteries II

NOVEL LI-ION CAPACITOR HAVING AN ULTRAHIGH SPECIFIC CAPACITY COMPARABLE TO THAT OF LI-ION BATTERY

TSUTOMU TAKAMURA

3-31-16, Azamino, Aobaku, Yokohama 225-0011, Japan

KYOUICHI SEKINE

5-5-8, Ouizumigakuenmachi, Nerimaku, Tokyo 178-0061, Japan

FUMINORI MOURI

3-34-1, Nishiikebukuro, Toshimaku, Tokyo 171-0021, Japan

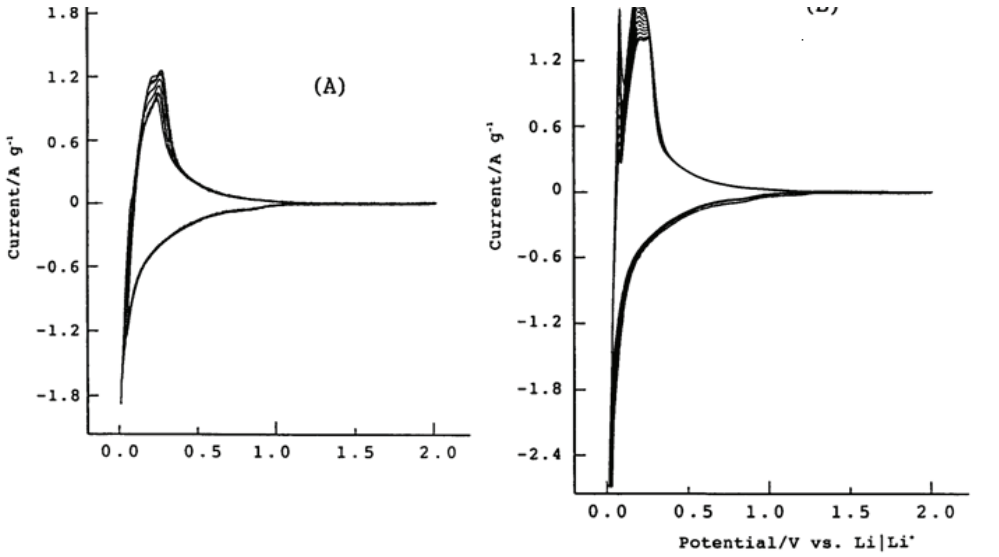
In an attempt to create a ultrahigh capacity capacitor we examined to apply the nanoionics mechanism proposed by J. Maier by the use of activated carbon fiber. By vacuum-deposition of Sn on the surface of the activated carbon fiber followed by oxidation by heating in the presence of oxygen to form SnO2 and immersing in an organic solvent containing 1 M of LiClO4 we could obtain very high capacity capacitor materials having the specific capacity of 250 mAh/g, i, e., the amount is as high as that of Li-ion battery. Instead of Sn we examined Pd, Cu, and Ag, When these metals were vacuum-deposited on the surface of activated carbon fiber, followed by heating in the presence of low pressure of oxygen.

Keywords: capacitor, carbon fiber, surface modification.

1. Introduction

During the course of examining the cyclic voltammogram (CV) of graphitized carbon fiber in PC containing 1 M of $LiClO_4$ we found incidentally the appearance of sharp prepeak when the sample was cleaning treatment by mild oxidation as shown in Fig. 1 (B). After a precise examination we could attribute this peak to be caused by the electrosorption of Li on the carbon surface. In case of activated carbon having a large specific surface area, we can expect the possibility to realize a capacitor having a huge double layer capacity, We examined an activated carbon sample.

Proceedings of the 14th Asian Conference on Solid State Ionics (ACSSI 2014)
Copyright © 2014 ACSSI 2014 Organizers. All rights reserved.
ISBN: 978-981-09-1137-9
doi:10.3850/978-981-09-1137-9_055



Pristine fiber After mild oxidation treated

Fig. 1 CV of graphitized carbon fiber in PC /1M $LiClO_4$

2. Experimental

As a sample we examined activated carbon fiber of Kureha Company made (Kuractive #2500 whose specific surface area is 2500 m^2 g-1). The fiber integrated felt was sandwiched between a folded Ni wire net and used as a test electrode.

3. Results and Discussion

The CV of the activated carbon fiber is shown in Fig. 2, where we see the presence of remarkable prepeak. The curve, however, is unstable and the double layer capacity becomes diminished gradually. After many trials we could stabilize this CV by modifying the surface with vacuum deposition of Sn which was converted to SnO2 by heating in air. The results are shown in Fig. 3.

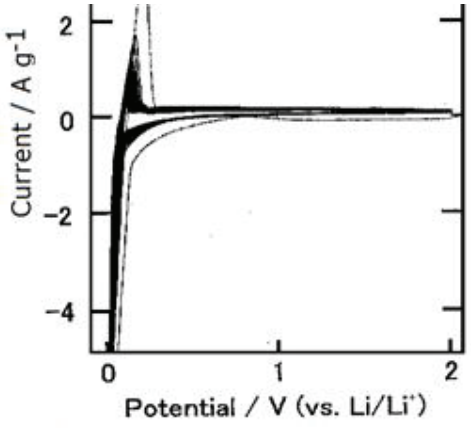


Fig. 2 CV curve of Kuractive #2500 in PC/1M $LiClO_4$ Potential sweep rate; 1mV s^{-1}

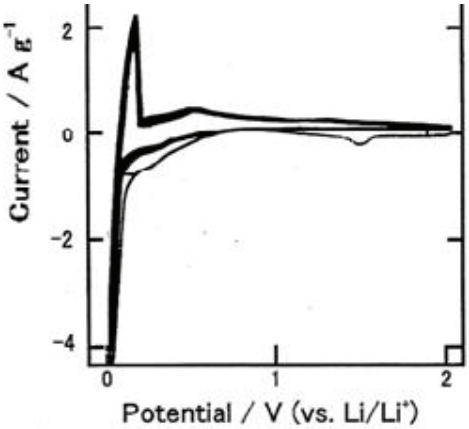


Fig. 3 CV curves of Kuractive # 2500 covered with a 400 A thick SnO_2 film (in PC/1M $LiClO_4$)

As seen in Fig. 3 the CV of the activated carbon fiber was successfully stabilized by the surface modification with very thin film of SnO_2. We tried to apply this method with transition metals other than Sn, i.e., Pd, Cu, Ag, and found that these metals are enable to give rise to modify the activated carbon fibers for emphasizing the available specific capacity.

References

[1] L.J. Fu, K. Endo, K. Sekine, T. Takamura, Y.P. Wu and H.Q. Wu, J. Power Sources, 162(1), (2006) 663-666.

[2] K. Endo, J. Suzuki, K. Sekine, and T. Takamura, Electrochemistry, 74(5), (2006) 374-378.

Fundamentals II

NON-DEBYE ELECTRICAL RELAXATION PROCESSES AND UNDERSTANDING OF DYNAMICAL CONDUCTIVITY IN ION CONDUCTING SOLIDS

G. GOVINDARAJ†
Department of Physics, School of Physical, Chemical and Applied Sciences, Pondicherry University, Pondicherry -605 014, India

Unique dielectric function in time and frequency domain are proposed for investigating the non-Debye relaxation (NDR). A detailed study is performed on the broadband dielectric loss data of glycerol over the temperature range 184 to 290 K and ac conductivity of β-AgI in 120 to 200K using the proposed NDR functions. The physical basis of NDR is shown to be the tailoring of Debye electric dipole charge $\{\rho^+, \rho^-\}$ into a non-trivially coupled interacting dipoles of charges $\{(1-g)\rho^+, (1-g)\rho^-\}$, $\{g\rho^+, g\rho^-\}$, hereafter referred as ensemble of g and (1-g) dipoles, due to the molecular interactions and defect disorder in the systems, where the fraction $0<g<1$ is an exponent in time and frequency domain and g=1 is non-interacting Debye electric dipole. The coupled interaction of ensemble of gg dipoles and their polarization processes lead to coexistence of slow and fast rates of relaxation times τ^g and τ^{2-g} with respect to the thermally activated Debye relaxation time τ. The proposed NRD function has unique features compared with existing NDR functions and it explains several experimental features of NDR. The NDR function explains α and β relaxation and broadband dielectric loss data of glycerol and ion dynamics of low temperature ac conductivity data of β-AgI systems. Coexistence of two Debye and corresponding NDR processes for structural (or rotational) and translational relaxation times are shown to be responsible broad dielectric loss spectra in glycerol, and α and β relaxation and ac conductivity spectra of β-AgI. Both glycerol and β-AgI data show excellent agreement with entire range of experimentally observed spectra of 16 decades and 9 decades respectively. The proposed NDR process predicts physics involved in the α and β relaxation in super-cooled liquids, polymers, plastic crystals and ac conductivity spectra of glassy, crystalline as well as super-cooled ionic melts.

1. Introduction

In general, the dielectric responses of liquid and solid dielectrics do not exhibit the Debye response characteristics, except in some liquid dielectrics. Hence, they are usually modelled by a modified Debye response functions called non-Debye relaxation (NDR) functions [1,2]. The time and frequency dependent empirical and phenomenological NDR function known in the literature are: (i) stretched exponential relaxation function $\phi(t)=\exp[-(t/\tau)^{\beta}]$ [1], where β is an exponent $0<\beta\leq1$ (ii) Havirliak-Nigami function [3] $\varepsilon^*_{HN}(\omega)\propto[(1+(i\omega\tau)^{(1-\alpha)}]^{\beta_{CD}}]^{-1}$, with $0<\alpha\leq1$ and $0<\beta_{CD}\leq1$; (iii) Cole-Cole function [4] is obtained when $\beta_{CD}=1$ and $0\leq\alpha<1$; (iv) Cole-Davidson [5] function is defined when $\alpha=0$ and $0<\beta_{CD}\leq1$,

† ggraj_7@yahoo.com

Proceedings of the 14th Asian Conference on Solid State Ionics (ACSSI 2014)
Copyright © 2014 ACSSI 2014 Organizers. All rights reserved.
ISBN: 978-981-09-1137-9
doi:10.3850/978-981-09-1137-9_064

and (v) Jonscher's power law [1] ac conductivity function $\sigma(\omega) \propto \omega^n$, and its corresponding dielectric loss $\varepsilon''(\omega) \propto \omega^{-(1-n)}$ (vi) coupling model of Ngai [1], (vii) Funke *et al*., concept of MIGRATION [6], (viii) macroscopic and microscopic models of Dyre, Dieterich, Sidebottom [7-9] and (ix) corrected model of Macdonald [10]. The exponents used in models (i)-(iv) are fit parameter and treated as a distribution of relaxation times. Whereas, in other models show certain unique features of universal behavior suggesting the dominant role of many-body interactions. All models are describing the experimental features of dielectric loss spectra and ac conductivity spectra of ion conducting solids. However, the transparent interpretation of non-Debye dielectric polarization relaxation dynamics is still appearing to be difficult. Also, it was *not* possible to establish the dependence of the exponents in (i)-(ix) on the physical characteristics of solids, for example, depolarization current, hopping frequency, activation energy for dipolar process and temperature. In addition to this, the concept of nonrandom bounce-back mechanism, coupling, and correlation are not clear in terms of hopping charge polarization process.

In the present paper, unique dielectric relaxation function and corresponding dielectric function is proposed based on our earlier work [11-14], with modifications, to investigate NDR. We have shown that NDR is a correlated polarization relaxation dynamics and sum of slow and fast polarization mechanisms with respect to Debye mechanisms. The physical basics for the fast and the slow polarization relaxation dynamics with respect Debye polarization relaxation dynamics is explained in terms non-Debye dipole formation and their interaction in the polarization process. The non-Debye dipole formation, their interaction, slow and fast relaxation rates are defined with respect to Debye polarization process. The proposed NDR function is used to explain the broadband dielectric loss spectra of glycerol, α relaxation in glycerol, and ion dynamics in the low temperature ac conductivity spectra of β-AgI. The model confirms the coexistence of two Debye and corresponding NDR processes for structural (or rotational) and translational relaxation times and they are shown to be responsible for broad dielectric loss spectra in glycerol [15] and ac conductivity spectra of β-AgI [6]. Both glycerol and β-AgI data show excellent agreement with experimentally observed spectra in the entire range of 16 decades frequency over the temperature range of 184 to 290 K for glycerol and 9 decades in ac conductivity spectra for β-AgI in the temperature range of 120 to 200K. The proposed NDR model predicts physics behind the α and β relaxation in super-cooled liquids, polymers, plastic crystals and ac conductivity spectra of glassy, crystalline as well as super-cooled ionic melts.

2. Unique non-Debye relaxation and dielectric functions

After a analyzing the existing non-Debye relaxation functions (i)-(ix) listed above and based on our earlier work [10-14] with a modifications, unique

dielectric relaxation function and corresponding dielectric function has been discovered for non-Debye dipolar polarization relaxation process and carrier charge polarization in ion conducting solids. These functions are found to be:

$$\phi^*(t)=P_\infty+(\Delta P)_s \exp[-(t/\tau^*)_s]+(\Delta P)_f \exp[-(t/\tau^*)_f] \quad (1)$$

$$\varepsilon^*(\omega)=\varepsilon_\infty+(\Delta\varepsilon)_s/(1+ i(\omega\tau^*)_s)+(\Delta\varepsilon)_f/(1+i(\omega\tau^*)_f), \quad (2)$$

$$Z^*(\omega)= R_s/(1+ i(\omega\tau^*)_s)+R_f/(1+i(\omega\tau^*)_f), \quad (3)$$

where $(\tau^*)_s=\tau/(i\tau)^{1-g}$, $(\tau^*)_f=\tau/((-i)\tau)^{-(1-g)}$, g is an exponent $0<g<1$, $i=\sqrt{-1}$, τ is thermally activated Arrhenius or non-Arrhenius Debye relaxation time with g=1, ω is the applied frequency, the suffix s and f denote slow and fast processes in NDR, $(\Delta P)_s=(P_s-P_\infty)_s$, $(\Delta P)_f=(P_s-P_\infty)_f$, are relaxation polarization with $(P_s)_s$ and $(P_s)_f$ as static value of polarization for slow and fast process, P_∞ is an instantaneous polarization, $(\Delta\varepsilon)_s=(\varepsilon_s-\varepsilon_\infty)_s$, $(\Delta\varepsilon)_f=(\varepsilon_s-\varepsilon_\infty)_f$, dielectric strengths for slow and fast process, $(\varepsilon_s)_s$ and $(\varepsilon_s)_f$ static value of dielectric constants for slow and fast relaxation process. The magnitudes of $(\Delta\varepsilon)_s$ and $(\Delta\varepsilon)_f$ are proportional to strength of the dipole, number of dipoles, and inversely proportional to temperature. The magnitudes of R_s and R_f are resistance offered in the complex impedance for slow and fast charge carrier polarization process with corresponding relaxation rates. The magnitudes of R_s and R_f may be equal or different depending on the systems, and proportional to strength and number of the carrier charge involved in the slow and fast carrier charge polarization, and inversely proportional to temperature.

Coexistence of slow and fast relaxation polarization ensembles and their corresponding relaxation processes ($0<g<1$) with respect to the Debye relaxation (g=1) is established with unique plausible non-Debye dipole formation and their coupled interactions. Fig. 1 illustrates the non-Debye dipole formation and their coupling. In the presence external perturbation, the dipole charge ρ associated with the non-interacting

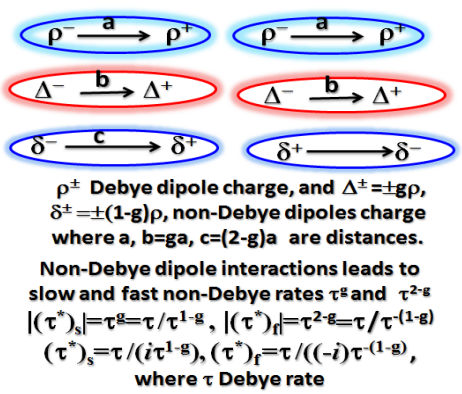


Fig. 1: Illustration of dipole structures for Debye and non-Debye polarization processes.

Debye dipole $\{\rho^+, \rho^-\}$ is tailored due to the molecule-molecule bonding and defect disorder in the systems. The net Debye dipoles charges ρ tailored into uneven charge $g\rho$ and $(1-g)\rho$ and forms non-Debye dipoles $\{(1-g)\rho^+, (1-g)\rho^-\}$, $\{g\rho^+, g\rho^-\}$, hereafter referred as non-Debye ensemble of g (1-g) dipoles. These ensemble of gg dipoles and their interactions are considered for defining the

slow and the fast relaxation rates τ^{g} and τ^{2-g} with respect to the Debye relaxation rate τ (g=1).

The following intuitive scheme is arrived for the slow and the fast relaxation process after complete exploration existing non-Debye relaxation process, in particular with Jonscher's "universal power law". The exponentials argument of Eq. (1) has been tailored into Debye and non-Debye polarization contributions to define the slow and fast relaxation times. The slow and fast relaxation processes are:

$$(t/\tau^{*})_{s}=(t/\tau)(\Gamma^{*}(t))_{s}=(t/\tau)(i\tau/t)^{1-g}=(t/\tau)^{g}i^{1-g} \quad (4)$$

$$(t/\tau^{*})_{f}=(t/\tau)(\Gamma^{*}(t))_{f}=(t/\tau)((-i)\tau/t)^{-(1-g)}=(t/\tau)^{(2-g)}i^{1-g} \quad (5)$$

where (t/τ) is Debye polarization with relaxation rate τ, the $(\Gamma^{*}(t))_{s}=(i\tau/t)^{1-g}$ impedes Debye relaxation process and becomes non-Debye slow relaxation time $|(\tau^{*})_{s}|=\tau^{g}$, $(\tau^{*})_{s}=\tau/(i\tau)^{1-g}$ whereas $(\Gamma^{*}(t))_{f}=((-i)\tau/t)^{-(1-g)}$ expedites Debye relaxation process τ and becomes non-Debye fast relaxation time $|(\tau^{*})_{f}|=\tau^{2-g}$, $(\tau^{*})_{f}=\tau/((-i)\tau)^{-(1-g)}$

In the frequency dependent dielectric function, the slow relaxation time and fast relaxation time are found in Eq. (2) and these are:

$$i(\omega\tau^{*})_{s}=i\omega\tau/(\Gamma^{*}(\omega))_{s}=i\omega\tau/(i\omega\tau)^{1-g}=(i\omega\tau)^{g} \quad (6)$$

$$i(\omega\tau^{*})_{f}=i\omega\tau/(\Gamma^{*}(\omega))_{f}=i\omega\tau/((-i)\omega\tau)^{-(1-g)}=i^{g}(\omega\tau)^{2-g} \quad (7)$$

where $(\Gamma^{*}(\omega))_{s}=(i\omega\tau)^{1-g}$ impedes Debye relaxation time τ and becomes non-Debye slow dielectric relaxation time $|(\tau^{*})_{s}|=\tau^{g}$, $(\tau^{*})_{s}=\tau/(i\tau)^{1-g}$, whereas $(\Gamma^{*}(\omega))_{f}=((-i)\omega\tau)^{-(1-g)}$ expedites Debye relaxation time τ and becomes fast relaxation time $|(\tau^{*})_{f}|=\tau^{2-g}$, $(\tau^{*})_{f}=\tau/((-i)\tau)^{-(1-g)}$. Since both slow and fast dielectric processes are governed by same loss mechanisms, the non-Debye loss $\tan(\delta)=-\tan(g\pi/4)$ at $\omega=1/\tau$ for both slow and fast relaxation process and also same for the sum of the slow and the fast relaxation process, where Debye loss $\tan(\delta)=-\omega\tau$, $\delta=\pi/4$ at $\omega=1/\tau$. Eqs. (1) and (2) are Laplace/inverse Laplace transform or Fourier/inverse Fourier transform pairs provided the differentials in the time domain are $d(t^{g})$ and $d(t^{2-g})$, and the differentials in the frequency domain are $d(\omega^{g})$ and $d(\omega^{2-g})$. The Laplace and Fourier transforms with these differentials in time and frequency domains make the transforms into the domain of slow and fast process.

3. Potential energy barrier and dissipation mechanisms for non-Debye slow and fast relaxation processes.

The potential energy barrier for Debye and non-Debye process is illustrated in Fig. 2. Initially, the charge density ρn_{c}, is involved in the Debye polarization process, where n_{c} is number density of dipole with Debye dipole moment $\boldsymbol{\mu_{D}=a\rho}$.

Since medium is actively involved with molecule-molecule bonding and interactions, and defect disorder, Debye dipole moments $\boldsymbol{\mu_D}$ becomes non-Debye dipole moments $\boldsymbol{\mu_s}$=**b**Δ, and $\boldsymbol{\mu_f}$=**c**δ, Δ=gρ δ=(1-g)ρ, where ρn_s and ρn_f dipole charge density for slow and fast processes dipoles. The interactions dipoles $\boldsymbol{\mu_s}$ and $\boldsymbol{\mu_f}$ modifies the Debye potential energy barrier as illustrated in Fig. 2.

In Fig. 2 the black curve is for Debye process, red and blue curves are for non-Debye slow and fast process respectively. An ensemble of identical non-interacting Debye dipoles of charge ρ free to rotate against some viscous liquid-like medium or jumping by the thermal excitation between two preferred orientations separated by a potential barrier E_D a situation likely found in Debye type polar liquids or solids. In the presence of external field ξ, interactions between the non-Debye dipole charges, gρ, and (1-g)ρ, changes the site energy

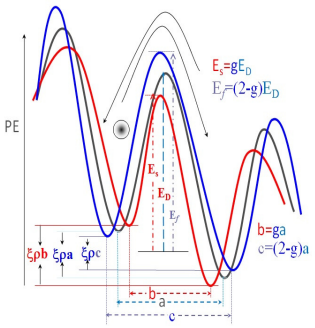


Fig. 2: Illustration of PE barrier for Debye and non-Debye polarization processes.

A and B and also potential energy barrier E_D and hence the time averaged occupancies f_A and f_B of two sites. For the charge ρ jumping towards A→B and B→A, the potential energy at sites A and B, potential energy barrier are: (i) E_D-$\xi\rho a/2$ and E_D+$\xi\rho a/2$ for Debye process with potential energy barrier E_D (ii) E_D-ξ(gρ)$b/2$ and E_D+ξ(gρ)$b/2$ for non-Debye slow process with potential energy barrier gE_D (iii) E_D-ξ(gρ)$c/2$ and E_D+ξ(gρ)$c/2$ for non-Debye fast process with potential energy barrier (2-g)E_D. where b=ga and c=(2-g)a is the distance between site A and B.

In a first step, the charge ρ has to surmount the energy barrier, E_D, between these sites of distance a. Because of change in site energy at A and B, and potential barrier energy, the dipole charge ρ tend to stay more time than the τ or less time than τ depends on the whether the potential barrier is E_s=gE_D or E_f=(2-g)E_D, where total shift in the potential energy barrier is E_f-E_s=2(1-g)E_D. After the time τ, *i.e.*, τ<t<∞, the neighboring charges rearrange in the course of their own motion and becomes slow relaxation rate τ^g, for example, τ=10^{-4}s, g=0.75, t=τ^g=10^{-3}s (delayed by a factor of $1/\tau^{1-g}$=10s), where effective potential barrier height for the slow process is E_s=gE_D and the reduction in the potential energy is (1-g)E_D. For the opposite case, *i.e.*, τ>t>∞, the neighboring mobile ions rearrange in the course of their own motion and becomes fast relaxation rate, for example for τ=10^{-4}s, g=0.75, t=τ^{2-g}=10^{-5}s (expedited by a factor of $1/\tau^{-(1-g)}$=0.1s) where effective potential energy barrier height for the fast rate process is E_f=

$(2\text{-}g)E_D$ and the reduction in the potential energy is $(1\text{-}g)E_D$. Since tailoring of Debye dipole charge into non-Debye dipole charge cannot follow the individual transitions, the tailoring of charges adjust itself to the time averaged occupancies f_A and f_B of the two sites. The application of external field ξ enhances the down-field rate and reduces the up-field rate resulting in a net change in occupancies by $\pm\Delta f_{AB}$ with respect to the equilibrium.

Every discrete transition is considered as the transfer of untailored charge ρ through the distance a, but the subsequent readjustment of the tailoring of charge gives rise to a final polarization $P_s=g\rho a\Delta f_{AB}$ for slow polarization process and $P_f=(2\text{-}g)\rho a\Delta f_{AB}$ for fast polarization process. Since all the net transitions take place in the field ξ, the energy derived from the field is $W_d=\xi\rho a\Delta f_{AB}$, but the energy stored in the system after relaxation for slow polarization process is $(W_s)_s=g\xi\rho a\Delta f_{AB}$ and the energy lost is: $(W_l)_s=W_d-(W_s)_s=(1\text{-}g)\xi\rho a\Delta f_{AB}$. Similarly, the energy stored in the system after relaxation for fast polarization process is $(W_s)_f=(2\text{-}g)\xi\rho a\Delta f_{AB}$, and the energy lost is: $(W_l)_f=W_d-(W_s)_f=-(1\text{-}g)\xi\rho a\Delta f_{AB}$. In both case of slow and fast process, the setting up of a given state of polarization in the system relaxing charges give rise a loss of energy $(W_l)_s$ or $-(W_l)_s$ which is proportional to the stored energy and which does not dependent on the rate at which these state of polarization has been established.

The energy loss $(W_l)_s$ or $(W_l)_f$ arising from the proposed tailoring of Debye dipole mechanism is additional to any loss that may arise in an alternating electric field ξ from the usual Debye relaxation. This is familiar energy criterion for Debye mechanism and at the loss at loss peak $\omega\tau=1$, where $\tan(\delta)=1$, $\delta=\pi/4$. The energy criterion for proposed non-Debye mechanism is $(\omega\tau^*)_s''/(\omega\tau^*)_s'=\cot(g\pi/2)$ or $(\omega\tau^*)_f''/(\omega\tau^*)_f'=\cot(g\pi/2)$, at the non-Debye loss peak $(\omega\tau)^g=(\omega\tau)^{2-g}=1$, $\tan(\delta)=1$, $\delta=g\pi/4$.

4. Salient features of the NDR function

The direct insight into the physical nature of loss peak may be obtained from an analysis of time domain response function $J^*(t)\propto d\phi^*(t)/dt$, of dielectric to step function electric field excitation, where $\phi^*(t)$ is given Eq. (1). Fig. 3 shows the time domain log-log plots for g=1, and for g=0.6 and g=0.3. Exponential plots on the left side show stretching in the in non-Debye relaxation in the time domain relaxation polarization for g=0.6, g=0.3. An explicit power law behavior in log-log plot are found in for both slow (red curves) and fast (blue curves) polarization processes and hence the in the sum of slow and fast processes (green curves in both left and right side figures). An astounding observation in both time and frequency domain curves are the that all the three type of transitions (Debye and non-Debye slow and fast processes) take place all at a time at

various relative rates as may be inferred from either in time domain Eq. (1) or frequency domain Eq. (2). For Debye mechanism, the peak frequency associated with the time t=τ, at which the slope goes through -1. Whereas, in the proposed NDR model, the loss peak is not caused by single 'homogenous' process as in Debye model, and it consists of sum of slow and fast rate processes with slopes greater than and less than -1.

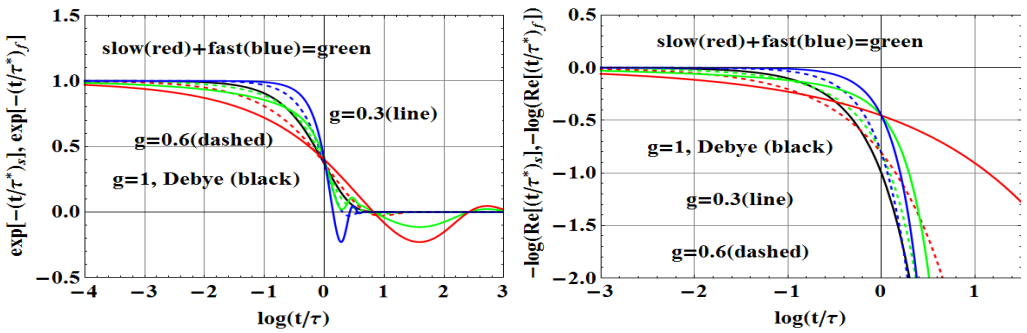


Fig. 3: Debye (g=1, black curve), and non-Debye relaxation functions for g=0.6 (dashed curve), 0.3 (continuous lines) are shown for slow (red), fast (blue) and sum of slow and fast (green) by plotting log(t/τ) against $\exp[-(t/\tau^*)_s]$, $\exp[-(t/\tau^*)_f]$, and $\exp[-(t/\tau^*)_s]+\exp[-(t/\tau^*)_f]$ (left side), and log(t/τ) against $-\log[\mathrm{Re}(t/\tau^*)_s]$, $-\log[\mathrm{Re}(t/\tau^*)_f]$, and $-\log[\mathrm{Re}((t/\tau^*)_s+(t/\tau^*)_f)]$ (right side).

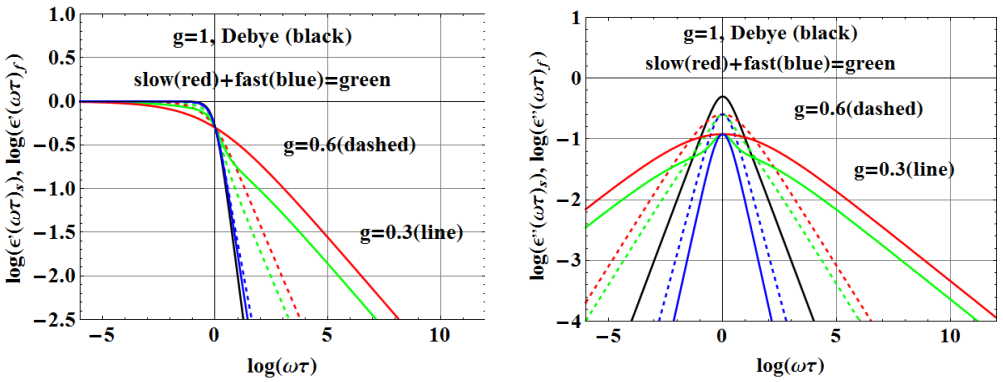


Fig. 4: Frequency domain Debye (g=1, black curve), and non-Debye dielectric functions for g=0.6 (dashed curve), 0.3 (continuous lines) are shown for slow (red), fast (blue) and sum of slow and fast (green) by plotting log(ωτ) against $\log(\varepsilon'(\omega\tau^*)_s)$ $\log(\varepsilon'(\omega\tau^*)_f)$, and $\log(\varepsilon'(\omega\tau^*)_s+\varepsilon'(\omega\tau^*)_f)$, (left side), and log(ωτ) against $-\log(\varepsilon''(\omega\tau^*)_s)$, $-\log(\varepsilon''(\omega\tau^*)_f)$, and $\log(\varepsilon''(\omega\tau^*)_s+\varepsilon''(\omega\tau^*)_f)$, (right side).

Though, the proposed NDR function has a similarity with Jonscher's "universal power law" empirical function $J(t)\propto((\omega_p t)^n+(\omega_p t)^k)^{-1}$ and its frequency domain numerical Fourier transform of J(t), where the physical basis for the exponents

0<n<1 and k>1 are still debated and no conclusive consensus so far. The present NDR function is completely different in terms of physical basis and functional form, when compared with all the existing empirical and phenomenological models. The proposed NDR model accommodates more than one Debye process with corresponding NDR, for example, structural or rotational and translation relaxations.

5. Glycerol (3μHz-40GHz, T=184-290K) and β-AgI (3mHz to 6MHz, T=120-200K) data analysis with proposed NDR function

Glycerol ($C_3H_5(OH)_3$) (melting temperature T_m=291K and glass transition temperature at T_g≈185K) is a hydrogen bonded material that easily can be supercooled and has been investigated in numerous attempt to test models and

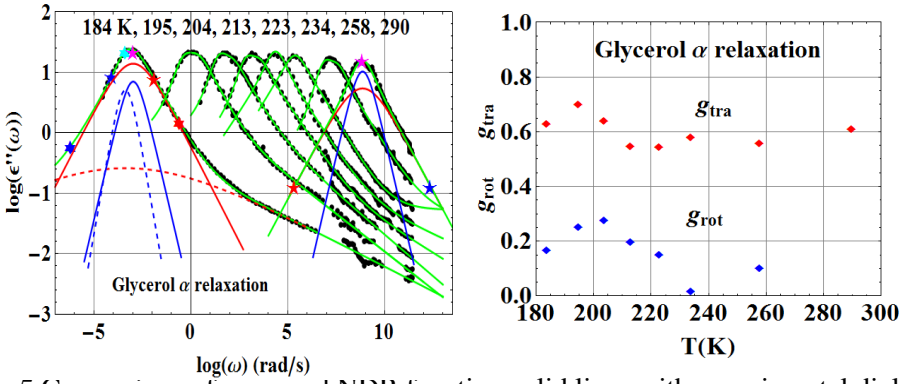


Fig. 5 Comparison of proposed NDR function solid lines with experimental dielectric loss data for glycerol (left side) and value of non-Debye dipole parameter g for rotational and translation relaxation (right side).

theories of glass transition. The reorentational relaxation in glycerol involves the tear and repair of hydrogen bonds. When hydrogen bonds ruptured, structural relaxation occurs, and this process may also involve a mass transport. Therefore, two active motions namely, reorentational and transitional motions relaxation are possible and these may be coupled or decoupled depending on the coupling strength. The glycerol dielectric loss data are collected literature [15] for the frequency range 3μHz-40GHz in the temperature between 184-290K and fitted with Eq. (2) by considering two NDR dielectric function $\varepsilon^*(\omega)_{tot}=\varepsilon^*(\omega)_{str}+\varepsilon^*(\omega)_{tra}$ and results are shown in Figs. 5 and 6. The

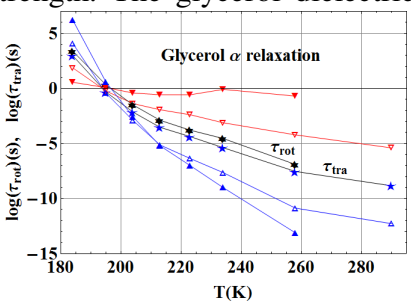


Fig. 6: Non-Arrhenius behavior of τ_{str} and τ_{rot} with corresponding slow and fast relaxation

magnitudes of g_{str} for structural and g_{tra} translational the two NDR process are shown right side of Fig. 5. Both g_{str} and g_{tra} are well separated and the interaction strength of non-Debye $g_{str}g_{str}$ dipoles and $g_{tra}g_{tra}$ dipoles completely different and responsible for α relaxation in glycerol. One can clearly see the glass dynamics relaxation having both very slow and fast relaxation in Fig. 6 with non-Debye $g_{str}g_{str}$ and $g_{tra}g_{tra}$ dipoles. For 184K, individual slow and fast relaxation contributions are shown for $\varepsilon^*(\omega)_{str}$ and $\varepsilon^*(\omega)_{tra}$ as red and blue continuous line and dashed curves and green curve is total dielectric loss curve of $\varepsilon^*(\omega)_{tot}$ of dielectric loss data. Similar features are observed for temperatures up to 258K. At 290K, the $\varepsilon^*(\omega)_{str}$ vanished, indicating that no contribution from structural relaxation, only translation relaxation contributes in the dielectric loss. Both τ_{str} and τ_{tra} show non-Arrhenius behavior as in Fig. 6. The standard error in fit parameters is less than 1% for all temperature.

The ac conductivity spectroscopy data of β-AgI are collected from the literature [6] for the temperature range 120-200K for the frequency range 3mHz to 1MHz. The ac conductivity is fitted with Eq. (3) by considering two NDR

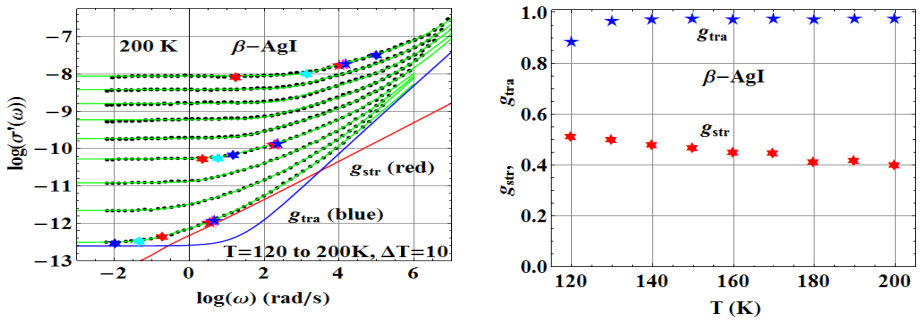
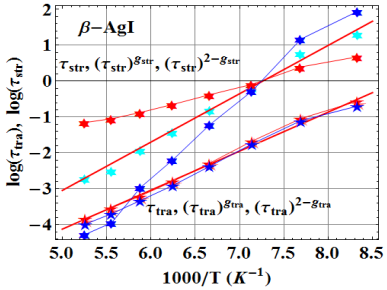


Fig. 7: Comparison of proposed NDR function solid lines with experimental dielectric loss data for glycerol (left side) and value of non-Debye dipole parameter g for rotational and translation relaxation (right side).



complex impedance functions $Z^*(\omega)_{tot}=Z^*(\omega)_{str}+Z^*(\omega)_{trs}$, in terms of complex conductivity $\sigma^*(\omega)_{tot}=1/\sigma^*(\omega)_{str}+1/\sigma^*(\omega)_{tra}$, where $\sigma^*(\omega)_{str}=1/Z^*(\omega)_{str}$ and $\sigma^*(\omega)_{tra}= 1/Z^*(\omega)_{tra}$ results are shown in Fig. 6 and 7. The two NDR functions showing existence of two

Fig. 8: Arrhenius behavior of τ_{str} and τ_{rot} with corresponding slow and fast relaxation.

different displacements of silver ion conceived via octahedral interstitial sites and other movements of silver ions that result from stacking faults of the hexagonal planes. Therefore, β-AgI has two NDR processes corresponding to structural and translational relaxation dynamics. The dc conductivity is found at

g_{str}=1 and g_{tra}=1, and follows the Arrhenius law with an activation energy 0.278±0.002eV.

6. Conclusions

A simple and general form NDR function has been envisioned in terms of ensemble of non-Debye dipoles $\{g\rho^+, g\rho^-\}$, $\{(1\text{-}g)\rho^+, (1\text{-}g)\rho^-\}$, referred as g and (1-g) dipoles. The origin for the gg dipoles is tailoring of Debye dipole charge ρ due to molecular interaction and defect disorder in the condensed matter system, where g=1 is non-interacting Debye dipole with charge ρ. The ensemble of gg dipole interactions and defect disorder leads to slow and fast relaxation rates with respect to the Debye polarization relaxation. The parameter g is an exponent in time and frequency domain and responsible for both slow and fast relaxation dynamics in the NDR processes. Dielectric loss data of Glycerol and β-AgI show excellent agreement with experimentally observed spectra in the entire range of 16 decades in frequency scale over the temperature range of 184 to 290 K for glycerol and 9 decades in the ac conductivity data of β-AgI in the temperature range120 to 200K. Both systems show two Debye and corresponding NDR for structural and translational relaxation dynamics.

Acknowledgements

Financial support from the CSIR research project 03/1279/13/EMR-II is gratefully acknowledged.

References

1. A.K. Jonscher, Dielectric Relaxation in Solids, Chelsea Dielectric Press, London, 1983.
2. K. L. Ngai, Relaxation and Diffusion in Complex Systems, Springer, New York 2011 and references within.
3. S. Havriliak, S. Nagami, J. Polym. Sci. **14**, 99 (1966).
4. K.S. Cole, R.H. Cole, J. Chem. Phys. **9**, 341 (1941).
5. D.W. Davidson, R.H. Cole, J. Chem. Phys. **19**, 1484 (1951).
6. K. Funke, *et al*., Phys. Chem. Chem. Phys. **4**, 3155 (2002).
7. J. C. Dyre, T.B. Schroder, Rev. Mod. Phys. **72**, 873 (2000); J. C. Dyre, J. Appl. Phys. **64**, 2456 (1988).
8. W. Dieterich, P. Maass, Chem. Phys. **284**, 439 (2002).
9. D. L.Sidebottom, Rev. Mod. Phys. **81**, 999 (2009).
10. J. R. Macdonald, Phys. Rev. B **71**, 184307 (2005).
11. G. Govindaraj, and R. Murugaraj, Mat. Sci. and Eng. B. **77**, 60 (2000).
12. R. Murugaraj and G. Govindaraj, Solid State Ionics, **176**, 109 (2005).
13. G.Govindaraj, Indian Journal of Pure & Applied Physics, **51**, 289 (2013).
14. G. Govindaraj, Solid State Ionics: Ionics for Sustainable World, World Scientific, Singapore, 661 (2012).
15. P. Lunkenheimer, *et al*., EuroPhys. Lett. **33**, 611 (1996).

STUDY OF STRUCTURAL PHASE TRANSITION AND DIELECTRIC BEHAVIOR OF $BiNaTiO_3$-$SrTiO_3$ (BNT-ST) SOLID SOLUTION

S. K. SAYYED*
Dep. of physics, Rashtrasant Tukadoji Maharaj Nagpur University, Nagpur-440033, M.S. India

S. A. Acharya
Email:saha275@yahoo.com

Bismuth sodium titanate (BNT) has been widely recognized as a lead free piezoelectric materials to replace PZT. Doping or substitution with other ferroelectric perovskite has been employed to improve the properties of BNT. In the present attempt, we have developed $SrTiO_3$ as a dopant to enhance dielectric behavior of BNT. (1-x)$BiNaTiO_3$-x $SrTiO_3$ (BNT-ST) solid solution x=0.24, 0.25, 0.26, 0.27, and 0.28 are synthesized by hydrothermal combustion method using metal nitrates, nitric acid and citric acid as a fuel. The structures of as-synthesized compositions of BNT-ST were confirmed by X-ray diffraction (XRD). XRD patterns for the composition (1-x) $BiNaTiO_3$-x $SrTiO_3$ [for x= 0.24] are matched with rhombohedral phase of BNT; however with the increasing ST concentration (x > 0.24) phase transition from rhombohedral-to-cubic are induced. For composition x = 0.25-0.26, both the phases are coexisted i.e rhombohedral and cubic phase. It clearly indicates that morphotropic phase boundary is developed in BNT-ST for ST composition between 0.25-0.26. These are also confirmed by RAMAN spectroscopy. The morphotropic phase boundary is the desired conditions for enhancement of dielectric and piezoelectric behavior. Enhancement of dielectric constant for these compositions is also observed.

Key words: Bismuth sodium titanate, morphotropic phase boundary, dielectric and piezoelectric behavior

1. Introduction:

Bismuth Sodium Titanate ($Bi_{0.5}Na_{0.5}TiO_3$, BNT) is ecofriendly and most widely studied lead free piezoelectric material [1,2]. Several researches is going on increasing the physical properties of BNT to replace lead based piezoelectric material which showing excellent properties at morphotrophic phase boundary (MPB). Similar to that the solid solution of BNT with other perovskite ferroelectric material can form the MPB. Recently, several studies reveal that the addition of second phase by adding certain dopants, enhances the physical and mechanical properties of the material. The most commonly studied solid solution of BNT is with $BaTiO_3$. The solid solution of BNT-BT shows morphotropic phase boundary at composition x=0.06 [3]. At this composition tetragonal phase

Proceedings of the 14th Asian Conference on Solid State Ionics (ACSSI 2014)
Copyright © 2014 ACSSI 2014 Organizers. All rights reserved.
ISBN: 978-981-09-1137-9
doi:10.3850/978-981-09-1137-9_114

induced which increase the dielectric properties. Similar to $BaTiO_3$ the solid solution of $BiNaTiO_3$- $SrTiO_3$ (BNT-ST) forms the morphotropic phase boundary at the composition range x=20-30 [4,5]. $SrTiO_3$(ST) is a highly symmetric and stable ferroelectrics at high temperature having a low temperature transition at -168^oC [6,7]. The incorporation of the Sr^{2+} ions at the A site and partially replacement of the Bi^{3+} and Na^+ reduces the transition temperature T_{max} i.e. antiferroelectric to paraelectric transition. Also the enhancement in dielectric properties is also observed.

Hence in the present report, we have studied the systematic structural changes in the (1-x)BNT-xST solid solution at the composition range x = 0.24-0.28 by using XRD and Raman spectroscopy. The effect of structural transition on dielectric properties was investigated.

2. Experimental Procedure

(1-x)BNT-xST, x=0.24-0.28 were successfully synthesized by Hydrothermal combustion method. Bismuth Nitrate ($BiNO_3.5H_2O$, Sigma Aldrich), Sodium Nitrate ($NaNO_3$,Merck), Strontium Nitrate ($SrNO_3$,Sigma Aldrich) and Titanium Isopropoxide ($Ti(OC_3H_7)_4$,Across) were used as an starting precursors. Nitric acid (HNO_3) was used as a solvent and Liquor ammonia (NH_4OH) was used for adjusting the pH of the solution. Citric acid was used as a chelating agent as well as fuel for combustion method. The synthesis was carried out in two steps. First a separate solution of Titanium Isopropoxide was prepared in citric acid with molar ratio of metal cation to citric acid 1:2. The pH of the solution was made to ~ 6 by adding liquor ammonia drop wise. Then the stoichiometric amount of Titanium isopropxide was added and stirred at 80^oC for 2 hours. Secondly all the metal nitrates were dissolved in nitric acid. Then the citric acid with a molar ratio of metals to citric acid 1:2 was added into it. The liquor ammonia was added to maintain the pH of the solution to ~ 6. After that the solution of the titanium was added and the total solution was stirred for 20 minutes at room temperature. The solution then transferred to Teflon line steel autoclave of capacity 300 ml. The autoclave was placed in hot air oven at temperature 120^oC for 30 hours. The resulting solution was combusted at 220^oC in a open muffle furnace. The resulting powder was calcined at 700 ^oC for 3 hours in a closed muffle furnace to obtain a well crystalline BNT-ST powder. The pellets of the sample were formed by adding polyvinyl alcohol as a binder. The pallets were sintered in a muffle furnace at temperature 800, 850,900,950^oC for 4 hours to optimize the sinterability.

3. Results and discussion

The X-ray diffraction pattern of different composition of BNT-ST systems are shown in Figure 1. The X-ray diffraction pattern of the (1-x)BNT-xST, composition with x=0.24-0.28 is well matched with rhombohedral BNT with JCPDS file no-36-0340.The XRD pattern shows the well crystalline (1-x)BNT-xST, powder with no other impurity or secondary phase. The peaks in the XRD pattern were shifted to lower angle side for the composition x=0.24, 0.25, 0.26 however for x=0.27 - 0.28, it is found to be shift to higher angle side. The shifting in the lower angle side indicates lattice parameter and cell volume expansion, which is observed for the composition x = 0.24 to 0.26 and the lattice contraction for x = 0.27 and 0.28. The changes in the lattice parameter and cell volume is attributed to the addition of Sr^{2+} ions having large ionic radii (1.26 Å) as compare to Bismuth Bi^{3+} and Sodium Na^{+} (1.17 Å, 1.18Å resp.). This changes in lattice parameter and lattice energy favors the phase transformation in order to stabilize the structure [8].

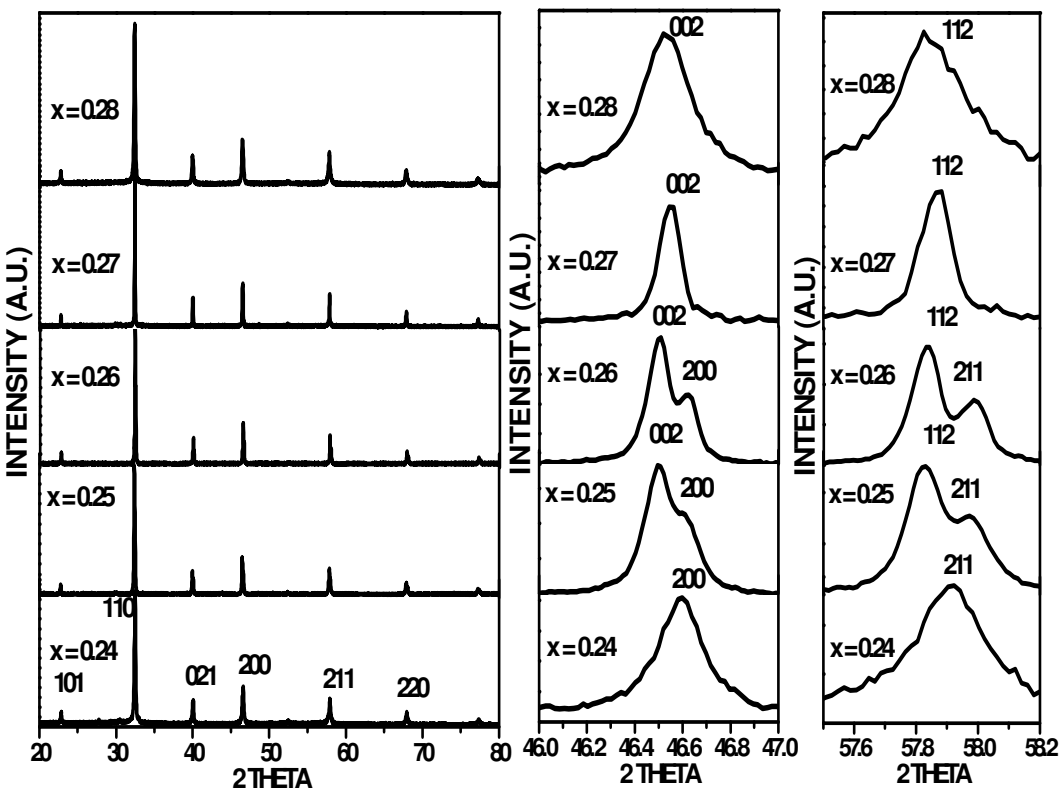


Figure 1: XRD pattern of 1-xBNT- xST (x=0.24-0.28)

Close view of XRD around 46.5^0 (200) clearly shows that at x = 0.25 the peak start splitting into two peaks, which can be indexed as (002), (200) related to pseudo cubic and rhombohedral phases, respectively. Similarly, the peak around 57.8(112) is splitted into two parts and can be manifested as (112), (211) planes related pseudo cubic and rhombohedral phase. The splitting is prominent for x=0.26; represents the existence of pseudo cubic and rhombohedral phases. It is clear evidence for morphotropic phase boundary (MPB) at composition x=0.25-0.26. Above this composition no splitting observed and there is complete transformation of structure from rhombohedral structure to pseudocubic phase. Hence the composition around x=0.25-0.26 have high aspect to show the good elctromechanical properties.

Raman Analysis

The structural order-disorder degree can be monitored by using Micro RAMAN Spectroscopy. Figure 2 shows the room temperature RAMAN spectrum of the (1-x)BNT- xST (x=0.24-0.28). It can be clearly seen that the Raman spectra of (1-x)BNT-xST, for x=0.24- 0.28 shows the broadening and shifting in the peak with the increase in the Sr concentration. To assign different vibrational mode of BNT-ST; earlier reported work are systematically revealed and compared with our results. According to the group theory calculation made by Kreisel et al [9] the rhombhedral structure of BNT showing 13 raman active modes Γ_{RAMAN} = 7A1+6E. Petzel et al [10] have reported 13 raman active modes as $4A_1$+9E due to the disorder in the A-site of the Perovskite BNT. According to work of Parija

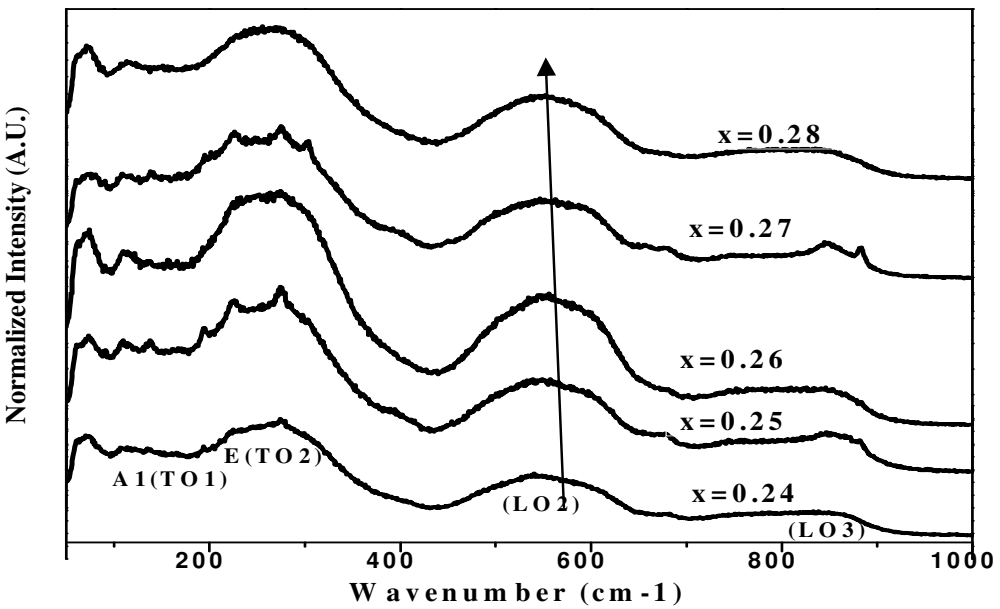


Figure 2: Room temperature RAMAN Spectrum of 1-xBNT- xST (x=0.24-0.28)

et al [11], the prominently observed 4 broad Raman bands in the BNT ceramic have been assigned to (i) band centered at 146 cm^{-1} $A_1(TO_1)$ related to the distorted octahedral BiO_6 and NaO_6 cluster. (ii) broad band near 281 cm^{-1} $E(TO_2)$ due to stretching of short range TiO_6 octahedral. (iii) band at 542 cm^{-1} (LO_2) attributed to O-Ti-O stretching symmetric vibration of the TiO_6 cluster. (iv) Broad band centered at 812 cm^{-1} (LO_3) mode has been assigned to longitudinal (LO) and transverse (TO) components, which is due to presence of the sites with containing octahedral distorted [TiO_6] clusters in the rhombohedral lattice [12].

In the present work, band observes at 146 cm^{-1} can be assigned to A1(TO1) and correlated with BiO_6 and NaO_6 octahedral distortion. It is found to be shifted to lower wavelength side (for x = 0.24) and there is the decrease in the intensity of this band with the further increase in x = 0.25-0.28 due to the addition of SrO_{12} cluster in the (1-x) BNT-xST, solid solution. In addition to that a shoulder start appearing in the lower wavenumber side with increasing Sr concentration upto x = 0.24 - 0.26 and this peak is emerging as a separated peak for x > 0.26. The bands in this region are also expected to be structure-sensitive toward phase transitions in which the A-site symmetry changes. Hence, the spectral changes at x = 0.24 - 0.28 are evident of a structural changes associated with Na-site symmetry change. The mode centered at around 260 cm^{-1} correspond to Ti-O vibration of (1-x)BNT-xST, x= 0.24 became broader and started splitting into two bands with the increasing concentration of Sr (x = 0.25 - 0.27) that shifted apart from each other, indicating particular phonon behavior in the structural evolution caused by the substitution of Sr^{2+} into $(Bi_{0.5}Na_{0.5})^{2+}$.

Dielectric Study

Figure 3 shows the dielectric constant versus temperature graph of pure BNT and (1-x)BNT-xST, x = 0.24,0.26 and 0.28 at frequency 10 KHz. As in the XRD no impurities is present so the dielectric constant is completely related to the grain size, oxygen deficiency and non uniform internal stresses due to this oxygen deficiency. The oxygen vacancy in the (1-x)BNT-xST, solid solution is created due to the partial replacement of Bi^{3+}, Na^{+} ions by the Sr^{2+} ions having large ionic radii.

From the XRD results and RAMAN analysis it is clearly seen that the addition of Sr^{2+} ions in BNT matrix introduces a structural changes in the BNT material. Therefore the dielectric constant is also get change with the doping of Sr^{2+}. An isovalent doping has been found to decrease curie temperature (Tc) [14]. In (1-x)BNT-xST solid solution the addition of $SrTiO_3$ is also act as an isovalent additives since the charge on Sr^{2+} is same as the charge on $Bi^{3+}_{0.5}Na^{+}_{0.5}$ and thus expected to decrease in T_m. Temperature versus variation in dielectric constant of BNT and BNT-ST systems (Fig 3a and insight) exhibits dielectric anomaly in BNT at around 320^{o}C, maximum temperature '*Tm*' for

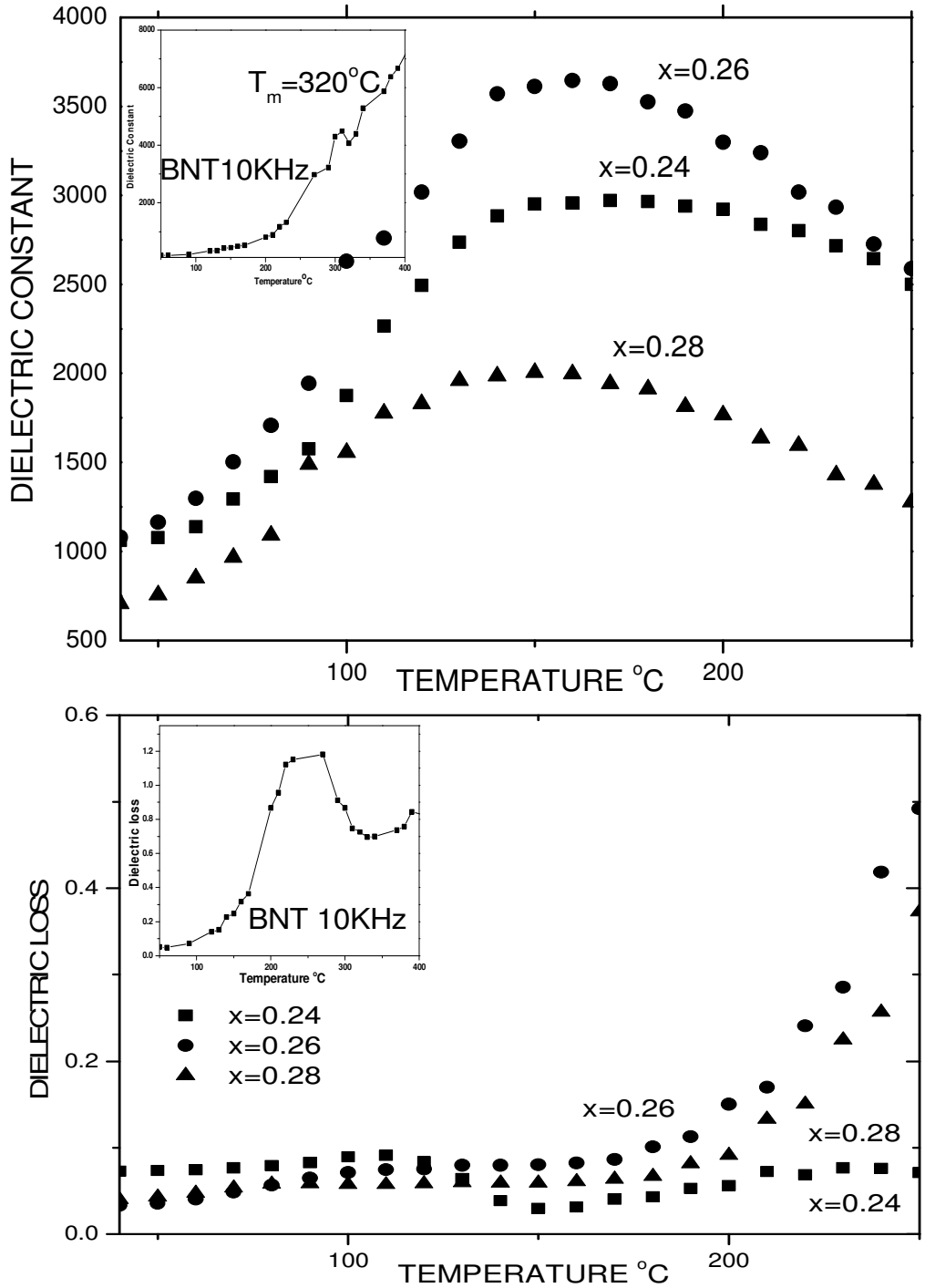


Figure 3: Dielectric Graph of BNT (Insight) and 1-xBNT- xST (x=0.24-0.28) at 10 KHz

antiferroelectric to paraelectric transition; however in BNT-ST it is observed

near 160°C. It provides a clear evidence to presume that the addition of Sr^{2+} ions at the A site of the BNT lowers the maximum temperature Tm (Antiferroelectric to paraelectric transition). It may be due to the change in the dipoles responsible for Transition as reported in [13]. Dielectric constant as well as loss of BNT-ST is found to be reduced as compared to BNT.

It can be understood as because ST is completely diffuses into the BNT lattice matrix and also the ST grows on the grain boundary of the BNT reducing the grain growth. The broadening in the dielectric graph represents the diffuse type behaviour of the (1-x)BNT-xST, solid solution. In case of (1-x)BNT-xST, solid solution the diffuse phase transition is depend on the oxygen deficiency which influence the distribution of local polarization [15]. The addition of Sr^{2+} ions favors' the oxygen deficiency.

The dielectric constant of the (1-x)BNT-xST, x=0.26 is larger than that of x = 0.24. Also the dielectric constant decreases for the concentration x = 0.28. This behaviour can be correlated to structural aspect as observed from XRD, it is clearly seen from the XRD that there is a optimal deviation in the structure for the composition x=0.24 and x=0.28. Hence at x = 0.26 is thought to be optimal composition showing good electromechanical properties due to coexisting phases of BNT ant ST.

4. Conclusion

The (1-x)BNT-xST (x=0.24-0.28) successfully synthesized by the hydrothermal combustion method. XRD characterization and the RAMAN analysis completely signify the structural changes in the BNT-ST solid solution. RAMAN active modes display the continuous shifting and broadening with the addition of Sr^{2+} revealing the characteristic feature of the phase transition. At composition x = 0.26 material shows the existence of MPB above this composition structure transformed to pseudocubic phase. The effect of additives on A site is completely seen in the dielectric study i.e. the transition temperature T_m decreases to 160°C and dielectric constant is also increases. The anomaly in the dielectric graph is broader as compare to pure BNT showing the diffuse type behaviour.

Acknowledgement

Authors acknowledge the financial support of the UGC New Delhi for providing funding under Maulana Azad National Fellowship.

References

1. R. Guo and A.S. Bhalla, *Appl. Phys. Lett.,* 89, 122909 (2006)
2. J. Wu, D. Xiao and J. Zhu, *Recent. Patents Mater. Sci*., 2, 140 (2009)
3. T. Takenaka, K. Maruyama, and K. Sakata, *Jpn. J. Appl. Phys.*, Part 130, 2236 (1991).
4. B. J. Chu, D. R. Chen, G. R. Li, and Q. R. Yin, J. *Eur. Ceram. Soc.* 22, 2115 (2002).
5. Jauch W and Palmer A, *Physical Review B,* (1999):2961–3.
6. A. Loetzsch, I. Lubcke, L.I. Uschmann, E. Forster and V. Grobe, *Appl Phys Lett* ,96, 071901 (2012) .
7. Y. Leow Chun, H. Junian and H. Mansor, *World Appl Sci J,* 14,1091 (2011) .
8. W. C. Lee, C. Y. Huang, L. K. Tsao, Y. C. Wu, *J Euro Ceram Soc*, 29,1443 (2009).
9. J. Kreisel, A. M. Glazer, G. Jones, P. A. Thomas, L. Abello, and G. Lucazeau, *J. Phys.: Condens. Matter,* 12, 3267, (2000).
10. J. Petzelt, S. Kamba, J. Fabry, D. Noujni, V. Porokhonskyy, A. Pashkin, I. Franke, K. Roleder, J. Suchanicz, R. Klein, and G. E. Kugel, *J. Phys.: Condens. Matter,*16, 2719 (2004).
11. B. Parija, S.K. Rout, L.S. Cavalcante, A. Z. Simões, S. Panigrahi, E. Longo and N.C. Batista, *Appl Phys A* , 109, 715 (2012).
12. J. Wang, Z. Zhou, and J. Xue, Acta Mater.,54, 1691,(2006).
13. J-K Lee, K.S. Hong, C. K. Kim, S.E. Park *J Appl Phys*, 91,4538 (2002).
14. S. Kasap and P.Capper , *Springer Handbook of Electronic and Photonic Materials New York: Springer Science + Business Media, Inc*(2006).
15. Marin Cernea, Gianluca Poli, Gheorghe Virgil Aldica, Ciceron Berbecaru , Bogdan Stefan Vasile and Carmen Galassi, *Current Applied Physics,* 12, 1100 (2012).

STUDY OF MORPHOLOGY, DIELECTRIC AND MAGNETIC BEHAVIOUR OF LEAD IRON NIOBATE (PFN) WITH SINTERING AIDS $4PbO\text{-}B_2O_3$ GLASS

T. QUAZI,*
Anjuman college of Engineering and Technology, Sadar, Nagpur

KAMAL SINGH
Department of Physics, Rashtrasant Tukdoji Maharaj Nagpur University, Nagpur-440033, M.S. India

Lead iron niobate [$Pb(Fe^{+3}_{1/2}Nb^{+5}_{1/2})O_3$] (PFN) is widely recognized for high relative permittivity. In the present work, PFN is synthesized by combustion route and liquid phase sintering (LPS) is used to enhance compactibility of the sample; Lead borate glass $4PbO\text{-}B_2O_3$ (LB) is used as sintering aid. Proportion of $PbO:B_2O_3$ was selected 40:60 on the basis of eutetic point of the phase diagram. The green pellets of PFN and PFN-LB are sintered at various temperatures. Relative density is obtained around 95% for 800°C sintering in case of xPFN-(1-x)LB [x= 0.01-0.03], however for pure PFN at 800°C, R.D.is found to be 92%. The XRD confirms the crystalline structure of as-synthesized PFN and LB-glass dispersed-PFN as well as amorphous nature of LB-glass. SEM and TEM techniques are used to investigate microstructure and exhibited nanoscale dimensions. Dielectric and magnetic behaviour of the compacted samples of pure PFN and PFN-LB are systematically studied and correlated with the microstructure. The dielectric response is found to be enhanced for 0.98PFN-0.02LB. The magnetic properties also are studied at room temperature for different composition.

.

1.Introduction

Lead iron niobate, $Pb(Fe^{+3}_{1/2}Nb^{+5}_{1/2})O_3$ (PFN) is well known Pb-based complex double perovskite $[A(B_IB_{II})O_3]$ ferroelectric family member, are most attractive due to their exceptionally high relative permittivity and low sintering temperature for making MLCC, actuator, sensor, memory devices, piezoelectric transducers, pyroelectric sensors [1-4]. At room temperature, PFN exhibits ferroelectric behavior due to Pb^{+2} on A-site and Nb^{+5} on B-site favoring the electric order. Mujumdar (2006) studied dielectric and magnetic properties of PFN. It also exhibit a (DPT) due to disordered cations arrangement on B-sites reported by Smolenskii and Bokov [5-7].

* *tanveerquazi05@gmail.com*

Proceedings of the 14th Asian Conference on Solid State Ionics (ACSSI 2014)
Copyright © 2014 ACSSI 2014 Organizers. All rights reserved.
ISBN: 978-981-09-1137-9
doi:10.3850/978-981-09-1137-9_116

In recent years, SHS technique (combustion route) has been established as a quick preparation process to produce multicomponent oxide ceramic powders without the intermediate decomposition and/or calcining steps [8-13]. Adoption of SHS-synthesis route for PFN, pyrochlore phase formation due to PbO losses can be reduced, as per ref. [14]. The attempts are focused here is to examine the PFN chemistry of synthesis, crystal structure, morphology and dielectric response at different temperature

2. Experimental

The initial ingredients used in this work were $Pb(NO_3)_2$ (99% Merck), $Fe(NO_3)_3.9H_2O$ (99% Merck) and Nb_2O_5 (99.5,Sigma-Aldrich) as cation precursors and urea, $CO(NH_2)_2$(99% Merck) as a fuel. The precursor were initially mixed in 50 ml distilled water and stirred for 15 min to obtain a homogeneous mixture. The homogeneous solution was heated at 250^0C (optimized temperature), the liquid frothed for a while, followed by ignition with evolution of gases and combustion occurred. To complete the combustion reaction, the reactants were further heated at 550^0C for 10 minutes in muffle furnace; reddish brown product of PFN was obtained. The product was grounded at room temperature in a mortar. The LB-glasses were prepared by following earlier reported conventional quenching technique; ingredients B_2O_3 and PbO (Merck) were used for synthesis [15]. LB-glass in different weight percentages (0.0 0.5, 1.0, 1.5, 2.0, 2.5 and 3.0 wt %) were dispersed in PFN to form different compositions. The compositions were mixed in presence of acetone with the help of ball mill (Pulverisette-6 Fritz, Germany). During ball milling, the milling rate was maintained at 600 rpm per hour. The powder was compacted using pressure of 5 ton/cm^2. The compacted pellets were sintered at temperature more than that of glass softening temperature. The density of the sintered pellet was determined using Archimedes principle [16] relative density was calculated. The Table 1 lists the nomenclature used in the present work to represent various compositions of PFN, LB and their sintering conditions. When the LB-glass percentage in PFN was increased above 3 wt%, then sintered pellet was found to melt, above 700^oC. This is due to softening temperature of LB-glass around 500^oC. Hence, maximum upto 3 wt% LB is added in PFN as sintering aids in the present work.

The crystal structure was confirmed by X-ray powder diffraction (XRD) using Cu-Kα_1 radiation, with the help of PANalytical X-ray powder diffractometer at 40 kV and 30 mA. Microstructure and surface morphology was examined by Transmission Electron Microscopy (TEM) CM200 TEM and Scanning electron microscope (JEOL:JSM-6380 Analytical SEM) The dielectric constant (ε_r) and dissipation factor (tan δ) were measured at different frequencies from 10 Hz to 1000 kHz in 25 to 200^0C temperature range by using computer

controlled HP-4192A LF impedance analyzer. The temperature during the measurements was controlled with an accuracy of $\pm 1^0$C using Eurotherm temperature controller.

3. Results

The XRD patterns of pure PFN and PFN-3-LB83 systems are shown in Figs 1(a), and (b), respectively. XRD patterns of PFN (Fig.1a) is well matched with the JCPDS data (file no. 0.032-0522) confirm the formation of single phase with monoclinic structure of PFN in 'Cm' space group symmetry. The observed XRD peaks are well matched with the lines of perovskite phase of PFN. No additional impurity phases are found. The amorphous nature of the LB-glass is not observed. XRD pattern of PFN-3-LB83 reveals the presence of sharp crystalline peaks of PFN (Fig. 1b).

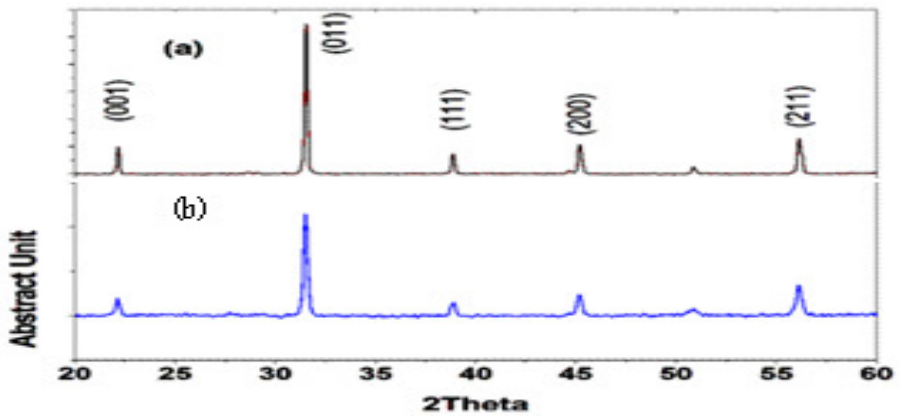


Figure 1. XRD patterns of (a) PFN and (b) PFN-3-LB83

TEM image of the as-synthesis PFN shows (Fig.2) oval shape of particles having diameter around 50 nm. It is existence of compositions fluctuation of the Fe^{3+} and Nb^{5+}, which leads to formation of many microscopic regions on the B-sites. The same trends of results have earlier been reported by Cross et al [17]. SEM images of sintered pellets of PFN-0-LB83 and PFN-2-LB83 samples are shown in Figs. 3 (a and b), respectively. Both the images reveal highly compacted structure with well defined grain and grain boundaries. However, glass deposition on the grain boundary can be clearly detected in SEM image of PFN-2-LB83. Grain size was determined by manual image analysis, matching digital pixel scale across each grain. The average grain size of PFN-0-LB83 and PFN-2-LB83 is obtained to be 1.9 μm and 2.4 μm, respectively. This clearly

shows that under the same sintering conditions grain size of PFN-2-LB-83 is more than PFN without LB. Relative density of both the system are determined and found more in PFN-2-LB83. Same trends of variation of grain size and relative density are observed in almost all samples (Table.1). However, if the LB concentration increases above 2 wt%, relative density and grain size both are found to decrease. The observed enhancement of sinterability of PFN by LB is understood on the basis of liquid phase sintering (LPS) process. The glass softening temperature of LB is around 500^{o}C, at which LB starts melting. In the present work sintering were performed above the glass softening temperature (at 700^{0}C and 800^{0}C), at which LB melt and liquid form of LB move around the grain boundaries of PFN grain due to capillary action. In capillary action, the capillary force arises due to surface tension at the interface (liquid-solid-vapour) leads the flow of liquid phase. On the same line, in the present case flow of LB through grain boundary fills the pores of PFN which leads to densification and grains-growth [18]. Thus increase in relative density using LB clearly shows that in PFN-LB sintering process is dominantly due to the liquid phase sintering (LPS) rather than solid-state sintering. However with an increase LB concentration above 2 wt%, decrease of sinterability is due to bridging of particle by glass materials, which can disintegrate the solid particles into smaller grains at the liquid-solid interface. The PFN-2-LB83 is found to optimize glass percentage in the liquid phase sintering.

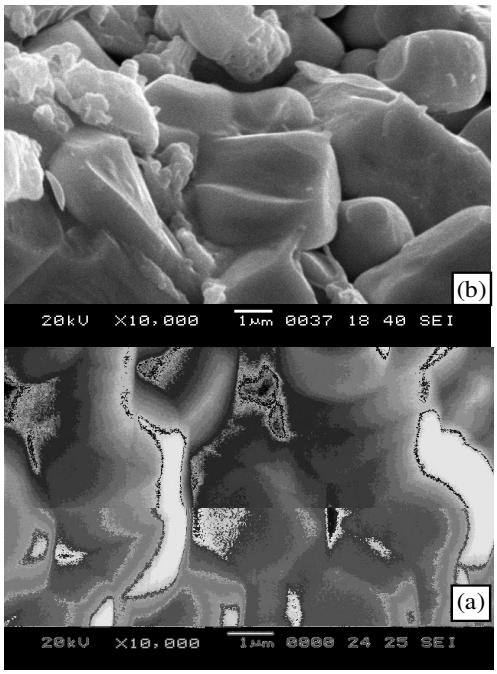


Figure 3. Scanning electron microphotograph of sintered sample
(a) PFN-0-LB83 (pure PFN) and
(b) PFN-2-LB-83 (PFN-2wt% LB glass) sintered
at 800^{0}C for 3hr

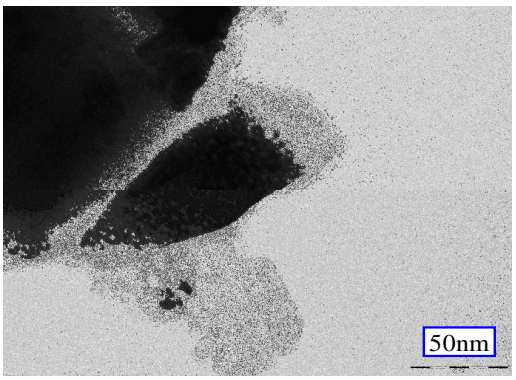


Figure 2. TEM of as prepared (before sintering) PFN prepared at 500^{0}C

Table 1. Density correction on observed dielectric constant, corrected dielectric constant, transition temperature and grain size for pure PFN

Sample code	T_{sinter} (^oC)	t_{sinter} (Hrs)	Density (%)	Porosity (%)	ε_r at 1kHz	$\tan\delta_{max}$	Grain Size (μm)	T_c (^oC)
PFN-0-LB72	700	2	88	12	13500	1.2	~ 1.2	112
PFN-0-LB73	700	3	80	20	11348	0.06	~ 1	115
PFN-0-LB82	800	2	90	10	14000	6	~ 1	110
PFN-0-LB83	800	3	92	8	15500	0.4	~ 1.9	118

The temperature profile of dielectric constant at 1 kHz frequency of PFN-LB samples sintered at 700 and 800^{o}C are displayed in figure.4. Dielectric anomaly around 100^{0}C can be clearly observed for both the samples. The dielectric maxima are shifted to lower temperature side from 118^{0}C to 90^{0}C with increasing LB percentage from 0 to 3 wt%. The dielectric anomaly can be correlated with monoclinic to cubic phase transition temperature (DPT) of PFN which has been reported at 114^{0}C [19-21].

The addition of LB in PFN is found to shift the transition temperature towards lower side. Same types of results have earlier been reported in the literature [22]. Comparison of dielectric behaviour of 700^{0}C and 800^{0}C sintered PFN-LB (Fig.5); indicate that LB influence on dielectric behaviour of PFN vary with sintering temperature. For 700^{0}C sintered sample, dielectric

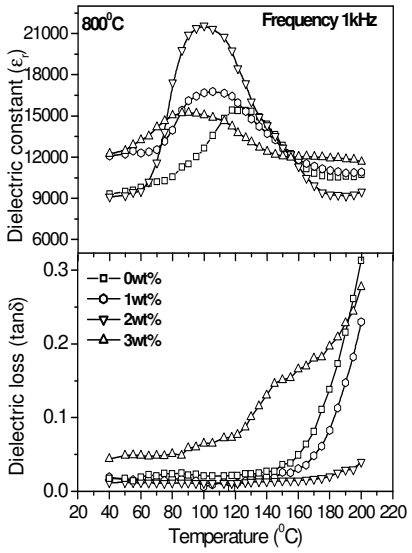
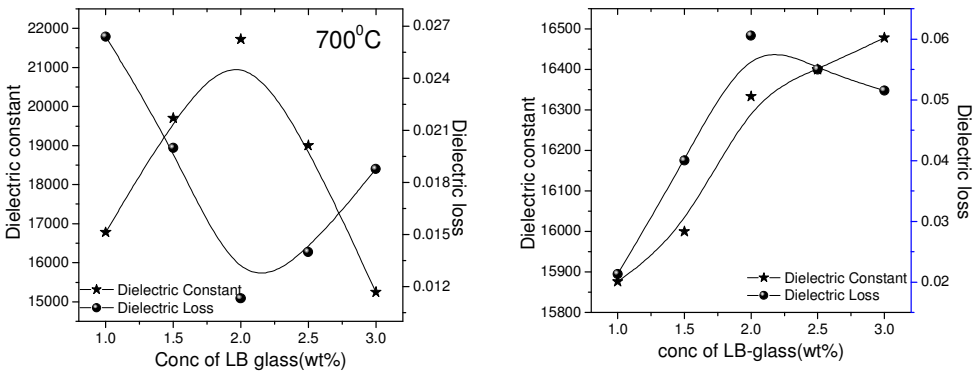


Figure 4. Variation of dielectric constant and loss with the temperature for LB-glass added PFN (1, 2, 3 wt %) at 1 kHz frequency for the pellets sintered at 800^0 C



(a) (b)

Figure 5: Dielectric constant and dielectric loss for different concentration of glass sample sintered at (a) 700^{0}C and (b) 800^{0}C, for 1 kHz frequency.

increases and loss tan δ followed the natural decrease with increase of LB glass content; however for 800^{0}C sintered sample, the dielectric constant enhanced, though loss factor (tanδ) decreases drastically as the glass concentration vary from 1 to 2 wt%; and thereafter it decreases for higher percentage of glass. In pure PFN shows the paramagnetic behavior, however the magnetic properties increases with the percentage of LB glass from 0 to3wt%.

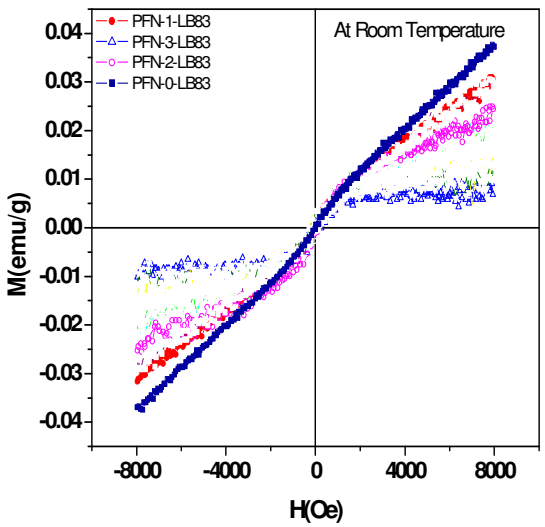


Figure 6. M-H hysthresis loop for pure-PFN and LB-PFN for 0 to3wt%

5. Conclusion

The upgrading of sinterability with the addition of LB in PFN are explained by liquid phase synthesis process. Liquid phase sintering by LB-glass in PFN is found strongly influencing on the compactness, morphology and dielectric behavior of nanostructure PFN material. The increase in densities of PFN-LB over pure PFN is also confirmed by SEM study. The dielectric behaviour is also studied. The magnetic behavior is also observed at RT

Acknowledgements

Authors are thankful to DRDO, New Delhi (INDIA) for providing financial assistance to carry out this study.

References

[1] R. Sobiestianskas,W. Peng, N. Leme, M. Karkut, J. Banys, J. Holc, and M. Kosec, *Applied physics letters*, 100, 122904(2012).
[2] D. Bochenek, P.Guzdek, *Journal of Magnetism and Magnetic Materials*, 323,369-374(2011).
[3] S.B. Majumder, S. Bhattacharyya, R.S. Katiyar, A. Manivannan, P. Dutta, M.S. Seehra, *J. Appl. Phys*. 99,024108(2006).
[4] Y. Sakabe, *Am. Ceram. Soc. Bull*. 66, 1338(1987).
[5] Y. Sakabe, Recent progress on multilayer ceramic capacitors, *MRS Int. Meet. Adv.Mater*. 10, 119-129(1989).
[6] G. Goodman, Ceramic capacitor materials, in: R.C. Buchanan (Ed.), *Ceramic Materials for Electronics, Marcel Dekker, NewYork,* pp. 79-138(1986).
[7] V. V. Bhat, A. M. Umarji, V. B. Shenoy, U. V. Waghmare, *Physical Review B*,72, 014104(2005).
[8] Y.Zhang, G.C. Stangle, *J. Mater. Res*.9(8),1997-2004(1994).
[9] M.M.A .Sekar, A.Halliyal, K.C. Patil, J. Mater. Res.11(5), 1210-1218(1996).
[10] D.A. Furno, J.R. Jurado, A.M. Segadaes, J.R. Frade, Mater. Res. Bull. 32(10), 1459-1470(1997).
[11] A.M. Segadaes, M.,R. Morelli, R.G.A. Kiminami, Combustion synthesis of aluminum titanate, *J.Eur. Ceramic. Soc*. 18(7), 771-781(1998).
[12] V.C. Sousa, A.M. Segadaes, M.R. Morelli, R.G.A. Kiminami, *Int. J. Inorg. Mater*.1 (2) 235-241(1999).
[13] S.R. Jain, K.C Adiga, V.R. Pai Verneker, *Combustion and Flame* 40(1981)71-79.
[14] M. P. Kassarjian, R. E. Newnham and J. U. Biggers: *Am. Ceram. Soc. Bull.* 64 (1985) 1108.
[15] Min, Pb., H. U. Anderson and C. C. Hodgkins, *US Patent* 4082906 (1978).
[16] ASTM Standard: Annual Book of ASTM Standards Vol.15.02, C373-88, P109-110. *ASTM, Philadelphia* P.A., pp.19103-18(1989).

[17] L. E Cross, Relaxor Ferroelectrics, *Ferroelectrics* 76–267(1987)241.
[18] W.D. Kingery:*J.Appl. Phys*., vol.30pp.301-06(1959).
[19] AIP Conf. Proc. 1512, pp. 1232-1233; doi:http://dx.doi.org/ 10.1063/ 1.4791496, Solid State Physics: Proceedings Of The 57th Dae Solid State Physics Symposium (2012).
[20] S.B. Majumder, S. Bhattacharyya, R.S. Katiyar, A. Manivannan, P. Dutta, M.S. Seehra, *J. Appl. Phys.* 99 (2006) 024108.
[21] R. Mazumder, A. Sen, *Journal of the European Ceramic Society* 28 (2008)2731-2737
[22] Chunz-Heuy Wang & Long Wu, Ceramics International 19 (1993) 391-398.

Abstracts

Cathode Materials for High Energy and Power Li-Ion Batteries

Jaephil Cho
Ulsan National Institute of Science & Technology (UNIST), Korea, Republic of
jpcho@unist.ac.kr

ABSTRACT

Recently, R & D activities of energy storage devices have been booming again after early 2000. Size of such devices have been expanded from small-sized to medium- and large-sized batteries. In terms of cathode materials for real usages in Li-ion batteries, many factors, such as tap density, capacity, pH, residual impurities should be considered and such factors are much more critical in high Ni-cathode materials. For instance, $LiNi_{0.80}Co_{0.15}Al_{0.05}O_2$ cathode exhibited must-be-solved many problems for Li-ion battery application and simple surface reactive metal oxide precursor coating demonstrated significantly improved the physical and electrochemical performances in the cell. In this talk, I am going to cover latest R & D activities of cathode materials for practical application for Li-ion batteries in my group at UNIST.

Keywords: Cathode, High power, High energy, Li-ion, Thermal stability.

Proceedings of the 14th Asian Conference on Solid State Ionics (ACSSI 2014)
Copyright © 2014 ACSSI 2014 Organizers. All rights reserved.
ISBN: 978-981-09-1137-9
doi:10.3850/978-981-09-1137-9_abstact1

Proceedings of the 14th Asian Conference on Solid State Ionics (ACSSI 2014)

Solid-State Thin-Film Batteries with 5-V-Class Cathode Materials

Naoaki Kuwata[a], Shota Kudo[b], Daichi Fujimoto[c], Yasutaka Matsuda[d] and Junichi Kawamura[e]
Tohoku University, Japan.
[a]*kuwata@tagen.tohoku.ac.jp*
[b]*kudo@mail.tagen.tohoku.ac.jp*
[c]*daichi@mail.tagen.tohoku.ac.jp*
[d]*matsuda@tagen.tohoku.ac.jp*
[e]*kawajun@tagen.tohoku.ac.jp*

ABSTRACT

All-solid-state thin-film batteries with a 5-V-class cathode material were fabricated. As the 5-V-class cathode, we have fabricated spinel structure $LiCoMnO_4$ thin films. In addition we have tried fabrication of olivine-type cathodes such as $LiMnPO_4$ and $LiCoPO_4$. Amorphous Li_3PO_4 thin films have been used as solid electrolytes in 4-V-class solid-state batteries with $LiCoO_2$ as a cathode and Li as an anode [1]. The electrochemical stability window of the amorphous Li_3PO_4 electrolytes was greater than 5 V at room temperature. Thus, the fabrication of solid-state thin-film batteries with higher-voltage cathode materials instead of $LiCoO_2$ is expected. These thin films were grown by pulsed laser deposition. X-ray diffraction and cyclic voltammetry were used to characterize the thin films. Effects of deposition parameters on the structure, morphology, and electrochemical properties of the thin films were investigated, particularly the influence of oxygen partial pressure, laser fluence, and substrate temperature. The CV curves of the $LiCoMnO_4$ thin films prepared under optimized conditions exhibited reversible 5-V charge/discharge peaks. Thin-film batteries fabricated with $LiCoMnO_4$ cathodes operated at potentials greater than 5 V, which is among the highest voltages reported for a thin-film battery. The thin-film battery also showed good cycling performance at 5 V, with an initial discharge capacity of 107 mAh/g and capacity retention of 99.4% after 20 cycles. In addition, the olivine type materials such as $LiMnPO_4$ have been operated in the thin-film batteries. However, the low lithium diffusion coefficient of the $LiMnPO_4$ limits the available capacity. Even though, the thin-film battery shows excellent cycle stability up to 500 cycles.

[1] N. Kuwata, N. Iwagami, and J. Kawamura, Solid State Ionics, 180 (2009) 644.
[2] N. Kuwata, N. Iwagami, Y. Tanji, Y. Matsuda, and J. Kawamura, J. Electrochem. Soc., 157 (2010) A521.

Keywords: All-solid-state battery, Thin film, Pulsed laser deposition, Spinel $LiCoMnO_4$, Olivine $LiMnPO_4$.

Proceedings of the 14th Asian Conference on Solid State Ionics (ACSSI 2014)

Synthesis of Nonstoichiometric LixCoO2(x>1) for All-Solid-State Lithium Ion Batteries Using $Li_2SP_2S_5$ Glass Ceramics

Sungwoo Noh[a], Junghoon Kim[b], Minjeong Kim[c] and Dongwook Shin[d]
Hanyang Univiersity, Korea, Republic of.
[a]*eva0818@hanmail.net*
[b]*nayak84@naver.com*
[c]*orangelove26@hanmail.net*
[d]*dwshin@hanyang.ac.kr*

ABSTRACT

Recently, attention has been focused on all-solid-state battery systems owing to safety concern in lithium ion battery with liquid electrolyte. Especially sulfide-based solid electrolytes are believed to be one of the most promising electrolytes for all-solid-state lithium batteries because of their high lithium ion conductivities. Nevertheless, it's well known that all-solid-state lithium ion battery with sulfide-based electrolyte has large interfacial resistance between cathode materials and solid electrolyte. In order to improve the electrochemical performance of all-solid-state lithium ion battery, nonstoichiometric LixCoO2(x>1) were synthesized by a solid-state reaction, and their characteristics has been studied. After synthesis of the stoichiometric LiCoO2, the remained excess lithium formed the lithium compounds, such as Li2CO3, are coated on the surface of cathode materials. In this reason, all the clear XRD peaks in LixCoO2(x>1) are well matched the standard pattern of the LiCoO2, and the Li2CO3 phase was gradually detected with increasing the lithium contents in LixCoO2. As the amount of lithium precursors increased, the surface of LixCoO2 became rough because of Li2CO3 coating. In initial charge discharge curves, the all-solid-state cell using cathode material as Li1.14CoO2 has the highest charge and discharge capacity. The lowest interfacial resistance between LCO and 78Li2S · 22P2S5 glass ceramic electrolyte was observed in the case of coatings amount of Li2CO3 adhered to the surface of Li1.15CoO2. From a comparison of the cycle stability of all-solid-state cell with LixCoO2(x>1), the coating weight of Li2CO3 in cathode material Li1.14CoO2 is appropriate amount for the best electrochemical properties in all-solid-state cells.

Keywords: All-solid- state lithium ion battery, Solid electrolyte, Lithium cobalt oxide, Surface modification.

Proceedings of the 14th Asian Conference on Solid State Ionics (ACSSI 2014)

Electrochemical Kinetics of $Li_3V_2(PO_4)_3$ Cathode by Parametric Impedance Spectroscopy Combined with GITT

Eui-Chol Shin[1,a], Jing Su[2,d], Yu-Guo Guo[2,e], Jaekook Kim[1,b] and Jong- Sook Lee[1,c]
[1]*Chonnam National University, Korea, Republic of.*
[a]*euichol@ejnu.net*
[b]*jaekook@chonnam.ac.kr*[c]
jongsook@jnu.ac.kr
[2]*Chinese Academy of ciences, China*
.[d]*sujing@iccas.ac.cn*
[e]*ygguo@iccas.ac.cn*

ABSTRACT

Lithium vanadium phosphate (LVP) is one of the promising cathode materials for Li-ion batteries, due to its good ionic mobility and high reversible capacity. Conventional galvanostatic or potentiostatic methods are widely used for the determination of the chemical diffusion coefficients, which is however applicable to solid solution regime only. Impedance spectroscopy is certainly indispensable tool but has been generally employed only at the limited state of charge conditions. We measured the impedance spectra down to the low frequency of 1 mHz at the steady state after intermittent galvanostatic titration steps. The impedance spectra of LVP exhibit distinct characteristics respectively for the solid solution regimes and the plateaus. The spectra in the solid solution regime can be modeled by the three dimensional transmission line model for the solid state diffusion process in addition to the charge transfer and solid-electrolyte-interface impedance. Lithium self-diffusivity and chemical diffusivity can be evaluated from the fitted circuit parameters of the transmission line models. The impedance feature in the plateau region indicates the contribution by the phase transition. The effects of the carbon-coating on the kinetic parameters evaluated by the impedance spectroscopy as well as the titration behavior were also examined.

Keywords: Lithium vanadium phosphate, Parametric impedance spectroscopy, Galvanostatic Intermittent Titration Technique(GITT), Carbon coating, Transmission line model.

Proceedings of the 14th Asian Conference on Solid State Ionics (ACSSI 2014)

Key Points and Materials Design for Rechargeable Lithium Sulfur Battery

Zhaoyin Wen[a], Jun Jin[b], Guoqiang Ma[c] and Xiangwei Wu[d]

Shanghai Institute of Ceramics, Chinese Academy of Sciences, China.
[a]*zywen@mail.sic.ac.cn*
[b]*jinger0623@163.com*
[c]*guoqiangma@student.sic.ac.cn*
[d]*xwwu@mail.sic.ac.cn*

ABSTRACT

Lithium sulfur battery is one of the most promising candidates for next generation secondary battery because of its high theoretical energy density, earth-abundant element and low cost. Nevertheless, Lithium sulfur battery suffers from severe capacity fading during cycling. This presentation reviews the systematic researches we did in the structural design of sulfur cathode and modification of electrolyte for lithium sulfur battery. We have designed a variety of sulfur conductive composite cathode, involving ordered mesoporous carbon sphere/S, S/tubular PPy, CNT/PPy/S, graphene/S paper and hollow S/PANi composite et al. A core shell structureed CNT/PPy/S composite contaning 70wt% sulfur content was synthesized , a discharge capacity of 725.8mAh/g after 100 cycles was maintained. Hollow PANI sphere@S composite was designed for prolonged cycling stability, which effectively suppressed shuttle effect and buffered the volume expansion. The discharge capacity is as high as 630mAh/g even after 1200 cycles at 0.5C. We studied the effect of different additives on electrochemical properties of the cell. The LiNO3 additive could retard the dissolution of polysulfides in the electrolyte. Pure sulfur cathode in the modified electrolyte shows improved cycling stability with 95% coulombic efficiency. An The average coulombic efficiency of lithium sulfur battery reaches 99.5% with appropriate amount PYR14TFSI ionic liquid as additive in the electrolyte. A discharge capacity maintained 638.1 mAh/g even after 100 cycles. With the improved materials, 5Ah lithium sulfur cells with energy density up to 300Wh/kg were assembled and investigated.

Keywords: Lithium sulfur battery, Composite, Cathode, Electrolyte additive.

Proceedings of the 14th Asian Conference on Solid State Ionics (ACSSI 2014)

Cathode Interface Structures in Solid-State Lithium Batteries with Sulfide Solid Electrolytes

Kazunori Takada
National Institute for Materials Science, Japan.
takada.kazunori@nims.go.jp

ABSTRACT

Lithium-ion batteries are now widely installed in portable electronics; however, they are still suffering from safety issues originated from combustible organic electrolytes. Moreover, they are anticipated to be used for vehicle and grid applications; however, batteries required in these applications are large. Increasing size increases amount of the electrolytes and lowering heat radiation to make the safety issues much more serious. Nonflammable solid electrolytes are expected to give a fundamental solution to the safety issues. In order to realize such solid-state lithium batteries, solid electrolytes having high ionic conductivities are necessary. High ionic conductivities have been often found in sulfides, because large sulfide ions leave wide openings for ionic conduction, and their high polarizability makes lithium ions highly mobile. However, the high polarizability causes a drawback. Noble potential of the cathode tends to decrease lithium-ion concentration on the electrolyte side of the cathode interface. Moreover, the decrease in the lithium-ion concentration is intense because of the weak attraction between sulfide and lithium ions, which forms a lithium-depleted layer at the interface. It is highly resistive due to the absence of charge carrier and should be eliminated in order to enhance the power density. Because the lithium depletion results from the noble potential of the cathode, the interfacial resistance will be reduced by shielding the sulfide-based solid electrolyte from the noble potential. In fact, surface coating onto the cathode material particles, which separates the sulfide-based electrolyte from the cathode material, has successfully reduced the interfacial resistance and enhanced the power density to be high enough for practical use. In addition, a self-organized core-shell structure found in LiAlyCo1?yO2 particles has the similar effect on the reduction of the interfacial resistance. Such interfacial structures will be presented in the conference.

Keywords: Lithium battery, Interface, Nanoionics.

Proceedings of the 14th Asian Conference on Solid State Ionics (ACSSI 2014)

Preparation and Cathodic Studies on α1-$LiVOPO_4$ and $LiVO(HPO_4)(C_2O_4)_{0.5}$

M. V. Reddy[a], A. Shahul Hameed[b], J. J. Vittal[c] and B. V. R. Chowdari[d]
National University of Singapore, Singapore.
[a]*phymvvr@nus.edu.sg*
[b]*a0068249@nus.edu.sg*
[c]*chmjjv@nus.edu.sg*
[d]*phychowd@nus.edu.sg*

ABSTRACT

Commercial lithium ion batteries (LIBs) use layer-type $LiCoO_2$ or $LiFePO_4$ as the cathode. LIBs with operating voltage of 3.6 V are extensively used in the present-day portable electronic devices like cell phones. However, for high-power applications like back-up power supplies and electric/hybrid electric vehicles, the LIBs need to satisfy several additional criteria, namely, cost-reduction, improvement in the energy density, safety-in-operation at high current charge/discharge rates and improvement in the low-temperature-operation. In this presentation, cathodic properties of two novel materials namely, α1-$LiVOPO_4$ and $LiVO(HPO_4)(C_2O_4)_{0.5}$ will be discussed. They were prepared by hydrothermal methods to obtain their hydrated precursors followed by dehydration. They are characterized by X-ray diffraction, Rietveld refinement, SEM, and BET surface area methods. Electrochemical investigations of these phases were carried out using cyclic voltammetry, galvanostatic cycling and electrochemical impedance spectroscopy techniques. α1-$LiVOPO_4$ has a layered structure with redox potential of 4 V and theoretical capacity of 166 mAh/g. Electrochemical studies showed a reversible capacity of 103 mAh/g at 0.1 C with low capacity fading. Hybrid frameworks with mixed oxalate and phosphate ligands have interesting structure and exhibit versatile chemistry. Novel Li containing framework of formula $LiVO(HPO_4)(C2O_4)_{0.5}$ has a layered structure with theoretical capacity of 125 mAh/g. These frameworks exhibit reversible lithium insertion/extraction at voltage of `4.0 V and a capacity of 80 mAh/g was obtained at 0.1 C. Annealing of lithium vanadyl oxalatophosphate at 800°C in Argon atmosphere resulted in $Li_3V_2(PO_4)3$-V_2O_3 composite material which exhibits excellent lithium storage.

Keywords: Cathodes, Aynthesis, α1-$LiVOPO_4$ and $LiVO(HPO_4)(C_2O_4)_{0.5}$.

Proceedings of the 14th Asian Conference on Solid State Ionics (ACSSI 2014)

NCL Behaviour and Ion Transport Property in Ion Conducting Polymers

Awalendra K. Thakur
Department of Physics, IIT Patna, Patna-800013, India.
akt@iitp.ac.in

ABSTRACT

In conducting solids with structural disorder such as; functional ceramics, non-stoichiometric crystals, glasses, transition metal oxides with multiple valence state, polymer salt complexes, polymer blends doped with salt in stoichimetric ratio etc. are considered structurally imperfect technologically class of materials. They hold key for the development of a wider variety of novel energy storage and surveillance devices, i.e. high energy density solid state batteries, super capacitors, fuel cell, sensors etc. However, such technological applications require a desirable set of parameters with unambiguous understanding of fundamental issue such as; (i) high ion transport with factors/mechanism controlling the same, (ii) separation of ionic (i.e. anionic / cationic) and electronic charge transport with exact determination of their magnitude (iii) role of external parameters like temperature, pressure, humidity, applied bias and bias frequency etc. on the electrical transport properties, (iv) role of internal parameters (stoichimetric composition defect) on ion dynamics and (v) control over tailored properties at desirable level for specific functionalities. The ever increasing demand of enhanced energy density and miniaturization is forcing the development of novel light weight ion conducting plastics (ICPS) with shape mouldability and design flexibility. However, an understanding of ion transport process in (ICPS) better known solid as polymer electrolyte (SPE) is not yet complete. It is believed that ion migration in multiphase ICPS takes place through two distinct pathway; (a) ionic motion via electron rich coordination sites in the host polymer matrix which is controlled by the ratio of electron rich sites (say Ä) and mobile cation (M+) and (b) ion transport occurring due to the motion of cation coordinated polymer chains, i.e.; mobility of polymer segments "segmental motion". Of the two possibilities noted above; the first one depends on composition of the ionic (cation/anion) species in the host polymer that can be controlled by varying salt (M+X-) concentration in host polymer. The other possibility is temperature dependent and characteristic of the polymer glass transition (i.e. ±- relaxation). ±- relaxation depends heavily on temperature as well as frequency of the applied bias. However, the exact mechanism and outcome of the coupling between ±- relaxation, ion transport and external parameters like temperature, frequency, and composition is yet to be understood completely. In the present studies, we report ion dynamics of a polymer blend based plastic conductor in the temperature limits +300C to -300C (`Tg of the blend). The role of ion concentration on relaxation, scaling and NCL response is reported for the first time.

Proceedings of the 14th Asian Conference on Solid State Ionics (ACSSI 2014)

Dynamic Heterogeneity in Organic Ionic Plastic Crystals

Fangfang Chen[a] and Maria Forsyth[b]
Deakin University, Australia.
[a]*chenf@deakin.edu.au*
[a]*maria.forsyth@deakin.edu.au*

ABSTRACT

Organic ionic plastic crystals (OIPCs) have gained considerable attention in recent years as solid-state fast ion conductors. However, their complicated microstructural and dynamic evolutions in the course of solid-solid phase transitions heighten the difficulty towards understanding their conduction mechanisms. Here we present our recent work on investigation of dynamic heterogeneity in OIPCs by means of molecular dynamics simulation. A small fraction of ions that possess above-average dynamics were identified in the plastic crystal phase, and the signature of this unusual motional behavior was found in the significant increase in the non-Gaussian parameter ±(t), which was directly related to the ion hopping between crystalline lattice positions. These unusual active ion motions could help to understand the ionic conduction in OIPC on the one hand, it also provides a reasonably possible cause for the observed NMR motional narrowing phenomena on the other hand.

Keywords: Dynamic heterogeneity, Plastic crystal, Ion transport, Ionic conduction mechanism, Molecular dynamics.

Proceedings of the 14th Asian Conference on Solid State Ionics (ACSSI 2014)

Relaxation Behavior in Clay Reinforced Polymer Nanocomposites

A. L. Sharma[1] and Awalendra K. Thakur[2]
[1]*Central University of Punjab, India.*
alsharmaiitkgp@gmail.com
[2]*Indian Institute of Technology (IIT) Patna, India.*
akt@iitp.ac.in

ABSTRACT

Polymer nanocomposite materials have evoked extensive academic and industrial attention in recent decade due to their unique properties. Ion conducting polymer nanocomposites (PNCs) have become increasingly important due to their potential applications in various electrochemical storage/conversion devices such as high energy density lithium ion batteries, PEM fuel cells, supercapacitors etc. PNCs are multicomponent system comprising of polar polymer having solvating heteroatoms, alkali metal salt having bulky anion and inert filler/clay as the adduct/dopant. Such a combination imparts structural disorder/amorphousity in the composite phase and it facilitates ion transport. The ion transport properties of PNC, in general, depends on wide ranging factors such as; (i) structural phase and pathway for ion migration, (ii) sites available for mobility of charge carriers, (iii) rate of carrier mobility, (iv) cation (charge carrier) coordination pattern with the polymer chain, (v) polymer chain motion and their orientation and (vi) flexibility of the polymer backbone structure etc. The present paper aims to analyze the effect of clay reinforcement on dielectric, conductivity and mechanical relaxation behavior of a polymer clay nanocomposite film. Macroscopic parameters like polymer glass transition temperature and available free mobile charge carriers have been analyzed properly using dynamic mechanical analysis and dielectric analysis. Dielectric analysis indicated distribution of relaxation time as a function of clay concentration whereas conductivity spectrum exhibited dispersion at lower frequency followed by saturation region at intermediate frequency. The dispersion behavior is related to the electrode polarization attributed to faster ion dynamics. The dielectric and conductivity relaxation are in excellent correlation with mechanical relaxation owing to changes in glass transition temperature due to polymer-ion-clay interaction.

Keywords: Polymer nanocomposites, Mechanical Relaxation, Dielectric Analysis, Renewable Energy Sources.

Proceedings of the 14th Asian Conference on Solid State Ionics (ACSSI 2014)

Probing Interfaces in Lithium Ion Conductors at the Atomic Level

Craig Fisher[1,a], Akihide Kuwabara[1,b], Hiroki Moriwake[1,c], Xiang Gao[1,d], Shijian Zheng[1,e], Saiful Islam[2], Hideki Oki[3,f], Keiichi Kohama[3,g] and Yuichi Ikuhara[4]

[1]*Japan Fine Ceramics Center, Japan*

.[a]*c_fisher@jfcc.or.jp*

[b]*kuwabara@jfcc.or.jp*

[c]*moriwake@jfcc.or.jp*

[d]*gaoxiang@jfcc.or.jp*

[e]*sjzheng@lanl.gov*

[2]*University of Bath, United Kingdom.*

m.s.islam@bath.ac.uk

[3]*Toyota Motor Corporation, Japan.*

[f]*4486533234@mail.ecc.u-tokyo.ac.jp*

[g]*kohama@keiichi.tec.toyota.co.jp*

[4]*The University of Tokyo, Japan.*

ikuhara@sigma.t.u-tokyo.ac.jp

ABSTRACT

Materials able to support high lithium ion conductivities are critical to the performance of lithium-ion batteries, whether as cathode, electrolyte, or anode. In conventional batteries, cathodes and anodes are typically prepared in nanocrystalline form to minimize transport lengths and maximize electrolyte- electrode contact. For all-solid-state batteries, which are garnering increasing interest, electrodes and electrolyte are deposited as thin films. In both instances, two-dimensional defects such as surfaces, grain boundaries, stacking faults, and heterointerfaces can strongly influence charge/mass transfer kinetics, and hence battery cell performance, cyclability and lifetime. One of the most powerful means of probing materials on the atomic level is atomistic computer simulation. Simulations can provide detailed insights into transport phenomena, as well as the nature and constitution of defects, including point defects and interfaces. In this paper we describe a number of studies combining results from advanced scanning transmission electron microscopy, electron energy loss spectroscopy, and atomistic simulation based on both classical forcefield models and first-principles calculations within the framework of density functional theory to reveal the structures and properties of various interfaces in Li-ion conductors such as layer- structured LiCoO2, olivine-structured phosphates such as LiFePO4, and silicates Li2MSiO4 (M = Fe, Mn) for cathode applications, as well as solid electrolytes La2/3-xLi3xTiO3 and Li3xLa1/3-xNbO3. The development of annular bright field detectors used in aberration-corrected STEMs now allows even the lightest elements to be visualized with sub-angstrom resolution in real time for direct comparison with simulation results, opening up an exciting new era for nanostructural analysis and design.

Keywords: Lithium-ion battery, Interface, First-principles calculations, Computer modeling, Atomic resolution.

Proceedings of the 14th Asian Conference on Solid State Ionics (ACSSI 2014)

In Situ Diffraction: Simultaneously Characterising Crystal Structure and Electrochemistry in Fully Functioning Batteries

Neeraj Sharma
UNSW Australia (University of New South Wales), Australia.
neeraj.sharma@unsw.edu.au

ABSTRACT

Electrochemical energy storage devices in the form of batteries are ubiquitous in society, used in everything from children's toys to mobile electronic devices, providing portable power solutions. There is a continuous drive for the improvement of batteries. A large proportion of the function of batteries arises from the electrodes, and these are in turn mediated by the atomic-scale perturbations or changes in the crystal structure during an electrochemical process (e.g. battery use). Therefore, a method to both understand battery function and improve their performance is to probe the crystal structure evolution in-situ while an electrochemical process is occurring inside a battery. Our work has utilized the benefits of in-situ neutron diffraction (e.g. sensitivity towards lithium) to literally track the time-resolved evolution of lithium in cathode materials used in rechargeable lithium-ion batteries. With this knowledge we have been able to directly relate electrochemical properties such as capacity and differences in charge/discharge to the content and distribution of lithium in the cathode crystal structure. In addition, the ability to test smaller samples (e.g. in coin cells) with in-situ X-ray diffraction has allowed us to probe other batteries types, such as primary lithium and ambient temperature rechargeable sodium-ion batteries. In particular, sodium evolution and distribution are tracked in electrodes of sodium-ion batteries. In-situ experiments that probe the time-resolved structural evolution during charge/discharge provide unparalleled insight into how electrodes evolve. Using this information a comprehensive atomic-scale picture of battery functionality can be created and permutations can be made to the electrodes that optimize battery performance. This talk will showcase some of our recent results on electrode structural evolution with respect to electrochemistry in fully functioning batteries.

Keywords: Lithium-ion batteries, Sodium-ion batteries, Neutron diffraction, X-ray diffraction, Crystal structure.

Proceedings of the 14th Asian Conference on Solid State Ionics (ACSSI 2014)

New Insights Into Novel Solid Electrolyte Materials from Magnetic Resonance Experiments

Luke O'Dell[a], Daniel Gunzelmann[b], Yogita Oza[c], Cameron Pope[d], Haijin Zhu[e], Konstantin Romanenko[f] and Maria Forsyth[g]
Deakin University, Australia.
[a]*luke.odell@deakin.edu.au*
[b]*daniel.gunzelmann@deakin.edu.au*
[c]*yoza@deakin.edu.au*
[d]*crpop@deakin.edu.au*
[e]*h.zhu@deakin.edu.au*
[f]*k.romanenko@deakin.edu.au*
[g]*maria.forsyth@deakin.edu.au*

ABSTRACT

VC is considered as a desirable additive for the anode side in Li-ion batteries, while $LiNO_3$ is also supposed to be effective for improving the performance of Li-S batteries in ether-based electrolytes. Here we explored the modification effects of VC-LiNO.

Keywords: Magnetic resonance, Solid electrolytes, Plastic crystals, Conducting polymers.

Proceedings of the 14th Asian Conference on Solid State Ionics (ACSSI 2014)

Ionic and Electronic Transport in Composite Electrodes for Lithium Batteries: In-Situ Dielectric Spectroscopy Study from Low Frequencies to Microwaves

Jean-Claude Badot[1], Kalid Ahmed Seid[2], Olivier Dubrunfaut[3], Patrick Soudan[4,a] and Bernard Lestriez[4,b]
[1]*IRCP, CNRS, Chimie ParisTech, France.*
jc.badot@chimie-paristech.fr
[2]*Adama Science and Engineering Materials Engineering Department, Adama, Ethiopia, Ethiopia.*
kalido96@yahoo.com
[3]*LGEP, CNRS, SUPELEC, UPMC, France.*
olivier.dubrunfaut@lgep.supelec.fr
[4]*IMN - CNRS - Université of. Nantes, France.*
[a]*Patrick.Soudan@cnrs-imn.fr*
[b]*Bernard.Lestriez@cnrs-imn.fr*

ABSTRACT

The improvement of battery performance requires the rationale optimization of composite electrodes. The developments of new experimental techniques as well as methodologies are needed to understand the relationships between the composition, the architecture and the performance of composite electrodes. The "ex-situ" broadband dielectric spectroscopy ("ex-situ" BDS) technique (40 Hz to 10 GHz) is used here to measure the electronic transport across all observed size scales of the composite materials for lithium batteries containing each an active material (e.g. LiFePO4, LiNi1/3Mn1/3Co1/3O2, etc.), a polymeric binder, carbon black and electrolyte. The frequency range is about 1 kHz – 5 GHz and the new device completes the traditional ex-situ measurements. In situ/operando BDS measurements will provide original data in the area in such a way that it is possible to see the evolution of the frequency dependent (complex) conductivity (ionic and electronic) at different scales with electrochemical performance. It is important to note that the classical impedance spectroscopy does not allow probing the electrical properties in the MHz – GHz range. The new device opens thus important prospects to determine the evolutions of the multi-scales electrical properties (ionic and electronic during electrochemical cycling. Our preliminary measurements show that the electronic transfer is changing with the environment: the wetting of the electrode by the liquid electrolyte leads to the formation of interactions between the polar molecules of the solvent or the ions from the salt and the active matter which influences the electronic transfer within it.

Keywords: Lithium-ion batteries, Composite electrodes, Ionic transport, Electronic transport, Dielectric spectroscopy, Dielectric relaxation, High frequencies and microwaves.

Proceedings of the 14th Asian Conference on Solid State Ionics (ACSSI 2014)

Electrode Materials for Li/Na Ion Batteries

Boddu Venkata Rami Reddy[a], Raman Ravikumar[b], Chandrashekaran Nithya[c] and Sukumaran Gopukumar[d]
CSIR-CECRI, India.
[a]*reddyphysical@gmail.com*
[b]*ravekhumaar14@gmail.com*
[c]*nithyajcs@gmail.com*
[d]*smbtapsun@gmail.com*

ABSTRACT

Electrochemical performance of reduced graphite oxide (rGO) anchored with nano-Sn particles synthesized by a reduction method is presented. The Sn nanoparticles are uniformly distributed on the surface of the rGO matrix and the particle size is `5-10 nm. The uniform distribution of Sn nano particles over rGO effectively accommodates the volume expansion experienced by Sn particles during cycling. Further, high electrochemical performance (97% capacity retention) can be ascribed to the flexible rGO matrix, which reduces the lithium-ion diffusion path lengths, thereby, providing a backbone for stabilizing the Sn particles. Sn/polypyrrole composite have been synthesized by coating polypyrrole on to the Sn particles and were investigated by physical characterization using XRD, FESEM and TEM. The Sn particles are believed to be stabilized and retain its electrochemical reactivity during charge/discharge cycling. Moreover, the composite exhibits better rate capability and cycle stability. Recently, research on Sodium ion battery is passionate due to the limitation of lithium resources and its cost. Present work on $NaxCoO_2$, synthesized by using sol gel method involving calcination up to 800°C for 12h. Charge/discharge studies have been performed at 0.1C, 0.2C, 0.5C and 1C rate in the voltage 2.0-4.2V using 1M $NaClO_4$ 1:1 (PC/EC) electrolyte delivering a capacity of 126 mAh/g. We also explored a new concept of storing Na+ ions in the rGO/Sb composites for sodium ion batteries. It delivers the highest discharge capacity (641 mAhg-1), good capacity retention (93%) and also performs well at high rate cycling (> 6600 mAg-1). Such a concept of storing Na+ in rGO/Sb composite is one of the simplest ways to enhance the electrochemical performance of metal based anodes for sodium ion batteries.

Keywords: Li-ion battery, Sn-nano particle, Sb-nano particle, Na-ion battery.

Proceedings of the 14th Asian Conference on Solid State Ionics (ACSSI 2014)

Development of $Li_2FeP_2O_7$ Cathode Glass, Glass-Ceramic and Polycrystalline Systems for Lithium Ion Batteries

Hariharan.K
Department of Physics,Universiti Putra Malaysia,43400 UPM Serdang,Selangor Darul Ehsan, Malaysia.
khariharan.iitm@gmail.com

ABSTRACT

The commercial cathode material lithium cobalt oxide ($LiCoO_2$) is expensive and cobalt has an adverse effect on environment. However, iron based cathode materials are in- expensive and environment friendly. They provide high energy density and operating voltage which find applications from house-hold devices to hybrid electric vehicles. Olivine structured materials such as lithium iron phosphate ($LiFePO_4$) has been predicted as potential cathode material. However, their poor electronic conductivity is a disadvantage. Hence, novel cathode materials and preparation techniques are much sought after. In the current work, we attempt to prepare the cathode material lithium iron (II) pyrophosphate ($Li_2FeP_2O_7$) in glass, glass-ceramic and crystalline phase. The phase pure ($Li_2FeP_2O_7$) is prepared using easily available and in-expensive starting materials. The Reitveld refinement of XRD data reveals Rwp as 0.97% and reduced-$\chi 2$ as 1.006. Impedance spectroscopy indicates electronically dominated conduction mechanism with a conductivity of 3.4×10^{-9} Scm^{-1} at 303 K in the pure phase of $Li_2FeP_2O_7$. The electronic transport in the glass phase is found to be poorer as compared to the crystalline phase, however, ionic transport improved significantly. The glass-ceramic phase depicted best electrical properties among the three phases. A comparative study of the electrical conduction characteristics in the three phases will be presented.

Keywords: Lithium iron(II) phosphate, Cathode for lithium ion batteries, Impedance spectroscopy.

Proceedings of the 14th Asian Conference on Solid State Ionics (ACSSI 2014)

Systematic Binder Design in High Capacity Silicon Anodes of Lithium Ion Batteries

Jang Wook Choi[a], You Kyeong Jeong[b], Tae-Woo Kwon[c] and Ali Coskun[d]
Korea Advanced Institute of Science and Technology (KAIST), Korea, Republic of.
[a]*jangwookchoi@kaist.ac.kr*
[b]*y.k.jeong@kaist.ac.kr*
[c]*taewookwon@kaist.ac.kr*
[d]*coskun@kaist.ac.kr*

ABSTRACT

High capacity silicon (Si) anodes have received considerable attention because its high capacity could facilitate the advent of emerging lithium ion battery (LIB) applications, such as advanced mobile electronics and hybrid electrical vehicles. For this achievement, fading mechanisms from large volume change of Si should be resolved. Along this direction, polymeric binder has turned out to play a decisive role in stable cycling of Si anodes, as the binder could stabilize the electrode films even during the large volume change of Si. In this discussion, I will cover three of my recent binder studies: 1) Mussel-inspired wet-adhesive binder designed by conjugation of catechol functional groups can be a universal approach for various polymer backbones.1 2) Hydrogen bonding was found to be very useful for Si polymeric binder because it could generate intimate interaction with Si while allowing for self-healing mechanism. As an example, I will introduce hyperbranched multidimensional ²-cyclodextrin polymer. This binder stabilizes Si electrodes by creating 3D hydrogen bonding.2 3) Finally, a more systematic binder study will be introduced. In this investigation, copolymer incorporating Meltrum's acid was designed to facilitate various binder functions such as self-healing, crosslinking, stiffness, etc. The systematic approach indicates that self-healing plays the most critical role in the Si anode performance among all the functions tested.

Keywords: Lithium ion battery, Silicon anode, Polymeric binder, Self-healing.

1 J. W. Choi et al., Adv. Mater., 2013, 25, 1571-1576. DOI: 10.1002/adma.201203981
2 J. W. Choi et al., Nano Lett., 2014, 14, 864-870. DOI: 10.1021/nl404237j

\

Proceedings of the 14th Asian Conference on Solid State Ionics (ACSSI 2014)

Development of Long Length MWCNTs/SnO_2 Nanocomposites with Increasing Capacity as Free- Standing Anode for Li Ion Batteries

Indu Elizabeth[a], Bhanu. P. Singh, S. Gopakumar and R. B. Mathur
CSIR- National Physical Laboratory, New Delhi, India.
[a]*induelizabeth20@gmail.com*

ABSTRACT

Various carbon materials have been extensively used as anode materials for rechargeable Li-ion batteries because of their consistent performance and potentialities. MWCNTs have also attracted attention as anode materials because of their high conductivity, high aspect ratio, good tensile strength etc. which makes them suitable for fabricating free standing anode. Multiwalled carbon nanotubes (MWCNTs) of length 100-150 nm prepared by Chemical Vapor Deposition is used to make free standing paper by simple vacuum filtration technique. The free standing paper when used as anode for Li ion battery shows a discharge capacity (rate C/10) of 181 mAh/g in the first cycle which increases to 197 mAh/g after the 50th cycle. SnO_2/long length MWCNTs nanocomposite is also prepared by chemical route. Free standing anode made from the nanocomposite shows a very high capacity 330 mAh/g in the first cycle which increases upto 383 mAh/g in the 50th cycle. Various characterization techniques like SEM, TEM, TGA, XRD and Raman spectroscopy have been carried out to evaluate the structure of the anode that is further correlated to its performance in Li-ion cell. This peculiar behavior of increase in capacity as cycling progresses is very remarkable and is promising for batteries.

Proceedings of the 14th Asian Conference on Solid State Ionics (ACSSI 2014)

Low Cost Synthesis Method and Characterization of $Li_2FeP_2O_7$/C as Cathode Material for Lithium Ion Battery

Zheng Zhenning[a], Liu Hanxing[b], Li Wenji and Yu Zhiyong
Wuhan University of Technology, China.
[a]*zhengzhenning@gmail.com*
[b]*lhxhp@whut.edu.cn*

ABSTRACT

In this paper, we reported a low cost synthesis method of $Li_2FeP_2O_7$/C composite via solid-state carbothermal reduction (CTR) method by using cheap Fe_2O_3 and ferric citrate as hybrid ferric source. XRD shows high purity of $Li_2FeP_2O_7$ while carbon from ferric citrate exists as amorphous carbon in the products. SEM images exhibit the size of particles is around 100-500nm, also amorphous carbon contributes to both enhancing the electrochemical performance and reducing the particle size significantly. The $Li_2FeP_2O_7$/C sample with 10% citrate content shows best electrochemical performance among the samples, has capacity of 108.6 mAh/g under 0.1C rate, which shows promising potential for cathode material of lithium-ion battery.

Keywords: Lithium ion battery, $Li_2FeP_2O_7$, Cathode materials, Solid-state carbothermal reduction (CTR) method.

Proceedings of the 14th Asian Conference on Solid State Ionics (ACSSI 2014)

Motion of Host Atoms in Some Cathodes in Li-Ion Batteries during Lithium Extraction and Insertion

Yinchun Lyu[1,a], Xiqian Yu[2,g], Rui Wang[1,b], Kyung-Wan Nam[2,h], Ruijuan Xiao[1,c], Lin Gu[1,d], Hong Li[1,e], Xiao-Qing Yang[2,i] and Liquan Chen[1,f]
[1]*Institute of Physics, CAS, China.*
[a]*yingchunlyu@gmail.com*
[b]*rui_wang@MIT.EDU*
[c]*rjxiao@iphy.ac.cn*
[d]*l.gu@iphy.ac.cn*
[e]*hli@iphy.ac.cn*
lqchen@iphy.ac.cn
[2]*Brookhaven National Laboratory, United States.*
[g]*yxqliphy@gmail.com*
[h]*knam@bnl.gov*
[i]*xyang@bnl.gov*

ABSTRACT

It is desirable that the lattice structure of cathodes in Li-ion batteries could maintain stable during lithium extraction and insertion in order to achieve excellent cyclic performance. Actually, very few materials can show high stability. Distortion of local structure, mixing of cations, appearance of new phases, dissolution of transitional metal and release of oxygen have been observed frequently in many cathodes. All these phenomena are related to the motion of host atoms during electrochemical reactions, caused by the thermodynamic instability of new formed lithium-rich or lithium-poor host structures. Therefore, it is necessary to understand the behaviors of the motion of host atoms during cycling and its impact on the electrochemical performances. Benefited from the rapid progress of characterization techniques, it is feasible now to study this problem. Local information about the motion of the host atoms in the lattice can be monitored by advanced aberration corrected scanning transmission electronic microscopy (STEM) technique. Average information can be tracked by X-ray and Neutron diffraction, X-ray absorption spectroscopy, nuclear magnetic resonance spectroscopy. In this report, the motion behaviors of host atoms in several cathode materials, including Li_2MnO_3-based, $LiCoO_2$-based, $LiCrO_2$-based, $LiNiO_2$-based materials have been investigated and compared. Typical structure variation, such as stacking changing, cation mixing, wave-like distortion of the atom plane, nucleation of new phases, formation of vacancies and phase boundaries, local amorphization, will be introduced. Impact on the thermodynamic and kinetic properties will be also discussed briefly.

Keywords: Motion of host atoms, Local structure, Cathode lithium ion batteries. Acknowledgement. Financial support from “Strategic Priority Research Program” of the Chinese Academy of Sciences, Grant No. XDA01010101 and National project 973 (2012CB932900) are appreciated.

Proceedings of the 14th Asian Conference on Solid State Ionics (ACSSI 2014)

Developing Solid Electrolytes for All-Solid-State Battery

Byoungwoo Kang
POSTECH, Korea, Republic of.
bwkang@postech.ac.kr

ABSTRACT

Our society faces energy challenges which are caused by the burning of fossil fuel. To address these challenges, fossil fuel's energy paradigm should be transformed into sustainable one through further utilizing renewable sources like solar power and wind. However, intermittent property and low quality of renewable sources make their utilization difficult. Energy storage technologies will be a key player for transforming fossil fuels energy paradigm into sustainable energy one by extending the utilization of renewable sources like wind and solar power. Among other technologies, lithium ion batteries are the most promising technology because of their high energy density and wide range of energy spectra coverage. However, the advent of novel applications such as energy storage system for renewable sources and electric vehicles makes present LIB technologies challengeable because these large-scale applications need much demanding requirements in terms of safety, cost, and cycle life. There are several approaches for solving these demanding requirements for novel applications. One of promising approach is the change of electrolyte from liquid to solid because solid electrolyte can easily address the safety issue. Furthermore, solid electrolytes have several advantages over liquid electrolyte with respect to chemical stability and high energy density originated from wide stable electrochemical window. However, solid electrolytes still suffer from their low ionic conductivity. To fully utilize solid electrolytes in all solid-state battery, the ionic conductivity should be improved by understanding ionic conduction mechanism. For this purpose, $Li_{1.5}Al_{0.5}Ge_{1.5}(PO_4)_3$ (LAGP) is chosen as a model system. In this talk, I will discuss about several parameters affecting ionic conduction with LAGP and briefly talk about our recent result.

Keywords: Battery, Solid electrolyte, All solid-state battery.

Proceedings of the 14th Asian Conference on Solid State Ionics (ACSSI 2014)

14 Years of Development in Garnet-Type Solid-State Li Ion Electrolytes and Future Trends

Venkataraman Thangadurai
University of Calgary, Canada.
vthangad@ucalgary.ca

ABSTRACT

Battery is an electrochemical device that stores electrical energy in the form of chemical energy. Among the various known batteries, Li ion batteries provide the highest gravimetric and volumetric densities, making them an ideal candidate for portable electronics and plug-in electric hybrid vehicles. The use of a ceramic electrolyte instead of organic electrolytes in solid-state Li ion batteries can eliminate safety issues. Also, solid-state batteries can operate at high voltage; thus, developing high power and energy density. Among the known solid- state metal oxide and non-oxides developed, the garnet-type metal oxide Li ion conductors show very interesting functional properties. The first studied Li-stuffed garnet-type compounds were $Li_5La_2M_2O_{12}$ (M = Nb, Ta), which show a Li-ion conductivity of $\sim 10^{-6}$ at 25°C. La and M sites can be substituted by various metal ions leading to Li-rich garnet-type, including $Li_6ALa_2M_2O_{12}$, (A = divalent ions) and $Li_7La_3C_2O_{12}$ (C = tetravalent ions). To date, Zr and Ta based garnet-type, $Li_{6.4}La_3Zr_{1.4}Ta_{0.6}O_{12}$ exhibits the highest bulk Li-ion conductivity of 10^{-3} Scm^{-1} at 25°C with an activation energy of 0.35 eV, which is an order or magnitude lower than the current used polymer. Here, we report current developments in the Li stuffed garnet-type oxides and discuss the chemical composition-structure-ionic conductivity relationship, as well as Li ion conduction mechanism of garnets.

Keywords: Solid State Li Battery, SolidLi Ion Electrolytes, Garnets Li stuffed garnets.

Proceedings of the 14th Asian Conference on Solid State Ionics (ACSSI 2014)

Effect of Li^+ Content On Lithium Ion Conductivity of Lithium Garnets

S. Ramakumar[a] and Ramaswamy Murugan[b]
Pondicherry University, India.
[a]*ramana_pec@hotmail.com*
[b]*moranamurugan@pec.edu*

ABSTRACT

The organic liquid electrolyte used in present lithium ion (Li+) rechargeable batteries are flammable and tend to leak and decompose at high temperatures. Therefore, recent research has been focused on solid state electrolytes which are expected to be electrochemically stable. Among them, garnet-type oxides came to the attention of researchers, with the stoichiometric composition of $Li^{3+x}B_3C_2O_{12}$, where B = Y, La; C = various metallic or metalloid cations and x is tuned according to the charge balance. In the present work, we have undergone a systematic investigation to understand the effect of Li^+ content on the Li^+ conductivity of $Li_xB_3C_2O_{12}$ (B = Y^{3+}, La^{3+}, Sr^{2+}, Ba^{2+}; C = Te^{6+}, Ta^{5+}, Zr^{4+}; 3 d x e 7.5 i.e., $Li_3Y_3Te_2O_{12}$, $Li_4La_{2.5}Sr_{1.25}Ta_2O_{12}$, $Li_5La_3Ta_2O_{12}$, $Li_6La_2BaTa_2O_{12}$, $Li_{6.5}La_{1.5}Ba_{1.5}Ta_2O_{12}$, $Li_7La_3Zr_2O_{12}$ and $Li_{7.5}La_{2.5}Sr_{0.5}Zr_2O_{12}$) garnet-like structure prepared by solid state reaction method. Powder X-ray Diffraction indicated that the entire selected compositional range was found to crystallize in the garnet- like structure with cubic symmetry. Scanning Electron Microscope images revealed that the grain size increases with increase in lithium content and were almost flattened like morphology for composition $Li_7La_3Zr_2O_{12}$. The total (bulk + grain boundary) ionic conductivity increases with the increasing lithium content and reaches a maximum of 5.1 x 10^{-4} S cm^{-1} at 33°C for the composition $Li_7La_3Zr_2O_{12}$ and then decreases with further increase of x in $Li_xB_3C_2O_{12}$. The Raman studies reveal the housing of lithium is exclusively on the tetrahedrally coordinated position for the $Li_3Y_3Te_2O_{12}$. Raman studies also revealed the decrease in the occupancy of the tetrahedrally coordinated lithium site with an associated increase of octahedrally coordinated lithium site with the increase of x in $Li_xB_3C_2O_{12}$.The present study revealed that the amount of Li^+ content plays a major role in the lithium ion conductivity of garnet structured electrolytes.

Keywords: Garnet-like structure, Ionic conductivity, Lithium-ion batteries.

Proceedings of the 14th Asian Conference on Solid State Ionics (ACSSI 2014)

Metastable Lithium Iron Phosphate Under Two Phase Electrochemical Reaction Between $LiFePO_4$ and $FePO_4$

Yuki Orikasa[a], Yukinori Koyama, Takashi Uyama, Katsutoshi Fukuda, Hajime Arai, Yoshiharu Uchimoto and Zempachi Ogumi
Kyoto University, Japan.
[a]*orikasa.yuuki.2a@kyoto-u.ac.jp*

ABSTRACT

Olivine structure lithium iron phosphate ($LiFePO_4$) shows a high power density. Understanding the mechanism of the phase transition can be of help in providing the origin of this fast charge-discharge ability. The material undergoes phase reactions between Li-rich Li_1-$FePO_4$ (LFP) and Li-poor Li-$FePO_4$ (FP). However, the LFP-FP phase transition model underlying battery operation has been the subject of debate for a decade. In this work, we conducted in situ time-resolved XRD and XAS measurements and studied the dynamic behavior of the $LiFePO_4$/$FePO_4$ phase transition. We examined XRD peak change during the charge-discharge reaction with a rate of 10C and relaxation process after the cycles. Before the charge, a peak at 19.15 degree can be observed, which corresponds to diffraction from the (211) and (020) planes of LFP. The charge reaction causes the appearance of peaks at 19.50 and 19.87 degrees, which reflect the (211) and (020) planes of the FP phase, respectively. In addition, an unexpected peak can be seen at 19.35 degree during the first discharge and the following charge-discharge reactions. The new peak reversibly forms and disappears in synchronization with the electrochemical cycling, and the new peak is located between the peaks of LFP and FP. These results suggest that the new peak is related to an olivine-type $LixFePO_4$ phase with an intermediate composition. This study experimentally observes the phase transition through the metastable phase under nonequilibrium battery operation for the first time.

Keywords: Lithium ion battery, Cathode, $LiFePO_4$, Phase transition, In situ measurement, XRD.

Proceedings of the 14th Asian Conference on Solid State Ionics (ACSSI 2014)

Impedance Spectroscopy for Beta-Alumina: Revisted and Settled

Jee- Hoon Kim[1,a], Eui-Chol Shin[1,b], Dong-Chun Cho[1,c], Sooseok Kim[2], Youngkoo Yoon[2], Keedeok Yang[2], Jinhyung Beom[2], Shu Yamaguchi[3], Jaekook Kim[1] and Jong-Sook Lee[1,d]
[1]*Chonnam National University, Korea, Republic of.*
[a]*jeehoonkim@ejnu.net*
[b]*euichol@ejnu.net*
[c]*dongchun@ejnu.net*
[d]*jongsook@jnu.ac.kr*
[2]*Fine Tech Co. Ltd., Korea, Republic of.*
[3]*University of Tokyo, Korea, Republic of*

ABSTRACT

In spite of being known as the archetypical solid electrolyte system since early seventies, vast amount of the literature published in the following decades, and the successful development into the commercialized NAS battery system, the electrical characteristics of the system seems not well established. The reported values are often vary by orders of the magnitude. In view of the extreme crystallographic conduction anisotropy, for polycrystalline beta (double prime) alumina in application a zig-zag conduction path across grains may be easily supposed. Grain boundaries may have additional blocking effects for the transport across or may promote the transport by providing parallel high conductive paths along them. Severely overlapped, strongly sample-sensitive impedance spectra falter mechanistic approaches. It will be shown that the presentation of the raw data measured over a wide range of temperature can illustrate clearly the AC characteristics and even allow the immediate quantitative evaluation of the conduction properties. AC-4-probe method is useful to distinguish definitely the sample and electrode effects, when applicable. Bulk frequency dispersion with the cube-root dependence, transmission line model with two parallel resistor network shunted by the capacitors where the high conduction path is selectively blocked, rather than the brick-layer model of the resistors in series, and huge current constriction effects are identified as characteristic features of polycrystalline beta alumina samples.

Keywords: Impedance spectroscopy, Beta alumina, grain boundary effects.

Proceedings of the 14th Asian Conference on Solid State Ionics (ACSSI 2014)

Mixed Glass Former Effect in Mol% $50Li_2O$-$50[xNb_2O_5$-$(1-x)P_2O_5]$ Glasses

Prashant Dabas[1] and K. Hariharan[2]
[1]*Indian Institute of Technology Madras, India.*
pra306843@gmail.com
[2]*Universiti Putra Malaysia, Malaysia.*
khariharan.iitm@gmail.com

ABSTRACT

The effect of incorporation of a second glass former niobium pentoxide (Nb_2O_5) on the physical and chemical properties of the notoriously hygroscopic glass system mol% $_{50}Li_2O$-$_{50}P_2O_5$ is investigated. The glass modifier (Li_2O) content is kept fixed at mol% 50 while the glass former P_2O_5 is sequentially replaced by another glass former Nb_2O_5. Essentially, the glass modifier to former ratio is kept unity and the structure is modified by replacing P_2O_5 with Nb_2O_5. The conductivity (Ã) of a conducting system depends on the concentration (n) and mobility (¼) of the charge carriers by the relation, Ã = nq¼ where q is the charge on the carriers. As, the concentration of the charge carriers is fixed (mol% 50), the effect of the change in the structure on the mobility of lithium ion is probed as Nb_2O_5 replaces P_2O_5 in the glass matrix. Glasses in the series mol% $50Li_2O$-$50[xNb_2O_5$-$(1-x)P_2O_5]$, x = 0 to 0.8 are investigated. The competitive network formation by two network formers influences the lithium ion motion and thermal stability of the glass. Variation of the following physical quantities with composition are investigated; (i) glass transition temperature, (ii) dissolution rate, (iii) density, (iv) Vickers hardness, (v) structure of the oxy-anion network, (vi), ionic conductivity (vii) activation energy for lithium ion conduction, (viii) fragility index, and (ix) crystallization behavior. Further, these variations will be discussed in the light of "Anderson-Stuart Model".

Keywords: Mixed Glass Former Effect, Glass Transition, Ionic Conductivity, Activation Energy.

Proceedings of the 14th Asian Conference on Solid State Ionics (ACSSI 2014)

Fast Proton Transport Mechanisms in the Triflic Acid Containing Guanidinium Triflate

Haijin Zhu[1,a], Usman Rana[2] and Maria Forsyth[1,b]
[1]*Deakin, Australia.*
[a]*h.zhu@deakin.edu.au*
[b]*maria.forsyth@deakin.edu.au*
[2]*King Saud University, Saudi Arabia.*
ranausmanalii4u@gmail.com

ABSTRACT

In our recent work, we have investigated the avenue of proton conductivity in the aprotic versions of organic ionic plastic crystals (OIPCs) by adding acids of various strengths and compositions.1,2 High proton conductivity was achieved in the plastic crystal phase of various acid-containing OIPCs. In line with the emergence of these new proton-conducting materials, there is an increasingly urgent need to fully understand the nature and mechanisms of the ionic transport and related molecular dynamics in these materials. In the present work, we investigate the solid-state dynamics of a protic organic solid which we hypothesised may display OIPC behaviour, guanidinium triflate. Several orders of magnitude enhancement of conductivity is observed upon addition of HTf to the organic solid, and this appears to follow percolation behaviour with a percolation threshold of approximately 2% HTf. The data support a structural diffusion (or Grotthus) mechanism of proton transport with a calculated Haven ratio significantly less than unity. 13C SUPER and 14N overtone NMR experiments were used to study the mobility and symmetry of the triflate anion and guanidinium cation respectively at molecular level. The former experiments shows that the CF_3 group in the anion displays fast and isotropic motion at room temperature. In contrast to the high mobility of the anion group, the 14N overtone experiments indicate that, the guanidinium cation is static in both the pure and the doped GTf samples at room temperature.

Keywords: Guanidinium Triflate, Transport, NMR, Organic Ionic Plastic Crystal(OIPC).

Proceedings of the 14th Asian Conference on Solid State Ionics (ACSSI 2014)

Preparation and Characterization of Novel Sulfobetaine Based Polymer Electrolyte Doped with NH_4PF_6

Manindra Kumar, Jagdish Kumar Chauhan, Madhavi Yadav and Neelam Srivastava
Banaras Hindu University, India.
manindra1986@gmail.com
[b]*jagdishchauhan34@gmail.com*
[c]*madhavi.phy13@gmail.com*
[d]*neelamsrivastava_bhu@yahoo.co.in*

ABSTRACT

Solid polymer electrolytes based on zwitterions have been prepared having different compositions of NH_4PF_6 by solution cast technique. XRD study indicates that pure polymer was semi-crystalline which chanced in to amorphous behavior with addition of salt. The maximum room temperature ionic conductivity has been found to be $\sim 10^{-3} Scm^{-1}$ for 50% salt doped electrolyte and conductivity obeys Arrhenius behavior with temperature. The broad peak in the Imaginary M•, Z• and μ• indicates the material is non-Debye in nature or distribution of relaxation. To recognize different relaxation, loss tangent curves have been deconvoluted and relaxation times have been calculated corresponding to each peak with salt concentration. The Kohlrausch-Williams-Watts (KWW) exponent ², is found to be nearly constant with salt concentration. Scaling of conductivity with salt and temperature is done successfully and it is found that a common phenomenon governs the conduction mechanism. Frequency dependent conductivity curves are analyses for conductivity power law. The power law exponent 'n' is > 1, which indicates the NCL/SLPL type behavior in the studies frequency range. NCL/SLPL type behavior is further supported by merging trend of conductivity spectra at higher frequency side, studied at different temperature.

Keywords: Polymer Electrolytes, Relaxation time, Loss tangent.

Proceedings of the 14th Asian Conference on Solid State Ionics (ACSSI 2014)

The Fabrication and Evaluation of Solid Oxide Fuel Cells Prepared by Spray Pyrolysis

Peter Hing[a], Montri Suklueng[b], Nyuk Yoong Voo and Lim Chee Ming[c]
Universiti Brunei Darussalam, Brunei Darussalam.
peter.ng@ubd.edu.bn
[b]*10h0602@ubd.edu.bn*
[c]*cheeming@ubd.edu.bn*

ABSTRACT

This paper describes the design and construction of a compact low cost spray pyrolysis system which can be heated up to 450°C. Micron thick layers of ceramic materials for devices have been deposited. The system has been used for the construction of symmetrical cells and experimental solid oxide fuel cells. Various processing parameters have been investigated to produce dense 20 micron thick GDC10 as oxide electrolyte on porous GDC10/NiO anode. The impedance of symmetrical cathodes have been studied and experimental SOFCs fuel cell evaluated up to 800C. The performance of the experimental SOFCs with dense GDC10 electrolyte, porous GDC10/NiO anode and experimental cobalt based cathode up to 800°C is highlighted.

Keywords: Spray pyrolysis, GDC10, Anode, Cathode, Symmetrical cathode, SOFCs, Impedance, Power density.

Proceedings of the 14th Asian Conference on Solid State Ionics (ACSSI 2014)

Enhancement of Ionic Conductivity of Dy-Doped Ceria: Role of Vacancy and Oxidation State

Smita Acharya[a] and Shradha Joshi[b]
Department of Physics, RTM Nagpur University, India.
[a]*saha275@yahoo.com*
[b]*acharya@yahoo.com*

ABSTRACT

High ionic conductivity is highly desired to develop oxide electrolytes for SOFC. In search of advanced materials, designing electrolytes which can exhibit better ionic conductivity is the prime focused of SOFC development. In recent years doped ceria electrolytes have emerged as a potential candidate materials as oxide electrolytes. Proper selection of dopants and fine tuning of microstructure can significantly improve ionic conductivity. In the present work, we report a simple hydrothermal techniques to synthesize Dy-doped ceria in different compositions ($Ce_{(1-x)}Dy_xO^{2-}$; x = 0.05 to 0.3). Structure and microstructure are studied by X-ray diffraction (XRD), Scanning Electron Microscopy (SEM) and Transmission Electron Microscopy (TEM). Ionic conductivity is studied by Impendence spectroscopy. To understand the correlation between microstructure and ionic conductivity, the structure, elemental analysis and oxidation state at micro-scale are analyzed by X-ray photoelectron spectroscopy (XPS) and UV-ViS spectroscopy. The micro-scale structural features and ionic conductivity showed an acute dependence on the concentration of oxygen ion vacancies and oxidation state of cerium, which in turn, could be modified by dopant concentration. Results from X-ray photoelectron spectroscopy showed an increased in concentration of oxygen ion vacancy with dopant concentration. The concentration of oxygen ion vacancy increased from 1.6 x 1020 cm^{-3} to 4.3 x 1020cm^{-1} with increase in dopant concentration from x = 0.05 to 0.3. Oxidation state of cerium is also found varying with dopant concentration. Maximum conductivity was obtained for 20 mol% Dy-doped ceria. The role of oxygen-ion vacancy and trivalent cerium in modifying ionic conductivity is discussed.

Keywords: Dy-doped ceria, Solid electrolytes, Solid oxide fuel cell, XPS and UV-VIS study, axygen vacancy.

\

Proceedings of the 14th Asian Conference on Solid State Ionics (ACSSI 2014)

Mixed Inorganic Salts Modified $CaZrO_3$-Based Proton Conductor with Improved Sinterability and Electrical Conductivity

Xiaowei Chi[a], Jingchao Zhang[b], Peng Peng[c], Zhaoyin Wen[d], Yu Liu[e] and Jinduo Han[f]
CAS Key Laboratory of Materials for Energy Conversion, Shanghai Institute of Ceramics, Chinese Academy of Sciences, China.
[a]*chixiaowei@student.sic.ac.cn*
[b]*jingchaozhang@mail.sic.ac.cn*
[c]*pengpeng@student.sic.ac.cn*
[d]*zywen@mail.sic.ac.cn*
[e]*yuliu@mail.sic.ac.cn*
[f]*hanjinduo@mail.sic.ac.cn*

ABSTRACT

$CaZr_{0.9}In_{0.1}O_{3-\delta}$ (CZI) has been considered to be one of the most promising proton conductors with considerable mechanical performances and excellent chemical stability against acidic atmospheres containing H_2O and CO_2. At present, the factors such as poor sinterability and low electrical conductivity still hindered their practical application. Recent research has demonstrated that some inorganic salts could improve the zirconate based conduction. Here, mixed inorganic compounds NaOH-Na_2CO_3 were for the first time used as an additive in CZI ceramic to improve its sinterability and conductivity. CZI powders synthesized by the sol-gel method were mixed with the additives via the ball-milling method. XRD, SEM and EIS techniques were then utilized to characterize the compositing powders and ceramics. The NaOH-Na_2CO_3 showed little influence on the phase structure of CZI powders and ceramics, but the densification temperature of CZI ceramics significantly decreased. Most importantly, the contribution of NaOH-Na_2CO_3 afforded the CZI ceramic under wet hydrogen at 800°C an electrical conductivity of as high as 10^{-2} S/cm, which were two orders of magnitude higher than that of pure CZI, verifying the feasibility of the method. Besides, the new method could be developed to improve the performances of other ionic conductors.

Keywords: $CaZrO_3$, Proton conductor, Inorganic salt, Electrical conductivity, Sol-gel.

Proceedings of the 14th Asian Conference on Solid State Ionics (ACSSI 2014)

A New Approach to AC Analysis of Solid Electrolytes

Dong-Chun Cho[a], Jee-Hoon Kim[b], Young-Hun Kim[c], Gye-Rok Kim[d], Eui-Chol Shin[e] and Jong-Sook Lee[f]

[1]School of Materials Science and Engineering, Chonnam National University, Korea, Republic of.

[a]dongchun@ejnu.net
[b]jeehoonkim@ejnu.net
[c]younghun@ejnu.net
[d]grkim3@ejnu.net
[e]euichol@ejnu.net
[f]jongsook@jnu.ac.kr

ABSTRACT

Impedance spectroscopy is the fundamental and essential tool for characterization of solid state electrochemical cells and the components. However, reliable and accurate analysis requires much experience and expertise. Errors and mistakes in the analysis of the impedance response covering a wide range of magnitude and frequencies could not be easily noted. It is not usually possible to evaluate the propriety of the analysis based on some individual spectra reported. It is supposed that more often the data are frustrating and confusing and thus could not be analyzed nor published. This work shows a clear overview of the AC characteristics can be given by AC conductivity curves at different frequencies in Arrhenius plots. Series of capacitance and admittance Bode plots can provide complimentary information. Especially, admittance Bode plots can indicate the characteristic frequency dependence irrespective of the presence of the ideal capacitors in parallel. The presentation can allow quantitative parameter evaluation, which may not be necessarily less accurate than the fitting analysis, which is strongly dependent on the modeling and procedures. The proper equivalent circuit model with well-defined power law dependence can be inferred from these plots. Simulated AC characteristics in comparison with the experimental data can unambiguously illustrate and explain the equivalent circuit models and the physical mechanism. The method has been found useful for many electroceramics with huge grain boundary impedance at low temperatures such as Y-doped $BaZrO_3$ and other proton conducting ceramics, Gd-doped ceria nanocrystals, LLZ ($Li_7La_3Zr_2O_{12}$) and lithium glass ceramics, LLT, and Na beta-alumina.

Keywords: Ac conductivity curve, Impedance spectroscopy, Capacitance and admittance Bode plots.

Proceedings of the 14th Asian Conference on Solid State Ionics (ACSSI 2014)

Ion Dynamics in $Na_2NbXP_3O_{12}$ (X=Cu, Cd, Pb, Zn) Glass with Unusual Complex Non-Debye Relaxation Function

N. S. Krishna Kumar[a] and G. Govindaraj[b]
Department of Physics, Ponduicherry University, Puducherry, India.
[a]*krishnanskumar@gmail.com*
[b]*ggraj_7@yahoo.com*

ABSTRACT

Understanding of ion dynamics through disordered solids are still challenging. Impedance spectroscopy is one of the relevant tools to understand the electric relaxation and ion dynamics. The impedance data of ion conducting glasses $Na_2NbXP_3O_{12}$ (X = Cu, Cd, Pb, Zn) are analysed with complex anomalous relaxation function, Æ*(t) = exp(-(t/Ä)⌈*) with ⌈* = (iÄ)^(1-g), i = sqrt(-1) and 0 < g d 1. This complex relaxation function corresponds to complex current density j*(t) directly proportional to exp(-(t/Ä)⌈*). The complex anomalous relaxation function has the analytical form in frequency domain Z*(É) = R/(1+iÉÄ)⌈*) and it is used to obtain the parameters from impedance data. The relaxation process originates as Debye relaxation with g = 1 and it is considered as fast process. A relatively slow relaxation with g < 1 generates due to non-random motion of ions. The physical picture for the slow and fast process is attributed in terms change in barrier energy and site energy due to trapping of mobile charge carriers. The fast relaxation process with Ncq charge carriers changed into a slow relaxation process with gNcq hopping charge carriers and (1-g)Ncq trapped charge carriers. Ion conduction occurs with a series of forward backward jumping through disordered host lattice of random energy barriers. Ion conduction and electrical relaxation of glass samples were analysed for coupled fast and slow relaxations. Both fast and slow process are thermally activated process and follows Arrhenius equation. Zn substituted glass shows lesser activation energy and higher conduction. The energy levels involved in hopping are obtained from activation energies of fast and slow process. The physical picture of ion dynamics and electric relaxation obtained from the complex anomalous relaxation function is compared with the Sidebottom's anomalous diffusion and model and mean squared displacement approaches.

Keywords: Ion dynamics, Non-Debye relaxation, Anomalous diffusion, Ion conducting glass, NASICON.

Proceedings of the 14th Asian Conference on Solid State Ionics (ACSSI 2014)

Hydration/Dehydration Kinetics in Protonic Ceramic Conductors: Moving Boundary Diffusion Problems

Gye-Rok Kim[1], Hyun-Ho Seo[1], Jung-Mo Jo[1], Eui-Chol Shin[1,a], Ji Haeng Yu[2] and Jong-Sook Lee[1,b]

[1]*Chonnam National University, Korea, Republic of*

[a]*euichol@ejnu.net*

[b]*jongsook@jnu.ac.kr*

[2]*Korea Institute of Energy Research, Korea, Republic of.*

jhyu@kier.re.kr

ABSTRACT

A high temperature van der Pauw method using a bulk disk sample was successfully applied to monitor non-monotonic conductivity relaxation upon water in-/ex-corporation of a protonic ceramic conductor, barium zirconates doped with 20 m/o yttrium (BZY20). Application of four electrodes along the entire lateral thickness of the disk sample and the averaging of the reciprocal and reversed polarity measurements allow a reliable estimation of the conductivity effects representing the one-dimensional diffusion processes. The faster hydrogenation process was found slightly more strongly activated than the slower oxygenation process and dehydrogenation kinetics upon water excorporation was slower than the hydrogenation. The observation can be explained by the moving boundary diffusion problem as previously directly evidenced by optical spectroscopy where the hydrogenation relaxations controlled by the development of the hydration fronts over the fraction of the sample thickness from the surface by the hydration-enhanced chemical diffusivity of water while the reoxidation is involved with the chemical diffusion over the entire sample thickness. The mechanism is shown to be general for the protonic ceramic conductors with non-monotonic conductivity relaxations.

Keywords: Protonic cermic conductors, Yttria-doped barium zirconate, van der Pauw method, Conductivity relaxation, Moving boundary diffusion.

Proceedings of the 14th Asian Conference on Solid State Ionics (ACSSI 2014)

Three-Dimensionally Ordered Macroporous Cu_2O/Ni Inverse Opal Electrodes for Electrochemical Supercapacitors

Chien-Chia Wang
National Chiao Tung University, Taiwan.
wang.cc@nsrrc.org.tw

ABSTRACT

With an ordered polystyrene (PS) template-assisted electrochemical approach we synthesized three-dimensional ordered macroporous (3DOM) Cu_2O/Ni inverse opals as electrodes for supercapacitors. The 3DOM Cu_2O/Ni electrodes display superior kinetic performance, and satisfactory rate capability and cycling performance. We demonstrate a novel nanoarchitecture consisting of a 3DOM Cu_2O/Ni inverse opal structure using electrodeposition of Ni metal within a polystyrene (PS) bead template. CuO nanostructures are subsequently deposited on the 3DOM Ni substrate to construct a nano-architectured pseudocapacitive electrode. The electrode nano-architecture might improve the power density in two ways: the 3DOM Ni substrate is expected to attain electrical conductivity greater than that of a conventional metal-oxide electrode, and the periodic pore structure inherent in ordered inverse opals should allow greater ionic conduction in the electrolyte-filled pores. The electrochemical characteristics of the resulting 3DOM Cu_2O/Ni architecture were examined for pseudocapacitor electrodes.

Keywords: Pseudocapacitor, Cu_2O, Polystyrene, Three-dimensionalordered macroporous Electrodeposition.

Proceedings of the 14th Asian Conference on Solid State Ionics (ACSSI 2014)

$Li(Ni_{1/3}Mn_{1/3}Co_{1/3-x}M_x)O_2$, M = Na, Mg, Ba and x = 0 - 0.33 as Potential Cathode Materials for Rechargeable Li-Ion Batteries

Gayani Amaraweera[1,a], Athula Wijayasinghe[1,b], Bengt- Erik Millander[2] and M. A. K. Lakshman Dissanayake[1]

[1]*Institute of Fundamental Studies, Sri Lanka.*

[a]*thngamaraweera@gmail.com*

[b]*athulawijaya@gmail.com*

[2]*Chalmers Institute of Technology, Sweden*

ABSTRACT

$Li[Ni_{1/3}Mn_{1/3}Co_{1/3}]O_2$ is presently being commercialized as cathode materials for rechargeable Li-ion batteries (LIB). However, LIBs have a high production cost partly due to the expensive cathode material containing Co. They are mainly used for consumer electronics but still costly for vehicular applications. Hence it is worthwhile to investigate $Li[Ni_{1/3}Mn_{1/3}Co_{1/3}]O_2$ based system, by fully or partially substituting expensive Co with other cheaper elements. Accordingly, this work is based on investigating $Li(Ni_{1/3}Mn_{1/3}Co_{(1/3-x)}M_x)O_2$, M = Na, Mg, Ba and x = 0 - 0.33, for the LIB cathode. Material synthesis was done by Glycine Nitrate Combustion technique by calcining at 900°C. X-ray diffractometry, scanning electron microscopy and thermo gravimetric analysis were used for the materials characterization. Solid pellets pressed at 100 MPa and sintered at 1000°C were used for electrical characterization by d.c. four probe technique. Composite $Li(Ni_{1/3}Mn_{1/3}Co_{1/3x}M_x)O_2$ electrodes were fabricated via tape casting and their electrical conductivity was determined by the van der Pauw technique. Electrochemical properties were examined with CR2032 coin cells using lithium metal foil as counter and reference electrodes with 1M $LiPF_6$ electrolyte. The cells were charged and discharged in a voltage range of 2.5 - 4.6 at a 0.2 C rate. The phase analysis revealed the formation of solid solutions of appropriate layered $Li(Ni_{1/3}Co_{1/3}Mn_{1/3})O_2$ phase of R3m structure in the prepared compositions over x = 0.11, except with Ba. The synthesized powders were quasi-spherical, sub micron size secondary particles formed by aggregating nano-scale primary particles. Further, most of these compositions showed higher electrical conductivity than the base material $Li(Ni_{1/3}Co_{1/3}Mn_{1/3})O_2$ for which the room temperature conductivity was 8.0×10^{-7} S/cm. In cell studies, the Na and Mg substituted materials with x = 0.04, showed an appropriate discharge capacity of 175 $mAhg^{-1}$ and 140 $mAhg^{-1}$ respectively. Hence this study revealed the possibility of preparing relatively cheaper cathode materials suitable for LIBs.

Keywords: Li-ion rechargeable battery, Cathode materials, Electrochemical performance.

Proceedings of the 14th Asian Conference on Solid State Ionics (ACSSI 2014)

Kinetic Study of Reactions between $LiFePO_4/FePO_4$ and Redox Species

Qizhao Huang[a], James Jennings[b] and Qing Wang[c]
National University of Singapore, Singapore.
[a]*qizhao@nus.edu.sg*
[b]*j.r.jennings@nus.edu.sg*
[c]*msewq@nus.edu.sg*

ABSTRACT

Lithium-ion battery is the most popular energy storage device for portable electronics due to its high energy density. It is not, however, suitable for large-scale applications before safety and other concerns are addressed. The Redox Flow Lithium-ion Battery (RFLB)1, a novel device, exploits the system design of redox flow battery, a popular choice for large-scale energy storage applications, and high energy density of lithium-ion battery. In the RFLB, electron transfer between the electroactive materials and the electrode relies on chemical lithiation/delithiation by dissolved redox species. The electron transfer process may compete with the lithium diffusion in the electroactive materials to be the rate-limiting step. The method we are going to introduce will help us to access the kinetics of electron transfer between the redox species and the electroactive materials. We have chosen step potential amperometry to study the reaction rate between the redox species and the electroactive materials. The test only requires a small amount of sample and is non-destructive. In this study, $LiFePO_4/FePO_4$ was used as the electroactive materials and $Fc/FcBr_2$ the redox species. Useful parameters such as the reaction rates between the redox species and electroactive materials could be extracted. We conclude that the electron transfer between the redox species and electroactive material is unlikely to be the rate-determining step. We also drew another important conclusion from the study, which is that reaction rate is faster on carbon-coated $LiFePO_4/FePO_4$, by comparing the results of carbon-coated and uncoated samples. The step potential amperometry proves to be a quick and versatile method to assess the reaction rate of the Li^+-coupled heterogenous charge transfer process, which is critical in finding better combinations of redox species and electroactive materials.

Keywords: Kinetics, Redox targeting, Redox flow, Lithium-ion batteries, Electrochemical.

Reference:
1. Q. Huang, H. Li, M. Grätzel, and Q. Wang, Reversible Chemical Delithiation/Lithiation of $LiFePO_4$: Towards A Redox Flow Lithium-ion Battery. Phys. Chem. Chem. Phys., 15 (6), 1793-1797 (2013)

Proceedings of the 14th Asian Conference on Solid State Ionics (ACSSI 2014)

Al Doping Improves Si Storage Energetics for Li, Na and Mg

Fleur Legrain[a], Oleksandr Malyi[b] and Sergei Manzhos[c]
National University of Singapore, Singapore.
[a]*fleur.legrain@gmail.com*
[b]*oleksandrmalyi@gmail.com*
[b]*mpemanzh@nus.edu.sg*

ABSTRACT

Silicon is a high-capacity anode material (up to 4200 mAh/g) which is on the verge of commercialization for Li ion batteries [1]. Pure Si is not, however, suitable neither for Na or Mg ion batteries [2]. These two technologies need to be developed for cheaper and large-scale use of metal ion batteries for grid as well as high-energy density mobile storage. Effective anodes still need to be developed for them. Despite having decent capacities of ~950 and ~3800 mAh/gSi based on NaSi and Mg_2Si (state of full charge), Si cannot serve as anode, because Na and Mg have positive defect formation energies Ef (unfavorable insertion thermodynamics) and high diffusion and insertion barriers at initial stages of charge (i.e. in diamond silicon) [2]. We show that doping Si with Al with Al number density of several % lowers Ef for all Li, Na, and Mg. In particular, it makes Na and Mg defect formation energies negative and competitive with metal cohesive energies. The Al concentrations studied are achievable by growing Si nanowires on a catalyst [3], i.e. this represents a feasible technology. Al doping could therefore enable Si-based anodes also for Na and Mg ion batteries.

Keywords: Al, Si, Anode, Li-ion batteries, Na-ion batteries, Mg-ion batteries, DFT.

[1] H. Wu and Y. Cui: Designing nanostructured Si anodes for high energy density lithium ion batteries, Nano Today 7 (2012) 414.
[2] F. Legrain, O. I. Malyi, S. Manzhos: Comparative computational study of the the diffusion of Li, Na, and Mg in silicon including the effect of vibrations, Solid State Ionics 253 (2013) 157; A. Carvalho, M. J. Rayson, P. R. Briddon, S. Manzhos: Effect of the adsorption of ethylene carbonate on Si surfaces on the Li insertion behavior, Chem. Phys. Lett. 585 (2013) 157; O. I. Malyi, T. L. Tan, S. Manzhos: A computational study of the insertion of Li, Na, and Mg atoms into Si(111) nanosheets, Nano Energy 2 (2013) 1149.
[3] O. Moutanabbir, D. Isheim, H. Blumtritt, S. Senz, E. Pippel, and D. N. Seidman, Colossal injection of catalyst atoms into silicon Nanowires , Nature 496 (2013) 78.

Proceedings of the 14th Asian Conference on Solid State Ionics (ACSSI 2014)

DFT Study on Feasibility of Two Step Redox Process in Li Battery Electrodes

Shamik Chakrabarti[1,a], Awalendra K. Thakur[2] and Koushik Biswas[1,b]
[1]*IIT Kharagpur, India.*
[a]*shamikiitkgp@gmail.com*
[b]*k_biswas@metal.iitkgp.ernet.in*
[2]*IIT Patna, India.*
akt@iitp.ac.in

ABSTRACT

Lithium battery has emerged as an important ionic device that established conceptual validity, technical feasibility and technological importance of solid state ionics. Starting with layered oxides such as; $LiCoO_2$, $LiNiO_2$, spinel $LiMn_2O_4$ cathode and lithiated carbon as anode material, the development has now moved a step further aiming at high rate capability, faster redox process and higher capacity electrodes for device applications. To continue with the pursuits, studies on $LiMPO_4$ and Li_2MSiO_4 (where M = Fe, Co, Ni) have opened new window for further analysis and evaluation. Out of these, phosphates ($-PO_4^{-3}$) are of special interest due to their high electrochemical stability during charge-discharge cycle arising due to strong covalent P-O bonds. On the other hand, silicates ($-SiO_4^{-4}$) are significantly important, with scope for multiple electron transfer prior to completion of redox process, due to the possibility of two stage intercalation-deintercalation process arising from transport of two Li^+ ions during redox reaction. This, in turn, doubles the electrode capacity in Li_2MSiO_4 compared to conventional electrode materials ($LiCoO_2$, $LiNiO_2$, $LiFePO_4$) in which only one or less than one Li^+ ion per formula unit takes part into electrochemical reaction. The same may be true with and possibly in Li_2MVO_4 as well. In the present work, we report DFT computation results on feasibility of two step electron transfer (redox) phenomenon in Li_2FeSiO_4, Li_2FeVO_4 etc. Electronic structure and Li+ intercalation voltage have also been calculated. Results showed that, in Li_2FeSiO_4, first stage Li ion de-intercalation occurs at 3.1 V corresponding to Fe^{+2}/Fe^{+3} redox couple while second stage de-intercalation occurred at 4.3 V corresponding to Fe^{+3}/Fe^{+4} redox couple. The two step charge transfer reaction delivers 330 mAh/g for the total reaction. Similarly, Li_2FeVO_4 showed first stage delithiation at 1.8 V corresponding to V^{+4}/V^{+5} redox couple while second stage de-intercalation occurred at 3.0 V corresponding to redox couple Fe^{+2}/Fe^{+3} with overall capacity of 290.5 mAh/g for the whole electrochemical reaction. Although silicate and vanadate exhibited redox reaction accompanying transfer of 2 electrons within electrochemical stability limit for electrolytes in the cell, large volume changes occurred during charge-discharge cycle. This may become a limitation for the materials in practical application. While full de-lithiation occurs with 9.7% volume change in vanadates, a volume change of more than 7% has been observed for the silicates. In sharp contrast, volume expansion-contraction during ion exchange in LiFeTiO4 is very small (0.8% for $LiFeTiO_4$ ' Li_2FeTiO_4 and > 2% for $LiFeTiO_4$' $FeTiO_4$) in comparison to silicate and vanadate materials. Further computational and experimental studies on these materials are going on in our lab and would be presented.

Keywords: Li ion battery, Electrode materials, DFT simulation, Geometric structure, Electronic structure, Li intercalation voltage.

Proceedings of the 14th Asian Conference on Solid State Ionics (ACSSI 2014)

Nickel Substituted $LiCoO_2$ as Cathode Materials for All-Solid-State Lithium Secondary Batteries Using Li_2S-P_2S_5 Solid Electrolytes

Minjeong Kim[a], Junghoon Kim[b], Sungbo Hong[c] and Dongwook Shin[d]
Hanyang University, Korea, Republic of.
[a]*orangelove26@hanmail.net*
[b]*nayak84@naver.com*
[c]*strland6@hanmail.net*
[d]*dwshin@hanyang.ac.kr*

ABSTRACT

Recently, all-solid-state lithium ion batteries based on solid electrolytes have attracted attention due to increased concerns on the safety problems of commercial lithium ion batteries using liquid electrolytes. Many researches have been conducted to enhance performance of the all-solid-state lithium batteries based on commercial $LiCoO_2$. In our previous work, nonstoichiometric $Li_{1+x}CoO_2$ were applied to the all-solid-state lithium batteries as cathode materials in an effort to enhance the cell performance. However, the performance of the all-solid-state lithium batteries based is still not sufficient to satisfy the market needs due to low reversible capacity and cycle life. In this study, in order to further increase the specific capacity of the all-solid-state lithium batteries, the mixed transition metal oxide $Li_{1+y}Ni_xCo_{1-x}O_2$ are proposed as cathode materials for the all-solid-state lithium batteries using Li_2S-P_2S_5 solid electrolytes by substituting some but not all of the cobalt with nickel which is known to have the advantages of low cost and reduced toxicity. To identify the effect of partial substitution of cobalt with nickel on the performance of the all-solid-state lithium batteries using Li_2S-P_2S_5 solid electrolytes, various compositions of $Li_{1+y}Ni_xCo_{1-x}O_2$ are prepared and their electrochemical properties are compared.

Keywords: All-solid-state lithium secondary batteries, Cathode materials, $Li_{1+y}Ni_x\ Co_{1-x}O_2$.

Proceedings of the 14th Asian Conference on Solid State Ionics (ACSSI 2014)

High Performance Dye-Sensitized Solar Cells with PEO Based Gel Polymer Electrolyte Using TiO_2 Nano Fibers Developed by Electrospinning

H. N. M Sarangika[1], G. K. R Senadeera[2], H. K. D. W. M. N. R. Divaratne[3,a], P. M. P. C. Ekanayake[3,b], C. A Thotawatthage[3,c] and M. A. K. L Dissanayake[3,d]
[1]*Sabaragamuwa University of Sri Lanka, Sri Lanka.*
sarangikah@gmail.com
[2]*The Open University of Sri Lanka, Nawala, Nugegoda, Sri Lanka,*
gkrsena@yahoo.com
[3]*Institute of Fundamental Studies, Kandy, Sri Lanka.*
[a]*nalika1128@gmail.com*
[b]*ekanayake.c@gmail.com*
[c]*thotawatthageca@yahoo.com*
[d]*makldis@yahoo.com*

ABSTRACT

Among the methods used to fabricate metal oxide nanostructures, electrospinning appears to be a convenient method due its ability to make continuous nanofibers with large surface area. Electrospinning can be used to fabricate nano fiber TiO_2 electrodes used in dye sensitized solar cells (DSSC). Although few researchers have attempted to use this method, the enhancements in the efficiencies reported so far are not that significant. Therefore, in this study we have explored the possibility of using electrospun TiO_2 nanofibers along with TiO_2 nano particles on the efficiency enhancement in quasi solid state DSSCs and compared their performance with the DSSCs prepared with TiO_2 (P25) nano particles made with the doctor blade method. The performance of these DSSCS was examined by I-V measurements under the illumination of 100 $mWcm^{-2}$. The composition of the quasi solid electrolyte used in these DSSCs was PEO (12.05 wt%), tetrapropylammonium iodide (14.46 wt%), ethylene carbonate (36.16 wt%), propylene Carbonate (36.16 wt%) and iodine (1.16 wt%). The room temperature conductivity of the electrolyte estimated by complex impedance analysis is $6.54 \times 10^{-3} Scm^{-1}$. While the DSSCs fabricated with TiO_2 nano particles alone showed an average efficiency of 4.4% with short circuit current density (Jsc) of 10.61 mA cm^{-2} and open circuit voltage (Voc) of 0.76 V respectively, the DSSCs fabricated with nano fiber incorporated composite TiO_2 electrodes showed an average efficiency of 6.2% with Jsc of 13.48 mA cm^{-2} and Voc of 0.70 V respectively. Therefore, this preliminary study shows that composite TiO_2 electrodes made with electrospun TiO_2 nano fibers combined with TiO_2 nano particles can enhance the efficiency of DSSCs by about 40%. The increased dye absorption due to the increased thickness and surface area of the TiO_2 electrode and the reduction of electron recombination of the excited electrons must have contributed to this efficiency enhancement.

Keywords: Electrospinning, Dye sensitized solar cells, Nanofibers.

Proceedings of the 14th Asian Conference on Solid State Ionics (ACSSI 2014)

Ion Dynamics in Nanocrystalline Graphene Wrapped $LiNiPO_4$ Composite

Rajesh Cheruku[a] and G. Govindaraj[b]
Pondicherry University, India.
[a]*rajeshche2003@gmail.com*
[b]*ggraj_7@yahoo.com*

ABSTRACT

Olivine family is widely used as cathodes in Li ion batteries because of their high energy density and high voltage. Out of these materials, $LiNiPO_4$ is interested because $LiNiPO_4$ has high redox potential, good thermal stability and high specific capacity but suffers from a low electronic conductivity. Research works are progressing to improve its electrical conductivity by carbon nano-coating or by inter-grain precipitation of conductive metallic particles or by different shapes of materials. Moreover, recent work indicated that the graphene two-dimensional edge plane site could aid lithium-ion adsorption and diffusion, leading to a reduced charging time and an increased power output. In the present study, $LiNiPO_4$ is synthesized by template free hydrothermal method. $LiNiPO_4$ material formed as spherical shaped particles which are prepared for the first time using hydrothermal method. The graphene oxide (GO) is prepared by Hummers method and GO was reduced by glucose as adopted by Chengzhou Zhu et.al. This technique has an advantage, since reducing agent as well as by products are environmentally friendly. The graphene wrapped $LiNiPO_4$ composite is crystallized in a stable orthorhombic structure of space group Pnma. Morphology was identified by the SEM, VSM was used to verify the magnetic behavior of the material and TEM results authenticated that the material crystallized in the nanocrystalline form. Electrical characterization was done through impedance spectroscopy and the results will be discussed.

Keywords: Nanostructured materials, Graphene, Olivine, Electrical studies.

Proceedings of the 14th Asian Conference on Solid State Ionics (ACSSI 2014)

Synthesis and Electrochemical Characterization of Tin-Hollandites, $K_2(M_2Sn_6)O_{16}$ (M = In, Co)

M. V. Reddy[1,a], Tran Thuy Linh[2,b], Dang Thu Hien[2,c], Stefan Adams[1,d] and B. V. R. Chowdari[1,e]
[1]*National University of Singapore, Singapore.*
[a]*phymvvr@nus.edu.sg*
[d]*mseasn@nus.edu.sg*
[e]*phychowd@nus.edu.sg*
[2]*S High School of Mathematics and Science, NUS, Singapore.*
[b]*h1130025@nushigh.edu.sg*
[c]*h1130003@nushigh.edu.sg*

ABSTRACT

Tin hollandites, $K_2(M_2Sn_6)O_{16}$ (M = In, Co) were synthesized by molten salt method (MSM) using 0.5M KCl:0.5MNaCl at 650°C for 3h in air. The compounds were characterized by Rietveld refined X-Ray Diffraction (XRD), Scanning Electron Microscopy (SEM), Density and Brunauer-Emmett-Teller (BET) surface area methods. The BET surface areas ranging from 1.82 (M = In) and 5.16 (M = Co) $m^2\ g^{-1}$, respectively and experimental density values are 7.6757 (M = In) and 7.633 (M = Co) gm cm^{-3}. The Electrochemical anodic behavior of M = Co and M = In were examined by galvanostatic cycling (GC) and cyclic voltammetry (CV) using Li-metal as the counter electrode in the voltage range 0.005-1.0V or 0.005-3.0V). Doctor blade technique was used to fabricate the electrode for Li-cycling studies. CV studies showed both compounds display main alloying (cathodic) peaks at ~0.25V and anodic peaks at ~0.5V vs. Li. Electrochemical properties showed a reversible capacity values in the range 630 to 700 mAh/g in the voltage range, 0.005-1.0 V vs. Li. When cycled to upper cut-off voltage (0.005-3.0V), high reversible capacity of 1050 to 1100 mAh/g and huge capacity fading was noted in both compounds due to huge volume variation conversion reaction of Sn, In.

Keywords: $K_2(M_2Sn_6)O_{16}$ (M = In Co), Molten salt method, Characterization, Anodes.

Proceedings of the 14th Asian Conference on Solid State Ionics (ACSSI 2014)

Influence of Liquid Phase Sintering by $ZnO\text{-}B_2O_3$ Glass on Sinterability of $b(Zr_{0.52}Ti_{0.48})O_3$

Shradha Joshi[a] and Smita Acharya[b]
Department of Physics, RTM Nagpur University, India.
[a]*acharya_shradha05@yahoo.co.in*
[b]*saha275@yahoo.com*

ABSTRACT

The piezoelectric ceramic material $Pb(Zr_{0.58}Ti_{0.42})O_3$ (PZT) has been intensively focused due to its high piezoelectric, ferroelectric and dielectric constant and found high potential to develop actuators and ultrasonic transducers. High sintering temperature hurdle the applicability of PZT. In this temperature range, loss of Pb from PZT due to high volatility is commonly observed, which alters the properties of PZT. A lot of effort has been done during the last two decades to reduce the sintering temperature of PZT while retaining good piezoelectric and dielectric properties. For lowering the sintering temperature of PZT different efforts have been attempted such as synthesize fine particle, doping or by additives of low melting point phases as sintering aids (i.e. Liquid phase sintering). The objective of the present work is to improve the sinterability of PZT by adding $0.4ZnO\text{-}0.6B_2O_3$ (ZB46) glass by liquid phase formation. The liquid phase speeds up the densification process by rearrangement of particles and enhance material transport. A Glass deposit on grain boundaries of PZT due to capillary action which is arises by surface tension at interface (liquid- solid - vapour). The PZT was synthesized hydrothermal route and ZB-glass by conventional quenching technique, separately. PZT was calcined at temperature 850°C to obtain perovskite phase. The compositions of PZT and ZB-glass (0 - 1.5 wt%) were prepared by mechanical milling. The tetragonal structure of calcined PZT, PZT-ZB and amorphous nature of ZB-glass are confirmed by XRD. Softening temperature of the glass has been found by Differential Thermal Analysis (DTA) and Thermal Gravimetric analysis (TGA). Microstructure was examined by Scanning Electron Microscope (SEM). Systematic sintering programme was used to sinter pellets of PZT and PZT-ZB. The enhancement in sinterability of PZT is observed by Liquid phase sintering with lowering sintering temperature; however no observable change are detected in dielectric constant by addition of ZB in PZT.

Keywords: $Pb(Zr_{0.58}Ti_{0.42})\ O_3$ (PZT), Liquid phase sintering, $_{0.4}ZnO_{\text{-}0.6}B_2O_3$ (ZB_{46}) glass.

Proceedings of the 14th Asian Conference on Solid State Ionics (ACSSI 2014)

Studies on Nano-Gel Polymer Electrolyte Based EDLCs

Amrita Jain[a] and S. K. Tripathi[b]
Jaypee University of Engineering and Technology, India.
[a]*amritajain86@yahoo.in*
[b]*sktripathi16@yahoo.com*

ABSTRACT

As an electrical energy storage device, supercapacitor finds attractive applications in consumer electronic products due to its attractive properties. In the present studies, electrochemical double layer capacitors (EDLCs) has been fabricated using nano gel composite polymer electrolyte comprising of poly(vinylidine fluoride-co-hexafluropropylene) PVdF(HFP) - propylene carbonate (PC) - magnesium perchlorate $Mg(ClO_4)_2$- nano-aluminium oxide (nano-Al_2O_3) as an inert nano filler which exhibits ionic conductivity of 5.9 x 10^{-3} S cm^{-1}, showing good mechanical and dimensional stability which is suitable for their application in EDLCs. Chemically treated and untreated activated charcoal was used as an electrode material. The electrochemical evaluation of EDLCs through cyclic- voltammetry, impedance spectroscopy and charge-discharge techniques demonstrate the excellent performance of chemically treated activated charcoal based EDLCs. The maximum capacitance of 303 mF cm^{-2} which is equivalent to single electrode specific capacitance of 202 F g-1 was achieved. It corresponds to energy-density of 28.0 W h kg^{-1} and power-density of 2.2 kW kg^{-1}.

Keywords: Electrochemical double layer capacitors, Nano gel polymer electrolyte, Activated charcoal.

Proceedings of the 14th Asian Conference on Solid State Ionics (ACSSI 2014)

Experimental Studies on Ionic Liquid Based Polymer Gel Electrolytes

S K Tripathi[a], Amrita Jain[b] and Ashish Gupta[c]
Jaypee University of Engineering and Technology, India.
[a]*sktripathi16@yahoo.com*
[b]*amritajain86@yahoo.in*
[c]*ashish_ssi@yahoo.co.in*

ABSTRACT

The optimized composition of free standing and mechanically stable polymer gel electrolytes film comprising of [PVdF(HFP) (30 wt%) - EMIM (Br) (70 wt%)] (30 wt%) - [PC-Mg $(ClO_4)_2$ (0.3M)] (70 wt%) has been synthesized using standard solution cast techniques. The synthesized electrolyte shows maximum room temperature ionic conductivity of 2.05 x 10^{-2} S cm^{-1} which is quite acceptable from device fabrication point of view. The temperature dependent plot confirms the VTF behavior of the synthesized polymer gel electrolyte system. The microscopic texture of the optimized electrolyte has been carried out by SEM micrograph. The surface morphology was studied by XRD which shows amorphous nature of the synthesized materials. The complexation of gel electrolyte was confirmed by FTIR studies.

Keywords: Ionic liquid, XRD, SEM, FTIR.

Proceedings of the 14th Asian Conference on Solid State Ionics (ACSSI 2014)

Synthesis and Impedance Analysis of Proton – Conducting Polymer Electrolyte Based on PAN: NH_4SCN

K. Selvakumar[a], M. Karthikeyan[b] and Ramesh Prabhu[c]
Alagappa University, India.
[a]*selvakumar21021024@gmail.com*
[b]*karthikeyanm747@gmail.com*
[c]*mkram83@gmail.com*

ABSTRACT

Recently polymer electrolytes have received considerable attention for application in rechargeable secondary batteries, fuel cells, supercapacitors, etc., since they can offer systems that are lighter, safer and more flexible in shape compared with their liquid counter parts. An attempt has been to prepare a new proton conducting polymer electrolyte based on poly acronitrile (PAN) with ammonium thiocyanate in different (wt%) ratios have been prepared by solution casting method, using DMF as solvent. The increase in amorphous nature of the polymer electrolyte has been confirmed by x-ray diffraction analysis (XRD). The FTIR spectroscopic study indicated the detailed interaction of PAN with proton. The ionic and dielectric permittivity has been calculated by a.c impedance spectroscopy. The linear variation of the proton conductivity of the polymer electrolytes with increasing temperature suggests the Arrhenius type thermally activated process proton (1H) Nuclear magnetic study made on PAN doped with ammonium thiocyanate. It reveals the conducting species is protons.

Keywords: Conductivity, NMR, XRD.

Proceedings of the 14th Asian Conference on Solid State Ionics (ACSSI 2014)

Structural and Electrical Characterisation of PVA:NH_4SCN Nanocomposite Polymer Electrolyte Films

Niharika Kulshrestha[a] and Prem Gupta[b]
Department of physics, Banaras Hindu University, Varanasi – 221005 (U.P.) India.
[a]*niharikakul@gmail.com*
[b]*guptapn07@yahoo.co.in*

ABSTRACT

Nanocomposite polymer electrolyte films are prepared by solution cast technique using polymer polyvinyl alcohol (PVA), salt ammonium thiocyante (NH_4SCN) and nanofiller silica nanoparticles of 14 nm average particle size. X-ray diffraction (XRD) confirms the amorphous nature of the sample with silica nanoparticles and the broad amorphous hump at around 23o indicates the interaction of silica nanoparticles with the polymer matrix. Fractals are observed in 70:30 PVA:NH_4SCN films containing 0-2% of silica nanoparticles. The images of the fractals are recorded through optical microscopy and the dimensions of fractals are calculated. Electrical and dielectric properties are analysed using impedance spectroscopy. The electrical conductivity at room temperature in 21% humidity is found to be maximum of the order of 10^{-3} S/cm for the sample containing 2% of silica nanoparticles. Dielectric constant, dielectric loss and loss tangent have been studied with frequency for various contents of silica nanoparticles.

Keywords: Polyvinyl alcohol, Silica nanoparticles, Electrical conductivity.

Proceedings of the 14th Asian Conference on Solid State Ionics (ACSSI 2014)

Cooling Rate Effects on Structure and Mobility of Garnet-related Fast-ion Conductor $Li_7La_3Zr_2O_{12}$

Wenyi Gu[a], Prasada Rao Rayavarapu[b] and Stefan Adams[c]
National University of Singapore, Singapore.
[a]*wenyigu@nus.edu.sg*
[b]*mserpr@nus.edu.sg*
[c]*mseasn@nus.edu.sg*

ABSTRACT

Aliovalently doped cubic $Li_7La_3Zr_2O_{12}$ (LLZ) has a strong application potential as solid electrolytes in all-solid-state batteries and as protective layers for anodes in Lithium-air batteries due to its favourable combination of fast ionic conductivity with chemical and electrochemical stability versus both lithium and cathode materials. Hysteresis of Li^+ ion conductivity has been observed in pentavalently (Ta and Nb) doped LLZ samples. In situ-neutron powder diffraction monitoring of the LLZ formation indicated that Li distribution of the annealed samples depends on the last cooling rate. High Li(1) site occupancy was observed in experiments employing high cooling rates while naturally furnace cooled samples yielded significantly lower Li(1) site occupancy implying a different degree of Li site ordering and local Li mobility as a function of the cooling rate. Systematic in situ X-ray powder diffraction and impedance spectroscopy results accordingly suggest that the last cooling rate can alter the distribution and ordering of Li+ ions in LLZ and hence the room temperature ionic conductivity of LLZ. Samples cooled with rates in the range 1 – 5 K/min showed at least two times higher conductivities than those quenched at a cooling rate higher than 25 K/min. The effect of cooling rates on Li+ conductivity is even more pronounced in the Ta-Ga or Nb-Ga co-doped LLZ, where conductivities of slowly cooled samples were up to two orders of magnitude superior to those of quenched samples though the origin of this pronounced effect may be more complex as the cooling rate may also affect the Ga distribution.

Keywords: Fast-ion conductors, Garnet-related solid electrolytes, in situ diffraction.

Proceedings of the 14th Asian Conference on Solid State Ionics (ACSSI 2014)

Electrical Evaluation of Chemical Gas Sensors Based on CuO Nanoflowers

Dang-Thanh Nguyen[1,a], Eui-Chol Shin[1,b], Duc-Vuong Dang[2] and Jong-Sook Lee[1,c]
[1]***Chonnam National University, Korea, Republic of.***
[a]*dangthanh@ejnu.net*
[b]*euichol@ejnu.net*
[c]*jongsook@jnu.ac.kr*
[2]***Hanoi University of Science and Technology, Viet Nam.***
vuong.dangduc@hust.edu.vn

ABSTRACT

Chemical gas sensors based on the surface-conductivity type metal oxide semiconductors have been developed for wide applications. The Schottky barriers at the surface/interface of the porous oxide films responsible for the sensing mechanism are modeled by the equivalent circuits of R and C elements in series to the bulk response from the core of the semiconductor grains. However, the model is hardly applied for the real sensor system, since the thin film geometry leads to the capacitance values close to the stray effects. An AC analysis has been recently performed on TiO_2 nanofiber sensor by the equivalent circuit analysis including the stray capacitance. In this work, CuO nanostructures were synthesized using $Cu(NO_3)_2$ precursor by hydrothermal method at 170°C. Morphology and crystal structure of CuO nano-flower was investigated by SEM and XRD. Powders after heat treatment at 500°C were deposited by drop-cast technique on Pt interdigital electrodes de-signed. The gas sensitivity was tested under different concentrations of ethanol vapor from about 50 to 500 ppm. As well as the conventional DC resistance, AC measurements of the sensors were performed. To understand the sensing mechanism in view of the bulk and surface electronic structure of CuO and the defect chemistry, bulk pellets were characterized under various treatments and measurement conditions.

Keywords: Cupric oxide, Gas sensor, Impedance spectroscopy.

Proceedings of the 14th Asian Conference on Solid State Ionics (ACSSI 2014)

Electrical Properties of Nanocrystalline Oxygen Deficient Barium Manganite

Namita Pandey[1] and Awalendra Kumar Thakur[2]
[1]*Indian Institute of Technology-Kharagpur*
namita205@gmail.com
[2]*Indian Institute of Technology-Patna, India.*
akt@iitp.ac.in

ABSTRACT

Oxygen ion conducting ceramics have been extensively studied due to their characteristic features of mixed charge permeation, high mobility of oxide ion/electrons, structural, phase and thermal stability etc. These are considered to be essential prerequisites for their suitability as electrode materials for solid oxide fuel cell (SOFC), gas sensors and oxygen pumps etc. Modification of structural properties by introducing intrinsic anion deficiency in the lattice structure leading to oxide ion conduction has come in vogue. Such an approach is expected to ensure fast oxygen ion conduction within lattice structure possibly via hopping. However, acceptable O_2^- ion transport occurs, as per reports in literature, at relatively higher temperature (= 800°C). Literature shows that their structural properties control the electrical conduction and other transport by the lattice defects present (including ionic and electronic defects). Hence, the oxygen vacancy created due to oxygen deficiency 'd' is represented by Kröger-Virk relation. Oxygen deficient perovskites (ABO_3-d) having Mn at B-site show mixed ionic conduction due to mixed valance states (III/IV). The electric properties become more prominent in nanocrystalline systems where the grain boundary effects play an important role in charge migration. But due to the heterogeneous particle size in nanocrystalline systems, the overall electrical studies suppress the actual grains and grain boundary effect on it. Hence, it is very important to study the ion dynamics and charge transport properties using impedance and modulus spectroscopy. In this paper, we report electrical properties of nanocrystalline $BaMnO_3$-d where, the oxygen deficiency d is created due to presence of mixed oxidation states Mn^{3+} and Mn^{4+}. The layered hexagonal-cubic crystal structure P63/mmc) of $BaMnO_3$-d as a result of high ionic radii (Ba^{2+} ~1.35Å) creates hexagonal layer in the system. The electrical properties studied using complex impedance analysis suggests thermally activated charge transport with only bulk contribution up to 300oC beyond which grain boundary effects is prominent. In order to understand the sample electric response in terms of the corresponding electrical equivalent counterpart, the complex impedance and modulus spectrum pattern has been modeled as an equivalent circuit representation in terms of the brick layer model for polycrystalline ceramics. The dc conductivity pattern shows the three regions following mixed conduction behavior at intermediate temperatures. The activation energy at this region >1 eV confirms this behavior.

Keywords: Layered hexagonal perovskite, Structural analysis, Oxygen deficiency, Complex impedance spectroscopy, Complex modulus spectroscopy.

Proceedings of the 14th Asian Conference on Solid State Ionics (ACSSI 2014)

AC Conductivity Analysis and Dielectric Relaxation Behaviour of a Conducting Polymeric System Based on PMMA - $LiClO_4$

Namrata Shukla[1], Awalendra K Thakur[2], Archana Shukla[3] and Ratnamala Chatterjee[4]
[1]*Illinois State University, USA.*
namrata3jan@gmail.com
[2]*Indian Institute of Technology Patna, Bihar, India.*
akt@phy.iitkgp.ernet.in
[3]*Indian Institute of Technology Bombay, Pawai,Mumbai, India.*
arsh25aug@gmail.com
[4]*Indian Institute of Technology Delhi, Hauz Khas, New Delhi, India.*
rmalac@physics.iitd.ac.in

ABSTRACT

Solid polymer electrolytes (SPEs) formed by distribution of alkali metal salts in polymer play an important role in the development of new energy sources, like solid state batteries, photo-electrochemical solar cells, sensors and electrochromic displays. Technological application of this class of materials requires high ionic conductivity (10-3 S cm^{-1}). Many research groups have endeavored for over three decades to synthesize the polymer with high conductivity but so far the conductivity of more than 10-3 S cm^{-1} has not been achieved. The main hurdle to achieve the goal is incomplete understanding of conduction mechanism in polymer electrolyte. The frequency dependent conductivity and dielectric relaxation both are sensitive to the motion of charged species and the dipoles of the polymer electrolyte. Their studies provide important information on the ionic transport mechanism of fast ion conductors. In this context, the present work is taken to explore the ion dynamics in Poly methyl methacrylate (PMMA) - $LiClO_4$ based polymer electrolyte using the analysis of frequency dependent dielectric relaxation and conductivity. Polymer electrolyte films have been prepared by solution cast technique. The dielectric behavior of the films has been analyzed in terms of frequency response of dielectric permittivity (μ•) and dissipation factor (tan´). Such an analysis has confirmed the presence of electrode polarization at lower frequency. The appearance of the loss peak in the low frequency (mHz to a few Hz) region is attributed to the losses due to conduction. The real part of ac conductivity spectra of the materials obeys Jonscher power law. It has been observed that the increase of salt concentration reduces the ionic conductivity relaxation time and hence increases the ionic conductivity. A correlation between ion hopping rate (Ép) and carrier concentration term (K) has been achieved from experimental results. The analysis appears to be consistent with the observed conductivity variation.

Keywords: Polymer electrolytes, Dielectric properties, Electrical conductivity, AC conductivity.

Proceedings of the 14th Asian Conference on Solid State Ionics (ACSSI 2014)

Oxygen Mobility and Lattice Dynamics in $Sr_2Fe_2O_5$ and $Ca_2Fe_2O_5$ Brownmillerites

Sergey Danilkin[1,a], Chris Ling[2,c], Josie Auckett[2,d] and Gordon J. Kearley[1,b]
[1]*Bragg Institute, ANSTO, Lucas Heights, NSW, Australia.*
[a]*sdz@ansto.gov.au*
[b]*gke@ansto.gov.au*
[2]*School of Chemistry, University of Sydney, Sydney, NSW, Australia.*
[c]*c.ling@chem.usyd.edu.au*
[d]*jauc3270@gmail.com*

ABSTRACT

Solid-state materials with high oxygen ion conductivity at moderate temperatures are of great importance and of much current scientific interest. One of few structures that intercalate oxygen fast belongs to the oxygen deficient Brownmillerite - type. It consists of alternating layers of Fe-O tetrahedra and Fe-O octahedra and has 1D ordered vacancy channels in the tetrahedral layers. According to the recent inelastic neutron scattering study the scattering pattern of Brownmillerites polycrystalline sample consists of the acoustic phonons emerging from the Bragg peaks and dominating low-frequency band of optical vibrations merging into acoustic modes [1]. The DFT simulations show that this is a result of large displacements of apical oxygen atoms, which even able to migrate into the vacancy channels of the tetrahedral layer. The oxygen migration in $Sr_2Fe_2O_5$ is based on structural instabilities and corresponding dynamical fluctuations of oxygen in the tetrahedral chains. [1]. We recently grew the large single crystals of $Sr_2Fe_2O_5$ and $Ca_2Fe_2O_5$ by the floating-zone method [2] and perform INS measurements of phonon dispersion curves with triple axis spectrometer TAIPAN at ANSTO [3]. We found that the acoustic transverse modes demonstrate linear increase in frequency at small phonon wave vectors and flatten up at energy of ~6 meV at $q > 0.5$. The optic modes have unusually low frequencies at Brillouin zone centre. At phonon energy below ~4 meV the optical mode is overdamped and merges into acoustic intensity. This agrees well with our DFT calculations of phonon dispersion curves in $Ca_2Fe_2O_5$. In the overdamped regime phonons are dynamical fluctuations with large amplitude coupled with oxygen migration motions. This gives some indications that that fast oxygen transport kinetics at ambient conditions in Brownmillerite is phonon-assisted.

Keywords: Brownmillerite, Oxygen transport, Lattice dymanics.

[1]W. Paulus, et al., J. Am. Chem. Soc., 130 (2008) 16080.
[2]J. Auckett, A. Studer, N. Sharma and C. Ling, Sol. St. Ionics, 225 (2012) 432.
[3]S. Danilkin and M. Yethiraj, Neutron News, 20 (2009) 37.ws, 20 (2009) 37.

Proceedings of the 14th Asian Conference on Solid State Ionics (ACSSI 2014)

Novel Bi-functional Perovskite Catalyst for Oxygen Reduction and Evolution

Jae- Il Jung[a] and Jaephil Cho[b]
Ulsan National Institute of Science & Technology (UNIST), Korea, Republic of.
[a]*jungji6013@unist.ac.kr*
[b]*jpcho@unist.ac.kr*

ABSTRACT

This study reports on the finding of novel bi-functional perovskite catalsyt, $La_{0.3}(Ba_{0.5}Sr_{0.5})_{0.7}Co_{0.8}Fe_{0.2}O_3$-($La_{0.3}$-5582). The newly introduced electrocatalyst exhibited a promising performance as a bi-functional catalyst in ORR and OER activities. The obtained electron transfer number (n) in ORR activities of $La_{0.}$3-5582 is 3.60~3.72, which are comparable with those of RuO_2 and $Ba_{0.5}Sr_{0.5}Co_{0.8}Fe_{0.2}O_{3-d}$ (BSCF5582), 3.63~3.77 and 3.20~3.26, respectively. The OER activity of $La_{0.3}$-5582 was 2~3 times higher than that of BSCF5582. HRTEM and XRD revealed that ~10 nm scale of rhombohedral $LaCoO_3$ particles are distributed as secondary phase particles on the surface of porous $La_{0.3}$-5582 grains. Such dynamic microstructure phenomena were attributed to the charge imbalance from the replacement of A-site cations with La^{3+} and local stress on Co-site sub-lattice with the cubic perovskite structure.

Keywords: Bi-functional electrocatalyst, Perovskite, BSCF, Oxygen reduction reaction, oxygen evolution reaction.

Proceedings of the 14th Asian Conference on Solid State Ionics (ACSSI 2014)

Novel Cathodes for Solid Oxide Fuel Cells

Peter Hing[a], Montri Suklueng[b], Nyuk Yoong Voo and Lim Chee Ming[c]
Universiti Brunei Darussalam, Brunei Darussalam.
[a]*peter.ng@ubd.edu.bn*
[b]*10h0602@ubd.edu.bn*
[c]*cheeming@ubd.edu.bn*

ABSTRACT

In this paper, the electrical conductivity and thermal expansion of ceramics in $Ba_{O.}Fe_{2O3.}Y_{2O3}$ and $Ba_{O.}Fe_{2O3.}Y_{2O3.}Co_{2O3}$ systems have been studied. These materials are being evaluated as possible cathodes for low and intermediate temperature solid oxide fuel cells. Conventional ceramic powder processing and solid state reactions are used to fabricate the electrodes with porosity ranging from 25% to 46%. A phase field has been identified in the $Ba_{O.}Fe_{2O3.}Y_{2O3}$ system with electrical conductivity of about $5Scm^{-1}$ at 800°C. The energy gap ranges from 0.2 eV to 1.2 eV. The electrical conductivity is, moreover, found to increase by several orders of magnitude with the addition of cobalt oxide. The relationship between processing, microstructures, electrical and thermal properties are presented and discussed.

Keywords: $Ba_{O.}Fe_{2O3.}Y_{2O3}$, $Ba_{O.}Fe_{2O3.}Y_{2O3.}Co_{2O3}$, Electrical conductivity, Thermal Expansion, Cathodes, SOFCs.

Proceedings of the 14th Asian Conference on Solid State Ionics (ACSSI 2014)

Novel Anode Catalytic Materials with Lithium-Ion Conducting Ability for Solid Oxide Fuel Cells with Improved Coking Resistance and Sulfur Tolerance

Wei Wang[a] and Zongping Shao[b]
Nanjing University of Technology, China.
[a]*wangwei414251823@163.com*
[b]*shaozp@yeah.net*

ABSTRACT

With increasing energy demand and diminishing fossil fuels resources, the development of new energy materials and technologies becomes important for a sustainable future. Solid oxide fuel cell (SOFC) is known as an environmental-friendly and highly efficient electrochemical energy conversion device, which is superior to the low-temperature fuel cells because a number of carbonaceous fuels could be utilized directly. The state-of-the-art anodes for SOFCs are the Ni-based cermets, which suffered from serious coke formation and sulfur poisoning when operated on carbon-containing fuels. These drawbacks have hindered the widespread application of this attractive technology. In this study, we focused on the design, fabricate and apply a series of novel cost-effective anode catalytic materials with lithium-ion conducting ability with improved coking resistance and sulfur tolerance for SOFCs operated on carbon and/or sulfur-containing fuels. We use the lithium-ion conducting materials as component of the catalyst layer and the anode to increase the coking resistance and/or sulfur tolerance for the first time. The relationship of element composition and lithium evaporation behavior in the anode catalyst layer with the carbon deposition behavior under carbon-containing fuel atmospheres would be specifically studied. On the other hand, novel 3D core-shell architecture with lithium-ion conducting ability from infiltration as highly efficient and sulfur-tolerant electrode for SOFCs would be developed and the sintering temperatures of the anodes would be optimized to achieve the best power output, operational stability as well as the sulfur tolerance. As a result, we would conduct a fundamental analysis of the reactions over the innovative anodes. This study offers a novel means for developing new coking and sulfur-resistant SOFCs that operate on widely available carbon-containing fuels with sulfur impurity for clean power generation to realize a sustainable future.

Keywords: Lithium ion conductor, Solid oxide fuel cell, Carbon deposition, Anode, Sulfur tolerance.

Proceedings of the 14th Asian Conference on Solid State Ionics (ACSSI 2014)

The Effect of NiO and MgO on the Sinterability of Yttria Stabilized Zirconia and Gadolinium Doped Ceria

Peter Hing[a], Andrew Jung[b], Daniel Dodzi Setssoafia[c] and Lim Chee Ming[d]
Universiti Brunei Darussalam, Brunei Darussalam.
[a]*peter.ng@ubd.edu.bn*
[b]*bruneijung@gmail.com*
[c]*setsoafiad@yahoo.com*
[d]*cheeming.lim@ubd.edu.bn*

ABSTRACT

This paper describes the effect of NiO and MgO doping on the sintering behaviour of YSZ and CGO. It is found that small amount of NiO and MgO assists the densification of both YSZ and GDC. Moreover, NiO is found to act as a grain size inhibitor. The sintering mechanisms discussed take into account the disappearance of the magnesia dopant. It is also found that dense YSZ.NiO and GDC.NiO are not reducible under butane flame at 800C. Thus the YSZ NiO and GdC.NiO can be used as solid oxide electrolytes. The implications of the findings on the fabrication of porous - dense - porous monolithic laminate structure for low cost and intermediate temperature solid oxide fuel cells are presented and discussed.

Keywords: NiO and MgO dopant, YSZ and GDC, Porous-dense-porous laminate, IT-SOFC.

Proceedings of the 14th Asian Conference on Solid State Ionics (ACSSI 2014)

Aqueous Lithium/Air Rechargeable Batteries with Protected Lithium Electrode

Nobuyuki Imanishi
Mie University, Japan.
Imanishi@chem.mie-u.ac.jp

ABSTRACT

Energy storage is one of the greatest challenges for our society in this century. With population increase and global economic development, we are facing increasing demand for energy and environmental impact by CO_2 emissions. It is important to develop good storage battery to store electricity to overcome these issues. Conventional lithium ion battery uses graphite anode. Possible limitation of energy density of the battery is considered about 250 Wh/kg. Lithium metal anode is expected to accomplish higher energy density. Lithium-air batteries are one of the systems which adopt lithium metal electrode. Our aqueous lithium-air battery has the following configuration; Li/polymer electrolyte/ceramic ion conductor/aqueous solution/Pt, air. One of the problems is low output power of the layered lithium electrode due to poor conductivity of the polymer electrolyte. It is, therefore, essential to develop a new interlayer material to achieve improved rate performance. The electrochemical properties of a composite solid polymer electrolyte consisting of poly(ethylene oxide) (PEO)-lithium bis(trifluoromethanesulfonyl)imide (LiTFSI) and polyether oligomers, e.g. tetraethylene glycol dimethyl ether (TEGDME), were examined as a protective layer between lithium metal and a lithium ion-conducting glass ceramic of $Li1+x+yAlx(Ti,Ge)_2$-xP_3-$ySiyO_{12}$ (LATP). Polyether is generally stable against lithium metal and reversible electrochemical reaction of lithium metal is achieved in polyether-based electrolytes. Those small molecular chains show high segmental motion and improved ion transport property is expected. The lithium ion conductivity and salt diffusion coefficient of PEO18LiTFSI were dramatically enhanced by the addition of TEGDME. The protected lithium electrode with PEO18LiTFSI-2TEGDME as the protective layer exhibited a low and stable electrode resistance of 85 & cm^2 at 60°C after 28 days and low overpotentials of 0.3 V for lithium plating and 0.4 V for lithium stripping at 4.0 mA cm^{-2} and 60°C. A Li/PEO_{18}LiTFSI-2TEGDME/LATP/saturated LiCl aqueous solution/Pt, air cell showed excellent cyclability up to 100 cycles at 2.0 mAh cm^{-2} and 1 mA cm^{-2}. Ether oligomers are attractive material for the interlayer between lithium metal and LATP in lithium-air batteries.

Keywords: Lithium-air battery, Polymer electrolyte, Polyether, LATP.

Proceedings of the 14th Asian Conference on Solid State Ionics (ACSSI 2014)

Phase Diagram and Sodium Ordering in Sodium Layered Oxides

Marie Guignard[a], Christophe Didier[b], Benoit Mortemard de Boisse[c], Dany Carlier[d], Jacques Darriet[e] and Claude Delmas[f]
ICMCB - CNRS, France.
[a]*guignard@icmcb-bordeaux.cnrs.fr*
[b]*Christophe.Didier@liverpool.ac.uk*
[c]*mortemard@icmcb-bordeaux.cnrs.fr*
[d]*carlier@icmcb-bordeaux.cnrs.fr*
[e]*darriet@icmcb-bordeaux.cnrs.fr*
[f]*delmas@icmcb-bordeaux.cnrs.fr*

ABSTRACT

Layered sodium oxides with the formula Na_xMO_2 (M is a transition metal) have been intensively studied these last thirty years either for their unique physical properties (high thermoelectric power, superconductivity ...) or with a view for their use in large sodium-ion batteries. In this context we have studied different Na_xMO_2 systems which differ one from another by the nature of the transition metal (M = V, Ni, Mo), by the type of site that sodium occupies, either octahedral or prismatic, and by the number of different MO_2 layers needed to describe the structure. The electrochemical study of these systems in sodium batteries, associated with in situ X-ray diffraction experiments, allowed for the first time to get a precise overview of their room temperature phase diagram. We then focused on the synthesis on the phases with the $Na_{1/2}MO_2$ composition. Their structure was determined from high resolution powder X-ray diffraction data and we found that a sodium/vacancy existed in those phases of each system. More precisely, three polymorphs $Na_{1/2}VO_2$ were studied. We have found that the three phases present not a sodium ordering between the VO_2 layers, but also a peculiar arrangement of the vanadium ions within the VO_2 slabs which form either pseudotrimers in the P2 phase (ABBA oxygen stacking, Na^+ in prisms) and in the P3 phase (AABBCCA oxygen stacking with a monoclinic distortion, Na^+ in prisms) or V-V pairs the O'3 phase (ABCA oxygen stacking with a monoclinic distortion, Na+ in octahedra). As a consequence the three polymorphs present very different magnetic and transport properties. As an example, we found that the P2 and the P'3 phases presented a first order transition near room temperature for which their electronic conductivity gained two orders of magnitude. Simultaneously a structural transition occured and the results obtained from high resolution powder diffraction and pair distribution function analysis indicated that the disappearance of the vanadium pseudotrimers was associated with this transition. This work on the Na_xVO_2 system showed that the arrangement of Na^+ ions between the VO_2 layers greatly affects the electron localization. This is a crucial point to keep in mind when considering sodium layered oxides with the general formula Na_xNO_2 for use as positive electrode materials in batteries, as transport properties can vary greatly during electrochemical cycling.

Keywords: Sodium batteries, Crystallography, New materials.

Proceedings of the 14th Asian Conference on Solid State Ionics (ACSSI 2014)

High-Voltage Sulphate Framework Cathode Materials for Na-Ion Batteries

Prabeer Barpanda[1], Gosuke Oyama[2], Shin-Ichi Nishimura[2], Sai-Cheong Chung[2], Chris D. Ling[2] and Atsuo Yamada[2]
[1]*Materials Research Center, Indian Institute of Science, India.*
prabeer@mrc.iisc.ernet.in
[2]*Department of Chemical System Engineering, The University of Tokyo, Japan.*

ABSTRACT

In the hunt for new cathode materials for next generation batteries, SO_{42}-based polyanionic framework compounds offer attractive platform to realize high-voltage cathodes owing to their electronegativity-induced inductive effect. Numerous SO_{42}-based cathodes have been reported for Li-ion batteries, such as tavorite and triplite polymorphs of $LiFeSO_4F$ achieving the highest Fe^{3+}/Fe^{2+} redox potential at 3.9 V. Parallel to the Li-ion story, there is growing focus on sodium-ion cathodes with the potential to develop low-cost large-scale batteries. Here, we will describe two new cathode candidates for sodium-ion batteries based on earth-abundant Na-Fe-S-O-H system. As sulphate compounds are prone to thermal decomposition and water dissolution, some non-aqueous low-temperature synthetic methods will be demonstrated. With the inductive effect and suitable open framework, two high-voltage cathode compounds will be introduced for large-scale sodium-ion batteries.

Proceedings of the 14th Asian Conference on Solid State Ionics (ACSSI 2014)

Reversible Chemical Lithiation/Delithiation of Anatase TiO_2 for Redox Flow Lithium-Ion Batteries

Feng Pan[a], Qizhao Huang[b] and Qing Wang[c]
National University of Singapore, Singapore.
[a]*panfeng@nus.edu.sg*
[b]*qizhao@nus.edu.sg*
[c]*qing.wang@nus.edu.sg*

ABSTRACT

Very recently, redox flow lithium-ion battery (RFLB) has emerged as a new electrochemical energy storage solution with great advantages over the conventional redox flow batteries and lithium-ion batteries. In RFLB the active electrode materials are reversibly delithiated/lithiated via redox targeting reactions without being attached to the current collector. The transport of electrons between the active material and current collector is mediated by the diffusion of redox shuttle molecules in the electrolyte. While $LiFePO_4$ have been successfully demonstrated in RFLB, so far there isn't report on the reversible chemical lithiation/delithiation of anodic materials. As a promising anodic material, anatase TiO_2 has drawn considerable attention and the electrochemical lithiation/delithiation of TiO_2 have been extensively investigated. In contrast, while chemical lithiation of TiO_2 by n- butyllithium has been reported by several groups, the reaction is irreversible and no chemical delithiation was reported. Here we report for the first time the reversible chemical lithiation/delithiation of TiO_2 and its application in RFLB. It was observed that anatase TiO_2 can reversibly be lithiated in the presence of bis(pentamethylcyclopentadienyl)cobalt (CoCp*2) in battery electrolyte and then be delithiated by cobaltocene (CoCp*2). The reactions can be described as follows:
xLi+ + TiO_2 + xCoCp*2 --> $LixTiO_2$ + xCoCp*2+
$LixTiO_2$ + xCoCp2+ --> xLi+ +TiO_2 + xCoCp2
The reversible Li+ insertion and extraction in the presence of the two redox mediators were confirmed by Raman, UV-vis, and XPS spectroscopic measurements. A redox flow lithium-ion battery was assembled based on CoCp*2, CoCp2 and TiO_2, and was tested galvanostatically. In a preliminary test, > 66% TiO_2 which was immersed in electrolyte away from the current collector, was reversibly charged/discharged through redox targeting reactions.

Keywords: Anatase TiO_2, Redox targeting, Redox flow, Lithium-ion batteries.

Proceedings of the 14th Asian Conference on Solid State Ionics (ACSSI 2014)

Application of Carbon Nanotube (CNT) Sheets as Current Collector of All-Solid-State Lithium Ion Batteries

Sunho Choi[a], Junghoon Kim[b], Chanhwi Park[c] and Dongwook Shin[d]
Hanyang University, Republic of Korea.
[a]*bdgjjang12@naver.com*
[b]*nayak84@naver.com*
[c]*howitzer86@hanmail.net*
[d]*dwshin@hanyang.ac.kr*

ABSTRACT

All-solid-state batteries using sulfide-based solid electrolytes have attracted attention in recent years due to their good safety and reliability. For constructing the all-solid-state battery system, composite cathodes should consist of active materials, solid electrolytes and conductive additives in order to intentionally create continuous lithium ion and electron conducting path. Additionally, physical contact using uniaxial cold pressing process should be established to maintain strong connection at the interfaces of composite cathode without binder. As a result, gaps and limited contact area between the composite cathode and current collector are formed owing to rough surface of the composite cathode, which results in poor performance of the cell. Usually, metal current collectors such as aluminum and copper foil are widely used for current collectors of commercial lithium ion batteries. However, it is difficult for the metal current collectors to adhere to the composite cathode without binder as well as fill the gaps on surface of the composite cathode due to rigid characteristic of the metals. In comparison with the metals, the CNT is one of the promising candidates for current collector because of excellent electrical and mechanical properties of the CNT. The CNT bundles were entangled into a continuous and robust three-dimensional network in carbon-based current collectors such as CNT sheets. The CNT sheets with such properties have been considered to help to increase the adhesion and contact area between the composite cathode and CNT sheets as current collector. In this study, the binder-free CNT sheets were prepared by simply ultrasonication and deposition for the current collector of the all-solid-state battery. The effects of the CNT sheets current collector will be discussed.

Proceedings of the 14th Asian Conference on Solid State Ionics (ACSSI 2014)

The 4th Missing Passive Circuit Element - A Memristor

S. R. S. Prabaharan
VIT University, India.
prabaharan.srs@vit.ac.in

ABSTRACT

The electrical switching arises from the coupled motions of electrons and ions within the oxide material, as one of the first recognized examples of a Memristor (memory-resistor) device, the fourth missing fundamental passive circuit element originally predicted by Chua in 1971 [1] and the first practical realization of the Memristor, in TiO_2, was reported in 2008 [2] by HP labs. Oxygen vacancy ordering is a prime cause for such correlation between high resistive and low resistive switching leading to data write and read respectively. In such memristive devices, the role of defects in the resistance-switching, in particular oxygen vacancy diffusion effects describing the transition between the high anf low resistive state has recently been a topic of great technological interest amongst various industries and academia. In this presentatation, the author explain the electroforming mechanism for a bipolar metal/oxide/metal switch by the aid of O_{2-} species responsible for the irreversible change, the behvaiour under bipolar forming voltages, and the relation to subsequent electrical switching correlating the write/read operation. A typical example of device fabrication and the understanding of various defects models supporting this phenomenon will be the highlight of the talk.

Keywords: Oxide ion conductors, Ionic defects, Resistive switching, Solids State Memories, Memristors ReRAM.

Proceedings of the 14th Asian Conference on Solid State Ionics (ACSSI 2014)

The Transformation of Conformers: A New Type of Solid-Solid Phase Transition

Liyu Jin[1,a], Haijin Zhu[2,d], Kate Nairn[1,b], Jiaye Li[1,c], Jenny Pringle[2,e], Patrick Howlett[2,f] and Maria Forsyth[2,g]
[1]*Monash University, Australia.*
[a]*liyu.jin@monash.edu*
[b]*katherine.nairn@monash.edu*
[c]*jiaye.li@monash.edu*
[2]*Deakin University, Australia.*
[d]*h.zhu@deakin.edu.au*
[e]*j.pringle@deakin.edu.au*
[f]*patrick.howlett@deakin.edu.au*
[g]*maria.forsyth@deakin.edu.au*

ABSTRACT

Organic ionic plastic crystals (OIPCs) is a unique type of ionic conductor which have been increasingly appealing to researchers for development of safe and effective electrolytes over the last two decades. Like ionic liquids, OIPCs also have negligible vapor pressure and are not flammability. However, unlike structureless ionic liquids, the ions within OIPCs form a lattice with long-range ordered lattice structure, while embodying certain degrees of short-range freedom which show rotational or orientational motions of the ions. It is these short-range motions that facilitate plastic deformation in OIPCs. More importantly, the motions also enhance the ions mobility thus increase the ionic conductivity. In this work, we are trying to understand the origin of an unusual OIPC solid-solid phase transition discovered in a recently synthesized OIPC, P1222FSI (triethylmethylphosphonium bis(fluorosulfonyl)imide). The phase transition is observed on the differential scanning calorimetry (DSC) as a plateau (the profile resembles an inverted glass transition) extending from -50°C to -30°C and is also highly reversible and consistent upon cooling and heating DSC cycles with different rates; this suggests it is thermodynamic in nature. 19F solid-state NMR spectra show distinct evolution of chemical shift anisotropy (CSA) over the transition temperature range. Raman spectra show variations in the peaks associated with P-C bonds of the P1222 cation and the cis and trans conformers of the FSI anion. Our results to date imply that the unusual phase transition may originated with the transformation of the anion from the trans conformers to cis conformers. This study therefore identify a new type of solid-solid phase transition, which we characterized with DSC, NMR and Raman. The origin of this unusual phase transition will be discussed.

Keywords: Unusual phase transition, Organic ionic plastic crystal, Solid electrolyte, Solid state NMR, Raman spectroscopy, Differential scanning calorimetry.

Author Index

Abhilash, K. P. 548
Acharya, S. A. 205, 215, 631, 677
Acharya, Smita 724, 738
Adams, S. 25, 127, 316, 355, 327, 391, 578, 595, 737, 743
Agrawal, S. L. 72, 569
Ahmed, Kalid 708
Amarasinghe, K. V. L. 32, 187, 528
Amaraweera, Gayani 730
Amaraweera, T. H. N. G. 270
Aniya, Masaru 93, 142, 225
Arai, Hajime 718
Araichimani, Arun 401, 408, 446, 467, 477, 560
Arof, A. K. 177
Arun, A. 436
Atsuo Yamada 3
Attanayaka, A. N. B. 270
Auckett, Chris Ling Josie 747
Aziz, M. F. 177

Badot, Jean Claude 708
Bahadur, S. Asath 63
Balasooriya, N. W. B. 270
Bandara, L. R. A. K. 187, 528
Barpanda, Prabeer 754
Beom, Jinhyung 719
Bhuvaneswari, R. 477
Biswas, Koushik 733
Boisse, Benoit Mortemard de 753
Buraidah, M. H. 177
Burke, Nick 288

Careem, M. A. 177
Carlier, Dany 753
Chakrabarti, Shamik 733
Chandrashekaran, Nithya 709
Chatterjee, Ratnamala 746
Chauhan, Jagdish Kumar 722
Chen, Fangfang 703
Chen, Liquan 714
Chen, Luo 259
Chen, M. H. 25
Chen, Wen 103, 118, 288
Cheruku, Rajesh 736
Chi, Xiaowei 642, 725
Chiang, Ken 288
Chidambaram, T. 560
Cho, Dong Chun 719
Cho, Dong-Chun 726
Cho, Jaephil 695, 748
Choi, Jang Wook 711
Choi, Sunho 756
Chowdari, B. V. R. 259, 297, 316, 343, 355, 701, 737
Chowdhury, Mohammed Tareque 150
Chung, Sai-Cheong 754
Coskun, Ali 711

Dabas, Prashant 720
Dang, Duc Vuong 744
Danilkin, Sergey 747
Darriet, Jacques 753
Delmas, Claude 753
Deswita 41
Devi, S. Siva 512
Didier, Christophe 753
Dissanayake, M. A. K. L. 32, 53, 187, 270, 528, 730, 735
Divaratne, H. K. D. W. M. N. R. 32, 735
Dong, Zhanmin 253
Dorai, Arunkumar 235
Dubrunfaut, Seid Olivier 708

Ekanayaka, E. M. T. K. 187
Ekanayake, P. M. P. C. 735
Elizabetha, Indu 712
Evangelin, N. Rubiya 467

Forsyth, Maria 703, 707, 721, 758
Fujimoto, Daichi 587
Fukuda, Katsutoshi 718

Gaikwad, V. M. 205, 215
Gao, Hiroki Moriwake Xiang 705
Genova, F. Kingslin Mary 512
Gopakumar, S. 709, 712
Govindan, K. 538, 560
Govindaraj, G. 667, 727, 736
Gu, Lin 714
Gu, Wenyi 578, 743
Guignard, Marie 753
Gunzelmann, Daniel 707
Guo, Jing 111
Guo, Yu- Guo 698
Gupta, Ashish 740
Gupta, Prem 742
Gupta, Ravindra Kumar 197
Gurunarayanan, Vinithra 401, 408

Hadip, Fitrah 488, 495, 503
Hameed, A. Shahul 701
Han, Chan Chin 488
Han, Jinduo 642, 725

Handal, Hala T. 619
Hanxing, Liu 365, 713
Haomin, Chen 595
Hariharan, K 720, 710
Haruhitosadakuni 93
Hassan, H. C. 177
Hellar, Nithya 235
Hema, M. 456
Hien, Dang Thu 737
Hing, Peter 723, 749, 751
Ho, Lim Ji 316
Hong, Sungbo 734
Honggowiranto, Wagiyo 163, 335
Howlett, Patrick 758
Huang, Qizhao 731, 755
Huang, Shengnan 118

Ibrahim, Ruhani 488, 522
Ikeda, Masahiro 142, 225
Ikuhara, Yuichi 705
Imanishi, Nobuyuki 752
Ishigaki, Toru 41
Islam, Saiful 705
Ismail, Ismariza 651
Itabashi, Haruka 587
Iwai, Yoshiki 150

Jahja, Aziz Khan 163, 335
Jain, Amrita 739, 740
Jani, Abdul Mutalib Md 651
Jennings, James 731
Jeong, You Kyeong 711
Jiang, Shanshan 118
Jin, Jun 381, 699
Jin, Liyu 758
Jo, Jung-Mo 728
Jodi, Heri 163
Joshi, Shradha 724, 738
Jung, Andrew 751
Jung, Jae Il 748

Kamaluddin, Norashima 488, 522
Kamiyama, Takashi 41
Kan, Wang Hay 619
Kang, Byoungwoo 715
Kannan, B. Rajesh 135
Karthikeyan, C. 512
Karthikeyan, M 741
Karthikeyan, S. 417, 436, 446, 456, 467, 477
Kartini, Evvy 41, 163, 335
Kawamura, J. 63, 150, 235, 587, 696
Kearley, Gordon J 747
Kim, Gye-Rok 726, 728
Kim, Jaekook 698, 719
Kim, Jee Hoon 719, 726
Kim, Junghoon 697, 734, 756
Kim, Minjeong 697, 734
Kim, Sooseok 719
Kim, Young-Hun quad 726
Kohama, Keiichi 705
Koyama, Yukinori 718
Kudo, Shota 696
Kulshrestha, Niharika 742
Kumar, Manindra 722
Kumar, N S. Krishna 727
Kumar, P. Senthil 13, 538
Kumari, J. M. K. W. 187
Kumhar, R. P. 72
Kuwabara, Craig Fisher Akihide 705
Kuwata, Naoaki 150, 235, 587, 696
Kwon, Tae-Woo 711

Latif, Famiza Abd 495, 488, 503, 522
Lee, Jong Sook 698, 719, 726, 728, 744
Lee, Yun Hong 391
Legrain, Fleur 85, 732
Lestriez, Bernard 708
Li, Hong 714
Li, Jiaye 758
Li, Junshen 288
Li, Yang 103
Li, Zhaolong 118
Ling, Chris D. 754
Linh, Tran Thuy 737
Liu, Heng 642
Liu, Yu 111, 307, 725
Liu, Yueli 103
Lu, Yan 278
Lyu, Yinchun 714

Ma, Guoqiang 381, 642, 699
Malyi, Oleksandr 85, 732
Mandal, B. P. 244
Mani, G. 417
Manoharan, Sindhuja 401, 408, 446, 467
Manzhos, Sergei 85, 374, 732
Maohua, Chen 127
Mardiyanto 335
Marka, Sandeep Kumar 259, 297
Mathavan, T. 467
Mathur, R B 712
Matsuda, Daichi Fujimoto Yasutaka 696
Matsuda, Yasutaka 587
Mellander, B. -E. 270, 730
Ming, Lim Chee 723, 749, 751
Mirfakhraei, Behzad 619
Mohd, Yusairie 522
Mouri, Fuminori 661
Muda, Kamariah Bt 495, 503
Murugan, R. 343, 717

Nairn, Kate 758
Nalini, B. 548
Nam, Rui Wang Kyung Wan 714
Nelson, P. Issac 538
Nguyen, Dang-Thanh 744
Nishimura, Shin-Ichi 754
Nithya, S. 417
Noh, Sungwoo 697

O'Dell, Luke 707
Ogumi, Zempachi 718
Okada, Yohei 142
Oki, Hideki 705
Orikasa, Yuki 718
Osman, Nafisah 651
Oyama, Gosuke 754
Oza, Yogita 707

Pan, Feng 755

Pandey, Namita 745
Pandi, D. Vinoth 401, 408, 417, 425, 436, 446, 456, 467, 477
Park, Chanhwi 756
Peng, Peng 307, 381, 725
Petnikota, Shaikshavali 259, 297
Pope, Cameron 707
Prabaharan, S. R. S. 63, 757
Prabeer Barpanda 3
Prabhu, Ramesh 741
Prabu, M. 13, 538
Pringle, Jenny 758
Putra, Teguh Yulius Surya Panca 41

Qi, Toh Wei 355
Qi, Yanyuan 103
Qian, Chen Ying 374
Quan, Chu Yao 316
Quazi, T. 685

Radha, K. P. 456
Rai, Neelesh 72, 569
Rajeswari, N. 63
Ramakrishna, S. 343, 717
Rana, Usman 721
Rani, Mohd Azri Ab 522
Rao, R. Prasada 25, 127, 327, 595
Ravikumar, Raman 709
Rayavarapu, Prasada Rao 743
Reddy, Boddu Venkata Rami 709
Reddy, M. V. 13, 25, 259, 297, 316, 343, 355, 391, 538, 701, 737
Rhee, Hee-Woo 197
Romanenko, Konstantin 707
Rui, Kun 278

Safanama, D. 25, 327
Sahara 142
Sakunthala, A. 13, 538
Sanjeeviraja, C. 417, 425, 456, 477
Sarangika, H. N. M. 32, 735
Sayyed, S. K. 677
Sekine, Kyouichi 661
Selvakumar, K 741
Selvasekarapandian, S. 63, 401, 408, 417, 425, 436, 446, 456, 467, 477, 512, 560
Selvin, P. Christopher 548
Senadeera, G. K. R. 32, 735
Senavirathne, V. A. 32, 187, 528
Seo, Hyun-Ho 728
Setssoafia, Daniel Dodzi 751
Sha, Wu 365
Shao, Zongping 750
Sharma, A. L. 704
Sharma, Neeraj 706
Shen, Chen 278
Shin, Dongwook 697, 734, 756
Shin, Eui-Chol 698, 719, 726, 728, 744
Shukla, Archana 746
Shukla, Namrata 746
Sikkanthar, S. 417
Sindhuja, S. 436
Singh, Bhanu. P. 712
Singh, Kalpana 619
Singh, Kamal 685
Somasundaram, K. 548
Soudan, Patrick 708
Srikanth, Vadali V. S. S. 259, 297
Srivastava, Neelam 722
Su, Jing 698
Sudaryanto 606
Suklueng, Montri 723, 749
Sun, Jia-Lin 253
Supardi 163

Takada, Kazunori 700
Takamura, Tsutomu 661
Takekawa, Reiji 150, 235
Teo, Keefe Wayne 259, 316
Thakur, Awalendra K 702, 704, 733, 745, 746
Thangadurai, Venkataraman 619, 716
Thotawaththage, C. A. 187, 735
Torii, Shuki 41
Tripathi, S. K. 739, 740
Tyagi, A. K. 244

Uchimoto, Yoshiharu 718
Uyama, Takashi 718
Uyen, Nguyen Ngoc Minh 355

Vasundhara, K. 244
Veeramanikandan, C. 401, 408
Venkataraman, B. Harihara 135
Vijaya, N. 425, 436, 446, 467, 477, 512
Vittal, J. J. 701
Voo, Nyuk Yoong 723, 749

Wahyudianingsih 163
Wang, Chien-Chia 729
Wang, Qing 731, 755
Wang, Qingsong 381
Wang, Wei 750
Weerasekera, W. A. R. B. 32
Wei, Jinquan 253
Wen, Zhaoyin 111, 278, 307, 381, 642, 699, 725
Wenji, Li 713
Wijayasinghe, Athula 730
Wijayasinghe, H. W. M. A. C. 270
Wu, Meifen 111
Wu, Xiangwei 699
Wu, Y. Z. 343

Xiao, Ruijuan 714

Yadav, Madhavi 722
Yamada, Atsuo 754
Yamaguchi, Shu 719
Yamashita, Yasunobu 3
Yang, Keedeok 719
Yang, Xiao- Qing 714
Yang, Xue 103
Yang, Yunxia 288
Yonemura, Masao 41
Yoon, Youngkoo 719
Yow, Zhen Feng 578
Yu, Ji Haeng 728
Yu, Xiqian 714
Yue, Wu Xiao 355
Yulianti, Evi 606

Zakharova, Galina S. 118
Zamri, Sharil Fadli Mohamad 488, 522

Zhang, Guowei 253
Zhang, Jingchao 642, 725
Zhao, Chunxia 118, 288
Zheng, Shijian 705
Zhenning, Zheng 713
Zhiyong, Yu 365, 713
Zhu, Haijin 707, 721, 758
Zhu, Jia-Lin 253
Zhu, Quanyao 118

Editors: S. Adams • J. Kawamura

ISBN 978-981-09-1137-9

www.rpsonline.com.sg